Biological and Medical Physics, Biomedical Engineering

Eugenijus Kaniusas

Biomedical Signals and Sensors III

Linking Electric Biosignals and Biomedical Sensors

Springer

Biological and Medical Physics, Biomedical Engineering

BIOLOGICAL AND MEDICAL PHYSICS, BIOMEDICAL ENGINEERING

This series is intended to be comprehensive, covering a broad range of topics important to the study of the physical, chemical and biological sciences. Its goal is to provide scientists and engineers with textbooks, monographs, and reference works to address the growing need for information. The fields of biological and medical physics and biomedical engineering are broad, multidisciplinary and dynamic. They lie at the crossroads of frontier research in physics, biology, chemistry, and medicine.

Books in the series emphasize established and emergent areas of science including molecular, membrane, and mathematical biophysics; photosynthetic energy harvesting and conversion; information processing; physical principles of genetics; sensory communications; automata networks, neural networks, and cellular automata. Equally important is coverage of applied aspects of biological and medical physics and biomedical engineering such as molecular electronic components and devices, biosensors, medicine, imaging, physical principles of renewable energy production, advanced prostheses, and environmental control and engineering.

Editor-in-Chief:
Bernard S. Gerstman, Department of Physics, Florida International University, Miami, FL, USA

Series Editors:
Masuo Aizawa, Tokyo Institute Technology, Tokyo, Japan

Robert H. Austin, Princeton, NJ, USA

James Barber, Wolfson Laboratories, Imperial College of Science Technology, London, UK

Howard C. Berg, Cambridge, MA, USA

Robert Callender, Department of Biochemistry, Albert Einstein College of Medicine, Bronx, NY, USA

George Feher, Department of Physics, University of California, San Diego, La Jolla, CA, USA

Hans Frauenfelder, Los Alamos, NM, USA

Ivar Giaever, Rensselaer Polytechnic Institute, Troy, NY, USA

Pierre Joliot, Institute de Biologie Physico-Chimique, Fondation Edmond de Rothschild, Paris, France

Lajos Keszthelyi, Biological Research Center, Hungarian Academy of Sciences, Szeged, Hungary

Paul W. King, Biosciences Center and Photobiology, National Renewable Energy Laboratory, Lakewood, CO, USA

Gianluca Lazzi, University of Utah, Salt Lake City, UT, USA

Aaron Lewis, Department of Applied Physics, Hebrew University, Jerusalem, Israel

Stuart M. Lindsay, Department of Physics and Astronomy, Arizona State University, Tempe, AZ, USA

Xiang Yang Liu, Department of Physics, Faculty of Sciences, National University of Singapore, Singapore, Singapore

David Mauzerall, Rockefeller University, New York, NY, USA

Eugenie V. Mielczarek, Department of Physics and Astronomy, George Mason University, Fairfax, USA

Markolf Niemz, Medical Faculty Mannheim, University of Heidelberg, Mannheim, Germany

V. Adrian Parsegian, Physical Science Laboratory, National Institutes of Health, Bethesda, MD, USA

Linda S. Powers, University of Arizona, Tucson, AZ, USA

Earl W. Prohofsky, Department of Physics, Purdue University, West Lafayette, IN, USA

Tatiana K. Rostovtseva, NICHD, National Institutes of Health, Bethesda, MD, USA

Andrew Rubin, Department of Biophysics, Moscow State University, Moscow, Russia

Michael Seibert, National Renewable Energy Laboratory, Golden, CO, USA

Nongjian Tao, Biodesign Center for Bioelectronics, Arizona State University, Tempe, AZ, USA

David Thomas, Department of Biochemistry, University of Minnesota Medical School, Minneapolis, MN, USA

More information about this series at http://www.springer.com/series/3740

Eugenijus Kaniusas

Biomedical Signals and Sensors III

Linking Electric Biosignals and Biomedical Sensors

Springer

Ao. Univ. Prof. Dipl.-Ing. Dr. techn. habil. Eugenijus Kaniusas
Head of Research Unit Biomedical Electronics
Head of Research Group Biomedical Sensing
Chairman of Study Commission Biomedical Engineering
Vienna University of Technology
Institute of Electrodynamics, Microwave and Circuit Engineering
Gusshausstrasse 27–29/E354
1040 Vienna
Austria
e-mail: kaniusas@tuwien.ac.at

ISSN 1618-7210 ISSN 2197-5647 (electronic)
Biological and Medical Physics, Biomedical Engineering
ISBN 978-3-319-74916-7 ISBN 978-3-319-74917-4 (eBook)
https://doi.org/10.1007/978-3-319-74917-4

Library of Congress Control Number: 2018960730

© Springer Nature Switzerland AG 2019
This work is subject to copyright. All rights are reserved by the Publisher, whether the whole or part of the material is concerned, specifically the rights of translation, reprinting, reuse of illustrations, recitation, broadcasting, reproduction on microfilms or in any other physical way, and transmission or information storage and retrieval, electronic adaptation, computer software, or by similar or dissimilar methodology now known or hereafter developed.
The use of general descriptive names, registered names, trademarks, service marks, etc. in this publication does not imply, even in the absence of a specific statement, that such names are exempt from the relevant protective laws and regulations and therefore free for general use.
The publisher, the authors and the editors are safe to assume that the advice and information in this book are believed to be true and accurate at the date of publication. Neither the publisher nor the authors or the editors give a warranty, expressed or implied, with respect to the material contained herein or for any errors or omissions that may have been made. The publisher remains neutral with regard to jurisdictional claims in published maps and institutional affiliations.

This Springer imprint is published by the registered company Springer Nature Switzerland AG
The registered company address is: Gewerbestrasse 11, 6330 Cham, Switzerland

Preface

This is the *third volume* in my series on "Biomedical Signals and Sensors" developing a bridge between physiology and theranostic human engineering. The *first volume* focuses on the interface between physiological mechanisms and the resultant biosignals that are commonplace in clinical practice. The physiologic mechanisms determining biosignals are described from the cellular level up to the mutual coordination at the organ level. In turn, the *second volume* considers acoustic and optic biosignals with the associated sensors. The formation path of acoustic and optic biosignals is considered on the physiological level, followed by their propagation within the body and coupling into the sensing device. The text follows biosignals on their academic journey from the source to the sensor.

This *third volume* bridges electric biosignals and biomedical sensors from a strategic point of view. The reader learns how electric, magnetic, and electromagnetic fields occur within the body, propagate through and interact with biological tissues, become shaped by homogeneous tissues and boundaries in-between, provoke neuromuscular stimulation and thermal effects, and finally pass the tissue-to-electrode boundary to be recorded. The *biosignal formation path* within the body is described in great depth, followed by the *biosignal sensing path*.

The book series emphasizes the common features of *acoustic*, *optic*, and *electric biosignals*, which are ostensibly entirely different in terms of their physical nature. Heterogeneous signals are discussed within a *common frame* from their formation within biological body up to their sensing by external devices outside the body. While crossing boundaries of different disciplines, such strategic approach mines knowledge of great value.

Electric biosignals and biomedical sensors pose a true *challenge* due to their highly interdisciplinary nature. However, the book helps in managing the challenge while presenting the basics of electrical engineering, physics, chemistry, biology, and physiology that are strategically necessary to understand and work with biosignals and sensors. *Applied basics* are covered at reasonable ease with numerous examples and great attention to detail, as reflected by the large number of footnotes with substantial insights. These academic basics should remain strong because these stand the test of time. It is a rewarding challenge giving the reader the

power to answer intriguing "Aha!" questions and bounding the own advancement to accelerate.

This book is directed primarily at graduate and postgraduate students in biomedical engineering. It is also accessible to those who are interested in physical, engineering, and life sciences, since the expected background knowledge is minimal and many fundamental phenomena are explained. The book should serve engineers and practitioners alike who have an interest in biomedical engineering since all examples are taken from real-world applications and research projects. The book is intended to provide a nice sequel into the effective and in-depth learning as well as into the basic research.

Discussed biosignals and sensing technologies substantiate nascent *wearable technologies*—the hot topic today—which comprise an appealing solution for pervasive monitoring and prompt novel approaches in diagnosis and therapy. These mobile developments have taken giant strides in recent years and truly resonate with the needs of society.

It is important to note that this book was significantly inspired by my *lectures* "Biomedical Sensors and Signals", "Biomedical Instrumentation", and "Biophysics" which constitute a significant part of a master's degree programme "Biomedical Engineering" at the Vienna University of Technology in Austria.

In the end, it is not the spot-like knowledge of diverse biosignals and engineering technologies coming from independent considerations that constitute a successful biomedical engineer with profound professional knowledge, but the *strategic and global expertise* in the genesis of heterogeneous biosignals and of the corresponding sensing technologies.

Vienna, Austria Eugenijus Kaniusas

Acknowledgements

My understanding and appreciation of biomedical issues have been boosted by permanent collaborative research and numerous interdisciplinary studies on national and international level. Years of experience as chairman of the study commission Biomedical Engineering at the Vienna University of Technology (VUT) taught me systematics in biomedicine and cross-topic competence, as reflected by the strategic structure of the present volume despite its profound heterogeneity and interdisciplinary.

This volume of more than 600 pages has claimed extraordinary mental and physical efforts over many years, not only from me but also from my cooperative colleagues and numerous diligent students of mine. I wish to express my sincere thanks and appreciation to Univ. Prof. Adalbert Prechtl from the Institute of Electrodynamics, Microwave and Circuit Engineering (EMCE), VUT, for instructive discussions on electrodynamics and proofreading, and to Dr. Karl Futschik from the EMCE for the support in the field of bioimpedance. I am grateful for numerical modelling of electric fields and careful proofreading by Dipl.-Ing. Stefan Kampusch from the EMCE.

I greatly acknowledge Univ. Prof. Frank Rattay from the Institute of Analysis and Scientific Computing (ASC), VUT, for his unlimited support in neuronal modelling. Special thanks go to Dipl.-Ing. Andreas Fellner, ASC, for numerical modelling of neuronal excitation. I would like to place on record my gratitude to Rene Hirtl, M.Sc., from the division Electromagnetic Compatibility and Optics, Seibersdorf Labor GmbH, for numerical modelling of electric and magnetic fields in different biological media. Cordial thanks go to Dipl.-Ing. Florian Thürk, Dipl.-Ing. Konstanze Krommer, and Mag. Vaiva Siauciunaite from the EMCE for careful proofreading. Special thanks go to Dipl.-Ing. Daniel Von-Chamier-Glisczinski from the Institute of Art and Design, VUT, who prepared the ball pen drawing prefacing this book volume.

I would like to express my deep gratitude to my family for the solid emotional background, especially to my daughter Ula and son Rokas. They have been given me the necessary time and strength while they have had to bear the loss of my time and effort at home.

Respectfully, I give my sincere thanks to all of them!

Contents

1 Sensing by Electric Biosignals—An Introduction 1
References 7

2 Formation of Electric Biosignals 9
2.1 Permanent Biosignals 10
2.2 Induced Biosignals 19
2.3 Transmission of Electric Signals 28
2.3.1 Propagation of Electric Signals 28
2.3.1.1 Lossless Medium 36
2.3.1.2 Lossy Medium 42
2.3.2 Effects on Electric Signals 49
2.3.2.1 Volume Effects 50
General Issues 50
Electric and Magnetic Fields 50
Current Density and Current 52
Electric Field and Voltage 54
Electrical Impedance 57
Simple Tissue Model 60
Electrical Properties of Biological Tissue 70
Mutual Field Coupling
and Quasi-electrostatic Situation 74
Incident Electric Fields 75
Conductive Phenomena 75
Polarization Phenomena 87
Conductive Versus Polarization Behaviour 96
Relaxation and Dispersion Effects on
Conductivity and Polarization 100
Alpha Dispersion 103
Beta Dispersion 111
Gamma Dispersion 117

Ionic and Displacement Dispersion 122
Dispersion Model Versus Experiment 124
Charge and Current Induction 133
Incident Magnetic Fields 150
Incident Electromagnetic Fields 162
2.3.2.2 Inhomogeneity Effects 170
Boundary Conditions 172
Conductive Phenomena 175
Dielectric Phenomena 180
Conductive and Dielectric Phenomena 183
Biological Boundaries 186
Diffraction 195
Reflection and Refraction 201
2.3.2.3 Volume and Inhomogeneity Effects—A Quantitative Approach 218
Incindent Electric Field 220
Incident Contact Current 234
Incident Magnetic Field 237
2.3.2.4 Physiological Effects 240
Electrical Stimulation Effects 243
Current Density Versus Electric Field 251
Nerve Activation 254
Single Cell Excitation 254
Natural, Intracellular, and Extracellular Stimulation 259
Activating Function 263
Charge Transfer During Stimulation 274
Stimulation Pattern 279
Single Monophasic Stimulus 279
Single Biphasic Stimulus 284
Periodic Stimulus 289
Strength-Duration Curve 297
Cathodic and Anodic Stimulation 309
Cathodic Block and Stimulation Upper Threshold 314
Current-Distance Relationship 317
Numerical Simulation—A Quantitative Approach 321
Axon Thickness and Its Distance to Electrode 328
Monopolar, Bipolar, and Tripolar Modes 331
Direct Current 336
Thermal Stimulation Effects 340

2.3.2.5 Adverse Health Effects and Exposure Limits 352
Basic Restrictions Versus Reference Levels 354
Contact Current 362
Cardiac Interference 373
Electric and Magnetic Field 378
Curent Density Field 383
Power Measures 387
Neural Stimulation 388
Subjective Versus Objective Stimulus 394
References 395

3 Sensing and Coupling of Electric Biosignals 399
3.1 Electrodes 401
3.1.1 Tissue, Skin, and Electrode Effects 405
3.1.1.1 Tissue Impedance 406
3.1.1.2 Skin Impedance 407
3.1.1.3 Electrode Polarization and Impedance 411
Metal Ion Electrode and Its Double Layer 413
Electrical Double Layer 421
Specific Adsorption 425
Water Relevance 429
Mass Transfer 431
Electric Potential and Debye Length 432
Half-Cell Voltage 436
Redox Electrode and Its Double Layer 439
Reference Ag/AgCl Electrode 442
Active Current or Voltage Application Between Electrodes 445
Charge Transfer and Activation Overvoltage 451
Diffusion and Diffusion Overvoltage 457
Coupled Reactions and Reaction Overvoltage 461
Dynamics of Electro-Kinetic Processes 462
Polarization of the Electrode/Tissue Boundary 463
Direct Voltage Application 468
Alternating Voltage Application 473
High Field Frequency 475
Low Field Frequency 476
Medium Field Frequency 477
Ag/AgCl and Pt Electrodes 490
Ag/AgCl Electrodes 490
Pt Electrodes 491
Recording Versus Stimulation 495

Electrode Impedance Model 496
Polarizable Electrode 502
Non-polarizable Electrode 504
Polarizable Versus Non-polarizable Electrodes 506
Experimental Issues 507
Measurement of Tissue Impedance 507
Tissue Conductivity/Cell Concentration 510
Movement Artefacts 511
Charge and Discharge of Monitoring Electrodes 513
3.1.1.4 Whole-Body Impedance 514
3.1.2 Signal Coupling in Diagnosis and Therapy 519
3.1.2.1 Diagnosis 519
3.1.2.2 Therapy 521
3.1.2.3 Non-contact Diagnosis 524
3.2 Biosignal and Interference Coupling 524
3.2.1 Capacitive Coupling of Interference 525
3.2.2 Inductive Coupling of Interference 529
3.2.3 Biosignal Coupling—Voltage Divider 531
3.2.4 Common-Mode Interference 532
3.2.5 Differential-Mode Interference 536
3.2.6 Inner Body Resistance 537
3.2.7 Electrode Area 539
3.2.8 Countermeasures Against Interference 539
3.2.8.1 Shielding 540
3.2.8.2 Driven-Right-Leg Circuit 541
3.2.8.3 Notch Filter 542
3.2.8.4 Preamplifier 542
3.2.9 Triboelectricity 543
3.3 Body Area Networks 547
References 549

Index 551

Symbols and Abbreviations

Note Variables used within limited contexts are not listed, for they are described within the relevant section.

a_{Me}	Activity of (metal) ions or species
A	Area
B	Magnetic flux density
c	Constant, specific heat capacity, (molar) concentration
c_{Me}	Concentration of (metal) ions
C	Capacitance
C''	Area-related capacitance
$CMRR$	Common-mode rejection ratio
d	Membrane thickness, distance, size, thickness
D	Axon diameter, electric flux density (electric displacement field)
D_{F}	Diffusion coefficient
e, e	Elementary charge, unit vector
E	Electric field
E_{I}	Incident electric field
E_{R}	Reflected electric field
f	(Oscillating, resonating) frequency
f_{C}	Heart rate
f_{Me}	Activity coefficient of (metal) ions
f_{r}	Relaxation frequency
f_{R}	Respiratory rate
F	Faraday's constant, force
G	Transfer function, electrical conductance
G''	Area-related electrical conductance
HCF	Heart current factor
i	Electric current, index
i_{AC}	Alternating current
i_{C}	(Capacitive) displacement current
i_{DC}	Direct current

i_E	(Electric, ionic) conductive current
I	(Complex) electric current amplitude, intensity of sensation
j_C	(Capacitive) displacement current density
j_E	(Electric, ionic) conductive current density
J	Current density amplitude
J_C	(Capacitive) displacement current density amplitude
J_E	(Electric, ionic) conductive current density amplitude
k	Index, wavenumber, Boltzmann constant
l	length, height, size
L	Inductance
m	Mass, ionic mobility
M	Torque
Me	Metal ion
n	Constant, turns ratio
N_A	Avogadro constant
p	Electric dipole moment
P	Power, electric polarization density field
P_{SAR}	Specific energy absorption rate
Q	Electric charge
r	Radius, distance, (ion) radius
R	Electrical resistance, gas constant
s	Biosignal
S	Substance
S	Power density
SNR	Signal-to-noise ratio
t	Time
T	Absolute temperature, time period
TEM	Transverse electromagnetic wave
u	Electric voltage, object velocity
U	(Complex) voltage amplitude
U_h	Half-cell voltage (or standard reduction potential)
U_{pol}	Polarization voltage
U_R	Resting (membrane) voltage amplitude
v	Electromagnetic wave propagation velocity, nerve conduction (propagation) velocity, drift velocity
V	Volume
W	Energy
x	Coordinate, distance
X	Physical quantity
y	Coordinate
z	Valence, number of electrons
Z	(Complex) electrical impedance, (complex) wave impedance
Z_C	(Complex) capacitive impedance
Z_E	(Complex) conductive impedance
α	Electric field attenuation coefficient, constant

β	Phase angle
δ	Skin depth, Debye length, diffusion layer thickness
Θ	Degree of coverage
Γ	Reflection factor
ε	(Complex) dielectric permittivity, step function
ε_0	Free space permittivity
ε_∞	Dielectric permittivity above the dispersion region
ε'	Real part of complex dielectric permittivity
ε''	Imaginary part of complex dielectric permittivity
ε_r	Relative electric permittivity
ϑ	Temperature
λ	Wavelength
μ	Dynamic viscosity, magnetic permeability
μ_0	Free space permeability
μ_r	Relative magnetic permeability
ρ	Density
τ	Relaxation time constant, time constant
γ	Electrical conductivity
γ_{eff}	Effective electrical conductivity
γ_I	Electrical conductivity of the intracellular medium
φ	Angle, phase angle, electric potential
ω	Angular frequency

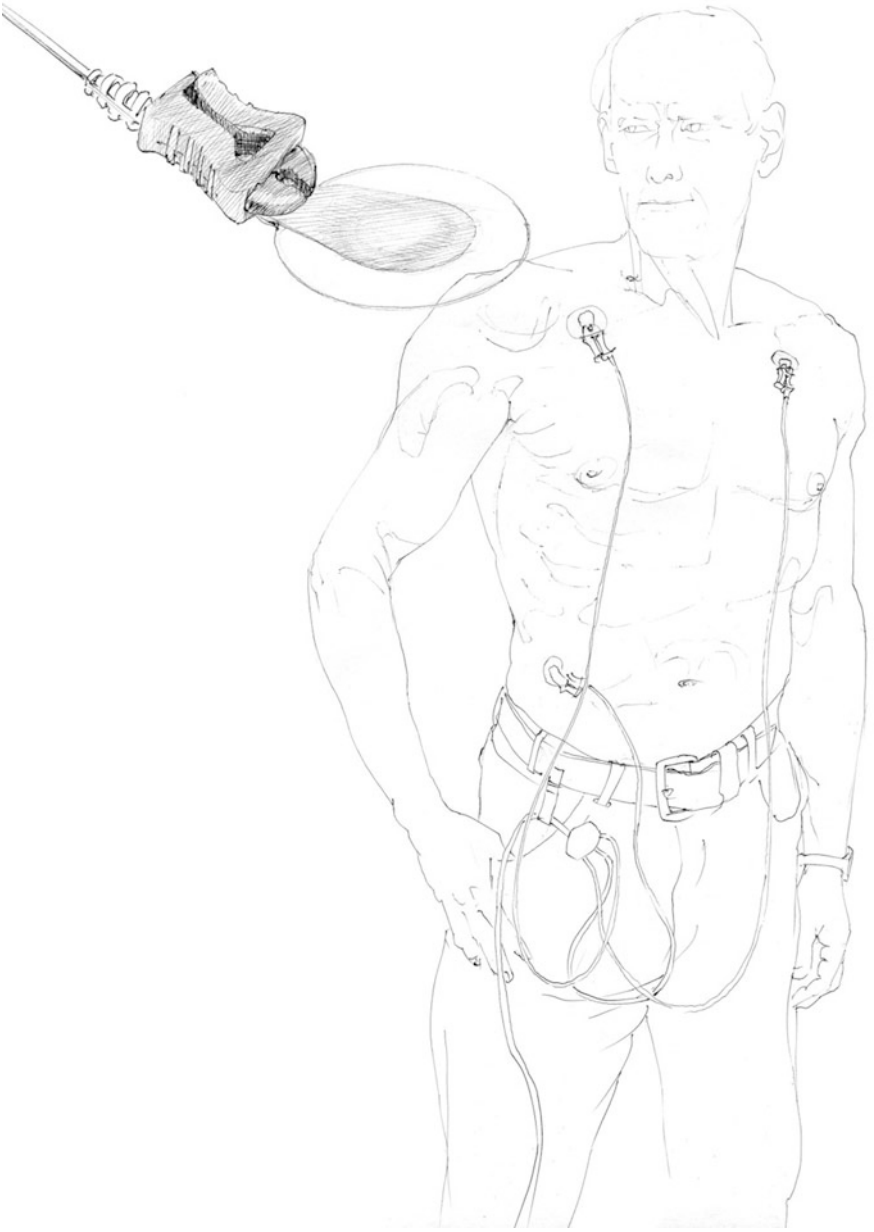

D. Chamier, unpublished ball pen drawing, Institute of Art and Design, Vienna University of Technology (2014)

Chapter 1
Sensing by Electric Biosignals—An Introduction

Abstract Biosignals facilitate an objective diagnosis of health status and provide an objective feedback for personalized therapy. A huge diversity of electric biosignals exists, including permanent and induced biosignals, which can be modelled with a simple electrical circuit. Multiple physiological parameters are usually extracted from a single electric biosignal that forms multiparametric monitoring.

The registration of electric biosignals is a timeless classic[1] in diagnosis for the assessment of cardiac, respiratory, or muscle status, among others. Biosignals facilitate an *objective diagnosis* of health status (Kaniusas 2012, Footnote 3) and provide an objective feedback for *personalized therapy* (Kaniusas 2012, Footnote 4), supporting individual selection of therapeutic measures and continuous monitoring of their impact (Kaniusas 2012, Fig. 1.4). Multiple physiological parameters can be usually attained from a single electric biosignal that allows *multiparametric monitoring* (Kaniusas 2012, Fig. 1.16).

A huge diversity of *electric biosignals* exists, including

- *permanent biosignals* being present without any artificial impact, with the biosignal source inside the body; and
- *induced biosignals* requiring an artificial stimulus, with the biosignal source outside the body;

compare the classification of biosignals from Kaniusas (2012, Fig. 1.15).

[1]Heinrich Müller (1820–1864) and Rudolph Albert von Kölliker (1817–1905), both German anatomists, were first in 1856 to demonstrate that each contraction of frog's ventricle produces an electric event (Geddes 2009). Etienne-Jules Marey (1830–1904), a French physiologist and cinematographer, and Gabriel Lippman (1845–1921), a French physicist, connected the electrodes from the frog's ventricle to the capillary electrometer and obtained an *integral of the first electrocardiogram*. Willem Einthoven (1860–1927), a Dutch physician, was the first to record an analog *non-integrated version of the electrocardiogram*, i.e., of the electrical activity of the heart by the use of string galvanometer.

© Springer Nature Switzerland AG 2019

E. Kaniusas, *Biomedical Signals and Sensors III*, Biological and Medical Physics, Biomedical Engineering, https://doi.org/10.1007/978-3-319-74917-4_1

Permanent Biosignals

Figure 1.1 demonstrates the basic principle of a *permanent electric biosignal* in terms of *electromyography*. Here an elongated single muscle fiber (or muscle cell) is locally excited while the excitation propagates from the left to the right. The excited region is spatially restricted, where *positive extracellular potentials* outside the membrane at its resting state (see the central region of the fiber at the time instance t_A in Fig. 1.1) are temporarily substituted by *negative extracellular potentials* during the local excitation (see the central region at the time t_C in Fig. 1.1). This is in line with basics of the excitation of a muscle fiber from Kaniusas (2012, Fig. 2.26).

If we assume *two electrodes* located in the extracellular space close to the cell membrane, it can be observed that the *voltage u* in-between is zero in both the resting and excited states (times t_A and t_C in Fig. 1.1). A non-zero *u* can only be expected when one of the electrodes resides in the excited region of the membrane and another in the non-excited region. The resulting course of *u* is depicted in Fig. 1.1b. We can conclude that the registered *biphasic waveform* of *u*—a

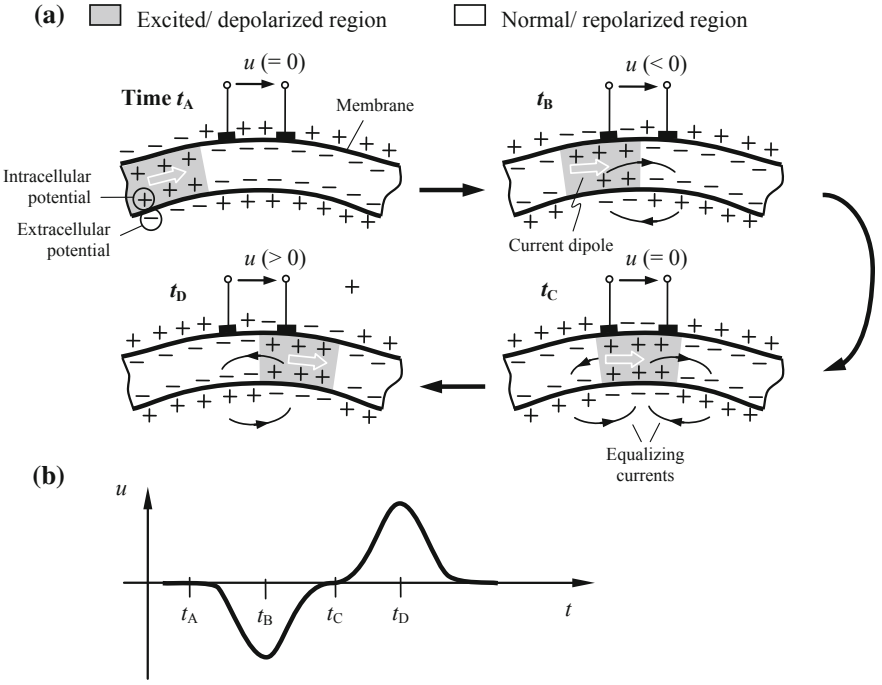

Fig. 1.1 Genesis of a permanent electric biosignal (electromyogram) with a single muscle fiber as the biosignal source. **a** Temporal and local depolarization of the muscle fiber propagating from the left to the right. **b** The corresponding voltage *u* measured on the membrane between two electrodes at the indicated time instants t_A, t_B, t_C, and t_D. The axial electrode distance is shorter than the axial expansion of the excitation region

permanent electric biosignal, known as *electromyogram*—conveys a differential picture of the *monophasic waveform* of a single action impulse propagating along the excitable fiber (Kaniusas 2012, Fig. 2.18b).

Please note that the *induced equalizing currents* outside and along the membrane (Kaniusas 2012, Fig. 2.18a) are absent or symmetric in the region between the two electrodes for $u = 0$ (see the times t_A and t_C in Fig. 1.1) and unsymmetric for $u \neq 0$ (times t_B and t_D in Fig. 1.1). For instance, the largest part of the extracellular equalizing current points to the left yielding $u < 0$ for the time t_B in Fig. 1.1b, whereas the largest extracellular current points to the right yielding $u > 0$ for the time t_D.

The formation of *permanent electric biosignals* up to their registration outside the body can be simplified as an *electrical circuit model*, satisfying (2.34)

$$\underline{I} = \frac{\underline{U}}{\underline{Z}_1 + \underline{Z}_2}. \tag{1.1}$$

As illustrated in Fig. 1.2a, we start with the *endogenous electric source* of a biosignal within the biological body (represented by the voltage source with its complex[2] amplitude $\underline{U}$). We go over the *lossy propagation* of generated biosignals throughout tissue and their simultaneous *modulation* by diverse physiological phenomena (propagation losses and modulation are represented by the complex electrical impedance $\underline{Z}_1$). As a certain portion of the generated biosignal leaves the body and thus is available for its registration above the body skin, we continue with the *coupling* of the endogenous biosignal into an external sensing device (coupling losses represented by the impedance $\underline{Z}_2$), e.g., via metal surface electrodes applied on the skin (compare Fig. 1.1). Lastly, the *conversion* of the endogenous biosignal into a registered electric signal is modelled (conversion losses as an additive part of $\underline{Z}_2$), preceding the *registration* of the permanent electric biosignal (modelled as ampere meter with the registered complex current amplitude $\underline{I}$).

Equation (1.1) highlights that the higher are the losses (proportional to the non-zero magnitudes $|\underline{Z}_1|$ and $|\underline{Z}_2|$), the weaker the registered electric biosignal (proportional to the magnitude $|\underline{I}|$) will be. Losses in *biological tissues* are mostly capacitive-ohmic, so that the inequality $-90° < \arg(\underline{Z}_1), \arg(\underline{Z}_2) < 0$ applies (Fig. 2.12).

To give another tangible *example* in terms of *electrocardiography*, the electric *source* ($\underline{U}$ in Fig. 1.2a) could be the heart with excited muscle fibers within (Fig. 2.1a). The induced *equalizing currents* in the extracellular space from each and every muscle fiber form additively electric and current density fields outside the heart ($\vec{E}$ and $\vec{J}_E$ fields in Fig. 2.1a) as well as the electric potential field (φ field in Fig. 2.1a). These fields extend (propagate) throughout tissue towards the skin and undergo attenuation due to increasing *distance* from the field source and, on the other hand, damping by the *lossy medium* itself ($\underline{Z}_1$ in Fig. 1.2a).

[2]All *complex quantities*—except complex vectors—are *underscored* in following sections.

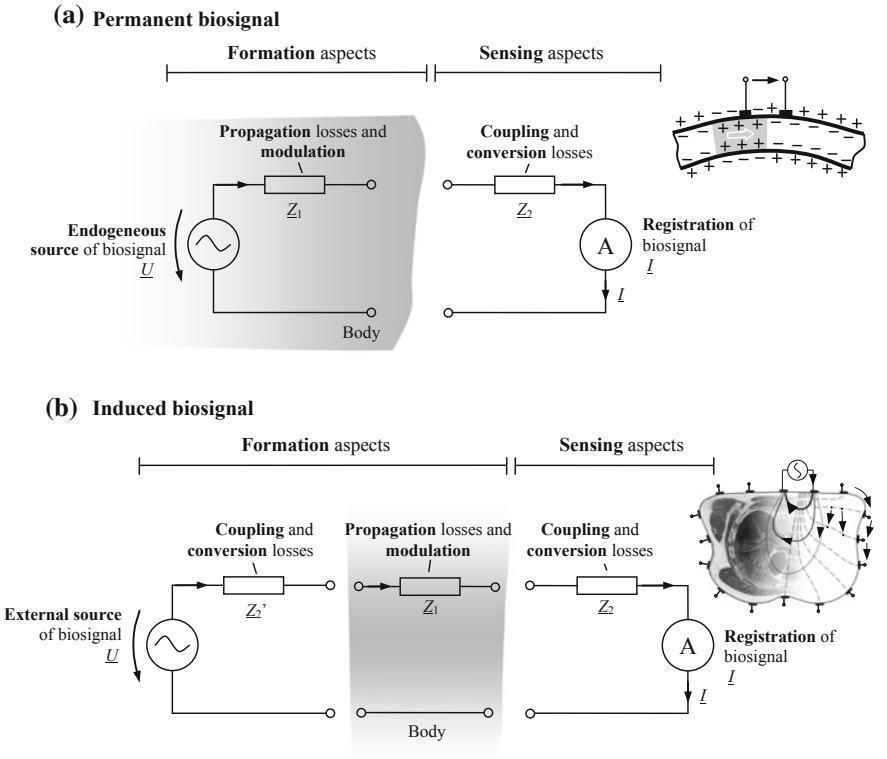

Fig. 1.2 Electrical circuit models of electric biosignals (Kaniusas 2012, Fig. 1.3). **a** Permanent electric biosignal, including its generation, propagation within the body, coupling out of the body, and registration. **b** Induced electric biosignal, including its generation, coupling into the body, propagation and modulation within the body, coupling out of the body, and its registration

For instance, high *frequency components* of these fields face a stronger damping than low frequencies (i.e., $|\underline{Z}_1|$ is larger for high frequencies than low frequencies, see Fig. 2.6). In addition, *conductive insets* on the way of the fields from the heart towards the skin, as depicted in Fig. 2.1b, reduce the spatial gradient of φ on the skin surface and thus the amplitude of the recorded signal (i.e., $\underline{Z}_1$ decreases for conductive and thus short-circuiting propagation media). On the way to the skin, the fields experience amplitude *modulation by respiration*, since the distance from the heart to the skin periodically changes in synchrony with the respiratory cycle and so the accumulated attenuation of fields is subjected to the respiratory cycle (Kaniusas 2012, Fig. 3.30b) (i.e., $\underline{Z}_1$ is modulated by respiration).

The *coupling* and *conversion* of electric biosignals is performed by electrodes on the skin, registering the local differences in φ (Fig. 2.1a). Here the boundary from the skin to electrodes (reflected by $\underline{Z}_2$ in Fig. 1.2a, see Fig. 3.19) shapes significantly the time course and spectral content of the recorded signal (given as $\underline{I}$ in Fig. 1.2a), i.e., of the recorded *electrocardiogram*.

Induced Biosignals

Figure 1.3 demonstrates the basic principle of *induced electric biosignals* in terms of *electrical field plethysmography* or *impedance tomography*. Multiple electrodes are placed circularly around the thorax in the horizontal plane so that the whole cross-section of the thorax is spanned. While an alternating current i with a constant amplitude (e.g., 1 mA at 50 kHz) is applied between two neighbouring *current electrodes* (e.g., electrodes 1 and 2 in Fig. 1.3a) as an *artificial stimulus*, the resulting voltages u are registered between other pairs of neighbouring *voltage*

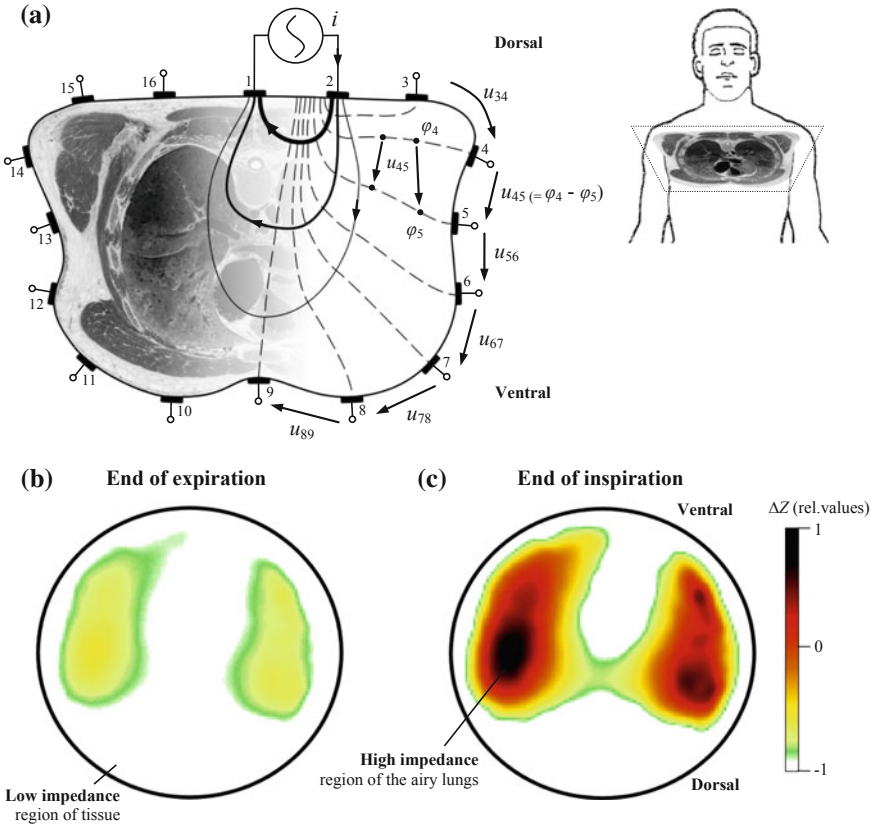

Fig. 1.3 Genesis of an induced electric biosignal (electric field plethysmogram). The basic principle and experimental results of the two-dimensional impedance tomography as applied across the thorax at the level of the heart. **a** An alternating current i is applied between electrodes 1 and 2, whereas the resulting voltage $u_{k,k+1}$ is registered between the neighboring electrodes k and $k+1$ with the index k ranging from 3 to 15. **b**, **c** Experimental results illustrate the distribution of the magnitude change ΔZ of the electrical impedance $\underline{Z}$ within the cross-section of the thorax. The inflation is illustrated over time from **a** the end of expiration to **b** the end of inspiration. Experimental horse data are provided by Schramel (2012), with the reference voltage taken at mid-inspiration

electrodes (e.g., electrodes 3 and 4, 4 and 5, etc.) as the *induced electric biosignal*. The location of the injection of i and the adjacent locations of multiple measurements of u are sequentially and electronically rotated after each time step; i.e. current electrodes become voltage electrodes and vice versa.

The larger is the impedance of the tissue section anchored between two equipotential surfaces (e.g., with the respective electric potentials φ_4 and φ_5 in Fig. 1.3a) connected to the two neighbouring electrodes (i.e., the electrode 4 and 5), the larger is the measured voltage between the electrodes (the voltage $u_{45} = \varphi_4 - \varphi_5$). From a *respiratory* point of view, when the local conductivity within a lung section residing between the two equipotential surfaces decreases with inspiration (since the isolating air inflates local alveoli), the potential difference and thus the registered voltage between these surfaces increases. In other words, the *induced electric biosignal* carries *respiratory information*.

Based on this principle, the two-dimensional spatial distribution of the impedance of small tissue sub-sections within the cross-section of the thorax can be calculated. Figure 1.3b shows the estimated change in this distribution from the *end of expiration* to the *end of inspiration*. The impedance of lung sub-sections clearly increases in the course of inspiration.

In analogy, during *late systole* there is less of conductive blood within ventricles of the heart than during *late diastole* (Kaniusas 2012, Fig. 2.38). Therefore, the voltage between equipotential surfaces encompassing ventricles can be expected to decrease from the late systole to the late diastole, which clearly reflects *cardiac activity*. Therefore, *cardiac information* can also be included within the *induced electric biosignal*.

The formation of *induced electric biosignals* up to their registration outside the body can be simplified as another *electrical circuit model*, satisfying

$$\underline{I} = \frac{\underline{U}}{\underline{Z}_2' + \underline{Z}_1 + \underline{Z}_2}. \tag{1.2}$$

As illustrated in Fig. 1.2b, the *artificial electric source* of the induced biosignal is external to the body (represented by the voltage source with the complex amplitude $\underline{U}$). The external stimulus is generated and then *coupled* from this source over the body skin into the body (coupling losses are represented by the impedance $\underline{Z}_2'$), e.g., via metal surface electrodes on the skin (Fig. 1.3a). The *propagation* of the induced biosignal through tissue follows, in the course of which the propagating biosignal is not only attenuated but also *modulated* by physiological phenomena of interest (propagation losses and modulation reflected by the impedance $\underline{Z}_1$). Again, a certain portion of the induced biosignal leaves the body and thus is available for its registration above the body skin. This portion is subjected to *coupling* and *conversion* losses while entering an external sensing device (represented by the impedance $\underline{Z}_2$), e.g., via the same or other electrodes on the skin (Fig. 1.3a). The *registration* of the induced electric biosignal follows (modelled as ampere meter), which is co-determined by all $\underline{U}$, $\underline{Z}_2'$, $\underline{Z}_1$, and $\underline{Z}_2$ (1.2).

In terms of the discussed electrical field plethysmography, the source $\underline{U}$ (1.2) corresponds to the applied artificial current i into the thorax (Fig. 1.3a), $\underline{Z}_2'$ models all electrode impedances of the applied current electrodes (Fig. 3.19), $\underline{Z}_2$ models all electrode impedances of the voltage electrodes, and $\underline{Z}_1$ accounts for the discussed cardiorespiratory modulations.

For *permanent biosignals*, it should be noted that *physiological phenomena* of interest are hidden in the voltage source $\underline{U}$ and the physiologically-modulated propagation losses $\underline{Z}_1$, both influencing the registered $\underline{I}$ (Fig. 1.2a). In contrast, for *induced biosignals*, physiological data are only provided by the propagation and modulation losses $\underline{Z}_1$ since the source $\underline{U}$ is an artificial source.

Permanent Versus Induced

Please note that the field plethysmography with its *induced electric biosignals* yields data on diverse *mechanical phenomena* within the body, tightly related to cardiovascular and cardiorespiratory activities, such as the pumping activity of the heart and circulation. Therefore induced biosignals are usually used for evaluation of mechanical body functions. This is in clear contrast to *permanent electric biosignals*, e.g., electrocardiogram (Fig. 2.1), which reflect electrical *excitation phenomena* but not mechanical phenomena. In fact, any muscular excitation serves as the input for a subsequent mechanical muscular action to be performed, such as the heart beat. From this perspective, permanent biosignals for excitation recording and induced biosignals for response recording perfectly complement each other in their diagnostic power.

References

L.A. Geddes, R.A. Roeder, Where do ideas come from? IEEE Eng. Med. Biol. Mag. **28**(5), 60–61 (2009)

E. Kaniusas, *Biomedical Signals and Sensors I: Linking Physiological Phenomena and Biosignals* (Springer Publisher, 2012)

J.P. Schramel, Unpublished tomographic image data, in *Clinic for Anesthesiology*, University of Veterinary Medicine, Vienna, 2012

Chapter 2
Formation of Electric Biosignals

Abstract Electric biosignals are subjected to highly instructive propagation within and outside of biological tissues. The transmission of electric, magnetic, and electromagnetic fields is governed by lossless and lossy media, conductive and dielectric media, as well as dispersive and non-dispersive media. Relaxation and dispersion effects as well as boundary conditions within heterogeneous media co-determine this insightful transmission. Electric biosignals within tissue yield physiological effects such as neuromuscular and thermal stimulation, depending on stimulus and tissue properties. Exposure limits assess potentially adverse health effects.

According to Fig. 1.2a, *formation aspects* of *permanent electric biosignals* include

- the *genesis of endogenous biosignals* and
- their *transmission* and *modulation* while propagating within the body,

on their way to the sensing device applied on the body skin. In analogy, *formation aspects* of *induced electric biosignals* (Fig. 1.2b) include

- an *artificial electric source* for the initial generation of induced biosignals,
- *coupling* of these biosignals into the body, and
- their *transmission* and *modulation* while propagating within the body,

on the way to the sensing device. The formation aspects reveal not only *clinically relevant correlations* between physiological phenomena of interest and recorded electric biosignals but also facilitate a proper and fundamental understanding of the *biosignal's diagnostic power*.

In the following section, we set the focus on the *transmission and propagation* of electric biosignals. We concentrate on a *common denominator* for most of electric biosignals propagating within biological tissue, irrespective of their origin and their specific physiological modulations (biosignals undergo during their propagation). In particular, instructive basics on the transmission of electric biosignals are provided for *lossless* and *lossy* media as well as for *homogeneous* and *heterogeneous* media. Physiological effects of *electrical stimulation* and *thermal*

© Springer Nature Switzerland AG 2019

E. Kaniusas, *Biomedical Signals and Sensors III*, Biological and Medical Physics, Biomedical Engineering, https://doi.org/10.1007/978-3-319-74917-4_2

stimulation are detailed and complemented subsequently by a qualitative and quantitative debate about potential *adverse health effects*.

2.1 Permanent Biosignals

There is a huge diversity of permanent electric biosignals, as can already be derived from their classification in Kaniusas (2012, Fig. 1.15). We will discuss here only a small *selection of biosignals*. In particular, we focus on well-known biosignals in clinical practice and on those which are usually derived based on *contact-based coupling*, in line with the model in Fig. 1.2a. That is, discussed biosignals are galvanically coupled out of the inner body via contact electrodes. Please note that most permanent biosignals are composed out of relatively *low frequency components* which are not able to propagate efficiently on their own (as an electromagnetic wave, see Fig. 2.2) so that, in fact, the contact-based approach is the most suited for their registration.

Cardiac Activity—Electrocardiogram

The most prominent source of electric biosignals is the *electrically exited heart*, with the so-called *electrocardiogram* as the resulting recorded biosignal *over time*; see Footnote 1 in Chap. 1 and Fig. 2.1. In particular, the electrical excitation of both the *myocardium of atria* and *myocardium of ventricles* (the two major muscles composing the heart) contribute to the whole excitation of the heart (Kaniusas 2012, Fig. 2.38). The very origin of the electrical excitation of myocardia is the cardiac muscle cell which composes both myocardia (Kaniusas 2012, Fig. 2.28).

The source of electrocardiogram is given by closed-loop *equalizing currents*, conductive and ionic currents in the extracellular space (Kaniusas 2012, Fig. 2.18). As shown in Fig. 1.1a, these currents flow along the inner surface of the membrane from the *excited region* of a single muscle cell towards its *resting regions* (as *conductive currents*), cross the membrane outwards (as *transmembrane displacement currents*), and then return back to the excited region along the outer surface of the membrane outside the cell (as conductive currents) and again cross the membrane inwards (as displacement current). It is like a passive transport of potential difference along the muscle fiber (Kaniusas 2012, Fig. 2.8).

The local density of these conductive *equalizing currents* in the extracellular space—to be precise, the density of all *accumulated equalizing currents outside countless muscle cells* of the cardiac muscle—is necessarily accompanied by the local *electric field* (2.32). This field, in turn, is given as the negative gradient of the electric *equipotential surfaces* (2.28). The resulting difference in the equipotential surfaces present at the two locations of conductive *electrodes* on the skin—or the resulting voltage drop u in-between the two skin electrodes, as shown in Fig. 2.1a by the electric potential difference $u = \varphi_3 - \varphi_1$—serves then as *electrocardiogram*. In other words, electric biosignals produced by both heart muscles are unavoidably conducted to other regions of the body closer to the skin surface because conductive

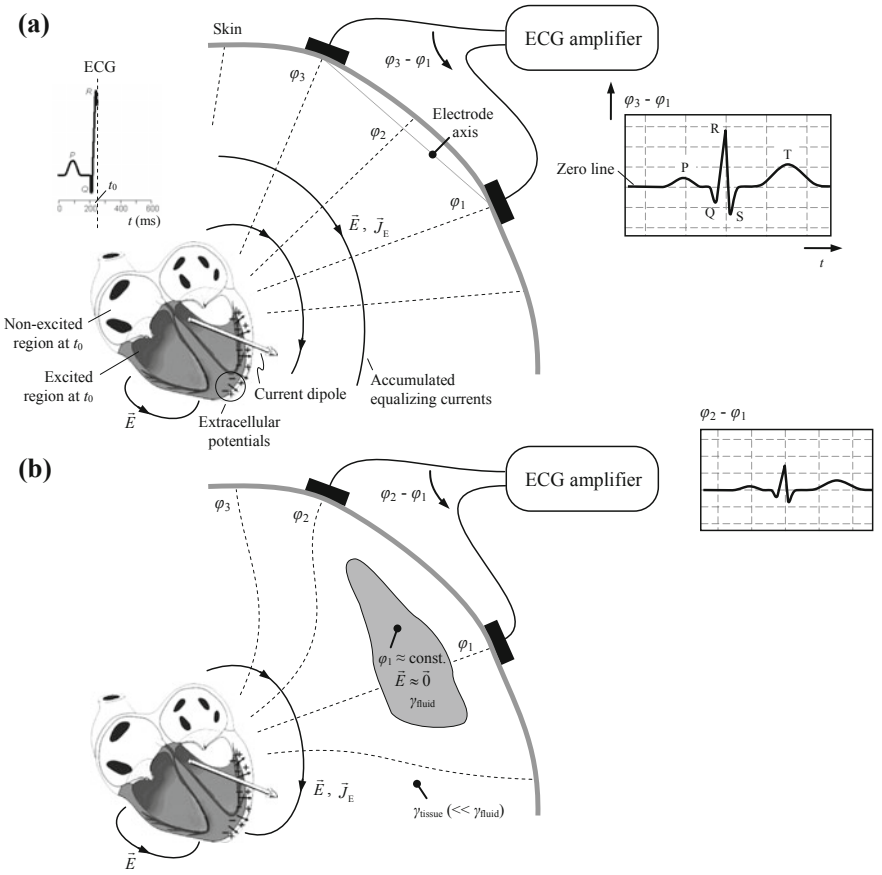

Fig. 2.1 Genesis of a permanent electric biosignal with the atria and ventricular heart muscles as biosignal sources, known as electrocardiogram (ECG). **a** Partially excited muscle regions of the heart with denoted extracellular potentials of the propagating excitation wave (Kaniusas 2012, Fig. 2.37) form the time-varying current dipole vector. The dipole is proportional to the total extracellular equalizing currents and thus to the associated electric $\vec{E}$ and current density $\vec{J}_E$ fields surrounding the heart. These fields determine the local gradient of the time-varying electric potential φ (2.28) and thus the resulting time-varying voltage u ($=\varphi_3 - \varphi_1$) between the two electrodes applied on the skin. The time course of u is known as ECG. **b** A well conducting inset is introduced between the heart and the skin, e.g., an accumulated fluid with its conductivity γ_{fluid} larger than γ_{tissue} of the surrounding tissue. Correspondingly, the conductive inset disperses the field lines of φ (Fig. 2.25a) and thus reduces the effective u ($=(\varphi_2 - \varphi_1) < (\varphi_3 - \varphi_1)$) between electrodes in comparison with (**a**) without any conductive inset

tissues are in contact with the heart and the skin. *Biological tissue* can be seen as a *volume conductor* featuring spatial and temporal *low-pass filter* behaviour (Fig. 2.62), i.e., causing high frequencies being damped stronger than low frequencies (Fig. 2.6). In addition, Fig. 2.1b illustrates how a conductive inset between the heart and the skin electrodes reduces the registered u from $(\varphi_3 - \varphi_1)$ to $(\varphi_2 - \varphi_1)$ and thus weakens the amplitude of the registered electrocardiogram.

It is important to keep in mind that a *resting muscle cell* or fully *excited muscle cell* does not generate any equalizing currents permeating the membrane. These currents are only generated in-between excited and non-excited regions of the cell, i.e., in-between excited and non-excited regions of myocardium. Therefore, *myocardium that is not fully excited* gives a non-zero electrocardiogram. In contrast, resting or fully excited myocardium is silent in electrocardiogram with the associated zero line. As denoted in Fig. 2.1a, please observe the *zero PQ interval* in electrocardiogram (with the fully excited myocardium of atria) or the *zero ST interval* (with the fully excited myocardium of ventricles) in the normal electrocardiogram. Likewise, if ventricles can not be fully excited (e.g., due to ischemic situation), the ST interval leaves the zero line and becomes usually elevated or depressed—a clear warning sign for clinicians.

The sequential *depolarization* and *repolarization* of atria and ventricles of the heart—in synchrony with the heart beat—produce differentiable deflections within electrocardiogram. These include well-known P, Q, R, S, and T waves (Fig. 2.1a). Electrocardiogram with differential electrodes on the body surface (e.g., bipolar electrodes with a finite inter-electrode distance, see Fig. 2.1) provides a *differential picture* of the cardiac muscle excitation, with the non-zero values for still ongoing depolarization or repolarization, and with zero values for both the resting and fully depolarized states, as instructively summarized in Kaniusas (2012, Fig. 2.37). Obviously, the differential picture applies only if the interelectrode distance is less than the spatial spread of the excitation potential (Kaniusas 2012, Eq. 2.13) and approximates even better the first spatial derivative of φ when the interelectrode distance decreases. Likewise, decreasing interelectrode distance shifts the cut-off frequency of the formed spatial high-pass filter toward higher frequencies.

Electrocardiogram, namely, the time course of u between the two skin electrodes, can be interpreted as the temporal *geometrical projection* of the so-called *current dipole vector* of the whole heart to the *electrode axis* (the connecting line between the two electrodes), as shown in Fig. 2.1a. The vector rotates and changes its magnitude in time and space within each single cardiac cycle (Malmivuo 1995). At the time instance when the dipole vector is parallel to the electrode axis, a *maximum projection* results and thus a maximum size of u is given. In analogy, the dipole vector perpendicular to the electrode axis shows a *zero projection* and thus a zero level of u. The momentary magnitude of this dipole vector can be interpreted as the momentary strength of the partial heart excitation, whereas the momentary dipole direction shows the momentary propagation direction of the excitation front. In particular, this current dipole vector of the muscle is additively composed out of single vectors of *cell-based dipoles* of individual *partially-excited muscle cells*

composing this muscle. The *current dipole vector* on the *cellular level* is defined—as indicated in Fig. 1.1—as the strength and direction of the intracellular *equalizing current* within the cell flowing *in the propagation direction* of the excitation front. Therefore, the current dipole vector of the whole heart accounts for all equalizing currents outside the heart muscle, i.e., extracellular to all muscle cells.

- The *current dipole is zero* for resting or fully excited myocardia and
- the *current dipole is non-zero* for partially-excited myocardia (Fig. 2.1a).

Ventricular fibrillation of the heart should be shortly mentioned, as being relevant for *adverse health effects* (Fig. 2.89). The genesis of ventricular fibrillation is detailed in Footnote 124. The associated waveform of *electrocardiogram* shows a highly irregular behaviour in the time domain, exhibiting fluctuations with rapidly changing instantaneous amplitude, shape, and frequency. The oscillation frequency is usually much higher than the regular heart rate because of the decreased lengths of closed pathways within the heart for the *re-entrant excitation waves* (Kaniusas 2015, Footnote 61 in Chap. 5).

Electrocardiogram can also be registered with *intracardial electrodes* located directly within the heart. The amplitude of *intracardial electrocardiogram* depends strongly on the inter-electrode distance. The larger this distance, the larger is the resulting voltage drop in-between (2.30 and Fig. 2.11). Therefore, the amplitude of intracardial electrocardiogram is lower in the bipolar configuration (with both electrodes on the heart and a relatively small inter-electrode distance) than in the unipolar configuration (with a single electrode on the heart); compare Fig. 2.83 and Footnote 130.

Muscular Activity—Electromyogram

Another typical electric biosignal is *electromyogram*, reflecting the *electrical excitation of muscle* over time. The genesis of electromyogram was already disclosed within Fig. 1.1a with two *implanted electrodes* located close to the membrane of a single muscle fiber. For a single action impulse with its *monophasic waveform* (Kaniusas 2012, Fig. 2.18b) propagating along the muscle fiber, namely, along the sarcolemma (Kaniusas 2012, Fig. 2.26), the voltage u between electrodes clearly reveals a *biphasic waveform*. There is a zero u for the resting fiber region under both electrodes and for the fully excited fiber region under both electrodes (times t_A and t_C in Fig. 1.1a). A non-zero u requires a partial excitation under both electrodes (times t_B and t_D in Fig. 1.1a). As in the case of electrocardiogram, electromyogram with its spatially dislocated electrodes provides a *differential picture* of the muscle cell excitation, i.e., the biphasic waveform of u follows out of the monophasic waveform of an action impulse.

Electromyogram can also be recorded with *external electrodes* on the skin, located *over the muscle* of interest.[1] On the skin surface, the aforementioned *equalizing currents* outside the muscle create their *equipotential surfaces* (2.28), the difference of which can be registered with conductive *skin electrodes*. This is in close analogy with the described principle in Fig. 2.1a.

The accessibility of muscular electric biosignals outside the muscle with skin electrodes is quite good. Since muscle cells are relatively large (Kaniusas 2012, Fig. 2.24) in comparison with nerve cells, equalizing transmembrane currents are relatively strong and give rise to relatively large potential gradients in the extracellular fluid around muscle cells. In addition, *numerous muscle cells* are *activated in synchrony*—in terms of *motor units* (Kaniusas 2012, Sect. 2.3.1)—so that *equalizing currents from individual cells sum up* and generate even stronger changes in electric potentials present at the locations of skin electrodes. In the case of an *asynchronous activation* of muscle cells (belonging to different motor units), the arising electric biosignals overlap and yield a relatively complex pattern on the skin level over the relevant muscle (bunch of muscle cells).

It can be said that the electrical activity of the muscle is *projected* across the *volume conductor* (tissues) to the skin surface where electrodes are applied; in close analogy with the discussed projection of the current dipole to the electrode axis (Fig. 2.1a). The *amplitude* of the surface electromyogram reflects the muscle activation, whereas the *frequency content* of electromyogram is partly determined by the average conduction velocity of the propagating action potentials along the muscle fiber.

Brain Activity—Electroencephalogram

The origin of *electroencephalogram* is not given by all-or-none action potentials travelling along nerve cells but by much slower and *graded postsynaptic potentials* (namely, inhibitory and excitatory postsynaptic potentials) of *activated nerve-to-nerve synapses* within the brain. Please consult (Kaniusas 2012, Fig. 2.23) comparing spiky action potentials and smooth postsynaptic potentials.

These postsynaptic potentials generate *extracellular equalizing currents* flowing between depolarized and resting regions of the postsynaptic membrane (Kaniusas

[1]For instance, the *abdominal uterine electromyogram*, known also as *electrohysterogram*, registers the electrical excitation of *smooth muscle cells*, the *uterus* is composed out of (Kaniusas 2012, Fig. 2.27), (Kaniusas 2012, Footnote 108). The electrical activity of the uterus can be assessed as the potential difference between each two surface electrodes located around the umbilicus on the abdomen (right/left and above/below by about 3 cm) (Di Marco 2014). The registered waveform of electromyogram occurs in-phase with intrauterine pressure increase in response to smooth muscle contractions. The waveform includes a *slow wave* (with components up to 0.03 Hz) and a *fast wave* (up to 3 Hz). The low frequency components of the fast wave (in the range of about 0.2–0.45 Hz) are associated with uterine contractions during *gestation*, whereas the high frequency components of the fast wave (in the range of about 0.8–3 Hz) are related to *parturition* contractions (more efficient labor contractions) and increase with estrus. It is suggested that changes in the excitation and contraction pattern of the uterus occur in response to the preparation for labour. The myometrium has to become more excitable and responsive in order to yield effective contractions which are capable of dilating the cervix.

2012, Fig. 2.19). In the region of multiple *dendrites* of a single nerve cell synaptically connected to other numerous associated neurons (up to 10,000 synapses per single nerve cell, see Kaniusas (2012, Fig. 2.21a)), these *equalizing currents sum up* (Kaniusas 2012, Fig. 2.23a) and generate spatially extended *electric and current density fields*. Individual fields of single synapses sum up and strong extracellular fields are generated when many synapses are simultaneously active. In analogy with Fig. 2.1a, these *volume fields* penetrate through the *volume conductor* (tissue) and generate differences in the *electric potentials* on the scalp (2.28). These differences can then be registered as *time-varying voltages* (2.29) between adjacent *electrodes on the scalp*, providing *electroencephalogram*. Consequently, the extent of *synchronization of synaptic activity* (networking of cells) within the recorded brain region is an important parameter favouring the evidence of electroencephalogram. For instance, *epileptic seizures* can be detected based on strong deflections in electroencephalogram due to an abnormally high synchronisity of nerve firing.

Since the cellular density in the brain is relatively high, extracellular *equalizing currents*—originating within a single synapsis—experience narrow *intercellular channels* on their way to resting membrane regions. The resulting high resistances (2.36) of these channels imply a relatively *wide distribution* of equalizing currents away from synapsis. This diffuse distribution of equalizing currents, in turn, indicate *diffuse spatial information* provided by electroencephalogram. In fact, a single derivation of electroencephalogram accounts for the activity from many thousands of neurons (e.g., 1 mm^3 of the cortex may host more than 10^5 neurons). Correspondingly, electroencephalogram reflects *overall brain functions* instead of the electrical activity from a single neuron.

The larger is the spatial distance from the activated synapsis, the lower are the induced local electric potentials. Therefore, electroencephalogram picks up the activity of *cortical neurons* in the cerebral cortex, i.e., of neurons sitting closest to the scalp where electrodes are located. Large *pyramidal neurons* seem to contribute most to the scalp electroencephalogram because they are perpendicular to the cortex surface, are well-aligned to each other and synchronized in their firing. The latter properties favour an efficient *projection* of equalizing currents to potential differences (or voltages) on the scalp.

For *skin electrodes*, bones of the skull and the scalp reside between the cerebral cortex (with *endogenous sources* of this electrical biosignal) and the electrodes (as *external sinks* for the biosignal). Therefore, there is a *capacitive coupling* of volume fields in the brain to the skin electrodes, which implies a high-pass filtering of this endogenous biosignal while crossing this isolating layer.

The *standardized 10–20 system* of electrodes can be used to record electroencephalogram (Kaniusas 2012, Footnote 251). The *monopolar modus*—when measured between each active electrode and a distant passive reference electrode (Fig. 2.83)—is usually used for the localization of the event of interest. The *bipolar modus*—when measured between adjacent electrodes—favours reduction of shared *artefacts* in electroencephalogram, which are assumed to affect adjacent electrodes in a similar way.

Challenges are still here while establishing a seamless *neurotechnological* link with the human brain in *naturalistic environments*. In particular, application and long-term wearing of scalp electrodes as well as signal corruption are problematic. Dominant *artefacts* from extracerebral sources are electrode/body movements, changes of the electrode contact impedance, eye movements or blinks, excitation of scalp muscles, tongue[2] movements, pulsatile heart activity, power lines, and others. The *reproducibility* of electroencephalogram is also impaired by the mechanical elasticity of the brain which may stretch significantly (>5%) during its normal physiologic motion as well as may displace significantly (mm to cm) relative to the skull (He 2013).

Eye Movements—Electrooculogram

The *cornea* of the eye—the anterior part of the eyeball—carries a *positive electric charge* while the *retina*—the posterior part of the eyeball—is *negatively charged*. The source of the retinal charge lies in the potential difference across the retina, to be more precise, in the potential difference generated by ionic currents across the retinal pigment epithelium (Berg 1991); compare (Kaniusas 2012, Fig. 2.10). The resulting *charge dipole* within each eye, referred to as *retino-corneal difference*, generates its own *electric and current density fields* as well as the associated *electric potential field*. For instance, the potential difference between the front and back of the eyeball is in the range 0.5–1 mV. When the eye or eyelid moves, the *charge dipole moves* and becomes spatially reoriented within the eye so that the related electric potential field undergoes a temporal change. The difference in the resulting time-varying electric potentials present at locations of contact *electrodes on the head skin* can then be registered as a *time-varying voltage* between the electrodes (Fig. 2.11), as in the case of the already discussed electric biosignals. This time course is known as *electrooculogram*. In other words, during the movement and reorientation of the dipole, the *projection* of the associated potential field to the head surface changes and so the voltage between the applied electrodes.

In particular, electrooculogram occurs in the course of *eyeball rotation* (horizontal and vertical eye movements) and *eyelid movements* (eye blinks). The electrodes measure local changes in the electric potential as the *charged cornea* moves nearer or further from the electrodes. For instance, for eyes looking straight, the cornea could be about the same distance from either side electrode, so that the associated voltage between these electrodes would be essentially zero. Likewise, when the positively charged cornea is closer to the positive electrode, a positive deflection in the recorded voltage is registered.

Interestingly, the *blink response*, namely, the upward or downward movement of the upper eye lid over the positively charged cornea, induces the opposite polarity

[2]The *tip of the tongue* has a *negative charge* with respect to the root. This difference in charges yields a potential difference along the tongue and along the conductive tissue structures close to the tongue. That is, when the tip touches tissues inside the mouth, the negative tip charge decreases the electric potential level at and near the point of contact, known as *glossokinetic potential*. Thus, *artefacts* in *electroencephalogram* due to tongue movements are called glossokinetic artefacts.

in electrooculogram to that induced by *vertical eye movements* of the same direction (Häkkinen 1993). Of course, this limits the separability of blinks and vertical movements out of the recorded electrooculogram.

In line with Fig. 1.2a, electrooculogram depends not only on the charge dipole itself and its variation during eye or eyelid movements, which comprises the time-varying *source* of the field and its variation (see $\underline{U}$ in Fig. 1.2a). Electrooculogram depends also on electric properties of lossy tissues surrounding this dipole as well as the source distance to the electrodes, which comprises the *medium-related damping* and *geometry-related damping* of generated fields, respectively (see $\underline{Z}_1$ in Fig. 1.2a). Correspondingly, electrodes should be placed as close to the eyes as possible to decrease the distance of electrodes to the charge dipole and thus to increase the *signal-to-noise ratio*. The amplitude of electrooculogram is inversely proportional to this distance. Please note that lowered eyelids (e.g., during eye blinks or looking downwards) increase the conductivity between the eyeballs and the skin the electrodes are applied on. This increased conductivity can be interpreted as a change in the *medium-related damping*. Therefore, the potential difference between electrodes, i.e., the time course of electrooculogram, becomes a clear function of eye blinks and gaze direction. In general, *inhomogeneous anatomical structures* around the eyeball influence strongly the resulting electric potential field, its projections at the site of electrodes, and thus the registered electrooculogram.

Quite *simple models*[3] of the eye can be used to model the charge dipole within the eye. The charge dipole can be even assumed to reside in a *fixed position* but with only a *varying spatial orientation* (Berg 1991). In line with the *monopolar model* (Footnote 3), electrooculogram shows a large deflection when the charged cornea moves directly towards the electrode, i.e., *moves along* the so-called *electrode-cornea line* (Häkkinen 1993). In contrast, when the cornea moves *perpendicular* to the electrode-cornea line, a small deflection in that electrode is expected.

[3] *Monopolar models* can even be used to model *electrooculogram* because of the relatively short distance of the applied skin electrodes from the eyeball (Häkkinen 1993). That is, this model represents the eyeball by a *positively charged monopolar cornea* only and neglects the effects of the *negatively charged posterior part* of the eyeball. When the eye or eyelid moves, this *positive monopolar source* moves in a homogeneous volume conductor. This simplest monopolar model reproduces changes of the local electric potential field near the anterior pole of the eyeball, namely, *near recording electrodes* applied closely to the eyeball.

However, with increasing distance of the applied electrodes from the eyeball, the behaviour of the electric potential field at the site of the electrodes gradually changes from

- *monopolar behaviour*, applicable for *short electrode-eyeball distances* with a single *charge monopol* (positive cornea only) within each eye, according to the *monopolar model*; to
- *dipolar behaviour*, applicable for *large electrode-eyeball distances* with a single *charge dipole* (positive cornea and negative retina) within each eye, according to the *dipolar model*. The relatively large distance can be approximated as more than 3 times the distance between the positive and negative charge poles within the eyeball (Häkkinen 1993).

The most *common eye movements* are (Larsson 2013):

- *fixation*, when the eyeball is more or less still and visual information is taken by the brain. It is characterized by low positional dispersion, low velocity, and a large period duration of about 200–300 ms;
- *saccade*, when the eyeball is shifting from one position to another, characterized by a very rapid movement, high velocity from 30 up to 500 deg/s, and a short period duration of about 30–80 ms.

Other Permanent Biosignals

Electroarthrography

Electroarthrography refers to recording of the induced *electric potentials* on the *knee* surface when the joint is subjected to the *compressive loading* (Han 2014). Here the source of the electric potentials is the load-induced flow of the interstitial fluid that transports electrically charged ions within the compressed cartilage.

In fact, the articular cartilage comprises mainly a large amount of extracellular matrix which is composed out of collagen fibers and is embedded in a gelatinous ground substance. This ground substance includes *negatively charged groups* which attract positively charged *cations* from the surrounding electrolyte to maintain electrical neutrality. When the compressive load is applied, the hydrodynamic drag displaces these cations (in the cartilage and the synovial fluid) away from the locally fixed and negatively charged groups. Consequently, a mechanically-induced electric field and the associated field of electric potentials are generated along the flow direction. Therefore, the induced potentials are also known as *streaming potentials*. For instance, *cartilage degeneration* (e.g., in patients with osteoarthritis) is tightly interconnected with diminished streaming potentials, whereas these potentials disappear completely in patients with knee *prostheses* (Han 2014).

Electrocochleography

Electrocochleography is a electrophysiological *stimulus-related recording* technique (Kumaragamage 2015). At the onset of an auditory stimulus, the technique captures the electrical activity from the cochlea, known as *cochlea potentials*, and from *action potentials* of the auditory/cochlear nerve. While cochlea potentials reflect the instantaneous displacement of the basilar membrane within the cochlea in response to the stimulus, action potentials represent a compound action potential as the summed response of a population of neurons (Ferraro 2006).

Mainly two recording approaches are used:

- *non-invasive extratympanic* and
- *invasive transtympanic*,

which differ in the placement of electrodes. In the former approach, the active sensing electrode is placed in the external ear within the ear canal proximal to the tympanic membrane. In the latter approach, a needle electrode is pierced through

the tympanic membrane and then placed in the promontory close to the round window (i.e., the opening from the middle ear into the inner ear, i.e., into the cochlea). The reference electrode can be applied on the earlobe of the contralateral or ipsilateral ear.

Due to the close proximity of the electrode to the cochlea, the signal amplitude of the invasive approach is approximately four times larger than that of the non-invasive approach (Kumaragamage 2015). Similar difference exists also for the *signal-to-noise ratio*. Please note that the total electrical activity registered in the outer ear is composed not only of the desired *inner ear activity* (in terms of electrocochleography) but also out of undesired *muscle activity* (from muscles within the ear and/or close to the ear) and interfering *cerebral activity*.

Usually recordings are carried out by *repeatedly capturing and averaging* cochlea activity in synchrony with the sound stimuli. Typically, the extratympanic approach requires averaging of up to 1000 evoked responses to attain a sufficient level of the *signal-to-noise ratio*. Please note that this ratio increases with the square root of the number of averaged responses. Averaged responses are then identified to correlate with disorders of the inner ear and pathologies of the cochlear nerve.

Contact-Less Assessment

Non-contact assessment of electrocardiogram, electroencephalogram, electro-oculogram and other electric biosignals should be shortly mentioned (Fig. 3.1). Here the *capacitive coupling* is used between the skin and *distant non-contact electrodes* in order to detect *displacement currents* emanating from the body surface in the course of various endogenous electric biosignals. Such electrodes are also known as *electric potential sensors*. It should be stressed that any non-contact registration requires *time-varying behaviour* of electric biosignals. The faster this variation, the lower is the *capacitive impedance* of the separating distance (2.43) and the stronger are displacement currents registered by the non-contact electrodes. In other words, time-constant components of endogenous biosignals can not be detected via displacement currents and thus via non-contact electrodes.

In practice, remote signals can be recorded through isolating clothes and the air with reasonable distances from 3 mm (for electroencephalogram) up to 1 m (for electrocardiogram) (Harland 2008); compare Fig. 3.31. In order to compensate for variations in the distance between the skin and electrodes and for variations in the composition of clothes, reference excitation signals may be used (Pinheiro 2010).

2.2 Induced Biosignals

Figure 1.3a has already described the basic principle of an induced electric biosignal, as a basis for the *electrical field plethysmography*, or more specifically, for the *impedance cardiography* or *impedance tomography*. In short, an *alternating*

current $i(t)$ is injected into a tissue section as the *system stimulus*, whereas the resulting *alternating voltage* $u(t)$ is registered across the section along the current flow as the *system response*, as shown in Fig. 2.9a. The voltage u serves as an *induced electric biosignal*.

For an assumed purely *conductive behaviour* of the tissue section with its time-varying *resistance* $R(t)$, the change in the time course of $u(t)$ clearly reflects the resistive behaviour through (2.31)

$$u(t) = R(t) \cdot i(t), \tag{2.1}$$

provided that the time course of $i(t)$ stays constant. Equation (2.1) is valid for any arbitrary waveforms of the applied $i(t)$.

If the section behaves as a *conductor and dielectric*, or as a lossy dielectric as most *biological tissues* do (Fig. 2.16), a similar relationship applies. Here the applied *sinusoidal* $i(t)$ with the constant complex peak value $\hat{\underline{I}}$ yields an amplitude-modulated and phase-modulated *sinusoidal* $u(t)$ with the time-varying complex peak value $\hat{\underline{U}}(t)$, given a time-varying complex *impedance* $\underline{Z}(t)$ of the tissue section permeated by $i(t)$ (2.34), to give

$$\begin{aligned} i(t) &= \hat{I} \cdot \cos(\omega t + \varphi_\mathrm{I}) = \mathrm{Re}\left\{\hat{I} \cdot \mathrm{e}^{\mathrm{j}\varphi_\mathrm{I}} \cdot \mathrm{e}^{\mathrm{j}\omega t}\right\} = \mathrm{Re}\left\{\hat{\underline{I}} \cdot \mathrm{e}^{\mathrm{j}\omega t}\right\}, \\ u(t) &= \hat{U}(t) \cdot \cos(\omega t + \varphi_\mathrm{U}) = \mathrm{Re}\left\{\hat{U}(t) \cdot \mathrm{e}^{\mathrm{j}\varphi_\mathrm{U}(t)} \cdot \mathrm{e}^{\mathrm{j}\omega t}\right\} = \mathrm{Re}\left\{\hat{\underline{U}}(t) \cdot \mathrm{e}^{\mathrm{j}\omega t}\right\} \text{ and} \\ \underline{Z}(t) &= Z(t) \cdot \mathrm{e}^{\mathrm{j}\varphi_Z(t)} \end{aligned} \tag{2.2}$$

with

$$\begin{aligned} &\hat{\underline{U}}(t) = \hat{\underline{I}} \cdot \underline{Z}(t) \text{ and} \\ &u(t) = \mathrm{Re}\left\{\hat{\underline{I}} \cdot \underline{Z}(t) \cdot \mathrm{e}^{\mathrm{j}\omega t}\right\} = \mathrm{Re}\left\{\hat{I} \cdot Z(t) \cdot \mathrm{e}^{\mathrm{j}(\omega t + \varphi_\mathrm{I} + \varphi_Z)}\right\} = \hat{I} \cdot Z(t) \cdot \cos(\omega t + \varphi_\mathrm{I} + \varphi_Z). \end{aligned} \tag{2.3}$$

Here ω is the angular frequency and φ the respective phase angle of $i(t), u(t)$, and $\underline{Z}(t)$. Again, the amplitude of $u(t)$ clearly reflects $\underline{Z}(t)$, i.e., reflects the conductive and dielectric behaviour of the considered tissue section.

Therefore, any temporal change in $R(t)$ or $\underline{Z}(t)$ is reflected by the induced biosignal $u(t)$, i.e., any increase in $R(t)$ or $|\underline{Z}(t)|$ increase the registered $u(t)$ and vice versa [(2.1) and (2.3)].

From a *physical point* of view,

- any *change in the spatial current distribution* within the tissue section—governed by geometrical boundaries present within the estimations for R (2.36) or $\underline{Z}$ (2.42)—and
- any *change in the electrical tissue properties*—governed by the local conductivity and permittivity present within the expressions for R or $\underline{Z}$—

determine the associated change in the registered amplitude of u, given a constant amplitude of i. In other words, any changes in *volume*, *conductivity*, and/or *permittivity* of the tissue section influence u.

From a *physiological point* of view,

- any *mechanical changes* in the *tissue morphology* such as shift in blood volume, shift in body fluid volume or lung water, or displacement of organs; as well as
- the presence of dynamic *physiological conditions* such as pulsating blood flow/volume in terms of cardiac activity, displaced and resized organs due to respiratory activity, respiratory-modulated stroke volume, and even blood flow velocity changes

produce changes in R or $\underline{Z}$ and thus changes in the registered u. For instance, an accumulation of conductive fluids within oedema yields reduction of $\underline{Z}$, whereas increasing velocity yields increase of $\underline{Z}$ due to elongated current pathways in-between adjacent red blood cells. Since blood is a good conductor and an important dielectric substance in tissue (Table 2.2), its volume fraction and pulsation determine significantly the instantaneous tissue conductivity and permittivity and thus determine significantly the momentary value of u.

In short, *cardiac component* of u reflects the regional blood perfusion while *respiratory component* reflects the regional air ventilation. *Cardiovascular* and *cardiorespiratory* properties can be assessed by u.

Measurements of static (or time-constant) and dynamic (time-varying) electrical properties of the body tissue can be performed via u. These properties can be basic properties, such as conductivity and/or permittivity, or clinically-relevant properties, such as the local perfusion level (Footnote 18). *Dynamic properties* of tissue reflect time-varying physiological functions that can be relatively easy revealed via induced biosignals. However, the measurement of *static properties* shows a restricted usability because of technological limitation (e.g., due to the time-varying electrode contact impedance) and the individual variability among tissue volumes (sampled by the permeating current i), which yields a large scatter of derived values.

Impedance Cardiography

Impedance cardiography is used for the registration of cardiac *blood shift*, especially for the registration of the absolute *stroke volume* (Patterson 1989; Malmivuo 1995; Mukkamala 2015). *Four skin electrodes* are typically applied. Two *current electrodes* are used for the *application of* i (e.g., 1 mA and 50 kHz): an upper electrode on the neck and a lower one on the abdomen. Another pair of *voltage electrodes* is used for the *registration of* u, one on the neck and another on the lower thorax located above the lower current electrode. Current electrodes form outer electrodes with respect to inner voltage electrodes.

Since the applied i follows the *path of least resistance*, the relatively thick *aorta with the conductive blood* inside can be expected to carry a significant amount of the total i flowing along the body axis. Please recall that blood is a better conductor

than the surrounding tissue (Table 2.2) so that the conductive i tends to travel through paths filled with blood, through the *blood-filled aorta*. Therefore when the aortic valve opens and the *systolic inflow* of highly conductive blood into the ascending aorta starts, the *thoracic impedance decreases* and thus the registered u becomes reduced in its amplitude.

Please note that the applied i does not travel in a straight line between both current electrodes (Fig. 2.57). Unfortunately, the low impedance current path of the chest wall shunts electric currents around the high impedance lungs, i.e., around instead of through the interior of the thorax. In other words, a significant portion of the induced current passes along the chest wall with relatively little current passing through the lungs and the interior. This shunting makes it difficult to attain a high *spatial resolution* of the interior, which is known as the *shunting effect of the wall*.

In addition, there are indications that changes in the blood volume in intrathoracic cardiovascular structures (e.g., in atria) other than the aorta are also likely to play a major role in the genesis of the waveform of u (Mukkamala 2015). Obviously, the specific current distribution depends strongly on the particular location of the applied electrodes, the tissue heterogeneity under the skin electrodes (Fig. 2.28), and the applied field properties (e.g., field frequency) determining the penetration depth of induced fields.

Impedance Pneumography

For monitoring of *lung function*, *impedance pneumography* can be used. Here impedance changes are evaluated with respect to the variation in the lung volume and in the pulmonary air flow (Seppa 2010). The total $\underline{Z}$ of the thorax varies mainly due to changes in the *lung volume*. *Inflated* and *deflated* lungs have already different electrical properties. As described in Section "Electrical Properties of Biological Tissue", deflated lungs exhibit increased conductivity and permittivity for field frequencies below β-dispersion, especially in the range of 10 kHz–100 MHz (Surowiec 1987).

Considering the flow of the part of the injected i through the lungs, it should be noted that the local *conductive currents* tend to *flow around alveoli* (along alveolar septum) but not directly through alveoli (Kaniusas 2012, Sect. 2.6). Again, the current i within the body seeks the *path of least resistance*, which is obviously given by the pathway through perfused conductive tissue in comparison with the optional pathway through the isolating alveolar air (Fig. 2.13). However, it can be expected that this tendency disappears with increasing field frequency since the contribution of *displacement currents* through the alveolar air to the total i through the lungs increases (2.42). During *inspiration*, alveolar volume increases, which stretches alveolar septum, prolongs the average current pathways around alveoli in the lungs, and thus increases the effective $|\underline{Z}|$ of the lungs (2.47). The reverse is true during *expiration*, during which the current pathways become shorter and thicker while $|\underline{Z}|$ decreases.

The *respiratory component* of u is much greater in amplitude than the *cardiac component*. The change in the thoracic $\underline{Z}$ by *pulsatile blood perfusion* is about one order of magnitude weaker than that induced by respiratory ventilation. For the

electrode pair at the neck and another pair at the upper abdomen (i.e., typical electrode application for the estimation of the stroke volume), the respiration component was 10–100 times greater than the cardiac component (Mukkamala 2015). This relationship imposes technical difficulties in the perfusion monitoring, especially in the derivation of cardiac-related parameters such as the stroke volume. However, the ratio between respiratory and cardiac components depends strongly on the application site of electrodes.

Body Impedance

Another application of induced biosignals comprises the measurement of the *body impedance* (Hong 2009; Grimnes 2008). It serves for the characterization of the composition and distribution of organic tissues and monitoring of their biological and physiological parameters. Not only the *whole human body* can be characterized by a set of electrical properties, but also separate biological tissues, and even *single cells*.

Again, four surface electrodes are typically used, where two of them are applied on the one foot sole and the other two on the other sole. The two outer electrodes provide i (e.g., 100 µA at 50 kHz) while the two inner electrodes permit measurement of u along the *foot-to-foot current path*. This current path permeats mainly the abdominal part of the body so that the measured impedance reflects, for instance, the *abdominal fat* portion (or the percentage body fat).

When limbs are involved in current pathways (Fig. 2.57), it should always be taken into account that the limb's cross-sections are typically much smaller than those of the trunk (Figs. 2.28 and 3.22). Therefore, limbs contribute much more to the total $\underline{Z}$ than the trunk. For instance, the magnitude $|\underline{Z}|$ of $\underline{Z}$ measured along the thigh-to-thigh path (around 30 Ω) was only about 10% of $|\underline{Z}|$ with the foot-to-foot current path (around 350 Ω) and hand-to-foot current path (around 400 Ω) (Hong 2009).

Two most common techniques for the *analysis of bioimpedance* are as follows (Gracia 2012):

- *Time domain analysis* with the time-varying impedance $\underline{Z}(t)$ as the final result. Here the time course in the variation of the tissue composition can be tracked by monitoring $\underline{Z}(t)$ over time. These tracked variations can be related to temporal changes in biological and physiological parameters to be derived. Typically, a single sinusoidal current $i(t)$ with a constant amplitude and *single frequency* ω is used as the system *stimulus*. The resulting variations of the registered magnitude $\left|\underline{\hat{U}}(t)\right| = \hat{U}(t)$ and the phase angle $\arg\left(\underline{\hat{U}}(t)\right) = \varphi_U$ of the sinusoidal voltage *response* $u(t)$ (2.2) reveal the quantitative and temporal changes of $\underline{Z}(t)$.
- *Frequency domain analysis* with the frequency-varying impedance $\underline{Z}(\omega)$ as the final result. The response of the system is assessed at *several individual* ω, i.e., $u(t)$ response to $i(t)$ is recorded at multiple ω. Multi-frequency response provides information about the composition of biological tissue. In an analogous way, the frequency response $\underline{Z}(\omega)$ can also be assessed by using a single wide-band excitation stimulus, e.g., a narrow impulse of $i(t)$ with a wide distribution of its spectral components, leading to a wide-band response in $u(t)$.

Impedance Tomography
This technique monitors the impedance distribution of small sub-sections of tissue using *multiple leads*. Leads are usually arranged in a *two-dimensional plane* (Fig. 1.3a), in order to

- resolve the spatial distribution of electrical properties,
- separate cardiac and respiratory components (in general, frequencies of cardiac and respiratory activities overlap (Nakesch 1994)), or simply
- remove (movement) artefacts.

Electrical impedance tomography can be used to register static structural data which resolve specific regions characterized by electrical properties that are different from surrounding tissues, known as *absolute electrical impedance tomography*. This tomography has the potential to differentiate between non-ventilated tissue areas containing pulmonary air and pathologically accumulated fluid (Leonhardt 2012). However, due to unknown electrode impedances and body boundaries, *time-difference electrical impedance tomography* is usually performed where a reference voltage is used. Moreover, *dynamic* variations of the aforementioned electrical properties can be monitored over time, known as *functional electrical impedance tomography*. For instance, the time course of lung inflation over respiration cycle can be assessed (*air ventilation/aeration*) as well as the spatial blood redistribution over cardiac cycle (*blood perfusion*). Provided electrodes for i and u are applied in a three-dimensional mesh (e.g., multiple rings of electrodes in different heights of the thorax, compare Fig. 1.3a), *three-dimensional electrical impedance tomography* can be realised, offering the three-dimensional conductivity distributions.

The methodology of electrical impedance tomography is applied in various biomedical fields such as monitoring of *regional pulmonary ventilation* in the thorax during intensive care or detection of breast tumors. For instance, regional ventilation correlates well with the regional changes in $Z = |\underline{Z}|$, whereas the change ΔZ in a certain spatial region of the lungs is linearly proportional to the corresponding lung volume change (Leonhardt 2012). In addition, mappings of the *regional blood perfusion* and the regional *ratios of the air ventilation to blood perfusion* are aimed at. The two-dimensional impedance tomography offers a non-invasive means of imaging the *internal conductivity distribution* within the body in vivo. Such distributions in the cross-section of the thorax—as shown in Fig. 1.3b—reveal, for instance, inflation status of the lungs which is highly useful to adjust/titrate settings of the artificial ventilation in intensive care units (Thürk 2017).

Experimental and clinical systems of the impedance tomography typically use 16 or 32 electrodes placed around the thorax and excited in the frequency range of about 50–200 kHz. The resulting *frame rate* amounts to 10 up to 50 images per second with the typical spatial resolution of 32 × 32 pixels (depends on the number of electrodes). Figure 1.3a shows a setting with 16 electrodes. The magnitude Z of $\underline{Z}$ is usually registered while neglecting the phase $\arg(\underline{Z})$ information. *Multifrequency tomography* has been also introduced, which can use up to 16 excitation

frequencies in the range of 10 kHz–1 MHz. Multiple frequencies are used to account for dispersion phenomena in tissues (Fig. 2.19) and thus to assess frequency-related changes of $\underline{Z}$ (Fig. 2.15).

The selection of the *oscillation frequency* of the injected current i is highly instructive. *Direct currents* are not used, especially in vivo, because of their harmful *electrolytic effects* developing over time (Fig. 2.84). In particular, irreversible electrochemical reactions at the electrode/tissue boundary have to be avoided where the charge neutrality of i is a prerequisite (Section "Charge Transfer During Stimulation"). Thus *alternating currents* in the *typical frequency range* from 20–200 kHz are used, which is a true *compromise*:

- Firstly, *neuromuscular excitation* has to be avoided. The lower limit of the frequency range is thus set by the *strength-frequency curve* of sinusoidal stimuli. As illustrated in Fig. 2.74, the safe level of the amplitude of i (stimulation threshold) increases with its increasing oscillation frequency above about 1 kHz, so that the *minimum frequency* of 20 kHz is selected to avoid neuromuscular stimulation. Please note that the increasing threshold for very low frequencies below about 10 Hz (Fig. 2.74) is not reasonable for tomography since electrolytic effects would start to develop with progressively decreasing frequency in this range. On the other hand,
- prominent *contrasts in electric properties*, conductivity and permittivity, of monitored tissues of interest should be present. The heterogeneity in electric properties of different tissues should be present for the reasonable use of induced biosignals. For instance, pulsating blood can yield significant changes in the amplitude of u only as long as the electric properties of blood and those of the surrounding tissue are different. Identical conductivities and permittivities would necessarily discard any pulsatile change in the amplitude of u over the cardiac cycle. These contrasts in properties clearly disappear with increasing frequency—in a step-wise manner according to Figs. 2.20 and 2.21—so that the *maximum frequency* of i is set to about 200 kHz. In other words, increasing field frequency progressively equalises permittivities and conductivities of different tissues within the body permeated by i, whereas the attainable *spatial resolution* of heterogeneous tissue sections decreases. In addition,
- increasing field frequency typically decreases the *inner resistance* of the *current source* for i (Gaggero 2012). The current source—with an ideally infinite inner resistance to keep the amplitude of i ideally constant in time irrespective of the time-varying load $\underline{Z}$ (2.3)—becomes less ideal with increasing frequency. Not only the amplitude of u but also that of i start to depend on $\underline{Z}$. Furthermore, the unknown and time-varying *contact impedances* of the current electrodes (Fig. 3.19) begin to influence u, forming the associated *movement artefacts*. This behaviour sets a reasonable *maximum frequency* of available tomographic systems to about 200 kHz. Furthermore,
- increasing field frequency short-circuits favourably *contact impedances* of the current and voltage electrodes. This favours both an easier injection of i into the

body (given a non-ideal current source) and a more precise measurement of u (given a non-ideal voltmeter). Finally,

- increasing frequency increases the *time resolution* and the achievable *frame rate*. This is particularly relevant when *multiple electrodes* and *multiple frequencies* are used so that the absolute time becomes a valuable resource.

The selected *oscillation frequency* determines also the *permissible amplitude* of the *current i* since neuromuscular and thermal effects have to be avoided. An increasing frequency allows injection of *larger i* into the body with still absent *neuromuscular effects* (Fig. 2.74). However, *thermal effects* become more likely with increasing strength of *i*. Both neuromuscular and thermal effects are accounted for by the applicable *reference levels* of contact currents (Fig. 2.87) which should not be exceeded by the effective amplitude of *i*. For instance, the reference level is 10 mA for 50 kHz (or 2 mA for 10 kHz, see Fig. 2.87), whereas a much lower level of 1 mA at 50 kHz is typically used in clinical practice. Obviously, the *signal-to-noise ratio* favourably increases with an increasing level of *i*.

The attained *spatial resolution* of the conductivity distribution is in the range 1.5–10% of the dimension of the volume conductor (Malmivuo 1995). The resolution is limited by the *distance between electrodes* on the thorax (in the range of 2–3 cm (Leonhardt 2012)) and improves with increasing *number of electrodes* and with increasing *signal-to-noise ratio*.

It is important to amend that the induced electric fields within biological tissue can be focussed or localized to a size no smaller than the wavelength of the field. There is always a compromise between the penetration depth and attained spatial resolution.

- The *penetration depth* of the field into tissue decreases (and the attenuation increases) with increasing frequency (Fig. 2.6), whereas
- the *spatial resolution* of tissue structures increases with increasing frequency and the decreasing wavelength (2.123);

for more details see Sect. 3.1.

The *reconstruction* of the conductivity distribution out of the measured u is an *inverse problem* which solution is far from straightforward and may yield different results. Therefore, numerous assumptions are typically met such as (i) circular, averaged or individual shape of the cross-section to be reconstructed, (ii) a typical conductivity mesh of the cross-section with only small spatial changes within, (iii) electrodes located on a plane and spaced at equal distances, and (iv) at least two-dimensional current density field.

Contact-Less Assessment

Artificially induced biosignals can be coupled into the body and, after being modulated within the body (see $\underline{Z}_1$ in Fig. 1.2b), can be coupled back out of the body for recording purposes via two different coupling mechanisms, namely,

- *contact-based* coupling (galvanic coupling, see Fig. 1.3a) and
- *contact-less* coupling (capacitive coupling, see Fig. 3.31b);

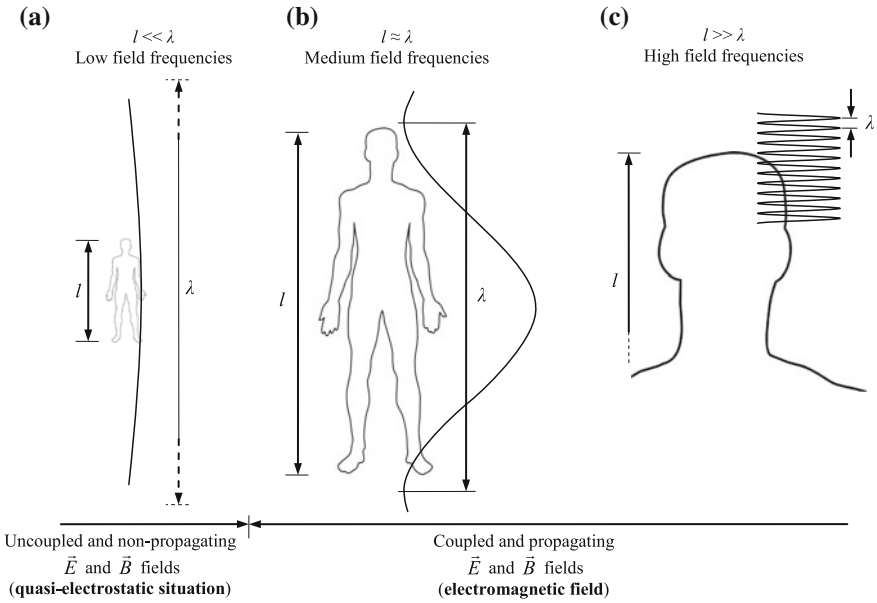

Fig. 2.2 Characteristics of fields as a function of the relationship between the (maximum) dimension l of the human body (of interest) and the field wavelength λ. **a** Uncoupled and non-propagating electric $\vec{E}$ and magnetic $\vec{B}$ fields at relatively low field frequencies f below MHz range (i.e., the coupling time-derivatives of $\vec{E}$ and $\vec{B}$ fields (proportional to f) are insignificant in their size, see Section "Incident Electromagnetic Fields"). The inequality $l \ll \lambda$ applies (2.52). **b** Coupled and propagating $\vec{E}$ and $\vec{B}$ fields above the MHz range, whereas the equality $l \approx \lambda$ applies. *c* Strongly coupled and propagating $\vec{E}$ and $\vec{B}$ fields in the even higher frequency range, whereas the inequality $l \gg \lambda$ applies

That is, not only contact electrodes (Fig. 3.1b, c) can be used for field coupling but also remote electrodes (Fig. 3.1a). The higher is the *field frequency* of the induced biosignal, the more efficient is the contact-less coupling of emanating electromagnetic fields into and out of the body (Fig. 2.2).

For *contact-less coupling*, fields are induced via *displacement currents*, e.g., via currents between two plate electrodes that face the skin and are located in a distance from the skin (Teichmann 2013). *Capacitors* are formed by both electrodes with the skin and biological tissue underneath, whereas tissue acts as a *lossy dielectric medium*. Displacement currents are coupled over these capacitors to and back from the medium. Conductive and dielectric properties of the medium—permeated by the remotely-induced current—and the spatial distribution of these properties vary in the course of *cardiovascular and cardiorespiratory activity* (e.g., due to motions of inner organs or local blood perfusion changes). These variations change capacitor properties and thus the characteristics of displacement currents

(amplitude, phase and direction) between electrodes or the characteristics of the associated voltage drop between electrodes; as a basis for the registered induced biosignal.

2.3 Transmission of Electric Signals

The *transmission of electric biosignals* throughout biological tissue—in addition to their genesis—comprises *formations aspects* of electric biosignals, according to the model of electric biosignals (Fig. 1.2). The transmission path of electric biosignals through tissue begins with the *electric source*. Please recall that

- *permanent biosignals* within tissue are generated by *endogenous electric sources* within the body (Fig. 1.2a); e.g., by muscle fiber in Fig. 1.1. In contrast,
- *induced biosignals* within tissue are generated by *external electric sources* in contact with the body (Fig. 1.2b). For instance, an artificial current is induced within tissue in Fig. 1.3a while the resulting voltage drop along the current path serves as an induced biosignal.

Starting at the source level, biosignals propagate through tissue along multiple paths and are subjected to changes in their intensity. Here *volume effects* in terms of conduction and polarization, relaxation and dispersion, charge and current induction, as well as electromagnetic induction are relevant. In addition, *inhomogeneity effects* significantly add to intensity changes of biosignals when they pass boundaries within heterogeneous tissues. These effects are related to boundary conditions along the propagation path and to scattering, diffraction, reflection, refraction and even to resonance. In fact, a large percentage of the biosignal intensity dissipates on the way and never reaches the skin surface where usually electrodes are located to register and record biosignals (Fig. 1.2).

Propagating biosignals within tissue

- may become *modulated by physiological activities* (as favourably used in *diagnosis*) and/or
- may *generate different physiological effects* as neuromuscular excitation or local heating (as deliberately used in *therapy*).

Therefore, possible *adverse health effects* of biosignals within tissue should be taken into account.

2.3.1 Propagation of Electric Signals

The *electric field* $\vec{E}$ and *magnetic flux density field* $\vec{B}$ can be *independently evaluated* with respect to their spread in tissue and their biological effects as long as they do not generate each other (Section "Incident Electromagnetic Fields").

Independent $\vec{E}$ and $\vec{B}$ fields are said to be *decoupled* and so they *can not propagate* as a wave within tissue (see below). Decoupled fields fulfil the so-called *quasi-electrostatic condition* from (2.52) (Footnote 15). In particular, *low frequencies* and/or *small geometrical size* of exposed objects of interest are required for the existence of decoupled fields. Interestingly, a fixed relationship between $\vec{E}$ and $\vec{B}$ is also missing in the *near field* (Footnote 5). For decoupled fields, *electrical equivalent circuit models*—as illustrated in Fig. 2.26b—can be simply used to model the behaviour of the exposed human body located within $\vec{E}$ and/or $\vec{B}$ fields.

Coupled $\vec{E}$ and $\vec{B}$ fields form the so-called *electromagnetic field* or *electromagnetic wave* (Fig. 2.2b, c). Within the wave, $\vec{E}$ and $\vec{B}$ fields mutually induce each other. Here the significant *time derivative* of one *high frequency field* acts as a source of the other high-frequency field; please recall that the derivative is proportional to the absolute value of the *frequency f* (Section "Incident Electromagnetic Fields"). In fact, this *mutual induction* or *mutual coupling* helps both fields in their *joint propagation* through tissue as a joint electromagnetic wave.

Figure 2.2a illustrates *uncoupled fields* $\vec{E}$ and $\vec{B}$ with the wavelength λ being much larger than the dimension $l(\ll\lambda)$ of the exposed body, i.e., the quasi-electrostatic condition in (2.52) is fulfilled. With increasing f of fields in Fig. 2.2b, the size of λ decreases (2.5) towards $\lambda \approx l$ and the quasi-electrostatic condition fails. The fields $\vec{E}$ and $\vec{B}$ *become coupled* and thus able to *propagate jointly* as a *wave*. In biological tissue, mutual coupling starts in MHz region with the associated λ in the range of the body size and its organs (see example below). Figure 2.2c depicts also the condition $\lambda \ll l$ for the highest f with the *intimately coupled* $\vec{E}$ and $\vec{B}$ fields. In particular, the associated λ is much smaller than dimensions of the body and its organs when *optical frequencies* are considered; here $\vec{E}$ and $\vec{B}$ fields propagate more like *rays*. Whether $\vec{E}$ and $\vec{B}$ fields are mutually coupled or not, it has a significant impact on the coupling efficiency of external fields down into the body (Fig. 2.33) and, on the other hand, on the radiation of fields out of the body (Fig. 3.31).

When the propagation *medium is unbounded*, the electromagnetic wave propagates as the so-called *transverse electromagnetic*[4] (TEM) *wave*, *TEM field*, or *TEM*

[4]In the *transverse electromagnetic (TEM) wave*, $\vec{E}$ and $\vec{B}$ field components at every point in space are contained in a *plane* and are *perpendicular* to the *propagation direction of the wave*. If the space orientation of these planes is the same—i.e., planes are parallel—then TEM wave forms the so-called *plane wave*, as shown in Fig. 2.3. If in addition to the presence of parallel planes, the amplitudes of $\vec{E}$ and $\vec{B}$ do not vary over each plane then TEM wave forms the so-called *uniform plane wave* (Fig. 2.3).

In contrast, if these *planes* with $\vec{E}$ and $\vec{B}$ components *are not aligned to each other*, a *spherical wave* can be formed by TEM wave, as illustrated in Fig. 2.4. Please observe misaligned planes at the regions A and C spanned by the corresponding unit vectors $\vec{e}_E$ and $\vec{e}_B$ (Fig. 2.4).

mode, as illustrated in Figs. 2.4 and 2.3. Here *far field*[5] conditions apply. The unbounded medium implies that there are *no specific boundary conditions* the propagating wave should meet. For instance, a bounded propagation applies for the

[5]*Near field* or near electromagnetic field is the region close to a source where $\vec{E}$ and $\vec{B}$ fields *are not necessarily perpendicular* to each other. In addition, near fields are mostly reactive, i.e., there is a local *out-of-phase propagation* of $\vec{E}$ and $\vec{B}$ fields. In other words, maxima and minima of $\vec{E}$ and $\vec{B}$ fields occur at different spatial points along the propagation direction, whereas these maxima and minima overlap in far field; compare Fig. 2.3.

Near field conditions may create *almost pure* $\vec{E}$ *fields* in some regions and *almost pure* $\vec{B}$ *fields* in other regions along the propagation direction. Therefore, the *wave impedance* Z—as the quotient of the amplitudes of $\vec{E}$ and $\vec{B}$ fields (2.10)—may vary throughout space, indicating highly inhomogeneous field structure in near field. There may be substantial variations of Z in near field from the space-independent Z in far field. In near field, the *inverse square law* [Footnote 9 and (2.14)] does not apply.

The *power density* (2.13) is not useful in near field as a descriptive quantity because there is no fixed relationship between the local $\vec{E}$ and $\vec{B}$ fields. In other words, the size of Z in (2.13) varies from one point to another. The *specific energy absorption rate* (2.58) is also highly non-uniform in space.

Near fields often vary more rapid with the *distance* r from the source than far fields. In particular, the amplitude of *near field declines* with factors $1/r, 1/r^2, 1/r^3$, and with even higher-order terms.

Far field conditions usually refer to plane TEM waves or spherical TEM waves (Footnote 7), where the radiation pattern does not change with r. In contrast to near field, higher-order terms $1/r^2$ and $1/r^3$ become negligible in far field at greater r compared with the remaining $1/r$ term in the spherical TEM wave (used as a possible transition condition from near to far field, see below). In fact, the higher-order terms decay much faster towards zero with increasing r than the term $1/r$. The *inverse square law* applies [Footnote 9 and (2.14)].

The largest dimension l of the *source antenna* and the wavelength λ determine the *distance r from the source to the onset of far field*, whereas this distance r is usually required to be larger than l and larger than λ.

- For *large antennas* satisfying $l > \lambda$, *far field approximately begins* for the distance

$$r > \frac{2 \cdot l^2}{\lambda}$$

  out to infinity.
- For *small antennas* with $l < \lambda$, *far field condition* can be derived where the $1/r$ and $1/r^2$ terms of $\vec{E}$ and $\vec{B}$ fields radiated by an electric dipole antenna become equal:

$$r > \frac{\lambda}{2\pi}.$$

  Please note that this case with $l < \lambda$ is usually applicable for electric biosignals in biomedical applications with the relatively small l and large λ.

Please note that the boundary for the onset of far field moves in space with the frequency of the antenna's emissions (2.5).

Obviously, the physical transition from near field to far field is not sharp but rather gradual, whereas the region of this transition depends strongly on the particular requirement used. Typical requirements are the $1/r$ and $1/r^2$ terms are already equal, Z is already constant with increasing r, or phase differences from different antenna's regions are already below a certain limit (of about $\pi/8$).

wave propagation between two conductive plates or along a coaxial cable, which set specific boundary conditions for $\vec{E}$ and $\vec{B}$ fields and thus excludes TEM wave as a potential propagation mode.[6] As the name of TEM wave already indicates, the mutually coupled $\vec{E}$ and $\vec{B}$ fields within TEM wave oscillate perpendicular to each other and perpendicular to the propagation direction $\vec{e}$ of the wave. The directions of the triplet $\vec{E}$, $\vec{B}$, and $\vec{e}$ are mutually *right-angled* and *right-handed*—see Figs. 2.3, 2.4, and 2.33—as can also be derived from the vector product in (2.4). Please note that both *lossless and lossy media* can carry TEM waves, whereas *biological tissues* represent typically lossy media. In general, *TEM waves* can propagate as *plane waves* or *spherical waves*.[7]

For *lossless media*, the simplest TEM wave results in which the perpendicular and associated $\vec{E}$ and $\vec{B}$ fields *oscillate in-phase* to each other, with

[6]Besides TEM mode, the electromagnetic field can also propagate in *other modes*. A mode is a particular configuration of the electromagnetic field which fulfils both

- *wave equations* and
- applicable *boundary conditions* (Fig. 2.34).

[7]*TEM wave*—in *far field* with the assumed *constant characteristics* v, λ, and Z throughout space—can propagate in different ways which can be approximated as

- *spherical wave* (Fig. 2.4) or
- *plane wave* (Fig. 2.3).

In the *spherical wave*, as illustrated in Fig. 2.4, the corresponding *wavefronts* (Footnote 10) propagate radially *outwards and uniformly in all directions* out from a small and relatively close *point source*. That is, wavefronts in spherical waves have *spherical surfaces*. The fields $\vec{E}$ and $\vec{B}$ composing the spherical TEM wave are perpendicular to each other and to the propagation direction, oscillate in-phase, and are tangential to spherical wavefronts (Fig. 2.4). On any spherical surface—for a given distance from the source or for a given radius of this surface—the fields $\vec{E}$ and $\vec{B}$ are necessarily the same. Even though the propagation *medium is lossless*, the amplitudes of $\vec{E}$ and $\vec{B}$ fields in the spherical wave decrease along the propagation distance $\vec{e}$ (Fig. 2.4). Here the *inverse square law* applies (Footnote 9). In practice, spherical waves are often summed to produce realistic TEM waves emanating by field sources residing relatively close to the field point of interest.

The *plane wave*, as illustrated in Fig. 2.3, has characteristics *similar to the spherical wave*, especially at field points far from the dedicated source of the spherical wave. Here, the curvature of the spherical wavefront—i.e., the reciprocal of the radius of the considered wavefront or reciprocal of the distance from the source to the considered field point—becomes so small that the resulting spherical wavefront appears to be almost planar. Figure 2.4 illustrates a *large curvature* $1/r_2$ of a wavefront close to the source versus a *small curvature* $1/r_1$ ($<1/r_2$) of a *more planar wavefront* more distant from the source. In the plain wave, the fields $\vec{E}$ and $\vec{B}$ oscillate in-phase perpendicular to each other and perpendicular to the propagation direction $\vec{e}$ of this wave (Fig. 2.3). In contrast to the *spherical wave*, the *amplitudes* of $\vec{E}$ and $\vec{B}$ fields within the *plain wave* remain constant along the propagation distance in *lossless medium*. In fact, the plane wave is a good approximation of TEM field in *far field*, i.e., far from the field source (Footnote 5).

The *spherical wave* and *plane wave* move with their troughs and crests along the propagation path. Please compare the propagating $\vec{E}$ in Fig. 2.3 for the later time instant $t = t_0$ (>0) running forward with respect to $\vec{E}$ at the earlier $t = 0$.

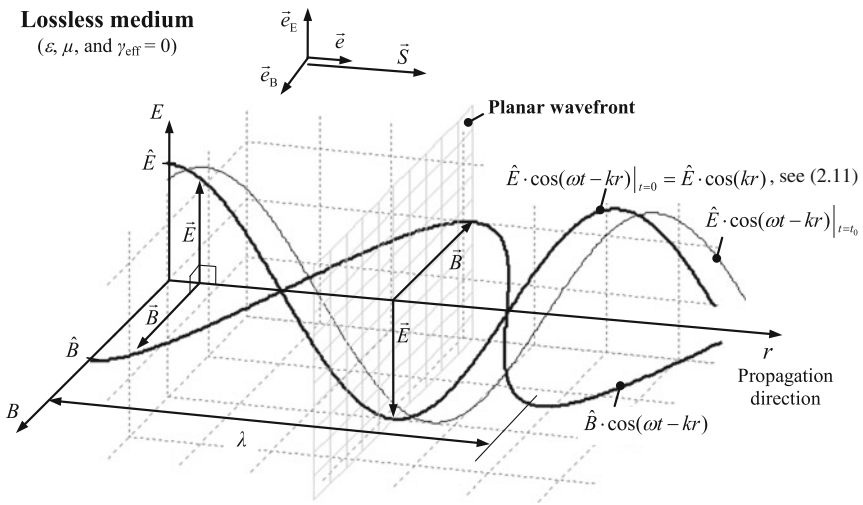

Fig. 2.3 Transverse electromagnetic (TEM) wave in far field as a uniform plane wave which approximates the spherical wave (Fig. 2.4) for large distances r from the field source. The TEM wave with its wavelength λ propagates in unbounded lossless medium. The electric field $\vec{E} = E \cdot \vec{e}_E$ pointing in the direction $\vec{e}_E$ is intimately coupled—via (2.4)—with the magnetic flux density field $\vec{B} = B \cdot \vec{e}_B$ in the direction $\vec{e}_B$. Both fields oscillate in-phase and perpendicular to each other, and perpendicular to the propagation direction $\vec{e}$ of TEM wave along the coordinate r. The traveling $\vec{E}$ wave over time is indicated as a function of r for the two time instants $t = 0$ and $t = t_0$ (>0)

$$\vec{e} \times \vec{E} = Z \cdot \frac{\vec{B}}{\mu}. \tag{2.4}$$

Here $\vec{e}$ is a unit vector pointing in the *propagation direction* of TEM wave, μ the magnetic permeability of the propagating medium, and Z the *wave impedance*. It is instructive to recognise that Z is given as the *ratio* of the amplitude E (of $\vec{E}$ field component) and the corresponding weighted amplitude B/μ (of the orthogonal magnetic field $\vec{B}/\mu$ component). From a practical point of view, (2.4) allows—in contrast to decoupled $\vec{E}$ and $\vec{B}$ fields—to calculate the corresponding $\vec{B}$ field out of the measured $\vec{E}$ field within the electromagnetic wave, and vice versa.

While for *lossless media* Z is a *real quantity* (2.10), for *lossy media* the wave impedance $\underline{Z}$ becomes a *complex quantity* (2.19). Complex vector amplitudes $\vec{E}$ and $\vec{B}$, and the complex $\underline{Z}$ in (2.4) would imply an *out-of-phase oscillation* of the associated *sinusoidal* $\vec{E}$ and $\vec{B}$ fields in *lossy media* (Kaniusas 2012, Footnote 145). Please compare lossless and lossy cases in Table 2.1.

The *electromagnetic wave* propagates in any medium with the *propagation velocity* v (also known as phase velocity, a *time-spatial* characteristic), oscillates with the frequency f in the time domain (a *time* characteristic), and oscillates with the wavelength λ along its propagation path (a *space* characteristic) according to

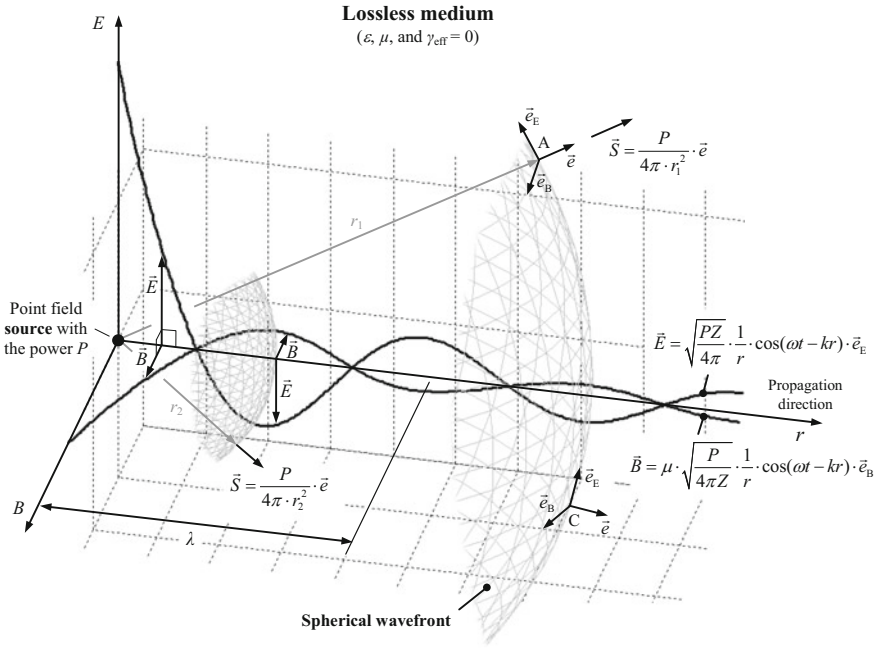

Fig. 2.4 Transverse electromagnetic (TEM) wave in far field as a spherical wave with its source located at the distance $r = 0$ (within near field) and the source power P; this wave mutates into a plane wave (Fig. 2.3) for large r from the field source. The TEM wave with its wavelength λ propagates in unbounded lossless medium. The two coupled fields, the electric field $\vec{E} = E \cdot \vec{e}_E$ and the magnetic flux density field $\vec{B} = B \cdot \vec{e}_B$ are shown for a single time instant (2.4). Both fields oscillate in-phase and perpendicular to each other, and perpendicular to the propagation direction $\vec{e}$ of TEM wave along the coordinate r. Instant values of $\vec{E}$ and $\vec{B}$ fields decay with $1/r$ due to the inverse square law (Footnote 9) while the associated power density $\vec{S}$ decays with $1/r^2$ (2.14); equations are valid for far field only

$$v = \lambda \cdot f = \frac{\omega}{k}. \tag{2.5}$$

Here ω is the *angular frequency* with $\omega = 2\pi \cdot f = 2\pi/T$, k the *wavenumber* or *phase constant* with $k = 2\pi/\lambda$, and T the time period. In other words,

- ω can be seen as the *temporal angular frequency* while
- k as the *spatial angular frequency*.

When wave radiates from one medium into another (Fig. 2.42), *electric and magnetic properties* of the respective medium will determine the respective v and λ [(2.6), (2.7) and (2.16), (2.15)]. Please note that the frequency f acts as a *fundamental quantity* that does not change when the radiation passes from one medium into another; however, the linearity of media is required here. In other words, the local size of λ depends on the local v, and vice versa.

Table 2.1 Propagation parameters of the transverse electromagnetic field in lossless medium (2.11) and lossy medium [such as biological tissue, see (2.20)] as a function of electrical properties of media and field frequency

Wave propagation parameters	Lossless medium ($\gamma_{\text{eff}} = 0$)	Lossy medium	
		Predominant dielectric medium [$\gamma_{\text{eff}} \ll \omega \cdot \varepsilon$, see (2.72)]	Predominant conductive medium [$\gamma_{\text{eff}} \gg \omega \cdot \varepsilon$, see (2.71)]
Wavenumber/phase constant k (rad/m)	$\omega\sqrt{\mu\varepsilon}$		$\sqrt{\frac{\omega\mu\gamma_{\text{eff}}}{2}}$
Propagation velocity v (=ω/k) (m/s)	$\frac{1}{\sqrt{\mu\varepsilon}}$		$\sqrt{\frac{2\omega}{\mu\gamma_{\text{eff}}}}$
Wavelength λ (=$2\pi/k$) (m)	$\frac{2\pi}{\omega\sqrt{\mu\varepsilon}}$		$2\pi\sqrt{\frac{2}{\omega\mu\gamma_{\text{eff}}}}$
Wave impedance $\underline{Z}$ (2.19) (Ω)	$\sqrt{\frac{\mu}{\varepsilon}}$		$\sqrt{\frac{\omega\mu}{2\gamma_{\text{eff}}}} \cdot (1+j)$
Skin depth δ [=1/α, (2.21)] (m)	∞	$\frac{2}{\gamma_{\text{eff}}} \cdot \sqrt{\frac{\varepsilon}{\mu}}$	$\sqrt{\frac{2}{\omega\mu\gamma_{\text{eff}}}}$

Data adopted from Balanis (1989)

Biological Tissue

Let us qualitatively and quantitatively consider λ, v, and Z within *biological tissue* when it is *transversed by the electromagnetic wave*. In general,

- the *wave's size* $\lambda(= v/f)$ in tissue becomes shorter than $\lambda_0(= v_0/f)$ in free space —with v_0 as the speed of light in vacuum of $3 \cdot 10^8$ m/s (2.8). Thus the inequality $\lambda < \lambda_0$ applies. For λ in *lossless case* ($\gamma_{\text{eff}} = 0$) see (2.7), whereas λ in *lossy case* ($\gamma_{\text{eff}} > 0$) is given by (2.16). The reduced λ of the coupled field into the biological body—as compared with λ_0 of the incident field outside the body —has significant consequences when inner fields interact with inner body structures of certain dimensions (such as organs). An example in Fig. 2.48 illustrates the relevance of the thickness of the fat layer in terms of the local energy deposition. In analogy,
- the *wave's speed* v in tissue is less than v_0; the inequality $v < v_0$ applies. For v in *lossless case* ($\gamma_{\text{eff}} = 0$) see (2.6), whereas v in *lossy case* ($\gamma_{\text{eff}} > 0$) is given by (2.15).
- The *wave's impedance* Z in biological tissue is less than Z_0 in free space. Equation (2.10) applies in *lossless case* while (2.19) in *lossy case*.

From a biophysical point of view, inequalities $\lambda < \lambda_0$, $v < v_0$, and $Z < Z_0$ apply because

- the *dielectric permittivity* $\varepsilon(\gg \varepsilon_0)$ of biological tissue is much higher than ε_0 in free space (Table 2.2) and, on the other hand,
- tissue has a non-zero *effective conductivity* $\gamma_{\text{eff}}(> 0)$.

In other words, *dielectric and conductive tissues slow down propagating waves.*

Table 2.2 Typical electrical properties of different physical and biological media for the field frequencies 50 Hz and 1 MHz; compare Figs. 2.20 and 2.21

Medium	Density ρ (kg/m^3)	Relative permittivity ε_r (1)	Effective conductivity γ_{eff} (S/m)	Attenuation coefficient α (1/m)	Relative permittivity ε_r (1)	Effective conductivity γ_{eff} (S/m)	Attenuation coefficient α (1/m)
		for 50 Hz			for 1 MHz		
Air	1.2	1	10^{-15}–10^{-14}	>1/10^{11}	1	10^{-15}–10^{-14}	>1/10^{11}
Water	1000	74	3	1/41	74	3	1/0.29
Blood	1057	$5.26 \cdot 10^3$	0.7	1/85	$3.03 \cdot 10^3$	0.82	1/0.61
Muscle	1050	$1.77 \cdot 10^7$	0.23	1/163	$1.84 \cdot 10^3$	0.5	1/0.79
Fat	900	$1.47 \cdot 10^6$	0.0196	1/564	27	0.0251	1/3.27
Bone (cortical)	1700	$8.87 \cdot 10^3$	0.02	1/503	144	0.024	1/3.83
Lung (deflated)	0.35	$8.69 \cdot 10^5$	0.2	1/160	$1.17 \cdot 10^3$	0.33	1/0.97

The relative dielectric permittivity ε_r and effective conductivity γ_{eff} are mainly taken from IFAC (2013), Gabriel (1996a), De Marco (2012), Furse (2009), Pawar (2009). The associated attenuation coefficient $\alpha = 1/\delta$ is inversely related to the skin depth δ (Fig. 2.6) and is calculated based on (2.21). Density ρ values are accumulated from different sources and are listed for comparison

For instance, at f = *300 MHz*, the size of λ *in muscle* amounts to only 12.3 cm as compared with 100 cm (=3 · 10^8 m/s / 300 MHz = λ_0) in free space. In fact, the value of 12.3 cm applies for muscle when considered as *lossy medium* (2.16) with numerical data from Figs. 2.20 and 2.21 (with $\varepsilon_r \approx 58$ and $\gamma_{eff} \approx 0.77\,S/m$). A larger value of 13.1 cm results for muscle approximated as *lossless medium* [(2.7) or (2.16) with $\gamma_{eff} = 0$]. As noted above, the non-zero γ_{eff} decreases the effective λ in tissue from 13.1 to 12.3 cm.

For comparison, the size of v *in muscle* at 300 MHz amounts to 3.69 · 10^7 m/s (<3 · 10^8 m/s in free space) when considering muscle as *lossy medium* (2.15). In analogy, a larger value of 3.94 · 10^7 m/s results when approximating muscle as *lossless medium* (2.17). The impedance magnitude Z *in muscle* at 300 MHz equals about 43.7Ω for *lossy muscle* (2.19) and increases to about 49.5Ω for *lossless muscle* (2.10), as compared with 377 Ω in free space.

Please note that the resulting λ_0 = 1 m in free space for the relatively high frequency of 300 MHz is already comparable with the size of the erect human body. Within the body, the size of λ is even in the lower range of about 12 cm and thus is comparable with the size of inner organs or extremities. That is, *coupling and joint propagation* of $\vec{E}$ and $\vec{B}$ fields can already be expected at the considered f of 300 MHz.

When we increase f to *2.4 GHz*, the estimated $\lambda = \lambda_0$ amounts to 12.5 cm in the *air* [with $\varepsilon_r = 1$ in (2.7)] while the level of λ within *muscle* decreases to even 1.7 cm (with the frequency-dependent $\varepsilon_r \approx 53$ in (2.7) for *lossless medium*, see Fig. 2.20 at 2.4 GHz). For the tenfold f of *24 GHz*, $\lambda = \lambda_0 \approx 12.5$ mm applies in the air and $\lambda \approx 2.4$ mm in muscle (with $\varepsilon_r \approx 26$ in (2.7) for lossless medium, see Fig. 2.20 at 24 GHz).

2.3.1.1 Lossless Medium

Lossless propagation of $\vec{E}$ and $\vec{B}$ fields forming *electromagnetic wave* is given in *lossless media* with the zero *effective conductivity* $\gamma_{eff} = 0$ (2.82). That is, there is

- *no medium-related damping* of the wave (Kaniusas 2015, Fig. 4.22), whereas the wave
- may still obey the *geometry-related damping* (due to the *inverse square law*, see Footnote 9).

Therefore, the lossless propagation does not generally imply constant *amplitudes of* $\vec{E}$ and $\vec{B}$ fields along the propagation pathway. For instance, Fig. 2.4 depicts the case of a *spherical TEM wave* (Footnote 7) in lossless medium with *vanishing amplitudes* with increasing propagation distance. In contrast, Fig. 2.3 depicts another case of a *plane TEM wave* (Footnote 7) in lossless medium with *constant amplitudes* of $\vec{E}$ and $\vec{B}$ fields along the propagation distance.

The *propagation velocity* v and *wavelength* λ (2.5) in *lossless medium* amounts to

$$v = \frac{1}{\sqrt{\mu \cdot \varepsilon}} = \frac{v_0}{\sqrt{\mu_r \cdot \varepsilon_r}} \approx \frac{v_0}{\sqrt{\varepsilon_r}} \tag{2.6}$$

and

$$\lambda = \frac{1}{f \cdot \sqrt{\mu \cdot \varepsilon}} = \frac{v_0}{f \cdot \sqrt{\mu_r \cdot \varepsilon_r}} = \frac{\lambda_0}{\sqrt{\mu_r \cdot \varepsilon_r}} \approx \frac{\lambda_0}{\sqrt{\varepsilon_r}} \tag{2.7}$$

with

$$v_0 = \frac{1}{\sqrt{\mu_0 \cdot \varepsilon_0}} \approx 3 \cdot 10^8 \text{ m/s} \quad \text{and} \quad \lambda_0 = \frac{1}{f \cdot \sqrt{\mu_0 \cdot \varepsilon_0}}, \tag{2.8}$$

as summarised in Table 2.1. Here ε is the dielectric permittivity of medium, μ the magnetic permeability of medium, whereas μ_r and ε_r are the relative permeability and relative permittivity, respectively. The constant ε_0 is the free space permittivity (=8.85 · 10^{-12} F/m) and μ_0 is the free space permeability ($\mu_0 = 4\pi \cdot 10^{-7}$ H/m). The speed v_0 is v of the *electromagnetic wave in free space* or in the *air* (with $\varepsilon_r = 1$ and $\mu_r = 1$), whereas, by analogy, the wavelength λ_0 is λ in the air.

Therefore, properties v and λ of waves *transversing lossless medium* are governed by electrical properties ε and μ of this propagation medium, and the field frequency f. Since $\varepsilon_r \gg 1$ (Table 2.2) and $\mu_r \approx 1$ (Footnote 17) apply in *biological tissue*, the aforementioned inequalities $v < v_0$ and $\lambda < \lambda_0$ are valid in pure *dielectric tissue*, as illustrated in Fig. 2.5. In other words, dielectricity *slows down* the *wave propagation* while *reducing the spatial spread* of a single wave cycle.

The associated *wavenumber* k (2.5)—the *spatial frequency* of travelling waves in *lossy media*—obeys

$$k = \frac{2\pi}{\lambda} = \frac{\omega}{v} = \omega \cdot \sqrt{\mu \cdot \varepsilon}. \tag{2.9}$$

The value of k increases with increasing ε_r. *Wavefronts* become *spatially accumulated* in a *high-permittivity medium* (with $\varepsilon_r \gg 1$) in comparison with free space. Here accumulated *planes of constant phase* shorten λ in dielectric tissue (2.7).

The associated *wave impedance* Z as the *quotient* of peak values of $\vec{E}$ and $\vec{B}$ fields (2.4) is *real-valued* and equals

$$Z = \frac{\hat{E}}{\hat{B}/\mu} = \sqrt{\frac{\mu}{\varepsilon}} = \sqrt{\frac{\mu_0}{\varepsilon_0}} \cdot \sqrt{\frac{\mu_r}{\varepsilon_r}} = Z_0 \cdot \sqrt{\frac{\mu_r}{\varepsilon_r}} \approx \frac{377\ \Omega}{\sqrt{\varepsilon_r}} \quad \text{with } Z_0 = \sqrt{\frac{\mu_0}{\varepsilon_0}}. \tag{2.10}$$

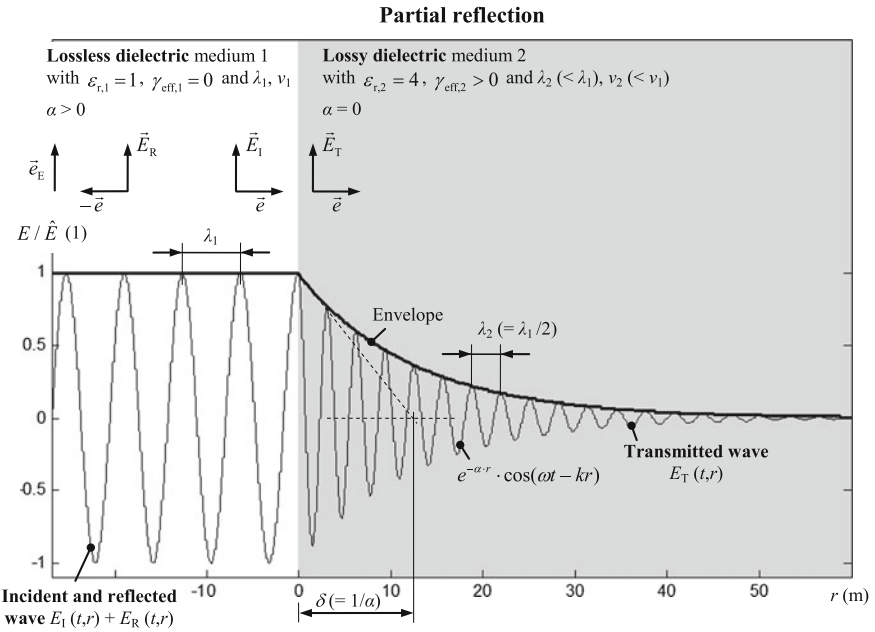

Fig. 2.5 The electric field $\vec{E} = E \cdot \vec{e}_E$ of the electromagnetic field (plane TEM wave, see Fig. 2.3) which propagates along the coordinate r in the direction $\vec{e}$ across and normally to the boundary surface separating lossless and lossy medium. At the boundary, reflection takes place so that the shown $\vec{E}$ before the boundary is the sum of incident and reflected waves; for details see Figs. 2.46 and 2.47. Correspondingly, the field $\vec{E}$ after the boundary is the transmitted wave only. Lossless dielectric medium before the boundary shows the relative permittivity $\varepsilon_r = 1$, a zero effective conductivity $\gamma_{eff} = 0$, and thus infinite skin depth $\delta \to \infty$ (Table 2.1). After the boundary, the lossy and predominant dielectric medium has $\varepsilon_r = 4$ and $\gamma_{eff} > 0$; i.e., $\gamma_{eff} \ll \omega \cdot \varepsilon$ applies (2.72). The field $\vec{E}$ has the instantaneous amplitude E, the angular frequency $\omega = 1$ rad/s, and points in the direction $\vec{e}_E$. Before the boundary, the field $\vec{E}$ exhibits the peak value $\hat{E}$ (2.11), the wavenumber $k = 2\pi/\lambda_1 = 1$ rad/m, and does not experience any spatial damping due to infinite $\delta \to \infty$. After the boundary, the propagating $\vec{E}$ exhibits increased $k = 2\pi/\lambda_2 = \sqrt{\varepsilon_r} = 2$ rad/m, reduced wavelength λ_2 ($<\lambda_1$), and is subjected to exponential damping with $\delta = 1/\alpha = 4 \cdot \pi$ m (Fig. 2.7)

Please recall from (2.4) that a real Z implies *in-phase propagation* of the local $\vec{E}$ and $\vec{B}$ fields within the electromagnetic field, as being characteristic for *lossless media*. In free space, $Z = Z_0 = 377\ \Omega$ applies. Since $\varepsilon_r \gg 1$ is valid in *biological tissues*, the impedance Z in dielectric tissue is always lower than $Z_0 (> Z)$.

For a *plane TEM wave* propagating over time t and along the distance r within unbounded medium, the *lossless propagation* of the associated $\vec{E}$ and $\vec{B}$ fields can be modelled by *undamped harmonic waves*:

$$\begin{aligned}\vec{E} &= E(t,r)\cdot\vec{e}_{\mathrm{E}} = \hat{E}\cdot\cos(\omega t - kr)\cdot\vec{e}_{\mathrm{E}} \quad \text{and}\\ \vec{B} &= B(t,r)\cdot\vec{e}_{\mathrm{B}} = \hat{B}\cdot\cos(\omega t - kr)\cdot\vec{e}_{\mathrm{B}}.\end{aligned} \tag{2.11}$$

Here $\hat{E}$ and $\hat{B}$ is the *peak value* of $\vec{E}$ and $\vec{B}$, respectively, ω the temporal angular frequency, and k the spatial frequency of the travelling $\vec{E}$ and $\vec{B}$ fields pointed in the direction of the unit vector $\vec{e}_{\mathrm{E}}$ and $\vec{e}_{\mathrm{B}}$, respectively. Models for the *spherical TEM wave* can be found in Fig. 2.4 and Footnote 9.

A very simple but instructive relationship results from (2.4) and (2.10), to give

$$\hat{E} = v\cdot\hat{B}. \tag{2.12}$$

That is, *amplitudes* of $\vec{E}$ and $\vec{B}$ fields in a *plane or spherical TEM wave* are *linearly dependent*, whereas the velocity v serves as the proportionality factor. When $\vec{E}$ rises in TEM wave, so does $\vec{B}$, and vice versa.

To define the *flow of electromagnetic energy* in space, the *power density* $\vec{S}$ can be used to describe propagation of the *plane or spherical TEM wave* in *far field* (Footnote 5). The density $\vec{S}$ is defined as the cross product of the perpendicular $\vec{E}$ and $\vec{B}$ fields:

$$\vec{S} = S\cdot\vec{e} = \vec{E}\times\frac{\vec{B}}{\mu} = \frac{E^2}{Z}\cdot\vec{e} = \frac{Z\cdot B^2}{\mu^2}\cdot\vec{e}. \tag{2.13}$$

The vector $\vec{S}$ is known as the instantaneous *Poynting*[8] *vector*, showing the strength S and the direction $\vec{e}$ of the *energy flow*. Please note that the power field $\vec{S}$ points in the propagation direction $\vec{e}$ of TEM wave (Figs. 2.3 and 2.4). The magnitude S is proportional to E^2 and inversely proportional to Z (2.10), as can be derived from (2.4). For instance, an instructive relationship $S = E^2/377\Omega$ applies in free space (with $\varepsilon_{\mathrm{r}} = 1$). In analogy, the magnitude S is proportional to B^2 and Z.

In fact, the power density *magnitude* S is the *power per unit area* normal to $\vec{e}$. For *spherical TEM waves* in Fig. 2.4, the level of S (in W/m^2) at a distance r from the point source corresponds to the quotient of the *total radiated power*, i.e., the source power P (in W), and the *spherical surface area*, i.e., the whole wavefront area $4\pi\cdot r^2$ (in m^2), enclosing the point source, to give

$$\vec{S} = \frac{P}{4\pi\cdot r^2}\cdot\vec{e}. \tag{2.14}$$

[8]John Henry Poynting (1852–1914) was an English physicist best known for the Poynting vector which gives the direction and magnitude to the flow of electromagnetic energy in space.

Equation (2.14) is known as the *inverse square law*.[9] Here we assume that the power P is equally distributed along the spherical area $4\pi \cdot r^2$. In fact, (2.14) accounts for the *geometry-related damping*, whereas the medium-related damping by definition is absent within *lossless medium*.

Consequently, the density S is inversely related to the square of r from the source to the considered field point of interest (2.14), just because of the aforementioned geometrical considerations. As the size of S is inversely related to r^2 for spherical waves while S can be derived from E^2 or B^2 in far field (2.13), it follows that the *amplitudes* E and B become *inversely related to* r for *spherical waves* in *far field*, as detailed by equations in Footnote 9.

Examples

Figure 2.3 demonstrates a *plane TEM wave* with intimately coupled $\vec{E}$ and $\vec{B}$ fields extending along the distance r. Both fields are clearly perpendicular to each other and to the propagation direction $\vec{e}$. The unit vectors $\vec{e}_{\mathrm{E}}, \vec{e}_{\mathrm{B}}$, and $\vec{e}$ are *right-angled* and *right-handed* (2.4). Here the propagating $\vec{E}$ wave (2.11) is indicated for two time instances $t = 0$ and $t = t_0$ (>0). *Planar wavefront*[10] can be recognized with *zero curvature*, whereas the local $\vec{E}$ and $\vec{B}$ fields are indicated within the shown wavefront in Fig. 2.3.

For comparison, a *spherical TEM wave* is shown in Fig. 2.4. The fields $\vec{E}$ and $\vec{B}$ are again perpendicular to each other and to the propagation direction $\vec{e}$ in each

[9]The *inverse square law* applies when electromagnetic waves (or electric biosignals) are radiated outward radially from a point source, as illustrated in Fig. 2.4 (compare (Kaniusas 2015, Footnote 25 in Chap. 4) and (Kaniusas 2015, Fig. 4.21)). For a *spherical wave* in *lossless media*, the total power in each complete *spherical wavefront* is the same. Since the original *source power* P is spread out over the *area* ($=4\pi \cdot r^2$) of a sphere—increasing in proportion to r^2 with the *propagation velocity* v (2.6)—the resulting *magnitude* S *of the power density* $\vec{S}$—passing through a unit area and facing directly the point source—at the distance r is inversely related to r^2 (2.14).

The corresponding *magnitude* E of $\vec{E}$ at the distance r for *spherical TEM wave* can be derived from (2.13) and (2.14) and amounts to

$$E = \sqrt{S \cdot Z} = \frac{1}{2} \cdot \sqrt{\frac{P \cdot Z}{\pi}} \cdot \frac{1}{r} \propto \frac{1}{r},$$

whereas the *magnitude* B of $\vec{B}$ at the distance r for *spherical TEM wave* can also be derived as

$$B = \mu \cdot \sqrt{\frac{S}{Z}} = \frac{\mu}{2} \cdot \sqrt{\frac{P}{\pi \cdot Z}} \cdot \frac{1}{r} \propto \frac{1}{r}.$$

In other words, the level of S *quadruples* while E *and* B *doubles* when r *is halved* (Fig. 2.4). Please note that $E = v \cdot B$ applies, in analogy with (2.12).

[10]*Wavefronts of the electromagnetic field* comprise *surfaces of constant phase*. Everywhere on a given wavefront, $\vec{E}$ and $\vec{B}$ fields are tangential to wavefronts and are the same in their magnitude, phase, and direction, at any instant of time. The *direction of wave propagation* is perpendicular to the wavefront surface, as illustrated in Fig. 2.4 at the points A and C with $\vec{e}$ as the vector of the propagation direction.

point of the propagation space. Again, the unit vectors $\vec{e}_E$, $\vec{e}_B$, and $\vec{e}$ are *right-angled* and *right-handed* (2.4). Two *spherical wavefronts* can be observed in Fig. 2.4 at the radial distances $r = r_1$ and $r = r_2$ from the field source at $r = 0$—a point source with the power P—with the wavefront's *non-zero curvature* $1/r_1$ and $1/r_2$, respectively. The instantaneous $\vec{E}$ and $\vec{B}$ fields are indicated on the wavefront located at $r = r_2$. Please note the flattening of spherical wavefronts with increasing propagation distance r from the source. Thus the propagating spherical wave necessarily *converges to a plane wave* with increasing r (Fig. 2.3). There is a spatial *decay of instantaneous amplitudes* of $\vec{E}$ and $\vec{B}$ fields in Fig. 2.4 with increasing r; in close analogy with the decline in the sound pressure with increasing distance from the sound source (Kaniusas 2015, Fig. 4.21).

Figure 2.5 demonstrates a *plane TEM wave*, namely, its $\vec{E}$ field component, permeating the *boundary* from a *lossless and weak dielectric* medium (like the air with $\varepsilon_r = 1$) down into a *lossy and strong dielectric* medium (with the assumed $\varepsilon_r = 4$). Please note that a *predominant dielectric medium* with $\gamma_{\text{eff}} \ll \omega \cdot \varepsilon$ (2.72) is assumed following the boundary (Table 2.1). The wave's v and λ *clearly decrease* by the factor $\sqrt{\varepsilon_r} = 2$ in the lossy dielectric medium since the local ε_r increases along the propagation path by the factor of 4 [(2.6) and (2.7)]; see Table 2.1. Please compare the doubled λ_1 in the incident medium with respect to λ_2 in the transmitted medium; $\lambda_1 = \sqrt{\varepsilon_r} \cdot \lambda_2 = 2 \cdot \lambda_2$ applies. Correspondingly, the equality $v_1 = 2 \cdot v_2$ applies. In addition, the *wave impedance* Z decreases with increasing ε_r (2.10). The reduced Z implies a reduced $\vec{E}$ field for a given $\vec{B}$ field within the joint TEM wave propagating in the strong dielectric medium as compared with the weak dielectric medium.

The *spatial frequency* k [$=\omega \cdot \sqrt{\mu \cdot \varepsilon}$, see (2.9)] increases by the factor $\sqrt{\varepsilon_r} = 2$ from the weak dielectric medium into the strong dielectric medium (Fig. 2.5). In other words, the raising k *accumulates spatial planes* of constant phase (wavefronts) of $\vec{E}$ and $\vec{B}$ fields in a *high-permittivity medium*. Please note that this accumulation of refracted planes of constant phase in the *electrically slow medium* (medium with high ε_r, see Fig. 2.5) is qualitatively comparable with the accumulation of refracted wavefronts of the sound pressure in the *acoustically slow medium* [medium with a low acoustic impedance, see Kaniusas (2015, Fig. 4.26)] and, on the other hand, is comparable with the accumulation of refracted light wavefronts in the *optically slow medium* [medium with a high index of refraction, see Kaniusas (2015, Fig. 5.13)].

In fact, *reflection* takes place in Fig. 2.5 at the boundary from the lossless and weak dielectric medium into the lossy and strong dielectric medium. Therefore, the shown wave $\vec{E}\left(=\vec{E}_I+\vec{E}_R\right)$ before the boundary is additively composed out of the *incident wave* $\vec{E}_I$ and *reflected wave* $\vec{E}_R$. The wave $\vec{E}\left(=\vec{E}_T\right)$ after the boundary is the *transmitted wave* $\vec{E}_T$ only. The field $\vec{E}_T$ experiences *exponential decay* within *lossy medium*. The decay is visualised by the shown envelope (Figs. 2.5 and 2.7) which steepness is determined by a finite *skin depth* δ (2.21). In particular, the propagating $\vec{E}$ field in Fig. 2.5 is analysed in Figs. 2.46 and 2.47 in much more detail.

2.3.1.2 Lossy Medium

Lossy propagation of $\vec{E}$ and $\vec{B}$ fields forming *electromagnetic wave* is given in *lossy media*[11] with the non-zero *effective conductivity* $\gamma_{\text{eff}} > 0$ (2.82). That is, there is

- the *medium-related damping* of the wave (Fig. 2.7), whereas the wave
- may additionally obey the *geometry-related damping* (due to the *inverse square law*, see Footnote 9).

Therefore, lossy propagation implies progressive *attenuation* of $\vec{E}$ and $\vec{B}$ fields. *Lossy medium* absorbs energy from the electromagnetic field—in terms of *conduction losses* (Fig. 2.16a) and *dielectric losses* (Fig. 2.19)—and converts it to *heat*. On the other hand, *geometrical spread* of wavefronts (Footnote 10)—if present in terms of an *attenuated spherical TEM wave*—adds to the effective attenuation.

The *propagation velocity* v and *wavelength* λ in *lossy medium* amounts to

$$v = \frac{1}{\sqrt{\frac{\mu\cdot\varepsilon}{2}}\cdot\sqrt{\sqrt{1+\left(\frac{\gamma_{\text{eff}}}{\omega\cdot\varepsilon}\right)^2}+1}} = v_{\gamma_{\text{eff}}=0}\cdot\frac{\sqrt{2}}{\sqrt{\sqrt{1+\left(\frac{\gamma_{\text{eff}}}{\omega\cdot\varepsilon}\right)^2}+1}} \tag{2.15}$$

and

$$\lambda = \frac{2\pi}{\omega\cdot\sqrt{\frac{\mu\cdot\varepsilon}{2}}\cdot\sqrt{\sqrt{1+\left(\frac{\gamma_{\text{eff}}}{\omega\cdot\varepsilon}\right)^2}+1}} = \frac{v_{\gamma_{\text{eff}}=0}}{f}\cdot\frac{\sqrt{2}}{\sqrt{\sqrt{1+\left(\frac{\gamma_{\text{eff}}}{\omega\cdot\varepsilon}\right)^2}+1}} \tag{2.16}$$

with

$$v_{\gamma_{\text{eff}}=0} = \frac{1}{\sqrt{\mu\cdot\varepsilon}}. \tag{2.17}$$

Here $v_{\gamma_{\text{eff}}=0}$ is the velocity in lossless case ($\gamma_{\text{eff}} = 0$). Therefore, properties v and λ of waves *transversing lossy medium* are governed by *electrical properties* ε, μ, and γ_{eff} of the propagation medium and the field frequency f. With increasing γ_{eff} in *biological tissue*, both v and λ clearly decrease [(2.15) and (2.16)]. In short, *losses*

[11] In general, if

- the *effective conductivity* γ_{eff} is *very high*, as in metals, we call the material a *conductor*. On the other hand, if
- γ_{eff} is *relatively low* and comparable with the product $\omega\cdot\varepsilon$, we call the material *lossy dielectrics*;

see (2.69) and Footnote 46.

slow down the wave propagation. The aforementioned inequalities $v < v_0$ and $\lambda < \lambda_0$ (2.8) are still valid in *lossy dielectric tissue* (Fig. 2.5).

The associated *wavenumber* k (2.5) in *lossy medium* obeys

$$k = \frac{2\pi}{\lambda} = \frac{\omega}{v} = \omega \cdot \sqrt{\frac{\mu \cdot \varepsilon}{2}} \cdot \sqrt{\sqrt{1 + \left(\frac{\gamma_{\text{eff}}}{\omega \cdot \varepsilon}\right)^2} + 1}. \tag{2.18}$$

That is, the value of k increases with increasing losses, i.e., with increasing γ_{eff}. *Wavefronts* become *spatially accumulated* in a *high-conductivity lossy medium* (with $\gamma_{\text{eff}} \gg 0$) that is qualitatively similar to the discussed accumulation of wavefronts in a *high-permittivity lossless medium* (with $\varepsilon_r \gg 1$). Therefore, accumulated *planes of constant phase* in conductive medium shorten λ (2.16).

The associated *wave impedance* $\underline{Z}$ as the *quotient* of complex amplitudes of $\vec{E}$ and $\vec{B}$ fields (2.4) is *complex-valued* and equals

$$\underline{Z} = Z \cdot e^{j\varphi_z} = \frac{\hat{\underline{E}}}{\hat{\underline{B}}/\mu} = \sqrt{\frac{j\omega\mu}{\gamma_{\text{eff}} + j\omega\varepsilon}}. \tag{2.19}$$

Complex $\underline{Z}$ implies a *non-zero phase shift* φ_Z ($\neq 0$) between the local $\vec{E}$ and $\vec{B}$ fields of the electromagnetic field in *lossy media*, as already discussed with respect to (2.4). For comparison, lossless media imply a real Z and thus the absent shift $\varphi_Z (= 0)$. Since $\varepsilon_r \gg 1$ and $\gamma_{\text{eff}} > 0$ are valid in *biological tissues*, the impedance magnitude Z in tissue is always lower than Z_0 (>Z).

Table 2.1 shows how equations describing v, λ, k, and $\underline{Z}$ in *lossy dielectric medium* reduce

- in *lossless medium* ($\gamma_{\text{eff}} = 0$);
- in *predominant dielectric medium* with a relatively *small* $\gamma_{\text{eff}} (\ll \omega \cdot \varepsilon)$, see (2.72); and
- in *predominant conductive medium* with a relatively *large* $\gamma_{\text{eff}} (\gg \omega \cdot \varepsilon)$, see (2.71).

For an *attenuated plane TEM wave* propagating over time t and along the distance r travelled into a lossy medium starting at $r = 0$, the *lossy propagation* of the associated $\vec{E}$ and $\vec{B}$ fields can be modelled by *damped harmonic waves*

$$\begin{aligned}
\vec{E} &= E(t,r) \cdot \vec{e}_E = \text{Re}\left\{\hat{\underline{E}} \cdot e^{-\alpha \cdot r + j(\omega t - kr)} \cdot \vec{e}_E\right\} = \hat{E} \cdot e^{-\alpha \cdot r} \cdot \cos(\omega t - kr + \varphi_E) \cdot \vec{e}_E \quad \text{and} \\
\vec{B} &= B(t,r) \cdot \vec{e}_B = \text{Re}\left\{\hat{\underline{B}} \cdot e^{-\alpha \cdot r + j(\omega t - kr)} \cdot \vec{e}_B\right\} = \hat{B} \cdot e^{-\alpha \cdot r} \cdot \cos(\omega t - kr + \varphi_B) \cdot \vec{e}_B.
\end{aligned} \tag{2.20}$$

Here $\hat{\underline{E}}$ and $\hat{\underline{B}}$ is the respective *complex peak value* of $\vec{E}$ and $\vec{B}$ fields, whereas φ_E and φ_B is the respective *angle* of the complex $\hat{\underline{E}}$ and $\hat{\underline{B}}$. Please note that

$\varphi_Z = \varphi_E - \varphi_B$ and $Z = E/(B/\mu)$ apply, as can be derived from (2.19) and (2.20). Such lossy propagation is illustrated on the right side of Fig. 2.5 for a plane wave impinging on a conducting halfspace. Models for the *attenuated spherical TEM wave* include additionally the weighting factor $1/r$ in line with the *inverse square law*; compare Fig. 2.4 and Footnote 9.

The propagation of *TEM waves* in *lossy medium* is subjected to the *exponential decay*, the *medium-related damping*. The coefficient α (>0) in (2.20) is the exponential *attenuation coefficient* of $\vec{E}$ and $\vec{B}$ fields. The size of α reflects how fast fields attenuate as they propagate through lossy medium. In fact, the *rationale* of the exponential law is given in Kaniusas (2015, Footnote 19 in Chap. 5), showing that the decay rate increases with α or, in other words, the local decay in $\vec{E}$ and $\vec{B}$ fields is proportional to the respective absolute amplitude of $\vec{E}$ and $\vec{B}$ fields themselves. Please compare the exponential decay of $\vec{E}$ field within lossy medium ($\alpha > 0$) starting at $r = 0$ (right side in Fig. 2.5) with the non-attenuated $\vec{E}$ field within lossless medium ($\alpha = 0$) extending for $r < 0$ (left side in Fig. 2.5); compare with the medium-related damping of sounds in Kaniusas (2015, Fig. 4.22).

Because of the field attenuation with increasing r, the *skin depth*[12] $\delta = 1/\alpha$—or the *penetration depth* of ambient fields into biological bodies—can be defined as the *inverse of* α. Generally speaking, the depth δ is the distance the effective field penetration into lossy tissue is limited to, to give

$$\delta = \frac{1}{\alpha} = \frac{1}{\left(\omega \cdot \sqrt{\frac{\mu \cdot \varepsilon}{2}} \cdot \sqrt{\sqrt{1 + \left(\frac{\gamma_{eff}}{\omega \cdot \varepsilon}\right)^2} - 1}\right)}. \tag{2.21}$$

According to the exponential term $e^{-\alpha \cdot r}$ (2.20), δ is the *space constant* or the *distance* the wave must travel into *lossy medium* to become attenuated by the factor 1/e to about 37%—or, roughly speaking, to *one-third*—of its original value at the incident surface of the lossy medium section (at $r = 0$).

Table 2.1 shows how the equation for δ (2.21) simplifies for *predominant dielectric medium* ($\gamma_{eff} \ll \omega \cdot \varepsilon$) and for *predominant conductive medium*

[12] *Biomedical relevance* of the skin depth δ can be illustrated based on clearly undesirable interactions of ambient electromagnetic fields with *medical implants* within the body, such as *cardiac pacemaker* under the skin surface (Footnote 130). Ideally, the level of δ should be much less than the implantation depth in order to avoid these interactions.

For instance, electrodes of cardiac pacemakers are usually implanted deeper than 2 cm under the skin (Heinrich 2015). If we assume *muscle* as the representative tissue, Fig. 2.6 yields the field *frequency of 2.5 GHz* at $\delta = 2$ cm as the minimal frequency at which the incident electric field on the body skin is already *attenuated to at least 37%* of its initial value at the skin, before this field reaches the *implanted electrodes* under the surface. In other words, the risk of coupling of interference signals from external electromagnetic fields into implanted electrodes located within conductive tissues decreases with continuing increase of the field frequency.

($\gamma_{\text{eff}} \gg \omega \cdot \varepsilon$). Interestingly, the approximation for $\gamma_{\text{eff}} \gg \omega \cdot \varepsilon$ describes the skin depth of electromagnetic induction (2.88).

The attenuation of $\vec{E}$ and $\vec{B}$ fields is clearly a function of *electrical properties* of lossy medium and the field frequency—as illustrated in (2.21)

- with *increasing* μ, the resulting α increases and δ decreases ($d\alpha / d\mu > 0$); i.e., the field penetration becomes *more shallow*;
- with *increasing* ε, the resulting α decreases and δ increases ($d\alpha / d\varepsilon < 0$); i.e., the field penetration becomes *more deep*;
- with *increasing* f, the resulting α increases and δ decreases ($d\alpha / df > 0$); i.e., the field penetration becomes *more shallow*; and
- with *increasing* γ_{eff}, the resulting α increases and δ decreases ($d\alpha / d\gamma_{\text{eff}} > 0$); i.e., the field penetration becomes *more shallow*;

as can also be derived from Table 2.1. It should be recalled that γ_{eff} varies strongly with f (Fig. 2.21), whereas γ_{eff} is one of the determinants of δ (2.21). Namely, when γ_{eff} increases with f, the associated α increases and δ decreases; i.e., the *field penetration* into *lossy tissue* becomes *more shallow* with *increasing f*. Likewise, the depth δ becomes semi-infinite ($\delta \rightarrow \infty$) in *lossless media* ($\gamma_{\text{eff}} = 0$) while *lossless penetration* prevails ($\alpha = 0$).

In *good conductors* (with high γ_{eff}, see Footnote 11), the wave attenuation is so rapid that $\vec{E}$ field already disappears within a very small distance $\delta = 1/\alpha$ (2.21) of the interface, e.g., following the air/conductor boundary at $r = 0$ in Fig. 2.5. Then the associated currents within conductors are confined to a thin layer of the thickness δ near the boundary surface, which is known as the *skin effect*. Please note that the field $\vec{E}$ in *ideal conductors* must be zero for any given conduction current (Footnote 56) so that in such conductors infinitely high $\alpha \rightarrow \infty$ and vanishingly small $\delta \rightarrow 0$ apply (see Table 2.1 with $\gamma_{\text{eff}} \rightarrow \infty$). In short, *highly conductive objects* do not allow the wave to penetrate it.

Please note that the *power density* $\vec{S}$ field (2.22) is subjected to an even stronger *exponential decay* than the associated $\vec{E}$ field (2.20). This is because the doubled exponent $2 \cdot \alpha$ applies for the attenuation of $\vec{S}$ as compared with the single exponent α for the attenuation of $\vec{E}$.

Figure 2.6 shows the decrease of δ with increasing f in lossy dielectrics, *muscle and fat*. The local loss of $\vec{E}$ and $\vec{B}$ fields increases with f and with the local γ_{eff}. Since muscle has higher γ_{eff} than fat at any f (Fig. 2.21), the loss of these fields in muscle is stronger than in fat at any f.

Tissues with high water content (such as *muscle*) show a high γ_{eff} and thus a small depth δ, whereas tissues with low water content (such as *fat*) show a low γ_{eff} and thus a large δ. To give a numerical example, only respective 40% and 5% of the incident $\vec{E}$ field of the electromagnetic wave is transferred through 5 cm of *muscle* at 300 MHz and 3 GHz with the respective $\delta \approx 5.5$ cm and $\delta \approx 1.7$ cm; as can be derived from (2.20) and Fig. 2.6. Correspondingly, a larger portion of 86% and

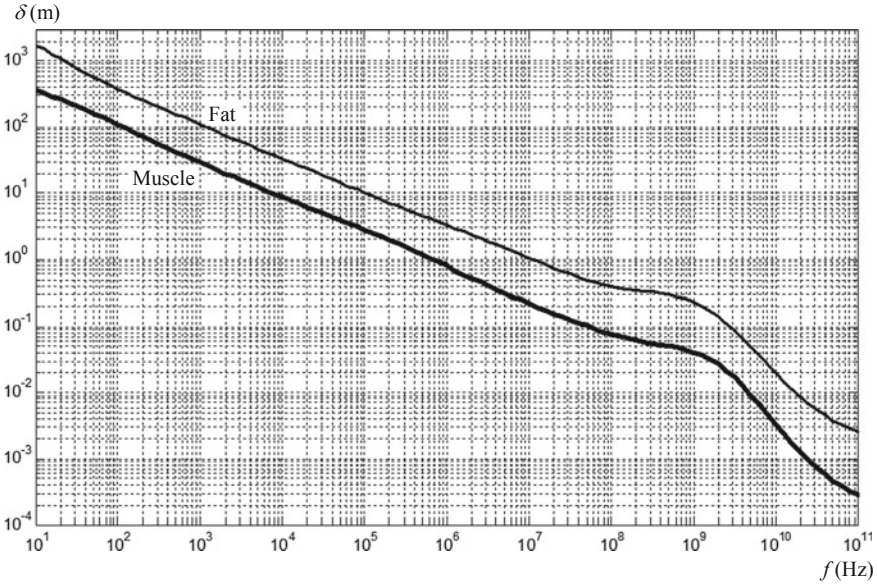

Fig. 2.6 Frequency variation of the skin depth δ in muscle and fat. The depth δ was estimated with (2.21) based on numerical data from Figs. 2.20 and 2.21. The estimated δ applies for a plane wave incident on a planar interface to muscle or fat section, i.e., incident on a lossy dielectrics halfspace with properties of muscle or fat (compare Fig. 2.5). The depth δ is the distance from the surface down into muscle or fat at which the local $\vec{E}$ and $\vec{B}$ fields have decreased by 1/e of their original value at the surface (2.20)

57% passes the same distance of 5 cm of *fat* at 300 MHz and 3 GHz with the respective $\delta \approx 32$ cm and $\delta \approx 8.8$ cm.

Figure 2.7 illustrates the instantaneous amplitude of $\vec{E}$ field along r and its exponential decay in lossy medium.

- *Low field frequencies* undergo low attenuation as they propagate through lossy *biological tissue*, with the associated high δ ($=\delta_2$ in Fig. 2.7) and low $\alpha\,(=1/\delta_2)$. There is *weak interaction* of the electromagnetic field with the penetrated tissue and thus *deep penetration* of this *weakly attenuated field* into tissue. *Diffuse heating* by deposited energy dominates.
- *High field frequencies* undergo high attenuation with low δ ($=\delta_1 < \delta_2$ in Fig. 2.7) and high $\alpha\,(=1/\delta_1 > 1/\delta_2)$ in terms of *strong interaction* of the electromagnetic field with the penetrated tissue. *Superficial penetration* of the *strongly attenuated field* results, leading to *locally restricted energy absorption* and thus to locally *concentrated heating*.

Compare with similar tendencies in acoustic biosignals from Kaniusas (2015, Fig. 4.23).

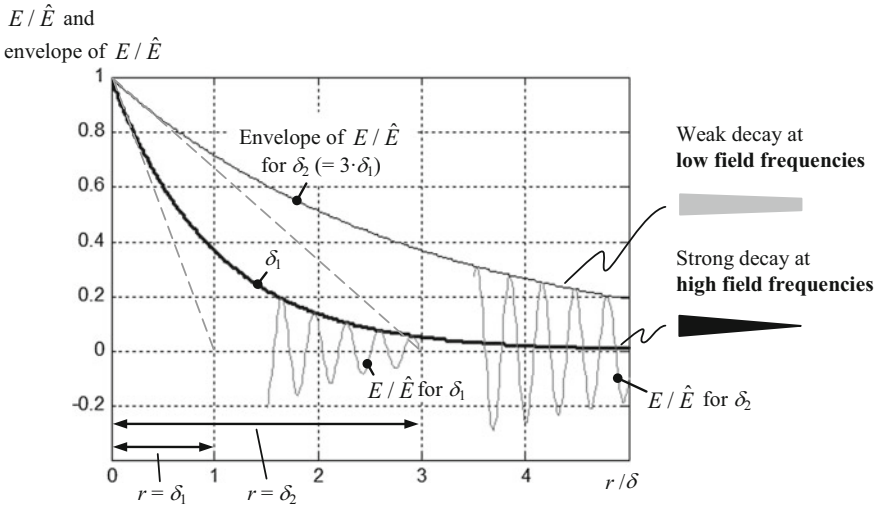

Fig. 2.7 The amplitude E of the electric field $\vec{E}$ (2.20) and its envelope of the electromagnetic field propagating along the coordinate r in a reflectionless semi-infinite lossy medium; compare Fig. 2.5 and Kaniusas (2015, Fig. 4.22). The envelope is subjected to the exponential decay with the skin depth δ (2.20). The corresponding tangents for a strong wave attenuation with $\delta = \delta_1$—e.g., at high field frequencies (Fig. 2.6)—and a slight wave attenuation with $\delta = \delta_2$ (=3 · $\delta_1 > \delta_1$)—e.g., at low field frequencies—are depicted at the medium boundary $r = 0$

For *very high field frequencies* with $f \to \infty$, the penetration is very slight with $\delta \to 0$ and whatever effects the electromagnetic field, especially, its $\vec{E}$ field component, has on the body are predominantly *surface effects* (Section "Incident Electromagnetic Fields"). The fields at very high frequencies simply *do not penetrate into or out of the lossy body*. From a therapeutic point of view, lowering frequency favours deep penetration of fields into the body while increasing frequency favours superficial treatment (Footnote 115).

Let us consider *attenuation of electromagnetic fields* in *lossy media*, i.e., a conductor,

- for time-varying $\vec{E}$ fields and
- for time-varying $\vec{B}$ fields

from a *physical perspective*. The *time-varying* $\vec{E}$ of the propagating electromagnetic wave transfers its wave energy to the kinetic energy of unbound charges within conductor. These charges start to move in terms of the resulting non-zero conductive current (2.55). While charges move, *collisions* start with less-mobile microscopic structures and *mutual friction* arises in-between moving charges. Both effects lead to *thermal losses*. Since mobility of charges is governed by γ_{eff} with $\vec{E}$ as the driving force [(2.53) and (2.54)], then the size of γ_{eff} governs also thermal losses for a given $\vec{E}$ field (2.58). Therefore, the body's $\gamma_{\text{eff}}(>0)$ determines the

coefficient α (>0) that increases with increasing γ_{eff} (2.21 and Table 2.1). The body's γ_{eff} attenuates propagating waves with increasing r (2.20).

The *time-varying field* $\vec{B}$ of the propagating electromagnetic wave sets *eddy currents* in conductor which, in turn, create their own magnetic field $\vec{B}_{\text{i}}$ opposing the incident $\vec{B}$ (Fig. 2.31a). This opposing $\vec{B}_{\text{i}}$ resists and thus limits the penetration of the incident $\vec{B}$ to the depth δ [(2.21) and (2.88)], e.g., from the air/conductor boundary down into the conductor by δ. Consequently, *current densities* and *electric fields* induced electromagnetically within the conductor will drop off in *exponential fashion* from the conductor's surface (Fig. 2.31b), in line with (2.20).

The *flow of electromagnetic energy* in space can also be defined with the *power density* $\vec{S}$ which is *complex-valued* in *lossy medium*, in contrast to the real-valued $\vec{S}$ in lossless case (2.13). The magnitude S can be written as (2.20)

$$|\vec{S}| = \left|\vec{E} \times \frac{\vec{B}}{\mu}\right| = \frac{E^2}{Z} = \frac{\hat{E}^2}{2 \cdot Z} \cdot \mathrm{e}^{-2\alpha \cdot r} + \frac{\hat{E}^2}{2 \cdot Z} \cdot \mathrm{e}^{-2\alpha \cdot r} \cdot \cos(2(\omega t - kr + \varphi_{\text{E}})). \tag{2.22}$$

Here an average time-constant component can be recognised, in addition to another oscillating component with doubled frequency.

It should be stressed that *resonance phenomena* in the body may lead to a much *higher local absorption* of wave energy at specific field frequencies than would be predicted by α only or by the simple exponential relationship (2.20). Resonance is related to *multiple reflections* within the body where travelling waves are *partially reflected*—back to the field source and forth from the field source—within *lossy and heterogeneous sections* of the body (Fig. 2.48). Reverberating waves lose progressively their energy after *multiple passage* of the same tissue section to a much larger extent as compared with a *single and straightforward passage* of this section. Given the *total reflection*—where the amplitude of the reflected wave equals to that of the incident wave (2.125)—waves reverberate in lossy tissue sections until they are completely absorbed by tissue.

The resulting maxima of *partial standing waves* during *partial reflection* (Fig. 2.47) and maxima of *standing waves* during *total reflection* (Fig. 2.45) denote

- local regions of *maximum* $\vec{E}$ *field* and thus
- local regions of *maximum energy absorption* (2.58);

compare Kaniusas (2015, Footnote 29 in Chap. 4). Therefore, standing waves create the potential for otherwise unexpected *overstimulation* of local excitable tissues or unexpected *overheating* of local tissues (Sect. 2.3.2.4).

If the *resonant body* shows relatively *high losses* (high α), propagating fields in the body will be absorbed already within a *few reverberations* back and forth. Such resonant body is said to have a *low quality factor* (Kaniusas 2015, Footnote 51 in Chap. 4). In contrast, relatively *small losses* within the resonant body (low α) mean

longer reverberations of fields within the body before a *steady state* of these fields is reached (Footnote 4 in Chap. 3). Then the associated *quality factor is high*. Resonance examples are provided in Section "Incident Electromagnetic Fields".

2.3.2 *Effects on Electric Signals*

After basic propagation phenomena of *electric, magnetic, and electromagnetic fields* have been discussed in Sect. 2.3.1, highly instructive *mutual interactions* of these fields with *biological tissue* should be discussed. In general, electric, magnetic, and electromagnetic fields within tissue are subjected to

- *volume effects* within *unbounded media*, such as *conduction* and *polarization*, *relaxation* and *dispersion*, *charge and current induction*, *electromagnetic induction*, whole-body and partial-body *resonances* (Sect. 2.3.2.1); as well as
- *inhomogeneity effects* when considering *bounded media*, such as *boundary conditions* for pure conductive, pure dielectric, and mixed conductive and dielectric media, *scattering*, *diffraction*, *reflection*, *refraction*, and *resonance* (Sect. 2.3.2.2).

Quantitative examples of modelled tissue sections when subjected to various field conditions offer practical and useful insights (Sect. 2.3.2.3).

When biological tissue is exposed to *electric fields* via *contact-less* and *contact-based coupling*, electric fields and currents are induced within tissue. Intensities of these fields and currents as well as their temporal and spatial distribution determine occurrence of diverse *physiological effects*:

- *neuromuscular excitation* effects (Section "Electrical Stimulation Effects") and
- *thermal* effects (Section "Thermal Stimulation Effects").

Here biological *exposure limits* are highly relevant to avoid *adverse health effects* of fields coupled into tissue (Section 2.3.2.5).

The physiological impact of *magnetic fields* incident on tissue is limited to time-varying magnetic fields (Section "Incident Magnetic Fields"), which again induce *electric fields and currents* within tissue. These fields, in turn, can excite and heat tissue (see above).

Induced electric fields and currents within tissue are strongly determined by

- *coupling mechanisms* of electric, magnetic, or electromagnetic field into tissue;
- strength, dynamic, frequency, and direction of the *field exposure* or of the *incident field* entering biological tissue;
- static and dynamic as well as microscopic and macroscopic *electrical properties* of the *exposed biological tissue*; and
- position, size, shape, and orientation of the *exposed tissue section* with respect to the incident directional field.

Lastly, it should be noted that the quantum *energy* of relevant frequencies (typically below GHz range) of electric biosignals related to biological tissues is relatively small. *No chemical interactions* between fields and molecular structures can be expected. Molecular structures can not be altered by electric biosignals. For instance, the energy of only 0.12 meV results for a very high frequency of 30 GHz (Kaniusas 2015, Eq. 5.3), the energy level which is still much less than the binding energy of weak chemical bonds (>40 meV) or even than thermal energy in living tissue (≈40 meV at 30 °C); compare cited energy levels in Kaniusas (2015, Sect. 5.1.1.1).

2.3.2.1 Volume Effects

General Issues

Electric and Magnetic Fields

Interestingly, all well-known and anticipated *interactions between electric and magnetic fields* and, on the other hand, *biological tissue* occur through mechanisms involving the *electric field* only. Even the ambient *magnetic field* may have electric consequences in terms of induced internal electric fields within tissue. Thus, the distribution of the electric field—and the *associated current density field*—in tissue is mostly sufficient to describe these interactions.

Before *interactions* between the *electric field and biological tissue* (Section "Incident Electric Fields") and, on the other hand, between the *magnetic field and tissue* (Section "Incident Magnetic Fields"), can be discussed, *basic concepts*[13] of the electric and magnetic fields should be very shortly introduced to provide their elementary understanding.

[13]The *conceptual origin* of the *electric and magnetic fields* as well as of the *capacitance* should be shortly described from a formal point of view, based on an example in Fig. 2.8. Here the magnitude E of the *electric field* $\vec{E}$ between two *plane-parallel plates of the capacitor* in the direction of a unit vector $\vec{e}_{\mathrm{E}}$ *normal to the plate's surface* equals to

$$\vec{E} = E \cdot \vec{e}_{\mathrm{E}} = \frac{u}{d} \cdot \vec{e}_{\mathrm{E}},$$

where u is the voltage drop across the gap between the plates and d is the distance between the plates. Obviously, the latter relationship assumes a *homogenous* $\vec{E}$ between the plates provided that d is very small with respect to lateral dimensions of plates.

As illustrated in Fig. 2.8, the *magnetic flux density* $\vec{B}$ with the magnitude B in the direction of a unit vector $\vec{e}_{\mathrm{B}}$ and in the normal distance r from a *wire carrying the electric current* i amounts to

$$\vec{B} = \frac{\mu_0 \cdot i}{2\pi \cdot r} \cdot \vec{e}_{\mathrm{B}}.$$

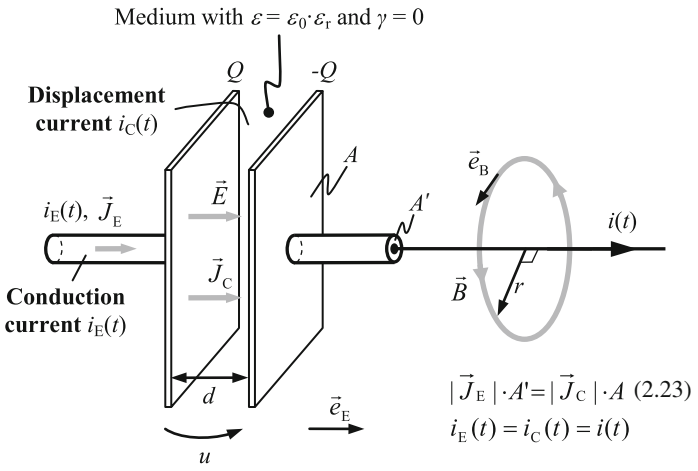

Fig. 2.8 The conceptual origin of the electric field $\vec{E}$ associated with electric excess charges Q and $-Q$ on the capacitor plates. In contrast, the magnetic field $\vec{B}$ is associated with moving electric charges in terms of a current i along the wire connected to the plates. For basic relationships between the latter physical quantities see Footnote 13

- The *electric field* is defined to account for forces among *electric charges* or, to be more precise, to account for the amplitude and direction of a *mechanical force* acting on an electric charge located in the electric field[14]; see Fig. 2.8. That is, the electric field is a *vector field* and is associated with the presence of electric charges (Kaniusas 2012, Footnote 21). In addition, the electric field can be induced by a *time-varying magnetic field* (see below).
- The *magnetic field* is also a *vector field* and is generated by *moving electric charges* (but not static charges), i.e., by *electric currents* including macroscopic currents [e.g., in wires, see Fig. 2.8 and (2.25)] and microscopic currents (e.g., in atomic orbits). The magnetic field can also exert a *mechanical force* on electric charges provided that these electric charges are in motion, i.e., there is a non-zero electric current (2.25). In analogy, a *time-varying magnetic field* induces *movements of unbound electric charges* (originally resting) and thus generates *electric currents* and the *associated electric fields* along conductive

This equation for $\vec{B}$ assumes an *infinitely long wire*. It should be noted that the vector $\vec{e}_B$ shows in the *circumferential* direction, i.e., the vector $\vec{B}$ encircles the wire carrying i according to the *right-handed association*; see Fig. 2.8 and Footnote 72.

[14]In fact, both *electric and magnetic fields* act in a *contact-less way*, i.e., there can be a *mechanical force* in between objects even though *objects are physically separated* from each other. For instance, one object could be the *source* of the electric and/or magnetic fields (e.g., power lines in the street, Footnote 80) while another object could be the *target* object experiencing this force (e.g., the human body exposed to fields of power lines).

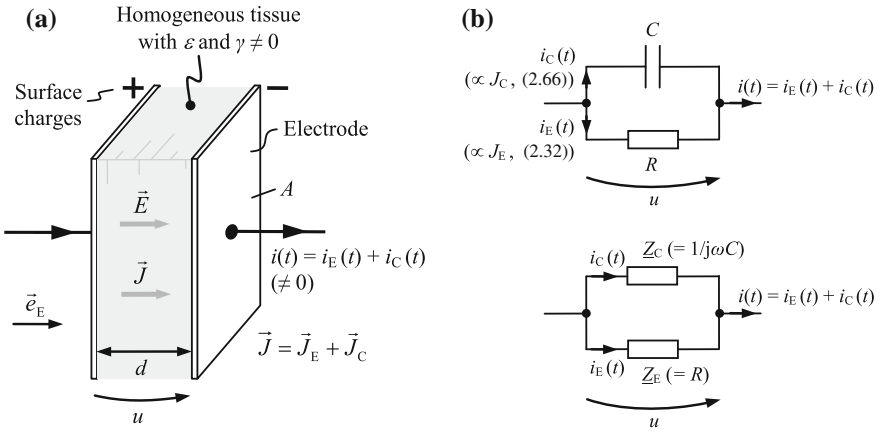

Fig. 2.9 Biological tissue and its principal electrical model. **a** Two electrodes and homogenous tissue in between with its electrical conductivity γ and dielectric permittivity ε. Local quantities of vector fields such as the time-varying electric field $\vec{E}(t)$ with its amplitude $\vec{E}$ and the total current density field $\vec{j}(t)$ with its amplitude $\vec{J}$ [$=\vec{J}_E + \vec{J}_C$, see (2.26)] determine global non-vector quantities such as the total current $i(t)$ that is additively composed of the conductive current $i_E(t)$ and capacitive/displacement current $i_C(t)$. **b** Electrical equivalent circuit models with the electrical resistance R in parallel to the capacitance C or, in analogy, the complex capacitive impedance $\underline{Z}_C$ in parallel to the conductive impedance $\underline{Z}_E$, see (2.36), (2.42), and Fig. 2.14

loops (e.g., within the human body exposed to time-varying magnetic fields, see Section "Incident Magnetic Fields").

Figure 2.8 demonstrates the *conceptual origin of the electric and magnetic fields*. In particular, the electric field $\vec{E}$ between plates of the capacitor is denoted, whereas the magnetic field $\vec{B}$ is denoted in a distance r from a wire carrying a time-varying electric current $i(t)$; see Footnote 13.

Current Density and Current

The *cross-section area A* of a *conductive body* permeated by a time-varying electric *conductive current* $i_E(t)$ with its *amplitude* I_E—as illustrated in Figs. 2.9a and 2.10—determines the resulting *instantaneous electric conductive current density* $\vec{j}_E(t)$ with its *vector amplitude* $\vec{J}_E$ (for *sinusoidal* $j_E(t)$ only) according to

$$\vec{j}_E(t) = j_E(t) \cdot \vec{e}_E = \frac{i_E(t)}{A} \cdot \vec{e}_E \quad \text{and} \quad \vec{J}_E = J_E \cdot \vec{e}_E = \frac{I_E}{A} \cdot \vec{e}_E. \tag{2.23}$$

The vector $\vec{e}_E$ is a unit vector in the direction of $\vec{J}_E$ and points in the normal direction $\vec{e}_n$ of the *cross-section surface* with its A. Simply speaking, the surface A is perpendicular to the current's direction; see $\vec{e}_n$ normal to A_1 in Fig. 2.10. That is, the amplitude I_E passing through A determines the amplitude J_E.

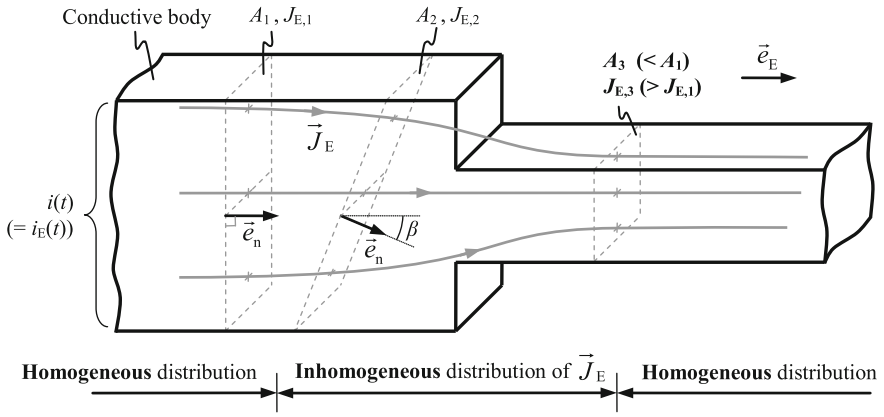

Fig. 2.10 The conceptual origin of the electric conductive current density $\vec{j}_E(t)$ with its magntiude $\vec{J}_E$ across the cross-section area A of a conductive body yielding the conductive current $i(t) = i_E(t)$ with its amplitude I_E (2.24). The current distribution is homogeneous within A as long as the size of A does not change along the current flow while the oscillation of $i_E(t)$—if any—is at a relatively low field frequency (i.e., without any current displacement towards the outer surface of the body, see (2.88) and Fig. 2.31b). An abrupt change in A along the current flow (see $A_1 > A_3$) yields an inhomogeneous distribution of $\vec{J}_E$ ($J_{E,1} < J_{E,3}$) in the body region between A_1 and A_3

Please note that

- $\vec{J}_E$ represents a *local vector quantity* (geometrical entity in space) with its local *signed magnitude* J_E *and its direction* $\vec{e}_E$ of
- I_E, a *global scalar quantity* which is a signed real quantity only (2.23).

In addition to the alignment of $\vec{J}_E$ and $\vec{e}_n$, (2.23) assumes a *homogeneous distribution* of $\vec{J}_E$ within the *cross-section surface* of the size A (i.e., a uniform distribution of $\vec{J}_E$ without any changes of J_E and its direction $\vec{e}_E$ from point to point within the cross-section surface). In other words, the area A can be assumed to be quite small for the current flow to stay homogeneous within the cross-section surface.

However, if the *current flow is not homogeneous* along the cross-section surface and/or the local $\vec{J}_E$ does not point in the direction of $\vec{e}_n$—at least, not everywhere within the cross-section surface—then a *surface integral*

$$i_E(t) = \int_A \vec{j}_E(t) \cdot d\vec{A} \quad \text{and} \quad I_E = \int_A \vec{J}_E \cdot d\vec{A} \tag{2.24}$$

applies with $d\vec{A} = dA \cdot \vec{e}_n$. According to this integral, the current amplitude I_E can be interpreted as the *surface integral of the normal projection* of $\vec{J}_E$ in the direction

$\vec{e}_n$ along the whole A, or, in analogy, as the *surface integral of the amplitude of the normal component* of $\vec{J}_E$ [$=J_{E,n}$ from (2.94)] in the direction $\vec{e}_n$.

Figure 2.10 illustrates that this *projection* equals to $\vec{J}_E \cdot d\vec{A} = J_E \cdot \vec{e}_E \cdot \vec{e}_n \cdot dA = J_E \cdot \cos(\beta) \cdot dA$ for the integration area $A = A_2$ (2.24). Here β is the *disorientation angle* between $\vec{e}_n$ and $\vec{e}_E$. The equality $I_E = J_{E,1} \cdot A_1 = J_{E,3} \cdot A_3$ applies in Fig. 2.10 when a homogeneous distribution of $\vec{J}_{E,1}$ and $\vec{J}_{E,3}$ within A_1 and A_3, respectively, is assumed. In other words, the amplitude $J_{E,3}$ is larger than $J_{E,1}$ because of the smaller cross-sectional area $A_3 (< A_1)$. Please note that the direction of the *local electric field* $\vec{E}$ is identical with that of the *local current density* $\vec{J}_E$ in *isotropic conductive bodies* only (2.32).

The *conductive current* $i_E(t)$ in the *conductive body* is always related to transport of a free *unbound electric charge* $Q(t)$ in line with

$$i_E(t) = \frac{dQ(t)}{dt} \quad \text{or} \quad Q(t) = \int i_E(t) dt. \tag{2.25}$$

In analogy with (2.23) and (2.24), similar relationships exist within a *dielectric body* for the time-varying *capacitive/displacement current density* $\vec{j}_C(t)$ with its *vector amplitude* $\vec{J}_C$ and the *amplitude* I_C of the time-varying *displacement current* $i_C(t)$ across the cross-section surface of the size A (2.66).

When both $\vec{J}_E = \underline{J}_E \cdot \vec{e}_n$ and $\vec{J}_C = \underline{J}_C \cdot \vec{e}_n$ are present along $\vec{e}_n$—within a *conductive and dielectric body* (also in *lossy dielectrics* with its *dispersive electrical properties*, see Footnote 11)—and *homogeneous distributions* of $\vec{J}_E$ and $\vec{J}_C$ are assumed within A, then (2.23) can be expanded as

$$\vec{j}(t) = \vec{j}_E(t) + \vec{j}_C(t) \quad \text{and} \quad \vec{J} = \vec{J}_E + \vec{J}_C \quad \text{with} \quad \underline{J} = \underline{J}_E + \underline{J}_C; \tag{2.26}$$

compare (2.68) and (2.69). As illustrated in Fig. 2.9a, $\vec{J} = \underline{J} \cdot \vec{e}_n$ is the *vector amplitude* of the time-varying *total current density* $\vec{j}(t)$ obeying

$$\vec{j}(t) = \mathrm{Re}\{\vec{J} \cdot e^{j\omega t}\} = \mathrm{Re}\{\underline{J} \cdot e^{j\omega t} \cdot \vec{e}_n\} \tag{2.27}$$

in response to the *total current* $i(t) = i_E(t) + i_C(t)$ across A (2.45). Please note that *amplitudes* $\underline{J}, \underline{J}_E$, and $\underline{J}_C$ in (2.26) should be considered as *complex quantities* (2.35), especially while adding $\underline{J}_E$ and $\underline{J}_C$, as illustrated in Fig. 2.18d.

Electric Field and Voltage

The *electric field* $\vec{E}$ can be derived from the *local electric potential* φ according to

$$\vec{E} = -\vec{\nabla}\varphi \quad \text{or} \quad \vec{E}(x,t) = E(x,t) \cdot \vec{e}_E = -\frac{d\varphi(x,t)}{dx} \vec{e}_x. \tag{2.28}$$

The minus sign in (2.28) implies that the vector $\vec{E}$ points in the direction of the strongest φ decrease. For the sake of simplicity, the right equation in (2.28) assumes spatial changes of $\varphi(x, t)$ in x direction only, which, in turn, yields $\vec{E}$ pointing along x direction only. That is, $\vec{E}$ points in the direction of a unit vector $\vec{e}_{\mathrm{E}}$, whereas the equality $\vec{e}_{\mathrm{E}} = -\vec{e}_{\mathrm{x}}$ applies.

Figure 2.11a illustrates an increase in $\varphi(x)$ with increasing coordinate x, i.e., $\varphi(x)$ increases linearly in the direction of a unit vector $\vec{e}_{\mathrm{x}}$. The associated $\vec{E}(x)$ field (2.28) points in the opposite direction to $\vec{e}_{\mathrm{x}}$, i.e., $\vec{E}(x)$ points in the direction $-\vec{e}_{\mathrm{x}}$. Its *magnitude* $E(x) = |\vec{E}(x)| = E$ does not change with increasing x due to a linear $\varphi(x)$ increase with x. In fact, the *size of E equals to the slope of φ(x)* increase over x.

In line with Fig. 2.11, the associated *instantaneous electric voltage u(t)* from the position A to B along the *line l* is given as the *difference of the respective electric potentials*

$$u(t) = \varphi_{\mathrm{A}}(t) - \varphi_{\mathrm{B}}(t). \tag{2.29}$$

It can be concluded from (2.29) that the resulting $u(t)$ does not depend on the particular *shape of the curve l* but only on $\varphi(x,t)$ values at the beginning A and the end B of l. Likewise, a *closed loop* with collapsed endpoints of l necessarily shows *zero u = 0*.

However, it should be stressed that (2.28) and (2.29) hold only if *electrostatic or quasi-electrostatic conditions*[15] apply (i.e., without any significant electromagnetic induction), see (2.52). In other words, electrostatic or quasi-electrostatic conditions are required for the *existence of φ field*.

Apart from electrostatic or quasi-electrostatic conditions, the *voltage u(t)* associated with the *curve l* connecting both positions A and B is generally defined as a *line integral* of $\vec{E}$ in the *tangential direction* $\vec{e}_{\mathrm{l}}$ along l, to give

[15] *Electrostatic* or *quasi-electrostatic conditions*—as detailed in Section "Mutual Field Coupling and Quasi-electrostatic Situation"—imply that the circumferential total voltage along the *closed loop* is zero or almost zero, respectively. That is, the *total voltage along the closed boundary* where the electric field is considered—more precisely, the total voltage given as a line integral of the tangential electric field along the closed boundary line, see (2.30)—should amount to zero or almost zero, respectively. *Zero voltage* along the closed loop strictly holds when the distribution of *electric charges* in space *does not change with time*.

In other words, (2.28) and (2.29) assume that the rate of change of *time-varying magnetic fields within this closed boundary* can be neglected. Here the *electromagnetic induction* (2.86) of the electric field along this boundary can be neglected in terms of the applicable *quasi-electrostatic conditions* [in line with (2.52)] or is not present at all in terms of *electrostatic conditions*.

Likewise, the electric field shows *no vortices or curls* in *electrostatic or quasi-electrostatic* case. This is in clear contrast to Fig. 2.31a with the illustrated *electromagnetic induction* and obvious *curls* of the electric field.

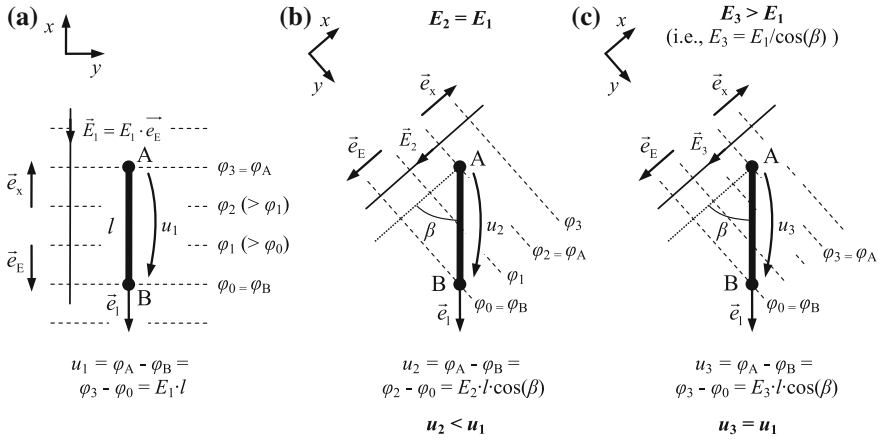

Fig. 2.11 The conceptual origin of the electric potential φ, the associated electric field $\vec{E}$, and the electric voltage u along the straight curve l connecting field points A and B under electrostatic conditions (Footnote 15). **a** $\vec{E}$ field in parallel to the straight line l yields a finite u_1 [(2.29) and (2.30)]. **b** The same $\vec{E}$ field is rotated with respect to l and now resides at a disorientation angle β to l, which yields a lower u_2 ($<u_1$). **c** A stronger $\vec{E}$ field is needed to reach again the level u_1 along l provided that β from (**b**) does not change

$$u(t) = \int_l \vec{E}(x,t) \cdot \mathrm{d}\vec{l} \tag{2.30}$$

with $\mathrm{d}\vec{l} = \mathrm{d}l \cdot \vec{e}_l$. The voltage $u(t)$ from (2.30) can be interpreted as the *line integral of the normal projection* of $\vec{E}(x,t)$ in the direction $\vec{e}_l$ along l or, in analogy, as the *line integral of the amplitude of the tangential component* of $\vec{E}(x,t)[= E_t(x,t)$ in (2.92)] in the direction $\vec{e}_l$.

Figure 2.11b illustrates that this projection equals to $\vec{E} \cdot \mathrm{d}\vec{l} = E_2 \cdot \vec{e}_E \cdot \vec{e}_l \cdot \mathrm{d}l = E_2 \cdot \cos(\beta) \cdot \mathrm{d}l$ with β as the *disorientation angle* between $\vec{e}_l$ and $\vec{e}_E$. If the angle β would equal 90° then the *tangential component* of $\vec{E}$ would disappear and the resulting u would equal zero. Please note that

- $\vec{E}(x,t)$ represents a *local vector quantity* with its local *signed magnitude* $E(x, t)$ *and its direction* $\vec{e}_E$ of
- $u(t)$, a *global scalar quantity* which is a signed real quantity only (2.30).

Figure 2.11 summarizes the aforementioned $\varphi(x)$ field from (2.28) (right side), the associated *homogeneous field* $\vec{E}(x)$ (i.e., $E(x) = |\vec{E}(x)| = \text{const}$ with varying x), and the resulting *voltage* u along the curve l connecting both positions A and B. The maximum drop in $u(= E_1 \cdot l)$ for a given $\vec{E}$ results when the orientation of l is in parallel to $\vec{E}$ with $\beta = 0$ and $\vec{e}_E = \vec{e}_l$ (Fig. 2.11a). With increasing β, the level of

$u\,(= E_1 \cdot l \cdot \cos(\beta))$ decreases by the *projection* factor $\vec{e}_E \cdot \vec{e}_l = \cos(\beta)$ in the range $0° < \beta < 90°$, as shown in Fig. 2.11b. Obviously, the absolute level of u can also be increased for $\beta \neq 0$ when rising the spatial change of $\varphi(x)$ field and thus the strength of the resulting $\vec{E}(x)$ field (2.28), as illustrated in Fig. 2.11c with $E_3 > E_1$. It should be recalled that the voltage u in Fig. 2.11 is independent on the particular *shape of the curve l* with its *fixed end points A and B* and depends on the associated φ difference of its end points (2.29) only if *electrostatic or quasi-electrostatic conditions* apply.

Electrical Impedance

The *global form of Ohm's law*[16] states that—in a *conductive body*, as shown in Fig. 2.12a, b—the *instantaneous electric conductive current* $i_E(t)$ through the body is proportional to the *instantaneous electric voltage* $u(t)$ along this body (in the direction of the current flow) divided by the *real resistance* R of this body (Kaniusas 2012, Footnote 2). An analogous relationship applies for the *amplitude* I_E of $i_E(t)$ and the *amplitude* U of $u(t)$, to give

$$i_E(t) = \frac{u(t)}{R} \quad \text{and} \quad I_E = \frac{U}{R}. \tag{2.31}$$

The *global form* in (2.31) considers global scalar quantities $i_E(t)$, I_E and $u(t)$, U (Fig. 2.12b) which describe the electric behaviour of the *whole conductive body*.

In contrast, the *local form of Ohm's law* in a *conductive body* considers the *local time-varying vector quantities* $\vec{j}_E(t)$ and $\vec{E}(t)$ with their *vector amplitudes* $\vec{J}_E$ and $\vec{E}$ of the corresponding $i_E(t)$ and $u(t)$, respectively [see (2.24) and (2.30)]. The local form describes the electric behaviour of *every spatial point within the conductive body* according to

$$\vec{j}_E(t) = \frac{\vec{E}(t)}{1/\gamma} \quad \text{and} \quad \vec{J}_E = \frac{\vec{E}}{1/\gamma} = \gamma \cdot \vec{E}, \tag{2.32}$$

see Fig. 2.12a. Here γ is the *local electrical conductivity* of the considered spatial point within the body; for detailed discussions see (2.54). Strictly speaking, (2.32) assumes

[16]Georg Simon Ohm (1789–1854) was a German physicist who stated that the current through a conductor is directly proportional to the voltage along this conductor and inversely proportional to the conductor's resistance, in terms of *Ohm's law*. Interestingly, Ohm's discovery was initially ridiculed and even reacted to with hostility by his contemporaries (compare Kaniusas (2012, Footnote 6)). Later, the importance of Ohm's law in electrical circuit analysis was recognized and Ohm was then considered the Mozart of electricity (Shukla 2008).

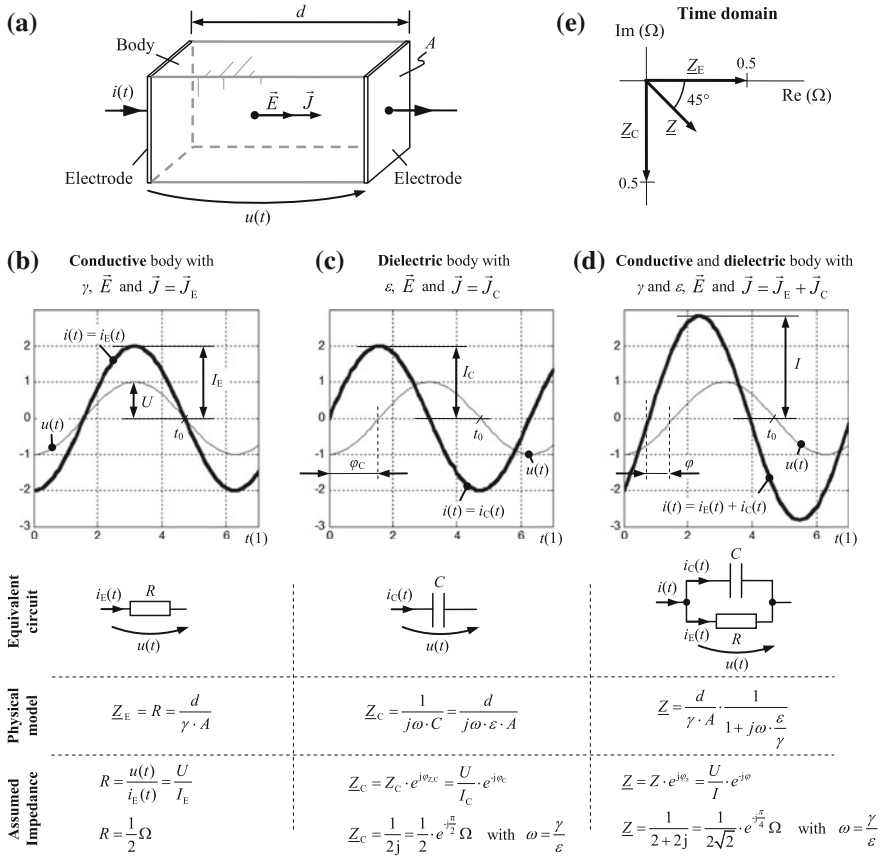

Fig. 2.12 The conceptual origin of the electrical impedance of a body between two electrodes (compare Fig. 2.18). **a** Body section between two electrodes. **b** Conductive body section yields in-phase changes of the conductive current $i(t) = i_E(t)$ through the body and the associated voltage $u(t)$ along the body with the resulting real resistance R (2.36). **c** Dielectric body section yields an out-of-phase relationship between the displacement current $i(t) = i_C(t)$ and the associated $u(t)$, i.e., the time course of $u(t)$ is delayed by 90° with respect to $i_C(t)$. The associated impedance $\underline{Z}_C$ has an imaginary part only (2.42). **d** Body section with conductive and dielectric properties yields an out-of-phase relationship between $i(t)$ and $u(t)$ with the resulting complex impedance $\underline{Z}$ (2.47). Plotted data in (**c**) and (**d**) assume $\omega = \gamma/\varepsilon = 1/\tau$ (2.49). The corresponding electrical equivalent circuit models, physical models of $\underline{Z}$, and assumed numerical $\underline{Z}$ values are shown. **e** The phasor diagram of $\underline{Z}_E$, $\underline{Z}_C$, and $\underline{Z}$ from (**b**)–(**d**) in the time domain (compare Fig. 2.18b–d)

- *isotropic body* (i.e., vectors $\vec{J}_E$ and $\vec{E}$ point in the *same spatial direction*, see Figs. 2.12a and 2.18a) and
- *linear body* (i.e., γ does not depend on the magnitudes J_E and/or E).

According to (2.32), time courses of $\vec{j}_E(t)$ and $\vec{E}(t)$ are *in-phase* without any temporal delay in-between, i.e., there is no rotational displacement between

complex amplitudes $\underline{J}_E$ and $\underline{E}$ in the *phasor diagram* from Fig. 2.18b. Please note that *biological media* can be *approximated as a conductor* at relatively *low field frequencies* (see Fig. 2.14).

However, (2.31) and (2.32) describe only the *amplitude/magnitude change*—based on the *real impedance R* or real γ—and are only valid for *conductive bodies*, as long as waveforms of $i_E(t)$ and $u(t)$ *oscillate in-phase* (Fig. 2.12b). In contrast, an *out-of-phase relationship* between the *total current* $i(t)[= i_E(t) + i_C(t)$, see (2.45)] and the associated sinusoidal $u(t)$ occurs in a *body* with *conductive and dielectric properties*. Here $i_C(t)$ is an additive component of $i(t)$ representing the *displacement current* through the polarizable medium of the body. Figure 2.12d illustrates the non-zero *phase shift* φ between sinusoidal waveforms $i(t)$ and $u(t)$. The *out-of-phase relationship* applies also to a *lossy dielectric* with its *dispersive dielectric permittivity* (Fig. 2.23) representing real *biological media*.

In fact, the *out-of-phase relationship* requires an introduction and use of a *complex impedance*—underscored in following sections—to describe not only

- the *amplitude change* between $i(t)$ and $u(t)$ but also
- the latter *phase shift* between $i(t)$ and $u(t)$.

Therefore, the *global form of Ohm's law* in a *conductive and dielectric body* states that the *complex amplitude* $\underline{I}$ of $i(t)$ through the body is directly proportional to the *complex amplitude* $\underline{U}$ of $u(t)$ along this body divided by the *complex impedance*

$$\underline{Z} = Z \cdot e^{j\varphi_Z} = R + j \cdot X \tag{2.33}$$

of this body, to give

$$\underline{I} = \frac{\underline{U}}{\underline{Z}} \quad \text{or} \quad I \cdot e^{j\varphi_I} = \frac{U \cdot e^{j\varphi_U}}{Z \cdot e^{j\varphi_Z}} = \frac{U}{Z} \cdot e^{j(\varphi_U - \varphi_Z)}. \tag{2.34}$$

Please note that the right side of (2.34) considers real magnitudes I, U, Z and the associated phases $\varphi_I, \varphi_U, \varphi_Z$ of the *complex amplitudes* $\underline{I} = I \cdot e^{j\varphi_I}$, $\underline{U} = U \cdot e^{j\varphi_U}$, $\underline{Z} = Z \cdot e^{j\varphi_Z}$, respectively. Figure 2.12d demonstrates U and I and their ratio U/I equalling Z.

The *real part* of $\underline{Z}$ is the *resistance R* and the *imaginary part* is the *reactance X*, as given in (2.33).

- For a *conductive body*—in line with (2.36) and (2.37)—a real $\underline{Z} = Z = R$ with zero $\varphi_Z = 0$ applies; with an *in-phase relationship* between $u(t)$ and $i(t) = i_E(t)$. Figure 2.12b depicts time courses $u(t), i_E(t)$ and the applicable physical model with an assumed numerical value of R determining the ratio $u(t)/i_E(t)$.
- For a *perfect lossless dielectric body*—in line with (2.42) and (2.43)—an imaginary $\underline{Z} = j \cdot X$ with $X < 0$ and $Z = |X|, \varphi_Z = -90°$ apply; with an *out-of-phase relationship* in terms of a delayed $u(t)$ with respect to $i(t) = i_C(t)$ by the *phase shift* of 90° (for sinusoidal courses). Figure 2.12c demonstrates the associated data.

- For a *conductive and dielectric body*, as well as for a *lossy dielectric*—in line with (2.47) and (2.48)—a complex $\underline{Z} = R + jX$ with $R > 0$, $X < 0$, and $Z = \sqrt{R^2 + X^2}$, $\varphi_Z = \arctan(X/R)$ with $-90° < \varphi_Z < 0°$ apply (compare Fig. 3.20c, e); with an *out-of-phase relationship* in terms of a delayed $u(t)$ with respect to $i(t) = i_E(t) + i_C(t)$ by the *phase shift* $|\varphi_Z|$. Figure 2.12d demonstrates an instructive case with $\varphi_Z = -45°$ with the assumed $\omega = \gamma/\varepsilon$.

The associated *local form of Ohm's law* for a *conductive and dielectric body* is

$$\vec{J} = \vec{J}_E + \vec{J}_C = \frac{\vec{E}}{1/(\gamma + j \cdot \varepsilon \cdot \omega)} = (\gamma + j \cdot \varepsilon \cdot \omega) \cdot \vec{E} \tag{2.35}$$

considering *vectors amplitudes* $\vec{J}_E$ and $\vec{J}_C$ with their *complex amplitudes* $\underline{J}_E$ and $\underline{J}_C$ (Fig. 2.18d) of the time-varying *conductive and displacement current density* $\vec{j}_E(t)$ and $\vec{j}_C(t)$, respectively. Here ε is the *dielectric permittivity* of the body and ω the *angular frequency*. In analogy with (2.32), (2.35) assumes an *isotropic and linear body*.

It is important to stress that γ and ε in *biological bodies* strongly depend on the *field frequency* due to diverse *dispersion phenomena* (see Figs. 2.20 and 2.21). In tissues acting as *lossy dielectrics*, ε becomes a complex quantity $\underline{\varepsilon}$ (2.77).

- The *global form of Ohm's law* considers *global electrical quantities*—such as *R and* $\underline{Z}$ in (2.31) and (2.34)—which are physical entities defined as *scalars* to describe the *global electric behaviour* of a delimited *tissue section*. In contrast,
- the *local form of Ohm's law* is obviously devoted to *local electrical quantities*—such as γ *and* ε in (2.32) and (2.35)—which are also *scalars* to describe the *local electric behaviour* of *each space point of tissue*.

Please note that *global quantities* can be *derived* from the corresponding *local quantities* and the relevant *geometric dimensions*, as exemplified in (2.47).

Global electrical impedance of a *tissue section* is relevant as it *dictates the current* in response to an applied *voltage stimulus*; see the *global Ohm's law* in (2.34). *Local electrical properties*, in analogy, *dictate pathways of the local current density* in response to an applied local *electric field*; see the *local Ohm's law* in (2.35).

Simple Tissue Model

Tissue as Conductor

Under the assumption that *biological tissue* behaves as an *electrical conductor*—with *unbound charges* in tissue acting as *mobile carriers* of the *conductive current* $i_E(t)$ through tissue (2.25)—a *tissue section* can be approximated as a *resistor* with its *resistance R* (Fig. 2.12a, b). Later, Section "Conductive Phenomena" describes conductive behaviour from a biophysical perspective.

The time course of the *voltage* $u(t)$ *across the resistor* is interrelated with the time course of the *current* $i(t) = i_E(t)$ *through the resistor* in accordance with (2.31). The two time courses $u(t)$ and $i_E(t)$ *do not show any phase shift* in-between and are graphically illustrated in Fig. 2.12b.

In general, the *conductive impedance* $\underline{Z}_E$ of a *conductive tissue section*—e.g., of an *electrolyte section* residing between two electrodes—equals the *ratio* between the *amplitude* $\underline{U} = U$ of $u(t)$ and the *amplitude* $\underline{I}_E = I_E$ of $i_E(t)$, and equals the real resistance R of this section (2.31). *Geometrical and electrical properties* of the *conductive tissue section* determine this R, to give

$$\underline{Z}_E = Z_E \cdot e^{j\varphi_{Z,E}} = \frac{\underline{U}}{\underline{I}_E} = \frac{U}{I_E} = R = \frac{d}{\gamma \cdot A} \tag{2.36}$$

with

$$Z_E = R \quad \text{and} \quad \varphi_{Z,E} = 0. \tag{2.37}$$

In accordance with Figs. 2.9a and 2.12a, b, the value of R is proportional to the *thickness* d of the conductive section *along the flow* of $i_E(t)$. By contrast, R is inversely proportional to the *homogeneous conductivity* γ of tissue within the section (*homogeneous section*) and to the *uniform cross-section area* A along the flow of $i_E(t)$. It should be recalled that γ *of biological bodies* strongly depends on the field frequency, i.e., γ shows *dispersive properties* with its size *increasing with frequency* (Fig. 2.21).

The right side of (2.36) assumes that the total current $i_E(t)$ is *homogeneously distributed* within the cross-section surface of the conductive body [at a relatively low frequency without any current displacement towards the outer surface of the body, see Figs. 2.10, 2.31b, and (2.88)]. The current $i_E(t)$ *penetrates perpendicularly this cross-section*, i.e., $i_E(t)$ penetrates the *face surface area* A. This is in analogy with the demonstrated current flow through A_1 and A_3 in Fig. 2.10.

Therefore, a restricted area for the current flow [i.e., a reduced A in (2.36)] and/or an increased length of the current path [i.e., an increased d in (2.36)] increase R and thus tend to decrease $i_E(t)$ along this path for a given $u(t)$ acting as a driving force.

- In global terms, the *conductive current* $i_E(t)$ takes the *spatial path of least resistance* R (2.31) or,
- in local terms, the *conductive current density* $j_E(t)$ takes the *spatial path of largest conductivity* γ (2.32).

The *total current* $i_E(t)$ within a *heterogeneous tissue* will always divide in such a way as to *minimize the total energy* expended—equal to the time integral of the product $u(t) \cdot i_E(t)$. For two parallel current branches with their resistances R_1 and R_2 and the respective *partial conductive currents* $i_{E1}(t)$ and $i_{E2}(t)$—as illustrated in Fig. 2.13a—the resulting *resistive current divider* yields

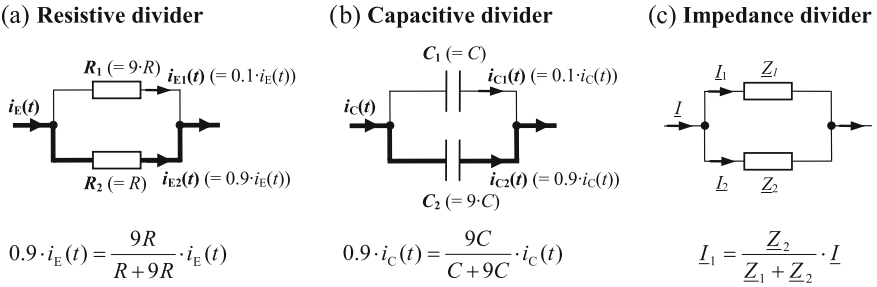

Fig. 2.13 Current divider with two branches indicating that the current takes the path of least impedance. **a** Resistive divider with the smaller resistor R carrying the most of the conductive current $0.9 \cdot i_E(t)$, see (2.38). **b** Capacitive divider in which the path with the largest capacitance $9 \cdot C$ carries the most of the displacement current $0.9 \cdot i_C(t)$, see (2.44). **c** Impedance divider where the complex amplitude $\underline{I}_1$ of the one current branch rises with increasing complex impedance $\underline{Z}_2$ of the other branch, see (2.51)

$$i_{E1}(t) = i_E(t) \cdot \frac{R_2}{R_1 + R_2} \quad \text{and} \quad i_{E2}(t) = i_E(t) \cdot \frac{R_1}{R_1 + R_2}. \tag{2.38}$$

Here the equality $i_E(t) = i_{E1}(t) + i_{E2}(t)$ necessarily applies.

For instance, the current $i_E(t)$ in Fig. 2.13a entering the parallel combination of the two resistances R and $9 \cdot R$ is split between resistances in inverse proportion to their size. The smaller resistor R carries $0.9 \cdot i_E(t)$, i.e., R carries the most of $i_E(t)$ according to the *division ratio* $9R/(R + 9R)$. It also follows that if the two resistances would have the same value (e.g., $9 \cdot R$ and $9 \cdot R$), the total current would be equally split (with $i_{E1}(t) = i_{E2}(t)$ in Fig. 2.13a).

Tissue as Dielectric

For comparison, if *biological tissue* is assumed to behave as a *dielectric body*—with *bound charges* in tissue acting as *immobile polarization centers* and thus carriers of the *displacement current* $i_C(t)$—a *tissue section* can be approximated as a *capacitor* with its *capacitance* C (Figs. 2.8 and 2.12a, c). Later, Section "Polarization Phenomena" describes dielectric and polarization phenomena in more detail.

The time course of the *voltage* $u(t)$ *across the capacitor*, i.e., across the arrangement of two identical *plane-parallel conductive capacitor plates* with the *dielectric body* between plates (Figs. 2.8 and 2.9b), is *proportional* to the accumulated *excess charge* $Q(t)$ and $-Q(t)$ *on the respective plate* (unbound charges) in line with

$$Q(t) = C \cdot u(t). \tag{2.39}$$

That is, the value of C *represents the proportionality factor* between $Q(t)$ and $u(t)$, whereas the *dielectric body* is assumed here to be *linear* (i.e., C in (2.39) does not depend on the actual level of $Q(t)$ and/or $u(t)$).

The time course of the *conductive current entering or leaving a capacitor plate* (via a wire connected to the plate) can be simply derived from the time derivative of $Q(t)$, see (2.25). On the other hand, this conductive current must simply equal the *displacement current* $i_C(t)$ *through the dielectric body of the capacitor* (see below), so that (2.25) and (2.39) yield

$$i_C(t) = \frac{dQ(t)}{dt} = \frac{d(C \cdot u(t))}{dt} = C \cdot \frac{du(t)}{dt} + u(t) \cdot \frac{dC}{dt} = C \cdot \frac{du(t)}{dt}. \tag{2.40}$$

Here we assume that C does not vary with time (i.e., $dC/dt = 0$); compare (Kaniusas 2012, Footnote 33) and Footnote 31 in Chap. 3. As the *capacitor is charged or discharged*—i.e., the capacitor plates *accumulate or lose progressively* $Q(t)$ in response to the *conductive current entering and leaving* the capacitor plate (2.25), respectively—the resulting *time course of* $u(t)$ becomes necessarily *delayed with respect to the time course of* $i_C(t)$ (by 90° for sinusoidal courses). This delay can be observed in (2.40) with $u(t)$ being a time integral of $i_C(t)$; the two sinusoidal time courses $u(t)$ and $i_C(t)$ are graphically illustrated in Fig. 2.12c.

Geometrical and electrical properties of a *dielectric tissue section* between plates determine its C equalling to

$$C = \frac{\varepsilon \cdot A}{d}. \tag{2.41}$$

In accordance with Figs. 2.9a and 2.12a, c, the value of C is proportional to the *homogeneous permittivity* ε ($=\varepsilon_0 \cdot \varepsilon_r$) of the dielectric body between plates (*homogeneous body*) and to the *area* A of a single capacitor plate. Likewise, the *cross-section surface* of the dielectric body with its area A is assumed to be *uniform along the flow* of $i_C(t)$ along the *distance* d between plates. By contrast, C is inversely proportional to d or, in other words, to the *thickness* d of the dielectric body between plates. It should be recalled that ε_r *of biological bodies* strongly depends on the field frequency, i.e., ε_r shows *dispersive properties* with its size *decreasing with frequency* (Fig. 2.20).

In analogy to (2.36), (2.41) assumes that the current $i_C(t)$ is *homogeneously distributed* within the cross-section surface of the dielectric body while $i_C(t)$ *penetrates perpendicularly this cross-section surface*, i.e., $i_C(t)$ penetrates the *face surface area* A. The homogeneous distribution of $i_C(t)$ implies a *homogeneous distribution of the electric field* $\vec{E}(t)$ between plates satisfying $E(t) = u(t)/d$ (Footnote 13). In fact, the homogeneous distribution requires a small d with respect to (maximum) lateral dimensions of capacitor plates; this assumption allows us to neglect *electric stray fields* (Kaniusas 2012, Footnote 13) on edges of plates, outside the dielectric body between plates.

The complex *capacitive impedance* $\underline{Z}_C$ of a *dielectric tissue section* (or of a capacitor) equals the *ratio* between the *complex amplitude* $\underline{U}$ of $u(t)$ and the *complex amplitude* $\underline{I}_C$ of $i_C(t)$ (2.34). The impedance $\underline{Z}_C$ is inversely related to

C (2.41) and to the *angular frequency* ω (=$2\pi \cdot f$), as can be derived from (2.40) and shown in Fig. 2.12a, c, to give

$$\underline{Z}_C = Z_C \cdot e^{j\varphi_{Z,C}} = \frac{\underline{U}}{\underline{I}_C} = \frac{1}{j \cdot \omega \cdot C} = \frac{d}{j \cdot \omega \cdot \varepsilon_0 \cdot \varepsilon_r \cdot A} = -j \cdot \frac{d}{\omega \cdot \varepsilon_0 \cdot \varepsilon_r \cdot A} \quad (2.42)$$

with

$$Z_C = \frac{1}{\omega \cdot C} \quad \text{and} \quad \varphi_{Z,C} = -\frac{\pi}{2}. \quad (2.43)$$

Please note that—strictly speaking—not only $\underline{Z}_C$ shows a frequency dependence with $1/\omega$ but also its parameter ε_r shows a sophisticated dependence on *frequency f* [modelled as (2.78)].

It is worth noting that (2.40) applies for *any time-varying waveforms* $u(t)$ across and $i_C(t)$ through the capacitor with its C. In contrast, (2.42) applies for complex amplitudes $\underline{U}$ and $\underline{I}_C$ of a *harmonic waveform* $u(t)$ and another *harmonic waveform* $i_C(t)$, respectively, with their identical f. In fact, it does not limit the application of (2.42) to *sinusoidal waveforms* only since any *time-varying waveform* can be decomposed into its frequency-dependent sinusoidal components (see *Fourier series* from Kaniusas (2012, Footnote 150)). Namely, any waveform (e.g., of $u(t)$) can be decomposed and then evaluated based on (2.42); finally, the resulting waveform (e.g., of $i_C(t)$) can be composed out of its sinusoidal components.

As the *conductive current* $i_E(t)$ takes the *path of least resistance* (see above),

- the *displacement current* $i_C(t)$ takes the *spatial path of least impedance* $|\underline{Z}_C|$ (2.42). In other words, $i_C(t)$ goes along the *path with largest capacitance* C.
- In local terms, the *displacement current density* $j_C(t)$ takes the *spatial path of largest permittivity* ε (2.35).

Figure 2.13b illustrates a *divider* with two parallel branches carrying *partial displacement currents* $i_{C1}(t)$ and $i_{C2}(t)$ across the respective capacitances C_1 and C_2. A *capacitive current divider* results with

$$i_{C1}(t) = i_C(t) \cdot \frac{C_1}{C_1 + C_2}, \quad i_{C2}(t) = i_C(t) \cdot \frac{C_2}{C_1 + C_2} \quad (2.44)$$

and the *total current* $i_C(t) = i_{C1}(t) + i_{C2}(t)$. The branch with the larger capacitance $9 \cdot C$ (>C) drains 90% of the total $i_C(t)$ according to the *division ratio* $9 \cdot C/(C + 9 \cdot C)$.

As illustrated in Fig. 2.8, a *conduction current* $i_E(t)$ flows along a *thin* wire (carried by unbound charges within the wire) while $i_E(t)$ continues as a *displacement current* $i_C(t)$ through a *dielectric non-conductive space* [without any unbound charges but bound, see (2.66)] between capacitor plates. In particular, $i_C(t)$ *substitutes* $i_E(t)$ in Fig. 2.8 at the left-conductive-plate/dielectric boundary while $i_E(t)$ originates again at the dielectric/right-conductive-plate boundary with

the equality $i_E(t) = i_C(t)$; compare (2.25) and (2.65). In addition, Figs. 2.27 and 3.26 illustrate also how displacement currents in the air surrounding a conductive body convert to conductive currents within the body (and vice versa).

Despite the equivalence $i_E(t) = i_C(t)$ in Fig. 2.8, the inequality of the associated *current density magnitudes* $|\underline{J}_E| \gg |\underline{J}_C|$ (2.23) applies. Obviously, this is because the *cross-section area A* of capacitor plates is large as related to a small cross-section area A' ($\ll A$) of wires connected to plates. Likewise, the *conduction current amplitude* $|\underline{J}_E| \cdot A' = I_E$ along wires equals the *displacement current amplitude* $|\underline{J}_C| \cdot A = I_C = I_E$ between plates.

Tissue as Conductor and Dielectric

In fact, the real *biological tissue* shows both *conductive and dielectric properties*, as indicated in Fig. 2.9a; see also Sect. 3.1.1.1. Here two *fundamental processes* occur in parallel:

- the *electrical conduction* of *mobile/unbound charges* and
- the *dielectric polarization* of *immobile/bound charges*

within tissue. Therefore, the electrical behaviour of a *tissue section can be modelled* as a *parallel combination* of

- a conductive element, a *resistor*, with its *resistance R* and
- a capacitive element, a *capacitor*, with its *capacitance C*,

as illustrated in Figs. 2.9b and 2.12a, d. Given this *simple tissue model*, it is clear that the *total current i(t) through the tissue section* can be additively split into a *conductive component* $i_E(t)$ (through R) and another *displacement component* $i_C(t)$ (through C) according to

$$i(t) = i_E(t) + i_C(t). \tag{2.45}$$

The time course of $i(t)$ in response to the voltage $u(t)$ *across the tissue section* can be simply derived from (2.31), (2.40), and (2.45) as

$$i(t) = \frac{u(t)}{R} + C \cdot \frac{\mathrm{d}u(t)}{\mathrm{d}t} \tag{2.46}$$

with a relevant observation that $u(t)$ across R is identical with $u(t)$ across C (Fig. 2.9b). Both time courses $u(t)$ and $i(t)$ are illustrated in Fig. 2.12d. Please note that—as in the case of dielectric tissue—the *time course of u(t)* is *delayed with respect to the time course of i(t)* (but by less than 90° for sinusoidal courses).

The associated *complex impedance* $\underline{Z}$ of a *tissue section* equals the *ratio* between the *complex amplitude* $\underline{U}$ of $u(t)$ and the *complex amplitude* $\underline{I}$ of $i(t)$, and can be directly derived from the *differential equation* in (2.46). Likewise, $\underline{Z}$ can be modelled as the *parallel connection* of the *conductive impedance* $\underline{Z}_E$ [$=R$, see (2.36)] and the *capacitive impedance* $\underline{Z}_C$ [$=1/j\omega C$, see (2.42)]; i.e., as R in parallel with C (Fig. 2.9b), to give

$$\underline{Z} = Z \cdot e^{j\varphi_Z} = \frac{\underline{U}}{\underline{I}} = \frac{\underline{Z}_C \cdot \underline{Z}_E}{\underline{Z}_C + \underline{Z}_E} = \frac{1}{\frac{1}{R} + j \cdot \omega \cdot C} = \frac{R}{1 + j \cdot \omega \cdot \tau} = \frac{d}{\gamma \cdot A} \cdot \frac{1}{1 + j \cdot \omega \cdot \frac{\varepsilon}{\gamma}} \tag{2.47}$$

with

$$Z = \frac{R}{\sqrt{1 + (\omega \cdot \tau)^2}} \quad \text{and} \quad \varphi_Z = -\arctan(\omega \cdot \tau). \tag{2.48}$$

The ratio ε/γ is known as the *relaxation time constant* τ

$$\tau = R \cdot C = \frac{\varepsilon}{\gamma} \tag{2.49}$$

in terms of *β-dispersion* from (2.74).

In analogy with (2.36) and (2.41), the right side of (2.47) assumes *homogeneous properties* γ and ε of tissue. It also assumes that the *cross-section surface* of the tissue section with its *area A* is *uniform along the flow* of $i(t)$, i.e., along the section's *thickness d* (Fig. 2.9a). In addition, the current $i(t)$ is *homogeneously distributed* within the cross-section surface while $i(t)$ *penetrates perpendicularly* this surface.

It should be recalled that electrical *tissue properties* $\varepsilon = \varepsilon_r \cdot \varepsilon_0$ and γ are *frequency-dependent* in terms of various *dispersion mechanisms* in tissue. Since ε_r decreases with increasing f while γ increases with increasing f (Figs. 2.20 and 2.21), the *derived ratio* $\tau = \varepsilon/\gamma$ (2.49) becomes *frequency-dependent* as well and τ decreases with increasing f.

It is important to observe that the share of $\underline{Z}_C$ in the total $\underline{Z}$ (2.47) decreases with increasing f [i.e., $\underline{Z}_C$ is proportional to $1/f$, see (2.42)] while the associated $i_C(t)$ and total $i(t)$ increase (2.45) given a certain frequency-independent $u(t)$. Please note that the *dispersive* ε also contributes to the dependence of $\underline{Z}_C$ on f (see Fig. 2.15 and the associated discussion). In contrast, the share of $\underline{Z}_E$ (2.36) in $\underline{Z}$ does not vary with f as well as the associated $i_E(t)$—for a given frequency-independent $u(t)$—under an assumption that γ is not subjected to any *dispersion* and thus is *constant* over f. In other words,

- at *low* f ($\ll 1/(2\pi \cdot \tau)$) *biological tissue* behaves like a *conductor*. With *decreasing f*, the magnitude of $\underline{Z}_C$ converges towards infinity [$|\underline{Z}_C| \to \infty$ for $f \to 0$ in (2.42)] and thus the approximation $\underline{Z} \approx \underline{Z}_E$ applies at low f in (2.47) and Fig. 2.9b. In contrast,
- at *high* f ($\gg 1/(2\pi \cdot \tau)$) *biological tissue* behaves as a *dielectric*. With *increasing f*, capacitive effects of tissue progressively dominate while $\underline{Z}_C$ progressively short-circuits $\underline{Z}_E$ ($|\underline{Z}_C| \to 0$ for $f \to \infty$) yielding $\underline{Z} \approx \underline{Z}_C$ at high f in (2.47) and Fig. 2.9b;

compare with a similar discussion of (2.69).

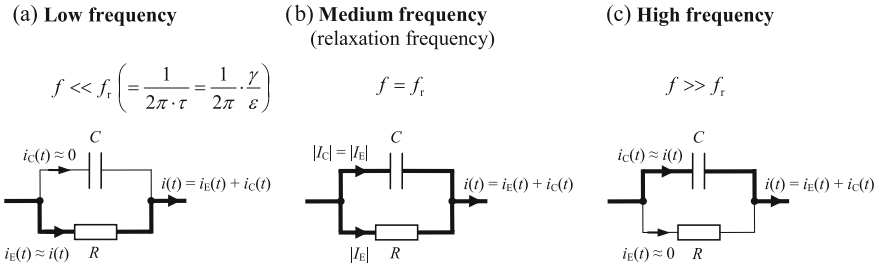

Fig. 2.14 Electrical equivalent circuit model of biological tissue with the electrical resistance R and capacitance C, see Figs. 2.9 and 2.12d. The qualitative distribution of the conductive current $i_E(t)$ and displacement current $i_C(t)$ is indicated **a** for the relatively low field frequencies $f \ll f_r$, with f_r as the relaxation frequency (2.50) and τ the relaxation time constant (2.49); **b** for the medium $f = f_r$, with the resulting equal magnitudes $|I_E| = |I_C|$ of $i_E(t)$ and $i_C(t)$; and **c** for the relatively high $f \gg f_r$

Figure 2.14a illustrates this behaviour, in that $i_E(t)$ across R dominates at the relatively *low* f ($\ll 1/(2\pi \cdot \tau)$) with $i_E(t) \approx i(t)$. By contrast, the current $i_C(t)$ across C dominates at the relatively *high* f ($\gg 1/(2\pi \cdot \tau)$) with $i_C(t) \approx i(t)$ (Fig. 2.14c). It is instructive that at the *relaxation frequency* f_r

$$f_r = \frac{1}{2\pi \cdot \tau} = \frac{1}{2\pi} \cdot \frac{\gamma}{\varepsilon} \tag{2.50}$$

both currents $i_E(t)$ and $i_C(t)$ become *equal in their respective magnitudes* $|I_E| = |I_C| = |\underline{U}/R|$ but not in their phase, see (2.49) and Fig. 2.14b. In fact, the equality $\underline{Z}_E = j \cdot \underline{Z}_C = R$ applies at $f = f_r$ that can be easily derived from (2.42) with $\omega = 1/\tau = \gamma/\varepsilon$.

Figure 2.13c illustrates an *impedance divider* given a *heterogeneous tissue* with its *conductive and dielectric properties*. The *total current* with its amplitude $\underline{I}$ branches into two *partial currents* $\underline{I}_1$ and $\underline{I}_2$ down to the impedances $\underline{Z}_1$ and $\underline{Z}_2$, respectively; in line with

$$\underline{I}_1 = \underline{I} \cdot \frac{\underline{Z}_2}{\underline{Z}_1 + \underline{Z}_2} \quad \text{and} \quad \underline{I}_2 = \underline{I} \cdot \frac{\underline{Z}_1}{\underline{Z}_1 + \underline{Z}_2}. \tag{2.51}$$

It can be observed that the branch with the smaller impedance drains the larger part of the total $\underline{I}$, similar to (2.38).

From Tissue Model to Real Data

It is instructive to *estimate the level of the resistance R and capacitance C* for a *rectangular section of muscle* residing between two electrodes, as illustrated in Fig. 2.12a. Let us assume *muscle's dimensions* of 1 cm × 1 cm × 10 cm (d = 0.1 m and $A = 1 \cdot 10^{-4}$ m^2 in Fig. 2.12a) and the following *muscle's electrical properties* γ = 0.23 S/m (approximated from Fig. 2.21) and $\varepsilon_r = 17 \cdot 10^6$ (from Fig. 2.20) at

the field frequency of 50 Hz. Then (2.36) yields $R \approx 4.35\ \text{k}\Omega$, i.e., *R in the range of kΩ*, whereas (2.41) yields $C \approx 0.15\mu\text{F}$, i.e., *C in the range of nF*.

The associated *complex impedance* $\underline{Z} = Z \cdot e^{j\varphi_Z}$ (2.33) of this *muscle section* (Fig. 2.12a) amounts to $4.17\ \text{k}\Omega - \text{j} \cdot 0.86\ \text{k}\Omega \approx 4.26\ \text{k}\Omega \cdot e^{-\text{j}\cdot 11.6^\circ}$ at 50 Hz according to (2.47) and (2.48). That is, the *magnitude Z* has decreased as compared with *R* ($4.26\ \text{k}\Omega < 4.35\ \text{k}\Omega$) while the resulting *phase shift* $\varphi_Z \approx -11.6^\circ$ becomes non-zero and is negative, as can be clearly seen in (2.48) ($Z < R$ and $-90^\circ < \varphi_Z < 0^\circ$ for $f > 0$) and is discussed with respect to Fig. 2.12d.

Of course, the capacitance *C* in parallel to the resistance *R* reduces *Z* with respect to *R* for any *non-zero frequency* (2.48). The phase φ_Z is zero for zero frequency only (direct current), whereas φ_Z is negative for any non-zero frequency. In analogy with the discussion of Fig. 2.14,

- *the lower the frequency*, the more close $\underline{Z}$ of the biological body approaches *R* and the more valid the approximation is of the *biological body as a conductor* (with $\underline{Z} = R$ and $\varphi_Z = 0$ at $f = 0$); see Sections "Relaxation and Dispersion Effects on Conductivity and Polarization" and "Biological Boundaries".
- *The higher the frequency*, the more close $\underline{Z}$ approaches $1/\text{j}\omega C$ and the more valid the approximation is of the *biological body as a dielectric* (with $\underline{Z} = 1/\text{j}\omega C$ and $\varphi_Z = -90^\circ$ at $f \to \infty$).

Figure 2.15 depicts the magnitude *Z* and the phase φ_Z of $\underline{Z}$ as a *dispersive function* of frequency—based on (2.47) and (2.48)—considering a *muscle section*, *fat section*, and *blood section* of identical dimensions. The associated *frequency-dependent* γ *and* ε_r are taken from Figs. 2.21 and 2.20, respectively. The fat section shows the highest *Z*, followed by muscle and blood, whereas *Z decreases step-wise* in each case (Fig. 2.15a) due to step-wise changes of γ and ε_r (Figs. 2.21 and 2.20).

For muscle and blood, comparisons are made when *dispersion phenomena are disregarded*. Plotted *approximations without dispersions* use the frequency-independent γ and ε_r with their constant numerical values taken at 50 Hz, i.e., $\gamma = 0.23$ S/m, $\varepsilon_r = 17 \cdot 10^6$ for *muscle* and $\gamma = 0.7$ S/m, $\varepsilon_r = 5260$ for *blood* (Fig. 2.15). Thick dots in Fig. 2.15 indicate locations at 50 Hz at which *Z* and φ_Z with and without dispersions clearly overlap. The only left frequency dependence in these approximations can be seen in (2.47).

Please note that the magnitude *Z with dispersions* decreases slower with frequency than *Z without dispersions* (Fig. 2.15a). This is because the *relaxation time constant* $\tau = \varepsilon/\gamma$ (2.49)—located in the denominator of the fraction of $\underline{Z}$ (2.47)—decreases with increasing frequency due to *dispersion mechanisms* (see above). This decreasing frequency-dependent *dispersive* τ elevates the associated *Z* as compared with *Z* when a *frequency-independent non-dispersive* τ is used. In analogy, as illustrated in Fig. 2.15b, the decreasing *dispersive* τ decreases the *imaginary part* of the denominator of $\underline{Z}$ (2.47) with increasing frequency; thus, it lowers the absolute size $|\varphi_Z|$ of φ_Z as compared with $|\varphi_Z|$ *without dispersions*.

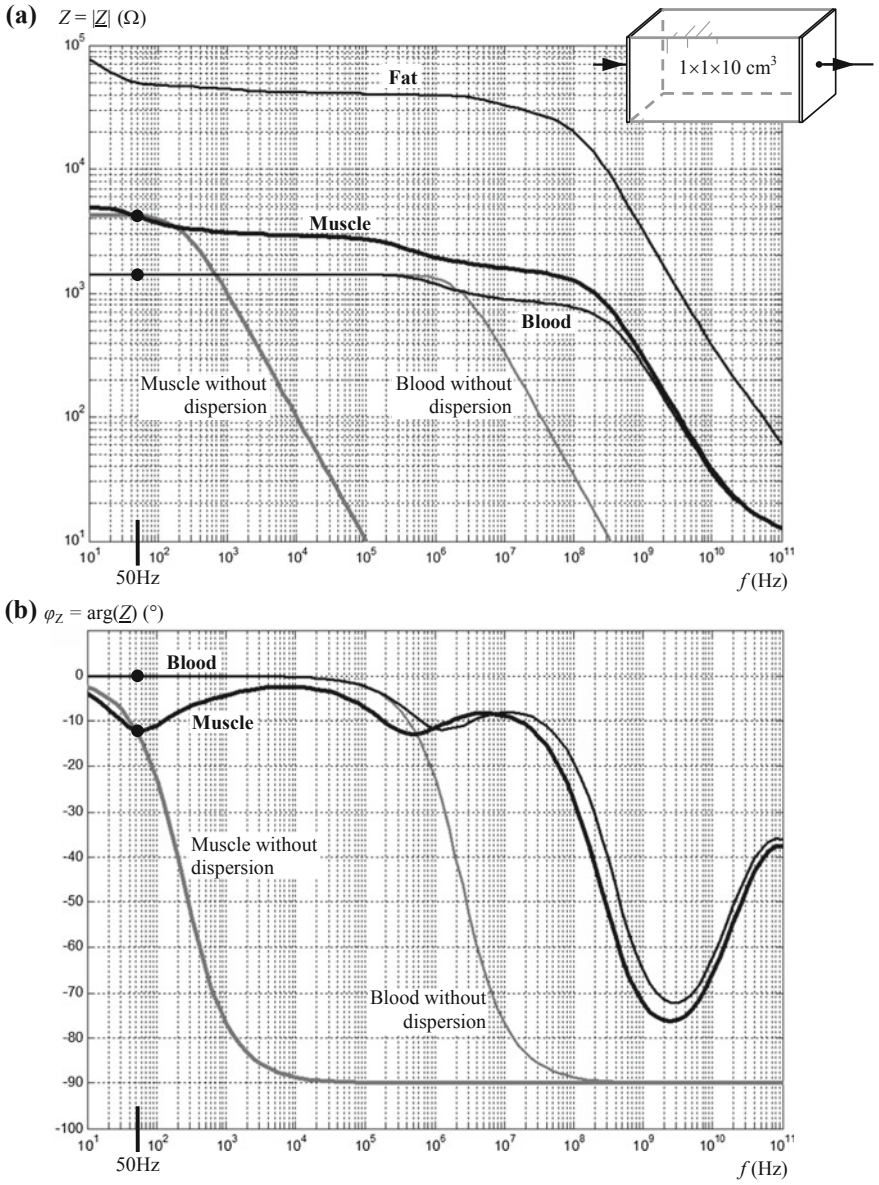

Fig. 2.15 Frequency variation of **a** the magnitude Z and **b** the phase φ_Z of the complex impedance $\underline{Z}$ of a rectangular section of muscle, fat, or blood with the section's dimensions 1 cm × 1 cm × 10 cm. Plotted estimations are based on 2.47 and 2.48 (with $d = 0.1$ m and $A = 0.01 \cdot 0.01$ m^2 = 10^{-4} m^2) with the frequency-dependent permittivity ε from Fig. 2.20 and the frequency-dependent conductivity $\gamma = \gamma_{\text{eff}}$ from Fig. 2.21 (see black curves). For comparison, Z and φ_Z are given without the frequency dependence of ε and γ (see grey curves), i.e., without dispersions considered and with constant values of ε and γ (taken at 50 Hz from Figs. 2.20 and 2.21)

Electrical Properties of Biological Tissue

The *bulk electrical*[17] *properties* of biological tissues are highly relevant for interaction of electric biosignals with tissues. These properties determine current pathways within heterogeneous tissues and the local amount of deposited energy within particular tissue along current pathways.

In particular, the local *effective conductivity* γ_{eff} determines the distribution of conductive currents (2.54) within tissue while the local relative *dielectric permittivity* ε_{r} determines the distribution of displacement currents (2.66). Obviously, the total current is given as the sum of both conductive and displacement currents (2.35). The *deposited energy* is a function of loss-related tissue properties. Since biological tissue acts as both the lossy conductor and lossy dielectric, the characteristic γ_{eff} determines the total amount of the deposited energy (2.58) but not the *ionic conductivity* γ alone accounting for lossy conductor only [$<\gamma_{\text{eff}}$, see (2.82)].

Macroscopic electrical properties γ_{eff} and ε_{r} are determined, among others, by

- *microscopic* structure of biological tissue, i.e., the tissue type,
- operation *frequency*, i.e., the field frequency within tissue,
- tissue *temperature*,
- *water* content in tissue, and by
- *intactness* of cellular membranes since most tissues act as suspension of cells.

Table 2.2 summarizes electrical properties for the most relevant types of physical and biological media involved in the generation, absorption, reflection, and transmission of electric biosignals. It can be observed that ε_{r} and γ_{eff} vary among diverse media and also strongly depend on the field frequency due to diverse *polarization and dispersion* mechanisms (Fig. 2.19). Please recall from (2.71) and (2.72) that biological tissue at *low frequencies* behaves as *conductor* and thus its γ_{eff} dominates the electrical behaviour of tissue (with $\gamma_{\text{eff}} \approx \gamma$ before dispersion regions, see Fig. 2.21). At *high frequencies*, the *dielectric behaviour* of tissue prevails with ε_{r} being the dominant property of tissue.

For instance, *blood* is a good conductor while *fat* is a poor conductor, whereas *muscle* is intermediate in its γ_{eff}. Detailed courses of ε_{r} and γ_{eff} over frequency can be observed in Figs. 2.20 and 2.21. For instance, ε_{r} of muscle decreases from about 10^6 to 10^3 with increasing frequency in the range from 1 kHz to 1 MHz, whereas γ_{eff} of muscle increases from about 0.3 S/m to 0.5 S/m in this frequency range.

The conductivity γ_{eff} of the *lungs* is a strong function of the air content. Deflating the lungs greatly increases γ_{eff} at relatively *low frequencies* (below β-dispersion of the lungs). A change from about 0.06 to 0.13 S/m is reported for *inflated* and *deflated lungs*, respectively, at 10 kHz and below (Surowiec 1987). The permittivity ε_{r} of the deflated lungs was also reported to be higher than that of the inflated lungs at these low frequencies around 10 kHz. In fact, the size of ε_{r} almost doubles for the

[17] *Magnetic body properties* can be well approximated by those of the air. Biological body behaves *neutral as the air*, whereas the body's magnetic permeability $\mu = \mu_0 \cdot \mu_{\text{r}} \approx \mu_0$ equals to the free space permeability μ_0 with the relative permeability $\mu_{\text{r}} \approx 1$.

deflated lungs at 10 kHz, whereas ε_r is in the range of about 10^5. In particular, charging of the cellular structures forming the alveoli seems to contribute to the *lung's polarization* below a *low-frequency β-dispersion*. In addition, the membrane polarization of the capillary erythrocytes in the lungs—i.e., polarization of the capillary blood in the lungs—seems to contribute to the lung's polarization below another *high-frequency β-dispersion*.

For comparison, please recall that γ_{eff} of *intracellular space* is about 1 S/m, whereas γ_{eff} of *extracellular space* is about 2 S/m (Kaniusas 2012, Sect. 2.1.2.1.2) for relatively *low frequencies* around 10 Hz (Foster 1996). At such low frequencies, the equality $\gamma_{eff} \approx \gamma$ applies for intracellular and extracellular media.

From a diagnostic and therapeutic point of view, *inhomogeneous properties* ε_r and γ_{eff} provide necessary contrasts for permanent and induced biosignals. These contrasts reflect *local volume changes*, *local polarizability changes*, and *local conductivity changes* over time, which, for instance, can be intentionally used

- to asses cardiac and respiratory activity (in *diagnosis*),
- to heat muscle and fat with different intensities (in *therapy*, see Footnote 115),
- to differentiate between *normal tissue and tumor tissue*[18] as well as

[18] *Electrical properties* of different tissues (Table 2.2) provide significant *contrasts* between *benign tissues* and *malignant tissues* (cancer) due to their different morphological structures present.

As the most constant difference between tumor and normal tissues (usually surrounding tumor tissues), *tumors* have significantly *higher water content* by about 10–20% (by weight) than intact normal tissues (Foster 1996). This is partly because of cellular necrosis in tumors (the loss of the cell membrane integrity), smaller volume fraction of intact cells (which act as insulating inclusions at relatively *low frequencies* below β-dispersion of cellular membranes, see Fig. 2.22), and irregular dense vascularization of tumors (abnormal formation of new blood vessels). Because of the increased water content, it can be expected that *tumor* tissues will exhibit somewhat *larger* ε_r and γ_{eff} in the frequency range of γ-dispersion (GHz range) than normal tissues; compare with an analogous discussion on the difference between seawater and soft tissues with respect to γ-dispersion in Section "Dispersion Model Versus Experiment".

With ongoing *necrosis*, γ_{eff} of tumor tissues increases in the kHz and MHz ranges while ε_r decreases. That is, the mechanical *breakdown of cell membranes* increases the volume fraction of tissue that can carry current at these low frequencies so that γ_{eff} *increases*; compare the widening of current pathways from Fig. 2.22a to 2.22b. In analogy, disintegrated membranes reduce the amount of interfacial polarization of cell membranes so that the effective ε_r *decreases*.

These discussed differences between tumor and normal tissues can be used for the *diagnosis* of malignant tissues. However, the particular tendencies of ε_r and γ_{eff} in tumor tissues as related to healthy tissues can not be generalized. Large differences exist between different tumor types (e.g., liver, spleen, or prostate) and between different development stages of the tumor (e.g., with or without necrosis). In particular, *good blood perfusion* and *large blood volume* in tissue (i.e., its high initial conductivity) and *absent necrosis* tend to *minimize any differences* in electrical properties between tumor and normal tissues (Foster 1996).

To give a quantitative example, prostate tumor tissue should be considered in more detail (Mishra 2012). From a physiological point of view, *benign prostate tissue* consists of fibromuscular structures surrounded by large amount of extracellular fluid, which provides a low impedance pathway for current to flow. In contrast, *malignant prostate tissue* is more cellular in its structure so that the cell membranes impose significant resistive elements that lead to reduced γ_{eff} of the bulk.

- for the assessment of tissue *changes after death*[19] (e.g., in food control).

It should be stressed that *converging* values of ε_r and γ_{eff} obscure these contrasts and thus reduce, for instance, the diagnostic power of physiological data as derived from biosignals. In fact, *high contrasts* in ε_r and γ_{eff} can be expected at *low frequencies*, whereas *low contrasts* prevail at *high frequencies*. This is because the frequency-dependent courses of ε_r and γ_{eff} in Figs. 2.20 and 2.21 are widely dispersed at low frequencies, whereas these courses approach each other at high frequencies. For instance, there is no more difference between muscle, blood, and water in electrical terms at high frequencies, as compared with low frequencies.

Fluid Content

In practice, the *fluid content* of a particular tissue is a major determinant of its electrical properties. The presence of water determines strongly electrical properties of tissues and their dependence on the frequency. *Water* accounts for about 70–80% of the volume of most *soft tissues* and for only about 20% of the volume of *fatty tissues*. Muscle and other tissues with *high-water and high-salinity content* are highly conductive and thus exhibit relatively *high losses*. These losses are especially prominent in the course of γ-dispersion, as can be seen in Fig. 2.21 based on the relatively strong change of γ_{eff} in muscle of about 60 S/m. In contrast, fat and

---

- The *effective* γ_{eff} was reported to increase from 0.18 S/m to 0.33 S/m for benign prostate tissue with increasing frequency in the range of 1–100 kHz using a bipolar configuration of electrodes (Mishra 2012); compare Fig. 2.21. In contrast, a much smaller increase of γ_{eff} from 0.07 S/m to 0.08 S/m was observed for malignant prostate tissue in the latter frequency range. Correspondingly,
- the *effective* ε_r was reported to decrease from $2 \cdot 10^6$ to $3 \cdot 10^4$ for benign tissue with increasing frequency in the latter frequency range, whereas a decrease from $7 \cdot 10^5$ down to $5 \cdot 10^3$ was observed for malignant tissue (Mishra 2012).

In short, *benign prostate tissue* tends to show higher γ_{eff} and higher ε_r than *malignant tissue*.

[19]The *dying tissue* exhibits specific and instructive changes in its γ_{eff} and ε_r, which can be derived from dielectric data (usually highly spread) of excised tissues at low field frequencies below about 1 MHz (Foster 1996).

- In the *short-term* (within a few minutes and hours after the death), cells undergo *swelling* that *decreases* γ_{eff} of the bulk tissue at *low field frequencies* (in the kHz range, i.e., *below β-dispersion* of cellular membranes). As shown in Fig. 2.22, this is because electrical currents largely pass through the extracellular spaces at these low frequencies so that the swelling constricts these extracellular spaces, decreases their effective cross-section area, and thus decreases the bulk γ_{eff}.
- In the *long-term* (within a one or few days up to weeks after the death), gross *disruption of cells* and *breakdown of cell membranes* (autolysis) occur in the dying tissue. It *increases* γ_{eff} of the bulk tissue at low frequencies. This is because cells as non-conducting particles in tissue—with their membranes acting as isolating barriers at these low frequencies—disappear and do not hinder anymore the current flow. The corresponding ε_r *decreases* at low frequencies due to disintegrated membranes, i.e., there is a progressive decline in the dominance of β-dispersion with the progressive disruption of cells.

In short, changes in electrical properties γ_{eff} and ε_r of the dying tissue are due to *fluid redistribution* within tissue (at *short times*) and due to *membrane breakdown* (at *long times*).

other *low-water content tissues* are less conductive and thus exhibit relatively *low losses* during γ-dispersion; see the relatively small change of γ_{eff} in fat of only about 3 S/m (Fig. 2.21). For instance, the *whole-body fat percentage* is usually assessed by measurements of the tissue impedance (e.g., at 50 kHz) because fat is a poorer conductor than water (Miklavcic 2006).

Anisotropy

Some tissues such as muscle exhibit an extreme *anisotropy in its structure* (Kaniusas 2012, Fig. 2.23) which clearly results in an extreme *anisotropy in electrical properties* ε_r and γ_{eff} (Footnote 30). The rationale of the anisotropy within *elongated muscle bundles or nerve fibers* can be simply demonstrated by considering spatial accumulations of individual elongated structures side by side and their exposure to electric and/or current density fields.

Conductive behaviour is subjected to the *anisotropy* because

- *longitudinal currents* can directly and easily travel along elongated structures. In contrast,
- *transversal currents*—mostly perpendicular to isolating membranes of muscle and nerve cells—must travel in *circuitous pathways* around individual cells and around individual bundles.

The resulting paths for transversal currents are less straightforward—as shown in Fig. 2.64—and thus are effectively longer than for longitudinal currents, which implies a higher γ_{eff} of the bulk for longitudinal currents (2.36). That is, the difference in the effective path length accounts for the *directional difference* in γ_{eff} within anisotropic tissue.

Such anisotropic variations are highly dominant for *low field frequencies* where the anisotropic tissue structure is still the major determinant of ε_r and γ_{eff}. Namely, anisotropy is relevant for frequencies below β-dispersion (below MHz) with still some degree of anisotropy left for even higher frequencies below γ-dispersion (below GHz). With increasing frequency, the aforementioned *transversal currents* start to bypass isolating cellular membranes via displacement currents (Fig. 2.22b) so that the anisotropic behaviour almost disappears with increasing frequency above β-dispersion.

For instance, electrical properties ε_r and γ_{eff} vary by the factor 7 to 10 in *muscle fibers* when the orientation of the incident electric field changes from parallel to perpendicular with respect to the muscle fiber axis (Foster 1996). For comparison, anisotropic γ_{eff} ratios of about 10 to 1 have been attributed to *nerve bundles* (Reilly 1998). As discussed above, γ_{eff} of muscle tends to be higher for currents along fibers (Footnote 30). The longitudinal ε_r of muscle fibers seems to be higher than the transversal ε_r for relatively low frequencies below 1 kHz, whereas this inequality reverses for higher frequencies approximately below β-dispersion (Gabriel 1996a).

Average Body Tissue

Electrical properties of the *average body tissue* are modelled using ε_r and γ_{eff} equal to two-thirds that of muscle tissue at the field frequency of interest (Furse 2009). However, this simplification is not applicable for evaluating near field effects and for the deposition of the peak power within heterogeneous tissues. The *mass density*

of the *average body tissue* is assumed to equal that of water, i.e., it equals 1 kg/m^3 (Furse 2009).

Usually, the homogenous $\gamma_{\text{eff}} \approx \gamma$ of *soft, high water content tissues* is assumed to be about 0.2 S/m[20] (CRP 1997) given relatively *low field frequencies* below β-dispersion (Figs. 2.19b and 2.21). This value is based on a particular *volume fraction of the extracellular fluid* since low frequency currents circumvent cells acting as isolating insets within a conducting medium (Fig. 2.22a). However, this fraction can significantly vary with physiological changes in tissues and cells (Foster 1996) and so does γ_{eff} of the bulk tissue.

Mutual Field Coupling and Quasi-electrostatic Situation

When *dimensions of the biological body*—exposed to ambient time-varying *electric and/or magnetic fields*—are small with respect to the field *wavelength* λ within the body, which implies

- relatively *low frequencies f* of fields (including constant fields with $f = 0$) and/or
- relatively *small geometrical size l* of exposed structures of the body,

the induced *electric and magnetic fields* within the body remain uncoupled. Please note that decoupled fields can be independently considered in their interactions with tissue.

In fact, this situation with *decoupled fields* is known as the *quasi-electrostatic situation*; see Footnote 15 and Fig. 2.2a. Here the *condition*

$$\frac{l \cdot \hat{B}}{T \cdot \hat{E}} \ll 1 \text{ transformed as } \frac{l \cdot f}{v} = \frac{l}{\lambda} \ll 1 \quad \text{or} \quad \frac{l/T}{v} = \frac{u}{v} \ll 1 \tag{2.52}$$

should be fulfilled, with $u = l/T$ as the material velocity of the moving body. It is instructive that the left equation within (2.52) can be rearranged into the other two equations based on (2.12). That is, even *relatively high f* may satisfy this condition as long as the *size l of considered structures* of the body—e.g., the maximum dimension l of the human body or of tissue structures of interest (Fig. 2.2a)—is sufficiently *small* with respect to λ.

[20]The average *effective conductivity* γ_{eff} of *biological tissue* is typically estimated with 0.2 S/m. This estimation stems from the observation that a typical *volume fraction* of the extracellular fluid in tissue is about 0.1, whereas γ_{eff} of the extracellular fluid amounts to about 2 S/m. Since *cells* themselves are considered as *nonconductive particles* in the dilute suspension (Foster 1996), the product $0.1 \cdot 2$ S/m approximates the aforementioned $\gamma_{\text{eff}} = 0.2$ S/m of *soft and high water content tissues*. In fact, this value 0.2 S/m is, strictly speaking, the *direct-current conductivity* with $\gamma_{\text{eff}} = \gamma$ (see text). However, 0.2 S/m also applies for *low field frequencies* below β-dispersion of cellular membranes (Fig. 2.19b) with $\gamma_{\text{eff}} \approx \gamma$ (Fig. 2.21).

Independent interactions of the constant and time-varying *electric fields* with *biological tissue* are discussed in Section "Incident Electric Fields". However, the *quasi-electrostatic situation* can be cancelled by an *electromagnetic induction* (Footnote 15)—provided that (2.52) does not hold—in which a time-varying magnetic field permeating the body induces significant curls of the time-varying electric field within the body (Fig. 2.31), as shown in Section "Incident Magnetic Fields". For instance, the left equation within (2.52) can be rewritten as $l^2 \cdot \hat{B}/T \ll \hat{E} \cdot l$ that clearly resembles the electromagnetic induction law from (2.86). Correspondingly, the rate of change $l^2 \cdot \hat{B}/T$ in the magnetic flux should be much smaller than the voltage drop $\hat{E} \cdot l$ for the quasi-electrostatic situation to be valid.

The following Section "Incident Electromagnetic Fields" discusses cases *outside the quasi-electrostatic situation* when f is relatively high and/or dimensions of the exposed body become comparable with or even larger than λ (Fig. 2.2b, c). Here the *electric and magnetic fields* in tissue *become mutually coupled*, start to *induce each other*, and then *propagate as a joint electromagnetic wave* through the biological body (2.4).

Incident Electric Fields

Various *interactions* of an *external electric field* $\vec{E}_{\text{ext}}$ with the *biological body* located within the field will be discussed in following sections. Since the electric field is defined to account for forces among *electric charges* (Section "Electric and Magnetic Fields"), it follows that the interaction between $\vec{E}_{\text{ext}}$ *and electric charges within biological tissue* (including its ional and polar structures, see Kaniusas (2012, Footnote 12)) should be considered. In particular, the latter interaction includes the following effects:

- induced *conductive currents* in tissue,
- *induced polarization* of non-polar structures in tissue,
- *alignment* of permanently polar structures in tissue,
- frequency-dependent *dispersion* of electrical tissue properties, and
- many other effects such as *electrostatic induction* due to induced surface charges.

Conductive Phenomena

As illustrated in Fig. 2.16a, *charged structures* within *conductive tissue*, which are *loosely bound and mobile* (such as *solvated ions*) are subjected to *electrostatic dragging forces* in response to a *local electric field* $\vec{E}$ *within tissue*. Please note that the resulting internal $\vec{E}$ in Fig. 2.16a is assumed to equal the applied $\vec{E}_{\text{ext}}$ (=$\vec{E}$) between both *charged electrodes*.

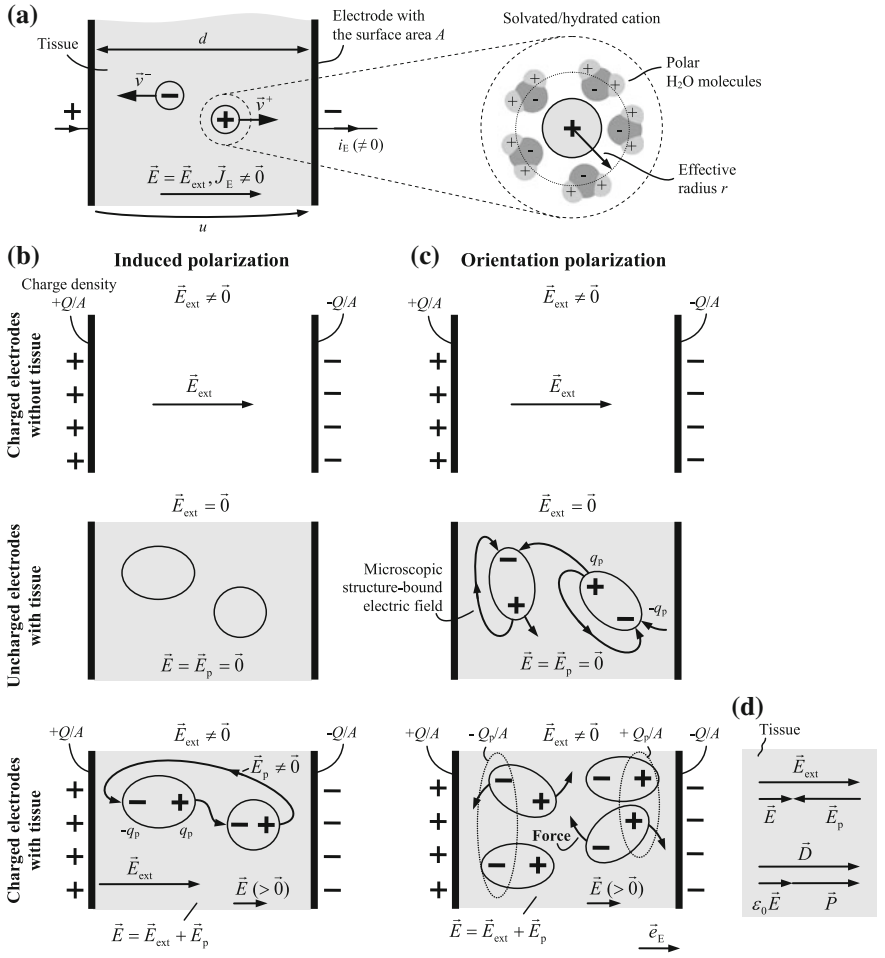

Fig. 2.16 The interaction of the external electric field $\vec{E}_{ext}$ with biological tissue as generated by the charged electrodes (with $E_{ext} = Q/(A \cdot \varepsilon_0)$ and Q as the electrode charge). **a** Flow of unbound electric charges in tissue (drift of solvated ions or charged particles with the drift velocity $\vec{v}$) when subjected to $\vec{E}_{ext}$ (as in electrolytic cell). This flow yields the conductive current i_E [$=\gamma \cdot E_{ext} \cdot A$ with the electric field in tissue $\vec{E} = \vec{E}_{ext}$, see (2.54)] in the external circuit, given ongoing electrode reactions (Fig. 3.13). **b** Polarization of charge-neutral non-polar structures due to charge separation within structures under the influence of $\vec{E}_{ext}$. Polarized structures obtain their own microscopic structure-bound electric fields which sum up to the macroscopic polarization electric field $\vec{E}_p$ opposing the applied $\vec{E}_{ext}$. Thus the resulting electric field $\vec{E}$ in tissue amounts to $\vec{E} = \vec{E}_{ext} + \vec{E}_p$. **c** Reorientation of permanently polar structures—such as electric dipoles—with the subsequent accumulation of the total polarization charge Q_p (<Q) yielding $\vec{E}_p \neq \vec{0}$. **d** Vector electric fields $\vec{E}$, $\vec{E}_{ext}$, and $\vec{E}_p$ (2.62) as well as charge density fields $\vec{D}$, $\varepsilon_0\vec{E}$, and $\vec{P}$ (2.64)

The *conductive tissue section* between electrodes carries a *non-zero current*. In addition, an accumulation of *surface charges* on boundaries of the section (facing electrodes) is assumed to be absent (e.g., due to ongoing electrode reactions, see Fig. 3.13), whereas these charges would reduce the resulting inner $\vec{E}$ with respect to the applied $\vec{E}_{\text{ext}}$ (as described in Fig. 2.25). Please note that the two electrodes under the voltage u are connected to and charged by a voltage source with the resulting homogeneous $|\vec{E}_{\text{ext}}| = u/d$ (for a relatively small distance d between electrodes as related to lateral dimensions of electrodes, see Footnotes 13 and 36).

Ionic Drift

Consequently, *unbound charges*, *ions* with a *non-zero net charge*[21] attain a certain *drift velocity* $\vec{v}$ (Fig. 2.16a)—in line with their limited *ionic mobility* m—while moving between (immobile) molecules, as detailed in Kaniusas (2012, Footnote 45) and Footnote 25, to give

$$m = \frac{|\vec{v}|}{|\vec{E}|} = z \cdot e \cdot \frac{D_{\text{F}}}{k \cdot T} = \frac{z \cdot e}{6\pi \cdot r \cdot \mu}. \tag{2.53}$$

Here z is the valence of ions drifting, e the elementary charge ($e = 1.6 \cdot 10^{-19}$ C), D_{F} the diffusion coefficient (see Kaniusas (2012, Footnote 24)), k the Bolzmann constant ($k = 1.38 \cdot 10^{-23}$ J/K), T the absolute temperature, r the *effective/actual radius*[22] of drifting/diffusing ions, and μ the dynamic viscosity of the surrounding medium.

In fact, the *average drift velocity* $\vec{v}$—and, to be precise, the validity of (2.53)—results from the *equality* of

- the *electrostatic dragging force* (equal to $ze \cdot \vec{E}$, i.e., proportional to the magnitude E and the total charge $z \cdot e$ of the drifting ion, see (Kaniusas 2012, Footnote 44)) acting on the drifting ion and
- the *frictional braking force* in the viscous medium *opposing the ion movements* (equal to $6\pi \cdot r \cdot \mu \cdot \vec{v}$, i.e., proportional to the viscosity μ and to the *effective* r including the *solvation/hydration shell*, see Footnote 22).

Please note that the latter equality does not consider *inter-ionic interactions* reducing the effective m (Footnote 28). In addition, (2.53) does not consider that the *frictional braking force* tends to increase with the *ionic concentration* due to progressively increasing friction of drifting ions with oppositely moving solvated ions (Hamann 1998).

[21] It is instructive to amend that charged structures with a *non-zero net charge* (e.g., ions) will experience a translational force even in an *homogeneous* $\vec{E}$, whereas polar structures with a *zero net charge* (e.g., dipoles) require a *non-homogeneous* $\vec{E}$ for their migration.

[22] As illustrated in Fig. 2.16a, the *effective radius* r is the distance from the ion's centre to the charge centre within the ion's *solvation/hydration shell*. Simply speaking, the effective radius exceeds the ion's atomic radius by the thickness of the solvation/hydration shell (Kaniusas 2012, Footnote 21).

As illustrated in Fig. 2.16a,

- positive ions (*cations*[23]) move towards the negative electrode (*cathode*) while
- negative ions (*anions*) move towards the positive electrode (*anode*);

see limitations of this behaviour from Footnote 7 in Chap. 3. Likewise, cations move in the direction of $\vec{E}$ *within electrolyte* while anions move in the opposite direction (Fig. 2.16a). For a specific *distribution of cations and anions* in electrolyte, see Fig. 3.9b and consult Footnotes 40 and 17 in Chap. 3. When electrolyte with dissociated charged ions is subjected to $\vec{E}$,

- the *direction of the ionic drift* with $\vec{v}$ is determined by the sign of the ionic charge $z \cdot e$ and the direction of $\vec{E}$, whereas
- the *magnitude*[24] v of the resulting ionic drift with $\vec{v}$ is determined by both ionic properties ($z \cdot e$ and r), as well as the applied field and medium properties (E and μ), in line with (2.53).

---

[23]It is instructive to observe that, since *positive ions* always move to the *cathode* (in both electrolytic and galvanic cells, see Footnotes 19 and 23 in Chap. 3), these positive ions are called *cations*. In analogy, *negative ions* travelling to the *anode* are called *anions*. In other words, cathode and anode are defined from the current/charge flow but not from the polarity of the voltage drop between electrodes.

[24]According to (2.53), the *drift velocity* v should increase with increasing *ionic charge* $z \cdot e$ of a single ion, if all other parameters in (2.53) are assumed to be constant. However, increasing z attracts more *polar water molecules* (see text), so that the thickness of the *hydration shell* increases as well, i.e., the effective r in (2.53) increases with z. This means that an increasing z—e.g., from *monovalent ions* with $z = 1$, such as K^+, to *bivalent ions* with $z = 2$, such as Ca^{2+}—can lead to either still balanced v (and m) or even reduced v (and m) in bivalent ions as compared with monovalent ions. However, there are some exceptions (Hamann 1998).

In contrast to *cations*, *anions* are usually weakly *hydrated* (compare the hydration level of cations and anions in Fig. 3.9b and Footnote 12 in Chap. 3), which then results in a higher v (and m) of anions with increasing z (Hamann 1998); i.e., the nominator in (2.53) ($\propto z$) increases to a larger extent than its denominator ($\propto r$). Likewise, *anions migrate usually faster than cations* for a given z, whereas this difference in v (and m) increases with increasing z of ions.

On the other hand, the velocity v (and m) varies also among ions with the same z (such as Na^+ and K^+), which is due to differences in the *radii of dehydrated ions*, as described in Kaniusas (2012, Footnote 21). In short, a decreasing radius of a dehydrated ion means an increasing thickness of its hydration shell, its larger *effective radius* r (Footnote 22), and thus smaller v (and m) (2.53).

Please note that the *migration v of H^+ and OH^-* ions in the solution with *water as solvent* is very high—e.g., v of H^+ and OH^- is higher by a factor of about 5 and 3, respectively, than v of K^+, given an ideally diluted solution without any inter-ionic interactions (Hamann 1998), see Footnote 28—which results in a relatively high H^+ and OH^- contribution to γ (2.54). In fact, *tunnelling processes*—with H_2O molecules and H_3O^+ ions involved—account for this *super-conductivity* of H^+ and OH^- ions (Hamann 1998) The abnormally high ionic mobility and conductivity are attributed to the ability of H^+ and OH^- ions to jump between successive H_2O molecules along a row of H_2O molecules, which is much faster than ordinary migration of H_3O^+ through the solution (Wright 2007). In other words, the general (2.53) does not apply for H^+ and OH^- ions in the water solution.

Interestingly, a *single H^+ ion*—because of its strong unsaturated *electric stray field* if considered in isolation (Kaniusas 2012, Footnote 13)—uses to adhere electrostatically to the negative side of the *water dipole* (namely, to the oxygen atom of the water molecule, see Kaniusas (2012,

Obviously, *collisions of travelling ions* with other particles in tissue (such as other ions or molecules) change the local direction of the ion's drift, so that Fig. 2.16a depicts only macroscopic average *drift velocity*.[25]

The *translational ionic drift* due to the local $\vec{E}$ is always connected with material transport in tissue, contributes to ionic m and thus to current transport. This $\vec{E}$-driven drift is superimposed on *random Brownian motion* of ions, whereas the drift of an ion (Fig. 2.16a) perturbs its *translational* Brownian motion with only a minor effect on its *rotational* Brownian motion. For instance, the interaction between the local $\vec{E}$ and dipolar structures (Fig. 2.16b) perturbs the *rotational* part of the Brownian motion (Wright 2007).

Ionic Conductivity

The movement or transport[26] of these free ionic charges—*cations and anions*, each moving in opposite directions—constitutes a *conductive ionic current* through tissue. That is, the *mechanism of conduction* in biological tissue is the *movement of solvated ions*. Because of mutual collisions and friction in-between ions and/or collisions with (less) mobile structures within tissue, movement of ions comprises a *lossy interaction* between drifting ions and microscopic tissue structures. The power loss primarily *heats tissue* (Fig. 2.85). This lossy interaction within tissue goes at

---

Fig. 2.4)) to form an *H_3O^+ ion*. This charged H_3O^+ ion attracts other polar water molecules from the solution to build its *hydration shell*, so that, in total, a complex $H_9O_4^+$ is typically formed, i.e., in total, a *single H^+ ion binds typically four H_2O molecules* (Hamann 1998).

[25]Please note that *direct current* in tissue is related to continuous and unidirectional movements of ions from one pole to the other; e.g., positive ions such as K^+ ions move from the positive pole to the negative one, see Fig. 2.16a. In contrast, *alternating current* in tissue imposes a synchronous *oscillation of ions* around their *resting positions*, i.e., ions move towards one pole during one half-cycle and towards the other pole during the following half-cycle.

In fact, the travelled distance from the resting position decreases with increasing *field frequency*, i.e., with decreasing duration of the half-cycle during which the travelling can take place. This is because the *ionic mobility m* is finite, see (2.53), which is given as the ratio of the ion's *drift velocity v* and the *electric field E* surrounding the ion (Kaniusas 2012, Footnote 45).

To give an example, the expected m of K^+ ions in water is in the range of 70 μm/s per 1 kV/m. From a microscopic point of view, this resulting v of ions of about 70 nm/s per 1 V/m is quite large, provided that the strength E is in the typical range of endogenous electric fields within tissue (a few V/m, see Section "Electric and Magnetic Field") and a typical radius of the non-hydrated K^+ ion is of only about 0.14 nm ($\ll$70 nm, see Kaniusas (2012, Footnote 21)). Likewise, a single K^+ ion passes more than 400 water molecules per second ($\approx$70 nm/0.15 nm with 0.15 nm as the approximate diameter of a single water molecule, see Kaniusas (2012, Fig. 2.4)) for an ambient E of only 1 V/m.

This fundamental behaviour of ions exposed to a local E in tissue is not only instructive in its nature but also strongly determines changes of the *tissue conductivity* γ_{eff} over frequency (see *dispersion mechanisms* in Fig. 2.19) and diverse effects of direct current on tissue (Fig. 2.84).

[26]Please note that an *induced direct current* in the ionic conductor (Footnote 25) leads to *concentration gradients* of the involved ions in the limited tissue region. For instance, positive ions become depleted to the left of the tissue region in-between both electrodes from Fig. 2.16a while these ions accumulate to the right; obviously, the reverse is true for negative ions. In addition, the *total concentration of ions* (i.e., the electrolyte composition) in this tissue region between electrodes can also change due to *chemical electrolytic reactions* on the electrode surface (Figs. 3.4 and 3.13).

the expense of the driving electric field energy, i.e., tissue losses withdraw energy from the driving field. The lossy interaction implies that the *tissue conductivity* γ has a non-zero and finite value, and determines *power loss* in tissue for a given driving field $\vec{E}$ (2.56).

In accordance with the *local form of Ohm's law*—see (2.32)—

$$\vec{J}_{\mathrm{E}} = \gamma \cdot \vec{E} = (\gamma^{+} + \gamma^{-}) \cdot \vec{E} = eN_{\mathrm{A}} \cdot (z^{+}c^{+}m^{+} + z^{-}c^{-}m^{-}) \cdot \vec{E}, \tag{2.54}$$

the induced *electric field* in tissue with the *vector amplitude* $\vec{E}$ provokes a non-zero (ionic) *conductive current density with the vector amplitude* $\vec{J}_{\mathrm{E}}$ (2.23) provided that the *ionic electrical conductivity* γ of the conductive tissue is non-zero; compare (Kaniusas 2012, Footnotes 21 and 45). In other words, the higher is γ, the less of the driving field $\vec{E}$ is necessary to end up with a certain impact $\vec{J}_{\mathrm{E}}$.

The right side of (2.54) denotes γ[27] as a function of characteristics of ions (2.53), *cations and anions*, involved in the *charge transport* (Fig. 2.16a) and thus contributing to the *magnitude* J_{E} of $\vec{J}_{\mathrm{E}}$. Here N_{A} denotes the Avogadro constant ($N_{\mathrm{A}} = 6.02 \cdot 10^{23}$ 1/mol), whereas z^{+} and z^{-} are the valence of these *cations and anions*, respectively. In analogy, c^{+} and c^{-} are the molar concentration of cations and anions involved in the charge transport (in mol/m^3), respectively. An identical interpretation applies also to superscripts of m and γ. Please note that (2.54) does not consider *inter-ionic interactions*—as described in Footnote 28—which tend to reduce the resulting γ.

It is instructive to rewrite (2.54) based on (2.53) that yields

$$\vec{J}_{\mathrm{E}} = (\gamma^{+} + \gamma^{-}) \cdot \vec{E} = eN_{\mathrm{A}} \cdot (z^{+}c^{+} \cdot \vec{v}^{+} - z^{-}c^{-} \cdot \vec{v}^{-}) \tag{2.55}$$

in close accordance with Kaniusas (2012, Footnote 45). It shows $\vec{J}_{\mathrm{E}}$ as a function of vector velocities $\vec{v}^{+}$ and $\vec{v}^{-}$ of cations and anions, respectively, drifting through conductive tissue, as illustrated in Fig. 2.16a. Please note the minus sign in (2.55) in contrast to the plus sign in (2.54); this is because *cations* with their $\vec{v}^{+}$ move in the direction of $\vec{E}$ while *anions* in the opposite direction to $\vec{E}$.

It is important to note that the inequality $m^{+} \neq m^{-}$ (2.54) usually applies because cations and anions differ in their physical size with their effective $r^{+} \neq r^{-}$ (2.53).

[27]For instance, the conductivity γ of the *extracellular space*—the conductivity mainly given by the dissociated ions Na^{+} and Cl^{-} of the *NaCl solution* (*table salt solution*) with its typical *concentration c of 0.15 mol/l* (Kaniusas 2012, Table 2.1)—can be easily estimated with (2.54). In an approximation, the following physical values apply $c^{+} = c^{-} = 0.15$ mol/l, $z^{+} = z^{-} = 1$, $m^{+} = 52 \cdot 10^{-9}$ m^2/(V · s) and $m^{-} = 79 \cdot 10^{-9}$ m^2/(V · s), yielding a calculated γ of about 2 S/m. This estimated value of 2 S/m is in good agreement with experimental values (Kaniusas 2012, Sect. 2.1.2.1.2). In fact, this estimation of γ applies to *0.9% NaCl physiological solution*, as given by 9 g NaCl dissolved within 1000 g H_2O, corresponding with the aforementioned c of 9 g/l / (23 g/mol + 35 g/mol) ≈ *0.15 mol/l*.

This means that *cations and anions contribute differently to the total conductivity* γ with the resulting $\gamma^{+} \neq \gamma^{-}$ (2.54). For instance, Cl^{-} anions in a diluted NaCl solution carry the most ionic current (about 60% of the total current), so that the following ratios $\gamma^{-}/\gamma \approx 0.6$ (for Cl^{-} anions) and $\gamma^{+}/\gamma \approx 0.4$ (for Na^{+} cations) result (Hamann 1998). Please recall that anions are usually less hydrated and thus migrate faster than cations, as elaborated in Footnote 24. The thicker the *hydration shell* of ions is in terms of *increasing r*, the *smaller the associated m and* γ tend to be within the bulk tissue. In addition, the latter ratios depend not only on the considered ion itself (e.g., Na^{+} in NaCl) but also on the relevant counterion (Cl^{-}).

In addition, an increasing z^{+} or z^{-} of ions in (2.54) does not necessarily mean increased γ^{+} or γ^{-}, respectively. This is because the *thickness of the solvation/hydration shell* of ions increases with increasing z which may lead to reduced m (2.53) and thus to reduced γ/z (2.54). Here, however, *cations and anions behave differently with increasing* z according to Footnote 24.

In addition, it should be noted that the *conductivity* γ of *organic ions* in tissue is usually smaller than γ of simple *inorganic ions* (such as Na^{+} and Cl^{-}) because the *radius* of (even dehydrated) organic ions is much larger than that of simple inorganic ions [(2.53) and (2.54)]. Organic ions are almost dehydrated because of their large radius and thus weak electric fields on the ion surface insufficient to attract electrostatically polar water molecules (in line with Kaniusas (2012, Footnote 21)).

It should be stressed that the *total conductivity* γ of an electrolyte solution (or of a biological tissue) is mainly a function of the *dissociated ions concentration*[28] c of *solute* (2.54) but not of ionic properties of *solvent*. Typically, *solvents* have a very

[28]The *total conductivity* γ increases *linearly* with increasing *electrolyte concentration* c (solute concentration) in the solution—in line with (2.54)

- only if the *electrolyte dissociates completely* irrespective of its effective c. In fact, this ideal behaviour applies only to *ideally diluted solutions*
- without any *inter-ionic interactions*; compare Footnote 7 in Chap. 3.

With increasing c of the electrolyte, these *inter-ionic interactions* progressively strengthen while the conductivity γ of the solution, in reality, increases less than the aforementioned linear increase from (2.54) would imply. In other words, there is a *non-linear dependence* between γ and c in non-ideal solutions (Footnote 7 in Chap. 3).

This *non-linear dependence* arises because of repelling and attractive *electrostatic forces* $\vec{F}$ between *charged ions* with the same or opposite polarity, respectively. In fact, $\vec{F}$ strongly increases in its magnitude $|\vec{F}|$ with decreasing distance d between the interacting ions in the solution ($|\vec{F}| \propto 1/d^2$ according to *Coulomb's law*). Please note that d tends to decrease with increasing c of *electrolyte*, so that *inter-ionic interactions* grow with gradual rapprochement of ions and with their increasing c. In contrast, infinite $d \rightarrow \infty$ and thus missing *inter-ionic forces* $|\vec{F}| \rightarrow 0$ apply for *ideally diluted solutions*. The increasing inter-ionic forces with increasing c lead to rising *mutual obstruction of charged ions* when moving in the electrolyte solution along the *directed* $\vec{E}$ (Fig. 2.16a). The attractive inter-ionic forces disfavour independent and opposite *migration of cations and anions* in the *applied local* $\vec{E}$ (Fig. 2.16a and Footnote 7 in Chap. 3). Obviously, these obstructed movements of ions *reduce the total* γ. In addition, the aforementioned divergence from the linear law in (2.54)—with increasing c of the electrolyte—becomes even more prominent with increasing *ionic charge* $z \cdot e$ since the *inter-ionic forces* increase with $z \cdot e$ as well ($|\vec{F}| \propto z \cdot e$ according to *Coulomb's law*).

low ionic concentration (low c^+ and c^-) due to their *weak autodissociation*[29] such as pure water with its weak *dissociation reaction* $2 \cdot H_2O \leftrightarrow H_3O^+ + OH^-$. Therefore, solvents have a *very low self-conductivity*. For instance, a very low value $\gamma \approx 6 \cdot 10^{-6}$ S/m applies for *pure water* (Hamann 1998), whereas a much larger estimated value of 2 S/m applies for 0.15 mol/l *NaCl aqueous solution* (Footnote 27). In other words, the better the dissociation of the electrolyte substance is (Kaniusas 2012, Footnote 13), the higher the resulting γ.

The local magnitude J_E depends strongly on the local γ in *heterogeneous tissues*, i.e., J_E increases with γ for a given magnitude E (see below). Provided an *isotropic tissue*,[30] i.e., its electrical properties (especially γ) are identical in all spatial directions, the induced directed fields $\vec{J}_E$ and $\vec{E}$ *point in the same direction* (see Figs. 2.16a and 2.18a). The associated *time courses* of $\vec{j}_E(t)$ and $\vec{E}(t)$ are *in-phase* (see Figs. 2.12b and 2.18b). Please note that γ also depends on the *tissue*

Another effect that contributes to *inter-ionic interactions* is the *mutual obstruction of ions* migrating together with their respective (relatively large) *clouds of counterions* (Fig. 3.9b) in opposite directions under the influence of the applied $\vec{E}$. Obviously, this mutual obstruction is particularly prominent at the relatively *high c* of ions in the solution.

It follows from above that the associated *mobilities m* of charge carrying ions (2.53) contributing to the total γ (2.54) decrease with the *onset and strengthening of inter-ionic interactions* or, in other words, decrease with increasing *c of the electrolyte* in the solution. For instance, the level of *m* of Na^+ ions of about $52 \cdot 10^{-9}$ $m^2/(V \cdot s)$ in an ideally diluted NaCl water solution at 25 °C decreases to about $44 \cdot 10^{-9}$ $m^2/(V \cdot s)$ in a *NaCl water solution* with the concentration of 0.1 mol/l at 25 °C (Hamann 1998). From a quantitative point of view, there is an effective decrease by about 15%. Please note that the latter NaCl concentration of 0.1 mol/l is comparable to the NaCl concentration of 0.15 mol/l within the *physiological solution* (Footnote 27).

[29]For instance, 1 L of water has about 55.5 mol of water (=1000 g / (16 g/mol + 2 g/mol)), whereas only about $1.17 \cdot 10^{-7}$ mol/l of *pure water* is intrinsically (auto) *dissociated* (Hamann 1998). Therefore, a *very low percentage* of only $2.1 \cdot 10^{-7}$ % or 0.002 ppm of pure water is dissociated. In contrast, *NaCl water solution* with its concentration of 0.1 mol/l at 25 °C is *completely dissociated* according to $NaCl(aq) \rightarrow Na^+(aq) + Cl^-(aq)$, i.e., about 100% of NaCl—of the so-called *strong electrolyte*—is dissociated into its ions Na^+ and Cl^-.

[30]Some biological materials such as *skeletal muscle* or *bone* are highly *anisotropic* in their inner structure—in order to support reasonably longitudinal forces (Kaniusas 2012, Sect. 2.3)—and thus are distinctly anisotropic in their *electrical properties*. Therefore, *longitudinal* static γ in the muscle tissue along muscle fibers (muscle cells (Kaniusas 2012, Fig. 2.24)) is up to 10 times higher than static γ in the *transversal* direction, especially at relatively *low frequencies* below about 10 MHz (Gabriel 1996a, b; Foster 1996). At *higher field frequencies the anisotropy progressively disappears* while membranes of muscle fibers become short-circuited by displacement currents. The two *effective conductivities* γ_{eff} for the longitudinal and transversal direction (2.82) *increase and approach a common value*. In other words, γ_{eff} *in the longitudinal orientation* is not only higher than γ_{eff} in the transversal direction (at low frequencies) but also *varies much less with frequency* (over the dispersion region of β-dispersion, compare Fig. 2.21). Therefore, effects of the tissue *anisotropy* on γ_{eff} (2.82) *are highly frequency-dependent*, especially below *β-dispersion* region up to about 500 kHz (Foster 1996); see Fig. 2.21 for the dependence of γ_{eff} on frequency.

temperature.[31] For *coupling factors* of an external electric field into a *biological body* located within the field, see Figs. 2.36, 2.38 and associated discussions.

Deposited Power

The resulting *power P* (the time rate of energy *W*) submitted to and deposited within a *homogenous tissue section* [as heat, see (2.154)] by ionic *conductive currents* through the section is given by

$$P = E \cdot J_E \cdot V = \gamma \cdot E^2 \cdot V = \frac{J_E^2}{\gamma} \cdot V. \tag{2.56}$$

Here V is the spatial volume of the affected homogeneous section encompassing constant $\vec{J}_E$ and $\vec{E}$ throughout this volume. The term $\gamma \cdot E^2$ represents the *spatial power density* and has physical units of W/m^3.

It can be observed from (2.56) that the *power P is proportional to* γ of tissue within the considered *homogeneous tissue section*.[32] Generally speaking, tissue

[31]Since the *mobility m of free charge carriers* (ions) in tissue increases with the *tissue temperature*—as the viscosity μ of the extracellular fluid decreases with increasing temperature [(2.53) and Kaniusas (2012, Footnote 45)]—the *ionic conductivity* γ of tissue increases by about +2%/°C for the relatively low field frequencies below 1 GHz (Foster 1995). Above about 1 GHz, the *dipolar loss* of tissue water contributes significantly to the *effective conductivity* γ_{eff} of tissue (2.81) with its reverse *temperature coefficient* of −2%/°C (see below).

In particular, as discussed in Section "Gamma Dispersion", the total *effective* $\gamma_{eff} = \gamma + \Delta\gamma$ of biological tissue (2.82) reflects both

- the *frequency-independent* γ and
- the *frequency-dependent contribution* $\Delta\gamma$ due to *dipolar losses*.

While γ increases with temperature (by about +2%/°C), the *relaxation frequency of* γ*-dispersion* (2.75) increases correspondingly. In fact, the gamma relaxation frequency of water increases by more than +2%/°C (≈100 · (26 GHz − 18 GHz)/((37 °C − 20 °C) · 18 GHz) with numbers taken from Footnote 43). Consequently, increasing temperature will result in a *decrease of dipolar losses* in water *below the gamma relaxation frequency* and thus result in a decrease of the dipolar contribution $\Delta\gamma$ (by about −2%/°C) to the total γ_{eff}. Since both contributions γ and $\Delta\gamma$ are *comparable* in their size *at a few GHz* in water (Fig. 2.21), it can be expected that the *temperature coefficient of* γ_{eff} should change its sign close to this frequency, i.e., a change in this coefficient from +2%/°C to −2%/°C can be expected at a few GHz. For instance, experimental data in Foster (1996) prove this sign change of the temperature coefficient of *muscle* near 2 GHz where the contribution γ from *ionic effects* and another contribution $\Delta\gamma$ from *dipolar effects* become equal (Fig. 2.21).

[32]If a *heterogeneous tissue section* with its *inhomogeneous conductivity* is subjected to an external electric field—determined by charged electrodes (2.60) enclosing the section (Fig. 2.35)—the deposited power within homogenous parts of tissue is a function of *conductivity ratios*. To give an example based on Fig. 2.35, in the case of

- the *series connection* of *two homogeneous tissue sections* of the same size with γ_1 and γ_2 (Fig. 2.35a), the deposited powers P_1 and P_2 within the respective sections fulfil the ratio

$$\frac{P_1}{P_2} = \frac{\gamma_2}{\gamma_1}.$$

with higher water content such as muscle is lossier than fat or bone for a constant $\vec{E}$ in these tissues; compare Fig. 2.21 and Table 2.2. On the other hand, *the power P is proportional to* E^2.

The *submitted energy* W ($=P \cdot \Delta t$ with P constant over time) over the time period Δt (>0) is *stored* in the affected tissue section as *heat* and, on the other hand, *dissipated* away from this affected site due to ongoing *blood perfusion*; see Footnote 107 and Section "Thermal Stimulation Effects".

In addition to the power P (2.56), another useful quantity is the *specific energy absorption rate*[33,34] P_{SAR}. It accounts for the *absorbed P*—or the *dissipated P* from the incident $\vec{J}_E$ and $\vec{E}$ field—per mass m of tissue due to ionic *conductive currents* within tissue:

$$P_{SAR} = \frac{P}{m} = \frac{E \cdot J_E \cdot V}{\rho \cdot V} = \frac{\gamma \cdot E^2}{\rho} = \frac{J_E^2}{\gamma \cdot \rho}. \tag{2.57}$$

The latter ratio can easily be derived from (2.54), (2.56) in combination with the *boundary condition* (2.104) which requires an identical conductive current density $\vec{J}_E$ through both sections in series. For instance, the series connection of different tissue sections can be found within the *multi-layered skin* (Fig. 3.2b) when the electric current enters the body perpendicular to the skin surface.

- The *parallel connection* of *two homogeneous tissue sections* (Fig. 2.35b) fulfils the ratio

$$\frac{P_1}{P_2} = \frac{\gamma_1}{\gamma_2},$$

as can be derived from (2.54) and (2.56) in combination with the *boundary condition* (2.96) which requires an identical tangential electric field $\vec{E}$ in both sections lying in parallel. For instance, the parallel connection of different tissue sections becomes relevant when the electric current flows along *blood vessels embedded within muscular tissue*.

[33]Please note that the *specific energy absorption rate* P_{SAR} from (2.57) and (2.58) can describe

- the *instantaneous absorption rate* with $E = E(t)$ as the *instantaneous value* of the time-varying $\vec{E}(t)$. In addition,
- for time-varying fields—such as *sinusoidal fields*—the estimated P_{SAR} can also give the *average absorption rate* with $E = E_{eff}$ as the *effective value* E_{eff} (or *root mean square* value) of the time-varying $\vec{E}(t)$.

[34]The *specific energy absorption rate* P_{SAR} is proportional to the *square of the effective value* E_{eff} of a time-varying field $\vec{E}(t)$ [see Footnote 33 and (2.57), (2.58)] while E_{eff} equals to $1/\sqrt{2}$ the *peak value* of a *time-varying sinusoidal field* $\vec{E}(t)$ (see $\hat{E}$ as the peak value of $\vec{E}(t)$ in (2.11) with $E_{eff} = \hat{E}/\sqrt{2}$). It follows that the *local* P_{SAR} (x) at the coordinate x is proportional to the square of the *local envelope width* of the *sinusoidal field* $\vec{E}(x,t)$. Since the envelope can vary in space along the propagation direction x of $\vec{E}(x,t)$—as illustrated in Figs. 2.45 and 2.47 in terms of a *standing wave* and *partial standing wave*, respectively—the associated *local* P_{SAR} *(x) can also vary from point to point* within the propagation medium. Another example with varying envelope of $\vec{E}(x,t)$ and varying P_{SAR} (x) is given by Fig. 2.48a, b.

Here ρ is the tissue density close to 1000 kg/m^3 for most tissues (Table 2.2). In other words, the measure P_{SAR} stands for the rate (in W/kg) at which energy is absorbed by tissue when exposed to a non-zero $\vec{J}_E$ and $\vec{E}$. The rate P_{SAR} offers a simple tool to quantify *power deposition* in the biological body due to *lossy interactions* of $\vec{J}_E$ and $\vec{E}$ with the conductive tissue [with $\gamma > 0$ in (2.57)]. For instance, *thermal interactions* of incident electromagnetic fields with living systems are based on the P_{SAR} deposition (see Section "Thermal Stimulation Effects").

It should be stressed that *lossy interactions* apply not only to *conductors* but also to *lossy dielectrics*, such as biological tissue is. The resulting *total lossy interactions* are thus determined by the *effective conductivity* γ_{eff} of *biological tissue* that exceeds the *ionic conductivity* γ (applies when tissue behaves as a pure conductor only) by the amount of $\Delta\gamma$ (>0) and *depends strongly on the oscillatory frequency* of the applied $\vec{E}$ (Fig. 2.21); see the dispersion-related discussion about (2.77)–(2.82). Please note that γ_{eff} considers not only losses due to directional and/or oscillatory movements of *free ionic charges* (and their *collisions* with other particles in tissue, as considered by γ only) in *conductors* but also losses due to oscillatory movements of *bound charges* (and their mutual *friction*) in *dielectrics*.

Therefore, the total P_{SAR} in biological tissue amounts to

$$P_{SAR} = \frac{\gamma_{eff} \cdot E^2}{\rho} = \frac{J_E^2}{\gamma_{eff} \cdot \rho}, \tag{2.58}$$

compare Footnote 33. In analogy with (2.57), P_{SAR} describes the *time rate of energy* transferred from an electromagnetic field to tissue per unit mass at a given local region with the applicable $\vec{E}$, γ_{eff}, and ρ.

Since γ_{eff} increases with the *field frequency* (Fig. 2.21), it can be deduced from (2.58) that P_{SAR} increases with frequency for a given $\vec{E}$ field. In other words, P_{SAR} tends to be higher in tissue for higher frequencies than for the lower ones, given the same $\vec{E}$ present in tissue. In general, P_{SAR} is not only a function of *field and tissue properties* but also of the *size and shape of the biological body* exposed to electromagnetic fields. This is because the body retroactively affects the distribution of fields within the body (Section "Incident Electromagnetic Fields" and Fig. 2.51). For critical values of P_{SAR} in terms of adverse health effects, see Section "Power Measures".

Salvation/Hydration of Ions

It should be recalled that *charged ions* in tissue are always *solvated/hydrated by molecules/polar molecules* of *solvent* due to electrostatic interactions. Figure 2.16a illustrates a hydrated cation with bound water molecules (compare Fig. 3.9b and Kaniusas (2012, Footnote 21)). For instance, dissociated Na^+ cations of the table salt NaCl—in water as solvent—are surrounded by water molecules with their *electronegative oxygen atoms* attracted to these positive cations and thus with oxygen atoms aligned towards the bodies of Na^+ ions, as illustrated in Fig. 2.16a. In contrast, the associated Cl^- anions in the NaCl solution are surrounded by water

molecules with their *electropositive hydrogen atoms* aligned towards negative Cl^- anions (Fig. 3.9b). This ion-dipole interaction between the charged ion and polar water molecules will be greater the larger the ionic charge and the smaller the bare ion size (Kaniusas 2012, Footnote 21).

Here primary and secondary solvation can be differentiated. The *primary solvation* means strongly bound and immobilised water molecules directly on the ion surface, which move altogether with the ion. Here the resulting arrangement of bound water molecules—usually *octahedral arrangement* around the ion—is considerably distorted from that of the pure water—usually *tetrahedral arrangement* around a central water molecule (forming water clusters). The *secondary solvation* shell is the next region of the solvent lying further out, whereas water molecules are affected but not immobilised by the ion, and do not move with the drifting ion. Here the structural arrangement gradually changes from the highly oriented water (bound water) to that of unmodified water (unbound water). The primary shell dominates in small and/or strongly charged ions (Na^+ or Al^{3+}, respectively, known as "structure makers") able to strongly *order and bound water molecules* around them, yielding a *loss in entropy* due to increase in order of the solvent. In contrast, other ions (such as K^+ and Cl^-, known as "structure breakers") induce less order which is not great enough to outweigh the disorder created in the secondary shell (i.e., with the transition from octahedral to tetrahedral order towards the bulk with increasing radius), yielding a *gain in entropy*.

Consequently, the *ions mobility m* (2.53) and thus the associated *ionic conductivity* γ (2.54) are strongly affected by the associated *water of hydration*, as already discussed in Footnote 24. In fact, the *polar structure of solvent molecules* is necessary for building a solvation/hydration shell around a central ion to reduce its *electric stray field* (as emitted by the central ion, compare Kaniusas (2012, Footnote 13) and Kaniusas (2012, Fig. 2.4)), for reorientation of solvent molecules within the shell in response to the directed stray field of the central ion, and even for breaking up ionic bonds within the NaCl salt and thus initiating *dissociation of NaCl* into its ions.

With increasing level of

- the *hydration of ions* (see Fig. 3.6a and Kaniusas (2012, Footnote 21)) and, on the other hand,
- the *hydration of polar proteins* (e.g., usually 0.3–0.4 g water is bound per gram protein (Foster 1996)),

the *bulk ionic* γ decreases; compare Footnote 41. The *mobility m of hydrated ions is reduced*, especially of hydrated ions near hydrated protein surfaces due to *frictional effects* among them (Foster 1996). *Hydrated proteins* may also act as *non-conducting particles* (in a conducting medium), impeding the directional ionic flow (i.e., migrating ions have to circumvent hydrated proteins) and thus limiting the resulting γ (compare Fig. 2.22a). To give a numerical example, the *calculated* γ of the *intracellular space* of the human erythrocyte amounts to 1.45 S/m if the known ionic composition is considered only. In contrast, the true value of γ is much less and amounts to only about 0.5 S/m while considering hydrated ions moving around hydrated proteins within the cell. Please consult also Footnote 28 and Footnote 7 in

Chap. 3 about *electrostatic inter-ionic interactions*, their changes with temperature, and their impact on the resulting γ.

Polarization Phenomena

Biological tissue can be imagined as an accumulation of a large number of *charge-neutral non-polar and polar structures* such as *molecules* hold inside by *molecular bonds* (or as non-polar *atoms* hold inside by *atomic bonds*). In fact, in

- a *non-polar structure*, the *two balance points* of the associated *positive and negative electric charges* within the structure *overlap in space* (Kaniusas 2012, Footnote 12), whereas in
- a *polar structure*, the *two balance points* do not completely overlap in space.

Induced Polarization

Microscopic electric fields of positive and negative charges within and around the non-polar structure necessarily cancel each other so that there is *no net electric field* right outside the *charge-neutral non-polar structure*. In analogy, there is no net macroscopic electric field within tissue. Here we assume the absence of any *external electric field* $\vec{E}_{\text{ext}} = E_{\text{ext}} \cdot \vec{e}_{\text{E}}$ applied to tissue, as can be applied by *two plane and large electrodes* surrounding a *thin tissue section* in-between (Fig. 2.16b).

When the field $\vec{E}_{\text{ext}}$ is actively applied to tissue composed out of *charge-neutral non-polar structures* via two *charged electrodes*—see Fig. 2.16b

- *positive charges within the structure move* on average by a fraction of an *atomic diameter* slightly towards the *negative electrode* (carrying a negative unbound charge $-Q$ on its surface) while
- *negative charges move* slightly towards the *positive electrode* (carrying a positive unbound charge $+Q$).

Likewise, positive charges—such as positively charged atoms within a single *molecule* or the positive nucleus of a single *atom*—move in one direction within the structure while negative charges move in the opposite direction; compare Fig. 2.19d. These movements keep going until the *attractive electrostatic force* between displaced *charges within the structure* is strong enough to balance the *repulsive electrostatic force* between these charges. In particular, this attractive force is inversely related to the squared distance between displaced charges (in line with Coulomb's law), whereas the repulsive force is proportional to the magnitude $E_{\text{ext}} = |\vec{E}_{\text{ext}}|$ of the applied $\vec{E}_{\text{ext}}$.

In fact, a *positive polarization charge* $+q_{\text{p}}$ is induced *within the structure* at the current balance point of now displaced *positive charges* while another *negative polarization charge* $-q_{\text{p}}$ is induced at the balance point of displaced *negative*

charges; see denoted q_p and $-q_p$ in Fig. 2.16b. The so-called *electric dipole moment* $\vec{p}$

$$\vec{p} = p \cdot \vec{e}_p = q_p \cdot d \cdot \vec{e}_p \tag{2.59}$$

is now induced within the structure due to non-zero $\vec{E}_{ext} \neq \vec{0}$, with d as the distance between q_p and $-q_p$, as illustrated in Fig. 2.17b. The unit vector $\vec{e}_p$ of $\vec{p}$ *points from the negative* $-q_p$ *to the positive* q_p (Fig. 2.17b), i.e., points in the opposite direction to the electric field inside the dipole, the field induced by q_p and $-q_p$ (compare the electric polarization field $\vec{E}_p = -\vec{P}/\varepsilon_0$ opposing the electric polarization density field $\vec{P} = \sum \vec{p}/V$ in Fig. 2.16d).

Thereby the originally *charge-neutral non-polar structure* (molecule and/or atom) remains electrically neutral as a whole but mutates into a *polarized structure* with its displaced and now *non-overlapping balance points* of positive and negative charges within the structure. An *electric dipole* (a *molecular dipole* and/or *atomic dipole*) is induced within the structure and an associated *structure-bound electric field*, a *microscopic electric field* between and around q_p and $-q_p$, is created right outside each single polarized structure within tissue; see Fig. 2.16b and Footnote 36. In analogy, the vector *superposition of these induced microscopic fields* of all polarized structures yields a non-zero *macroscopic electric polarization field* $\vec{E}_p$ within and around the tissue section between the two electrodes. An associated *total*

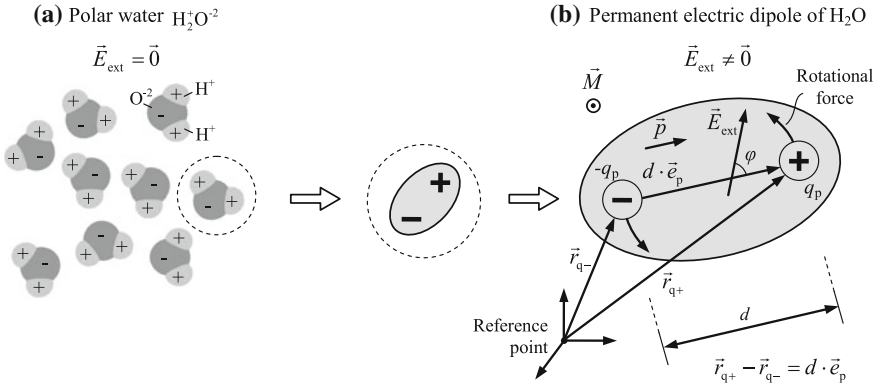

Fig. 2.17 Orientation polarization of water molecules H_2O under the influence of an external electric field $\vec{E}_{ext}$; compare Fig. 2.16b, c. **a** Random orientation of polar H_2O molecules with their negative oxygen sides and positive hydrogen sides under zero $\vec{E}_{ext} = \vec{0}$. **b** A single H_2O molecule as a permanent electric dipole with its polarization charges q_p and $-q_p$ at a distance d, and its dipole moment $\vec{p}$ (2.59). When the dipole is exposed to a non-zero $\vec{E}_{ext} \neq \vec{0}$, it experiences rotational forces and thus a torque $\vec{M}$ (Footnote 35)

excess polarization charge Q_p and $-Q_p$ is created at the respective *boundary of the tissue section* facing electrodes.

It should be stressed that the considered positive and negative charges within the structure are *elastically bound* to each other and held in place by mutual *molecular bonds*. In other words, these *bound charges* are elastically arrested and *are not free to move* from one structure to another within or through tissue. The resulting *quasi-elastic movements* of bound charges within the structure—when a non-zero $\vec{E}_{ext}$ is applied—are minimal and *locally restricted*, and thus can not contribute to a *conductive current* within tissue. These local movements do not contribute to a net current flow of *unbound charges* in line with (2.54). Obviously, this is in clear contrast to Fig. 2.16a with *unbound charges* that are free to move through tissue and can transfer a net electric charge from one electrode to another in terms of a non-zero conductive current.

If there is an *alternating time-varying* $\vec{E}_{ext}(t)$ applied to tissue, i.e., $\vec{E}_{ext}(t)$ with an alternating direction, *polarized structures* (electric dipoles) change their polarization directions every *half cycle* of $\vec{E}_{ext}(t)$ (Footnote 45). This alternating *repolarization* goes on as long as the *temporal dynamic* of $\vec{E}_{ext}(t)$ changes is sufficiently slow as compared with the time needed to repolarize *structure with its certain mass* and thus its *non-zero inertance*; see the *displacement dispersion* from Fig. 2.19d.

Orientation Polarization

If the *two balance points* of positive and negative charges within a *biological structure* do not completely overlap in space—already without any external application of a polarizing field $\vec{E}_{ext}$—this structure is said to be a *polar structure* or *permanent electric dipole* with its own non-zero $\vec{p}$ at zero $\vec{E}_{ext} = \vec{0}$ (2.59). Figure 2.16c illustrates *permanent polarization charges* q_p and $-q_p$ within polar structures, charges located at the respective balance points of permanently dislocated positive and negative charges within the polar structure. Consequently, the polar structure has already its own *structure-bound electric field*, a *microscopic electric field*. As illustrated in Fig. 2.17, the most prominent polar structure in tissue is that of the *water molecule* H_20 (Kaniusas 2012, Footnote 12 and Kaniusas 2012, Fig. 2.4). The oxygen side of H_20 is somewhat negative and represents $-q_p$, whereas the hydrogen side is somewhat positive and represents q_p (Fig. 2.17a).

In the absence of an applied $\vec{E}_{ext}$, *permanently polar structures* are *randomly oriented* within tissue due to their inherent *thermal motions*, as shown in Fig. 2.16c. A net *macroscopic electric polarization field* $\vec{E}_p$ structures produce within and around a *tissue section* is still zero, i.e., the vector *superposition of permanent microscopic fields* of polar structures is on average non-constructive (Footnote 36).

However, when polar structures within tissue located between two *charged electrodes* are subjected to a non-zero $\vec{E}_{ext} \neq \vec{0}$ (Fig. 2.16c), each polar structure

experiences a *torque*,[35] as illustrated in Fig. 2.17b. The torque arises because *attractive and repulsive electrostatic forces* act between polar ends of the dipole (represented by q_p and $-q_p$) and electrode charges (Q and $-Q$); see Fig. 2.16c. In other words, charges q_p and $-q_p$ experience *rotational forces* when subjected to the external $\vec{E}_{ext}$ (Fig. 2.17b). In fact, polar structures become *slightly aligned* to each other *with the applied* $\vec{E}_{ext}$ (2.76)—i.e., *structures rotate* into the same alignment under the influence of $\vec{E}_{ext}$—despite of omnipresent thermal motions (Fig. 2.16c). *Microscopic electric fields* of polar structures become mutually aligned (Footnote 36). In contrast to zero $\vec{E}_{ext} = \vec{0}$, the *macroscopic field* $\vec{E}_p$- the less-random aggregation of polar structures in tissue produces—is no longer zero while a *total excess polarization charge* Q_p and $-Q_p$ is induced at the respective *boundary of the tissue section* facing electrodes (Fig. 2.16c).

When an *alternating time-varying* $\vec{E}_{ext}(t)$ is applied, *permanent dipoles rotate* in one direction during one *half cycle* of $\vec{E}_{ext}(t)$ and then in the opposite direction during the subsequent half cycle. This alternating *alignment* is only effective as long as the temporal dynamic of $\vec{E}_{ext}(t)$ changes is sufficiently slow; see *γ-dispersion* from Fig. 2.19c.

Tissue Polarization Model

The applied electric field $\vec{E}_{ext}$ *polarizes a tissue section* between two *charged electrodes* (with Q and $-Q$) from a *macroscopic point* of view in both discussed cases of

- the *induced polarization* of *non-polar structures* (Fig. 2.16b) and
- the *orientation polarization* through alignment of already *polar structures* (Fig. 2.16c).

In fact, *polarizable tissue* behaves as a *dielectric*.

In the presence of $\vec{E}_{ext}$ obeying

$$\vec{E}_{ext} = E_{ext} \cdot \vec{e}_E = \frac{Q}{A \cdot \varepsilon_0} \cdot \vec{e}_E, \tag{2.60}$$

[35]The magnitude M of the *torque* $\vec{M}$ is greatest when the *permanent electric dipole* is at right angle to the *externally applied electric field* $\vec{E}_{ext}$. To be precise, the torque

$$\vec{M} = \vec{p} \times \vec{E}_{ext} = p \cdot E_{ext} \cdot \sin(\varphi) \cdot \vec{e}_M$$

is proportional to $\sin(\cdot)$ of the *displacement angle* φ between the *electric dipole moment* $\vec{p} = q_p \cdot d \cdot \vec{e}_p$ (2.59) of the considered dipole and the vector field $\vec{E}_{ext}$. Figure 2.17b depicts the dipole of H_2O with its $\vec{p}$ displaced by φ with respect to the direction of $\vec{E}_{ext}$. The resulting *rotational forces*—both acting on q_p and $-q_p$ with their *force magnitude* $|\vec{M}|/(2 \cdot d)$—and the vector $\vec{M}$ are also illustrated in Fig. 2.17b. In addition, Fig. 2.19c illustrates φ between $\vec{p}$ and the local electric field $\vec{E}_{ext}$ within *polarizable tissue*.

there is an *accumulation*[36] of an *excess negative charge* $-Q_p$ directly at the left *boundary of the tissue section*—as illustrated in the lower subfigure of Fig. 2.16c—and, on the other hand, an accumulation of a corresponding *excess positive charge* Q_p at the right boundary. This *induced polarization charge* Q_p is distributed over the boundary's surface with its *contact area A* (i.e., the contact area with the electrode surface) and is locally *uncompensated, exposed, and bound*. The unit vector $\vec{e}_E$ in (2.60) points in the direction of $\vec{E}_{ext}$ (Fig. 2.16c).

Please note that (2.60) assumes a *constant charge Q and −Q on the respective electrode*—irrespective of the polarizable tissue presence between electrodes—distributed over the electrode's *surface area A*. As discussed in Footnote 36, constant Q and $-Q$ imply that both *electrodes are charged but isolated* from any external charge source (for instance, electrodes were charged by an external *voltage source* and then disconnected from the source). Moreover, it should be stressed that

[36]The *induced electric fields* or *aligned electric fields* outside microscopic *polarized structures* or *polar structures*, respectively, cancel each other *within polarizable tissue* in terms of *microscopic interactions* because there is *no excess charge* inside tissue. In contrast, at the *outer boundaries* of a *tissue section* (namely, boundaries facing *charged electrodes* with Q and $-Q$), the induced *excess polarization charges* Q_p *and* $-Q_p$ are uncompensated and thus have a *macroscopic impact* (Fig. 2.16b, c). Namely, the charges Q_p and $-Q_p$ produce a *macroscopic electric polarization field* $\vec{E}_p$ *which opposes the applied external* $\vec{E}_{ext}$ within the scope of both

- the *induced polarization* of non-polar structures (Fig. 2.16b) and
- the *orientation polarization* of already polar structures (Fig. 2.16c).

In terms of the geometric *superposition principle*, the resulting inner *electric field* $\vec{E}$ *within tissue* is *reduced* in its magnitude E *in relation to the magnitude* E_{ext} of the applied $\vec{E}_{ext}$ by the amount of the magnitude E_p of $\vec{E}_p$ (2.62). Figure 2.16d demonstrates the associated vectors $\vec{E}$, $\vec{E}_{ext}$, and $\vec{E}_p$. Here we assume that the *charge density* on the surface of the two electrodes ($=Q/A$ and $-Q/A$)—surrounding the tissue section between electrodes—*remains constant* throughout the polarization process. That is, both *charged electrodes are assumed to be isolated* to prevent flow of *unbound charges* to or from the electrodes when polarizable tissue is inserted; compare with the origin and changes of the charge density on the cell membrane from Kaniusas (2012, Fig. 2.7). In fact, the *factor of this reduction* of E_{ext} within tissue is given by the *relative permittivity* ε_r *of tissue* (2.62). For the *electric flux density* $\vec{D}$ in tissue (2.64), it must be pointed out that the magnitude D is a function of the *unbound* Q (but not *bound* Q_p), so that the field $\vec{D}$ *without polarizable tissue* between electrodes is equivalent to the field $\vec{D}$ *with polarizable tissue* between *electrodes* (charged with Q and $-Q$); compare upper and lower subfigures in Fig. 2.16b, c.

In contrast to isolated electrodes, when the two *electrodes are connected* to a *voltage source*, i.e., unbound charges can flow to and from these electrodes, the *electric field* $\vec{E}$ between electrodes *remains constant* irrespective of the presence of polarizable tissue between electrodes. That is, the equality $\vec{E} = \vec{E}_{ext}$ applies within tissue between charged and connected electrodes. Here the *magnitude D* of the field $\vec{D}$ between electrodes, *in contrast to isolated electrodes*, increases from $D = Q/A$ without polarizable tissue between electrodes to $D = (Q + Q_p)/A$ with polarizable tissue inserted between electrodes. In fact, an *excess unbound electric charge* is delivered to both electrodes by the connected *voltage source* when tissue is inserted. To be precise, an additional positive charge of the size $+Q_p$ is delivered to the positive electrode with its original Q while a negative $-Q_p$ to the negative electrode with its original $-Q$. This delivery of excess charges compensates for the induced polarization charges $+Q_p$ and $-Q_p$ residing on the *outer boundaries* of the *tissue section* facing the two electrodes; with $Q_p = Q \cdot (\varepsilon_r - 1)$ and thus $Q_p > Q$ for $\varepsilon_r > 1$.

the *unbound charge* Q *and* $-Q$ on *isolated electrodes* are always larger than the induced *bound charge* Q_p *and* $-Q_p$ on *tissue boundaries*, respectively; with $Q_p = Q \cdot (1 - 1/\varepsilon_r)$ and thus $Q_p < Q$ for finite $\varepsilon_r > 1$.

The *uncompensated charges* Q_p and $-Q_p$ necessarily induce a *macroscopic polarization field* $\vec{E}_p$ within tissue

$$\vec{E}_p = E_p \cdot (-\vec{e}_E) = \frac{Q_p}{A \cdot \varepsilon_0} \cdot (-\vec{e}_E), \tag{2.61}$$

with its magnitude $E_p = Q_p/(A \cdot \varepsilon_0)$, compare (2.60)—as demonstrated in Fig. 2.16b. In particular, the induced vector field $\vec{E}_p = E_p \cdot (-\vec{e}_E)$ *opposes* the externally applied $\vec{E}_{ext} = E_{ext} \cdot \vec{e}_E$ so that the resulting *electric field* $\vec{E} = E \cdot \vec{e}_E$ within *polarizable tissue* obeys

$$\vec{E} = \vec{E}_{ext} + \vec{E}_p = \frac{\vec{E}_{ext}}{\varepsilon_r} \quad \text{and} \quad E = E_{ext} - E_p = \frac{E_{ext}}{\varepsilon_r}, \tag{2.62}$$

as illustrated in Fig. 2.16d. Please note that $\vec{E}$ is reduced in its *magnitude* E by the *relative permittivity* ε_r of *polarizable tissue* in comparison to the applied *magnitude* E_{ext} (Footnote 36); e.g., the induced polarization in typical dielectrics yields reduction factors of about $\varepsilon_r = 2$ to 5 while the orientation polarization in water yields a much larger reduction factor in the range of 80. In other words, the *applied field* $\vec{E}_{ext}$ is *partially compensated* by the *polarization field* $\vec{E}_p$ of tissue while the resulting *inner field* $\vec{E}$ $(=\vec{E}_{ext} + \vec{E}_p)$ within tissue turns to be finite in size. This is in clear contrast to *currentless conductive tissue* with a *complete compensation* of the applied electric field within tissue (see below).

The amount of the *accumulated polarization charge* Q_p in response to $\vec{E}_{ext}$ is accounted for by the *dielectric permittivity* $\varepsilon = \varepsilon_0 \cdot \varepsilon_r$ of *polarizable tissue*, namely, by ε_r of tissue (ε_0 is the permittivity of free space). Thereby, the *charge density* Q_p/A of Q_p, namely, the induced *electric polarization density field*[37] $\vec{P}$ in polarizable tissue is given by

[37]The *polarization density field* $\vec{P}$ can be given as

$$\vec{P} = \frac{Q_p}{A} \cdot \vec{e}_E = \frac{\sum \vec{p}}{V}$$

and can be interpreted as the *volume density* of *all* induced and aligned *electric dipole moments* $\vec{p}$ (2.59) within the volume V of the *polarizable tissue* (Figs. 2.17 and 2.19c). In other words, $\vec{P}$ is the *total amount of* $\vec{p}$ of all polarizable and polar structures per unit volume of tissue. The latter equation illustrates that *polarized dielectric* can be imagined as an *accumulation* of a large number of *atomic and molecular dipoles*.

$$\vec{P} = \frac{Q_p}{A} \cdot \vec{e}_E = \varepsilon_0 \cdot (\varepsilon_r - 1) \cdot \vec{E}. \tag{2.63}$$

Here the term $(\varepsilon_r - 1)$ is known as the *electric susceptibility*.[38] Please note that vector fields $\vec{P}$ and $\vec{E}$ point in the same direction within an *isotropic polarizable tissue* with its electrical property ε_r being identical in all spatial directions. In contrast, fields $\vec{P}$ and $\vec{E}_p$—compare (2.61) and (2.63)—point in opposite directions according to their relation $\vec{E}_p = -\vec{P}/\varepsilon_0$; compare fields $\vec{P}$, $\vec{E}$, and $\vec{E}_p$ in Fig. 2.16d.

A reasonable combination of the *external impact on polarizable tissue* [i.e., due to non-zero $Q \neq 0$ on electrodes surrounding the tissue section, see (2.60)] and the resulting $\vec{P}$ in tissue (2.63) yields an instructive relationship:

$$\frac{Q}{A} \cdot \vec{e}_E = \varepsilon_0 \cdot \vec{E} + \frac{Q_p}{A} \cdot \vec{e}_E \quad \text{and} \quad \vec{D} = \varepsilon_0 \cdot \vec{E} + \vec{P} = \varepsilon \cdot \vec{E} = \varepsilon_0 \varepsilon_r \cdot \vec{E}. \tag{2.64}$$

Here $\vec{D}$ is the field of the *electric flux density* (or the *electric displacement field*) in tissue. Its magnitude D can also be interpreted as the *charge density* Q/A of the *electrode charge* Q distributed over the area A. Please note that the fields $\vec{E}$ and $\vec{D}$ point in *the same spatial direction* and are *in-phase* in the time domain when an *isotropic polarizable tissue* with *lossless polarization processes* is considered, respectively (compare Fig. 2.23b).

It can also be derived from (2.64) that the field $\vec{D}$ is not a function of the induced *bound* Q_p on tissue boundaries but only of the *unbound* Q residing on electrodes. Therefore, the externally induced $\vec{D}$ within polarizable tissue can be interpreted—in line with Fig. 2.16d—as being received by both

- the resulting $\vec{P}$ field [due to an *excess polarization* of tissue with respect to the *residual polarization* of free space, i.e., proportional to $\varepsilon_0 \cdot (\varepsilon_r - 1)$, see (2.63)] and
- the residual $\varepsilon_0 \cdot \vec{E}$ field in tissue (the *residual polarization* of free space, i.e., proportional to ε_0 only).

In contrast to $\vec{D}$, the *electric field* $\vec{E}$ in tissue is a function of both the applied *unbound* Q on electrodes and the induced *bound* Q_p on tissue boundaries, as illustrated in (2.64) (Footnote 36). As already discussed, the magnitude E within polarizable tissue decreases with increasing ε_r given a constant $\vec{D}$ [or a constant Q which stimulates polarization processes, see (2.60)].

---

[38] In general, the relative permittivity ε_r *is a non-linear function* of the inner field $\vec{E}$, especially in the case of the *alignment* of permanently polar structures when *exposed to* $\vec{E}$ (Fig. 2.16c); compare Footnote 45. Usually, the level of ε_r tends to increase with increasing magnitude E (i.e., the alignment of permanent dipoles overwhelms progressively thermal motions), reaches a peak (the maximum possible alignment is already reached), and then decreases and converges towards 1 ($\varepsilon = \varepsilon_0 \cdot \varepsilon_r$ converges towards $\varepsilon = \varepsilon_0$ of free space).

Capacitive Displacement Current

Provided that an *alternating time-varying* $\vec{E}_{\text{ext}}(t)$ is applied via charged electrodes, the associated *electrode charge* $Q(t)$ (2.60) as thus the associated *flux density* $\vec{D}(t)$ (2.64) are necessarily subjected to continuous *temporal changes*. In parallel, *bound charges* within *polarizable tissue* (residing between electrodes) undergo an alternating *repolarization*, in terms of both polarization processes: *induced polarization and orientation polarization* (Fig. 2.16b, c). The associated *electric dipoles* $\vec{p}$ (2.59) alternate in their *strength and spatial direction*, whereas not only $\vec{p}$ of a single dipole alternates but also the averaged field $\vec{P}$ of all $\vec{p}$ fields within tissue (Footnote 37), in terms of an alternating *polarization field* $\vec{P}$.

Bound charges can be said to *move locally* (by a fraction of an *atomic diameter*) and to be *reposited locally* inside polarizable tissue.

- These *local movements*[39] of *bound charges* constitute the so-called *capacitive/displacement current* $i_{\text{C}}(t)$ through *polarizable tissue*. By analogy,

[39]It is instructive to show that the *displacement current* in *polarizable tissue* (2.66) accounts for *local movements of electric charges*; in analogy with *global movements of charges* accounting for the *conductive current* in *conductive tissue* (2.54). Namely, the *displacement current* accounts for movements of *polarization charges* q_{p} and/or $-q_{\text{p}}$ of the *electric dipole* within *polarizable structure* (Fig. 2.17b).

For this purpose, (2.64) and (2.66) can be rewritten as

$$\vec{j}_{\text{C}}(t) = \varepsilon_0 \cdot \frac{\mathrm{d}\vec{E}(t)}{\mathrm{d}t} + \frac{\mathrm{d}\vec{P}(t)}{\mathrm{d}t},$$

showing that the time derivative of $\vec{P}(t)$—known as the *polarization current density* $\mathrm{d}\vec{P}(t)/\mathrm{d}t$—contributes to the *displacement current density* $\vec{j}_{\text{C}}(t)$. The density $\mathrm{d}\vec{P}(t)/\mathrm{d}t$—based on Footnote 37—can be expressed as

$$\frac{\mathrm{d}\vec{P}(t)}{\mathrm{d}t} = \frac{\mathrm{d}}{\mathrm{d}t}\left(\frac{1}{V}\sum \vec{p}(t)\right) = \frac{\mathrm{d}}{\mathrm{d}t}\left(\frac{q_{\text{p}}}{V}\sum\left(\vec{r}_{\text{q}+}(t) - \vec{r}_{\text{q}-}(t)\right)\right) = \frac{q_{\text{p}}}{V}\sum\left(\vec{v}_{\text{q}+}(t) - \vec{v}_{\text{q}-}(t)\right)$$

with $\vec{p}$ given as

$$\vec{p}(t) = q_{\text{p}} \cdot d(t) \cdot \vec{e}_{\text{p}}(t) = q_{\text{p}} \cdot \left(\vec{r}_{\text{q}+}(t) - \vec{r}_{\text{q}-}(t)\right);$$

compare (2.59). Here $\vec{r}_{\text{q}+}$ and $\vec{r}_{\text{q}-}$ are the two radial vectors from a *reference point* to point charges q_{p} and $-q_{\text{p}}$ (at a mutual distance d), respectively, of a considered single dipole $\vec{p}$. Figure 2.17b illustrates field vectors $d \cdot \vec{e}_{\text{p}}$, $\vec{r}_{\text{q}+}$, and $\vec{r}_{\text{q}-}$. Correspondingly, the time derivative of $\vec{r}(t)$ gives the *movement velocity* $\vec{v}(t) = \mathrm{d}\vec{r}(t)/\mathrm{d}t$ of the respective charge q_{p} and/or $-q_{\text{p}}$ with respect to the *reference point*.

Please note that the resulting proportionality between $\vec{j}_{\text{C}}(t)$ and $\vec{v}(t)$ (of *bound charges*) is qualitatively in line with the proportionality between $\vec{j}_{\text{E}}(t)$ and $\vec{v}(t)$ (of *unbound charges* from (2.55), see Kaniusas (2012, Footnote 45)). In both cases, the proportionality coefficient has the physical unit of the charge per volume.

As can be clearly seen in the latter equation breaking down $\mathrm{d}\vec{P}(t)/\mathrm{d}t$, any change of $\vec{p}$ due to *positional changes* of q_{p} and/or $-q_{\text{p}}$ (with $\vec{v}(t) \neq \vec{0}$)—such as

- *non-local movements* of *unbound charges* constitute the *conductive current* (2.25) through *conductive tissue*.

In fact, the current $i_C(t)$ equals to the *rate of Q(t) change* on the electrode (Fig. 2.16b, c):

$$i_C(t) = \frac{dQ(t)}{dt}; \tag{2.65}$$

see the discussion on $i_E(t) = i_C(t)$ from Fig. 2.8 in Section "Simple Tissue Model". The associated *capacitive/displacement current density* $\vec{j}_C(t)$ through *polarizable tissue* with its *vector amplitude* $\vec{J}_C$—compare (2.32)—can be derived from (2.64) and (2.65) and equals to

$$\vec{j}_C(t) = \frac{d\vec{D}(t)}{dt} = \varepsilon \cdot \frac{d\vec{E}(t)}{dt} \quad \text{with} \quad \vec{J}_C = \frac{d\vec{D}}{dt} = \varepsilon \cdot \frac{d\vec{E}}{dt} = \varepsilon_0 \varepsilon_r \cdot \frac{d\vec{E}}{dt}. \tag{2.66}$$

Here $\vec{D}$ and $\vec{E}$ are the respective *vector amplitudes* of the time-varying $\vec{D}(t)$ and $\vec{E}(t)$ in tissue. In accordance with (2.66), the *rate of change* of $\vec{D}(t)$ field or, in analogy, the rate of change of $\vec{E}(t)$ field—with an assumed time-invariant ε_r—determines the size of the *magnitude* of $\vec{J}_C$. It can be observed from (2.66) that time courses of $\vec{E}(t)$ and $\vec{D}(t)$ are *delayed* with respect to the time course of $\vec{j}_C(t)$; for sinusoidal courses, this delay amounts to 90°.

For a *harmonic sinusoidal waveform* of $\vec{E}(t)$—and thus for the resulting *harmonic waveform* of $\vec{j}_C(t)$—with the *angular frequency* ω (=$2\pi \cdot f$), (2.66) can be rewritten for *vector amplitudes* $\vec{J}_C$ and $\vec{E}$ as

$$\vec{J}_C = \underline{J}_C \cdot \vec{e}_E = j\varepsilon_0 \varepsilon_r \cdot \omega \cdot \vec{E} \tag{2.67}$$

with the *complex amplitude* $\underline{J}_C$ of $\vec{J}_C$ [compare (2.40) with (2.42)]. Figure 2.18 illustrates both vectors $\vec{J}_C$ and $\vec{E}$ pointing into the *same spatial direction* $\vec{e}_E$ (Fig. 2.18a), whereas complex $\underline{J}_C$ and $\underline{E}$ are dislocated by 90° in the *phasor diagram* (Fig. 2.18c) due to the complex factor $j \cdot \varepsilon \cdot \omega$ in-between $\underline{J}_C$ and $\underline{E}$ (2.67). Equation (2.67) shows also that the particular involvement of polarization phenomena within $\vec{J}_C$ depends on the speed of the field change, i.e., the field frequency

---

- *reciprocal movements* of q_p and $-q_p$ from or to each other (i.e., with a time-dependent $d(t)$ in terms of *induced polarization* from Fig. 2.16b) and/or
- *joint rotation* of q_p and $-q_p$ (i.e., with a time-dependent $\vec{e}_p(t)$ in terms of *orientation polarization* from Fig. 2.16c)

contributes to $d\vec{P}(t)/dt$ and thus to $\vec{j}_C(t)$ in *polarizable tissue*. In *free space*, zero $d\vec{P}(t)/dt = \vec{0}$ applies while $\vec{j}_C(t)$ is then carried by the term $\varepsilon_0 \cdot d\vec{E}(t)/dt$ only.

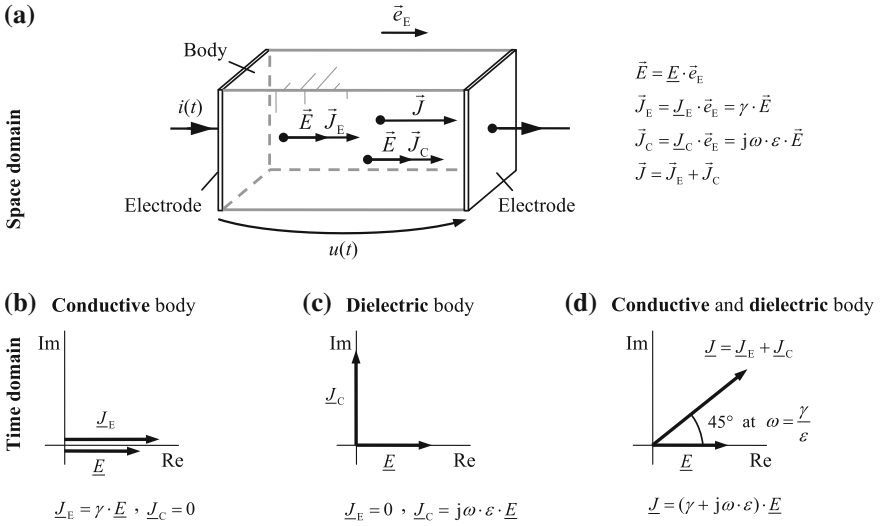

Fig. 2.18 The conceptual origin of **a** the electric field vector $\vec{E}$ with its complex amplitude $\underline{E}$, the conductive current density $\vec{J}_E$ with $\underline{J}_E$, the displacement current density $\vec{J}_C$ with $\underline{J}_C$, and the total current density $\vec{J}$ with $\underline{J}$ in **b** a pure conductive body, **c** a pure dielectric body, and **d** conductive and dielectric body (compare Fig. 2.12). While all vectors point in the same spatial direction of the unit vector $\vec{e}_E$, their complex amplitudes $\underline{E}$, $\underline{J}_E$, $\underline{J}_C$, and $\underline{J}$ are generally twisted to each other in the phasor diagram. In particular, the amplitude $\underline{J}_E$ is aligned with $\underline{E}$, $\underline{J}_C$ precedes $\underline{E}$ by 90°, and $\underline{J}$ precedes $\underline{E}$ by 45° at the assumed angular frequency $\omega = \gamma/\varepsilon = 1/\tau$ (2.49) and thus with the resulting $|\underline{J}_E| = |\underline{J}_C|$ and $|\underline{J}| = \sqrt{2} \cdot |\underline{J}_E|$

f, and, on the other hand, the size of ε_r. It should be said in advance that the effective size of ε_r is also a strong function of f (Fig. 2.20).

Conductive Versus Polarization Behaviour

It should be recalled that *conductive effects* are related to interaction of an *externally applied electric field* $\vec{E}_{ext}$ with *unbound charges* in tissue, whereas *polarization effects* are related to interaction of $\vec{E}_{ext}$ with *bound charges*. The resulting strength of conductive and polarization effects are governed by the two major *macroscopic electrical properties of tissue*, the *conductivity* γ and *permittivity* ε, respectively. Namely,

- the strength of the induced *conductive current density* $\vec{j}_E(t)$ with its *vector amplitude* $\vec{J}_E$ (2.54) is proportional to the size of γ, a *frequency-dependent measure* of the *local tissue* (Fig. 2.21). The conductivity γ describes the ability of *conductive tissue* to *transport or move unbound free charges* within and through tissue in response to the prevailing *electric field* $\vec{E}$ *within tissue*.

The *conductive current* $i_E(t)$ (2.24) yields a *net current flow* and a *net charge flow* (2.25) through a *conductive tissue section*. On the other hand,

- the strength of the induced *electric polarization density* $\vec{P}$ (2.63) and its *rate of change* $d\vec{P}/dt$—contributing to the *displacement current density* $\vec{j}_C(t)$ (Footnote 39) with its *vector amplitude* $\vec{J}_C$ (2.66)—are proportional to the size of the *relative permittivity* ε_r, a *frequency-dependent measure* of the *local tissue* (Fig. 2.20). The permittivity ε_r describes the ability of *polarizable tissue* to *separate bound charges* within polarizable structures (induced polarization) and/or to *rotate bound charges* within polarizable structures (orientation polarization)—or, in general, to *move locally bound charges*—in response to the prevailing $\vec{E}$ within tissue. The *displacement current* $i_C(t)$ does not carry any unbound free charge and thus can not accumulate any unbound charge (e.g., *no surface charge* according to (2.107) can be accumulated by $\vec{J}_C$). Likewise, there is *no net current flow* and *no net charge flow* through a polarizable tissue section in response to $i_C(t)$.

When comparing the *polarization and conductive behaviour*, it is instructive to observe that

- *polarizable tissue* (dielectric body or polarizable isolator) with the resulting *non-zero* $\vec{E} \neq \vec{0}$ within tissue is characterized by a *partial compensation* [after a certain *relaxation time*, see (2.74) and (2.75)] of the external charges Q and $-Q$ (applied on electrodes facing opposite boundaries of a polarizable tissue section between electrodes) by the induced *surface charges* Q_p and $-Q_p$ (induced on tissue boundaries) with $Q_p < Q$ for finite ε_r, as illustrated in Fig. 2.16b, c. In analogy, the *applied* $\vec{E}_{ext}$ (2.60) is *partially compensated* by the *polarization field* $\vec{E}_p$ within tissue [generated by Q_p and $-Q_p$, see (2.61)] that results in a *non-zero* $\vec{E}$ ($=\vec{E}_{ext} + \vec{E}_p \neq \vec{0}$). In contrast,
- *currentless conductive tissue* (currentless conductive body) with the resulting *zero* $\vec{E}$ ($=\vec{E}_{ext} + \vec{E}_i = \vec{0}$) within tissue is characterized by a *complete compensation* (after a certain *relaxation time*, see Footnote 55) of the externally applied $\vec{E}_{ext}$ by the inner electric field $\vec{E}_i$ within tissue (generated by induced *surface charges* on tissue boundaries which face *sources and sinks* of the external $\vec{E}_{ext}$ field, see Fig. 2.25a).

Furthermore, it is important to stress that the *conductive current* $i_E(t)$ with its density $\vec{j}_E(t)$ represents a *lossy current component* within conductive and polarizable tissue and accounts for losses in *tissue regions* acting as *conductors*. In contrast, the *displacement current* $i_C(t)$ with its density $\vec{j}_C(t)$ represents a *lossless current component* in tissue and characterizes *tissue regions* acting as *lossless dielectrics*. In addition, biological tissue also typically behaves as a *lossy dielectric* so that the resulting *total losses* in tissue—including *conductive and dielectric*

losses—are determined by the *effective conductivity* γ_{eff} [$=\gamma + \Delta\gamma$, see (2.82)]. In particular,

- *lossy current* is marked by an *in-phase relationship* (0° offset) between time courses of $j_E(t)$ and $E(t)$ within tissue [Fig. 2.12b and (2.32)], i.e., marked by an *in-phase movement velocity of unbound charges* within tissue in response to the *time-varying* $E(t)$ (2.55). In contrast,
- *lossless current* is marked by an *out-of-phase relationship* (90° offset for sinusoidal courses) between $j_C(t)$ and $E(t)$ within tissue [Fig. 2.12c and (2.66)], i.e., marked by an *out-of-phase movement velocity of bound charges* within tissue in response to $E(t)$ (only local motions and local accumulations over atomic distances, see Footnote 39).

Consequently, *sinusoidal* currents densities $j_E(t)$ and $j_C(t)$ within *biological tissue* with *conductive and dielectric properties* are out-of-phase by 90° provided that the applicable γ and ε of tissue are *real quantities*. To be precise, $j_E(t)$ is delayed with respect to $j_C(t)$ by 90° given a certain $E(t)$ field in tissue (2.69); compare Fig. 2.12b, c.

Taking into account (2.26), (2.32), and (2.66), the *total current density* $\vec{j}(t)$ in tissue with conductive and dielectric properties—as illustrated in Fig. 2.9a—amounts to

$$\vec{j}(t) = \vec{j}_E(t) + \vec{j}_C(t) = \gamma \cdot \vec{E}(t) + \varepsilon \cdot \frac{d\vec{E}(t)}{dt} \tag{2.68}$$

in response to $\vec{E}(t)$ within tissue. Equation (2.68) confirms that

- *time courses* of $j_E(t)$ and $E(t)$ show *0° phase shift* in-between (Fig. 2.12b),
- *sinusoidal time courses* $j_C(t)$ and $E(t)$ show *90° phase shift* in-between, with $j_C(t)$ preceding $E(t)$ (Fig. 2.12c), whereas
- *sinusoidal time courses* $j(t)$ ($=j_E(t) + j_C(t)$) and $E(t)$ show an out-of-phase relationship with a *finite phase shift* of larger than 0° but smaller than 90°, with $j(t)$ preceding $E(t)$ (Fig. 2.12d).

For *harmonic waveforms* of $\vec{E}(t)$ such as *sinusoidal fields*, (2.68) and (2.26) can be rewritten with the *vector amplitudes* $\vec{J} = \underline{J} \cdot \vec{e}_E$, $\vec{J}_E = \underline{J}_E \cdot \vec{e}_E$, $\vec{J}_C = \underline{J}_C \cdot \vec{e}_E$, and $\vec{E} = \underline{E} \cdot \vec{e}_E$ and their respective *complex amplitudes* $\underline{J}$, $\underline{J}_E$, $\underline{J}_C$, and $\underline{E}$ as

$$\vec{J} = \vec{J}_E + \vec{J}_C = \gamma \cdot \vec{E} + j\varepsilon \cdot \omega \cdot \vec{E} = \gamma \cdot \vec{E} + \varepsilon \cdot \omega \cdot \vec{E} \cdot e^{j\frac{\pi}{2}}; \tag{2.69}$$

While γ represents the *real conductivity* when considering conductive currents, the term $j\omega \cdot \varepsilon$ can be interpreted as the *imaginary conductivity* for displacement currents.

Figure 2.18 illustrates all vectors $\vec{J}$, $\vec{J}_E$, $\vec{J}_C$, and $\vec{E}$ in the space and time domain. While vectors point in the *same spatial direction* of $\vec{e}_E$ (Fig. 2.18a), their *complex amplitudes* are twisted to each other in the *phasor diagram* (Fig. 2.18d). In particular, the amplitude $\underline{J}_E$ is aligned with $\underline{E}$ (i.e., *unbound charges* oscillate in

phase with the applied $\underline{E}$), $\underline{J}_C$ precedes $\underline{E}$ by 90° (i.e., *bound charges* oscillate out-of-phase with the applied $\underline{E}$), and $\underline{J}$ ($=\underline{J}_E + \underline{J}_C$) precedes $\underline{E}$ by less than 90°.

For the real *biological tissue* that acts as both

- *conductor*, i.e., with *conductive losses* described by γ, and
- *lossy dielectric*, i.e., with *dielectric losses* described by $\Delta\gamma$ and *lossless polarization* described by real ε,

the *ionic conductivity* γ in (2.69) should be substituted by the *effective conductivity* γ_{eff} [$=\gamma + \Delta\gamma$, see (2.82)] considering conductive and dielectric losses. Then (2.69) mutates into

$$\vec{J} = \vec{J}_E + \vec{J}_C = \gamma_{eff} \cdot \vec{E} + j\varepsilon \cdot \omega \cdot \vec{E}; \tag{2.70}$$

compare (2.81) and Footnote 11. Likewise, *lossy dielectric* implies its *complex permittivity* $\underline{\varepsilon}$ (2.77).

It can be *qualitatively* derived from (2.69) that the *higher the field frequency f*, the larger is the produced *displacement* $\vec{J}_C$ for a given $\vec{E}$. In other words, the faster *oscillate bound charges* within polarizable structures in tissue with increasing *f*, the larger is the *movement velocity* of these charges (see velocity $\vec{v}(t)$ in Footnote 39), and thus the larger is the magnitude $J_C = |\vec{J}_C| = \varepsilon \cdot \omega \cdot E$. That is, the *frequency-dependent component* $\vec{J}_C$ in (2.69) increases with f while the *frequency-independent component* $\vec{J}_E$ does not, provided that both properties γ_{eff} and ε are assumed to be independent on the size of *f*. Consequently, $\vec{J}_E$ dominates $\vec{J}$ at *low f* where biological tissue is essentially *conductive*, whereas $\vec{J}_C$ dominates $\vec{J}$ at *high f* where tissue is essentially *dielectric*; compare Fig. 2.14.

This dominance can be easily detailed from a *quantitative* point of view:

- the *predominant conductive behaviour* in biological tissue requires inequalities

$$|\vec{J}_E| \gg |\vec{J}_C| \quad \text{and} \quad \gamma_{eff} \gg \omega \cdot \varepsilon \tag{2.71}$$

  to be fulfilled (2.69). It is obvious that (2.71) applies rather at the *relatively low f*. Please note that the *condition* $\gamma_{eff} \gg \omega \cdot \varepsilon$ is equivalent to the discussed condition $f \ll 1/(2\pi \cdot \tau)$ [from (2.49) and Fig. 2.14 with γ substituted by γ_{eff}]. On the contrary,
- the *predominant dielectric behaviour* is characterized by

$$|\vec{J}_E| \ll |\vec{J}_C| \quad \text{and} \quad \gamma_{eff} \ll \omega \cdot \varepsilon, \tag{2.72}$$

  applicable at the *relatively high f*. In analogy, the condition $f \gg 1/(2\pi \cdot \tau)$ applies.

It is obvious that when *dielectric losses* can be *neglected* ($\Delta\gamma = 0$) then the equality $\gamma_{eff} = \gamma$ applies and the resulting *modified conditions* $\gamma \gg \omega \cdot \varepsilon$ and $\gamma \ll \omega \cdot \varepsilon$

discriminate between predominant conductive and predominant dielectric behaviour, respectively. It should be reiterated that biological *tissues* are overwhelmingly *resistive* at *low f*, i.e., the condition $\gamma_{eff} \gg \omega \cdot \varepsilon$ (2.71) applies although the applicable ε_r values may attain impressive levels of more than 10^7 at very low f (Fig. 2.20); compare the discussion related to (2.122).

Please note that if inert *relaxation processes* dominate within tissue—with their necessarily *finite speed* (Section "Relaxation and Dispersion Effects on Conductivity and Polarization")—the response of tissue to a step in the inner $E(t)$ will become necessarily a function of time. Namely, the time course of the resulting *conductive* $j_E(t)$ (2.32) and that of the *accumulated* $P(t)$ (2.63) within tissue will be an *(exponential) function* of time in response to a *step function* in $E(t)$ (compare Fig. 2.29c). That is, the *static* value of γ (2.32) and the *static* value of ε_r (2.63) apply only in the limit of *semi-infinite time*. In contrast, the *dynamic response* of *conductive tissue* and/or *dielectric tissue* to a sinusoidal $E(t)$ field is characterized by the *frequency-dependent conductivity* γ_{eff} and/or *frequency-dependent permittivity* ε_r, which sizes vary strongly with f of $E(t)$ according to Figs. 2.21 and 2.20, respectively.

Relaxation and Dispersion Effects on Conductivity and Polarization

The concept of *electric conduction* refers to moving unbound charges in response to the *ambient electric field* $\vec{E}_{ext}$ (Fig. 2.16a) and reflects conductive properties of tissue (2.36). The concept of *electric polarization* means separation and/or rotation of bound charges in response to $\vec{E}_{ext}$ (Fig. 2.16b, c) and reflects dielectric properties of *heterogeneous biological tissues* (2.41). The *relaxation* refers to alternating movement direction of unbound charges—in terms of the local *conduction*—when $\vec{E}_{ext}$ alternates in its local direction. In analogy, the relaxation refers to alternating changes in the accumulated polarity of bound charges—in terms of *polarization*—when the applied $\vec{E}_{ext}$ is an *alternating field*. The relaxation of charges can follow directional changes of $\vec{E}_{ext}$ only up to a certain field frequency, known as the *relaxation frequency* f_r. This is because the *inertness* of involved charges requires a certain time for their effective displacement and/or for the mechanical charge separation in terms of conduction and/or polarization, respectively.

The *inertness of unbound charges* in conduction processes was already discussed with respect to (2.53). In terms of polarization, the larger is the *inertness of bound charges*, i.e., the larger is the size of the polarized structure with imbedded bound charges, the more time is required for their separation and/or rotation, and the smaller is the resulting f_r. Therefore, with increasing field frequency, the relaxation progressively ceases since polarization of charges can follow the *dynamics* of the incident $\vec{E}_{ext}$ only up to a certain frequency.

The *relaxation frequency* $f_{r,k}$ is an inverse measure of the time required for the *k*-th polarization mechanism to develop. This time is known as the *relaxation time constant* τ_k [$=1/(2\pi \cdot f_{r,k})$, see (2.50)]. Therefore, each relaxation process as determined by a specific polarization mechanism is usually characterized by, as a

rough *approximation*, a single τ_k [e.g., based on the simple Debye expression from (2.78)]. However, electrical properties of only a few biological media such as pure water can be very closely fitted by a *single* τ_k. In many biological tissues, *several polarization mechanisms* may occur in parallel so that the associated electrical response at a certain field frequency can then be described by *several* τ_k only. In particular, the relevant size of τ_k in various tissues covers a wide range of values from seconds to milliseconds (alpha dispersion), from microseconds to nanoseconds (beta dispersion), to picoseconds (gamma dispersion), and even down to femtoseconds (displacement dispersion). Therefore, the response of polarizable tissue to a single step in $\vec{E}_{ext}$ involves a *delayed physical displacement* of bound charges *forming polarization*. In analogy, the alternating $\vec{E}_{ext}$ forces periodical and physical redistribution of charges *forming relaxation*.

The *dispersion of conduction* denotes the non-linear impact of the frequency of the applied $\vec{E}_{ext}$ field on the transport of unbound charges and dissipated energy. In particular, the dispersion describes the strength and the *progressive gain* of conduction—e.g., transport of unbound charges—with increasing frequency. In analogy, the *dispersion of polarization* denotes the non-linear impact of the frequency of $\vec{E}_{ext}$ on the strength and the *progressive loss* of polarization with increasing frequency. The intrinsic kinetics of the polarization governs its frequency dependence and thus determines dispersion. In fact, dispersion of polarization is an intrinsic property of *lossy dielectrics* (Footnote 11). Accordingly, electrical properties of tissue characterising its conductive and polarization behaviour, namely, the *effective conductivity* γ_{eff} and *permittivity* ε necessarily show *frequency dependence*.

In fact, the *structural heterogeneity* of biological tissues is essential for underlying phenomena of conduction and polarization; i.e., structure and composition of tissues determine the presence or absence of particular conduction and polarization mechanisms. The interaction of $\vec{E}_{ext}$ with biological tissue is characterised by specific *microscopic interactions* at the ional, molecular, and cellular level (Fig. 2.16). These interactions include *frequency-dependent relaxation* phenomena due to redistribution of ion layers (e.g., around charged ions), interfacial recharging/polarization around heterogeneous structures (e.g., cell membranes), as well as rotation of polar molecules (e.g., water molecules or proteins) when tissue is exposed to $\vec{E}_{ext}$, as will be detailed in the following sections. These *microscopic interactions*, in turn, determine *macroscopic bulk properties* such as γ_{eff} and ε. Therefore, the highly *non-uniform structure* of tissue is crucial in determining its γ_{eff} and ε, and their frequency-dependent behaviour. Likewise, *dispersion* always refers to the heterogeneous tissue behaviour at various frequencies.

The *conduction and dielectric spectrum* of biological tissue—as described in Gabriel (1996a, b, c), Reilly (1998), WHO (1993), Foster (1996)—is basically characterized by three main *interaction mechanisms*, relaxation regions, or dispersion phenomena (Fig. 2.19):

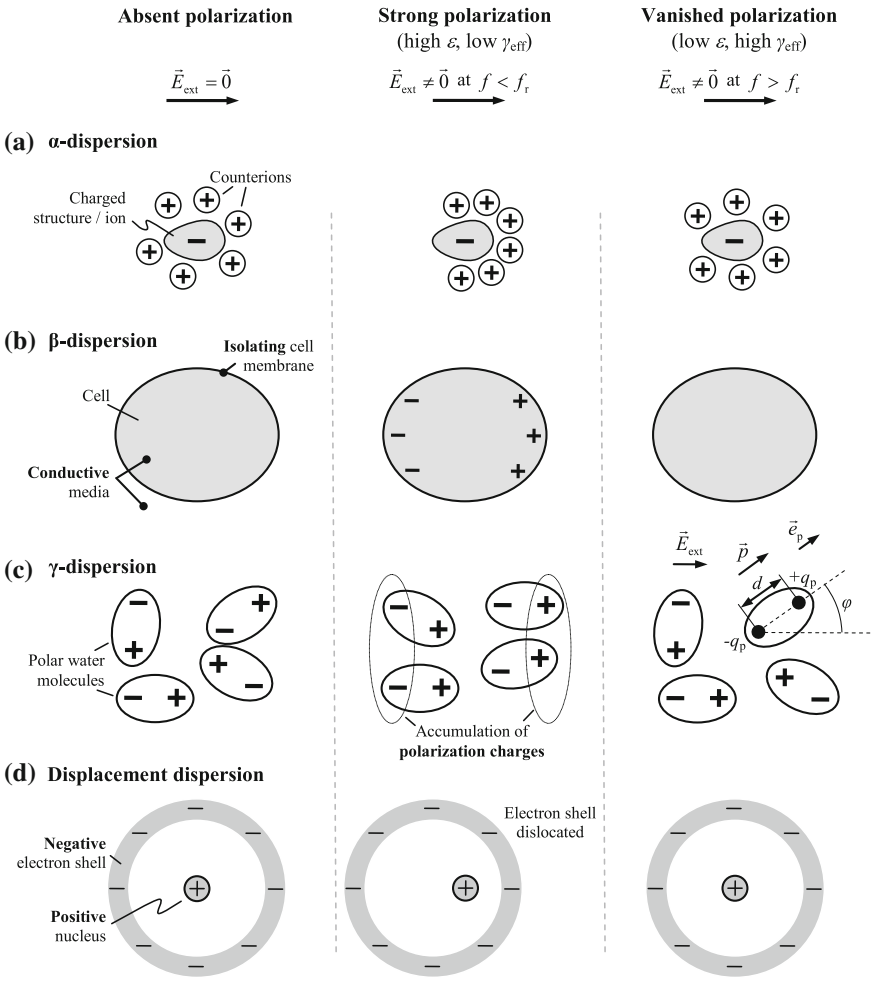

Fig. 2.19 Different dispersion/polarization phenomena in biological tissues in response to the external electric field $\vec{E}_{ext}$ oscillating with the field frequency f. **a** Polarization due to asymmetric accumulation of (positive) counterions around a (negatively) charged biological particle, known as α-dispersion. **b** Recharging of cell membranes, known as β-dispersion. **c** Reorientation of polar water molecules, known as γ-dispersion; compare Fig. 2.16c. **d** Induced polarization of non-polar atomic structures, known as displacement dispersion; compare Fig. 2.16b. Columns in (**a**)–(**d**) refer to three distinct cases; namely, absent polarization due to missing stimulus with $\vec{E}_{ext} = \vec{0}$ (left subfigures), strong polarization at relatively low f below the respective relaxation frequency f_r (i.e., the specific mechanical inertness of polarizable structures can still be neglected, see central subfigures), and again absent polarization at relatively high f above the respective f_r (i.e., the specific inertness of polarizable structures can not be neglected any more, see right subfigures)

- *alpha dispersion* (α-dispersion) at low frequencies with f_r in *kHz range*, a large τ as a fraction of *milliseconds* (2.73), and the lowest repolarization speed due to inert ionic diffusion;
- *beta dispersion* (β-dispersion) at medium frequencies with f_r in *MHz range* and smaller τ as a fraction of *microseconds* (2.74) due to faster interfacial polarization;
- *gamma and delta dispersion* (γ-dispersion and δ-dispersion) at high frequencies with f_r in the higher *GHz range* and even smaller τ in the range of *picoseconds* (2.75) due to even more faster dipolar orientation; and
- *ionic and displacement dispersion* at *optical frequencies* with f_r in *infrared and visible range* and the smallest τ as a fraction of *picoseconds* and *femtoseconds*, respectively, due to the smallest inertance of and thus fastest polarization of electronic clouds.

Therefore, with increasing field frequency of the incident $\vec{E}_{ext}$, α-dispersion occurs first in biological tissue, followed by β-dispersion, then by δ and γ-dispersions, and lastly by ionic and displacements dispersion located at the highest frequency. Successive dispersions with increasing frequency are illustrated in Figs. 2.20 and 2.21 based on experimental data. Please note that *underlying physical mechanisms* of all these dispersions are *basically different*, as clearly reflected by different origins of parameters determining the respective τ_k (2.73–2.75).

Alpha Dispersion

The so-called *alpha dispersion* (α-dispersion) is based upon numerous *inert mechanisms* within biological tissue, which have major impact on both polarization and conductance of tissue.

Polarization

Polarization mechanism of α-dispersion is based on an *asymmetric counterion distribution* in and near the charged surface of structures (or membranes) in response to the outer stimulus, the ambient electric field $\vec{E}_{ext}$ with the field frequency *f*, as illustrated in Fig. 2.19a. The asymmetry in the counterion distribution represents an *asymmetric charge distribution* and thus leads to *counterion polarization*.

With the alternating direction of $\vec{E}_{ext}$, counterions redistribute in synchrony with the applied $\vec{E}_{ext}$ in terms of *relaxation*. Since relatively *large structures* are involved in the redistribution, the counterion polarization contributes to the polarization of tissue only in the relatively *low frequency range* up to a few kHz and below, usually below about 10 kHz. Therefore, the formed *electronic bilayers* yield dominant *α-dispersions* to various degrees.

In fact, *charged structures* and *charged surfaces* provoke prominent *counterion polarization*, as described below.

- Diffusion and relaxation of counterions at the site of the *charged cellular structures* and *charged intracellular structures* (e.g., proteins) contribute to polarization at low *f* ($<f_r$ with f_r as the *relaxation frequency*), whereas the failure of polarization at higher *f* denotes the ionic dispersion process, α-dispersion. For

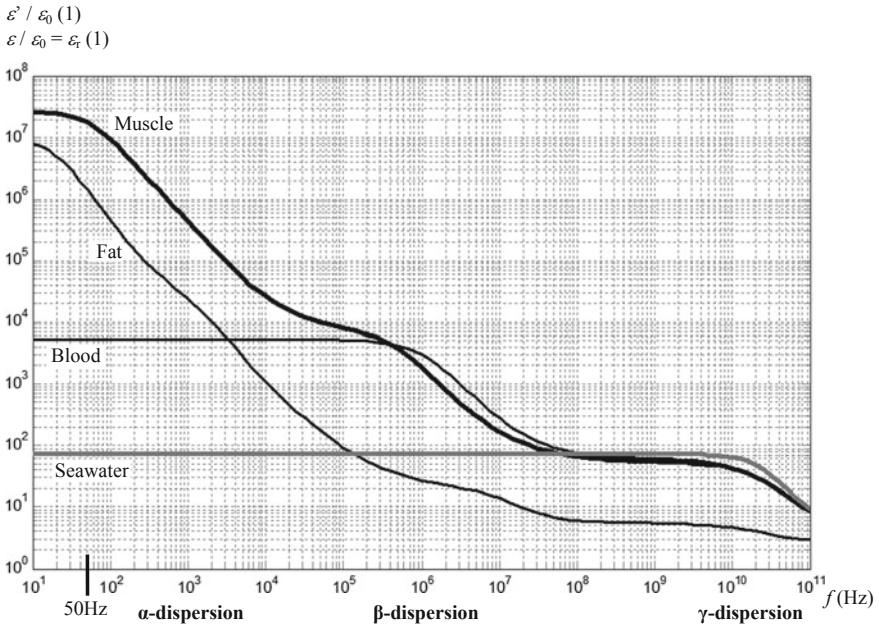

Fig. 2.20 Frequency variation of the effective, real dielectric permittivity ε ($=\varepsilon'$) of different biological media in the course of multiple dispersion phenomena; compare Fig. 2.24. Data on blood, muscle, and fat was taken from (IFAC 2013). Data on seawater at 37 °C was modeled with the parameters from Gabriel (1996c) which are used within the real part of the Debye expression considering γ-dispersion only [i.e., $\Delta\varepsilon / \varepsilon_0 = 69$, $\varepsilon_\infty / \varepsilon_0 = 5$, and $\tau = 6.2$ ps in (2.78)]. This modeling is a reasonable approximation in the considered frequency range up to 100 GHz (Somaraju 2006)

instance, relaxation of counterions about the tubular apparatus within muscle cells (Kaniusas 2012, Fig. 2.26) or about charged cell membranes (Kaniusas 2012, Fig. 2.3) comprises such polarization mechanisms.

- Relaxation and alternating polarization due to asymmetric distribution of counterions near *charged surfaces* and near large *charged membrane-related structures* contributes to the tissue polarization at low f ($\lesssim f_r$). The failure of this polarization at higher f denotes α-dispersion. In fact, there is an *alternating diffusion* of ions driven by electrochemical and electrostatic forces, as generated by the applied alternating $\vec{E}_{ext}$ and the induced inner electric fields within electrolyte. In addition, ions are necessarily subjected to hydrodynamic forces (2.53). Therefore, the *alternating ionic diffusion* in the *electrolytic double layers* adjacent to charged surfaces polarizes the structure (Fig. 3.16). For instance, diffusion of ions within surface layers on the extracellular and intracellular side of the cell membrane comprises such polarization mechanisms.

Molecular phenomena of α-dispersion are the least understood when compared with other dispersion mechanisms.

The applicable *relaxation time constant* τ for *counterion polarization* of α-dispersion has the characteristic order of l^2/D_F (Foster 1996), i.e.,

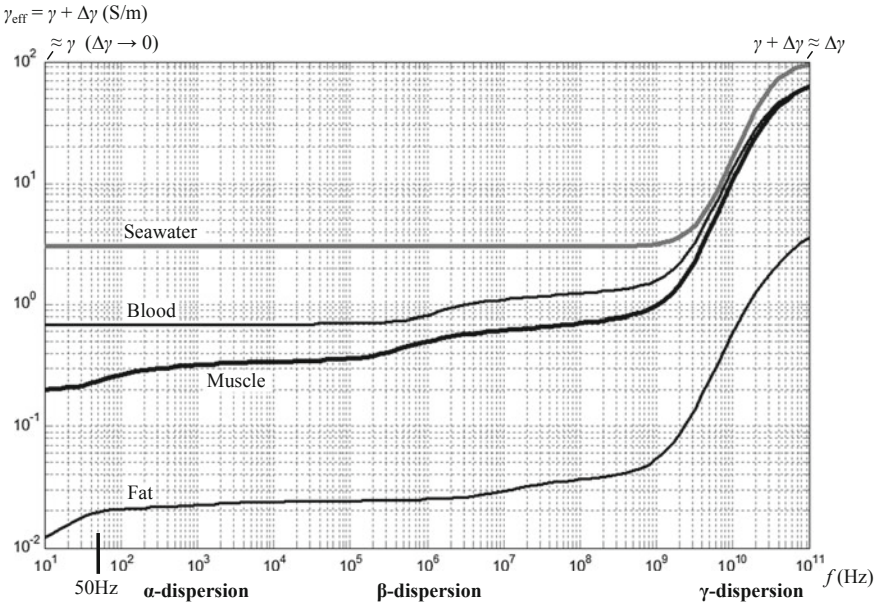

Fig. 2.21 Frequency variation of the effective, real conductivity $\gamma_{eff} = \gamma + \Delta\gamma$ [$=\gamma + \omega \cdot \varepsilon''$, see (2.82)] of different biological media in the course of multiple dispersion phenomena; compare Fig. 2.24. Data on blood, muscle, and fat was taken from IFAC (2013). Data on seawater at 37 °C was modeled with the parameters from Gabriel (1996c), which are used within the imaginary part of the Debye expression considering γ-dispersion only [i.e., the static conductivity of seawater due to free ions is $\gamma = 3$ S/m, $\Delta\varepsilon / \varepsilon_0 = 69$, and $\tau = 6.2$ ps in (2.78)]. This modeling is a reasonable approximation in the considered frequency range up to 100 GHz (Somaraju 2006)

$$\tau \propto \frac{l^2}{D_F}. \tag{2.73}$$

Here l is the distance over which the *ionic diffusion* occurs in response to the alternating $\vec{E}_{ext}$, whereas D_F is the diffusion coefficient of ions (Kaniusas 2012, Footnote 24). Obviously, the associated f_r equals $1/(2\pi \cdot \tau)$ (2.50).

Heterogeneous tissue structures may yield extremely high values of ε due to trapping of charges at internal interfaces within tissue; see experimental data in Fig. 2.20 with ε in the region of $10^7 \cdot \varepsilon_0$ for muscle. The strength and presence of α-dispersion, i.e., the *relative change* in both γ_{eff} and ε in the frequency range of α-dispersion, is relatively *strong* for ε but *hardly apparent* for γ_{eff} [in line with (2.83)]. In particular, the size of ε decreases steeply with f while γ_{eff} hardly increases with f in the course of α-dispersion; compare Footnote 45. The affected frequency range of α-dispersion is relatively *broad* (2.80), as reflected by a large value of the distribution parameter α_k of about 0.4 (Foster 1996). That is, α-dispersion is far broader than the Debye dispersion with its $\alpha_k = 0$ (2.78) by virtue of its kinetics.

Figure 2.19a demonstrates a thin *counterion layer* built out of positive charges that surrounds a negatively charged large particle[40] (e.g., a large ion or charged structure) in response to mutual electrostatic attractive forces. Provided that the external $\vec{E}_{\text{ext}}$ is not yet applied, a *symmetric cloud of counterions* results around the central ion (left subfigure in Fig. 2.19a). These counterions are *electrostatically bound* to the surface charges of the large particle but are *free to move laterally* along the surface of this large particle. Please note that any *electrostatic interactions* produce *spatial correlations* between charged structures (ions) in the solution.

When such a large particle with counterions is subjected to a non-zero $\vec{E}_{\text{ext}}$ with its *f*, *counterions will redistribute* along the surface under the influence of all three

- the resulting local *electric field*,
- *electrostatic forces* between counterions in the cloud and the charged particle in the middle of the cloud, and
- permanent *diffusion*;

as illustrated in Fig. 2.19a (central subfigure). That is, positive counterions tend to move towards the negative cathode but without leaving the surface of the large negatively charged particle. At the same time, negative charges tend to move towards the positive anode. *Balance points* of positive and negative ions become displaced and an *asymmetric cloud of charges* results near each moving large particle. An *electric dipole* is induced, in close analogy with induced polarization

[40]Please note that the final *distribution* of (solvated or hydrated) *charged structures* in the solvent obeys—in an approximation—an *equilibrium* between

- *electrostatic forces* (among charged structures) and
- *thermal motion*;

in line with the discussion in Footnote 7 in Chap. 3. For instance, an *energetically optimal near-order* of (hydrated) positive cations and (hydrated) negative anions is determined by attractive and repelling electrostatic forces in-between these ions. Therefore, a *single ion aims at inversely charged counterions* in its close vicinity to reduce *electric stray fields* of this single ion (Kaniusas 2012, Footnote 13). In the meantime, thermal motions of all involved ions tend to destroy the latter near-order and thus prevent formation of rigid and tight order between cations and anions.

As the result of the aforementioned equilibrium, on *time average*, a *central single ion* becomes surrounded by a *cloud of ions* (from electrolyte) with *spherical symmetry*—a cloud composed predominantly out of *counterions*, as illustrated in Fig. 2.19a (left subfigure)—*without any external electric fields* being applied. Likewise, the *total charge of the ionic cloud* around the central ion must equal the *charge of the central ion* (Footnote 17 in Chap. 3). As illustrated in Fig. 3.9b, *each and every ion* in the cloud acts for its part as another central ion with its *own cloud of counterions*.

In addition, *solvent molecules*, such as *water molecules*, residing in the *hydration shell* of ions and in-between (Fig. 3.9b) tend to *reduce the attractive electrostatic forces* between cations and anions because water has a relatively high *permittivity*; compare the related discussion on *electric stray fields* from Kaniusas (2012, Footnote 13). Because of weakened electrostatic forces, *thermal motion* leads to even stronger *smearing of the near-order* (favoured by pure electrostatic forces).

from Fig. 2.16b. Consequently, an associated large ε results within the suspension, i.e., accumulation of large particles surrounded by small counterions. Obviously, the *diffusion* counteracts the influence of $\vec{E}_{\text{ext}}$ on directed movements of counterions along the surface of large particles.

The induction of electric dipoles—i.e., the asymmetric cloud of charges—occurs for relatively long half-periods $1/(2 \cdot f)$ of the alternating $\vec{E}_{\text{ext}}$ below the size of τ or, in analogy, for relatively *low frequencies* $f < f_{\text{r}}$ (or for $\omega \cdot \tau \ll 1$); see the middle subfigure of Fig. 2.19a. As soon as the inert cloud can not follow the relatively fast oscillatory changes of $\vec{E}_{\text{ext}}$ with the relative *high frequency* $f > f_{\text{r}}$ ($\omega \cdot \tau \gg 1$), i.e., the relative cloud displacement with respect to the central charged particle is too inert, the *induction of electric dipoles ceases*; see the right subfigure of Fig. 2.19a. In other words, ions are impelled backwards and forwards so rapidly that the build-up of the asymmetric ionic atmosphere cannot be formed fast enough, the relaxation disappears. The associated ε decreases and denotes the occurrence of α-dispersion.

Likewise, after the external field $\vec{E}_{\text{ext}}$ is *switched off*, the original counterion atmosphere is re-established by *restoring electrostatic forces* (attractive forces) between counterions and the central charged particle with the same *relaxation time constant* τ (2.73). In particular, the *asymmetric* ionic atmosphere relaxes back to the *symmetric* distribution while counterions migrate across the ionic atmosphere of the central particle. For instance, the size of τ can be estimated from the time a counterion takes to move across the *diameter of the ionic atmosphere* from behind the central ion to in front of the central ion (Wright 2007); compare Fig. 2.19a and see below. Please note that these *restoring forces* increase with decreasing average distance in-between counterions and the central charged ion so that these forces increase with increasing *concentration of ions* in the solution (Hamann 1998).

Please note that for a given constant value of $\vec{E}_{\text{ext}}$, *ions tend to leave their respective clouds of counterions*—since cations and anions move in opposite directions—and tend to establish new clouds of counterions. At the stage of movement, this rebuild of clouds around the central charged particle—i.e., around the particle which is subjected to *spatial migration* in the solution—takes some time, again, the *relaxation time* τ (2.73). The ionic atmosphere has to build-up in front of the moving ion and to decay behind the ion, both processes occurring continuously. In general, any translational motion of an ion requires neighbouring ions to adjust their relative positions, with the change of the shape of the ionic atmosphere around the ion/particle under migration; known as *Debye-Falkenhagen effect*.

Because of the finite values of τ—i.e., the process of the rebuild can not occur instantaneously—the central charged particle hurries always a little bit ahead of the charge *center of gravity of counterions* cloud in the solution for a momentary constant $\vec{E}_{\text{ext}}$ (Fig. 2.19a). Therefore, there is more of the ionic atmosphere behind the central ion than in front of it, i.e., an *asymmetric counterion distribution* results,

in clear contrast to the symmetry of the distribution obtained for zero $\vec{E}_{ext}$, as can be observed in Fig. 2.19a. Here the aforementioned *restoring electrostatic forces* between the mutually displaced central particle and the oppositely charged counterions act as *braking forces* for migration of particles and ions. The restoring force hinders an independent migration of cations towards cathode and anions towards anode, i.e., limits the resulting conductivity, as described in Footnote 28. In other words, the *asymmetric atmosphere* around a drifting anion "pulls the anion back" and the velocity of the anion results to be less than it would be for the *symmetric atmosphere* for $f < f_r$ (Fig. 2.19a).

Since the ionic atmosphere is composed not only of counterions (Fig. 3.9b), the ionic drift of inversely charged ions in opposite directions within the cloud around the central ion contributes to the *asymmetric charge distribution* (Wright 2007). For instance, if the central ion is an anion, this anion and other anions within the ionic atmosphere will move towards the positive pole, whereas cations (true counterions) within the ionic atmosphere will move in the opposite direction towards the negative pole. Therefore, in front of the moving central anion, there will be a deficit of positive charge and an excess of positive charge behind the central anion, which forms the asymmetric charge distribution.

Interestingly, it should be amended that the *relaxation of the ionic cloud* around the central particle or central ion—in line with Fig. 2.19a—is a function of the ionic concentration and can also arise at much higher field frequencies (>10 kHz) than the discussed α-dispersion. From a biophysical point of view, *low ionic concentrations* tend to yield relatively large clouds of counterions because spacious clouds do not hinder each other in the diluted solution. Correspondingly, *large clouds* stand for their large mechanical *inertness*, especially when counterions in these clouds are periodically dislocated with respect to the central ion in response to the applied alternating $\vec{E}_{ext}$. This great inertness also stands for the associated large τ and thus for low f_r. Therefore, *increasing ionic concentration* shifts the dispersion towards higher frequencies, i.e., the value of f_r increases and that of τ decreases with concentration. For instance, a relatively low f_r of about 300 kHz results for KCl solution in water with the low ionic concentration of 10^{-4} mol/l, whereas an increased concentration up to 10^{-2} mol/l raise f_r into MHz range to about 30 MHz (Anderson 1994). Authors in Hamann (1998), Wright (2007) cite short τ of ions in the range of only 10^{-7} to 10^{-9} s that yields a relatively high f_r ($=1/(2 \cdot \tau)$) in the range of 5–500 MHz ($\gg$10 kHz).

Finally, it should be mentioned that the size of the driving *electric field* $\vec{E}$ in electrolyte (Fig. 2.16a) also influences the *asymmetry of the ionic cloud*. For relatively small $\vec{E}$ (e.g., 10 V/cm), the resulting drifting velocities $\vec{v}$ are also relatively low (e.g., $5 \cdot 10^{-5}$ m/s, with the assumed typical ionic mobility m of $5 \cdot 10^{-8}$ m^2/(V s), see (2.53) and Footnote 27) so that the time taken by an ion to move a distance in the order of the *diameter of the ionic cloud or atmosphere* (e.g., 3 nm) is much larger than τ (i.e., 3 nm / $5 \cdot 10^{-5}$ m/s = $6 \cdot 10^{-5}$ s $\gg 10^{-7}$ s). Therefore, for low $\vec{E}$, there is ample time for the asymmetry to reach its state. As $\vec{E}$ gets stronger, the drifting $\vec{v}$ increase and there is progressively less time for

the build-up of the asymmetric ionic atmosphere because ions simply "run away"; the relaxation effect disappears. Consequently, the *asymmetric atmosphere* at *low strengths* of $\vec{E}$ reduces $\vec{v}$ of drifting ions and reduces the net conductivity. This *asymmetry* of ionic charges disappears at *high field strengths* while symmetric distributions remain with the associated increased $\vec{v}$ and conductivity.

Conductance

When free *unbound charges* in tissue such as *ions* are set in *motion* in response to the ambient electric field $\vec{E}_{\text{ext}}$ with its *f*—as illustrated in Fig. 2.16a and (2.53)—ions *collide* with immobile or less mobile structures within tissue as well as are subjected to *mutual friction*. During collisions and frictional interactions with other atoms and molecules, migrating ions lose their energy and thus generate *heat* in tissue.

- At relatively *low f*, unbound charge carriers travel during each half-cycle of $\vec{E}_{\text{ext}}$ relatively *large distances in tissue* over which a greater chance exists for *collision* with or trapping at immobile particles or interfaces in tissue. *Collisions decelerate* migrating ions and so the corresponding *conductivity* γ_{eff} *is relatively small*, as can be easily observed from (2.55). In fact, moving ions oscillate around their resting positions during each half-cycle of $\vec{E}_{\text{ext}}$ (Footnote 25). In contrast to low *f*,
- at *high f* unbound charge carriers cover relatively *short distances in tissue* and thus are less likely to collide or be trapped. The reduced deflection amplitude of ions exposed to the alternating $\vec{E}_{\text{ext}}$ and thus the reduced collision rate render the corresponding γ_{eff} *to be relatively high*.

Therefore, the *size of* γ_{eff} tends to increase with *f* of the field in qualitative terms, especially in a step-wise manner within the frequency range of α-dispersion, as illustrated in Fig. 2.21. The inequality $\gamma_{\text{eff}} > \gamma$ (2.82) dominates with increasing *f*, with γ as the only ionic conductivity at 0 Hz. In addition, we can conclude that *large-scale structures* in tissue become less important at high *f* where ionic charges travel only short distances in response to $\vec{E}_{\text{ext}}$ so that large-scale structures do not hinder movements of ionic charges anymore.

A finite value of γ_{eff} denotes *lossy interactions* between migrating ions and the microscopic tissues structure, whereas this interaction withdraws energy from the applied $\vec{E}_{\text{ext}}$ within tissue. The *absorbed power* increases with increasing *f*—in close analogy with the aforementioned increase in γ_{eff} with *f*—in the course of a particular dispersion mechanism. Please recall the direct proportionality of the specific absorption rate to γ_{eff}, given a certain value of $\vec{E}_{\text{ext}}$ (2.58).

The behaviour of γ_{eff} in biological tissue can also be discussed based on electrostatic forces which keep a *cloud of counterions* around a *central charged particle or ion*, as introduced in Fig. 2.19a. When the central ion is relaxed, this ion, on time-average, occupies its *equilibrium position* in the centre of the spherical cloud of counterions. Under the influence of the local $\vec{E}_{\text{ext}}$, or the resulting electrostatic dragging force, the central ion moves to an off-center position and experiences an electrostatic *restoring force* due to the present and inversely charged counterions

(Bisquert 2005). In addition, counterions are dragged by $\vec{E}_{ext}$ in the opposite direction to the direction of the central ion so that the latter restoring force even increases. Therefore, the central ion is *electrostatically bound* to its counterions as well as counterions to the central ion. Since the central ion and counterions are supposed to move in opposite directions while carrying charges (of an electric current, see Fig. 2.16a), the restoring force in-between tends to reduce the respective contributions of the central ion and counterions to the total γ_{eff} (2.55), i.e., the restoring force reduces drifting velocities of cations and anions. Please recall that all mobile ions can be considered as charge carriers contributing to γ_{eff}. In fact,

- the *restoring force* slows down the *long range displacements* of the central ion accompanied by the confinement cloud for the *direct* $\vec{E}_{ext}$ or the relatively *low* f [$<f_r$, see (2.73)] of the alternating $\vec{E}_{ext}$, which then implies a *relatively low* γ_{eff}.
- At the relatively *high* f ($>f_r$), the effect of the elastic restoring force can be neglected because the central ion is subjected to *short range displacements* only (see above). The central ion behaves as if it were freely moving around only under the limiting influence of the viscous force (*microscopic friction*). This behaviour implies an increased γ_{eff} as compared to low f.

In other words, periodic formations of the *asymmetric cloud* of counterions in synchrony with the alternating $\vec{E}_{ext}$ at $f < f_r$ denotes a reduced γ_{eff}, as illustrated in the central subfigure of Fig. 2.19a. The retarding effect of the asymmetry on the ions movement in response to $\vec{E}_{ext}$ ceases at $f > f_r$ and the *symmetric cloud* denotes an increased γ_{eff}, see the right subfigure in Fig. 2.19a; which is in line with *Debye-Falkenhagen effect*.

When the central ion is displaced from its equilibrium position within its ionic cloud, then either this ion follows the opposite restoring force and returns back to its equilibrium position (as discussed above), or the *cloud of counterions becomes rearranged*[41] towards the new position of the central ion. In the latter case, the motion of the central ion is accompanied by the *creation and destruction of its ionic cloud* along the trajectory of this central ion. The *relaxation of the ionic atmosphere*

[41]If a *small ion* becomes accelerated by the ambient *direct electric field* to a relatively high velocity —in line with (2.53)—so that the ion transverses the *effective diameter of its ionic cloud* (of the approximate size of 10 nm or 10^{-8} m (Hamann 1998)) in less time than the *cloud needs to be physically established* (in the range of 10^{-8} s (Hamann 1998))—i.e., faster than the *relaxation time constant* τ in (2.73)—then the ionic cloud can not be built at all and stays out. The *missing ionic cloud* means also an *increased effective conductivity* γ_{eff} at such a high velocity v of ionic migration (of about 10^{-8} m / 10^{-8} s = 1 m/s) or at the relatively *strong electric field* leading to such a high v in the electrolyte. Please recall that the strength of the electric field can be estimated from (2.53) for a given ionic m and v. In analogy, it should be stressed that

- *increasing ionic concentration* as well as
- *increasing valence of ions* in the electrolyte

also lead to a *reduced size of the ionic cloud* and thus lead to an *increased* γ_{eff} of the solution.

—i.e., its creation and destruction around the central ion—is relatively long and is determined by τ. Therefore, this relaxation slows down the migration of the central ion and thus reduces γ_{eff}, especially for the direct $\vec{E}_{\text{ext}}$ or the relatively low f. Please recall that the displacement of the central ion as the charge carrier contributes to the electric current and thus co-determines γ_{eff} (2.55). It follows from the above discussion that (Bisquert 2005)

- for the *direct* $\vec{E}_{\text{ext}}$ and at *low* f ($<f_{\text{r}}$), the central ion migrates downwards along the direction of the dragging force while its associated *cloud of counterions* is alternatingly *created and destructed* in synchrony with the alternating $\vec{E}_{\text{ext}}$. The resulting γ_{eff} is relatively low and constant over f; compare $\Delta\gamma = 0$ at low $f < f_{\text{r}}$ in Fig. 2.24.
- At *medium* f ($\approx f_{\text{r}}$), the central ion *relaxes partly back* to its *cloud of counterions*. The size of γ_{eff} increases nearly quadratically with increasing f; see $\Delta\gamma \propto f^2$ (2.83) in the region close to f_{r} in Fig. 2.24. Finally,
- at *high* f ($>f_{\text{r}}$), the central ion is subjected to *microscopic friction* only, whereas the restoring force can be neglected. The associated γ_{eff} is relatively high and constant over f, see $\Delta\gamma = 0$ at high $f > f_{\text{r}}$ in Fig. 2.24.

In short, the *effective conductivity* γ_{eff} of the electrolyte at *low frequencies*—below α-dispersion—can be seen as a slow motion of the bound central ion coupled electrostatically to its surrounding counterions relaxation. In contrast, γ_{eff} at *high frequencies*—above α-dispersion—can be understood as a much faster motion of the central ion, limited by the microscopic friction only.

It is interesting to observe that small positive counterions in the cloud—as illustrated in Fig. 2.19a—can freely exchange with ions of the same sign in the bulk electrolyte, i.e., *small positive ions* in the bulk act here as *good conductors*. That is, ions of the same sign can enter the counterion layer and their charge is then quickly conducted to the opposite side of the central large particle; in analogy with fast *tunnelling processes* (Footnote 24). However, *small negative ions* in the bulk would have to travel—i.e., migrate in response to $\vec{E}_{\text{ext}}$—around this *large particle*. The effective migration pathway elongates while circumventing this particle so that small negative ions can only act as *less good conductors* (Foster 1996). This is in clear contrast to small positive ions and their good conductivity in the bulk. Please recall (2.55) considering contributions of both positive and negative ions to the total conductivity of the bulk. In other words, the effective contribution of an ion to the conductivity of the solution depends on whether its charge has the same or opposite polarity than that of prevailing counterions within ionic clouds.

Beta Dispersion

The so-called *beta dispersion* (β-dispersion) is based upon heterogeneous tissue structure, e.g., interfacial *cell membranes* within biological tissue, and the resulting boundary phenomena, which have major impact on both polarization and conductance of tissue.

Polarization mechanism of β-dispersion is based on *charging of interfaces* in between different tissue regions. Charging occurs when *unbound charges* on at least

one side of the interface are *set in motion* in response to the outer stimulus, the ambient electric field $\vec{E}_{\text{ext}}$ with the field frequency f, and accumulate a *non-zero surface charge* on the interface, as illustrated in Fig. 2.19b. Thus, a *conductive medium* is required on at least one side of the interface for its recharging (Footnote 78). When opposite surface charges are accumulated on joint/coherent interfaces, e.g., on inner surfaces of the cell membrane facing each other (Fig. 2.19b), an *asymmetric charge distribution* is attained, which forms *interfacial polarization*.

Based on the aforementioned *polarization mechanism*, with each half-cycle of the time-varying $\vec{E}_{\text{ext}}$, the interface is discharged and then charged again with the surface charge of another polarity, forming *relaxation mechanism*. Obviously, local *conductive currents* transfer this surface charge from/to the interface; compare with the associated recharging currents from Fig. 2.29c. This build-up and *redistribution of the surface charge* is an inert mechanism (Footnotes 55 and 78)—with the *relaxation time constant* τ (2.74)—that ceases with decreasing duration of the half-cycle of $\vec{E}_{\text{ext}}$ below τ and thus with increasing f of $\vec{E}_{\text{ext}}$ above the *relaxation frequency* f_{r} (=1/(2π · τ)). In fact, the midpoint of this transition (halfway) between present and absent polarization at low and high f, respectively, corresponds to f_{r}. This is then known as *β-dispersion mechanism*. In other words, the formed *electronic bilayers* yield dominant dispersions to various degrees in the bulk properties of the heterogeneous tissue.

The applicable τ for *interfacial polarization* of β-dispersion has the characteristic form—in analogy with (2.49)—

$$\tau = \frac{\varepsilon}{\gamma_{\text{eff}}}. \tag{2.74}$$

It is instructive to observe that with increasing ε the polarization process progressively requires more time so that the associated τ increases. In contrast, increasing γ_{eff} strengthens conductive currents, accelerating recharging and surface charge redistribution processes so that τ decreases.

Isolating Boundaries—Polarization

Recharging of cell membranes is a prominent mechanism of interfacial polarization in tissue. Membranes separate intracellular and extracellular regions with intrinsic conductive properties. Thus conductive currents through these regions allow accumulation of surface charges and recharging of membranes in response to $\vec{E}_{\text{ext}}$. The polarization and relaxation arise in the *medium frequency range* up to hundreds of kHz, typically in the range of about 20 kHz–100 MHz, i.e., the relevant f_{r} resides in the latter range.

Figure 2.19b demonstrates how charges arrested within the cell move and become dislocated in response to the electrostatic force governed by $\vec{E}_{\text{ext}}$; in analogy with Fig. 2.25. Positive ions move along the direction of $\vec{E}_{\text{ext}}$ while negative ions move against. An *asymmetric charge distribution* results for low $f < f_{\text{r}}$ (or for $\omega \cdot \tau \ll 1$) leading to polarization of the cell (see the left subfigure of

Fig. 2.19b). However, charge separation ceases for high $f > f_r$ ($\omega \cdot \tau \gg 1$) due to finite charge mobility (right subfigure of Fig. 2.19b). Figure 2.64 confirms charge accumulation on both sides of the cell and its polarization, whereas the accumulated charge inside of the cell attracts the opposite charge from extracellular space.

In fact, the *constant* τ is the time constant for *charging of the cell membrane capacitance* through currents between extracellular and intracellular spaces (compare with the membrane time constant as the *quotient of the capacitance and electrical conductance* of the membrane from Kaniusas (2012, Eq. 2.3) and Kaniusas (2012, Fig. 2.9). For instance, authors in Sanchez (2016) demonstrate that f_r of the *muscle* (around 30 kHz) decreases (by about 25%) with the *muscular contraction*. It is consistent with the concept that the diameter size of the muscle fiber increases slightly with the contraction so that the *capacitance of the muscle cell membrane* increases with the contraction (Kaniusas 2012, Footnote 32), which leads to the increased τ of the membrane (Kaniusas 2012, Eq. 2.3).

Recharging of membranes below f_r—or *below β-dispersion*—yields accumulation of polarization charges and thus a relatively high ε of tissue. The size of ε increases in proportion to the cell size and membrane capacitance. For f above f_r—or *above β-dispersion*—the interfacial polarization diminishes due to finite mechanical inertness of ion movements polarizing the cell membrane. Correspondingly, the associated effective value of ε decreases that gives rise to *β-dispersion*.

Isolating Boundaries—Conduction

The current flow at f below f_r (>f)—or *below β-dispersion*—covers only *extracellular space* in-between cells, which yields a relatively low γ_{eff} of biological tissue. In particular, predominantly conductive currents within tissue at this *low* f can not pass through isolating cell membranes with its high leakage resistance (Fig. 2.64) which acts as a barrier for continuous (passive) ion transport from/to extracellular and intracellular spaces (Kaniusas 2012, Fig. 2.3). Therefore, the effective *cross-section area*—permeated by the current line around the cell, as illustrated by the current i_1 and its area A_1 in Fig. 2.22a—is relatively small so that the associated resistance along this current line is relatively large (2.36). From a macroscopic point of view—and γ_{eff} is a *macroscopic tissue property*—the small area for the current flow through extracellular space implies a small γ_{eff} of tissue. In other words, the size of the bulk conductivity γ_{eff} below f_r reflects the *volume fraction of extracellular space* and thus the conduction of this extracellular space (Footnote 19). Cells in tissue can be regarded as *insulating inclusions* in a conducting fluid (Fig. 2.22a). For instance, early researchers in the 19th century already recognised that *erythrocytes* appear at low frequencies as *non-conducting particles* in a conductive medium (Foster 1996).

The isolating *membrane shields* the interior of the cell from ambient fields with their f below f_r while the ambient conductive current through tissue can only flow around the cells (Fig. 2.64). In fact, the *induced voltage drop* across the membrane

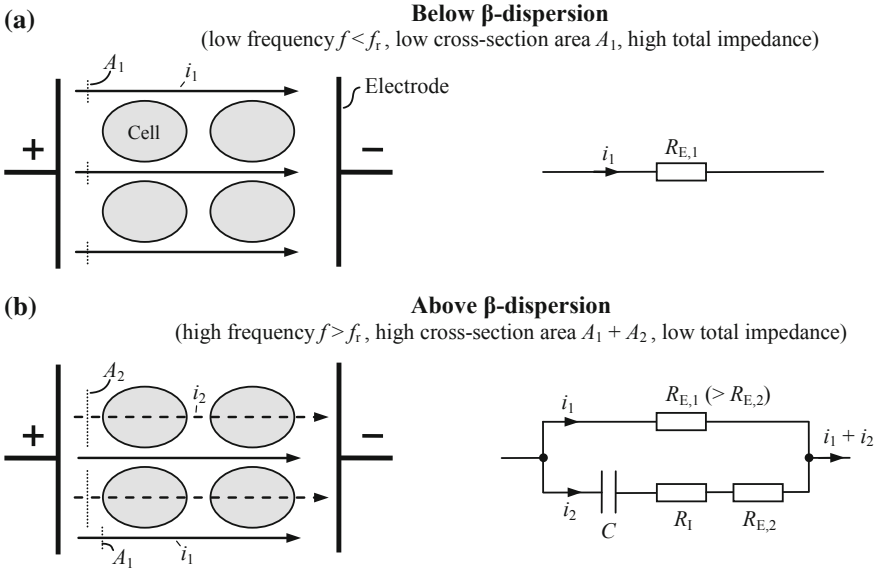

Fig. 2.22 Biological tissue with tightly packed cells and its principal behavior in the course of β-dispersion. **a** Below β-dispersion, there is a strong polarization of cells while the effective electrical conductivity γ_{eff} of tissue is relatively low due to extracellular currents only (Fig. 2.64). **b** Above β-dispersion, the polarization of cells vanishes (Fig. 2.20) while γ_{eff} increases (Fig. 2.21). The respective electrical equivalent circuit models depict the extracellular current i_1 through the relatively small cross-section area A_1 along the associated extracellular resistance $R_{E,1}$ (Kaniusas 2012, Fig. 2.9). For the case (**b**), the current i_2 passes the relatively large cross-section area A_2 ($>A_1$) through the cell membranes with the capacitance C, the associated intracellular resistance R_I, and along $R_{E,2}$ [$<R_{E,1}$ due to shorter current pathways in-between than around the cells, see (2.36)]

on both opposite sides of the cell (2.140) takes over the whole voltage drop across the cell so that the residual voltage drop inside the cell vanishes. The strength of the induced electric field and current density within the cell is still zero (Fig. 2.25a). In short, the induced voltage across the membrane shields the interior of the cell.

In contrast to the current flow below f_r, the current flow at f above f_r ($<f$)—or *above β-dispersion*—permeats both *extracellular and intracellular spaces*, which yields a relatively large γ_{eff} of tissue (Footnote 30). At this *high f* the capacitive impedance (2.42) of the cell membrane is significantly reduced and short-circuits the relatively high leakage resistance of the membrane, which resides in parallel to the capacitive impedance (Kaniusas 2012, Fig. 2.9). Therefore, we end up with a *displacement current* coupled through the capacitor of the cell membrane, flowing into the cell, passing the cell as a *conductive current* and then leaving the cell again through the membrane (see i_2 with its A_2 in Fig. 2.22b). Of course, this current flow

is in addition to the simultaneous *conductive current* around the cell (see i_1 with its A_1 in Fig. 2.22b). Please note that $|i_1 + i_2| > |i_1|$ applies, provided an identical voltage across the electrodes in Fig. 2.22a, b. Please compare similar discussions on Fig. 2.14 for the different f above and below f_r.

That is, within the *intracellular space*, this displacement current is carried by a conductive current. Ambient extracellular currents enter the intracellular space without restriction at high f (Fig. 2.22b). Therefore, the effective *cross-section area* $A_1 + A_2$ (Fig. 2.22b) is now available for the current flow in-between and through the cells, which is larger than only A_1 relevant for the current flow below f_r (Fig. 2.22a). From a macroscopic point of view, an increased area for the current flow through extracellular and intracellular spaces implies an increased γ_{eff} of the bulk above f_r as related to γ_{eff} below f_r. In other words, the size of the bulk conductivity γ_{eff} above f_r reflects the *volume fractions of both extracellular and intracellular spaces*, and thus reflects the sum of their respective conductivities. In particular, the size of γ_{eff} increases from the *extracellular conductivity* (valid for $f < f_r$) up to the sum of extracellular and intracellular conductivities (valid for $f > f_r$) in a *step-wise manner* within the scope of the single β-dispersion mechanism (Fig. 2.21). Likewise, the increase $\Delta\gamma$ in the conductivity γ_{eff} (2.82) with increasing f reflects the size of the *intracellular conductivity*.

Figure 2.22 demonstrates *electrical equivalent circuit models* for both discussed cases $f < f_r$ and $f > f_r$. The *total impedance* of a considered *cellular tissue* section between electrodes clearly decreases from the extracellular resistance R_E (at low $f < f_r$ below β-dispersion, see Fig. 2.22a) to R_E short-circuited by another complex impedance (at $f > f_r$ above β-dispersion, see Fig. 2.22b). The latter complex impedance is given by the capacitive impedance $1/(\omega C)$ of the membrane in series with intracellular and extracellular components along the current flow. Likewise, the bulk conductivity γ_{eff} of the cellular tissue at $f < f_r$ is lower than γ_{eff} at $f > f_r$ because R_E is larger than the short-circuited R_E, given fixed geometrical dimensions of the tissue section between electrodes (2.36) for $f < f_r$ and $f > f_r$.

The *shielding effect of the membrane* is lost above f_r. In particular, the *induced voltage drop* across the membrane—proportional to the *cell radius* or to the cell size below f_r (2.140) and effectively shielding the cell—falls off as the *inverse of* f [(2.42) and (2.140)]. The cell's interior becomes exposed to ambient fields for $f > f_r$. In the limit of high frequencies, the induced voltage across the membrane converges towards a finite but rather small value which is proportional to the *membrane thickness* only (2.142) (much smaller than the *cell radius*). In other words, the shielding efficiency has decreased with increasing f by the ratio the cell radius to the membrane thickness.

In summary, the *major β-dispersion* of the cell membrane is noticeable in both the decrease of ε and the corresponding increase in γ_{eff}. However, there are also other *minor dispersions* due to *membrane-bound structures* which overlap in frequency with β-dispersion:

- charging of the *nuclear membrane* and other *membranes of intracellular organelles*[42] and
- polarization and relaxation of proteins and other organic macromolecules.

These additional dispersions are typically weaker and lead to a rather *broad, smeared, and smooth course* of ε and γ_{eff} over f, as can be observed in Figs. 2.20 and 2.21, respectively. This is in clear contrast to a step-wise behaviour, as being applicable for a *single dispersion mechanism* (Fig. 2.24). In particular, the large range of spatial dimensions of membrane-bound structures within tissue—from the cell, to nucleus, to organelles (Kaniusas 2012, Fig. 2.2)—contributes to a relatively broad distribution of the associated values of relaxation frequencies. It is not surprising therefore that experimental homogenization of tissue eliminates most of β-dispersion by disruption of cell membranes (Foster 1996); compare Footnote 19.

Conducting Boundaries

Interfaces between different tissues can be not only isolating—as in the case of the isolating cell membranes—but simply represent *physical boundaries* between two tissue regions (or phases) with *different electrical properties*, i.e., different γ_{eff} and/or ε. Figure 2.37 illustrates the muscle/fat boundary with incident fields within muscle and refracted fields within fat. In other words, *heterogeneous tissue*—when subjected to the external $\vec{E}_{\text{ext}}$—can be *charged at its inner boundaries* between *homogeneous regions* of the tissue; see the boundary from Fig. 2.56a.

[42]In fact, at relatively *low frequencies* of the incident field—below the relaxation frequency of *β-dispersion of the outer cell membrane*—this cell membrane *shields the interior of the cell* (subcellular components) from the external electric field and thus prevents the *nuclear membrane* and membranes of *intracellular organelles* from being polarized (Foster 1996); compare Kaniusas (2012, Fig. 2.2). The interiors of the cell are increasingly exposed with rising field frequency, i.e., the voltage drop induced across the nuclear membrane is largest at frequencies between the *β-relaxation frequency of the outer cell membrane* and the *β-relaxation frequency of the nucleus membrane*. In particular, the β-relaxation frequency of the nucleus membrane is usually much higher than that of the outer cell membrane; e.g., 1.6 MHz versus 0.7 MHz in liver (Foster 1996). The *voltage drop* across the nucleus membrane above its β-relaxation frequency *falls off as the inverse of frequency* [in qualitative analogy with (2.141)] and then converges towards the *product of the inner electric field and the nuclear radius* [in analogy with (2.142)].

In analogy, it can be expected that

- the maximum voltage drop *across the organelle* (not connected with the outer cell membrane or with the extracellular medium) and
- the maximum voltage drop across *internal membranes* within the cell

are larger for the *low frequency process* than for the *high frequency*. Namely, this *maximum voltage drop* is larger for field frequencies below the *β-relaxation frequency of the organelle* (i.e., the organelle should still comprise a barrier for inner currents within the cell) but above the *β-relaxation frequency of the outer cell membrane* (i.e., the interiors of the cell should be already exposed). In particular, the β-relaxation frequency of the organelle is usually much higher than that of the outer cell membrane; e.g., 13 MHz for mitochondria versus 0.7 MHz in liver (Foster 1996).

Interestingly, above the β-relaxation frequency of the organelle, the maximum voltage drop *across the organelle* is roughly and simply equal to the product of the *inner electric field* strength and the *mean dimension* of the organelle; in close analogy with (2.142).

Neighbouring boundaries carrying opposite surface charges—e.g., opposite boundaries of a well-conducting inset embedded within less-conducting tissue exposed to $\vec{E}_{\text{ext}}$ (Fig. 2.59)—comprise another *polarization mechanism*.

The accumulated surface charge at boundaries is then quantitatively given by *boundary conditions* of the induced normal fields on both sides of the boundary; see (2.117) for the rather general case considering conducting and displacement currents across the boundary. For conditions of the *non-zero surface charge*, see discussion on (2.107). Obviously, the physical boundary as well as the surface charge disappear between two identical tissue regions. As in the case of isolating interfaces, the time-varying $\vec{E}_{\text{ext}}$ periodically changes the size and thus the polarity of the surface charge in terms of *relaxation mechanism*. The repolarization ceases with increasing f due to inert buildup of the surface charge (Footnote 78), forming *dispersion mechanism*.

Gamma Dispersion

The so-called *gamma dispersion* (γ-dispersion) is based upon polar structure of *water molecules* and their reorientation in tissue, which have major impact on both polarization and conductance of tissue.

Polarization

Polarization mechanism of γ-dispersion is based on the partial *orientation polarization* and relaxation of water molecules in biological tissues with a high water content. The *polar water molecule* is composed out of two opposite charges bound to each other with their non-overlapping balance points, acting as a permanent *molecular dipole* (Kaniusas 2012, Footnote 12). The water dipoles are subjected to their *rotational reorientation* in response to the outer stimulus, the ambient electric field $\vec{E}_{\text{ext}}$ with the field frequency f, as illustrated in Fig. 2.19c. Polar structures become slightly aligned to each other so that *polarization charges* are induced at the *boundaries* of the considered tissue section, as already described in Figs. 2.17 and 2.16c.

With the alternating direction of $\vec{E}_{\text{ext}}$, polar water molecules become reoriented in synchrony with the applied $\vec{E}_{\text{ext}}$ in terms of *dipolar relaxation*, the local polarization charges alternate in their sign. This reorientation of molecular dipoles is an inert mechanism—with the *relaxation time constant* τ (2.75)—that ceases with decreasing duration of the half-cycle of $\vec{E}_{\text{ext}}$ below τ and thus with increasing f of $\vec{E}_{\text{ext}}$ above the *relaxation frequency* f_{r} ($=1/(2\pi \cdot \tau)$) in GHz region. The disappearance of rotational reorientation forms *γ-dispersion mechanism*.

At relatively *low* $f < f_{\text{r}}$ (or $\omega \cdot \tau \ll 1$), the water dipoles orient in response to the change in $\vec{E}_{\text{ext}}$ and *polarization charges* become accumulated. According to (2.63), the associated ε is relatively high (and at maximum for fields close to 0 Hz). However, for relatively *high* $f > f_{\text{r}}$ (or $\omega \cdot \tau \gg 1$), the mechanical inertness of dipoles dominates as well as microscopic molecular forces hindering the dipole reorientation. The dipoles become progressively unable to follow the change in $\vec{E}_{\text{ext}}$ since temporal changes of $\vec{E}_{\text{ext}}$ are too rapid. Reduced or missing reorientation of dipoles at this high f no longer contributes to the accumulation of polarization

charges while dipoles in tissue retain their random orientations. The associated polarization disappears, forcing ε to diminish for $f > f_r$.

Figure 2.19c depicts a random orientation of water dipoles at zero $\vec{E}_{ext} = \vec{0}$ (left subfigure). Dipoles align collectively for and in synchrony with the non-zero $\vec{E}_{ext}$ at the relatively low $f < f_r$, whereas polarization charges become accumulated on both boundaries facing incident and outbound $\vec{E}_{ext}$ (central subfigure). For high $f > f_r$, dipoles are unable to follow directional changes of $\vec{E}_{ext}$ and, again, a random orientation of dipoles results (right subfigure).

While the *dominant effect* of γ-dispersion is the dipolar reorientation of free *unrestricted water molecules* in tissue with their dispersion centered at f_r of about 20 GHz,[43] other *less dominant contributions* to γ-dispersion are due to rotational dipolar relaxation of

- *bound water molecules*[44] in tissue and
- *polar proteins* in tissue.

All dispersive effects broaden and smear the whole dispersion in tissue.

In particular, *bound water molecules* (associated with protein surfaces) tend to have lower f_r than *unrestricted water molecules* in the bulk water because bound molecules are hindered in their reorientation. Equation (2.75) supports qualitatively this observation since an increasing viscosity increases τ required for reorientation and thus decreases f_r. In particular, the fraction of bound water contributes significantly to γ-dispersion at f near 1 GHz ($\ll$20 GHz, see Footnotes 43 and 44) (Foster 1996). The amount of motionally-restricted water molecules corresponds roughly to a single layer of water molecules surrounding protein surfaces and forming their *hydration shells* (Fig. 3.6a and Kaniusas (2012, Footnote 21)). Obviously, the amount of unrestricted water molecules in the bulk-like water equals the difference between the total water content and that being motionally restricted.

While the size of τ for *small water molecules* is in the range of *picoseconds* (Footnote 43), *large polar proteins* and their relaxation can have values of τ as

[43]The particular value of f_r of unrestricted *water* in terms of *γ-dispersion* depends strongly on its *temperature*. Namely, the size of τ (=$1/(2\pi \cdot f_r)$) decreases with increasing temperature while f_r concurrently increases by about +2% / °C, as illustrated in (2.75). For instance, $\tau \approx 9$ ps and $f_r \approx 18$ GHz apply at room temperature of 20 °C, whereas $\tau \approx 6$ ps, $f_r \approx 26$ GHz apply at body temperature of 37 °C.

[44]Dipolar relaxation of *bound water molecules*—including water associated with tissue surfaces—is usually referred to as *delta dispersion* (δ-dispersion). In contrast, γ-dispersion mainly refers to relaxation of *unrestricted water molecules*. In addition, the *rotational relaxation* of polar side groups of proteins is suggested to contribute to δ-dispersion, as well as *interfacial polarization* and *counterion diffusion* along small regions of charged surfaces (Foster 1996). However, the interpretation of δ-dispersion is still under debate since a single dominant dispersion mechanism lacks here.

Changes of electrical properties of tissue during δ-dispersion are relatively weak. The associated decrease $\Delta\varepsilon/\varepsilon_0$ is in the range of 10–20 while the simultaneous increase $\Delta\gamma$ is about 0.4–0.5 S/m when f of the applied field passes the *relaxation frequency* f_r of δ-dispersion; compare Fig. 2.24. This relaxation f_r of δ-dispersion resides in the range of 0.1–3 GHz.

large as *microseconds*. *Small polar proteins* show τ values in the range of *nanoseconds* [e.g., hemoglobin shows f_r of about 300 MHz (Pfützner 2003)]. Equation (2.75) quantifies the direct dependency between the dipole size and τ. The associated f_r of large polar proteins extends down to MHz range (i.e., into the frequency range of β-dispersion). In addition, *polar side-chains on protein molecules*—which are smaller than polar proteins themselves—can also relax but at much higher f_r of about 100–1000 MHz (Foster 1996). These side-chains have been suggested as contributing to small dispersions in the latter range of f_r.

Following the difference between motionally-unrestricted and motionally-restricted water molecules, it can be recognised that τ is generally longer for *tissue water* (i.e., restricted water in biological material) than for *pure water*. For instance, water in bone yields $\tau \approx 13$ ps, water in fat $\tau \approx 8$ ps, and water in muscle $\tau \approx 7$ ps, whereas the smallest $\tau \approx 6$ ps applies for pure water (Footnote 43); all τ values are given at 37 °C (Gabriel 1996c). The rotational ability of some water molecules within tissues is mechanically restricted due to organic environment that interacts electrostatically with polar water molecules. The mechanical restriction is less dominant in body fluids due to their low organic content, i.e., their low solute concentration.

The higher is the *content of tissue water*, the higher is ε at $f < f_r$ below the relaxation region as compared with ε at $f > f_r$ above the relaxation region. A high water content contributes to an increased change $\Delta\varepsilon$ (2.79) in the course of γ-dispersion. For low $f < f_r$ just below γ-dispersion—as partly illustrated in Fig. 2.20—the size of $\varepsilon/\varepsilon_0$ ($=\varepsilon_r$) in pure *water* amounts to about 74, in *muscle* with a still relatively high water content to about 50, and in *bone* with a relatively low water content amounts to only about 20 (Gabriel 1996c).

The applicable τ for *dipolar relaxation* of γ-dispersion has the characteristic form of the Debye type (2.78)

$$\tau = \frac{4\pi \cdot \mu \cdot r^3}{k \cdot T}. \tag{2.75}$$

Here μ denotes the dynamic viscosity of the medium, T the absolute temperature, k the Bolzmann constant ($k = 1.38 \cdot 10^{-23}$ J/K), and r the *effective radius* of the relaxing dipole (Footnote 22) such as water molecule or polar protein. Equation (2.75) applies for all kinds of dipolar relaxation within the scope of γ-dispersion, from dipolar relaxation of water molecules, to dipolar relaxation of polar proteins, and to that of polar side-chains on proteins.

It follows from (2.75) that the periodic reorientation of dipoles in response to alternating $\vec{E}_{ext}$ accelerates—and f_r increases—with the *temperature* T of tissue (Footnote 43) as well as with decreasing *volume* r^3 of the single *relaxing dipole*. The smaller the dipole, the less inert is this dipole and the faster can be its rotation. Likewise, the smaller the dipole, the higher is the frequency f such dipole can follow in its rotation without restriction (Fig. 2.16c).

It is interesting to note that the maximum *orientation energy* of the dipole (proportional to the product of the inner $\vec{E}_{\text{ext}}$ at the dipole and the electric dipole moment $\vec{p}$, see (2.59) and Fig. 2.17) is typically much less than its mean kinetic *thermal energy* (in the order of $k \cdot T$). This inequality assumes reasonable but not exceedingly high strengths[45] of the incident $\vec{E}_{\text{ext}}$. The *random thermal agitation* of dipoles opposes strongly the orientated torque on dipoles (torque $\vec{M}$ due to non-zero $\vec{E}_{\text{ext}}$, see Footnote 35) so that the ensemble of dipoles approaches a *thermal equilibrium* in its orientation. The resulting mean cosine angle $\langle \cos(\varphi) \rangle$ between the moment $\vec{p}$ (2.59) and the incident $\vec{E}_{\text{ext}}$ at the position of the dipole—as illustrated in Fig. 2.19c—obeys

$$\langle \cos(\varphi) \rangle \approx \frac{p \cdot E_{\text{ext}}}{k \cdot T}. \tag{2.76}$$

The mean $\langle \cos(\varphi) \rangle$ becomes proportional to the magnitude E_{ext} and inversely proportional to T, namely, to *thermal agitation*. In other words, the average misalignment angle φ between $\vec{p}$ and $\vec{E}_{\text{ext}}$ tends to decrease with increasing magnitude E_{ext} and/or decreasing T, or, in analogy, with increasing *orientation energy* and/or decreasing *thermal energy*. From a practical point of view, increasing temperature disturbs the alignment of $\vec{p}$ and $\vec{E}_{\text{ext}}$.

The effective size of the *permittivity* ε was shown to increase with *temperature* by about 0–2%/°C, depending on the absolute value of f. In particular, this increase rate applies for f below the GHz range, i.e., below the region of γ-dispersion (Foster

[45]Theories of the *counterion polarization* and *dipolar relaxation* within the scope of α-dispersion and γ-dispersion, respectively, apply to linear responses to relatively *weak electric fields* only. These *linear responses* or linear effects mean that the perturbation of the system by the applied electric field is relatively small. In particular, only a *small net polarization* of the system is caused. The resulting motions of individual counterions or molecular dipoles are hardly affected by the applied electrostatic forces (generated by external electric fields) exerted on ensembles of counterions or dipoles. For instance, the linear response holds as long as the *orientation energy* of molecular dipoles (i.e., the interaction energy with the applied electric field) is much less than their *thermal energy* (2.76).

In contrast, if the *orientation energy* exceeds the *thermal energy*, the affected dipoles are substantially all aligned with incident the electric field. The non-linear *dielectric saturation* occurs while the *permittivity* decreases strongly (Footnote 38). A high orientation energy—or a *high inner electric field*—implies an almost maximum polarization of polarizable structures, including mechanisms of the *induced and orientation polarization* (Fig. 2.16b, c). Here an additional increase in the inner electric field adds progressively less *surplus polarization* and thus the *permittivity* of the polarizable structure—as a measure of accumulated polarization charges per unit of the electric field (2.63)—has to *decrease*.

The condition for the exceedingly high orientation energy applies only for very high inner electric fields of the order of 10^6–10^7 V/m (for polar proteins according to Foster (1996)). Please compare with the *relatively high electric fields* within the cell membrane ($\approx 10^7$ V/m) and within the double layer ($\approx 10^9$ V/m) on the electrode surface (from Footnote 13 in Chap. 3), and with the *relatively low endogenous electric fields* within the body (Section "Electric and Magnetic Field").

1996). The increase in ε with temperature can be expected due to varying f_r that also tends to increase by about +2%/°C with rising temperature (according to Footnote 43). Consequently, the increasing f_r shifts the spectral course of ε over f towards higher values of f—compare the course of ε in Fig. 2.20 being shifted to the right—which, in turn, increases ε of tissue at a particular f of $\vec{E}_{ext}$ with increasing tissue temperature.

Conductance

The effect of γ-dispersion (reorientation of polar molecules) on γ_{eff} is less straightforward than in the case of α-dispersion (obstructed movement of ions carrying current) or β-dispersion (current flow obstructed by isolating cells). However, the concept of *energy* can be favourably used here since *γ-dispersion dissipates* submitted energy through production of *heat* within tissue, as described below.

Please recall that the *dissipated energy* within tissue is proportional to its γ_{eff} according to (2.58) when $\vec{E}_{ext}$ in tissue is given. In other words, the larger is the absorbed energy by tissue—or dissipated from the incident field $\vec{E}_{ext}$—the larger is the associated γ_{eff} of tissue. In particular,

- for very *low* $f \ll f_r$ below γ-dispersion, an ordered and slow rotational reorientation of all permanent water dipoles takes place so that there is *no friction* among dipoles. No friction losses, *no heat* is produced, and thus no energy is withdrawn from the applied $\vec{E}_{ext}$. Reorientation of dipoles is relatively *slow* (low f) in comparison with fast thermal motions of dipoles so that this reorientation does not contribute to the actual temperature. Correspondingly, the relevant γ_{eff} does not change over f for $f \ll f_r$.
- For f *close to and at* f_r, all dipoles exposed to $\vec{E}_{ext}$ can only *partially follow* periodic changes in the direction of $\vec{E}_{ext}$ because of the *dipole inertness*. Some *water dipoles* rotate more while others rotate less, which necessarily yields a desynchronised rotation of dipoles and generates a mutual friction in-between bound charges within dipoles during their oscillatory movements. The friction decelerates involved dipoles and generates *friction losses* in terms of produced *heat* within tissue (2.154). In addition, reorientation of dipoles—even though restricted by their inertance—is already relatively *fast* (high f) and thus adds to thermal motions of dipoles and effectively contributes to the temperature. In fact, this heat represents the absorbed energy by tissue at the cost of the incident energy from $\vec{E}_{ext}$. These losses are known as *dipolar losses* or *dielectric losses*. For non-zero losses, the relevant γ_{eff} increases (2.58). Right at f_r, the friction among dipoles is most dominant and so dipolar losses in tissue become maximal; the associated γ_{eff} shows maximum rate of increase with f at $f = f_r$ (Fig. 2.24). In addition, the dipolar relaxation of *polar proteins* and their *polar side-chains* might contribute a noticeable amount to γ_{eff} [especially, because of the high value of f_r, see (2.84)].
- For very *high* $f \gg f_r$ above γ-dispersion, exposed inert dipoles can not follow at all changes in the alternating $\vec{E}_{ext}$. Dipolar reorientation ceases as well as the

heat generating friction in-between dipoles. Obviously, missing reorientation does not contribute to thermal motions. *Dipolar losses disappear*. The relevant γ_{eff} does not change over f for $f \gg f_{\text{r}}$, just as γ_{eff} does not change for $f \ll f_{\text{r}}$.

In fact, the change in the *conductivity* γ_{eff} is given as the product of the *angular frequency* $2\pi \cdot f$ and the *loss factor* describing the dissipated energy, as shown in (2.83). Therefore, the level of γ_{eff} is subjected to a maximum rise over f directly at $f = f_{\text{r}}$, where the loss factor is at its maximum. The conductivity γ_{eff} rises nearly quadratically with f below f_{r}, as can be derived from (2.83) with $\omega \cdot \tau \ll 1$. For f above f_{r}, the size of γ_{eff} converges towards a constant value, as can also be derived from (2.83) with $\omega \cdot \tau \ll 1$. Therefore, the course of γ_{eff} increases in a *step-wise manner* over f for a single dispersion mechanism, as shown in Fig. 2.24. For *thermally* induced changes in γ_{eff}, see Footnote 31.

Interestingly, in *tissues with high water content*, the effective conductivity γ_{eff} [$=\gamma + \Delta\gamma$, see (2.82)] shows roughly equal contributions from the *ionic conductivity* γ and $\Delta\gamma$ considering *dipolar losses within tissue water* at f around 3 to 5 GHz. This equal proportion can be easily estimated for seawater when $\gamma = 3$ S/m, $\Delta\gamma = 3$ S/m, and $\gamma_{\text{eff}} = 6$ S/m are considered in Fig. 2.21 in the course of γ-dispersion. In other words, in the course of γ-dispersion, dipolar losses start to dominate over conductive losses (due to collisions of ions, see Section "Conductive Phenomena") with increasing f.

When *dielectric losses are absent*—as applicable for $f \ll f_{\text{r}}$ and $f \gg f_{\text{r}}$—the resulting *electric field* $\vec{E}$ in polarizable tissue and the resulting *electric flux density field* $\vec{D} = \varepsilon \cdot \vec{E}$ are *in phase* (2.64), as illustrated in the phasor diagram of Fig. 2.23c. Here the factor ε connecting $\vec{E}$ and $\vec{D}$ must be a real quantity, whereas the inequality $|\vec{E}| < |\vec{E}_{\text{ext}}|$ applies for $\varepsilon/\varepsilon_0 > 1$ (2.62). However, when *dielectric losses are present*—as applicable for f close to and at f_{r}—the inert orientation of dipoles follows the applied electric stimulus with some phase lag. More formally, the field $\vec{D}$ describing accumulated polarization charges is temporally delayed with respect to the stimulus field $\vec{E}$, as can be observed in Fig. 2.23b. In fact, this *out-of-phase behaviour* enables a lossy dielectric to draw energy from the ambient electric field and then to dissipate it in the form of heat.

Ionic and Displacement Dispersion

Following α to γ dispersions, it is instructive to discuss shortly ionic and displacement polarizations, with the associated relaxation and dispersion mechanisms. In fact, *ionic polarization* is based on displacement of ions from their resting state within molecule. Again, when the half-period of the incident $\vec{E}_{\text{ext}}$ with its frequency f becomes too short with respect to the associated relaxation time constant, inert *ionic relaxation* ceases and *ionic dispersion* occurs. *Ionic relaxation* persists up to *infrared region* with the relevant *relaxation frequency* of about 10^{12} Hz.

Another polarization mechanism—the fastest one among all discussed polarization phenomena and existing up to *ultraviolet region*—is *electronic or atomic polarization*, known also as *displacement polarization*. As illustrated in Fig. 2.19d, here polarization

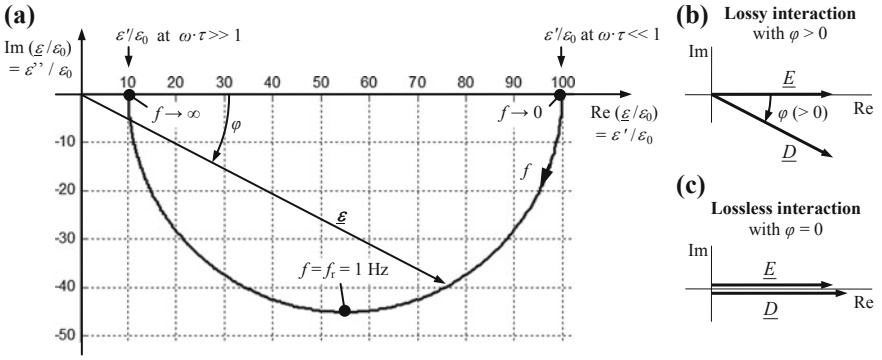

Fig. 2.23 The complex permittivity $\underline{\varepsilon}$ (=$\varepsilon' - j\varepsilon''$) as a Nyquist plot (Footnote 38 in Chap. 3) in view of lossy and lossless interactions in tissue. **a** Lossy interaction with the loss angle φ in the complex plane as a function of the field frequency f in the course of a single dispersion mechanism, located at the relaxation frequency f_r. The used numerical data is identical with that in Fig. 2.24. **b** Lossy interaction is characterized by the temporally delayed electric flux density $\vec{D} = \underline{D} \cdot \vec{e}_E$ with respect to the incident electric field $\vec{E} = \underline{E} \cdot \vec{e}_E$ by the phase angle φ (>0) in the phasor diagram within the time domain. In the space domain, the fields $\vec{D} = \underline{\varepsilon} \cdot \vec{E}$ and $\vec{E}$ point in the same direction of the vector $\vec{e}_E$ because of the assumed isotropy (Fig. 2.16d). The permittivity $\underline{\varepsilon}$ is a complex quantity. **c** For lossless interaction, the fields $\vec{D} = \varepsilon \cdot \vec{E}$ and $\vec{E}$ are in-phase and $\varphi = 0$ applies. Here the permittivity $\varepsilon = \varepsilon'$ is a real quantity

of electronic clouds occurs on atomic level. In particular, the field $\vec{E}_{ext}$ displaces the negative cloud of electrons around positive atomic nuclei in a direction opposite the field. The resulting slight separation of positive and negative charges, namely, the separation of their balance points, makes one side of the atom somewhat positive and the opposite side somewhat negative (compare Fig. 2.16b). With alternating $\vec{E}_{ext}$, polarization direction alternates in terms of *displacement relaxation*. Of course, this polarization ends when the cloud becomes too inert to be timely dislocated in synchrony with $\vec{E}_{ext}$ (right subfigure in Fig. 2.19d) and *displacement dispersion* occurs. The relevant *relaxation frequency* resides at about 10^{15} Hz. However, all polarizations are lost within ultraviolet region and for even higher f.

Both ionic and displacement dispersions contribute to a very *small decrease in* ε with increasing f. This is because the respective *displacement magnitudes* are also very small, amounting to only a fraction of atomic diameter.

In clear contrast to β and γ dispersions (Fig. 2.19b, c), ionic and displacement polarizations (Fig. 2.19d) face a *restorative force*, acting against the separation of charges and thus against the polarization of the structure. This elastic repelling force and the opposing polarizing force favour oscillation in the separation of charges for f close to the respective *relaxation frequency*. For instance, a mutual oscillation of the electron cloud and the associated nucleus within the cloud may result out of the two opposed electrostatic and interacting forces. Therefore, ionic and displacement polarizations are based on *resonant polarization mechanisms*, whereas β and γ

dispersions are *non-resonant* in their nature since the restorative force is missing here. The resonant behaviour yields an increased ε close before and close after the respective relaxation frequency in the course of ε over f.

Dispersion Model Versus Experiment

Biological tissues are *lossy*.[46] When a current or propagating wave passes through tissue, some power will be deposited within tissue as heat. Please recall that the propagating wave experiences not only

- *conductive losses* but also
- *dielectric losses*

in the course of a single *dispersion* around the *relaxation frequency* f_r, which *heats* up tissue. From a physical point of view, the two different kinds of losses can not be modelled with real values of the classical electrical conductivity γ and dielectric permittivity ε. This is because the real γ describes *conductive losses* only (Fig. 2.16a) while the real ε describes the *lossless oscillation* of bound charges only (Fig. 2.16b, c).

In order to consider the missing *dielectric losses*, it is appropriate to introduce the *complex permittivity* $\underline{\varepsilon}$, to give

$$\underline{\varepsilon} = \varepsilon' - \mathrm{j}\varepsilon''. \tag{2.77}$$

The *real part* of $\underline{\varepsilon}$ is the classical *permittivity* $\varepsilon' = \varepsilon = \varepsilon_0 \cdot \varepsilon_r$—in line with (2.64)—that is a measure of the *stored energy* in the electric field $\vec{E}$ with the frequency f within tissue. Please note that ε' represents the *lossless interaction* of $\vec{E}$ with polarizable tissue. The value of ε' stands for the portion of the *oscillatory motion of bound charges* that is 90° *out-of-phase* with the prevalent $\vec{E}$, whereas this motion forms the *displacement current* (2.69).

The *imaginary part* ε'' in (2.77) stays for the dielectric *loss factor* that describes a fraction of *energy dissipated* in tissue per cycle of $\vec{E}$. The dissipation is due to the *friction* in-between fastly and continuously reoriented dipoles within molecules and from molecules nearby, which heats up tissue and withdraws energy from the inner $\vec{E}$. *Bound charges* forming dipoles are hindered in their oscillations (see γ-dispersion in Fig. 2.19c). Consequently, we end up with an additional oscillatory *motion component* of bound charges that is *in-phase* with $\vec{E}$, as if it were a

[46] In fact, *lossy materials* are

- *good conductors* (with numerous free *unbound charges*) and/or
- *lossy dielectrics* (with *bound charges* oscillating and rubbing on each other).

In contrast, *lossless materials* are

- *good isolators* (without available free *unbound charges*) and/or
- *perfect dielectrics* (with oscillation of *bound charges* unhindered by neighbouring charges);

compare Footnote 11.

conductive current in-phase with $\vec{E}$ [compare in-phase fields from (2.54)]. This friction-related motion component represents *dielectric losses* and is determined by ε''. Therefore, *lossy dielectric materials* are characterized by $\varepsilon'' \neq 0$ and $\gamma_{\text{eff}} > \gamma$, whereas *lossless dielectric materials* are characterised by $\varepsilon'' = 0$ with $\gamma = 0$ in *perfect dielectrics* (without any power deposited within this lossless material); compare Footnote 11.

Polarization—Single Dispersion

In *lossy dielectric tissue*, the *electric flux density field* $\vec{D} = \underline{\varepsilon} \cdot \vec{E}$ follows a step-wise temporal increase in the local $\vec{E}$ with a certain time delay because the relevant dispersion effect needs always a certain time to develop. Please recall that, for instance, charge separation on membrane interfaces (β-dispersion, see Fig. 2.19c) or reorientation of dipoles (γ-dispersion, see Fig. 2.19c) is intrinsically an *inert mechanical process* (leading to losses). From a mathematical point of view, the negative *imaginary part* $-\mathrm{j}\varepsilon''$ of $\underline{\varepsilon}$ (2.77) delays $\vec{D}$ with respect to $\vec{E}$ (and not the other way around). Figure 2.23b illustrates the resulting *phase lag* φ (>0) between complex amplitudes $\underline{E}$ and $\underline{D}$ in the phasor diagram of the time domain.

In particular, there is an *exponential increase* in the magnitude of $\vec{D}$ (*system output* in terms of generated polarization) for the *step-wise increase* in the magnitude of $\vec{E}$ (*system input* in terms of polarization stimulation) in the time domain; compare Kaniusas (2012, Fig. 2.8a, b). Therefore, a *single dispersion mechanism* can be modelled in the frequency domain in terms of the *Debye expression* (Footnote 16 in Chap. 3) as

$$\underline{\varepsilon} = \frac{\underline{D}}{\underline{E}} = \varepsilon_\infty + \frac{\Delta\varepsilon}{1 + \mathrm{j} \cdot \omega \cdot \tau} = \varepsilon_\infty + \frac{\Delta\varepsilon}{1 + (\omega \cdot \tau)^2} - \mathrm{j} \cdot \frac{\Delta\varepsilon \cdot \omega \cdot \tau}{1 + (\omega \cdot \tau)^2} \tag{2.78}$$

This is a *transfer function* of the first order from $\underline{E}$ to $\underline{D}$, as could be obtained by Laplace transformation of the exponential change in $\vec{D}$ in response to the step-wise change in $\vec{E}$. The real and imaginary components of $\underline{\varepsilon}$ (2.77) result to

$$\varepsilon' = \varepsilon_\infty + \frac{\Delta\varepsilon}{1 + (\omega \cdot \tau)^2} \quad \text{and} \quad \varepsilon'' = \frac{\Delta\varepsilon \cdot \omega \cdot \tau}{1 + (\omega \cdot \tau)^2}. \tag{2.79}$$

Here τ is the *relaxation time constant* of the relevant polarization mechanism which manifests and then ceases within the considered dispersion mechanism. The permittivity ε_∞ is the real permittivity ε' well *above the dispersion region* at relatively *high frequencies* where $\omega \cdot \tau \gg 1$ or, in analogy, where $f \gg f_\mathrm{r}$ applies. Therefore, ε_∞ describes residual and relatively fast polarization mechanisms well above the considered dispersion region, i.e., much faster than the polarization mechanism with the dynamic of τ. For instance, if (2.78) describes γ-dispersion, the size of ε_∞ accounts for the even faster and still present displacement polarization. Figure 2.24 illustrates the residual ε_∞ for high $f \gg f_\mathrm{r}$.

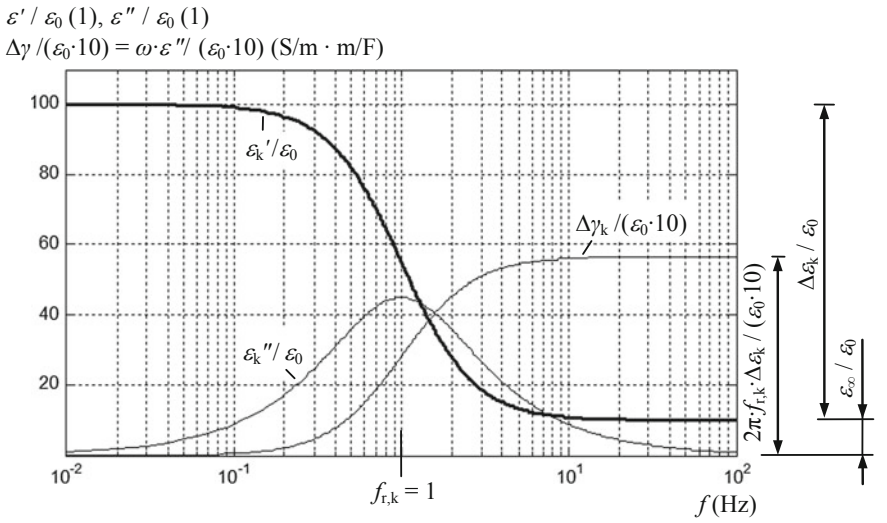

Fig. 2.24 The complex permittivity $\underline{\varepsilon}_k$ ($=\varepsilon_k' - j\varepsilon_k''$) and the increase $\Delta\gamma_k$ of the effective conductivity of tissue (2.82) as a function of the field frequency f in the course of the k-th dispersion mechanism, located at the assumed relaxation frequency $f_{r,k} = 1$ Hz (Fig. 2.23). In accordance with (2.78), the permittivity change $\Delta\varepsilon_k/\varepsilon_0$ was assumed to be 90, $\varepsilon_\infty/\varepsilon_0 = 10$, and $\tau_k = 1/(2\pi \cdot 1\text{ Hz})$. The total increase $\Delta\gamma_k$ for $\omega \cdot \tau \gg 1$ amounts to $2\pi \cdot 1\text{ Hz} \cdot 90 \cdot \varepsilon_0 \approx 565 \cdot \varepsilon_0 \cdot (1\text{ rad/s})$ (2.83), which is fully in line with the depicted course of $\Delta\gamma_k/(\varepsilon_0 \cdot 10)$

The *strength of the dispersion* is given by the maximum *permittivity change* $\Delta\varepsilon$ (>0) of ε' within the dispersion region. The size of $\Delta\varepsilon$ equals the difference between ε' ($>\varepsilon_\infty$)—as related to relatively *low frequencies* ($\omega \cdot \tau \ll 1$ or $f \ll f_r$) well below the dispersion region—and ε_∞ ($\omega \cdot \tau \gg 1$ or $f \gg f_r$). Figure 2.24 illustrates $\Delta\varepsilon$ for a single dispersion mechanism, as modelled with (2.78). It should be noted that this $\varepsilon' = \varepsilon_\infty + \Delta\varepsilon$ at low f and for a single dispersion mechanism denotes *static permittivity* in the limit of *semi-infinite time*; i.e., it describes the response in $\vec{D}$ (the system response) long after the application of a step in $\vec{E}$.

In particular, for a *single dispersion mechanism*,

- the *real* ε' of the complex $\underline{\varepsilon}$ experiences a *step-wise decrease* when increasing f passes f_r, as illustrated in (2.79) and Fig. 2.24. Therefore, the tissue *polarization* loses its strength with f, as already discussed for different dispersion mechanisms from phenomenological perspective (Fig. 2.19). Please note in Fig. 2.24 that the modelled decrease in ε' extends approximately over *two frequency decades*.
- The *imaginary* ε'' of the complex $\underline{\varepsilon}$ shows a single maximum at $f = f_r$ with the peak value of $\Delta\varepsilon/2$ while ε'' decreases to zero for low $f \ll f_r$ and high $f \gg f_r$. Equation (2.79) shows the calculus of ε'' while Fig. 2.24 depicts it. In physical

terms, the frequency-dependent *dielectric losses* are at maximum at $f = f_r$ while they disappear for $f \ll f_r$ and $f \gg f_r$.

Figure 2.23a illustrates both ε' and ε'' in the *complex plane*, showing clearly how the *loss angle* φ (i.e., the phase lag between $\vec{E}$ and $\vec{D}$) increases and then decreases with increasing f. This is in full agreement with the discussed courses of ε' and ε'' over f (Fig. 2.24). The plot in Fig. 2.23a is known as *Nyquist plot* (Footnote 38 in Chap. 3) showing the dielectric relaxation behaviour.

Polarization—Multiple Dispersions

In analogy with a *single dispersion mechanism* modelled as a *single step* in $\underline{\varepsilon}$ of the bulk, *multiple dispersion* mechanisms yield *multiple steps* in $\underline{\varepsilon}$ of the bulk. As illustrated in Fig. 2.20 based on experimental data, biological tissues are truly subjected to multiple dispersions (α-dispersion, β-dispersion, and others). Multiple dispersions, i.e., their total spectrum, can be modelled as the *summation*[47] of the respective single dispersions [from (2.78)]—known also as the *Cole-Cole expression*[48]

$$\underline{\varepsilon} = \varepsilon_\infty + \sum_{k=1,2,\ldots}^{K} \frac{\Delta\varepsilon_k}{1 + (j \cdot \omega \cdot \tau_k)^{1-\alpha_k}}. \tag{2.80}$$

Here K denotes the total number of considered and relevant dispersion mechanisms in tissue with the respective permittivity change $\Delta\varepsilon_k$ and the relaxation time constant τ_k of the k-th dispersion. Usually K amounts up to 4 or 5 in the frequency range of 10 Hz–100 GHz (Gabriel 1996c); compare with Fig. 2.20.

In addition, (2.80) accounts empirically for a possible *spectral broadening*[49] of the particular dispersion region by the *distribution parameter* α_k. In particular,

[47]This simple approach of the *summation* in (2.80) has its *physical limitations* and represents only an approximation (Foster 1996). For instance, the interior of cells is shielded from the external incident electric field at *low frequencies* (i.e., below f_r of β-dispersion of the outer cell membrane) and thus the absent polarization of intracellular organelles and nucleus will not contribute to the *bulk permittivity* $\varepsilon = \varepsilon'$; for details see Footnote 42. Consequently, the summation in (2.80) tends to *overestimate* $\varepsilon = \varepsilon'$ of cellular tissue at these low field frequencies.

[48]The name of the Cole-Cole diagram derives from brothers Kenneth Stewart Cole (1900–1984) and Robert H. Cole (1914–1990), both American biophysicists, who performed experimental investigations on impedance of biological media.

[49]The *spectral broadening of the dispersion* in biological tissue may indicate the presence of numerous *overlapping Debye-type dispersions* (2.78) each with a slightly *different relaxation time constant* τ. The resulting distribution of these slightly different τ values is due to *several polarizing structures* of similar type, size, shape, and kinetics; e.g., due to a broad range of (irregular) cell size and shape, varying size of membrane-bound organelles in the cell, as well as the existence of cellular junctions (Kaniusas 2012, Footnote 67) (Foster 1996).

In addition, there are also indications that fundamental *charge transport and dipole reorientation* mechanisms in tissues are *mutually interrelated*. This is especially true in concentrated suspensions (due to intermolecular interactions, compare Footnote 50) so that as the degree of this interrelation increases, the dispersion width increases, the *broadening parameter* α_k rises and attains non-zero values (2.80).

complex structure and composition of biological tissue as well as *intermolecular interactions*[50] widen dispersion regions. For instance, $\alpha_k = 0$ applies for the relatively narrow dispersion width of the *k*-th dispersion (Fig. 2.24) in accordance with the *Debye expression* (2.78), whereas the width increases for $0 < \alpha_k < 1$.

- The size of α_k is about 0.4 for *α-dispersion*, i.e., the dispersion width is relatively broad.
- For *β-dispersion*, α_k resides in the range of 0.1–0.4 in cell suspensions and close to 0.1 in suspensions of blood cells (Foster 1996).
- The value of α_k for *γ-dispersion* is almost zero for body fluids (including pure water) and resides in the range of 0.1–0.2 for most biological tissues. That is, pure water undergoes nearly a single relaxation with τ_k within a relatively narrow γ-dispersion.

In other words, the spectral broadening is typical for biological tissues with a relatively low water content but not for pure water.

Conductance

Using the complex $\underline{\varepsilon}$ from (2.77), conductive and displacement currents in (2.69) with their *complex vector amplitudes* $\vec{J}$, $\vec{J}_E$, $\vec{J}_C$, and $\vec{E}$ can be rewritten[51] as

---

Likewise, *electrostatic interactions* among the different (suspended) particles may lead to a distribution of τ in the bulk, although the individual particles themselves may exhibit relaxation with a single τ. Furthermore, some *dielectric processes* of relaxation are suspected to have kinetics of higher order than the *first order of the Debye expression* (2.78) (Foster 1996).

[50]For instance, the static *dielectric permittivity* $\varepsilon = \varepsilon'$ of seawater depends on the *water salinity* and is generally reduced as related to that of pure water. This is because salt ions are hydrated to some extent, i.e., there are some water molecules in the immediate vicinity of the ion; see *hydrated ions* in Fig. 3.6a. *Water molecules* that are in the close vicinity of a salt ion orient themselves with respect to this ion but less with respect to the ambient electric field. Therefore, it can be expected that these partly arrested water molecules do not contribute to the *orientation polarization* of seawater (Somaraju 2006). In other words, ions from dissolved salts will impede *dipolar relaxation* of water molecules (Fig. 2.16c).

In addition, seawater has several dissolved salts—with the presence of different ions—and therefore is a significantly better conductor than pure water.

[51]In practice, (2.81) can be simplified to a single term, to give

$$\vec{J} = \gamma \cdot \vec{E} + \mathrm{j} \cdot \underline{\varepsilon} \cdot \omega \cdot \vec{E} = \mathrm{j} \cdot \omega \cdot \underline{\varepsilon}^* \cdot \vec{E}.$$

Please note that the introduced *modified complex permittivity* $\underline{\varepsilon}^*$ ($\neq \underline{\varepsilon}$) considers also the static ionic conductivity γ (2.54) and thus represents a *composite quantity*. This is an advantageous approach from an *experimental point of view* (Gabriel 1996c) but less from a physical and descriptive one. This modification yields then

$$\underline{\varepsilon}^* = \underline{\varepsilon} + \frac{\gamma}{\mathrm{j}\omega} = \varepsilon' - \mathrm{j} \cdot \left(\varepsilon'' + \frac{\gamma}{\omega}\right) \quad \text{and thus} \quad \gamma_{\mathrm{eff}} = \omega \cdot \mathrm{Im}\left(\underline{\varepsilon}^*\right) = \gamma + \omega \cdot \varepsilon'',$$

which shows that the *effective conductivity* γ_{eff} can be assessed with the imaginary part of $\underline{\varepsilon}^*$ only, although two basically different physical mechanisms contribute to this net conductivity γ_{eff} [conductive losses and dielectric losses, see (2.82)].

$$\begin{aligned}\vec{J} &= \vec{J}_E + \vec{J}_C = \gamma \cdot \vec{E} + j \cdot \underline{\varepsilon} \cdot \omega \cdot \vec{E} = (\gamma + \omega \cdot \varepsilon'') \cdot \vec{E} + j \cdot \varepsilon' \cdot \omega \cdot \vec{E} \\ &= (\gamma + \Delta\gamma) \cdot \vec{E} + j \cdot \varepsilon' \cdot \omega \cdot \vec{E} = \gamma_{eff} \cdot \vec{E} + j \cdot \varepsilon \cdot \omega \cdot \vec{E}\end{aligned} \tag{2.81}$$

with

$$\gamma_{eff} = \gamma + \Delta\gamma = \gamma + \omega \cdot \varepsilon''. \tag{2.82}$$

In (2.81), the first real term $\gamma_{eff} \cdot \vec{E}$ represents the *effective conductive current* considering *conductive and dielectric losses* with involved unbound charges and bound charges, respectively. The second imaginary term $j \cdot \varepsilon \cdot \omega \cdot \vec{E}$ represents the lossless oscillation of bound charges and thus constitutes the classical *displacement current* (2.67).

It can be observed in (2.82) that ε'' contributes to the total *effective conductivity* γ_{eff}. The *negative sign* of the *imaginary part* $-j\varepsilon''$ of $\underline{\varepsilon}$ (2.77) yields a positive increase $\Delta\gamma$ ($=-j \cdot j \cdot \omega \cdot \varepsilon'' = \omega \cdot \varepsilon'' \geq 0$) in γ_{eff}, as required by the discussed physics of *dielectric losses* (Section "Gamma Dispersion"). It should be stressed that γ_{eff} considers all *friction-related heat losses* given by γ and $\omega \cdot \varepsilon''$, as caused by the motion of *free and bound charges*, respectively. In particular,

- the *frequency-independent portion* γ of γ_{eff} is due to ionic conduction only. The portion γ ($=\gamma_{eff}$) is the only present conductivity at the direct $\vec{E}$ field (Fig. 2.21). Thus the inequality $\Delta\gamma \ll \gamma$ applies at *low frequencies* with $f \ll f_r$, which yields $\gamma_{eff} = \gamma + \Delta\gamma \approx \gamma$; i.e., the *effective conductivity* is determined by the *ionic conduction* only.
- The *frequency-dependent portion* $\Delta\gamma = \omega \cdot \varepsilon''$ is due to dielectric losses in (or failure of) various polarization/relaxation phenomena. In fact, the portion $\Delta\gamma$ is zero for the direct $\vec{E}$ field (Fig. 2.21). In contrast to low frequencies, at *high frequencies* with $f \gg f_r$, the change $\Delta\gamma$ typically dominates over γ with $\Delta\gamma \gg \gamma$. This yields $\gamma_{eff} = \gamma + \Delta\gamma \approx \Delta\gamma$, i.e., the *effective conductivity* is dominated by *dielectric losses* only. In fact, $\Delta\gamma$ accounts for the component of $\vec{J}$ that is in-phase with $\vec{E}$ (2.81).

Consequently, the propensity of *tissue* to generate *heat losses*—for a given strength of the inner sinusoidal $\vec{E}$ field and its oscillation f—is determined proportionally to the applicable γ and ε'' of tissue, or equivalently, to the level of the *frequency-dependent* γ_{eff}. Please recall that *relaxation processes* in tissue lead to *losses* which, in turn, manifest as generated *heat* in tissue. Therefore, the *specific energy absorption rate* P_{SAR} (2.58)—or the rate at which the field energy is given to the permeated tissue—depends on γ_{eff} but not on γ only. Both *field frequency* and *tissue properties* determine P_{SAR}. The higher is f, the larger is γ_{eff} (Fig. 2.21), the

larger is the field $\vec{E}$ absorption within tissue, and the faster the electromagnetic wave loses (deposits) its energy as it travels through tissue. As a practical conclusion, the *higher is f*, the *shallower is the tissue heating*, which is in qualitative agreement with Fig. 2.6. As illustrated in Fig. 2.21,

- tissues with a *low water content*—such as skin, bone, and fat—exhibit relatively *low losses*, whereas
- tissues with a *high water content* and thus with a dominant γ-dispersion—such as muscle and brain—are *much lossier*.

Such observations are highly relevant and instructive for the proper operation of *therapeutic thermal treatment*, as discussed in Footnote 115.

Polarization Versus Conductance

Interestingly, the *permittivity* ε and *conductivity* γ_{eff} of tissue *can not vary independently* with *f*. On the other hand, not all dispersions residing in different frequency ranges affect ε and γ_{eff} in the same way. The *modelled data* from Fig. 2.24 as well as the *experimental data* from Figs. 2.20 and 2.21 reveal that any step-wise decrease in ε with f is necessarily accompanied by the associated step-wise increase in γ_{eff}.

In fact, it can be derived from (2.79) and (2.82) that the *dispersion-dependent increase* $\Delta\gamma_k$ of the *k*-th dispersion obeys

$$\Delta\gamma_k = \omega \cdot \varepsilon_k'' = \frac{\Delta\varepsilon_k \cdot \omega^2 \cdot \tau_k}{1 + (\omega \cdot \tau_k)^2}. \tag{2.83}$$

For high $f \gg f_{r,k}$ ($\omega \cdot \tau_k \gg 1$) an instructive relationship results

$$\Delta\gamma_k \approx \frac{\Delta\varepsilon_k}{\tau_k} = 2\pi \cdot f_{r,k} \cdot \Delta\varepsilon_k. \tag{2.84}$$

It shows that $\Delta\gamma_k$ levels off above the dispersion region and even becomes

- *proportional to* $f_{r,k}$ and, on the other hand,
- *proportional to* $\Delta\varepsilon_k$.

Please recall that $f_{r,k}$ (=1/(2π · τ_k)) is the respective *relaxation frequency* for the *k*-th dispersion and denotes halfway between high and low limits of ε' and $\Delta\gamma$, as well as the maximum of ε'', as can be observed in Fig. 2.24. Likewise, the *maximum change* $\Delta\gamma_k$ in the effective γ_{eff} over a single dispersion region is directly related to the product $f_{r,k} \cdot \Delta\varepsilon_k$.

Therefore—from a physical point of view

- α-*dispersion* with the relatively *low* f_r in kHz range can be expected to be associated with a small, *almost absent increase* $\Delta\gamma$, whereas the corresponding *decrease* $\Delta\varepsilon$ *is very large*. This is in full agreement with experimental data; e.g., see muscle in Figs. 2.20 and 2.21. In contrast,

- *β-dispersion* with the *medium* f_r in the higher MHz range can be expected to yield a *pronounced increase* $\Delta\gamma$ given a *pronounced decrease* $\Delta\varepsilon$. Again, experimental data confirm this behaviour; see blood in Figs. 2.20 and 2.21. Lastly,
- *γ-dispersion* with the *high* f_r in GHz range yields the *largest increase* $\Delta\gamma$ with the relatively *small* $\Delta\varepsilon$; see seawater in Figs. 2.20 and 2.21.

In short, ε' decreases in subsequent steps of different sizes—as related to α, β, γ dispersions of biological tissue—while the associated γ_{eff} increases in subsequent steps of different sizes. It is important to note that these electrical properties vary over quite a few orders of magnitude with f, the level of ε' more than γ_{eff} (Figs. 2.20 and 2.21).

In line with predominant *conductive behaviour* at low f or predominant *dielectric behaviour* at high f [(2.71) and (2.72)], the conductivity γ_{eff} of tissue (conductive property) determines its behaviour in the electromagnetic field at low f ($<f_r$). At high f ($>f_r$), the permittivity ε' (dielectric property) determines the tissue behaviour. Obviously, not only the absolute size of f influences the transition from conductive to dielectric behaviour but also the *frequency-dependent* γ_{eff} [(2.71) and (2.72)]. Compare instructive *examples* from Section "Biological Boundaries".

Experiment

Experimental data in Fig. 2.20 show courses[52] of the *permittivity* ε versus f for different media, whereas Fig. 2.21 shows courses of the *effective conductivity* γ_{eff}. Clearly resolved *dispersion regions* are visible with the associated f_r in kHz, MHz, and GHz ranges, separated by plateaus at intermediate f. In particular, *intermediate plateaus* are dominant in the course of γ_{eff}; here most tissues approach a plateau in the range 10–100 MHz after β-dispersion (Foster 1996). Please recall that *heterogeneity of tissues* favours increased number of dispersions. Therefore, relatively wide dispersion regions typically overlap in a heterogeneous tissue while ε and γ_{eff} in tissue undergo an almost continuous monotonic decrease and increase, respectively, over the considered range of f.

As expected from (2.84), α-dispersion at low f manifests in a strikingly large decrease in ε with increasing f while the corresponding increase in γ_{eff} is hardly noticeable. The reverse is true for γ-dispersion at high f. In particular, *muscle* with its complex cellular structure exhibits complex polarization and relaxation mechanisms, including partly overlapping α, β, and γ dispersion regimes. In contrast, *blood* as a diluted suspension of cells exhibits only β and γ dispersions without α-dispersion. In analogy, *seawater* exhibits γ dispersion only. Correspondingly, almost identical ε of muscle and blood can be observed after β-dispersion. Identical values of ε of muscle, blood, and seawater after γ-dispersion illustrate that the residual ε of these media reflects properties of inert water dipoles only. This is in analogy with identical γ_{eff} of muscle, blood, and seawater after γ-dispersion at high f.

[52]Please note that the *logarithmic scaling* in Figs. 2.20 and 2.21 *strengthens subjectively* the depicted changes in the dielectric permittivity ε and effective conductivity γ_{eff} for an observer when their corresponding absolute levels are relatively small, and, on the contrary, *weakens subjectively the objective changes* when the absolute levels are high.

For instance, *muscle* exhibits a large amount of *α-dispersion*; i.e., ε shows a more than 100-fold decrease with increasing f, whereas f_r is centered at about 100 Hz (Fig. 2.20). Contributing mechanisms are both *counterion polarization* (Fig. 2.19a) and *polarization of the transverse tubules* (complex membraneous channels permeating the muscle cell and being continuous with the membrane of the muscle cell, see Kaniusas (2012, Fig. 2.26)). The dominance of α-dispersion is more pronounced for incident electric fields in the *longitudinal orientation* of elongated muscle cells than in the *transverse orientation* (Foster 1996). In terms of *β-dispersion*, the size of f_r of *muscle* is about 500 kHz, whereas the dielectric increment $\Delta\varepsilon/\varepsilon_0$ (2.79) is about 7000 (Foster 1996). For the impact of the *anisotropy of muscle* on the frequency dependence of γ_{eff} in terms of *β-dispersion* see Footnote 30.

For comparison, *blood* shows $\Delta\varepsilon/\varepsilon_0$ (2.79) of about 5000 for *β-dispersion* with its estimated f_r of about 2 MHz (Fig. 2.20), whereas the associated $\Delta\gamma$ (2.83) amounts to about 0.5 S/m (Fig. 2.21); data are quantitatively in line with Foster (1996). Interestingly, latter numbers of $\Delta\varepsilon/\varepsilon_0$ and $\Delta\gamma$ fulfil (2.84) with $2\pi \cdot 2 \cdot 10^6$ Hz $\cdot$ 5000 $\cdot$ ε_0 = 0.55 S/m $\approx$ 0.5 S/m. The given value of f_r is comparable with 1.2 MHz as estimated in IFAC (2013), (Gabriel 1996c) based on a dispersion model with α_k = 0.1 (2.80).

Please note that f_r of *β-dispersion in blood* is higher than f_r of *β-dispersion in muscle*, whereas $\Delta\varepsilon/\varepsilon_0$ tends to be lower in blood than muscle, as can be derived from Fig. 2.20. That is, the static ε and the size of τ of β-dispersion in liquid *blood* are typically smaller than in soft *tissues*. This is the consequence of the typically smaller cells in blood and thus smaller capacitors to be recharged during polarization; please recall the direct proportionality between the capacitance and the surface area of the capacitor (2.41).

The associated courses of ε of muscle, blood, and seawater are quite similar in the frequency range of *γ-dispersion* (Fig. 2.20). This is not surprising since present water in these media, namely, the dipolar relaxation of water dipoles, determines this dispersion (Fig. 2.19c). Therefore, *biological water* and its motional properties (i.e., water in tissue exposed to hydration effects, see Footnote 44) govern dielectric properties of *soft tissues* (i.e., tissues with a *high water content*) and of blood in GHz range. When we consider tissues with a relatively high water content (muscle and blood) versus pure water, we can recognise that $\Delta\varepsilon/\varepsilon_0$ of *muscle* and *blood* for *γ-dispersion* is about 50 and is less than $\Delta\varepsilon/\varepsilon_0 \approx 69$ of *seawater* (Fig. 2.20). This is due to the fact that water amounts to about 80% of the volume of most *soft tissues* such as muscle (Foster 1996). Therefore, the size of $\Delta\varepsilon$ of muscle and blood—with only a limited water content—must be less than $\Delta\varepsilon$ of pure seawater. The corresponding increase $\Delta\gamma$ of muscle and blood in the range of *γ-dispersion* is about 60 S/m (Fig. 2.21). With the estimated f_r of water of about 26 GHz (Footnote 43), (2.84) again confirms qualitatively the aforementioned experimental values of muscle and blood with $2\pi \cdot 26 \cdot 10^9$ Hz $\cdot$ 50 $\cdot$ ε_0 = 72 S/m $\approx$ 70 S/m. This *estimated value* of 70 S/m is a bit higher than the *experimental value* of 60 S/m because water in muscle and blood is rather bound and not unrestricted (Footnote 44) so that the associated f_r of γ-dispersion should be definitely lower in (2.84) than 26 GHz.

Lastly, *fat* shows a relatively large $\Delta\varepsilon/\varepsilon_0$ in the course of *α-dispersion* while its *β-dispersion* is less pronounced in comparison to that of muscle (Fig. 2.20). Since

fat has a relatively *low water content* of only about 20%, its γ-*dispersion* in terms of $\Delta\varepsilon/\varepsilon_0$ is also less pronounced. The corresponding $\Delta\gamma$ of γ-dispersion is relatively small and amounts to about 3 S/m ($\ll$60 S/m, see Fig. 2.21).

Charge and Current Induction

Electrostatic Induction

A *homogenous electric field* $\vec{E}_{\text{ext}}$ which is *external to a conductive body* surrounded by the *isolating air*—namely, $\vec{E}_{\text{ext}}$ external to a *currentless conductive body*[53]—induces *surface charges* in the body parts facing sources and sinks of $\vec{E}_{\text{ext}}$. It is known as *electrostatic induction*.

As illustrated in Fig. 2.25a, the distribution of these induced *surface charges* results from the movement of (loosely bound or unbound) *positive charges* in the body in the direction of the external $\vec{E}_{\text{ext}}$ while (loosely bound or unbound) *negative charges* move in the opposite direction after the external field $\vec{E}_{\text{ext}}$ has been switched on. Obviously, these *charge movements* mean *transient conductive currents* within the exposed conductive body during the accumulation of these surface charges (2.25); compare Fig. 2.16a. Likewise, charges of the same polarity are repelled while charges of the opposite polarity are attracted to each other if electrode charges producing the applied $\vec{E}_{\text{ext}}$ and, on the other hand, unbound charges within the conductive body are mutually considered; compare Fig. 2.16b, c. In fact, charges within the body continue to separate and accumulate to surface charges—given a *static field* $\vec{E}_{\text{ext}}$ (see Footnote 55)—until an *own electric field* $\vec{E}_{\text{i}}$ is created by the body. The *final* $\vec{E}_{\text{i}}$ *inside the body*—as determined by the *induced surface charges*—equals the *external field* $\vec{E}_{\text{ext}}$ in its magnitude. Obviously, the direction of this induced *inner field* $\vec{E}_{\text{i}}$ *opposes* that of the external field $\vec{E}_{\text{ext}}$. Therefore, *transient currents* within the body ceases as soon as the net driving force [$ze \cdot \vec{E}_{\text{i}}$, see (2.53)]—proportional to the net field $\vec{E}_{\text{i}}$ within the body—acting on unbound charges $z \cdot e$ goes to zero; a further accumulation of *surface charges* stops.

Consequently, the resulting *effective electric field* $\vec{E}$ *within and outside the conductive body* is given by a *vector superposition* of the homogenous $\vec{E}_{\text{ext}}$ and the induced $\vec{E}_{\text{i}}$, to give

$$\vec{E} = \vec{E}_{\text{ext}} + \vec{E}_{\text{i}}. \tag{2.85}$$

The resulting *magnitude* E of $\vec{E}$ *inside conductive tissue becomes zero* with $E = E_{\text{ext}} - E_{\text{i}} = 0$; see the region A in Fig. 2.25. The induced surface charges can be said to

[53]From a practical point of view, an isolated *human body* surrounded by the isolating air can already be approximated as a *currentless conductor* in the ambient *electric field*. This is because the conductance of the air is much less than that of body tissues, especially at relatively *low field frequencies* (Table 2.2); see examples in Section "Biological Boundaries".

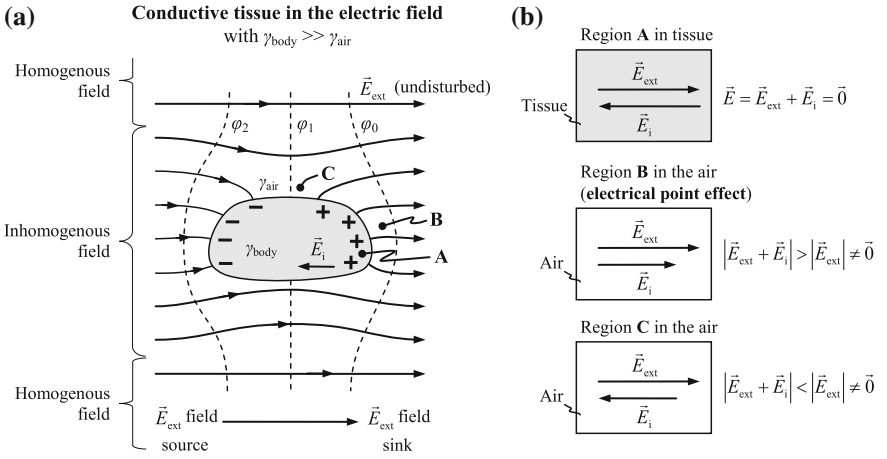

Fig. 2.25 Induction of surface charges in the (non-ideally) conductive human body (with its electrical conductivity $\gamma_{body} \neq \infty$) surrounded by isolating air (with $\gamma_{air} \ll \gamma_{body}$, see Table 2.2) when exposed to an external electric field $\vec{E}_{ext}$; compare Figs. 2.49 and 2.50. **a** The accumulated surface charges induce their own electric field $\vec{E}_i$ inside the body, which equals to $\vec{E}_{ext}$ in its magnitude given the conductive body. Thus, the resulting electric field $\vec{E}$ throughout the body amounts to zero, i.e., the magnitudes obey $E = E_{ext} - E_i = 0$ (region A). The field lines of $\vec{E}_{ext}$ are indicated, whereas the local density of field lines reflects the local magnitude of the effective $\vec{E}_{ext}$. Equipotential surfaces of the electric potential φ are indicated ($\varphi_2 > \varphi_1 > \varphi_0$ with $\varphi_2 - \varphi_1 = \varphi_1 - \varphi_0$). **b** The geometric proportions of the vectors $\vec{E}_{ext}$ and $\vec{E}_i$ inside and outside of the conductive body at the marked regions A, B, and C

screen the inner region of the conductive body from the outer incident $\vec{E}_{ext}$. Please note that this implies also a negligible interference of external electric fields with *medical implants* within conductive tissues of the body.

Likewise, the *final state in the charge distribution* should encompass *resting charges* only, the condition which necessarily implies inside $\vec{E} = \vec{0}$ (otherwise highly mobile charges within the conductive body would still experience a non-zero force). The induced surface charges are exactly the right size to cancel the external $\vec{E}_{ext}$ throughout the interior of the conductive body. That is, the size of the induced charge in the body is proportional to the magnitude E_{ext} of the external $\vec{E}_{ext}$, whereas the sum of all induced surface charges equals necessarily zero (i.e., no surplus charge is induced in the isolated body exposed to $\vec{E}_{ext}$).

The induced charges *accumulate only on the surface*[54] of the conductive body. Because of the aforementioned movements of charges, the resulting *charge density is unevenly distributed* on the body surface, see Fig. 2.25a. Local peaks in the

[54]The *conductive body* is assumed to be *homogeneous*. Otherwise, *space charges* would accumulate on inhomogeneities within the body. In particular, *surface charges* would accumulate on boundaries between inner body regions with different γ and/or ε, or, in general, with different *relaxation time constants* (2.49).

charge density—as well as peaks in the local outer electric field—arise around the sharp corners and points of the outer body surface, which is known as the *electrical point effect* (see below). Please note that if an *alternating time-varying* $\vec{E}_{\text{ext}}(t)$ with its *alternating direction* is applied, the *polarity* of the *accumulated surface charges* alternates as well as the aforementioned *transient currents* with alternating direction persist within the conductive body with each directional change in $\vec{E}_{\text{ext}}(t)$; compare Fig. 2.29c (and text below).

Because of the *absent electric field* $\vec{E} = \vec{0}$ *inside* the considered *isolated body* (strictly speaking, at a *constant temperature* within the body),

- this *currentless and*
- *conductive body*

represents a region of *constant electric potential*. Likewise, free *unbound charges* within the body *distribute regionally*[55] in a way that each *macroscopic point* of the body attains the same *electric potential* (but not necessarily zero potential) with the resulting *inside* $\vec{E} = \vec{0}$ (2.28). Likewise, the electric potential within and outside the body can be interpreted as a *scalar superposition* of potentials pertaining to the two fields $\vec{E}_{\text{ext}}$ and $\vec{E}_{\text{i}}$.

[55]In fact, *unbound charges distribute regionally* with a certain finite time constant, i.e., with the so-called *relaxation time constant* τ which is given as the ratio of the dielectric permittivity ε to the *electrical conductivity* γ of the (homogeneous) body [$\tau = \varepsilon/\gamma$, see (2.74)]. Consequently, this constant τ increases with decreasing γ of the body. This implies that a *redistribution of charges* in terms of *conductive currents* within the body (2.25) occurs relatively slowly in *poor conductors* (or isolators with small γ), whereas the redistribution occurs almost instantaneously in very *good conductors* (as metals with large γ).

It follows that a *static electric field outside a conductive body* leads always to a completed charge redistribution in the body after a relatively long time ($\gg\tau$). Likewise, the static electric field induces surface charges which sizes do not change with time anymore leading to *zero inner electric field* (Fig. 2.25a).

In contrast, if the half-period $1/(2f)$ (inverse to the field frequency f) of a *time-varying electric field* (residing outside the *isolated conductive body*) comes into the range of the body's τ ($\geq 1/(2f)$) then the charge redistribution in the body can not be completed during the respective half-period of the electric field. Consequently, the *electric field* inside of a *non-ideally conductive body never goes to zero* at this relatively high f because this body *never becomes currentless* due to *inert charge redistribution* with the non-zero $\tau \geq 1/f$. For an *ideally conductive body*, the charge redistribution is instantaneously finished [with $\tau \to 0$ for $\gamma \to \infty$, see (2.74)] with the resulting currentless situation and zero electric field established within the body.

Figure 2.29c demonstrates these currents within the body in response to a *switched electric field* (switched in a rectangular way) outside the *non-ideally conductive body*. These currents necessarily *redistribute induced surface charges* from/to the body surface. It can be derived from this figure that abrupt changes in the outer electric field yield *exponentially decreasing currents* in the body and thus *exponential changes in the local charges* [in line with (2.25)]. This temporal behaviour and presence of currents is determined through the indicated time constant τ of the body (compare Kaniusas (2012, Fig. 2.8c)).

The *isolated conductive body* in Fig. 2.25a has the *potential* φ_1 while the inequality $\varphi_2 > \varphi_1 > \varphi_0$ applies; consequently, the equipotential surfaces are dispersed (widened) at the location of the conductive body (compare Figs. 2.49 and 2.52). It can be observed in Fig. 2.25a that *equipotential surfaces* are always *perpendicular to the electric field* lines passing through these surfaces; compare Fig. 2.26, (2.28), and Kaniusas (2012, Footnote 26). The *boundary of the conductive body* also comprises an *equipotential surface*, so that the *electric field* lines enter the body with an angle *perpendicular to the body surface*. Likewise, the *tangential component of the electric field* right at the boundary of the *currentless and conductive body* is always zero,[56] which, in fact, results from *boundary conditions* [compare (2.96) and (2.106)].

Electrical Point Effect

Moreover, the *electric field lines become dense* in the air regions close to the accumulated surface charges, i.e., to the left and right of the conductive body in Fig. 2.25a. This means that the magnitude of the *effective* $\vec{E}$ in these air regions is increased[57] related to other regions outside the body, e.g., related to above and below the conductive body as shown in Fig. 2.25a. Figure 2.25b demonstrates the geometric superposition of the external field $\vec{E}_{\text{ext}}$ and the induced *opposing field* $\vec{E}_{\text{i}}$ (due to induced surface charges) that yields the effective $\vec{E}$ at the highlighted regions A, B, and C located inside and outside of the conductive body. Likewise, the local concentration of $\vec{E}$ lines outside the body, i.e., the local magnitude of $\vec{E}$, increases with increasing local *surface curvature* of the conductive body, such as of the human head; compare Fig. 2.51. Obviously, the *conductive body* (with its induced surface charges) *perturbs the external field* $\vec{E}_{\text{ext}}$ only in the close vicinity of

[56]Since the *boundary conditions* require the *tangential component* of the electric field to be continuous (2.96) and the electric field inside the *currentless and conductive body* is zero, it follows that the tangential component of the electric field at the surface of an *isolated and thus currentless conductive body* (i.e., right outside the body surface) must also be zero. Likewise, the electric field—if any—at the outer boundary of the *isolated conductive body* must be everywhere *normal to this boundary*, as illustrated in Figs. 2.25 and 2.26a.

On the other hand, the *electric field* inside an *ideally conductive body* with its *infinite conductivity* [$\gamma \to \infty$ in (2.54)] must always be zero because otherwise the *conductive current density* within the body would be infinite given a *finite electric field* within the body, which is not possible.

[57]It is interesting to note that the *maximum electric field* on the surface of an uncharged and *conductive spherical body* amounts to $3 \cdot E_{\text{ext}}$ with E_{ext} as the strength of the (otherwise homogenous) external field $\vec{E}_{\text{ext}}$, which comprises the *electrical point effect* (see text). The location of the maximum electric field is the point on the curved surface facing directly the source (or sink) of the electric field; comparable with the region B in Fig. 2.25a (with $\gamma_{\text{body}} / \gamma_{\text{air}} \gg 1$) or with top and bottom regions of the body insert in Fig. 2.49a.

In comparison with the spherical body, an uncharged and *conductive cylindrical body* yields the maximum electric field of only $2 \cdot E_{\text{ext}}$ on its outer surface facing normally the ambient electric field.

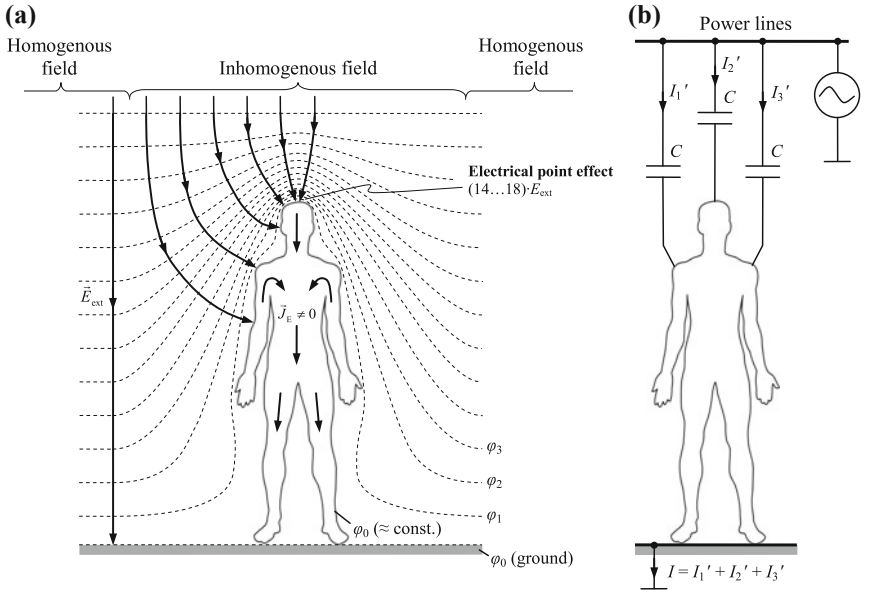

Fig. 2.26 Electrical point effect of the conductive and grounded human body in an external electric field $\vec{E}_{ext}$ along with the induced electric current density $\vec{J}_E$ in the body. **a** The field lines of $\vec{E}_{ext}$ and equipotential surfaces of the electric potential φ are indicated ($\varphi_{k+1} > \varphi_k$ and $\varphi_{k+1} - \varphi_k = \varphi_k - \varphi_{k-1}$ with k as the index); compare Fig. 2.25. The time-varying $\vec{E}_{ext}$ induces conductive currents with the density $\vec{J}_E$ within the body (Fig. 2.29), whereas all induced currents sum up to the total current I leaving the body through the feet. The potential step within the body is non-zero (due to inner $\vec{J}_E \neq \vec{0}$ within the body) but is much smaller than within the air (due to isolating air in comparison with conductive body) so that the body potential is approximated by φ_0. **b** The conceptual model of the grounded body in the external electric field generated by ambient power lines; compare Fig. 2.27. The body is virtually connected via the capacitances C to the power line, whereas the total current I equals to $I_1' + I_2' + I_3'$

the body. It should be emphasised that the field lines of the current density are aligned with those of the electric field (2.54), provided that the affected media (air and conductive body) are isotropic.

Figure 2.26a demonstrates electric field lines and equipotential surfaces (surfaces of a constant potential) when a *grounded human* stands in an *ambient electric field* $\vec{E}_{ext}$. As already noted, the human body can be approximated as a (non-ideally) *conductive body in the electric field*, whereas the potential of this grounded body equals the ground potential. In analogy with Fig. 2.25a (see the region B), *electric field lines become dense* and crowded in *the head region*—a *curved region* with non-zero *surface charge* and with only *normal components of the electric field* present on the air/head boundary (Footnote 56)—so that locally *increased magnitude of the resulting* $\vec{E}$ arises here; compare Footnote 57. It turns out that the

maximum $\vec{E}$ *above the head* amounts in its magnitude to $14 \cdot E_{\text{ext}}$ up to $18 \cdot E_{\text{ext}}$ of the (homogenous) unperturbed $\vec{E}_{\text{ext}}$ with its magnitude E_{ext} when the oscillating $\vec{E}_{\text{ext}}$ with the frequency of 50–60 Hz is considered (ILO 1994; CRP 1997; Heinrich 2015); see Fig. 2.26.

This effect of the locally increased magnitude of the resulting $\vec{E}$—in general, at *conducting sharp corners*, points, or edges—is known as the *electrical point effect*[58] or *hot spot effect*; see numerous examples in Sect. 2.3.2.3. The increased and focussed $\vec{E}$ on geometrical inhomogeneities increases also the associated local *current density field* (2.54). In particular, low frequency fields with the wavelength larger than the object size focus themselves on metallic corners. The presence of the normal component of $\vec{E}$ on conductive and isolated surfaces (Footnote 56) supports the existence of non-uniform electric fields around curved metallic isolated objects.

Obviously, this *manifold electric field* just *outside the head* implies manifold strength of the induced internal electric field *within the head*; see boundary conditions from Sect. 2.3.2.2 and Fig. 2.30. For instance, the numerical example in Fig. 2.52b illustrates that the increased field strength outside the spherical body by the factor 2.4 increases the inner field in the body by 2.4 to 237 V/m, as related to only 1000 V/m / 10 = 100 V/m without considering the electrical point effect.

---

[58]Instructive insights into the *increased electric field magnitude* E_{r} just outside of *conducting corners, points* or *edges* are given by a *spherical capacitor*. The capacitor is composed out of an *inner conductive sphere* with the radius r_1 and an excess charge Q on the surface of this sphere and, on the other hand, a concentric *outer conductive shell* with the inner radius r_2 and $-Q$ on the inner surface of the shell (compare Fig. 2.8).

The *electric field* $\vec{E}$ in-between both conductors in the radial range $r_1 \leq r \leq r_2$ and the *voltage drop* U from the inner conductor to the outer conductor equals

$$\vec{E} = E_{\text{r}} \cdot \vec{e}_{\text{r}} = \frac{Q}{4\pi \cdot \varepsilon} \cdot \frac{1}{r^2} \cdot \vec{e}_{\text{r}} \quad \text{and} \quad U = \frac{Q}{4\pi \cdot \varepsilon} \cdot \left(\frac{1}{r_1} - \frac{1}{r_2} \right),$$

respectively (compare Footnote 17 in Chap. 3). Here ε is the *dielectric permittivity* of the medium between the sphere and the shell and $\vec{e}_{\text{r}}$ a unit vector in the radial direction.

If we assume that the outer *shell is far away from the sphere* (with $r_2 \gg r_1$), the resulting arrangement resembles a single small sphere embedded in a large medium. Here the sphere's U is related to a *distant conductor* far away from this sphere. Under this assumption, the *magnitude* E_{r} *at the surface of the sphere* results as an *instructive function of* U *and* r_1 according to

$$E_{\text{r}} = \frac{U}{r_1}.$$

In other words, a conducting *sharp corner or edge* can be approximated as a *sphere surface of a small radius* r_1, whereas the *resulting* E_{r} *on the corner or edge* can then be estimated by the latter equation. The smaller this r_1, the less is the influence of the other large *distant conductor* (former shell before the approximation) on the size of E_{r} and, on the other hand, the larger is E_{r} in close proximity to the corner or edge. Please note that the electric field concentrates around the corner or edge due to decaying E_{r} with $1/r^2$ (see above).

Exposed Human Body

As illustrated in Fig. 2.26a, the resulting *field lines of* $\vec{E}$ *are perpendicular to the body surface* (i.e., perpendicular to the conductor surface, Sect. 2.3.2.2) while most of field lines enter the body in the region of the *head and shoulders* (see below). In fact, field lines which enter the body signify the non-zero *current density* in the body (2.54), i.e., the *induced current* in the *grounded body* flows towards the ground (Fig. 2.26a). In other words, the current prefers the *conductive body* as its pathway over the *non-conductive air* so that the external $\vec{E}_{\text{ext}}$ lines (and current lines) enter preferably the upper human body in the region of the head and shoulders. Likewise, mainly *displacement currents* in the air [predominant dielectric medium, see (2.72)] enter the body and then propagate as *conductive currents* through the conductive body [predominant conductive medium, see (2.71)] towards the ground.

Figure 2.26b demonstrates the corresponding *conceptual model* of the *grounded body* in the ambient $\vec{E}_{\text{ext}}$ generated by ambient power lines. The grounded body is coupled to the electric field in proportion to the body's *capacitance to the power line* (i.e., to the voltage source with a low output impedance). Simply speaking, the greater this capacitance, the greater is the *current flow* into the body. This *capacitance* and, thus, this *current flow* in the body, *decrease*

- for increasing *distance to the power line* (in analogy with increasing d in (2.41) and increasing capacitive impedance (2.42), see Fig. 2.8) and
- for decreasing *surface area of the body skin* which faces the power line (in analogy with decreasing A in (2.41) and increasing capacitive impedance (2.42), see Fig. 2.8).

In fact, this capacitance depends on the size, shape, and the orientation of the body in the ambient $\vec{E}_{\text{ext}}$ (see below). Since field lines of $\vec{E}$ enter the body all along its surface (Fig. 2.26a), multiple capacitors connecting the body and the power line can be assumed as a model, see Fig. 2.26b. Consequently, all *currents* through these capacitors *sum up* in the region of the bottom of the *grounded feet* and then enter the ground line.

Interestingly, for a given external $\vec{E}_{\text{ext}}$ *in parallel to the long axis of the body*, the strongest electric and current density fields are induced in the human body when the *body is grounded* through the feet (ICNIRP 2010; Reilly 1998). There is a low-resistance electrical contact between the feet and the ground (Fig. 2.26). On the contrary, the weakest fields are induced when the *body is insulated* from the ground.

In particular, Fig. 2.27 compares qualitatively the *grounded body* (e.g., the barefoot person standing in wet grass) and the *ungrounded body* (e.g., the person standing on a dry surface) in terms of the induced currents in the body. Once more, the resulting $\vec{E}$ *field lines* enter almost the whole *grounded body* standing upright (Fig. 2.27a). Therefore the amount of the current passing through any given

horizontal cross-section of the body—see the indicated current I_X and the corresponding cross-section in Fig. 2.27a—increases when the cross-section moves from the head (upper body region) to the feet (lower body region) along inner field lines of $\vec{E}$. The *maximum current* results at the *point of the ground contact* (e.g., bare feet or a hand grasping an earthed pole), also known as *short-circuit current*.[59] In Fig. 2.27a, this maximum current I_1 passes out mainly through the *bottoms of the feet* and may result in a perceptible electric shock. In fact, this maximum current is the sum of all *displacement currents* accumulated over the *skin surface* or, to be more precise, is the product of the (average) displacement current density and the (average) surface area of the body (2.23). However, the current density distribution over the skin is highly inhomogeneous (see below). The subfigure in Fig. 2.27a reveals the current strength passing through the *body cross-section*[60] at the particular body height or, in other words, reveals the increase in the current towards the feet as related to the fractional body height. The *slope* of this experimentally determined curve confirms again that most of the current enters the body in the upper region of the *head and shoulders*, whereas most of the current leaves the body through *feet*; compare Fig. 2.51.

If the conductive *body is ungrounded*, the situation significantly changes. That is, if the body is situated above the ground in a vertically oriented electric field (Fig. 2.27b), the resulting $\vec{E}$ *field lines* enter the upper body (through the *head and shoulders*) and leave from the lower body (through the *legs and feet*). The current in the body becomes *maximum at the midsection of the body*, contrary to the grounded body; see the maximum current I_2 in Fig. 2.27b. Consequently, the current goes to zero in the upper region of the head and the lower region of the feet. The inequality $I_2 < I_1$ applies because the ambient electric field lines enter and leave the

[59]In fact, the *short-circuit current* I_1 to ground for a *grounded person* amounts to Reilly (1998)

$$I_1 = 9 \cdot 10^{-11} \cdot l^2 \cdot f \cdot E_{\text{ext}} \cdot 1 \frac{\text{A} \cdot \text{s}}{\text{V} \cdot \text{m}},$$

where l is the *height of the person* (Fig. 2.27a). The above expression results from theoretical approach to an upright cylinder with its *height-to-radius ratio* of 12 located in the electric field which is directed along the axis of the cylinder.

That is, the maximum current I_1 increases disproportionately with l, i.e., with increasing surface area of the body and thus with increasing area for the coupling of the ambient electric field into the body. On the other hand, increasing *field frequency f* increases displacement currents in the air. In terms of the model in Fig. 2.27a, the capacitance C_1 increases with increasing l^2 (2.41), whereas the magnitude of the capacitive impedance in the air [=1/(2π · f · C_1), see (2.42) and Kaniusas (2012, Footnote 33)] decreases with increasing C_1 and increasing f.

To give a *quantitative example*, an ambient field of 5 kV/m at 50 Hz (compare Footnote 80 and Fig. 2.87) would yield the current I_1 of about 0.07 mA for a typical body height of 1.8 m.

[60]The *current distribution* from Fig. 2.27 can be used to calculate the *distribution of* P_{SAR} [according to (2.57)] along the axis of the body provided that areas of cross-sections and tissue conductivities are known. This calculus assumes also that the wavelength of the electric field—the human body is exposed to—is large compared with the body size; see Section "Incident Electromagnetic Fields".

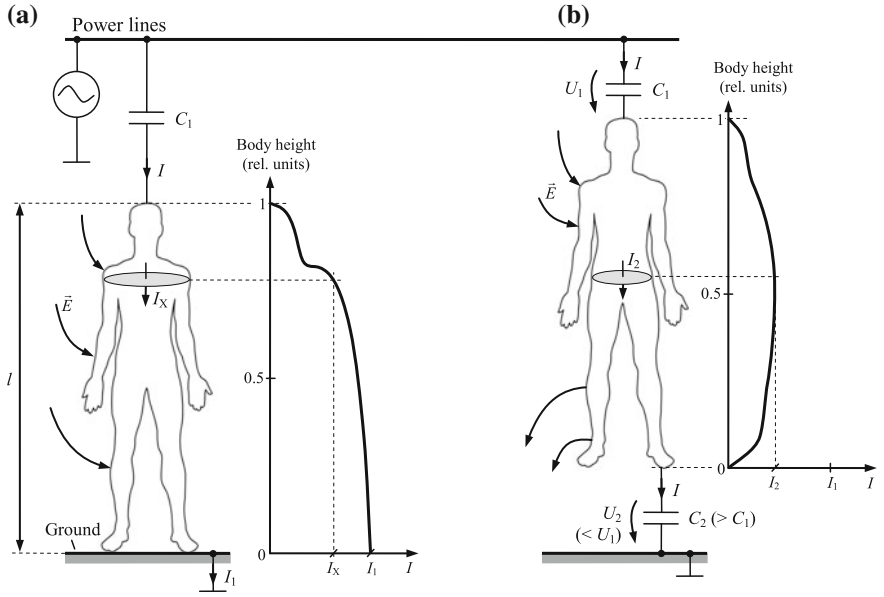

Fig. 2.27 Induction of the electric field and current I in the body standing upright in a vertically oriented electric field $\vec{E}$ (as generated by ambient power lines); compare Fig. 2.26b. **a** The conceptual model of the grounded body connected via the capacitance C_1 to the power line, with the greatest current I_1 passing through the bottoms of the feet; compare Figs. 2.26b and 3.26. **b** Ungrounded body with the capacitances to the power line and the ground. Because of $C_2 > C_1$, the voltage divider places the body potential more close to the ground than to the potential of the power line (with voltage amplitudes $U_2 < U_1$). The greatest current I_2 ($<I_1$) passes through the midsection of the body; compare Fig. 2.51. Subfigures to the left indicate the size of I as a function of the fractional body height, with experimental data adopted from Reilly (1998)

ungrounded body (Fig. 2.27b), whereas the field lines only enter the grounded body (Fig. 2.27a).

When the human body resides in an ambient $\vec{E}_{\text{ext}}$, especially when the *body is grounded* (Fig. 2.26), the *total current* flowing through the body (I_X or I_1 in Fig. 2.27a) is strongly determined by

- *field parameters* (exposure conditions) and
- *geometric properties* of the body, namely, the body size, shape, and posture,

rather than tissue conductivity (ICNIRP 2010). Obviously, the induced internal field strength as well as the resulting total current (2.23) increase in direct proportion to the

outer field strength E_{ext}. Induced currents, electric and current density fields[61] in tissue also increase in *direct proportion* to the *field frequency*[62] for a given E_{ext}, especially for field frequencies below about 10 MHz (ICNIRP 1998; WHO 1993). That is, the latter proportion applies as long as the field frequency remains *below whole-body and partial-body resonances*; compare with the frequency behaviour of P_{SAR} (2.58) in Fig. 2.33. This proportion is based mainly on the *capacitive impedance* of the air, which decreases with increasing frequency [Footnote 59 and (2.42)] and thus more $\vec{E}$ lines enter the body; compare with the discussion related to (2.121). As a minor effect contributing to decreased inner electric fields (2.122), it should be mentioned that the *effective conductivity* γ_{eff} in tissue rises with increasing field frequency (Fig. 2.21). In addition, a reduced amount of the induced *surface charges* can be expected with increasing *field frequency* because of inert movements of charges (ions) towards the body surface (see Fig. 2.25 and Footnote 78). In that regard, the reduced charge necessarily implies reduced currents in the body for their discharge (see below).

All three geometric properties (body size, shape, and posture) govern the spatial extension of the conductive body in the direction of the ambient $\vec{E}_{ext}$. That is, the *upright posture*—exposed to $\vec{E}_{ext}$ perpendicular to the ground, see Figs. 2.26 and 2.27a—constitutes rather a *worst-case scenario* in terms of a relatively *strong total current* (at the point of the ground contact). The associated *effective height* l in Footnote 59 is relatively large. This is in contrast to the *lying posture* where the body extends over only a few equipotential surfaces along $\vec{E}_{ext}$ and the resulting *total current is relatively weak*; i.e., the *effective height* l is relatively small. Obviously, the effective distribution of inner currents passing through various organs and tissues within the body depends on the respective conductivities (2.54); compare Fig. 2.35 and Footnote 32.

Distribution of Current Density

Since the *current density* (but not the current, such as I_1 or I_2 in Fig. 2.27) is a useful quantity to assess quantitatively stimulation and thermal effects

---

[61]The magnitude J_E of the *induced current density* $\vec{J}_E$ in the bodily tissue in response to the *external field* $\vec{E}_{ext}$ at *frequency* f can be approximated as (WHO 1993)

$$J_E = c \cdot f \cdot E_{ext};$$

compare (2.122). Here c is a constant which depends on the body orientation in the field (i.e., on the coupling geometry, see Fig. 2.30) and on the body part considered (i.e., on its local conductivity). For instance, the constant c amounts to about $3 \cdot 10^{-9}$ S/(Hz · m) for the cardiac region and head, whereas c increases generally for the upright posture in the ambient electric field perpendicular to the ground (i.e., *worst-case coupling*, see text). The above equation also discloses the relationship between outer and inner electric fields; compare with *attenuation factors* out of boundary conditions (Sect. 2.3.2.2).

[62]For instance, in order to induce a *current density* of 2 mA/m^2 in the body, a time-varying external *electric field* of 5 kV/m is needed at the field frequency of *50 Hz*, whereas a threefold strength of 15 kV/m is needed at *one third of 50 Hz* (≈17 Hz) to induce the same current density (CRP 1997); compare Footnote 112 and Fig. 2.87.

(Sect. 2.3.2.4), it should be stressed that the *current density* in the body depends not only on

- the *current* itself but also on
- the *effective area* of the cross-section perpendicular to the current flow (2.23).

That is, increasing area (e.g., in the height of the chest) would reduce the local current density (2.36). In analogy, *highest current densities* arise in the bony regions of the *ankle and knee* (Reilly 1998) for the grounded body. This is because there is a *small cross-section* of conductive material since bone does not conduct much (Table 2.2) while a *large current* passes through (Fig. 2.27a); compare Fig. 2.57. For instance, the peak P_{SAR} (2.58) was reported to occur—as expected—in muscles and blood vessels of the ankle (WHO 1993).

On the other hand, the *distribution of the conductive current density* $\vec{J}_E$—e.g., within a tissue section between two electrodes carrying a certain current—depends on the local *distribution of the tissue conductivity* γ_{eff}. That is, the higher is the local γ_{eff} of an embedded organ considered such as muscle, the higher is the resulting local $\vec{J}_E$. In analogy, regions of *low* γ_{eff} such as fat layers or bony regions show lower $\vec{J}_E$ (Fig. 2.35). The current will tend to flow through tissues of *high* γ_{eff} such as blood accumulation or muscle (preferentially along muscle fibers due to their *anisotropy*, see Footnote 30) and around tissues of *weak* γ_{eff} such as bone, fat, and lung (Fig. 2.31c). The resulting dispersing field lines of $\vec{J}_E$ field are illustrated in Fig. 2.52b, c for conductive and isolating insets. The current always follows the path of least impedance that is not necessarily a straight-line path (Figs. 2.13c and 2.54). Therefore, the highly *heterogeneous human body*—as illustrated in Fig. 2.28 for a cross-section of the thorax at the level of the heart—with a highly *non-uniform composition* out of tissues with different electrical properties necessarily yields a highly *non-uniform distribution of* $\vec{J}_E$.

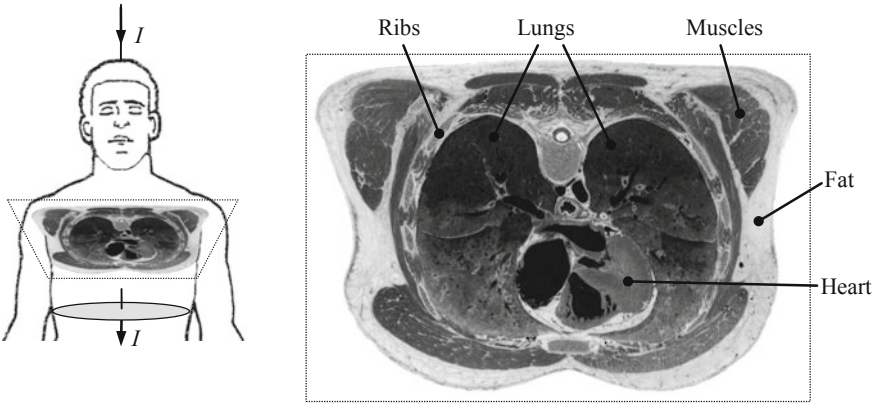

Fig. 2.28 Heterogeneous composition of bodily tissues, as faced by the current *I* flowing along the long axis of the body; compare Fig. 2.27. A cross-section of the thorax at the level of the heart illustrates its highly non-uniform composition out of lung, muscle, fat, and bone tissues, as well as air and blood. Photographic image is taken from Bulling (1997)

The *effective* γ_{eff} of tissue is a strong function of the *field frequency* (Figs. 2.20 and 2.21). Since *electrical properties of tissues* match more closely for higher frequencies, the *distribution* of $\vec{J}_{\text{E}}$ progressively *becomes uniform* with *increasing frequency*.

Surface Charges and Currents

It can be expected that

- equal *surface charges of opposite polarity*—with a *zero net surface charge* in the body—are induced in the *isolated conductive body* subjected to ambient $\vec{E}_{\text{ext}}$; compare Figs. 2.25a, 2.27b, and Fig. 2.29. In contrast,
- a *non-zero net surface charge* is induced in the *grounded conductive body*. For instance, a negative charge is induced in the grounded body in proportion to C_1 at the time instant when the power line has a positive potential (Fig. 2.27a); as if this body would represent one of the two conducting plates of a plate capacitor (i.e., with C_1 in Fig. 2.27a).

As already discussed, the induced opposite charges in the *ungrounded body* generate their inner electric field $\vec{E}_{\text{i}}$ which opposes the external $\vec{E}_{\text{ext}}$ (Fig. 2.25a) and

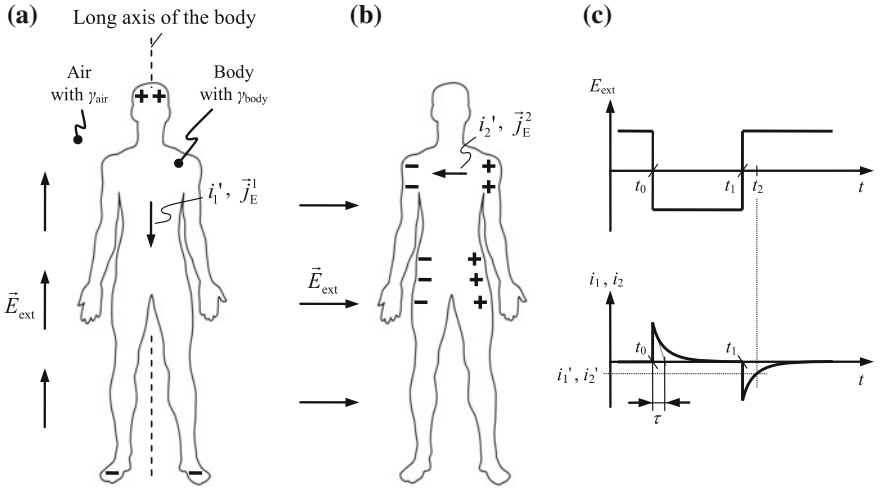

Fig. 2.29 Effects of the position of the human body (with the electrical conductivity γ_{body}) in the ambient time-varying electric field $\vec{E}_{\text{ext}}$ in the air (with $\gamma_{\text{air}} \ll \gamma_{\text{body}}$, see Table 2.2) on the induced surface charges, conductive currents i, and conductive current density $\vec{j}_{\text{E}}$ within the body; compare Figs. 2.25, 2.49, and 2.51 for detailed distributions of inner and outer electric fields. **a** The alternating incident field $\vec{E}_{\text{ext}}$ in parallel to the long axis of the body yields relatively small surface charge, low rate of its change, and thus relatively weak current i_1' ($<i_2'$). However, the inequality of amplitudes $j_{\text{E}}^1 > j_{\text{E}}^2$ possibly applies due to smaller cross-sections in (**a**) than (**b**) the inner currents pass through. **b** The alternating incident field $\vec{E}_{\text{ext}}$ perpendicular to the long axis of the body with the relatively strong i_2'. **c** Qualitative time courses of the magnitude E_{ext} and $i(t)$ are given under the assumption of a rectangular waveform of $\vec{E}_{\text{ext}}$ field and a relaxation time constant τ

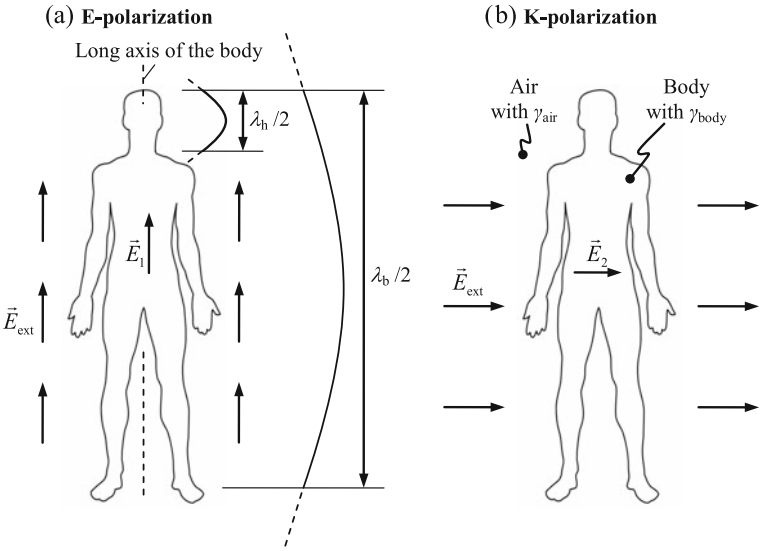

Fig. 2.30 Effects of the position of the human body (with the electrical conductivity γ_{body}) in the ambient external electric field $\vec{E}_{ext}$ in the air (with $\gamma_{air} \ll \gamma_{body}$, see Table 2.2) on the induced field $\vec{E}$ within the body. **a** The incident field $\vec{E}_{ext}$ in parallel to the long axis of the body yields relatively large internal $\vec{E}$ directed along the long axis (with magnitudes $E_1 > E_2$); compare Fig. 2.49 and consult Footnote 75 for field polarizations. The whole-body resonance (ungrounded body) with the resulting wavelength λ_b and the resonance of the head only with λ_h are indicated ($\lambda_b > \lambda_h$). **b** The incident field $\vec{E}_{ext}$ perpendicular to the long axis of the body; compare Fig. 2.50

thus reduces effectively the resulting electric field $\vec{E}$ within the body. According to (2.85), the magnitude of $\vec{E}$ equals $E_{ext} - E_i$, as an approximation for tangential field components on the body surface (see discussions related to Fig. 2.30).

The *human body* significantly perturbs the *spatial distribution* of the static and time-varying *electric field* external to the body. As illustrated in Fig. 2.26 (and Fig. 2.25a), in the region close to the body an *inhomogeneous field* results with perturbed both electric field lines and equipotential surfaces (2.28). This is in contrast to the *static magnetic field* and to the *time-varying magnetic field of low frequency*, which are not perturbed by the human body residing in this field. In fact, there is no perturbation as long as the resulting skin depth (2.88) is much larger than body dimensions so that the magnetic field permeates the body without changes.

If a *human body* is considered within the external $\vec{E}_{ext}$ then the sign, size, and local density of the induced *surface charge* depend greatly on the *size, shape, and even the position of the exposed body* with respect to the directional vector field

$\vec{E}_{ext}$. Figure 2.29 illustrates the strong dependence of the *distribution of charges* on the *position of the human body* in $\vec{E}_{ext}$. The field $\vec{E}_{ext}$ parallel to the long axis of the body (Fig. 2.29a) induces fewer charges in comparison with the field perpendicular to the long axis (Fig. 2.29b). This is because of the *varying face area* for the surface charge accumulation. Namely, the face area of the body in its sagittal plane (Fig. 2.29b) or frontal plane is much larger than that in the body's transverse plane (Fig. 2.29a).

It should be noted that the *sign and size of induced surface charges* on the conductive body (Fig. 2.25a) vary in synchrony with the *alternating* $\vec{E}_{ext}$. This *continuous redistribution of charges* (in their position) on the surface of the body results in *alternating electric currents* $i(t)$ inside the body. In other words, these *alternating currents* account for temporal *changes of the surface charge* provided that the external $\vec{E}_{ext}$ varies in time. It should be recalled that the current amplitude is defined as the rate at which the charge changes (2.25). In fact, the *induced current between surfaces with opposite charges* reduces the charge on the one side—i.e., reduces the positive charge upwards the current flow—while the charge is accumulated on the other side—i.e., the positive charge is accumulated downwards the current flow. As shown in Fig. 2.29a, the non-zero *conductive current* i_1' at the selected time instance t_2 (i.e., $t_2 - t_1 < \tau$ in Fig. 2.29c so that $i_1' \neq 0$) reduces the positive charge in the head while this current i_1' increases the positive charge in feet (or, in analogy, decreases here the negative charge). In analogy to Fig. 2.29a, the non-zero i_2' at t_2 in Fig. 2.29b determines the rate of the charge change on the left and right sides of the body.

It can be expected that the resulting amplitude of the *alternating current in the body* depends also on the *position of the body* in the external field; compare with other effects of the body position from Figs. 2.30 and 2.32. That is, the induced current is stronger for the alternating $\vec{E}_{ext}$ field perpendicular to the long axis of the body (Fig. 2.29b) in comparison with the same $\vec{E}_{ext}$ field parallel to the long axis (Fig. 2.29a). This is because more charges are induced in the former case than in the latter case. Consequently, the *inequality* $i_1' < i_2'$ applies for currents (at t_2 in Fig. 2.29c) as well as for the associated current amplitudes if a sinusoidal $\vec{E}_{ext}$ is applied.

However, the situation for the instantaneous *conductive current density* $\vec{j}_E(t)$ in the body differs completely from that of the instantaneous *current amplitudes* $i(t)$ if both body positions from Fig. 2.29a, b are compared. In fact, the direction of $i(t)$ in the body differs for both body positions and thus the resulting $\vec{j}_E(t)$ *varies inversely* in its amplitude $j_E(t)$ with the *cross-section area* of the body region which is crossed by $i(t)$. The *maximum local* $j_E(t)$ can be expected for *narrow regions* of the body, such as the neck or ankles (ICNIRP 1998); compare (2.23) and Fig. 2.57. Therefore, induced $i(t)$ along the long axis of the body, e.g., currents crossing the *neck and ankles* with $\vec{E}_{ext}$ field parallel to the long axis (Fig. 2.29a), tend to produce

local peaks in $j_E(t)$.[63] In other words, although $i_1' < i_2'$ applies in Fig. 2.29a, b for the time instant t_2, the reverse *inequality* $j_E^1 > j_E^2$ may apply in certain local regions with small cross-section areas. Provided that conductive regions of the body are highly heterogeneously distributed in the body, a highly *non-uniform distribution of local currents*—i.e., a highly non-uniform $\vec{j}_E(t)$—can be expected inside the body.

Figure 2.29c depicts the schematic *time course* of the magnitude E_{ext} of $\vec{E}_{ext}$ and the corresponding course of $i(t)$ in the body to account only for changes in the induced surface charge. In fact, the *relaxation of surface charges* takes place with a certain *relaxation time constant* τ which is small in highly conductive bodies and large in less conductive bodies (2.49); see Footnote 55. The current $i(t)$ peaks when $\vec{E}_{ext}$ reverses its polarity and thus the sign of the induced surface charge has to reverse. With the progressing charge reversal, the size of $i(t)$—carrying unbound charges—decreases *exponentially*. As already noted, *displacement currents* (2.66) flow outside the body while *conductive currents* (2.54) dominate in the conductive human body (inverse capacitor) under the application of the alternating external $\vec{E}_{ext}$ (Fig. 2.29a).

Please note that grounded or ungrounded (isolated) *conductive human body—charged* due to its presence within the static electric field, as illustrated in Fig. 2.27—may be *discharged through physical contact* with other *charged conducting objects* (e.g., exposed to the same electric field) but residing at a *different electric potential*, as shown in Fig. 2.86a. This discharge process may yield substantial *contact currents* in the contact region of the body, which also implies non-zero *inner currents* within the body. In particular, the discharge occurs when

- the *ungrounded human body* at a non-zero potential touches a *grounded object* at zero potential; likewise, the discharge follows when
- the *grounded human body* at zero potential touches an *ungrounded object* at a non-zero potential. For instance, Fig. 2.86a illustrates the potential φ_G of the grounded body and another potential φ_B ($>\varphi_G$) of the ungrounded object leading to a non-zero contact current through the body.

as elaborated in Footnote 116 in detail. Obviously, such inner currents within the body can influence the proper function of *medical implants*.

Orientation of the Human Body

Another interesting phenomenon of the electrobiological interaction is illustrated in Fig. 2.30. In fact, the *orientation of the human body* and its *slenderness* with respect to the external electromagnetic field (in the air) influences strongly the induced

[63] For instance, the exposure with E_{ext} = *5 kV/m* at 50 Hz *parallel to the long axis of the body* (Fig. 2.29a) induces the current density of about *2 mA/m²* in the *neck* (ICNIRP 1998), i.e., in the narrow cross-section of the body downwards the current flow (Footnote 62). It should be noted that this level of E_{ext} and that of the current density still comply with the corresponding *reference level* and the corresponding *basic restriction*, respectively, for the general public exposure (Fig. 2.87).

electric field in the body, the *induced field which is constant throughout the interior* of the assumed homogenous body (Fig. 2.49).

When the *long axis of the body* is parallel to the *external electric field vector* $\vec{E}_{ext}$ with the magnitude E_{ext}, the induced *internal electric field* $\vec{E}_1$ is relatively strong (Fig. 2.30a). In contrast, the same external $\vec{E}_{ext}$ perpendicular to the long axis causes a weaker internal electric field $\vec{E}_2$ (Fig. 2.30b); i.e., the incident *undisturbed* $\vec{E}_{ext}$ is identical in both cases and only its direction varies. Consequently, the induced *internal* $\vec{E}_1$ along the long axis of the body (i.e., with its magnitude E_1 in Fig. 2.30a) is much stronger[64] than the induced $\vec{E}_2$ perpendicular to the long axis (with its magnitude E_2 in Fig. 2.30b); see Figs. 2.49 and 2.50.

Boundary conditions (Fig. 2.36) and *charge accumulation* (Figs. 2.25 and 2.29) account for this *inequality* $E_1 > E_2$:

- Namely, the incident $\vec{E}_{ext}$ in Fig. 2.30a is *mostly tangential* to the body surface over a large portion of the body surface. Thus the *condition for tangential components* of the electric field (2.96) applies and forces the *continuity of the electric field* entering tissue over a large portion of the body surface with $E_1 \approx E_{ext}'$, i.e., directly at the charge-free boundary (Fig. 2.36). It is important to note that the magnitude E_{ext}' of the *effective electric field just outside the body surface* is less than E_{ext} ($>E_{ext}'$) of the undisturbed $\vec{E}_{ext}$. This is because the accumulated surface charges create their own electric field which opposes the incident and undisturbed $\vec{E}_{ext}$, as illustrated in the region C in Fig. 2.25. Consequently, both the phenomenon of *opposing fields* and the condition for tangential components yield the inequality $E_1 < E_{ext}$. In general terms, the *tangential coupling* of the incident $\vec{E}_{ext}$ (Fig. 2.30a) yields a relatively *high internal* $\vec{E}_1$.
- In contrast, the incident $\vec{E}_{ext}$ in Fig. 2.30b is *mostly normal* to the body surface over a large portion of the body surface. Thus the *condition for normal components* of the electric field (2.104) applies and forces the *discontinuity of the*

[64] A *quantitative idea* about the effects of the position of the body with respect to the direction of the incident electric field can be provided by a *prolate spheroid* (Furse 2009); see Figs. 2.49 and 2.50. In fact, internal electric fields in two *spheroids* can be compared, i.e., in spheroids *orientated differently* with respect to the external time-varying electric field. The *prolate spheroid* (with the ratio 6.3 of its long axis to short axis) resembles *elongated body shape* and shows electrical properties of the (average) tissue in the body (Table 2.2). It turns out that the ratio of the internal to incident electric field (at the field frequency of 60 Hz) in the case of the body (spheroid) orientation shown in Fig. 2.30a is more then *14 times greater* than in the case of the body (spheroid) orientation shown in Fig. 2.30b, even though body dimensions (spheroid dimensions) are the same (Furse 2009). Thus, the approximation $E_1 \approx 14 \cdot E_2$ applies in Fig. 2.30 provided that the magnitude E_{ext} of the incident field is identical for both orientations of the body. The *relatively low frequency* (60 Hz) of the electric field indicates that mainly *conductivity of the spheroid determines the size of the internal field*; compare (2.122). The resulting inner field in the *prolate spheroid* depends—generally speaking—not only on its *orientation* within the incident field but also on its *axial ratio*.

electric field entering tissue over a large portion of the body surface to $\vec{E}_2$ disadvantage. Directly at the charged boundary, the boundary condition requires $E_2 \approx E_{ext} \cdot \gamma_{air}/\gamma_{body} \ll E_{ext}$ due to the inequality $\gamma_{air} \ll \gamma_{body}$ (Table 2.2). In general terms, the *normal coupling* of the incident $\vec{E}_{ext}$ (Fig. 2.30b) yields a relatively *low internal* $\vec{E}_2$.

The *accumulation of surface charges* takes place because of the interaction between a non-zero $\vec{E}_{ext}$ and conductive body, as illustrated in Figs. 2.25 and 2.29. Please recall that this accumulation tends to reduce the electric field inside the body. If the incident $\vec{E}_{ext}$ is oriented according to Fig. 2.29a, the face area of the body for the accumulation of surface charges is much smaller than that for the $\vec{E}_{ext}$ field orientation according to Fig. 2.29b. Consequently, fewer charges are accumulated in the case of Fig. 2.29a as related to Fig. 2.29b. The resulting and *counteracting inner field* due to these surface charges—corresponds to the inner field $\vec{E}_i$ from Fig. 2.25—is less pronounced in Fig. 2.30a than Fig. 2.30b. In other words, the resulting magnitude E_1 within the body (Fig. 2.30a) is less compensated/reduced by the induced inner field than the magnitude E_2 (Fig. 2.30b).

Once again, the *inequality* $E_1 > E_2$ applies in Fig. 2.30, which determines also that P_{SAR}—proportional to E^2 (2.58)—is larger for the external $\vec{E}_{ext}$ along the long axis of the body in comparison with the external $\vec{E}_{ext}$ perpendicular to the long axis (Fig. 2.33).

In light of the above, it should be stressed that induced *inner electric fields* in the body—as induced by *outer electric fields* the body is exposed to—depend on both

- *boundary conditions* for the fields to cross the body surface and
- induced *surface charges* with their own induced electric fields opposing outer fields.

Obviously, these conditions and charges are tightly interrelated with each other. To give a tangible example, if an *elongated body* is considered in an ambient electric field—such as the human body in Fig. 2.30—then all applicable boundary conditions should be fulfilled, including those for tangential and normal field components. At a first glance, it may appear confusing that *tangential coupling* yields a relatively high internal electric field while *normal coupling* yields a relatively low internal field. However, the *internal electric field* throughout the homogenous, non-currentless, and non-ideally conductive body is expected to be *constant* (Fig. 2.49). Induced surface charges generate opposing electric fields which reduce outer tangential fields close to the surface (the region C in Fig. 2.25b), in the course of which inner electric fields (i.e., fields coupled tangentially from outside across the body surface into the body) are reduced as well. That is, only the combination of both boundary conditions and surface charges provides a constant electric field throughout the volume of the conductive body.

Incident Magnetic Fields

In contrast to the static and time-varying *electric field* (Fig. 2.26), the external *static magnetic field* is *not perturbed*[65] by (spatially delimited) biological tissue. This is because magnetic properties of the air and tissues are the same, i.e., the magnetic permeability $\mu \approx \mu_0$ of the air equals that of tissues, whereas μ_0 is the permeability of free space (Footnote 17). Therefore, the time-constant magnetic field does not encounter any (magnetically relevant) boundary while entering and propagating through the non-magnetic human body.

However, the external *time-varying magnetic field*[66] with the magnitude B of the *magnetic flux density* $\vec{B}$ *induces the electric field* $\vec{E}$ *with the magnitude* E circulating around the magnetic field lines. The induced electric field generates its own magnetic field which superimposes the incident external magnetic field, so that the total time-varying magnetic field in the body region and around it *becomes perturbed* and displaced (see below). In fact, this induced *electric field* is subjected to *diverse interactions with tissue*, as already described in Section "Incident Electric Fields".

This phenomenon of the electric field induction is known as *electromagnetic induction* described by the *Maxwell-Faraday equation*[67]:

$$\vec{\nabla} \times \vec{E} = -\frac{\mathrm{d}\vec{B}}{\mathrm{d}t} \quad \text{or} \quad \int_{\partial A} \vec{E} \cdot \mathrm{d}\vec{l} = -\frac{\mathrm{d}}{\mathrm{d}t} \int_{A} \vec{B} \cdot \mathrm{d}\vec{A} \quad \text{or} \quad U(\partial A) = -\frac{\mathrm{d}(B \cdot A)}{\mathrm{d}t}. \tag{2.86}$$

- The above differential equation in the *local form* (on the left side with the curl as operator) assumes the *right-handed association* of the involved vector fields $\vec{E}$ and $-\mathrm{d}\vec{B}/\mathrm{d}t$. That is, as illustrated in Fig. 2.31, the actual association of the incident field $\vec{B}$ and the induced $\vec{E}$ is *left-handed* due to the minus sign in (2.86).

[65]The *static magnetic field* becomes *perturbed* in the regions of the metallic (ferromagnetic) *medical implants* within the body. In addition, *mechanical forces* arise on such implants, which should be limited to avoid malfunctioning of implants and tissue damage.

[66]For instance, the *time-varying magnetic field* $\vec{B}(t)$ is generated around a power line carrying a non-zero *alternating current* $i(t)$; see Fig. 2.8.

[67]Michael Faraday (1791–1867) was an English physicist and chemist who contributed greatly to the understanding of electromagnetism, induction, and electrochemistry. He formed the foundation of electric motors so that it was largely to his efforts that electricity became practical for human use.

James Clerk Maxwell (1831–1879) was a Scottish physicist best known for his formulation of classical electromagnetic theory which was also based on Faraday's observations. This theory was a unified model of electricity, magnetism, and light.

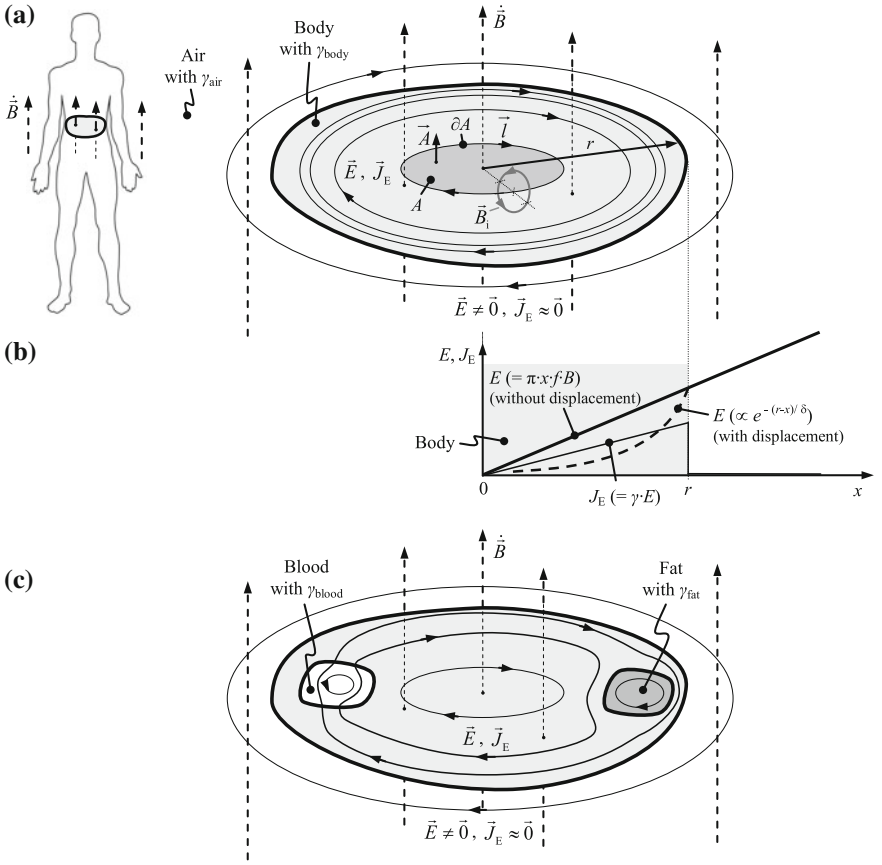

Fig. 2.31 Basic principle of electromagnetic induction in the conductive biological tissue surrounded by the air and exposed to a spatially-uniform time-varying magnetic field. **a** The incident field lines of the time-varying sinusoidal magnetic flux density $\vec{B}$ (i.e., the external field with $\dot{\vec{B}} = d\vec{B}/dt \neq \vec{0}$), the induced field lines of the electric field $\vec{E}$ [the induced field in line with (2.86)], and the resulting induced field lines of the conductive current density $\vec{J}_E$ [in line with (2.87)] in an (assumed) homogenous cross-section area of tissue. The area is delimited in space by the radius r. **b** Qualitative courses of the magnitudes E and J_E as a function of increasing distance x from the centre of the homogenous body. Solid lines refer to the induction only while the dashed line results from both the induction and magnetic field displacement towards the outer boundary of tissue. *c* A heterogeneous tissue delimited in space with the associated incident $\vec{B}$ field and the resulting $\vec{E}$, $\vec{J}_E$ fields; compare Fig. 2.59. For the electrical conductivities γ of the different media, the following inequality applies $\gamma_{blood} > \gamma_{body} > \gamma_{fat} > \gamma_{air}$; compare Table 2.2

- The *integral form* [in the middle of (2.86), compare (2.30)] illustrates that the line integral of the $\vec{E}$ field component in the direction $\vec{e}_l$ (with $d\vec{l} = dl \cdot \vec{e}_l$) of the border line (i.e., the integral of the tangential $\vec{E}$ field component) along the closed boundary ∂A of the surface with the area A (see Fig. 2.31a) equals the

negative rate of change of the surface integral of $\vec{B}$ field component *normal to the area A* (i.e., the integral of the normal $\vec{B}$ field component) along this surface A. In other words, the electromagnetic induction arrives at its maximum for the orientation of the incident $\vec{B}$ field *perpendicular* to the surface A, whereas the induced $\vec{E}$ field amounts to zero for a *parallel orientation* of $\vec{B}$ field and A. Thus the mutual *orientation angle* between $\vec{B}$ field and A is highly relevant.

- Finally, the *global form* of the equation in (2.86) (on the right side) illustrates that the induced voltage U along the boundary ∂A (Fig. 2.31a) equals the negative rate of change in the magnetic flux $B \cdot A$ *permeating perpendicularly this surface*, whereas the right-handed association between the voltage and flux is assumed here.

Therefore, the external time-varying magnetic field—but not the static magnetic field—manifests physically as induced *internal electric fields* in *tissue* or in *medical implants* if such are present. *Magnetic origin* leads to *electric consequences*. Please note that the relevant consequences (or interactions) between the internal electric field and the (predominantly) *conductive tissue* are already discussed within the scope of (2.54), Figs. 2.16a, and 2.25a. In analogy, the relevant consequences between the internal electric field and the (predominantly) *dielectric tissue* are discussed within the scope of Figs. 2.16b, c and 2.19. The (adverse) interactions of electric fields with *medical implants* are described in Section 2.3.2.5.

Thus, provided a *conductive body*—such as *biological tissue*—resides within the time-varying magnetic field, the *induced electric fields* in tissue are necessarily associated with the *electric current density* in this tissue. To be precise, the *tissue conductivity* γ governs the latter relationship (2.54); please note that lossy interactions in dielectrics are excluded when using γ only (see (2.82) for *lossy dielectric*). The resulting *electric currents* are known as *eddy currents*. Figure 2.31 shows the field lines of the *electric field and current density circulating in parallel*.

The magnitude of the *induced electric field* (and thus the magnitude of the *induced current density*) in any voluminous *tissue* (conductive and/or dielectric) is *proportional* to

- the *magnitude B* of the magnetic flux density [see $\vec{B}$ in (2.86)],
- the *rate of change* in the magnetic flux density [provided A is constant, see $\mathrm{d}/\mathrm{d}t$ in (2.86)], and
- the *cross-section area* of the body permeated by the magnetic flux, i.e., the *size of the exposed body* [see A in (2.86)].

Consequently, the induced electric fields are greatest when the time-varying magnetic field is aligned along the body's sagittal plane, e.g., aligned from the front to the back of the body crossing the relatively *large body surface* (in the body's frontal plane), and is perpendicular to the principal long body axis. In analogy, the induced electric fields are weakest when the magnetic field is aligned along the long body

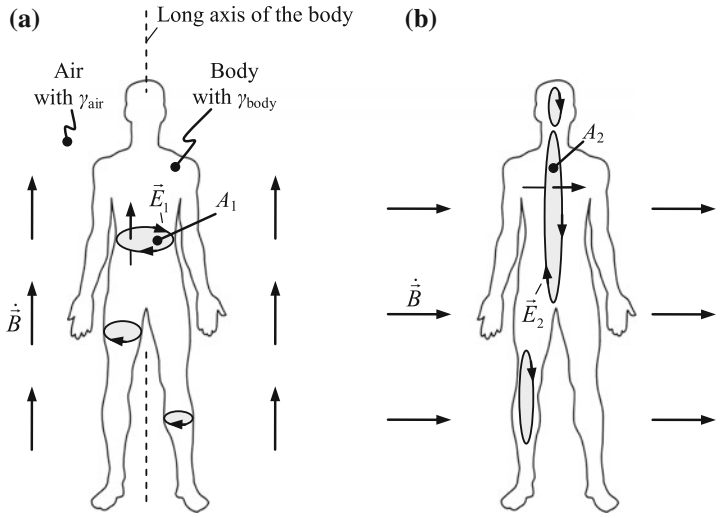

Fig. 2.32 Effects of the position of the human body (with the electrical conductivity γ_{body}) in the ambient external magnetic field $\vec{B}$ in the air (with $\gamma_{air} \ll \gamma_{body}$, see Table 2.2) on the induced field $\vec{E}$ within the body; compare Fig. 2.31. **a** The field $\vec{B}$ in parallel to the long axis of the body yields small internal $\vec{E}$ due to small cross-section area A [with magnitudes $E_1 < E_2$ for $A_1 < A_2$, see (2.86)]. In the body, the $\vec{E}$ field circulates around its long axis and shows maximal values at its outer surface. **b** The field $\vec{B}$ perpendicular to the long axis of the body

axis, e.g., aligned from the head to the feet crossing the relatively *small body surface*.

Figure 2.32 illustrates the effects of the body position in the ambient time-varying magnetic field on the induced electric field in the body. The *different orientations of the body* yield $E_1 < E_2$ (and $U_1 < U_2$) because of the inequality $A_1 < A_2$ (compare Fig. 2.31b). Please note that the considered A_1 and A_2 in Fig. 2.32 are *perpendicular to the incident magnetic field*. However, for *single organs* in the body, different field alignments may yield the highest values of the induced electric field. In analogy, higher electric fields are induced in the bodies of *larger people* for a given B, d/dt and a given spatial orientation of the incident magnetic field $\vec{B}$ with respect to the body (Fig. 2.32). This is because the current conduction loops tend to be more spacious for larger bodies; compare Figs. 2.31 and 2.32. It should be noted that the induced $\vec{E}$ fields tend to circulate not only around the *centre of the trunk* (where A is relatively large) but also to a lesser extent around the *centre of the head* and the *centre of the legs* (see examples in Fig. 2.32b).

As a practical approximation of (2.86), the *magnitude* J_E of the *induced current density* $\vec{J}_E$ along a *conductive loop* of the radius *r within the conductive body* with its *homogenous anisotropic ionic conductivity* γ amounts to

$$J_E = \gamma \cdot E = \gamma \cdot \pi \cdot r \cdot f \cdot B \tag{2.87}$$

in response to a pure sinusoidal[68] and homogenous magnetic field $\vec{B}$ with its *magnitude B* at the frequency[69] *f*; compare Fig. 2.31a. The latter approximation assumes a *spatially-uniform* external time-varying *magnetic field* and a *negligible displacement* of this magnetic field (permeating the body) towards its surface (see below). For the circular loop, approximations $A = \pi \cdot r^2$ and $U(\partial A) = 2\pi \cdot r \cdot E$ were used here. Equation (2.87) confirms the aforementioned dependencies between the magnitude J_E and all three, namely, *B*, d/d*t*, and *A*. The resulting *specific energy absorption rate* P_{SAR}—as induced by the time-varying magnetic field at any location of the exposed tissue—can be easily derived from (2.57) and (2.87).

Obviously, the *induced* J_E within the *conductive body* increases with increasing *local* γ given a local induced electric field [(2.54) and (2.87)]. The resulting magnitude of the *local current density* induced in any part of the *conductive body* will then be dependent on both the induced local electric field and the *distribution of* γ within the body. In other words, in bodies with low or even *negligible* γ, the incident time-varying magnetic field shows small or even no effects, respectively, in terms of the induced current density.

Figure 2.31 demonstrates the resulting current distribution in a *homogenous conductive body* (Fig. 2.31a) compared with that in a *heterogeneous conductive body* (Fig. 2.31c); see also numerical example in Fig. 2.59. In the heterogeneous body, the highly *conductive regions* within the body (e.g., local blood accumulations) act as *sinks for the field lines of* $\vec{E}$ *and* $\vec{J}_E$ because *surface charges* are generated in these conductive regions by the electromagnetically-induced electric

[68]For *non-sinusoidal magnetic fields*, such as square-wave or pulsatile fields, the *rise and decay times* are of paramount importance because these determine the maximum rate of change in the magnetic flux density [d/d*t* in (2.86)] and thus determine the maximum magnitude J_E in tissue. On the other hand, peak strengths and temporal dynamics of the inner J_E [and inner magnitude *E*, (2.54)] govern the stimulation of nerves and muscles; see Section "Electrical Stimulation Effects".

[69]It is instructive to observe that a *high frequency f* in combination with a *low magnitude B* is usually used for *energy coupling and data exchange* along a *contact-less transmission line* throughout tissue; e.g., for recharging of a *medical implant* deep within the body with a coil outside the body. The high *f* prevents favourably *stimulation of nerves and muscles* (residing close to the transmission line) while the low *B* keeps the resulting magnitude J_E (2.87) within tissue below *excitation thresholds of nerves and muscles*; see Kaniusas (2012, Fig. 2.16c) and Section "Electrical Stimulation Effects".

In contrast, a *low f* in combination with a *high B* is preferred for *neuromuscular stimulation* in terms of *therapy*. Here the low *f*—still above 50–100 Hz, see Kaniusas (2012, Fig. 2.16c)—implies a high *excitability* of nerves and muscles while the high *B* induces a large J_E which exceeds *excitation thresholds*.

field (2.86); see below for more details. In contrast, the *less conductive regions* (e.g., local fat accumulations or airways filled with the isolating air) act as dispersive units for the field lines.[70] It can be expected that the induced current across the highly conductive regions would increase with increasing geometrical *size of such conductive regions*; i.e., the larger is the highly conducting path for the current induced, the larger is this current. In addition, *local circular loops* (closed pathways) of $\vec{E}$ and $\vec{J}_E$ usually occur within the insets themselves because of their *finite cross-section area* that the insets present to the perpendicular $\vec{B}$ field [in line with the induction law in (2.86)], as schematically illustrated in Fig. 2.31c. Likewise, an extremely thin conductive inset would imply no local circular loops of currents within this inset itself, just the global current that passes through this inset.

In other words, *macroscopic structures* in the body, such as spatially limited organs and tissues, as well as *microscopic structures*, such as biological cells isolated via their membranes from the conductive extracellular space (Kaniusas 2012, Fig. 2.2a), affect significantly the *spatial distribution of induced electric fields and conductive currents*. The exact pathway of the induced current in the conductive body, simply speaking, is a function of electrical conductivities γ of various tissues involved while the resulting *current pattern* is usually highly *inhomogeneous*.

It is highly instructive to observe that *conductive insets* (e.g., muscles) experience low inner electric fields but high inner current densities (2.54), whereas *isolating insets* (e.g., fat) experience high electric fields and low current densities. The numerical example in Fig. 2.59 confirms this behaviour. In other words, the induced voltage U (2.86) drops mainly in the regions with a high resistance [low conductivity, see (2.36)] and less in the regions with a low resistance (high conductivity); in terms of a voltage divider.

Please note that *electrical point effects* (such as in Fig. 2.26a, see Footnote 58) can also arise in highly heterogeneous tissue permeated by time-varying magnetic fields, provided that sharp edges of some highly conducting structures or objects

---

[70]Concerning the resulting distributions of $\vec{E}$ und $\vec{J}_E$ field lines within *insets of different conductivities* embedded within tissue that is exposed to an alternating spatially-uniform magnetic field (Fig. 2.31c), the following observations can be made:

- Given a *conductive inset* within less conductive tissue, induced $\vec{E}$ *fields* within the inset decrease as related to induced ambient $\vec{E}$ fields (surrounding the inset) because of *boundary conditions*; see discussions related to a similar case in Fig. 2.52b. At the same time, the corresponding $\vec{J}_E$ *fields* within the conductive inset increase as related to $\vec{J}_E$ fields surrounding the inset; see Fig. 2.53a. Simply speaking, the currents prefer the low conductance pathway and thus flow through the conductive inset. *Numerical example* in Fig. 2.60a illustrates this behaviour. On the contrary,
- Given an *isolating inset* within conductive tissue, induced $\vec{E}$ *fields* within the inset increase as related to induced ambient $\vec{E}$ fields (surrounding the inset); see discussions related to a similar case in Fig. 2.52c. At the same time, the associated $\vec{J}_E$ *fields* within the isolating inset decrease as related to $\vec{J}_E$ fields surrounding the inset; see Fig. 2.53b. Simply speaking, the currents are forced to flow around the isolating inset. *Numerical example* in Fig. 2.60b illustrates this behaviour.

reside within tissue (e.g., metallic wires of implants); see the electrical point effect in the numerical example in Fig. 2.61c.

Figure 2.31b demonstrates spatial courses of the *magnitudes E and* J_E in the radial direction of the *homogenous body*, as can be derived from (2.87). Provided that the external time-varying magnetic field is homogenous (spatially-uniform) and here is no (significant) displacement of the inner magnetic field towards the body surface (i.e., the inequality for the the skin depth $\delta \gg r$ applies, see below), both *E and* J_E increase in proportion to the *distance x* from the body's centre (solid lines in Fig. 2.31b). Correspondingly, outer (*peripheral*) regions of the homogenous body show *more dense lines of* $\vec{J}_E$ *and* $\vec{E}$; see Fig. 2.31a. In other words, J_E and E are greatest at the periphery (or at the outer surface) of the homogenous body, where the current paths are longest; compare Fig. 2.59b. In contrast, the fields $\vec{E}$ and $\vec{J}_E$ (and the deposited power in tissue, see below) disappear right in the middle of the homogenous body.

Therefore, if the *whole body is exposed* to a time-varying $\vec{B}$, e.g., within the scope of *magnetic resonance imaging* with switched $\vec{B}$ fields, the *outermost body surfaces* experience largest induced fields. Please recall from Fig. 2.32 that switched $\vec{B}$ fields perpendicular to the long axis of the body are expected to induce largest inner fields. Therefore, outer *skin regions* may undergo the peripheral *neuromuscular stimulation* or *thermal effects*. The neuromuscular stimulation is even favoured by the relatively *low skin conductivity*, increasing the local voltage drop across the skin layer, increasing the local electric field within the skin, and thus rendering peripheral stimulation more likely (Fig. 2.63b).

Outside the *boundary of the body* in the air, i.e., for $x > r$ with r as the *radial extension of the body* from Fig. 2.31a, the $\vec{E}$ field continues to increase with x; i.e., the magnetic field is present not only in the body region but also outside the body, see Fig. 2.31b. The corresponding J_E in the air is approximately zero because the conductivity of the air is relatively low related to that of the body ($\gamma_{air} \ll \gamma_{body}$, see Table 2.2); compare Fig. 2.59b. Please note that the *deposited (induced) power* (2.56) in tissue due to the non-zero E and J_E grows quadratically with x, as a consequence of a linear increase of both magnitudes E and J_E with x (Fig. 2.31b). This spatial *non-linear behaviour* of the deposited power is a significant issue if heat has to be locally deposited in tissue (Footnote 115), favouring *superficial heating* of voluminous tissues exposed to time-varying magnetic fields.

From a *quantitative* point of view, if a *human body* with the assumed (homogenous) γ of 0.2 S/m (Table 2.2) is considered in an *external magnetic field* at 50 Hz with the amplitude of 100 μT,[71] the induced current densities in the *peripheral body regions* are in the range of 0.2–2 mA/m^2 (CRP 1997); compare

[71]For comparison, the strength of the *magnetic field* is at most 15 and 10 μT at a height of 1 m above ground under *overhead power transmission lines* (with the cable height of about 30 m above ground) with the voltage 380 and 220 kV, respectively, at 50% of the maximum load and the field frequency of 50 Hz (CRP 1997); compare Footnote 80.

Footnote 73. In fact, the *local current density* is proportional to the local γ of the considered body region (2.54) and this density increases with increasing distance of this region from the centre of the body; see J_E as a function of x ($\leq r$) in Fig. 2.31b. In analogy with Fig. 2.32, magnetic fields of about 300–600 μT at 50 Hz are required to induce 1 mA/m^2 in the head (with its relatively *small cross-section*), whereas only 100–200 μT are required to induce the same current density in the periphery of the trunk and in the heart region (with relatively *large cross-section*) (CRP 1997). For instance, guidelines in ICNIRP (2010) refer to local electric fields of about 23–33 mV/m per mT in the *brain* induced by 50 Hz ambient magnetic field, which are relevant for effects of these fields on the *central nervous system* (Section 2.3.2.5). The above guidelines also refer to fields of about 20–60 mV/m per mT in the *skin* induced by 50 Hz ambient magnetic field, which, in analogy, are relevant for effects of these fields on the *peripheral nervous system* with its nerve endings residing in the skin. The latter values correspond roughly to those from CRP (1997) with the assumed γ of tissue of 0.2 S/m.

Interestingly, the *direction of the induced conductive currents*—e.g., the local direction of ideal vortices of eddy currents in the ideally *homogeneous tissue* (heterogeneous tissue shows a mixture of both eddy-related and source-related fields, see below)—is such that it produces[72] an own magnetic field which *opposes the incident change* dB/dt already present in tissue. Thus, it can be considered as a *feedback effect*. In other words, induced currents, in turn, create their own magnetic field which opposes the incident magnetic field and thus resists its penetration into tissue. Consequently, the total magnetic field as well as the induced current will drop off in an exponential way from the surface (see below).

For instance, Fig. 2.31a demonstrates this *produced magnetic field* $\vec{B}_i$ *opposing* the incident $d\vec{B}/dt$ *inside any loop* in tissue; consider the right-handed association between the induced field lines $\vec{J}_E$ and $\vec{B}_i$ (see Footnote 72). Likewise, this produced magnetic field inside any loop in tissue always acts to *keep the magnetic flux* ($=B \cdot A$) *constant* in time and in this loop. There is a tendency to reduce the *initial time-varying magnetic field in the loop* (within the conductive body with its induced $\vec{J}_E$), whereas the produced magnetic field $\vec{B}_i$ strengthens the initial time-varying magnetic field *outside the loop*; compare Fig. 2.31a. The *initial time-varying*

[72]In general, the local *conductive and displacement currents* (e.g., in tissue) are necessarily related to the local magnetic field by the *Maxwell-Ampere equation*:

$$\vec{\nabla} \times \frac{\vec{B}}{\mu} = \gamma_{\text{eff}} \cdot \vec{E} + \varepsilon \cdot \frac{d\vec{E}}{dt} = \vec{J}_E + \vec{J}_C = \vec{J}.$$

This differential equation in the *local form* assumes the *right-handed association* of the original fields $\vec{J}_E$ or $\vec{J}_C$ and, on the other hand, the resulting vector field $\vec{B}$. In analogy, there is the right-handed association between the inner field $\vec{E}$ in tissue and the associated inner field $\vec{B}$. For instance, the magnetic field of an infinitely long wire carrying a conductive current is shown in Fig. 2.8, with the corresponding equation given in Footnote 13.

magnetic field is said to be *displaced towards the boundary of the (predominantly) conductive tissue*.

Therefore, the *skin depth* δ can be given (see Table 2.1), which is the depth below the surface of the *conductive body*—with its *effective conductivity* γ_{eff} [$\gamma_{\text{eff}} = \gamma$ for ionic currents only and $\gamma_{\text{eff}} > \gamma$ with present dielectric losses, see (2.82)]—at which the incident *time-varying magnetic field* has fallen by 1/e (i.e., has been displaced towards the surface, as discussed above), or dropped to about 37% of the initial value of the external magnetic field at the body surface (compare Fig. 2.5 and Kaniusas (2015, Fig. 5.6)); to give (compare Table 2.1)

$$\delta = \sqrt{\frac{2}{\omega \cdot \gamma_{\text{eff}} \cdot \mu}}. \tag{2.88}$$

Here ω is the angular frequency of the time-varying field ($\omega = 2\pi \cdot f$ with f as the oscillation frequency) and μ is the magnetic permeability of tissue ($\mu = \mu_0 \cdot \mu_r \approx \mu_0$ with $\mu_r \approx 1$ for biological tissues according to Footnote 17); compare (2.21). Here μ_0 is the permeability of free space ($\mu_0 = 4\pi \cdot 10^{-7}$ H/m) and μ_r the relative magnetic permeability. Please note that (2.88) assumes a *predominant conductive body* but not dielectric body; namely, the inequality $\gamma_{\text{eff}} \gg \omega \cdot \varepsilon$ applies for the predominant conductive body (2.71 and Table 2.1).

The depth δ can also be interpreted as the depth in the *conductive body* traversed by the time-varying magnetic field for its amplitude decrease of 1/e. Consequently, the *magnetic field* as well as the induced *electric fields and current density fields* within the body are mainly located *within the tissue layer* of the *thickness* δ adjacent to the boundary of the body. The main conclusion of this observation is that the *inner region of the conductive body* remains *free of any fields* under the assumption of a relatively large body with $r \gg \delta$; compare Fig. 2.31a, b.

In fact, the fields experience an *exponential decay* with increasing distance inwards from the boundary, as illustrated in Fig. 2.31b (dashed line) and (2.20). The effective *length constant* (or space constant) for this decay is the above depth δ; compare with the length constant $1/\alpha$ from (2.20) (and Kaniusas (2012, Fig. 2.8c)). For instance, the *estimated depth* δ—to be precise, for the predominant *conductive body* in line with Table 2.1—amounts to about 2.5 m according to (2.88) for the field frequency *100 kHz*, *average body conductivity* $\gamma_{\text{body}} = 0.4$ S/m (Table 2.2 and Fig. 2.21), and $\mu = \mu_0$. In contrast, the depth δ is only about 2 mm ($\ll$2.5 m) for the frequency *10 GHz* (from (2.88) with $\gamma_{\text{body}} = 10$ S/m from Fig. 2.21); compare with the plotted values of δ from Fig. 2.6 that does not assume the predominant conductance of the body and see Section "Incident Electromagnetic Fields" concerning the field absorption on the body surface at such high field frequencies.

Thus, the *time-varying magnetic fields penetrate the human body* without any noticeable attenuation—in analogy to *static magnetic fields* at 0 Hz (see above)—provided that the corresponding field *frequencies are relatively low* (<100 kHz). That is, the internal magnetic field within the body differs negligibly from the

external field, assuming that the body thickness is much less than δ. However, here the estimated δ is already in the range of typical body dimensions, which means a slight (linear) decrease of the magnetic fields within the body, as compared with that at the body surface. For instance, *10 MHz* is suggested in Reilly (1998) as the field frequency above which the skin depth ($\delta \approx 0.2$ m from (2.88) at 10 MHz with the assumed $\gamma_{body} = 0.6$ S/m from Fig. 2.21) becomes a significant consideration in most cases.

Equation (2.88) discloses important relationships of the depth δ with the *parameters* of the time-varying magnetic field and parameters of the (predominantly) *conductive body*. In particular, the *penetration depth* δ of the external field into tissue

- *decreases with increasing* ω of the *time-varying field* because the induced electric field in tissue is proportional to the rate of change in the magnetic flux [see d/d*t* in (2.86)]. Correspondingly, the opposing magnetic field B_i (Fig. 2.31a) strengthens with increasing ω, which displaces the magnetic net field to a larger extent towards the body's boundary. Furthermore, the depth δ
- *decreases with increasing* γ_{eff} *of tissue* because the induced current density (and thus the associated opposing field B_i, see Footnote 72) in tissue is proportional to its γ_{eff} at a given induced electric field in tissue (see (2.54) for $\gamma_{eff} = \gamma$ and (2.81) for $\gamma_{eff} \geq \gamma$).

It is important to observe that the *electromagnetically-induced electric field*—proportional to the temporal decrease of the incident time-varying magnetic field (2.86)—within the *heterogeneous tissue* with its conductive and dielectric properties acts as *stimulus* for

- (periodic) *induction* of *surface charges* (alternating in their sign) out of *freely moving charges* in the predominantly *conductive regions* within the heterogeneous tissue (i.e., dislocation of free unbound electric charges due to the electromagnetically-induced electric field; in analogy with the electrostatic induction from Fig. 2.25a) and
- (periodic) *polarization of non-polar structures* (i.e., dislocation of bound electric charges due to the electromagnetically-induced electric field; in analogy with the induced polarization from Fig. 2.16b) and even (periodic) *alignment of polar structures* (in analogy with the reorientation of permanent polar structures from Fig. 2.16c) with their *bound charges* involved within the predominately *dielectric regions* of the heterogeneous tissue.

Please note that *surface charges* also account for the aforementioned *electrical point effect* (Footnote 58), as illustrated in Fig. 2.61c, d.

As the result of the above phenomena, the *effective electric field*

$$\vec{E} = \vec{E}_E + \vec{E}_S \tag{2.89}$$

within the *heterogeneous body*—exposed to the *time-varying magnetic field*—results as a *vector superposition* of

- *the eddy electric field* $\vec{E}_E$ due to electromagnetic induction, with the field *vortices* involved only (as shown in Fig. 2.31a), and, on the other hand, its stimulated/linked fields, namely,
- *the source electric fields* $\vec{E}_S$ due to both
  - dislocated free unbound charges in conductors and
  - dislocated bound charges in isolating polarizable media, dielectrics,

with the *source-related* fields involved only (compare Figs. 2.16b, c and 2.25a).

Such resulting electric field $\vec{E}$ within the heterogeneous body is demonstrated in Figs. 2.31c and 2.59a. It follows from above that this *superposed electric field* $\vec{E}$ within the heterogeneous body induces both

- local *conductive currents*

$$\vec{J}_E = \gamma_{eff} \cdot (\vec{E}_E + \vec{E}_S) = \gamma_{eff} \cdot \vec{E} \tag{2.90}$$

  due to the local conductive property γ_{eff} of tissue permeated by the time-varying magnetic field [compare (2.87)] and during build-up of *surface charges*; as well as
- local *displacement currents*

$$\vec{J}_C = \varepsilon \cdot \frac{d(\vec{E}_E + \vec{E}_S)}{dt} = \varepsilon \cdot \frac{d\vec{E}}{dt} \tag{2.91}$$

  due to the local dielectric property ε of the permeated tissue, i.e., due to the aforementioned *induced and reorientation polarizations* in tissue.

The *total current* $\vec{J}_E + \vec{J}_C$ is illustrated in (2.68) (without considering dielectric losses, i.e., with $\gamma_{eff} = \gamma$) or (2.81) (with dielectric losses, i.e., with $\gamma_{eff} \geq \gamma$); compare Fig. 2.59.

Likewise, if the heterogeneous body is composed out of a few conductive regions regionally limited by an isolating/dielectric region, we can expect *conductive currents* within the conductive regions as well as conductive currents leaving these regions and thus acting as charging currents for the *surface charge* [between the conductive and isolating regions, compare (2.117)]. Please note that the latter conductive currents continue as *displacement currents* in the dielectric region in-between conductive regions; compare continuation of the conductive current $i_E(t)$ by the displacement current $i_C(t) = i_E(t)$ at the capacitor plates from Fig. 2.8.

Please note that with increasing *dimensions of the exposed body* with respect to the field wavelength—which implies either

- increasing *field frequency* of the ambient time-varying magnetic field or
- increasing physical *dimensions of the body*—

the induced electric and magnetic fields become mutually coupled (Fig. 2.2b, c) and thus can not be independently considered [e.g., in terms of their spatially-limited *diffusion* into the conductive biological tissue in line with (2.88)]. That is, when the effective wavelength decreases towards the range of body dimensions (2.52), the aforementioned *electromagnetically-induced displacement currents* within the (dielectric) body start to generate their own *magnetic field* (Footnote 72) while this magnetic field, in turn, generates displacement currents due to *electromagnetic induction* (2.86). This process then manifests as the *propagation of electromagnetic waves*—composed out of electric and magnetic fields oscillating perpendicular to each other (2.4)—within the body. That is, the propagation of waves should be additionally considered when qualifying interactions between the incident *high frequency* time-varying magnetic fields and *large biological tissues* exhibiting *conductive and dielectric properties*; see Sects. 2.3.1 and "Incident Electromagnetic Fields".

Static Magnetic Field

As discussed above, the *time-varying* $\vec{B}$ field yields a non-zero induced U in a stationary or moving body in line with (2.86). However, please note that a non-zero U—and thus a non-zero *inner electric field*[73] also results when a *macroscopic body* is moved within a *spatially heterogeneous* but *static magnetic* $\vec{B}$ field (i.e., $dB/dt = 0$); that is, when the magnetic flux $B \cdot A$ through the body still varies over time [see the right equation in (2.86)]. In analogy, a finite U results when the relevant A of the body *changes over time* (i.e., $dA/dt \neq 0$), even if the permeating $\vec{B}$ field is still static; which again is due to the time-varying magnetic flux $B \cdot A$. Interestingly, a finite U also results within a non-symmetrical body when the body *changes its spatial orientation* relative to the spatial vector of the still static $\vec{B}$ field. Here the resulting time-varying A—i.e., the area normal to the $\vec{B}$ field—yields the associated U (compare Fig. 2.32). Therefore, *time and spatial gradients* are key factors in terms of the *electromagnetic induction*.

From a *microscopic point* of view, the static $\vec{B}$ can induce different *physical effects* (ICNIRP 2004):

- *Translation* and *orientation* of molecular and cellular *substances*. It affects structures with diamagnetic, paramagnetic, and ferrimagnetic properties, such as hemoglobin, collagen, fibrin, or even retinal rods.

[73]Interestingly, *static magnetic fields* can also induce *inner electric fields* within tissue, provided there is a *relative motion of the tissue* in relation to the ambient static magnetic field. Thus, there is still a non-zero *rate of change in the magnetic flux* $B \cdot A$ in (2.86).

For instance, the static *magnetic field of the earth* with the magnitude B in the range of 50 μT yields *electric fields* of about 50 μV/m in the body when standing up or moving quickly the head (CRP 1997). Consequently, *current densities* of about 10 $\mu A/m^2$ result in tissues (2.54) for the assumed (homogenous) conductivity γ of 0.2 S/m (Table 2.2). Please note that this induced current density does not surpass the *basic restriction* of the inner current density of 2 mA/m^2 at 50 Hz from *exposure guidelines* (Fig. 2.87).

- *Electrodynamic forces* on moving electrolytes, e.g., on *moving ions* with the velocity $\vec{v}$ in blood (2.53). These forces generate an electric field $\vec{v} \times \vec{B}$ (due to Hall effect) and an associated current density $\gamma \cdot (\vec{v} \times \vec{B})$ (2.54) with the assumed electrolyte conductivity γ. Across a blood vessel with its width d, a non-zero voltage $d \cdot v \cdot B$ results (2.30), i.e., a voltage normal to the flow direction. For instance, a constant $\vec{B}$ field of 5 T induces endogenous electric fields in the range of 0.5 V/m at the location of the sinoatrial node (ICNIRP 2004). Fortunately, 0.5 V/m is lower than 30 V/m as required for cardiac stimulation (see section on endogenous fields in Section "Electric and Magnetic Field").
- Electron spin states of chemical reaction intermediates are affected.

However, *clinically significant effects* for short-term and long-tern exposure to *static magnetic fields* are still *lacking*.

Incident Electromagnetic Fields

Electric and magnetic fields are said to be *coupled* (Sect. 2.3.1) as soon as

- the *time-varying electric field* (namely, the displacement current) induces a significant *time-varying magnetic field* (according to the equation in Footnote 72) and, on the other hand,
- the *time-varying magnetic field* induces a significant *time-varying electric field* [according to (2.86)],

i.e., the *time derivatives* of both fields become significant in size in Maxwell's equations and the *derivatives of fields act as sources* of each other. That is, in contrast to independent and decoupled external electric and magnetic fields, both fields *induce mutually each other* and thus can propagate as *electromagnetic field* or *electromagnetic wave* through the air (or dielectric media).

Likewise, the lower the *field frequency*, the *less coupled* the *electric and magnetic fields* are (Fig. 2.2a). Please note that the field frequency f is proportional to the aforementioned *time derivative* $\mathrm{d}/\mathrm{d}t$ of the time-varying field; i.e., $\mathrm{d}E(t)/\mathrm{d}t = 2\pi \cdot f \cdot E(t)$ with $E(t)$ as the sinusoidal electric field. *Uncoupled fields* imply also that effects of the electric and magnetic fields can be considered separately, as assumed in Section "Incident Electric Fields". This is particularly so when frequencies are below about 0.1–1 MHz (or lower than about 10 MHz (Furse 2009)) and the *wavelength* of the field is much *larger than the geometrical size* of the source (WHO 1993); compare (2.52) and Fig. 2.2a. For instance, this absent (or only weak) coupling justifies the use of the electric current density only (or the electric field only) for low frequencies when considering interactions of ambient fields with biological tissues (Section "Electric and Magnetic Field").

That is, the *strengthened coupling* arises with *increasing frequency* of fields (with their increasing derivatives), along with *decreasing wavelength* [(2.5) and (2.52)]. Consequently, the effective wavelength may go down to body dimensions

and even structure size of heterogeneous tissues for relatively high frequencies; see Fig. 2.2b, c.

In general, incident *electromagnetic fields penetrate into the biological body*, in the course of which the body *absorbs some energy* that is then converted to *body heat*; consequently, the temperature of the body rises (Section "Thermal Stimulation Effects"). Obviously, *medical implants* inside the body can also absorb some energy and become warmed up.

According to ICNIRP (1998),

- *external electromagnetic fields* at frequencies *below about 100 kHz* results in *negligible energy absorption* by exposed biological tissue (without any physical contact with the source of the electromagnetic field) and thus in no measurable temperature rise in tissue (compare Sect. 2.3.2.4 and Footnotes 105 and 107). The induced inner *electric and current fields* increase in proportion to the *field frequency* (compare Section "Charge and Current Induction" and Footnote 61). The relevant *penetration depth* of incident fields into exposed tissue—or the *skin depth* according to Fig. 2.6 and Table 2.1—is very large because of the low field frequencies. In contrast,
- fields at frequencies *above 100 kHz* can lead to significant absorption and thus to markable increase in the *tissue/body temperature* (Section "Thermal Stimulation Effects"). In general, *uniform exposure* leads to a highly *non-uniform deposition* of energy within the exposed body, which depends on
  - the size of the body compared to the wavelength of the radiation,
  - the incident field parameters (e.g., field frequency),
  - electrical characteristics of the exposed body (e.g., electrical and dielectric properties), and
  - ground/reflector effects (see below).

The *energy absorption* in tissue is usually quantified with P_{SAR} (2.58) and, for very high frequencies, with the power density (see below).

In particular, fields in the approximate range of *100 kHz–20 MHz* are mainly absorbed by the *whole body* longer than the free-space wavelength. Much of the energy is absorbed within the body below the skin layers, whereas the energy absorption increases with increasing field frequency (see below). The relevant *penetration depth* (or skin depth) of incident fields into tissue is still relatively large because of the relatively low field frequencies.

In the range of about *20–300 MHz*, a relatively *high and very non-uniform* absorption can occur in the *entire body*. As illustrated in Fig. 2.30a, this is because of

- *whole-body resonances* or
- *partial-body resonances*,

i.e., when *whole-body dimensions* or *head/torso dimensions* are in the range of the ambient field *wavelength (outside the body or head)*, respectively. Typically, *whole-body resonances* occur in the approximate range of about 20–200 MHz,

whereas *partial-body resonances* are located in the frequency range of about 200–300 MHz (or even up to 400 MHz according to Heinrich (2015)).

The *non-uniformity in the absorption* is caused by multiple *reflections and refractions* at the interfaces between materials of different electrical properties such as air and body (Fig. 2.48 and Section "Reflection and Refraction"). These non-uniformities are further increased by *heterogeneous structure of the body* and that of body's tissues.

In fact, this relatively *high and non-uniform absorption* (i.e., locally peaked) at *specific frequencies*, as discussed in Sect. 2.3.1.2, is due to (*partial*) *reflection* of travelling waves back and forth in some lossy and heterogeneous sections of the body (Section "Reflection and Refraction"). The wave loses progressively its energy after *multiple passage* of the same section (*multiple reverberation*) to a much larger extent as compared with a *single and straightforward passage* of the travelling wave through the whole heterogeneous body. In analogy, maxima of (partial) standing waves (Figs. 2.45, 2.47, and 2.48) indicate spatial regions of maximum electric field and thus regions of maximum absorption in heterogeneous tissue (2.58). That is, more power is absorbed by tissue at specific frequencies—i.e., *body resonances*—than would be predicted by simple wave attenuation (2.20). Likewise, body resonances occur within a small band of field frequencies with ranges on either side that show reduced absorption (Kaniusas 2015, Footnote 51 in Chap. 4).

In particular, the *whole-body resonance* can be reasonable approximated by treating the whole *ungrounded body* (Footnote 76) as a *half-wave dipole*, i.e., when the body height is about one-half of the free-space wavelength; compare Fig. 2.30a and Kaniusas (2015, Fig. 4.24b, c). Because of the *limited conductivity* and substantial *thickness* of the *human body*, the resonance occurs when the *body height* is about *four-tenths*[74] *of the free-space wavelength* (Furse 2009). In addition, the *quality factor* of the resulting body resonator (Kaniusas 2015, Footnote 51 in Chap. 4) is relatively low due to the relatively low conductivity of biological tissue (Furse 2009), as related to highly conducting metallic objects (Footnote 74).

Ambient electromagnetic fields at even higher frequencies in the range from about *300 MHz to several GHz* are subjected to predominantly *local non-uniform absorption*. Please recall that exponential attenuation effects alone already imply an *increasing absorption* with *increasing field frequency*; see (2.20) and the diminishing *skin depth* with increasing frequency in Fig. 2.6. Finally, fields at frequencies above *about 10 GHz* are primarily *absorbed* already at the *body surface*, in the course of which the body temperature is elevated only at the body surface.

[74]The *resonance in objects* with their length of about *one-half of the wavelength* occurs only in long, thin, metallic objects, i.e., in *slim conducting objects* (like a wire antenna) located in non-conducting free space.

Please note that at such high frequencies the associated wavelengths are already in the millimetre range [see (2.6) and the corresponding examples], especially within tissue. In particular, this suggests the absorption of the incident field energy already in the outer tissue layers—containing thermal sensors in the skin, see Section "Thermal Stimulation Effects"—with their thickness in the millimetre range.

Such high frequency fields can not be expected to affect *medical implants* residing deep within the body due to the negligible penetration depth of these fields into the body. From a *therapeutic* point of view, high frequencies of incident electromagnetic fields are favourable for *surface heating* of the human body, whereas low frequencies foster *deep heating* of the inner body.

Although the measure P_{SAR} (2.58) is the quantity to assess the energy absorption, this *volume-related quantity* is less reasonable for these very high frequencies above 10 GHz when the energy is already absorbed at the body surface, i.e., when the *penetration depth* of the external field into tissue is very small (Fig. 2.6); compare the skin depth from (2.88) for high field frequencies and Sect. 2.3.1.2. Here the incident *power density* of the ambient field (plane wave in far field), i.e., the incident power per unit area (in W/m^2), is a more appropriate quantity to assess the energy absorption at the body surface; see (2.13), (2.22) and Section "Power Measures".

Since the human body is an *elongated body*—with the height-to-radius ratio of about 12 (in line with Footnote 64)—the *coupling of electromagnetic energy* can be expected to be highly sensitive to the *orientation of the human body* within the ambient electromagnetic field[75] (in the air). As shown in Fig. 2.33, the *orientation of the body* influences strongly the whole-body *energy absorption* in terms of P_{SAR}; compare with the influence of the position of the conductive body on the induced surface charges (in Section "Charge and Current Induction" and Fig. 2.29) and the descriptive numerical simulations (e.g., Fig. 2.49 vs. Fig. 2.50).

For instance, an average man has a *resonance absorption frequency* close to 70–80 MHz for *E-polarization* (in Fig. 2.33), which corresponds to the approximate wavelength λ_b of free space (in Fig. 2.30a). In particular, a 1.6 m tall standing *ungrounded human* ($=\lambda_b \cdot 4/10$) yields the resonance frequency of 75 MHz at $v = v_0$ [(2.5) and (2.6)]. *Seated individuals* or babies exhibit higher frequencies (>100 MHz) because of smaller body dimensions. In analogy, *shorter subjects* exhibit higher resonance frequencies, whereas *grounding* of an exposed individual

[75]If the *electric field* vector in the *plane wave* is incident and parallel to the long axis of the body, it is usually referred to as *E-polarization*. In contrast, if the *propagation vector* is parallel to the long axis, which implies that the electric field vector is perpendicular to the long axis, it is known as *K-polarization*. Two triplets of field vectors in Fig. 2.33—including vectors of the electric and magnetic fields and the propagation vector (compare Fig. 2.3)—illustrate both polarizations.

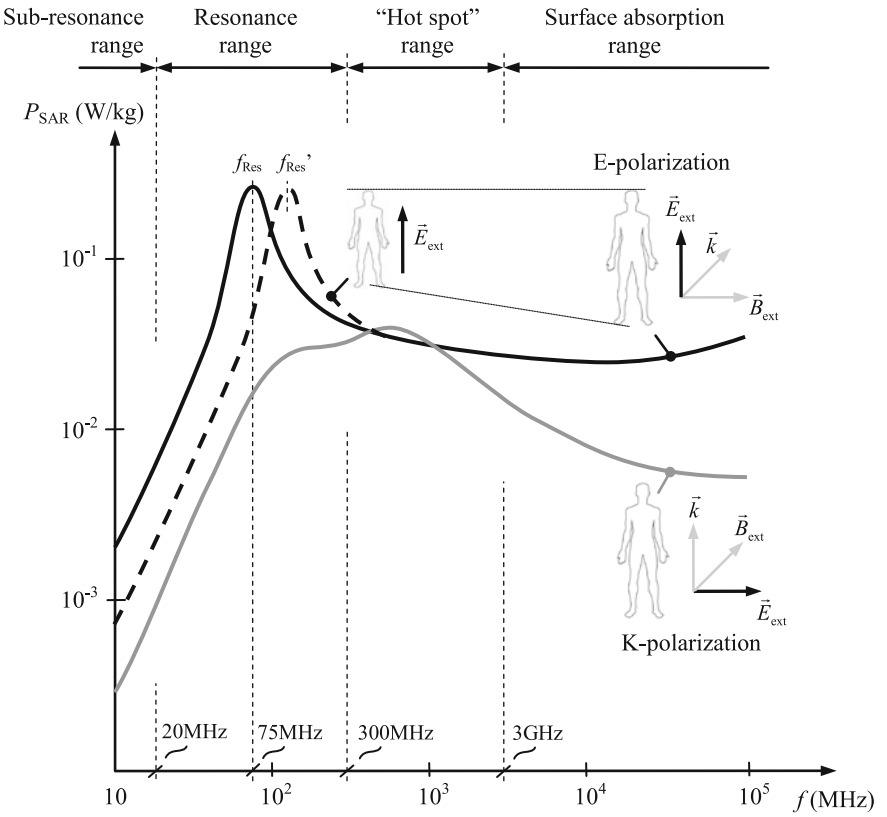

Fig. 2.33 Average whole-body specific energy absorption rate P_{SAR} (2.58) as a function of field frequency f for an average erect man in free space. The ambient electric field $\vec{E}_{ext}$ in the incident plane wave with the power density of 10 W/m^2 (2.13) is directed either parallel to the long axis of the body (known as E-polarization, solid and dashed black lines) or perpendicular to the long axis (K-polarization, grey line); see Footnote 75. The effect of a reduced human size is indicated for E-polarization, leading to an increased resonance frequency f_{Res}' ($>f_{Res}$). In addition, the propagation vector $\vec{k}$ of the plane wave is indicated, whereas $\vec{k}$, $\vec{E}_{ext}$, and the magnetic field $\vec{B}_{ext}$ vectors of the plane wave are perpendicular to each other (Fig. 2.3). Data on P_{SAR} taken partially from Furse (2009)

lowers its resonance frequency.[76] Distinct parts of the body such as the *head* show *partial-body resonances* at even higher resonance frequencies because of even

[76]In addition, *grounding* of the feet of an exposed individual impacts strongly its *resonance frequency* because, simply speaking, the conducting (grounding) plane acts as a mirror for electric fields; i.e., the conductor forces the tangential components of the electric field to vanish (2.96 and Fig. 2.25a). An ideal grounding makes the individual appear to be twice as tall and thus lowers its resonance frequency (e.g., 75 MHz in free space for *standing ungrounded body*, see Figs. 2.30a and 2.33) by a factor of 2 down to 37.5 MHz for *standing body with grounded feet* (Furse 2009). Likewise, imperfect grounding leads to resonance frequencies between 37.5 and 75 MHz.

smaller dimensions[77]—which e.g., correspond to the wavelength λ_h ($<\lambda_b$) in Fig. 2.30a—at *more than 200 MHz* (Furse 2009). The *resonance frequency typically scales* with the *size* of the resonating body (or body part) *relative to the wavelength*.

At the resonance, the absorbed power is increased as would be predicted from the reflection-free wave attenuation (2.20). For instance, this *power increase factor* is about 3.9 for the whole-body resonance (at about 75 MHz), whereas it amounts to about 2.8 for the *partial-body resonance* of the head (at about 205 MHz), both factors being applicable in ungrounded adults (Furse 2009).

Interestingly, *below the resonance region*—where the body dimensions are much greater than the field wavelength—P_{SAR} *increases with* f^2 (for *all polarizations*) for frequencies up to about 10 MHz; see Fig. 2.33. This becomes obvious when the increase of the inner electric field in proportion to f along with (2.58) is recalled; see discussion related to Figs. 2.26, 2.27, and Footnote 61. Just beyond the resonance frequency, the rate P_{SAR} falls off as $1/f$ and then reaches a plateau.

The *maximum absorption* of energy out of the ambient field—or the *maximum* P_{SAR}—occurs at the specific *field frequency* which is a function of both

- field polarization (Footnote 75) and
- the shape and size of the exposed subject; see Fig. 2.33.

Simply speaking, if the (partial or whole-body) *resonance is prominent*, e.g., as applies in E-polarization (Fig. 2.33), the maximum fields in the body result at the corresponding *resonance frequency* and thus the maximum absorption occurs at the resonance (2.58). For instance, *longer and thinner bodies* with E-polarization exhibit higher average whole-body P_{SAR} because the resonance peak becomes more pronounced.

In particular, the rate P_{SAR} is higher for *E-polarization* than for *K-polarization* (Footnote 75), especially *below the resonance frequency*, which is due to the two following principles:

In analogy with the comparison between *grounded and ungrounded body* in terms of *induced currents* in the body (Fig. 2.27), the *average whole-body* P_{SAR} (Fig. 2.33) is higher for the grounded individual than the ungrounded one (WHO 1993). From a practical point of view, it can be concluded that isolating *footwear* reduces the average whole-body P_{SAR} in individuals exposed to ambient electromagnetic fields.

[77]It is interesting to note that *resonances* of the body impose some difficulties when applying electromagnetic fields on *animals* and then extrapolating test results to *humans*; for instance, in order to assess biological effects as a function of the deposited electromagnetic energy (Section 2.3.2.5). In fact, animals and humans have different resonance frequencies because of their different body dimensions. If a rat is being treated at its *whole-body resonance frequency* (of about 600 MHz according to (Furse 2009)), the deposited energy at this field frequency (or the average whole-body P_{SAR}) can be much greater than it would be in a human given the same frequency and the same incident power density (2.13); i.e., the human is resonant at a different and much lower frequency (of about 75 MHz) than the rat.

- P_{SAR} tends to increase when the *incident electric field* is mostly tangential (but not normal) to the body surface because then the *induced electric fields* $\vec{E}_E$ in tissue are maximal (see discussion related to Fig. 2.30). On the other hand,
- P_{SAR} tends to increase when the *incident magnetic field* intercepts perpendicularly a relatively large cross-section area of the body because then the *induced electric fields* $\vec{E}_H$ in tissue are maximal (see discussion related to Fig. 2.32).

Therefore, it can be derived from Fig. 2.33 that both principles apply additively for *E-polarization* in terms of the total P_{SAR}. That is, the incident electric field is mostly parallel to the body surface and, on the other hand, the cross-section area (in the body's sagittal plane in Fig. 2.33) permeated by the incident magnetic field is relatively large. Both facts contribute to a (relatively) large total internal electric field ($=\vec{E}_E + \vec{E}_H$) and thus to a *large total* P_{SAR} *resulting from E-polarization* (2.58). In contrast, the incident electric field for *K-polarization* is mostly normal to the body surface with the resulting (relatively) small $\vec{E}_E$ contributing little to the total P_{SAR} (Fig. 2.33). On the other hand, the cross-section (in the body's frontal plane in Fig. 2.33) perpendicular to the incident magnetic field is relatively large for K-polarization so that the resulting (relatively) large $\vec{E}_H$ contributes to the total P_{SAR} to a large extent. In total, the net P_{SAR} for E-polarization exceeds that for K-polarization.

Additional insights into the effects of the particular polarization are already offered by Fig. 2.30a (Section "Charge and Current Induction"). It should be reiterated that, when the *long axis of the body* is parallel to the *external electric field vector* $\vec{E}_{ext}$, the induced *internal electric field* $\vec{E}_1$ is relatively large; especially, for field frequencies below the *resonance frequency*. Therefore, the whole-body absorption and the average whole-body P_{SAR}—proportional to the squared E_1 (2.58)—*reach maximal values* under the assumption of *plane wave* and *far field* conditions (Sect. 2.3.1). In contrast, the field $\vec{E}_{ext}$ perpendicular to the long axis of the body causes smaller *internal electric field* $\vec{E}_2$ (Fig. 2.30b), smaller whole-body energy absorption, and thus smaller whole-body P_{SAR}, provided that the magnitude E_{ext} of the incident field is identical in both cases (in Fig. 2.30a, b) and the incident field direction varies only. In other words, the *inequality* $E_1 > E_2$ *applies* in Fig. 2.30, which determines that the resulting P_{SAR} is larger for the external E_{ext} along the long axis of the body as related to the external E_{ext} perpendicular to the long axis.

Local resonances arise in terms of local maxima in the spectral behaviour of the average whole-body P_{SAR} at higher frequencies, which are related to local resonance effects of the head, arms, and neck. In addition, a *heterogeneous body* with differing frequency-dependent permittivities and conductivities of the various tissues causes P_{SAR} to vary throughout the body (mainly due to reflections and resonances) and to depend on the field frequency. Even in a *homogenous body* P_{SAR} generally varies (or is spatially non-uniform) throughout the body. This is

because boundary conditions apply for the incident and inner field at the (skin) surface of the body and, on the other hand, the body's permittivities and conductivities are never infinitely large or infinitesimally small, which results in finite field penetration depth [see (2.88)].

In fact, it is a matter of the *ratio of the body size to wavelength*, which determines the *spatial variation of* P_{SAR} in the *homogenous body*:

- If the body *size* is much *smaller than the wavelength*, i.e., the field frequency is below the resonance region, the internal P_{SAR} would be relatively *constant* over the volume of the body. For instance, it would apply for a rat at 80 MHz, whereas the rat's resonance frequency for E-polarization is about 600 MHz ($\gg$80 MHz, see (Furse 2009)). On the other hand,
- if the *size* is in the range of and *larger than the wavelength*, i.e., the field frequency is in the resonance region and above it, the internal P_{SAR} would *significantly vary* in the body space. For instance, it would apply for a human body at 80 MHz, i.e., at the resonance frequency of the human body for E-polarization.

In other words, similar internal P_{SAR} distributions result in two conducting objects of different sizes when each object is irradiated at a frequency which yields the same ratio of the object size to wavelength.

In addition, *high local* P_{SAR} occurs at locations such as the *ankles* and *wrist*, as already noted in Section "Charge and Current Induction". These bony locations show small total cross-sections and even much smaller cross-sections of conductive tissues along which the current can pass through. This yields high local current densities (2.23) and thus high local P_{SAR} (2.58) in bony locations. Obviously, at high frequencies *above several GHz*, high local P_{SAR} occurs at the *skin level*.

The *distribution of* P_{SAR} in the human body exposed to *near field* is even more non-uniform than in *far field* (WHO 1993). It should be noted that the frequency dependence of the *energy absorption* by the body under *near field* conditions (e.g., within the scope of short wave diathermy at about 10 MHz (and less) for therapeutic aims, compare Footnote 115) is very different from that under *far field* conditions. In short, near field conditions may create almost pure electric fields in some body regions and almost pure magnetic fields in other regions, which may result in high *local energy absorption* and thus in highly *non-uniform distribution of* P_{SAR}; compare Sect. 2.3.1. The strength of this local absorption depends strongly on the *separation distance* between the electromagnetic source and the considered body (region).

As a consequence of a *heterogeneous conductivity* of the body, large ratio of the body size to wavelength, and *near field* conditions, areas of intense local P_{SAR} can arise in the body, known as local "*hot spots*", with a very rapid spatial variation of the inner fields. In addition, *reflections* on tissue boundaries may generate *standing waves* (Kaniusas 2012, Footnotes 161 and 170), (Kaniusas 2015, Footnote 29 in Chap. 4) which necessarily produce local hot spots; compare Figs. 2.45 and 2.47.

Such hot spots lead to a significant local increase in the tissue temperature (Fig. 2.48). As described in Section "Thermal Stimulation Effects" and Footnote 107, the latter increase is determined not only by the amount of absorbed energy ($=P_{SAR} \cdot \Delta t$) but also by the (active regulatory) thermal properties of tissue. It should be noted that the high localized fields at the hot spot usually do not have the capacity to significantly increase the whole-body P_{SAR} (WHO 1993).

Figure 2.33 illustrates the average *whole-body* P_{SAR} as a function of the incident field frequency for an *average man* exposed to a plane wave in free space and for the considered *two polarizations* of the incident field (Footnote 75). It can be observed that P_{SAR} specifically depends not only on frequency but also on the polarization. The P_{SAR} curves of both polarizations exhibit resonating behaviours close to and at the respective resonance frequency, whereas the *greatest values of* P_{SAR} and the most *prominent resonance* arise for *E-polarization*.

The dominant maximum of *K-polarization* in Fig. 2.33 is located at a higher frequency than that of *E-polarization*. This can be expected due to smaller dimensions of the body cross-sections perpendicular to the long axis of the body (i.e., in the direction of the field E_{ext} for K-polarization, Fig. 2.33) than the dimensions of cross-sections parallel to the long axis (i.e., in the direction of the field E_{ext} for E-polarization, Fig. 2.33). Likewise, smaller *resonating wavelengths* result for K-polarization.

In general, the following ranges can be recognised within the course of P_{SAR} as a function of frequency (WHO 1993), as also indicated in Fig. 2.33:

- the *sub-resonance range* up to about 20 MHz, where *energy absorption increases with frequency*; then
- the *resonance range* up to about 300 MHz, where the body dimensions and the ambient field wavelength are in the same range; then
- the *"hot-spot" range* up to about 3 GHz, where a significant *local energy absorption* can occur (in the spatial range of a few centimetres) and the *energy absorption decreases with increasing frequency*; and lastly
- the *surface absorption range* for frequencies greater than 3 GHz, where ambient energy is primarily absorbed at the *body surface*.

In addition, Fig. 2.33 indicates *increased resonance frequency* for a *reduced human size* for E-polarization. This is in line with the previously discussed behaviour of the *whole body* as a *half-wave dipole*.

2.3.2.2 Inhomogeneity Effects

In addition to the geometry-related damping of propagating *electromagnetic wave* (Fig. 2.4) and the medium-related damping in *homogenous media* (Fig. 2.7), the *heterogeneous structure* of biological tissues impacts strongly the *attenuation of the wave* propagating in a specific direction, e.g., towards the skin surface. In general, the electromagnetic wave interacts with *microscopic structures* such as cells and *macroscopic structures* such as organs and layered tissues (Fig. 2.48),

depending on the field frequency. Non-propagating *electric fields* and non-propagating *magnetic fields* are similarly affected by the heterogeneous structure. A highly heterogeneous structure of the thoracic region is demonstrated in Fig. 2.28. The wave-tissue interaction is rather complex, in the course of which the wave may experience *spatial redirection* and *accumulated attenuation* while heading towards the sensor on the skin (for diagnosis) or towards the target organ from the applicator (for therapy).

For instance, when an *electromagnetic field* passes the boundary from one medium into another—e.g., an ambient field *enters an exposed biological body*—the field can be reflected and refracted on the boundary, transmitted through the boundary, or absorbed within media (Fig. 2.42). These phenomena depend not only on electrical properties of both media but also on field properties such as the field frequency (Fig. 2.22). The *absorbed energy* by the exposed body—mainly governed by the conductivity and dielectric losses of the body—is converted to inner *heat* (Fig. 2.48). The absorbed fields can even *stimulate nerves or muscles* within the body in terms of wanted or unwanted *Interference* with endogenous biosignals (Fig. 2.63).

In particular, the following effects govern the propagation of the *electromagnetic wave* in the heterogeneous tissue as well as spreading of non-propagating *electric and magnetic fields*:

- scattering
- diffraction
- reflection,
- refraction, and
- resonance.

Please recall that acoustic sounds (Kaniusas 2015, Sect. 4.1.2.2.2) and light (Kaniusas 2015, Sect. 5.1.2.2.2) are subjected to identical effects. This similarity emphasizes the *common features of acoustic, optic, and electric biosignals*, which —at first glance—are entirely different in their physical nature.

Scattering describes dispersion of the incident electromagnetic wave from a straight trajectory in all random directions when the wave encounters local *non-uniformities* in the electrical properties (Kaniusas 2015, Fig. 5.10). In particular, scattering within tissue is dominant when the size of local non-uniformities matches the wavelength λ of the propagating wave; namely, the scattering is dominant for relatively *high frequencies* in the higher MHz range (2.5). For details on the scattering, see (Kaniusas 2015, Sect. 5.1.2.2.2) considering the light scattering, i.e., the scattering of the very high frequency electromagnetic waves. In particular, isotropic Rayleigh scattering occurs when λ is much smaller than the size of non-uniformity (Kaniusas 2015, Fig. 5.11a), whereas anisotropic Mie scattering is relevant for λ similar to or larger than this size (Kaniusas 2015, Fig. 5.11b).

Diffraction is the bending of electromagnetic waves around relatively small non-uniformities or spreading past small openings, i.e., small compared with the propagating λ; see Section "Diffraction". *Reflection* refers to the bouncing off of waves of the non-uniformity provided that the dimensions of the non-uniformity are

larger than λ; see Section "Reflection and Refraction". *Refraction* means redirection or bending of the wave when it passes across the boundary from one medium into another (with different electrical properties), whereas the dimensions of the refracting surface are larger than λ; see Section "Reflection and Refraction". Please note that all four scattering, diffraction, reflection, and refraction describe *digression from straight line travel*. Lastly, *resonance* indicates the presence of cavities with reverberating waves within and thus the associated increased absorption of waves at the resonance frequency; see Section "Incident Electromagnetic Fields". The basis for all inhomogeneity effects are formed by *boundary conditions* applicable to any electric, magnetic, and electromagnetic fields—so we begin with boundary conditions.

Boundary Conditions

Normal and Tangential Components

The electric field, flux density field, and current density field are all *local vector quantities*, having a certain *magnitude* and *spatial direction*. Therefore, any vector field can be split into its *normal and tangential components* when the field crosses the *boundary* between two media with *different electrical properties*. This splitting facilitates not only the mathematical modelling of the field's behaviour but also the physical understanding of fields across the boundary. As illustrated in Fig. 2.34,

- the *normal field component* defines the portion of the considered field that is perpendicular to the boundary surface.
- The *tangential field component* defines the portion of the considered field that lies on the boundary surface.

That is, the *electric field* $\vec{E}$ (2.28) can be split according to

$$\vec{E} = \vec{E}_\mathrm{n} + \vec{E}_\mathrm{t} = E_\mathrm{n} \cdot \vec{e}_\mathrm{n} + E_\mathrm{t} \cdot \vec{e}_\mathrm{t}, \tag{2.92}$$

the *electric flux density field* $\vec{D}$ (2.64)

$$\vec{D} = \vec{D}_\mathrm{n} + \vec{D}_\mathrm{t} = D_\mathrm{n} \cdot \vec{e}_\mathrm{n} + D_\mathrm{t} \cdot \vec{e}_\mathrm{t}, \tag{2.93}$$

the *conductive current density field* $\vec{J}_\mathrm{E}$ (2.54)

$$\vec{J}_\mathrm{E} = \vec{J}_\mathrm{E,n} + \vec{J}_\mathrm{E,t} = J_\mathrm{E,n} \cdot \vec{e}_\mathrm{n} + J_\mathrm{E,t} \cdot \vec{e}_\mathrm{t}, \tag{2.94}$$

and lastly the *capacitive/displacement current density field* $\vec{J}_\mathrm{C}$ (2.66)

$$\vec{J}_\mathrm{C} = \vec{J}_\mathrm{C,n} + \vec{J}_\mathrm{C,t} = J_\mathrm{C,n} \cdot \vec{e}_\mathrm{n} + J_\mathrm{C,t} \cdot \vec{e}_\mathrm{t}, \tag{2.95}$$

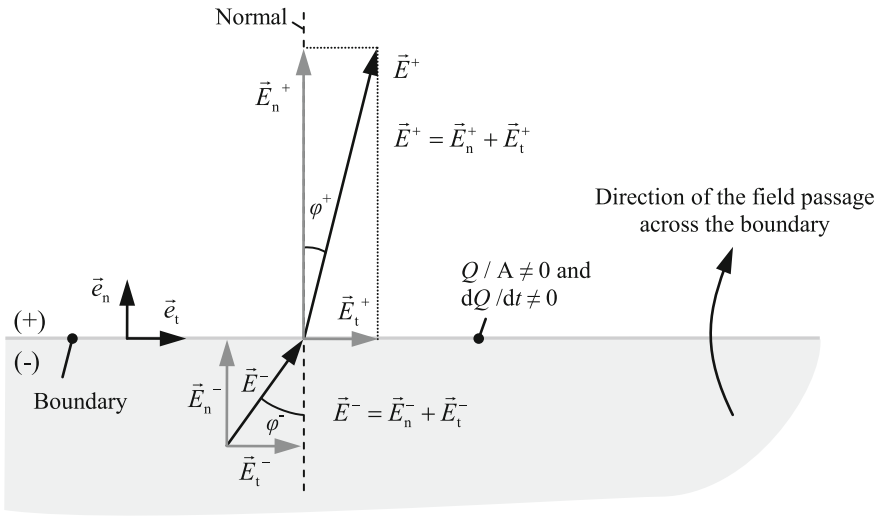

Fig. 2.34 The boundary surface given as the interface between two bodies with different electrical properties. The change of properties along the field passage across the boundary may change normal and tangential field components. Here the field vector of the electric field $\vec{E}$ experiences a change in its magnitude and direction when $\vec{E}$ crosses the boundary from the lower medium (−) to the upper medium (+). The normal component $\vec{E}_n$ is subjected to a step-wise change (2.99) while the tangential component $\vec{E}_t$ does not change at all (2.96)

Vectors $\vec{e}_n$ and $\vec{e}_t$ are *unit vectors* normal and tangential to the boundary surface, respectively, as illustrated in Fig. 2.34.

General Boundary Conditions

Boundary conditions explicitly define the behaviour of *normal and tangential field components* across the boundary. *Different electrical properties* on both sides of the boundary generally imply that local fields can experience specific changes in their components when passing this boundary.

As illustrated in Fig. 2.34, local electric fields $\vec{E}$ immediately above and below the boundary can possess different values, i.e., not only *different magnitudes* but also *different directions*. The superscript "−" denotes the *preceding medium* while the superscript "+" denotes the *following medium*. The shown $\vec{E}$ in Fig. 2.34 passes the boundary from the lower medium into the upper medium.

The following *general boundary conditions* must be satisfied for both *conductive and dielectric phenomena* at the boundary of two different media or tissues. In addition, *specific boundary conditions* should be fulfilled for

- *conductive phenomena* only (Section "Conductive Phenomena") or
- *displacement phenomena* only (Section "Dielectric Phenomena").

Field Components

The *tangential components* E_t of the *electric field* $\vec{E}$ (Fig. 2.34), i.e., the portions of $\vec{E}$ that lie on the surface just above and below the boundary, are necessarily steady across the boundary according to

$$[[E_t]] = E_t^+ - E_t^- = 0 \quad \text{or} \quad E_t^+ = E_t^-. \tag{2.96}$$

Equation (2.96) follows from the zero net voltage along a closed loop situated just outside the boundary with its vanishing area. This condition in (2.96) has a few important implications:

- the *tangential field* on the outer surface of a *currentless conductor* (non-ideal or ideal) *is always zero* because there is no electric field inside such a conductor; see discussion about Fig. 2.25a and Footnote 56. Consequently,
- the *electric field must perpendicularly enter an isolated and thus currentless conductor* (Figs. 2.51 and 2.55), as can also be derived from (2.106).
- The *tangential electric field is steady* in its size across any boundary between two media with different electrical properties (Figs. 2.5 and 2.56).

It follows from (2.96) that the *tangential components* D_t of the *electric flux density* $\vec{D}$ (Fig. 2.36a) obey

$$\frac{D_t^+}{\varepsilon_+} = \frac{D_t^-}{\varepsilon_-}, \tag{2.97}$$

where ε_- and ε_+ are the *dielectric permittivities* of the medium preceding and following the boundary, respectively (Fig. 2.36a).

For the *normal components* D_n of $\vec{D}$—the portions of the fields that are perpendicular to the boundary surface (Fig. 2.36a)—a step-wise change of D_n applies according to the accumulated[78] *electric charge* Q *on the surface area* A of the

[78] *Electric charge* Q - composed of only *free unbound charges*—on the *boundary* between tissues with *different electrical properties* [(2.107) and (2.117)] decreases with increasing *field frequency* and even disappears for infinitely *high field frequencies*; see the interfacial *β-dispersion* from Fig. 2.19. There is progressively less time for the unbound Q to be accumulated at the boundary—or periodically re-located/induced at the opposite boundary in Fig. 2.25a via *conductive currents* from Fig. 2.29c—with decreasing duration of half-periods of the external alternating electric field. Electric charges have a *limited accumulation speed* due to their finite inertness and *finite mobility* (2.53).

In fact, the speed of the charge accumulation is limited by the *finite relaxation time constant* of tissue [(2.49) and (2.74)]. It should be reiterated that free unbound charges can be *accumulated by conductive currents* only (2.25), whereas *displacement currents* do not carry free unbound charges (2.66).

On the other hand, the accumulated Q on the boundary disappears also for negligibly small *electrical conductivities* of involved tissues on both sides of the boundary because such tissues can not transfer free unbound charges [(2.54) and (2.107)].

boundary, i.e., according to the resulting *charge density Q/A* residing right at the discontinuity:

$$[[D_\mathrm{n}]] = \frac{Q}{A} \quad \text{or} \quad D_\mathrm{n}^+ - D_\mathrm{n}^- = \frac{Q}{A}. \tag{2.98}$$

Equation (2.98) follows from the equality of the *electric flux* through the closed surface—the flux equals the surface integral of $\vec{D}$ normal to the surface—with the electric charge residing inside this surface. It should be noted that this charge Q considers only *free unbound charges*, i.e., it does not consider any polarization charges from (2.64). These true charges can only be *created by conductive currents* crossing the boundary (2.25) but not by *displacement currents* which do not carry free unbound charges (2.66).

In analogy to (2.98), the *normal component* E_n of $\vec{E}$ is subjected to

$$\varepsilon_+ \cdot E_\mathrm{n}^+ = \varepsilon_- \cdot E_\mathrm{n}^- + \frac{Q}{A}. \tag{2.99}$$

Assuming the boundary *surface free of charge* ($Q = 0$) the condition for D_n follows as a *special case*

$$D_\mathrm{n}^+ = D_\mathrm{n}^-, \tag{2.100}$$

or for E_n as

$$\varepsilon_+ \cdot E_\mathrm{n}^+ = \varepsilon_- \cdot E_\mathrm{n}^-, \tag{2.101}$$

which is usually used as an approximation for high frequency fields (Footnote 78).

Conductive Phenomena

We start with *conductive phenomena* which are related to movement of free *unbound charges* (Fig. 2.16b, c) and are thus related to *conductive currents*. Please recall that unbound charges can be accumulated by conductive currents only, in clear contrast to *displacement currents*.

Field Components

The *normal component* $J_\mathrm{E,n}$ of the *conductive current density* $\vec{J}_\mathrm{E}$—as illustrated in Fig. 2.36a for the muscle/fat boundary—increases at the boundary by the amount of the negative rate of change in the *charge density Q/A* at the discontinuity, to give

$$[[J_\mathrm{E,n}]] = -\frac{1}{A} \cdot \frac{\mathrm{d}Q}{\mathrm{d}t} \quad \text{or} \quad J_\mathrm{E,n}^+ - J_\mathrm{E,n}^- = -\frac{1}{A} \cdot \frac{\mathrm{d}Q}{\mathrm{d}t}. \tag{2.102}$$

In other words, the conductive component $J_\mathrm{E,n}$ that carries a charge naturally loses its magnitude at the cost of the charge Q at the boundary when passing this

boundary. Again, the accumulated or depleted charge Q is only the *free unbound charge*. The boundary can only be charged by the *conductive current* determined by the rate $\mathrm{d}Q/\mathrm{d}t$ (2.25) that is proportional to the difference $J_{\mathrm{E,n}}^{+} - J_{\mathrm{E,n}}^{-}$ (2.102). For instance, the varying Q is a major issue within the genesis of *β-dispersion* as interfacial polarization (Fig. 2.19b).

The *tangential component* $J_{\mathrm{E,t}}$ of $\vec{J}_{\mathrm{E}}$ (Fig. 2.36a) easily results from (2.54) and (2.96) to

$$\frac{J_{\mathrm{E,t}}^{+}}{\gamma_{+}} = \frac{J_{\mathrm{E,t}}^{-}}{\gamma_{-}} \tag{2.103}$$

for *conductive phenomena*.

Provided the rate of the Q *change is negligible*, i.e., *stationary conditions* apply with $Q \neq 0$ and $\mathrm{d}Q/\mathrm{d}t = 0$, the boundary condition for the *normal component* E_{n} of the *electric field* $\vec{E}$ (Fig. 2.34) within the scope of *conductive phenomena* follows from (2.54) and (2.102):

$$\gamma_{+} \cdot E_{\mathrm{n}}^{+} = \gamma_{-} \cdot E_{\mathrm{n}}^{-}. \tag{2.104}$$

Here γ_{-} and γ_{+} are the *electrical conductivities* of the medium preceding and following the boundary, respectively (Fig. 2.36a). The remaining boundary condition for the *tangential component* E_{t} of $\vec{E}$ is already given in (2.96). Please note that the assumed $\mathrm{d}Q/\mathrm{d}t = 0$ is in line with the condition $\gamma_{\mathrm{eff}} \gg \omega \cdot \varepsilon$ (2.71) pertaining to the *predominant conductive behaviour*.

Equation (2.104) confirms that for an *isolated conductor* with its conductivity $\gamma_{+} \gg \gamma_{-}$, i.e., with $(\gamma_{-}/\gamma_{+}) \to 0$, and an incident ambient $\vec{E}$ field necessarily *normal to the conductor's surface* (see above), the inner electric field within the conductor goes to zero when $Q \neq 0$ and $\mathrm{d}Q/\mathrm{d}t = 0$ apply (i.e., no equalising currents as shown in Fig. 2.29c). As illustrated in Fig. 2.25a, the inner $E_{\mathrm{n}}^{+} = 0$ applies even though the incident $E_{\mathrm{n}}^{-} \neq 0$ outside the conductor is non-zero; see the region A in Fig. 2.25b.

Furthermore, (2.104) forms the basis for the boundary condition of the *normal component* D_{n} of the *electric flux density* $\vec{D}$ (Fig. 2.36a) for *conductive phenomena*, to give

$$D_{\mathrm{n}}^{+} \cdot \frac{\gamma_{+}}{\varepsilon_{+}} = D_{\mathrm{n}}^{-} \cdot \frac{\gamma_{-}}{\varepsilon_{-}}. \tag{2.105}$$

Again, we assume that the boundary surface carries some charge $Q \neq 0$ which, however, does not change over time with $\mathrm{d}Q/\mathrm{d}t = 0$. Please note that this (2.105) is fully equivalent to (2.98) with Q from (2.107). Lastly, the boundary condition for the *tangential component* D_{t} of $\vec{D}$ is already given in (2.97).

Angles

It should be stressed that the *electric field* $\vec{E}$ is in parallel to and in synchrony with the *electric flux density field* $\vec{D}$ in *lossless and isotropic media*, as illustrated in Figs. 2.16d and 2.23b. That is, the permittivity ε is a *real quantity*, whereas lossy media would require a complex quantity [see (2.64) versus (2.77)] and anisotropic media would require ε as a matrix. On the other hand, the *conductive current density field* $\vec{J}_{\mathrm{E}}$ flows always in the direction of and in synchrony with the field $\vec{E}$ in *isotropic media*—with γ as a *real quantity* (2.54) but not a matrix—as shown in Fig. 2.16a. Correspondingly,

- the *incident angles* φ^- to the normal of all three associated fields $\vec{E}$, $\vec{D}$, and $\vec{J}_{\mathrm{E}}$ *before the boundary* are *identical in size*. Similarly,
- an identical *refraction angle* φ_{E}^+ to the normal applies *after the boundary* for all three fields $\vec{E}$, $\vec{D}$, and $\vec{J}_{\mathrm{E}}$.

Figure 2.36a illustrates the equality of φ^- pertaining to incident fields $\vec{E}$, $\vec{D}$, and $\vec{J}_{\mathrm{E}}$ as well as the equality of φ_{E}^+ ($<\varphi^-$) of refracted fields $\vec{E}$, $\vec{D}$, and $\vec{J}_{\mathrm{E}}$ for the muscle/fat boundary.

For *conductive phenomena*, the quantitative relation between φ^- and φ_{E}^+ results to

$$\tan\varphi_{\mathrm{E}}^+ = \frac{E_{\mathrm{t}}^+}{E_{\mathrm{n}}^+} = \frac{D_{\mathrm{t}}^+}{D_{\mathrm{n}}^+} = \frac{J_{\mathrm{E,t}}^+}{J_{\mathrm{E,n}}^+} = \frac{\gamma_+}{\gamma_-} \cdot \tan\varphi^-, \tag{2.106}$$

which can be easily derived under the assumption of $\mathrm{d}Q/\mathrm{d}t = 0$; for instance, considering components of the field $\vec{D}$ from (2.97) and (2.105).

Equation (2.106) illustrates that for an *isolated conductor* with $(\gamma_-/\gamma_+) \to 0$ and an incident ambient $\vec{E}$ field, the incident $\varphi^- \to 0$ applies. This confirms that the incident field $\vec{E}$ *enters perpendicularly* with $\varphi^- = 0$ the *isolated conductor* embedded within a non-conductive medium (Fig. 2.25a).

It can be observed from (2.106) that the *angles* φ_{E}^+ *and* φ^- *differ* ($\varphi_{\mathrm{E}}^+ \neq \varphi^-$) only if both media show *heterogeneous conductivities* ($\gamma_+ \neq \gamma_-$). In other words, different conductivities imply a directional change of the considered fields crossing the boundary for $Q \neq 0$ and $\mathrm{d}Q/\mathrm{d}t = 0$ at this boundary, except for *perpendicular entrance* ($\varphi_{\mathrm{E}}^+ = \varphi^- = 0$).

Surface Charge

As already discussed, a non-zero *conductive current*—but not the displacement current—across the boundary between two electrically different and *isotropic media* creates a non-zero *surface charge* at the boundary, i.e., a charge composed out of *free unbound charges*. The surface charge (2.98) equals

$$\begin{aligned}\frac{Q}{A} &= D_{\mathrm{n}}^+ - D_{\mathrm{n}}^- = D_{\mathrm{n}}^- \cdot \left(\frac{\varepsilon_+ \cdot \gamma_-}{\varepsilon_- \cdot \gamma_+} - 1\right) = E_{\mathrm{n}}^- \cdot \left(\frac{\varepsilon_+ \cdot \gamma_- - \varepsilon_- \cdot \gamma_+}{\gamma_+}\right) \\ &= J_{\mathrm{E,n}}^- \cdot \left(\frac{\varepsilon_+}{\gamma_+} - \frac{\varepsilon_-}{\gamma_-}\right)\end{aligned} \tag{2.107}$$

under the assumption of $dQ/dt = 0$. It is instructive to observe that the accumulated Q depends not only on the conductive characteristic γ—which governs the conductive current in the bulk—but also on the dielectric characteristic ε (since D_n in (2.98) is a function of ε).

Consequently, the surface remains free of charge only if

- both γ_- and γ_+ disappear ($\gamma_-, \gamma_+ \to 0$), i.e., there are no unbound charges to accumulate Q (Footnote 78),
- equalities $\varepsilon_- = \varepsilon_+$ and $\gamma_- = \gamma_+$ apply, i.e., the physical boundary between both identical media disappear, or, alternatively, if
- the equality $\varepsilon_+/\varepsilon_- = \gamma_+/\gamma_-$ applies.

Likewise, if the boundary is assumed to be free of charge with $Q = 0$ then the equality $\varepsilon_+/\varepsilon_- = \gamma_+/\gamma_-$ of ratios $\varepsilon_+/\varepsilon_-$ and γ_+/γ_- applies (2.107). Based on this equality, the boundary condition for E_n^+ and E_n^- from (2.101) and, on the other hand, the condition from (2.104) become—as expected from the respective assumptions—identical.

Equation (2.107) is instructive in considering, once again, an *isolated conductor* with $(\gamma_-/\gamma_+) \to 0$ and an incident ambient $\vec{E}$ field with E_n^-. Equation (2.107) predicts $Q/A = -D_n^- = -\varepsilon_- \cdot E_n^-$, i.e., an incident positive $E_n^- > 0$ outside the conductor creates a *negative charge density* $Q/A < 0$ at the point of incidence at the conductor surface; compare Fig. 2.34. The point of incidence is comparable with the left side of the *conductive body* from Fig. 2.25a, which receives a non-zero outer electric field. Indeed, the left side of the body carries a negative surface charge. This accumulated surface charge effectively *screens* the inner of the body from any induced inner electric fields, which causes $E_n^+ = 0$ just outside the boundary and already inside the body. Figure 2.25a confirms that the inner electric field within the conductor is zero. From a theoretical point of view, the negative surface charge Q receives and equals in its size the *electric flux* $D_n^- \cdot A$ entering this charge Q so that there is *no net flux* left to leave the boundary down into the conductor.

Examples

An instructive example for a practical applicability of boundary conditions is shown in Fig. 2.35. A *series connection* of two *homogeneous tissue sections* of the same size with the respective conductivities γ_1 and γ_2 ($>\gamma_1$) is depicted in Fig. 2.35a, whereas a *parallel connection* of the two homogeneous tissue sections of the same size is depicted in Fig. 2.35b. The two electrodes surrounding tissues carry constant and equal charges of opposite polarity, i.e., a *constant outer voltage* is applied between electrodes. Therefore, *stationary conditions* can be assumed with $dQ/dt = 0$ at the boundary in-between homogeneous tissue sections.

The boundary between tissue sections connected in *series* shows only *normal components* of fields, see equations listed under Fig. 2.35a. Stationary conditions and (2.102) require continuity in the *normal* $J_{E,n}$ across the boundary. The associated *normal* E_n across the boundary obeys (2.104) so that E_n is higher within the tissue

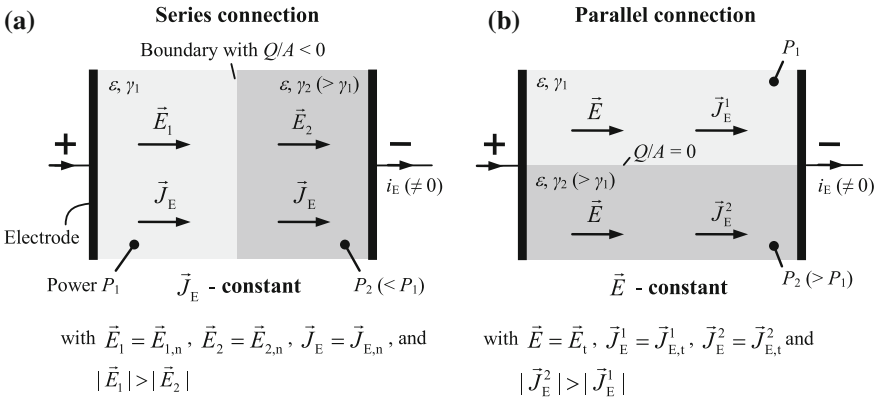

Fig. 2.35 The local electric field $\vec{E}$ and local conductive current density $\vec{J}_E$ within a heterogeneous tissue showing two different electrical conductivities γ_1 and γ_2 ($>\gamma_1$), and identical dielectric permittivities $\varepsilon_1 = \varepsilon_2 = \varepsilon$; compare Footnote 32. **a** Two homogeneous tissues are connected in series. An identical $\vec{J}_E$ results in both tissues, with only the normal component $J_{E,n}$ at the boundary. **b** Both homogeneous tissues are connected in parallel. An identical $\vec{E}$ results in both tissues, with only the tangential component E_t at the boundary

section showing a lower γ_1 (i.e., $|\vec{E}_1| > |\vec{E}_2|$ applies). The accumulated *charge density* Q/A on the boundary follows from (2.107) and equals $D_n^- \cdot (\gamma_1/\gamma_2 - 1) < 0$, i.e., it is negative due to $\gamma_2 > \gamma_1$ with the assumed $\varepsilon_1 = \varepsilon_2$ (compare Footnote 79). In other words, the *electric flux* directed from the left towards the boundary—the flux is proportional to $E_{1,n}$—is partly sunk by the *negative surface charge* on the boundary. Consequently, the remaining electric flux to the right away from the boundary—proportional to $E_{2,n}$ ($<E_{1,n}$)—becomes reduced. Please note that the amount of Q/A can also be independently varied by changing the ratio ε_1 to ε_2, as can be observed in (2.107). The *dissipated power* P within each tissue section—as already discussed in Footnote 32—is proportional to the respective product $J_{E,n} \cdot E_n$ (2.56) so that the dissimilarity $P_1 > P_2$ applies. In fact, both tissue sections form a *voltage divider* with respect to the applied outer voltage, whereas this divider determines the absolute values of E_n, $J_{E,n}$, and lastly Q/A.

The boundary between tissue sections connected in *parallel* shows only *tangential components*, see equations under Fig. 2.35b. Equation (2.96) requires continuity in the *tangential* E_t across the boundary. The associated *tangential* $J_{E,t}$ across the boundary obeys (2.103) so that $J_{E,t}$ is higher within the section showing a higher γ_2 (i.e., $|\vec{J}_E^2| > |\vec{J}_E^1|$ applies). In other words, the current density field follows the path of the largest conductivity. The accumulated Q/A on the boundary (2.107) is zero since normal field components on the boundary are absent. The *dissipated power* P within each tissue section (Footnote 32) is proportional to the respective product $J_{E,t} \cdot E_t$ (2.56) so that $P_1 < P_2$ applies. Both tissue sections form a *current divider* with respect to the total current flowing between electrodes—see (2.38) and Fig. 2.13a—whereas this divider determines the absolute values of E_t and $J_{E,t}$.

Therefore, in any *heterogeneous body*, *inhomogeneous electric fields* can be met due to varying local conductivities. For instance, local regions of increased and reduced conductivity tend to show weaker and stronger electric fields, respectively, along the current flow (Figs. 2.35a and 2.59).

Figure 2.30 illustrates the practical relevance of *boundary conditions* when an isolated *human body*, an elongated conducting body, is exposed to an ambient $\vec{E}$ field. The predominant *tangential coupling* of $\vec{E}$ field into the body is discussed where relatively *small surface charges* are induced in the relatively small regions facing perpendicularly the incident $\vec{E}$ field (Fig. 2.30a). This tangential coupling is compared with the predominant *normal coupling* of $\vec{E}$ field with the relatively large facing surface and thus *large surface charges* (Fig. 2.30a). In fact, boundary conditions have a major impact on the resulting size of induced internal $\vec{E}$ fields within the body, which, in turn, may generate *neuromuscular and/or thermal effects*.

Dielectric Phenomena

Dielectric phenomena are related to *bound charges* in terms of induced polarization and orientation polarization (Fig. 2.16b, c). Therefore, any free unbound charge Q and its rate of change $\mathrm{d}Q/\mathrm{d}t$ are irrelevant and thus can be set to zero in the following discussions (i.e., $Q = 0$ and $\mathrm{d}Q/\mathrm{d}t = 0$). *Displacement currents* to be considered can neither carry nor accumulate any unbound net charge at the boundary, in clear contrast to *conductive currents*.

Field Components

The boundary condition for the *normal component* $J_{\mathrm{C,n}}$ of the *displacement current density* $\vec{J}_{\mathrm{C}}$—as illustrated in Fig. 2.36b for the muscle/fat boundary—can be attained when (2.98) is differentiated with respect to time and the definition of $\vec{J}_{\mathrm{C}}$ is used from (2.66), which yields

$$J_{\mathrm{C,n}}^{+} = J_{\mathrm{C,n}}^{-} + \frac{1}{A} \cdot \frac{\mathrm{d}Q}{\mathrm{d}t}. \tag{2.108}$$

With the applicable condition $Q = 0$ for dielectric phenomena, $J_{\mathrm{C,n}}$ obeys to

$$J_{\mathrm{C,n}}^{+} = J_{\mathrm{C,n}}^{-}. \tag{2.109}$$

Equation (2.109) shows that the normal $J_{\mathrm{C,n}}$ is continuous across the boundary since there are no surface charges that can be accumulated by $\vec{J}_{\mathrm{C}}$.

The *tangential component* $J_{\mathrm{C,t}}$ of $\vec{J}_{\mathrm{C}}$ (Fig. 2.36b) is subjected to the following condition

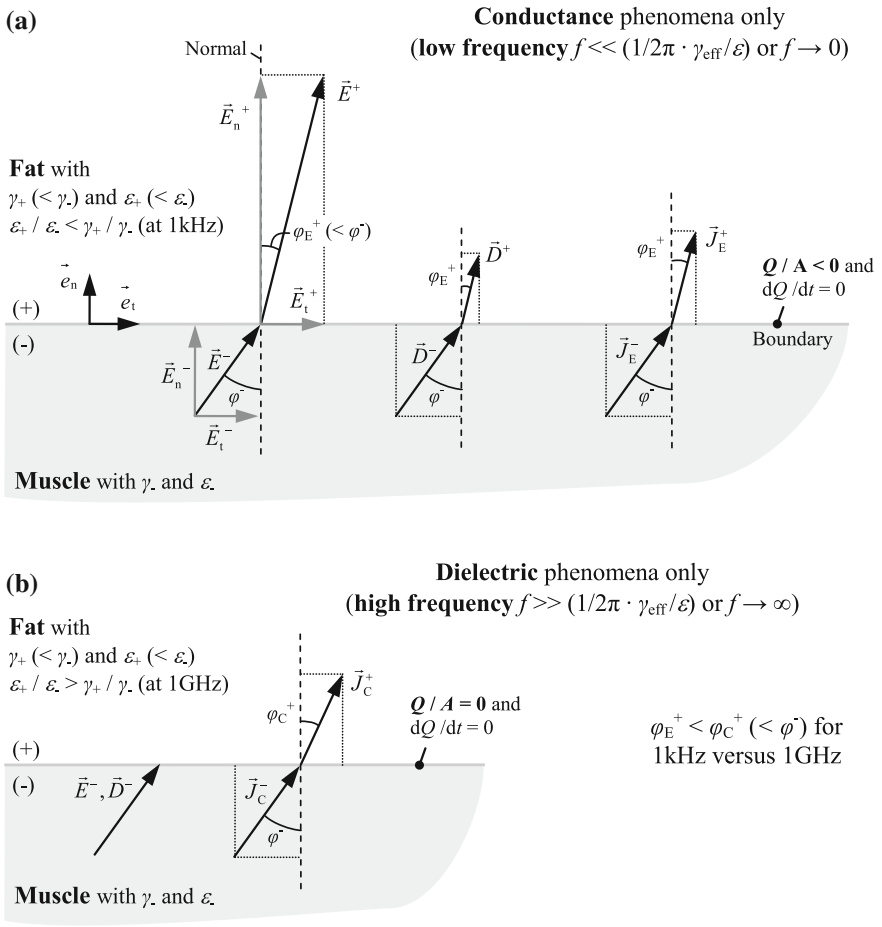

Fig. 2.36 Discontinuity between muscle and fat with the associated boundary conditions for vectors of the electric field $\vec{E}$, electric flux density $\vec{D}$, the conductive current density $\vec{J}_E$, and the displacement current density $\vec{J}_C$; compare Figs. 2.37 and 2.56. Isotropic muscle and isotropic fat have different electrical conductivities γ and dielectric permittivities ε. **a** Predominant conductive phenomena at the assumed relatively low field frequency 1 kHz yield a negative unbound electric charge $Q < 0$ at the boundary due to the inequality $\varepsilon_+/\varepsilon_- < \gamma_+/\gamma_-$ at 1 kHz (2.107). The charge Q is accumulated by $\vec{J}_E$ permeating the boundary, whereas temporal changes of Q at the boundary are neglected ($dQ/dt = 0$). **b** Predominant dielectric phenomena at the assumed relatively high field frequency 1 GHz determine $Q = 0$ because $\vec{J}_C$ across the boundary can not accumulate any free electric charges at the boundary

$$\frac{J_{\mathrm{C,t}}^{+}}{\varepsilon_{+}} = \frac{J_{\mathrm{C,t}}^{-}}{\varepsilon_{-}}, \tag{2.110}$$

which similarly follows from the boundary condition in (2.96) via differentiation. Please note a qualitative similarity of tangential conditions from (2.103) and (2.110) for the conductive and dielectric phenomena, respectively. Here γ accounting for conductive behaviour (2.103) is substituted by ε for dielectric behaviour (2.110).

The applicable boundary condition for the *normal component* E_{n} of the *electric field* $\vec{E}$ is already given in (2.101) (with the condition $Q = 0$). The condition for the *tangential component* E_{t} of $\vec{E}$ is given by (2.96). The *normal component* D_{n} of the *electric flux density* $\vec{D}$ follows the condition in (2.100) (with $Q = 0$), whereas the *tangential component* D_{t} of $\vec{D}$ obeys (2.97).

Angles

Equation (2.66) shows that the *displacement current density field* $\vec{J}_{\mathrm{C}}$ in *isotropic media*—with ε as a real quantity—flows in the direction of the associated *electric field* $\vec{E}$ and the *electric flux density field* $\vec{D}$. For the temporal behaviour between $\vec{J}_{\mathrm{C}}$ and $\vec{E}$, see Fig. 2.18. Correspondingly,

- the *incident angles* φ^{-} to the normal of all three associated fields $\vec{E}$, $\vec{D}$, and $\vec{J}_{\mathrm{C}}$ *before the boundary* are *identical in size*. Similarly,
- an identical *refraction angle* φ_{C}^{+} to the normal applies *after the boundary* for all three fields $\vec{E}$, $\vec{D}$, and $\vec{J}_{\mathrm{C}}$.

Figure 2.36b illustrates the equality of φ^{-} pertaining to incident fields $\vec{E}$, $\vec{D}$, and $\vec{J}_{\mathrm{C}}$ as well as the equality of φ_{C}^{+} ($<\varphi^{-}$) of refracted fields $\vec{E}$, $\vec{D}$, and $\vec{J}_{\mathrm{C}}$ for the muscle/fat boundary.

For *dielectric phenomena*, the quantitative relation between φ^{-} and φ_{C}^{+} results to

$$\tan\varphi_{\mathrm{C}}^{+} = \frac{E_{\mathrm{t}}^{+}}{E_{\mathrm{n}}^{+}} = \frac{D_{\mathrm{t}}^{+}}{D_{\mathrm{n}}^{+}} = \frac{J_{\mathrm{C,t}}^{+}}{J_{\mathrm{C,n}}^{+}} = \frac{\varepsilon_{+}}{\varepsilon_{-}} \cdot \tan\varphi^{-}, \tag{2.111}$$

as can be derived under the condition $Q = 0$; for instance, considering field components of $\vec{J}_{\mathrm{C}}$ from (2.109) and (2.110).

It can be observed from (2.111) that the *angles* φ_{C}^{+} *and* φ^{-} *differ* ($\varphi_{\mathrm{C}}^{+} \neq \varphi^{-}$) only if both media show *heterogeneous permittivities* ($\varepsilon_{+} \neq \varepsilon_{-}$). In other words, different permittivities imply a directional change of the considered fields crossing the boundary. Again, a qualitative similarity of conditions from (2.106) and (2.111) for the conductive and dielectric phenomena, respectively, can be observed (with ε instead of γ).

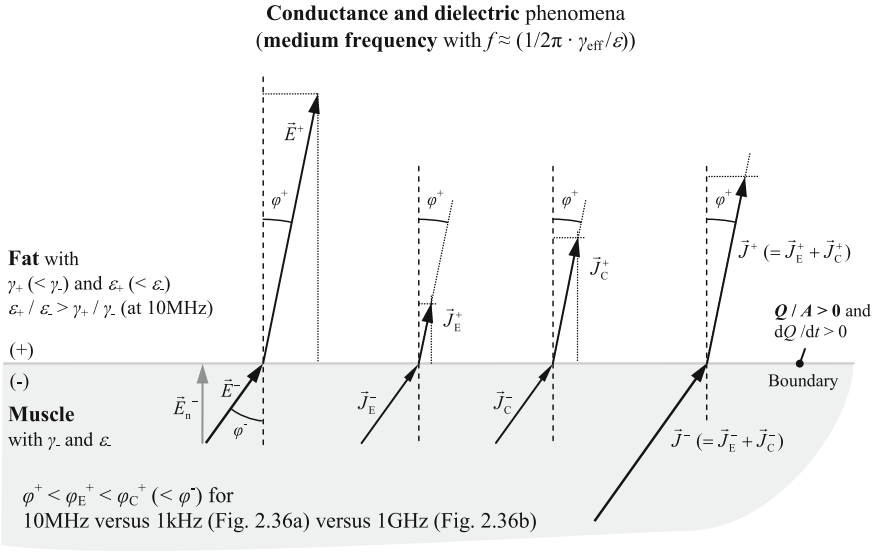

Fig. 2.37 Discontinuity between muscle and fat with the associated boundary conditions for vectors of the electric field $\vec{E}$, the conductive current density $\vec{J}_E$, the displacement current density $\vec{J}_C$, and the total current density $\vec{J}$ (2.112); compare Fig. 2.36. Isotropic muscle and isotropic fat have different electrical conductivities γ and dielectric permittivities ε. Conductance and dielectric phenomena prevail at the assumed field frequency 10 MHz. A positive unbound electric charge $Q > 0$ at the boundary and its positive rate of change $dQ/dt > 0$ result due to the inequality $\varepsilon_+/\varepsilon_- > \gamma_+/\gamma_-$ at 10 MHz (2.117) for the shown time instance with $E_n^- > 0$

Conductive and Dielectric Phenomena

Please recall that

- *conductive behaviour* in biological tissue is dominant for large γ when the condition $\gamma_{eff} \gg \omega \cdot \varepsilon$ (2.71) is fulfilled. Conductive behaviour prevails at relatively *low field frequencies* (2.118) with boundary conditions from Section "Conductive Phenomena" being applicable. In contrast,
- *dielectric behaviour* in biological tissue dominates for large ε when the reverse condition $\gamma_{eff} \ll \omega \cdot \varepsilon$ (2.72) is fulfilled. Dielectric behaviour is favoured at relatively *high field frequencies* (2.119), whereas boundary conditions from Section "Dielectric Phenomena" apply.

However, in most practical cases and for *finite field frequencies* both *conductive and dielectric phenomena* are present with the associated simultaneous *conductive and displacement currents*, respectively. The resulting total current density field $\vec{J}$ can be given as a vector sum of the conductive current density field $\vec{J}_E$ and the displacement current density field $\vec{J}_C$ according to

$$\vec{J} = \vec{J}_{\mathrm{E}} + \vec{J}_{\mathrm{C}}, \tag{2.112}$$

as detailed in (2.35). In fact, boundary conditions are needed to account for this practical situation, as elaborated below.

Field Components

The *normal components* $J_{\mathrm{E,n}}$ and $J_{\mathrm{C,n}}$ of the *conductive current density* $\vec{J}_{\mathrm{E}}$ and the *displacement current density* $\vec{J}_{\mathrm{C}}$, respectively—as illustrated in Fig. 2.37 for the muscle/fat boundary—obey

$$\frac{J^{+}_{\mathrm{E,n}}}{J^{-}_{\mathrm{E,n}}} = \frac{\gamma_{+}}{\gamma_{-}} \cdot \frac{\gamma_{-} + \omega \cdot \varepsilon_{-}}{\gamma_{+} + \omega \cdot \varepsilon_{+}} \quad \text{and} \quad \frac{J^{+}_{\mathrm{C,n}}}{J^{-}_{\mathrm{C,n}}} = \frac{\varepsilon_{+}}{\varepsilon_{-}} \cdot \frac{\gamma_{-} + \omega \cdot \varepsilon_{-}}{\gamma_{+} + \omega \cdot \varepsilon_{+}}. \tag{2.113}$$

The *tangential component* $J_{\mathrm{E,t}}$ of $\vec{J}_{\mathrm{E}}$ conforms to (2.103), whereas the *tangential component* $J_{\mathrm{C,t}}$ of $\vec{J}_{\mathrm{C}}$ to (2.110). The *normal component* J_{n} of the *total current density* $\vec{J}$ follows from (2.112) and satisfies $J_{\mathrm{n}} = J_{\mathrm{E,n}} + J_{\mathrm{C,n}}$, whereas for the associated *tangential component* the analogous equality $J_{\mathrm{t}} = J_{\mathrm{E,t}} + J_{\mathrm{C,t}}$ applies.

It can be verified that for very *low field frequencies* with $\omega \to 0$, where only *conductive currents* are present, the condition for $J_{\mathrm{E,n}}$ in (2.113) mutates into $J^{+}_{\mathrm{E,n}} = J^{-}_{\mathrm{E,n}}$. That is, the condition for $J_{\mathrm{E,n}}$ in (2.113) mutates into the *conductive condition* from (2.102) with $\mathrm{d}Q/\mathrm{d}t = 0$ (due to $\omega \to 0$). Likewise, the condition for $J_{\mathrm{C,n}}$ in (2.113) transforms into the *dielectric condition* $J^{+}_{\mathrm{C,n}} = J^{-}_{\mathrm{C,n}}$ from (2.109) for very *high frequencies* with $\omega \to \infty$, where only *displacement currents* are present.

It is interesting to observe the change in the *normal component* E_{n} of the *electric field* $\vec{E}$ (Fig. 2.37)—as can be derived from (2.99) and (2.117)—across the boundary, to give

$$\frac{E^{+}_{\mathrm{n}}}{E^{-}_{\mathrm{n}}} = \frac{E^{-}_{\mathrm{n}} \cdot \frac{\varepsilon_{-}}{\varepsilon_{+}} + \frac{Q}{A \cdot \varepsilon_{+}}}{E^{-}_{\mathrm{n}}} = \frac{\gamma_{-} + \omega \cdot \varepsilon_{-}}{\gamma_{+} + \omega \cdot \varepsilon_{+}}. \tag{2.114}$$

Equation (2.114) applies when simultaneous conductive and displacement currents are present. The *tangential component* E_{t} of $\vec{E}$ conforms to (2.96).

Please note that (2.114) mutates into the conductive condition from (2.104) for $\omega \to 0$ and conductive currents only. In analogy, (2.114) mutates into (2.101) for $\omega \to \infty$ and displacement currents only. In general, (2.114) offers a reasonable basis for practical estimations, for instance, as used in (2.121).

The boundary condition of the *normal component* D_{n} of the *electric flux density* $\vec{D}$ can be easily derived from (2.114) and $\vec{D} = \varepsilon \cdot \vec{E}$ (2.64) and follows

$$\frac{D^{+}_{\mathrm{n}}}{D^{-}_{\mathrm{n}}} = \frac{\varepsilon_{+} \cdot E^{+}_{\mathrm{n}}}{\varepsilon_{-} \cdot E^{-}_{\mathrm{n}}} = \frac{\varepsilon_{+}}{\varepsilon_{-}} \cdot \frac{\gamma_{-} + \omega \cdot \varepsilon_{-}}{\gamma_{+} + \omega \cdot \varepsilon_{+}}. \tag{2.115}$$

The *tangential component* D_t of $\vec{D}$ is given in (2.97).

Please note that (2.115) mutates into the condition from (2.105) for $\omega \to 0$ and conductive currents only. In analogy, (2.115) mutates into (2.100) for $\omega \to \infty$ and displacement currents only.

Angles

The assumed *isotropic medium* on both sides of the boundary—in the case of both *conductive and dielectric phenomena*—requires

- the *incident angles* φ^- to the normal of all three associated fields $\vec{E}, \vec{D}$, and $\vec{J}$ *before the boundary* to be *identical in size*. In addition, the *charge density* Q/A and its *temporal change* $1/A \cdot \mathrm{d}Q/\mathrm{d}t$ on the boundary are formed in a way that
- an identical *refraction angle* φ^+ to the normal results *after the boundary* for all these fields $\vec{E}$, $\vec{D}$, and $\vec{J}$.

Figure 2.37 illustrates the equality of φ^- pertaining to incident fields $\vec{E}, \vec{D}$, and $\vec{J}$ as well as the equality of φ^+ ($<\varphi^-$) of refracted fields $\vec{E}, \vec{D}$, and $\vec{J}$ for the muscle/fat boundary.

For *conductive and dielectric phenomena*, the quantitative relation between φ^- and φ^+ results to

$$\tan\varphi^+ = \frac{E_t^+}{E_n^+} = \frac{D_t^+}{D_n^+} = \frac{J_{C,t}^+}{J_{C,n}^+} = \frac{J_{E,t}^+}{J_{E,n}^+} = \frac{J_t^+}{J_n^+} = \frac{\gamma_+ + \omega \cdot \varepsilon_+}{\gamma_- + \omega \cdot \varepsilon_-} \cdot \tan\varphi^-. \qquad (2.116)$$

It can be verified that for very *low field frequencies* with $\omega \to 0$, where only conductive currents are present, (2.116) mutates into (2.106). On the other hand, (2.116) mutates into (2.111) for very *high frequencies* with $\omega \to \infty$, where only displacement currents are present. Therefore, the refracted value of φ^+ remains between φ_E^+ [from (2.106) for conductive currents only] and φ_C^+ [from (2.111) for displacement currents only] provided that a non-zero and finite frequency $\omega \geq 0$ is given and *electrical properties* γ and ε do not depend on frequency. However, properties γ and ε do strongly change over frequency; see Fig. 2.21 for the realistic course of γ over frequency and Fig. 2.20 for the realistic course of ε over frequency.

Surface Charge

Since both conductive and displacement currents are present across the boundary—between two electrically different and *isotropic media*—the *conductive current* may create a non-zero *surface charge density* Q/A directly at the boundary with its non-zero *rate of change* $1/A \cdot \mathrm{d}Q/\mathrm{d}t$, to give

$$\frac{Q}{A} = E_n^- \cdot \left(\frac{\varepsilon_+ \cdot \gamma_- - \varepsilon_- \cdot \gamma_+}{\gamma_+ + \omega \cdot \varepsilon_+} \right) \quad \text{and} \quad \frac{1}{A} \cdot \frac{\mathrm{d}Q}{\mathrm{d}t} = \omega \cdot E_n^- \cdot \left(\frac{\varepsilon_+ \cdot \gamma_- - \varepsilon_- \cdot \gamma_+}{\gamma_+ + \omega \cdot \varepsilon_+} \right). \qquad (2.117)$$

Please observe that Q/A from this equation equals Q/A from (2.107) for only conductive phenomena at $\omega \to 0$.

Conductive and Displacement Currents

Inhomogeneous tissue entails specific boundary conditions that have important effects on the *distribution of electric currents* within that tissue; namely, on the distribution of conductive and/or displacement currents. This distribution strongly depends on the *field frequency*.

- At *low frequencies* (2.118) for the predominant *conductive behaviour* ($\gamma_{\text{eff}} \gg \omega \cdot \varepsilon$), the *conductive current* follows pathways of the *least ohmic resistance* (2.36), e.g., from live electrode to ground electrode. It is like the flow of water in the river given a few parallel riverbeds, whereas most water follows down the widest riverbed. In local terms, the local conductive current density increases in high-conductivity regions (2.54). Here a sufficient ground for conductive currents can be easily created with a single *ground electrode*.
- The situation at *high frequencies* (2.119) for the predominant *dielectric behaviour* ($\gamma_{\text{eff}} \ll \omega \cdot \varepsilon$) is quite different. Here the *displacement current* follows pathways of the *largest capacitance* (2.41) and/or the *least inductance*, but not pathways of the least ohmic resistance. In local terms, the local displacement current density increases in high-permittivity regions (2.66). Here a single *ground electrode* will usually not be adequate to provide a sufficient ground. This is because displacement currents may choose not only the direct path to the ground electrode (even though closely located to the live electrode) carrying the ground potential but also can choose many other indirect paths to reach this ground potential (e.g., via longer paths through the air, see Fig. 3.31).

The total *current* takes always pathways of the *least impedance* (Fig. 2.13c). Please recall that the capacitive impedance is inversely related to the capacitance (2.42), whereas the conductive impedance equals to the ohmic resistance (2.36).

Biological Boundaries

From Muscle into Fat

Figure 2.36 demonstrates boundary conditions for the different fields permeating the discontinuity *from muscle into fat*, i.e., the *muscle/fat boundary*. Therefore, properties of the *muscle* and fields within the muscle carry the *superscript "−"*, whereas properties of the *fat* and fields within the fat carries the *superscript "+"*, in close analogy with Fig. 2.34. Please note that inequalities $\gamma_+ < \gamma_-$ and $\varepsilon_+ < \varepsilon_-$ apply irrespective of the field frequency; see frequency-dependent electrical properties of muscle and fat from Figs. 2.20 and 2.21.

From Muscle into Fat—Conductive Behaviour

Figure 2.36a assumes a *predominant conductive behaviour* at the *low field frequency* of 1 kHz. Here a predominant *conductive current* crosses this discontinuity from *muscle towards fat*. In fact, conductive behaviour is characterised by the *condition* $\gamma_{\text{eff}} \gg \omega \cdot \varepsilon$ (2.71) so that a direct non-alternating field with the field frequency $f = 0$, a relatively low frequency f

$$f \ll \frac{1}{2\pi} \cdot \frac{\gamma_{\text{eff}}}{\varepsilon} = f_{\text{r}}, \tag{2.118}$$

a large γ_{eff}, or a small ε is required. It should be stressed that the *effective conductivity* γ_{eff} is relevant here but not the pure ionic conductivity γ (2.82).

For muscle and fat at 1 kHz, the inequality $\gamma_{\text{eff}} \gg \omega \cdot \varepsilon$ still applies. That is, the term $(1/2\pi \cdot \gamma_-/\varepsilon_-)$—known as the *relaxation frequency* f_{r} (2.50)—equals about 13 kHz ($\gg$1 kHz) with electrical properties at f = 1 kHz for muscle with γ_- = 0.32 S/m and $\varepsilon_- = 435 \cdot 10^3 \cdot \varepsilon_0$ (Figs. 2.20 and 2.21). The relaxation frequency f_{r} $(=1/2\pi \cdot \gamma_+/\varepsilon_+)$ equals about 17 kHz ($\gg$1 kHz) with properties at 1 kHz for fat with γ_+ = 0.022 S/m and $\varepsilon_+ = 24 \cdot 10^3 \cdot \varepsilon_0$. Because of the low frequency, the rate $\mathrm{d}Q$ / $\mathrm{d}t$ of the accumulation of *unbound charges* directly at the boundary can be neglected, i.e., *stationary conditions* apply with a non-zero $Q \neq 0$ and $\mathrm{d}Q$ / $\mathrm{d}t = 0$.

Let us start with

- the *electric field* $\vec{E}$ $[=\vec{E}_{\text{n}} + \vec{E}_{\text{t}}$, see (2.92)] in Fig. 2.36a. Tangential components E_{t} are identical (2.96) while for normal components the inequality $E_{\text{n}}^{+} > E_{\text{n}}^{-}$ applies due to $\gamma_+ < \gamma_-$ at 1 kHz (i.e., 0.022 S/m < 0.32 S/m according to Fig. 2.21) (2.104).
- The *electric flux density field* $\vec{D}$ $[=\vec{D}_{\text{n}} + \vec{D}_{\text{t}}$, see (2.93)] in Fig. 2.36a shows the inequality $D_{\text{t}}^{+} < D_{\text{t}}^{-}$ due to $\varepsilon_+ < \varepsilon_-$ at 1 kHz (2.97) and, on the other hand, the inequality $D_{\text{n}}^{+} < D_{\text{n}}^{-}$ due to $D_{\text{n}}^{+} = D_{\text{n}}^{-} \cdot (\varepsilon_+ \cdot \gamma_-)/(\varepsilon_- \cdot \gamma_+) = D_{\text{n}}^{-} \cdot (24 \cdot 10^3 \cdot \varepsilon_0 \cdot 0.32$ S/m$)/(435 \cdot 10^3 \cdot \varepsilon_0 \cdot 0.022$ S/m$) \approx D_{\text{n}}^{-} \cdot 0.8$ (2.105). Concerning
- the *electric current density field* $\vec{J}_{\text{E}}$ $[=\vec{J}_{\text{E,n}} + \vec{J}_{\text{E,t}}$, see (2.94)] in Fig. 2.36a, the inequality $J_{\text{E,t}}^{+} < J_{\text{E,t}}^{-}$ holds due to $\gamma_+ < \gamma_-$ (2.103), whereas $J_{\text{E,n}}$ does not change across the boundary in view of $\mathrm{d}Q/\mathrm{d}t = 0$ (2.102).
- The accumulated *charge density* Q/A in Fig. 2.36a at the muscle/fat boundary surface turns to be negative[79] ($Q/A < 0$) because the term $\varepsilon_+/\gamma_+ - \varepsilon_-/\gamma_-$ $(=24 \cdot 10^3/0.022$ S/m $- 435 \cdot 10^3/0.32$ S/m $< 0)$ is negative provided that the incident component $J_{\text{E,n}}^{-}$ is positive (2.107). Please recall that the conductive current coming from the muscle and entering the fat creates this surface charge. The rate of the *charge density change* $1/A \cdot \mathrm{d}Q/\mathrm{d}t$ for conductive behaviour is zero.
- The *refraction angle* φ_{E}^{+} is less than the *incident angle* φ^{-} $(>\varphi_{\text{E}}^{+})$ in Fig. 2.36a due to $\gamma_+ < \gamma_-$ at 1 kHz (2.106).

[79] It is interesting to discuss separately the effect of the ratio γ_-/γ_+ and that of the ratio $\varepsilon_-/\varepsilon_+$ on the sign of Q for the muscle/fat boundary, in close analogy with the discussion of the sign of Q in Fig. 2.35a. Since $\gamma_- > \gamma_+$ applies, the inequality $\gamma_-/\gamma_+ > 1$ is valid, which would imply a positive Q (>0) at the boundary with the theoretically assumed $\varepsilon_- = \varepsilon_+$ (2.107). However, in reality, $\varepsilon_- > \varepsilon_+$ and $\varepsilon_-/\varepsilon_+ > 1$ apply also, which would imply a clearly negative Q (>0) at the boundary with the theoretically assumed $\gamma_- = \gamma_+$. Altogether, since the ratio γ_-/γ_+ ($\approx$14.5) is smaller than $\varepsilon_-/\varepsilon_+$ ($\approx 18.1 > \gamma_-/\gamma_+$), the resulting Q at the muscle/fat boundary turns to be negative (Fig. 2.36a).

Figure 2.36a illustrates the incident and refracted fields $\vec{E}$, $\vec{D}$, and $\vec{J}_E$ across the discontinuity from *muscle to fat* at 1 kHz. Please note that incident fields in *muscle* were assumed to have an identical magnitude to visualize their respective changes when passing this boundary. After the boundary, refracted fields in *fat* show different magnitudes because different boundary conditions apply. It can be observed in Fig. 2.36a that the incident angle φ^- to the normal of all considered vector fields is identical in size since an *isotropic preceding medium* was assumed before the boundary. Likewise, the same refraction angle φ_E^+ applies for all three fields in an *isotropic following medium*. In other words, all incident fields point in one direction as a consequence of the assumed *muscle isotropy* while all refracted fields point in another direction within the assumed *isotropic fat*.

From Muscle into Fat—Dielectric Behaviour

Figure 2.36b assumes a *predominant dielectric behaviour* at the *high field frequency* of 1 GHz. Here a predominant *displacement current* crosses this discontinuity from *muscle towards fat*. In fact, dielectric behaviour is characterised by the *condition* $\gamma_{eff} \ll \omega \cdot \varepsilon$ (2.72) so that a relatively high frequency f

$$f \gg \frac{1}{2\pi} \cdot \frac{\gamma_{eff}}{\varepsilon} = f_r, \tag{2.119}$$

a small γ_{eff}, or a large ε is required. For instance, the current magnitude $J_E \to 0$ for $\gamma_{eff} \to 0$ while the magnitude $J_C \neq 0$ (2.68). For muscle and fat at 1 GHz, the inequality $\gamma_{eff} \ll \omega \cdot \varepsilon$ already applies. That is, the *relaxation frequency* f_r (=1/2$\pi \cdot \gamma_-/\varepsilon_-$) equals about 0.32 GHz (<1 GHz) with electrical properties at f = 1 GHz for muscle with γ_- = 0.98 S/m and $\varepsilon_- = 55 \cdot \varepsilon_0$, whereas the size of f_r (=1/2$\pi \cdot \gamma_+/\varepsilon_+$) equals about 0.18 GHz (<1 GHz) with properties at 1 GHz for fat with γ_+ = 0.05 S/m and $\varepsilon_+ = 5.4 \cdot \varepsilon_0$ (Figs. 2.20 and 2.21).

- The *field* $\vec{E}$ in Fig. 2.36b passing the boundary shows identical E_t (2.96) but different $E_n^+ > E_n^-$ due to $\varepsilon_+ < \varepsilon_-$ at 1 GHz (2.101).
- The *field* $\vec{D}$ in Fig. 2.36b reveal $D_t^+ < D_t^-$ due to $\varepsilon_+ < \varepsilon_-$ (2.97) and $D_n^+ = D_n^-$ (2.100).
- The *displacement current density field* $\vec{J}_C$ [=$\vec{J}_{C,n} + \vec{J}_{C,t}$, see (2.95)] in Fig. 2.36b obeys the inequality $J_{C,t}^+ < J_{C,t}^-$ due to $\varepsilon_+ < \varepsilon_-$ (2.110) while the component $J_{C,n}$ does not change across the boundary (2.109).
- The *charge density* Q/A and its *rate of change* $1/A \cdot dQ/dt$ in Fig. 2.36b are zero because displacement currents do not accumulate any unbound charges.
- The *refraction angle* φ_C^+ is less than the *incident angle* φ^- (>φ_C^+) in Fig. 2.36b due to $\varepsilon_+ < \varepsilon_-$ at 1 GHz (2.111).

Figure 2.36b illustrates the incident fields $\vec{E}^-$, $\vec{D}^-$, and $\vec{J}_C^-$ and the refracted field $\vec{J}_C^+$ across the discontinuity from *muscle to fat* at 1 GHz. Again, all incident fields point in one direction as a consequence of the assumed *muscle isotropy* while all refracted fields point in another direction within the assumed *isotropic fat*. If we

compare the muscle/fat boundary behaviour at 1 GHz (Fig. 2.36b) with that at 1 kHz (Fig. 2.36a), we recognise $\varphi_C^+ > \varphi_E^+$ ($<\varphi^-$) because the relevant ratio $\varepsilon_+/\varepsilon_-$ [$\approx$0.1 at the high frequency of 1 GHz, see (2.111)] is larger than the ratio γ_+/γ_- [$\approx$0.068 at the low frequency of 1 kHz, see (2.106)]. Obviously, the relation between $\varepsilon_+/\varepsilon_-$ and γ_+/γ_- is a strong function of the field frequency—as illustrated in Figs. 2.20 and 2.21—which implies a frequency dependence in the relation between φ_E^+ and φ_C^+.

From Muscle into Fat—Conductive and Dielectric Behaviour
Figure 2.37 demonstrates a case where both *conductive and displacement currents* cross the boundary *from muscle to fat* at the field frequency of 10 MHz, i.e., at a *medium frequency f*

$$f \approx \frac{1}{2\pi} \cdot \frac{\gamma_{\text{eff}}}{\varepsilon} = f_r \tag{2.120}$$

in the range of the *relaxation frequency* f_r. The relaxation frequency f_r (=$1/2\pi \cdot \gamma_-/\varepsilon_-$) equals about 65 MHz with the muscle's electrical properties at f = 10 MHz with γ_- = 0.62 S/m and ε_- = 171 · ε_0, whereas f_r = $1/2\pi \cdot \gamma_+/\varepsilon_+$ equals about 38 MHz with the fat's properties at 10 MHz with γ_+ = 0.03 S/m and ε_+ = 14 · ε_0 (Figs. 2.20 and 2.21).

- The *field* $\vec{E}$ in Fig. 2.37 across the boundary is subjected to identical E_t (2.96) but different $E_n^+ > E_n^-$ due to $E_n^+ = E_n^- \cdot (0.62\ \text{S/m} + 2\pi \cdot 10 \cdot 10^6 \cdot 171 \cdot \varepsilon_0)/(0.03\ \text{S/m} + 2\pi \cdot 10 \cdot 10^6 \cdot 14 \cdot \varepsilon_0) \approx 19 \cdot E_n^-$ at 10 MHz (2.114).
- The *field* $\vec{D}$ across the boundary reveals $D_t^+ < D_t^-$ due to $\varepsilon_+ < \varepsilon_-$ (2.97) and $D_n^+ > D_n^-$ due to $D_n^+ \approx D_n^- \cdot 19 \cdot (14/171) \approx 1.55 \cdot D_n^-$ (2.115).
- The *field* $\vec{J}_C$ in Fig. 2.37 obeys the inequality $J_{C,t}^+ < J_{C,t}^-$ due to $\varepsilon_+ < \varepsilon_-$ (2.110) and $J_{C,n}^+ > J_{C,n}^-$ due to $J_{C,n}^+ = J_{C,n}^- \cdot 19 \cdot (14/171) \approx 1.55 \cdot J_{C,n}^-$ (2.113).
- The *field* $\vec{J}_E$ in Fig. 2.37 obeys $J_{E,t}^+ < J_{E,t}^-$ due to $\gamma_+ < \gamma_-$ (2.103) and $J_{E,n}^+ < J_{E,n}^-$ due to $J_{E,n}^+ = J_{E,n}^- \cdot 19 \cdot (0.03/0.62) \approx 0.9 \cdot J_{E,n}^-$ (2.113).
- The *charge density* Q/A and its *rate of change* $1/A \cdot \mathrm{d}Q/\mathrm{d}t$ in Fig. 2.37 are both positive because the inequality $\varepsilon_+/\varepsilon_- > \gamma_+/\gamma_-$ (14/171 > 0.03/0.62) holds for the assumed incident positive E_n^- (2.117).
- The *refraction angle* φ^+ is less than the *incident angle* φ^- ($>\varphi^+$) in Fig. 2.37 due to (1/19) < 1 at 10 MHz (2.116).

Figure 2.37 illustrates the incident and refracted fields $\vec{E}$, $\vec{J}_E$, $\vec{J}_C$, and $\vec{J}$ across the discontinuity from *muscle to fat* at 10 MHz. Again, all incident fields point in one direction as a consequence of the assumed *muscle isotropy* while all refracted fields point in another direction within the assumed *isotropic fat*. If we compare behaviours of the muscle/fat boundary at 1 kHz with the relevant φ_E^+ (Fig. 2.36a), at 10 MHz with φ^+ (Fig. 2.37), and at 1 GHz with φ_C^+ (Fig. 2.36b), we recognise the inequality $\varphi^+ < \varphi_E^+ < \varphi_C^+$ ($<\varphi^-$) driven by the inequality (1/19) < (0.068) < (0.1). Please note that the *unbound charge* $Q \neq 0$ at the boundary *alternates in its size and*

sign—as governed by the temporal variation speed $dQ/dt \neq 0$—in synchrony with the incident alternating fields, as can be derived from (2.117).

The discussed behaviour of the *electric field* $\vec{E}$ across the *muscle/fat boundary* at 1 kHz, 10 MHz, and 1 GHz—as illustrated in Figs. 2.36 and 2.37—reveals a few *general tendencies*. The field $\vec{E}$ with its only *tangential component* on the boundary, will pass through the boundary *without changing*. Behind this boundary, the field $\vec{E}$ will propagate without significant attenuation through the medium if the field frequency is relatively low and thus lossy interactions with the medium can be neglected (Fig. 2.6). Obviously, multiple reflections may increase accumulated losses due to the medium-related damping (Fig. 2.48).

In clear contrast to the tangential $\vec{E}$ field, the incident *normal component* of $\vec{E}$ is subjected to strong changes across the *muscle/fat boundary*. Since fat shows lower values of γ_{eff} and ε than muscle at any frequency (Figs. 2.20 and 2.21), the refracted normal component in fat has more than the tenfold size after the boundary than the incident normal component in muscle before the boundary. For instance, the increase factor is 14 at 1 kHz, 19 at 10 MHz, and 10 at 1 GHz (see above). In particular, this *increase factor* from *muscle into fat* is formed by the ratio

- γ_-/γ_+ for conductive behaviour (2.104),
- $\varepsilon_-/\varepsilon_+$ for dielectric behaviour (2.101), and
- $(\gamma_- + \omega \cdot \varepsilon_-)/(\gamma_+ + \omega \cdot \varepsilon_+)$ for mixed behaviour (2.114).

Consequently, the larger $\vec{E}$ field in fat than in muscle may imply a *higher heating rate in fat than in muscle*. Please note that there is a disproportionate increase in the deposited power within tissue with increasing inner $\vec{E}$ field; namely, the power varies as E^2 (2.56). Such considerations have important practical consequences, for instance, for shortwave diathermy, in which external fields have to be coupled into particular inner tissues such as muscle or fat for heat generation within that tissue in terms of therapy (Footnote 115).

From Air into Tissue

The *air/tissue boundary* is another prominent example of inhomogeneity effects. If we consider an isolated and conductive body, the outer electric field $\vec{E}$ in the air incident at the air/tissue boundary will be dominated by its *normal component* entering the body (Fig. 2.25). As already discussed, this is because the tissue's conductivity is much higher than that of the air (2.106). In fact, the surface of the conductive body—i.e., the surface of the air/tissue boundary—represents an equipotential surface, which forces the *tangential component* of $\vec{E}$ on this surface to disappear. For instance, a human body exposed to the electric field $\vec{E}$ in the air represents such conductive body with the normal incidence of $\vec{E}$ (Fig. 2.26a).

Since the external $\vec{E}$ field is normally incident on the body surface ($\vec{E} = \vec{E}_{\text{n}}^{-}$ in the preceding medium, see Fig. 2.34), the *boundary conditions* for the normal component determine the inner field within that body ($\vec{E} = \vec{E}_{\text{n}}^{+}$ in the following medium). As in the discussed case of the muscle/fat boundary, *high values of* γ_{eff}

and ε *of bodily tissue* (γ_{body} and $\varepsilon_{\text{body}}$) as related to those in the air (γ_{air} and ε_{air}) reduce strongly the inner $\vec{E}_{\text{n}}^{+} = \vec{E}_{\text{body}}$ field as related to the incident $\vec{E}_{\text{n}}^{-} = \vec{E}_{\text{air}}$ field. In fact, the inequality of magnitudes $E_{\text{n}}^{+} = E_{\text{n}}^{\text{body}} \ll E_{\text{n}}^{-} = E_{\text{n}}^{\text{air}}$ applies. In particular, the inner $\vec{E}_{\text{body}}$ within tissue is reduced by

- the factor $\gamma_{\text{air}}/\gamma_{\text{body}}$ (2.104) for *conductive behaviour* at relatively *low frequencies* (2.118), i.e., reduced by the ratio of *effective conductivities* of both interfacing media;
- the factor $\varepsilon_{\text{air}}/\varepsilon_{\text{body}}$ (2.101) for *dielectric behaviour* at relatively *high frequencies* (2.119), i.e., reduced by the ratio of *permittivities* of both interfacing media; and
- the factor $(\gamma_{\text{air}} + \omega \cdot \varepsilon_{\text{air}})/(\gamma_{\text{body}} + \omega \cdot \varepsilon_{\text{body}})$ (2.114) for *mixed behaviour* at medium frequencies (2.120); as determined by all three the *effective conductivities* γ_{air} and γ_{body} as well as the *imaginary conductivities* $\mathrm{j}\omega \cdot \varepsilon_{\text{air}}$ and $\mathrm{j}\omega \cdot \varepsilon_{\text{body}}$ (2.69) depending on the frequency.

If we assume *muscle* properties as being representative for *bodily tissue*—the outer field $\vec{E}$ is incident upon—it can be easily estimated that tissue behaves as a *dominant conductor* for relatively *low field frequencies up to MHz region* using the *conductor condition* $\gamma_{\text{eff}} \gg \omega \cdot \varepsilon$ (2.71).

- For *50 Hz* the relevant product $\omega \cdot \varepsilon_{\text{r}}^{\text{body}} \cdot \varepsilon_0$ in the body amounts to $2 \cdot \pi \cdot 50 \cdot 17 \cdot 10^6 \cdot \varepsilon_0 \approx 0.05$ S/m (for experimental values of $\varepsilon_{\text{r}}^{\text{body}}$ see Fig. 2.20 at 50 Hz) with the resulting inequality 0.05 S/m $\ll \gamma_{\text{body}}$ ($=\gamma_{\text{eff}} = 0.2$ S/m from Fig. 2.21 at 50 Hz). It is instructive to observe that although $\varepsilon_{\text{r}}^{\text{body}}$ of soft tissues is extraordinarily high in the order of 10^7, the *conductive behaviour* of tissue is still dominant.
- For *1 kHz*, the product $\omega \cdot \varepsilon_{\text{r}}^{\text{body}} \cdot \varepsilon_0$ amounts to 0.02 S/m with 0.02 S/m $\ll \gamma_{\text{body}}$ (=0.3 S/m at 1 kHz); the *conductive behaviour* is dominant.
- For *1 MHz*, $\omega \cdot \varepsilon_{\text{r}}^{\text{body}} \cdot \varepsilon_0 \approx 0.11$ S/m with 0.11 S/m $\ll \gamma_{\text{body}}$ (=0.5 S/m at 1 MHz); the *conductive behaviour* is still dominant.
- For *1 GHz*, the product $\omega \cdot \varepsilon_{\text{r}}^{\text{body}} \cdot \varepsilon_0 \approx 3$ S/m yields already the inequality 3 S/m $\gg \gamma_{\text{body}}$ (=1 S/m at 1 GHz). At this high frequency the conductive behaviour of tissue does not dominate any more but the *dielectric behaviour*.

In contrast to the exposed tissue, the surrounding *air* with its *very low conductivity* γ_{air} of about 10^{-15} S/m ($\ll \gamma_{\text{body}}$) behaves as a *dominant dielectric* for frequencies already as low as 50 Hz. That is, the relevant product $\omega \cdot \varepsilon_{\text{r}}^{\text{air}} \cdot \varepsilon_0$ in the air for 50 Hz amounts to $2 \cdot \pi \cdot 50 \cdot 1 \cdot \varepsilon_0 \approx 2.8 \cdot 10^{-9}$ S/m with $2.8 \cdot 10^{-9}$ S/m $\gg \gamma_{\text{air}}$. Obviously, the product $\omega \cdot \varepsilon_{\text{r}}^{\text{air}} \cdot \varepsilon_0$ increases with frequency so that its dominance over γ_{air} even progressively increases with frequency.

Let us consider a special case of the *power line frequency of 50 Hz*, which is highly relevant in terms of an unintended body's exposure (Fig. 2.89) and thus for field coupling into the body (Fig. 2.26). For instance, this situation applies when a *human body* resides *within the air* in the close vicinity of overhead *transmission*

lines (Footnote 80). As detailed above, the *body behaves as a conductor* at 50 Hz with dominating conductive currents within the body while the surrounding *air behaves as a dielectric* at 50 Hz with dominating displacement currents in the air. Therefore, the general boundary condition from (2.114)

$$E_{\mathrm{n}}^{\mathrm{body}} = \frac{\gamma_{\mathrm{air}} + \omega \cdot \varepsilon_{\mathrm{r}}^{\mathrm{air}} \cdot \varepsilon_0}{\gamma_{\mathrm{body}} + \omega \cdot \varepsilon_{\mathrm{r}}^{\mathrm{body}} \cdot \varepsilon_0} \cdot E_{\mathrm{n}}^{\mathrm{air}} \tag{2.121}$$

can be simplified for the relatively *low field frequencies* as

$$E_{\mathrm{n}}^{\mathrm{body}} \approx \frac{\omega \cdot \varepsilon_{\mathrm{r}}^{\mathrm{air}} \cdot \varepsilon_0}{\gamma_{\mathrm{body}}} \cdot E_{\mathrm{n}}^{\mathrm{air}}. \tag{2.122}$$

Equation (2.122) is known as the *low-frequency approximation*. At 50 Hz, (2.122) yields $E_{\mathrm{n}}^{\mathrm{body}} = E_{\mathrm{n}}^{\mathrm{air}} \cdot 1.4 \cdot 10^{-8} \approx E_{\mathrm{n}}^{\mathrm{air}} \cdot 10^{-8}$ with values taken from Figs. 2.20 and 2.21. This approximation is used in many research reports (Heinrich 2015). In addition, the *electrical point effect* on the curved body's surface such as the *head* should be considered as an *additional multiplication factor* in (2.122); this factor is usually referred to as the *field distortion factor*. With an assumed multiplication factor of 15—a reasonable local amplification factor in the head region (Fig. 2.26a)—the amended approximation for 50 Hz reads as $E_{\mathrm{n}}^{\mathrm{body}} = 15 \cdot E_{\mathrm{n}}^{\mathrm{air}} \cdot 1.4 \cdot 10^{-8} \approx E_{\mathrm{n}}^{\mathrm{air}} \cdot 10^{-7}$ for the normal field coupling from the air into the human body.

This approximation illustrates that the induced *internal* $\vec{E}$ field in the body is strongly attenuated as related to the strength of the ambient *external* $\vec{E}$ field within the air. The induced field resides even *7 orders of magnitude* below that outside the body. It is as if the inner volume of the *biological body* is efficiently *shielded* from the ambient $\vec{E}$ fields. Amongst other things, this implies a *reduced interference* of ambient $\vec{E}$ fields with *medical implants* within the body. However, this interference can still not be neglected, as clearly illustrated for the case of an implanted *cardiac pacemaker* (Footnote 130).

These considerations based on (2.122) apply to the case of a standing human body in the ambient $\vec{E}$ field (Fig. 2.29) or a prolate spheroid exposed to $\vec{E}$ field (Fig. 2.49) to estimate inner $\vec{E}$ field strengths. However, such estimations are valid only up to about 10 MHz, i.e., up to the *resonance* range of the human body (Fig. 2.33).

Figure 2.38 demonstrates the *variation of the ratio* $E_{\mathrm{n}}^{\mathrm{body}}/E_{\mathrm{n}}^{\mathrm{air}}$ over *frequency* (2.121) when the body is approximated either as *muscle* or *fat*; in other words, when the *air/muscle boundary* or *air/fat boundary* is considered, respectively. The ratio is numerically evaluated with experimental data from Figs. 2.20 and 2.21. As expected from (2.122), *muscle* tends to show lower inner $\vec{E}$ fields than *fat* because of higher muscle conductivity (Fig. 2.21). In addition, the *general case* for the normal coupling (2.121) is compared with its *low-frequency approximation*

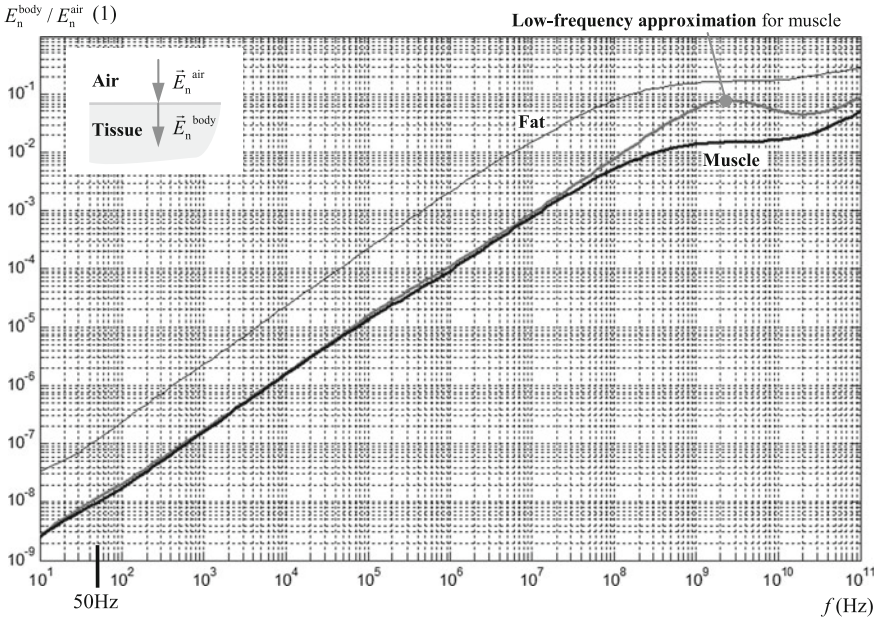

Fig. 2.38 Frequency variation of the ratio E_n^{body}/E_n^{air} of the magnitude E_n^{body} of the normal component of the electric field within the human body to the normal magnitude E_n^{air} in the air, given a planar air/tissue boundary. Here the body tissue is approximated either as muscle or fat. The ratio was estimated with (2.121) based on numerical data from Figs. 2.20 and 2.21. For comparison, the low-frequency approximation for the air/muscle boundary is shown (2.122). This ratio indicates the reduction factor of the normally incident electric field on the conducting body in the air when entering the body (Fig. 2.26a). The electrical point effect is not considered in the ratio

(2.122) for muscle. Here a clear overlap of both curves is evident in the relatively wide frequency range up to about 100 MHz, which confirms the validity of this approximation.

It can be observed from Figs. 2.38 and (2.122) that the aforementioned *shielding* weakens with increasing *field frequency*, i.e., the inner $\vec{E}$ field increases with frequency. The strength of the inner $\vec{E}$ field within the body scales roughly proportional to the field frequency up to about 100 MHz, as clearly seen in Fig. 2.33. In other words, while the nominator in (2.122) increases steeply with frequency—and the resulting ratio E_n^{body}/E_n^{air} too—the denominator with γ_{body} does not. Please compare this with the discussed proportional scaling of the inner current density in response to an external $\vec{E}$ field from Footnote 61.

The typical increase in the *effective conductivity* γ_{body} with increasing frequency —as shown in Fig. 2.21, where the body is approximated as muscle or fat— counteracts only insignificantly the increase in the inner $\vec{E}$ field with increasing frequency (2.122). Please recall from Fig. 2.35a that the inner $\vec{E}$ field tends to

decrease with increasing local conductivity. From a quantitative point of view, the relative increase in γ_{body} is much weaker than the associated increase in the corresponding frequency, provided that the absolute frequency is up to about 100 MHz. However, for even higher frequencies in the GHz range, γ_{body} raises steeply with frequency—in terms of γ-dispersion (Fig. 2.21)—so that the increase rate of E_n^{body}/E_n^{air} clearly loses its intensity in this frequency range (Fig. 2.38).

Examples

Let us consider a few *quantitative examples* for field coupling into an exposed human body from the air at typical *power line frequencies* 50/60 Hz, as illustrated in Fig. 2.26. With the assumed strength of the external $\vec{E}_{air}$ field in the air of 10 kV/m at 50 Hz and the spatial lines of the $\vec{E}_{air}$ field located in parallel to the long axis of the body (Fig. 2.30a), the inner $\vec{E}_{body}$ field in the body amounts to only 5 mV/m up to 25 mV/m depending on the body region (CRP 1997). Please note that 10 kV/m represents a quite reasonable level for exposed bodies located under *overhead transmission lines*.[80] The latter external and inner field levels yield the *attenuation factor* of $2.5 \cdot 10^{-6}$ up to $5 \cdot 10^{-7}$ ($=E_{body}/E_{air}$) which is well comparable to the estimated attenuation of about 10^{-7} from (2.122). In general, internal $\vec{E}$ fields are reported to be 6–7 orders of magnitude below that of incident external $\vec{E}$ fields (Foster 1996; Furse 2009).

Guidelines (ICNIRP 2010) provide other quantitative examples. Here local electric fields of about 1.7–2.6 mV/m in the *brain* are referred, as induced per kV/m of the ambient electric field at 50 Hz. The induced fields in the brain are relevant for their neurostimulation effects on the *central nervous system*. On the other hand, guidelines state much larger induced electric fields of about 12–33 mV/m in the *skin* per kV/m of the ambient electric field. These induced fields in the skin are relevant for their neurostimulation effects on the *peripheral nervous system* since peripheral nerve endings reside within the skin. Therefore, *technical electric fields* in the range of kV/m (Footnote 80) yield *inner electric fields* in the range of only mV/m. According to Section "Electric and Magnetic Field", these induced fields have comparable strengths as *natural endogenous electric fields* (1–50 mV/m).

If the human body is approximated by a *prolate spheroid* (Footnote 64), the *attenuation factor* amounts to about $2.5 \cdot 10^{-7}$ ($=E_{body}/E_{air}$ or $=E_1/E_{ext}$ in Fig. 2.30a) for the incident electric field at 60 Hz directed *parallel* to the long axis of the body (Furse 2009). For the *perpendicular* orientation of the incident field to the long axis of the body, the attenuation becomes even stronger with about $2 \cdot 10^{-8}$ ($=E_{body}/E_{air}$ or $=E_2/E_{ext}$ in Fig. 2.30b). As already discussed, the *body's exposure* to mainly tangential fields along the long axis (Fig. 2.30a) comprises the

[80]For comparison, the strength of the *electric field* is at most 6 and 4 kV/m at a height of 1 m above the ground under *overhead power transmission lines* (with the cable height of about 30 m above the ground) with the voltage 380 and 220 kV, respectively, and the field frequency of 50 Hz (CRP 1997); compare Footnote 71. In contrast, the electric field directly at the surface of *household devices* used in the daily routine amounts to only 10 V/m up to 100 V/m (CRP 1997).

worst-case scenario with the strongest induced inner fields for this field/body orientation, as compared with the normal incidence of fields on the body surface (Fig. 2.30b).

Own simulations with a *prolate spheroid* in Fig. 2.49 show the *attenuation factor* of $3 \cdot 10^{-7}$ (=300 μV/m / 1000 V/m) for the *longitudinal orientation* of the incident electric field along the long axis of the spheroid. For the *transversal orientation* of the incident field in Fig. 2.50, the attenuation, as expected, increases to $2.7 \cdot 10^{-8}$ (=27 μV/m / 1000 V/m). It can be observed in Fig. 2.49 that the *electrical point effect* significantly increases the local electric field right on the outer curved body surface where the local curvature is high. To be precise, on the top of the prolate spheroid, the field raises by a significant factor of 22 (=22 kV/m / 1 kV/m).

In response to the *induced electric field* within tissue, a certain *inner current density* results within tissue, as determined by the local conductivity (2.54). For instance, the induced electric field of 5 mV/m yields the current density of 1 mA/m^2 for the assumed homogenous conductivity of 0.2 S/m at 50 Hz (Table 2.2). It should be noted that this density level of 1 mA/m^2 is still below but already close to the related basic restriction of 2 mA/m^2 (Fig. 2.87).

Diffraction

The rationale of *diffraction of electromagnetic waves* can be best seen when the wavelength λ of the electromagnetic field is considered in relation to the size of an object or body the field is incident upon (Fig. 2.39).

- If the size of λ *is large* in relation to the body the field hits during its propagation (Fig. 2.39a), the larger part of the incident wave will *readily diffract* around the body and remains unaffected in its propagation, as discussed below. Likewise, for longer λ the particle behaves as a point source of diffracted waves, whereas the body's shape is of little importance. In analogy, the wave can also spread outward beyond *small openings* in the otherwise absorbing surface, i.e., openings in the order of a few λ or smaller. Consequently, the diffracted wave can not be a plane wave in the close vicinity of the body or opening, even though the incident wave is a simple plane wave.
- If the size of λ *is in the same order* of magnitude as the size of the body (Fig. 2.39b), the diffraction becomes less pronounced than for longer λ; i.e., bending of waves towards the particle past this particle lessens (compare Kaniusas (2015, Fig. 4.25b)). In addition, the *interference* usually arises among diffracted waves creating (alternating) regions of greater wave intensity (due to constructive interference) and lesser wave intensity (destructive interference); compare Fig. 2.40.
- For an even *smaller* λ below the size of the body (Fig. 2.39c), most of the incident wave is reflected back according to the *reflection* laws (Section "Reflection and Refraction") and a *wave shadow* is formed behind this particle; compare (Kaniusas 2015, Fig. 4.25a). Here the diffraction is small and

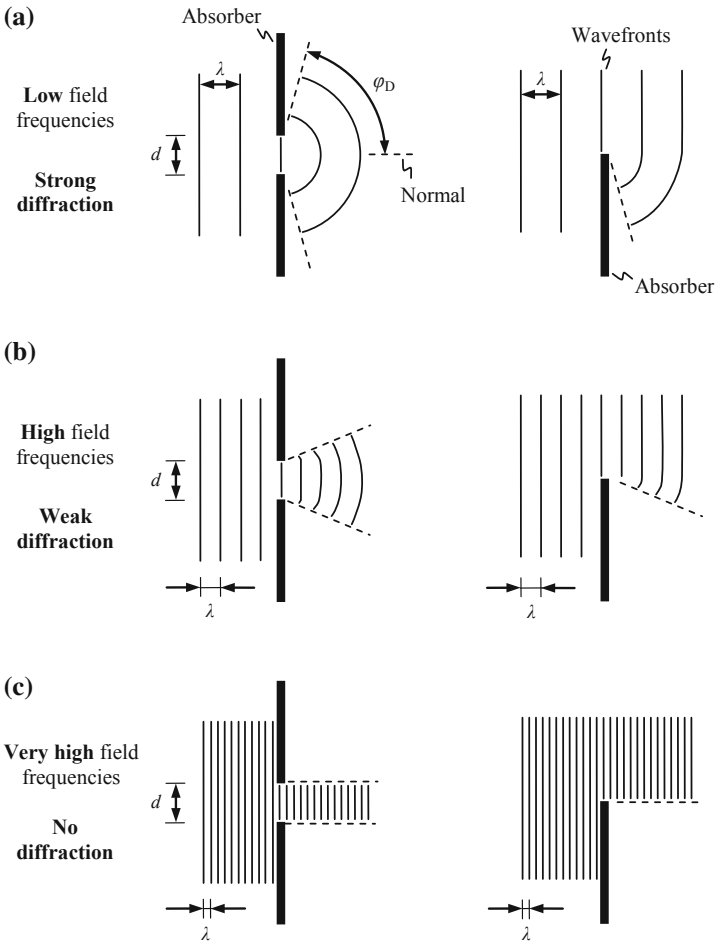

Fig. 2.39 Plane electromagnetic waves subjected to diffraction effects when incident on an opening, i.e., a window within an absorbing surface (left subfigures), and an absorbing barrier (right subfigures); compare (Kaniusas 2012, Fig. 4.25). **a** Strong diffraction (spreading and bending of waves) results for relatively low field frequencies with relatively large wavelengths λ ($\geq d$ with the opening width d). **b** Weak diffraction yields blurred geometric shadows casted behind openings and barriers for relatively high field frequencies with relatively small λ. **c** Very high field frequencies with very small λ cast sharp shadows behind relatively large absorbing objects; geometrical optics apply

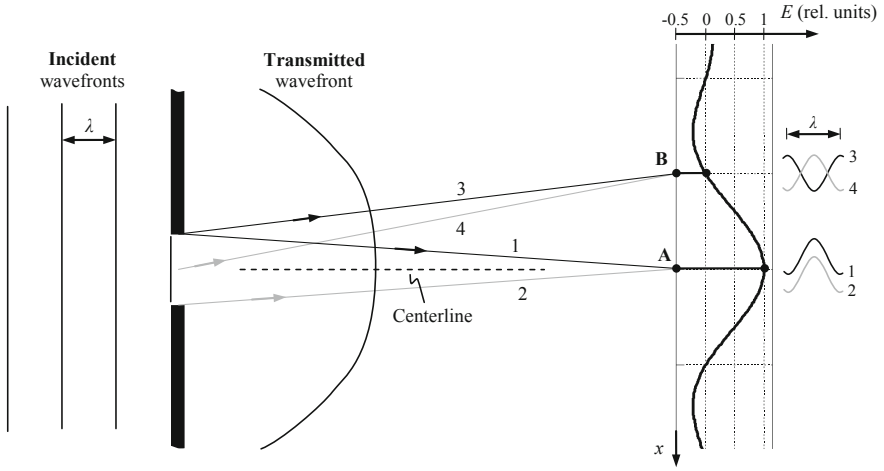

Fig. 2.40 Diffraction due to interference effects of the electric field E beyond the opening; compare Fig. 2.41. The points on the wavefront residing directly in the opening act as sources of the secondary spherical waves (Footnote 81). The resulting travelling waves beyond the opening interfere with each other. Constructive interference of the waves 1 and 2, and, on the other hand, destructive interference of the waves 3 and 4 are shown in far field. Constructive interference in the region A yields the global maximum in the spatial course of E. In contrast, destructive interference results in the region B where both waves arrive 180° out-of-phase; this interference yields zero local E. In fact, the resulting spatial course of E follows the sinc function $\sin(x)/x$. Please note that the local E^2 is related to the local power density $\vec{S}$ according to (2.13), i.e., related to the magnitude S from Fig. 2.41

can be neglected in the behaviour of the propagating electromagnetic wave. Likewise, the back scattered energy is much larger for the reflection than diffraction, as illustrated schematically in Kaniusas (2015, Fig. 4.25).

In fact, the *diffraction*—as illustrated in Fig. 2.39—manifests as

- the apparent *bending* of waves around *small particles* or *opaque barriers* (into the region of their geometrical shadow), i.e., around an aggregation of material with different Z (2.19) from the particle's or barrier's surrounding (compare Kaniusas (2015, Fig. 4.25)), and
- the *spreading* of waves past *small openings* (e.g., windows of absent absorption, located within a strongly absorbing surface).

Here small particles or openings mean that their size is small compared to the size of λ or is maximally in the order of λ.

In terms of the *diffraction of waves throughout an opening*, the extent of the spreading beyond an aperture in *far field* (see Fig. 2.41) is inversely proportional to the size of the opening d related to λ (in the propagation medium), to give

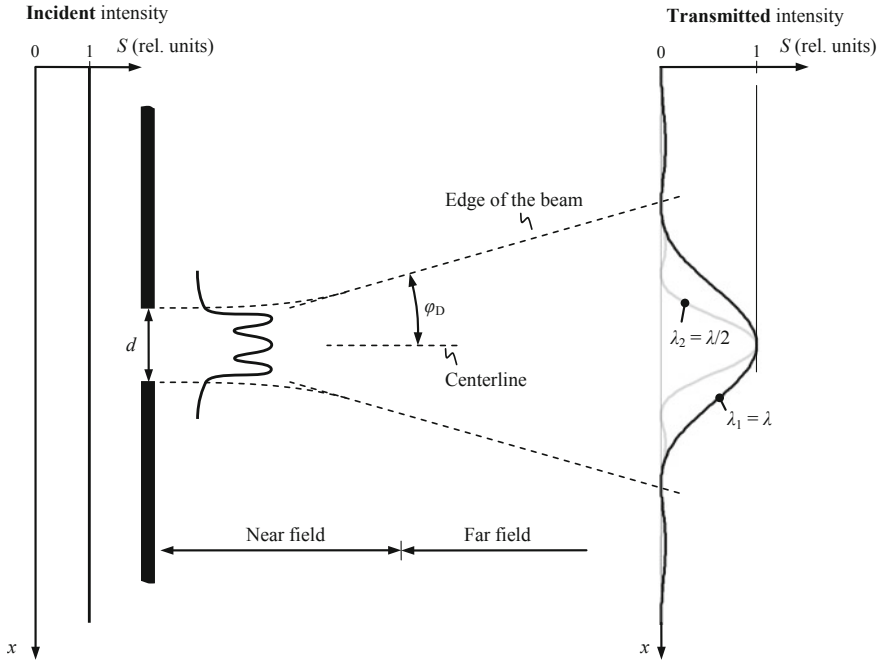

Fig. 2.41 Diffraction effects on the power density $\vec{S}$ (2.13) of the electromagnetic wave spread beyond a single opening with the size d. While the spatial profile of the magnitude S is highly irregular in near field close to the opening, this profile becomes much smoother in far field. Here it follows the squared sinc function $(\sin(x)/x)^2$. The diffraction angle φ_D (2.123) is indicated for the field wavelength $\lambda_1 = \lambda$. In contrast to this field, another electromagnetic field with the halved $\lambda_2 = \lambda/2$ yields a more narrow profile of S, i.e., the diffraction effects are less pronounced for smaller λ_2 and higher field frequencies; compare Fig. 2.39a, b

$$\sin(\varphi_D) = \frac{\lambda}{d}. \tag{2.123}$$

Here φ_D is the *diffraction angle*, i.e., the angle between the direction of the spreading wave (behind the opening) at which the first minimum intensity occurs (or the first minimum in the absolute value of the electric field) and the normal to the opening surface; see the indicated φ_D in Figs. 2.39a and 2.41. Here it should be recalled that depicted wavefronts of the electromagnetic field in Fig. 2.39 do not reflect the local wave intensity or the local magnitude of the electric field but instead indicate the field surfaces of constant phase. In contrast, Fig. 2.40 shows the spatial behaviour of the magnitude of the electric field, whereas Fig. 2.41 shows the spatial behaviour of the field intensity.

Please note that

- the smaller d,
- the longer λ, or
- the smaller the field frequency (2.5),

the larger is the *spreading* due to diffraction; namely, the spreading angle φ_D increases. Figure 2.39 illustrates the spreading for the relatively large and small λ. Likewise, there is no spreading (with $\varphi_D \to 0$) if the opening is much wider than λ [$\lambda/d \to 0$ in (2.123)]. Consequently,

- *low field frequencies* with large λ are likely to diffract throughout relatively small and large openings—or around relatively *small and large bodies*—whereas
- *high field frequencies* with small λ tend to diffract only beyond relatively small openings—or around relatively *small bodies* (Fig. 2.2).

It can be derived from Figs. 2.39a and (2.123) that a very *small opening* ($\ll\lambda$) has a large φ_D and thus acts as a *point field source* (Fig. 2.4) in far field with a *uniform radiation* pattern of *spherical waves*. Obviously, these spherical waves converge to *plane waves* at very far distances from the opening (Sect. 2.3.1.1). In addition, ideally *sharp shadows* are never produced at the *absorbing corners* (or opaque barriers for the electromagnetic waves) or after passage of waves through *openings* (Fig. 2.39); this is because of the residual diffraction around the corner or the edge of the opening.

In fact, the diffraction is the result of *interference of secondary spherical waves* in the opening,[81] i.e., superimposed secondary waves reinforce each other or cancel each other out. As already noticed, the interference is most pronounced when λ is comparable to the dimensions of the obstacle or opening.

Figure 2.40 illustrates the nature of the single opening (slit) *diffraction* in terms of the *wave interference*. For instance, the waves from all element pairs (directly in the opening) symmetric to the centerline of the opening—e.g., the waves 1 and 2 in Fig. 2.40—arrive in-phase at the region A and thus undergo *constructive interference*. In consequence, the resulting total electric field in the region A shows the global maximum. Likewise, this region is the most favourable location for constructive interference of all *secondary spherical waves* (see Footnote 81). In contrast, the waves 3 and 4 (Fig. 2.40) arrive 180° out-of-phase or $\lambda/2$ different in their travelled path; here *destructive interference* occurs. The resulting total electric field in the region B represents an overall minimum in its absolute magnitude. In

[81] In fact, every unobstructed point on the *incident wavefront* momentarily present in the *opening* (or slit) acts as a source of a *secondary spherical wave*. The superposition of all spherical waves determines the form of the *resulting transmitted wavefront* at any subsequent time behind the slit, i.e., the superposition determines the resulting *diffraction pattern* of the slit. Obviously, not only amplitudes but also relative phases of the individual spherical waves govern their *interference pattern* and thus the resulting transmitted wavefront beyond the opening.

Fig. 2.40 demonstrates two interference patterns:

- *constructive interference* of waves 1 and 2 leading to the maximum of the transmitted intensity, as well as
- *destructive interference* of waves 3 and 4 leading to the first null (from the centerline) in the transmitted intensity.

addition, Fig. 2.40 illustrates schematically the incident and transmitted wavefronts, in analogy with wavefronts from Fig. 2.39.

Figure 2.41 illustrates the *diffraction* with the *incident homogenous power density* $\vec{S}$ before the opening (i.e., the incident wave is a plane wave) and the *transmitted heterogeneous* $\vec{S}$ beyond the opening. Please note that the magnitude S of $\vec{S}$ (from Fig. 2.41) is a quadratic function of the electric field (from Fig. 2.40) according to (2.13). In the region of *near field*, the transmitted wave is not yet spread out appreciably while the width of the opening still determines the approximate width of the *laterally confined beam*. Here *spatial irregularities* dominate; namely, irregular local minima and maxima in the total *magnitude of the electric field* and in the resulting *magnitude of* $\vec{S}$ (Fig. 2.41). These irregularities are caused by the aforementioned constructive and destructive interference of secondary spherical waves (propagating from all points in the aperture, see Footnote 81).

Away from the opening in Fig. 2.41, *near field* transforms gradually into *far field*. The approximate distance of this transition (from the opening) is discussed in Footnote 5. In particular, the *spatial extension of near field* increases with larger opening (or with larger antenna). In far field, the wave profile of S becomes much more regular with a single central smooth peak dropping to null on both sides (Fig. 2.41). More importantly, the *edges of the beam* in far field—defined here by the first nulls on both sides of S from the centerline, see dotted lines in Fig. 2.41—start to spread laterally with increasing distance from the opening. The distance between both edges becomes linearly proportional to the distance of the considered S profile from the opening. The width of the central peak is inversely proportional to the width of the opening and is proportional to λ; in line with the definition of the angle φ_D in far field (2.123).

In analogy with the principle of the *inverse square law* [Footnote 9, (2.14), and Fig. 2.4], the incident power in the opening is spread out and distributed along the *surface area of wavefronts* beyond and surrounding the opening (i.e., the area with the local non-zero electric field or with the local non-zero S, see Figs. 2.40 and 2.41). Since the width of the spreading (or φ_D) beyond the opening increases with the diffraction strength, the latter surface area gets larger with stronger *diffraction* and, on the other hand, this area enlarges with the *ongoing propagation* of wavefronts away from the opening (i.e., enlarges with increasing distance of wavefronts from the opening).

Correspondingly, the local *power density* $\vec{S}$ (i.e., the power per unit area) at an observation point beyond the opening tends to decrease

- with stronger diffraction and
- with increasing distance from the opening (Footnote 9),

as also does the local *electric field* (2.13). In other words, the *peak electric field* and the *peak S* at a certain distance beyond the opening decrease when the diffraction becomes stronger (e.g., the ratio λ/d increases).

In *far field*, the curvature of the diffracted wavefront has a radius which is approximately equal to the distance of the wavefront from the opening. Here the

wavefront shape approximates a segment of a *spherical wave*—the stronger the diffraction, the larger is this segment (see Fig. 2.39a, b)—that emanates virtually from a point source centered in the opening; compare Fig. 2.4. Likewise, the *absolute amplitudes* of *sinc courses of the electric field* and that of *squared sinc courses of S* in far field—as demonstrated in Figs. 2.40 and 2.41—decrease with increasing distance of the observation point from the opening.

To give a tangible biomedical example, the diffraction is highly relevant when the *electromagnetic field* has to be coupled into the biological body for *hyperthermia* treatment (Footnote 115). The finite size of the aperture of the field applicator and thus the resulting non-zero spreading of beam in far field [in line with (2.123)] make a *localized energy deposition* impossible at deep regions of the body tissue. On the other hand, the *field frequency* should be kept relatively low to allow for a deep penetration of the wave within tissue (and thus for a deep heating); see Fig. 2.6. Since low frequency implies large λ (2.5), it unfortunately implies also a relatively large spreading of the field (2.123); see the discussion on the field penetration and focussing in Sect. 3.1.

Reflection and Refraction

Reflection

When a propagating electromagnetic wave impinges on the boundary between two *different media* (e.g., from the air on a biological object), a part of the incident wave bounces back into the incident medium while another part of the incident wave enters the medium behind the boundary. That is, the incident wave experiences

- *reflection* off the boundary surface and
- *refraction* across the boundary surface,

as illustrated in Fig. 2.42. The applicable *reflection and refraction laws*—as will be discussed below—assume that the *wavelength* of the wave is much smaller than the dimensions of the interface or of the body the wave is incident upon. Under this condition, *geometrical optics* can be applied for reflection and refraction laws. If the latter condition is not fulfilled, scattering phenomena (Kaniusas 2015, Fig. 5.11) and diffraction phenomena (Fig. 2.39) apply, whereas scattering is also known as diffuse reflection. In fact, reflection and refraction laws for the *electric field* $\vec{E}$ and *magnetic flux density field* $\vec{B}$ fields—both forming the *electromagnetic wave* (Fig. 2.3)—can be derived from *boundary conditions* (Section "Boundary Conditions") and wave equations (Balanis 1989).

In particular, *reflection laws* state that an electromagnetic wave incident upon a boundary will be reflected off the boundary surface at an *reflection angle* φ'_1 equal to the *incident angle* φ_1 (=φ'_1). Figure 2.42 demonstrates the incident and reflected wavefronts (Footnote 10) of a plane *TEM wave* (Footnote 4) on the boundary between two *different media*, whereas the equality of φ_1 and φ'_1 can be observed. Here the incident φ_1 comprises the angle between the direction $\vec{e}_1$ of the wave

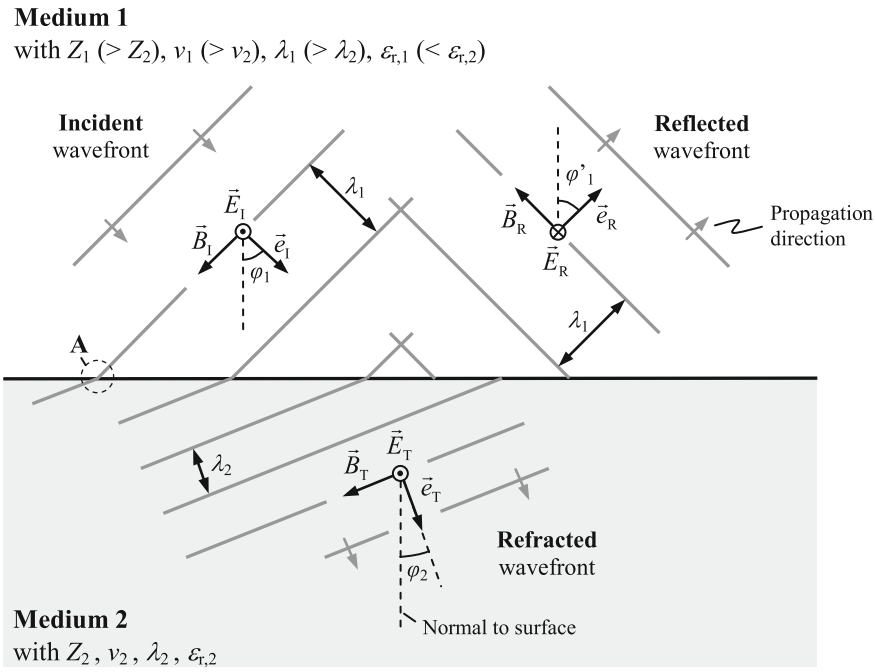

Fig. 2.42 Reflection and refraction of the plane TEM wave at oblique incidence on the boundary of two different media, shown in the plane of incidence. Right-angled and right-handed vectors of the electric field $\vec{E}$ (with the perpendicular polarization to the plane of incidence), the magnetic flux density $\vec{B}$, and the propagation direction $\vec{e}$ are shown. The respective index I, R, and T stands for the incident, reflected, and transmitted wave. Here v is the wave propagation velocity, λ the wavelength, φ_1 the incident angle (in the fast medium 1 before the boundary), φ'_1 the reflection angle (=φ_1, still in the medium 1), and φ_2 the refraction angle (in the slow medium 2 after the boundary)

incidence and the normal to the *reflective surface* at the point of the incidence; the direction $\vec{e}_I$ corresponds with the propagation direction $\vec{e}$ from (2.4) and Fig. 2.3. The reflection φ'_1 is defined in an analogous way with $\vec{e}_R$ as the propagation direction of the reflected wave (Fig. 2.42). Please note that all three $\vec{e}_I$, $\vec{e}_R$, and the normal lie in the same plane, known as the *plane of incidence*. This reflection law is mainly a consequence of the continuity of the tangential $\vec{E}$ field at the boundary (2.96), whereas the tangential $\vec{E}$ is zero for conducting surfaces (Fig. 2.25). The equality $\varphi_1 = \varphi'_1$ is valid irrespective of the *wave polarization* (Footnote 75).

The amount of the *reflected wave* $\vec{E}_R = E_R \cdot \vec{e}_E$ propagating along $\vec{e}_R$ at the boundary—as related to the *incident wave* $\vec{E}_I = E_I \cdot \vec{e}_E$ propagating along $\vec{e}_I$ and *obliquely incident* ($\varphi_1 = \varphi'_1 \neq 0$) on the boundary—from one *lossless medium* on another lossless medium is determined by the *reflection factor* Γ_E:

$$\Gamma_{\mathrm{E}} = \frac{E_{\mathrm{R}}}{E_{\mathrm{I}}} = \frac{Z_2 \cdot \cos(\varphi_1) - Z_1 \cdot \cos(\varphi_2)}{Z_2 \cdot \cos(\varphi_1) + Z_1 \cdot \cos(\varphi_2)}. \tag{2.124}$$

Here *perpendicular polarization* of the incident $\vec{E}_{\mathrm{I}}$ and $\vec{E}_{\mathrm{R}}$ waves is assumed to the *plane of incidence*, as depicted in Fig. 2.42. In (2.124), E_{I} and E_{R} are the respective magnitudes of $\vec{E}_{\mathrm{I}}$ and $\vec{E}_{\mathrm{R}}$, whereas Z_1 and Z_2 are the respective real-valued wave impedances (2.10) of the preceding and following medium at the boundary. The angle φ_1 and φ_2 is the *incident angle* and *refraction angle*, respectively.

The reflection-relevant *difference in media* present on both sides of the boundary is clearly described by the *difference in their Z* (2.124). For *lossless biological tissue*, the impedance Z is mainly determined by their relative *dielectric permittivity* ε_{r} (2.10). Consequently, when a wave is incident on a dielectric medium with the different ε_{r}, a reflected wave is necessarily produced; i.e., $\varepsilon_{\mathrm{r},1} \neq \varepsilon_{\mathrm{r},2}$ leads to $Z_1 \neq Z_2$ and then to $\Gamma_{\mathrm{E}} \neq 0$. Likewise, the reflected $\vec{E}_{\mathrm{R}}$ wave increases in its magnitude $E_{\mathrm{R}} = \Gamma_{\mathrm{E}} \cdot E_{\mathrm{I}}$ with increasing difference between $\varepsilon_{\mathrm{r},1}$ and $\varepsilon_{\mathrm{r},2}$ for lossless biological tissues. The reflected $\vec{E}_{\mathrm{R}}$ wave propagates in the *opposite direction* with the same *propagation velocity* as the incident $\vec{E}_{\mathrm{I}}$ wave [see (2.6) for lossless case]. Please compare the *incident direction* $\vec{e}$ with the opposite *reflected direction* $-\vec{e}$ in Fig. 2.45.

It is instructive to observe in Fig. 2.42 that if the refracted medium is a stronger *dielectric* than the incident medium (i.e., $\varepsilon_{\mathrm{r},1} < \varepsilon_{\mathrm{r},2}$, as applicable for the *boundary from the air to muscle or to fat*) then the inequalities $\varphi_1 > \varphi_2$ (2.130), $\cos(\varphi_1) < \cos(\varphi_2)$ (for $\varphi_1, \varphi_2 < 90°$), and $Z_1 > Z_2$ (2.10) apply. Consequently, the nominator $(Z_2 \cdot \cos(\varphi_1) - Z_1 \cdot \cos(\varphi_2))$ in (2.124) becomes negative with the resulting negative $\Gamma_{\mathrm{E}} < 0$. The negative Γ_{E}, in turn, implies that the *reflected* $\vec{E}_{\mathrm{R}}$ field points into the opposite direction than the *incident* $\vec{E}_{\mathrm{I}}$ field, as illustrated in Fig. 2.42. For instance, if we assume $\varphi_1 = 45°$, $\varepsilon_{\mathrm{r},1} = 1$, and $\varepsilon_{\mathrm{r},2} = 4$ in lossless media (with ε_{r} values from Fig. 2.5) then φ_2 results to about 20.7° (2.130), $Z_1 \approx 377\ \Omega$, $Z_2 \approx 377/2 \approx 188\ \Omega$ (2.10), and $\Gamma_{\mathrm{E}} \approx -0.45$.

The case with *oblique incidence* of the electromagnetic wave (2.124) can be simplified to *normal incidence* (with $\varphi_1 = \varphi'_1 = 0$). Here the propagation direction $\vec{e}_{\mathrm{I}} = -\vec{e}_{\mathrm{R}}$ is *normal* to the boundary surface, which renders both $\vec{E}$ and $\vec{B}$ fields to be purely *tangential* to this surface, as illustrated in Fig. 2.45. The factor Γ_{E} from (2.124) reduces to

$$\Gamma_{\mathrm{E}} = \frac{E_{\mathrm{R}}}{E_{\mathrm{I}}} = \frac{Z_2 - Z_1}{Z_2 + Z_1} \tag{2.125}$$

for *lossless media* on both sides of the boundary [with the assumed $\varphi_1 = 0$ and thus the resulting $\varphi_2 = 0$, see (2.130)]; compare similar (Kaniusas 2015, Eq. 4.15) for reflection of acoustic sounds and similar (Kaniusas 2015, Eq. 5.11) for reflection of light. In addition, the difference between *perpendicular and parallel polarizations* disappears for *normal incidence*.

For *normal incidence* and *lossless media*, the corresponding *transmission factor* T_E for the transmitted $\vec{E}_T = E_T \cdot \vec{e}_E$ with the magnitude E_T propagating along $\vec{e}_T$ behind the boundary as related to the incident $\vec{E}_I$ can be written as

$$T_E = \frac{E_T}{E_I} = 1 + \Gamma_E = \frac{2 \cdot Z_2}{Z_2 + Z_1}, \tag{2.126}$$

based on the simple condition

$$\vec{E}_T = \vec{E}_I + \vec{E}_R \quad \text{or} \quad E_T = E_I + E_R. \tag{2.127}$$

This boundary condition results from the continuity of the *tangential* $\vec{E}$ field at the boundary (2.96); compare Fig. 2.45 with indicated $\vec{E}_I$, $\vec{E}_R$, and $\vec{E}_T$. In fact, we can differentiate between

- the *partial reflection* marked by $|\Gamma_E| < 1$. As the ratio $\varepsilon_{r,2}/\varepsilon_{r,1}$ increases, the discontinuity met by the incident wave becomes stronger so that the *reflection strength* $|\Gamma_E|$ increases while the *transmission efficiency* $|T_E|$ decreases. The reflected field $\vec{E}_R \neq \vec{0}$ is present only if $\vec{E}_I \neq \vec{E}_T$ (or $\varepsilon_{r,2}/\varepsilon_{r,1} \neq 1$) applies. The magnitudes E_I, E_R are inversely related to $\varepsilon_{r,1}$ while E_T is inversely related to $\varepsilon_{r,2}$ (2.10); thus E_I, E_R, and E_T are never zero for finite ε_r ($\neq \infty$) in real dielectrics.
- The *total reflection*—or the *maximum possible reflection*—is marked by $|\Gamma_E| = 1$. For instance, $\Gamma_E = -1$ leads to $T_E = 0$ and thus to $\vec{E}_I = -\vec{E}_R$ and $\vec{E}_T = \vec{0}$ (2.126). There is no transmitted wave at all (Fig. 2.44). In analogy,
- the *absent reflection* implies $\Gamma_E = 0$ with $Z_1 = Z_2$ (2.125) and thus $T_E = 1$ with $\vec{E}_R = \vec{0}$, $\vec{E}_I = \vec{E}_T$ (2.126). The electromagnetic wave does not experience any electrically-relevant boundary and propagates without any changes from the incident medium into the refracted medium.

It is instructive to discuss the case of the *partial reflection* of the *normally incident* wave on a medium with stronger dielectric properties, such as the boundary from the *air to muscle or to fat* (Table 2.2). The inequality $\varepsilon_{r,2} > \varepsilon_{r,1}$ implies $Z_2 < Z_1$, i.e., there is an *inverse relationship* between Z and ε_r (2.10). The inequality $Z_2 < Z_1$ yields *negative reflection* with $\Gamma_E < 0$ (2.125), as illustrated in Figs. 2.46 and 2.47. In other words, the inequality $\varepsilon_{r,2} > \varepsilon_{r,1}$ forces the incident field $\vec{E}_I$ to decrease towards $\vec{E}_T$ at the onset of the medium following the boundary so that a specific $\vec{E}_R$ must arise in front of the boundary in order to compensate for this decrease. The compensation fulfils the *continuity requirement* for the total tangential $\vec{E}$ at the boundary (2.127). In short, $\varepsilon_{r,2} > \varepsilon_{r,1}$ forces $E_T < E_I$ and thus requires $E_R < 0$ with the negative $\Gamma_E < 0$. The negative Γ_E means that the *reflected* $\vec{E}_R$ is *out-of-phase* by 180° as compared with the incident $\vec{E}_I$.

For *normal incidence* and *lossy media*—with the non-zero *effective conductivity* γ_{eff}—the *reflection factor* $\underline{\Gamma}_{\text{E}}$ becomes a *complex-valued number* with

$$\underline{\Gamma}_{\text{E}} = \frac{\underline{E}_{\text{R}}}{\underline{E}_{\text{I}}} = \Gamma_{\text{E}} \cdot \mathrm{e}^{\mathrm{j}\varphi_{\Gamma}} = \frac{\underline{Z}_2 - \underline{Z}_1}{\underline{Z}_2 + \underline{Z}_1}. \tag{2.128}$$

Here $\Gamma_{\text{E}} = |\underline{\Gamma}_{\text{E}}|$ is the magnitude of $\underline{\Gamma}_{\text{E}}$, $\varphi_{\Gamma} = \arg(\underline{\Gamma}_{\text{E}})$ the phase angle of $\underline{\Gamma}_{\text{E}}$, and $\underline{Z}$ the complex wave impedance in lossy media (2.19). The complex $\underline{\Gamma}_{\text{E}}$ means an *out-of-phase relationship* by the phase φ_{Γ} between the incident $\vec{E}_{\text{I}}$ field and reflected $\vec{E}_{\text{R}}$ field, as revealed by the ratio of the *complex amplitudes* $\underline{E}_{\text{R}}$ and $\underline{E}_{\text{I}}$. Please note that φ_{Γ} is related to fields present *right on the boundary* because of the field's *lossy propagation*. For real $\underline{\Gamma}_{\text{E}} = \Gamma_{\text{E}}$ (2.125) in *lossless media*, there is either *zero phase* shift between $\vec{E}_{\text{I}}$ and $\vec{E}_{\text{R}}$ for $\Gamma_{\text{E}} > 0$ or even *180° shift* for $\Gamma_{\text{E}} < 0$, as discussed above. The reflected $\vec{E}_{\text{R}}$ wave increases in its magnitude $|\underline{E}_{\text{R}}|$ with increasing difference between $\underline{Z}_1$ and $\underline{Z}_2$—as determined by both the difference between $\varepsilon_{\text{r},1}$ and $\varepsilon_{\text{r},2}$ as well as the difference between $\gamma_{\text{eff},1}$ and $\gamma_{\text{eff},2}$ (2.19)—for *lossy biological tissues* (Table 2.2).

The *transmission factor* $\underline{T}_{\text{E}}$ in *lossy media* becomes also a complex-valued number with—in analogy with (2.126)

$$\underline{T}_{\text{E}} = \frac{\underline{E}_{\text{T}}}{\underline{E}_{\text{I}}} = 1 + \underline{\Gamma}_{\text{E}} = \frac{2 \cdot \underline{Z}_2}{\underline{Z}_2 + \underline{Z}_1} \tag{2.129}$$

connecting the transmitted $\vec{E}_{\text{T}}$ and incident $\vec{E}_{\text{I}}$ directly on the boundary.

In analogy with lossless media where increasing ε decreases its impedance Z (2.10), increasing γ_{eff} of *lossy media* contributes also to the magnitude Z decrease of the complex $\underline{Z}$ (2.19); see numerical examples related to muscle in Sect. 2.3.1. There is not only the aforementioned inverse relationship between Z and ε_{r} but also an *inverse relationship* between Z and γ_{eff}. In particular, the magnitudes E_{I} and E_{R} are inversely related to $\gamma_{\text{eff},1}$ while E_{T} is inversely related to $\gamma_{\text{eff},2}$. Not only different electrical properties $\varepsilon_{\text{r},1} \neq \varepsilon_{\text{r},2}$ but also different $\gamma_{\text{eff},1} \neq \gamma_{\text{eff},2}$ contribute to the inequality $\underline{Z}_1 \neq \underline{Z}_2$ (2.128) and thus render a reflected $\vec{E}_{\text{R}}$ to occur at the boundary. As in the case of lossless media, the boundary condition in (2.127) forces $\vec{E}_{\text{R}}$ to be produced in the incident lossy media as a compensation for the inequality $\vec{E}_{\text{I}} \neq \vec{E}_{\text{T}}$ right at the boundary; in short, $\vec{E}_{\text{R}}$ has to fulfil this boundary condition.

Figures 2.44 and 2.45 illustrate *normal incidence* from the air on a medium with the wave impedance obeying $\underline{Z}_2 \to 0$. The *total reflection* occurs with $\Gamma_{\text{E}} \to -1$ (2.125), $T_{\text{E}} \to 0$ (2.126) and thus with $\vec{E}_{\text{I}} = -\vec{E}_{\text{R}}$, $\vec{E}_{\text{T}} = \vec{0}$ right at the boundary. In other words, the *transmitted* $\vec{E}_{\text{T}}$ *field disappears* and the *total reflection* of the incident $\vec{E}_{\text{I}}$ field occurs on a medium

- with very high permittivity, i.e., total reflection occurs on a *perfect dielectric* with $\varepsilon_{\text{r},2} \to \infty$ and thus $\underline{Z}_2 \to 0$ (2.19), or

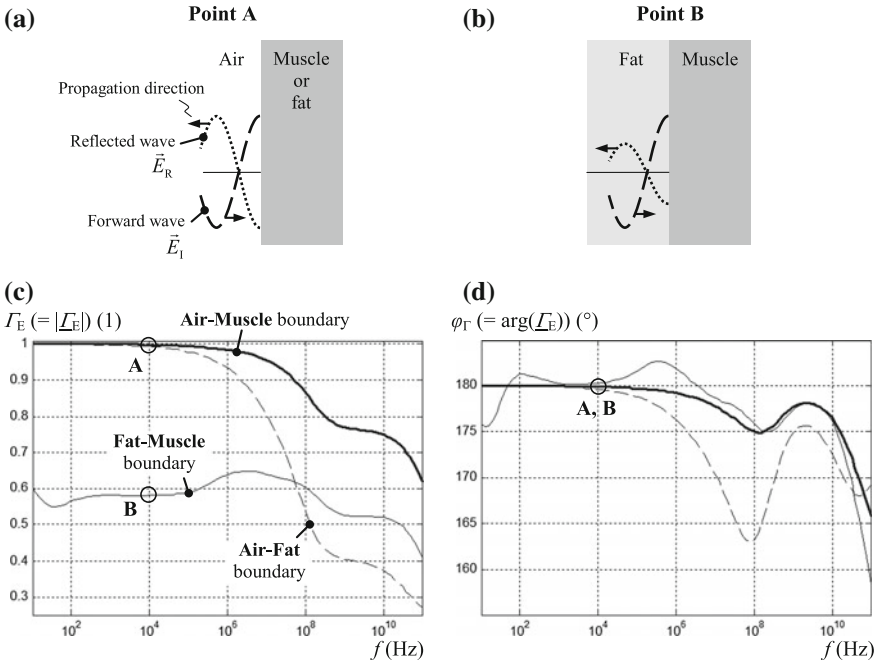

Fig. 2.43 Reflection of the plane TEM wave at normal incidence on the boundary **a** from the air into lossy muscle, the air into lossy fat; and **b** from the lossy fat into lossy muscle. Plotted time instances of waves of the incident and reflected electric field $\vec{E}$ are comparable with the time instant $\pi/2$ from Fig. 2.44c. The reflected wave is stronger and the corresponding magnitude Γ_E of the reflection factor $\underline{\Gamma}_E$ is higher at lower field frequencies *f*. $\underline{\Gamma}_E$ is stronger for the air as the incident medium than fat when entering muscle, especially at lower *f*. **c–d** The magnitude and phase of $\underline{\Gamma}_E$ (2.128) as a function of *f* considering the air/muscle, air/fat, and fat/muscle boundaries. The complex wave impedances of tissues were estimated with (2.19) based on numerical data of muscle and fat (Figs. 2.20 and 2.21), whereas the impedance of the air was approximated with 377 Ω (2.10)

- with very high conductivity, i.e., total reflection occurs on a *perfect conductor* with $\gamma_{\text{eff},2} \to \infty$ and thus $\underline{Z}_2 \to 0$ (2.19);

in analogy with the discussion in Footnote 56 related to *zero electric fields* within and on *ideally conductive bodies*. For instance, the electromagnetic wave reflects off a metal surface, e.g., as light reflects from a metallized mirror (Kaniusas 2015, Footnote 2 in Chap. 5). Obviously, a strong reflected $\vec{E}_R$ wave is also produced on a good, but not perfect, dielectric or, in analogy, on a good but not perfect conductor; the resulting $\vec{E}_T$ wave within this dielectric or this conductor, respectively, will be small but not zero.

Figure 2.43 evaluates quantitatively (2.128) based on *different boundaries* that are common when considering interactions of $\vec{E}$ fields with biological tissues. In particular, the boundary from the air to muscle (Fig. 2.43a) yields a higher

reflection strength Γ_E than the boundary from fat to muscle (Fig. 2.43b). In both cases, there is a clear *out-of-phase relationship* between $\vec{E}_I$ and $\vec{E}_R$ fields with $\varphi_\Gamma \approx 180°$.

From a quantitative point of view, $\Gamma_E \approx -0.77$ results at 1 GHz for the *air/muscle boundary*, whereas $\Gamma_E \approx -0.53$ results at 1 GHz for the *fat/muscle boundary*. This inequality $|-0.77| > |-0.53|$ occurs because electrical properties (ε_r and γ_{eff}, see Figs. 2.20 and 2.21) as well as the derived $\underline{Z}$ (2.19) differ to a larger extent between the air and muscle than between the fat and muscle. The larger is the difference in the respective $\underline{Z}$, the larger is $\underline{\Gamma}_E$ (2.128). In addition, the change in $\underline{Z}$ is larger for the *air/muscle boundary* than *air/fat boundary*, especially at higher frequencies (Fig. 2.43c); e.g., the air/fat boundary shows $\Gamma_E \approx -0.4$ at 1 GHz fulfilling the inequality $|-0.77| > |-0.4|$.

With *increasing frequency*, frequency-dependent properties ε_r and γ_{eff} of different tissues become progressively similar (Figs. 2.20 and 2.21) so that the associated $\underline{Z}$ values converge into each other. Consequently, the *reflection strength* Γ_E on considered boundaries within Fig. 2.43c tends to decrease with increasing frequency. In contrast, the *angle* φ_Γ remains rather constant close to 180° on all considered boundaries (Fig. 2.43d), which highlights the *out-of-phase relationship* between $\vec{E}_R$ and $\vec{E}_I$.

Refraction

A part of the incident electromagnetic wave, which was not reflected at the boundary, enters the medium behind the boundary (2.127). As shown in Fig. 2.42, the refracted wave experiences a redirection (or *bending*) owing to a change in electrical properties across the boundary.

In *lossless media*, the redirection owes to a change in the *propagation velocity* v (2.6) across the boundary. When a wave passes from a *fast medium* with v_1 into a *slow medium* with v_2 ($<v_1$), the propagation direction $\vec{e}_T$ of the refracted wavefronts is bent closer to the normal (to the *refracting surface*) with the resulting *refraction angle* φ_2 ($<\varphi_1$), as shown in Fig. 2.42. As soon as the incident wavefront hits the slow medium, this local wavefront is slowed down at its point of incidence, for instance, at the denoted point A in Fig. 2.42. Meanwhile, the rest of the incident wavefront—residing to the right of the point A—still continues to spread with the high v_1 until it also hits the slow medium. Therefore, the total incident wavefront is clearly rotated to the right when it enters the slow medium. It is as if the refracted wavefronts were flattened in the slow medium in relation to wavefronts in the fast medium.

As shown in Fig. 2.42, the slow medium decreases the distance between neighbouring *wavefronts* which implies a decreased *wavelength* λ_2 (2.7) with respect to the incident λ_1 ($>\lambda_2$). It should be reiterated that the frequency of the wave does not change when the wave enters another linear medium so that the lower v_2 in the slow medium yields necessarily a shorter λ_2, and vice versa.

For *lossless media*, the amount of bending is subject of *Snell's*[82] *refraction law*

$$\frac{\sin(\varphi_2)}{\sin(\varphi_1)} = \frac{k_1}{k_2} = \frac{\lambda_2}{\lambda_1} = \frac{v_2}{v_1} = \frac{\sqrt{\varepsilon_1 \cdot \mu_1}}{\sqrt{\varepsilon_2 \cdot \mu_2}} \cong \frac{\sqrt{\varepsilon_1}}{\sqrt{\varepsilon_2}}. \tag{2.130}$$

Please note that all three $\vec{e}_I$ of the incident wave, $\vec{e}_T$ of the refracted wave, and the normal to the refractive surface lie in the same plane. This law is applicable to waves irrespective of their *polarization*. In other words, for a given φ_1 and ε_1 of the incident medium, the refraction angle φ_2 decreases as ε_2 of the refracted medium—i.e., the dielectric medium into which the transmitted wave propagates—increases. Please compare (2.130) with the refraction law in Kaniusas (2015, Eq. 4.16) for refraction of acoustic sounds and in Kaniusas (2015, Eq. 5.12) for refraction of light.

The refraction in-between *lossy media* has to consider attenuated and *non-uniform waves* of $\vec{E}_I$, $\vec{E}_R$, and $\vec{E}_T$ on both sides of the boundary, in contrast to uniform plane waves (Footnote 4). Here the *complex form* of *Snell's refraction law* applies (Balanis 1989):

$$\frac{\sin(\phi_2)}{\sin(\phi_1)} = \frac{\alpha_1 + \mathrm{j}k_1}{\alpha_2 + \mathrm{j}k_2}. \tag{2.131}$$

The wavenumber k for lossless media (2.9) in (2.130) is substituted here by the complex *propagation constant* $\alpha + \mathrm{j}k$. The *attenuation coefficient* α (>0) accounts for *losses* and increases with increasing γ_{eff} (>0); see (2.21) and Table 2.1. The wavenumber k accounts for lossy media (2.18). The angles ϕ_1 and ϕ_2 in (2.131) are *complex angles* for $\alpha \neq 0$, whereas their physical meaning is not as immediate as a real angle. In other words, the *true physical angle of refraction* φ'_2 is not ϕ_2 which is complex and not real.

For instance, let us consider a boundary from dielectric to conductor, such as the *air/tissue boundary* [with $\alpha_1 = 0$ and $\alpha_2 \neq 0$ in (2.131)]. Within the conductor, a weak transmitted wave arises, which is exponentially damped in the *direction of the surface normal* but propagates in the *direction* $\vec{e}_T$ *of the refraction*. This direction $\vec{e}_T$ is inclined at the angle φ'_2 ($\neq\phi_2$) to the surface normal (Fig. 2.42). Therefore, the resulting *constant amplitude planes* in the conductor are parallel to the boundary surface, whereas the resulting *constant phase planes* are inclined at the true angle φ'_2 (see refracted wavefronts in Fig. 2.42). For a very *good conductor* behind the boundary, the refraction φ'_2 approaches zero ($\phi_2 \rightarrow 0$ and $\varphi'_2 \rightarrow 0$) and the refracted λ_2 strongly decreases (Table 2.1), whereas the reflection factor approaches unity ($\underline{\Gamma}_E \rightarrow -1$ with $\arg(\underline{\Gamma}_E) = 180°$, see Fig. 2.43c, d). For very good conductors, both φ'_2 and $\underline{\Gamma}_E$ are essentially independent on the incident φ_1.

[82] Willebrord Snellius (1580–1626) was a Dutch astronomer and mathematician after which *Snell's law* was named. This law relates the degree of the wave bending to the physical properties of materials which surround the bending surface.

Example—Standing Wave

The *total reflection* is demonstrated in Fig. 2.44 based on *normal incidence* of the plain TEM wave on the surface of a *perfect dielectric* ($\varepsilon_{r,2} \to \infty$) or a *perfect conductor* ($\gamma_{eff,2} \to \infty$); e.g., incident on a *metallic surface*. The time domain behaviour of the *harmonic waveform* E_I (t,r) of the *incident* $\vec{E}_I = E_I(t,r) \cdot \vec{e}_E$ is illustrated. Here the field $\vec{E}_I$ is *tangential* to the boundary surface and propagates into the direction $\vec{e}_I = \vec{e}$ towards the boundary with increasing coordinate r. In addition, the resulting harmonic waveform $E_R(t,r)$ of the *reflected* $\vec{E}_R = E_R(t,r) \cdot \vec{e}_E$ is shown that propagates into the opposite direction $\vec{e}_R = -\vec{e}$ away from the boundary towards decreasing r. The factor $\Gamma_E \to -1$ of the total reflection applies (2.128). It is as if $\vec{E}_R$ is *inverted* with respect to $\vec{E}_I$ (= $-\vec{E}_R$) *right at the boundary*

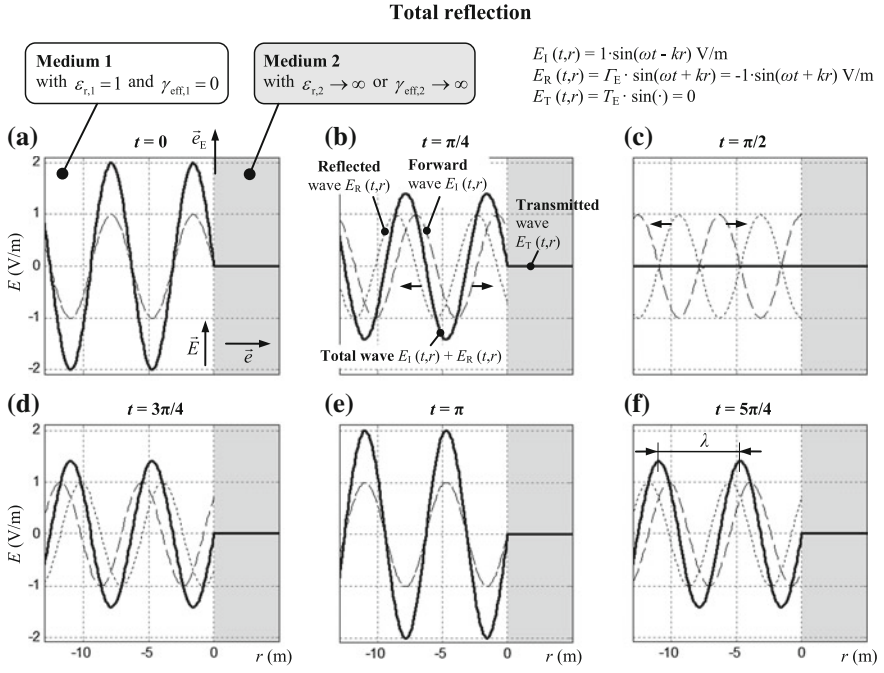
Total reflection
Medium 1
with $\varepsilon_{r,1} = 1$ and $\gamma_{eff,1} = 0$
Medium 2
with $\varepsilon_{r,2} \to \infty$ or $\gamma_{eff,2} \to \infty$
$E_I(t,r) = 1 \cdot \sin(\omega t - kr)$ V/m
$E_R(t,r) = \Gamma_E \cdot \sin(\omega t + kr) = -1 \cdot \sin(\omega t + kr)$ V/m
$E_T(t,r) = T_E \cdot \sin(\cdot) = 0$
(a) $t = 0$
(b) $t = \pi/4$
(c) $t = \pi/2$
(d) $t = 3\pi/4$
(e) $t = \pi$
(f) $t = 5\pi/4$
Reflected wave $E_R(t,r)$
Forward wave $E_I(t,r)$
Transmitted wave $E_T(t,r)$
Total wave $E_I(t,r) + E_R(t,r)$
E (V/m)
r (m)
λ

Fig. 2.44 Total reflection of the plane TEM wave at normal incidence on the boundary. The instantaneous waveforms $E(r)$ of the electric field $\vec{E} = E \cdot \vec{e}_E$ are shown along the coordinate r for the indicated equidistant time t instants (time step is $\pi/4$) in **a**–**f**. The incident wave $E_I(t,r)$ (with the peak value of 1 V/m propagating in the direction $\vec{e}$), the reflected wave E_R (t,r) (propagating in the opposite direction $-\vec{e}$), and the transmitted wave $E_T(t,r)$ (propagating in the direction $\vec{e}$) are shown; compare Fig. 2.45. The associated harmonic courses are given in the upper right part. Lossless dielectric medium (such as the air) is assumed before the boundary with its relative permittivity $\varepsilon_{r,1} = 1$, the effective conductivity $\gamma_{eff,1} = 0$, and the skin depth $\delta \to \infty$, whereas the associated $E_I(t,r)$ and $E_R(t,r)$ exhibit the wavenumber $k = 1$ rad/m (=$2\pi/\lambda$) and the angular frequency $\omega = 1$ rad/s. After the boundary, perfect dielectric ($\varepsilon_{r,2} \to \infty$) or perfect conductor ($\gamma_{eff,2} \to \infty$) is assumed, which yields the total reflection and thus a vanishing E_T (t,r). The reflection factor is $\Gamma_E = -1$ [=$(0 - Z_1)/(0 + Z_1)$, see (2.125)] while the transmission factor is $T_E = 0$ [=$(2 \cdot 0)/(0 + Z_1)$, see (2.126)]

surface; here $\vec{E}_R$ is 180° *out-of-phase* from $\vec{E}_I$. The *net field* $\vec{E}_I + \vec{E}_R$ with the amplitude $E_I(t,r) + E_R(t,r)$ is additively formed in front of the boundary along r (Fig. 2.44). Please note that this *sum field* $\vec{E}_I + \vec{E}_R$ with incident and reflected components represents the *effective field* $\vec{E}$ existing to the left of the halfspace (e.g., to the left of the metallic halfspace). For the total reflection, the *transmitted* $\vec{E}_T = E_T(t,r) \cdot \vec{e}_E = \vec{0}$ with the waveform $E_T(t,r) = 0$ disappears due to $T_E \to 0$ (2.126). Please note that the magnetic flux density field $\vec{B}$ of the plain TEM wave—see triplets of right-angled field vectors $\vec{e}_E$, $\vec{e}_B$, and $\vec{e}$ in Fig. 2.3—is not shown in Fig. 2.44 for the sake of simplicity.

All waveforms are shown at six *different instants of time*, with the time step of $\pi/4$ (Fig. 2.44). For all instants of time, the tangential $\vec{E}_T$ is zero on the surface of perfectly dielectric or perfectly conductive object (see above). Therefore, the *sum field* $\vec{E}_I + \vec{E}_R$ on the outer *boundary surface* (e.g., on the *metallic surface*) is also necessarily *zero* (Fig. 2.44a–f). This is because tangential $\vec{E}$ fields are continuous across any boundary satisfying $\vec{E}_I + \vec{E}_R = \vec{E}_T = \vec{0}$ at the boundary (2.127).

Figure 2.45 accumulates different time instants of the *sum field* $\vec{E}_I + \vec{E}_R$ along r with a smaller time step of $\pi/8$ within a single plot, whereas electric properties of media on both sides of the boundary remain the same as in Fig. 2.44. Interestingly, the wave $E_I(t,r) + E_R(t,r)$ amounts to zero at *certain positions* along the propagation path (in front of the boundary surface) and for all instants of time. In particular, all spatial points that lie at *multiple λ/2 intervals* from the boundary show zero effective field $\vec{E}$ $(=\vec{E}_I + \vec{E}_R = \vec{0})$ at all times. These *zero points* are known as *nodes* and are explicitly marked in Fig. 2.45. At these nodes, $\vec{E}_I$ and $\vec{E}_R$ fields—each propagating in opposite direction—are equal in their amplitude and opposite in sign so that they cancel each other at all times.

In-between nodes the total $E_I(t,r) + E_R(t,r)$ wave moves up and down over time in a sinusoidal fashion, as demonstrated in Fig. 2.45. *Minima and maxima* are formed, known as *antinodes*, which are also spaced at *λ/2 intervals*. This behaviour of nodes and antinodes is called *standing wave* which is the result of the local *constructive superposition* (forming antinodes) and the local *destructive superposition* (forming nodes) of the incident $\vec{E}_I$ and reflected $\vec{E}_R$ waves along r; compare Kaniusas (2012, Footnote 170) and Kaniusas (2015, Footnote 29 in Chap. 4)). Please note that $\lambda/2$ spacing is only valid for *normal incidence*,[83] whereas the

[83]For the sake of completeness it should be noted that *standing wave* patterns occur also for *oblique incidence* ($\varphi_1 \neq 0$) of the plane TEM wave. The resulting interference pattern of the incident $\vec{E}_I$ and reflected $\vec{E}_R$ waves (Fig. 2.42) resembles a *checkerboard pattern* of the magnitude of the sum field $\vec{E}_I + \vec{E}_R$. The resulting *nodes* are further apart than $\lambda/2$. In fact, the distance $\lambda/2 \,/\, \cos(\varphi_1)$ between two consecutive nodes—along the normal to the boundary surface—increases with the rising incident angle φ_1 (Furse 2009). As time progresses, this *pattern pulsates* while the positions of the nodes do not change, similar to normal incidence from Fig. 2.45.

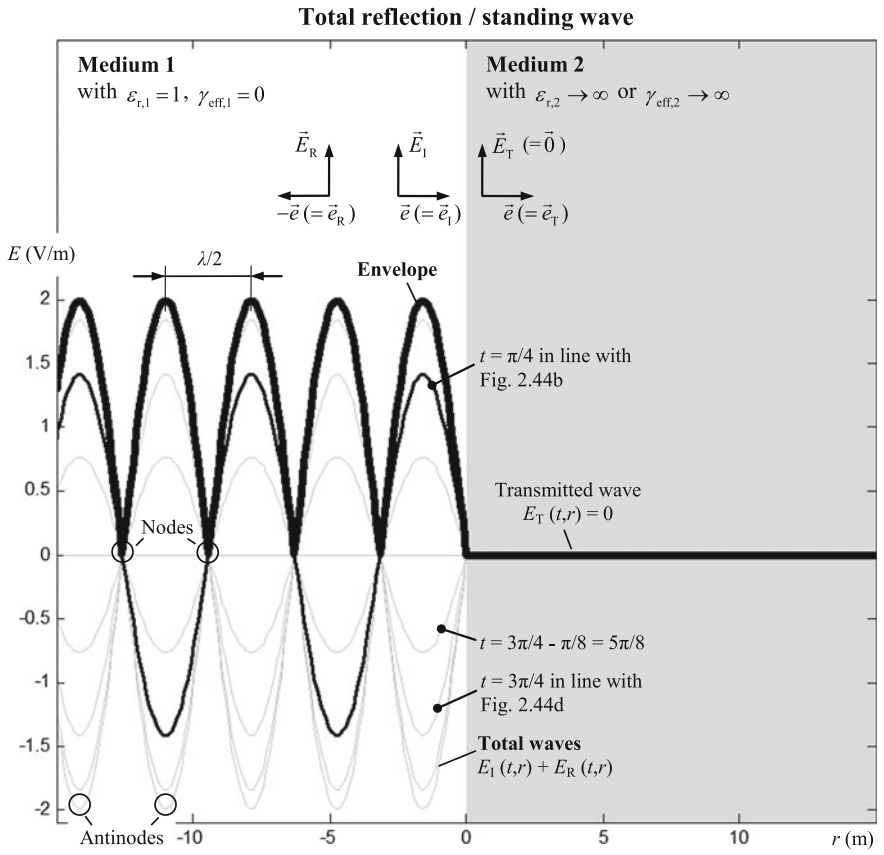

Fig. 2.45 Standing wave based on the total reflection of the plane TEM wave at normal incidence on the boundary; in analogy with Fig. 2.44. The instantaneous waveforms $E(r)$ of the electric field $\vec{E} = E \cdot \vec{e}_E$ are shown along the coordinate r for the indicated equidistant time t instants (time step is $\pi/8$). The total wave $E_I(t,r) + E_R(t,r)$ is illustrated before the boundary, given as the sum of the incident wave $E_I(t,r)$ and reflected wave $E_R(t,r)$. The transmitted wave $E_T(t,r)$ after the boundary amounts to zero for the total reflection. Adopted media on both sides of the boundary, the reflection and transmission factors are identical with that in Fig. 2.44. The envelope of $E_I(t,r) + E_R(t,r)$ is introduced with marked nodes and antinodes; compare Fig. 2.47 for the partial reflection

effective length of $\lambda/2$ is clearly proportional to the given *propagation velocity* v and inversely proportional to the used *field frequency* f (2.5).

Standing wave pattern is often represented by the *envelope* of the effective sum wave $E(t,r) = E_I(t,r) + E_R(t,r)$ or, in analogy, the envelope of the *effective field* $\vec{E}$ with the magnitude E, as depicted in Fig. 2.45. The envelope clearly shows the local positions of *nodes and antinodes*. In fact, the local amplitude of the *envelope* determines the local probability of electrical stimulation and thermal effects (Sect. 2.3.2.4).

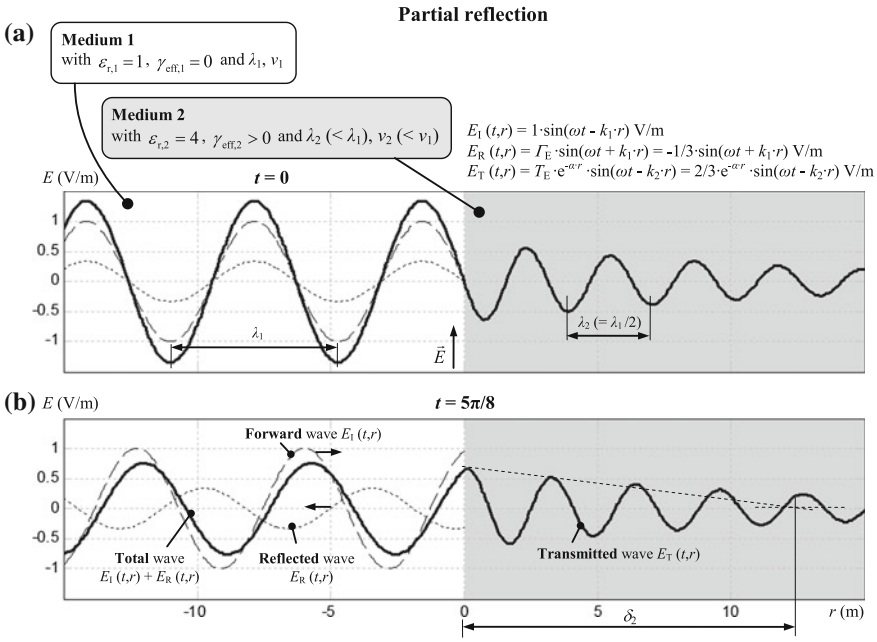
Partial reflection
(a)
Medium 1
with $\varepsilon_{r,1} = 1$, $\gamma_{eff,1} = 0$ and λ_1, v_1
Medium 2
with $\varepsilon_{r,2} = 4$, $\gamma_{eff,2} > 0$ and λ_2 (< λ_1), v_2 (< v_1)
$E_I(t,r) = 1 \cdot \sin(\omega t - k_1 \cdot r)$ V/m
$E_R(t,r) = \Gamma_E \cdot \sin(\omega t + k_1 \cdot r) = -1/3 \cdot \sin(\omega t + k_1 \cdot r)$ V/m
$E_T(t,r) = T_E \cdot e^{-\alpha r} \cdot \sin(\omega t - k_2 \cdot r) = 2/3 \cdot e^{-\alpha r} \cdot \sin(\omega t - k_2 \cdot r)$ V/m
E (V/m)
t = 0
1
0.5
0
-0.5
-1
λ_1
λ_2 (= λ_1/2)
$\vec{E}$
(b) E (V/m)
t = 5π/8
Forward wave $E_I(t,r)$
Total wave $E_I(t,r) + E_R(t,r)$
Reflected wave $E_R(t,r)$
Transmitted wave $E_T(t,r)$
-10
-5
0
5
10
δ_2
r (m)

Fig. 2.46 Partial reflection of the plane TEM wave at normal incidence on the boundary. The instantaneous waveforms $E(r)$ of the electric field $\vec{E} = E \cdot \vec{e}_E$ are shown along the coordinate r for two time t instants **a** $t = 0$ and **b** $t = 5\pi/8$. The incident wave $E_I(t,r)$ (with the amplitude of 1 V/m propagating in the direction $\vec{e}$), the reflected wave $E_R(t,r)$ (propagating in the opposite direction $-\vec{e}$), and the transmitted wave $E_T(t,r)$ (propagating in the direction $\vec{e}$) are shown; compare Fig. 2.47. The associated harmonic courses are given in the upper right part. Lossless dielectric medium (such as the air) is assumed before the boundary with its relative permittivity $\varepsilon_{r,1} = 1$, the effective conductivity $\gamma_{eff,1} = 0$, and the skin depth $\delta_1 \to \infty$, whereas the associated $E_I(t,r)$ and $E_R(t,r)$ exhibit the wavenumber $k_1 = 1$ rad/m ($=2\pi/\lambda_1$) and the angular frequency $\omega = 1$ rad/s. After the boundary, the lossy and predominant dielectric medium has $\varepsilon_{r,2} = 4$ and $\gamma_{eff,2} > 0$, which yields the partial reflection [$\gamma_{eff,2} \ll \omega \cdot \varepsilon_{r,2} \cdot \varepsilon_0$ applies, see (2.72)]. The propagating $E_T(t,r)$ shows increased $k_2 = 2\pi/\lambda_2 = k_1 \cdot \sqrt{\varepsilon_r} = 2$ rad/m, reduced wavelength λ_2 ($<\lambda_1$), and is subjected to exponential damping with $\delta_2 = 1/\alpha = 4 \cdot \pi$ m (Fig. 2.7). The reflection factor is $\Gamma_E = -1/3$ [$=(Z_1/\sqrt{4} - Z_1)/(Z_1/\sqrt{4} + Z_1)$, see (2.125) and Table 2.1] while the transmission factor is $T_E = 2/3$ [$=(2Z_1/\sqrt{4})/(Z_1/\sqrt{4} + Z_1)$, see (2.126)]

In particular, the local absolute size of the envelope indicates the local level of the *specific energy absorption rate* P_{SAR} (Fig. 2.48a, b) since the local P_{SAR} is a function of the local effective E^2 (2.58); compare Footnote 34. Therefore, the course of the envelope within *biological bodies* co-determines—jointly with γ_{eff}—the regional distribution of P_{SAR} inside bodies (e.g., exposed to electromagnetic radiation) and thus co-determines the local heat generation (2.155). In other words, spatial changes in P_{SAR} within a homogeneous tissue region showing a constant γ_{eff} are only determined by spatial changes in E^2. However, the resulting local increase in the tissue temperature depends not only on the local P_{SAR} but also on regulatory properties (Footnote 107).

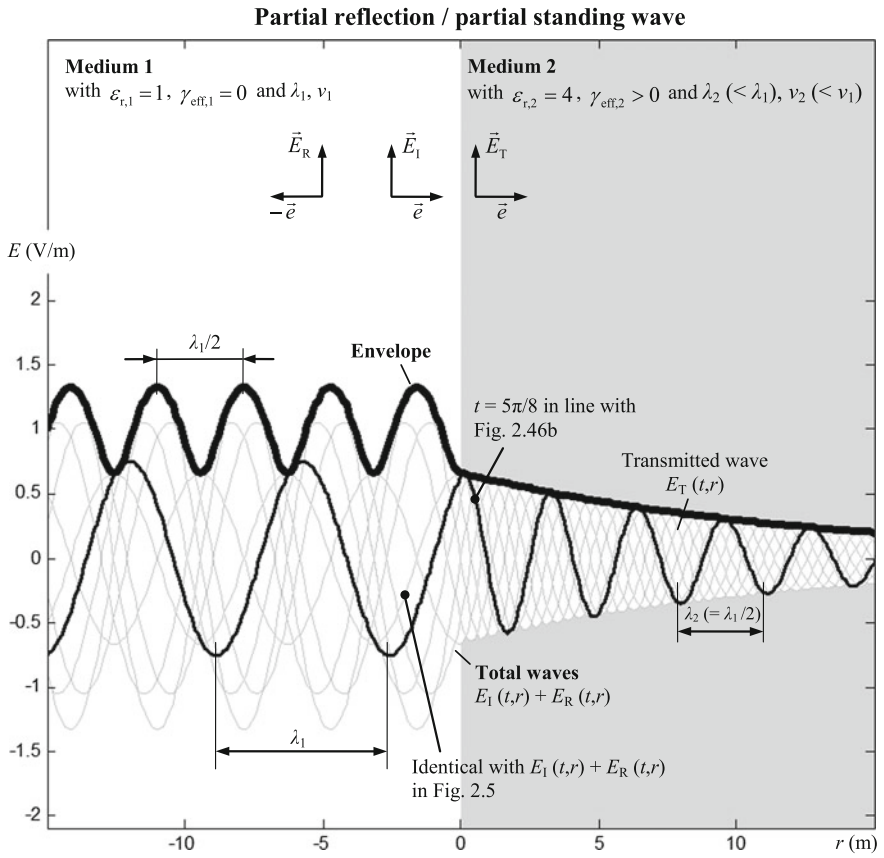

Fig. 2.47 Partial standing wave based on the partial reflection of the plane TEM wave at normal incidence on the boundary; in analogy with Fig. 2.46. The instantaneous waveforms $E(r)$ of the electric field $\vec{E} = E \cdot \vec{e}_E$ are shown along the coordinate r for the indicated equidistant time t instants (time step is $\pi/4$). The total wave $E_I(t,r) + E_R(t,r)$ is illustrated before the boundary, given as the sum of the incident wave $E_I(t,r)$ and reflected wave $E_R(t,r)$. After the boundary, the transmitted wave $E_T(t,r)$ is illustrated (Fig. 2.5). Adopted media on both sides of the boundary, the reflection and transmission factors are identical with that in Fig. 2.46. The envelope of $E_I(t,r) + E_R(t,r)$ before the boundary and the envelope of $E_T(t,r)$ after the boundary are introduced; compare Fig. 2.45 for the total reflection

Since the spatial course of the *standing wave* and its *envelope* is determined by λ (Fig. 2.45), it is obvious that the distribution of P_{SAR} within an exposed body becomes a strong function of the body size compared to λ. In particular, when the size is larger or equal to λ (Fig. 2.2b), the *distribution of* P_{SAR} can be expected to be highly *non-uniform* throughout the body.

Example—Partial Standing Wave

While Figs. 2.44 and 2.45 illustrate the *total reflection*, Figs. 2.46 and 2.47 detail quantitatively the *partial reflection* on the boundary between two different media.

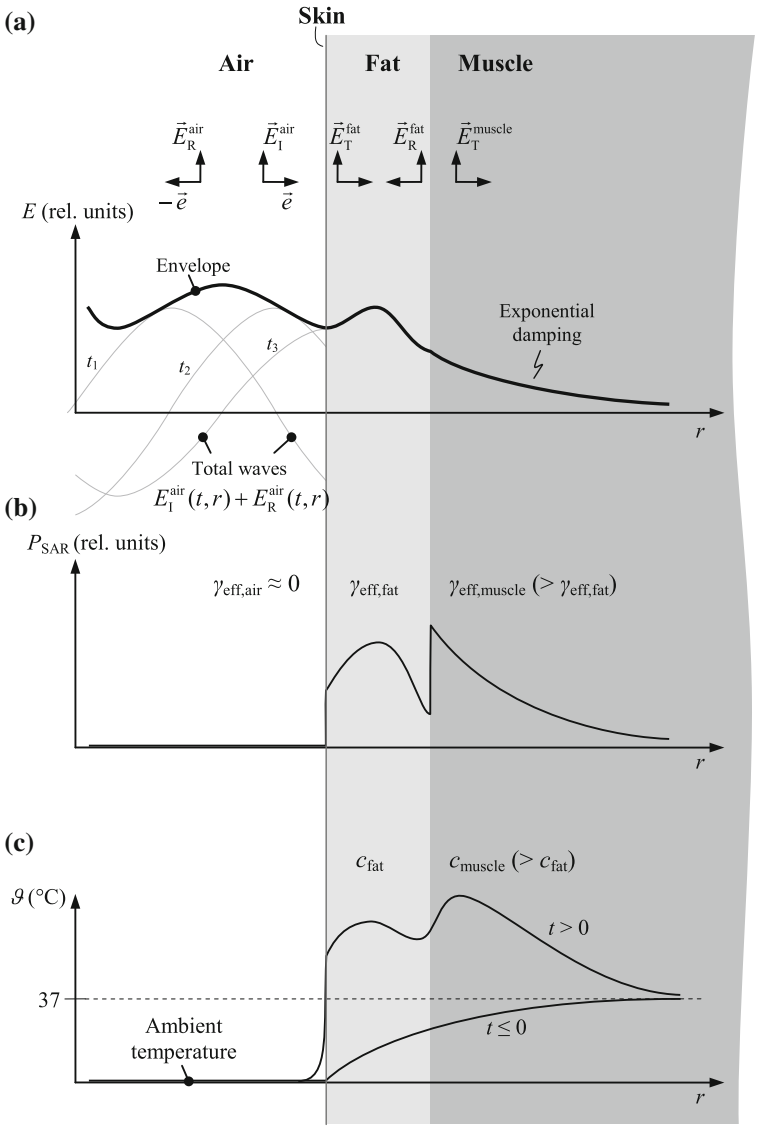
(a)
Skin
Air
Fat
Muscle
$\vec{E}_R^{air}$
$\vec{E}_I^{air}$
$\vec{E}_T^{fat}$
$\vec{E}_R^{fat}$
$\vec{E}_T^{muscle}$
$-\vec{e}$
$\vec{e}$
E (rel. units)
Envelope
Exponential damping
t_1
t_2
t_3
r
Total waves
$E_I^{air}(t,r) + E_R^{air}(t,r)$
(b)
P_{SAR} (rel. units)
$\gamma_{eff,air} \approx 0$
$\gamma_{eff,fat}$
$\gamma_{eff,muscle}$ (> $\gamma_{eff,fat}$)
r
(c)
c_{fat}
c_{muscle} (> c_{fat})
ϑ (°C)
37
$t > 0$
$t \leq 0$
Ambient temperature
r

◀**Fig. 2.48** Multiple reflections of the plane TEM wave at normal incidence on multiple boundaries, formed by the lossy heterogeneous body within the air. The body is approximated by a fat layer of a finite thickness followed by a semi-infinite muscle layer. **a** The incident wave $E_{\mathrm{I}}^{\mathrm{air}}$ of the electric field $\vec{E} = E \cdot \vec{e}_{\mathrm{E}}$ yields multiple partial reflections and re-reflections at the air/fat and fat/muscle boundaries, with reflected waves $E_{\mathrm{R}}^{\mathrm{air}}$ in the air and $E_{\mathrm{R}}^{\mathrm{fat}}$ in fat, and transmitted waves $E_{\mathrm{T}}^{\mathrm{fat}}$ in fat and $E_{\mathrm{T}}^{\mathrm{muscle}}$ in muscle. The sum waves $E_{\mathrm{I}}^{\mathrm{air}} + E_{\mathrm{R}}^{\mathrm{air}}$ and $E_{\mathrm{T}}^{\mathrm{fat}} + E_{\mathrm{R}}^{\mathrm{fat}}$ form partial standing waves in the air and fat, respectively (Fig. 2.47). The spatial wave $E_{\mathrm{I}}^{\mathrm{air}} + E_{\mathrm{R}}^{\mathrm{air}}$ is shown in the air for time instants t_1 to t_3. The continuous envelope of $E_{\mathrm{I}}^{\mathrm{air}} + E_{\mathrm{R}}^{\mathrm{air}}$, $E_{\mathrm{T}}^{\mathrm{fat}} + E_{\mathrm{R}}^{\mathrm{fat}}$, and $E_{\mathrm{T}}^{\mathrm{muscle}}$ is highlighted. The waves $E_{\mathrm{T}}^{\mathrm{fat}} + E_{\mathrm{R}}^{\mathrm{fat}}$ and $E_{\mathrm{T}}^{\mathrm{muscle}}$ are subjected to the exponential absorption in lossy fat and muscle, with their effective conductivities $\gamma_{\mathrm{eff,muscle}} > \gamma_{\mathrm{eff,fat}}$ (Table 2.2). **b** The non-zero $\gamma_{\mathrm{eff,muscle}}$ and $\gamma_{\mathrm{eff,fat}}$ yield a specific energy absorption rate P_{SAR} with its local maxima within the body. The course of P_{SAR} follows roughly the course of the envelope within the body (2.58) with a prominent discontinuity at the fat/muscle boundary (due to $\gamma_{\mathrm{eff,muscle}} > \gamma_{\mathrm{eff,fat}}$). **c** The resulting continuous distribution of the temperature ϑ. Before the body's exposure to the TEM wave (for time $t \leq 0$), a continuous increase of the local ϑ from the ambient temperature (<37 °C at the skin) towards the core body temperature (37 °C in muscle) can be observed. With ongoing exposure, the spatial distribution of ϑ leads to local maxima in ϑ. Some data are adopted from Pfützner (2003)

For the partial reflection, the incident medium is assumed to be a *lossless dielectric* while the transmitted medium behind the boundary is a *lossy and predominant dielectric medium*. Their electrical properties yield $\Gamma_{\mathrm{E}} = -1/3$ (2.128) and $T_{\mathrm{E}} = 2/3$ (2.129) using approximations for $\underline{Z}$ from Table 2.1. That is, the resulting $\vec{E}_{\mathrm{R}}$ is inverted with respect to $\vec{E}_{\mathrm{I}}$ but with a lower scaling factor of 1/3 (<1) than in the case of the total reflection (Fig. 2.44b).

The *transmitted* $\vec{E}_{\mathrm{T}}$ does not disappear at the boundary, travels behind the boundary down into the lossy dielectric medium (Fig. 2.47), and is subjected to the *exponential decay* (2.20). In general, a spatially extended decay arises in poor conductors or lossy dielectrics; otherwise, the total reflection would occur in front of good or perfect conductor with disappearing $\vec{E}_{\mathrm{T}}$ already at the boundary surface inside the conductor. Please recall that the attenuation forces $\vec{E}_{\mathrm{T}}$ to disappear within a certain *skin depth* δ under the boundary (2.21). The associated currents in response to $\vec{E}_{\mathrm{T}}$ within this lossy dielectric (Fig. 2.47) are therefore confined to a surface layer of the thickness δ. Since the lossy halfspace after the boundary is semi-infinite, *reflections are missing* below the boundary. In analogy with Fig. 2.5, increased permittivity $\varepsilon_{\mathrm{r},2}$ (=4) of the lossy dielectric medium with respect to the incident $\varepsilon_{\mathrm{r},1}$ (=1) reduces the refracted λ_2 with respect to the incident λ_1 ($= \sqrt{\varepsilon_{\mathrm{r},2}/\varepsilon_{\mathrm{r},1}} \cdot \lambda_2 = 2 \cdot \lambda_2$) and slows down the wave propagation with v_2 with respect to v_1 ($= 2 \cdot v_2$) (Table 2.1).

Figure 2.46 details two *different time instants*, $t = 0$ and $5\pi/8$, whereas Fig. 2.47 accumulates different time instants with a much smaller time step of $\pi/4$. In contrast to the total reflection, the net wave $E_{\mathrm{I}}(t,r) + E_{\mathrm{R}}(t,r)$ within the incident medium—in front of the boundary to a lossy dielectric halfspace—does not show any zero nodes for the *partial reflection*. Instead of nodes, clear *minima* can be observed within the *envelope* of $E_{\mathrm{I}}(t,r) + E_{\mathrm{R}}(t,r)$, occurring at regular spatial intervals. Such pattern is referred to as a *partial standing wave*.

A comparison of Fig. 2.45 with $\Gamma_E = -1$ and Fig. 2.47 with $\Gamma_E = -1/3$ demonstrates that *maxima of the envelope* increase (towards the maximum level of 2 at the regions of antinodes) with increasing magnitude $|\Gamma_E|$ while *minima of the envelope* decrease (towards the minimum level of 0 at nodes). In other words, the deflection width of the envelope increases with $|\Gamma_E|$ or, in analogy, the deflection increases with increasing difference between $\underline{Z}_2$ and $\underline{Z}_1$ (2.128), or between $\varepsilon_{r,2}$ and $\varepsilon_{r,1}$ (for lossy and predominant dielectric medium, see Table 2.1). The pattern of the *partial standing wave* (Fig. 2.47) approaches that of the *pure standing wave* (Fig. 2.45) for high values of $\varepsilon_{r,2}$ ($>\varepsilon_{r,1}$) behind the boundary, i.e., when the wave enters a strong dielectric. In addition, as $\varepsilon_{r,2}$ increases, Z_2 decreases (2.10) and so the magnitude of $\vec{E}_T$ at the boundary decreases (2.129). While

- a *standing wave* arises in front of
  - a *perfect dielectric* or
  - a *perfect conductor*

due to the *total reflection*,

- a *partial standing wave* is typically built in front of
  - a *weak conductor* or
  - a *lossy dielectric*

due to the *partial reflection*.

If the *incident medium* were also a *weakly lossy medium* (e.g., a weak conductor) in contact with a *strongly lossy medium* (e.g., a good or perfect conductor), both the incident $\vec{E}_I$ and reflected $\vec{E}_R$ would be subjected to the exponential damping during their propagation. Therefore, the resulting *envelope* of the *standing wave* or the envelope of the *partial standing wave* located within the weakly lossy medium would significantly differ in its shape from that within the lossless incident medium (Figs. 2.45 and 2.47).

Example—Multi-layered Tissue

Until now, we have considered a single boundary only. However, biological bodies are usually layered out of *different tissues* forming *multiple boundaries* within the body. Therefore, *multiple reflections* and *re-reflections* can occur between different boundaries facing each other (Fig. 2.48).

The reflection and transmission conditions—based on boundary conditions (Section "Boundary Conditions")—tend to yield *different strengths* of the inner electric $\vec{E}$ field within the *adjacent tissue layers* and so favour different levels of the resulting P_{SAR} within layers (2.58). For instance, the normal $\vec{E}$ fields tend to be larger in *fat* than in *muscle* when considering the *muscle/fat boundary* (Fig. 2.37).

In particular, *standing waves* (Fig. 2.45) and *partial standing waves* (Fig. 2.47) can be created between boundaries, especially at *higher field frequencies*, where the resulting λ approaches the thickness of tissue layer between boundaries (Fig. 2.2). Here the *ratio* of the layer thickness to λ strongly determines whether a standing

wave will arise within this layer. As already discussed, the standing wave shows local *minima* and *maxima* in the *spatial course* of the *envelope* of total $\vec{E}$ field ($= \vec{E}_I + \vec{E}_R$) and thus in the spatial course of the deposited P_{SAR}. Likewise, the ratio determines the *non-uniform spatial distribution* of $\vec{E}$ and P_{SAR} fields within individual tissue layers.

Figure 2.48 demonstrates qualitatively *multiple reflections* on and within a heterogeneous, multi-layered, and lossy biological body. In particular, an incident plane TEM wave within the air is *normally incident* on a *two-layered biological body* composed out of a fat layer with a finite thickness followed by a muscle layer with a semi-infinite thickness. Therefore, two boundaries are formed:

- the *air to fat boundary* with the reflection factor $\underline{\Gamma}_E \approx \Gamma_E \approx -0.4$ and the transmission factor $\underline{T}_E = 1 + \underline{\Gamma}_E \approx T_E \approx 0.6$ (2.129) at the assumed field frequency of 1 GHz; and
- the *fat to muscle boundary* with $\Gamma_E \approx -0.53$ and $T_E \approx 0.47$ (Fig. 2.43c).

Since $|\Gamma_E| < 1$ apply, *partial reflections* and *partial standing waves* can be expected within the *air* and the *fat* layer. In particular, *reflections* and *re-reflections* at the air/fat and fat/muscle boundaries lead to *partial standing waves*. In addition, the incident $\vec{E}_I$, reflected $\vec{E}_R$, and transmitted $\vec{E}_T$ waves within the lossy layers of fat and muscle are subjected to the *exponential decay* with increasing propagation distance (Fig. 2.48a), which certainly smoothes minima and maxima of standing waves.

Please recall that λ and v of propagating waves are the largest in the *air*, smaller in *fat*, and the smallest in *muscle*. This is because ε_r and γ_{eff} in the air are the smallest, increase in fat, and are the largest in muscle; see approximations for λ and v in Table 2.1 with numerical data in Table 2.2. In fact, increasing ε_r and γ_{eff} *slow down the wave propagation* while *accumulating wavefronts* in space.

As disclosed by Fig. 2.48a, *local maxima* result in the *envelope* of the total $\vec{E}$ in the *air* and *fat* in terms of partial standing waves. The *exponential damping* of the envelope can be observed in lossy *fat* and *muscle*, whereas the damping in muscle is stronger than in fat (Fig. 2.6); compare Fig. 2.5.

In the *air*, P_{SAR} is negligibly small because of the extremely low γ_{eff} [≈ 0, see (2.58) and Table 2.2)]. A local maximum of P_{SAR} arises in the *fat* layer (Fig. 2.48b). A strong discontinuity in P_{SAR} can be clearly observed at the *fat/muscle boundary*. While the tangential $\vec{E}$ is strictly continuous across all boundaries (2.96), as can be observed in Fig. 2.48a with the shown *tangential* $\vec{E}$ *field* only, the local P_{SAR} may change across boundaries in a step-wise manner. Namely, the size of P_{SAR} may jump when the local γ_{eff} abruptly changes across the boundary, given an even constant $\vec{E}$ across the boundary (2.58). In Fig. 2.48b, the conductivity γ_{eff} in fat before the boundary is smaller than γ_{eff} in muscle after the boundary so that the deposited local P_{SAR} steeply increases from fat to muscle across the boundary.

Since P_{SAR} is *unevenly distributed* across the different layers (Fig. 2.48b), the resulting local *heat* generation as well as the increase in the local *temperature* ϑ can also be expected to be uneven (2.155). Figure 2.48c illustrates the expected

temporal and spatial courses of ϑ within different tissues along the coordinate r. The *spatial distribution of* ϑ changes from the stationary distribution *before the exposure* by the incident TEM wave (for time $t \leq 0$) to another stationary distribution valid for the continuous and *constant exposure* ($t \gg 0$).

- *Before the exposure* ($t < 0$), the local *steady-state level* of ϑ increases continuously with r, i.e., increases naturally from the low ambient value at the skin level towards an increased value of the core body temperature (=37 °C) within the muscle (Kaniusas 2012, Sect. 3.1.5).
- With the *onset of the exposure* ($t = 0$), the local ϑ does not change at all due to its inertness; compare with ϑ (t) = 37 °C at $t = 0+$ and 0- in Fig. 2.85.
- With *ongoing exposure* ($t > 0$)—comparable with $t > 0$ in Fig. 2.85—the spatial distribution of ϑ elevates until local *equilibriums* along r are reached between
  - the locally *deposited* P_{SAR} (the external heating rises the local ϑ),
  - the local *storage* of heat by tissue itself (increasing *specific heat capacity* c reduces the local ϑ), and
  - compensatory *thermoregulatory mechanisms* (large contact area of blood vessels and fast blood flow reduce the local ϑ, see Footnote 107).

Figure 2.48c illustrates a possible *steady state* for ϑ over r for $t \gg 0$ when all involved local processes have reached their individual steady states; i.e., for t much larger than any time constants involved in thermoregulatory processes (Footnote 107).

The discussed increase in the deposited P_{SAR} after the *fat/muscle boundary* (Fig. 2.48b) favours a higher ϑ in muscle as related to fat. However, *thermoregulatory mechanisms* in *muscle* can be expected to be more pronounced and faster than in *fat*, which is due to dense vascularization and better perfusion of muscle. The thermoregulation in muscle limits the local increase in ϑ as related to fat. Therefore, both latter mechanisms counteract each other and avoid any prominent increase in ϑ after the fat/muscle boundary.

On the other hand, the heat capacity c of muscle is higher than that of fat (Fig. 2.48c). The higher c rises the *time constant* of the thermoregulation in muscle but do not influence the final value of the elevated ϑ (Footnote 107). There is also a continuous exchange of heat in between all three air, fat, and muscle layers, which leads to a smooth and steady spatial course of the local ϑ across all these layers. The impact of a fast or slow thermoregulation on the final ϑ is demonstrated in Fig. 2.85b.

2.3.2.3 Volume and Inhomogeneity Effects—A Quantitative Approach

Volume and inhomogeneity effects of electric, magnetic, and electromagnetic fields have been discussed in Sects. 2.3.2.1 and 2.3.2.2. Below a few quantitative examples will be provided to facilitate the basic understanding of the interaction between these fields and *heterogeneous biological tissue*.

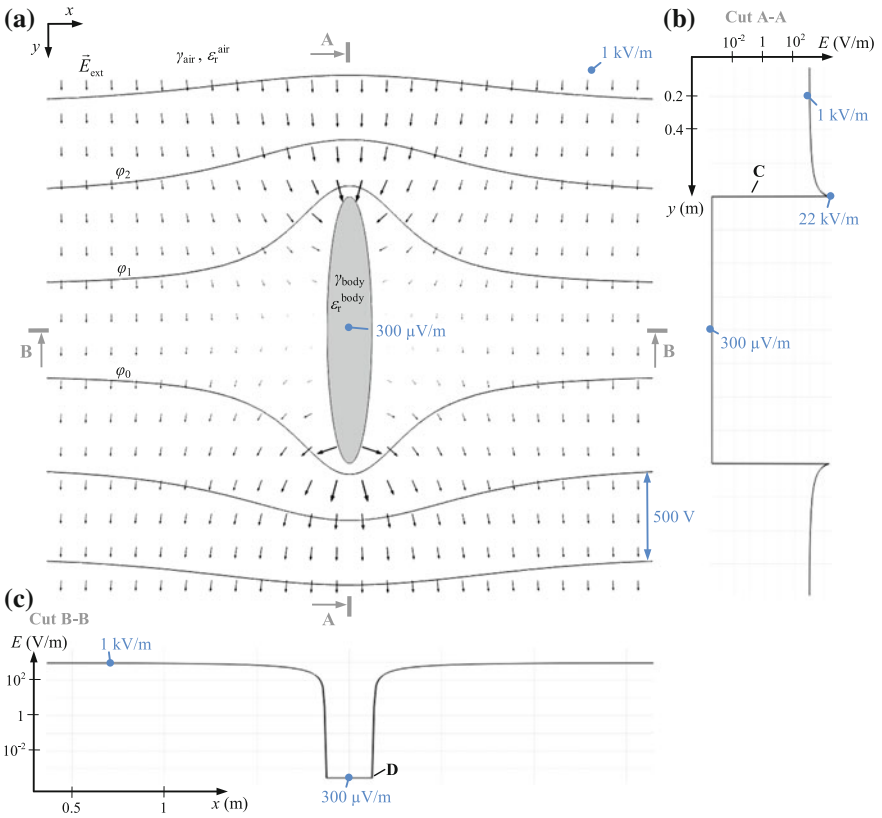

Fig. 2.49 Inhomogeneity effects on the distribution of the effective electric field $\vec{E}$ and electric potential field φ with an elongated voluminous body insert exposed to an external electric field $\vec{E}_{ext}$ directed along the long body axis; compare Figs. 2.25 and 2.50. **a** A prolate spheroid with the ratio 6 of its long axis (=1.6 m) to short axis (=0.27 m)—resembling elongated human body shape (Footnote 64)—is surrounded by air. The external (homogenous) field E_{ext} (=1 kV/m) at the frequency of 50 Hz in the isolating air with its electrical conductivity γ_{air} ($=10^{-15}$ S/m) is significantly disturbed by the presence of the conductive body with γ_{body} (=0.2 S/m, i.e., $\gamma_{body} \gg \gamma_{air}$, see muscle characteristics from Table 2.2). The relative permittivity ε_r^{body} ($=17 \cdot 10^6$) of the body at 50 Hz is much higher than ε_r^{air} (=1) of the air (Table 2.2). **b** The corresponding course of the effective magnitude E of $\vec{E}$ is depicted for outside and inside of the body along its long axis (see cutting line A-A), whereas the magnitude is logarithmically scaled. **c** As in (**b**) but along the body's short axis (see cutting line B-B). The spatial distribution and direction of $\vec{E}$ are shown by arrows; the longer the arrow, the larger the local field magnitude E. Equipotential surfaces of the electric potential φ are also indicated as lines with $\varphi_2 > \varphi_1 > \varphi_0$ and $\varphi_2 - \varphi_1 = \varphi_1 - \varphi_0 = 500$ V. All numerical data were calculated using finite-element method with a three-dimensional model (Kampusch 2017)

Incindent Electric Field

Figure 2.49 provides quantitative data on the effective *electric field* and *electric potential* around and inside of an *elongated conductive body* surrounded by the *air* and exposed to an external electric field $\vec{E}_{\text{ext}}$ with the magnitude E_{ext} of 1 kV/m (the field strength comparable with that under the overhead power transmission lines, see Footnote 80). This prolate spheroid serves as a model of the human body in the air (Footnote 64). This calculated situation is similar to the qualitative one in Fig. 2.30a with the human body in the ambient field, whereas the vector field $\vec{E}_{\text{ext}}$ is parallel to the long axis of the body. As could be expected from Fig. 2.25, the otherwise homogenous $\vec{E}_{\text{ext}}$ is significantly disturbed by the presence of the conductive body. The electric field lines (or field vectors) tend to enter the body because it provides a pathway of (relatively) low conductivity for the lines of the electric field and electric current density (2.32); likewise, the *current* always takes the *pathway of least resistance* (Fig. 2.13a). The magnitude of the electric field $\vec{E}$ inside the body amounts to very low values (about 300 μV/m versus 1 kV/m outside the body) because of the inequality $\gamma_{\text{air}} \ll \gamma_{\text{body}}$; see Sect. 2.3.2.2 for boundary conditions. The coupling of the *normal* $\vec{E}$ can be observed on the top and bottom of the body, whereas the relevant boundary condition (for normal components) forces a significant change in the field magnitude (2.114). In contrast, *tangential* $\vec{E}$ *coupling* on both sides of the body demonstrates a continuous change of the electric field across the boundary. It can be easily observed that the $\vec{E}$ *field just outside the body surface* is

- significantly increased on the top and bottom of the body (due to *electrical point effect*, compare with the region B in Fig. 2.25 and Footnote 58) and
- significantly decreased on both sides of the body (due to *opposing electric fields* generated by *induced surface charges*, compare with the region C in Fig. 2.25).

Concerning the distribution of the *equipotential surfaces* in the presence of the *conductive body*, it can be observed in Fig. 2.49a that surfaces in the region of the body are *dispersed and widened*; compare Fig. 2.25a. This is because a conductive body represents the region of constant potential so that adjacent equipotential surfaces must sheer away from the body to keep constant the potential difference between neighbouring equipotential surfaces.

Figure 2.49b provides the course of the effective magnitude E of the resulting $\vec{E}$ for outside and inside of the body along its long axis (see the cutting line A-A in Fig. 2.49a). This course confirms the *electrical point effect* with the peak value of 22 kV/m given the (otherwise homogenous) external electric field of only 1 kV/m. The latter peak is not very dominant in the plot because of its *logarithmic scaling*, as compared with the dominant peak in Fig. 2.51b given its *linear scaling*. In addition, an abrupt *step-wise decrease* of E can be observed at the boundary when

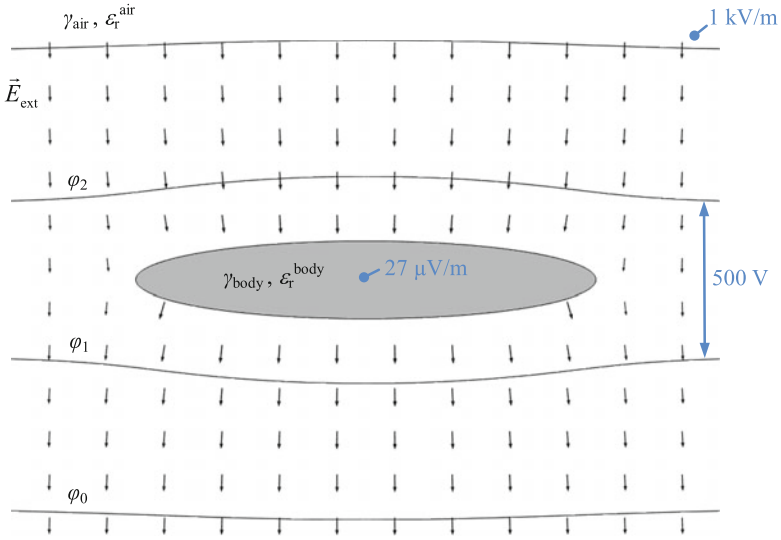

Fig. 2.50 Inhomogeneity effects on the distribution of the effective electric field $\vec{E}$ and electric potential field φ with an elongated voluminous body insert exposed to an external electric field $\vec{E}_{ext}$ directed along the short body axis; compare Figs. 2.25 and 2.49. For numerical data on the body characteristics, surrounding air, and parameters of the applied external field see caption of Fig. 2.49. Numerical data were calculated using finite-element method with a three-dimensional model, whereas given numbers are effective values (Kampusch 2017)

the field enters the conductive body (drop from 22 kV/m down to 300 µV/m), i.e., a steep decrease by seven orders of magnitude due to *normal coupling*. In contrast to Fig. 2.49b, Fig. 2.49c provides the effective magnitude E along the body's short axis (see the cutting line B-B in Fig. 2.49a). This course confirms the *continuous decrease* of $\vec{E}$ at the boundary due to *tangential coupling* into the conductive body. Only a *kink* in the magnitude E can be observed directly at the boundary (at the point D in Fig. 2.49c) but no *jump* (as at the point C in Fig. 2.49b).

Similar to Fig. 2.49, Fig. 2.50 provides the field distribution around and inside of an *elongated conductive body* exposed to an external $\vec{E}_{ext}$ in the *air*. However, here the ambient $\vec{E}_{ext}$ is *perpendicular to the long axis of the body* (as depicted in Fig. 2.30b). The distribution reveals that the *electrical point effect* (with the peak value of 2 kV/m) is much less dominant in the upper and lower regions of the body surface in comparison with Fig. 2.49 (with the peak value of 22 kV/m) because the *local curvature* of the boundary for the *incident normal field component* in Fig. 2.50 is much less than in Fig. 2.49. In addition, the effects of the *opposing electric fields* can be observed in Fig. 2.50 that yield diminished net field strength on both sides of the body. In analogy to the discussion of the inequality $E_1 > E_2$ from Fig. 2.30 (see above), it can be expected that the resulting inner E in the body from

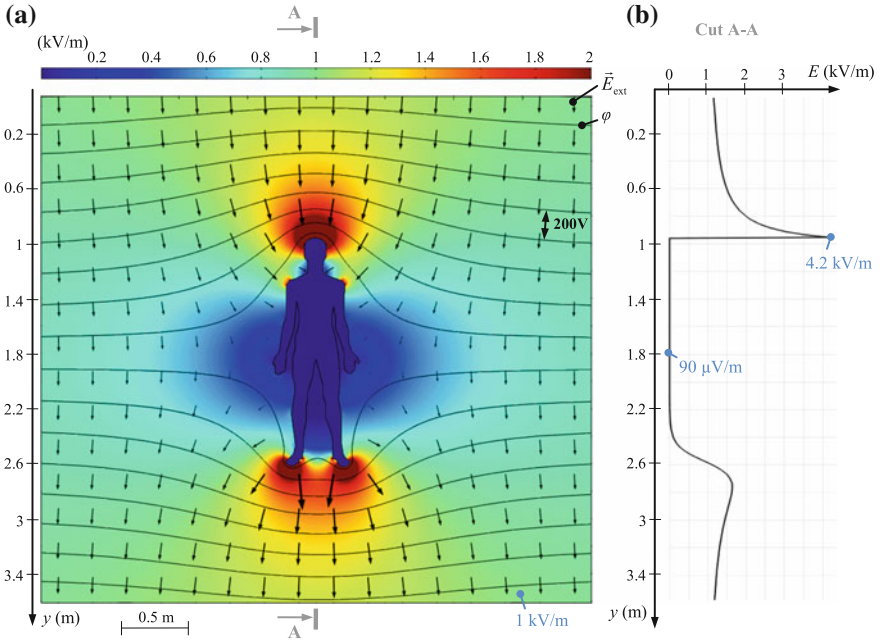

Fig. 2.51 Ungrounded human body in the air exposed to an external electric field $\vec{E}_{ext}$ (with the magnitude E_{ext} = 1 kV/m) directed along the long body axis; compare Fig. 2.57. **a** The distribution of the resulting electric field $\vec{E}$ (field vectors coded as arrows while the field's local effective magnitude E is coded as background color) and the distribution of the electric potential field φ (depicted as lines of the equipotential surfaces) are shown; compare Figs. 2.27b and 2.49. The field frequency is 50 Hz, whereas the electrical conductivity of the body and air is assumed as 0.2 S/m and 10^{-7} S/m, respectively. The longer the arrow, the larger the local magnitude E. The relative permittivity amounts to $17 \cdot 10^6$ in the body and to 1 in the air. The difference between two neighboring equipotential surfaces equals to 200 V. **b** The course of the effective E is depicted along the body axis (see cutting line A-A). All numerical data were calculated using finite-element method based on a two-dimensional model of the human body (Kampusch 2017)

Fig. 2.49 is higher than that from Fig. 2.50. Namely, the external $\vec{E}_{ext}$ parallel to the long body axis yields 300 μV/m in the centre of the conductive body (Fig. 2.49) while the external $\vec{E}_{ext}$ perpendicular to the long axis yields only 27 μV/m (Fig. 2.50). The *equipotential surfaces are dispersed* to a smaller extent in Fig. 2.50 than in Fig. 2.49 because the spatial extension of the elongated conductive body is less in the direction of the electric field in Fig. 2.50 than in Fig. 2.49.

That is, the *ratio of the internal to incident electric field* in the case of the *longitudinal body orientation* in $\vec{E}_{ext}$ (Fig. 2.49) amounts to about $3 \cdot 10^{-7}$ (=300 μV/m / 1 kV/m), whereas the ratio in the case of the *transversal body orientation* (Fig. 2.50) amounts to about $3 \cdot 10^{-8}$ (27 μV/m / 1 kV/m), provided the body size is identical; compare with *attenuation factors* from Sect. 2.3.2.2. In

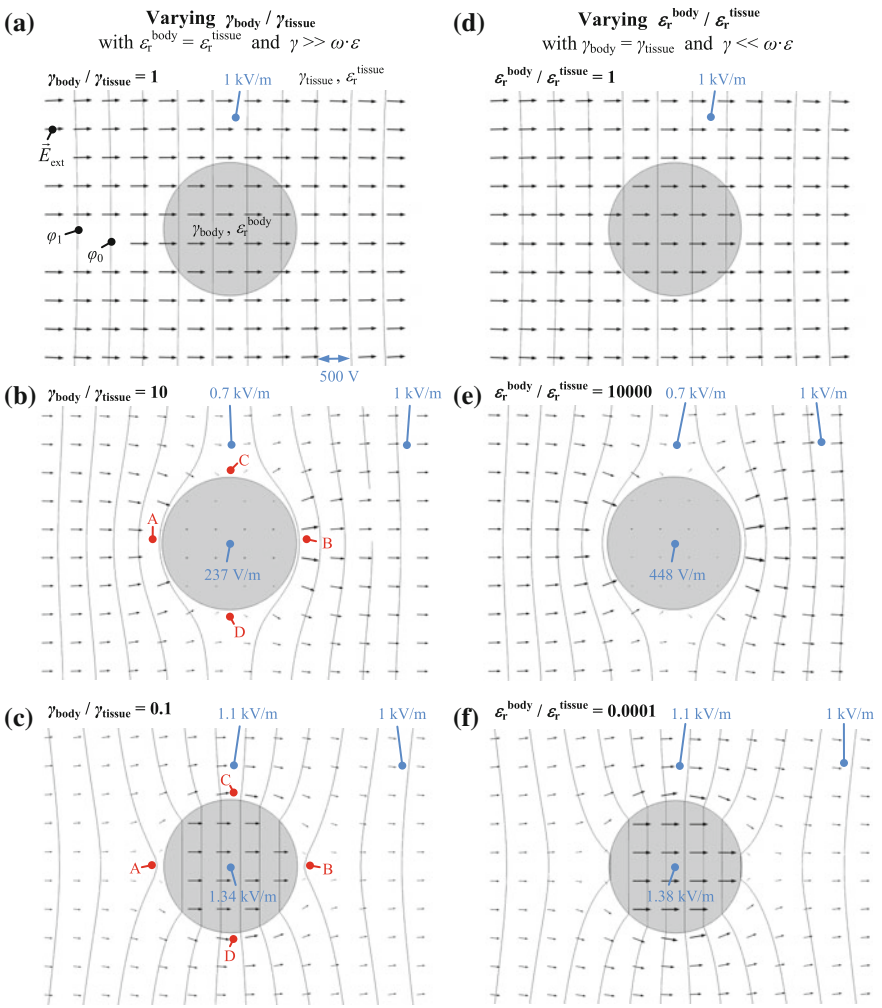

Fig. 2.52 Inhomogeneity effects on the distribution of the effective electric field $\vec{E}$ and electric potential field φ with a spherical body insert exposed to an external electric field $\vec{E}_{ext}$ prevailing in the otherwise homogenous surrounding tissue; compare Figs. 2.25, 2.49, and 2.50. **a–c** Varying ratio of the electrical conductivity γ_{body} of the body insert to the conductivity γ_{tissue} of tissue, whereas the corresponding relative permittivities are equal, i.e., $\varepsilon_r^{body} = \varepsilon_r^{tissue} = 1$. The radius of the sphere is 1 m, the external field magnitude $E_{ext} = 1$ kV/m is applied at the frequency 0 Hz; i.e., only the conductive behavior is present ($\gamma \gg \omega \cdot \varepsilon = 0$). The distance between two neighboring equipotential surfaces is $\varphi_1 - \varphi_0 = 500$ V. The longer the arrow, the larger the local magnitude E. **d–f** Varying ratio $\varepsilon_r^{body}/\varepsilon_r^{tissue}$ with $\gamma_{body} = \gamma_{tissue} = 1$ S/m at the applied field frequency 10 MHz with dominating dielectric behavior (due to $\gamma \ll \omega \cdot \varepsilon$). **a** $\gamma_{body} = \gamma_{tissue} = 1$ S/m. **b** $\gamma_{body} = 10$ S/m and $\gamma_{tissue} = 1$ S/m, in analogy with Fig. 2.53a. **c** $\gamma_{body} = 1$ S/m and $\gamma_{tissue} = 10$ S/m, in analogy with Fig. 2.53b. **d** $\varepsilon_r^{body} = \varepsilon_r^{tissue} = 1$. **e** $\varepsilon_r^{body} = 10000$ and $\varepsilon_r^{tissue} = 1$. **f** $\varepsilon_r^{body} = 1$ and $\varepsilon_r^{tissue} = 10000$. All numerical data were calculated using finite-element method with a three-dimensional model, whereas given numbers are effective values (Kampusch 2017)

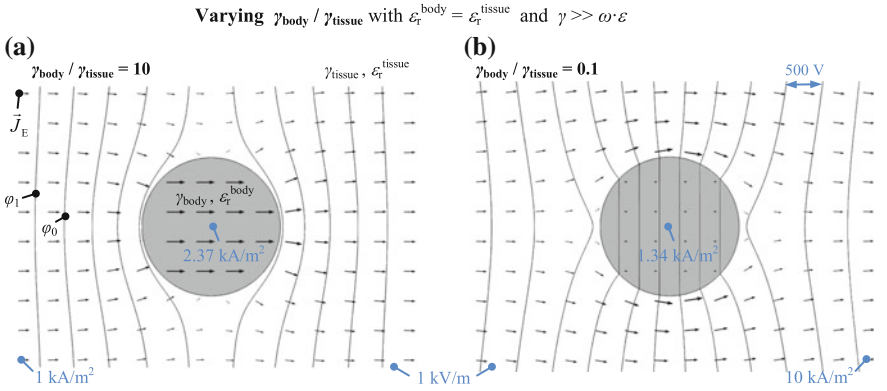

Fig. 2.53 Inhomogeneity effects on the distribution of the conductive current density field $\vec{J}_E$ and electric potential field φ with a spherical body insert exposed to an external electric field $\vec{E}_{ext}$ prevailing in the otherwise homogenous surrounding tissue; compare Figs. 2.52 and 2.54. Varying ratio of the electrical conductivity γ_{body} of the body insert to the conductivity γ_{tissue} of tissue, whereas the corresponding relative permittivities are equal, i.e., $\varepsilon_r^{body} = \varepsilon_r^{tissue} = 1$. The radius of the sphere is 1 m, the external field magnitude $E_{ext} = 1$ kV/m is applied at the frequency 0 Hz; i.e., the conductive behavior clearly dominates (due to $\gamma \gg \omega \cdot \varepsilon = 0$). The distance between two neighboring equipotential surfaces is $\varphi_1 - \varphi_0 = 500$ V. The longer the arrow, the larger the local magnitude J_E of $\vec{J}_E$. **a** $\gamma_{body} = 10$ S/m and $\gamma_{tissue} = 1$ S/m, in analogy with Fig. 2.52b. **b** $\gamma_{body} = 1$ S/m and $\gamma_{tissue} = 10$ S/m, in analogy with Fig. 2.52c. All data were calculated using finite-element method with a three-dimensional model (Kampusch 2017)

qualitative analogy with Footnote 64, the former ratio is greater by a factor of more then 11 (=300 μV/m / 27 μV/m) than the latter ratio.

Figure 2.51a illustrates the distribution of the electric field $\vec{E}$ and electric potential around and inside of a modelled *human body* exposed to an otherwise homogenous external field $\vec{E}_{ext}$ in the *air*. The incident field is aligned with the body axis, whereas the depicted situation matches qualitatively that with the *elongated conductive body* in the external field directed along the long axis of the body (from Fig. 2.49); compare Footnote 64. This figure, in turn, confirms the *electrical point effect* at *curved regions* of the upper and lower body (surface), such as head and feet where most of the electric field (or electric current) enters and leaves the body, respectively; compare Fig. 2.27b. The effects of the *opposing fields* can be also recognized in that they reduce the net magnitude of the electric field on both sides of the upright body.

Figure 2.51a provides insights into effective magnitudes E of $\vec{E}$ along the body axis, with the obvious *peak value* of 4.2 kV/m occurring above the *head* and another peak in the region of the *feet*. Interestingly, the small magnitude of 90 μV/m results in the centre of the human body (modelled in two dimensions) that corresponds well with the magnitude of 93 μV/m in the centre of a modelled ellipse

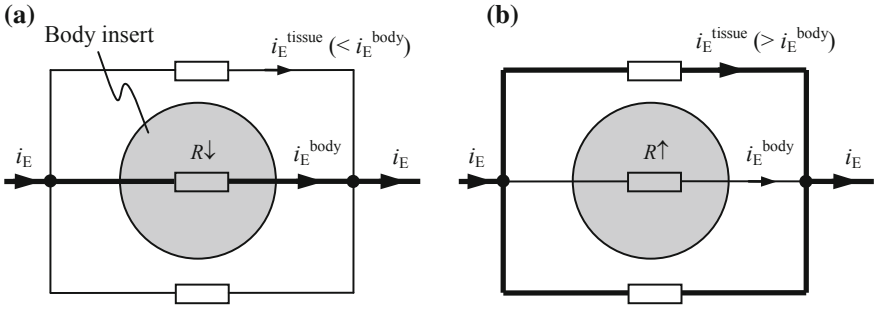

Fig. 2.54 Equivalent circuit models of an inhomogeneity in biological tissue. A body insert with the electrical resistance R (=$\underline{Z}_E$, see Fig. 2.9b) is located within the otherwise homogenous surrounding tissue at the field frequency 0 Hz; i.e., the conductive behavior prevails (with $\underline{Z}_C \to \infty$ in Fig. 2.9b so that $\underline{Z}_C$ can be neglected). **a** Conductive body insert is located in isolating tissue, in analogy with Fig. 2.52b. The major current i_E^{body} of the total conductive current i_E passes through the body insert while the remaining current $2 \cdot i_E^{tissue}$ flows around the insert through tissue (i.e., $i_E = i_E^{body} + 2 \cdot i_E^{tissue}$). **b** Isolating body insert is located in conductive tissue, in analogy with Fig. 2.52c

(as a two-dimensional analogue of an elongated voluminous spheroid in Fig. 2.49), given almost identical longitudinal size of 1.6 m of both models, the identical strength of the ambient $\vec{E}_{ext}$ of 1 kV/m in the air, and identical tissue properties.

Figure 2.52 offers a more general and instructive picture of the field distribution considering a *spherical body* of varying electrical conductivity γ and relative permittivity ε_r—with respect to the surrounding tissue—exposed to an ambient $\vec{E}_{ext}$. Likewise, a body insert is considered within the *surrounding tissue*. Obviously the ambient $\vec{E}_{ext}$ and equipotential surfaces remain undisturbed if *electrical properties* of the body insert and tissue *are identical*, as shown in Fig. 2.52a, d. That is, there is no *electrical boundary* (interface) and the electric field retains its magnitude and direction across the *physical boundary* between the body insert and the surrounding tissue.

To begin with the interpretation of the field distribution, an *increased γ of the body insert* is assumed in Fig. 2.52b, i.e., a *conductive body* is located in (poorly) *isolating tissue*. A *predominant conductive behaviour* is assumed here, i.e., the inequality $\gamma \gg \omega \cdot \varepsilon$ (=0 at $\omega = 0$) applies (2.71). The resulting lines (or vectors) of the electric field tend to enter the body (see above). Thus, the *conductive current density* $\vec{J}_E$ in the body region (2.54) and also the total current through the body increase (as related to the homogenous case in Fig. 2.52a), whereas the total current is given as the surface integral of the local magnitude J_E (2.24). Figure 2.53a depicts the corresponding field $\vec{J}_E$ with an evidently increased J_E in the body region. In addition, Fig. 2.54a illustrates the increased current i_E^{body} through the conductive body related to the current i_E^{tissue} heading around this body throughout isolating tissue, as based on the equivalent circuit model from Fig. 2.9. It should be noted

that the assumed field frequency is 0 Hz (direct field in Figs. 2.52a–c, 2.53, and 2.54) so that the *capacitive impedance* of tissue (2.42) is infinitely large and thus the corresponding displacement currents are zero. Therefore, only *conductive currents dominate* here and the capacitive impedance can be neglected in Fig. 2.9b.

Paradoxically, the vectors of the *electric field within the body* in Fig. 2.52b seem to shorten as related to the non-disturbed regions of the electric field (distant from the body). This is because the local γ in the body is higher than γ of tissue, which means that the local electric field in the body should decrease by the ratio $\gamma_{body}/\gamma_{tissue} = 10$ [see the condition for the *normal components*[84] in (2.104) and Fig. 2.52b], given an identical J_E in the body (2.54) and in the *non-disturbed field regions* of tissue. In other words, the later simplification resembles a *series connection of the body insert and tissue* where only normal field components prevail on the boundary; compare Fig. 2.35a. However, the density J_E increases in the body region by the factor of about 2.4 as related to the non-disturbed regions of the J_E field in tissue (Fig. 2.53a), so we would expect a decreased electric field in the body by the factor of 10 / 2.4 ≈ 4.2; in fact, the numerical simulation in Fig. 2.52b confirms quantitatively this consideration and yields a *reduction factor* of about 4.2 (=1 kV/m / 237 V/m); compare Fig. 2.49b with an extremely large ratio $\gamma_{body}/\gamma_{air}$. Please note that the ratio of the resulting value of J_E and that of the electric field within the body insert (=2.37 kA/m^2 / 237 V/m from Figs. 2.53a and 2.52b) necessarily yields the assumed conductivity γ_{body} of this insert [=10 S/m, see (2.54)]. Consequently, the electric field and $\vec{J}_E$ field decrease directly above and below the body insert as related to the non-disturbed regions of the field; compare the electric field of 0.7 kV/m versus 1 kV/m in Fig. 2.52b and observe the distribution of $\vec{J}_E$ field in Fig. 2.53a, respectively.

In addition, the *electrical point effect* can be observed to the left and right of the body insert in Fig. 2.52b (comparable with the regions A and B), with the peak fields of about 2.4 kV/m on the outer body surfaces, given the otherwise homogenous $\vec{E}_{ext}$ of only 1 kV/m; compare Footnote 57 with 2.4 kV/m being close to the maximum possible value of 3 kV/m (=3 · E_{ext}) for conductive spherical bodies. It should be noted that at the outer surface of the spherical body where the *peak field* occurs the electric peak field has only its *normal component* and thus the boundary condition of (2.104) (for normal components) should be fulfilled. Consequently, the *inner electric field below the surface* and *within the body* increases by the factor of 2.4 kV/m / 1 kV/m = 2.4, the increase factor we have already correctly observed in the increase of J_E within the body region (see above). The inner electric field throughout the body insert is almost constant.

[84]Please note that the ambient *electric field* in Fig. 2.52b is *mostly normally coupled* into and out of the *conductive body* via its front surfaces, see marked regions A and B, so that boundary conditions for the normal components (2.104) apply. On the contrary, a pure *tangential coupling* in the regions C and D is of minor importance because here the tangential electric field is relatively small and goes even to zero for an *ideally conductive body*; compare Footnote 85.

In particular, the observed *electrical point effect*

- on the *sphere* (proportional to the ratio 2.4 kV/m / 1 kV/m, Fig. 2.52b) is less dominant than that
- on the *prolate spheroid* (22 kV/m / 1 kV/m, Fig. 2.49b)

because the *local curvature* of the sphere surface is less than the local curvature of the prolate spheroid surface at its peaked end.

Figure 2.52c illustrates a field situation in contrary to that in Fig. 2.52b. Here γ of the body insert is less than γ of surrounding tissue, i.e., a (poorly) *isolating body* is located in *conductive tissue*. Thus, the electric field lines tend to avoid the body because it does not represent the spatial region of least resistance. The corresponding Fig. 2.53b confirms that the field $\vec{J}_E$ circumvents the isolating body. In addition, Fig. 2.54b illustrates the increased current i_E^{tissue} through conductive tissue surrounding the body related to the current i_E^{body} throughout the isolating body insert, as based on the equivalent circuit model from Fig. 2.9.

Paradoxically, the vectors of the *electric field within the body* in Fig. 2.52c seem to elongate as related to the ambient non-disturbed regions of the field (distant from the body). This is because the local γ in the body is lower than γ of tissue, which means an increased inner electric field in the body (2.54) while transferring a particular amount of current through the body insert, although this amount of current in Fig. 2.52c is even decreased in comparison with the homogenous case in Fig. 2.52a.

From a formal point of view, the predominantly *tangential coupling*[85] of the electric field into the body in Fig. 2.52c (comparable with marked regions C and D) yields an increased electric field in the body by the factor of only 1 [according to the condition for the tangential field coupling in (2.96)], given a concurrently decreased J_E in the body by the ratio $\gamma_{tissue}/\gamma_{body} = 10$ (2.103) in comparison with the non-disturbed field regions of tissue. In other words, the later simplification resembles a *parallel connection of the body insert and tissue* where only tangential field components prevail on the boundary; compare Fig. 2.35b. However, the density J_E decreases in the body region only by the factor of about 7.4 as related to the non-disturbed regions of $\vec{J}_E$ in tissue (Fig. 2.53b), so we would expect an increased electric field in the body by the factor of 10 / 7.4 $\approx$ 1.3; in fact, the numerical simulation in Fig. 2.52c confirms quantitatively this consideration and yields an *amplification factor* of about 1.3 (=1.3 kV/m / 1 kV/m). Please note that the ratio of the resulting value of J_E and that of the electric field within the body insert (=1.3 kA/m^2 / 1.3 kV/m from Figs. 2.53b and 2.52c) necessarily yields the assumed conductivity γ_{body} of this insert [=1 S/m, see (2.54)]. Consequently, the

[85]Please note that the ambient *electric field* in Fig. 2.52c is *mostly tangentially coupled* into and out of the *isolating body* via its upper and lower surfaces, see marked regions C and D, so that boundary conditions for the tangential components (2.96) apply. On the contrary, a pure *normal coupling* in the regions A and B is of minor importance because here the normal electric field is relatively small and goes even to zero for an *ideally isolating body*; compare Footnote 84.

electric field and $\vec{J}_E$ field increase directly above and below the body insert as related to the non-disturbed regions of the field; compare the electric field of 1.1 kV/m versus 1 kV/m in Fig. 2.52c and observe the distribution of J_E field in Fig. 2.53b, respectively.

Interestingly, the *electric field on the outer surface* of the upper and lower part of the body in Fig. 2.52c (comparable with the regions C and D) amounts to about 1.3 kV/m, i.e., the local field increases by the factor of 1.3 as related to the non-disturbed regions of the field in tissue. Since only tangential components of the electric field dominate in these surface regions and the corresponding boundary condition (2.96) requires their continuity across the boundary, the *inner electric field below the surface* and *within the body* amounts also to about 1.3 kV/m, i.e., the value we have already correctly observed above.

It can also be observed that *equipotential surfaces* in Fig. 2.52b are *dispersed and widened* by the presence of the *conductive body insert* (compare Fig. 2.49a). In contrast, equipotential surfaces are *concentrated and narrowed* by the *isolating body insert*.

In the case of Fig. 2.52e, ε_r of the body insert is increased with respect to surrounding tissue, whereas γ of the body and tissue are identical. A *predominant dielectric behaviour* is assumed but not the conductive one, i.e., the inequality $\gamma \ll \omega \cdot \varepsilon$ applies (2.72). In fact, a *dielectric body* is located in a *less dielectric tissue*. In global terms, the capacitive impedance of the body is less than that of surrounding tissue (2.42). Therefore, the *alternating electric field* (and the *displacement current density* $\vec{J}_C$ field) tend to pass through the body insert instead of circumventing it. This behaviour is especially pronounced at *high field frequencies* when

- the low *capacitive impedance of the body* (2.42) starts to dominate over
- the *conductive impedance of the body* [i.e., the body resistance which does not depend on frequency, see (2.36)] and thus lowers
- the *total impedance of the body* [given as parallel connection of the latter impedances, see (2.47) and Fig. 2.9b].

It favours the passage of ambient currents through the body insert, in contrast to a homogenous distribution of currents across the body and tissue (Fig. 2.52d). In addition, the *electrical point effect* can also be observed to the left and right of the body insert in Fig. 2.52e with the peak fields of about 2.6 kV/m on the body surfaces, given the incident field of 1 kV/m.

Paradoxically, the vectors of the *electric field within the body* in Fig. 2.52e seem to shorten as related to the ambient non-disturbed regions of the field (distant from the body). This is because the local ε_r in the body is higher than ε_r of tissue, so that the electric field has to decrease in the body in proportion to ε_r [in line with (2.62)]; see the relevant discussion in Section "Polarization Phenomena". In addition, the density magnitude J_C of $\vec{J}_C$ throughout the body insert increases as related to the non-disturbed regions of the field. This is because increasing ε_r in the body increases J_C (2.66) and the dielectric body insert focusses $\vec{J}_C$ field, despite the

reduced electric field in the body. Consequently, the electric field and $\vec{J}_C$ field decrease directly above and below the body insert as related to the non-disturbed regions of the field; compare the effective electric field of 0.7 kV/m versus 1 kV/m in Fig. 2.52e.

Figure 2.52f signifies a field situation in contrary to that in Fig. 2.52e, whereas a predominant dielectric behaviour is still assumed (see above). Here ε_r of the body insert is less than ε_r of surrounding tissue, i.e., a *less dielectric body* is located in *dielectric tissue*. Because of the increased capacitive impedance of the body (2.42), the alternating electric field and the density $\vec{J}_C$ field tend to avoid and circumvent the body insert.

Paradoxically, the vectors of the *electric field within the body* in Fig. 2.52f seem to elongate as related to the ambient non-disturbed regions of the field (distant from the body). This is because the local ε_r in the body is lower than ε_r of tissue, so that the inner electric field in the body has to increase (2.62); compare with the analogous change of the electric field across the muscle-fat boundary in Fig. 2.37. In addition, the density J_C throughout the body insert decreases as related to the non-disturbed regions of the field. This is because J_C decreases with decreasing ε_r in the body (2.66) and the body insert disperses $\vec{J}_C$ field, despite the increased electric field in the body. Consequently, the electric field and $\vec{J}_C$ field increase directly above and below the body insert as related to the non-disturbed regions of the field; compare the effective electric field of 1.1 kV/m versus 1 kV/m in Fig. 2.52f.

In general, the resulting field pattern in Fig. 2.52b resembles strongly that in Fig. 2.52e. That is, an *increasingly conductive body insert or increasingly dielectric body insert* in tissue tends to

- focus *electric field* and *current density* field in the body region while
- *equipotential surfaces* are dispersed in this region; compare Fig. 2.56a.

In an analogous way, the resulting field pattern in Fig. 2.52c resembles strongly that in Fig. 2.52f. That is, an *increasingly isolating body insert or less dielectric body insert* in tissue tends to

- disperse *electric field* and *current density* field in the body region while
- *equipotential surfaces* are focussed in this region; compare Fig. 2.56b.

It should be stressed that the total *current density*—as depicted in Fig. 2.9a—is generally given as the sum of $\vec{J}_E$ and $\vec{J}_C$ vectors (2.68). Therefore, the magnitude and direction of the total current density and thus the corresponding electric field depend on both

- conductive phenomena [with *free charges* involved, (2.54)] and
- dielectric phenomena [with *bound charges* involved, (2.66)].

In other words, the behaviour of the electric field around and across the boundary tissue-body strongly depends on both *conductive and dielectric properties* of both the body and tissue (Section "Incident Electric Fields").

Lastly, *boundary conditions* for the *discontinuity* between the body insert and surrounding tissue from Fig. 2.52 should be discussed in more detail, in analogy with the more general discussion from Fig. 2.36. As already mentioned, *identical electrical properties* of both involved media imply that there is no *electrical boundary* and thus the electric field retains its magnitude and its direction across the *physical boundary* (interface) between the body insert and tissue. Provided that both media are *isotropic*, the fields of the current densities $\vec{J}_E$ and $\vec{J}_C$ [(2.54) and (2.66)] and electric flux density $\vec{D}$ (2.64) follow exactly the direction of the electric field.

If *electrical properties* of two adjacent media are *different* then the field usually changes its direction and magnitude while crossing the boundary from one medium into another (Section "Boundary Conditions"). For instance, Fig. 2.55 depicts a zoomed version of Fig. 2.52b where the resulting *boundary condition* of the electric field can be observed. Namely, this field is *focussed* into the conductive body due to $\gamma_{body} > \gamma_{tissue}$, whereas *conductive properties prevail over dielectric* due to $\gamma \gg \omega \cdot \varepsilon$ (especially at $\omega = 0$ in Fig. 2.52b). Here the observed vectors of the electric field in tissue tend to be almost normally incident on the surface of the *conductive body*; compare the related discussion about Fig. 2.25. Within the body,

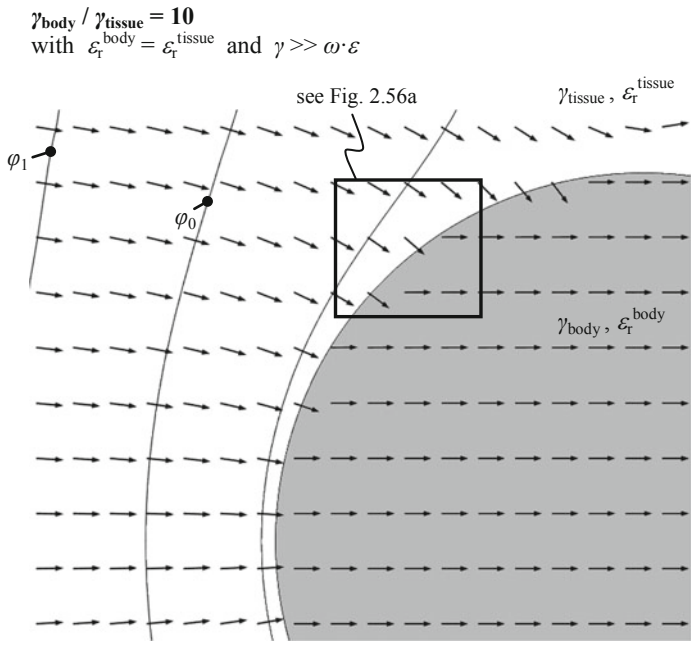

Fig. 2.55 Boundary condition for the direction of vectors of the electric field $\vec{E}$ when entering the conductive body insert, in analogy with the quantitative data from Fig. 2.52b. The length of all arrows is kept constant so that these vectors depict the field direction only but not its magnitude. All data were calculated using finite-element method (Kampusch 2017)

vectors are horizontally aligned, i.e., aligned in the direction of the undisturbed external $\vec{E}_{\text{ext}}$ (distant from the body insert that acts as the source of disturbance). Please note that the length of all arrows was kept constant in Fig. 2.55 in order to illustrate *only the directional change of the electric field* while crossing the boundary tissue-body. In fact, the magnitude of the electric field in the body is much less than that in surrounding tissue, as already discussed and observed in Fig. 2.52b.

Figure 2.56a demonstrates geometrically the corresponding *boundary conditions* for the *electric field incident on the body surface* in more detail if the inequality $\gamma_{\text{body}} > \gamma_{\text{tissue}}$ applies under the assumption of $\gamma \gg \omega \cdot \varepsilon$ (*dominance of conductance*). That is, tangential components E_{t} and normal components E_{n} of the electric field on the body surface in Fig. 2.52b underlie the following conditions, to give

$$E_{\text{t}}^{+} = E_{\text{t}}^{-},\ E_{\text{n}}^{+} = E_{\text{n}}^{-} \cdot \frac{\gamma_{\text{tissue}}}{\gamma_{\text{body}}} < E_{\text{n}}^{-} \quad \text{and} \quad Q < 0, \tag{2.132}$$

which can be easily derived from (2.96), (2.104), and (2.107). Here the tissue carries the superscript "−", whereas the body insert carries "+", see Fig. 2.56. Please note that only *conductive currents* are involved in Fig. 2.52b because the direct field (at 0 Hz) is applied only. Obviously, (2.132) can also be derived from *other relevant boundary conditions* from (2.98) and (2.107) with $\varepsilon_{\text{r}}^{\text{body}} = \varepsilon_{\text{r}}^{\text{tissue}}$ (as applies for Fig. 2.52b).

A similar behaviour of the *focussed electric field* into the body results also in Fig. 2.52e, provided that the inequality $\varepsilon_{\text{r}}^{\text{body}} > \varepsilon_{\text{r}}^{\text{tissue}}$ holds under the assumption of

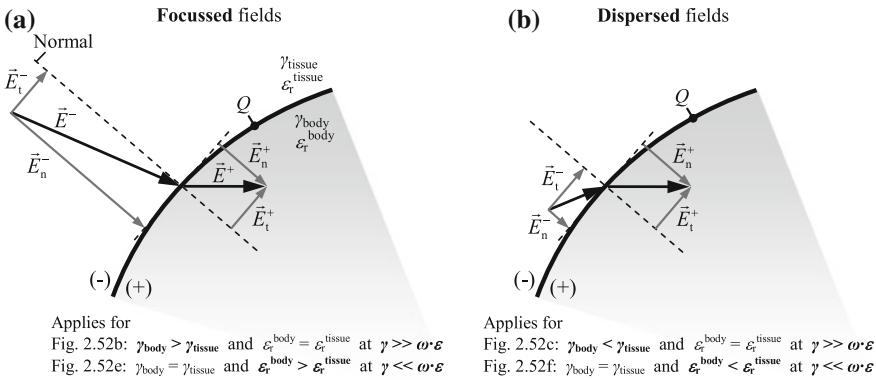

Fig. 2.56 Boundary conditions of the electric field $\vec{E}$ at the discontinuity between tissue and a body insert within the tissue. Applicable relations are given between electrical conductivities γ and relative permittivities ε_{r} of the tissue and body insert, whereas the resulting (unbound) electric charge Q at the boundary varies in each case (2.107); compare Fig. 2.36. **a** Focussing of $\vec{E}$ field into the body region, in analogy with Fig. 2.52b, e. **b** Dispersion of $\vec{E}$ field out of the body region, in analogy with Fig. 2.52c, f

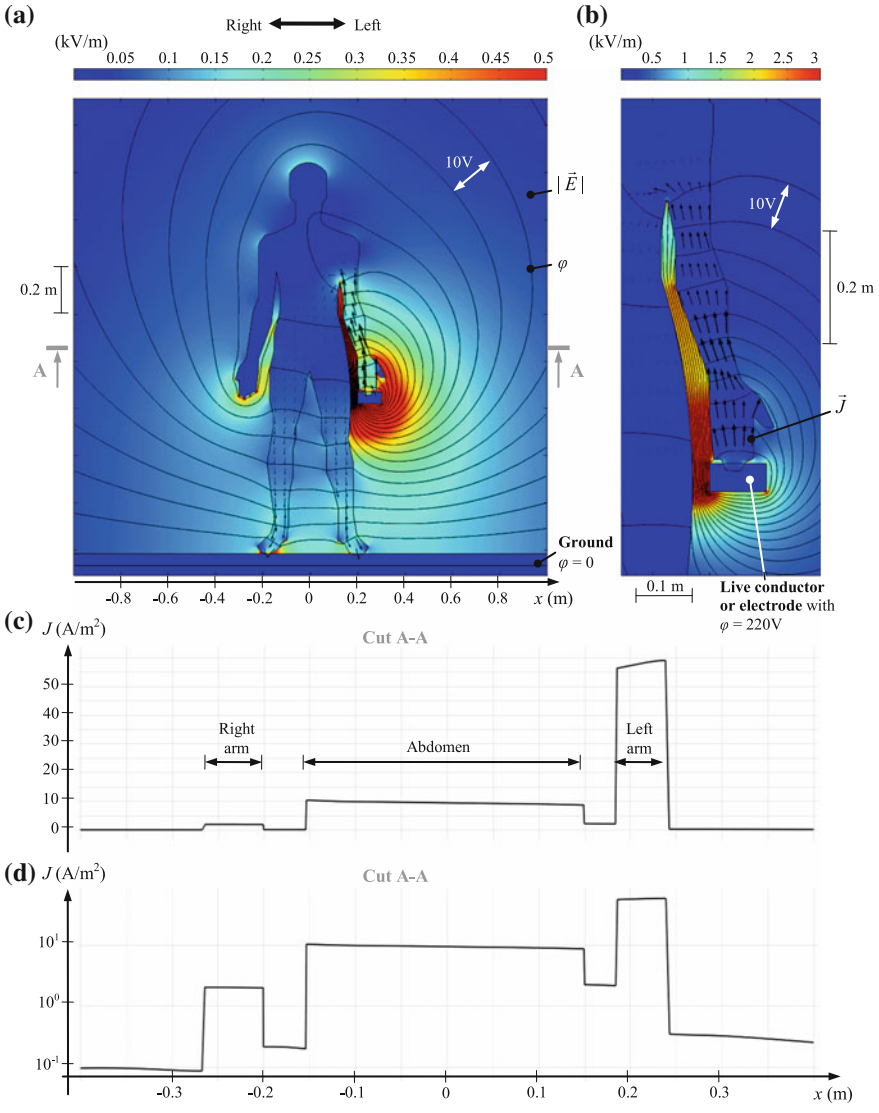
(a)
Right
Left
(kV/m)
0.05 0.1 0.15 0.2 0.25 0.3 0.35 0.4 0.45 0.5
10V
$|\vec{E}|$
φ
0.2 m
A
A
Ground
$\varphi = 0$
-0.8 -0.6 -0.4 -0.2 0 0.2 0.4 0.6 0.8 x (m)
(b)
(kV/m)
0.5 1 1.5 2 2.5 3
10V
0.2 m
$\vec{J}$
0.1 m
Live conductor or electrode with $\varphi = 220$V
(c)
J (A/m^2)
Cut A-A
50
40
30
20
10
0
Right arm
Abdomen
Left arm
(d)
J (A/m^2)
Cut A-A
10^1
10^0
10^{-1}
-0.3 -0.2 -0.1 0 0.1 0.2 0.3 x (m)

◀**Fig. 2.57** Grounded human body in the air with the left hand in contact with a live conductor at the voltage of 220 V which oscillates with the frequency of 50 Hz. **a** The distributions of the effective magnitude E of the electric field $\vec{E}$ (coded as background color), the electric potential field φ (depicted as lines of the equipotential surfaces), and of the effective current density field magnitude J of $\vec{J}$ (local field vectors coded as arrows which length is proportional to the local magnitude J) as the sum of conductive and displacement current densities (2.68) are shown; compare Fig. 2.51. The electrical conductivity of the body and air is assumed as 0.2 S/m and 10^{-7} S/m, respectively. The relative permittivity amounts to $17 \cdot 10^6$ in the body and 1 in the air. The difference between two neighboring equipotential surfaces amounts to 10 V (i.e., in total 21 equipotential lines between the live conductor and ground). **b** An excerpt of (**a**). **c** The course of the effective J is depicted along the cutting line A-A using linear scaling. **d** As (**c**) but with logarithmic scaling. All numerical data were calculated using finite-element method based on a two-dimensional model of the human body (Kampusch 2017)

$\gamma \ll \omega \cdot \varepsilon$ (*dominance of dielectric properties*). In fact, the applicable geometrical *boundary conditions* are again those depicted in Fig. 2.56a, to give

$$E_t^+ = E_t^-,\ E_n^+ = E_n^- \cdot \frac{\varepsilon_{tissue}}{\varepsilon_{body}} + \frac{Q}{A \cdot \varepsilon_{body}} < E_n^- \quad \text{and} \quad Q > 0, \tag{2.133}$$

which can be easily derived from (2.96), (2.98), and (2.107). Please note that predominantly *displacement currents* are involved in Fig. 2.52e so that (2.133) applies for these currents only [in line with (2.66)]. On the contrary, the condition in (2.104) with $\gamma_{body} = \gamma_{tissue}$ from Fig. 2.52e and thus the resulting steady components of the normal and tangential electric field apply for (insignificant) residual *conductive currents* only. In other words, these conductive currents pass through the tissue and body insert in Fig. 2.52e as if there were no boundaries (comparable with the distribution in Fig. 2.52a).

In contrast to Fig. 2.56a, *boundary conditions* in Fig. 2.56b illustrate the case where the incident *electric field*—instead of being focussed by the body insert (Fig. 2.56a)—circumvents the body and becomes *dispersed* in the body region. In particular, the boundary conditions in Fig. 2.56b refer to the field case in Fig. 2.52c where the inequality $\gamma_{body} < \gamma_{tissue}$ applies under the assumption of $\gamma \gg \omega \cdot \varepsilon$ (*dominance of conductance*); it yields (2.132):

$$E_t^+ = E_t^-,\ E_n^+ = E_n^- \cdot \frac{\gamma_{tissue}}{\gamma_{body}} > E_n^- \quad \text{and} \quad Q > 0. \tag{2.134}$$

In addition, the latter conditions of the dispersed electric field in Fig. 2.56b apply also to the field case in Fig. 2.52f with the inequality $\varepsilon_r^{body} < \varepsilon_r^{tissue}$ under the assumption of $\gamma \ll \omega \cdot \varepsilon$ (*dominance of dielectric properties*) fulfilling (2.133):

$$E_t^+ = E_t^-,\ E_n^+ = E_n^- \cdot \frac{\varepsilon_{tissue}}{\varepsilon_{body}} + \frac{Q}{A \cdot \varepsilon_{body}} > E_n^- \quad \text{and} \quad Q < 0. \tag{2.135}$$

Again, only *conductive currents* are involved in Fig. 2.52c, whereas predominantly *displacement currents* are involved in Fig. 2.52f.

Incident Contact Current

An instructive example of the resulting fields in response to the incident *contact current* is given in Fig. 2.57. Here a *grounded body* is considered, which is in contact with a *live conductor* (or a bare electrode). Both feet of the body are grounded (to the zero potential), whereas the *left hand* contacts a conductive body connected to the *power lines* (at the potential of 220 V time-varying with 50 Hz). In fact, this arrangement imitates a rather unfavourable situation of the effective current pathway within the body with the resulting *heart current factor* of 1 (Fig. 2.92a), the situation relevant to assess (adverse) physiological effects (Figs. 2.89 and 2.90).

In the *air*, as shown in Fig. 2.57a, strong *electric fields* result in the vicinity of the left arm, especially between the left arm and the thorax (because of their different local potentials); compare also the corresponding excerpt in Fig. 2.57b. In analogy with Fig. 2.51, the *electrical point effect* can be observed at curved regions of the right hand and both feet.

In the *body*, strongest *electric fields*—i.e., the regions with dense lines of the *equipotential surfaces*—can be found in the *left arm* and *both feet* (Fig. 2.57a). In fact, these are the regions with the increased local *current densities*, as can be observed from the corresponding, relatively long arrows of the current density field (Fig. 2.57a). As discussed in Section "Charge and Current Induction", *narrow regions of body extremities*, such as the *wrist* or *ankles*, can be expected to show *maximum current densities*. In particular, Fig. 2.57b illustrates that the local current density in the left arm (i.e., the length of the local arrows) increases noticeably in the regions of decreasing cross-section areas of this arm (2.23), whereas the local current density decreases when the current transverses widened regions of the body (extremities).

It can also be observed in Fig. 2.57a that the current density within the *thorax* at the height of the *heart* is larger on the left side in comparison with the right side. In fact, this is a disadvantageous situation in terms of adverse physiological effects since the vulnerable heart resides on the left (Fig. 2.92). In contrast, at the height of the *abdomen*, the current density loses the aforementioned left-to-right dominance, as depicted in Fig. 2.57c. The latter figure confirms also our expectations that the local current densities within the *left arm* are significantly larger than that within the *abdomen* or the *right arm*.

It is highly instructive that the effective current down the *right arm* to the *right hand* and then to the *ground* through the *isolating air* is not zero, even though the *left hand* is in contact with the live conductor and both feet of the *conductive body* are grounded. This is because the field frequency of the power lines (50 Hz) is not zero. That is, the involved time-varying fields imply the presence of *non-zero displacement currents* (2.66) through the *isolating air* (mainly between both hands

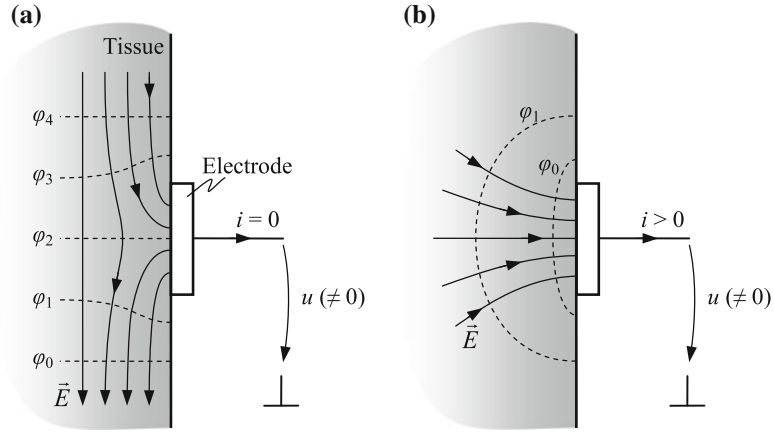

Fig. 2.58 Distributions of the electric potential φ and electric field $\vec{E}$ within tissue at the electrode/tissue boundary close to **a** the voltage sensing metal electrode (with the output current $i = 0$) and **b** the current sensing metal electrode ($i > 0$). Equipotential surfaces of φ are indicated with $\varphi_{i+1} > \varphi_i$ and a constant step potential ($\varphi_{i+1} - \varphi_i$)

and the ground). In particular, logarithmic scaling in Fig. 2.57d reveals that the resulting current densities in the air to the left and to the right of the human body are small but finite in size. As expected, these current densities in the air are larger on the left than on the right due to stronger electric fields on the left. Please note that Fig. 2.57 depicts the *total current density* as the sum of both *conductive* and *displacement current densities* (2.68).

The presence of the *contact current* determines significantly the distribution of the *electric potential* and the associated *electric field* at the *electrode/tissue boundary*. Figure 2.58 illustrates schematically these distributions for

- *voltage sensing metal electrode* (with a zero current $i = 0$ leaving the electrode, see Fig. 2.58a) and
- *current sensing metal electrode* (with a finite $i > 0$ leaving the electrode, see Fig. 2.58b).

These spatial distributions are basically different in that *electric field lines* do not accumulate within the *voltage electrode* (with the resulting $i = 0$), whereas these field lines do accumulate in the *current electrode* ($i > 0$). Please recall that equipotential surfaces are always perpendicular to electric field lines [due to the gradient function in-between, in line with (2.28)]. The electric field within tissue enters and leaves perpendicularly the currentless conductive *voltage electrode*, as shown in Fig. 2.58a (compare Fig. 2.25). In Fig. 2.58b, the electric field is still perpendicular to the surface of the *current electrode* because the accumulated

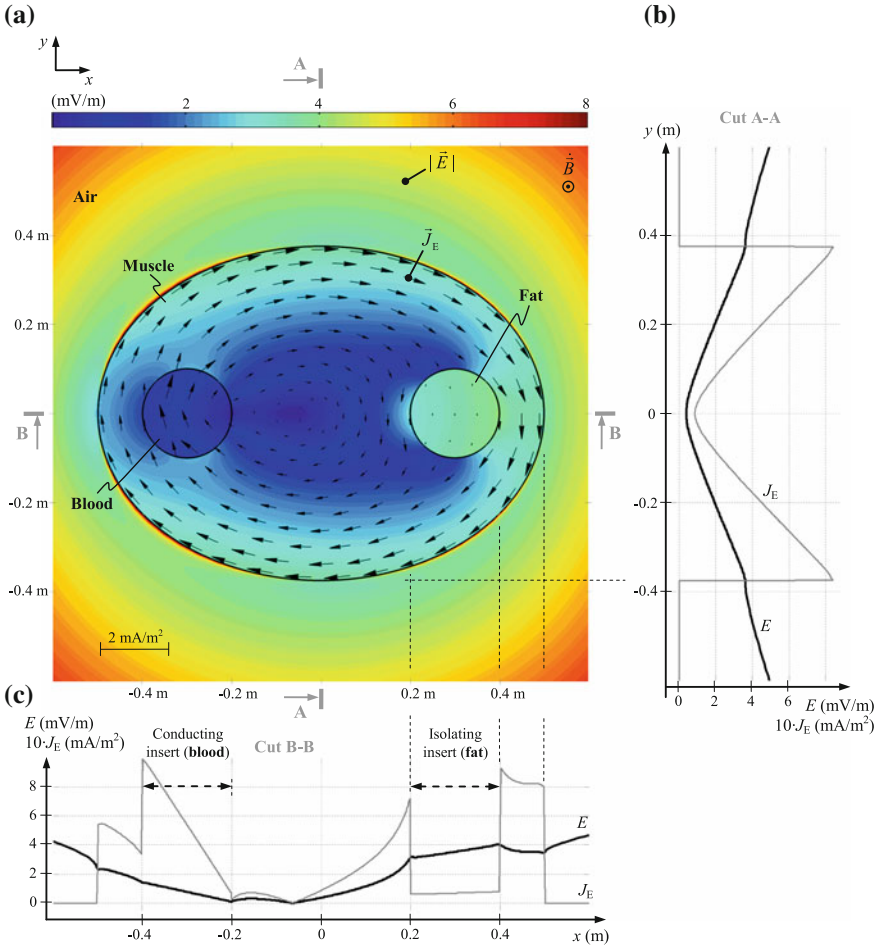

Fig. 2.59 Schematic cross-section of the human body in the air exposed to a spatially-uniform time-varying magnetic field $\vec{B}$ (with its effective value **B** of 50 μT and $\dot{\vec{B}} = \mathrm{d}\vec{B}/\mathrm{d}t \neq \vec{0}$) directed along the surface normal of the cross-section; compare with the analogous set-up in Fig. 2.31c. **a** The distribution of the effective magnitude E of the induced electric field $\vec{E}$ (the field's local magnitude E is coded as background color) and the distribution of the effective magnitude J_E of the resulting conductive current density field $\vec{J}_\mathrm{E}$ (field vectors coded as arrows which length is proportional to the local J_E) are shown in terms of electromagnetic induction. The heterogeneous cross-section is composed out of muscular tissue with a blood insert (i.e., a conducting insert with respect to the muscle) and another fat insert (an isolating insert); see detailed representations in Fig. 2.60. The field frequency is 50 Hz, whereas the electrical conductivity of the muscle, blood, fat, and air is assumed as 0.2, 0.7, 0.02, and 10^{-7} S/m, respectively. The relative permittivity amounts to $17 \cdot 10^6$ in the muscle, 5260 in the blood, $1.5 \cdot 10^6$ in the fat, and 1 in the air; in line with the electrical properties of muscle, fat, and blood from Figs. 2.20 and 2.21 (at 50 Hz). **b**, **c** The courses of the effective magnitude E and J_E are depicted along the cutting lines A-A and B-B, i.e., along the coordinates $x = 0$ and $y = 0$, respectively. Plotted numerical data were calculated using finite-element method based on a two-dimensional model of the human body (Hirtl 2014)

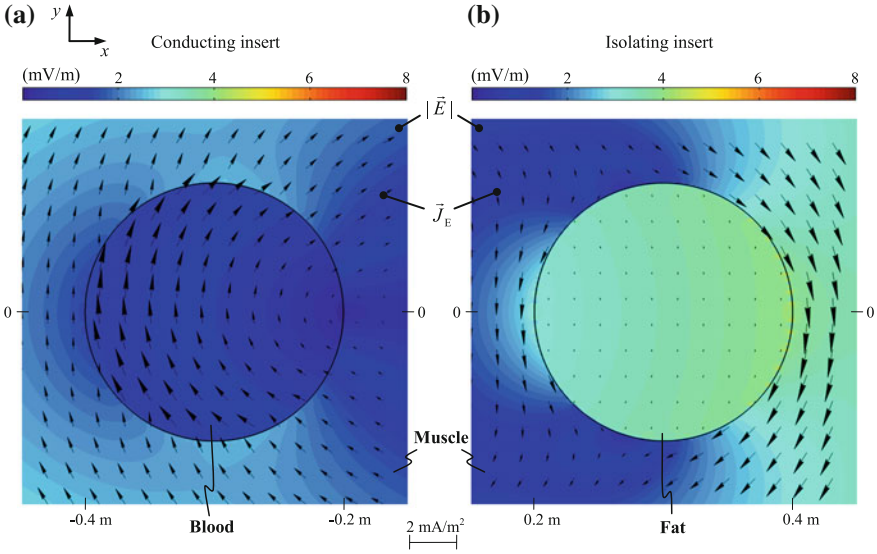

Fig. 2.60 An excerpt of Fig. 2.59 illustrates electromagnetic induction in more detail, in the region of the conducting body insert (blood) and the isolating body insert (fat), both embedded within body tissue (muscle)

current within this electrode has no tangential component (along the surface); i.e., current lines within the electrode take the shortest path to the wire connected to this electrode.

Incident Magnetic Field

In close analogy with Fig. 2.31c showing a *heterogeneous body* permeated by the ambient *time-varying magnetic field* $\vec{B}$, Fig. 2.59 illustrates the effective *electric field* $\vec{E}$ (2.89) and the *conductive current density field* $\vec{J}_E$ (2.90) in the heterogeneous body. The fields are shown for the inner body region and outside it, at the power line frequency of 50 Hz and the effective magnitude of 50 μT of $\vec{B}$. Please note that the latter field strength is comparable with that below the overhead power transmission lines (Footnote 71). In particular, the body is assumed to be composed out of *muscular tissue* with a more *conductive blood insert* (see this *conductive insert* to the left in Fig. 2.59a) and with a *less conductive fat insert* (see this *isolating insert* to the right in Fig. 2.59a). The assumed conductive and dielectric properties of all three involved biological media come close to reality and are taken from Figs. 2.20 and 2.21 (at 50 Hz).

Vectors of $\vec{E}$ and $\vec{J}_E$ field spin within the heterogeneous body, as expected from Fig. 2.31c. *Inside the body*, these fields increase in their magnitudes E and J_E almost linearly from the centre of the body to its outer surface, as can be observed in

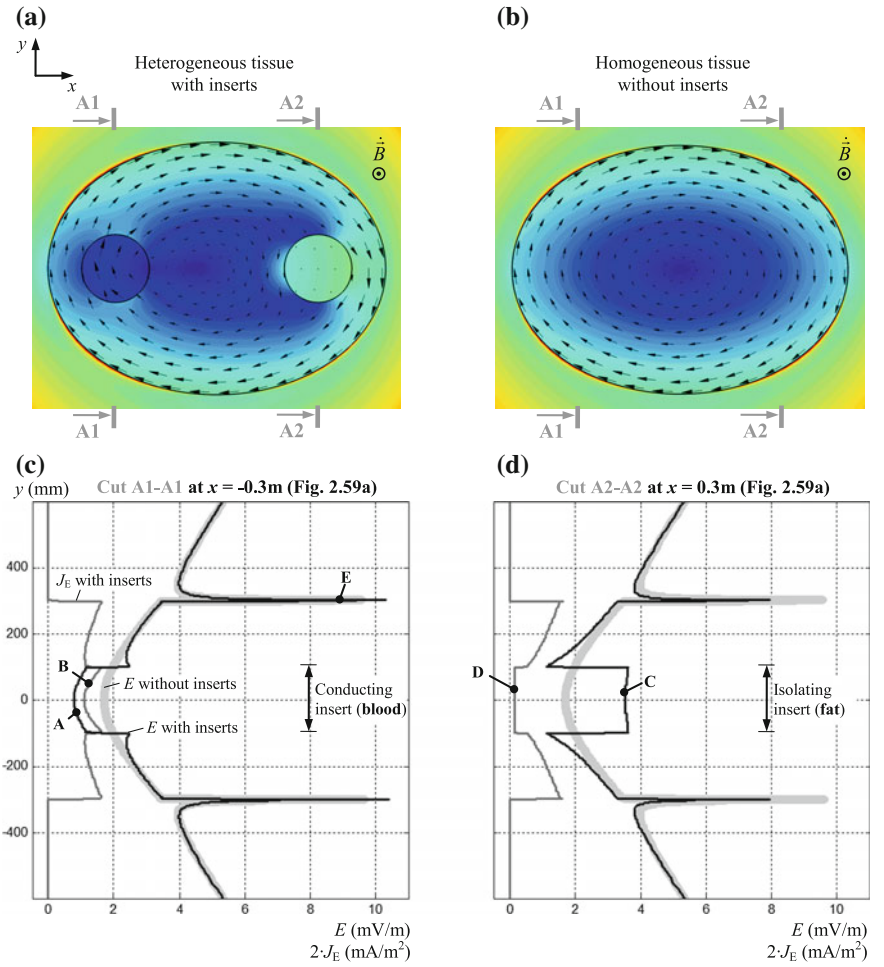

Fig. 2.61 Heterogeneous and homogenous cross-sections of the schematic human body in the air exposed to a spatially-uniform time-varying magnetic field $\vec{B}$ directed along the surface normal of the cross-section. **a** Heterogeneous cross-section with the distribution of the induced electric field $\vec{E}$ and the distribution of the resulting conductive current density $\vec{J}_E$ in terms of the electromagnetic induction (Fig. 2.31). For characteristics of the fields and body with its inserts see caption of Fig. 2.59. **b** Homogeneous cross-section from (**a**) without body inserts. **c**, **d** The courses of the effective magnitude E and J_E are depicted along the cutting lines A1-A1 and A2-A2, i.e., along the coordinates $x = -0.3$ m and $x = 0.3$ m, respectively (according to Fig. 2.59a). Plotted numerical data were calculated using finite-element method based on a two-dimensional model of the human body (Hirtl 2014)

Fig. 2.59b. The $\vec{E}$ field *outside the body* still continues to increase while the associated $\vec{J}_E$ field is almost zero (because of the isolating air), in analogy with Fig. 2.31b and (2.87). Please note that the *conductive and displacement current* components in the air can be neglected because of the relatively low air conductivity and low field frequency, respectively [see (2.90) and (2.91)].

However, a clear *asymmetry* with respect to x axis can be observed in the body fields (Fig. 2.59) because of both insets with their different electric properties. It is instructive that the zero point in $\vec{E}$ and $\vec{J}_E$ fields is not at $x = 0$ (as in Fig. 2.31b for the homogeneous body) but at $x = -63$ mm (Fig. 2.59c), i.e., the zero point is more closely located to the conductive insert. This is because (symmetric) *eddy fields* (due to electromagnetic induction) are superimposed by (asymmetric) *source fields* (due to induced surface charges around the blood and fat inserts); see Section "Incident Magnetic Fields". The blood insert acts as the *sink* for lines of $\vec{E}$ and $\vec{J}_E$ fields, whereas the fat insert acts as the *dispersive region* for these field lines (Figs. 2.59a and 2.31c). More detailed illustrations of $\vec{E}$ and $\vec{J}_E$ fields in the regions of inserts are provided in Fig. 2.60.

It can be inferred from Figs. 2.59c and 2.60a that, in analogy with the discussion in Footnote 70, the *conductive insert* shows decreased inner E and increased inner J_E, as related to the respective levels outside this conductive insert. The reverse is true for the *isolating insert*, as shown in Figs. 2.59c and 2.60b.

Figure 2.61 illustrates numerical comparisons of fields between the *heterogeneous body* (with two inserts, in full agreement with Fig. 2.59) and the *homogeneous body* (without both inserts). Once again, the courses of E and J_E magnitudes in the heterogeneous body in Fig. 2.61c confirm that the conductive insert yields a decreased inner $\vec{E}$ field and increased inner $\vec{J}_E$ field (see points A and B in Fig. 2.61c). The reverse situation applies for the isolating insert (see points C and D in Fig. 2.61d). In contrast to the heterogeneous body, the homogenous body shows continuous changes of $\vec{E}$ within the body because there are no inner boundaries (Fig. 2.61c, d).

Please note that the courses of E in Fig. 2.61c, d—across the *boundaries* between the (conductive/isolating) inserts and the surrounding tissue—are subjected to a *step-wise behaviour*. This is because the *normal components* of $\vec{E}$ are mostly involved in the depicted course of E (Fig. 2.61c, d), whereas the normal components can definitely jump on these boundaries [in line with (2.99)]. In contrast, the courses of E in Fig. 2.59c across these insert/tissue *boundaries* are *continuous* in their spatial behaviour because the *tangential components* of $\vec{E}$ are mostly involved in the depicted course of E and the tangential components can not jump at all [in line with (2.96)].

It is interesting to observe the *electrical point effect* at the *muscle-air boundary* in Fig. 2.61c, d, in both heterogeneous and homogeneous bodies (see the point E in Fig. 2.61c). This point effect dominates more on the side of the conductive insert, whereas this effect becomes even less dominant on the side of the isolating insert within the heterogeneous body than on the surface of the homogeneous body.

2.3.2.4 Physiological Effects

Physiological effects within biological tissue in response to a stimulus of electrical, chemical, mechanical, or thermal origin depend on

- the *spatial distribution* of stimulus within tissue,
- the *type and temporal pattern* of stimulus, and
- the subject/organ/tissue *susceptibility* to stimulus.

Here we focus on the *electrical stimulus* with the associated

- *electrical stimulation effects* on excitable tissues (Section "Electrical Stimulation Effects") and
- *thermal stimulation effects* on all tissues (Section "Thermal Stimulation Effects").

Since the electrical stimulus is typically delivered by a source external to the body, *coupling* of the *outer field* (i.e., external electric, magnetic, and/or electromagnetic field) into the bodily tissues is highly relevant (Sect. 2.3.2.2). The coupling determines the induced *inner field* [i.e., electric and current density field, see (2.54)] within tissue and thus the associated physiological effects of electrical and thermal stimulation. When these effects become exceedingly strong, *adverse effects* may occur (Section 2.3.2.5).

Field Coupling

Inner body fields—leading to *electrical stimulation* and/or *heating* of tissues—can be *induced* via mechanisms of

- *contact-less coupling*, where inner electric and current density fields are induced within the human body *without any physical contact* between the body and the *external field source*, known as *direct coupling* (e.g., when the *body is exposed* to external ambient electric, magnetic, and/or *electromagnetic fields*, see Fig. 2.63b); as well as
- *contact-based coupling*, where inner electric and current density fields are induced within the body *based on a physical contact* of the *external field source* with the body, known as *indirect coupling* (e.g., body's contact with charged objects or the skin electrode lead to *contact currents*, see Fig. 2.57);

compare direct and indirect coupling from Sect. 3 and Fig. 3.1. For instance, *alternating electric fields* (Fig. 2.26) or *alternating magnetic fields* (Fig. 2.31) around the human body can be coupled into this conductive body and then induce electric and current density fields within tissue. It should be recalled that *ambient fields are significantly perturbed* by the presence of the human body, i.e., by the presence of a conductive body within the isolating air (Fig. 2.26).

Since *coupling mechanisms* greatly depend on the field frequency (Fig. 2.33), the field coupling down into tissue shows strong *frequency dependence*. Therefore, any *physiological effects* due to induced inner fields will also exhibit frequency dependences.

Electrical Stimulation Versus Thermal Effects

Major interaction mechanisms are through *electric and current density fields* within biological tissues (Fig. 2.63), whereas *physiological effects* generally depend on frequency, intensity, and waveform of fields (Figs. 2.73 and 2.74). An established *interaction mechanism* of electric and current density fields for field frequencies

- *below about 100 kHz* is *stimulation of excitable tissues*, i.e., field interactions with *nerves and muscles*, with an associated relatively *small energy deposition*[86] of $\ll$ 1 W/kg (Section "Electrical Stimulation Effects"). These interactions comprise the most important mechanism for *hazard assessment* (Section "Adverse Health Effects and Exposure Limits") because of increased sensitivity of excitable tissues to inner fields in this frequency range. For higher frequencies, increasingly stronger fields are required to recruit the electrical excitability of excitable tissues, i.e., at frequencies where the polarization of the cell membrane (i.e., determining depolarization of the membrane, see Fig. 2.64) due to surrounding electric fields weakens and even disappears (above β-dispersion), while only non-excitatory displacement currents across the membrane are left.
- *Thermal interaction* predominates for higher frequencies *above 100 kHz*[87] with a quite *large required energy deposition* of about 1 W/kg (Section "Thermal Stimulation Effects"). In other words, neuromuscular excitations become less dominant while the thermalization of absorbed energy becomes the major

[86]To give a quantitative example, the estimated *energy absorption rate* P_{SAR} at *100 kHz* amounts to about 0.06 W/kg for the *basic restriction of the inner electric field* of 13.5 V/m in tissue or, alternatively, amounts to about 0.1 mW/kg for the *basic restriction of the current density* of 200 mA/m^2 in tissue; see Fig. 2.87 and (2.57) with the assumed tissue conductivity of 0.36 S/m (from muscle in Fig. 2.21 at 100 kHz). As described in Section "Electrical Stimulation Effects", the inner electric and current density fields account for the *stimulation of excitatory tissues*. On the other hand, the basic restriction of P_{SAR} is in the much higher range of 2–4 W/kg for frequencies above *100 kHz* (Section "Power Measures") to account for the *local heating* of the body (e.g., the head or trunk).

In analogy, the *inner current density* and the *inner electric field* in tissue can be estimated to amount to about 19 A/m^2 ($\gg$200 mA/m^2) and 53 V/m (>13.5 V/m), respectively, with the assumed tissue conductivity of 0.36 S/m and the assumed absorption rate P_{SAR} = *1 W/kg* (2.57). That is, the energy deposition level is assumed where thermal interactions start to dominate. Figure 2.87 demonstrates the latter level of the current density approximately corresponding to P_{SAR} = 1 W/kg, which is much higher than the basic restriction of the current density.

It follows from above that the estimated P_{SAR} *for excitatory interactions* is much lower than P_{SAR} *for thermal interactions*; compare Footnote 105. In addition, the assumed (relatively) high frequency of 100 kHz for excitatory interactions provides a rather worst-case scenario in this specific comparison (where basic restrictions of the inner electric and current density fields tend to increase with increasing field frequency, see Fig. 2.87).

[87]However, for pulsed sinusoidal stimuli or *non-continuous pulsed exposure*, the frequency separating stimulation of excitable tissues and thermal stimulation can extend well into the MHz region (Reilly 2011). Namely, the *delineation frequency* increases inversely with the square root of the *duty cycle* for non-continuous exposure (Footnote 134) because the *effective value of the exposure*—determining the *heating capacity* (Section "Thermal Stimulation Effects")—is proportional to the square root of the duty cycle.

mechanism. In contrast to the strong frequency dependence of neuromuscular excitation below 100 kHz, there is *no significant frequency dependence* of *thermal effects* for frequencies above 100 kHz; e.g., there are no significant changes of perception thresholds in Fig. 2.88 above 100 kHz.

In other words, as the frequency of the electromagnetic exposure increases *from about 100 kHz* (Section "Incident Electromagnetic Fields"), the dominant effects change from neuromuscular excitation to thermal excitation, namely, to heating of tissue. However, heating requires higher strengths of the electromagnetic field than neuromuscular excitation (Footnote 86 and 105). At high frequencies *above about 10 MHz* (up to 300 GHz (ICNIRP 1998)), *voluminous heating* is the *major effect* of interactions between the electromagnetic field and tissue. Higher frequencies *above about 10 GHz* are already absorbed at the body surface which necessarily ends in *superficial heating* of the body. Section 2.3.2.5 addresses the associated limits of heating.

For *contact-less coupling*, the *dominance* of both mechanisms of interaction depends on the *field frequency* since much less of the electromagnetic *field energy* is absorbed by the exposed biological tissue for frequencies below about 100 kHz (Fig. 2.33); especially absorbed in the approximate range 300 Hz–100 kHz (WHO 1993). Here the *electrical excitation* of tissues predominates at these low frequencies *below 100 kHz*, i.e., excitation is the most important mechanism of interaction between an external electromagnetic field and tissue. This is because *thermal interactions* occur at much higher energy levels than those needed for electrical excitation (Footnote 86). To give an example, an *electrical stimulus at 50 Hz* is not perceived as thermal stimulus (e.g., with a typical perceivable temperature rise in excess of 1 °C) even though this stimulus obviously heats tissue. This is because the relatively high energy level necessary to produce thermal perception would also yield severe *pain masking any thermal sensation*. On the other hand, an electrical stimulus *at 100 kHz* can be sensed as warmth but not as a tingling sensation.

In summary, *stimulation of excitable tissues* and *thermal interaction* show the following differences:

- *electrical excitation* of neuromuscular tissues mainly depends on the particular *waveform* of stimulus (e.g., the waveform of the electric current density, see below) and largely depends on the *field frequency*, whereas
- *thermal impact* largely depends on the *effective value* of stimulus (e.g., the root mean square value of the electric current density, see below) and is rather independent on the *field frequency*.

Let us consider an *example* for electrical *skin stimulation*. At the *lowest levels of stimulation*, large-diameter myelinated fibers with the lowest excitation thresholds (Fig. 2.81) residing close to the skin surface (Fig. 2.76) become excited. Here relatively thick sensory fibers for *mechanoreception* are stimulated (Footnote 101). Neural end and bend structures (Fig. 2.65)—with lower excitation thresholds than straight structures—represent most likely sites of excitation. With *increasing*

strength of the stimulus, small-diameter myelinated fibers and unmyelinated fibers (e.g., nociceptors leading to *pain*, see Footnote 101) become additionally excited. Recruitment of fibers residing in greater depths starts. At even *higher stimulation levels*, thermal sensation due to local tissue *heating* arises.

Interestingly, both electrical stimulation and thermal interaction may be accompanied by *counteracting mechanisms*:

- *electrical stimulation* reveals different *blocking phenomena* working against excitation, whereas
- *thermal effects* are counteracted by *thermoregulatory actions*.

In particular, *blocking phenomena* are due to sophisticated and non-linear excitation mechanisms within membrane including cathodic block, stimulation upper threshold (Section "Cathodic Block and Stimulation Upper Threshold"), high frequency conduction block (Section "Periodic Stimulus"). Counteracting *thermoregulatory actions* are due to vasodilation, heat convection, and radiation (Section "Thermal Stimulation Effects"). Interestingly, both counteracting mechanisms can be *favourably used in practice*. For instance, blocking phenomena facilitate *selective stimulation* of different fiber qualities (Footnote 99), whereas thermoregulatory actions improve *blood perfusion* (Footnotes 107 and 115).

It should be amended that *ambient electric fields* that act on an exposed human body (*contact-less coupling*) not only induce electric and current density fields acting *inside of the body* but also act *outside the body*. For instance, outer electric fields can cause body hair on the skin surface to vibrate and thus can be perceived.

Electrical Stimulation Effects

The discussed bulk properties of biological tissues account mainly for the *passive linear electrical properties* of tissues, excitable and non-excitable. However, *electrical stimulation*, i.e., applied *electric and current density* fields (Kaniusas 2012, Fig. 2.13), may potentially provoke *depolarization of membranes* of embedded *excitable cells* and—if thresholds are exceeded—*active cell response* due to activation of voltage-gated ion channels within membrane (Kaniusas 2012, Fig. 2.10). As a result, a highly *non-linear behaviour* of the membrane manifests in terms of induced *all-or-none action potentials* (Kaniusas 2012, Sect. 2.1.3.2). Local action potentials lead to spatially propagating nerve impulses (Kaniusas 2012, Fig. 2.13) and/or muscle contractions (Kaniusas 2012, Fig. 2.31).

- *Depolarization* of the cell membrane still below the excitation threshold implies an *increased excitability of the cell*, i.e., the cell can respond with action potentials to any stimulus, even to otherwise subthreshold stimulus. On the contrary,
- *hyperpolarization* of the cell membrane implies a *decreased excitability of the cell*, i.e., the cell can ignore otherwise suprathreshold stimuli.

In addition, other non-linear mechanisms such as *breakdown of cell membranes* (Footnote 90) may arise during *hyperpolarization* in response to applied electric fields.

Electrical stimulation targets excitable cells, in particular,

- stimulation of *sensing organs* (e.g., retinal phosphenes),
- stimulation of *nerves* (sensory or motor neurons), and
- stimulation of *muscles* (direct excitation of denervated muscles),

which are *non-thermal effects* in their nature and known as *neuromuscular effects* (Kaniusas 2012, Sect. 2.1.3.2). Although excitation can also be reached by different physical stimuli such as chemical, thermal, or mechanical, we focus here solely on the electrical stimulation.

Sensing organs typically show the lowest *stimulation thresholds*, followed by thresholds for nerve stimulation and then by the highest thresholds for denervated muscles (Fig. 2.73). In fact, muscle fibers are most easily excited by stimulating motor neuron connecting with muscle fibers (Kaniusas 2012, Fig. 2.24). Therefore, an *involuntary muscle contraction* can be due to three reasons, namely,

- a *strong stimulating current* through the *muscle* itself (direct excitation of the muscle),
- a *weaker current* along or through the connecting *nerve* which innervates this muscle (muscle excitation via motor neuron), or due to
- an *even weaker current* through the associated motoric *brain* region (governing this muscle).

Neuromuscular effects range from stimulation perception, to muscle spasms, or even to shocks and ventricular fibrillation (Fig. 2.88). Thresholds for neuromuscular effects tend to be lower for neurons closer to the stimulation electrode, for larger fiber diameters, and for elongated fibers aligned with the excitatory electric field in tissue.

Only specific stimuli in combination with a specific experimental set-up are able to stimulate and potentially excite excitable cells or fibers (Kaniusas 2012, Sect. 2.2). That is, a *particular fiber* reacts only to a *specific stimulus* delivered by a *specific experimental set-up*. The stimulus—e.g., *electric field* or *current density field*—is characterized by *three excitation-related quantities*

- *dynamic change* of stimulus,
- *duration* of stimulus, and
- *strength* of stimulus.

These quantities and their relationships determine whether the fiber will be excited or not for a given experimental setting.

In particular, for active membrane depolarization of a nerve or muscle cell, a *dynamic change* in the *momentary stimulus* is required, so that excitation effects at the cellular level can be expected to *vary with frequency*. In contrast, *constant stimuli* are counterbalanced through various *accommodating or adaptation mechanisms* and can not lead to excitation (Kaniusas 2012, Sect. 2.1.3.2.3). Therefore, alternating

stimuli such as *alternating currents* across the membrane are typically used for excitation (Kaniusas 2012, Fig. 2.13).

For *periodic stimulus*, neuromuscular effects are strongest in the *frequency range* of about 10–100 Hz (Fig. 2.74 and Kaniusas (2012, Fig. 2.16c)), whereas *accommodating mechanisms* limit neuronal effects below the latter range. That is, a certain minimum rate of the temporal change of stimulus is required for excitation; otherwise, *adaptation effects* prevail for slowly changing stimuli (Fig. 2.73). For instance, the excitatory depolarizing stimulus should be fast enough to open the relatively fast voltage-gated Na^+ channels depolarizing the membrane but not the relatively slow voltage-gated K^+ channels repolarizing the membrane.

Above the aforementioned frequency range, non-linear mechanisms of the membrane polarization buildup (*high frequency conduction blockade*), *refractoriness* of any excitable cell and capacitive *displacement currents* across the cell membrane limit neuronal effects and rise the excitability threshold, whereas neuronal effects almost disappear above 30 kHz. In particular, too short *depolarizing half-periods* (e.g., only 5 μs for 100 kHz) prevent excitation at high frequencies. In other words, excitation fails if the depolarizing stimulus ends too early (Fig. 2.69). This is because *cells need some time* to become excited (Kaniusas 2012, Fig. 2.13c) so that stimulation thresholds exhibit strong *frequency dependence* for high frequencies or short phase durations (Fig. 2.74). As illustrated in Fig. 2.73 (and Kaniusas (2012, Fig. 2.16a)), increasing stimulus amplitude can even compensate for decreasing phase duration of the depolarizing stimulus; however, a certain *minimum duration* is always needed to excite the cell.

At high frequencies, *displacement currents* which are *non-excitatory* dominate across the membrane at the cost of reduced *conductive currents* which are *excitatory* (Fig. 2.71a). With increasing frequency, the *polarization of membrane*—in response to the electric field outside of the cell (Fig. 2.64)—progressively decreases, whereas the polarization is strongest below β-dispersion [Fig. 2.19b and (2.141)]. The decreasing polarization disfavours induction of depolarizing voltages superposing the resting membrane voltage (2.139) and thus disfavours excitation of the cell.

In general, neither *continuous direct current* nor *continuous high frequency current* can excite cells (except for special cases with very high stimulus amplitude (Reilly 1998)). However, *direct current* may influence *excitability of cells* (Fig. 2.84). Subthreshold levels of electric and current density fields—unable to excite—may still affect both the *excitability of cells* (especially of *nerve cells* with a lower excitation threshold) and *ongoing electrical activity* (of nerve cells).[88] Please compare with effects of weak inhibitory shunts from Kaniusas (2012, Fig. 2.23a).

[88]There are suggestions that *weak electric fields* in the brain (with minimum thresholds as low as 100 mV/m below 100 Hz) contribute to the *electrical polarization* of neurons in the *central nervous system* and thus affect the *synchronization* of active groups of neurons (ICNIRP 2010). Consequently, cognitive processes like *memory* may be sensitive to the effects of these physiologically weak electric fields.

Sinusoidal stimulus comprises an interesting example in which the *duration of the depolarizing half-period* and the *dynamics* of the stimulus (i.e., two of the three excitation-related quantities from above) are tightly interrelated and can be represented by the *oscillatory frequency f* alone. In particular, the half-period equals to $1/(2f)$ while the level of dynamics is proportional to f; compare discussion on Fig. 2.74. Therefore, the relationship between the *strength* of stimulus (the third quantity) and f considers *all three excitation-related quantities* and determines excitation for a given experimental set-up, as illustrated in Fig. 2.74 (and Kaniusas (2012, Fig. 2.16c)).

To give an example, *muscle response* to electrical stimulation strongly depends on *stimulation parameters*.

- Relatively *low stimulation rate* up to about 30 Hz and the associated synchronous but low contraction rate of skeletal muscle produce *muscle twitches* (Kaniusas 2012, Fig. 2.31). Higher rates produce merged twitches and thus a *smooth contraction* (*tetanus*) with a reasonable muscle force. However, high firing rates, especially above 50 Hz, *fatigue* the contracting muscle very fast.
- The *pulse duration* and *pulse magnitude* of the stimulation current—in other words, the delivered *stimulation charge per pulse* (2.25)—govern the muscle force and are usually varied in order to intentionally control it.

Spatial and Temporal Stimulation Parameters

Spatial parameters of the stimulation set-up—as illustrated in Fig. 2.75b–f—and *temporal parameters* of the applied stimulation waveform—as illustrated in Fig. 2.72—determine *neuromuscular excitation*.

- *Spatial parameters* of stimulation are mainly given by the electrode design, skin conditions, and heterogeneity of underlying tissues with embedded excitable cells. These parameters govern the *spatial distribution* of the local *current density* around and across excitable structures and thus their resulting responsiveness to temporal parameters of stimulation. To demonstrate the spatial relevance, it should be noted that *transversal currents* across the axon are less likely to excite it than *longitudinal currents* of the same magnitude along the axon; compare Fig. 2.63a with Fig. 2.63b. As another example, *spatial gradients of electric fields* favour excitation of elongated axons (Fig. 2.66), whereas *high levels of electric fields* favour excitation of terminal and bend regions of axons (Fig. 2.65).

On the other hand, *weak electric fields* in the brain (above the thresholds for the induction of retinal phosphenes, Footnote 128) with frequencies in the range of 10–20 Hz (but not at higher or lower frequencies) seem to interact with rhythmical electrical activity in the *visual and motor cortices* of the brain and thus slightly affect *visual processing* and *motor co-ordination* (ICNIRP 2010). In addition, some *people* claim to be *hypersensitive* to weak electric and magnetic fields; however, double-blind studies suggest that reported symptoms are unrelated to such exposure (ICNIRP 2010).

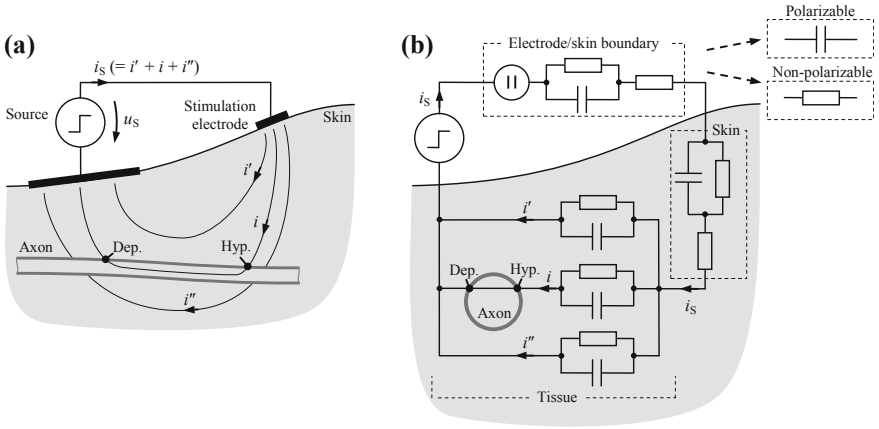

Fig. 2.62 Typical set-up for the neuromuscular stimulation of an axon below the skin with surface electrodes. **a** A small stimulation and a large reference electrode are applied on the skin to inject the source current i_S into tissue (with $i_S = i' + i + i''$). A fraction current i of i_S (>i) permeates the axon's membrane in terms of intracellular stimulation (Fig. 2.63a) while fractions i' and i'' contribute to extracellular stimulation (Fig. 2.63b). **b** The equivalent electrical circuit model for the electrode/skin boundary, the skin, and tissues with the embedded axon

- *Temporal parameters*, i.e., the shape of the stimulation waveform (see *excitation-related quantities* from above), govern excitation and its threshold. As already discussed, an excitatory stimulus requires a certain dynamic. The stimulus should be *not too slow* in order to override *accommodation* of the cell, *not too fast* to avoid both the *refractory behaviour* of the cell (Kaniusas 2012, Fig. 2.14) and non-depolarizing *displacement currents* (Fig. 2.63a) across the cell membrane draining the stimulators battery (Kandel 2000), and *not too short* to give the cell sufficient time for the excitation process to develop.

Figure 2.62a shows a typical set-up for *neuromuscular stimulation* of an axon below the skin with surface electrodes. Here the source current i_S (or the source voltage u_S) is applied between the stimulation and reference electrodes, whereas the resulting distribution of current lines—to be precise, of the current density field—within tissue is determined by *spatial parameters*.

- The shown current fraction i of i_S (=$i' + i + i''$) transverses the axon's membrane and may lead to its excitation in terms of *intracellular stimulation* (Fig. 2.63a). As illustrated in Fig. 2.62a, the inward *i hyperpolarizes* the membrane while the outward *i depolarizes* it.
- The two other fractions i' and i'' contribute to excitation in terms of *extracellular stimulation* (Fig. 2.63b). Here the axon region being closest to the electrode and facing *approaching currents* (i.e., facing *anodic stimulation*) experiences *hyperpolarization* (Fig. 2.67f). In contrast, another region being closest to the electrode and facing *departing currents* (i.e., facing *cathodic stimulation*) experiences *depolarization* (Fig. 2.67e).

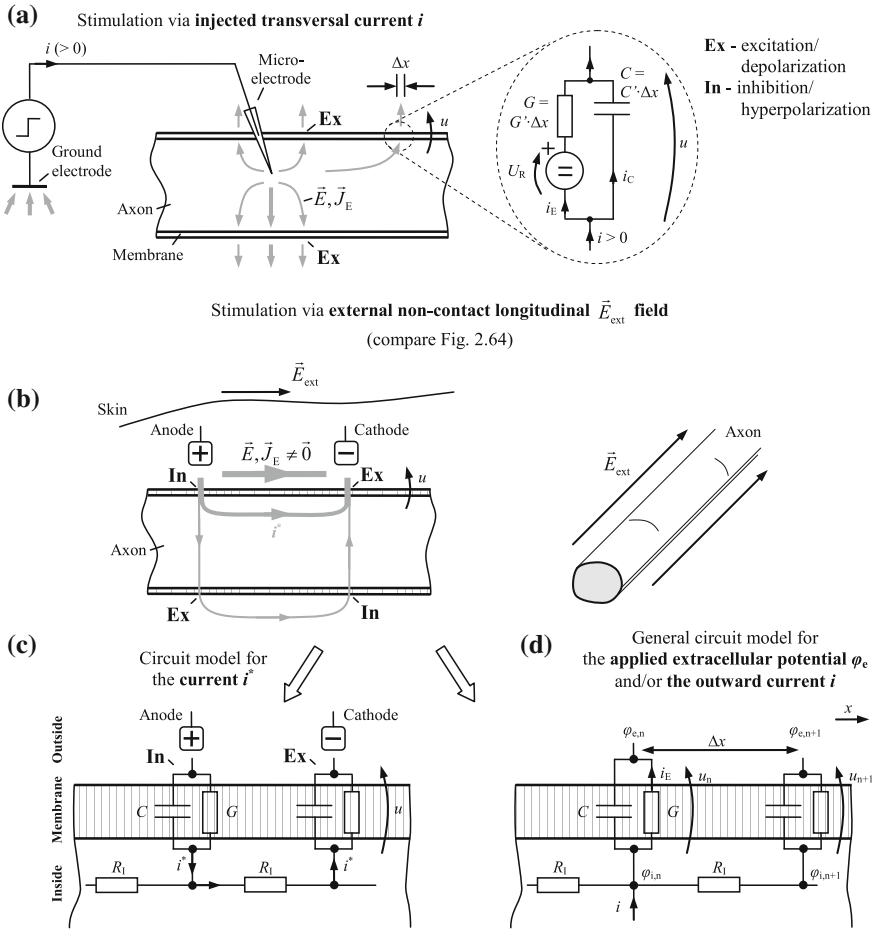

Fig. 2.63 Stimulation of an excitable cell. **a** Stimulation via injection of the transversal stimulating current i (>0) into the axon of a nerve cell; compare (Kaniusas 2012, Fig. 2.13). **b** Stimulation via the local electric field $\vec{E}$ and the conductive current density $\vec{J}_E$ (2.54) in tissue surrounding the axon. The axon's longitudinal axis is located in parallel to the direction of $\vec{E}$; in contrast to the transverse electric field from Fig. 2.64. These inner $\vec{E}$ and $\vec{J}_E$ fields arise, for instance, in response to the ambient electric field $\vec{E}_{ext}$ coupled through the skin into tissue (Fig. 2.30). As a model for the inner fields coupled into tissue, two oppositely charged electrodes —anode and cathode—can be assumed within tissue, with the shown local distribution of $\vec{E}$ and $\vec{J}_E$ field lines outside and inside of the axon. Alternatively, the setting in Fig. 2.66a can be assumed. Depolarized and hyperpolarized regions of the membrane are indicated. **c** Simplified electrical equivalent circuit model for the spatial pathway of the current i^* in and out of the axon from (**b**) with C as the membrane capacitance, G its non-linear conductance, and R_I the intracellular resistance (compare Fig. 2.18). **d** Segmented axon as a network for extracellular stimulation from (**b**)

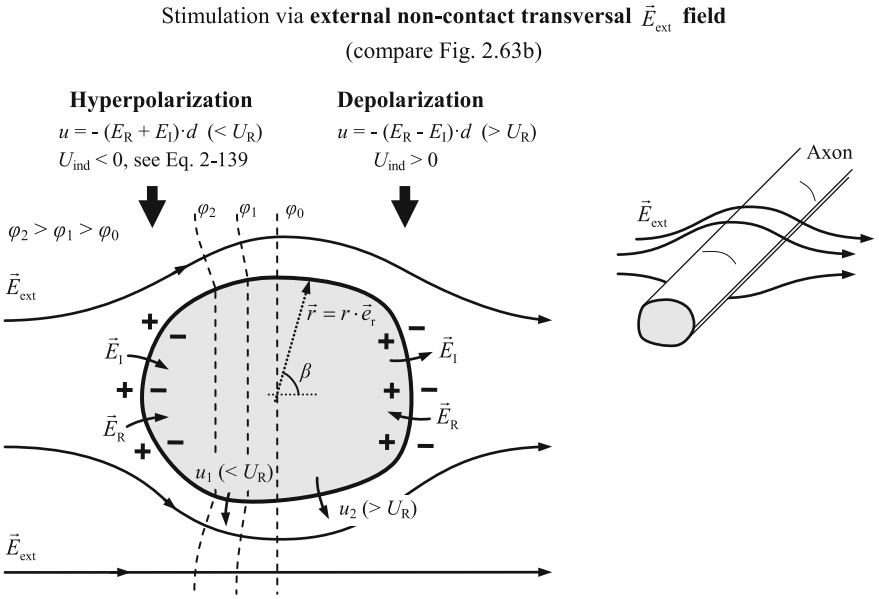

Fig. 2.64 An excitable elongated cell (e.g., neuron's axon) exposed to a transverse external electric field $\vec{E}_{ext}$ with its electric potential φ surfaces; in contrast to the longitudinal electric field from Fig. 2.63b. The field frequency of $\vec{E}_{ext}$ is below β-dispersion region (Fig. 2.22a) so that ambient currents circumvent the cell. The induced surface charges (as in Fig. 2.19b) generate their own electric field $\vec{E}_I$ inside the cell membrane, which interferes constructively with the resting membrane electric field $\vec{E}_R$ on the left side of the cell. Here the membrane voltage u decreases from its resting level U_R (≈ -70 mV < 0) and thus becomes even more negative, i.e., the membrane is hyperpolarized in response to $\vec{E}_{ext}$. In contrast, on the right side of the cell, the induced field $\vec{E}_I$ opposes $\vec{E}_R$ so that the resulting voltage u increases towards more positive values, i.e., the membrane becomes depolarized here

Therefore, *spatiotemporal transfer functions* between the resulting i', i, and i'' and, on the other hand, the applied stimulus i_S (or u_S) determine the probability of excitation. These functions imply that the applied waveform of i_S (or u_S) differs significantly from the resulting waveforms of i', i, and i''. In general, spatiotemporal transfer functions are highly *non-linear*, especially when polarizable electrodes are used with their highly non-linear electrode/skin boundary (Fig. 3.14).

While Fig. 2.62a gives an idea about *transfer functions* in *space domain*, Fig. 2.62b illustrates linearized transfer functions in *frequency domain*. The associated *electrical circuit model* is shown in Fig. 2.62b (for modelling see Sect. 3.1.1). It can be observed that, for instance, the temporal behaviour of i close to the axon is coupled to the applied waveform of i_S via spatiotemporal transfer functions of the electrode/skin boundary, the skin/tissue boundary, and tissue.

The *electrode/skin* transfer function can be approximated as RC model (Fig. 3.20b)—the charge transfer resistor (considering the charge-transfer-limited electrode reaction) in parallel to the double layer capacitor (accounting for the contact between metallic electrode and ionic electrolyte), and in series with the electrolyte resistor (due to electrode gel). For *polarizable electrodes*, the total model simplifies to a single capacitor (Fig. 2.62b), whereas the charge transfer resistance is relatively high and thus can be neglected (Fig. 3.21). In contrast, for *non-polarizable electrodes*, a single resistor results; i.e., the charge transfer resistor is dominant with its relatively small value. The *skin* can be modelled as another RC model (Fig. 3.3), with the corneal resistance and capacitance connected in parallel, and in series with the subcorneal resistor (due to the well-perfused dermis). Lastly, *biological tissue* can be modelled as a cell suspension which behaves as another RC model (Fig. 3.2) mainly acting as spatial *low-pass filter*. Because of the low-pass behaviour, for instance, a pair of recording electrodes records spatially steeper changes in the electric potential due to propagating action potentials along closely located muscle units than along units located more distant. Likewise, closely located muscle units generate higher frequencies in the surface potential than distant units.

Cell Orientation

Provided the *induced electric field* within *extracellular space*—or the associated *current density field* (2.54)—around an *excitable nerve or muscle cell* is sufficiently strong to depolarize the membrane above its threshold, the reviewed *active cell response* follows. The minimum strength of the electric field to induce excitation strongly depends on

- the *cell's orientation* with respect to the ambient electric field and
- the *cell's spatial extension*.

Namely, if the *long axis of an elongated cell* is in *parallel to the incident electric field* (Fig. 2.63b), a lower strength of the field is required for excitation as related to the cell's orientation with its long axis *perpendicular to the field* direction (Fig. 2.64). The more elongated is the cell, the larger is this difference in the required excitatory fields incident from different directions (*anisotropic excitation*), whereas spherical cells experience identical excitation from all directions (*isotropic excitation*). Please compare discussions related to Fig. 2.49 versus Fig. 2.50 concerning longitudinal and tangential electric fields, as well as related to Figs. 2.29 and 2.30.

Therefore, the *maximum probability* of excitation—or effectiveness of electrical stimulation—is given for nerve fibers aligned along the *direction* of the induced electric field (or the induced current density field) within tissue. Here the induced *gradients of the extracellular electric potential* point in the propagation direction of action potentials, i.e., point in the *most sensitive direction of elongated fibers* to external electrical excitation.

Magnetic Stimulation

Magnetic stimulation of nerves and muscles should be shortly addressed. Here a *time-varying magnetic field* (e.g., as generated by a discharge of a capacitor into an inductive coil) outside the human body induces *time-varying electric fields* within the body based on the *electromagnetic induction* (2.86). The induced electric fields and the associated conductive currents (eddy currents) within tissue can stimulate nerve and muscle fibers.

It should be recalled that the *temporal dynamics* of the incident magnetic field strongly influences not only the dynamics but also the size of the induced inner electric field. Both latter quantities are relevant for excitation (see above). As an important advantage, the induced electric field has already a *charge-balanced waveform* so that potential *tissue damage* is minimized (Section "Charge Transfer During Stimulation"). In addition, the magnetic field *penetrates more easily through tissues*—especially through weakly conductive fatty tissues (Fig. 2.6)—down to excitable fibers located at great depths, in comparison with transcutaneous stimulation of superficial fibers with contact electrodes on the skin surface. The magnetic stimulation does not require a direct physical contact between the body and the stimulation device so that a patient-friendly stimulation through clothes can be realised.

Current Density Versus Electric Field

To start with a detailed analysis of electrical *stimulation effects on excitable cells*, it is advisable to consider *driving forces* with respect to excitation. In fact,

- the induced *conductive current density* $\vec{J}_E$ across the cell membrane and
- the induced *electric field* $\vec{E}$ along the outer membrane.

comprise such forces. While guidelines in (ICNIRP 1998) take $\vec{J}_E$ in tissue as a *basic restriction* (Section "Basic Restrictions Versus Reference Levels"), more recent guidelines in (ICNIRP 2010) take $\vec{E}$ in tissue as a *basic restriction*, although both quantities are tightly interrelated (2.54). One of the reasons for this switch is certainly the fact that uncertainties in calculating directly the inner $\vec{E}$ are much less than uncertainties in $\vec{J}_E$ due to errors in the assumed tissue conductivity (2.54) (Reilly 2011).

Current Density as Driving Force

The *rationale for* $\vec{J}_E$ as the appropriate physical quantity responsible for the membrane *excitation* (i.e., nerve and muscle cells in the body) was already discussed in Kaniusas (2012, Sect. 2.1.3.2). In short, the *transversal injection* of a *conductive current* in or out of the excitable cell through its membrane—compare Figs. 2.63a, 2.71a, and Kaniusas (2012, Fig. 2.13)—leads to a net flow of ions in or out of the cell, mainly of K^+ ions through passive K^+ resting channels in the membrane. This net flow, in turn, alters the charge separation across the membrane and thus alters the polarization of the membrane. The *membrane voltage u* changes. Consequently,

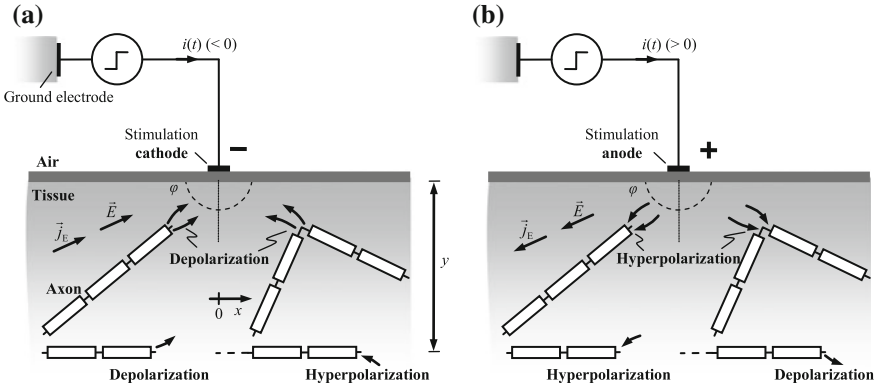

Fig. 2.65 Recruitment of axon at its end (end mode, see Footnote 92) and/or its bend in the trajectory of the axon (bend mode) by extracellular stimulation with the electrode set-up from Fig. 2.67a. In contrast to a straight axon (central mode excitation, see Fig. 2.67), the electric field $\vec{E}$—but not the gradient of $\vec{E}$—within tissue is the responsible metric for excitation. **a** Cathodic stimulus with the resulting current outflow out of the end region and out of the bend region, which depolarizes the axon at these points of efflux (Fig. 2.23a). **b** Anodic stimulus with the current inflow, resulting in hyperpolarization at the points of influx

- local *depolarization* results for local *conductive outward transmembrane currents* ($i > 0$ in Fig. 2.63a) which *favour excitation* of the cell (when stimulating closed/resting voltage-gated Na^+ channels within the membrane). In contrast,
- local *hyperpolarization* results for local *conductive inward transmembrane currents* ($i < 0$ in Fig. 2.63a) which *hinder excitation*.

Figure 2.63a depicts outward currents $i > 0$ and depolarized regions of the membrane causing u to increase in its absolute value; compare with outward excitatory ionic currents during propagation of action impulses in Kaniusas (2012, Fig. 2.18a). In short, the *transmembrane* $\vec{J}_E$ is the driving force for *intracellular stimulation*.

Electric Field as Driving Force

Figure 2.63b illustrates the induced inner $\vec{E}$ and $\vec{J}_E$ fields within tissue but outside an embedded axon. These fields arise in response to the *external electric field* $\vec{E}_{ext}$ coupled in a *contact-less* way into tissues.

The *rationale for the inner* $\vec{E}$ as the physical quantity responsible for the membrane *excitation* is given by the fact that the induced local *longitudinal* $\vec{E}$ (Fig. 2.30a) outside an excitable cell embedded within tissue produces a non-zero *voltage drop* or, in other words, a non-zero *gradient of the electric potential* (2.28) along the outer membrane surface of the cell (Fig. 2.63b). In fact, the relevant *integration distance* for $\vec{E}$ in the axial direction of the cell in order to estimate the *voltage drop* (2.30) is in the range of the applicable *length constant* of the membrane (Kaniusas 2012, Table 2.2). Obviously, the voltage drop increases with

increasing integration distance. For instance, this integration distance is in the range 2–5 mm for unmyelinated axons and 1–2 mm for myelinated axons (comparable with *internodal distance* in myelinated axons).

This *voltage drop* forces *equalising currents* to originate along and across the surface of the membrane; similar to induced equalising currents within the scope of the passive spread of depolarization (Kaniusas 2012, Figs. 2.7 and 2.18a) or the postsynaptic spread of depolarization (Kaniusas 2012, Fig. 2.19). In particular, the induced local $\vec{E}$ necessarily generates a local conductive $\vec{J}_{\mathrm{E}}$ *along the membrane's surface* [in accordance with (2.32)] as well as a blend of a local conductive $\vec{J}_{\mathrm{E}}$ and another displacement current density $\vec{J}_{\mathrm{C}}$ *across the membrane's surface* [in accordance with (2.32) and (2.66), respectively]. Figure 2.63a depicts the applicable equivalent circuit model of the membrane.

In fact, a *non-zero gradient* of $\vec{E}$ (2.145) along an elongated and straight axon—i.e., excitation in terms of *central mode* (Fig. 2.66 and Footnote 92)—and external to the axon drives *transmembrane currents* (Fig. 2.63d). In other words, a gradient of *potential differences*—or a change in the voltage gradient—across adjacent nodes drives *extracellular stimulation* (2.145). Please note that a strictly *constant* $\vec{E}$ along the straight (and infinite) axon *can not drive any net transmembrane currents*, as can be inferred from Fig. 2.63d. This is because every local membrane region along the infinitely long axon (or every node in myelinated case) experiences outward and inward currents in response to the constant $\vec{E}$, whereas these currents are identical in their size and have opposite directions. Therefore, the associated *net transmembrane current* across any membrane region (or any node) amounts to zero and there is neither regional hyperpolarization, depolarization, nor excitation. However, the field $\vec{E}$ within the real biological tissue is never uniform, either because axon changes its orientation with respect to the local $\vec{E}$ or because the resulting $\vec{E}$ distribution in tissue is non-uniform (due to heterogeneous tissues and local stimulation electrodes, compare Fig. 2.57). In short, a *non-zero gradient* of $\vec{E}$ is thus the driving force for *extracellular stimulation* in *central mode*. However, a *constant* $\vec{E}$ is a sufficient condition for extracellular stimulation of axon endings and/or bend regions in terms of *end mode* and *bend mode*, respectively (Fig. 2.65).

Since *potential differences* are induced along the *outer side of the membrane*, the local *membrane voltage* u is necessarily affected due to the *superposition principle* (Kaniusas 2012, Footnote 195). Please recall that the induced electric potential outside the membrane decreases downwards $\vec{E}$ field lines, i.e., the potential decreases along the direction of $\vec{E}$ [Fig. 2.11 and (2.28)]. It follows that—in the course of superposition—the voltage u tends to decrease on *the left side* of Fig. 2.63b below a *virtual anode* (positive electrode acting as *current source*, see Fig. 2.75c). Here the local u decreases in absolute units and becomes even more negative than its resting value: the local membrane patch under the anode becomes *hyperpolarized*. In other words, the outer side of the membrane experiences more positive potential and thus reduces the local u. The reverse behaviour can be

expected on the *right side* of Fig. 2.63b below a *virtual cathode* (negative electrode acting as *current sink*, Fig. 2.75b). The associated absolute u tends to increase in absolute units favouring *depolarization* of the affected membrane region.

Based on the *voltage drop* between the virtual anode and cathode and, on the other hand, the simplified electrical equivalent circuit model of the membrane (Fig. 2.63c and Kaniusas (2012, Fig. 2.18a)), it is obvious that *induced currents should enter the axon* through the membrane at the site of the *virtual anode*. In particular, this voltage drop—in response to $\vec{E}$ outside the axon—induces *displacement* i_C and *conductive* i_E currents through the membrane *capacitance* C and *conductance* G (Fig. 2.63a), respectively, as discussed in Fig. 2.71a. Then these currents flow jointly as a *conductive* current $i^*(=i_C + i_E)$ along the *intracellular resistance* R_I and subsequently leave the axon's inside at the site of the *virtual cathode* (Fig. 2.63c). The pathway of i^* is also depicted in Fig. 2.63b. In fact, the conductive i_E through G determines the *membrane hyperpolarization or depolarization* but not the displacement i_C through C; see Fig. 2.71a and the associated discussion.

In accordance with the discussed depolarization for outward currents and hyperpolarization for inward currents, it is clear that

- the inward current below the *virtual anode* serves as *hyperpolarizing stimuli* while
- the outward current below the *virtual cathode* serves as *depolarizing stimuli*.

However, these currents entering the axon through the membrane are usually much weaker than currents outside the axon, as qualitatively illustrated by the thickness of field lines in Fig. 2.63b. In addition, relatively small currents—see Fig. 2.63b—can also be expected to cross the whole axon and thus to affect the polarization of the opposite membrane.

Therefore, two *virtual electrodes* with opposite charges—anode and cathode—act as a *simple model* for excitation effects of the induced $\vec{E}$ within tissue (Fig. 2.63b). Please note that the only two considered virtual electrodes assume a *non-zero gradient* of $\vec{E}$ external to the axon, as needed for excitation in central mode.

Nerve Activation

Electrical *excitation of a single nerve cell* is considered first, followed by phenomenological comparison of *natural, intracellular, and extracellular stimulation*. We conclude with the concept of *activating function*.

Single Cell Excitation

Figure 2.64 depicts an elongated axon of a nerve cell located in the external *transverse electric field* $\vec{E}_{ext}$, i.e., the field is transversal to the long axis of the cell in terms of *extracellular stimulation*. Please compare it with the axon stimulation from Fig. 2.63b where the stimulating external $\vec{E}_{ext}$ and the associated inner $\vec{E}$ are in

parallel to the long axis. The pattern of field lines in Fig. 2.64 around and within the cell—acting as a less conducting inset with respect to its surrounding—is comparable with that in Fig. 2.52c.

Mobile *ionic charges* inside the cell experience electrostatic forces which strength and direction are determined by the applied directional $\vec{E}_{\text{ext}}$ field. Namely, *negative charges* (diverse intracellular anions, see (Kaniusas 2012, Sect. 2.1.1)) move to the left in Fig. 2.64 towards a virtual positive electrode acting as the source of $\vec{E}_{\text{ext}}$ lines. *Positive charges* (intracellular cations, mainly K^+ ions) move to the right towards a virtual negative electrode acting as the sink of $\vec{E}_{\text{ext}}$ lines (Fig. 2.16a). Intracellular charges become separated and a *net charge accumulates* on the membrane inside the cell (*electrostatic induction*, see Fig. 2.25a). Accumulated charges attract complementary charges from the extracellular space to reduce their stray fields (Kaniusas 2012, Footnote 13), so that a *finite electric field* $\vec{E}_{\text{I}}$ is *induced* across the membrane in response to external $\vec{E}_{\text{ext}}$. The membrane becomes *polarized*.

The resulting *total electric field* $\vec{E} = E \cdot (-\vec{e}_{\text{r}})$ within the membrane is given by the vector sum of the *resting membrane electric* field $\vec{E}_{\text{R}} = E_{\text{R}} \cdot (-\vec{e}_{\text{r}})$ and the induced $\vec{E}_{\text{I}}$. The field $\vec{E}_{\text{R}}$ is determined by

$$\vec{E}_{\text{R}} = \frac{U_{\text{R}}}{d} \cdot (-\vec{e}_{\text{r}}), \tag{2.136}$$

where U_{R} is the *resting membrane voltage* ($\approx$−70 mV), d the membrane thickness ($\approx$7 nm), and $\vec{e}_{\text{r}}$ a unit vector pointing in the radial direction of the assumed *spherical cell*; see Fig. 2.64. For the *left side of the cell*, constructive interference

$$\vec{E} = \vec{E}_{\text{R}} + \vec{E}_{\text{I}} = (E_{\text{R}} + E_{\text{I}})\ (-\vec{e}_{\text{r}}) \tag{2.137}$$

occurs while for the *right side* destructive interference

$$\vec{E} = \vec{E}_{\text{R}} + \vec{E}_{\text{I}} = (E_{\text{R}} - E_{\text{I}})\ (-\vec{e}_{\text{r}}) \tag{2.138}$$

results. Correspondingly, the total $\vec{E}$ increases in magnitude with respect to $\vec{E}_{\text{R}}$ on the *left*, whereas the absolute value of the *membrane voltage* u ($=-(E_{\text{R}} + E_{\text{I}}) \cdot d < U_{\text{R}}$) decreases to even more negative values than U_{R}. The membrane patch to the left in Fig. 2.64 becomes *hyperpolarized*. On the *right*, the total $\vec{E}$ decreases, whereas the absolute value of u ($=-(E_{\text{R}} - E_{\text{I}}) \cdot d > U_{\text{R}}$) increases and the membrane becomes *depolarized*.

Obviously, the *polarization process* requires a certain time for *inert intracellular charges* [with their finite mobility, see (2.53)] to become separated. Therefore, the described *hyperpolarization* and *depolarization* arise only at relatively *low frequencies*, where each half-cycle of the applied $\vec{E}_{\text{ext}}$ is long enough for separation of charges. Accumulated charges on the membrane decrease in their size with

increasing frequency and so the magnitude of $\vec{E}_I$ decreases with frequency. Namely, the described polarization process is dominant for oscillation frequencies of $\vec{E}_{ext}$ below *β-dispersion* (Fig. 2.19b).

While strong local *depolarization* may lead to local *excitation* of the cell membrane, strong local *hyperpolarization* may lead to local *breakdown*[89] of the membrane. The voltage u in the range of a *few hundred mV*[90] is required for breakdown, whereas a change in U_R of about *20 mV* is necessary for excitation (Kaniusas 2012, Fig. 2.14a). For instance, sensory and muscular reactions may result from the alterations in u.

Please recall for comparison that the absolute level of U_R is about *70 mV*. Breakdown and excitation comprise examples of the *non-linear behaviour* on the cell (Kaniusas 2014). The *risks of breakdown and excitation* decrease with increasing *frequency* because of the inert charge separation. In other words, missing charge separation and zero induced $\vec{E}_I$ at high frequencies imply missing breakdown and missing excitation. In general, knowledge of the net electric field which acts on specific parts of the cell membrane is important in predicting excitation and/or breakdown.

Below β-dispersion, external currents related to $\vec{E}_{ext}$ do not enter the exposed cell (Fig. 2.64), whereas *above β-dispersion* currents flow not only along the cell but also through the cell (Fig. 2.22). Consequently, *warming* of *extracellular* space results for relatively low frequencies of $\vec{E}_{ext}$ below β-dispersion, whereas warming of both *extracellular and intracellular* spaces results above β-dispersion.

---

[89]The *breakdown of the cell membrane* (Footnote 90) imposes failure of its mechanical and isolating properties. The membrane becomes *perforated* which is known as *electroporation*. Generated holes may close by itself after the external stimulus has ceased (*reversible electroporation*); however, holes may even become larger and instable, especially in response to periodic stimulus, leading to breakdown of the whole cell membrane and thus the cell death (*irreversible electroporation*). The amplitude of the membrane voltage of about 200 mV ($\geq |2 \cdot U_R| = 2 \cdot 70$ mV = 140 mV) is required for reversible electroporation, whereas about 800 mV ($\geq |10 \cdot U_R|$) for irreversible electroporation (Reilly 1998).

[90]The *breakdown of the cell membrane* (Footnote 89) requires *exceedingly high strengths* of the inner *electric field* within the membrane and thus requires high voltages across the membrane (2.30) in the order of *0.1–1 V* (WHO 1993). As an approximation, at least twice the strength of the *inner resting electric field* in the membrane is needed for its breakdown (Pfützner 2003). Please recall that the resting membrane voltage is about −70 mV while the inner resting electric field in the membrane is already impressively high in the order of 100 kV/cm (Kaniusas 2012, Footnote 49).

For instance, the *external field strength* required to rupture the membrane of a 10 μm cell is in the range of 10–30 kV/m (Foster 1996). This required field strength can be estimated from (2.140) with U_{ind} = 0.1–1 V, $\varphi = 0$, and for low field frequencies with $\omega \cdot \tau \ll 1$ (with the radius r effectively determining the required field strength).

It is important to note that the *probability of the breakdown* decreases with increasing *field frequency*, i.e., the probability is highest before *β-dispersion* at low frequencies when the *membrane polarization* (Fig. 2.19b) is most dominant (2.140). Likewise, this probability decreases with predominant *displacement currents* through the cell membrane at high frequencies, the currents that short-circuit the membrane and thus prevent its excessive polarization and, in turn, its potential breakdown.

In analogy with stimulating effects of the *longitudinal electric field* along the long axis of an excitable cell (Fig. 2.63b), the *external* $\vec{E}_{\text{ext}}$ outside the depicted cell in Fig. 2.64 also creates *differences in the electric potential* φ along the *outer membrane surface*. In particular, a gradient in φ is created in membrane regions *above and below the cell* in Fig. 2.64, where $\vec{E}_{\text{ext}}$ is *tangential* to the membrane surface. The size of the induced φ decreases in the direction of $\vec{E}_{\text{ext}}$ along the membrane surface. Thus the potential φ decreases from left to right in Fig. 2.64 in regions above and below the cell; compare $\varphi_2 > \varphi_1 > \varphi_0$. This implies that the *resulting membrane voltage u* in these regions also decreases in its absolute value in the direction of $\vec{E}_{\text{ext}}$; compare $u_2 > u_1$ in Fig. 2.64. In consequence, the *membrane excitability* in the *hyperpolarized* region with its u_1 is less than in the *depolarized* region with its u_2. Please note that since the inside of the cell is assumed to carry a finite current (the interior is not currentless), we have a non-zero but constant electric field within the cell (Fig. 2.64).

In analogy with the *virtual anode* from Fig. 2.63b, *approaching anodic currents* in Fig. 2.64 hyperpolarize the membrane. Similarly, *departing cathodic currents* in Fig. 2.64 depolarize, in qualitative analogy with effects of the *virtual cathode* in Fig. 2.63b.

The *total voltage u* across the membrane (Fig. 2.64) can be given as

$$u = U_{\text{R}} + U_{\text{ind}}, \tag{2.139}$$

where U_{ind} is the *induced voltage across the membrane* in response to the applied external $\vec{E}_{\text{ext}}$ in the extracellular space. In fact, the discussed polarization generates U_{ind} in terms of *β-dispersion* (Fig. 2.19b). For *spherical cells*, the voltage U_{ind}—and thus the probability of its *excitation or breakdown*—is proportional not only to the *strength* E_{ext} of the homogenous incident $\vec{E}_{\text{ext}}$ but also to the *cell size* (WHO 1993; Foster 1996), to give

$$U_{\text{ind}} = \frac{1.5 \cdot E_{\text{ext}} \cdot r \cdot \cos(\beta)}{\sqrt{1 + (\omega \cdot \tau)^2}}. \tag{2.140}$$

Here r is the effective cell radius, β the angle between $\vec{E}_{\text{ext}}$ and $\vec{r}$ (Fig. 2.64), ω the angular frequency of $\vec{E}_{\text{ext}}$, and τ the relaxation time constant of *β-dispersion* (2.74). Figure 2.64 demonstrates *depolarized membrane regions* at $\cos(\beta) > 0$ with the resulting $U_{\text{ind}} > 0$ and $u > U_{\text{R}}$, and *hyperpolarized regions* at $\cos(\beta) < 0$ with $U_{\text{ind}} < 0$ and $u < U_{\text{R}}$.

Equation (2.140) assumes a purely *conductive behaviour* of extracellular and intracellular spaces inclosing the membrane; i.e., the *inequality* $\gamma_{\text{eff}} \gg \omega \cdot \varepsilon$ applies for both spaces (2.71). In other words, (2.140) assumes relatively *low frequencies* where conductive behaviour dominates; compare the discussion about the air-tissue boundary as a function of frequency in Section "Biological Boundaries".

Maximum values of U_{ind} [$=\pm 1.5 \cdot E_{ext} \cdot r$ at $\omega \cdot \tau \ll 1$, see (2.140)] are given at the *low frequency* limit below the *beta relaxation frequency* and in the regions of the membrane that face the incident $\vec{E}_{ext}$ (at $\beta = 180°$ with $U_{ind} = -1.5 \cdot E_{ext} \cdot r$, see the *left side of the cell* in Fig. 2.64) and the departing $\vec{E}_{ext}$ (at $\beta = 0$ with $U_{ind} = 1.5 \cdot E_{ext} \cdot r$, see the *right side of the cell* in Fig. 2.64). In short, maximum values are induced in the direction of the ambient non-disturbed $\vec{E}_{ext}$.

Since polarization of the membrane diminishes with *increasing frequency* (see above), the voltage U_{ind} *falls off* as the inverse of frequency *above β-dispersion* according to

$$U_{ind} \approx \frac{1.5 \cdot E_{ext} \cdot r \cdot \cos(\beta)}{\omega \cdot \tau}, \tag{2.141}$$

which can be easily derived from (2.140) with $\omega \cdot \tau \gg 1$.

It is instructive to discuss the *dielectric behaviour* of a cell exposed to the ambient $\vec{E}_{ext}$. In contrast to the condition on the conductive behaviour from (2.140), the dielectric behaviour requires the *inequality* $\gamma_{eff} \ll \omega \cdot \varepsilon$ for extracellular and intracellular spaces. The dielectric behaviour dominates in the limit of *high frequencies* of $\vec{E}_{ext}$ far *above β-dispersion*, e.g., in the GHz range according to the discussion about the air-tissue boundary in Section "Biological Boundaries". In addition, the dielectric behaviour may dominate when extracellular medium of a relatively *low conductivity* is used around cells.

If permittivities of the membrane and both media surrounding the membrane are assumed to be identical, the *induced voltage* U_{ind}^{∞} *across the membrane* at *very high frequencies* equals (Foster 1996)

$$U_{ind}^{\infty} = E_{ext} \cdot d \cdot \cos(\beta), \tag{2.142}$$

i.e., equals simply to the projection of the incident $\vec{E}_{ext}$ field in the radial direction $\vec{r}$ of the cell (Fig. 2.64) over the thickness d (2.30). *Displacement currents* across the membrane prevail.

From a qualitative perspective, the *maximum* U_{ind} possible is proportional to the radius r (2.140) which serves as a projection distance for $\vec{E}_{ext}$ (2.30). The *entire voltage* that is applied to the cell by the incident $\vec{E}_{ext}$ at *low frequencies* is developed only *across the opposite membranes* of the cell (Figs. 2.64 and 2.19b) yielding a relatively large level of U_{ind} (2.140). Likewise, interiors of the cell—such as *nucleus* and *organelles*—do not carry any voltage drop in response to the incident $\vec{E}_{ext}$ and thus are effectively *shielded* from $\vec{E}_{ext}$ outside the cell at *low frequencies*.

With *increasing frequency*, the level of U_{ind} decreases (2.142). Above β-dispersion, U_{ind} decreases as the inverse of frequency (2.141). Interiors of the cell become increasingly exposed to the incident $\vec{E}_{ext}$, the shielding effect of the membrane progressively disappears. In the limit of *high frequencies*, the entire

applied voltage by the external stimulus—as a projection of the external $\vec{E}_{ext}$ over the cell width/diameter $2 \cdot \vec{r}$ (2.30)—is developed *across the whole cell* or mainly across the *intracellular space*, the cytoplasm (since $r \gg d$). Interiors of the cell are now fully exposed to $\vec{E}_{ext}$, whereas the membrane carries only a tiny amount (2.140) of the low-frequency voltage (2.142) because of its thinness ($r \gg d$).

- The maximum U_{ind} [proportional to r, see (2.140)] at *low frequencies* (below *β-dispersion*) is by about *three orders of magnitude* higher than
- U_{ind}^{∞} [proportional to d, see (2.142)] at *high frequencies* (above *β-dispersion*),

as induced by comparable $\vec{E}_{ext}$ outside the cell. In fact, the maximum U_{ind} decreases to U_{ind}^{∞} by the *ratio r/d* with r being in the µm range and d in the nm range (Kaniusas 2012, Sect. 2.1.1). The induced voltage drop across the nuclear membrane and that across intracellular organelles obey similar mechanisms, as discussed in Footnote 42.

It should be noted that induced differences in φ and induced levels of U_{ind} in asymmetrical cells strongly depend on the direction of the ambient $\vec{E}_{ext}$ prevailing outside the cells, with the highest local differences in φ and highest local U_{ind} when $\vec{E}_{ext}$ points in the axial direction of nerve or muscle cells (WHO 1993). Therefore, the resulting changes in the cell's excitability are stronger in *elongated cells* when they are oriented in *parallel to the external* $\vec{E}_{ext}$. Elongated cells are subjected to higher risks of *excitation and breakdown* for a given $\vec{E}_{ext}$ along the cell, which is known as *anisotropic excitation*. In particular, tube-like axons of nerve cells and fiber-like muscle cells are affected by anisotropic excitation.

Natural, Intracellular, and Extracellular Stimulation

It is instructive to identify origins of possible activating stimuli, whereas three major cases can be distinguished.

Natural Activation

Natural activation and propagation of action impulses—e.g., natural activation of *sensorial endings* of neurons (Kaniusas 2012, Fig. 2.21)—is *forced* by a non-zero second *spatial derivative* d^2u/dx^2 of the *membrane voltage u* along the axis x of the axon (Kaniusas 2012, Fig. 2.18b) scaled by the factor $(\gamma_I \cdot D/(4 \cdot C''))$, to give

$$\frac{du}{dt} = \frac{\gamma_I \cdot D}{4C''} \cdot \frac{d^2u}{dx^2}. \tag{2.143}$$

Here γ_I is the intracellular conductivity, D the axon diameter, and C'' the membrane area related capacitance. In fact, this relationship can be derived from the *cable equation* for the onset of activation with the initial reduced voltage $u = 0$ and $\varphi_e = 0$ (Footnote 93). Likewise, the *virtual "forcing current density"*—in line with (2.40)—favouring depolarization of the membrane with the *required rate of change* $du/dt > 0$ equals $(\gamma_I \cdot D/4) \cdot d^2u/dx^2$ (A/m^2).

Intracellular Activation

Intracellular activation—with an *intracellular electrode* permeating the membrane (Fig. 2.69a)—is *forced* by an externally applied non-zero *current density* j (A/m^2) *crossing outwards the membrane* and depolarizing it (comparable with the injected current i in Fig. 2.63a, d), to give

$$\frac{\mathrm{d}u}{\mathrm{d}t} = \frac{1}{C''} \cdot j. \tag{2.144}$$

This relationship can be derived from the *cable equation*[91] (for *weak subthreshold stimulus* or for the *onset of activation* with initial values $u = 0$, $\mathrm{d}^2u/\mathrm{d}x^2 = 0$, and $\varphi_\mathrm{e} = 0$). Equation (2.144) also results from a simple consideration that the *applied* j at its onset will *first cross the capacitor* of the membrane so that the basic capacitor relationship in (2.40) is reflected by (2.144) (Fig. 2.63d). Equation (2.144) confirms that the applied *anodic current* with $j > 0$ *depolarizes* the membrane with the resulting $\mathrm{d}u/\mathrm{d}t > 0$, whereas *cathodic current* with $j < 0$ *hyperpolarizes* it with $\mathrm{d}u/\mathrm{d}t < 0$ (Fig. 2.69).

Extracellular Activation—Straight Axon

Extracellular activation—with an extracellular electrode distant from the axon to be stimulated (Fig. 2.67a)—is *forced* by an externally applied non-zero second *spatial derivative* $\mathrm{d}^2\varphi_\mathrm{e}/\mathrm{d}x^2$ of the *extracellular potential* φ_e along x *just outside the axon* (Fig. 2.63d) scaled by the factor $(\gamma_\mathrm{I} \cdot D/(4 \cdot C''))$, to give

$$\frac{\mathrm{d}u}{\mathrm{d}t} = \frac{\gamma_\mathrm{I} \cdot D}{4C''} \cdot \frac{\mathrm{d}^2\varphi_\mathrm{e}}{\mathrm{d}x^2}. \tag{2.145}$$

In analogy to (2.143), this relationship can be derived from the *cable equation* for *weak subthreshold stimulus* or for the *onset of activation* with the initial $u = 0$ and $\mathrm{d}^2u/\mathrm{d}x^2 = 0$ (Footnote 93). Likewise, the *virtual "forcing current density"*

[91] It is instructive that equations for the *simplified electric network* of connected *membrane segments* from Footnote 93 can be easily amended with an additional *stimulation current* i or with its *current density* j $(=i / (\pi D \cdot \Delta x))$ permeating the membrane in an *outward direction*, as illustrated in Fig. 2.63d. That is, the equation for the nth intracellular node from Footnote 93 can be rewritten as

$$C \cdot \frac{\mathrm{d}(\varphi_{\mathrm{i,n}} - \varphi_{\mathrm{e,n}})}{\mathrm{d}t} + \frac{\varphi_{\mathrm{i,n}} - \varphi_{\mathrm{i,n-1}}}{R_\mathrm{I}} + \frac{\varphi_{\mathrm{i,n}} - \varphi_{\mathrm{i,n+1}}}{R_\mathrm{I}} + i_\mathrm{E} = i$$

with the associated differential equation for *unmyelinated cylindrical fibers*

$$\frac{\mathrm{d}u}{\mathrm{d}t} = \frac{1}{C''} \cdot \left(\frac{\gamma_\mathrm{I} \cdot D}{4} \cdot \left(\frac{\mathrm{d}^2u}{\mathrm{d}x^2} + \frac{\mathrm{d}^2\varphi_\mathrm{e}}{\mathrm{d}x^2} \right) - G'' \cdot u + j \right)$$

This equation shows the informative relationship between the resulting $\mathrm{d}u/\mathrm{d}t$ across the membrane and the applied j through the membrane.

favouring depolarization of the membrane with the *required* $du/dt > 0$ equals $(\gamma_I \cdot D/4) \cdot d^2\varphi_e/dx^2$ (A/m^2). Equation (2.145) illustrates that $d^2\varphi_e/dx^2 > 0$ is needed to *depolarize* the membrane patch at x with $du/dt > 0$, whereas $d^2\varphi_e/dx^2 < 0$ *hyperpolarizes* the membrane with $du/dt < 0$. Here both *anodic and cathodic currents*—as delivered by the extracellular electrode—can *depolarize* and *hyperpolarize* the membrane but at its *different regions*. However, cathodic current requires lower current thresholds and thus is more effective for excitation of the membrane (Fig. 2.67).

It should be stressed that a *non-zero spatial gradient* $d^2\varphi_e/dx^2$ of the applied *electric field* $d\varphi_e/dx$ (2.28) is required for *extracellular stimulation* of a *straight axon* (and ideally infinite axon). Please recall from Section "Current Density Versus Electric Field" that a *constant electric field* along the elongated axon (with $d\varphi_e/dx \neq 0$ and $d^2\varphi_e/dx^2 = 0$) would lack the driving force for the net ionic transfer across a local membrane patch and thus lack depolarization of the membrane along the axon (Fig. 2.63d).

Extracellular Activation—Terminal and Bend Axon

In contrast to the *straight axon* excitation (*central mode*[92]), a *constant electric field* is sufficient to drive locally net *transmembrane currents* and thus to stimulate *terminal endings* of axon (*end mode*) or *bend regions* of axon (*bend mode*), see Fig. 2.65.

Figure 2.65a illustrates that the *terminus of the axon* and the *bend of the axon* directed towards *cathode* experience currents exiting this axon (*outward transmembrane currents*), along the electric field lines created by cathode. In line with Fig. 2.63a, the axon becomes *depolarized* at the points of efflux. If the cathodic stimulus is sufficiently strong, excitation will be initiated at the site of maximum current efflux. *Anodic* stimulus in Fig. 2.65b with the opposite direction of the electric field in tissue shows the opposite behaviour. Here the inflow of currents into the axon (*inward transmembrane currents*) *hyperpolarizes* the terminus and the bend of the considered axon.

In practical cases, the applied gradient $d^2\varphi_e/dx^2$—the *second derivative* of φ_e—may be insufficient to excite the elongated fiber at an interior node but the corresponding electric field $d\varphi_e/dx$—the *first derivative* of φ_e—itself may be sufficient to excite *termini* and/or *bend regions* of the fiber. Therefore, the bend axon region is more likely to be excited than a *straight axon region*, whereas a *sharp bend* has a lower excitation threshold than a *gradual bend*. As in the case of central mode (2.145), the threshold for *end mode* excitation is inversely related to the *diameter* of the fiber end, so that excitation of *thick fiber endings* implies a *larger recruitment volume* than excitation of thin endings. Even the *second derivative* $d^2\varphi/dx^2$—and thus the excitation sensitivity of the elongated fiber—

[92] In general,

- excitation of a straight axon region is referred as *central mode*,
- excitation of a fiber terminus as *end mode*, and
- excitation of a bend region as *bend mode*.

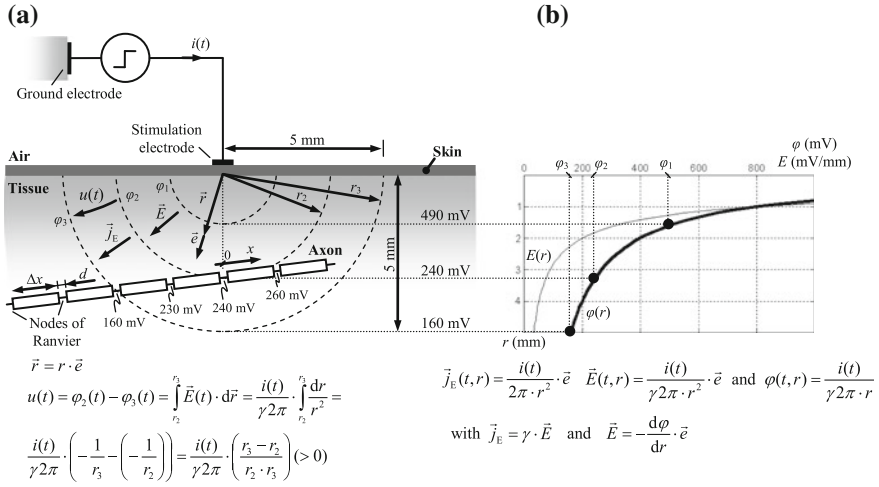

Fig. 2.66 Extracellular stimulation of a myelinated axon (central mode excitation) embedded within semi-infinite homogeneous isotropic tissue under the skin with a small monopolar stimulation electrode located on the skin surface and with a remote ground electrode; compare with Fig. 2.67. **a** The injected conductive current $i(t)$ distributes homogeneously across the half-spherical surface with its area $2\pi \cdot r^2$ at the radial distance r from the electrode. The resulting conductive current density $\vec{j}_E(t,r)$ within tissue obeys (2.23), the electric field $\vec{E}(t,r)$ (2.32), the voltage $u(t)$ between two points in tissue follows (2.29) while the extracellular electric potential $\varphi_e(t,r) = \varphi(t,r)$ obeys (2.28); see the corresponding equations. Consequently, subsequent nodes of Ranvier of the axon experience different levels of $\varphi(t)$, which may yield excitation of the axon. The gradient of $\vec{E}$ determines the excitation (2.145). **b** Numerical estimation of $\varphi(r)$ and $E(r)$ for the considered volume within $0 < r < 5$ mm assumes $i(t) = 1$ mA and the homogeneous isotropic tissue conductivity $\gamma = 0.2$ S/m (see muscle characteristics from Table 2.2)

increases in *bend axon regions* and in regions where the density of the local stimulus current strongly changes (Fallon 2016; Reilly 1998).

For excitation of a terminal ending and a bend region, the *first derivative* $d\varphi/dx$ comprises the *driving force*. Given the *bell-like shape* of φ along the axon axis x (Fig. 2.67c, d)—for a typical extracellular stimulation set-up with an electrode on the skin surface and the *axon lying in parallel to the skin* at a certain depth y (Fig. 2.67a)—it is clear that the spatial derivative $d\varphi/dx$ will show two extreme values. One extreme is at $x > 0$ (namely, at $x = y/\sqrt{2}$, see equations in Fig. 2.67b with $2x^2 - y^2 = 0$) and another at $x < 0$ (at $x = -y/\sqrt{2}$), both extremes reside in lateral regions where φ experiences largest spatial changes over x. Therefore, the terminus of the axon located at the region nearest to the stimulation electrode (i.e., right under the electrode at $x = 0$) will not experience the maximum excitation. Maximum excitation of the terminus takes place at the region more lateral to it; namely, at $x = y/\sqrt{2}$ for anodic stimulus or $x = -y/\sqrt{2}$ for cathodic stimulus in line with Fig. 2.65. In general, the *stimulation pattern* (cathodic or anodic, reversing minima of $d\varphi/dx$ to maxima and vice versa) and *orientation* of the axon end (pointing towards or away from the electrode) will determine the spatial region under the electrode where fields with the maximum excitation occur.

Interestingly, the *recruitment volume* with *end mode* excitation is about 40–50 times greater than that with *central mode*, for equal energy of monophasic or biphasic test pulses (Reilly 2011). For a given recruitment volume, *end mode* requires the *least stimulation energy*. Therefore, end mode excitation can be expected to dominate over central mode in biological tissue with *randomly oriented neurons*. In practical applications, the dominance of any mode (Footnote 92) will obviously depend on the details of neuronal structure and geometry as well as the stimulation set-up. More than one mode can be simultaneously activated, depending on the respective thresholds.

Activating Function

Intracellular stimulation (Fig. 2.69a) and its depolarizing and hyperpolarizing effects are straightforward, as can be seen from the simple (2.144). In contrast, *extracellular stimulation* depends on many more parameters while relationships between anodic and cathodic current and, on the other hand, depolarization and hyperpolarization of different membrane regions are rather sophisticated. All the more, *practical applications* typically use extracellular stimulation where stimulation electrodes are placed in a distance from the stimulation object, such as nerve or muscle. Therefore, in the following discussion, we will consider extracellular stimulation from a qualitative and quantitative perspective while using the highly instructive concept of *activating function*, as proposed by Rattay (1986a).

Experimental set-up for *extracellular stimulation* defines spatial field distributions of the time-varying electric field $\vec{E}$, the associated current density field $\vec{j}_{\mathrm{E}}$, as well as the extracellular electric potential field φ within tissue inclosing *excitable structures* of interest. In this context, Fig. 2.66a illustrates a monopolar *current electrode* located on the skin surface delivering the current i for *extracellular excitation* of a *myelinated axon* residing below the skin. The resulting distributions of $\vec{E}$, $\vec{j}_{\mathrm{E}}$, and φ are indicated for the *homogeneous isotropic tissue* under the skin, with the assumed *spherical symmetry* of these fields around the stimulation electrode. In fact, the spherical symmetry requires the *stimulation electrode* to act as a *current point source*, i.e., the electrode is either *small* (for flat electrode shape) or has a *spherical shape*. The *ground electrode* is far away from the stimulation electrode (and may be in the infinity) and thus does not influence field distributions around the axon of interest; likewise, field distributions around the myelinated axon are determined by the stimulation electrode only.

The *neighbouring nodes of Ranvier* of the axon are subjected to different φ and different $\vec{E}$, as can be observed from numerical values in Fig. 2.66b. A *non-zero spatial gradient* of $\vec{E}$ along the axis x of the axon can be recognized in Fig. 2.66a based on the inequality of φ differences [or inequality of voltages, see (2.29)] in-between neighbouring nodes, i.e., 260–240 mV $\neq$ 240–230 mV $\neq$ 230–160 mV. A *net transmembrane current* results at any node experiencing non-constant voltage drops with respect to the next node to the right and the next node to the left (Section "Current Density Versus Electric Field"). An inward transmembrane current generates hyperpolarization of the affected node, whereas an outward current depolarization (Fig. 2.63a). Thus the *condition for extracellular activation* from (2.145) is *fulfilled*, whereas the *straight axon* is locally *stimulated* and can be *excited* in response to the external i (*central mode* excitation).

Please note that numerical values in Fig. 2.66b assume a *small electrode* with respect to the *depth* of the axon under the surface or with respect to the considered radius r of the spherical field distribution. Accordingly, the used calculus—as shown by equations in Fig. 2.66—assumes a *current point source*.

The example in Fig. 2.66 illustrates that—provided distributions of induced $\vec{E}$, $\vec{j}_E$, and φ fields within tissue are known, as imposed by an *extracellular electrical stimulation*—*spatial gradient* of $\vec{E}$ along the axon embedded within tissue can be estimated to determine *transmembrane currents* and thus to determine if stimulation of the axon is present or not. In other words, a relationship is required between *extracellular fields* and the *rate of change* du/dt of the local membrane voltage u, as already suggested by (2.145). For myelinated axon, the rate du/dt at each node of Ranvier is crucial for its potential excitation in response to extracellular fields. Here the concept of *activating function*[93] $f(x) = \mathrm{d}^2\varphi_e/\mathrm{d}x^2$ is designed to estimate

[93]The *axon's membrane* can be approximated as a *simplified electric network* composed out of connected *membrane segments* with their length Δx, as illustrated in Fig. 2.63d. In fact, every segment represents a space clamped region or a space clamp experiment (Rattay 1990). For the nth intracellular node, the sum of all four outgoing currents yields (Rattay 1986a)

$$C \cdot \frac{\mathrm{d}(\varphi_{i,n} - \varphi_{e,n})}{\mathrm{d}t} + \frac{\varphi_{i,n} - \varphi_{i,n-1}}{R_I} + \frac{\varphi_{i,n} - \varphi_{i,n+1}}{R_I} + i_E = 0,$$

whereas the *stimulation current* i from Fig. 2.63d is set to zero (Footnote 91). Here C is the membrane capacitance of the axon's length Δx, R_I the associated intracellular resistance, φ *electric potentials*, and i_E the outward *ionic current* (composed out of sodium, potassium, and chloride ions, including conductive leakage currents, see Kaniusas (2012, Fig. 2.12) through the membrane conductance G (highly non-linear). Please note that Fig. 2.63d does not need to consider any extracellular resistances since *extracellular potentials* φ_e *are clamped* by *extracellular stimulation*.

With the *reduced membrane voltage* $u_n = \varphi_{i,n} - \varphi_{e,n} - U_R$ (i.e., the membrane voltage is reduced by the offset of the *resting membrane voltage* $U_R = -70$ mV) at the nth node, the latter equation can be rewritten as

$$\frac{\mathrm{d}u_n}{\mathrm{d}t} = \frac{1}{C} \cdot \left(\frac{1}{R_I} \cdot (u_{n-1} - 2u_n + u_{n+1} + \varphi_{e,n-1} - 2\varphi_{e,n} + \varphi_{e,n+1}) - i_E \right).$$

This equation provides a basis to estimate the *rate of change* du/dt which sign is essential for excitation, i.e.,

- du/dt > 0 for membrane *depolarization* and potential *excitation*, whereas
- du/dt < 0 for membrane *hyperpolarization* (2.145).

It is instructive that this rate du/dt is a function of the *spatial distribution of the extracellular potential* φ_e along the axis x of the axon, whereas the distribution of φ_e is determined by *electrode positons* and *electrical properties* of the medium the axon is embedded within.

For *myelinated cylindrical fibers* with Δx as the internodal length (isolated membrane with typical length of 1–2 mm, see Fig. 2.66a), d the width of the nodal gap (nonisolated membrane, 1–2 μm), D the axon diameter (2–20 μm, including the myelin), C'' the membrane area related capacitance (about 1μF/cm^2), γ_I the intracellular conductivity (about 1 S/m (Rattay 1988)), the following approximations apply:

$$C = \pi D \cdot d \cdot C'' \text{ (Kaniusas 2012, Eq. 2.2)}, \quad R_\mathrm{I} = \frac{\Delta x}{\gamma_\mathrm{I} \cdot \pi D^2/4} \quad \text{and} \quad j_\mathrm{E} = \frac{i_\mathrm{E}}{\pi D \cdot d}$$

with j_E as the magnitude of the ionic current density $\vec{j}_\mathrm{E}$. That is, the membrane of myelinated fibers is active only at nodes of Ranvier with their width d; likewise, the capacitive and ionic currents will enter the fiber only at nodes.

Then the equation for $\mathrm{d}u_\mathrm{n}/\mathrm{d}t$ considering *myelinated cylindrical fibers* reads as

$$\frac{\mathrm{d}u_\mathrm{n}}{\mathrm{d}t} = \frac{1}{C''} \cdot \left(\frac{\gamma_\mathrm{I} \cdot D}{4} \cdot \left(\frac{u_{\mathrm{n}-1} - 2u_\mathrm{n} + u_{\mathrm{n}+1}}{\Delta x \cdot d} + \frac{\varphi_{\mathrm{e,n}-1} - 2\varphi_{\mathrm{e,n}} + \varphi_{\mathrm{e,n}+1}}{\Delta x \cdot d} \right) - j_\mathrm{E} \right).$$

In the case of *unmyelinated cylindrical fibers*, $\Delta x = d$, with the limit for $\Delta x \to 0$ and $j_\mathrm{E} = u \cdot G/(\pi D \Delta x) = u \cdot G''$ with G'' as the area related membrane conductance, we find

$$\frac{\mathrm{d}u}{\mathrm{d}t} = \frac{1}{C''} \cdot \left(\frac{\gamma_\mathrm{I} \cdot D}{4} \cdot \left(\frac{\mathrm{d}^2 u}{\mathrm{d}x^2} + \frac{\mathrm{d}^2 \varphi_\mathrm{e}}{\mathrm{d}x^2} \right) - G'' \cdot u \right).$$

The latter equation is similar to the *cable equation*, connecting u, $\mathrm{d}u/\mathrm{d}t$, and $\mathrm{d}^2u/\mathrm{d}x^2$ in long cables. It illustrates the influence of fiber parameters on the *propagation velocity* of action impulses along fibers, whereas the velocity is directly related to $\mathrm{d}u/\mathrm{d}t$. For instance, $\mathrm{d}u/\mathrm{d}t$ increases with the *fiber diameter* D and/or its *inner conductivity* γ_I so that the *propagation velocity* increases with

- *increasing* D and/or with
- *increasing* γ_I

(compare Kaniusas (2012, Eqs. 2.11 and 2.12)). *Prior to and at the onset of the stimulus* with the *fiber resting*, it can be observed from the above equation that for zero $u = 0$ (i.e., the effective membrane voltage equals U_R and stays constant right at the onset due to the non-zero C; compare Footnote 33 in Chap. 3) and zero spatial derivatives ($\mathrm{d}^2u/\mathrm{d}x^2 = 0$), only the second *spatial derivative* $\mathrm{d}^2\varphi_\mathrm{e}/\mathrm{d}x^2$ determines the *temporal derivative* $\mathrm{d}u/\mathrm{d}t$ according to

$$\frac{\mathrm{d}u}{\mathrm{d}t} = \frac{\gamma_\mathrm{I} \cdot D}{4C''} \cdot \frac{\mathrm{d}^2 \varphi_\mathrm{e}}{\mathrm{d}x^2}.$$

In fact, we arrived at (2.145) for *extracellular stimulation*. In order to get an action potential, i.e., to *start depolarization of the membrane*, the voltage u has to increase in the area where excitation is to be produced with the positive depolarization rate $\mathrm{d}u/\mathrm{d}t > 0$ and has to approach the threshold voltage. For $\mathrm{d}u/\mathrm{d}t > 0$, the *inequality* $\mathrm{d}^2\varphi_\mathrm{e}/\mathrm{d}x^2 > 0$ *should be fulfilled* (Fig. 2.67). In particular, the polarity of the initial response of $\mathrm{d}u/\mathrm{d}t$ follows that of $\mathrm{d}^2\varphi_\mathrm{e}/\mathrm{d}x^2$ in line with (2.145). It is instructive to summarize that the *second spatial derivative* $\mathrm{d}^2\varphi_\mathrm{e}/\mathrm{d}x^2$ *of the extracellular potential* φ_e *in the direction* x *of the axon is responsible for activation inside the axon*.

In particular, $\mathrm{d}^2\varphi_\mathrm{e}/\mathrm{d}x^2$ *is the forcing function* because it is responsible for activating an imbedded fiber by *extracellular stimulation*. The term $\mathrm{d}^2\varphi_\mathrm{e}/\mathrm{d}x^2$ is thus known as the *activating function*,

- $f(t,n)$ for *myelinated fibers* (with *difference* quotients of φ_e) and
- $f(t,x)$ for *unmyelinated fibers* (with *differential* quotients of φ_e), to give

$$f(t,n) = \frac{\varphi_{\mathrm{e,n}-1}(t) - 2\varphi_{\mathrm{e,n}}(t) + \varphi_{\mathrm{e,n}+1}(t)}{\Delta x \cdot d} \quad \text{and} \quad f(t,x) = \frac{\mathrm{d}^2 \varphi_\mathrm{e}(t)}{\mathrm{d}x^2}.$$

du/dt given the spatial distribution of φ along the *long axis* x of the axon and outside the axon's membrane.

The *activating function* $f(x)$ provides the spatial *extent of depolarization or hyperpolarization* of local membrane regions and its *spatial decay* along x of the axon.

- A *high positive value* of the activating function $f(x)$ correlates with a strong *depolarization* at the region x and thus indicates a *low excitation threshold* of the *external current* i for excitation at x (Footnote 93).
- A *small positive value* of $f(x)$ correlates with a *high excitation threshold* of i for excitation at x. In contrast,
- a *negative* $f(x)$ is associated with *hyperpolarization* of the membrane at x. The more negative is $f(x)$, the stronger is the associated hyperpolarization.

It should be stressed that the *activating function* $f(x)$ is determined by *geometrical and medium factors*, including

- the *electrode current* and *electrode shape*,
- the *distance* of the fiber from the electrode,

- Accordingly, *depolarization* of the membrane with du/d$t > 0$ is produced and an action potential can be generated at the coordinate $x = n \cdot \Delta x$ (at nodes only) for $f(t,n) > 0$ in *myelinated fibers* and at x (at any membrane location) for $f(t,x) > 0$ in *unmyelinated fibers*. In contrast,
- *hyperpolarization* of the membrane is produced where $f(t,n) < 0$ in *myelinated fibers* or $f(t,x) < 0$ in *unmyelinated fibers* applies.

It should be reiterated that the latter interpretation of $f(t,n)$ and $f(t,x)$ with respect to du/dt is valid only for the *onset of the stimulus* before the membrane becomes strongly depolarized (above threshold).

Provided that $f(\cdot)$ does not vary much within the *internodal distance* Δx, $f(t,n)$ can be well approximated by $f(t,x)$ and the response of myelinated and unmyelinated fibers to extracellular stimulation becomes quite similar (Rattay 1988). In particular, this similarity applies when the shortest *distance y between the fiber and electrode* exceeds Δx, i.e., when the stimulation electrode is far away from the fiber as related to Δx (e.g., when $y > 2$ mm for $\Delta x = 1$ mm and $D = 2.4$ µm (Rattay 1987)).

For extracellular stimulation and every configuration of electrodes, the *sum of depolarizing/activating influences* is equal to the *sum of hyperpolarizing/deactivating influences*, in line with

$$\int_{-\infty}^{\infty} f(t,x)\,\mathrm{d}x = 0.$$

The external stimulation current can only depolarize certain regions at the cost of hyperpolarized regions. This is because the equalising *transmembrane current* flows always along a *closed loop* while depolarizing one region and hyperpolarizing another region (Fig. 2.67g, f). Since hyperpolarized regions are always present along the fiber, the propagation of *action impulses can even be blocked* in these regions which show a strongly negative $f(x) \ll 0$ (requiring quite strong stimulation currents; compare Fig. 2.78c, e and Footnote 99).

- the *extracellular medium* surrounding the fiber, and
- the *axial direction* of the fiber with respect to induced fields.

The function $f(x)$ predicts how easily the particular axon region is activated for a particular *experimental set-up* and a particular *electrical* stimulus. For instance, Fig. 2.67e, f shows $f(x)$ for the experimental set-up from Fig. 2.67a with cathodic and anodic stimuli from Fig. 2.67b. These properties of $f(x)$ make this function very attractive for *practical computations*.

However, the *rate of change* $\mathrm{d}u/\mathrm{d}t$ effectively *determines depolarization or hyperpolarization* at the membrane region x. This rate $\mathrm{d}u/\mathrm{d}t$ (2.145) is proportional not only to the second spatial derivative $f(x) = \mathrm{d}^2\varphi_e/\mathrm{d}x^2$, the activating function, along the neuron's axon (*unmyelinated axon*) or along the exposed nodes of Ranvier (*myelinated axon*) but also to the *factor* $(\gamma_I \cdot D/(4 \cdot C''))$. Therefore,

- the *depolarization rate* $\mathrm{d}u/\mathrm{d}t$ increases—and thus the *excitation threshold* decreases—with rising *diameter* D (Fig. 2.81) and rising *intracellular conductivity* γ_I. This is because rising D and γ_I favour equalizing currents within the fiber and lower its electrical resistance (Kaniusas 2012, Footnote 30). In addition,
- the rate $\mathrm{d}u/\mathrm{d}t$ decreases—and the *excitation threshold* increases—with rising *capacitive coating* C'' of the membrane because more time is needed to recharge the membrane capacitance.

Afterwards, when $\mathrm{d}u/\mathrm{d}t$ is known for the region x, the time $\Delta t = \Delta u \,/\, (\mathrm{d}u/\mathrm{d}t)$ taken for u to change by the required amount Δu to excite the cell region can be easily estimated; compare with the change Δu in u in Kaniusas (2012, Fig. 2.14a) from the resting level U_R of −70 mV to the threshold level −50 mV by $\Delta u = 20$ mV. This calculated time interval Δt determines then the *pulse width* $t_p = \Delta t$ needed for effective excitation at x, see Fig. 2.75a. Please note that the latter estimation of Δt as the simple ratio $\Delta u \,/\, (\mathrm{d}u/\mathrm{d}t)$ represents a *linear approximation* which holds only for relatively *short pulse widths*[94] and weak depolarizations.

In fact, the *activating function* strongly varies along fibers with electrodes implanted very close to these fibers, especially, when the inequality $y \leq \Delta x$ is fulfilled. Here y is the *shortest distance* between fiber and electrode (Fig. 2.67a), and Δx is the *internodal distance* (typically 1–2 mm, see Fig. 2.66a). Here, the response of the myelinated fiber strongly depends on the distance between the electrode and the *closest node of Ranvier*. A weak stimulation current is sufficient

[94]For the *linear approximation* to hold, each stimulation phase—see Fig. 2.67b—is assumed to be shorter than the *time constant* τ (2.49) of the membrane (Kaniusas 2012, Table 2.2) according to $t_p < \tau$. For instance, if t_p is in the range of 100 μs, the linear approximation holds rather for *unmyelinated fibers* (with τ in the range of 200–500 μs) but not for myelinated fibers (20–70 μs). Please compare the related discussion on the linear/exponential increase of the membrane voltage during the *short current stimulus* from Section "Single Monophasic Stimulus".

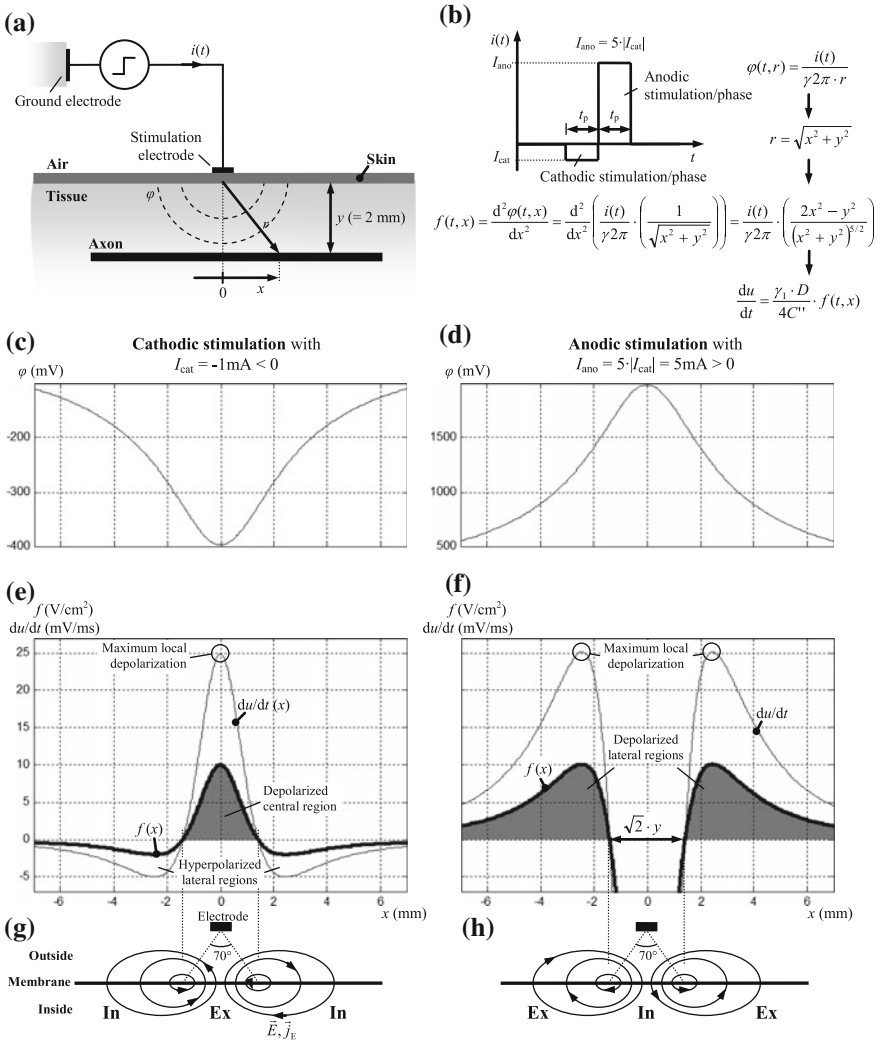

Fig. 2.67 Extracellular stimulation of an unmyelinated axon surrounded by semi-infinite homogeneous isotropic tissue; in close analogy with Fig. 2.66. **a** The axon lays in parallel to the skin surface at the assumed depth y of 2 mm. **b** The anodic phase of the biphasic current pulse has the fivefold amplitude of the cathodic phase; i.e., the current pulse is a charge-unbalanced biphasic pulse. This intended inequality yields similar local levels of the maximum membrane depolarization (at different axon's regions) during both equally long phases; compare Fig. 2.77. **c**, **d** The extracellular electric potential $\varphi_e(x) = \varphi(x)$ along the axon for cathodic and anodic stimulations. **e**, **f** The associated activating function $f(x)$ and the initial membrane depolarization rate du/dt (Footnote 93). **g**, **h** Directed field lines across the axon's membrane with the resulting excited/depolarized (Ex) and inhibited/hyperpolarized regions (In); compare Figs. 2.63c, d and 2.75b, c. Numerical estimation for -7 mm $< x < 7$ mm assumes $I_{cat} = -1$ mA, $I_{ano} = 5$ mA, the intracellular axon's conductivity $\gamma_I = 1$ S/m, the axon diameter $D = 10$ µm, the axon's area related capacitance $C'' = 1$ µF/cm^2, and the tissue conductivity $\gamma = 0.2$ S/m (Table 2.2)

for excitation when the electrode is directly *above a node*, whereas a stronger current is needed when the electrode resides just in the *middle of two neighbouring nodes* (Rattay 1987). This difference between nodal and internodal stimulation becomes dominant for the electrode located very close to the fiber. Therefore, for a small distance y, e.g., below 0.3 mm for $\Delta x = 1$ mm and $D = 2.4$ µm (Rattay 1987), the stimulation threshold current depends mainly on the *electrode's distance* from the *closest node* but not from the *fiber*. This situation in the myelinated fiber implies that only a *single node* or a *few nodes*—spatially close to the electrode—are involved in the fiber excitation due to extracellular stimulation.

The influence of (resting or firing) axons in tissue on externally-induced extracellular fields can be neglected so that these fields are solely determined by the external stimulation electrode and tissue properties. For the considered axon, it can be assumed that the *finite volume of the axon* as well as its *resting and action membrane potentials* do not significantly influence (or superimpose) axial extracellular fields along the axon as induced by the active electrode (Malmivuo 1995). An axon changes its *extracellular potential* by only about 1–3 mV when it is firing (Rattay 1986a, 1987), which is much less than the necessary depolarization amount of about 20 mV to excite the axon. Likewise, more than 95% of the membrane voltage is carried by changes of the *intracellular potential* (Rattay 1990). Therefore, the resulting spatial distribution of φ_e can be simply evaluated from the field of the stimulation electrode alone without considering the particular geometry and activity of fibers within tissue and the axon's contribution to φ_e. Obviously, the geometry of fibers can only be neglected for *central mode* excitation.

It is instructive to analyse how a typical *extracellular experimental set-up* determines the current direction and strength at the stimulation electrode, which are needed to reach positive and depolarizing $f(t,x) > 0$ at a particular location x along the axon. For this purpose, Fig. 2.67a illustrates quantitatively an *unmyelinated axon* located within *homogeneous isotropic tissue* at the *depth* y below a *skin surface electrode*. The axon lies in parallel to the skin surface. The *electrode* is assumed to be *small* so that discussed *spherical fields* prevail in tissue, in close analogy with Fig. 2.66.

The axon is subjected to different *gradients of the extracellular electric potential* $\varphi(x)$ along its long axis x during the cathodic stimulation phase (Fig. 2.67c) or anodic stimulation phase (Fig. 2.67d) of the *biphasic current pulse* with subsequent cathodic and anodic phases (Fig. 2.67b). Obviously, extreme values of $\varphi(x)$, maximum and minimum values, occur in axon's regions which are located closest to the stimulation electrode, i.e., in regions located at a minimum radius r from the stimulation electrode. For the axon located in parallel to the surface, extreme values reside at $x = 0$ (see unmyelinated axon in Fig. 2.67a), whereas the axon not parallel to the surface shows extremes at $x \neq 0$ (see myelinated axon with its extreme value at $x > 0$ in Fig. 2.66a).

The *activation function* $f(x)$ and the *initial membrane depolarization rate* $\mathrm{d}u(x)/\mathrm{d}t$—i.e., the initial increase rate of u—of the set-up in Fig. 2.67a are shown in

Fig. 2.67e, f. The applicable equations for calculus of $f(x)$ and $\mathrm{d}u(x)/\mathrm{d}t$ are given in Fig. 2.67b and Footnote 93. It is instructive that

- during *cathodic stimulation* the central membrane region of the axon for $|x| < y/\sqrt{2}$ of the axial width $2 \cdot y/\sqrt{2} = \sqrt{2} \cdot y$ is *depolarized* (see grey area in Fig. 2.67e); this width can be derived out of $2x^2 - y^2 = 0$ (Fig. 2.67b). The depolarized region is characterized by positive $f(x) > 0$ throughout the cathodic negative phase $i(t) < 0$. Thus, it should be pointed out that the applied *i(t) has to be negative* to *depolarize* the local *region at x = 0* closest to the electrode (since $2x^2 - y^2 = -y^2 < 0$ and $i(t) < 0$ apply for $f(t,x) > 0$ in equations from Fig. 2.67b). Here the *region at x = 0* experiences a *maximum of the depolarization* and represents the *most excitable point* of the shown unmyelinated axon; $f(x)$ is at its maximum at $f(0)$. The level of $f(x)$ and the associated depolarization strength increase non-linearly with decreasing depth y; in fact, $f(0) = -i(t)/(2\pi\gamma \cdot y^3)$ applies for $x = 0$ (Fig. 2.67b). In other words, the activating function $f(x)$ shrinks in its magnitude with y but not in the width of the central region $\sqrt{2} \cdot y$ that even increases with y. The closer is the axon to the electrode (superficial axon), the less stronger $i(t)$ is needed for its depolarization and eventual excitation.
  The *width* $\sqrt{2} \cdot y$ of the depolarized region—and thus the depolarized membrane area of the axon—*increases in proportion to increasing distance y* of the axon from the electrode and is *independent on the size of i(t)*. The deeper is the excitable fiber, the less *focussed* is its stimulation. In particular, lateral to and outside of the central region $|x| > y/\sqrt{2}$, *hyperpolarization* occurs (with $i(t) < 0$ and $f(x) < 0$), with a *maximum hyperpolarization* at $x \approx \pm 1.2 \cdot y = \pm 2.4$ mm (see below).
  From the point of view of a *single monopolar electrode*, both border lines between depolarized and hyperpolarized regions comprise an *opening angle* of about 70.5° (Fig. 2.67g). This angle is *independent on* the *fiber depth y*, *fiber parameters*, and the *extracellular conductivity*, as long as the extracellular medium is homogeneous and isotropic (Rattay 1987). In fact, a simple *geometrical relation* between the depolarized width $\sqrt{2} \cdot y$ and the depth y requires this constant angle of 70.5° (= $2 \cdot \mathrm{arctg}\,(1/\sqrt{2})$).
  The associated ionic *transmembrane currents* point outwards in the depolarized central region and inwards in the adjacent hyperpolarized lateral regions (Fig. 2.67g). Please recall that *outward currents* are indicative of the membrane *depolarization* and are typical for excitatory transmembrane current stimuli (Fig. 2.63a). In contrast to cathodic stimulation,
- the *anodic stimulation depolarizes* lateral regions of the axon for $|x| > y/\sqrt{2}$ and *hyperpolarizes* the central region $|x| < y/\sqrt{2}$ (including $x = 0$). Here two symmetrical local regions at $x \approx \pm 1.2 \cdot y = \pm 2.4$ mm experience a *maximum of the depolarization*, whereas a *maximum of the hyperpolarization* occurs at $x = 0$. Please note that there is *no excitation of the region x = 0* closest to the electrode. In contrast to cathodic stimulation, *anodic stimulation* with $i(t) > 0$ inverts $f(t,x)$ which now becomes negative $f(t,x) < 0$ at $x = 0$ and thus *hyperpolarization* results at $x = 0$ (Fig. 2.67f).

Therefore, lateral excitatory *transmembrane currents* point outwards while central inhibitory transmembrane currents point inwards. The *opening angle* is obviously the same (Fig. 2.67h). Please note that if the depolarization in lateral regions reaches the threshold, initiated action impulses can only propagate outwards from the central region. This is because the even stronger hyperpolarization of the central region—fivefold strength if compared with the lateral depolarization (see below)—would block the propagation inwards (see *collision block* in Section "Single Monophasic Stimulus").

It is also instructive to amend that for *surface electrodes* and fibers—positioned below the surface in a distance y *comparable with the electrode size*—the width of depolarizing regions ($f(\cdot) > 0$) and hyperpolarizing regions ($f(\cdot) < 0$) along fibers are in the order of the electrode size (Rattay 1988).

An important message from a practical and clinical point of view is that *extracellular stimulation* always gives rise to both local *depolarization* and local *hyperpolarization*, even along a single fiber. It is impossible to excite some fiber regions without having simultaneously hyperpolarized other regions which may even inhibit propagation of action impulses generated in depolarized regions (see *cathodic block* from Fig. 2.78c, e).

It can be seen from Fig. 2.67e, f that both $f(x)$ and $\mathrm{d}u(x)/\mathrm{d}t$ *quickly decay along the axon* and *effectively disappear* for $|x| > 5 \cdot y$. To be precise, $f(x)$ has already decreased to about 1.4% of its extreme value (at $x = 0$) at the distance $x = \pm 5y$ ($=\pm 10$ mm for $y = 2$ mm) or decreased to 5.4% at $x = \pm 3y$ ($=\pm 6$ mm for $y = 2$ mm). Therefore, axon parts distant from the stimulation electrode—here distant means relative to y—do not need to be considered in the stimulation, even though the local $\varphi(x)$ has still significant levels there. For instance, $\varphi(x)$ has only decreased to about 20% ($\gg 1.4\%$) of its extreme value (at $x = 0$) at the region $x = \pm 5y = \pm 10$ mm or decreased to 32% ($\gg 5.4\%$) at $x = \pm 3y = \pm 6$ mm.

Please note that the depicted *cathodic and anodic phases* in Fig. 2.67b have the same *pulse widths* t_p but different amplitudes. In particular, the amplitude I_ano ($=|5 \cdot I_\mathrm{cat}|$) of the *anodic current stimulus* has the *fivefold size* of the *cathodic current stimulus* I_cat. This is because we aim at a similar maximum $\mathrm{d}u(x)/\mathrm{d}t$ in local depolarized regions—i.e., aim at a similar strength of the local stimulus, even though at different x—during both the anodic and cathodic stimuli. This similar local impact is indicated in Fig. 2.67e, f by empty circles at the same level of $\mathrm{d}u(x)/\mathrm{d}t$. In particular, the latter *factor of five* results out of the fact that the central peak of $f(x)$ (at $x = 0$ in Fig. 2.67e) has approximately the fivefold magnitude of the neighbouring lateral peaks (at $x = \pm 2.45$ mm). Consequently, cathodic stimulus requires less current amplitude for the axon's depolarization (at $x = 0$) than anodic stimulus (depolarization at $x = \pm 2.45$ mm) and thus is more effective for the axon's excitation. However, different magnitudes $|I_\mathrm{ano}| \neq |I_\mathrm{cat}|$ but identical t_p give a *charge-unbalanced biphasic current pulse* (Fig. 2.67b) that is potentially harmful to tissues (Section "Charge Transfer During Stimulation"), in clear contrast to a desired *charge-balanced biphasic current pulse* (Fig. 2.75a).

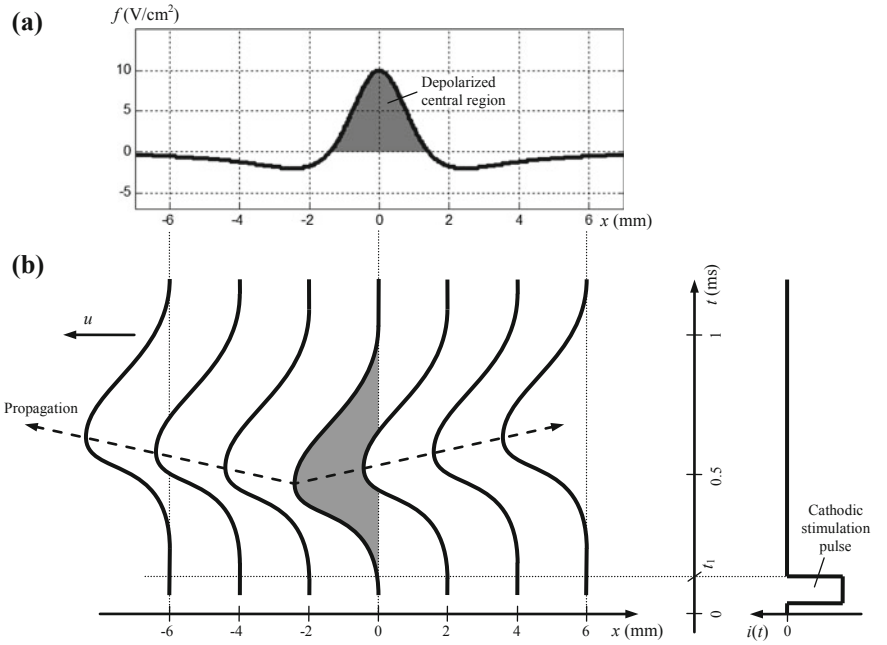

Fig. 2.68 Cathodic stimulation of an unmyelinated axon from Fig. 2.67a by the threshold current $i(t)$ (<0) yielding an action impulse at the region $x = 0$. **a** The activating function $f(x)$ (Fig. 2.67e). **b** The associated propagation of the action impulse—in terms of the membrane voltage u—for $|x| > 0$ with the propagation velocity of about 36 m/s; in close analogy with Rattay (1986a). Horizontal axis is the axon's axis, vertical axis is the time elapsed. The stimulation pulse, the cathodic rectangular current pulse, of 100 μs duration and with the threshold amplitude is plotted along the time axis

Identical levels of $du(x)/dt$ at the region x yield identical local levels of the absolute membrane depolarization $\Delta u = du(x)/dt \cdot t_p$ at the end of equally long phases (cathodic and anodic). Again, the latter estimation of Δu is based on the *linear approximation* (Footnote 94), assuming short phases and weak depolarizations. According to the approximation $\Delta u = du(x)/dt \cdot t_p$, it is interesting to infer that *after the end of a short current pulse*, the *membrane voltage u* along the fiber obeys qualitatively the *waveform of the activating function f(x)* (Rattay 1990).

That is, $u(x)$ becomes proportional to $f(x)$ providing a *practical and easy to establish association* (without solving differential equations for ionic membrane currents). This proportionality applies all the more so when the aforementioned linear approximation holds. It is valid for *subthreshold behaviour* of the membrane, for its *passive depolarization and hyperpolarization* without any active processes of excitation; in other words, valid for constant subthreshold membrane conductance G'' along the fiber.

To give some *examples*, Fig. 2.68a illustrates $f(x)$ while the associated scaled image of $f(x)$ is given by a horizontal cross-section $u(x)$ in Fig. 2.68b at the time instance t_1. Numerical example in Fig. 2.77b, c—see bold lines at $t = 1.1$ ms—clearly proves this proportionality between $u(x)$ and $f(x)$ for cathodic and anodic cases, whereas Fig. 2.67e, f illustrates $f(x)$ for these both cases.

Figure 2.68 illustrates *cathodic stimulation* and the associated *propagation of action impulses* along an *unmyelinated fiber* for the experimental set-up in Fig. 2.67a. The *threshold current* level of $i(t) < 0$ is applied to excite only the most excitable axon's region at $x = 0$ showing the highest value of $f(x)$ (Fig. 2.68a). With a certain *time delay of a few hundred μs* after the start of the *cathodic stimulation* pulse, an action impulse is generated at $x = 0$ (Fig. 2.68b). The propagation of the impulse starts to the right and left of the excited central region towards resting fiber regions, i.e., *bifurcation* occurs, with an estimated *conduction/propagation velocity* of about 36 m/s (Kaniusas 2012, Table 2.2). This velocity can be geometrically estimated in Fig. 2.68b from the slope of the dashed line connecting peaks of action impulses, i.e., the slope equals 6 mm / 0.166 ms ≈ 36 m/s.

Please recall that the *axon's diameter* is a major determinant of the *velocity*; see notice in Footnote 93 (Kaniusas 2012, Eqs. 2.11 and 2.12). For unmyelinated fibers, the propagation doubles in its speed when the diameter increases by a factor of four; e.g., increases from 9.6 to 38.4 μm (Fig. 2.76). As we know, propagation in unmyelinated fibers is much slower than in myelinated fibers (Kaniusas 2012, Table 2.2).

The *spatial extension* of an action impulse in the axial direction of the axon is addressed by Kaniusas (2012, Eq. 2.13) and amounts to about 36 m/s · 1 ms = 36 mm, with 1 ms as the assumed impulse duration, or as *temporal extension* (Fig. 2.68b). Likewise, it is instructive to highlight that the excited region has a typical length of a few cm.

The *threshold current* is applied in Fig. 2.68 without any suprathreshold stimulation. Correspondingly, the associated *hyperpolarization* in lateral regions around the depolarized central region at $x = 0$, starting at $x = \pm y/\sqrt{2} = \pm 1.4$ mm, is quite weak so that the generated and bifurcated action impulse passes easily along these lateral regions to the right and left of the central region with its width $\sqrt{2} \cdot y = 2.8$ mm. Weak hyperpolarization implies missing *cathodic block* (Fig. 2.78c, e).

In contrast to cathodic stimulation, *anodic stimulation* with $i(t) > 0$ would generate *two symmetrical action impulses* at two different locations $x = \pm 1.2 \cdot y$ (Fig. 2.77c). One action impulse from $x = -1.2 \cdot y$ would successfully propagate in the negative x direction while another originating from $x = +1.2 \cdot y$ in the positive x direction. Action impulses propagating towards $x = 0$ would necessarily extinguish each other in terms of *collision block*.

It should be recalled that *natural stimulation* always leads to *one-way propagation* of action impulses (e.g., along the axon from dendrites in receptors towards synapses, see Kaniusas (2012, Fig. 2.21)). This is in clear contrast to *artificial stimulation* which may lead to symmetrical *two-way propagation* (Fig. 2.68b) when a resting fiber is stimulated.

Charge Transfer During Stimulation

Charge Transfer Mechanisms

The stimulation current or *charge can be transferred* by electrodes to excitable tissue by *three mechanisms* (Weissenrieder 2009)—when using stimulation electrodes in contact with tissue (Fig. 3.1b, c)—

- *reversible Faradaic reactions* within the electrode/tissue boundary, i.e., with conductive currents across the boundary and thus connected with a *net charge transfer* into tissue (see Section "Electrode Impedance Model"). Electrons are transferred across the boundary via electrochemical reactions (Fig. 3.4), whereas reaction products are bound to the electrode surface and can be completely reversed by alternately passing equal and opposite charges;
- *irreversible Faradaic reactions* within the boundary, i.e., with still conductive currents across the boundary but irreversible reaction products introducing new species into tissue; and
- *non-Faradaic reactions* within the boundary, i.e., with displacement currents leading to capacitive charging or discharging of the double layer of the boundary and thus connected with an *absent net charge injection* into tissue.

The relative contribution of these different mechanisms to the total transferred charge into tissue depends on both waveform properties of the stimulus and material/geometric properties of the electrode/tissue boundary. As discussed in Section "Ag/AgCl and Pt Electrodes", different chemical reactions may occur on the electrode surface (e.g., water electrolysis to H_2 at cathode and to O_2 at anode). *Irreversible reactions* challenge tissue's and/or electrode's ability to buffer and/or suppress deleterious effects. Irreversible reactions are usually harmful to both *tissue and electrode material* and should be avoided, in contrast to *reversible reactions* with the associated *safe charge injection limit*. For more details on the *limited validity* of the safe charge injection limit see Section "Neural Stimulation".

Obviously, the charge transfer through *non-Faradaic reactions* is the *most attractive mechanism* since it is based on the *capacitive behaviour* of the electrode/tissue boundary *without any electrochemical reactions* and thus *without any potentially harmful reaction products*. Here ionic charges are *moved transiently* in tissue regions close to the boundary, which generates *non-zero excitatory electric fields* within these tissue regions. In particular, these charges move from or to the boundary in synchrony with the alternating electric field within tissue if *periodic stimuli* are applied. However, with only capacitive currents through the boundary it is usually difficult to generate a sufficient strength of the electric field that is strong enough to excite nerve and/or muscle cells within tissue. This is especially difficult for the relatively *low oscillating frequencies* of excitatory electric fields within tissue since low frequencies are *difficult to couple* through the capacitive boundary

but are required for an *efficient excitation* (Kaniusas 2012, Fig. 2.16c). Please recall that an increasing field frequency facilitates displacement currents and thus easies field coupling through the capacitive boundary (2.43).

As an advantage, *non-Faradaic reactions without reaction products* typically precede *Faradaic reactions with reaction products* when an electric stimulus is abruptly applied across the boundary; for instance, in terms of a biphasic current pulse (see the associated discussion in Section "Pt Electrodes"). In short, this is because the polarization overvoltage (3.16) governing Faradaic reactions is zero at the onset of the pulse and then is exponentially developed during the pulse (Kaniusas 2012, Fig. 2.8b).

The *inert behaviour of the boundary* and the *temporal dynamic of the applied stimulus*—in the simplest case, of a single *monophasic pulse*—also plays a significant role in the *onset of Faradaic reactions* (following in time non-Faradaic reactions). While the *time constant* of the boundary is determined by the product of its double layer capacitance (3.5) and the electrode resistance (3.16)—see Fig. 3.19c—the *duration of the stimulus pulse* is set by the user. When the time constant is comparable to or longer than the pulse duration, the *net charge injection* into tissue via *Faradaic reactions* becomes *limited*. This is because the boundary and its double layer capacitance are not even completely recharged during the pulse duration, which *weakens* the resulting *polarization overvoltage* and thus weakens the associated *Faradaic reactions* within the boundary (compare Section "Pt Electrodes"). This limitation particularly applies to electrodes that employ porosity to enhance the *safe charge injection limit* due to their increased electrochemical surface area (Cogan 2016); see discussions in (2.158) and Section "Pt Electrodes".

Irreversible Reactions To Charge Neutrality

Irreversible reactions within the electrode/tissue boundary have to be avoided to prevent *tissue damage* by residual and potentially *harmful reaction products*. It is natural to expect that if cathodic and anodic reactions are equally strong—in synchrony with cathodic and anodic phases of the stimulus (Fig. 2.75a)—then *reversibility of the reaction* should be given. However, the *charge neutrality* of the stimulation pulse—i.e., the total delivered charge over its whole period amounts on average to zero (see below)—does not necessarily imply reversibility of induced reactions.

This is because *electrochemical reactions* within the boundary typically underlie different diffusion processes (e.g., including gas evolution), have different decomposition voltages (see U_{dec} in Fig. 3.14), and show *different kinetics* (3.20). Consequently, *reactants* (reaction input) at the beginning of the next stimulating pulse period typically differ from *reaction products* (reaction output) after the end of the preceding stimulating pulse period. Strictly speaking, the charge neutrality is not capable of reversing products of *irreversible reactions* back to reactants.

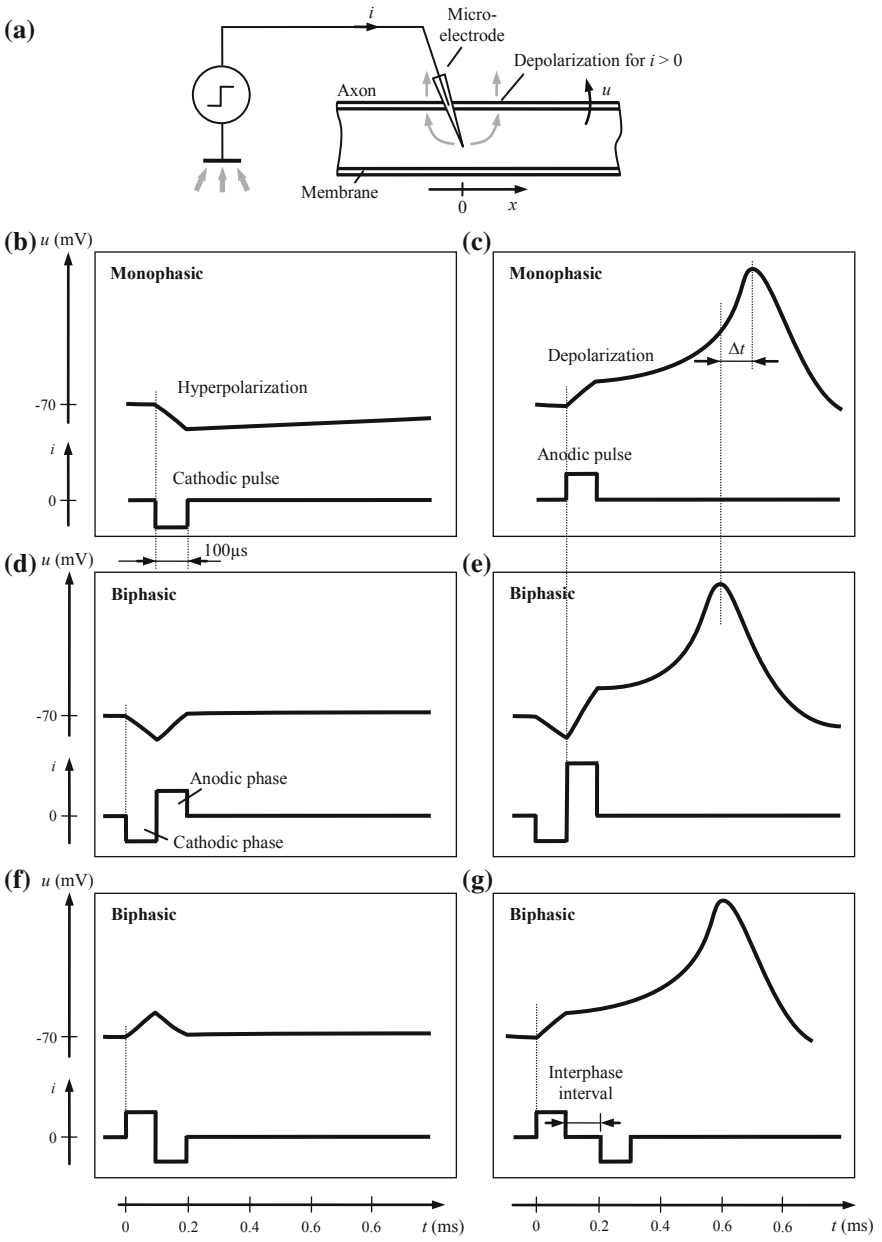
(a)
i
Micro-
electrode
Depolarization for i > 0
Axon
u
Membrane
0
x
(b) u (mV)
Monophasic
Hyperpolarization
-70
i
Cathodic pulse
0
(c)
Monophasic
Depolarization
Δt
Anodic pulse
100µs
(d) u (mV)
Biphasic
-70
i
Anodic phase
0
Cathodic phase
(e)
Biphasic
(f) u (mV)
Biphasic
-70
i
0
(g)
Biphasic
Interphase
interval
0
0.2
0.4
0.6
0.6
t (ms)
0
0.2
0.4
0.6
0.6
t (ms)

◂**Fig. 2.69** Intracellular stimulation of an excitable unmyelinated cell with a single monophasic or biphasic stimulus. **a** Stimulation via injection of the transversal stimulating current *i* into the axon of a nerve cell, using rectangular current pulses with 100 µs duration; compare Fig. 2.63a and Kaniusas (2012, Fig. 2.13). **b** Starting from the resting state of the membrane with its resting voltage u (=−70 mV), a monophasic cathodic pulse produces hyperpolarization which dies away very slowly. **c** A monophasic anodic pulse—just above the threshold—leads to an action impulse. **d** A biphasic pulse with its hyperpolarizing phase followed by depolarizing anodic phase of equal duration and amplitude—the fiber still remains at rest. **e** The depolarizing phase with the doubled amplitude generates an action impulse. **f** Hyperpolarizing phase follows immediately depolarizing phase and prevents an action impulse. **g** Interphase interval triggers an action impulse, in contrast to (f). Data taken from Rattay (1990)

A tangible example of irreversible reactions in view of charge neutrality is given below. *Reduced products* (Fig. 3.4d) of Faradaic reactions in the leading *cathodic phase* of a *biphasic current pulse* may diffuse too far from the electrode surface to be *oxidized* (Fig. 3.4c) during the subsequent *anodic phase* of the pulse. Here we assume identical charges per phase in the anodic and cathodic phases (Fig. 2.75a). Consequently, the electrode surface would be charged with a positive *excess charge* during the anodic phase, with the resulting *polarization voltage* $u_{\mathrm{pol,i}} > U_{\mathrm{pol}}$ (Fig. 3.13c). The affected electrode/tissue boundary would leave its *electrochemical equilibrium* (3.13) towards values more positive than U_{pol}, raising one-way electrochemical reactions and the possibility of *tissue harm and/or electrode corrosion* (Cogan 2016). Likewise, if $u_{\mathrm{pol,i}}$ before and after the current pulse is unchanged, given a fully reversible redox reaction (3.12), the electrochemical equilibrium is maintained.

Excess Charge and Polarization

Therefore, an *excess charge* or *excess polarization* of the electrode/tissue boundary should be avoided. In fact, the excess charge determines the *polarization overvoltage* ($u_{\mathrm{pol,i}} - U_{\mathrm{pol}}$) across the *capacitive boundary* (see 3.5 and Fig. 3.20c), which, in turn, determines the associated one-way *electrochemical reactions* (Fig. 3.14) for a given value of ($u_{\mathrm{pol,i}} - U_{\mathrm{pol}}$) within the boundary (potentially with unidirectional gas evolution). These reactions may have *harmful effects on tissue and/or electrode*, especially for *long-term chronic applications*.

A progressive charge accumulation on the boundary over time should be prevented by *avoiding or minimizing any direct current* across the boundary during stimulation. This current would steadily recharge the double layer capacitance of the boundary and progressively increase the amplitude of the *polarization overvoltage*. For a *periodic stimulus*, a direct current component should be avoided within the stimulus. However, it should be amended that the *direct current* can also be favourably used to *change the excitability of cells*, as discussed with respect to Fig. 2.84.

For instance, let us consider a *periodic stimulus* formed by *monophasic rectangular anodic current pulses* with a necessarily *non-zero direct component*; like a series of single monophasic pulses shown in Fig. 2.69c. The associated *polarization overvoltage* of the electrode would strongly increase throughout each rectangular

pulse (due to *charging of the boundary* by the finite current) and then would slightly decrease during the *inter-pulse interval* with zero current applied (due to *discharging of the boundary* along leakage resistances of the boundary, see the resistance in Fig. 3.20c). In total, the *average unipolar polarization overvoltage* would disadvantageously increase after each period of the monophasic stimulus until *stationary conditions* with a finite polarization overvoltage are reached.

Safety Countermeasures

Absent excess polarization can be ensured by a strict balance in the charge carried by the *stimulating phase* (or *depolarizing phase*) and another following *charge-balancing phase* (or *hyperpolarizing phase*) of a single stimulating current pulse. In other words, a reversed current pulse is applied following the stimulus, which passes an equal electric charge backwards through the electrodes to avoid deleterious electrochemical reactions.

A common approach to attain such a *charge-balanced pulse*—as illustrated in Fig. 2.75a—is the use of a *biphasic current pulse* (but not a biphasic voltage pulse) in which the phase-related charge in the leading phase (*cathodic phase* with the negative charge $-i_p \cdot t_p$ in Fig. 2.75a) and the phase-related charge in the trailing phase (*anodic phase* with the positive charge $i_p \cdot t_p$ in Fig. 2.75a) are equal and opposite. Likewise, the *net charge* delivered to tissue after each pair of phases or each pulse amounts to *zero*. It should be recalled that the *charge* is given as the *time integral of the current* (2.25) so that the *charge per phase* equals the area under the waveform of a current pulse during the considered phase, as illustrated in Fig. 2.75a by lined areas.

For instance, the *anodic phase* of the *biphasic current pulse* in the stimulation set-up from Fig. 2.69d–g (*intracellular stimulation*) *depolarizes* the axon membrane, whereas the *cathodic phase* neutralises the total charge of the pulse but *hyperpolarizes* the membrane. In the simplest case, the positive and negative parts of a rectangular current stimulus should be of the same size.

If even a *very small charge* is left on the electrode *following each stimulation pulse*—when a *periodic series* of current pulses is delivered to the electrode—then the *net charge* across the electrode/tissue boundary builds up over time with repeated pulsing. Eventually the *accumulated excess charge* density in the boundary will reach a point where the resulting *polarization overvoltage* is high enough for *electrochemical reactions* to begin.

It may be technically difficult to maintain precisely the *charge-balance* and the resulting *direct current* below *required limits* (Section "Neural Stimulation"). Here, as a very simple and typical *countermeasure* in neural stimulators is

- to include *capacitors* in series with stimulation electrodes to *block the delivery of any direct current* over time or any excess charge to the boundary. Another typical countermeasure comprises
- *shorting* of the *stimulation electrode* to the *ground/reference electrode* or even to

- the *metal case* of the implanted stimulator for the time *between two neighbouring stimulating pulses* in order to avoid the excess polarization, which is known as *inter-pulse potential control* (Cogan 2016).

When shorting to the case, the excess charge of the electrode/tissue boundary of the stimulation electrode becomes redistributed over both the electrode surface and over the much larger surface of the metal case. In doing so, the resulting excess polarization of the boundary is reduced and is then mainly dominated by the polarization of the much larger case. Simply speaking, the accumulated excess charge of the boundary is recovered back by shorting.

However, please note that the use of *charge-balanced pulses* is a *necessary but not sufficient* condition for harmless stimulation. Strong *polarizations* of the boundary driven by *large charge densities* and/or *large current densities* across the boundary *during a single phase* can already induce *irreversible electrochemical reactions* and/or *metabolic stress*. Both can be *harmful* to the electrode and biological tissue (Section "Neural Stimulation"). Especially when *current densities are different* in their amplitudes during consecutive anodic and cathodic phases within a still *charge-balanced pulse* (i.e., widths t_p of phases differ between anodic and cathodic phases, see Fig. 2.75), irreversible reactions are strongly favoured due to the varying strength of the boundary polarization from one phase to another (Fig. 3.14).

Stimulation Pattern

Different stimulation patterns can be applied for neuromuscular stimulation. *Monophasic stimulus* refers to *unidirectional* current or voltage application (Fig. 2.69b). In contrast, *biphasic stimulus* refers to *bidirectional* current or voltage application, in which two unidirectional phases follow each other (Fig. 2.69d).

Single Monophasic Stimulus

Short stimuli

The reaction of the nerve fiber depends on the *charge of stimulus* for short stimuli. This useful *rule of thumb* applies only when a relatively *short monophasic current stimulus* across the fiber's membrane is used for its excitation. The rule assumes a typical short stimulus duration in the range of 100 µs. Figure 2.69b, c illustrates such short stimuli. In fact, this rule is suggested by Fig. 2.71b, i.e., the *strength-duration curve* of a monophasic rectangular current pulse. The curve shows that the *excitatory threshold charge* is constant for a relatively short current stimulus—irrespective of the associated excitatory current level—and thus determines excitation (see below).

Here the terminus *short* relates to the *pulse duration* shorter than

- the *time constant of the membrane* (applies to simplified excitatory models such as Fig. 2.63a for intracellular stimulation) or shorter than

- the *chronaxie* of the strength-duration curve (applies for realistic stimulation scenarios and extracellular stimulation).

The applied *electric charge* is decisive here because the membrane—as a capacitor with its *capacitance C*—has to be *recharged and depolarized* by a certain amount of the charge for the membrane's excitation. It should be amended that this rule applies to just one *depolarizing phase* or one depolarizing pulse polarity of *biphasic current stimulus* (such stimulus is usually used to balance the applied charge, as described later in Section "Single Biphasic Stimulus").

The particular and fine shape of the used *current waveform is not important* for this short stimulus. This is because a single fiber can not respond to waveform changes of the stimulus shorter (or faster) than the fibre's *recovery period* (or *refractory period*) in the order of 1 ms (Rattay, 1986b, 1987); see Kaniusas (2012, Fig. 2.14). What counts is the charge threshold.

A *short suprathreshold stimulus* leads to a *single firing*, to a single action impulse; in contrast to multiple firing for longer stimulus (see below). When a *bunch of nerve fibers* are considered within a single *nerve*, the *charge of stimulus* determines also how many single fibers within that nerve are excited, as discussed in Footnote 100. In short, higher charge levels recruit greater number of fibers, which, of course, places larger *metabolic stress* on the whole nerve and may even lead to nerve injury (Section "Neural Stimulation").

A relatively *short current stimulus* has a prominent *practical advantage*. It allows a reasonable control of the extent of depolarization or hyperpolarization Δu of the voltage u across the stimulated membrane in response to this stimulus. Namely, if the stimulus duration is shorter than the *time constant of the membrane* (Kaniusas 2012, Table 2.2)—or shorter than the *chronaxie* of the strength-duration curve (Fallon 2016), see Fig. 2.73—the size of Δu becomes roughly *linearly proportional* to the product of

- the *currentamplitude* and
- the *duration* of the stimulus (2.25).

In other words, Δu becomes linearly proportional to the *applied charge* [$=C \cdot \Delta u$, see (2.39)] by the delivered stimulation pulse. From a practical point of view, the size of Δu can be rather easily and *linearly controlled* by changing either the current amplitude and/or the time for which the current flows. In analogy, *depolarizing* Δu (>0) or *hyperpolarizing* Δu (<0) can be controlled by varying the depolarizing charge ($C \cdot \Delta u > 0$) or hyperpolarizing charge ($C \cdot \Delta u < 0$), respectively, of a *single monophasic stimulus*. Likewise, the polarity and size of the *charge* of the respective phase of *biphasic current stimulus* determine the sign and size of the resulting Δu. Please compare the following discussion concerning the linear response and time constant.

Obviously, the current direction across the membrane determines whether depolarization ($\Delta u > 0$) or hyperpolarization ($\Delta u < 0$) takes place. For instance, *depolarization* of the membrane region *closest to the stimulation electrode* requires either

- *anodic current* for *intracellular stimulation* (Fig. 2.69 and Kaniusas (2012, Fig. 2.13)) or
- *cathodic current* for *extracellular stimulation* (Fig. 2.67).

The reverse is true for *hyperpolarization* of this closest membrane region.

Figure 2.69 illustrates *responses of a nerve fiber* stimulated with an *intracellular electrode* delivering a *single monophasic current stimulus*; in close analogy with Kaniusas (2012, Fig. 2.13). While a *single cathodic pulse* hyperpolarizes the membrane towards more negative u (Fig. 2.69b), a *single anodic pulse* depolarizes it. When the *excitation threshold* of the fiber is reached, depolarization ends with excitation of the fiber (Fig. 2.69c).

Long Stimuli

For long monophasic current stimuli, the *current amplitude* matters but not the delivered charge. This can also be derived from the *strength-duration curve* in Fig. 2.71b. It indicates that the *excitatory threshold current* is constant for a relatively long current stimulus—irrespective of the associated excitatory charge level—and thus determines excitation (see above).

When the *duration of the monophasic current stimulus* is more than five times that of the *refractory period*, the firing behaviour will be different. A constant and *long suprathreshold stimulus* leads to *repetitive firing*, as used, for instance, for cochlea implants (Rattay 1990). For instance, a *fiber close to the stimulation electrode* will reach its threshold soon—i.e., the local $f(x)$ along the fiber and thus its $\mathrm{d}u/\mathrm{d}t$ are quite high (in terms of *extracellular stimulation*, see Fig. 2.67e, f)—and may fire many times during this single long stimulus. Likewise, *multiple firing* may occur when the current electrode is located inside the fiber (in terms of *intracellular stimulation*, see Fig. 2.69a). However, from a practical point of view, long monopolar stimulation phases should be avoided to limit *charge accumulation* at the electrode/tissue boundary and to avoid *irreversible reactions*.

For instance, a single *depolarizing half-period* of 100 Hz *sinusoidal electrical stimulus* can produce up to *three action impulses* within this period when fibers *close to the stimulation electrode* are considered (Rattay 1986b). In fibers further away from the electrode, *two action impulses* are generated with a *larger delay* with respect to the depolarizing half-period. In contrast, most *distant fibers* still within reach of the electrical stimulation—i.e., at the outer border of the *active area*, see stimulation thresholds at the outer border of the suprathreshold region B in Fig. 2.76b—will *fire once and lately* in response to the single depolarizing stimulus. In analogy, *higher stimulating currents* will reach even more distant fibers and their thresholds (Fig. 2.76b). The *firing rate* of a particular fiber within the *active area* increases with decreasing *distance* of this fiber from the electrode and with increasing *stimulation current* of a *relatively long stimulus* (Rattay 1986b, 1987).

Strong Stimuli

Increasing current strength increases the frequency of firing (compare Kaniusas (2012, Fig. 2.22)). However, for *extracellular stimulation*, this *periodic firing* occurs only up to a certain current strength after which an *aperiodic firing* sets

(Rattay 1990). The aperiodic reaction results from a strong hyperpolarization of lateral segments of the fiber—according to negative parts of the *activating function* (Fig. 2.67e)—when the central segment is strongly depolarized by cathodic stimulation. This hyperpolarization inhibits propagation of periodic action impulses; compare with cathodic block from Section "Cathodic Block and Stimulation Upper Threshold". Please note that *bringing the stimulation electrode closer to the fiber* (Fig. 2.67a) at a constant simulation strength increases also the frequency of firing; in qualitative analogy with increasing current but constant distance to the fiber.

Waveform of Stimulus
The particular *waveform* of the stimulus plays a critical role in the firing behaviour. Basic waveforms of

- *rectangular* current,
- *sawtooth* current, and
- *sinusoidal* current

with the respective excitation thresholds have already been discussed in Kaniusas (2012, Fig. 2.16). According to Rattay (1990), periodic *rectangular stimulus* at 125 Hz during its depolarizing half-period yields *triple firing* in fibers close to the electrode (with the period's duration $1/(2 \cdot 125\ \text{Hz}) = 4$ ms) but only *double firing* occurs for periodic *trapezoid stimulus*. At higher frequency 250 Hz with much shorter depolarizing half-periods (2 ms), *double firing* occurs for these both waveforms, whereas at even more higher 500 Hz only a *single firing* occurs (1 ms).

Temperature
Please note that *raising the temperature* shortens reactions within the membrane. Increased temperature shortens *refractory periods*, shortens *duration of action impulses*, and reduces their *peak amplitudes* (Rattay 1990). In addition, stimulation and excitation become easier at higher temperatures, which is noticeable when the temperature changes by 5–10 °C (as estimated from Rattay (1990)). The excitation threshold tends to increase with decreasing temperature (Reilly 1998). However, at exceedingly high temperatures—more than 10–15 °C above nominal temperature—action impulses are no more able to propagate along axons because of their essentially reduced strength. It is known as *heat block* (Rattay 1990).

Collision Block
When *two action impulses* propagate towards and meet each other, no one can travel through and both impulses disappear. That is, *no bifurcation* occurs even though a strong local depolarization arises at the site of collision. This is because a finite refractory time and hyperpolarized tails of both oncoming action impulses (Kaniusas 2012, Fig. 2.14a) allow for only a unidirectional propagation of action impulses (Kaniusas 2012, Fig. 2.18). In other words, the strong depolarization at the

site of collision could not overcome hyperpolarized regions enclosing this site. This phenomenon is known as *collision block*[95] and may easily arise when a fiber is stimulated at two different locations (Figs. 2.75f and 2.77c).

Unmyelinated Versus Myelinated Fibers

The onset of an artificial excitation precedes by a certain *time delay* the onset of a triggered action impulse (Fig. 2.68b). For *unmyelinated fiber*, this delay can be more than 200 μs and strongly depends on the stimulus amplitude; compare Fig. 2.69c with Fig. 2.69e. Obviously, the *delay is maximal* for the least strong stimulation/depolarization already leading to excitation, i.e., the delay is maximal for the *threshold stimulation*. This delay decreases with increasing amplitude of the depolarizing stimulus, as illustrated by numerical data in Fig. 2.79c with a maximum simulated delay of more than 1 ms. The time delay is much less for *myelinated fibers* than unmyelinated fibers (Rattay 1990) and can be in the range of 100 μs or more (Van den Honert 1979). A strong suprathreshold stimulus may reduce this delay essentially to zero. In other words, *unmyelinated fibers* show *slow subthreshold responses* in comparison with *myelinated fibers*.

For *unmyelinated fibers*, the membrane voltage u in the subthreshold region—the foot or starting phase of an action impulse—shows rather a *linear increase or decrease* when the resting membrane is depolarized or hyperpolarized, respectively, *for the duration of a short rectangular current pulse* in the range of 100 μs. Figures 2.69 and 2.77d, e illustrate these clearly linear changes during the short stimulus for unmyelinated fibers. In contrast, the subthreshold region for *myelinated fibers* shows an *exponential increase or decrease* during a depolarizing or hyperpolarizing *short current pulse* of 100 μs, respectively (Kaniusas 2012, Fig. 2.13c). This exponential behaviour can be expected from an almost complete recharging of RC circuit of the membrane (Kaniusas 2012, Fig. 2.13a). Obviously, when the generated impulse propagates along the axon away from the site of stimulation, this particular stimulus-dependent shape of the *leading edge* of action impulse—i.e., linear for unmyelinated or exponential for myelinated fibers— vanishes quickly; in fact, this shape converges towards an exponential increase (Rattay 1990).

In *unmyelinated fibers*, both

- the *large time delay* and
- the *linear increase during depolarization*

are mainly the consequence of the *large capacity* C and thus the *large time constant* τ (2.49) of the relatively *large membrane region* which is exposed to and permeated by depolarizing currents. In contrast, both C and τ are smaller in *myelinated fibers* where only their *narrow nodes* are exposed to currents (Kaniusas 2012, Fig. 2.18a). τ in the range of 200–500 μs for unmyelinated fibers versus 20–70 μs for

[95]The *collision block* is of special interest for medical applications, by which, for instance, spastic signals can be stopped via electrical stimulation. Here *artificially produced* action impulses (antidromic impulses) travel against and stop *naturally evoked* impulses (orthodromic impulses) along *motor nerves* leading naturally to spastic signals.

myelinated fibers are contrasted in Kaniusas (2012, Table 2.2). Therefore—as depicted in Kaniusas (2012, Fig. 2.8b)—*unmyelinated fibers* exhibit only the *initial linear part* of the overall exponential increase of u during their depolarization for the duration of a *short current impulse of 100 μs* below the applicable τ (>100 μs). Likewise, the opposite inequality $\tau < 100$ μs applies for *myelinated fibers* implying that the whole *exponential increase* dominates during their depolarization (Kaniusas 2012, Fig. 2.8b) throughout this short current impulse of 100 μs. In addition, *voltage-gated sodium channels of different speeds* contribute to the aforementioned differences in the *time delay* between unmyelinated and myelinated fibers.

Single Biphasic Stimulus

Single *biphasic stimulus* consists of two phases or two pulses of opposite polarities (Fig. 2.69d, e), in clear contrast to *monophasic stimulus* with a single phase or single pulse (Fig. 2.69b, c). For *extracellular stimulation* (Fig. 2.75), it can be recognized that the *primary function* of

- the *initial cathodic phase* of *biphasic current pulse* (Fig. 2.75a) is used to *depolarize and excite the fiber* (namely, the fiber region closest to the electrode, see Fig. 2.67), whereas the function of
- the *following anodic phase* is to *balance the delivered charge* and thus to *reverse electrochemical processes* within the electrode/tissue boundary (Section "Charge Transfer During Stimulation").

Obviously, the *anodic phase* has also a *hyperpolarizing effect* on the fiber and may reduce the *depolarizing effect* of the preceding *cathodic phase*. Thus, the aimed excitation of the fiber may even fail.

Please recall that *depolarization* of the membrane is an *inert process* which dynamics is governed by the *membrane time constant* τ (Kaniusas 2012, Table 2.2); i.e., ionic inflow and outflow through the membrane and recharging of the membrane have finite speeds (Kaniusas 2012, Fig. 2.14b). The process of depolarization is a kind of regenerative process within the membrane in response to the already removed depolarizing stimulus. Therefore, depolarization can be diminished and excitation abolished by a hyperpolarizing phase which follows closely the depolarizing phase, namely, closer than τ. This abolition occurs during the early stage of the excitation process of the membrane (Van den Honert 1979). In particular, this *destructive interference* results when the *cathodic phase is relatively short* and the anodic phase follows immediately or very shortly after the cathodic phase. Likewise, a short depolarizing stimulus should be slightly above threshold depolarization *during the stimulus* itself in order to produce excitation because *passive repolarization* towards the resting state is permanently active (working against depolarization) and the build-up of excitation is an inert process (Van den Honert 1979).

Obviously, these discussed phenomena apply also for *intracellular stimulation* (Fig. 2.69a). Here

- *the anodic phase* of biphasic current pulse *depolarizes*, whereas
- *the cathodic phase balances the charge* and *hyperpolarizes* the membrane.

Figure 2.69 illustrates *excitation of a fiber* stimulated with an *intracellular electrode* based on a *single biphasic current stimulus*. According to Fig. 2.69d, the *preceding cathodic phase* hyperpolarizes, whereas the *following anodic phase* depolarizes the membrane. If both phases are equally long and strong, the *membrane voltage* u remains close to its resting level (≈ -70 mV). However, the doubled amplitude of the anodic phase leads to an excitation, as shown in Fig. 2.69e. This increased amplitude (Fig. 2.69e) leads to an earlier generation of the associated *action impulse* by the time window Δt than in response to the anodic pulse with non-increased amplitude (Fig. 2.69c); compare Fig. 2.79c. This is because a stronger depolarizing current i in Fig. 2.69e yields a larger *ratio* $\mathrm{d}u/\mathrm{d}t$ (>0) depolarizing the membrane. Even the simplified relationship between i and u from (2.40) suggests this dependency without considering the non-linear membrane behaviour.

Figure 2.69f illustrates an example of the *destructive interference* for *intracellular stimulation*. The depolarizing anodic phase with the short duration of only 100 µs does not excite the membrane because of the subsequent hyperpolarizing cathodic phase, even though a single anodic pulse of equal amplitude and equal duration is sufficient for excitation, as shown in Fig. 2.69c.

In fact, an *initial hyperpolarization* of fiber can be intentionally used to avoid its subsequent excitation (Fig. 2.69f). Since fiber responses to hyperpolarization strongly depend on their properties (including fiber thickness), the initial hyperpolarization provides a basis for a *selective excitation of different fibers* (e.g., enabling thick A fibers but blocking thin pain-related C fibers; see Footnote 101).

Interphase Interval

An *interphase interval*, a delay introduced between the consecutive cathodic and anodic phases of *biphasic current stimulus*, often helps to avoid this destructive interference and allows still greater development of the excitation process. In practical applications, the *interphase interval* in the range up to 300 µs resides in-between the relatively short phases, as illustrated in Fig. 2.75a for *extracellular stimulation*. This interval gives sufficient time for the relatively *inert fiber's excitation* to be developed in response to the preceding cathodic depolarization and well before the following anodic repolarization/hyperpolarization takes place.

Even a very low level *hyperpolarizing anodic phase* (Fig. 2.75a)—immediately following the *depolarizing cathodic phase*—may be sufficient to *abolish excitation* in cases where the cathodic phase alone was near the *excitation threshold*. The introduction of a small *interphase delay* will assure excitation of these fibers by raising the *abolition threshold* of the anodic phase above the actual amplitude of the anodic phase. In fact, the abolition threshold is the hyperpolarizing phase amplitude required to suppress the action potential. On the other hand, with increasing amplitude of the depolarizing cathodic phase in the suprathreshold range, excitation

develops more rapidly making the membrane less susceptible to abolition by the following anodic phase. For *example*, with a depolarizing cathodic phase of 125% of the monophasic stimulus threshold, a change in the interphase delay from 0 to 20 μs raises the *abolition threshold* of the following hyperpolarizing phase from 68 to 200% of the stimulus threshold, as experimentally observed in myelinated fibers (Van den Honert 1979).

In particular, the *interphase interval* tends to *reduce the current threshold amplitude* for biphasic stimulus, i.e., the *depolarizing phase needs less charge* (and energy) to excite the fiber because of more distant hyperpolarizing phase. This reduction especially applies when relatively short biphasic phases (<200 μs) are used for stimulation (Rattay 1990). An instructive example is given in Fig. 2.69g where an interphase interval of 100 μs allows generation of an action impulse, in clear contrast to Fig. 2.69f with an identical depolarizing phase but without an interphase interval and without any subsequent action impulse.

The *latency* or the time delay between the end of the depolarizing stimulus and the rising phase of action potential—as discussed in Section "Single Monophasic Stimulus"—is even referred to as *vulnerable period* (Van den Honert 1979). The rationale for this label is as follows. A hyperpolarizing phase immediately following the depolarizing phase falls necessarily into this vulnerable period so that this *hyperpolarizing phase* accelerates *repolarization* and thus may *prevent excitation*. During this period the fiber is vulnerable to abolition of excitation.

A *substantially elongated vulnerable period* develops when the depolarizing stimulus is only very slightly *suprathreshold* (see latencies in Fig. 2.79c). Please recall from Section "Single Monophasic Stimulus" that the expected latencies or vulnerable periods can be greater than about 100 μs for *myelinated fibers* and greater than about 1 ms for *unmyelinated fibers*. For instance, such slight *suprathreshold stimuli* apply to *distant fibers* located within the outer spatial boundary of the suprathreshold region (see the outer boundary of the region B in Fig. 2.76b). Therefore, it is obvious that the *interphase delay* greater than the *vulnerable period* would have no sense in terms of the *abolition threshold*—a hyperpolarizing pulse can not prevent an action potential which has already peaked.

- At *small amplitudes* of the hyperpolarizing phase an increase in the *latency* of the response is produced in comparison with absent hyperpolarizing phase.
- At *greater amplitudes* the hyperpolarizing phase causes a rapid repolarization of the membrane toward its resting potential, *abolishing action potential*.

Decreasing interphase interval increases the *latency* until the associated action potential is completely *abolished*. In other words, the abolition threshold is proportional to both

- the depolarizing phase amplitude and
- the interphase delay.

In addition, varying interphase intervals can be used to stimulate selectively fibers of different diameters (Reilly 1998); compare Footnotes 101 and 99.

Waveform of Charge-Balancing Phase

Please recall that the charge-balancing phase, e.g., the *anodic phase* of *extracellular stimulation* in Fig. 2.75a, is to avoid the *charge accumulation* across the electrode/tissue boundary (Section "Charge Transfer During Stimulation"). Therefore, the particular *waveform* of the charge-balancing phase is not of primary importance. Above all, the time integral (2.25) is of importance since it determines the total charge delivered by this waveform. In contrast to depolarizing phase with its high rectangular dynamics required for excitation (Kaniusas 2012, Fig. 2.16), the charge-balancing phase is usually realized as an arbitrary *exponential decay* (capacitive discharge), as long as the charge-balance results between cathodic and anodic phases. Therefore, the *anodic phase* in *extracellular stimulation* is usually realized as an *exponential decay*, which is relatively easy to implement from an *engineering perspective*.

Strictly speaking, the particular *waveform of the charge-balancing phase* is still important. This is because momentary current levels within this waveform determine non-linearly both the type and strength of *electrode reactions* (Fig. 3.14) which are potentially harmful. On the other hand, when a capacitively coupled *exponential anodic phase* is employed for charge-balancing (with zero interphase delay), the peak anodic current depends on the *time constant* of the resulting RC circuit for discharge. *Short time constants* produce large and early peak currents, *stronger destructive interference*, and thus *greater loss of excitation*. Conversely, *long time constants* cause *abolition of excitation in fewer fibers* (Van den Honert 1979), especially in *distant fibers* experiencing only slightly suprathreshold stimulation. Please note that *interphase interval* can also be added before the onset of the exponential decay to reduce the current threshold.

Biphasic Versus Monophasic Threshold

The *biphasic excitation threshold* is typically higher than the *monophasic excitation threshold* because of the discussed *destructive interference*. The *current reversal* within biphasic pulse tends to reverse an action potential that was already started by the initial phase of the pulse. That is, the threshold amplitude of the *depolarizing phase of biphasic pulse* is higher than the threshold amplitude of the *depolarizing monophasic pulse*. An increase in the amplitude of biphasic stimulus is needed to overcome the desensitizing effect of the hyperpolarizing phase of biphasic pulse. In particular, *thresholds* for biphasic stimulus are elevated more when *pulse/phase is short* so that the repolarizing current reversal immediately follows the depolarizing initial phase, before an action potential has had a chance to unfold. Current thresholds from Fig. 2.73 (cases A and B) as well as thresholds from Fig. 2.80 (cases with 10 μm diameter and 2 mm distance comparing monophasic cathodic and biphasic pulses) confirm this behaviour. Here *monophasic cathodic rectangular stimulus* shows lower thresholds than *biphasic rectangular stimulus* (with the preceding cathodic phase), whereas this difference disappears for longer pulses in the range of 1 ms.

According to experimental data in Van den Honert (1979), the biphasic threshold amounts to about 130% of the monophasic threshold for zero *interphase*

delay, decreases with increasing delay to 120% for 20 μs delay, and then converges down to about 100% for 100 μs and longer delays. In particular, 100% applies for *infinite delay* where biphasic pulse clearly mutates into monophasic pulse with the resulting *equal excitation thresholds*. This means also that the *strength-duration curve* (Fig. 2.71b) of biphasic stimulus is located at higher strength levels than that of monophasic stimulus, whereas both curves necessarily converge for higher pulse/phase durations (>1 ms, i.e., above the refractory period), as illustrated in Fig. 2.73 (cases A and B), Fig. 2.80 (see above), and also in Reilly (1998, 2011) based on numerical data. The latter numbers apply for dissected *myelinated fibers*, charge-balanced biphasic pulses, and equal phase durations of 50 μs. From a practical point of view, it is important to stress that the introduction of the *interphase delay* can substantially reduce the amplitude required of a biphasic stimulus to elicit a neuromuscular response.

For *extracellular stimulation*, using *cathodic and anodic pulses*—with different excited regions along the axon and even different thresholds for a single monophasic pulse, see Fig. 2.67—the relationship between monophasic and biphasic thresholds becomes more intricate (Reilly 2011). In fact, *cathodic monophasic pulse* shows a lower threshold than an *initially cathodic biphasic pulse* (charge-balanced), in line with the discussion from above. However, for an axon experiencing *anodic monophasic pulse* or *initially anodic biphasic pulse* (charge-balanced), just the opposite is true, especially for phase durations >100 μs. The threshold lowers from anodic monophasic pulse to initially anodic biphasic pulse, i.e., the recruitment increases relative to monophasic pulse of the same amplitude and phase duration. In contrast to cathodic stimulation, here the phase reversal lowers the threshold; however, in no case, the resulting anodic threshold is lower than the threshold of *cathodic monophasic pulse*. The decrease in the anodic threshold is noteworthy at longer phase durations, especially above 100 μs; e.g., the threshold of the initially anodic biphasic pulse at 100 μs decreases by a factor of about 4 relative to anodic monophasic pulse.

Therefore, *cathodic monophasic thresholds* are the lowest when an individual nerve fiber is considered. However, if we are interested in maximising the *total recruitment volume* inclosing multiple fibers at both *anode and cathode*, *biphasic waveform* seems to be in favour of *monophasic waveform*. Numerous fibers below anode and cathode—disjoint fiber populations—would experience successive cathodic stimulation (with a low threshold) and anodic stimulation (with a high threshold). Likewise, with biphasic stimulation, fibers under anode are more efficiently excited, whereas an increased amplitude of about 5 times (Fig. 2.67) would be required to reach the same degree of recruitment under anode with a monophasic waveform (Reilly 2011). In other words, more fibers under both electrodes can be considered as being "favourably" oriented when the biphasic waveform is applied. In particular, the largest *recruitment volume* results when the biphasic waveform includes an *interphase interval* lowering the stimulation threshold and thus increasing the recruitment volume at a given stimulus strength.

Another advantage of *biphasic waveform* is that it may enhance the total recruitment of neurons excited by the *end mode* or *bend mode* (Fig. 2.65).

Depending on the orientation of the bend region and/or the terminus of the neuron—as illustrated in Fig. 2.65—*monophasic stimulation* (*cathodic or anodic* stimulation) leads only either to depolarization or hyperpolarization of an exposed bend region or exposed terminus close to the electrode, respectively. If the stimulus is strong enough, excitation occurs. In contrast, *biphasic stimulation* (*cathodic andanodic* stimulation) may lead to depolarization (and excitation) of exposed bend regions and termini within a single cycle of biphasic waveform under each electrode. Therefore, biphasic stimulation may favourably enhance the number of excited disjoint fibers at each electrode due to the phase reversal—an *enhanced recruitment* is achieved.

Electrochemical Consequences

Biphasic stimulus with its *charge-balanced waveform* implies that the charge injected through an electrode during depolarizing phase can be safely and substantially extended beyond the level which would cause *tissue damage* with *monophasic stimulus* (Van den Honert 1979). Hence, biphasic stimulation appears particularly well suited for permanent *chronic stimulation*, extending electrode lifetime and minimizing unwanted biological reactions.

In analogy with Section "Charge Transfer During Stimulation", *biphasic current stimulation* reduces electrochemical reaction products by partial *reversal of electrochemical reactions* taking place at the electrode/tissue boundary. The introduction of the *interphase interval* may partly defeat the purpose of biphasic waveform by allowing slightly greater *diffusion* of reaction products away from the electrode surface during the interval and thus by reducing the effective reversal rate. However, this disadvantageous effect is opposed by the favourable *reduction of depolarizing current amplitude* necessary for excitation when the current reversal phase is delayed (see above). This reduction of the amplitude yields fewer reaction products and *less electrochemical stress*. Therefore, *biphasic charge-balanced stimulus* tends to reduce electrically induced *tissue damage* while decreasing *threshold current* levels needed for excitation.

Periodic Stimulus

After single monophasic stimulus and single biphasic stimulus have been described with respect to their excitation properties, a series of biphasic stimuli—a *periodic stimulus*—will now be considered for excitation. To start with, *switching on* any *periodic stimulus*—as in the case of any monophasic or biphasic stimulus—produces a single action impulse if and when the *excitation threshold* is reached.

Rectangular Pulses

For *rectangular shape* with its *long duration* in the order of the *refractory period* (0.5–1 ms), *current thresholds* are almost identical for

- a *single monophasic rectangular pulse*,
- a *single biphasic rectangular pulse*, and
- *periodic biphasic rectangular pulses*,

according to numerical data (Rattay 1986b, 1990) from *intracellular stimulation*. Here periodic pulses are given by a series of biphasic rectangular pulses without

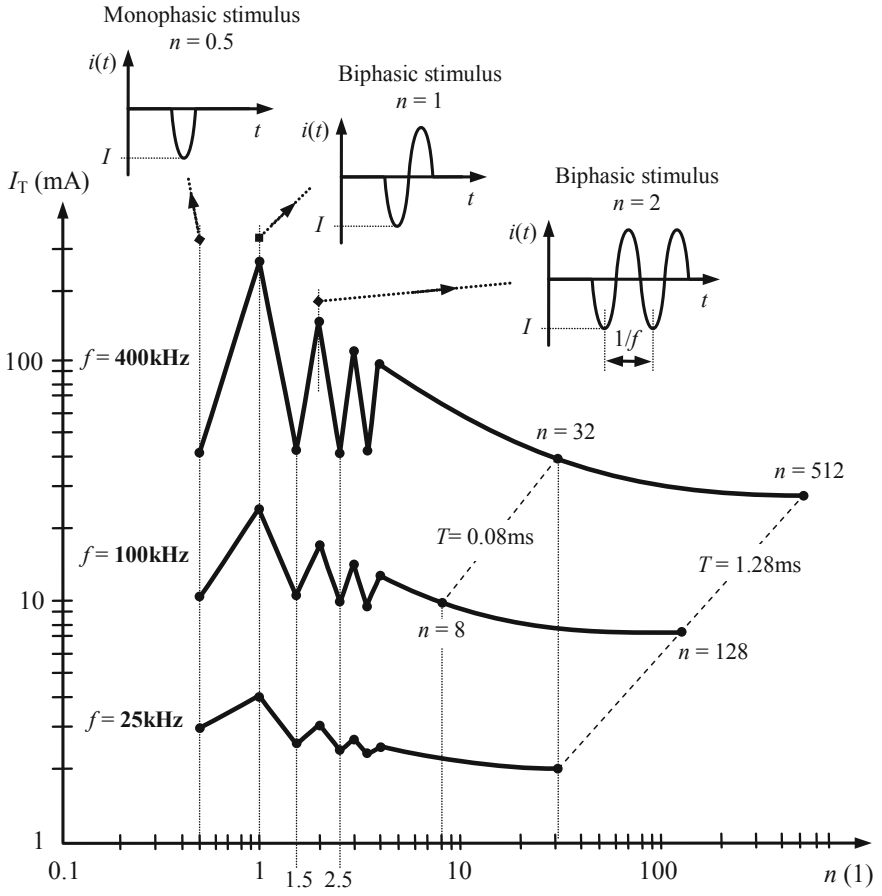

Fig. 2.70 Excitation current thresholds I_T for monophasic sinusoidal stimulus ($n = 0.5$), biphasic sinusoidal stimulus (with even n), and periodic sinusoidal stimulus as a function of the number n of full cycles of sinusoidal waveform. Three full-cycle oscillation frequencies are considered such as 25 kHz (with the single phase duration of 20 μs), 100 kHz (5 μs), and 400 kHz (1.25 μs). Numerical data is taken from Reilly (2011), calculated using SENN model with a point current electrode located in 2 mm distance from 20 μm diameter myelinatedfiber. Dashed lines indicate the total stimulus duration T [as in (2.151)]

any interphase intervals or gaps in-between; compare a biphasic rectangular pulse with an interphase interval from Fig. 2.75a. Comparable thresholds result out of the fact that the *initial rectangular pulse or phase* is identical in shape and amplitude in all three stimuli and is *long enough* for the temporal evolution of the relatively *inert excitation process*. Thus, the following waveform of the stimulus is of minor relevance since the initial segment has already determined excitation and its threshold.

For *rectangular shape* with its *short duration* in the range of 100 μs—i.e., shorter than the refractory period, see Section "Single Monophasic Stimulus"—

current thresholds depend strongly on the morphology of the stimulation pulse. For *periodic biphasic rectangular pulses* with their short phase durations of about 100 μs,

- the *first cathodic phase depolarizes* the axons region closest to the electrode (Fig. 2.67e),
- the *second anodic phase hyperpolarizes* and thus inhibits the formation of an action impulse in this region, whereas
- the following *third cathodic phase favours* again the formation of the action impulse;

in close analogy with the behaviour of biphasic pulses (Section "Single Biphasic Stimulus"). Please note that *extracellular stimulation* is assumed here (Fig. 2.75b).

Therefore, short *biphasic pulses*—both single and periodic (at a relatively *high frequency*)—*inhibit formation of action impulses* in comparison with short *monophasic pulses*. Because of this inhibition, the *firing rate* is lower than the *stimulation rate* for stimulation periods shorter than the *refractory period*, even when strong stimuli are applied (see below).

This inhibition implies that these *biphasic pulses* require larger *thresholds of current densities* than *monophasic pulses*, especially for ≤ 100 μs as a single phase duration. For *single and periodic biphasic rectangular pulses* of short duration of 100 μs, current densities are larger by the factor of about 2 and 1.2 for *unmyelinated and myelinated fibers*, respectively, and by the respective factor of about 5 and 1.4 for 20 μs duration (Rattay 1986b). Thus, threshold differences tend to increase for *shorter pulses* (Fig. 2.73, compare cases A and B) and are larger for unmyelinated fibers. Absolute threshold currents for myelinated fibers are still lower by a factor of 2–3 than for unmyelinated ones of the same diameter, which is qualitatively in line with Fig. 2.81b.

Simulated data in Fig. 2.70 confirms that a single sinusoidal pulse (for $n = 0.5$, i.e., for a half of a full cycle) has a significantly lower excitation threshold than a biphasic sinusoidal pulse ($n = 1$, one full cycle). These *threshold differences* clearly increase for *shorter phases* or, in analogy, for *higher oscillation frequencies*.

A *sequence of biphasic rectangular pulses*, i.e., periodic biphasic stimulus, tends to show *lower thresholds* than a *single biphasic pulse*. In particular, this applies for *short phases* ≤ 100 μs with this difference increasing with decreasing phase duration, and for *short interphase intervals* <500 μs with this difference increasing with decreasing interval. For instance, threshold current densities are lower by about 9% and 20% for 100 μs and 10 μs, respectively, in *unmyelinated fibers*; and by about 3–17% and 20–50% for 100 μs and 10 μs, respectively, in *myelinated fibers* (Rattay 1986b, 1990).

Again, Fig. 2.70 confirms lower thresholds of *repeated biphasic pulses* in comparison with a single biphasic pulse. Please note that this difference increases with increasing oscillation frequency—i.e., with decreasing duration of a single phase—and with increasing number of cycles passed. When evaluated at half-cycle

multiples, there is an *oscillating threshold* with *minima* at odd numbers of passed half-cycles (transferring the maximum net charge to the site of excitation) and with *maxima* at even numbers (zero net charge transferred) (Reilly 1998). Figure 2.74 offers similar insights in that *repeated sinusoidal pulses* show lower thresholds than a single pulse for higher oscillation frequencies (or for shorter phases), whereas the onset of threshold differences depends on the onset of membrane integration effects (see below).

Lower thresholds of *pulses sequences* can be explained by *membrane integration effects*. In particular, repeated pulses with the repetition intervals up to a few multiples of the membrane time constant τ [for intracellular stimulation and simplified RC model, see (2.148)] or up to a few multiples of the *empirical time constant* τ_e [for extracellular stimulation, considering real fiber and real set-up, see (2.151)] will be integrated in a *non-linear fashion* by the membrane (Reilly 2011). That is, τ and/or τ_e determine the effective integration time. Interestingly, the non-linear integration applies not only to depolarizing monophasic pulses but also to biphasic pulses due to non-linear voltage-dependant ionic conductances within the membrane in response to its *depolarization close to excitation*.

In particular, for *oscillatory stimulus*, a *bias voltage* on the membrane asymptotically increases with each successive cycle of stimulation due to *differing conductivity of the membrane* to *inward and outward currents*, even in the subthreshold range where the membrane is only slightly non-linear but exposed to *numerous cycles*. In the course of integration, a *depolarizing bias voltage* in *the membrane voltage* is built on each cycle of stimulation. Thus, such *integration lowers the excitation threshold* of repeated pulses in relation to both a single monophasic pulse and a single biphasic pulse, as clearly illustrated in Fig. 2.70. The absolute magnitude of integration effects seems to be stronger for higher *stimulus frequencies*; please consider logarithmic scaling in Fig. 2.70. The lower is the frequency, the lower is the threshold in fibers with a relatively long τ or τ_e (as in Kaniusas (2012, Fig. 2.16c)). The degree of the threshold reduction increases with the number of cycles passed and then levels off in the range of τ or τ_e. Figure 2.70 illustrates this convergence of thresholds towards a *constant plateau* with increasing number of cycles after about 1.28 ms. It is instructive that this plateau is very close to the *threshold* that would apply to a *cathodic monophasic rectangular pulse* having a duration equal to the half cycle duration of the relevant sinusoidal stimulus (Reilly 1998). These membrane integration effects can be interpreted as *constructive interference lowering the excitation threshold* that is in clear contrast to *destructive interference* for short biphasic pulses *raising the threshold* (Section "Single Biphasic Stimulus").

Sinusoidal Pulses

Sinusoidal pulses are less efficient in excitation than *rectangular pulses* because the *rate of rise* is lower in sinusoidal pulses than rectangular pulses. Sinusoidal pulses are thus less efficient in timely overriding the passive repolarization towards the resting state and in timely overriding the membrane *leakage currents* (preventing depolarization). In fact, for short phase durations with the prominent mechanism of

the *destructive interference* (or of the potential current reversal before excitation is finally triggered), the *duration of the depolarizing phase* determines the *excitation threshold* for sinusoidal pulses. For long phase durations, the threshold depends rather on the *rate of rise* and the *peak value* of the sinusoidal stimulus (Reilly 1998).

In fact, a *monophasic rectangular pulse* has the lowest threshold, followed by a *biphasic rectangular pulse* with a higher threshold and then by a *biphasic sinusoidal pulse* with the highest threshold, as illustrated in Fig. 2.73 (cases A, B, and C). These differences, as already discussed, almost disappear for longer pulses. Note that with long durations in Fig. 2.73, thresholds for rectangular waves remain at rheobase but rise for *sinusoidal wave* (case C). This exceptional rise demonstrates effects of *accommodation* that are strongest for sinusoidal waveform (Kaniusas 2012, Fig. 2.16c).

The thresholds of *periodic biphasic sinusoidal pulses* are higher by about 10–60% than of *periodic biphasic rectangular pulses* of the same oscillating frequency in *unmyelinated fibers* (Rattay 1986b). Depending on the phase duration, an increase by about 35% results for phase duration of 100 μs (i.e., for $1/(2 \cdot 100\ \mu s)$ = 5 kHz oscillation) and by about 10% for 20 μs (25 kHz). Similar tendencies can be expected in *myelinated fibers*. Figure 2.70 illustrates excitation current thresholds for sinusoidal stimulus and myelinated fibers, as discussed above.

Repetitive Firing

Periodic current stimulus with suprathreshold amplitude leads to *repetitive firing*.

- At *very low frequencies*, *multiple firing* occurs within the half-period of the stimulating current, especially for strong suprathreshold stimuli. This is in close analogy with a suprathreshold monophasic current stimulus of long duration (Section "Single Monophasic Stimulus").
- At *low frequencies*, generated action impulses are well *synchronized* with the stimulating current. The excitation synchronizes with the depolarizing phase of periodic stimulus. Namely, the onset of action impulse synchronizes with *maximum* or *anodic phase* of the injected current in *intracellular stimulation* (Fig. 2.69) or, on the other hand, with *minimum* or *cathodic phase* in *extracellular stimulation* (Fig. 2.67). The harmonic stimulus is approximately phase-locked with the generated series of action impulses.
- At *high frequencies*, excitation needs *higher currents* while *synchronization* with each depolarizing phase *is lost*.

To give a quantitative example, let us consider a sinusoidal electrical stimulus. The stimulus at *100 Hz*—at *very low frequency* (see above)—can produce *up to three action impulses* within a single *depolarizing half-period* or single *depolarizing phase* with the duration of 5 ms $(=(1/2) \cdot (1/100\ \text{Hz}))$ (Rattay 1986b).

For oscillating frequencies of the stimulus below about *500 Hz*—at *low frequencies* (see above)—action impulses are generated in *synchrony* with each and every depolarizing phase of periodic biphasic pulses (Rattay 1986b). Please note that at the frequency of 500 Hz, the duration of a single depolarizing phase is already quite short and equals 1 ms $(=(1/2) \cdot (1/500\ \text{Hz}))$. That is, the depolarizing

half cycle is already in the range of the *refractory period*.[96] Even in the region around *800 Hz*, a synchronous firing with each depolarizing phase is still possible but only for a *strong suprathreshold stimulating current*.

At *high frequencies* (see above), certain *action impulses are already missed* altogether even though the synchronization between the periodic stimulus and the remaining impulses prevails. For instance, every third depolarizing phase leads to an action impulse at *2 kHz* (Rattay 1986b). The excitation rate of individual neurons can follow a *sub multiple of the stimulation rate* which is above the *inverse of the refractory period* (Fallon 2016), see Footnote 96.

High frequencies need stronger depolarizing currents but action impulses are lost even for these high currents. At about *10 kHz*, a single action impulse results only from *switching on* the stimulus (or from outer disturbances) if the excitation threshold is surpassed. In fact, there is an almost continuous change from *synchronized action impulses* (until about 2 kHz (Rattay 1990)) to irregular *non-synchronized action impulses* with increasing frequency of the periodic stimulus. Non-synchronized impulses are due to *self-excitation* or "ringing" of axons and/or small disturbances in the stimulation signal (Rattay 1990).

However, *fatigue effects* should be mentioned which become prominent at relatively high stimulation frequencies from 100 Hz to 10 kHz according to Reilly (1998). The fatigue decreases the firing rate to subharmonics of the stimulation frequency due to *metabolic stress* (Section "Neural Stimulation"). Over a few minutes, an axon often fires at the same rate as the stimulus, shifts to firing with every other stimulus, then to every third or even fourth. An increasing amplitude of the stimulus solely delays this downward shift of the firing rate.

The perceived intensity and quality of the artificial stimulation usually increases with increasing *stimulation rates* and with *elongated pulse trains* (Fallon 2016); compare Fig. 2.70 and dependency of α on the train length in (2.159). This is in line with and mimics the *natural operation* of nerve fibers (Kaniusas 2012, Fig. 2.22). Here a single isolated action impulse will hardly evoke a physiological response but

---

[96]Please recall that a *minimum time interval* exists between successive action potentials, determined by the relative and absolute refractory periods (Kaniusas 2012, Fig. 2.14a), i.e., action potentials never overlap. While

- the *relative refractory period* can be overridden by an increasingly stronger suprathreshold stimulus,
- the *absolute refractory period* can not.

In fact, the momentary excitation *threshold* is elevated during the relative refractory period.

Thus the absolute refractory period determines the upper limit for the instantaneous frequency of action impulses—or *maximum firing frequency*—of about 1 kHz (=1/1 ms with 1 ms as the typical duration of the absolute refractory period in neurons). For frequencies higher than about 500 Hz (=1/2 ms, i.e., the inverse of 2 ms), the depolarizing half-period starts to overlap with the *relative refractory period* (in the range of 2–4 ms in neurons), *rising the threshold* and thus impeding the generation of new action potentials in synchrony with every depolarizing phase.

It should be added that myelinated fibers tend to have a shorter *absolute refractory period* (0.4–1 ms according to Reilly (2011)) than unmyelinated fibers (about 2 ms). Consequently, the *maximum firing frequency* is higher for *myelinated fibers*.

a train of action impulses. Please recall that instantaneous frequency of action potentials (not a single impulse) and their total number code graded/analogous stimulus. In other words, natural activation rates of targeted fibers are artificially mimicked by repeated pulse trains. If the artificial stimulation is successful in producing *natural patterns*, then presumably the nerve would not experience more *metabolic stress* (Section "Neural Stimulation") than it would be the case in its natural firing. *Stimulation rates* well above the *natural firing rates* may induce metabolic stress, especially, in cases where an uncomfortable perception of the stimulation is present.

High Frequency Conduction Blockade

Similar to *collision block* (Footnote 95), *high frequency sinusoidal stimulation* can *reversibly block action impulses* within fiber. It is known as *high frequency blockade* or *high frequency conduction block*. As discussed in Footnote 99, this blockade can be used to select a special window of fiber diameters to be recruited. In analogy, *selective block* of conduction through pain fibers (e.g., C fibers, see Footnote 101) is aimed during neuromuscular functional stimulation to avoid simultaneous perception of pain.

In particular, a local fiber region stimulated with a high frequency biphasic sinusoidal signal—e.g., with 2 kHz or even 20 kHz in terms of *intracellular stimulation* (Solomonow 1984) or up to 300 kHz for *extracellular stimulation* (Zhao 2015)—experiences *strong oscillations of its local membrane voltage*. These oscillations force the affected fiber region to stay in its refractory period so that all action impulses propagating along this region experience a *full blockade*. Constant high-frequency activation of both voltage-gated K^+ channels and voltage-gated Na^+ channels under the blocking electrode appear to contribute to *conduction block* (Zhao 2015; Reilly 2011). These channels lose their ability to regulate K^+ and Na^+ currents during intact action potential generation. In addition, differing conductivities of the membrane for inward and outward currents (compare membrane integration effects from above) may lead to *buildup of polarization* (e.g., at nodes for myelinated fiber) to the high level where voltage-gated Na^+ channels become inactive through self-inactivation (Kaniusas 2012, Footnote 39).

The *kinetics of ion channel gating* play a major role in the conduction block (Zhao 2015). In particular, K^+ channels are slow compared to sodium channels (Kaniusas 2012, Fig. 2.14b) so that *K^+ channels* do not follow high-frequencies very well; these channels become constantly open as the frequency increases to the kHz range. For frequencies above 20 kHz, the fast kinetics of *Na^+ channels* also saturates causing these channels to be constantly open. Interestingly, non-symmetric charge-unbalanced waveforms with a longer positive or negative phase block nerve conduction by inducing either a *constant hyperpolarization or depolarization*, respectively, of membrane during *extracellular stimulation* (Zhao 2015). Please recall that *charge-unbalanced* current waveforms lead to disadvantageous accumulation of electric charges which may cause *irreversible electrochemical reactions*.

When strong stimuli are applied, the amplitude of these oscillations can even be greater than the deflection amplitude of action potential. However, even

subthreshold levels of the high frequency sinusoidal stimulation can inhibit propagation of action impulses that were initiated elsewhere (Reilly 2011). These high frequency oscillations disappear within a few mm with increasing distance from the stimulation site, according to the *length constant* of the membrane (Kaniusas 2012, Table 2.2). Decreased amplitude of the high frequency stimulation allows some of action impulses to pass by affected regions, i.e., a *partial blockade* with the associated *asynchronous firing* occurs.

The *blocking threshold*, defined as the amplitude of the high frequency stimulus below which complete block did not occur, was found to *monotonically increase with frequency* in *myelinated fibers* (e.g., A fibers). In contrast, *unmyelinated fibers* (e.g., C fibers) show a *non-monotonic behaviour* of the blocking threshold over frequency (e.g., threshold increases up to 30 kHz and then decreases up to 50 kHz (Joseph 2011)). Accordingly, a *selective block* of either A fibers or C fibers can be obtained by choosing the appropriate combination of frequency and amplitude of the blocking stimulus (Joseph 2011).

In fact, the *blockade* proceeds from the *thickest to the thinnest fibers* with *increasing amplitude* of the high frequency stimulus (Footnote 99). The *blocking threshold* is inversely proportional to *axon diameter* with smaller axons having higher thresholds than larger axons at the same frequency.

An interesting detail is that the high frequency stimulus may once generate propagating action impulses when *switched on* and surpassing threshold. That is, this stimulus may even generate two impulses (after bifurcation) travelling in opposite directions; compare bifurcation in Fig. 2.77d. Please recall that these impulses may collide with other oncoming propagating impulses and thus extinguish each other in terms of *collision block*.

Spatial Activation

For *periodic stimuli*, the *spatial area* of *activated fibers* is qualitatively similar to the area depicted in Fig. 2.76b for short monophasic stimulus. In fact, *high frequency stimulation* tends to show a *smaller spatial range* within which excitation is possible as compared with *low frequency stimulation*. This is because the high frequency stimulus gives less time Δt for recharging of membranes. Here only fibers close to the electrode—experiencing large depolarization ratio $\mathrm{d}u/\mathrm{d}t$ [>0 with $\mathrm{d}u/\mathrm{d}t \propto f(x)$, see (2.152)]—become timely depolarized to the threshold level $\Delta u \approx \mathrm{d}u/\mathrm{d}t \cdot \Delta t = 20$ mV. Please note that the latter product assumes constant $\mathrm{d}u/\mathrm{d}t$ throughout Δt, implying linear increase of u during depolarization (applicable rather to unmyelinated fibers, see Section "Single Monophasic Stimulus").

Fiber Selectivity

Periodic stimulus of a *high frequency* shows a high threshold (Fig. 2.70) so that only easily excitable nerve fibers, i.e., *thick fibers*, become excited (Fig. 2.81). In contrast, *low frequencies* exhibit low thresholds and tend to excite both *thick and thin fibers*. However, please recall that thick fibers at low frequencies may even underlie *cathodic block* due to suprathreshold stimulation (Fig. 2.78c, e) and thus become ineffective.

Therefore, different fiber classes—as described in Footnote 101—are excited at different frequencies. As reviewed in Reilly (2011), sinusoidal stimulation at low 5 Hz tends to recruit only *C fibers* with the smallest diameter (0.5–1.5 μm), the medium frequency of 250 Hz excites both *thick Aβ and thin Aδ fibers* (7–10 μm and 2–5 μm, respectively), whereas the highest stimulation frequency of 2000 Hz favours only *thick Aβ fibers*.

Strength-Duration Curve

The *strength-duration curve* depicts the *threshold* of the *stimulus strength* as a function of the *stimulus duration*. In fact, the curve reflects the fact that the stimulation intensity (e.g., stimulation current, voltage, charge, or even energy) has to be high enough and last long enough for the inert membrane voltage to reach its excitation threshold. The strength-duration curve considers excitation of nerve or muscle fibers. Here we start with a simplified theoretical model and conclude with realistic considerations. In addition, the strength-frequency curve is introduced.

Simplified Strength-Duration Curve

The *strength-duration curve* can be theoretically derived based on a simple and linear equivalent *electrical circuit model* from Fig. 2.63a. This RC model considers a small patch of membrane—a single spatially-limited membrane of excitable cell—subjected to *intracellular stimulation*. This consideration of the isolated membrane provides some useful and basic insights, even for large-scale *macroscopic excitations* that are the result of individual excitations of multiple excitable cells.

This *RC model* considers only the passive response of the *membrane voltage u* to an external time-varying source current $i(t)$ permeating the membrane. The model accounts only for the membrane's *pre-excitation state* or its *subthreshold behaviour*. The following simple closed-form mathematical expressions reflect underlying electrical processes and the resulting *subthreshold relationships*. As an additional limitation, *inneraxional current leaking* away from the site of electrode within the cell is assumed to be finite and constricted to the axial extension Δx (Fig. 2.63a). We neglect a specific *spatial distribution* of i along the membrane's coordinate x, which is typically governed by the electrode design and heterogeneity of intracellular medium along the current pathway.

The considered model in Fig. 2.63a includes the resting membrane voltage U_R, the *electrical conductance* $G' \cdot \Delta x$ of the membrane (with G' as the conductance related to the axon's axial length x) determined mainly by the number of passive K^+ resting channels in the membrane, and the *capacitance* $C = C' \cdot \Delta x$ determined by the lipid double layer of the membrane. Typically, U_R is around −70 mV, $G'' = G'/(\pi D)$ is about 1 mS/cm^2, and $C'' = C'/(\pi D)$ is about 1 μF/cm^2, with D as the axon diameter in the typical range of 0.5–20 μm (Kaniusas 2012, Table 2.2).

The *resting state of the membrane* is denoted by $u = U_R$ for zero disturbance $i = 0$. An external *inward current* i (<0 in Fig. 2.63a) into the cell yields a graded *hyperpolarization* of the membrane with the associated $u < U_R$; i.e., the inward current hyperpolarizes. In contrast, an *outward current* i (>0 in Fig. 2.63a) yields a

graded *depolarization* with $u > U_R$; compare Fig. 2.62a. The extent of depolarization determines if the membrane becomes finally *excited* or not in the non-graded all-or-none fashion, and generates an all-or-none action potential. Typically, the change Δu of about 20 mV is needed to reach the *excitation threshold level* of $u = U_R + \Delta u = u_T \approx -50$ mV ($>U_R$, see Kaniusas (2012, Fig. 2.14a)). Please recall from Section "Single Biphasic Stimulus" that the build-up of *excitation is an inert process* so that the actual threshold level depends strongly on the waveform.

For the *derivation* of the *strength-duration curve*, it is important to recognise that not the external i is primarily responsible for the membrane's u *depolarization* towards u_T but only its *conductive current component* i_E, which passes the *leakage resistance* $R = 1/(G' \cdot \Delta x)$ of the RC model (Fig. 2.63a). In fact, real conductive currents—mainly across passive K^+ resting channels—are needed for depolarization so that the component i_E can be considered as the *depolarizing component* of i. The residual component of i ($=i_E + i_C$), the *displacement current component* i_C—in parallel to i_E, see the RC model—crosses the membrane capacitor with its C in order to discharge it during depolarization (or upcharge it during hyperpolarization). Consequently, the inequality $|C \cdot u_T| < |C \cdot U_R|$ applies for the capacitor charge during depolarization. In engineering terms, the component i_C can be considered as a *reactive component* of i, which does not directly contribute to depolarization but unfavourably increases the total level of i and thus energy costs of stimulation.

As a next step, it is important to recognise that not only the *temporal dynamic of the applied current* $i(t)$ ($=i_E + i_C$) governs excitation but also the *RC behaviour of the membrane* since only the partial current i_E determines the excitation-relevant $\Delta u = i_E \cdot R$ (Fig. 2.63a). Namely, the RC behaviour determines the amount of i_E within i and thus the size of Δu.

The *relationship* between Δu and *waveform parameters* of i (e.g., its pulse duration) should be instructive and practical in the design of energy-efficient depolarization just at the threshold. Such resulting parameters would prevent both under-threshold depolarization (with $u < u_T$) without excitation and over-threshold depolarization ($u > u_T$) with wasted stimulation energy. These optimised waveform parameters of i would make sure that the resulting waveform of i has just the necessary but *minimum amplitude and duration* for a successful excitation right at $u = u_T$.

In order to derive the latter relationship, let us assume a *step current pulse* of $i(t)$ for the external excitation with the *amplitude* I (Heaviside step function), entering the membrane's RC circuit (Fig. 2.63a). The associated component $i_E(t)$ can be readily solved as

$$i_E(t) = I \cdot (1 - e^{-t/\tau}) \tag{2.146}$$

based on the *transfer function* $G(j\omega)$ between $i_E(t)$ as output and $i(t)$ as input, to give

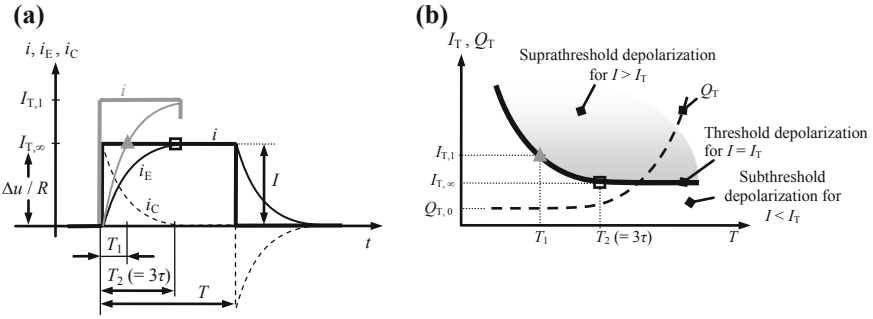

Fig. 2.71 Origin of the strength-duration curve for intracellular stimulation with a single monophasic rectangular current pulse based on a simple RC model (Fig. 2.63a). **a** The pulse i (=i_E + i_C, see Fig. 2.63a) with its duration T, the amplitude I, and the associated conductive i_E and displacement i_C components. **b** The strength-duration curve quantified as the threshold current amplitude I_T in relation to T (2.148)

$$G(j\omega) = \frac{1}{1 + j\omega \cdot RC} \tag{2.147}$$

with $\tau = R \cdot C$ as the *membrane time constant* and $\omega = 2\pi f$ the angular frequency. That is, the necessary *threshold amplitude* $I_T = I$ of the now *single rectangular pulse* $i(t)$ with its pulse *duration* T (Fig. 2.71a) in order to reach the excitation-relevant $\Delta u = i_E \cdot R$ follows from (2.146) as

$$I_T = \frac{\Delta u/R}{1 - e^{-T/\tau}} = \frac{I_{T,\infty}}{1 - e^{-T/\tau}} \quad \text{with} \quad I_{T,\infty} = \Delta u/R. \tag{2.148}$$

In fact, this equation already represents the *strength-duration curve*, as illustrated in Fig. 2.71b. Please note that as $T \to \infty$, $I_T \to I_{T,\infty} = \Delta u/R$. From a practical point of view, we can already approximate $I_T \approx I_{T,\infty}$ for durations $T \geq 3\tau$. This is because the equality $I_T = 1.05 \cdot I_{T,\infty}$ applies at $T = 3\tau$ with only about 5% difference between I_T and $I_{T,\infty}$; likewise, the threshold I_T increasingly converges to $I_{T,\infty}$ with increasing T [see (2.148) and Fig. 2.71b].

For comparison, the *threshold charge* Q_T of the monophasic rectangular $i(t)$ that is necessary to achieve the excitation threshold I_T, can be easily derived from (2.25) and (2.148), and is

$$Q_T = I_T \cdot T = \frac{I_{T,\infty} \cdot T}{1 - e^{-T/\tau}} = Q_{T,0} \cdot \frac{T/\tau}{1 - e^{-T/\tau}} \quad \text{with} \quad Q_{T,0} = I_{T,\infty} \cdot \tau, \tag{2.149}$$

as qualitatively plotted in Fig. 2.71b. Please note that the relationship $Q_{T,0} = I_{T,\infty} \cdot \tau$ provides a simple and *practical means* of *determining* τ, without having to trace the entire strength-duration curve. That is, it is sufficient to evaluate

thresholds $I_{T,\infty}$ and $Q_{T,0}$ at only two durations T of the rectangular $i(t)$, one very long ($T \gg \tau$) and another very short ($T \ll \tau$), respectively.

Interestingly, the *threshold energy* of a *monophasic rectangular stimulus* attains minimum value at $T = 1.25 \cdot \tau$ which can be derived from the local minimum in the course of the energy $(I_T)^2 \cdot T$ in relation to T [with I_T from (2.148)]. Energy considerations are important when considering systems powered by a *battery*. In addition, minimum energy favours *chronic stimulations* in terms of *safety* (Section "Neural Stimulation").

The *strength-duration curve* of I_T in (2.148) and Fig. 2.71b can be interpreted as two *straight-line asymptotes* at small T ($\ll\tau$) and large T ($\gg\tau$) with strong *variation* in the curve shape in the vicinity of $T = \tau$. *Experimental data* typically suggests either an *exponential fit* (2.151) or a *hyperbolic fit* (in the form of $(1 + \tau/T)$).

The *threshold excitation* is given along the *strength-duration curve* of Fig. 2.71b for different monophasic rectangular pulses $i(t)$ with their interrelated parameters $I = I_T$ and T from (2.148). Likewise, the inequality $I > I_T$ corresponds to an energetically unfavourable *suprathreshold depolarization* at a given T, with $i(t)$ then having too high I (see grey area in Fig. 2.71b). In analogy, the inequality $I < I_T$ implies *subthreshold depolarization* without any subsequent action potential.

In other words, as soon as the *excitation condition* ($\Delta u = i_E \cdot R$) is met by the rather inert course of i_E over time (see (2.146) and Fig. 2.71a), the *momentary waveform* of i—or the momentary waveform parameters of i—can already be considered as excitatory and energy-efficient in line with the *strength-duration curve* (2.148). If this condition is surpassed, the excitation still takes place but the energy budget of stimulus is not optimal.

In practical terms, (2.148) yields a *threshold-related* $I_T = I$ given a certain T, which can be considered as an *optimization or design guideline* for threshold depolarization. In analogy, a *threshold-related* duration $T_T = T$ can be expressed from (2.148) as

$$T_T = \tau \cdot \ln\left(\frac{R \cdot I}{R \cdot I - \Delta u}\right) \tag{2.150}$$

given a certain I. This equation composes another *optimization or design guideline* for *threshold depolarization*. Please note that since $R \cdot I > \Delta u$, the duration T_T in (2.150) is necessarily positive. Likewise, the inequality $T > T_T$ corresponds to an energetically unfavourable *suprathreshold depolarization* at a given I (see grey area in Fig. 2.71b), whereas $T < T_T$ implies *subthreshold depolarization*.

Figure 2.71a demonstrates i_E (2.146) and i_C ($=i - i_E$) for the rectangular $i(t)$. Since the *conductive component* i_E is crucial for the membrane depolarization, please note that a high momentary *displacement component* i_C necessarily indicates a relatively weak depolarization due to the associated low i_E. At this *particular time moment*, a relatively high $I_T = I$ would be required to reach Δu. In contrast, a disappearing i_C indicates the maximum possible depolarization by i_E and thus a relatively low $I_T = I$ required to reach Δu.

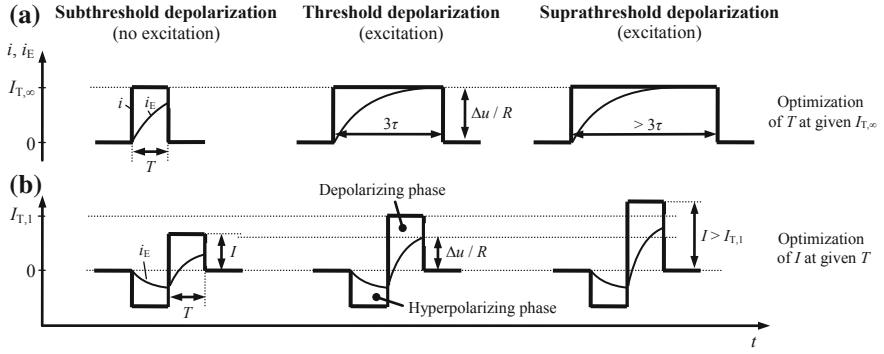

Fig. 2.72 Waveform optimization of the stimulation current i for intracellular stimulation based on the strength-duration curve (Fig. 2.71b). **a** Optimization of monophasic rectangular pulse with the varying duration T but constant amplitude I ($=I_{T,\infty}$). **b** Optimization of biphasic rectangular pulse (a charge-unbalanced pulse, as in Fig. 2.67b) with respect to the varying amplitude I of the depolarizing phase but constant phase duration T

The associated *strength-duration curve* (2.148) in Fig. 2.71b illustrates two threshold amplitudes $I_{T,\infty}$ and $I_{T,1}$ ($>I_{T,\infty}$) with the respective pulse duration T_2 ($\approx 3\tau$) and T_1 ($<T_2$). These parameters are also depicted in the time courses of Fig. 2.71a to illustrate the mutual relationship between the time course of $i(t)$ (Fig. 2.71a) and the strength-duration curve (Fig. 2.71b).

Figure 2.72 illustrates the use of the *strength-duration curve* for *optimization* of the depolarizing *monophasic rectangular waveform* $i(t)$. Please recall that the *intracellular stimulation* set-up from Fig. 2.63a is assumed here, with $i(t)$ (>0) permeating the membrane *outwards*. In particular, Fig. 2.72a facilitates the *guideline* from (2.150) in finding the *optimum* $T = T_T$ ($\approx 3\tau$) for a given $I = I_{T,\infty}$ (see subfigure in the middle of Fig. 2.72a).

Another typical stimulation waveform of $i(t)$, a *biphasic stimulus*, is considered in Fig. 2.72b along the other *guideline* from (2.148). The first *negative phase* leads to the graded *hyperpolarization* of the membrane (inward current) and the associated decrease of i_E. The following *positive phase* leads to the graded *depolarization* (outward current) with the associated increasing i_E (2.146). The amplitude I of the positive phase is optimised based on (2.148) for a given T so that *threshold depolarization* takes place (see subfigure in the middle of Fig. 2.72b). The increasing I of the positive phase in Fig. 2.72b shows a transition from

- *subthreshold depolarization* without excitation ($I < I_T$), to
- *optimal depolarization* with excitation ($I = I_T$), and then to
- *suprathreshold depolarization* with excitation but with wasted stimulation energy ($I > I_T$).

Even though the derived *RC model* for the *strength-duration curve* (2.148) is highly instructive, it has some *limitations*. This simple model considers only *transversal currents* (Fig. 2.63a) across the membrane in terms of *intracellular stimulation*, neglecting *longitudinal currents* along the membrane (Fig. 2.63b). Another limitation is that the accommodation behaviour of the membrane is ignored, i.e., an increase in Δu during extended subthreshold stimulation. For instance, the accommodation is highly relevant when saw-tooth waveforms of the stimulation current are used (Kaniusas 2012, Fig. 2.16b). Furthermore, the leakage resistance R (Fig. 2.63a) is generally a non-linear function of u; compare (Kaniusas 2012, Fig. 2.12). In the resting state and during subthreshold stimulation the used R is determined by passive K^+ resting channels in the membrane and stays constant only up to about 80% of the action potential threshold u_T (Reilly 1998). For suprathreshold stimulation, R decreases and becomes now mainly governed by voltage-gated Na^+ and K^+ channels.

Realistic Strength-Duration Curve

Please recall that the discussed simple RC model considers only *subthreshold relationships* with *experimental conditions* being *idealized*. In practice, the strength-duration curve and its parameters (*rheobase and chronaxie*, see below) are determined by both

- *properties of the exitable fiber* and
- *stimulation set-up*, including all geometrical and material factors of the *experimental setting*;

compare Figs. 2.73 and 2.80. In particular, the *realistic strength-duration curve* and its parameters are strongly influenced by the membrane time constant τ (Fig. 2.63a), the time constant of activation and deactivation of voltage-gated ion-specific channels within membrane, membrane integration effects (Section "Periodic Stimulus"), accommodation effects (Kaniusas 2012, Fig. 2.16b), refractory effects (Kaniusas 2012, Fig. 2.14a), stimulation pattern (Section "Stimulation Pattern"), anodic versus cathodic stimulation (Fig. 2.67), spatial current distribution accounting for the electrode distance to the fiber and for the electrode size (Fig. 2.66), and current versus voltage application. In other words, a lot of *non-linear membrane mechanisms* co-determine the *strength-duration curve*.

Figure 2.73 depicts typical *strength-duration curves* of a single nerve fiber in comparison with a denervated muscle fiber. Two different diameters of the nerve fiber and four different stimulation patterns are considered; compare Fig. 2.80 and Kaniusas (2012, Fig. 2.16). For instance, *anodic* monophasic stimulation (case D) shows higher thresholds than *cathodic* monophasic stimulation (case A), in analogy with the key message from Fig. 2.67. The influence of different *experimental set-ups* is illustrated in Fig. 2.80.

It can be observed in Fig. 2.73 that *nerve fibers* can be activated with lower and shorter stimuli than *muscle fibers*. Typically nerves are stimulated with pulse durations <1 ms, whereas muscles require durations from 20 to 100 ms (Mayer 2017). Thus, *nerve fibers* are more sensitive to electrical stimulation than *muscle*

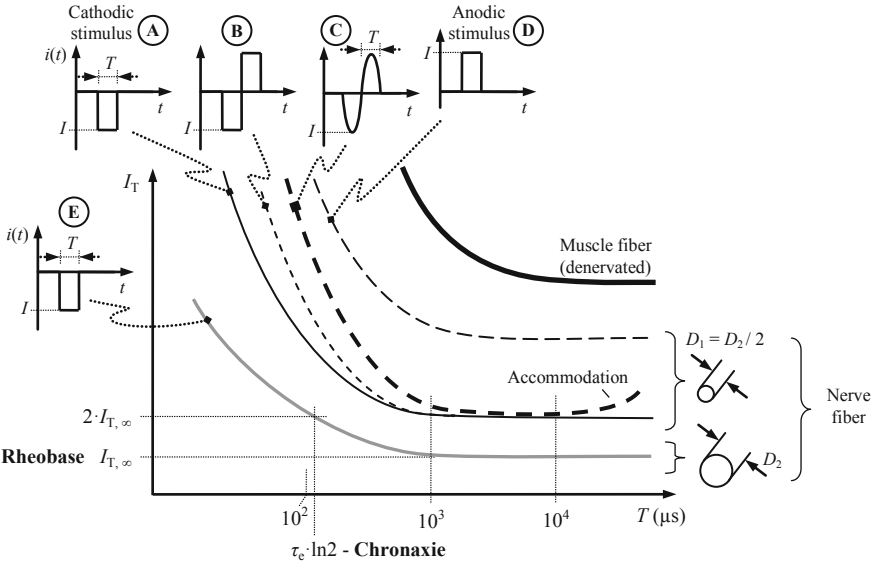

Fig. 2.73 Qualitative strength-duration curves (Fig. 2.71b) of myelinated nerve fibers and denervated muscle fibers with I_T as the absolute current amplitude of the excitation threshold and T as the phase duration. The curves are determined by properties of excitable fibers and the experimental set-up for extracellular stimulation. For nerve fibers, two different diameters D and four different stimulation patterns are considered: monophasic rectangular pulse (cathodic and anodic), biphasic rectangular pulse, and biphasic sinusoidal pulse; compare Figs. 2.74 and 2.80. The rheobase $I_{T,\infty}$ and chronaxie ($\tau_e \cdot \ln 2$) are indicated for exponential fit (2.151) for the fiber with D_2. For quantitative data, see Reilly (2011), Malmivuo (1995), Rattay (1990)

fibers (Reilly 1998; Malmivuo 1995). For instance, muscles—if directly stimulated without prior recruitment of the associated motor neurons (denervated muscle)—require electric fields that are about 10 times greater than those for nerve stimulation (Furse 2009).

Strength-Frequency Curve

The duration T of a single phase for periodic stimuli in Fig. 2.73 can easily be transformed into the *oscillation frequency* f (=1/(2T)) in order to arrive at the *strength-frequency curve*. This curve clearly indicates if *frequency dependence* of neuronal or muscular excitation prevails (Kaniusas 2012, Sect. 2.1.3.2.3).

Figure 2.74 compares strength-frequency curves for *single cycle* and *continuous sinusoidal stimulus*. The former one was directly derived from the *strength-duration curve* of a single sinusoidal pulse in Fig. 2.73 (case C) and shows identical thresholds except the replaced abscissa. In other words, the *high-frequency upturn* in Fig. 2.74 corresponds to the *low-duration upturn* in Fig. 2.73. As already discussed in Section "Periodic Stimulus", repeated stimulus tends to decrease the stimulation threshold due to *membrane integration effects*, i.e., thresholds for single

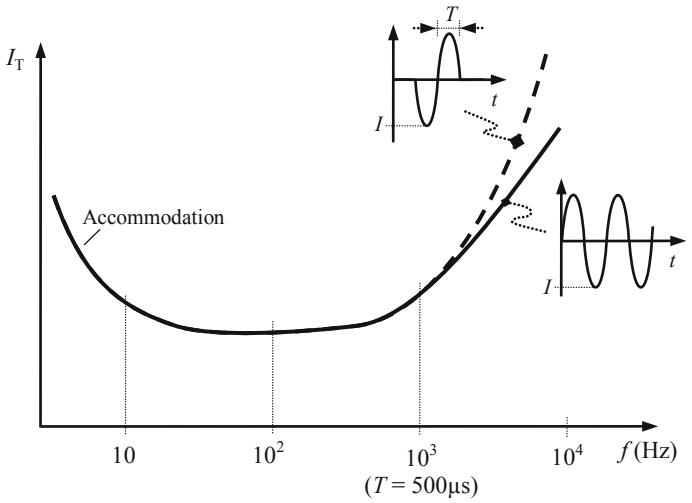

Fig. 2.74 Qualitative strength-frequency curves of nerve fibers for single cycle and continuous sinusoidal stimulus; compare Kaniusas (2012, Fig. 2.16c). Here I_T is the current amplitude of the excitation threshold, f (=1/(2T)) the oscillation frequency, and T the single phase duration. The curves are plotted in close analogy to Fig. 2.73 but with the rescaled horizontal axis

cycle stimulus rise at steeper rate (Fig. 2.74). For higher frequencies, thresholds converge to a frequency-proportional asymptote in each case (Reilly 2011).

As can be inferred from Figs. 2.73 and 2.74, for *periodic stimuli*, *thresholds for stimulation* depend on all three:

- *stimulus strength* (e.g., of the applied current density or electric field)
- oscillation *frequency*, and also on
- particular *waveform* of a single cycle.

As shown in Fig. 2.74 and Kaniusas (2012, Fig. 2.16c), threshold current densities for sinusoidal stimulation *increase progressively* at frequencies below several tenth of Hz and above 1–3 kHz. Correspondingly, low, medium, and high frequencies will be addressed below.

At the *direct current* (0 Hz), stimulation may only be elicited at the *onset or interruption* of direct current (as with a rectangular pulse); compare Fig. 2.91. *Steady direct current* produces thermal effects rather than neuromuscular excitations. At *low frequencies* (<10 Hz), *accommodation mechanisms* dominate while a slowly depolarizing stimulus is applied (Kaniusas 2012, Sect. 2.2.2). In particular, *sinusoidal thresholds* rise at low frequencies—around 10–50 Hz for nerve stimulation (Reilly 1998)—because the associated slow *rate of change* of the stimulus prevents a timely recharging or depolarization of the membrane towards its excitation in view of present *leakage currents* across the membrane counteracting its depolarization. Please recall

that the oscillation frequency f of any harmonic stimulus $i(t)$ $(=I \cdot \sin(2\pi f \cdot t))$ determines its rate of change $\mathrm{d}i/\mathrm{d}t$ $(=2\pi f \cdot I \cdot \cos(2\pi f \cdot t))$. The nerve is said to adapt to slowly varying or constant stimulus, known as *accommodation*. In contrast, periodic or single *rectangular stimulus* does not show such a threshold increase at low frequencies (or long phase durations), as contrasted in Fig. 2.73 for single rectangular versus single sinusoidal stimulus. This is because the *rate of change* of rectangular stimulus does not depend on the frequency (given as the inverse of the phase duration). In practice—aside from the ideal step-wise rectangular waveform—the rate of change of rectangular stimulus is mainly determined by its amplitude.

At *medium frequencies* in the range of 10–100 Hz, *lowest threshold values* occur, whereas thresholds for *peripheral* nerve excitation remain low for frequencies up to several kHz (ICNIRP 1998). The *minimum* in Fig. 2.74 discloses that the dynamics and duration of the sinusoidal stimulation are optimal in the range of the mains frequencies 50/60 Hz. Here the stimulus allows not only an effective therapeutic stimulation but also imposes serious *hazards from power lines* (Sect. "Contact Current").

At *high frequencies* above 1–3 kHz, the rise of thresholds accounts for the progressively shorter time available for the *charge accumulation* on the neuronal membrane (ICNIRP 2010). In fact, the cell membrane can easily be *polarized* only below *β-dispersion* region (Fig. 2.19b) so that the membrane voltage is externally affected only at relatively *low field frequencies* below the beta dispersion (Section "Relaxation and Dispersion Effects on Conductivity and Polarization"). Equation (2.140) confirms the polarization decrease with increasing frequency. It follows that the membrane stimulation towards its excitation becomes stronger with decreasing frequency considering only this *polarization mechanism*.

In addition to the polarization, the threshold's rise above 1–3 kHz accounts for diverse electrophysiological phenomena such as a non-linear buildup of the membrane polarization (*high frequency conduction blockade*), *refractory behaviour*, and *capacitive/displacement currents*. Refractory mechanisms increase stimulation thresholds (due to *relative refractory period*) and even hinder synchronous excitation irrespective of the stimulus strength (*absolute refractory period*) at higher frequencies (Footnote 96). On the other hand, the proportion of the *displacement current component* to the total current crossing the membrane increases at higher frequencies (see the displacement i_C and the total i in Fig. 2.63a); compare (Kaniusas 2012, Sect. 2.1.3.2.3). Consequently, the residual *conductive current component* (see the conductive $i_E = i - i_C$ in Fig. 2.63a) across the membrane—the component responsible for depolarization—decreases with increasing frequency.

Current density thresholds for *nerve fibers* rise above about 0.5–1 kHz and already above about 100 Hz for *muscles* due to larger time constants of muscle fibers compared with nerve fibers (ICNIRP 2010). Please compare nerve and muscle from Fig. 2.73 with rescaled abscissa ($f = 1/(2T)$). The excitation of *cardiac*

muscle deserves special attention because it can be life-threatening and may lead to atrial or *ventricular fibrillation*[97] (Footnote 124).

Myelination reduces significantly the *membrane time constant* of myelinated fibers compared with unmyelinated fibers (Kaniusas 2012, Table 2.2). Therefore, thresholds for *myelinated fibers* start to increase at a lower phase duration of biphasic stimulus (i.e., start to increase towards decreasing duration, compare Fig. 2.73) or, in analogy, start to increase at a higher frequency (i.e., towards increasing frequency, compare Fig. 2.74) than for *unmyelinated fibers*; as can also be inferred from Reilly (2011).

Experimental data usually suggest an *exponential fit* for the threshold

$$I_{\mathrm{T}} = \frac{I_{\mathrm{T},\infty}}{1 - \mathrm{e}^{-T/\tau_{\mathrm{e}}}} \tag{2.151}$$

in analogy with (2.148). While $I_{\mathrm{T},\infty}$ still represents the residual threshold amplitude for long experimental stimulus with the duration T ($\gg\tau_{\mathrm{e}}$), the resulting *empirical time constant* τ_{e} is different from the actual *membrane time constant* τ (Kaniusas 2012, Table 2.2).

Rheobase and Chronaxie

A few useful parameters such as rheobase and chronaxie can be derived from the *strength-duration curve*. As illustrated in Fig. 2.73 (for the diameter D_2 of nerve fiber), the *rheobase current* is the minimum current which evokes a response or excites for an infinitely long stimulus duration T. To be precise, rheobase applies

- for T significantly larger than τ [with the simplified RC model from (2.148)] or
- for T significantly larger than τ_{e} [applicable for the general case including experimental data, see (2.151)].

According to (2.148) and (2.151), *rheobase is the current* $I_{\mathrm{T},\infty}$; compare Fig. 2.71b. In real-world applications, (experimental) *rheobase* current $I_{\mathrm{T},\infty}$ (2.151) differs from the *modelled rheobase* $\Delta u/R$ as derived from the simplified RC model (2.148). In fact, the *rheobase current* represents *excitability of fiber* and thus—as already mentioned—depends on the *fiber properties* and the *stimulation set-up*.

[97]Fortunately, electrical stimulation thresholds for *ventricular fibrillation* (Footnote 124) exceed significantly those for the electrical stimulation of cardiac muscle by a factor of about 10–20 (ICNIRP 2004; Reilly 1998) or about 50 (ICNIRP 2010). This is because, to produce ventricular fibrillation, the cardiac excitation must be externally generated during the *early phase of ventricular recovery*, i.e., during the so-called *vulnerable period* of the cardiac cycle (Footnote 126). Here the *excitability* of cardiac muscle is still relatively low because it has *not fully recovered* yet. Thus a higher current density is required to re-excite this *partly recovered cardiac muscle* than for excitation of the *resting cardiac muscle*. In addition, a *critical mass of the heart* should be excited for fibrillation and not a few cardiac muscle cells. Interestingly, the apex of the heart (Kaniusas 2012, Fig. 2.32b), showing the greatest muscle thickness, has the lowest ventricular fibrillation threshold. Correspondingly, a chest electrode over the apex has the lowest threshold with respect to other anatomical positions on the chest.

From a biophysical point of view, rheobase is a measure of *leakage effects* and increases with increasing leakage. These effects are especially apparent in spatial models with *current distribution* where stimulation current is applied close to the fiber region to be stimulated.

For *intracellular stimulation*, a microelectrode is inserted into a fiber to stimulate/depolarize it with outward currents that are necessarily subjected to current distribution along the fiber, see Figs. 2.63a and 2.69a. Namely, the *applied current leaks away* inneraxionally along the axis of the fiber and lifts up the membrane voltage down the electrode *outside the targeted region* to be stimulated (compare Kaniusas (2012, Fig. 2.13a)). Because of this finite leakage, the applied strength of stimulation current should be above a certain limit to reach the excitation threshold at the target region, whereas rheobase results to be finite. On the other hand, the rheobase current is zero if the membrane *leakage resistance R* within the simple subthreshold RC model (Fig. 2.63a) is assumed to be infinite. This relationship can also be derived from $I_{T,\infty} = \Delta u/R$ (2.148) showing that the *rheobase* $I_{T,\infty} \to 0$ with $R \to \infty$.

For *extracellular stimulation*, a surface electrode can be used to stimulate fibers under the skin, see Fig. 2.66. The applied current experiences a particularly strong widening of the resulting current density field (shaped as hemisphere), whereas the *currents leakage* past the targeted fiber increases with increasing *distance of this fiber from the electrode*. Consequently, rheobase increases with the widening of the field and with the distance.

Chronaxie is the pulse or stimulus width at which twice the reobase current evokes a response, as shown in Fig. 2.73 (again, for the nerve fiber with D_2). Please recall that *chronaxie* can be *practically derived* from the very simple relationship $Q_{T,0} = I_{T,\infty} \cdot \tau_e$ using only two durations T. The experimental chronaxie is a measure of time constants of both the *nerve fiber* to be excited and the *stimulation set-up*; hence, chronaxie can also be interpreted as the *effective stimulation time constant*.

For the simple RC model and *intracellular stimulation*, chronaxie amounts to $\tau \cdot \ln 2 \approx 0.7 \cdot \tau$, as can easily be derived from (2.148) with $I_T = 2 \cdot I_{T,\infty}$. In the general case, including most experimental cases, *chronaxie* equals $\tau_e \cdot \ln 2$ (2.151) and is very different from the *modelled chronaxie* $\tau \cdot \ln 2$ (due to the excitable membrane only and its time constant τ only).

Chronaxie typically amounts to about 100 µs for *myelinated fibers* and 500–600 µs for *unmyelinated fibers* (Rattay 1990); however, it strongly depends on experimental set-up. Larger values are a consequence of a larger *capacity* of a much larger exposed *membrane* in unmyelinated fibers than myelinated fibers (here only narrow nodes are exposed).

As already mentioned, *rheobase* and *chronaxie* vary with the *distance of the electrode* from the fiber and depend on the *spatial distribution of the stimulation current* (Reilly 1998, 2011). Namely, the empirical τ_e generally increases with increasing distance and with currents becoming distributed in a more gradual, less focal, fashion; i.e., τ_e increases with increasing spatial region exposed to depolarizing currents.

In analogy, the size of τ_e increases with the *size of the contact electrode*. The larger is the electrode, the less focal is the resulting current distribution. Consequently, the resulting *distribution of transmembrane currents* is more diffuse and engages a greater number of nodes (in myelinated fibers), which obviously increases the time τ_e needed for the discharge of all these nodes during depolarization. In addition, the resulting *diffuse distribution of extracellular potentials* decreases the spatial gradient of the electric field and thus increases the excitation threshold (2.145). Therefore, *rheobase* increases with increasing electrode size and/or increasing distance between the fiber and electrode. Figure 2.80 illustrates an increase in rheobase (by a factor of about 4.8) for extracellular stimulation with a single cathodic monophasic pulse when the *distance* between a small monopolar electrode and a 10 µm unmyelinated fiber is doubled (from 1 to 2 mm).

Rheobase is inversely related to the *fiber diameter*, as illustrated in Fig. 2.73 (cases A and E), whereas this relationship applies for both *central mode* and *end mode* (Footnote 92). Numerical data in Fig. 2.80 confirm an increase in rheobase (by a factor of about 1.7) when the diameter is halved from 10 to 5 µm given a cathodic monophasic pulse. Please note that the *polarity ratio* is given as the ratio of the respective rheobases. For instance, the polarity ratio ideally equals five (compare this factor five from Fig. 2.67) when anodic and cathodic stimulation from Fig. 2.73 (case D versus A) are contrasted; realistic numerical data from Fig. 2.80 yields polarity ratios between 4.2 and 4.3 depending on the cathodic pulse duration. In addition, *denervated muscle fibers* show significantly increased values of τ_e (in the range of ms up to about 60 ms (Reilly 1998)) and rheobase in comparison with *motor neurons*.

Applications

The *strength-duration curve* can be used to *optimise waveforms* and *safety margins* when stimulating different fibers. For instance, stimulation of afferent *thick Aβ fibers* is favourable since it reduces *pain perception*. However, a simultaneous stimulation of *thin Aδ fibers* should be avoided since it would induce sharp, fast-onset pain. Please consult Footnote 101 for different fiber qualities. In fact, we look for a *waveform* that has the stimulation potency in exiting Aβ fibers but not Aδ fibers.

Fortunately, thick Aβ fibers have higher propagation speed of action potentials and thus exhibit *lower* τ_e (and lower τ) than thin Aδ fibers. In addition, thick fibers can be excited more easily than thin ones so that *rheobase* for Aβ fibers is lower than rheobase for Aδ fibers. Figure 2.73 confirms qualitatively that a nerve fiber with *doubled diameter* has only *half of the original rheobase*; numerical data in Fig. 2.80 yield a factor of 1/1.7 = 0.59. Consequently, the larger is the difference in *fiber diameters*, the larger is the expected *safety margin*.

A *monophasic stimulation pulse* with the duration in the range of τ_e of Aβ fibers can rather excite Aβ fibers but not Aδ fibers. Here the large τ_e of Aδ fibers does not give sufficient time for excitation to be developed in these fibers. However, for longer pulse durations, the *safety margin* between Aβ fibers and Aδ fibers decreases

and reaches a plateau. This is indirectly confirmed in Reilly (2011) where the safety margin between 20 μm A fiber and 1 μm C fiber is lowest for long pulse durations (>10 ms) of a monophasic rectangular pulse and amounts to about 20. That is, the margin is lowest considering *rheobases* of both fibers. This margin increases to about 40 for the pulse duration of 1000 μs which is the size of τ_e of the C fiber. For the duration of only 100 μs, i.e., the approximate duration of τ_e of the A fiber, the margin increases to even higher levels of about 100. According to Reilly (2011), *biphasic waveforms* tend to have higher safety margins than *monophasic waveforms*.

The *strength-duration curve* can also be used to *characterise nerve and muscle pathologies* when current pulses of different durations are applied and the associated current levels required to achieve nerve excitation are measured. Monophasic, biphasic, and other wave shapes as well as single and bursted stimulation can be applied, all of which modify stimulation thresholds and the resulting form of the strength-duration curve; see examples in Kaniusas (2012, Fig. 2.16). For instance, sawtooth current stimulus and the resulting strength-duration curve can be used to differentiate between *innervated muscle* and *denervated muscle* since accommodation mechanisms are absent in denervated muscles; compare Kaniusas (2012, Fig. 2.16b) with the rise due to accommodation (for innervated muscle) and (Kaniusas 2012, Fig. 2.16b) without this rise (for denervated muscle).

Cathodic and Anodic Stimulation

The difference between cathodic and anodic stimulation is highly instructive. Please recall that

- *cathodic stimulation* is given by an active stimulation electrode acting as a *current sink* with the current $i(t)$. In contrast,
- *anodic stimulation* is given by a *current source*; see instructive Fig. 3.11c, Fig. 3.13c, and Footnote 19 in Chap. 3 for detailed definitions.

Concerning the site of the stimulation, we can differentiate between

- *intracellular stimulation*—see Fig. 2.69a—and
- *extracellular stimulation*—see Fig. 2.75b, c.

Intracellular Stimulation

Intracellular cathodic stimulation is given by an electrode inserted into an axon. The electrode is negatively charged with respect to a neutral reference electrode placed outside the axon, see Fig. 2.69a, b and the associated discussion. This arrangement yields *inward currents* permeating the membrane, which decreases the absolute membrane voltage, hyperpolarizes the membrane, and thus *disfavours its excitation*. Obviously, the membrane region closest to the electrode—at the region $x = 0$ along the axon in Fig. 2.69a—experiences the strongest hyperpolarization. The hyperpolarization level decreases exponentially with increasing distance $|x|$ (>0). The smaller is the *length constant* of the membrane, the steeper is this

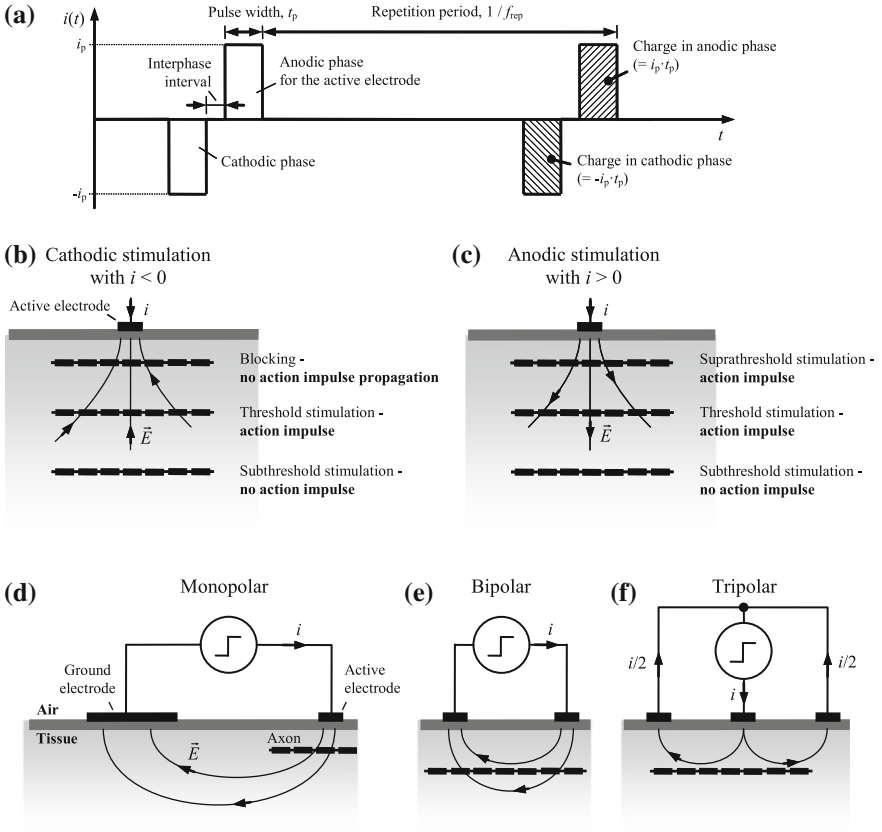

Fig. 2.75 Typical extracellular stimulation settings. **a** Biphasic current pulses with the preceding cathodic phase—i.e., the active surface electrode acts as current sink, see **b**—and the following anodic phase—i.e., the electrode acts as current source, see *c*. Electrical charge ($=i_p \cdot t_p$) of cathodic phase equals to that of anodic phase in (**a**), which yields a charge-balanced biphasic pulse. **d** Monopolar stimulation of an axon located under the active electrode with the current between the active electrode and the ground electrode (relatively large). **e** Bipolar stimulation with the spatially constricted current between two active electrodes. **f** Tripolar stimulation with currents between the central electrode and the two return electrodes

decrease, as illustrated in Kaniusas (2012, Fig. 2.8c). Please compare the associated discussion on Kaniusas (2012, Fig. 2.13) concerning inhibitory stimulus.

In contrast, *intracellular anodic stimulation* is given by a positively charged electrode located inside an axon and the associated *outward currents* through the membrane (Fig. 2.69a, c). Here the absolute membrane voltage increases while the membrane is depolarized and *its excitation is favoured*. In fact, the local membrane regions become excited as soon as the local depolarization level reaches the local threshold level. Again, depolarization is strongest in the membrane region closest to

the stimulation electrode, whereas depolarization decreases exponentially with increasing $|x|$.

Extracellular Stimulation

The situation is far more sophisticated for *extracellular stimulation* (Fig. 2.75b, c). In particular, *extracellular cathodic stimulation* is given by a negatively charged electrode located in a distance from an axon to be stimulated (with $i(t) < 0$ in Fig. 2.75b). In contrast to intracellular cathodic stimulation, *depolarization* from extracellular cathodic stimulation is confined to a relatively small *central axon's region* $|x| < y/\sqrt{2}$ (or $|x| < 0.7 \cdot y$) along the axon's coordinate x. In fact, this is the region where the *activating function* $f(x) > 0$ is positive, as illustrated in and discussed with respect to Fig. 2.67e. Likewise, cathodic stimulation allows *depolarization of the axon* only for the region width determined by and *approximately equal to the distance* y of the axon from the stimulation electrode (Fig. 2.67a). The smaller is this y, i.e., the closer is the stimulation electrode to the axon, the narrower is this depolarized region. The axon's region *most sensitive to excitation* is the region nearest to the electrode, i.e., the region at $x = 0$ marked by the highest positive level of $f(x)$. In fact, the local *axon activation* results as soon as the local stimulus intensity reaches the local threshold level and *a single action impulse* is released. However, cathodic block may also apply (Section "Cathodic Block and Stimulation Upper Threshold"). The resulting action impulse at $x = 0$ bifurcates and propagates outwards away from this region (Fig. 2.77b, d).

In the *depolarized* central region, the current *leaving outwards the closest axon's regions* (or closest nodes for myelinated axons) must be accompanied by another equally strong current *entering inwards more distant axon's regions* (or distant nodes for myelinated axons), as illustrated in Fig. 2.67g. This equality is because of the *conservation of the electric current* since here is no net charge accumulation anywhere along the current pathway (2.25). In accordance with the current direction within these distant regions, these regions must experience *hyperpolarization* (compare Kaniusas (2012, Fig. 2.13)). Therefore, in addition to the central depolarization, lateral regions experience *hyperpolarization* (Fig. 2.67e). This is in clear contrast to intracellular stimulation where cathodic stimulation produces only hyperpolarization varying in its strength along the axon.

Extracellular anodic stimulation is given by a positively charged electrode (with $i(t) > 0$ in Fig. 2.75c). In contrast to extracellular cathodic depolarization of the central region, extracellular *anodic depolarization* is generated in two symmetrical lateral areas around the central region for $|x| > y/\sqrt{2}$ (or $|x| > 0.7 \cdot y$) where $f(x) > 0$ applies, as shown in Fig. 2.67f. The axon's regions *most sensitive to this depolarization* are located at $x \approx \pm 1.2 \cdot y$ (for the set-up in Fig. 2.67a) and marked by the highest local levels of $f(x)$. If the local axon's thresholds are surpassed, *two symmetrical action impulses* are produced at distances *approximately equal to* $\pm y$ from the axon's region closest to the electrode (at $x = 0$). Both impulses naturally bifurcate (Fig. 2.77c, e). Impulses propagating inwards towards the centre $x = 0$ experience either blocking due to the central hyperpolarization or *collision block* with oncoming impulses, i.e., they become extinct. In contrast,

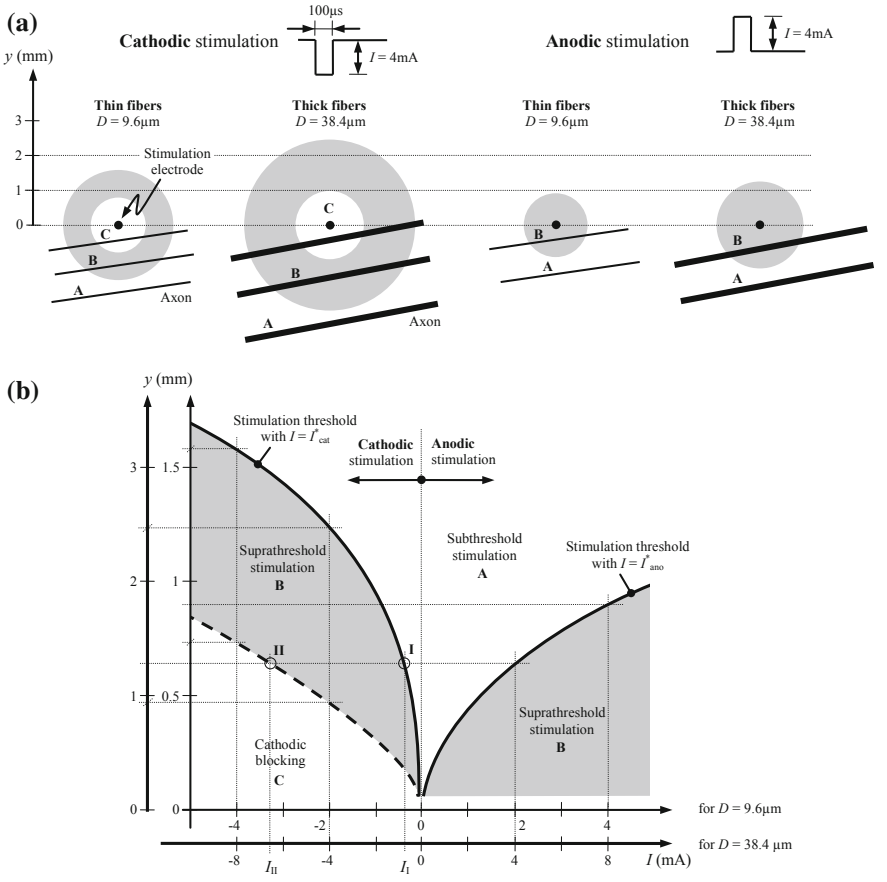

Fig. 2.76 Relationship between the electrode current amplitude I and the fiber distance y to the electrode for unmyelinated fibers, known as the current-distance relationship. The stimulation electrode is an implanted monopolar spherical electrode—acting as a current point source with a rectangular pulse of 100 µs duration—within homogeneous isotropic tissue with its conductivity of 0.3 S/m (as in Fig. 2.81a). **a** Three regions with imbedded fibers result around the stimulation cathode: the subthreshold region A without any generated action impulse, thesuprathreshold region B with a propagating action impulse (grey color), and the suprathreshold region C with a local excitation but without impulse propagation (cathodic block). The stimulation anode generates only regions A and B. The illustrated absolute size of regions corresponds to I = 4 mA. **b** The inner axes belong to the axon diameter of 9.6 µm, the outer ones to 38.4 µm. For cathodic stimulation, a minimum distance y exists at the point where cathodic block prevents an escape of a generated action impulse. For anodic stimulation, the blocking does not exist. The firing B regions are larger for the thick axon than for the thin axon given the same I. Computational data is taken from Rattay (1987)

impulses propagating outwards away from $x = 0$ can successfully leave the site of the stimulation.

In the *hyperpolarized* central region, the hyperpolarizing current enters the closest axon's regions (or nodes), as shown in Fig. 2.67h. Likewise, the same current must leave more distant and lateral axon's regions (or nodes) depolarizing them.

Cathodic Versus Anodic Stimulation
In the case of *intracellular* stimulation,

- *cathodic* stimulation yields *hyperpolarization* only, whereas
- *anodic* stimulation *depolarization* only.

In the case of *extracellular* stimulation, in clear contrast to intracellular stimulation,

- *cathodic* stimulation yields both *depolarization and hyperpolarization*, whereas
- *anodic* stimulation yields also both *depolarization and hyperpolarization*.

From a practical point of view, it is important to know whether extracellular cathodic stimulation or extracellular anodic stimulation is appropriate for excitation of nerve fibers. As already discussed in Fig. 2.67b–d, *anodic stimulation* needs a *much stronger excitatory current* than *cathodic stimulation*; compare Fig. 2.73 (cases A and D) and Fig. 2.80. Namely, the *fivefold* magnitude is required to reach the local excitation threshold provided that durations of anodic and cathodic phases of the current stimulus are identical. In other words, anodic stimulation pulses require higher *charge levels* than cathodic pulses for the same configuration of the electrode and axon; likewise, a greater volume of excited tissue is recruited around cathode than anode for the same stimulation amplitude (Fig. 2.76). Please recall that this factor applies for *unmyelinated fibers* and monopolar *current electrodes* acting as *point sources*. In general, this ratio of anodic to cathodic threshold is known as *polarity ratio* (Reilly 2011).

This approximate factor of five arises because the lateral positive peaks in $f(x)$ during *anodic stimulation* are only one-fifth of the central peak which is the positive peak during *cathodic stimulation*. For instance, the factor of five can also be derived from Fig. 2.76b considering the ratio $I^*_{\text{ano}}/I^*_{\text{cat}}$ of the threshold current amplitudes I^* for anodic and cathodic stimulation at a constant axon depth y from the electrode. Namely, the ratio $I^*_{\text{ano}}/I^*_{\text{cat}} \approx 2$ mA / 0.4 mA = 5 results for $D = 9.6$ µm and the horizontal line crossing points I and II in Fig. 2.76b.

For *myelinated fibers*, the author in (Rattay 1990) shows that the *anodic stimulation threshold* is about 4.5 to 8 times (mostly 6 times) greater than the *cathodic stimulation threshold*, with a monopolar stimulation electrode situated at a variable distance y of 0.5 to 4 mm directly above the node. For an *unmyelinated fiber*, numerical data in Fig. 2.80 illustrate that the observed polarity ratio is between 4.2 and 4.3.

However, if the stimulation electrode is moved towards the terminus of neuron (*end mode* stimulation, see Fig. 2.65), this ratio of anodic to cathodic threshold differs much from 5 and may even decrease to 1 or even become fractional. In the

fractional case, the anodic threshold is actually lower than the cathodic threshold. Please recall that in the end mode not the gradient of the extracellular electric field drives depolarization but the electric field.

Therefore, *extracellular cathodic stimulation*—with an electrode *close to excitable structures* acting as *current sink* (Fig. 2.75b)—is more effective than *extracellular anodic stimulation* (Fig. 2.75c) with the same *charge per phase* (Fig. 2.75a). In clinical applications, local *cathodic* stimulation is usually applied with a remote large reference electrode connected as *anode*. Figure 2.75a illustrates cathodic stimulation during the initial *cathodic phase*, whereas anodic stimulation is given during the following *anodic phase*.

Finally, please recall that cathodic and anodic spikes are generated in different axon's regions below the stimulation electrode and propagate generally in the negative and positive direction of x, as discussed above (compare Fig. 2.68b). Consequently, *cathodic and anodic stimulation* may yield *different time delays* of action impulses at their point of destination.

Cathodic Block and Stimulation Upper Threshold

Cathodic block

The *strength of cathodic stimulus* with respect to a *nerve fiber* located in a distance from the stimulation electrode

- is proportional to the *current strength* $i(t)$ delivered by the stimulation electrode and
- inversely proportional to the *distance* y between the stimulation electrode and the fiber;

as can be derived from (2.152) (for $x = 0$ with x as the axon axis). In other words, increasing $i(t)$ and/or decreasing y rise the fiber-related stimulus.

A continued *increase in the strength* of *suprathreshold cathodic stimulus* is followed by only little change in the already *suprathreshold depolarization* and in the *already successful excitation* of the central region of the *fiber* located right *under the stimulation electrode* (around $x = 0$, as illustrated in Fig. 2.67e). However, the associated *simultaneous hyperpolarization* of lateral regions of the fiber elevates with increasing stimulus strength. Please recall that for *extracellular stimulation* (Fig. 2.67e) the cathodic depolarization of the central region is marked by positive values of the *activating function* while the associated hyperpolarization of lateral regions shows negative values.

For strong *extracellular cathodic stimuli*, the hyperpolarization *lateral* to the active central region (Fig. 2.67e) can even be strong enough to *block propagating action impulses* originating in and coming from this *central* region (Fig. 2.78c, e). Likewise, it is known that (remote) *hyperpolarized* axon regions can *stop propagation* of (centrally) induced action potentials. In particular, this block arises when *cathodic stimulation* $i(t)$ of the fiber reaches a level of some *eight times the current threshold* and above (Rattay 1988, 1990; Malmivuo 1995). This *suprathreshold*

blocking phenomenon is known as *cathodic block*,[98] *anodal surround block*, or even *high current blockade*, and is applicable for both *myelinated and unmyelinated* fibers. In other words, *nerve fibers residing close to the stimulation electrode* (fibers with small y), which delivers a *high cathodic current* (electrodes with high $i(t)$), are mostly susceptible to cathodic block. Please note that *cathodic block* applies only to *extracellular stimulation* (Fig. 2.67a) but not *intracellular stimulation* (Fig. 2.69a).

In particular, this aforementioned *factor of eight* applies for an implanted *spherical electrode* acting as a *current point source* with respect to an unmyelinated fiber. For instance, this factor can be derived from any horizontal line in Fig. 2.76b considering cathodic stimulation. Namely, the ratio I_{II}/I_I equals about eight when the associated current amplitudes I at the denoted point I (with the threshold current I_I at which excitation starts) and at the denoted point II (with the current I_{II} at which propagation ceases due to cathodic block) are related.

It is important to recognize that for a *successful cathodic stimulation*

- a necessary *minimum distance* or *lower limit* for y exists. This distance is at the point where the *lateral* anodic surround block (which occurrence depends on y, see above) still prevents an escape of an action impulse induced *centrally*, as illustrated in Figs. 2.75b and 2.78. Obviously,
- an *upper limit* for y is given at the point where *subthreshold depolarization* starts which—per definition—is insufficient to induce any impulse.

It is instructive to recognise that the *duration of a cathodic current impulse* plays a major role when *cathodic block* has to be triggered. As illustrated in (Rattay 1990), a *relatively short impulse* with a *decreasing duration* (<0.1 ms) requires an over-proportionate higher current level for a monopolar electrode to reach cathodic block (for y considered in the range of 0.5–4 mm); compare Footnote 98. Here, the block-related current level rises with increasing y. In contrast, a *relatively long impulse* in the modelled range 0.1–1 ms requires an almost constant current amplitude for cathodic block. In other words, this *block is less likely for short current pulses* since high current amplitudes are required.

From a biophysical point of view, *short current pulses* imply less charge for *hyperpolarization* of lateral axon regions than long pulses given the same current amplitude. Consecutively, short pulses imply lower hyperpolarization level of these axon regions. In addition, for short pulses, *spontaneous discharge* of the hyperpolarized *lateral* regions—i.e., discharge with the membrane *time constant* τ

[98]The *cathodic block* can also be intentionally used to *block propagation of action impulses* (Rattay 1990); compare Footnotes 95 and 99. For *short pulse durations* below 100 µs, necessary cathodic currents become very strong and may *damage tissue and fibers* (Section "Charge Transfer During Stimulation"). Please recall that the applied charge—i.e., the time integral of the applied instantaneous current (2.25)—is responsible for depolarization and hyperpolarization of the membrane (Section "Single Monophasic Stimulus"). Therefore, *long pulse durations* with reduced current levels are preferred in blockade applications.

In addition, a relatively *long*, linear or *exponential falling phase* typically follows the plateau phase of the applied cathodic current impulse to *prevent axon's firing* when this impulse is abruptly *switched off*.

(Kaniusas 2012, Table 2.2) towards its resting state—has more time before the arrival of action impulses from the excited *central* region. Therefore, the associated blocking by short pulses becomes less likely because of the membrane discharge in progress.

Please note that *extracellular anodic stimulation* does not show such block because action potentials are produced laterally and can propagate away from the hyperpolarized central region, as shown in Figs. 2.67f and 2.75c. Thus there is *no lower limit* for y for a *successful anodic stimulation*; however, higher stimulation intensities are needed than for a *successful cathodic stimulation* (Fig. 2.76). In analogy with cathodic stimulation, an *upper limit* for y for anodic stimulation is given by *subthreshold depolarization*.

In view of aforementioned phenomena, lower and upper limits of the *electrode current* $i(t)$ and the associated *impulse duration* for generation of *action impulses* which are able to *propagate* depend on the electrode *distance* y from the fiber, as discussed in the following Section "Current-Distance Relationship".

Stimulation Upper Threshold

There is a mechanism—known as *stimulation upper threshold* from Boinagrov (2012))—which prevents generation of action impulses. In particular, an action impulse is not triggered in the depolarized axon region during *extracellular stimulation* even though, for instance, a strong *depolarizing cathodic stimulus* is applied in *suprathreshold range*. There are even indications that this mechanism is also applicable for intracellular stimulation (Rattay 2017).

The biophysical explanation is the *reversal of the sodium* Na^+ *ionic flow*—or *reversal of the current*—through open voltage-gated Na^+ channels within the cell membrane during its strong depolarization (Kaniusas 2012, Fig. 2.10a). Namely, instead of

- a *depolarizing inflow of* Na^+ *ions* into the cell in the *depolarized membrane region*, the *strong membrane depolarization* leads to
- a *hyperpolarizing outflow of* Na^+ *ions*

according to the resulting *electrochemical driving force* affecting Na^+ ions within channels. During the *strong depolarization*, the membrane voltage exceeds the *equilibrium voltage* for Na^+ ions of about +61 mV (according to Kaniusas (2012, Table 2.1) and the Nernst equation in Kaniusas (2012, Eq. 2.5)). Thereby, the associated electrical force driving Na^+ ions out of the cell exceeds the diffusional force driving Na^+ ions into the cell, which leads to a *net outflow of* Na^+ *ions* out of the cell. Consequently, the net outflow of positive ions contributes to hyperpolarization of the membrane and thus favours missing excitation of the cell; compare with the efflux of positive potassium K^+ ions in Kaniusas (2012, Fig. 2.14b) and the associated hyperpolarization phase in Kaniusas (2012, Fig. 2.14a).

It is instructive to stress the difference between stimulation upper threshold and cathodic block. While

- the *current reversal* within the membrane prevents *generation of action impulses* in view of a strong local depolarization,

- *cathodic block* prohibits *propagation of already generated action impulses* in view of a strong local hyperpolarization.

Current-Distance Relationship

Distant and *thin fibers* require stronger stimulation currents $i(t)$—i.e., larger excitation *thresholds*—than *near* and *thick fibers*. This simple rule on distant versus near fibers can easily be derived from the *inverse proportionality* between the *depolarization rate* $\mathrm{d}u/\mathrm{d}t$ and the *electrode distance* y to the fiber from equations in Figs. 2.67b and (2.145), to give

$$\frac{\mathrm{d}u}{\mathrm{d}t} = \frac{\gamma_\mathrm{I} \cdot D}{4C''} \cdot f(t, x = 0) = -\frac{\gamma_\mathrm{I} \cdot D}{4C''} \cdot \frac{i(t)}{2\pi\gamma \cdot y^3} \tag{2.152}$$

at the central axon region $x = 0$ being closest to the electrode. For practical relevance of this distance relationship, see functional electrical stimulation from Footnote 99.

On the other hand, the simple rule on thin versus thick fibers can be derived from the direct proportionality between $\mathrm{d}u/\mathrm{d}t$ and the axon diameter D from (2.152) (compare Footnote 93). In other words, *thick fibers* are stimulated first before *thin fibers* are activated, which, for instance, can be advantageously used to avoid pain-related stimulation (Footnote 101).

Therefore the *number of firing fibers* (within a nerve) increases with the stimulation strength. The *probability of excitation* of *all thick fibers*[99] within the

[99]The *recruitment* of thick axons before thin axons with increasing stimulation strength is unfortunately disadvantageous within the scope of *functional electrical stimulation* (FES) of motor nerves (compare Footnote 101). FES typically uses a varying *stimulus amplitude* and varying *pulse width* (at a fixed stimulation frequency) to recruit low to moderate muscle forces, whereas variation of the *stimulation frequency* can be used to generate high forces.

The latter disadvantage in the recruitment results because *thick efferent motor neurons* (e.g., around 20 µm, myelinated Aα motor fibers) govern *fast-twitch muscles* which are responsible for high contraction/force levels, heavy exercise, subjected to large fatigue, and are *naturally quite seldom used*. Only when great and fast muscular force is desired, these readily fatigued motor units are recruited. They are known as *type II motor units* which are relatively *large* in size. Please recall that a single motor neuron and all muscle cells that it innervates are called as a *motor unit* (Kaniusas 2012, Fig. 2.24).

An artificial and *easy stimulation of thick fibers* with relatively low current levels is disadvantageously *unnatural*. Such stimulation leads to a *fast fatigue* of stimulated muscles. In addition, there is only a *little control* of the muscle contraction force (90–100% of the total force available) within a relatively *narrow range of the stimulation current*; see the aforementioned steep increase of the *excitation probability* for thick fibers with increasing current strength. Smooth and low-force levels required for frequent daily functions (e.g., eating) are not possible while stimulating thick motor neurons.

In contrast, *thin efferent motor neurons* (e.g., around 10 µm, myelinated Aα motor fibers) can only be stimulated with relatively *strong currents* after thick fibers have already been recruited. These thin neurons govern *slow-twitch muscles* which are responsible for mild exercise, most resistant to fatigue, and are *naturally quite often used*; known as *type I motor units* which are relatively *small* in size. These thin motor neurons have also the lowest *threshold for synaptic*

activation, whereas this synaptic threshold increases with increasing neurons size. Thus an artificial stimulation of *thin fibers* is more natural and would be preferred within FES; however, it *requires high current levels*.

Furthermore, *thick motor fibers* are usually located rather *close to the skin surface* so they are even more excitable with skin surface electrodes than *thin motor fibers* embedded rather deep *inside muscles*. This is because of the reduced electrode distance to the thick fibers and thus their increased excitability (2.152).

The *natural recruitment order*—for increasing muscle force—starts from *thin neurons* of the small type I motor units and ends with *thick neurons* of the large type II motor units. In contrast, the so-called *inverse recruitment order* in FES—for increasing current strength—starts from *thick neurons* of the large type II motor units and ends with *thin neurons* of the small type I motor units. The inverse recruitment order will inappropriately utilize more readily fatigued and large muscles for low-force tasks, whereas fatigue resistant small muscles will be recruited at stronger stimuli only. This contributes to the aforementioned unfavourably steep relationship between the muscle contraction force and the stimulation strength, implying only *little control* in the gradual muscle force.

A few *techniques* can be used to counteract or *circumvent the inverse recruitment order*. Since *thick fibers* are stimulated first before *thin fibers* with increasing stimulation currents (Fig. 2.81), *thick fibers are also blocked first* at *high stimulation currents* by the discussed mechanisms of

- the *high current blockade* or *cathodic block* (Fig. 2.76 and Footnote 98) and
- the *high frequency blockade* (Section "Periodic Stimulus")

using *extracellular electrodes*. Therefore, since the activation of thick fibers is blocked, this inhibits large type II motor units which we do not want to stimulate at the first place within FES. In other words, action impulses can not propagate along regions x of fibers, which experience either a strongly negative activating function $f(x) \ll 0$ or the high frequency stimulation of the membrane at x.

The *high current blockade* is introduced in Fang (1987). Here relatively long (>350 μs) and strong current pulses (1–2.3 mA) were used to stimulate and excite small axons while large axons still remain in the *cathodic block* and do not generate any propagating action impulses. Decreasing the amplitude of the applied current pulses, allows some additional larger axons to fire in the *natural recruitment order*. Finally, at a certain minimum current level (1 mA), no blockade is active, all axons fire, and the *muscle force* becomes maximal. Likewise, the highest current stimuli produce lowest mechanical forces. Further decrease of the current amplitude (below 1 mA) is not reasonable since it decreases the muscle force following the *inverse recruitment order*; in this low range of the current, the highest current stimuli would produce highest forces.

According to the *high frequency blockade*, another special set-up with two stimulation electrodes can be used for a *selective blockage* to realise the *natural recruitment order* within FES (Solomonow 1984). While the *first electrode* stimulates all fibers (e.g., with a typical stimulation rate of 20–70 Hz), the *second electrode* applies a high frequency stimulation with its adjustable amplitude. At the high amplitude, only *small axons* (e.g., 10 μm in diameter) and those more distant from the second electrode escape the *high frequency blockade* and become stimulated and excited by the first electrode. Here small type I motor units become activated at the start of the muscle recruitment, with *small contraction forces*. With the ongoing recruitment, the amplitude of the high frequency stimulation is reduced. Now both small and large axons (e.g., 10 and 15 μm) escape the blockade and become excited by the first electrode. Consequently, small and large type I+II motor units become activated while now recruited *large contraction forces* add to smaller ones and thus add to the overall force. The resulting recruitment order is qualitatively in line with the natural recruitment order.

For the sake of completeness, it should be noted that not only the cathodic block and high frequency blockade can be used for diameter and distance *selective fiber excitation* but also

nerve (e.g., with their D of 20 μm) is larger than that of all thin fibers within the same nerve (e.g., D = 10 μm) for a given $i(t)$. Interestingly, the *excitation probability* for *thick fibers increases steeper* with increasing current strength than the excitation probability for thin fibers (Rattay 1990). Thus a *gradual control*[100] of the number of firing fibers within the nerve is easier for thin fibers. In fact, this behaviour is disadvantageous for functional stimulation of motor nerves. Namely, easily recruitable thick motor fibers with the associated little control of high force contractions of muscles (Footnote 99) disfavours generation of controllable, smooth, and low force levels which are required during daily activities.

The discussed differences between the cathodic and anodic stimulation are instructively summarized in Fig. 2.76 for *unmyelinated fibers* embedded within *homogeneous isotropic tissue* and being *at rest before stimulation*. Here the so-called *current-distance relationship* is illustrated. In particular, this relationship considers jointly

- the *current amplitude I* of an implanted monopolar spherical electrode acting as a *current point source*,
- the *electrode distance y to the fiber*, and
- the resulting *subthreshold*, *threshold*, and *suprathreshold stimulation* of the fiber (including cathodic block).

In other words, *depolarization*, *excitation* of the fiber as well as *propagation* along the fiber are jointly studied. For the *cathodic current*, Fig. 2.76a shows that

- the fiber closest to the electrode experiences the *cathodic blocking phenomenon* because of the strong cathodic stimulus, see the *spherical suprathreshold region C*. Here a strong central excitation is accompanied by strong lateral hyperpolarizations inhibiting any propagation of action impulses away from the central region.
- A more distant fiber experiences normal excitation with propagating impulses along this fiber, see the grey-coloured *suprathreshold region B*. All fibers which pass through the outer border of the region B but do not enter the region C—or

depolarizing *sub-threshold prepulses* (Vuckovic 2008). Prepulses increase the excitation threshold of the most excitable fibers—thick and close to the stimulation electrode—due to *accommodation* processes.

Finally, it is interesting to note that the type II fast-twitch motor units can *favourably* be transformed into the type I slow-twitch motor units by *chronic electrical stimulation*. On the contrary, *muscle disuse* (e.g., after spinal cord injuries) *unfavourably* tends to shift the metabolism of the type I fatigue resistant motor units towards that of the type II readily fatigued motor units.

[100]Careful *control of the delivered stimulus charge* can be used to obtain a *gradual neural response*, namely, to obtain a *controlled number of excited fibers* within a single *nerve bundle*. In fact, the *excitation probability*—or the relative number of excited fibers—is a function of the applied *stimulus charge* and usually reveals a *sigmoid shaped recruitment curve*. After the activation threshold is reached by increasing charge, the curve *climbs steeply* with ongoing charge increase so that the associated number of activated individual fibers rises steeply, until the curve finally *plateaus* with all the available fibers within the nerve being already activated.

pass through the outer sphere but do not enter the inner sphere—experience both successful excitation and propagation.
- The most distant fiber experiences depolarization below the threshold level being insufficient for its excitation, see the *subthreshold region A* without any generated action impulse.

In contrast to three cathodic regions A, B, and C, the *anodic current* in Fig. 2.76a generates only two denoted regions A and B, *without any blocking phenomenon*:

- A fiber close to the electrode experiences normal excitation with propagating impulses, as the fiber resides within the grey-coloured *spherical suprathreshold region B*.
- A more distant fiber experiences depolarization below the threshold without any induced action impulse, see the *subthreshold region A*.

In short, *grey regions* in Fig. 2.76a denote regions in which *propagating action impulses* are produced, denote the *recruitment volume*. Diameters of these regions depend, among others, on the diameter D, current stimulus I, and stimulus duration (for the influence of the duration, see Section "Cathodic Block and Stimulation Upper Threshold").

It is instructive that

- only *thicker fibers* are *excited in greater distances y* from the electrode, whereas exited fibers closer to the electrode will include thin fibers. The same level of the excitation current reaches fibers more distant to the electrode if their D is greater; see the absolute axis for y in Fig. 2.76a. In particular, the grey *cathodic spherical ring* in Fig. 2.76a is thicker and the grey *anodic sphere* is larger for the shown thick fiber (D = 38.4 μm) than for the thin fiber (D = 9.6 μm). Inner and outer spheres for cathodic excitation as well as the sphere for anodic excitation are smaller for smaller D. This is in full agreement with the *greater excitability of thicker fibers* from Fig. 2.81b. Large fibers have a larger *recruitment volume*.

It is also instructive from a practical point of view that

- the *lower limit of y* for an effective cathodic fiber stimulation—*cathodic block* sets this limit—rises with increasing D, as can be derived from Fig. 2.76a comparing D = 9.6 μm with 38.4 μm.
- When *cathodic spherical rings* for D = 9.6 and 38.4 μm in Fig. 2.76a are compared with each other, it is obvious that there is a small volume, defined by both spherical rings, in which *small fibers* are already stimulated by a *given current pulse* (small fibers are just above their region C) but *large fibers* are not stimulated (large fibers are still in *cathodic block* within the outer range of their region C). This behaviour offers a way to stimulate small fibers over large fibers, which could be advantageously used to counteract *inverse recruitment order* (Footnote 99).

Figure 2.76b offers a more detailed picture on the *current-distance relationship* for *unmyelinated fibers*. While *inner axes* in Fig. 2.76b belong to the *axon diameter* of $D = 9.6$ µm, the *outer ones* are scaled with the factor of *two* and belong to the *fourfold* diameter of $D = 4 \cdot 9.6$ µm $= 38.4$ µm. In fact, the diagram in Fig. 2.76b can be applied to *arbitrary fiber diameters D* (in µm)—to estimate their individual *current-distance relationship*—by multiplying values of the inner axes for I and y with the factor $\sqrt{D/9.6\,\mu\text{m}}$ (Rattay 1990).

All aforementioned regions A, B, and C can be recognized in Fig. 2.76b. For *cathodic stimulation*, a minimum distance y exists at the point where *cathodic block* prevents an escape of an induced action impulse. This *lower limit* of the electrode distance y *rises with increasing* I and *increasing* D. For *anodic stimulation*—as already discussed—such *blocking* does not exist. *Cathodic stimulation* reaches to *greater depths* and has *smaller current thresholds* (at a fixed depth) than anodic stimulation. This is in agreement with the shape of the activating function in Fig. 2.67 showing the central peak (relevant for cathodic stimulation) with the fivefold amplitude in comparison with amplitudes of lateral peaks (relevant for anodic stimulation). The grey-coloured region B with the effective excitation and propagation extends to larger y for the considered thick axon than for the thin axon at a given level of I. In Fig. 2.76b, the associated *stimulation thresholds* $I = I^*_{\text{cat}}$ and $I = I^*_{\text{ano}}$ are highlighted for cathodic and anodic stimulation, respectively. Please note that horizontal lines in Fig. 2.76b allow to extract I^*_{cat} and I^*_{ano} which rise with the distance y, qualitatively similar to the representation in Fig. 2.82b. In addition, horizontal lines depict the *lower and upper boundaries* for I for *cathodic stimulus* as well as the lower boundary for I for *anodic stimulus* for an effective *excitation* of and *propagation* along a fiber at a given distance y from the electrode.

Thin *dashed lines* in Fig. 2.76b apply for $I = 4$ mA and both considered diameters D of 9.6 µm and 38.4 µm. These lines denote minimum and maximum values of y for *cathodic excitation and propagation* as well as denote maximum values of y for *anodic excitation and propagation*; in short, denote spatial boundaries of the region B for $I = 4$ mA. Please note that the same boundaries and the current $I = 4$ mA apply for the scaling of y axis in Fig. 2.76a.

The *current-distance relationship* is *fairly linear* for small currents I and small distances y. As discussed in Rattay (1990), the *threshold current* in myelinated fibers is *proportional* to the *distance* y for only small $y \ll 1$ mm; i.e., doubling y requires double threshold current. For larger y in the order of 1 mm, the current is *proportional to* y^2; i.e., doubling y requires fourfold current. Even for greater distances, the current *proportionates to* y^3; i.e., doubling y requires even eightfold current. This is in qualitative agreement with flattened curves in Fig. 2.76b of stimulation thresholds at large y for cathodic and anodic stimulation.

Numerical Simulation—A Quantitative Approach

Instructive *numerical data* on *cathodic and anodic stimulation* of an *unmyelinated nerve fiber* is demonstrated in Fig. 2.77. A single monopolar electrode acting as a *current point source* is modelled in a distance of 2 mm from the fiber, whereas the electrode and fiber are surrounded by a homogenous isotropic tissue (Fig. 2.77a).

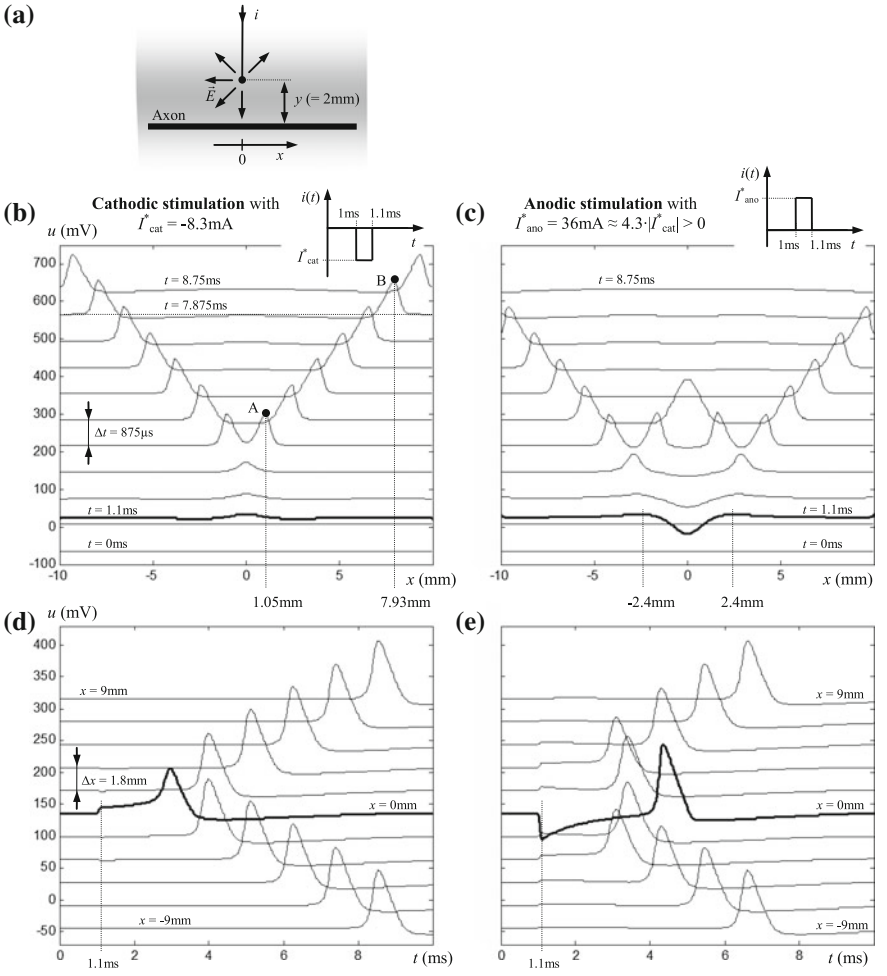

Fig. 2.77 Stimulation and excitation of an unmyelinated axon surrounded by semi-infinite homogeneous isotropic tissue; compare Fig. 2.67. **a** The axon lays at the distance y of 2 mm from a small monopolar stimulation electrode. **b**, **d** Cathodic threshold stimulation with a rectangular current impulse of the amplitude I^*_{cat} and its duration of 100 µs, starting at the time t = 1 ms. **c**, **e** Anodic threshold stimulation with $I^*_{ano} \approx 4.3 \cdot |I^*_{cat}|$. **b**, **c** Space evolutions of the membrane voltage u along the axon axis x for different time instants. **d**, **e** Time evolutions of u along t for different axon regions x. All numerical data were calculated using Hodgkin-Huxley model at 18 °C (Rattay 1990) with the intracellular axon's conductivity γ_I = 1 S/m, the axon diameter D = 10 µm, and the tissue conductivity γ = 0.2 S/m

A single relatively short rectangular *current pulse* of 100 µs is used for the stimulation at the fiber *threshold*. Please recall that the selected duration of 100 µs is shorter than the *refractory period* and shorter than the *time constant* τ of unmyelinated fibers. Therefore we expect only a *single action impulse* in response

to the stimulus and a *linear change in the membrane voltage u* during this stimulus, as detailed in Section "Single Monophasic Stimulus".

The *anodic threshold stimulus* requires a higher amplitude by the factor of 4.3 than the *cathodic threshold stimulus* (close to the aforementioned factor of 5, see polarity ratio and Fig. 2.67c, d). The *cathodic stimulation* yields maximum depolarization and generates a single action impulse at the central axon region $x = 0$ being closest to the electrode (Fig. 2.77b, d). Here the activation function $f(x)$—or the *necessary gradient of the electric field* along the unmyelinated fiber—at $x = 0$ amounts to 9.95 V/cm^2 · (8.3 mA/1 mA) ≈ 830 mV/mm^2 (with 9.95 V/cm^2 taken from Fig. 2.67 at $x = 0$). In contrast, the *anodic stimulation* excites both lateral regions $x = \pm 2.4$ mm experiencing maximum depolarization (Fig. 2.77c) and clearly hyperpolarizes the central region $x = 0$ with maximum hyperpolarization at the end of the current pulse (at $t = 1.1$ ms in Fig. 2.77e). This is in full agreement with the discussion on Fig. 2.67.

Generated action impulses clearly *bifurcate* and propagate along x with the estimated *propagation velocity* of about 1.6 m/s; i.e., with the estimated velocity of (7.93–1.05 mm)/(5 · 0.875 ms) ≈ 1.57 m/s considering points A and B in Fig. 2.77b. The *spatial extension* is in the range of 1 cm, including a quite long hyperpolarized tail of the propagating single action impulse (see the dashed line in Fig. 2.77b at the time instance $t = 7.875$ ms to recognize this extended tale); compare with the discussion of Fig. 2.68b.

In the anodic case (Fig. 2.77c), the aforementioned *collision block* occurs at $x = 0$ where colliding action impulses disappear. It is also instructive to observe that, at the end of the applied stimulation pulse, the associated space evolutions of the *voltage u*—see bold lines at $t = 1.1$ ms in Fig. 2.77b, c—clearly resemble the shape of the applicable *activating function* (see Fig. 2.67e, f). Please recall that the activating function reflects the local rate du/dt of the change of u (Footnote 93) so that the *observed change of u* in Fig. 2.77 during the current pulse can be interpreted as the *activating function scaled with time*. Please observe the expected *linear increase* in u (depolarization) at $x = 0$ during the *cathodic current stimulus* for the time period from 1 ms to 1.1 ms (Fig. 2.77d). In analogy, a *linear decrease* in u (hyperpolarization) at $x = 0$ can be observed during the *anodic current stimulus* (Fig. 2.77e); see the associated discussion on the *subthreshold behaviour* in Section "Single Monophasic Stimulus".

Figure 2.78 details data on *cathodic stimulation* but for a *varying distance* y between the electrode and the unmyelinated fiber. The electrode approaches the fiber; namely, the distance y was numerically reduced from 2 mm (Fig. 2.77b, d), to 1 mm (Fig. 2.78b, d), and to 0.35 mm (Fig. 2.78c, e). At the smallest selected $y = 0.35$ mm, the *cathodic block* started (Section "Cathodic Block and Stimulation Upper Threshold"). As illustrated in Fig. 2.78c, this block is characterized by a very strong depolarization and a subsequent action impulse at $x = 0$ while both lateral sides experience a strong concurrent hyperpolarization. The hyperpolarization blocks the *bifurcation* of the action impulse and its further propagation to the left and right from the central region. Please note that the current amplitude of the stimulation impulse was kept constant at -8.3 mA for all three different values of y,

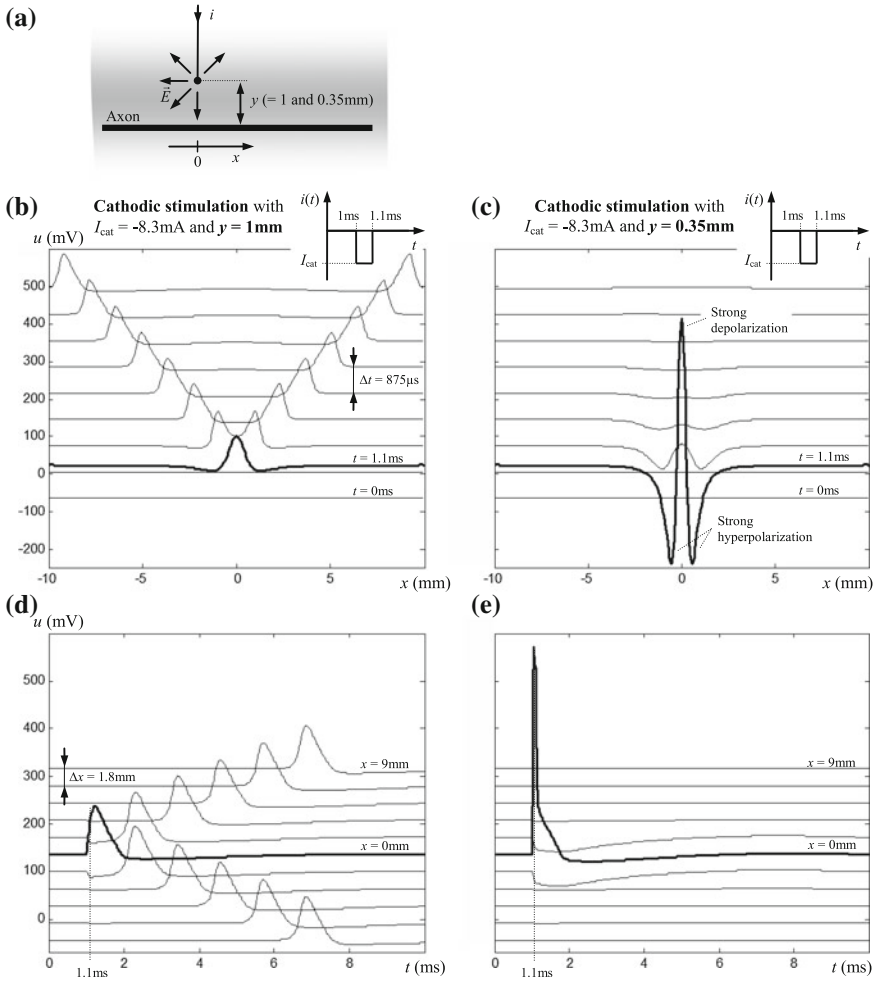

Fig. 2.78 Cathodic stimulation and excitation of an unmyelinated axon from Fig. 2.77 with a variable distance y between the electrode and axon. **a** Stimulation set-up. **b**, **d** Cathodic stimulation with $y = 1$ mm and the amplitude $I_{cat} = -8.3$ mA (i.e., with the cathodic threshold amplitude $I^*_{cat} = I_{cat}$ for $y = 2$ mm according to Fig. 2.77b). **c**, **e** Cathodic stimulation with $y = 0.35$ mm and I_{cat} yielding already cathodic block. **b**, **c** Space evolutions of the membrane voltage u along the axon axis x for different time t instants. **d**, **e** Time evolutions of u along t for different axon regions x. All numerical data were calculated using Hodgkin-Huxley model; for model parameters see Fig. 2.77

whereas this current level represents both the threshold current for $y = 2$ mm (Fig. 2.77b, d) and the cathodic block current for $y = 0.35$ mm (Fig. 2.78c, e).

While decreasing y, the *accumulated depolarization* of the fiber central region at $x = 0$—i.e., the accumulated $\Delta u = \mathrm{d}u/\mathrm{d}t \cdot \Delta t$ (>0) over the time interval Δt with $\mathrm{d}u/\mathrm{d}t$ (>0) being proportional to the *activating function* (see above)—progressively

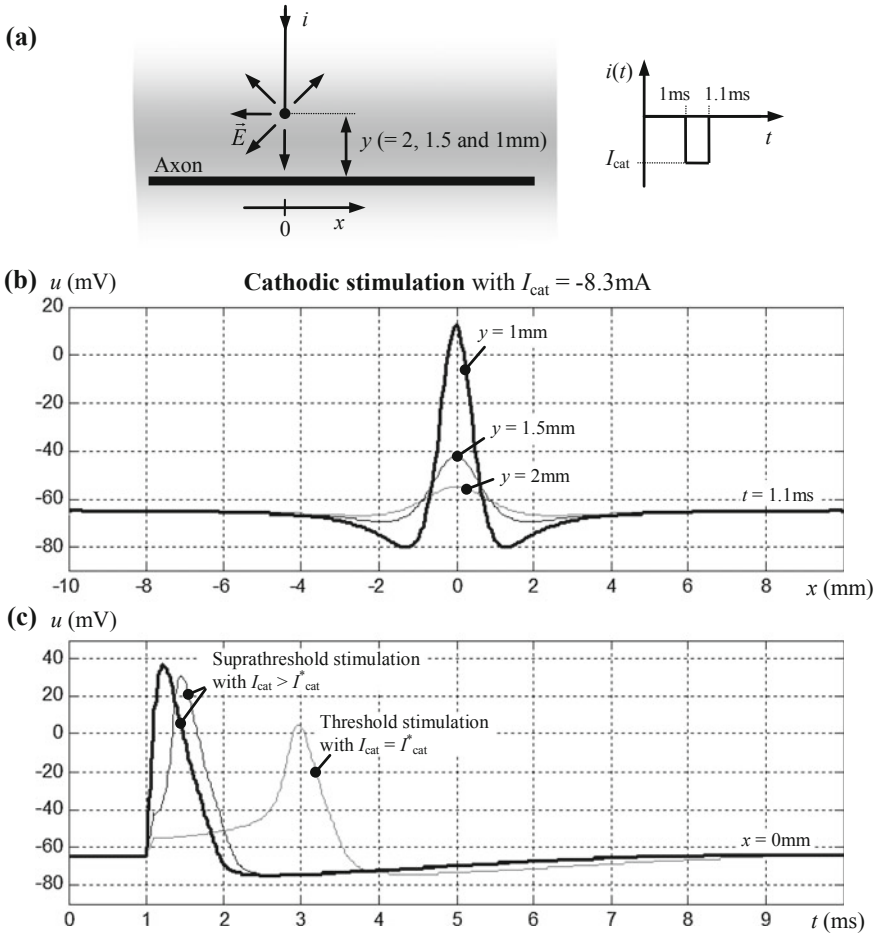

Fig. 2.79 Cathodic stimulation and excitation of an unmyelinated axon from Figs. 2.77 and 2.78 with a variable distance y between the electrode and axon. **a** Stimulation set-up of cathodic stimulation with y = 2, 1.5 and 1 mm and the current impulse amplitude $I_{cat} = -8.3$ mA (i.e., with the cathodic threshold amplitude $I^*_{cat} = I_{cat}$ for y = 2 mm according to Fig. 2.77b). **b** Space evolutions of the membrane voltage u along the axon axis x for the time t instant at 1.1 ms, i.e., right after the current impulse, see (**a**). **c** Time evolutions of u along t for the axon region x = 0 closest to the stimulation electrode. All numerical data were calculated using Hodgkin-Huxley model; for model parameters see Fig. 2.77

increases during the current pulse. Therefore, the associated *time delay* between the delivered short current pulse and the following action impulse decreases with decreasing y (Section "Single Monophasic Stimulus"). Please compare the longest delay of more than 1 ms for the *threshold stimulation* in Fig. 2.77d (y = 2 mm) with an almost absent delay for the strong *suprathreshold stimulation* in Fig. 2.78d (y = 1 mm).

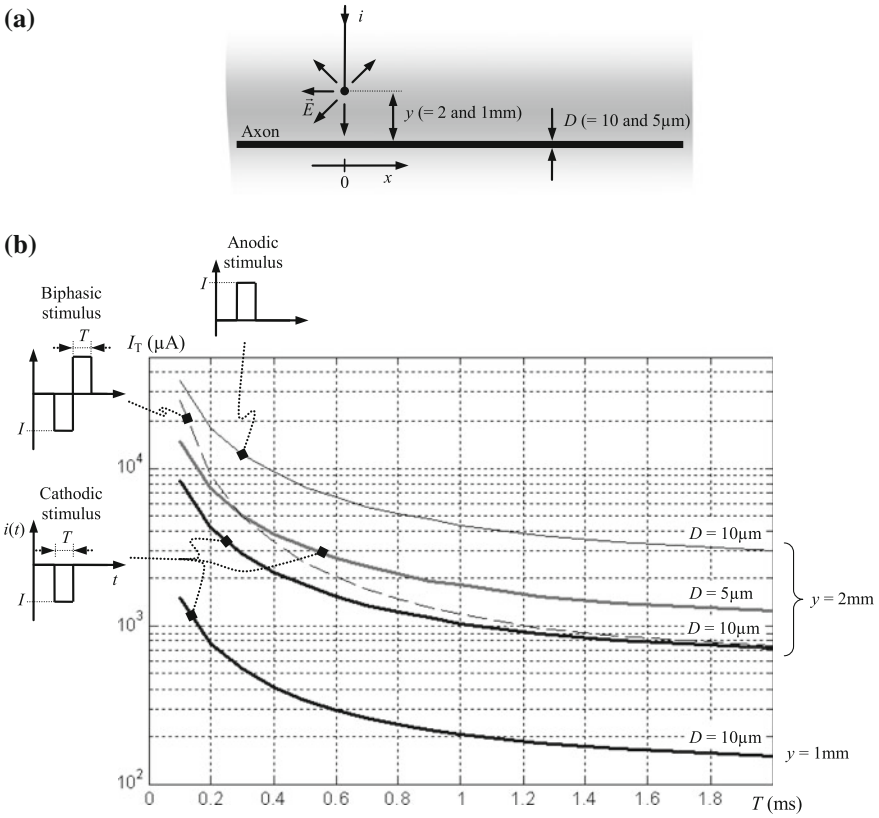

Fig. 2.80 Strength-duration curves of unmyelinated axons for different experimental set-ups with I_T as the absolute current amplitude of the excitation threshold and T as the phase duration; compare Fig. 2.73. **a** Stimulation set-ups with a variable distance y (=2 and 1 mm) between the electrode and axon, a variable axon diameter D (=10 and 5 μm), and variable stimulation patterns: monophasic rectangular pulse (cathodic and anodic) and biphasic rectangular pulse. **b** Strength-duration curves. All numerical data were calculated using Hodgkin-Huxley model; for model parameters see Fig. 2.77

Figure 2.79 complements insights from Figs. 2.77 and 2.78 while showing *space evolutions* of $u(x)$ directly *after the stimulus* (at t = 1.1 ms) as well as *time evolutions* of $u(t)$ at the *central fiber region* (at x = 0) residing *closest to the stimulation electrode*. As expected, the *activating function* in Fig. 2.79b increases in its amplitude with decreasing distance y from 2 mm, to 1.5 mm, and to 1 mm (before the cathodic block is reached at y = 0.35 mm). This is qualitatively in line with the peak $f(0) = -i(t)/(4\pi\gamma \cdot y^3)$ of the activating function $f(x)$ at $x = 0$ and the peak's increase with decreasing y [as derived from equations in Fig. 2.67b with the factor 4π considering the full-spherical surface instead of 2π for the half-spherical surface in Fig. 2.67b; compare (2.152)]. The *time delay* in Fig. 2.79c clearly decreases from the threshold stimulation (at y = 2 mm), to a suprathreshold

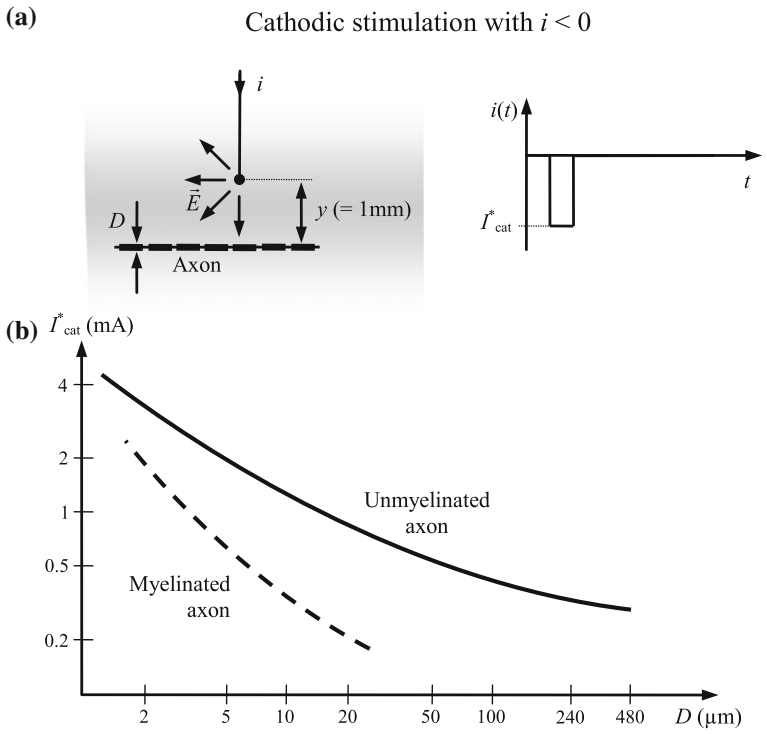

Fig. 2.81 Cathodic stimulation of unmyelinated and myelinated axons with the associated current thresholds over the axon's diameter D. **a** Implanted monopolar stimulation electrode acts as a current point source situated at a distance of 1 mm from the fiber. A cathodal rectangular pulse with the threshold amplitude I^*_{cat} and 100 µs duration is applied. The conductivity of the isotropic and homogeneous tissue is 0.3 S/m. **b** The threshold I^*_{cat} as a function of D with simulation data taken from Rattay (1986a)

stimulation (y = 1.5 mm), and to an even stronger suprathreshold stimulation (y = 1 mm).

Figure 2.80 illustrates the associated strength-duration curves while varying the distance y (from 2 to 1 mm), the diameter D (from 10 to 5 µm), the stimulation pattern (monophasic and biphasic), and the phase duration of the applied pattern (from 100 µs to 2 ms). Please note that the current threshold I_T from Fig. 2.80 corresponds exactly with the cathodic threshold from Fig. 2.77b, d, to give $I_T = |I^*_{cat}| = 8.3$ mA, considering monophasic cathodic pulse with 100 µs duration. In analogy, the equality $I_T = |I^*_{ano}| = 36$ mA applies for 100 µs monophasic anodic pulse in Figs. 2.80 and 2.77c, e.

It can be observed in Fig. 2.80 that thresholds decrease with decreasing y and increasing D. Anodic stimulation shows highest thresholds. As already discussed, the difference between monophasic cathodic stimulus and biphasic stimulus (with

cathodic phase first) is prominent for short durations and disappears for long durations above 1 ms (above the refractory period).

Axon Thickness and Its Distance to Electrode

Axons' Thickness

It is instructive to reiterate that *thick axons can be excited more easily than thin ones*, as already discussed with respect to (2.152). It should also be recalled that the local depolarization rate $\mathrm{d}u/\mathrm{d}t$ $(=\gamma_\mathrm{I} \cdot D/4C'' \cdot f(\cdot)$ at the onset of an external stimulus) for *unmyelinated and myelinated fibers* is proportional to the *axon's diameter* D, as derived in Footnote 93. The thicker is the axon, the larger is its $\mathrm{d}u/\mathrm{d}t$, and thus the more excitable the axon is.

Another reason for an easy excitability of thick *myelinated axons* in comparison with thin myelinated axons is that the *internodal length* increases with the thickness. In fact, the ratio of the outer axon diameter and the internodal length of approximately 1:100 is typical for most axons. Thus, the resulting *differences in the electric potentials* at the neighbouring nodes of Ranvier—or the *voltage drop* from one node to the next one (2.29)—are proportionally larger for thick axons. Since this voltage drop accounts effectively for the force that drives current across the membrane and thus for *depolarization* of myelinated axons, thick axons are more likely to be excited by external stimulation. From a mathematical point of view, the term $(\varphi_{\mathrm{e},n-1} - 2\varphi_{\mathrm{e},n} + \varphi_{\mathrm{e},n+1})$ considers these *extracellular potential differences* and determines the size of the activation function $f(n)$ (Footnote 93).

Figure 2.81b illustrates how *current thresholds* for unmyelinated and myelinated axons decrease with D. Namely, the *threshold amplitude* I^*_{cat} of the cathodic *rectangular pulse* $i(t)$ (<0) with 100 µs duration is plotted over D. Here *cathodic stimulation* is considered with an *implanted monopolar stimulation electrode* acting as a *current point source* and situated at a distance of 1 mm from the fiber (Fig. 2.81a).

It is important to observe in Fig. 2.81b that

- *myelinated axon* is more excitable than
- *unmyelinated axon* at a given D

when *extracellular stimulation* is considered. Therefore, the resulting *ratio* of I^*_{cat} for unmyelinated axon to I^*_{cat} for myelinated axon is larger than one at a given D. In accordance with Fig. 2.81b, this ratio even increases with increasing D. We want to address these phenomena by the following qualitative *biophysics*.

A smaller *time constant of the membrane* of myelinated axons (for *radial currents* across the membrane, see Kaniusas (2012, Table 2.2) favours their faster depolarization in response to an extracellular current stimulus if compared with unmyelinated axons; see the related discussion on the linear/exponential increase from Section "Single Monophasic Stimulus". Therefore, *myelinated axons* can be

expected to be more excitable than *unmyelinated ones* for a given stimulus strength and duration. In addition, unmyelinated axons can be thought of as myelinated axons with a very little distance between "virtual nodes" (Fallon 2016). The associated depolarizing *differences in the electric potentials* at these nodes are relatively small, meaning that the associated excitation thresholds of unmyelinated axons are quite high.

Myelination results in a proportionately greater decrease in the *axial time constant of the membrane* than does the same increase in D (Kaniusas 2012, Eqs. 2.11, 2.12). Please recall that the axial time constant is relevant for the axial spread of depolarization (and equalising currents, see Kaniusas (2012, Fig. 2.18)) and determines its propagation speed (Kaniusas 2012, Footnote 63). Consequently, the aforementioned ratio of I^*_{cat} for unmyelinated axon to I^*_{cat} for myelinated axon can be expected to increase with increasing D.

Figure 2.81b illustrates that the threshold I^*_{cat} over the diameter D is highly *non-linear*. Experimental data for the set-up in Fig. 2.81a with the point cathode located 1 mm above a node of Ranvier indicates that I^*_{cat} for thick fibers is inversely proportional to $\sqrt{D}$, whereas I^*_{cat} for thin fibers is inversely proportional to D^2 (Reilly 1998).

In short, *large myelinated axons* are more easily excited than *small unmyelinated axons*. This difference in the axon's susceptibility to *external stimulation* has significant *practical consequences* in the recruitment[101] of different *sensory and motor fibers* during neural or neuromuscular stimulation; compare Footnote 99. For the sake of completeness, it should be amended that large myelinated axons have also higher *conduction velocities* than small unmyelinated axons; compare Kaniusas (2012, Eqs. 2.11, 2.12, and Table 2.2).

[101] Usually *unmyelinated fibers* are called *C fibers* while *myelinated fibers A fibers* (Reilly 2011).

- *Motor efferent fibers* are A fibers with their diameter typically larger than 5 µm.
- *Sensory afferent fibers* comprise both A and C fibers. *A fibers* include subclasses of
  - *Aδ fibers* with the diameter of about 2–5 µm (for fast-sharp cutaneous pain and temperature sensation),
  - *Aβ fibers* with about 7 to 10 µm (for cutaneous mechanoreception), and
  - *Aα fibers* with about 11 to 15 µm (for proprioception, receptors of muscle spindle);
  - *C fibers* have the smallest diameter of about 0.5 to 1.5 µm (for slow-chronic pain sensing which even tends to become greater over time).

As shown above, *motor fibers and sensory fibers—not related to pain*—are *large* and myelinated in comparison with *thin* unmyelinated and myelinated sensory fibers *for pain sensing*. Therefore—since motor fibers and non-pain sensory fibers are usually *targeted by the electrical stimulation*—it is fortunate that these fibers have lower stimulation thresholds than pain-related fibers which activation is to be avoided; compare the relevant discussion on (2.152) and Footnote 99.

Please recall that Fig. 2.81 is valid for a small *implanted monopolar electrode* acting as a *current point source*. For comparison, let us consider a small *surface monopolar electrode* located on the skin (Fig. 2.67a), as typically used for stimulation purposes. Provided that both compared electrodes act as *current point sources*, the *half-spherical surface* ($2\pi \cdot r^2$ in equations of Fig. 2.66b) should be used for the resulting current distribution around the surface electrode instead of the *full-spherical surface* ($4\pi \cdot r^2 = 2 \cdot 2\pi \cdot r^2$) applicable to implanted electrode. This halving of the effective current surface doubles the size of the resulting extracellular potential (φ_e in Fig. 2.63d) on the axon's surface and thus doubles the size of the associated activating function $f(x)$; see equations in Fig. 2.67b. Therefore, the *current threshold* for a successful fiber excitation is approximately halved for the *surface electrode* in comparison with the current threshold for the *implanted electrode* (Fig. 2.81b), if axon parameters, its distance to the stimulation electrode, and the surrounding tissue are identical.

Axon's Distance to Electrode

The *current threshold* I_{cat}^* obviously changes with the *distance* y of a nerve fiber to the current electrode, i.e., the distance of the target stimulation object from the current source. The size of I_{cat}^* should intuitively increase with increasing y, as already discussed with respect to Fig. 2.76. Distant fibers need a stronger electrode current to be excited while the number of firing fibers increases with the amplitude of this current. In other words, the current $i(t)$ has to increase in its amplitude in order to keep $f(x)$ constant with increasing y, as can be derived from equations in Fig. 2.67b (for $x \neq 0$) or from (2.152) (for $x = 0$). Please note that Figs. 2.67 and 2.81 consider a *fixed* y of 2 mm and 1 mm, respectively.

In contrast, Fig. 2.82 considers *varying* y. Here *cathodic stimulation* of unmyelinated and myelinated axons is performed with a surface monopolar stimulation electrode (Fig. 2.82a). Figure 2.82b depicts the *ratio* of I_{cat}^* at the variable distance y to I_{cat}^* at a fixed distance $y = 2$ mm (from Fig. 2.67a), as can be derived from (2.152). Obviously, stimulation thresholds refer to the excitation of the *most excitable axon's region* at $x = 0$; see cathodic stimulation in Fig. 2.67e.

The shown ratio *non-linearly increases* with y^3 with increasing y, whereas the ratio obviously equals one at the *reference distance* $y = 2$ mm. To give a tangible example, when y is *halved* with respect to the reference distance—e.g., y decreases from 2 to 1 mm—the associated threshold I_{cat}^* decreases by a factor of 8. In contrast, *doubling the distance*—e.g., y increases from 2 to 4 mm—requires an 8-fold increase in I_{cat}^* .

Please note that this ratio is inversely proportional to the relative decrease of $f(x)$ with increasing y at the most excitable region $x = 0$. In fact, this ratio from Fig. 2.82b is valid for *current point sources*, as, for instance, applicable for *small surface or small implanted stimulation electrodes* from Fig. 2.67a or Fig. 2.81a, respectively.

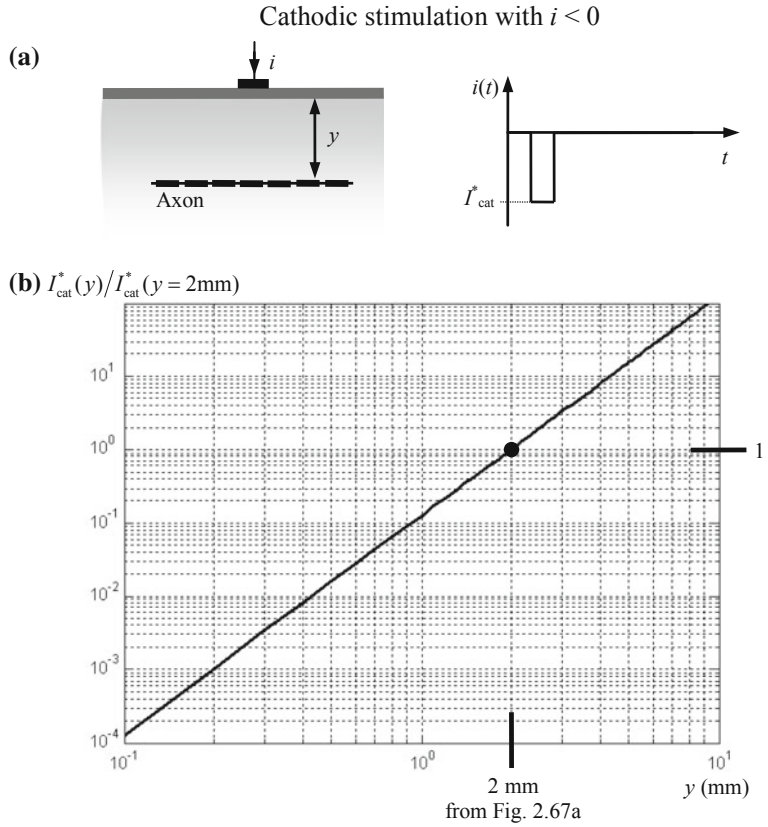

Fig. 2.82 Cathodic stimulation of unmyelinated and myelinated axons with the associated relative change of current thresholds over the distance y of the fiber from the electrode. **a** Surface monopolar stimulation electrode acts as a current point source, equivalent to Fig. 2.67a. A cathodal rectangular pulse with the threshold amplitude I^*_{cat} is applied. **b** Ratio of I^*_{cat} at the distance y to I^*_{cat} at y = 2 mm non-linearly increases with y

Monopolar, Bipolar, and Tripolar Modes

Practical applications in recording and stimulation can typically use not only one but also a few electrodes close to biological tissue being sensed or stimulated, respectively. Therefore, it is important and highly instructive to consider advantages and disadvantages of the resulting different *recording and stimulation modes*. In particular, the discussed concept of the *activating function* $f(x)$ proves to be very useful here (Fig. 2.67).

Monopolar Mode

In *monopolar recording mode*, circulating electrical current or present voltage is sensed between an *active electrode near to biological tissue* being *monitored* and another *remote ground electrode*. The ground electrode is also known as *return electrode or reference electrode*. The ground electrode should be located within a

bioelectrically inactive area as far away from the monitored tissue as possible so that sensed current or voltages are not influenced by bioelectric behaviour of tissues close to the ground electrode; the exact position of the ground electrode is immaterial.

In analogy, *monopolar stimulation mode* applies a current or voltage between an *active electrode* near to biological tissue to be *stimulated* and a *remote ground electrode*. Figure 2.75d illustrates a typical monopolar stimulation setting with surface skin electrodes acting as active and ground electrodes, whereas the axon to be stimulated is located beneath the active electrode.

As an *advantage* of the monopolar stimulation mode, the current needed for an effective stimulation is relatively low if compared with bipolar or tripolar modes (see below). That is, the associated *stimulation current threshold* is relatively low. As a *disadvantage*—in terms of either recording or stimulation—the *spatial averaging or spatial spread* of recorded or applied biosignals, respectively, is greater than in bipolar or tripolar modes. In fact, the *averaging and spread* are undesirable if we want to listen to and target at, respectively, small and confined groups of nerve or muscle fibers.

Thus there is a *compromise* between the *local strength of stimulation* and the *spatial width of the depolarized region*:

- while the *strength* is proportional to the *amplitude* of $f(x)$ at the depolarized local region x (where $f(x) > 0$),
- the *spatial width* of the depolarized region is determined by the *interval size* Δx of x values (again, obeying $f(x) > 0$).

Figure 2.83 illustrates this compromise (as also discussed below).

In addition, the *electrode size* can be favourably varied to *control the recruited volume* of fibers. For highly selective and regionally restricted stimulation under the *active electrode*, the size of this electrode should be reduced in order to increase the local *current density* (2.23) and the associated excitatory electric field right under the electrode. On the other hand, the size of the *ground electrode* should be increased to avoid activation of fibers under the ground electrode. Please recall that the position of the active electrode with respect to the fiber, especially *myelinated fiber*, has also a strong influence on its excitability (Footnote 93).

Bipolar Mode

In *bipolar recording mode*, circulating electrical current or present voltage is sensed between an *active electrode* and a *return electrode*, *both electrodes located near the target tissue* (Fig. 2.75e). This electrode setting is also known as *dipole electrode*. In analogy, *bipolar stimulation mode* passes current or applies voltage between these two electrodes close to each other.

Therefore, the current sensed or applied is confined to a rather small tissue region so that a *fine spatial control* of the monitoring or stimulation region, respectively, can be obtained. Figure 2.83 confirms this in that the depolarized region for *bipolar mode* in Fig. 2.83b (with $\Delta x \approx 2.5$ mm for $f(x) > 0$ and the *cathode-anode distance* $d = 1$ mm) is more narrow than that for *monopolar mode* in Fig. 2.83a ($\Delta x \approx 2.8$ mm > 2.5 mm). Likewise, an *unwanted stimulation* of distant

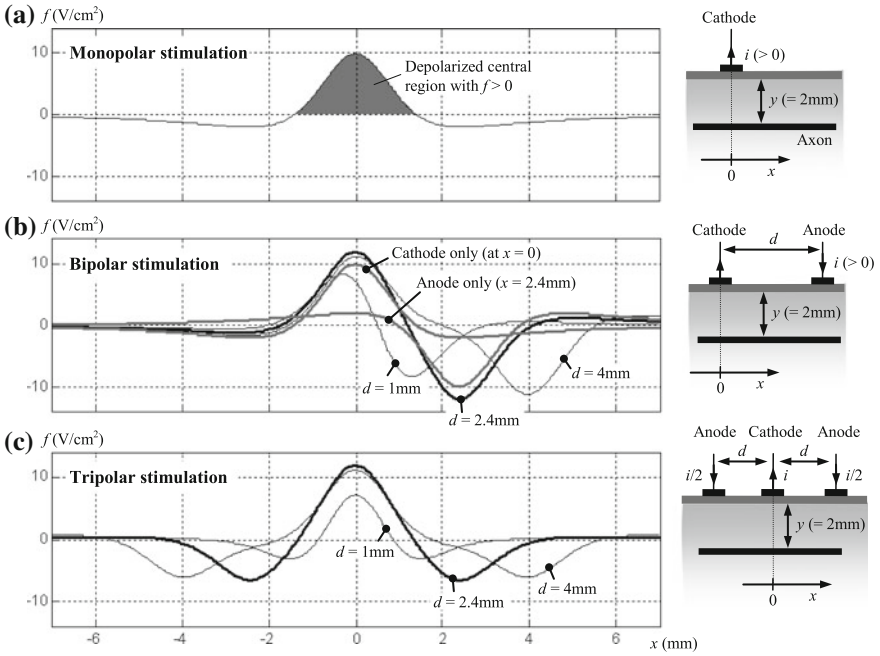

Fig. 2.83 Activating functions $f(x)$ of unmyelinated fiber for **a** monopolar stimulation (with a remote anode, identical with Fig. 2.67e), **b** bipolar stimulation (cathode and anode separated by the varying distance d), and **c** tripolar stimulation (with varying d); compare Fig. 2.75d–f. Current stimulation electrodes reside on the flat skin surface. The unmyelinated axon lays in parallel to the surface at the depth of 2 mm. $f(x)$ for bipolar and tripolar modes are calculated by superposition of $f(x)$ of single electrodes (2.153). Numerical estimation assumes i = 1 mA and the homogeneous isotropic tissue conductivity γ = 0.2 S/m (Table 2.2)

excitable neuromuscular structures can be advantageously *avoided* in praxis when selecting *proper mode and appropriate d*. In general, small electrodes applied close to each other activate primarily superficial tissue layers, whereas electrodes placed farther apart tend to activate deeper layers (compare Kaniusas (2015, Eq. 5.26)).

As already mentioned, the *stimulation threshold* is typically higher for bipolar than monopolar mode. This is illustrated by lower maximum values of $f(x)$ (>0) for bipolar mode (in Fig. 2.83b with d = 1 mm) than monopolar mode (Fig. 2.83a) given a *relatively small d*. In other words, the small d implies a local overlap of depolarizing effect from one electrode and hyperpolarizing effect from another electrode (*destructive superposition*)—compare Fig. 2.67e, f—which effectively reduces the total local depolarization and thus increases the associated stimulation threshold of bipolar mode. For larger values of d, the threshold can even decrease (*constructive superposition*), as discussed below.

Tripolar Mode

Tripolar recording and stimulation modes have also been proposed. For instance, *tripolar stimulation mode* is illustrated in Fig. 2.75f in which a current of one polarity is applied on a central electrode and usually half the *return current* of the opposite polarity on two adjacent electrodes.

Tripolar stimulation has been shown to provide a more focussed, spatially selective stimulation than bipolar stimulation but, however, at the cost of a reduced stimulation efficiency (Fallon 2016). Therefore, the *stimulation threshold* is higher for tripolar mode as related to monopolar and bipolar modes. Eventually, the *return current* can also be shared between the two adjacent electrodes and another distant ground electrode in order to widen the stimulation focus if needed.

For instance, Fig. 2.83c with $d = 1$ mm illustrates a highly *focussed* but rather *weak depolarization* for *tripolar mode*, as can be derived from a narrow $\Delta x \approx 1.7$ mm (for $f(x) > 0$) but a low maximum peak of $f(x)$ of only 7.1 V/cm^2. In contrast, a rather *blurred* but *strong depolarization* can be observed for *monopolar mode* in Fig. 2.83a, characterized by a wide $\Delta x \approx 2.8$ mm (for $f(x) > 0$) but a high maximum peak of $f(x)$ of about 10 V/cm^2.

Superposition of Activating Functions

Figure 2.83 compares *monopolar*, *bipolar*, and *tripolar stimulation modes* based on their $f(x)$. Stimulation electrodes are located on the skin surface carrying identical stimulation current i (=1 mA); compare Fig. 2.75d–f. Electrodes are assumed to be relatively *small* with respect to the axon's depth y below the surface so that electrodes approximately act as *current point sources* (with the half-spherical surface, see Section "Axon Thickness and Its Distance to Electrode"). While the depth y (=2 mm, in analogy with Fig. 2.67a) within *homogeneous isotropic tissue* is constant for all compared modes, the *electrode distance d* between cathode and anode is varied from 1 mm, to 2.4 mm, to 4 mm for bipolar and tripolar modes.

The activating function $f(x)$ along the axis x of the axon for

- *monopolar mode* (Fig. 2.83a)—using a *single small electrode*—is calculated with equations from Fig. 2.67b (compare similar plots from Fig. 2.67e, f).
- *Bipolar and tripolar modes* (Fig. 2.83b, c) are estimated by geometric *superposition*[102] *of* $f_k(x)$ describing each displaced *single small electrode* (Rattay 1987). The effective *total f(x)* for the shown *bipolar mode* in Fig. 2.83b results as

[102]Please note that the *superposition principle* allows to consider and compare *arbitrary geometries of the stimulation electrodes* with respect to recruitment of fibers close to electrode(s). Namely, any geometrical type of electrode can be approximated by a number of single electrodes and thus by a *superposition of f(x)* from single electrodes [for bipolar case, see (2.153)]. For instance, a *ring electrode* around a bundle of fibers (around a nerve) can be reasonably compared in its recruitment efficiency with a single monopolar electrode close to the nerve or a *dipole electrode* encompassing the nerve (Rattay 1990).

$$f(x) = \sum_{k=1,2} f_k(x) = \sum_{k=1,2} \frac{i(t) \cdot (-1)^k}{\gamma 2\pi} \cdot \left(\frac{2(x - x_k)^2 - y^2}{\left((x - x_k)^2 + y^2\right)^{5/2}} \right). \quad (2.153)$$

Here γ is the tissue conductivity, whereas the displacement $x_1 = 0$ (at $k = 1$) considers the single cathode located at $x = 0$ and the displacement $x_2 = d$ ($k = 2$) the single anode located at $x = d$. Accordingly, grey waves in Fig. 2.83b illustrate $f(x)$ of the single cathode and single anode (dislocated by $d = 2.4$ mm) and their effective superposition yielding the total $f(x)$ drawn in black.

It is interesting to observe for *biphasic mode* in Fig. 2.83b that a *depolarizing maximum* of the total $f(x)$ down under the *cathode* (at the region $x = 0$) is spatially followed by a *hyperpolarizing minimum* of the total $f(x)$ down under the *anode* (at $x > 0$ depending on d). For *triphasic mode* drawn in Fig. 2.83c, an anodic minimum precedes a cathodic maximum followed by another anodic minimum, which is qualitatively in line with the arrangement of all three anode, cathode, and anode electrodes on the skin surface.

It is highly instructive that in the shown *bipolar case* an induced *action impulse* in the region of cathode can always *propagate in at least one direction*; i.e., the one-sided lateral hyperpolarization can only block propagation into one direction. In other words, when the cathodic stimulus is already in the higher *suprathreshold region*—e.g., at least eight times the threshold (see the discussed ratio I_{II} / I_I from Fig. 2.76b)—the discussed *cathodic block* does not strictly apply. There is no upper limit of i to excite the fiber using bipolar mode. In the simple case of *stimulation slightly over the threshold* without any blocking, the induced impulse experiences *bifurcation* and propagates in both directions.

In particular, the case in Fig. 2.83b shows that the induced action impulse can always escape to the left *away from the anode* irrespective of the stimulation strength, i.e., the level of i. The potentially strong *hyperpolarization* on the right side of the depolarized region *can block propagation* only to the right side *towards the anode*.

Consequently, *reversal of the stimulation current i* in bipolar mode leads to the same threshold behaviour but the *propagation direction* of impulses will be *reversed* if a *strong suprathreshold stimulus* is given. This may be relevant when an *alternating current* $i(t)$ is used.

The *superposition* (2.153) for bipolar case (Fig. 2.83b) makes also clear that a *maximum local depolarization* occurs when one of *lateral depolarized regions* of $f(x)$ from *anodic stimulus* (Fig. 2.67f) spatially overlaps with the *central depolarized region* of $f(x)$ from *cathodic stimulus* (Fig. 2.67e). Under the cathode, the anode electrode may add up to 20% (or one-fifth) to the total depolarization from the cathode electrode when the separation distance $d = 1.2 \cdot y = 2.4$ mm applies; compare the factor of five in Fig. 2.67.

In other words, there is an *optimal distance* $d = 1.2 \cdot y$ between cathode and anode for an axon to be *maximally stimulated* at the depth y. Please note that this

optimal d depends on y. Likewise, the local intensity of the axon depolarization can be varied by varying d, as illustrated by Fig. 2.83b.

It can also be observed from Fig. 2.83b that for $d \gg y$, *depolarization* is maximal at the position of *cathode* while *hyperpolarization* is maximal at the position of *anode*. Please observe $f(x)$ for the largest $d = 4$ mm ($\gg y = 2$ mm) with its resulting bipolar peaks. In practical terms this means that if the axon depth y is much less than the regional displacement d of anode and cathode, the discussed *superposition* can be neglected and both electrodes can be independently considered in their effects on the axon.

It is important to recognize that the *width* Δx *of the depolarized region* (for $f(x) > 0$) tends to decrease with decreasing d (Fig. 2.83b). A spatially *focussed stimulation* (small Δx) occurs at the expense of a reduced *stimulation strength* (reduced $f(x)$); see the aforementioned compromise. For instance, when d gets smaller from 2.4 mm down to 1 mm, the range Δx decreases from $\Delta x \approx 2.9$ mm to 2.5 mm while the maximal depolarizing amplitude of $f(x)$ decreases from about 12 to 8.3 V/cm^2.

Tripolar mode is demonstrated in Fig. 2.83c. In analogy with bipolar mode, it confirms a more focussed stimulation with decreasing d at the cost of a reduced stimulation efficiency. A greater stimulation current i is generally needed when focussed stimulation is aimed at. Again, a compromise has to be found between focus sharpness and stimulation efficiency.

Finally, a case should be shortly considered where the *distance y to an axon* is different for multiple electrodes carrying the same stimulation current. This case, for instance, is applicable for *multiple implanted electrodes* close to the axon to be stimulated (compare Fig. 2.81a). It turns out that a distant electrode with its y about three times of y of another near electrode *can be neglected* (Rattay 1987) since the *distant electrode* contributes only very little to the geometrical superposition result (2.153). In particular, $f(x)$ of each single electrode is subjected to a strong decrease with y according to $f(0) = -i(t)/(2\pi\gamma \cdot y^3)$; compare (2.152).

Direct Current

Neuromuscular excitation requires a certain *dynamic in the stimulus* to circumvent various effects in excitable structures, which are attributed to decreased excitability for too slow dynamic and for too fast dynamic of the stimulus (Fig. 2.74). In contrast, *thermal interaction* does not require any dynamic, the interaction depends mainly on the effective value of the stimulus (Section "Thermal Stimulation Effects").

Therefore, a steady stimulus, a continuous *direct current*, can not stimulate excitable cells. However, an *onset or interruption* of the direct current permeating tissue can still lead to temporary *neuromuscular effects*. A relatively quick and strong change in the current amplitude is required to exceed stimulation thresholds. For instance, the current's onset and interruption can lead to a transient tingling sensation. This is in full contrast to *alternating currents* which can stimulate excitable tissues throughout the *whole exposure duration* provided that the relevant

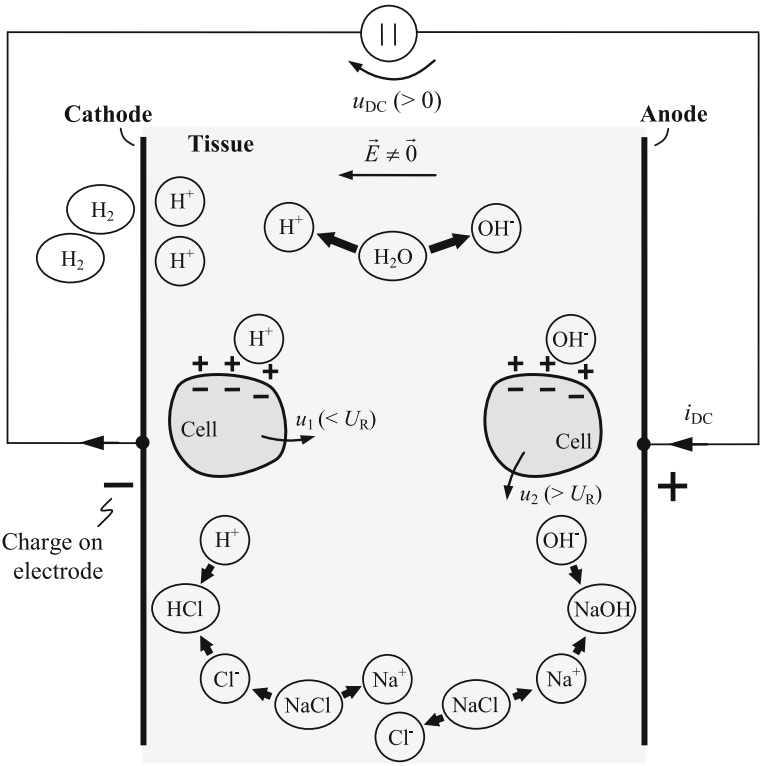

Fig. 2.84 Excitability-related and electrolytic effects of the imposed direct current i_{DC} between two electrodes, anode and cathode. Both electrodes enclose biological tissue with embedded excitable cells and their membrane voltage u (with $u = U_R \approx -70$ mV in the resting state). The excitability of cells is increased at the anode while it is decreased at the cathode. Weak dissociation of water molecules ($H_2O \leftrightarrow H^+ + OH^-$) and strong dissociation of table salt ($NaCl \rightarrow Na^+ + Cl^-$) in tissue (Footnote 29)—combined with electrostatic forces due to accumulated charges on electrodes (compare Fig. 2.16b)—lead to formation of the acid H^+Cl^- ($=H^+ + Cl^-$) below the cathode and the base Na^+OH^- ($=Na^+ + OH^-$) below the anode. The reactive acid and base can irritate and damage tissue

thresholds are exceeded. Please note that the threshold depends on many contributing factors, as discussed with respect to Fig. 2.88. *Thermal effects* persist also throughout the *whole exposure duration* of tissue to direct currents.

Gradual changes in the amplitude of the *direct current* yield rather sensations of *internal heating*. *Sudden changes* of this amplitude—including its interruptions—usually produce *neuromuscular effects* such as muscular contractions or even severe shock.

Cathodal Make and Anodal Break

When the *electrical circuit* carrying the *direct current* is closed, i.e., the current starts to flow, *neuromuscular stimulation* can occur

- at the *onset of the direct current* in the regions close to the *cathode electrode*, which is known as *cathodal make*. In contrast,
- when the circuit is opened and the direct *current ceases*, the stimulation is likely in the region of the *anode electrode*, known as *anodal break*.

The *cathodal make* can be derived from *extracellular stimulation* in which the cathodic current stimulus depolarizes—and excites if local thresholds are exceeded—axon regions residing closest to the current electrode (Fig. 2.67c, e, g).

The *anodal break* is less obvious. As any excitation, the anodal break is based on a *transient depolarization* of excitable structures under the electrode. Please recall that before the circuit is opened or disconnected, the continuous *anodic current* hyperpolarizes excitable cells right under the anode (Fig. 2.67d, f, h). In particular, *hyperpolarization* opens the *slow inactivation gates* of the *voltage-gated* Na^+ *channels* within the membrane (Kaniusas 2012, Footnote 39). When now the hyperpolarizing anodic current is abruptly terminated, the voltage-controlled and *fast activation gates* of the *voltage-gated* Na^+ *channels* quickly increase the inflow of Na^+ ions back to the level of the membrane's *resting state*. However, the *slow inactivation gates* still remain open for a longer time due to their inertness (Lee 2016). In total, the resulting *net conductance of* Na^+ inwards into the cell is briefly higher than the conductance of Na^+ in the resting state, which means that the membrane depolarizes and a potential neuromuscular excitation may follow. In addition to the depolarizing effect of the accelerated recovery of the voltage-gated Na^+ channels, a decreased conductance of the *voltage-gated* K^+ *channels* during hyperpolarization contributes to the aforementioned *transient depolarization* and thus to the anodal break (Reill 1998).

In other words, when the hyperpolarizing *anodic current ceases*, the membrane *hyperpolarization breaks down*. The local hyperpolarizing current (inward current) through the membrane must reverse its direction to dismantle hyperpolarization; the *hyperpolarizing current* reverts to a *depolarizing current* (outward current). If this depolarizing current is strong enough, neuromuscular excitation can originate in terms of the anodal break.

Please note that *cathodal make* and *anodal break* can be *prevented* by avoiding abrupt termination of the current. Here exponential or trapezoidal shapes have been successfully used in electrotherapy.

Excitability of Cells

Direct currents may yield other manifold effects (Leitgeb 2010), as illustrated in Fig. 2.84. In particular, the direct current may change *excitability of cells* (Footnote 88) which reside in the *vicinity of current electrodes*.

Please recall that the applied direct current via two electrodes surrounding a section of biological tissue creates a *direct electric field* inside tissue, as shown in Figs. 2.16a and 2.84. In response to this field, *unbound ionic charges* start to *move*

unidirectionally and continuously within tissue (Footnote 25). For instance, *positive H^+ ions* (from the water autodissociation $H_2O \leftrightarrow H^+ + OH^-$, although very weak in line with Footnote 29) follow the electrostatic attraction force and tend to accumulate at the *negative electrode*, cathode (Fig. 2.84). The corresponding *negative OH^- ions* tend to accumulate at the *positive electrode*, anode.

Consequently, *excitable cells* within tissue in the region of

- *cathode* become surrounded by *positive ions* (Fig. 2.84). The *excess* of positive charges in the *extracellular space* decreases the membrane voltage u ($=U_R \approx -70$ mV in the resting state) to even more negative values ($u_1 < U_R$ at the cathode in Fig. 2.84). Please recall that u across the cell membrane is defined as the potential difference between the intracellular and extracellular spaces (Kaniusas 2012, Fig. 2.6). A weak *hyperpolarization* of the membrane results that implies a *reduced excitability* of the affected cells residing close to *cathode* (*cathodic inhibition*). Excitable cells in the region of
- *anode* become surrounded by *negative ions* (Fig. 2.84). The *excess* of negative charges in the *extracellular space* increases the absolute u to more positive values ($u_2 > U_R$ at the anode in Fig. 2.84). A weak *depolarization* of the membrane results that implies an *increased excitability* of the affected cells residing close to *anode* with a *reduced excitation threshold*. In other words, the *responsiveness* to any stimuli is *increased* (*anodic excitation*[103]).

Electrolytic Effects

The *direct current* drives otherwise non-spontaneous chemical reactions at the *electrode surface* permeated by this current, known as *electrolytic effects*. In particular, electrolytic effects are relevant for electrodes in contact with *biological tissue*. Section "Ag/AgCl and Pt Electrodes" as well as Fig. 3.13 up to Fig. 3.15 provide a lot of relevant examples on electrolytic effects at the electrode/tissue boundary and their scientific background.

As illustrated in Fig. 2.84, the aforementioned *movements* of ionic charges H^+ and OH^- towards the cathode and anode, respectively, and their likely *reactions* with chemical counterparts under electrodes contribute to relevant *electrolytic effects* within tissue. At *cathode*, H^+ ions are bound to Cl^- ions—please note that Cl^- ions are reaction products of the table salt NaCl dissociation in tissue (Footnote 27)—and produce the hydrochloric *acid* HCl. At *anode*, OH^- ions are bound to

[103]These *excitability-related effects* of *direct currents* are applied in different *therapeutic* settings (Footnote 88). To give a few practical examples, the excitability of receptors (nerve cells) is reduced on purpose in the *pain relieve therapy* using direct currents. On the other hand,

- *anodic excitation* and
- *cathodic inhibition*

are suggested as the relevant mechanisms acting on the brain neurons in terms of the *clinical neuromodulation* within the scope of the *transcranial direct current stimulation*. Here electrodes are applied to specific locations on the scalp for the direct current application to treat depression, chronic pain, craving, or even improve cognitive function.

Na^+ ions and yield the sodium hydroxide *base* NaOH.[104] The produced acid and base can *damage biological tissues* close to electrode surfaces, especially in the *long-term current application* and even in the course of *small direct currents* (Leitgeb 2010).

In addition, accumulated H^+ ions within tissue below cathode may *outgas as* H_2 gas into the air (Fig. 2.84) and may even form a potentially explosive mixture of H_2 and O_2 (oxyhydrogen). These disadvantageous electrolytic effects are especially relevant for diverse *therapeutic applications* such as radiofrequency surgery, galvanic baths, or iontophoresis, in which a direct current is actively applied on the body.

Thermal Stimulation Effects

Please recall that *neuromuscular stimulation effects* are determined by both *properties of excitable tissue* and *stimulus properties*. As relevant stimulus properties, the delivered *electric charge* mainly governs electrostimulation for short pulses of stimulus, whereas the *current amplitude* governs stimulation for long pulses. Here the particular *waveform* of stimulus as well as its *instantaneous frequency* are of major importance, but not the *electrical energy of stimulus*.

In fact, this latter insight related to the energy of stimulus is supported by the *strength-duration curve* of the threshold *stimulus energy* [proportional to $(I_T)^2 \cdot T$, see (2.148)] over the *phase duration* T of stimulus. This curve for $(I_T)^2 \cdot T$ over T typically shows a minimum—located at $1.25 \cdot \tau$ for a simple RC membrane model from Fig. 2.63a—and not a gradual change, as observed in the case of the strength-duration curve (Fig. 2.71b) for the threshold current I_T over T (2.148) and for the threshold charge $I_T \cdot T$ over T (2.149). The non-gradual behaviour of the threshold energy $(I_T)^2 \cdot T$ excludes the stimulus energy as a primary metrics for electrostimulation but indicates its usability as a secondary metrics for the design of energy-efficient waveforms (e.g., to reduce battery demands).

In the case of *thermal effects*, again,

- stimulus properties and
- properties of exposed tissue

are major determinants (Footnote 115). In terms of *stimulus properties*, the *stimulus energy* is of *primary importance*, in clear contrast to neuromuscular stimulation. Please recall from Footnote 86 that thermal excitation of tissue requires much more energy than electrical excitation.[105]

---

[104] Please note that there is (must be) also an *inverse neutralization reaction* in which acid HCl and base NaOH react and form again salt NaCl and water H_2O in line with HCl + NaOH → NaCl + H_2O.

[105] To provide some perspective in the *comparison of the thermal and electrical excitation of tissue*—in addition to their comparison in Footnote 86—let us *estimate* P_{SAR} as needed for a *temperature increase* $\Delta\vartheta$ *of 1* °C *in tissue*, i.e., as needed for a significant *thermal impact*, and compare it with

Since the delivered power or energy of stimulus is directly proportional to the square of the root mean square value (or the *effective value*, see Footnote 34) of stimulus (2.58), the *effective value* determines thermal responses of the exposed tissue. For instance, in the case of current application to tissue, the effective value of the current stimulus governs *temperature increase* within tissue. The *frequency of stimulus* is of *secondary importance* for thermal stimulation. Consequently, *perception thresholds for neuromuscular stimulation* are rather frequency-dependent, whereas *perception thresholds for thermal stimulation* are not (see the plateau above 100 kHz in Fig. 2.88).

In terms of exposed *tissue properties* determining thermal effects, the *effective conductivity* γ_{eff} (2.82) is the relevant parameter for power deposition and heating of tissue (2.58). In particular, the conductivity γ_{eff} accounts not only

- for *conductive losses* but also
- for *dipolar dielectric losses*,

both being involved in the power deposition within tissue. Namely, the effective γ_{eff} considers ionic *conductive currents* due to directional and/or oscillatory motions of loosely bound or even *unbound charges* in tissue (2.53), whereas the associated *losses* are generated by obstructed movements of these unbound charges (2.54). In addition, γ_{eff} considers *displacement currents* in the course of lossy tissue polarization due to oscillatory motions of *bound charges* (2.82), whereas the associated *losses* are generated by friction between continuously reoriented bound charges (dipoles) at and close to the relaxation frequency. In short, *local lossy currents* cause *local energy deposition* and thus *local tissue heating*.

At *low frequencies heat* in tissue is due to losses in the course of *conductance* currents; see the region with $\gamma_{\text{eff}} \approx \gamma$ in Fig. 2.21. In contrast, at *high frequencies relaxation processes* determine generation of heat; see the region where $\gamma_{\text{eff}} \approx \Delta\gamma$ applies in Fig. 2.21.

---

another P_{SAR} as derived from the *basic restrictions* of the inner electric field (13.5 V/m at 100 kHz, see Fig. 2.87) to avoid the *electrical excitation* of tissue. It should be stressed that these basic restrictions indicate sub-threshold levels of the electrical excitation. In addition, the chosen level of 13.5 V/m (at this relatively high frequency) indicates rather a *worst-case scenario* for this comparison since endogenous thresholds for local nerve stimulation are usually below 10 V/m (though, for much lower field frequencies, see Section "Electrical Stimulation Effects").

That is, the needed level of P_{SAR} for $\Delta\vartheta = 1$ °C of muscular tissue (with $c = 3.6$ W · s/(K · g) according to Footnote 107) over a relatively short time interval $\Delta t = 1$ s of energy deposition amounts to $c \cdot \Delta\vartheta/\Delta t = 3.6$ W/g. Here an assumption was met that all the absorbed energy in tissue is transformed into heat, while the relatively inert *thermoregulatory mechanisms can be neglected* during this short time period $\Delta t = 1$ s; see Footnote 106. On the other hand, in analogy with Footnote 86 and (2.57), the upper threshold of P_{SAR} to avoid the *electrical excitation* amounts to 0.06 W/kg = $6 \cdot 10^{-5}$ W/g (at 100 kHz).

This obvious inequality of both values 3.6 W/g and $6 \cdot 10^{-5}$ W/g shows that the resulting $\Delta\vartheta$ in the case of the electrical excitation only would be extremely low (in the order of only $2 \cdot 10^{-5}$ °C ≈ 1 °C · $6 \cdot 10^{-5}$/3.6). This comparison underlines much *larger energies* involved in *thermal excitation* as related to *electrical excitation*.

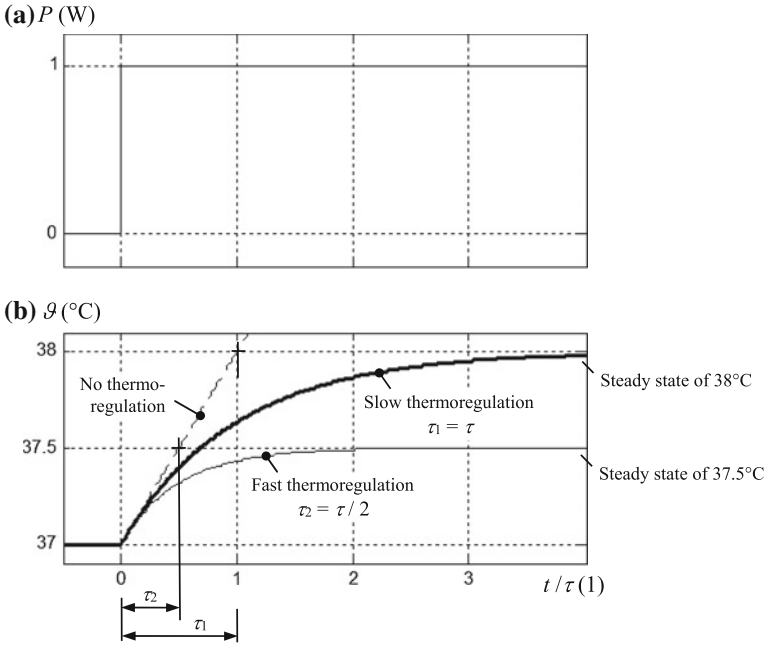

Fig. 2.85 Thermoregulatory response of biological tissue. **a** A step-wise supply of the electromagnetic power P into tissue as a thermal stimulus. **b** The resulting increase in the tissue temperature ϑ is shown in response to this stimulus, whereas a steady state of ϑ (=37 °C) is assumed before the stimulus is applied ($P = 0$ and $\vartheta = 37$ °C for $t < 0$); compare Fig. 2.48c. The linear increase in ϑ results for missing thermoregulatory mechanisms; i.e., passive tissue is heated, see Footnote 106. The non-linear increase in ϑ results for relatively slow and fast thermoregulatory mechanisms; i.e., heat is applied to tissue with its active thermoregulatory response, see Footnote 107. In fact, the slow mechanisms show smaller product $A \cdot \alpha$ (Footnote 107), larger time constant $\tau_1 = \tau$, and larger steady-state level of ϑ during the persistent stimulus as related to fast thermoregulatory mechanisms with $\tau_2 = \tau/2$

Please note that while some *thermal effects* in biological tissues mainly depend on

- the local *absolute temperature-time profile* as induced in tissue (i.e., an increase in the local temperature, see Fig. 2.85b), other thermal effects depend on
- the local *rate of the temperature change* with a negligible rise in the local absolute temperature (e.g., *microwave hearing*, see below).

Passive Tissue

To start with detailed considerations of thermal effects, let us start with a *passive homogeneous tissue* exposed to electrical stimulus. Any active *thermoregulatory mechanisms* on the vascular and metabolic level are assumed to be *negligible* (Footnote 107).

The relationship between the magnitude J_E of the conductive *current density* permeating passive tissue and the resulting increase $\Delta\vartheta$ in the *tissue temperature* ϑ generated by this current can be easily derived from (2.58), to give

$$J_E^2 = \gamma_{eff} \cdot \rho \cdot P_{SAR} = \gamma_{eff} \cdot \rho \cdot c \cdot \frac{\Delta\vartheta}{\Delta t} \quad \text{and} \quad J_E \propto \sqrt{\Delta\vartheta} \tag{2.154}$$

using

$$\Delta W = m \cdot c \cdot \Delta\vartheta = P_{SAR} \cdot m \cdot \Delta t \tag{2.155}$$

Here ρ is the tissue density, c the specific heat capacity of tissue, m the mass of the homogeneously exposed tissue, P_{SAR} the specific energy absorption rate, and ΔW the submitted/induced heat over the time interval Δt. Equation (2.155) assumes[106] that the total submitted electrical energy $P_{SAR} \cdot m \cdot \Delta t$ is stored as the inner heat $\Delta W = m \cdot c \cdot \Delta\vartheta$ in tissue; please consider Footnote 107 with P_{SAR} instead of P/m.

It is instructive that the temperature ϑ increases in proportion to P_{SAR} but neither in proportion to J_E nor in proportion to the magnitude E of the inner electric field. There is a non-linear relationship between P_{SAR} and J_E and, on the other hand, between P_{SAR} and E (2.58). Therefore—in the worst case without thermoregulation limiting $\Delta\vartheta$ in tissue—the *maximum* $\Delta\vartheta$ *is highly disproportional to both* J_E *and* E (2.154). It should be recalled that J_E and E are interrelated via the scaling factor γ_{eff} (2.81).

The greatest *rise in* ϑ occurs in regions of highest J_E or *lowest cross-section areas* (2.23) the current passes through, such as ankles or wrists (compare narrow arm and wide abdomen in Fig. 2.57). Likewise, an increased area of the skin contact will require an increased current to produce the same local rise in the tissue's ϑ (e.g., for therapeutic aims).

---

[106] If the *heat transfer mechanisms* are relatively slow or heat losses due to *thermoregulatory mechanisms* in tissue *can be neglected* (e.g., as always applicable for a short time period $t \to 0$; in practice, it may be up to a few minutes in hyperthermia treatment (Furse 2009)), then the local P_{SAR} (2.57) is simply proportional to the *initial rate of local temperature increase* $\Delta\vartheta$, to give

$$P_{SAR} = c \cdot \left.\frac{\Delta\vartheta}{\Delta t}\right|_{t \to 0}.$$

Here c is the specific heat capacity of tissue. Figure 2.85b demonstrates a *steady increase of* $\Delta\vartheta$ over time given *constant* P_{SAR} [$=P/m$, see (2.57)] and missing thermoregulatory mechanisms. This approximation can be easily derived from Footnote 107 and can be used for the *experimental* P_{SAR} *estimation*.

In particular, the latter approximation applies for a relatively short period Δt of applied current or voltage pulses—e.g., for tissue healing—and thus allows for a simple *estimation of the resulting temperature change* $\Delta\vartheta$ without considering complex thermoregulatory mechanisms.

Active Tissue

However, the submitted ΔW is not only accumulated in tissue but also transported away[107] via *active thermoregulatory mechanisms*. In fact, heating of a local part of

[107]Considering *electrobiological interactions*, it is interesting to observe that the induced *heat* ΔW is

- *accumulated* within the exposed tissue, and, on the other hand,
- *actively transported* away from the local site of impact to maintain *local homeostasis* of the exposed site and to maintain *global homeostasis* of the whole body; compare Section "Thermal Stimulation Effects", (Kaniusas 2012, Sect. 3.1.5) as well as Footnote 115 and Footnote 4 in Chap. 3.

The accumulated heat increases primarily the tissue temperature ϑ by $\Delta\vartheta$; compare Footnote 106. As the time t passes, the local *blood perfusion* increases and transports a part of the induced heat away from the impact site. Thus, the regulatory *vasodilation of vessels* in tissue (Kaniusas 2012, Footnote 130)—with their contact area A (or heat exchange area) penetrating the tissue volume—performs important *thermal regulatory functions*, preventing overheating of tissue and balancing and limiting its local ϑ.

The sum of the accumulated heat (proportional to $\Delta\vartheta$) and the transported heat (proportional to the product $\vartheta \cdot \Delta t$) can be expressed as

$$\Delta W = m \cdot c \cdot \Delta\vartheta + \alpha \cdot A \cdot \vartheta \cdot \Delta t$$

or, as a *differential equation*,

$$\frac{\mathrm{d}W}{\mathrm{d}t} = m \cdot c \cdot \frac{\mathrm{d}\vartheta}{\mathrm{d}t} + \alpha \cdot A \cdot \vartheta,$$

where m is the mass of the exposed tissue, c the specific heat capacity, and α represents a measure of the blood flow velocity in (regulatory) dilated vessels. In fact, increasing both A and α facilitates the thermal regulation in tissue, whereas the resulting *time constant* τ of regulatory processes is determined by the following ratio, to give

$$\tau = \frac{m \cdot c}{\alpha \cdot A}.$$

As can be derived from the *differential equation*, a *step-wise supply* of the (heat-inducing) *power* $P \cdot \varepsilon(t)$ (=$\mathrm{d}W/\mathrm{d}t \cdot \varepsilon(t)$) into biological tissue with $\varepsilon(t)$ as the Heaviside step function (i.e., $\varepsilon(t) = 0$ for $t < 0$ and $\varepsilon(t) = 1$ for $t \geq 0$) yields the *exponential increase of* ϑ in tissue according to

$$\vartheta(t) = \frac{P}{\alpha \cdot A} \cdot \left(1 - \mathrm{e}^{-t/\tau}\right) \cdot \varepsilon(t);$$

compare Kaniusas (2012, Footnote 29) and Fig. 2.85. Likewise, this *step response* $\vartheta(t)$ (Fig. 2.85b) as a response of tissue residing in its *zero initial state*—i.e., the response of the resting tissue with its temperature $\vartheta(0) = 37$ °C—to a *step input* $P \cdot \varepsilon(t)$ (Fig. 2.85a) can be easily derived from the above equation. The tissue is considered here as a system with a single input $P \cdot \varepsilon(t)$ and a single output $\vartheta(t)$.

Please note that the *initial rate* $\mathrm{d}\vartheta/\mathrm{d}t$ of the temperature increase in tissue is *proportional to* P, see Footnote 106. In particular, the resulting $\mathrm{d}\vartheta/\mathrm{d}t$ is inversely proportional to c of the exposed tissue. That is, the higher c, the lower is the resulting rate $\mathrm{d}\vartheta/\mathrm{d}t$ because more thermal energy can be uptaken by tissue with higher c (for a given change in ϑ). For instance, this initial rate $\mathrm{d}\vartheta/\mathrm{d}t$ is less in *muscle* than in *fat* because the heat capacity c of muscle is larger than fat (3600 versus

the body and/or the whole body by deposition (absorption) of the electromagnetic energy from any external artificial source (or even due to solar radiation) tends to

- increase the *local body temperature* and/or *core body temperature* related to the whole-body (Kaniusas 2012, Sect. 3.1.5). In parallel,
- *thermoregulatory responses* are provoked by ΔW to *limit increase in the temperature* and to maintain *homeostasis* in the body (Footnote 4 in Chap. 3) through dissipation of the thermal load without unduly stressing local and global physiological systems involved.

In fact, *homeostasis* is the condition necessary for proper and stable functioning of the body. Thermoregulatory responses minimize the heat load on the body and counteract acute exposure (Footnote 107). Typically this response depends on ambient conditions, e.g., the *active response threshold* is reduced at increased ambient temperatures.

Thermoregulatory responses counteract the *proportional increase* in the tissue temperature with the passing of time in response to the submitted or deposited heat (2.155). In particular, thermoregulatory mechanisms lead to a *disproportionately smaller increase* in the *temperature*, as could be derived from the *exponential increase* of the temperature when tissue is subjected to a *step-wise supply* of the power P (Footnote 107).

Figure 2.85 illustrates how thermoregulatory responses *limit increase in the tissue temperature* (Fig. 2.85b) in response to a step-wise supply of P (Fig. 2.85a). Here the temperature reaches its plateau after a few *time constants* τ (e.g., after $5 \cdot \tau$, see Footnote 107 for definition of τ). This is in clear contrast to the case without thermoregulation showing a *proportional increase* without any steady state given a non-zero incident power. Therefore, thermoregulation is an *inert process* with a non-zero τ, which needs a certain time to develop. In particular, the local slope of the exponential increase, i.e., the rate of increase, decreases with increasing time (Fig. 2.85b).

2000 W · s/(K kg) according to Pfützner (2003). The rate $d\vartheta/dt$ decreases as t increases—see Fig. 2.85b—because the (inert) *thermoregulatory responses come progressively into action*, i.e., the local slope of the exponential increase decreases with increasing t.

Time courses in Fig. 2.85b confirm such behaviour in that the local slope of the tissue response *without any thermoregulatory mechanisms* is constant over t; i.e., ϑ steadily increases over t. In contrast, the local slope of the tissue response with *active thermoregulatory mechanisms* (slow and fast) decreases over t. That is, the final ϑ plateaus over t if thermoregulatory mechanisms are strong enough to counter-balance the artificially delivered heat power $P \cdot \varepsilon(t)$.

In particular, the thermoregulatory response such as vasodilation causes the *temperature rise* $d\vartheta/dt$ to be *non-linear* over t. The temperature rise is *linear* (Footnote 106) before vasodilation increases the blood flow to a level high enough to reduce the rate $d\vartheta/dt$ of the temperature rise; this linear range may last up to a few minutes after a hyperthermia treatment has been started (Furse 2009). Given a continuous power supply into tissue and following a time interval of a few τ (e.g., after $5 \cdot \tau$), the blood flow reaches its *steady-state response*, the temperature rise $d\vartheta/dt$ converges to zero, and the temperature ϑ itself plateaus at a steady-state level of $\vartheta(t \to \infty) = P/(\alpha \cdot A)$; see Fig. 2.85b and the last equation from above.

Figure 2.85b compares *slow and fast thermoregulation*, differing in their respective product $A \cdot \alpha$ which considers the area A for the *heat exchange* and the factor α proportional to the blood flow velocity (Footnote 107). All A, α, and $A \cdot \alpha$ favour the efficiency of thermal regulation. The *slow thermoregulation* exhibits a smaller $A \cdot \alpha$ due to *sparse vascular network* involved in thermoregulation. The smaller $A \cdot \alpha$ implies a larger *time constant* $\tau_1 = \tau$ and a larger steady-state end value (Footnote 4 in Chap. 3) of the tissue temperature for a still persisting power deposition in comparison with the *fast thermoregulation* based on *dense vascular network* with $\tau_2 = \tau/2$ (for relevant equations consult Footnote 107). For instance, *muscle* with its dense vascularization tends to have a larger $A \cdot \alpha$ than *fat* with its sparse vascularization. Please recall that τ also depends on the *specific heat capacity* which is larger for muscle than fat.

Thermoregulatory mechanisms are composed out of

- *physiological responses* and
- *behavioural responses*,

including thermal conduction of the local heat to adjacent tissues, convection, and/or radiation (Kaniusas 2015, Footnote 3 in Chap. 5). These mechanisms usually target *conduction of the inner body heat to the body surface* for both the body cooling and for the heat dissipation into the environment. In particular, *physiological responses* of thermoregulatory origin include the following

- increased *blood perfusion* in the skin through vasodilation (in line with decreased total peripheral resistance, see (Kaniusas 2012, Eq. 2.20)) leading to increased thermal conductance of the skin;
- initiated *sweating* also favouring thermal conductance of the skin;
- increased *heart rate* improving blood flow (Kaniusas 2012, Eq. 2.30) and thus improving heat exchange between the blood flow and environment across the skin barrier; and
- reduced *metabolic heat production* reducing inner heat production and the total heat load on the body (e.g., through reduced locomotor activity of the body).

All these physiological reactions belong to the *natural repertoire* of thermoregulatory responses that serve to maintain the *core body temperature* in its normal range (ICNIRP 1998; WHO 1993). For instance, regulatory *skin blood flow*[108] can increase from about 0.2–0.5 l/min in thermally neutral conditions to about 7–8 l/min during severe hyperthermia; i.e., there is room for a *20-fold increase* in the peripheral skin blood flow (ICNIRP 2004).

[108] An increased *skin blood flow* requires an increased *cardiac output* and thus a *non-compromised cardiac function* and *perfusion*. In other words, atherosclerosis, heart failure, impaired sweating and vasodilation, or arterial thrombosis (e.g., due to dehydration in the elderly making blood more prone to clot) render *thermoregulatory responses* less efficient and potential *thermal damage* more likely.

It is instructive to recognise that the response of the *cardiovascular system* to strong *electromagnetic exposure* is consistent with that associated with *conventional heating*. Namely, the system responds with an increase in the *heart rate* and *cardiac output* (Kaniusas 2012, Eq. 2.30) as well as with a decrease in the *total peripheral resistance* (Kaniusas 2012, Eq. 2.20) through relaxed smooth muscles surrounding arterioles.

Thermoregulatory Capacity

Thermal interactions are *not necessarily accompanied* by a significant *rise in the absolute temperature* of a body part or the whole body because of counteracting thermoregulatory effects (Fig. 2.85). Of course, this assumes intact and *sufficient thermoregulatory capacity* of the body. *Thermoregulatory responses* are highly *dominant*[109] if the applied whole-body P_{SAR} exceeds 4 W/kg (Footnote 131). However, the *thermoregulatory capacity* of the body may be exceeded given much higher P_{SAR}. This upper level of P_{SAR} strongly depends on *environmental conditions* which mainly affect perspiration-based cooling as a major physiological countermeasure; consult Footnote 115 for exposure conditions. *Thermal stress* from exposure to P_{SAR} is *more severe* when the body is in *hot and humid environment*—e.g., due to impaired sweating—or the body is covered with heavy clothing. Otherwise, thermal effects of the energy absorption could be even beneficial and stress reducing given a *cold environment* of the body (Kaniusas 2015, Sect. 5.2.1.4). Even most sensitive tissues can withstand < 4 W/kg without irreversible effects under *normal environmental conditions*. Interestingly, the body's thermoregulation is more efficient against heat than cold since the skin typically loses heat faster than it can be restored (Reilly 1998).

In addition, a *prolonged exposure* to levels of radiation—raising the core body temperature—ultimately leads to *failure of thermoregulatory mechanisms*. An insufficient thermoregulatory capacity would lead to *harmful effects* of tissue heating, especially when the inner temperature rises *in excess of 1–2 °C*; i.e., when the internal *core body temperature* rises from 37 °C to more than 39 °C. Normally, the *metabolic heat production* in a limited volume of tissue may typically increase its temperature by not exceeding 0.8 °C above the core body temperature (WHO 1993).

In particular, *lesions* (thermal damage) occur when local temperatures exceed 42 °C for periods of more than about 1 h (ICNIRP 2004). The rapidity of lesions increases with rising temperatures so that at around 45 °C lesions—e.g., in the skin and/or muscle (Reilly 1998)—are likely within 10–30 min in many tissues (ICNIRP 2004). *Adverse effects* will be avoided with a margin of safety if temperatures

- in the *head* are less than 38 °C,
- in the *trunk* less than 39 °C, and
- in the *limbs* less than 40 °C.

[109]Interestingly, thermoregulatory behaviour (in monkeys) starts when the temperature in the *hypothalamus region*—the control centre in the brain for thermal regulating mechanisms (Kaniusas 2012, Sect. 3.1.5)—increases by only as little as 0.2–0.3 °C without any noticeable increase in the rectal temperature (ICNIRP 1998).

The more dominant is the active *thermoregulatory response* and the less sensitive is the tissue or organ to heat, the less are the risks of a potential thermal damage. For instance, the better is the *vascularity* and flow of blood through tissue in question, the better is the thermoregulatory response. Therefore, biological tissues that *lack blood supply*—such as the *lens* of the eye—are very sensitive to the high frequency exposure (>100 kHz). *Tissues without vessels* or poorly perfused have a reduced ability to dissipate heat and thus are subjected to a potential thermal impact. For instance, the opacity can be formed in the lens due to a contact-less exposure to a high frequency electromagnetic field (WHO 1993). In addition, very high frequencies above about 10 GHz (see below) lead to *superficial heating* and are especially dangerous for *superficial not-perfused tissues* such as the *lens* of the eye. On the other hand, the *hypothalamus* is a particularly *sensitive organ* to heat.

For quantitative comparison, the metabolic rate of the *human body* is about 4 W/kg for *moderate activity* (Footnote 131) and may reach levels of up to 6 W/kg in healthy people (WHO 1993). In thermally *neutral environments*, the total heat production of the *resting body* is about 100 W that is obviously offset by simultaneous heat loss of about 100 W (WHO 1993).

Coupling of and Thermoregulatory Response to Electromagnetic Fields

Absorption of the electromagnetic energy causes *tissue heating*, whereas ambient fields can be coupled into the human body via different mechanisms of *direct coupling* and *indirect coupling* (Sect. 2.3.2.4). For instance, ambient time-varying electric fields (Fig. 2.26) or time-varying magnetic fields (Fig. 2.31) can be coupled into the body and then induce *conductive and displacement currents* within tissue. The resulting distribution of the current density field in *heterogeneous tissues* is highly non-uniform (Figs. 2.51 and 2.57) so that the resulting *energy deposition and heat generation*—non-linearly dependent on the local current density according to (2.58)—are even more *non-uniform* within tissues.

In fact, a finite *penetration depth* of the incident electromagnetic field into tissue (Fig. 2.6) determines the local field strength within tissue. This strength determines the local P_{SAR} (2.58), the local deposited energy, and thus local thermal effects (2.155) and lastly induced *thermoregulatory effects* in response to P_{SAR} (Footnote 107). In short, local thermoregulatory responses depend on the local distribution of the absorbed energy within tissue.

On the other hand, the *penetration depth* decreases with increasing *field frequency* (Fig. 2.6), especially for frequencies above the whole-body resonance (Fig. 2.33). In addition to finite penetration depth, *partial-body resonances* and locally peaked *non-uniform absorption*—also strongly depending on the field frequency (Section "Incident Electromagnetic Fields")—contribute to a *non-uniform distribution* of the local deposited P_{SAR} within the body. Please recall from Fig. 2.22 that *low frequency* fields (below β-dispersion) mainly lead to extracellular

currents and thus *extracellular heating*, whereas *high frequencies* (above β-dispersion) progressively bridge cell membranes and thus lead to *intracellular heating* as well. In short, exposure of tissue to ambient electromagnetic fields usually leads to a spatially *non-uniform* P_{SAR} within tissue, to non-uniform spatial patterns of energy deposition, and thus to non-uniform thermoregulatory responses.

Figure 2.48 illustrates a schematic *example* with a normally incident electromagnetic wave entering a layered body composed out of skin, fat, and muscle layers connected in series. The deposited P_{SAR} (Fig. 2.48b) as well as the resulting tissue temperature (Fig. 2.48c) show spatially *heterogeneous patterns* along the wave penetration through the skin down into tissue; compare Fig. 2.47.

Therefore, at *relatively low frequencies* the external incident electromagnetic fields penetrate tissues to *great depths* and thus are characterised by *deep heating* (Fig. 2.6). The submitted energy and heat become distributed within a *volume* of the human body. Therefore

- for field frequencies from about *100 kHz up to 10 GHz* the whole-body and/or localized specific energy absorption rate P_{SAR}—i.e., a *volume-related quantity* expressed in W/m^3, see (2.57)—are used as *basic restrictions* when assessing *exposure limits* in terms of tissue heating. In fact, major *voluminous heating* of tissues occurs between *10 MHz and 10 GHz*. In contrast, external electromagnetic fields
- of higher frequencies from about *10 GHz to 300 GHz* are already largely *absorbed at the body surface* (Section "Incident Electromagnetic Fields"), i.e., the epidermal upper layer of the skin and superficial subcutaneous tissues are heated as well as the outer part of the eye. Thus the *power density*—i.e., an *area-related quantity* in W/m^2, see (2.13)—is reasonably used here as a *basic restriction*. High local power densities lead to strong *superficial heating*.

Please recall that all basic restrictions *limit an increase in the tissue temperature by less than 1 °C* (Section "Power Measures"), which has been suggested as the upper limit of the temperature increase that yields no *detrimental health effects* (ICNIRP 1998). Please note that *medical implants* can be unfavourably heated through coupled fields.

It is important to recognize that the local and whole-body thermoregulatory responses are initiated by *thermal receptors* within the skin (Kaniusas 2012, Footnote 14)—or thermal sensors at the body surface—involving their afferent input to the brain. Therefore, *superficial heating* by incident fields at *high frequencies above 10 GHz* can be expected to trigger more efficient *thermoregulation*. In other words, cutaneous perception depends on the field frequency, whereas thermal receptors respond more efficiently to these high frequencies. *Deep heating* of tissues at low frequencies is presumably related to *less efficient*

thermoregulation. Consequently, *perception thresholds*[110] *of thermal sensors* within the skin—above which the thermoregulatory response is triggered—can be expected to decrease with decreasing *penetration depth* of incident electromagnetic fields.

For instance, *thermoregulatory responses* of *animals* were less effective in preventing an increase in their skin and core body temperatures during exposure at their corresponding *whole-body resonance* (usually < 1 GHz, see Section "Incident Electromagnetic Fields") than at their *supra-resonant frequencies* (>1 GHz) (WHO 1993). Because of this diminished response, internal human organs subjected to their *partial-body resonances* in the course of *deep heating* may even suffer *thermal damage*, without any sensation of warmth during the exposure (WHO 1993). Even the *task performance* by animals was affected by lower exposure levels at the whole-body resonance than at supra-resonant frequencies, even though the resulting core body temperature was raised by about 1 °C in both cases (WHO 1993). This confirms that the deeper is heating, the less efficient is thermoregulation, especially for the whole-body resonance.

Thermoelastic Interactions

Thermoelastic interactions should be shortly discussed which are still the subject of scientific dispute. The origin of these interactions lays in the *pulsed electromagnetic exposure* which seems to be more effective in producing a biological response than *continuous exposure* with the same average energy level and the same P_{SAR} (ICNIRP 1998; WHO 1993). For instance, pulsed microwave fields with short duration pulses in the range of 1–10 μs seem to be more effective than non-pulsed microwave fields. The *microwave hearing* comprises such an example of the biological response, where pulse-modulated electromagnetic fields with frequencies in the range of about 200 MHz–6.5 GHz are heard by people with normal hearing *as buzzing, clicking, or popping sounds*.

The microwave hearing due to even *single and repeated electromagnetic pulses* with the duration <30 μs at 2.45 GHz has been attributed to *thermoelastic interactions* in the auditory cortex of the brain (ICNIRP 1998). A rapid increase in the local temperature due to absorption of electromagnetic energy is suggested

[110]The *perception threshold* of thermal sensors (thermal receptors, see Kaniusas (2012, Footnote 14) in the skin to incident high frequency fields (at 2.4 GHz) is around 0.6 up to 2.4 W/kg in *animals* (WHO 1993); compare Footnote 132. The thresholds of between 0.05 and 5 W/kg were reported to induce in animals an increased *thermal conductance* of their skin and reduced *metabolic heat production*, depending on environmental conditions. Thresholds of about 1 W/kg led to *behavioural responses* in the thermoregulation, e.g., animals selected cooler environments. In general, thresholds for the activation of a given thermoregulatory response vary inversely with *body mass* of animal; thus an extrapolation of experimentally determined thresholds from animals to humans is not straightforward (WHO 1993).

In *humans*, the *perception threshold* of warming from the exposure depends on the incident field *frequency*, the *area*, and *location* of the exposed part of the body. Please recall the increased efficiency of the thermoregulation for high frequencies above 10 GHz due to superficial heating (see text). In addition, there is a *response delay* from the onset of expose to the perception of warmth, ranging from fractions of a second to many seconds (WHO 1993).

(WHO 1993), which, in turn, yields an abrupt thermal expansion and thus a thermoeleastic pressure wave in the acoustic range that is perceived by the intact human ear. It should be stressed that in this particular case of the microwave hearing, the large *rate of the local temperature change* in tissue is the critical parameter but not the very small *absolute increase* in the local temperature level (WHO 1993). In addition, thresholds for hearing are dependent on the *energy density per single pulse* (i.e., J/m^2 per pulse) or the peak electric field strength rather than the *average power density* (W/m^2) that indicates the presence of *non-linear mechanisms* within thermoelastic interactions.

Athermal Effects

For the sake of completeness, it should be noted that there is some *in-vitro evidence* on specific *biological effects with the associated response windows*[111] when tissue is exposed to either

- low intensity and *very low frequency electromagnetic fields* (below 300 Hz, known also as *extremely low frequency fields*) or
- low intensity but high frequency *electromagnetic fields* that are *amplitude-modulated* at these very low frequencies.

In particular, *non-thermal* (*athermal*) biological effects of *amplitude-modulated* high frequency *electromagnetic fields* (with the base frequency above 100 kHz) have been suggested, other than the classical heating effects (WHO 1993). Here the applied levels of P_{SAR} are too low to involve any response to heating. The base frequency of the latter electromagnetic fields usually resides in the *GHz range*, whereas the frequency of the amplitude-modulation is very low below 300 Hz, in most cases even in the range of *1–100 Hz*. Potential athermal effects on the cellular basis potentially include membrane permeability changes for cation fluxes (across the membrane) and suppression of some immune responses. Non-thermal interactions may even imply a "demodulation" of the amplitude-modulated fields at the level of the cellular membrane (WHO 1993). However, since it is almost impossible to eliminate any induced *thermal gradients* within biological tissue exposed to an ambient field (i.e., eliminate any local *thermal stress*), the validity, replication, and identification of athermal effects are currently rather poor.

It is remarkable that there is a large body of data indicating that the aforementioned very *low frequency electromagnetic fields* and *amplitude-modulated high*

[111]Specific *biological effects* in response to *amplitude-modulated electromagnetic fields* above 100 kHz (base frequency) apparently indicate the existence of *windows of response* (ICNIRP 1998; WHO 1993). That is, there are responses only in particular regions of the incident *power density* and *modulation frequency* of the applied field. In other words, there are *power density windows* and *modulation frequency windows* of response; compare with (narrow) response windows in the energy domain from Kaniusas (2015, Fig. 5.4a) and frequency domain from Kaniusas (2015, Eq. 5.3). These *apparent windows* challenge the classical concept model of a monotonic relationship between the intensity of the electromagnetic field and the severity of the induced biological effects.

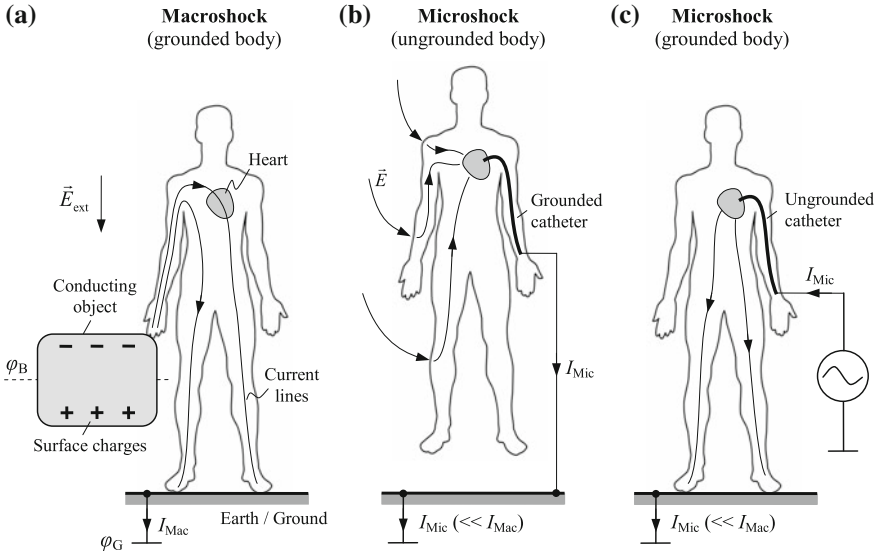

Fig. 2.86 Effects of entry points of the electric current into the human body. **a** Macroshock due to an external current I_{Mac}. This current I_{Mac} results from a direct contact of the grounded human body with its electric potential φ_G with an ungrounded conducting object carrying the potential φ_B ($>\varphi_G$). Both the body and object are subjected to a strong ambient electric field $\vec{E}_{ext}$, whereas the object shows surface charges in response to $\vec{E}_{ext}$ (Fig. 2.25a); see Footnote 116. **b** Microshock in the ungrounded body subjected to the electric field $\vec{E}$ (Fig. 2.27) due to a grounded intracardial catheter located close to the susceptible heart. An inner current I_{Mic} occurs directly in the heart region. **c** Microshock in the grounded body with a non-zero I_{Mic} due to an ungrounded intracardial catheter close to the heart

frequency electromagnetic fields interact with biological tissue at miniature *energy levels* that are even lower than energy needed for

- neuromuscular excitation (with the associated relatively *low energy* deposition in tissue at *low field* frequencies) or
- thermal stimulation (with the associated relatively *high energy* deposition in tissue at *high frequencies*);

compare Footnote 86. However, the involved hypothetical mechanisms are not fully understood and there is no convincing evidence (WHO 1993; ICNIRP 1998); compare Footnote 88.

2.3.2.5 Adverse Health Effects and Exposure Limits

Biological body subjected to

- non-ionizing electromagnetic radiation or to an *ambient electromagnetic field* (known as *contact-less* or *direct coupling*) as well as the body

- experiencing *physical contact* with an external current or voltage source (known as *contact-based* or *indirect coupling*)

will be considered within the scope of *exposure limits* to avoid *adverse biological effects*. Mainly *short-term biological effects* are considered since the currently existing scientific evidence for *long-term and chronic biological effects* is unfortunately too weak to provide the basis for exposure limits (ICNIRP 2010). In fact, biological effects can be either detrimental (e.g., in chance exposures) or beneficial (e.g., used in controlled fashion for diagnostic or therapeutic purposes in medicine), depending on circumstances. For instance, even induced biosignals within the body for diagnostics (Kaniusas 2012, Fig. 1.15a) are also subject to restrictions and thus can not be arbitrarily strong.

Effects to Be Avoided

The exposure to *external fields*—such as time-varying *electric, magnetic, and electromagnetic fields*—as well as to *contact currents and contact voltages* result in *internal fields*—such as electric and current density fields—within bodily tissues. These inner fields may primarily generate the following *biological effects*

- *neuromuscular excitations* (Section "Electrical Stimulation Effects") and/or, if inner fields are strong enough and become significantly absorbed by tissue,
- *tissue heating* (Section "Thermal Stimulation Effects").

Strictly speaking, characteristics of both mechanisms are *frequency-dependent* (e.g., superficial versus deep heating at different field frequencies of an incident electromagnetic field) and depend strongly on the *coupling mechanisms* involved (Sect. 2.3.2.4).

In addition to consideration and avoidance of the aforementioned *biological effects*, electromagnetic exposure and the associated risks should be especially considered with respect to Heinrich (2015)

- *passive medical implants* in humans (such as endoprosthesis, stents, or artificial heart valves) to avoid
  - an invalid *force application* on the implant (Footnote 65),
  - an adverse *increase of electric fields* close to *curved implants*, especially with sharp metallic edges (i.e., to circumvent the electrical point effect from Fig. 2.26a), or to avoid,
  - an excessive *warming up of conductive implants* or tissues close to such implants,
- *active medical implants* with an intrinsic energy source to avoid any interference with
  - cardiac pacemakers (to mimic natural endogenous biosignals),
  - cochlea or retinal implants (to substitute sensorial biosignals),
  - implantable defibrillators (to overwrite abnormal endogenous biosignals), or
  - neuromuscular stimulators (to generate endogenous biosignals).

That is, any *malfunction* of or *functional interference* with passive and active implants should be avoided while external fields are present outside implants.

Basic Restrictions Versus Reference Levels

Guidelines for limiting exposure to time-varying electric, magnetic, and electromagnetic fields serve to avoid *adverse health effects*, i.e., to avoid detectable impairment of the health of the exposed individual (ICNIRP 1998, 2010).

Well-established biological effects serve as a *basis for guidelines*. For frequencies *up to about 100 kHz*, neuromuscular effects (Section "Electrical Stimulation Effects") form this basis. These effects include the perception of up to annoyance by *time-varying surface charges* induced on the body and by the resulting *time-varying currents* within the body (Fig. 2.86a), the *stimulation of nerves* in the *peripheral* and *central* nervous system, the *stimulation of muscles*, as well as the induction of *retinal phosphenes*. For even higher frequencies above 100 kHz, *thermal effects* (Section "Thermal Stimulation Effects") become dominant and start to form the basis for guidelines.

However, guidelines do not necessarily protect against the most extreme combinations of diverse sensitivity factors favouring adverse health effects (Footnote 130). As already mentioned, the above *guidelines* are limited on *short-term health effects*, such as stimulation of excitable tissues (nerves and muscles), elevated tissue temperature, shocks and burns caused by touching of conducting objects (e.g., due to contact currents). *Guidelines* are intended to provide an *acceptable margin of safety*.

Two levels of guidance are usually introduced by guidelines:

- *Basic restrictions* in terms of *crucial physical quantities* are directly related to the established and adverse *biological effects*. Such quantities are
  - the *internal current density* in tissue,
  - the *internal electric field* in tissue (Fig. 2.63),
  - the whole-body averaged and localized specific *energy absorption rate* P_{SAR} in tissue [in W/kg, see (2.58)], and
  - the *power density* incident on the tissue surface [in W/m^2, see (2.22)],

  depending upon the exposure situation and the field frequency (Fig. 2.87). A protection against adverse health effects requires that *basic restrictions are not exceeded*. However, basic restrictions are *not conveniently measurable quantities* in practical exposure situations so that another level of restrictions is required.
- *Reference levels* in terms of *practical physical quantities* can be easily used for the *exposure assessment*, such as
  - the *ambient electric field*,
  - the *ambient magnetic field*,
  - the *ambient power density*,

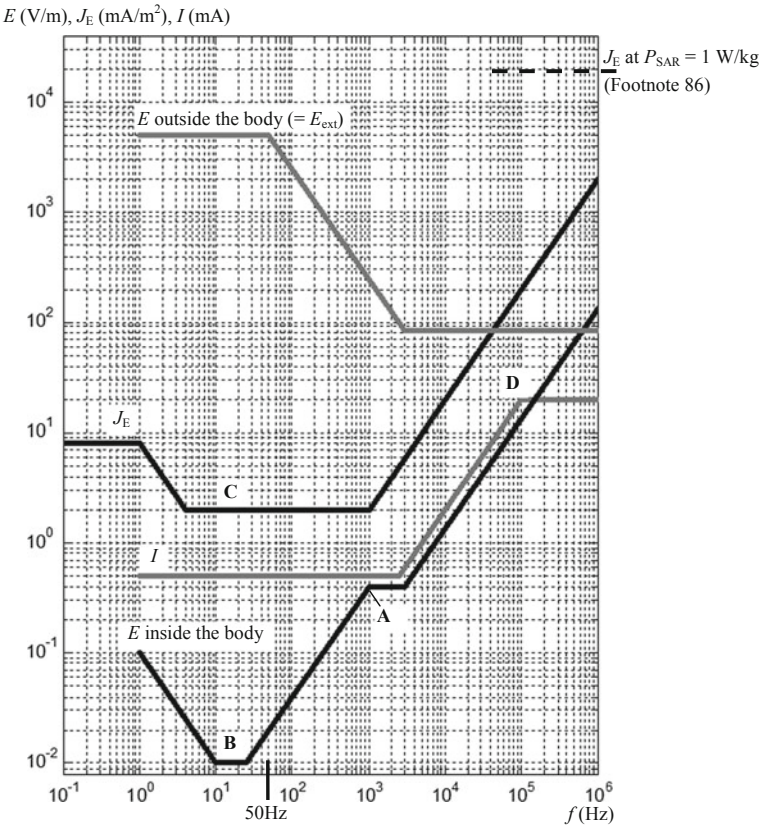

Fig. 2.87 Restrictions on human exposure to time-varying electric and electromagnetic fields in accordance with the guidelines ICNIRP (1998) and ICNIRP (2010). Basic restrictions (black lines) of the magnitude J_E of the current density in biological tissue (especially for the head and trunk, (ICNIRP 1998)) and the magnitude E of the internal electric field in biological tissue (especially for the head, (ICNIRP 2010)) are given for the general public exposure. The restrictions are directly based on established (adverse) health effects. Reference levels (grey lines) of the magnitude E of the ambient electric field outside the body ($=E_{ext}$) and the (point) contact current I are indicated (ICNIRP 2010), to which the general public can be exposed without exceeding basic restrictions and thus without (validated) health effects. All values are given as effective values (or root mean square values)

– the (short-circuit) *contact current*, and
– the *current flowing through the limbs*;

compare Fig. 2.87. That is, the compliance or comparison of the latter physical quantities—*experimentally measured* (e.g., in vivo) or *mathematically calculated* (e.g., in silico) in any particular realistic *exposure situation*—with the

corresponding *reference levels*[112] will ensure the compliance with the relevant *basic restrictions* and thus will ensure the absence of adverse biological effects. For instance, the actual level of the ambient electric field (in a particular exposure situation) below the relevant reference level of the ambient electric field ensures the compliance with the relevant basic restriction.

It can be easily recognised that the *major difference* between basic restrictions and reference levels is that

[112]In fact, *reference levels* are obtained from relevant *basic restrictions* by *mathematical modeling* (using published data) and extrapolations from *experimental data* (ICNIRP 1998, 2010). The reference levels are calculated for the condition of *maximum coupling* of the external field to the exposed individual (e.g., a stronger coupling of the time-varying magnetic field according to Fig. 2.32b is preferred for calculations over that in Fig. 2.32a). Reference levels thereby provide maximum protection of the individual even under *worst-case conditions* in such a way that *basic restrictions will not be exceeded*.

For instance, *reference values* pertaining to the ambient *electric field and magnetic field*—as derived from basic restrictions such as from the whole-body P_{SAR} in the range of 100 kHz–10 GHz [see (2.58)]—consider only the *far field* region and *unperturbed homogenous field* of exposure. That is, objects in the field such as the conductive body are not assumed to perturb the field, in contrast to the depicted behaviour in Fig. 2.25a.

On the other hand, *reference values* pertaining to the ambient *electric field and magnetic field*—as derived from basic restrictions such as from the *current density* in the body in the range up to about 100 kHz—consider *electrostatic induction* (Section "Charge and Current Induction") and *electromagnetic induction* (Section "Incident Magnetic Fields"), respectively. In addition, some reference levels are not directly derived from basic restrictions, these reference levels address perception (of the electric field) and adverse *indirect effects* of exposure (via limited *contact currents* based on indirect coupling).

In most cases, however, the *distance* from the *field source* and the *exposed body* is relatively close, i.e., the body resides in the *near field*. Consequently, an *inhomogeneous field* occurs over the space occupied by the body and can even be localized to a small part of this body. In these cases, the *maximum field* strength in the (relevant) space occupied by the body should be used for the safe exposure assessment, albeit very conservative exposure assessment (ICNIRP 2010).

Alternatively, the *spatial average* of the inhomogeneous field along the body or the (relevant) part of it can be used for the exposure assessment. For instance, authors in (ICNIRP 2010) suggest a tissue volume of $2 \times 2 \times 2$ mm^3 for the *vector average* of the *internal electric field*, whereas the 99th percentile value for a specific tissue is then the relevant value to be compared with the basic restriction. In analogy, a minimum of 1000 interacting cells—which amounts approximately to 1 mm^3 in most nerve tissues—is suggested as the *averaging volume* for the internal electric field. In fact, the size of the averaging volume and the *length constant* of the membrane (Kaniusas 2012, Table 2.2) suggest a biologically reasonable *averaging distance* in the range of about 1–5 mm for the measurement and computation of *internal electric fields* in tissues, except for thin tissues such as the retina and skin.

The resulting *spatial average* should not exceed the *reference level*. In contrast to this simple rule, the point-wise and local exposure level may exceed the reference level under the important provision that the *basic restriction is not exceeded*.

- *basic restrictions*—strongly frequency-dependent—consider only *biological effects*, whereas
- *reference levels*—strongly frequency-dependent—consider both
  - *biological effects* and
  - *coupling effects* of ambient fields into the body.

Consequently, the frequency dependence of reference levels accounts for both frequency dependence of basic restrictions (or frequency dependence of biological effects) and, on the other hand, frequency dependence of the field coupling. Discussed *coupling effects* comprise different mechanisms, including conductive currents, polarization phenomena, surface charges, electromagnetic induction, and the resonant absorption of energy from electromagnetic fields of a relatively high frequency.

A proper choice of an applicable *basic restriction*—by choosing an appropriate physical quantity—is a strong function of the *field frequency*, as indicated by the frequency dependence of the interaction between electromagnetic fields and biological tissues (Sect. 2.3.2.4).

- The induced *internal current density* within the body (especially for the head and trunk, as used in (ICNIRP 1998)) and the *internal electric field* (especially for the head with its brain tissue and other tissues, as used in (ICNIRP 2010))—tightly interrelated via (2.54)—are mainly used as *basic restrictions* in the lower frequency range *up to about 100 kHz* (up to a maximum of 10 MHz). The usage of these physical quantities accounts for *neuromuscular excitation*, prevent shocks and burns; see instructive discussions in Section "Current Density Versus Electric Field". Please recall that at these low frequencies, *electric and magnetic fields* are uncoupled (Fig. 2.2), which means that biological effects pertaining to electric and magnetic fields can be separately considered and accounted for. In fact, *uncoupled fields* even justify the use of the current density and electric field as applicable basic restrictions instead of P_{SAR} (accounting for *coupled fields* as an electromagnetic wave).
- The quantity P_{SAR} is used as the basic restriction in the higher frequency range of *100 kHz–10 GHz* to account for the *energy deposition* within tissue out of the traveling electromagnetic wave. Please recall that the high frequency in the range of MHz couples electric and magnetic fields through their derivatives (2.86). The basic restriction P_{SAR} accounts for *thermal excitation* and is used to prevent *excessive heating* of local body regions (head, trunk, and limbs) and of the *whole body*.
- The incident *power density* is used in the range from *10 GHz to 300 GHz* to account for a *superficial absorption* of the electromagnetic energy and to prevent *heating of tissues* at or near to the *body surface* (Section "Incident Electromagnetic Fields").

Reference levels are provided for the *occupational exposure* and *general public exposure*,[113] whereas levels for the general exposure are obviously lower than those for the occupational exposure. Usually reference levels for the general public exposure are derived from reference levels of the occupational exposure using *safety factors* (usually ≥ 2); see an example in Footnote 131. Please note that reference levels do not apply for *medical exposure*[114] which necessarily exceeds exposure limits to induce favourable and therapeutic biological effects. Medical exposure comprises numerous applications.[115]

---

[113]In terms of the *occupational exposure* in *controlled environments*, different measures can be used for the protection of *adult* workers at their workplaces under *known exposure conditions*. These measures include

- *engineering controls* (e.g., reduction of electromagnetic emissions by devices, reduction of stray fields, avoidance of interference in terms of standing waves) as a first step,
- *administrative controls* (e.g., access limitation, alarms, exposure limitation to working hours only, such as *8 h a day*), and
- *personal protection measures* (e.g., protective clothing) as a last resort when engineering and administrative controls turn to be insufficient.

With the exception of personal protection measures, engineering and administrative controls can also be applied for the protection of the *general public*.

It should be stressed that the *general public* in *uncontrolled environments* includes *sensitive subpopulations* of all ages such as infants, pregnant women, and the frail elderly, individuals with *varying health status* and *varying susceptibilities*, individuals *unaware of their exposure* up to *24 h a day* to ambient electromagnetic fields, and individuals who can not be expected to avoid or minimize reasonably their exposure (e.g., via protective clothing). In addition, the *thermoregulatory capacity* of sensitive subpopulations may be reduced so that their tolerance to the *combined effects* of artificial exposure, solar exposure, exercise, heat from inner metabolism, and high ambient temperature could be much lower, which dictates more strict guidelines for the general public.

These differences between *workers* and the *public* underlie the adoption of more strict *exposure restrictions* for the public than for workers; compare Footnote 131.

[114]It should be stressed that both *occupational exposure* and *general public exposure* of standard guidelines *exclude* exposure for medical purposes, i.e., *medical exposure*, where the risks and benefits of exposure, *above the basic restrictions*, must be properly weighed (CR 1999). In other words, compliance with the guidelines (ICNIRP 1998, 2010) may not necessarily preclude interference with diverse medical devices or implants such as cardiac pacemaker or cochlear implant; see Footnote 130.

[115]To give an example for a reasonable *medical exposure* in order to *deposit electromagnetic energy* in a particular quantity in a specific location and volume, *therapeutic treatments* based on

- shortwave diathermy and
- microwave diathermy

should shortly be discussed. In the case of *shortwave diathermy*, plate electrodes are applied on the body with low field frequencies at about 1 MHz yielding *deep penetration* of fields into tissue (Fig. 2.6). Here *fat* layers experience higher inner electric fields and thus are heated more than adjacent *muscle* layers; see the associated discussion on Fig. 2.37. Alternatively, a wire is wound around an extremity forming a coil operated at 13 MHz or 27 MHz with the resulting *superficial penetration* of fields into tissue. Here inner but superficial *electric fields* are induced due to electromagnetic induction (2.86) with a specific *skin depth* (2.88), whereas the resulting *current*

Field Distribution

Exposure conditions and assessment in guidelines—based on basic restrictions and reference levels—normally assume *unperturbed homogenous fields*. However, in practice, the exposure is complicated by the highly non-uniform *distribution of induced fields and currents* within and outside the *exposed body* (Footnote 112). In particular,

- *properties of the body*—its dimensions, shape, heterogeneous structure, electrical properties, and its geometrical alignment with respect to the incident field—and
- *properties of incident and induced fields*—especially its oscillatory frequency and waveform

determine distribution patterns of fields and thus the *degree of perturbation* of homogeneous fields. An example of perturbation is shown in Fig. 2.31c. *Complex*, *focussed*, and *non-homogenous field distributions* can occur inside, outside, and on the surface of *biological objects* exposed to incident electromagnetic fields; including *body resonance phenomena* (Fig. 2.30a), *electrical point effects* (Fig. 2.26a), and other effects.

For low frequencies and uncoupled fields, the type of the field is also relevant, i.e., whether and where *electric and/or magnetic field* are present, since uncoupled

---

density (2.87) is determined by the *tissue conductivity*. That is, conductive *muscle* inserts experience stronger inner fields and thus are heated more than isolating *fat* inserts in the course of the electromagnetic induction. This is because the induced current in tissue chooses the way of least resistance (Fig. 2.13a), i.e., the current prefers to cross conductive muscle instead of isolating fat (Footnote 70). In the case of *microwave diathermy* at 2.45 GHz for superficial penetration and treatment, electromagnetic fields are applied without any body contact, i.e., the hyperthermia device irradiates external to the body.

Usually targeted *deep heating* is accompanied by disadvantageous *surface overheating* due to finite penetration depth (finite skin depth). Please note that the effective *penetration depth* and thus the *thermal treatment depth* decrease with increasing *field frequency* (Fig. 2.6) which is an important operation parameter. In addition, *focussing* of fields within the body increases with increasing field *frequency* (Sect. 3.1). Frequency determines also the *size of the applicator* which becomes an effective field source only when the radiating structure is one-half of a wavelength or larger, i.e., low frequency fields with favourably deep penetration and large wavelength (2.5) require an unfavourably large applicator. Lastly, the diffraction or the *field divergence* in tissue increases with increasing ratio of the wavelength to the aperture size (2.123), i.e., to the size of the radiating structure. Consequently, low frequency fields and a favourably small applicator signify a large disadvantageous spread of spatial inner fields in tissue and their missing focus.

In diathermy, the induced electric fields in body tissues yield *conductive currents* and *dipole rotation* which, in turn, generate *collision and friction* in-between ions and molecules within tissue. The collision and friction generate *heat in tissue* (Fig. 2.16). The heat is partially accumulated in the local tissue and, on the other hand, is transported away by the local *blood perfusion* to maintain *homeostasis* (Footnote 107). To prevent a local overheating, the local perfusion is actively improved, which accelerates oxygen supply and removal of metabolic waste. Consequently, to give a tangible example, *healing of wounds* is promoted as well as *pain is relieved*.

In addition, hyperthermia devices are used in *cancer therapies* in combination with radiotherapy and chemotherapy (WHO 1993).

fields can be spatially separated and separately considered. For instance, largest power deposition in the body occurs when the *long axis of the body* is aligned with the electric field vector of the incident electromagnetic wave. The orientation of the exposed body is schematically addressed in Fig. 2.30, highlighted with numerical data in Fig. 2.33, or even discussed from the cellular level in Figs. 2.63 and 2.64.

An instructive *example* is shown in Fig. 2.25a where the *presence of a biological conducting object* (e.g., human body) embedded within a non-conducting environment (e.g., human body located in the air) considerably alters exposure conditions. This constellation gives rise to electric field strengths higher than those expected from homogenous situations due to the *electrical point effect*. Conducting objects act as *diffracting elements* for the ambient electromagnetic field (Fig. 2.39). Since the magnitude and direction of the electromagnetic field vary in time, induced *surface charges* (Fig. 2.25a) are subjected to temporal changes and, in turn, induce *electric currents* within the conducting object (Fig. 2.29) accumulating these charges (2.25). These charges and currents become sources of additionally induced electric fields in these objects. These fields are highly localized and—under certain circumstances—can constructively or destructively add to the original incident (homogenous) field (2.85). For instance, the region B in Fig. 2.25 demonstrates *constructive interference* while the region C *destructive interference*.

The *non-uniform distribution* requires different models for the estimation of peak values of *basic restrictions* and/or average values of basic restrictions. For instance, for *localized effects* of the incident electromagnetic fields and calculation of the *peak* P_{SAR} (e.g., per 1 g of tissue for cellular phone dosimetry), *precise anatomical models* must be used (Furse 2009). This is because the resulting local field within the body is highly dependent on the local electrical properties of the heterogeneous body. In contrast, for the *whole-body* P_{SAR}, *approximated anatomical models* are usually used to provide a rough understanding of the absolute P_{SAR} values and their relative changes (e.g., with the frequency of the incident field, as illustrated in Fig. 2.33).

It should be stressed that exposure guidelines usually assume *far field* conditions (Footnote 5), especially when the *power density* is used as the *basic restriction* (Footnote 112). In order to assess the exposure situation in *near field*—with a potentially high local P_{SAR} as the *basic restriction*—local strengths of *electric and magnetic fields* should be separately measured and then compared with the corresponding stipulated *reference levels*. Please recall that local maxima of electric and magnetic fields do not necessarily overlap in near fields; i.e., Equation (2.13) for the calculation of the power density does not apply in near fields. In other words, physical quantities such as the power density are of limited use in near fields.

However, this approach in *near field* leads to a rather *conservative and unreliable exposure assessment* (WHO 1993; ICNIRP 1998). This is because the *coupling of energy* from the *electric or magnetic near field* into tissue can not exceed the basic restriction of P_{SAR} in *far field* from which the reference levels of the *electric or magnetic far field* are derived (Footnote 112). On the other hand, direct field measurements at distances from the source of less than about 20 cm or $\lambda/2$, whichever is smaller, are experimentally not reliable; in such cases, direct measurements of induced currents flowing through the body are more reasonable (WHO 1993).

Simultaneous and Non-sinusoidal Exposure

For *simultaneous exposure* to ambient fields or contact currents composed out of *different frequencies*, the *multiple frequency rule*

$$\sum_{f=f_{\min}}^{f_{\max}} \frac{X^{\mathrm{f}}}{X_{\mathrm{R}}^{\mathrm{f}}} \leq 1 \tag{2.156}$$

can be applied (ICNIRP 2010). Here X is the *physical quantity* used for the exposure assessment and subsequent comparison with the corresponding *reference level*, e.g., X can be the *ambient electric field* (=E_{ext} in Fig. 2.87) or the *contact current* (=I in Fig. 2.87). Consequently, the quantity X^{f} indicates the strength of the assessed quantity at the considered *frequency* f (in the ambient field) for the relevant frequency range from $f_{\min}$ to $f_{\max}$. The quantity $X_{\mathrm{R}}^{\mathrm{f}}$ acts as a *weighting factor* and is the corresponding *reference level* for X^{f}. The criteria in (2.156) should be fulfilled to comply with exposure guidelines provided the ambient field or contact current is composed out of multiple frequencies.

In the case of a *non-sinusoidal ambient field* or a *non-sinusoidal contact current* —e.g., a distorted or pulsed field at frequencies below 100 kHz where neuromuscular effects are prominent—it is also possible to apply the *multiple frequency rule* (2.156). That is, this rule can be applied after the non-sinusoidal waveform has been decomposed into its discrete spectral components according to *Fourier analysis* (Kaniusas 2012, Footnote 150). However, this approach may be *unnecessarily conservative* because the procedure in (2.156) assumes that all spectral components add constructively in their phase, i.e., all maxima of components coincide at the same time resulting in a sharp peak. This assumption does not apply in most realistic cases of non-sinusoidal fields with fixed non-random phases of their components.

Alternatively, decomposed *spectral components* of an *external field* or a *contact current* can be *weighted* in their *amplitude and phase*, which accounts for the relevant reference level or basic restriction (ICNIRP 2010), to give

$$\left| \sum_{f=f_{\min}}^{f_{\max}} \frac{X^{\mathrm{f}}}{X_{\mathrm{R}'}^{\mathrm{f}}} \cdot \cos(2\pi \cdot f \cdot t + \gamma^{\mathrm{f}} + \varphi^{\mathrm{f}}) \right| \leq 1. \tag{2.157}$$

In other words, a *filter function* is applied in (2.157) on the field or current considered. Here $X_{\mathrm{R}'}^{\mathrm{f}}$ can be judged as an *adjusted reference level* (or exposure limit according to ICNIRP (2010) acting as the *weighting factor* for the amplitude X^{f} of a particular spectral component oscillating over the time t with the frequency f; compare (2.156). The angle γ^{f} is the phase angle of the spectral component at f, which results out of Fourier analysis. The angle φ^{f} is another phase angle at f reflecting the applied filter function. In analogy with (2.156), the criteria in (2.157) should be fulfilled for the ambient non-sinusoidal field and/or non-sinusoidal contact current in question in order to comply with guidelines.

Contact Current

The *contact current* results from *physical contact* of the *conductive human body* with *energized or charged conductive objects*; compare Figs. 2.27b and 2.86a. In particular, conducting objects located in an ambient *electromagnetic field* with a necessarily *electric field component* (Fig. 2.3) at frequencies *below about 100 MHz* can accumulate electrical *surface charges*.[116] Such conducting objects can be ungrounded or poorly grounded metallic objects such as cars or fences, whereas missing or poor ground allows the object to obtain an *electric potential* different

[116] *Surface charges* of opposite sign but equal amount—to be discharged by a subsequent contact—in the *conducting object* (or in the *conducting human body*) isolated from the ground are induced by a strong *ambient electric field* (Fig. 2.25a), or, more generally, by the *electric field component* of an ambient electromagnetic field. Likewise, an isolated and exposed conducting object or body acts as a capacitor plate to store surface charges (capacitive coupling, see Fig. 2.27b) and therefore obtains a specific *electric potential* given by the ratio of the accumulated surface charge to the capacitance (2.39).

Please note that this is the reason for *potential differences* [non-zero *driving voltages*, see (2.29)] between different *passive conducting objects* or bodies located in different locations of an ambient electric field. Here passive means that objects and bodies are not connected to any external source so there is no inflow or outflow of unbound charges; compare Footnote 36.

The size of the *accumulated surface charge* is proportional to

- the *strength of the ambient electric field*,
- the *body size* (applicable for the accumulated charge in the isolated body, Fig. 2.29), and
- the *object size* (applicable for the accumulated charge in the isolated object, see the *comparison between car and truck* in Section "Electric and Magnetic Field"). In addition, the *accumulated charge* size is inversely proportional to
- the *field frequency*;

see Footnote 78 and Section "Charge and Current Induction". The larger is the accumulated charge, the larger is the *driving voltage* (2.39), and the stronger is the resulting *contact current* (Footnote 117) during the *spark discharge* when the conducting object and conducting body approach and touch each other; see Fig. 2.86a and (2.25).

In particular, two major cases can be distinguished for this discharge:

- the resulting *contact current* can flow through the body to the ground when the *charged conducting object is ungrounded* (or poorly grounded) and the *body is grounded* (both exposed to the ambient electric field); compare Figs. 2.86a and 2.27a. For instance, a grounded person may touch an ungrounded car exposed to a strong ambient electric field. The contact current flows from higher to lower electric potentials, whereas the potential difference provides the *driving voltage* (2.29). On the other hand,
- the resulting contact current can also flow through the body when the exposed *conducting object is grounded* and the exposed *charged body is ungrounded*; compare Fig. 2.27b. For instance, an ungrounded person wearing isolating shoes may collect surface charges and then discharge them through a spark when he or she touches a grounded conducting object (such as a light switch).

Obviously, *perception and annoyance thresholds* (Fig. 2.88) for the *spark discharge* depend on the aforementioned parameters which determine the accumulated charge size. Furthermore, it should be noted that spark discharges at high field frequencies can arise at much lower electric fields in comparison with low frequencies (Furse 2009).

from that of the human body (grounded or ungrounded). Figure 2.86a illustrates different potentials φ_G and φ_B ($>\varphi_G$) of a grounded human body and an ungrounded conducting object, respectively. A driving *voltage drop* results in-between, i.e., the voltage $\varphi_B - \varphi_G$ in Fig. 2.86a in line with (2.29).

When a person touches such a charged object, a net *contact current* of a certain strength[117] can start flowing between the person and the object. The accumulated surface charge of the object is discharged (2.25) in terms of *indirect coupling*. Even when the person approaches closely the charged object, a current can start to flow in terms of a *spark discharge*. In the case of Fig. 2.86a, the conducting object with a *zero net charge* before the contact—with separated surface charges only—attains a *negative net charge* after the discharge. That is, after the contact current ceases, which, per definition, carries positive charges along the current flow (2.25) directed from the object through the body towards the ground (Fig. 2.86a).

The resulting *contact currents*[118] can stimulate peripheral nerves (excitable tissues) and thus can cause

---

[117]When a *grounded person* (or a body part of it) comes into contact with a conducting charged *ungrounded object* (Footnote 116), the resulting strength of the *contact current* through the person depends—in line with Ohm's law from (2.34)—on the *driving voltage* between the object and the ground, and the total *impedance* along the current flow. This *driving voltage*, in turn, depends on

- the *accumulated surface charge* on the object and
- the *capacitance* of this object with respect to the ground (2.39).

For the parameters determining the *charge size* please consult Footnote 116, whereas the *capacitance size* depends mainly on the object's size, its surface area, and orientation (2.41).

On the other hand, the total *impedance* along the current pathway—compare with the whole-body impedance from (3.37)—is determined by a *series connection* of

- the *contact impedance* from the object to the person's body; this impedance depends on the area of the contact surface and surface conditions such as dry or wet;
- the *inner body impedance*; its effective size is mainly determined by body parts permeated by the current and showing narrowest cross-sections and lowest conductivities, such as joints, ankles, or fingers (2.36); and
- the *contact impedance* from the body to the ground; for grounded person this low-ohmic impedance can be neglected (Fig. 2.27a) while for ungrounded person it is quite large, is mainly capacitive (Fig. 2.27b), and decreases with increasing field frequency (2.42).

Strictly speaking, all the latter contributions to the total impedance are *frequency-dependent*.

[118]Within the scope of safety considerations of *point contact currents*,

- *macroshocks* and
- *microshocks*

—as illustrated in Fig. 2.86—can be differentiated according to the specific points of current entry.

When an external current, known as *macroshock* (Fig. 2.86a), is applied at two points *far from the susceptible organ* (usually the heart), e.g., on the skin surface of the body, the *current spreads* significantly across tissues. The resulting *current density* in the body is relatively low because the current spreads across quite a large area (2.23). Usually only a small fraction of the total current flows though the susceptible organ, whereas the size of this fraction depends strongly on the spatial location of current pathways; compare the riskiness of pathways from Fig. 2.92.

- *tingling or prickling sensation* up to *shock* at higher current levels, especially for field *frequencies below 100 kHz* (in line with neuromuscular excitations up to 100 kHz). Provided that this current is strong enough (or the current density is sufficiently high), *heating* or even *burn*[119] of affected skin regions can occur. In particular, precautions should be taken near *high power* and *low frequency* systems, as indicated in Fig. 2.87 by the obvious frequency dependence of reference levels of the contact current.
- At higher field frequencies *between about 100 kHz and 100 MHz*, *heat sensations* can result and thus hazards of *burns* from contact currents of sufficiently high density will predominate (WHO 1993).

Reference Levels

Figure 2.87 depicts *reference levels* for the sinusoidal *point contact current I* from *conducting objects* in serve for the prevention of *shock and burn hazards* in the general public. It should be noted that these reference levels *do not prevent perception* of the current in the general public but avoid painful shock and burns.

The *lowest reference level* of 0.5 mA in Fig. 2.87 is valid up to 2.5 kHz. For high frequencies above 100 kHz, the *highest reference level* of 20 mA is proposed; see point D in Fig. 2.87. This proposal originates from experimental data suggesting a *reference level* of 45 and 100 mA for the *high frequency current* between 10 and 110 MHz flowing through a *human limb* in terms of the general public exposure and occupational exposure, respectively, to avoid excessive *heating effects* (ICNIRP 1998). Here the current of about 100 mA is likely to produce a localized increment of temperature of less than 1 °C. Likewise, the reference level of 45 mA assures that

---

The approximate *safety limit for macroshocks* is *relatively large* and amounts to *50 mA* (at 50/60 Hz) in order to avoid *ventricular fibrillation* (Grimnes 2008); compare Footnote 124 on ventricular fibrillation and Figs. 2.88 and 2.89 on fibrillation thresholds.

In contrast to macroshock, *microshock* situation refers to a *direct contact* of a single (current) electrode with the susceptible organ. For instance, it applies for an invasive device or intracardial catheter electrodes located close to the heart.

Fig. 2.86b illustrates an *ungrounded human body* with an implanted *grounded catheter*, whereas the ambient electric field couples into the body and induces currents within the body towards the ground along the catheter line (Fig. 2.27). In analogy, Fig. 2.86c illustrates a *grounded body* and an *active ungrounded catheter* yielding again conductive currents along the body towards the ground.

Then even very small electrode currents—as well as *leakage currents* of applied parts in contact with the heart—can already induce ventricular fibrillation because the resulting *current density* at the point of the electrode contact with the heart tissue can be quite high due to *small contact area* (2.23). In fact, the reference (current) electrode can be at any point of the body.

The approximate *safety limit for microshocks* is *10 μA* (at *50/60 Hz* at the contact area of 1–3 mm^2) to avoid *ventricular fibrillation* (Grimnes 2008). Please recall that this safe level of the current in the external circuit is very low (i.e., is *very strict*) as compared with the macroshock situation.

[119] *Local burn* is related to rapid elevation of the local tissue temperature to levels that *denature proteins*, whereas normal avenues of heat transfer from the exposed site are inadequate due to relatively *slow thermoregulatory mechanisms*.

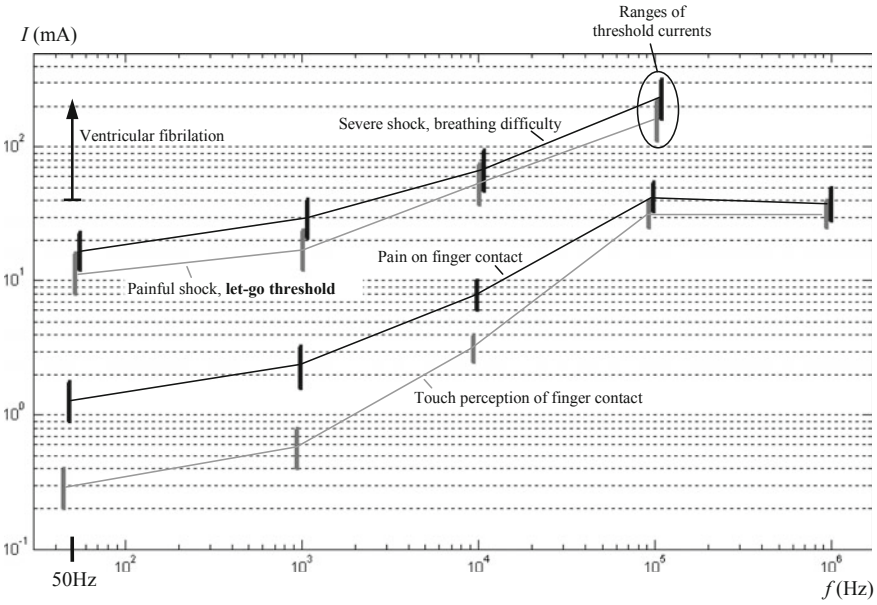

Fig. 2.88 Experimental threshold values (50th percentile values) for the point contact current with its effective value I at frequencies of 50/60 Hz, 1 kHz, 10 kHz, and 100 kHz. The indicated ranges of threshold currents apply to children, women, and men. Thresholds consider different physiological effects from pure touch perception of finger contact, to the let-go current (Fig. 2.91), to severe shock. Different contact situations with metallic electrodes were evaluated, including contact of the index finger with a conductive electrode, whereas a metallic armband served as the ground electrode. Image data extracted from ICNIRP (1998) and WHO (1993)

basic restrictions on the *localized* P_{SAR} in terms of thermal effects are not exceeded by the *induced current* within the limb (ICNIRP 1998).

Threshold Values

For comparison, *threshold values* for *point contact currents* at 100 kHz are depicted in Fig. 2.88, whereas *different perception levels* are considered in a wide population[120] including children, women, and men (at 50th percentile values[121] only). It can be observed that—as expected—the selected *reference level* of the contact

[120] As an approximation, particular *thresholds of the point contact current* (Fig. 2.88) for

- *women* comprise *two-thirds* of that for *men* and thresholds for
- *children* comprise *one-half* of that for *men* (WHO 1993).

In other words, *women* proved to be more sensitive than *men*, while *children* were more sensitive than women.

[121] It should be recalled that this *50th percentile* reflects experimental data for 50% of children, women, and men or, in analogy, it reflects *mean values* in children, women, and men provided that the *Gaussian* (or *normal*) *distribution* applies.

current of 20 mA at 100 kHz in Fig. 2.87 for the *general public exposure* does not exceed the touch perception threshold in Fig. 2.88, whereas contact currents above 50 mA may severely *burn* the site of the conductor contact with tissue. In general, safety considerations dictate reasoning in terms of *minimal threshold values* rather than *mean threshold values* when considering populations.

To give an *example*, typical diagnostic settings for *impedance tomography* (Fig. 1.3) use effective amplitudes of about 5 mA of injected sinusoidal currents at 50 kHz (Leonhardt 2012). This value is clearly below the relevant reference level of 10 mA at 50 kHz (Fig. 2.87) and perception thresholds approximately located between 10 and 20 mA at 50 kHz (Fig. 2.88).

Figure 2.88 summarizes ranges of experimental *threshold values* for sinusoidal *point contact currents* not only for various *physiological effects* ranging from

- pure *touch perception*, to
- *pain on contact*, to
- *let-go current*,[122] to
- *severe shock* and *breathing difficulty*, to even
- *ventricular heart fibrillation*

but also for the varying *current frequency*. Obviously, *rising contact currents* yield increasing severity of adverse *health effects*.

With stronger stimulation, *bare perception* goes into *discomfort* and then lastly into *intolerable pain*. For stimulation based on the *electromagnetic induction* (ICNIRP 2004), the lowest percentile for the intolerable stimulation occurs at the *rate of change of the magnetic field* which is about 20% above the median of the perception threshold. It can be observed in Fig. 2.88 that thresholds for *perception* and *pain* are well below *let-go* thresholds. There is a relatively *narrow margin* between the *perception* of the peripheral nerve stimulation and the corresponding *pain* thresholds, especially at higher frequencies (Fig. 2.88). Current thresholds leading to involuntary muscle contractions depend on the *recruited volume of muscles* and/or *recruited nerves* innervating these muscles, whereas the positioning of current pathways through the body determines local recruitments.

Thresholds for smallest measurable *muscle reactions* (muscle twitch) can be expected to be slightly above those for *perception* (Reilly 1998). For electromagnetic induction and stimulation, *motoric thresholds* (contraction of muscles) were

[122]The *let-go current* is the lowest current which starts to control nerves and muscles in terms of a sustained muscular contraction or cramped muscles (see *tetanus* in Kaniusas (2012, Sect. 2.3.2). A *voluntary control of muscles is just lost* including reflex withdrawals. For instance, a subject experiencing the let-go current is unable to let go of a gripped conductor as long as the stimulus persists, e.g., the subject is unable to open his hand and drop a live electrode. This is because grip muscles (flexors) of the hand are usually stronger than opening muscles (extensors). The voluntary control of skeletal muscles is lost at high current levels (even through these muscles) and involuntary movements occur, i.e., *"freezing" to a live conductor* held in hand is possible.

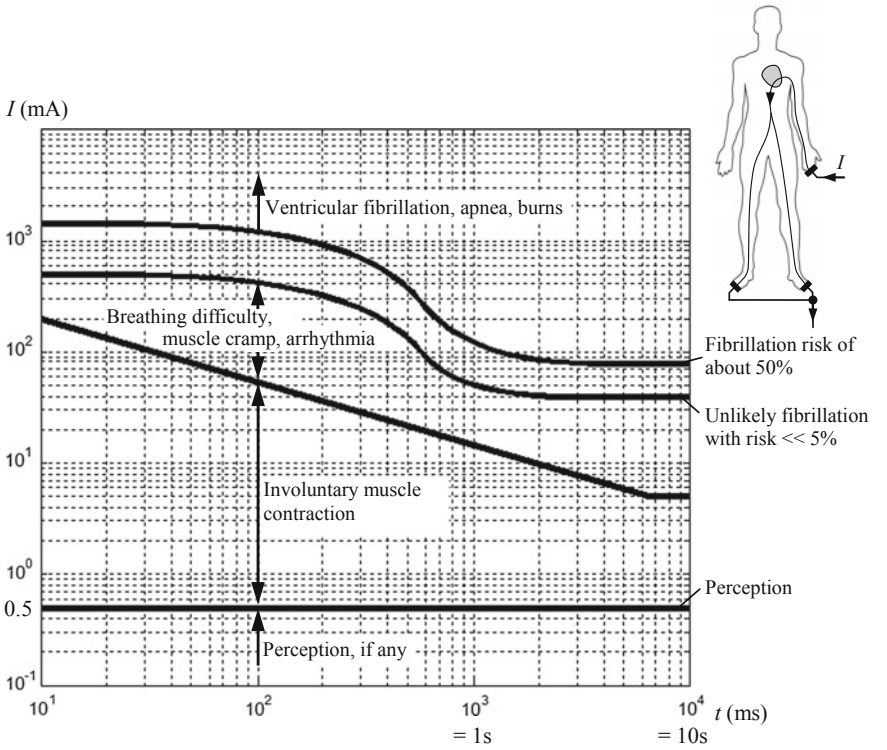

Fig. 2.89 Experimental regions of diverse physiological effects of the alternating current with its effective value *I* flowing from the left hand to both feet in the total population for the mains frequency 50 Hz (namely, for the range of 15–100 Hz) as a function of the exposure duration *t* ranging from 10 ms to 10 s; compare Figs. 2.57 and 2.88. For ventricular fibrillation, the applicable heart current factor is 1 (Fig. 2.92a). Image data extracted from DIN 60479-1 (2007)

reported to be about 50% greater than *sensation thresholds*, whereas about twice the sensation threshold was already described as *intolerable* (ICNIRP 2004).

In general, the effective impact of the contact current and the associated threshold values for different perception levels depend on many *contributing factors* such as

- *current strength* (Fig. 2.88)
- *contact area* of electrodes (Fig. 3.23),
- *wetness* of the skin (Sect. 3.1.1.4),
- field *frequency* (Fig. 2.88),
- *exposure duration* (Fig. 2.89),
- applicable *whole-body impedance* (Fig. 2.90),
- *person's impedance* to the ground (Fig. 2.27),
- spatial *location of the major current pathway* within the body (Fig. 2.92),
- size and shape of the *conductive object* (Fig. 2.86a), and even

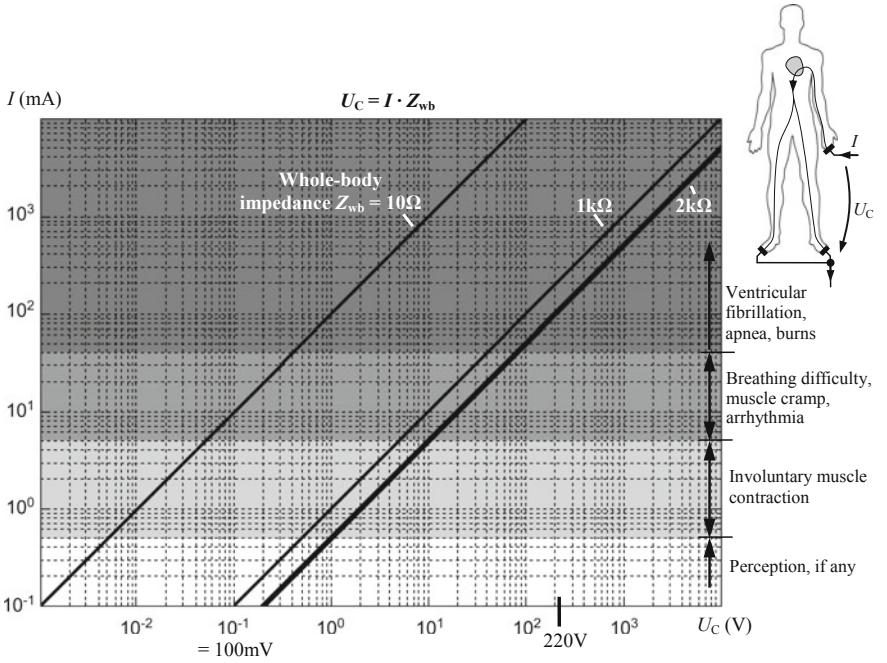

Fig. 2.90 Experimental regions of diverse physiological effects of the alternating current with its effective value I flowing from the left hand to both feet in the total population for the mains frequency 50 Hz and a long exposure duration >10 s as a function of the effective value U_C ($=I \cdot Z_{wb}$) of the contact voltage and the whole-body impedance Z_{wb} (Fig. 3.22). Image data is derived from Fig. 2.89. For ventricular fibrillation, the applicable heart current factor is 1 (Fig. 2.92a). Please note that the voltage-dependant behaviour of the skin impedance is not considered here

- *individual susceptibility* (Footnote 120).

For instance, a small cross-section of the contact area, such as that of a fingertip touching a charged object, implies a high local current density (2.23) and thus a high risk of local *burns* at higher frequencies.

Exposure Duration

Since the neuromuscular stimulation of excitable tissues clearly depends on the *stimulus duration* (Fig. 2.73), touch perception, let-go, and other thresholds also depend on the *exposure duration*. In contrast to Fig. 2.88 showing experimental current thresholds for diverse physiological effects as a function of the *field frequency*, Fig. 2.89 illustrates *experimental current thresholds for physiological effects* as a function of the *exposure duration* at the *mains frequency* of 50 Hz (to be precise, for the range of 15–100 Hz), as derived from a *safety publication* (DIN 60479-1 2007).

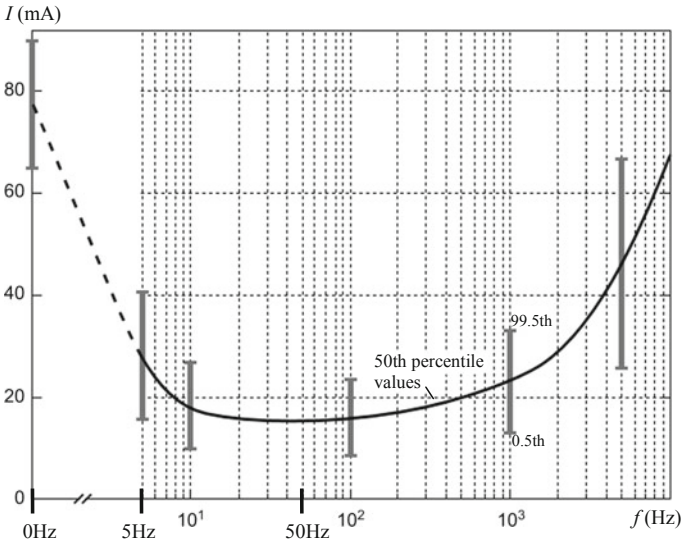

Fig. 2.91 Let-go current thresholds. The effective value I of the point contact current—a tetanizing sinusoidal current, see Footnote 122—for hand contact with a live conductor, for adult men as a function of the current frequency. The curve provides 50th percentile values while grey bars indicate the variability of this threshold from its 0.5th up to 99.5th percentile. Dashed line shows interpolated values between experimental points at 0 Hz (direct current) and 5 Hz; compare Figs. 2.74 and 2.88. Image data extracted from Reilly (1998) and WHO (1993)

Figure 2.89 demonstrates decrease of thresholds with increasing *exposure time* below about 10 s, whereas above 10 s thresholds remain almost constant (Leitgeb 2010; DIN 60479-1 2007). Correspondingly, the associated risks and the severity of *physiological effects* tend to increase with increasing exposure time below 10 s and to level off above 10 s. A remarkable exception is given by *ventricular fibrillation* (Footnote 124) in Fig. 2.89. Here threshold is almost constant below and above the exposure time of about 1 s while this threshold increases steeply at exposure times of about 500 ms towards decreasing time; the *vulnerable period* (Footnote 126) is responsible for this behaviour.

The *perception threshold* to contact currents in Fig. 2.89 is denoted at 0.5 mA, irrespective of the exposure duration, when the body is in contact with a conducting live surface. Here a sort of *worst-case scenario* is considered in this *safety publication* (DIN 60479-1 2007) since the threshold of 0.5 mA is a bit higher than perception thresholds of less than 0.5 mA from Fig. 2.88. The indicated current range above 0.5 mA evokes *involuntary muscle contractions* which usually exclude any deleterious health effects.

Even stronger and longer lasting contact currents yield severe muscle contractions such as *muscle cramps* which *severity* rises with increasing current strength and/or exposure duration. Strong and persisting currents within the body may even affect *breathing muscles* and thus *impair normal breathing* up to complete cramp

of muscles and thus *respiratory arrest*, known as *apnea*; see Figs. 2.88 and 2.89. Thresholds leading to *breathing difficulties* reside above *let-go* thresholds while thresholds leading to *respiratory tetanus* are somewhat above them. The associated nerves and the respiratory centre in the brain may also be overstimulated, which may also end with *apnea* in response to a very strong current stimulus. In addition, *severe burns* (Fig. 2.89) can occur for large currents and long exposure durations (>1 s). Fatal *ventricular fibrillation* may also occur (Footnote 124).

Please note that Fig. 2.89 considers only the *current pathway* from the left hand to both feet. Other pathways through the body may have *different thresholds* for different physiological effects. In particular, the *heart current factor* from Fig. 2.92 can be used to estimate *fibrillation thresholds* for other pathways.

In addition, a safety limit—comparable with a reference level—for *macroshocks* (Fig. 2.86a) is defined and amounts to 50 mA at 50/60 Hz to avoid *ventricular fibrillation*, as shortly discussed in Footnote 118. This level is in quantitative agreement with experimental data from Fig. 2.89 for long and thus *high-risk exposure times* (≥ 10 s). The safety limit for *microshocks* (Fig. 2.86b, c) is much lower and amounts to 10 μA.

Contact Voltage

The effective value I of the *contact current* through the body—which determines *physiological effects* according to Fig. 2.89—is given by the ratio U_C/Z_{wb} [$=I$, see Ohm's law in (2.34)] of the effective value U_C of the *contact voltage* to the *whole-body impedance* Z_{wb} (Fig. 3.22). Therefore, the contact U_C could be easily depicted as a function of the resulting I for practically relevant values of Z_{wb}. In fact, the voltage U_C is a relevant *safety parameter* in the case of the accidental contact of the body with *live parts*.

Figure 2.90 illustrates the resulting *current-voltage diagram*. Diverse *physiological effects* from Fig. 2.89 are shown as a function of U_C for a few relevant values of Z_{wb}, the mains frequency 50 Hz, and a long exposure duration >10 s. Here a typical value of Z_{wb} of 2 kΩ (3.37) is considered which is the relevant value for *safety publications* and *macroshocks* (Fig. 2.86a). Another more critical value of 1 kΩ for the hand to hand contact as well as a low value of only 10 Ω—relevant for *microshocks* (Fig. 2.86b, c)—are reflected by Fig. 2.90.

This current-voltage diagram instructively shows which levels of U_C must be considered as dangerous, given a certain Z_{wb}. Obviously, the lower is Z_{wb}, the higher are adverse risks for a given U_C (Fig. 2.90). Thus the impedance Z_{wb} always acts as a *current-limiting barrier*. For instance, the *mains voltage of 220 V*- as applicable in daily life—is highly likely to induce *ventricular fibrillation* with the assumed typical $Z_{wb} = 2$ kΩ in terms of *macroshock*. Lower voltages U_C above 10 V may already yield unfavourable muscle cramps while U_C above 1 V may yield muscle twitches. Apparently *small voltages* in the range of only *100 mV* may even generate severe muscle cramps, breathing difficulties, and arrhythmic beats provided that the applicable Z_{wb} is very low and resides in the ohms region (Fig. 2.90). For instance, this is applicable for *open surgery* and thus *microshocks*.

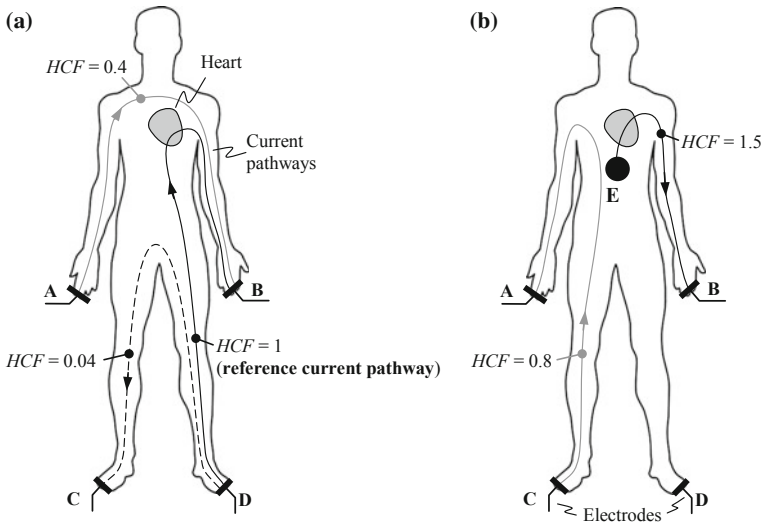

Fig. 2.92 Current pathway and its dependence on the electrode locations or on the location of the body part in contact with live parts. **a** The reference current pathway between the left hand and any foot (or both feet) goes through the vital organ, the heart, with the risk of ventricular fibrillation. The associated heart current factor *HCF* is defined as 1 (Leitgeb 2010); compare Fig. 2.57. In contrast, the foot-to-foot current pathway does not cross the heart, yielding a much lower *HCF* of only 0.04. The pathway hand-to-hand yields an intermediate value of *HCF* = 0.4. **b** The current pathway between right hand and right foot is indicated in comparison with that between the chest and the left hand, showing the relevant *HCF* levels

Let-Go Current

Figure 2.91 illustrates the *50th percentile* of experimental thresholds of the *let-go current* (Fig. 2.88) of *men* as a function of the *current frequency*. As described in Footnote 122, this current is related to the incapability to release a live conductor due to tetanizing sinusoidal currents. In addition to 50th percentile, the ranges of thresholds are indicated in Fig. 2.91, which start at the 0.5th percentile and extend up to 99.5th percentile of men. It should be pointed out that while the shown ranges of thresholds in Fig. 2.88 depict the variability among *children*, *women*, *and men* (at 50th percentile values only), the illustrated ranges in Fig. 2.91 depict the variability among *different percentiles in men* only.

Unfortunately, *minimal let-go currents* apply for frequencies between 10 and 100 Hz including typical frequencies 50/60 Hz of *power lines*, imposing high hazards from power lines in humans, as already discussed with respect to Fig. 2.74. At 50/60 Hz, the 50th percentile of the let-go current threshold in adult male volunteers amounts to about 15 mA. Here *minimum thresholds* of 9, 6, and 4.5 mA apply for *men*, *women*, *and children*, respectively, when considering the lowest 0.5th percentile (Reilly 1998; WHO 1993). Please note that this threshold for

women is decreased by a factor 2/3 (=6 mA/9 mA) as related to men, whereas the threshold for children is decreased by a factor 1/2 (=4.5 mA/9 mA); see Footnote 120.

In fact, Fig. 2.91 represents the *strength-frequency curve* from Fig. 2.74 for the *let-go current*, suggesting increasing thresholds for both low frequencies below and high frequencies above the range 10 to 100 Hz. In particular, the upper frequency of the threshold upturn resides in a quite wide range from 100 to 1500 Hz with a median of about 500 Hz for different *perception levels* (Reilly 1998). The lower frequency of the upturn resides in the range from 20 to 100 Hz with a median of about 30 Hz. Obviously, these upturn frequencies strongly depend on experimental conditions such as electrode size. Figure 2.91 illustrates the estimated *let-go thresholds* for the direct current at 0 Hz.

Figures 2.91 and 2.74 propose an infinite increase for increasing frequency. However, in practice, thresholds for different *perception levels* cease to rise above a frequency of about 100 kHz and reach *plateaus*, as illustrated in Fig. 2.88. At plateaus, *perception levels* will become dominated by frequency-independent *thermal effects* occurring at strong electrical stimuli (Footnote 86) instead of frequency-dependent *neuromuscular effects*. Please recall that thermal effects are largely independent on frequency, whereas the frequency above which thermal perception dominates depends also on the duty factor for *non-continuous pulsed stimulation* (Footnote 87).

Not only *strength-frequency curves* (Fig. 2.74) but also the related *strength-duration curves* (Fig. 2.73) can be used to asses perception levels and adverse events; e.g., perception thresholds, motor/muscular responses, pain, and pain tolerance (Reilly 1998). Here *rheobase* and *chronaxie* can be used as descriptive parameters; please recall that these parameters depend not only on the stimulus itself but also on experimental settings.

Direct Current

Direct currents of about 2 mA can be perceived as *tingling sensation or warmth* for the hand-hand pathway (Fig. 2.92) or for another pathway from one hand to both feet (Leitgeb 2010; DIN 60479-1 2007). This *perception threshold* of 2 mA at 0 Hz is higher than the perception threshold of 0.5 mA for alternating 50 Hz currents (Fig. 2.89). Increasing *amplitude* and *prolonged exposure* of the direct current intensify its sensation, in qualitative analogy with thresholds from Fig. 2.89.

Increasing discontinuities in the direct current and extended exposure may even lead to involuntary cramp-like *contractions of muscles*, the associated *pain*, *cardiac and/or respiratory arrest*, *ventricular fibrillation* (Footnote 124), and even *severe burns*. Figure 2.91 illustrates the estimated *let-go thresholds* (Footnote 122) for the direct current. Current amplitudes above 40 mA tend to disturb reversibly the *excitation propagation* in the heart (Leitgeb 2010). Again, an elongated *exposure duration* to direct currents decreases thresholds of diverse (adverse) physiological effects, except for perception.

Cell Membrane

Lastly, *perforation of cell membranes* should be mentioned that can occur at very *high current* strengths within the body and even for relatively *short exposures*. Alternating and direct currents can lead to perforation. Large currents yield strong electric fields in cellular tissues and across cell membranes, especially at low field frequencies [below β-dispersion, see (2.140)] where the membrane voltage carries the whole voltage drop across the cell. These strong fields within membranes can lead to *breakdown of membranes* (Footnotes 89 and 90). Biological tissues such as muscles can be irreversibly damaged by this *non-thermal mechanism* leading to tissue necrosis.

Cardiac Interference

The distribution of tissue conductivities determines the *distribution of the conductive current density* within the body in response to *contact currents* (Section "Charge and Current Induction"). Inner currents prefer conductive tissues such as blood and muscles over isolating tissues as fat, lung, and bone. In fact, the current in the chest even prefers to cross the *heart region* because of its relatively high conductivity. The heart is an organ that is susceptible to electric currents and shows different non-lethal and lethal risks. It means that the amount of the current passing through the heart is an important factor for the human safety (Leitgeb 2010).

In particular, *the contact current* of

- at least *5 mA at 50/60 Hz* with a relatively long exposure duration of about 10 s (Fig. 2.89) may yield a reversible interference with the *excitation of heart muscles*, known as *reversible cardiac arrhythmia*. *Higher levels*
- of above about *40–500 mA—at 50/60 Hz* depending on the exposure duration and other aforementioned contributing factors, see Figs. 2.88 and 2.89—may even induce the *lethal risk* of *ventricular fibrillation* (see below). When the current through the heart continues to increase to levels
- higher than *1 A at 50/60 Hz*, *all heart muscles* can become *excited at once* and contract altogether. This is then known as reversible and *sustained myocardial contraction* or *cardiac arrest*, with the heart beat being completely ceased. In contrast to ventricular fibrillation, the normal heart rhythm is re-established as soon as the strong current that triggered the sustained myocardial contraction disappears. This is in qualitative analogy to *ventricular fibrillation with defibrillation*, since the strong excitation current not only arrests the heart beat but also favourably defibrillates the whole heart muscle.[123]

[123]This would explain that *fatalities* due to *cardiac failure* usually occur at relatively *low voltages* and thus relatively *low currents* (Fig. 2.90) which trigger ventricular fibrillation without the essential *defibrillation* of the heart. In contrast, accidents with *high voltages* yield most often *burns* because relatively high currents through the body not only burn the permeated tissue but also defibrillate the heart (Reilly 1998).

Ventricular Fibrillation

Ventricular fibrillation[124] occurs when part of the current passing through the chest flows through the heart and excites only a *part of the heart muscle*—but not the whole heart muscle—disrupting the normal excitation pathway of the heart (Kaniusas 2012, Fig. 2.35). Ventricular fibrillation does not stop on its own when the current that triggered it ceases. Here *defibrillation*[125] is necessary to stop ventricular fibrillation to avoid death (Footnote 124).

---

[124] *Ventricular fibrillation* refers to highly *uncoordinated and irregular excitation and contraction of ventricles* in the heart, preventing the heart from being properly filled by blood and thus from pumping blood into arteries. Thus, the vital blood circulation of the body and of the heart itself is arrested and death results within minutes unless circulation is restored via electric *defibrillation* (Footnote 125). In other words, *ventricular fibrillation does not stop on its own* (e.g., even when the current that triggered it is ceased), this *self-sustaining fibrillation* has to be discontinued by defibrillation.

Concerning the *genesis of ventricular fibrillation*, the action impulse in ventricles—or an induced electrical impulse due to *external electrical stimulation* during the *vulnerable period* of the cardiac cycle (Footnote 126)—may encounter some muscular regions in ventricles (accumulation of cardiac muscle cells) which are *fully recovered*, others *partially recovered*, and others still *absolutely refractory* (Kaniusas 2012, Sect. 2.1.3.2.2). In fact, there is a strong *non-uniformity in the recovery of excitability* in ventricles after the ventricular systole.

In the case of *electrical stimulation*, only *certain parts of the heart muscle* become excited, which disrupts the normal electrical excitation of the heart along its conductive system (Kaniusas 2012, Fig. 2.35). Therefore, the *excitation wave* may preferentially *propagate unidirectionally* in a certain (unpredictable) direction *along a closed pathway* (i.e., propagate in a *loop* within the heart) such that the excitation wave front *returns* to a previously excited tissue after a certain time delay, i.e., at least after the *refractory period*, and then unfortunately *re-excites* this tissue again.

This is known as *re-entry mechanism* (Kaniusas 2015, Footnote 61 in Chap. 5). Multiple passages along these closed pathways lead to the so-called *multiple re-entry*—the electrophysiological basis for *ventricular fibrillation*. In fact, re-entry and ventricular fibrillation are favoured by

- myocardial *ischemia* (e.g., occlusion of coronary arteries facilitating the aforementioned non-uniformity in the recovery of excitability);
- electrical *stimulation* with an external stimulus (which introduces an additional non-uniformity as required for fibrillation, i.e., introduces additional depolarization below the cathode and additional hyperpolarization below the anode, see Fig. 2.63);
- *premature ventricular contraction* or *extrasystole* (i.e., the vulnerable period is elongated and non-uniformity in excitability increases after a premature beat, reducing the fibrillation threshold by about 35% (Reilly 1998); repetitive extrasystoles reduce the threshold even more, see Kaniusas (2015, Footnote 61 in Chap. 5);
- *deprivation of oxygen*, and many other pathological causes.

In general, any *temporal and spatial dispersion of the recovery* of excitability in cardiac muscles, e.g., due to local ischemia, increases the degree of ventricular vulnerability. The *diseased heart* is much more susceptible to ventricular fibrillation.

[125] *Defibrillation* administers electric shocks to the heart (typically via large contact electrodes on the chest) in order to depolarize the *whole heart simultaneously* (or, at least, critical mass of ventricles) and to convert the heart into the absolute refractory state. *Re-entry mechanisms* can not reappear, uncoordinated activity ceases as well as ventricular fibrillation.

In particular, defibrillation allows the *sinoatrial node* to re-establish *coordinated excitation and contraction of ventricles* after defibrillation. In fact, the sinoatrial node resumes its pacemaker function after all *cardiac muscle cells repolarize and relax together*—following their collective

The heart muscle is susceptible to ventricular fibrillation during the heart's *vulnerable period*.[126] Outside the vulnerable period, the electrical stimulation may only induce single *extrasystoles* (Kaniusas 2015, Footnotes 377 in Chap. 5). The *probability of fibrillation* increases with

- increasing *current strength* and
- increasing *exposure duration*;

see Fig. 2.89. In particular, the necessary current level to induce ventricular fibrillation decreases steeply if the *exposure duration* exceeds the duration of a *single cardiac cycle* (of about 1 s), so that the external stimulation of the heart is definitely present during the vulnerable period. Factors such as the size and position of electrodes, the current waveform, and the applicable whole-body impedance co-determine the fibrillation threshold.

---

depolarization due to the external defibrillation—and thus become again excitable via the regular conductive system of the heart (Kaniusas 2012, Fig. 2.35).

A typical *defibrillation shock* has *energy* of about 200 J or more, resulting in brief *current pulses* up to 50 A over a few ms, e.g., 250 J = $(50A)^2 \cdot 50\Omega \cdot 2$ ms with the assumed *whole-body impedance* of 50 Ω (3.37). Please note that the applicable *skin impedance* is quite low because of the *high contact voltage* and even decreases with increasing shock energy. This is in analogy with the high-voltage spark discharges which short-circuit the skin and thus the skin impedance.

[126]The *atrial and ventricular fibrillation* can only be induced when the time instant of the electrical stimulation coincides with the *late atrial or ventricular systole*, respectively; or, in analogy, with the *early phase of atrial or ventricular recovery* from excitation, respectively. This time period is known as the *vulnerable period* (Reilly 1998). During the vulnerable period electrical excitability gradually recovers following contraction. This leads to very important practical conclusions that for

- *short current durations* <1 s the risk of fibrillation is determined by the temporal coincidence of the exposure event and the vulnerable late systole—i.e., no coincidence, no risk—whereas for
- *long durations* >1 s the vulnerability of the late systole manifests definitely during the exposure duration (Fig. 2.89).

In particular, the onset of *ventricular fibrillation* is most likely preceding the apex of the *T wave* of the electrocardiogram (Kaniusas 2012, Fig. 2.38c) because the *non-uniformity in the recovery of excitability* in *ventricles* is maximal at this time interval (Footnote 124). Simply speaking, the temporal coincidence of the electrical stimulation with the T wave should be avoided to escape ventricular fibrillation. As an approximation, the vulnerable period comprises about 10% of the cardiac cycle (about 100 ms in the absolute time) in terms of ventricular fibrillation. In addition, the *stimulation threshold* for ventricular fibrillation *decreases significantly* when the heart is *repeatedly stimulated* during the *vulnerable period* (ICNIRP 2010).

Likewise, the electrical stimulation at times *outside the vulnerable period* either

- is *ineffective* and nothing happens; i.e., cardiac muscles are already excited or still remain in their refractory state *before the vulnerable period*, or
- may yield only a single *extrasystole*; i.e., cardiac muscle cells are fully recovered and excitable *after the vulnerable period* but there is no *re-entry mechanism* (Footnote 124) because the non-uniformity in the recovery of excitability is missing.

It should be noted that *ventricular fibrillation* can be lethal while *atrial fibrillation* reduces the atrial filling only and thus is not lethal (Kaniusas 2012, Footnote 113).

It can be observed in Fig. 2.89 that strong but short-exposure currents of about 1 A for less than 100 ms are highly likely to induce ventricular fibrillation provided that the exposure occurs during the *vulnerable period*. It should be reiterated that the risk of fibrillation at such high current levels increases drastically with increasing *exposure duration* beyond a *single cardiac cycle*.

Figure 2.89 illustrates empirically derived thresholds for *ventricular fibrillation* —as a function of the contact current and exposure duration—below which fibrillation is highly unlikely, i.e., with the fibrillation risk $\ll$5%. Provided that the current pathway from the *left hand to both feet* is considered, fibrillation may start at 40 mA at 50 Hz given a long exposure duration >1 s. This pathway is known as the *reference current pathway* with the associated *heart current factor HCF* of 1 (Fig. 2.92a, see below).

Please note that a more *unfavourable current pathway* going through or closer to the heart region would decrease this threshold. For instance, a more risky pathway from the *breast to the left hand* increases *HCF* to 1.5 yielding a lower fibrillation threshold of only 40 mA/1.5 $\approx$ 27 mA for long exposure durations > 1 s. On the contrary, a more *favourable current pathway* more distant to the heart increases the fibrillation threshold. The pathway from the *one hand to another hand* has $HCF = 0.4$ and yields a higher fibrillation threshold of 40 mA/0.4 = 100 mA for long exposure durations > 1 s.

In analogy, if electric currents are introduced close to or *directly into the heart*— e.g., through *intracardial catheter electrodes* (Fig. 2.86b, c) or during open *cardiac surgery* in operating theatres—fibrillation risks are significantly increased and the associated fibrillation thresholds amount to only 10 µA. Please note that thresholds for *microshocks* are reduced by more than the factor 1000 in comparison with *macroshocks*, as described in Footnote 118.

The *current-voltage diagram* from Fig. 2.90 illustrates ventricular fibrillation as a function of the *contact voltage* U_C for the *reference current pathway*. As already mentioned, the *mains voltage* with U_C = 220 V is clearly capable to induce *ventricular fibrillation* given a typical Z_{wb} = 2 kΩ in terms of *macroshock*. A more *unfavourable current pathway* such as that from the *breast to the left hand* reduces the fibrillation threshold so that the risk of fibrillation increases even more.

Moreover, the *fibrillation threshold* for currents of 10 µA introduced *directly into the heart* (Footnote 118) yields even lower thresholds for U_C in the range of only several *10 µV*, given the electrical resistance of the heart in the range of *several ohms* (Leitgeb 2010). A more realistic case of the *hand to hand contacts during cardiac surgery* and an applicable Z_{wb} of 1 kΩ yields dangerous voltages of about *10 mV* (=10 µA · 1 kΩ) capable of triggering ventricular fibrillation. Consequently, maximum potential differences in operating theatres intended for critical *cardiac and thorax surgery* are typically limited to 10 mV.

Heart Current Factor

The risk of *ventricular fibrillation* increases with decreasing distance of the *effective current pathway* to the heart region and with increasing amount of the current through the heart. Therefore, for safety considerations in terms of ventricular fibrillation, different current pathways can be compared with each other and with respect to the aforementioned *reference current pathway*. In particular, this pathway results when electrodes or live parts contact the *left hand and any foot* (or *both feet*). This resulting reference pathway—as illustrated in Figs. 2.92a and 2.57 with the associated risk of fibrillation given in Fig. 2.89—is already quite dangerous and yields a relatively high fibrillation risk.

This *fibrillation risk* is quantitatively assessed by the aforementioned *heart current factor HCF* = 1. In an approximation, *HCF* provides the ratio of the *current density* in the heart for a *given current pathway* to the current density in the heart for the contact current of equal amplitude along the *reference current pathway*. As shown in Fig. 2.92a, the hazard of fibrillation decreases by 60% if the pathway *hand-to-hand* (*HCF* = 0.4) is considered instead of the reference pathway. On the contrary, the hazard increases by 50% for the current pathway from the *breast to the left hand* (*HCF* = 1.5) since the cardiac region is strongly involved within this pathway (Fig. 2.92b). A few more *current pathways*[127] with the indicated *HCF* are depicted in Fig. 2.92a, b for comparison aims.

From a practical point of view, the factor *HCF* can be easily used to *estimate the risk* of fibrillation for any given current pathway through the body with its associated *HCF* value. Please recall that the *reference current pathway* with its *HCF* = 1, the reference current amplitude I_{ref}, and the reference exposure duration t_{ref} leads to the *experimental fibrillation risk* from Fig. 2.89. Correspondingly, any *given current pathway* within the body with its *HCF*, the current amplitude $I = I_{ref} / HCF$, and exposure duration $t = t_{ref}$ leads to a quantitative fibrillation risk evaluated from Fig. 2.89 at the levels I_{ref} and t_{ref}. In other words, the current I_{ref} / HCF of any current pathway represents an identical risk of ventricular fibrillation as the reference current I_{ref} flowing from the left hand to any foot (or both feet). To give a quantitative example, a current of 100 mA for the pathway from the *left hand to both feet* (*HCF* = 1, see Fig. 2.92a) yields the same risk of ventricular fibrillation as another current of 250 mA (=100 mA /0.4) for the pathway *hand-to-hand* (*HCF* = 0.4).

---

[127]It is interesting to note that in the case of *lightning* and thunderstorm it is advisable to kneel down (with both feet close to each other) but not to lie down, even though kneeling may attract lightning more than the lying position. That is, provided there is a lightning stroke nearby, a huge surge of current creates large *potential differences* in the radial direction around the entry point of stroke and along the surface of the ground. A so-called *step voltage* between both feet in contact with the ground results, whereas the voltage rises with both increasing potential differences and increasing distance between feet.

The kneeling position with both feet close to each other has two advantages as related to lying on the ground. Firstly, it reduces the step voltage and thus the resulting *total current through the body*. Secondly, the *fibrillation risk* is reduced for kneeling since inner currents avoid the cardiac region; the associated *HCF* is only 0.04 for the foot-to-foot current pathway (Fig. 2.92a), i.e., kneeling tends to protect the heart from its fibrillation.

Direct Current

Direct currents above 500 mA flowing from one hand to both feet—along the *longitudinal axis* of the human body (Fig. 2.89)—for short exposure *durations of less than 100 ms* may lead to *ventricular fibrillation* (Footnote 124). By qualitative analogy with fibrillation thresholds at 50 Hz (Fig. 2.89), the associated thresholds for fibrillation increase and level off with *decreasing exposure duration* (DIN 60479-1 2007). For instance, the aforementioned threshold of 500 mA at the short exposure <100 ms decreases down to about 150 mA at the large exposure >1 s (Leitgeb 2010).

As in the case of alternating currents, exposure to the direct current with a *short exposure duration <200 ms* can induce ventricular fibrillation only if the direct current exceeds the relevant exposure-dependant threshold during the *vulnerable period* of the heart cycle (Footnote 126) (DIN 60479-1 2007). By analogy with alternating currents, the *heart current factor* (Fig. 2.92) applies also for *direct currents* in order to assess the fibrillation risk as a function of the local current pathway within the body.

For *short exposures* <200 ms, fibrillation thresholds of the amplitude of the direct current are almost equal to the thresholds of the effective value of the alternating current. However, *prolonged exposures* exceeding a single *cardiac cycle* raise fibrillation thresholds of the direct current significantly above those of the alternating current. For instance, a rather conservative fibrillation *threshold of 150 mA*—conservative because most healthy persons have a bit higher fibrillation threshold of 200 mA (DIN 60479-1, 2007)—applies for the direct current at a large exposure *duration of 10 s* versus the threshold of only 40 mA for 50 Hz and 10 s (from Fig. 2.89).

Electric and Magnetic Field

An outer *time-varying electric field* surrounding a conductive human body can yield local elevations of the electric field on the skin, especially in combination with the *electrical point effect* (Fig. 2.26). These elevations can induce *sensations* of this ambient field due to

- vibrations of the body hair—where an alternating recharging of hairs and skin surface yields vibration of hairs with twice the field frequency and thus activation of mechanoreceptors within the skin (Kaniusas 2012, Footnote 81)—and
- stimulation of peripheral receptors in the skin.

Pure perception or *annoyance* is mainly induced through accumulated *surface charges* on the body surface (Fig. 2.29) and their *discharge via currents* through the body (Fig. 2.86a) in the presence of the ambient *time-varying electric field* in the relatively *low frequency range up to 100 kHz* (ICNIRP 2010). Please recall from Section "Incident Electromagnetic Fields" that below 100 kHz the exposed body absorbs only a negligible amount of energy from the outer field. For instance,

the outer field amplitude of 10 and 20 kV/m (Footnote 80) can be perceived by 20 and 50% of population, respectively (CRP 1997).

In contrast to the time-varying electric field, the ambient *time-varying magnetic field* in the latter range up to 100 kHz induces electric and current density fields within tissue in the course of *electromagnetic induction* (Fig. 2.31). These fields, in turn, stimulate central and peripheral nerves as well as induce retinal phosphenes (Footnote 128).

Please recall that the *direction* of the ambient time-varying electric or magnetic field with respect to the body orientation strongly impacts the strength of the *induced inner electric field* within the body. While the *maximum inner electric field* is induced when

- the external *electric field* is directed *parallel* to the long body axis (Fig. 2.30a),
- the external *magnetic field* directed *perpendicular* to the long axis induces the maximum inner electric field (Fig. 2.32b).

Figure 2.87 illustrates the *basic restriction* of the *inner electric field* with its magnitude E within the human body (Fig. 2.63b) as a function of the *field frequency* and the associated *reference value* of the *outer electric field* with its magnitude E_{ext} outside the body. The *general public exposure* is considered only.

Basic Restrictions over Frequency

The *basic restriction* of E *inside* bodily tissues up to 1 kHz (see point A in Fig. 2.87) limits the induced electric field strength inside of tissues of the *central nervous system*, namely, inside the *brain* and *retina*. These restrictions are mainly supposed to avoid the induction of *retinal phosphenes*,[128] i.e., to avoid a well-established *physiological effect* with the *lowest excitation threshold*. Here the

[128] *Retinal phosphenes* are perceptible *faint flashes of light* in the periphery of the visual field *without light* actually entering the eyes. Phosphenes can be induced by

- *mechanical stimulation* (rubbing of closed eyes) and
- *electromagnetic stimulation* (due to *ambient time-varying electric and magnetic fields* which induce *inner electric fields and currents* in the retina)

of *mechanically and electrically excitable cells in the retina*, including photoreceptors (Reilly 1998). Although photoreceptors in the retina are primarily sensitive to light (Kaniusas 2012, Footnote 88), they show a cross-sensitivity to other stimuli such as *local mechanicaland electrical stimuli* producing a *visual sensation* in the brain (Kandel 2000). It should be noted that the internal electric fields in the retina corresponding to phosphenes perception are much lower—a factor of 100 or so (Reilly 1998)—than those necessary for nerve or muscle excitation (Fig. 2.73). *Synaptic junctions* in the retina are the likely region of the local electrical stimulation in terms of phosphenes, with induced depolarizing changes in the presynaptic membrane potential (Kaniusas 2012, Fig. 2.19).

It should be noted that the *retina* with its phosphenes is usually considered as an appropriate, albeit conservative, *model* for induced *electric field effects* in the *central nervous system*. This is simply because the retina—as an outgrowth of the forebrain—is part of the central nervous system (ICNIRP 2010).

retina as an *outgrowth of the forebrain* with its retinal phosphenes serves as a model for the brain in order to asses transient effects of the brain stimulation on brain functions.

Stimulation thresholds for *phosphenes*—as well as the associated *basic restrictions* of *E*—are *lowest* between 10 and 25 Hz (see point B in Fig. 2.87). When considering such *weak electric fields* inducing retinal phosphenes, the collective effect of interacting nerve cells, the network effect, should be accounted for (ICNIRP 2010); see the averaging volume of 1000 interacting cells from Footnote 112. This *collective effect* finds its expression in the summation and integration of small induced voltages and currents in *synaptic junctions* of nerve cells (Footnote 128).

The thresholds for phosphenes induction as well as *basic restrictions* of *E* rise rapidly at lower and higher *f* around the mentioned range 10–25 Hz (Fig. 2.87). At 50 Hz, the restriction of the inner *E* amounts to 0.02 V/m (ICNIRP 2010). The rising threshold at higher *f* intersects with the stimulation thresholds of the central and *peripheral myelinated nerves* at 1 kHz (ICNIRP 2010). Namely, for *f* above 1 kHz, basic restrictions on the stimulation of the peripheral nerve system apply. Since the inner *E* fields required for excitation of *peripheral nerves* are lower than those required for excitation of *central nerves* (see below), the basic restrictions above 1 kHz—based on the thresholds of peripheral nerves—protect against the adverse stimulation of both *central nerves* and *peripheral myelinated nerves*.

In particular, at 1 kHz, the *stimulation threshold* of 4 V/m—applicable to stimulation of *peripheral myelinated fibers* (see below)—with a *reduction factor* of 10 yields the relevant *basic restriction* of the inner *E* of 0.4 V/m (see point A in Fig. 2.87). Above 3 kHz, the restrictions of *E* for all parts of the body rise again due to diverse mechanisms, as detailed with respect to the rising current threshold in Fig. 2.74 towards increasing *f*.

Reference Values over Frequency

In the *low frequency range*, especially below 1 kHz, i.e., where negligible energy absorption from ambient electromagnetic fields (Section "Incident Electromagnetic Fields") and minor electromagnetic induction (Section "Incident Magnetic Fields") apply, the *reference levels* of E_{ext} are intended to prevent *neuromuscular stimulation* from mainly *contact currents*, to prevent shocks and burns. In addition, the reference levels of E_{ext} up to 50 Hz include a sufficient margin to prevent effects related to *surface charges* and their *discharge* (Figs. 2.29 and 2.86a), yielding *perception and annoyance* in most people. For *higher frequencies* up to about 100 kHz, the *reference levels* of E_{ext} are based on the basic restriction of the induced *E* within the body (Fig. 2.32).

The ambient electric field E_{ext} of about 4–5 kV/m at 50/60 Hz (typical for an overhead power transmission line, see Footnote 80) yields *perception of a finger contact* of a *grounded person* with an exposed and *isolated passenger car* (located close to the transmission line) (CRP 1997), in close analogy with Fig. 2.86a. Please note that the acceptable *reference level* of E_{ext} is at 5 kV/m at 50 Hz (Fig. 2.87), i.e., this level is comparable with the aforementioned perception threshold of a finger contact. In contrast, for an exposed and *isolated truck* (under the transmission line),

the *threshold* of E_{ext} that induces the same perception of the finger contact is *smaller by a factor of 6* than that for the isolated passenger car. In line with Footnote 116, this is because the induced *surface charge*—and the subsequent *discharge current* through the body—increases with the *size* of the conducting and isolated object located in the ambient E_{ext} and subjected to separated surface charges. Larger charges and currents obviously lower this perception threshold of E_{ext} when a grounded person contacts an isolated truck. For comparison, the *perception threshold of a spark discharge* between the finger and small objects caused through charging of a person amounts to about 1 kV/m at 50/60 Hz while considering the most sensitive 10% of adult persons (CRP 1997). The related annoyance threshold for spark discharges amounts to about 2–3 kV/m.

Therefore, the *reference level* of E_{ext} of 5 kV/m at 50 Hz (Fig. 2.87) *does not completely exclude the perception* of ambient electric fields (close to transmission lines) for the *general public exposure*. However, adhering to this reference level reduces the possibility of spark discharges but does not eliminate it, and thus *protects* against considerable disturbances and *adverse health effects*.

For the *occupational exposure*, the reference level of E_{ext} of 20 kV/m is given for the low frequency range 1–25 Hz (ICNIRP 1998, 2010) and the reference E_{ext} of 30 kV/m is given for *static electric fields* at 0 Hz (Heinrich 2015). However, there are further limitations of this level if there is a risk of contact with (grounded or ungrounded) conducting objects at a different potential than the human body potential; in other words, if there is an increased *risk of discharge* (Footnote 116).

It can be expected that the *sharp decrease* of the reference E_{ext} from 50 Hz to 3 kHz (Fig. 2.87) compensates for an increase of the inner E within the body with increasing *frequency* f given a constant E_{ext} outside the body in the air. In particular, this increase of E follows from the *boundary condition* (2.101) of the dominating normal components E and E_{ext} at the air/tissue boundary (Fig. 2.55). Here the boundary equality $E = E_{ext} \cdot \varepsilon_{air}/\varepsilon_{body}$ applies. Therefore, E increases for a constant E_{ext} since the *permittivity* ε_{body} of biological tissue decreases with increasing f (Fig. 2.20) but not the permittivity ε_{air} ($\ll \varepsilon_{body}$) of the air in the latter frequency range.

The increased E in tissue for a constant outer E_{ext} tends to increase the magnitude J_E of the associated *conductive current density field* (2.54) within the body. Thus the *outer* E_{ext} has to decrease with f to keep the *inner* J_E constant or, likewise, in order to comply with the almost constant *basic restrictions* of J_E in the range from 50 Hz to 3 kHz (Fig. 2.87). In addition, please note that the tissue *conductivity* —connecting E and J_E—slightly increases with increasing f in the latter range so that E is required to stay constant even more in order to keep J_E rather constant.

Figure 2.87 considers reference values of E_{ext} only up to 1 MHz according to (ICNIRP 2010). For members of the *general public* and for even *higher frequencies* up to 300 GHz, reference values for the ambient E_{ext} are considered in (ICNIRP 1998). In particular, the reference E_{ext} decreases from 87 V/m at 1 MHz towards a *minimum value* of 28 V/m at 10 MHz and then stays constant up to 400 MHz. In this high frequency range, the minimum reference E_{ext} accounts for the *maximum energy* coupled into the body; i.e., the coupling of ambient fields is quite efficient in this range (Section "Incident Electromagnetic Fields"). Between 400 MHz and

2 GHz, the reference E_{ext} increases from 28 V/m to 61 V/m and then remains constant up to 300 GHz.

Paradoxically, *basic restrictions* of the inner *E* field intersect and even exceed the *reference levels* of the E_{ext} field outside the body at frequencies close to 1 MHz. This inadequacy can only be justified by *uncertainties* in the applied methodology to set the reference levels, whereas the methodology includes mainly mathematical modelling and extrapolation from laboratory investigations (ICNIRP 1998, 2010).

Endogenous Fields

Depicted values of the *inner electric field* in Fig. 2.87—i.e., basic restrictions—should be put into perspective with the size of *endogenous electric fields* of diverse well-established *biological effects*. Please recall that all biological *effects have their own thresholds* below which they do not occur; i.e., these effects can still be avoided when *basic restrictions* on the inner electric fields within the body are not exceeded. In the following, we start with the strongest fields within the body and end with the weakest.

The *strongest electric field* is found within the resting *membrane of the cell*, attaining impressively high absolute levels of about 10^7 V/m (=100 kV/cm = 70 mV / 7 nm, see Kaniusas (2012, Footnote 49)). Decaying electric fields outside the cell in the extracellular space are already much weaker and decrease strongly with increasing distance from their origin[129] (Footnote 58). *Close to the excitable cells* fields may be only up to *200 V/m* (CRP 1997), i.e., these fields are already many orders of magnitude smaller than intramembrane fields.

The minimum threshold of the *inner electric field* (endogenous field) for the stimulation and excitation of *myelinated nerve fibers* of the *peripheral nervous system* in humans has been estimated in the range of about 4–6 V/m, based on the assumption that the stimulation takes place in the skin or immediately below the skin (ICNIRP 2010). For instance, the *threshold* for excitation of *peripheral nerves* at 50 Hz are above *2 V/m*. The minimum threshold for the excitation of *myelinated nerve fibers* of the *central nervous system* in humans has been suggested of about 10 V/m up to 20 V/m according to different sources. It is instructive to observe that the excitation threshold pertaining to the *central nervous system* is significantly higher than that of the *peripheral nervous system*. In addition, fields in the order of 1 V/m can influence the excitability of neurons in the brain (ICNIRP 2004); compare Footnote 88 and Fig. 2.84.

The threshold for excitation of *cardiac muscle* is much higher and reside above *30 V/m* (CRP 1997). The *fibrillation threshold* of the cardiac muscle during the *vulnerable period* (Footnote 126) is about 10 to 20 times (ICNIRP 2004; Reilly 1998) up to 50 times (ICNIRP 2010) higher than for the cardiac muscle stimulation (Footnote 97) for short stimulation pulses.

[129]The electric field usually decreases non-linearly with increasing distance from the site of origin. For instance, the electric field from a *line dipole* (i.e., opposite charges on two straight wires located at a relatively small distance in comparison with the distance from the wires to the point of interest) is *inversely proportional to squared distance* from the dipole.

The only robustly established effects of the stimulation *below the thresholds for nerve or muscle stimulation* are the induction of *retinal phosphenes* (Footnote 128). The minimum threshold for this induction of phosphenes is about *50–100 mV/m* at *20 Hz* and rises rapidly at higher and lower frequencies (ICNIRP 2010). As expected, the threshold for phosphenes is above the *basic restriction* of the inner electric field of 10 mV/m at 20 Hz (see point B in Fig. 2.87). Avoiding retinal phosphenes is intended to protect against any possible stimulation effects on *brain* functions.

The *electric fields in peripheral sites* in response to distant excitable cells are in the range of *1–50 mV/m*, composing *permanent biosignals* (Kaniusas 2012, Fig. 1.15) and, ultimately, having their origin in the recurrent excitation of cells. Please note that these *natural endogenous electric fields* of 1–50 mV/m correspond with *natural endogenous current densities* of 0.2–10 mA/m^2 (or 0.02–1 μA/cm^2) under the assumption of the tissue conductivity of 0.2 S/m (2.54 and Table 2.2). Please compare the associated discussion on the *endogenous current density fields* from Section "Curent Density Field".

Curent Density Field

When currents are applied on or within the body, it should be recognised that usually not the absolute *current level* itself is the quantity determining biological effects and adverse risks but the resulting *current density* field (2.23). In other words, the larger is the *contact area* of electrodes or live parts in contact with the body and the larger are the *cross-section areas* along which the resulting currents flow within the body, the less are the risks of expected adverse effects due to these currents. Obviously, the local *dynamic and peaks* of instantaneous current density fields within tissue are decisive in determining *neuromuscular excitation*.

It should be reiterated that the *inner conductive current density* can be induced via contact-less (or direct) coupling or via contact-based (indirect) coupling. That is, ambient electric and magnetic fields can induce *inner currents* within the exposed body in terms of *contact-less coupling* (Figs. 2.26a and 2.31). On the other hand, a physical contact of the body with a charged object leads also to *inner currents* in terms of *contact-based coupling* (Fig. 2.86a). The discussed coupling and induction mechanisms show that *properties of incident fields* (including its waveform, frequency, etc.) as well as *properties of the body* (including its size, orientation, etc.) —i.e., exposed and/or connected body to the field source, see section on the field distribution in Section "Basic Restrictions Versus Reference Levels"—are important factors for the *coupling efficiency*.

The impact of the *current density* transversing the *human skin* is quantified in DIN 60479-1 (2007):

- No changes of the skin are usually observed for densities below 10 mA/mm^2 (or 1 A/cm^2), whereas prolonged exposure of more than a few seconds may lead to a *whitish discoloration of the skin*.

- For higher densities between 10 and 20 mA/mm^2, the skin under the current electrode *reddens*, whereas
- between 20 and 50 mA/mm^2 the skin becomes *brownish* with blisters around the electrode; known as *current brands*.
- Even higher current densities > 50 mA/mm^2—especially for an extended exposure above a few seconds—lead to *carbonisation* of the skin.

Thresholds of the *current density* through the skin with respect to *various (adverse) effects*—such as no changes, red skin, current brands, and carbonisation—decrease non-linearly with increasing *duration* of the skin exposure. In analogy with Fig. 2.89, these thresholds of the current density level off for durations above about 10 s.

Figure 2.87 illustrates the *basic restriction* of the *inner current density field* with its magnitude J_E within the human body (Fig. 2.63b) as a function of the *field frequency*. The *general public exposure* is considered only. The shown course of J_E demonstrates a minimum of 2 mA/m^2 in the range of 4 Hz–1 kHz, whereas below 4 Hz and above 1 kHz the restriction J_E increases. This course of J_E is comparable with the qualitative course of the threshold current over the frequency f for sinusoidal stimulus and neuromuscular stimulation (Fig. 2.74). Therefore, the discussed biophysical mechanisms with respect to Fig. 2.74 equally apply to the course of J_E in Fig. 2.87 in order to avoid *neuromuscular stimulation* effects.

In particular, the density level of 100 mA/m^2—leading to consistent neuronal excitation within the head (see below)—is used as a *starting point* for the derivation of the *basic restriction* of J_E in exposure guidelines. Here a safety factor of 10 is applied for the occupational exposure and an additional factor of 5 for the *general public exposure* (ICNIRP 1998). Therefore, the restriction J_E for the *general public exposure* amounts to $100/(10 \cdot 5) = 2$ mA/m^2 in the frequency range from 4 Hz to 1 kHz (see point C in Fig. 2.87).

With *increasing frequency* above a few hundreds of Hz (above 300 Hz (WHO 1993)), *neurostimulation effects* become less likely due to diminished membrane polarization, refractory behaviour, and displacement currents (Fig. 2.74). Reduced risks of stimulation imply that the associated level of the *basic restriction* J_E increases with frequency. However, the restriction J_E continuous to rise only up to frequencies of about 100 kHz where *thermal effects* start to dominate and then levels off with increasing frequency.

This is because the thermally-relevant and frequency-independent *basic restriction* P_{SAR} should be used for *thermal effects* (Section "Power Measures") instead of the basic restriction J_E. In other words, the equivalent thermally-relevant threshold for J_E levels off because the thermally-relevant threshold for P_{SAR} determines this J_E [via (2.57)] while P_{SAR} is independent on the field frequency. Therefore, for instance, the basic restriction for J_E for frequencies around 2–3 MHz (>100 kHz) is equivalent in its effect to the restriction for the peak P_{SAR} (WHO 1993).

In short, the relevant *threshold*—or the applicable *reference value* (Fig. 2.87) from *exposure guidelines*—for the *ambient* E_{ext} *outside the body* at the dominating

frequency 50 Hz of power lines is *5 kV/m*. The relevant threshold for the *inner* J_E *inside the body* at 50 Hz amounts to *2 mA/m*^{2}. However, please recall that these guidelines provide an acceptable margin of safety in the general case only. Exposure guidelines do not consider special circumstances such as a potential interference with implanted *medical devices*, e.g., with *cardiac pacemaker*[130]

[130]The coupling of *electric and magnetic fields* into (implanted) *medical devices* worn by individuals is considered as the *indirect* or *contact-based coupling*. The coupling into cardiac pacemakers is highly relevant in praxis (CRP 1997; Heinrich 2015) and should be considered here (Footnote 12 in Sect. 2). *Two types* of *cardiac pacemakers* exist:

- the *unipolar cardiac pacemaker*, in which only one *stimulation/sensing electrode* goes from the pacemaker to the cardiac muscle to be stimulated (Kaniusas 2012, Sect. 2.3), whereas the casing of the pacemaker or the surrounding body tissue acts as the second *reference electrode*. In contrast,
- the *bipolar cardiac pacemaker* has two electrodes, the *stimulation/sensing electrode* and the *reference electrode*, both going from the pacemaker directly to the cardiac muscle.

The *unipolar cardiac pacemaker* is regarded as the most sensitive medical implant (CRP 1997), especially with respect to *external electric fields* at the relatively low frequencies up to 1 kHz (Heinrich 2015). This is because the *interference voltage at the sensing input of the pacemaker*—i.e., the voltage due to the external electric field—is proportional to the *geometrical distance* between both electrodes of the pacemaker. To be more precise, the interference voltage is proportional to the aforementioned distance in the direction of the non-zero electric field component, see (2.30) and the influence of the angle β in Fig. 2.11a, b. In particular, this distance is much larger for the unipolar cardiac pacemaker (i.e., the distance between the electrode in the heart and the stimulator casing located further away from the heart) than that in the bipolar cardiac pacemaker (i.e., the distance between both electrodes located directly in the heart). Therefore, the *bipolar pacemaker* turns to be more *robust* to external electric fields than *unipolar pacemaker*.

In addition, the relatively large size of the *reference electrode* of the *unipolar pacemaker* implies that this electrode is highly sensitive to coupled *electric fields* from surroundings into tissue. The ambient electric field at 50 Hz of more than *2.5 kV/m* in its magnitude already *disturbs* the proper function of the *unipolar pacemaker* (CRP 1997). As noted in Section "Curent Density Field", this field magnitude of >2.5 kV/m is unfavourably lower than the proposed *reference value* of 5 kV/m for outer electric fields at 50 Hz (Fig. 2.87) to protect general public and prevent adverse health effects. Likewise, an individual with the implanted unipolar cardiac pacemaker should avoid the stay under overhead *power transmission lines* with the voltage 380 kV or 220 kV, where electric fields of 6 kV/m or 4 kV/m, respectively, may easily prevail above the ground (Footnote 80).

However, *external time-varying magnetic fields* at the relatively low frequencies up to 1 kHz—which are usually highly *inhomogeneous in space* and are *limited* to local spots within the body (e.g., magnetic fields are generated by field sources of small physical dimensions residing close to the human body)—may yield a larger *interference voltage* at the sensing input in *bipolar pacemakers* than that in *unipolar pacemakers* (Heinrich 2015). This is due to a local, regionally limited, and relatively small integrating area in between electrodes of the bipolar pacemaker (both electrodes are located in the heart). This small area, i.e., the effective loop area A in (2.86), can be fully permeated by local *peaks of the inhomogeneous magnetic field*, which then results in a relatively high induced/interference voltage. In contrast, the area encompassed by electrodes of the unipolar pacemaker is relatively large (see above), which implies integrating, smoothing, and averaging effects on the inhomogeneous time-varying magnetic field permeating this large area. Correspondingly, this results in a relatively small induced/interference voltage in the *unipolar pacemaker* and thus its higher *robustness* in comparison to the *bipolar pacemaker* when the body with implants is exposed to locally constricted time-varying magnetic fields.

within the body (Footnote 114). Such circumstances tend to reduce exposure limits and render them more strict than presented in Fig. 2.87 and considered as harmless for the general public.

Endogenous Fields

Depicted values of the *inner current density field* in Fig. 2.87—i.e., *basic restrictions*—should be put into perspective with the size of *endogenous current density fields* of diverse well-established *biological effects*. In the following, we start with the strongest fields within the body and end with the weakest.

Pulsed and high *current densities above 1000 mA/m²* within the body may lead to *life-threatening effects* due to excitation of neuronal and muscular structures. These severe effects include cardiac extrasystoles (Kaniusas 2015, Footnote 61 in Chap. 5), muscular tetanus (Kaniusas 2012, Fig. 2.31b), *ventricular fibrillation* (Footnote 124), and even respiratory failure (ICNIRP 1998). For instance, current densities above 3 A/m² (above 300 μA/cm²) were reported to induce *pump failure* of the heart (comparable to extrasystoles), whereas densities above 5 A/m² induced *ventricular fibrillation* (Roy 1976). The latter thresholds were assessed in dogs at 60 Hz for a relatively long exposure duration of 15 s. Please recall that this relatively long exposure (>10 s) implies minimum thresholds in line with Fig. 2.89.

Current densities exceeding *several 100 mA/m²* in the frequency range of about 10–1000 Hz induce consistently *neuromuscular excitation*. Current densities *above 100 mA/m²* in the *head* in the latter frequency range induce *acute changes* in the excitability of the *central nervous system* in human, whereas densities *lower than 100 mA/m²* in the head alter visual and mental functions; compare Footnote 88. Current densities of only *about 10 mA/m²* at 20 Hz in the *retina* are sufficient to induce *retinal phosphenes* (Footnote 128).

No established *adverse health effects* are reported for the inner current density *below 10 mA/m²* at frequencies up to 1 kHz. In fact, current densities up to 10 mA/m² are generated by *permanent biosignals* in bodily tissues, composing *natural endogenous current density fields*. Please compare the associated discussion on the *endogenous electric fields* from Section "Electric and Magnetic Field".

Finally, it should be noted that the *robustness* of an implanted system to external *electric and magnetic fields* is determined not only by the used *configuration of electrodes*—as illustrated above—but also by the used *amplification of input signals*. Usually, the amplification of bipolar input signals is higher than that of unipolar signals. This is because the expected amplitude of the relevant input signal—e.g., the intracardial electrocardiogram—is lower in the bipolar case, which necessitates its higher amplification in the bipolar system. The higher amplification—or the higher sensitivity of the cardiac pacemaker to input signals—implies also a higher sensitivity of *bipolar wired systems* to external noise related to that of *unipolar systems*.

Summing up, the *noise immunity* of the *bipolar cardiac pacemaker* in comparison with the *unipolar cardiac pacemaker* is determined by all three:

- the pacemaker sensitivity to external *constant and time-varying electric fields*,
- the pacemaker sensitivity to external *time-varying magnetic fields*, and
- the *amplification* level of input signals.

Basically, an induced *artificial field* exceeding *endogenous fields*—naturally present in tissue—tends to induce *physiological effects*. The author in Leitgeb (2010) gives the threshold of *10 mA/m²* (or 1 μA/cm²) for the excitation of a *single cell*, whereas a conscious perception requires simultaneous excitation of *multiple cells* and starts at about *100 mA/m²* (or 10 μA/cm²). As expected, natural endogenous current densities are in the range of *basic restrictions* of the *inner current density* (Fig. 2.87), whereas these restrictions imply safety factors for the general public exposure.

Power Measures

Specific Energy Absorption Rate

The *basic restriction* (ICNIRP 1998) in terms of

- the *localized* specific *energy absorption rate* P_{SAR} (2.58) is in the range of 2–4 W/kg for frequencies *above 100 kHz* and for the *general public exposure*. The value of 2 W/kg applies for the head and trunk while 4 W/kg applies for limbs. Please consult Section "Incident Electromagnetic Fields" for the significance of the frequency as a vital parameter governing the spatial absorption of ambient fields. For comparison, the *basic restriction* for
- the *whole-body average*[131] P_{SAR} is only 0.08 W/kg for the *general public exposure*.

These restrictions limit the *rise of the body temperature to less than 1 °C* to *avoid heat stroke*, whereas the body's ability to deposit and dissipate the heat is already

[131]The origin of the basic restriction pertaining to the *whole-body average* P_{SAR} stems from the fact that exposure of healthy adults under *moderate environmental conditions* to the whole-body average P_{SAR} of less than 4 W/kg for about 30 min yields a still acceptable *increase in the body temperature of less than 1 °C* (ICNIRP 1998). For instance, the exposure of 4 W/kg for about 20–30 min rises the average body temperature of the *resting body* by about 0.1–0.5 °C with minimal changes in blood pressure and respiration rate, which is quite acceptable in healthy people (WHO 1993).

Therefore, the whole-body average P_{SAR} of *0.4 W/kg*—i.e., with a *safety factor* of 10—has been chosen as the *basic restriction* that provides adequate protection for the *occupational exposure*. The latter *safety factor* provides a large margin of safety with respect to other limiting conditions such as

- high physical activity of the body during the work,
- high ambient temperature, and
- high air humidity (i.e., thermally unfavourable environmental conditions).

For the *general public exposure* including sensitive subpopulations (Footnote 113), an additional safety factor of 5 is introduced, which yields the aforementioned basic restriction of *0.08 W/kg* for the *whole-body average* P_{SAR}.

Interestingly, the *metabolic rate of the human body* is about *4 W/kg for moderate activity* (such as a light house cleaning). A safety factor of 10 could be used to derive an additional whole-body heat stress which can still be tolerated; it would amount to the aforementioned *0.4 W/kg* as the *basic restriction* for the *occupational exposure*.

considered[132] (Footnote 107). The restrictions prevent excessive heating of tissue at or near the body surface (Section "Thermal Stimulation Effects").

Power Density

Another relevant *basic restriction* is the *power density* which accounts for the *superficial absorption* of the incident energy (by the skin) at relatively high field frequencies (Section "Incident Electromagnetic Fields"). This basic restriction amounts to 10 W/m^2 for field frequencies in the range from 10 to 300 GHz for the *general public exposure* (ICNIRP 1998), whereas an exposure of 10 W/m^2 may already result in the perception of heat. The associated *reference level*[133] of the *power density* is 2 W/m^2 in the range from 10 to 400 MHz for the *general public*, increases linearly from 2 to 10 W/m^2 in the range from 400 MHz to 2 GHz, and then remains at the level of 10 W/m^2 up to 300 GHz.

Neural Stimulation

There are a few *mechanisms* by which neural stimulation can *damage tissue*:

- *electrochemical stress*,
- *metabolic stress* as *two major mechanisms*, as well as
- *thermal stress* and
- *mechanical stress*.

Electrochemical Stress

Electrochemical stress occurs when electrochemical reactions, *irreversible Faradaic reactions*, take place while the resulting *reaction products harm tissue and/or electrode material* at the site of stimulation. These reactions are discussed in Section "Charge Transfer During Stimulation" from a *general perspective* and in Section "Ag/AgCl and Pt Electrodes" from a *detailed perspective*.

Metabolic Stress

Metabolic stress is due to *unnatural nerve stimulation*. That is, an overly *quick, strong, and/or extended stimulation* may render neurons to become *less responsive*

[132]In analogy, *animal* data indicate *biological effects* of *acute exposure* to electromagnetic fields, which are consistent with responses to *induced heating*; compare Footnote 110. That is, biological effects result when either

- the *tissue temperature* (or body temperature) *rises by about 1 °C* or more, or
- *thermoregulatory responses* are triggered to minimize the total heat load (WHO 1993).

Most biological effects have been reported at incident levels of P_{SAR} above about *1–2 W/kg*. In other words, any long-term adverse effects are not likely from exposures below thermally significant levels.

[133]Please note that *reference levels* of the *electric and magnetic fields* outside the body in this high frequency range from 10 MHz to 300 GHz can be easily derived from the *power density* using (2.13) and $Z = 377\ \Omega$.

in that their *threshold for excitation elevates*. Neurons can even become *depressed* and completely *refractory*.

The inner *homeostasis* of the stimulated nerve (bunch of neurons) may break down when a strong and frequent nerve excitation requires and even exceeds the total available homeostasis capacity. Natural homeostatic limits are different for different nerves so that the associated metabolic limits also differ. In response to abnormal stimulation, a morphological *axonal injury* may even occur where axon's myelin sheath prolapses into the axons space (McCreery 2016), reducing or even obliterating the effective axon's diameter (which is critically needed for the propagation of excitation in line with Kaniusas (2012, Fig. 2.18)).

The stimulation-induced depression of the neuronal activity and its excitability is usually *reversible* and temporary so that neurons eventually recover. However, the recovery may require up to many days after termination of the stimulus. Hence, the rather inert physiological phenomena involved in the depression are very different from transient and short accommodating mechanism (from Kaniusas (2012, Fig. 2.16)). There is also a risk of producing *irreversible* and permanent damage if the stimulus intensity is progressively increased while attempting to compensate for a depressed response and an elevated stimulation threshold.

In fact, either a high *amplitude of the stimulation current* at a medium *stimulation rate* or a medium amplitude at a high rate yields *metabolic stress* within the nerve (McCreery 2016). *Pulse timing* plays also a decisive role so that a high *duty cycle*[134] and/or long duration of the stimulation time lead to *nerve damage* due to metabolic stress.

Interestingly, *metabolic stress* can also be expected when subjective responses are induced well beyond the *comfortable level* (of humans and animals) for prolonged periods (Fallon 2016). Therefore, the provision of a comfortable state provides an approximate *limit to the metabolic harm* (even though the stimulation rate is well above the natural firing rate (Fallon 2016)). This very simple rule of insuring comfortable state can be applied to *sensory prostheses* where *perception of the stimulation* is possible, such as cochlear implants and the auricular vagus nerve stimulation. Please note that this simple rule does not apply for cortical prostheses where a sensory feedback is hardly likely.

Thermal Stress

For the sake of completeness, *thermal stress* or *heating of tissue* from *neural stimulation* should be shortly mentioned. A potential heating due to electrical power dissipation is *rarely a problem*, except for *high-power stimulation* devices such as cardiac *defibrillators* (Footnote 124). Tissue heating has been shown to be generally negligible at normal physiological stimulating frequencies (<100 Hz) for relatively short pulse durations (e.g., as small as 10 μs) (Van den Honert 1979). Please recall that electrical stimulation of nerves and muscles requires much less energy than thermal stimulation, as reflected by the relevant levels of *basic restrictions* (in Footnote 86 and Fig. 2.87).

[134]The *duty cycle* is the fraction of the time period in which the stimulation is active.

Mechanical Stress

Electrodes are typically made out of *biocompatible metals* (Footnote 136), especially when implanted within the body (Fig. 3.1c). However, intrinsically hard metals present a *hard abiotic interface* to intrinsically *soft biological tissues* and thus cause *mechanical stress* to tissues. In particular, neural and muscular tissues suffer under this stress.

An apparent *mismatch* in the *Young's modulus* (Kaniusas 2012, Footnote 135) between common *metals* used for electrodes and *biological tissues* amounts to several orders of magnitude. For instance, the modulus of 170 GPa applies for *platinum* while only 3–10 kPa applies for *brain tissue* and about 400–700 kPa for *peripheral nerves* (Patil 2016). This mismatch can easily cause *tissue trauma* and *inflammatory responses*, especially when *long-term applications* of metal electrodes are considered. The mismatch is an essential issue while maintaining a *stable recording interface* within or on *constantly moving body tissues*. Please recall that softness of tissues—especially of neural tissues—is needed to withstand these body movements.

An improved matching of mechanical properties between the *electrode material* and the target tissue is needed in future. Currently, these critical issues are addressed by *incorporating metals* (i.e., coating of metals), *substituting metals* (with electroactive organic materials such as flexible conductive polymers with the Young's modulus in the lower range of 1–10 GPa as compared with metals), or by other *sophisticated materials* (e.g., carbon nanotubes and graphene (Patil 2016)). In contrast to metal surfaces, *surfaces of conductive polymers* can be advantageously *functionalised* to release drugs or mitigate inflammatory responses of tissue at the site of stimulation and/or recording.

Stimulation Parameters Versus Stress

A fundamental understanding of instructive *relationships* between *parameters of the neural stimulus* and the different *stress mechanisms* allow us to shape the stimulus in a way that keeps tissue and electrode material harmless. Major mechanisms such as *electrochemical and metabolic stress* are mostly sensitive to stimulation parameters and are described below in detail. For *thermal stress* and the associated parameters, see (2.154) in Section "Thermal Stimulation Effects". In particular,

- the *charge density Q*/*A* (*local quantity*) per single phase of the stimulation pulse accumulated at the *electrode surface area A*, or the accumulated current density across the electrode/tissue boundary per phase, determines how much the double layer capacitance (3.5) of the *capacitive boundary* is charged or discharged by the current density. The resulting *opposite charges* across the boundary, in turn, determine
  - the *polarization overvoltage* ($(u_{\mathrm{pol,i}} - U_{\mathrm{pol}})$ from (3.16))—as the voltage drop between the metal electrode and tissue—and thus govern

– *electrochemical electrode reactions* (based on Butler-Volmer equations from Footnote 22 in Chap. 3, as described in Section "Ag/AgCl and Pt Electrodes") and finally account for
– *electrochemical stress*.

The *safe level* of *Q/A* to avoid *irreversible reactions* is known as the *safe charge injection limit*, *charge density limit*, or even *electrochemically safe limit*. For instance, this limit equals approximately 50–150 μC/cm^2 per phase for Pt electrodes (depending on the stimulus pulse duration (McCreery 2016)). In contrast,

- the *charge Q* (*global quantity*) per phase determines the occurrence and the rate of neural excitation, governs the number of excited fibers within a nerve—as described in Section "Single Monophasic Stimulus"—and thus is a *major determinant* of *metabolic stress*. Greater delivered charge corresponds to greater number of excited fibers within the nerve, which places more metabolic stress on the nerve. The *safe level* of *Q* per phase can be approximated as <1μC per phase according to Fallon (2016). In addition,
- the delivered *total charge per stimulation period* of a periodic stimulus determines the *excess charge* across the boundary and thus the *polarization overvoltage*. Again, this overvoltage determines *electrochemical electrode reactions* and thus contributes to *electrochemical stress*. Therefore, *charge-balanced pulses* of the stimulus are aimed at with the required *zero direct current* across the boundary, as described in Section "Charge Transfer During Stimulation" and shown in Fig. 2.75a. For instance, the *safe level* of the allowed residual *direct current* in implantable devices is defined with <100nA (Fallon 2016).

Please note that *electrochemical stress*[135] can occur if either the *density Q/A* per phase or a non-zero *direct current*—as delivered by the stimulation electrode—

[135] As another *minor factor* affecting *electrochemical reactions*, the *timing of periodic stimulation pulses* defined through the pulse width, duty cycle, and rate should be shortly discussed. Since the *electrode/electrolyte boundary* shows *inert dynamics* with its *finite time constant*—determining the extent of *Faradaic reactions* within the boundary (Section "Charge Transfer During Stimulation" and Fig. 3.19c)—the timing of pulses co-determines the level of *electrochemical stress*. For instance,

- stimulation pulses with a *stimulation rate* of 1 kHz will move the electrode voltage towards its electrochemically active regions 10 times more frequently than the same pulses at 100 Hz. On the other hand,
- an *increasing pulse width* may generate *more reaction by-products* and *more electrochemical stress* (even for a constant injected charge per pulse) because the potentially harmful polarization overvoltage across the boundary is active over a longer period of time (Fallon 2016). However, an *increasing pulse width* with *decreasing stimulation frequency* increases also the *double layer capacitance* (due to inert and delayed accumulation of ionic counter-charges, see Section "Polarization of the Electrode/Tissue Boundary"). Then the associated excursions of the overvoltage become weaker for longer pulse widths and may lead to *less reaction by-products* than for short pulses (even for a constant charge per pulse).

There are numerous *sophisticated mechanisms* connecting the timing of stimulation pulses and electrochemical stress, which are still under review.

exceeds their respective *safe limits* (see above) while *tissue and/or electrode material*[136] are harmed. If the direct current is not adequately controlled, a very low *Q*/*A* even below the *charge density limit* can cause *electrochemical damage*. Equally, for stimulators delivering no direct current, the applied *Q*/*A* above the *charge density limit* can also cause electrochemical damage.

In terms of *metabolic stress*, a safe and damage-free operation of a *single stimulation electrode* can be empirically predicted by just two variables, the charge *Q* per single phase (cathodic or anodic phase of an a priori charge-balanced current pulse) and the density *Q*/*A* per single phase (Fallon 2016). The following *inequality* (Shannon 1992)

$$\log(Q/1\mu\mathrm{C}) + \log((Q/A)/(1\mu\mathrm{C}\cdot\mathrm{cm}^{-2})) \leq n \tag{2.158}$$

approximately holds for and predicts safe stimulation of neurons. The constant n is found to reside in-between 1.5 and 1.9 to define the safe region of Q and Q/A. More conservative and lower values of n around 1.5 are applicable for electrodes lying in direct contact with the neural tissue, whereas less conservative but higher values around 1.75 apply for electrodes located in a distance from the neural tissue. In fact, the latter inequality describes the *safe area* under a straight line in the Cartesian space with the logarithmic scaling of Q and Q/A.

Empirical investigations justify (2.158) (McCreery 2016). In particular, *Pt electrodes* were implanted over the parietal cortex (in anaesthetized cats) and *charge-balanced current pulses* with 400 μs phase duration (symmetric phase pairs with anodic first) and the repetition rate of 50 Hz were used; see Fig. 2.75a with $t_p = 400$ μs and $f_{rep} = 50$ Hz. *Histological evaluations* served as *reference* for nerve damage. Since the observed damage was mainly of *metabolic origin*, the condition in (2.158) reflects mainly *metabolic stress*. Please note that tissue responses to *short-term stimulation* over 7–8 h underlie (2.158) but not over months.

While Q per phase increases in (2.158), the associated Q/A has to decrease for a still safe stimulation, and vice versa. Both *measures interact* mutually while determining the threshold n of the *stimulation-induced nerve injury*.

It is instructive to observe from (2.158) that

[136]It is interesting that many *noble materials* of electrodes, which are *biocompatible and safe* within the body in their *passive state* (i.e., electrodes are unconnected from any voltage or current source) become unsafe when used as *stimulating electrodes* (i.e., when electrodes are connected to a source). For instance, *gold* is well tolerated in its passive state but readily *dissolves and oxidises* when the electric potential of a gold electrode (with respect to the potential of the electrolyte) is raised above the *half-cell voltage* of gold or above its *polarization voltage* (3.11) by a few hundred mV. In other words, the gold electrode easily *dissolves when used as anode* for stimulation purposes (compare Figs. 3.13c and 3.14).

In contrast, *platinum, titanium, and iridium* are metals which *do not easily dissolve* when their potentials are raised significantly from their respective potentials of the passive state. Therefore, these metals are preferred for stimulation electrodes.

- *small electrodes* (with $A < 0.5$ mm^2) are likely to induce *electrochemical stress* since the density *Q/A tends to be large* and *can easily exceed the charge density limit*.
- *Large electrodes* ($A > 0.5$ mm^2) are likely to induce *metabolic stress* since the associated relatively *small Q/A* is usually *below the charge density limit* and does not induce irreversible reactions (Fallon 2016). In other words, even though the *charge density limit* is not exceeded, *large electrodes* can still damage neurons.

In fact, the prediction from (2.158) does not apply for very *small electrodes* with the associated large densities *Q/A* (>100 μC/cm^2). In this case, the *charge density limit* on *Q/A* (representing *electrochemical safety*) should be applied *in addition to* the metabolic limit from (2.158) (representing *metabolic safety*).

Please recall from Section "Pt Electrodes" that reversible reactions with the associated charge density limit are usually considered as biologically safe. On the basis of the above, this rule appears as an *assumption with limited validity* and applies rather for *charge-balanced pulses* and *small electrodes*. In other words, the required electrochemical safety is likely to include metabolic safety for small electrodes. This demonstrates that adhering to *safe charge injection limits* is a necessary but not a sufficient condition for safe operation to avoid both electrochemical and metabolic stress (compare Section "Charge Transfer During Stimulation").

Please note that the *anatomy* of the stimulation site, the *electrode location*, and the *electrode's geometry*[137] play a decisive role in determining neural damage. This is especially true of the *electrode* which is *not in direct contact* with the *nerve to be excited*. The applied stimulation current can leak away from this nerve and thus can reduce the risk of nerve damage for a given current strength. In particular, the prevailing *electroneural anatomy* governs the current distribution and thus the resulting *charge density Q/A* in spatial regions of the neural tissue; compare with a heterogeneous current distribution from Fig. 2.57.

Finally, let us consider a *simple example* of the relatively small Pt *needle electrode* with the effective area of 4 mm^2 (e.g., as used for percutaneous auricular vagus nerve stimulation) to deliver charge-balanced *biphasic current pulses*. As illustrated in Fig. 2.75a, the amplitude $i_p = 2$ mA and the pulse width $t_p = 500$ μs apply. The charge Q per phase equals 2 mA · 0.5 ms = 1 μC and its density $Q/A = 1$ μC / 0.04 cm^2 = 25 μC/cm^2. Thus the electrochemically safe limit is not exceeded following the conservative condition 25 μC/cm^2 < 50 μC/cm^2, which

[137] *Non-uniform surface* of the *stimulation electrode* requires a heterogeneous distribution of the electric field and the associated current density along this surface, as detailed with respect to the *electrical point effect* (Figs. 2.25a and 2.26a). Therefore, increased current densities in local regions of sharp corners, points, or edges of the electrode favour the rise of local *polarization overvoltages* (3.16) and thus the rise of local *electrochemical reactions*, in close analogy with Footnote 37 in Chap. 3. From a practical point of view, electrode shapes with minimum number of corners and edges (e.g., spheres or discs) induce a lower *electrochemical stress* than electrodes with more corners and edges (for the same electrode area and delivered charge) (Fallon 2016).

indicates that *electrochemical stress* can be theoretically excluded. Since current pulses are charge-balanced, the discussed contribution of *charge-unbalanced pulses* to the electrochemical stress can also be excluded. Equation (2.158) yields log(25) = 1.4 < 1.5 demonstrating that *metabolic stress* can also be theoretically excluded for *short-term stimulation* over hours. However, for *long-term application* clinical studies are always needed to prove the needed *integrity of the electrode and biological tissue*.

Subjective Versus Objective Stimulus

The *subjective perception amplitude* I_S strongly differs from the *objective stimulation intensity* I (or stimulation power), especially their *rates of growth*, which complicates the assessment of suprathreshold responses for electrical stimulation. Typically, a non-linear *psychophysical relationship* in the form

$$I_S = c \cdot I^{\alpha} \tag{2.159}$$

applies (Reilly 1998). Here c is the scaling factor and α the *exponential factor* or the rate of growth of sensory magnitude; compare with the neural perception from Kaniusas (2012, Footnote 92). The exponent α has values from 1 to 3. In other words, the growth of the sensation I_S is usually greater than the growth of the stimulus I as long as $\alpha > 1$.

For instance, the size of α for stimulation of the finger ($\alpha \approx 2.5$) is greater than that of the arm (1.6) or leg (1.4) given *contact currents* via *spark discharges*. The fast growing of sensation in the finger may be due to the fact that the current flow through the finger is more volume limited than in the arm or leg (2.5 > 1.6, 1.4). A high current density results along the finger and thus a spatially extensive sensory excitation far beyond the stimulation point, in contrast to spatially limited sensation on the leg or arm.

Interestingly, the exponent α peaks for 50/60 Hz stimulation in the most sensitive frequency range (Fig. 2.91). In addition, α tends to increase with increasing *number of pulses* in the stimulation train. For instance, a train of 100 μs long pulses of constant current strength, delivered at 60 Hz rate yields a sixfold increase in the sensory I_S when the number of pulses increases from 1 to 30 (Reilly 1998). The enhancement of the sensory response due to repetitive stimuli is not only due to integration effects on the membrane level (Fig. 2.70) but also on the level of the central nervous system receiving a series of action impulses. This central integration process influences also the effective *integration time* which typically increases from a few multiples of the *empirical time constant* τ_e (2.151) amounting to <1 ms (for membrane integration effects) up to 50 ms for both membrane and central integration effects. However, for increasing I, additional nonlinearities become dominant due to interactions between excitatory and inhibitory processes, due to change in the population of excited fibers from large-diameter to small-diameter fibers (Fig. 2.81), as well as other processes.

References

J.E. Anderson, The Debye-Falkenhagen effect: experimental fact or fiction? J. Non-Cryst. Solids **172–174**, 1190–1194 (1994)

C. A. Balanis, *Advanced Engineering Electromagnetics* (Wiley, London, 1989)

P. Berg, M. Scherg, Dipole models of eye movements and blinks. Electroencephalogr. Clin. Neurophysiol. **79**(1), 36–44 (1991)

J. Bisquert, V. Halpern, F. Henn, Simple model for ac ionic conduction in solids. J. Chem. Phys. **122**, 151101 (2005)

D. Boinagrov, S. Pangratz-Fuehrer, B. Suh, K. Mathieson, N. Naik, D. Palanker, Upper threshold of extracellular neural stimulation. J. Neurophysiol. **108**(12), 3233–3238 (2012)

A. Bulling, F. Castrop, J.D. Agneskirchner, W.A. Ovtscharoff, L.J. Wurzinger, M. Gratzl, *Body Explorer. An Interactive Program on the Cross-Sectional Anatomy of the Visible Human Male* (Springer, Berlin, 1997)

S.F. Cogan, D.J. Garrett, R.A. Green, Electrochemical principles of safe charge injection, in *Neurobionics: The Biomedical Engineering of Neural Prostheses*, ed. by R.K. Shepherd (Wiley, London, 2016), pp. 55–88

Commission on Radiological Protection, Protection against low-frequency electric and magnetic fields in energy supply and use, in Recommendation of the commission on Radiological Protection of the Federal Ministry for the Environment, Nature Conservation and Nuclear Safety (in Germany), vol 7 (1997)

Council recommendation of 12 July 1999 on the limitation of exposure of the general public to electromagnetic fields (0 Hz to 300 GHz). Off. J. Eur. Commun. L199/59–L199/70 (1999)

T. De Marco, F. Ries, M. Guermandi, R. Guerrieri, EIT forward problem parallel simulation environment with anisotropic tissue and realistic electrode models. IEEE Trans. Biomed. Eng. **59**(5), 1229–1239 (2012)

L.Y. Di Marco, C. Di Maria, W.C. Tong, M.J. Taggart, S.C. Robson, P. Langley, Recurring patterns in stationary intervals of abdominal uterine electromyograms during gestation. Med. Biol. Eng. Comput. **52**, 707–716 (2014)

J.B. Fallon, P.M. Carter, Principles of recording from and electrical stimulation of neural tissue, in *Neurobionics: The Biomedical Engineering of Neural Prostheses*, ed. by R.K. Shepherd (Wiley, London, 2016), pp. 89–120

Z.P. Fang, J.T. Mortimer, A method for attaining natural recruitment order in artificially activated muscles, in Proceedings of 9th Annual International Conference of the IEEE Engineering in Medicine and Biology Society (1987), pp. 657–658

J.A. Ferraro, J.D. Durrant, Electrocochleography in the evaluation of patients with Meniere's disease/endolymphatic hydrops. J. Am. Acad. Audiol. **17**(1), 45–68 (2006)

K.R. Foster, Dielectric properties of tissues, in *The Biomedical Engineering Handbook*, ed. by J.D. Bronzino (1995), pp. 1385–1394 (1995)

K.R. Foster, H.P. Schwan, Dielectric properties of tissues, in *Handbook of Biological Effects of Electromagnetic Fields*, ed. by C. Polk, E. Postow (CRC Press, Boca Raton, 1996), pp. 25–102

C. Furse, D.A. Christensen, C.H. Durney, *Basic Introduction to Bioelectromagnetics* (CRC Press, Boca Raton, 2009)

C. Gabriel, S. Gabriel, E. Corthout, The dielectric properties of biological tissues: I. Literature survey. Phys. Med. Biol. **41**(11), 2231–2249 (1996a)

S. Gabriel, R.W. Lau, C. Gabriel, The dielectric properties of biological tissues: II. Measurements in the frequency range 10 Hz to 20 GHz. Phys. Med. Biol. **41**(11), 2251–2269 (1996b)

S. Gabriel, R.W. Lau, C. Gabriel, The dielectric properties of biological tissues: III. Parametric models for the dielectric spectrum of tissues. Phys. Med. Biol. **41**(11), 2271–2293 (1996c)

P.O. Gaggero, A. Adler, J. Brunner, P. Seitz, Electrical impedance tomography system based on active electrodes. Physiol. Meas. **33**(5), 831–847 (2012)

J. Gracia, V.P. Seppa, J. Viik, J. Hyttinen, Multilead measurement system for the time-domain analysis of bioimpedance magnitude. IEEE Trans. Biomed. Eng. **59**(8), 2273–2280 (2012)

S. Grimnes, O.G. Martinsen, Bioimpedance and Bioelectricity Basics (Elsevier, Amsterdam, 2008)
V. Häkkinen, K. Hirvonen, J. Hasan, M. Kataja, A. Värri, P. Loula, H. Eskola, The effect of small differences in electrode position on EOG signals: application to vigilance studies. Electroencephalogr. Clin. Neurophysiol. **86**(4), 294–300 (1993)
C.H. Hamann, W. Vielstich, *Electrochemistry* (in German: Elektrochemie) (Wiley-VCH Publisher, London, 1998)
Q. Han, M.D. Buschmann, P. Savard, The forward problem of electroarthrography: modeling load-induced electrical potentials at the surface of the knee. IEEE Trans. Biomed. Eng. **61**(7), 2020–2027 (2014)
C.J. Harland, R.J. Prance, H. Prance, Remote monitoring of biodynamic activity using electric potential sensors. J. Phys Conf. Ser. **142**(1), 1–4 (2008)
B. He, T. Coleman, G.M. Genin, G. Glover, X. Hu, N. Johnson, T. Liu, S. Makeig, P. Sajda, K. Ye, Grand challenges in mapping the human brain: NSF workshop report. IEEE Trans. Biomed. Eng. **60**(11), 2983–2992 (2013)
H. Heinrich, F. Börner, Electromagnetic fields at work: safety of employees with active and passive medical implants under exposure to electromagnetic fields (in German: Elektromagnetische Felder am Arbeitsplatz: Sicherheit von Beschäftigten mit aktiven und passive Körperhilfsmitteln bei Exposition gegenüber elektromagnetischen Feldern). Research report 451 of Federal Ministry of Labour and Social Affairs (2015)
R. Hirtl, *Unpublished Numerical Data* (Electromagnetic Compatibility Lab, Seibersdorf Laboratories, Austria, 2014)
K.H. Hong, Y.G. Lim, K.S. Park, Effectiveness of thigh-to-thigh current path for the measurement of abdominal fat in bioelectrical impedance analysis. Med. Biol. Eng. Compu. **47**(12), 1265–1271 (2009)
Institute of Applied Physics, Italian National Research Council, niremf.ifac.cnr.it/tissprop (2013)
International Commission on Non-Ionizing Radiation Protection, ICNIRP guidelines for limiting exposure to time-varying electric, magnetic and electromagnetic fields (up to 300 GHz). Health Phys. **74**(4), 494–522 (1998)
International Commission on Non-Ionizing Radiation Protection, ICNIRP statement on medical magnetic resonance. Health Phys. **87**(2), 197–216 (2004)
International Commission on Non-Ionizing Radiation Protection, ICNIRP guidelines for limiting exposure to time-varying electric and magnetic fields (1 Hz–100 kHz). Health Phys. **99**(6), 818–836 (2010)
International Labour Organisation, Protection of workers from power frequency electric and magnetic fields. Occup. Safety Health Series **69** (1994)
L. Joseph, R.J. Butera, High frequency stimulation selectively blocks different types of fibers in frog sciatic nerve. IEEE Trans. Neural Syst. Rehabil. Eng. **19**(5), 550–557 (2011)
E.R. Kandel, J.H. Schwartz, T.M. Jessell, *Principles of Neural Science* (McGraw-Hill, New York, 2000)
E. Kaniusas, *Biomedical Signals and Sensors I: Linking Physiological Phenomena and Biosignals* (Springer, Berlin, 2012)
E. Kaniusas, Nonlinear behaviour of vital physiological systems, in *International Conference on Theory and Application in Nonlinear Dynamics (ICAND 2012)*, ed. by V. In, A. Palacios, P. Longhini (Springer, Berlin, 2014), pp. 113–121
E. Kaniusas, Biomedical Signals and Sensors II: Linking Acoustic and Optic Biosignals and Biomedical Sensors (Springer, Berlin, 2015)
S. Kampusch, *Unpublished Numerical Data* (Biomedical Sensing Lab, Institute of Electrodynamics, Microwave and Circuit Engineering, Vienna University of Technology, Austria, 2017)
C. Kumaragamage, B. Lithgow, Z. Moussavi, A new low-noise signal acquisition protocol and electrode placement for electrocochleography (ECOG) recordings. Med. Biol. Eng. Compu. **53**, 499–509 (2015)
L. Larsson, M. Nyström, M. Stridh, Detection of saccades and postsaccadic oscillations in the presence of smooth pursuit. IEEE Trans. Biomed. Eng. **60**(9), 2484–2493 (2013)

K.H. Lee, P.S. Duffy, A.J. Bieber, *Deep Brain Stimulation: Indications and Applications* (CRC Press, Boca Raton, 2016)
N. Leitgeb: Safety of Electromedical Devices (Springer Publisher, 2010)
S. Leonhardt, B. Lachmann, Electrical impedance tomography: the holy grail of ventilation and perfusion monitoring? Intensive Care Med. **38**(12), 1917–1929 (2012)
J. Malmivuo, R. Plonsey, *Bioelectromagnetism, Principles and Applications of Bioelectric and Biomagnetic Fields* (Oxford University Press, Oxford, 1995)
W. Mayer, in Private communication (2017)
D. McCreery, Preclinical testing of neural prosthesis, in *Neurobionics: The Biomedical Engineering of Neural Prostheses*, ed. by R.K. Shepherd (Wiley, London, 2016), pp. 89–120 (2016)
V. Mishra, H. Bouayad, A. Schned, A. Hartov, J. Heaney, R.J. Halter, A real-time electrical impedance sensing biopsy needle. IEEE Trans. Biomed. Eng. **59**(12), 3327–3336 (2012)
D. Miklavcic, N. Pavselj, F.X. Hart, Electric properties of tissues. Wiley Encycl. Biomed. Eng. 1–12 (2006)
R. Mukkamala, J.O. Hahn, O.T. Inan, L.K. Mestha, C.S. Kim, H. Toreyin, S. Kyal, Toward ubiquitous blood pressure monitoring via pulse transit time: theory and practice. IEEE Trans. Biomed. Eng. **62**(8), 1879–1901 (2015)
H. Nakesch, H. Pfützner, C. Ruhsam, P. Nopp, K. Futschik, Five-electrode field plethysmography technique for separation of respiration and cardiac signals. Med. Biol. Eng. Compu. **32**(4), 65–70 (1994)
A.C. Patil, N.V. Thakor, Implantable neurotechnologies: a review of micro- and nanoelectrodes for neural recording. Med. Biol. Eng. Compu. **54**(1), 23–44 (2016)
R.P. Patterson, Fundamentals of impedance cardiography. IEEE Eng. Med. Biol. Mag. **8**(1), 35–38 (1989)
S.D. Pawar, P. Murugavel, D.M. Lal, Effect of relative humidity and sea level pressure on electrical conductivity of air over Indian Ocean. J. Geophys. Res. Atmos. **114**(D2), 1–8 (2009)
H. Pfützner, *Applied Biophysics* (in German: Angewandte Biophysik) (Springer, Berlin, 2003)
E. Pinheiro, O. Postolache, P. Girao, A survey on unobtrusive measurements of the cardiovascular function and their practical implementation in wheelchairs. Sens. Trans. J. **9**, 182–199 (2010)
F. Rattay, High frequency electrostimulation of excitable cells. J. Theor. Biol. **123**, 45–54 (1986a)
F. Rattay, Analysis of models for external stimulation of axons. IEEE Trans. Biomed. Eng. **33**(10), 974–977 (1986b)
F. Rattay, Ways to approximate current-distance relations for electrically stimulated fibers. J. Theor. Biol. **125**, 339–349 (1987)
F. Rattay, Modeling the excitation of fibers under surface electrodes. IEEE Trans. Biomed. Eng. **35** (3), 199–202 (1988)
F. Rattay, Electrical Nerve Stimulation: Theory, Experiments and Applications (Springer, Berlin, 1990)
F. Rattay, in Private communication (2017)
J.P. Reilly, *Applied Bioelectricity: From Electrical Stimulation to Electropathology* (Springer, Berlin, 1998)
J.P. Reilly, A.M. Diamant, *Electrostimulation: Theory, Applications, and Computational Model* (Artech House Publisher, 2011)
O.Z. Roy, J.R. Scott, G.C. Park, 60-Hz ventricular fibrillation and pump failure thresholds versus electrode area. IEEE Trans. Biomed. Eng. **BME-23**(1), 45–48 (1976)
Safety publication and preliminary standard DIN IEC/TS 60479-1 (VDE V 0140-479-1): effects of current on human beings and livestock (2007)
B. Sanchez, J. Li, T. Geisbush, R.B. Bardia, S.B. Rutkove, Impedance alterations in healthy and diseased mice during electrically induced muscle contraction. IEEE Trans. Biomed. Eng. **63**(8), 1602–1612 (2016)
R.V. Shannon, A model of safe levels for electrical stimulation. IEEE Trans. Biomed. Eng. **39**(4), 424–426 (1992)

V.P. Seppa, J. Viik, J. Hyttinen, Assessment of pulmonary flow using impedance pneumography. IEEE Trans. Biomed. Eng. **57**(9), 2277–2285 (2010)

A.K. Shukla, T.P. Kumar, Pillars of modern electrochemistry. Electrochem. Soc. Inter. **17**(3), 31–39 (2008)

M. Solomonow, External control of the neuromuscular system. IEEE Trans. Biomed. Eng. **BME-31**(12), 752–763 (1984)

R. Somaraju, J. Trumpf, Frequency, temperature and salinity variation of the permittivity of seawater. IEEE Trans. Antennas Propag. **54**(11), 3441–3448 (2006)

A.J. Surowiec, S.S. Stuchly, M. Keaney, A. Swarup, Dielectric polarization of animal lung at radio frequencies. IEEE Trans. Biomed. Eng. **34**(1), 62–67 (1987)

F. Thürk, S. Böhme, D. Mudrak, S. Kampusch, A. Wielandner, H. Prosch, C. Braun, F.P.R. Toemboel, J. Hofmanninger, E. Kaniusas, Effects of individualized electrical impedance tomography and image reconstruction settings upon the assessment of regional ventilation distribution: comparison to 4-dimensional computed tomography in a porcine model. PLOS ONE **12**(8), e0182215, 1–16 (2017)

D. Teichmann, J. Foussier, J. Jia, S. Leonhardt, M. Walter, Noncontact monitoring of cardiorespiratory activity by electromagnetic coupling. IEEE Trans. Biomed. Eng. **60**(8), 2142–2152 (2013)

C. Van den Honert, J.T. Mortimer, The response of the myelinated nerve fiber to short duration biphasic stimulating currents. Ann. Biomed. Eng. **7**(2), 117–125 (1979)

A. Vuckovic, M. Tosato, J.J. Struijk, A comparative study of three techniques for diameter selective fiber activation in the vagal nerve: anodal block, depolarizing prepulses and slowly rising pulses. J. Neural Eng. **5**, 275–286 (2008)

A.N. Weissenrieder, *Stimulation Electrodes for Pacemaker Applications: Electrochemistry of bioelectrodes* (VDM Publisher Dr, Müller, 2009)

World Health Organization, in Electromagnetic fields (300 Hz–300 GHz). Environ. Health Criteria **137** (1993)

M.R. Wright, *An Introduction to Aqueous Electrolyte Solutions* (Wiley, London, 2007)

S. Zhao, G. Yang, J. Wang, J.R. Roppolo, W.C. Groat, C. Tai, Conduction block in myelinated axons induced by high-frequency (kHz) non-symmetric biphasic stimulation. Front. Comput. Neurosci. **9**(86), 1–10 (2015)

Chapter 3
Sensing and Coupling of Electric Biosignals

Abstract For diagnostic sensing and therapeutic coupling of electric biosignals they have to cross the electrode/tissue boundary across the skin. Thereby metal ion and redox electrodes as well as polarizable and non-polarizable electrodes are subjected to direct and alternating voltage application. Boundaries become polarized while charge transfer, diffusion, and coupled reactions take place on the electrode surface. The formed electrode impedance contributes to the whole body impedance that determines the effectiveness of diagnosis and therapy using electrodes. Any measurement or application of electric biosignals is subjected to capacitive and inductive coupling of interference signals as well as to common-mode and differential-mode interferences. Potential countermeasures include passive and active shielding, driven-right-leg-circuit, notch filters, and preamplifiers.

According to Fig. 1.2, *sensing aspects* of electric biosignals include

- *coupling* of biosignals—emanating from the biological body—into a sensing device applied on the skin, and
- *conversion* of the coupled biosignal into a registered electrical signal within the sensing device.

Reception or *sensing of electric biosignals* originating within the biological body is performed for *diagnostic purposes*, e.g., via *surface electrodes* on the body skin to register electrical heart excitation in terms of electrocardiogram. On the other hand, *coupling of electric biosignals* into the body is usually used for *therapeutic purposes* to stimulate and excite bodily tissues, e.g., for functional electrical stimulation of muscles or hyperthermia treatment. The active coupling can also be used for *diagnostic generation* of induced biosignals (Kaniusas 2012, Fig. 1.15a), e.g., for electrical impedance tomography (Fig. 1.3). The undesired coupling may also occur during the *body's exposure* to ambient electromagnetic fields with potentially adverse health effects.

Both *diagnostic sensing* (Fig. 3.24) and *therapeutic coupling* (Fig. 3.25) are governed by many factors related to characteristics of

© Springer Nature Switzerland AG 2019

E. Kaniusas, *Biomedical Signals and Sensors III*, Biological and Medical Physics, Biomedical Engineering, https://doi.org/10.1007/978-3-319-74917-4_3

- the applied *electrode*,
- the type of *biological tissue*, and
- the *electrode/tissue boundary*, which is practically most important.

In particular, material and geometrical properties of electrodes (including its surface conditions), physical and biophysical tissue properties (including inhomogeneity, anisotropy, and local blood perfusion) are relevant factors on the part of the electrode and tissue. At the electrode/tissue boundary, a double layer manifests with the associated polarization of electrodes, which are other crucial factors for sensing and coupling.

Diagnostic sensing of biosignals as well as *therapeutic coupling* of biosignals can be realised using either

- *contact-less approach* using *capacitive mechanisms* (known as *direct coupling*) or
- *contact-based approach* using *conductive mechanisms* (known as *indirect coupling*).

Contact-less approach presumes a missing physical contact (Fig. 3.1a) between the body and the *external field meter* (for *diagnostic sensing*) or, on the other hand, between the body and the *external field source* (for *therapeutic coupling*). The body can serve as a source of the time-varying electric, magnetic, or electromagnetic field (for *diagnostic sensing*) or, on the other hand, can be exposed to the time varying electric, magnetic, or electromagnetic field (for *therapeutic coupling*). In particular, the contact-less approach is based upon displacement currents coupled out of or into the body (Fig. 2.26), induced polarization and alignment of permanently polar structures (Fig. 2.16), electrostatic induction (Fig. 2.25), and electromagnetic induction (Fig. 2.32). The higher is the field frequency, the better the coupling. For instance, time-varying *electric and current density fields* can be induced within the body to generate therapeutic *neuromuscular and thermal effects*.

Contact-based approach presumes a real physical contact (Fig. 3.1b, c) between the body and the *external field meter* (for *diagnostic sensing*) or, on the other hand, between the body and the *external field source* (for *therapeutic coupling*). For therapeutic setting, *steady and time-varying electric and current density fields* can be induced within the body since electric charges are transferred (mediated) via the physical *contact current* (2.25). For instance, *contact currents* result through the human body—staying in a direct skin contact with a conductive (metallic) object—when the body and object have *different electric potentials* (Fig. 2.86a).

In terms of the *contact-based approach*, transient *spark discharges* can occur when the human body approaches a charged *conductive object* in the air (Fig. 2.86a) and the *breakdown* electric field of the air is exceeded (Kaniusas 2012, Footnote 49). For instance, charges to be discharged could be surface charges of the isolated conductive object (e.g., an isolated passenger car), whereas these charges are induced in the course of the object's exposition to a strong ambient electric field (Footnote 116 in Chap. 2). Please recall that spark discharges can cause local transient current densities capable of shocks and burns (Fig. 2.88).

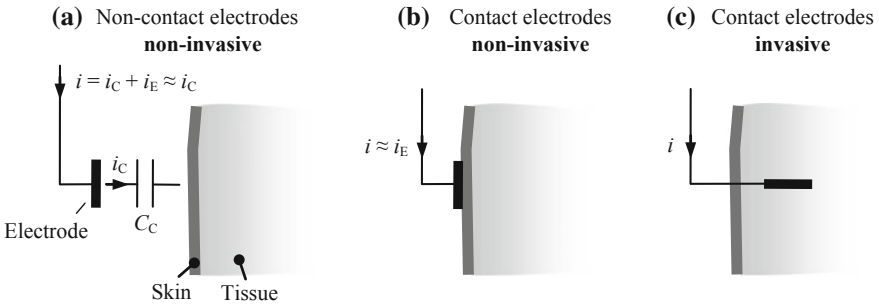

Fig. 3.1 Metallic electrodes as interfaces between biological tissue and technical device. **a** Non-contact electrode situated in a distance with the capacitive coupling across the capacitance C_C to/from the human body. The electrode senses mainly the capacitive current i_C between the electrode and body. **b** Contact non-invasive electrode applied directly on the body skin. The type of this electrode, polarizable or non-polarizable (Fig. 3.21), determines the type of coupling and the composition of the resulting current i ($=i_C + i_E$) between the electrode and body. Usually the conductive current i_E dominates with $i \approx i_E$ when a conductive electrode gel is applied. **c** Contact implanted electrode can also be polarizable or non-polarizable

3.1 Electrodes

Electrodes are the *interfaces* between the technical device and biological tissue and play an important role in the performance of the measurement system. In particular, electrodes interface *ionic currents* prevailing within biological tissue with *electronic current* in the wire within technical devices. This conversion from the ionic into electronic conduction during biosignal recording (for diagnosis), or the opposite conversion during biosignal application (for therapy), occurs at the *electrode/tissue boundary*, to be more precise, at the electrode/electrolyte boundary.

The conversion is effective during both the build-up of the electrical *double layer*, i.e., during the temporary charge separation at the boundary, and the *current flow* across this boundary with the electrode acting as a source or sink of electrons (Fig. 3.13). That is, the metal *electrode exchanges charges* with arriving *ions* in terms of electron transfer (3.12), whereas charge-neutral and charged substances may be *ionised* and *neutralised*, respectively, at the boundary. In addition, the electrode metal can be *oxidized/dissolved* where metal atoms enter the solution as charged cations (Fig. 3.4a), or, conversely, metal ions in the solution can be *reduced/deposited* onto the electrode surface and then become neutral atoms of the electrode metal (Fig. 3.4b).

Properties of the boundary can even dominate the *overall performance* of the diagnostic or therapeutic system. Thus, a proper understanding of this boundary is crucially important, as discussed in depth in this section. Please note that *electrodes* can significantly contribute to the *noise* and even determine the *noise susceptibility* of the whole system. The brown noise ($1/f^2$ noise) is dominant in electrodes, with the associated strong *baseline drifts*. Here *movement artefacts*, *triboelectric effects*, and *power line interference* are strong contributors to the noise.

Future electrodes face a number of *challenges* such as

- registration of the inner *electrode condition* since the electrode/tissue boundary undergoes significant temporal and structural changes (Roach et al. 2007) and so the momentary electrode impedance;
- development of mechanically *strong but highly flexible electrodes* which can perfectly mimic and integrate with soft muscular and neural tissues (in vivo stability); and
- *functionalisation of the electrode surface* to counteract local inflammatory responses, e.g., of implanted electrodes throughout the whole implant period.

Contact Electrodes

In general, we can differentiate between

- wet or dry *contact electrodes* (Fig. 3.1b) and
- dry *non-contact electrodes* (Fig. 3.1a).

Contact electrodes utilise *conductive sensing* or read out of endogenous fields from the inner body (for diagnosis), and *conductive coupling* or application of external fields down into the body (for therapy), known also as galvanic sensing or coupling, respectively. The presence of gel in *wet electrodes*—a conductive gel or electrolytic layer between the electrode surface and the body—mainly eases the resulting electrical *contact with the body skin*. Gel favourably lowers the *electrode impedance* and reduces the noise drift. The galvanic contact to the body raises the quality of recorded or applied biosignals over that from non-contact electrodes. Usually wet electrodes are considered as *gold standard*; e.g., Ag/AgCl electrode coated by wet hydrogel containing chloride ions.

However, there are a lot of drawbacks. Wet electrodes tend to degenerate over time since the gel moisture evaporates limiting the electrode's lifetime. The *skin can easily be irritated* by the gel during the long-term monitoring, especially in premature babies with highly sensitive skin. In contrast, *dry electrodes* tend to improve over time. This is because moisture from the skin, i.e., sweat, as well as from the environment tend to accumulate within the electrode/tissue boundary, which lowers and stabilizes the *electrode impedance*.

In addition, special coatings around implantable electrodes are used to prevent buildup of nonconductive fibrous tissue (scar tissue) and avoid electrode corrosion. Coatings formed by *well-conducting layers* (e.g., conducting polymers) allow large charges to be easily transmitted across the electrode/tissue boundary without significantly rising the *polarization overvoltage* (3.16). The limited overvoltage advantageously restrains *electrochemical reactions* within the boundary, whose by-products are potentially harmful to tissue and/or electrode material.

Please note that contact electrodes can be *applied externally* on the skin, forming *surface-seated electrodes* such as adhesive surface electrodes from Fig. 3.1b. Alternatively, contact electrodes can be *implanted* within tissue, comprising *deep-seated electrodes* such as intramuscular needle electrodes from Fig. 3.1c inserted like a cannula.

Biocompatible metals are needed for *implanted electrodes*, whereas *platinum*, *gold*, *titan*, *iridium*, *stainless steel*, and *tungsten* are considered as biocompatible (Patil and Thakor 2016) (Footnote 136 in Chap. 2). As an advantage, these metals are highly conductive and can be patterned with high resolution. Interestingly, implanted electrodes are exposed to a *chemically rough environment*.

Non-contact Electrodes

Non-contact electrodes—or *remote-seated electrodes*—utilise *capacitive sensing* of inner body fields (for diagnosis) or *capacitive coupling* of external fields into the body (for therapy). These electrodes are *necessarily dry* (Figs. 3.1a and 3.31). These electrodes are either in an isolating distance from the body (e.g., reside on the person's clothing) or are still in contact with the body skin but carry a thin dielectric layer to form an isolating barrier to the skin. The isolation from the body implies that non-contact electrodes can mainly sense the time-varying *displacement currents*. This is because the *direct current impedance* of the (air) gap between the electrode and body—the effective pathway for potential conductive currents (2.36)—is usually much higher than the frequency-dependent *alternating current impedance* of this gap—the effective pathway for displacement currents (2.42)—at a non-zero and typically relatively high frequency of the biosignal (Fig. 2.14c).

Non-contact electrodes offer a chemically inert surface and thus are best suited for *long-term applications*. However, capacitive coupling excludes registration or application of direct currents (or direct voltages), has the highest *electrode impedance* among all mentioned electrodes, is very prone to movement artefacts and to *triboelectric effects*, and may show *long settling times*.

For instance, the greater is the *capacitance* between the *non-contact electrode* for capacitive coupling and the *grounded conductive body*, the greater is the induced *therapeutic current* through the body (2.42 and Fig. 2.26b). In addition, if the *body is isolated* (Fig. 2.27b), the increasing capacitance between the body and the ground increases the current through the body (Fig. 3.26). Both capacitances depend on the size, surface area, and orientation of all three the conductive coupling electrode, the conductive body, and the ground. Therefore, the induced currents will differ, for instance, for small and large coupling electrodes as well as for slim and obese persons.

Contact electrodes on the body cause *limited compliance* in mobile patients including limitations due to *connected cables* to the electrodes. In contrast, *non-contact electrodes* can measure through clothes and could be integrated into everyday objects (such as office chair or bed at home) to perform continuous measurements *without constraints* on the patient in terms of *pervasive monitoring* (Kaniusas 2007).

Penetration and Focusing

The *penetration depth* δ (or *skin depth*) of the electromagnetic field down the electrode decreases with increasing frequency; for *qualitative data* on muscle and fat see Fig. 2.6. That is, *high frequency* fields hardly penetrate into or out of the body. For instance, electrodes on the body skin are useless in producing some therapeutic electrophysiological effects in the interior of the body at the desired high frequencies. In fact, a highly *localized applicator* is required within the body in the

close vicinity to the application region of interest in order to have localized high frequency fields within the body. In contrast, local *low frequency* fields can be induced via a *distant contact electrode* on the skin surface.

However, the *focussing capability* of the electromagnetic field via the electrode into the body—with the electrode acting as a field source—*increases with increasing frequency* or with decreasing *wavelength* (2.5). From a *qualitative perspective*, the focussing capability increases with the ratio d/λ of the aperture d of the field source to the wavelength λ (2.123). Therefore,

- *low frequency fields* (with $d/\lambda \ll 1$) do not allow deep focussing—as illustrated in Fig. 2.39—although they penetrate well within a large penetration region (δ is large with respect to body dimensions). Low frequencies favour their usage for *unfocussed deep applications*. In contrast,
- *high frequency fields* ($d/\lambda \gg 1$) support their focussing but do not penetrate far from the electrode (δ is small with respect to body dimensions). High frequencies favour their usage for *focussed superficial applications*. Consequently,
- *medium frequency fields* is the best choice to attain *some penetration* (i.e., the frequency is not too high) and *some focussing* (i.e., the frequency is not too low) at the same time.

For instance, these frequency-related issues are highly relevant for *hyperthermia treatment* of targeted superficial or deep tissues in the body (Footnote 115 in Chap. 2). In particular, contact-based *localized applicators* such as metallic electrodes help to *focus low frequency fields*, especially for read out of inner fields or localized deposition of large power. Please note that electromagnetic power can be *maximally focussed* to a spatial region of size in the order of a single *wavelength*. This confirms indirectly that low frequencies with large wavelengths are poorly focussed.

Sensing, Stimulation, and Reference Electrodes

For *sensing* or *coupling* of biosignals at least *two electrodes* are required so that the biological body in question becomes part of the electrical circuit. Electric *voltages* can be registered or applied, respectively, between both electrodes. In analogy, electric *currents* can be registered or applied, respectively, flowing from one electrode to the other.

One of the two electrodes is typically located over a bioelectrically active area to be investigated for *diagnosis*, known as the *sensing electrode*, or over an area to be treated for *therapy*, known as the *stimulation electrode*. The sensing and active electrodes are also referred to as *active electrodes* or *different electrodes*.

The other electrode is the *reference electrode*. This electrode is placed on a most *bioelectrically inactive area*, i.e., with ideally absent or at least steady local electric potentials being recorded, especially, when operated together with the *sensing electrode*. For instance, the reference electrode on the skin surface is preferably positioned over bony structures but not over large bioelectrically active muscles. Therefore, the sensing electrode measures voltages relative to some body location with a steady reference potential where the reference electrode is placed. The bioelectrically inactive area implies that the reference electrode is also called *neutral electrode* or *indifferent electrode*.

The *reference electrode* has a preferably *large surface area* (Footnote 30) to avoid large current densities on the electrode surface (2.23) when used in conjunction with the *stimulation electrode*. Please recall that minimised current densities minimise unwanted neuromuscular and thermal effects at the site of the reference electrode. For monopolar sensing or coupling (Fig. 2.75d), the reference electrode is *placed as far as possible* from the sensing or stimulation electrode, respectively. The reference electrode can also be located on the electrical ground; however, there is no perfect ground with absolute zero potential. Please note that

- an *ideal reference electrode* should have zero *polarization voltage* (Fig. 3.4). This polarization voltage should not depend on the current flowing through this electrode. Consequently,
- a *real reference electrode* is required to exhibit a small polarization voltage and a small *polarization overvoltage* (Fig. 3.14).

The requirement for the *small polarization overvoltage* can be practically fulfilled either with a *low electrode impedance* or a *small current* through the electrode/electrolyte boundary of the reference electrode. The low impedance can be attained when using a reference electrode with a *large surface area*; see the associated discussion in Section "Electrode Impedance Model". The small current results when a high-end recording amplifier with a *high input impedance* is used for sensing purposes.

Electrode Shape

The *current density field* concentrates and *electric field* lines become crowded on metallic corners, points, and edges in terms of the *electrical point effect* (Fig. 2.26a and Footnote 58 in Chap. 2). *Non-uniform fields* are formed around *metallic electrodes*, especially around small, slim, and pointed electrodes, which, among others, increase the local *electrochemical stress* (Footnote 137 in Chap. 2). Therefore, *metallic electrodes* meant to provide *uniform coverage of current* (e.g., for therapy), especially for long-term applications, are generally *circular* in their shape and have *rounded corners* to minimise the focussing of the current density and electric fields.

The more localized and pointed is the electrode, the more detailed is the spatial information obtained (for diagnosis) or the more precise is the current applied (for therapy). Large *surface electrodes* are the least localised (but non-invasive) while tiny *needle electrodes* are highly localised (but usually invasive).

3.1.1 Tissue, Skin, and Electrode Effects

Inner biosignals are generated by nerve and muscle activity within the body and can be registered by means of metallic electrodes applied on the skin surface for *diagnostic aims*. In analogy, induced biosignals within the body can be applied for *therapeutic aims*. In both cases, *contact coupling* and *non-contact coupling* of these inner biosignals—namely, of *electric and current density fields*—can be applied (Fig. 3.1).

For this field's coupling into or out the body, the electrical behaviour of *biological tissues* and the *skin* is highly relevant because these fields permeate tissues and skin while experiencing unwanted *losses* (to be precise, fields experience changes in the time, frequency, and spatial domains) and unfavourable *interferences*, as discussed in the following sections. In fact, these fields permeate tissues and skin in order to reach the *electrode sites* or *target organs* for diagnostic and therapeutic aims, respectively.

For instance, *skin effects* are dominant when metallic electrodes are applied on the skin to record inner (permanent) biosignals emanating from the inner body. Here the skin can act as an *isolating barrier* under certain circumstances such as when very low field frequencies dominate in biosignals to be recorded. That is, the skin impedance is usually of a value much greater than the impedance of the bodily tissue and thus contributes significantly to the aforementioned field losses.

Inner biosignals pass the complex *skin/electrode interface* to be conducted along electrode wires to the diagnostic device. This interface also imposes significant *losses* and *reshapes the recorded biosignal*. Obviously, the reverse passage of biosignals across the boundary is valid for the therapeutic device. In practice, the skin/electrode impedance is aimed to be as small as possible to minimize the associated voltage drop and thus the associated biosignal losses within this impedance. The behaviour of the *electrode* itself—with its complex *impedance* and *electric polarization*—is crucial for the quality of the diagnostically recorded and therapeutically applied biosignals, as described below.

3.1.1.1 Tissue Impedance

The *impedance* $\underline{Z}_\mathrm{b}$ *of biological tissue*—can be seen as a *cell suspension*—is modelled as a parallel connection of a resistor with the *body resistance* R_b and a capacitor with the *body capacitance* C_b, as illustrated in Fig. 3.2a [see also Fig. 2.9 and (2.47)], to give

$$\underline{Z}_\mathrm{b} = \frac{\underline{U}_\mathrm{b}}{\underline{I}} = \frac{R_\mathrm{b}}{1 + \mathrm{j} \cdot \omega \cdot R_\mathrm{b} \cdot C_\mathrm{b}} \approx R_\mathrm{b}. \tag{3.1}$$

Here $\underline{U}_\mathrm{b}$ is the *complex amplitude* of the *voltage drop* u_b across tissue and $\underline{I}$ the *complex amplitude* of the *current* i through this tissue [compare (2.34)]. In fact, (3.1) is based on both the *conductive and dielectric properties* of tissue (Section "Simple Tissue Model").

However, the *capacitive component* of this model can be neglected if inner or induced fields (electric and current fields) in tissue show relatively *low frequencies*; compare the instructive discussions related to (2.122) and Fig. 2.14a. To be more precise, this simplification assumes $|1/\mathrm{j}\omega C_\mathrm{b}| \gg R_\mathrm{b}$, i.e., the charge transfer within tissue via mobile ions is unconstrained and fast so that its R_b [derived from (2.36) and (2.54)] turns to be quite low. The latter approximation yields a *simplified model* of tissue with $\underline{Z}_\mathrm{b} \approx R_\mathrm{b}$ (3.1), as illustrated in Fig. 3.2a. In particular,

- in terms of *global quantities of tissue*, the *capacitive impedance* $|1/j\omega C_b|$ goes to infinity for very *low field frequencies* (2.42). Then the *conductive resistance* R_b of tissue only determines the relationship between the (conductive) current and voltage applicable to a finite-sized piece of tissue [see instructive discussions related to (2.47)]. Likewise,
- in terms of *local quantities of tissue*, time derivatives of local fields in tissue go to zero for very *low field frequencies*, which, in turn, implies disappearing *displacement current* density (2.66). Then the electrical *conductivity* of tissue only determines the local relationship between the local *conductive current* density and the local *electric field* (2.32).

In line with this *simplified model*, biological tissue is modelled as the *body resistance* R_b only—according to the approximation in (3.1)—in Figs. 3.22, 3.24 and 3.25 for the sake of simplicity.

3.1.1.2 Skin Impedance

The *electrical behaviour of the skin*—when *surface electrodes* (typically with electrode paste acting as *electrolyte*) are applied on the skin and the electric current crosses it—is determined by conductive properties of the different skin layers permeated by this current in the *transversal direction*, see Fig. 3.2b. Thus the different skin layers determine the applicable *electrical equivalent circuit model* of the skin, as also illustrated in Fig. 3.2b.

In particular, the outermost skin layer of the *epidermis* (with its thickness of about 100 µm), known as the *corneum layer* (composed out of about 15–30 dead cells with its total thickness of about 10–40 µm), acts as a relatively poor conductor (when dry). Deeper below the skin surface, in the *subcorneal medium*, the local electrical conductivity rises, especially in the well-perfused *dermis* of the skin (below the epidermis, see Fig. 3.2b).

Consequently,

- the *conducting (metallic) electrode* on the skin or the *conducting electrolyte* following the electrode surface,
- the adjacent *isolating layer of the corneum*, and
- the following *conductive tissues* beneath the corneum (i.e., the conductive subcorneal medium),

all three form the *corneal capacitor* with its capacitance C_{cor} (in analogy with two conductive plates and an isolating layer in-between the plates forming a capacitor in Fig. 2.8); in the order of 0.02–0.06 µF/cm^2 (Reilly 1998). In order to account for the poor conductivity of the corneum layer (isolating layer), a relatively *large resistor* R_{cor}—in the order of 100–1000 k$\Omega \cdot$ cm^2 in the low frequency range up to about 1 Hz (Reilly 1998), compare Fig. 3.23—resides in parallel to C_{cor} in the equivalent circuit model, as depicted in Fig. 3.2b. In addition, a relatively *small resistor* R_{subcor} lies in series with the latter parallel circuit and models the

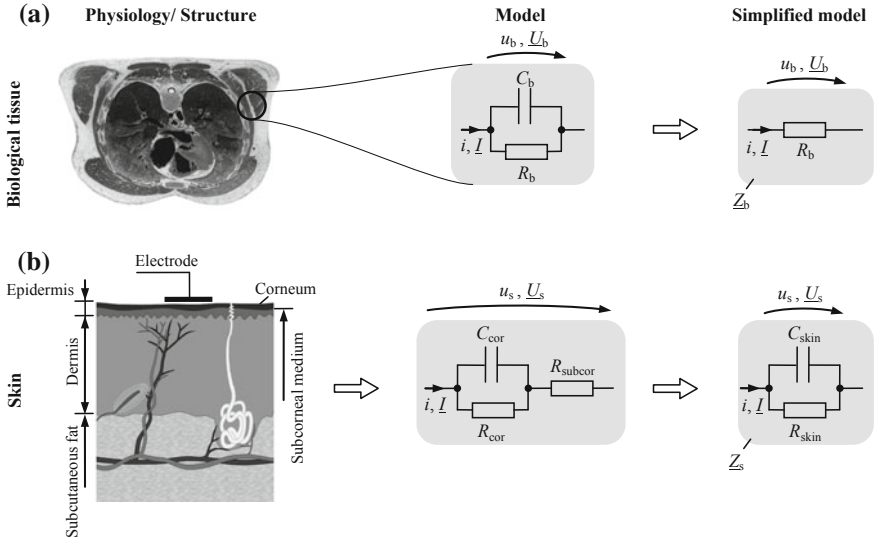

Fig. 3.2 The electrical equivalent circuit models of **a** biological tissue [according to Fig. 2.9 and (3.1)] and **b** the skin (3.2); compare Fig. 3.19. The associated models and their simplified versions are shown

well-conductive subcorneal medium. The total *skin impedance* $\underline{Z}_s$ (Fig. 3.2b) amounts to

$$\underline{Z}_s = \frac{\underline{U}_s}{\underline{I}} = \frac{R_{cor}}{1 + j \cdot \omega \cdot R_{cor} \cdot C_{cor}} + R_{subcor} \approx \frac{R_{cor}}{1 + j \cdot \omega \cdot R_{cor} \cdot C_{cor}}, \tag{3.2}$$

with $\underline{U}_s$ as the *complex amplitude* of the *voltage drop* u_s across the skin and $\underline{I}$ the *complex amplitude* of the *current i* through this skin. Please note that the magnitude of the impedance $\underline{Z}_s$ (3.2) equals $R_{cor} + R_{subcor}$ for *low frequencies* ($\ll 1/(2\pi \cdot R_{cor} \cdot C_{cor})$) and then decreases with *increasing field frequency*, so that the equality $\underline{Z}_s \approx R_{subcor}$ results at *high frequencies* ($\gg 1/(2\pi \cdot R_{cor} \cdot C_{cor})$).

Typically, the value of R_{subcor} is much smaller than that of the parallel connection of R_{cor} and $1/(j\omega C_{cor})$ (2.47) so that R_{subcor} can be neglected. Then a *simplified model* of $\underline{Z}_s$ results, as approximated in the above equation and shown in Fig. 3.2b.

Figure 3.3 shows the skin response to a *voltage stimulus* u ($=u_s$) applied via an (active) surface *sensing electrode* on the skin. The large *reference electrode* (Footnote 30) is considered to be *indifferent*. The polarization voltage and electrode impedance of both electrodes (Fig. 3.19) as well as the tissue impedance (Fig. 3.2a) are neglected in the subsequent discussion, so that the stimulus u drops across the skin and the equality $u = u_s$ applies.

As can be derived from the applicable *electrical model of the skin* (Fig. 3.3b), the rectangular waveform of the applied $u = u_s$ (Fig. 3.3c) leads to a spiky and

differential response of the *resulting current i* permeating the skin (Fig. 3.3d). That is, the *high-pass behaviour* of the skin dominates here, with the stimulus u as the input signal and the resulting i as the output signal. In particular, the initial relatively high *spike* in i (at the time instant $t = t_0$, i.e., at the onset of the pulse in u) is only limited by the relatively small R_{subcor} of the *well-conductive subcorneal medium*. This is because the corneal C_{cor} is short-circuited and thus only R_{subcor} limits i at $t = t_0$ (Fig. 3.3b). With the passage of time $t > t_0$, the current i through the skin decays exponentially to its *end value*, limited by the sum $R_{cor} + R_{subcor}$; see the labelled current axis in Fig. 3.3d. In practice, this decay of the skin i is relatively steep and the end value goes usually towards zero because R_{cor} ($\gg R_{subcor}$) is relatively high yielding $R_{cor} + R_{subcor} \approx R_{cor}$ and thus $1/R_{cor} \rightarrow 0$; see Fig. 3.3d.

Figure 3.3d demonstrates also the response in i of the *skin without corneum* for comparison aims. That is, the corneal layer is stripped away by adhesive tape, i.e., the skin is abraded to remove the outermost isolating layer of the epidermis in order to improve the electrical contact of the surface electrode (or the electrode's electrolyte) with the skin. Here the aforementioned *high-pass behaviour* in the waveform of i *disappears* and only R_{subcor} determines the strength of i (Fig. 3.3d) through the skin in response to the applied u pulse (Fig. 3.3b).

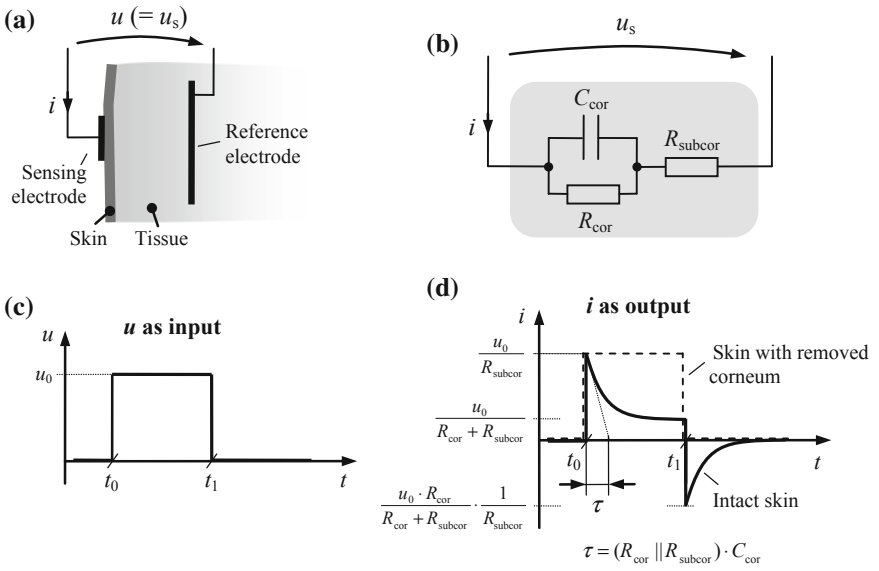

Fig. 3.3 Current response of the skin to voltage stimulus. **a** An active/sensing surface electrode is applied on the skin. The corresponding reference electrode (large and indifferent) is assumed to be deep within the tissue. **b** The used electrical equivalent circuit model of the skin with the capacitance C_{cor} and resistance R_{cor} of the isolating corneum (the outermost layer of the epidermis, see Fig. 3.2b, as well as with the resistance R_{subcor} ($\ll R_{cor}$) of the well-conductive subcorneal medium. **c** The applied voltage pulse u ($=u_s$) which equals the voltage drop u_s across the skin. **d** The resulting current i through the skin, with and without the corneum layer (e.g., removed by skin abrading)

It should be noted that the described *model of the skin* in Fig. 3.3b with its capacitive behaviour is a rough approximation only. Just to give an idea of an *improved model*, the skin with an applied surface electrode can also be considered as a *series connection* of

- the *conducting electrode* or its *conducting electrolyte*,
- the *isolating corneum*,
- the *conducting subcorneal medium* (including *conducting dermis*) down to the subcutaneous fat,
- the *isolating subcutaneous fat* and, lastly,
- the *conductive tissues* deeper under the skin (e.g., conducting muscles); see Fig. 3.2b.

That is, the current transverses all these different layers in series. Correspondingly, *two capacitors* connected in series would result within an improved model, in contrast to a single capacitor from Fig. 3.3b.

The conductive *current* across the dry skin appears to be conducted through *discrete channels* (Reilly 1998), with a density of about 1 channel per mm^2. The punctuate nature of the skin conductance suggests that *sweat ducts* (*sweat glands*) form these channels, acting as conductive tubes through the isolating corneum. Sweat typically contains a *saline NaCl solution*, roughly comparable to 0.9% physiological solution (Footnote 27 in Chap. 2).

In addition, the *skin* can also be approximated as a *semi-permeable diaphragm* residing between two solutions containing the same ions and of different ionic concentrations—the electrolyte on the electrode surface and the body fluids. These concentration differences yield a voltage drop across such a permeable diaphragm [compare (Kaniusas 2012, Eq. 2.5)], in accordance with phenomena discussed in Fig. 3.4 and Footnote 15. This voltage drop, known as *contact voltage*, acts as a direct *voltage source* in series with the equivalent circuit from Fig. 3.2b. Such an electrolyte/fluids boundary also behaves as a parallel connection of an *additional capacitor* (due to a charge separation across the diaphragm) and *resistor* (associated with the electrical conductance of the diaphragm), which resides in series with the contact voltage. Please note that the contact voltage is a strong function of the skin preparation and the type of the used electrode/electrolyte.

It should be stressed that the skin, in general, exhibits also highly *non-linear* and markedly *time-varying electrical properties*—for instance, see the *voltage-dependence of the skin impedance* (Fig. 3.23)—that become complicated even more by chemical interactions at the electrode/skin interface (Figs. 2.84 and 3.17). Obviously, these non-linear and time-varying properties can not be readily expressed in terms of a simple (linear and time-invariant) *passive electrical circuit model*, as proposed in Fig. 3.2b. In other words, the applied skin models in Figs. 3.22, 3.24 and 3.25 exclude the non-linear and time-varying properties of the skin.

3.1.1.3 Electrode Polarization and Impedance

Direct contact between a metal electrode and biological tissue (e.g., a surface electrode applied on the skin or implanted into the body, see Fig. 3.1b, c) leads to various *chemical*, *electrical*, and *adsorption processes* on and close to the electrode surface. These processes result in the *electrode polarization*, i.e., an accumulation of *counter-charges* with the resulting *voltage drop* between the metal electrode and the surrounding tissue (Fig. 3.4). Basically, counter-charges accumulate only when one type of charge carriers penetrate the phase boundary, the metal/tissue interface, easier than another complementary type of carriers, whereas both types of carriers ensure charge neutrality. The polarization occurs even though there is *no active application of voltages or currents* on the electrode (a *currentless situation* is

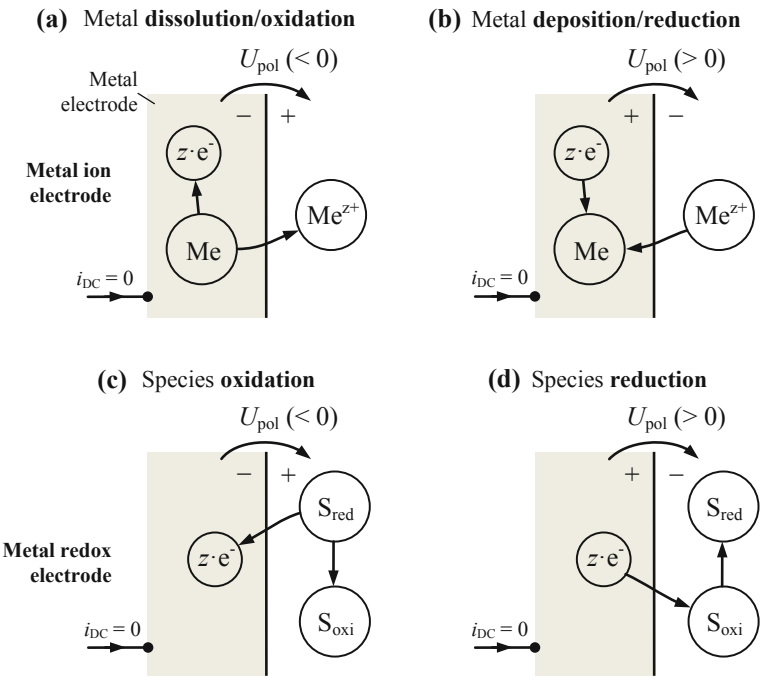

Fig. 3.4 Basic chemical processes on the electrode/tissue boundary. The metal ion electrode is associated with **a** the metal dissolution (Fig. 3.6a) and **b** the metal deposition. The metal redox electrode is associated with **c** the predominant oxidation of species in the tissue/electrolyte and **d** the predominant reduction of species in the tissue/electrolyte. Me and Me^{z+} denote the metal ion in the electrode and tissue/electrolyte, respectively (3.3). The substance S_{oxi} indicates the oxidized state of the substance S, whereas S_{red} indicates the associated reduced state (3.12). The charge distribution is shown for **a**–**d** with the associated polarization voltage U_{pol}

assumed with the electrode being disconnected from any external circuits), whereas this polarization becomes even more prominent when a *finite current* crosses the electrode/tissue boundary.

The *electrode impedance* is another important property which determines the extent of an additional *electrode polarization* in response to the *electrode current*. This impedance depends on the electrode material, its geometry, used electrolytes on the electrode surface (their concentration, temperature, resting or in motion due to stirring) as well as the signal frequency and even the current density across the boundary.

For the sake of simplicity, we assume that *biological tissue* (cell suspension)—in contact with and directly adjacent to the electrode—can be roughly *approximated* as a *solution of mobile ions* for charge transport. That is, the tissue is already assumed to act as an *electrolyte* (also perspiration of the skin acts as an electrolyte), which will be referred to as *tissue/electrolyte* in the following sections. Likewise, the *metal/tissue* interface or, as an approximation, the *metal/electrolyte* interface is described in this section.

In particular, another *electrolyte layer* (e.g., *electrode paste* or jelly) is usually employed as an interface between the *metallic electrode* and the *bodily tissue* (typically, the surface of the body in line with Fig. 3.1b). This conductive layer establishes a clearly defined contact with an advantageously *low contact impedance*. Therefore, the whole electrode/tissue interface is composed out of the *metal/electrolyte interface* and the *subsequent electrolyte/skin interface* (Sect. 3.1.1.2).

As discussed in the following sections (Fig. 3.4), the electrode can act as

- *metal ion electrode* or
- *redox electrode*, whereas the associated *electrode polarization* (the voltage drop across the electrode/electrolyte boundary) depends on many factors including the composition of the surrounding *tissue/electrolyte*. In addition, the electrode can also act as
- *reference electrode* with a relatively small (or even negligible) and constant *electrode polarization* that—as a very important condition for practical sensing of electric biosignals—does not directly depend on the *tissue/electrolyte* surrounding this electrode and, on the other hand, is preferably independent on the electric current through this electrode.

Metal Ion Electrode and Its Double Layer

In the case of the *metal ion electrode*, *osmotic pressure*[1] of metal Me ions in the electrode,[2] forces them to leave the electrode (*metal dissolution*) and convert to *positive cations* Me^{z+} *in the tissue/electrolyte* close to the electrode surface (with their valence z), to give

$$Me \leftrightarrow Me^{z+} + z \cdot e^{-}, \tag{3.3}$$

provided that the opposite osmotic pressure of ions in the tissue/electrolyte is less than that in the electrode,[3] see Fig. 3.4a. Obviously, dissolved *metal cations* become solvated (or *hydrated*).

[1] *Osmosis* refers to the *selective diffusion of solvent*—but not solute—from one region to another; namely, from the *low-solute-concentration solution* to the *high-solute-concentration solution*. Likewise, highly concentrated regions absorb the solvent (usually water). In osmosis, both regions with the different solute-concentrations are separated by a *semi-permeable structure* (such as a semi-permeable membrane) which is permeable to the solvent only (e.g., due to smaller solvent molecules which can pass through the membrane but not the large solute molecules).

This process of the selective diffusion is driven by the *internal thermal energy of the solvent*. Namely, the pure solvent can be assumed to have a higher energy density than a mixture of the solvent and solute, since the pure solvent has more solvent molecules and the thermal energy of the solute does not contribute to the aforementioned *selective transport* from one region to another (presuming that the semi-permeable membrane is impermeable to the solute).

This internal energy of the solvent can be assumed to be proportional to the *driving osmotic pressure*. That is, the solvent moves from "high pressure" regions (e.g., with the pure solvent and with the highest energy density) to "low pressure" regions (e.g., towards a solution of the solvent and solute, showing lower energy density) across the semi-permeable structure. This is in analogy with the normal fluid flow through a pipe from the high pressure region to low (Kaniusas 2012, Eq. 2.18). Consequently, the *osmotic pressure* increases with

- the absolute *temperature* and with
- the *differential in the solute-concentrations* on both sides of the semi-permeable structure.

Finally, it should be noted that *osmosis* is highly relevant in diverse *biological processes*, such as the selective transport of (small) water molecules across the *semi-permeable cell membrane* (Kaniusas 2012, Fig. 2.3) driven by the difference in the solute-concentrations between intracellular and extracellular regions.

[2] *Osmosis* from Footnote 1 can also be applied to the *electrode/electrolyte interface* in which *metal ions* act as solvent subjected to the *selective diffusion*. Metal ions can leave the metal surface and enter the electrolyte or, on the other hand, deposit on the surface from the electrolyte, depending on the *osmotic pressure*. In other words, the *metal surface* acts as a kind of *semi-permeable membrane*.

[3] Please note that—instead of the *osmotic pressure*—also the *electrochemical potential energy* of *metal ions* in the *metal electrode* and that of metal ions in the *electrolyte* could be considered to discuss quantitatively the dissolution of the metal electrode or the metal deposition on the electrode (Hamann and Vielstich 1998). In short, the *electrochemical potential energy* of a substance is given as $W_{Ch} + W_{El}$, i.e., as the sum of

- the *chemical potential energy* $W_{Ch} = W_{Ch,0} + k \cdot T \cdot \ln a$, i.e., W_{Ch} is proportional to the product of the absolute *temperature* T and the logarithm of the associated *activity* a (Footnote 7), with $W_{Ch,0}$ as W_{Ch} under *standard thermodynamic conditions* (Footnote 8) and k as the Bolzmann constant; and

Likewise, metal "vaporizes" into the electrolyte—or metal has a tendency to send its (positively charged) ions into the electrolyte—until a *chemical equilibrium* (i.e., a *dynamic equilibrium* as a *steady state*[4]) would be reached (in fact, it is not reached, see below) in which the *same number of metal ions* leaves the metal surface and, on the other hand, comes back to the surface, as averaged over time [see reversible process in (3.3)]. In the *chemical equilibrium state*, the electrolyte would be saturated with metal ions (in analogy with the air layer over liquid, with the air being saturated with the vapour of the liquid).

However, this *chemical equilibrium can not be reached* since, when metallic ions with an *excess of positive nucleus charge* leave the electrode, this *electrode becomes negatively charged* (to be precise, the electrolyte-sided electrode surface

---

- the *electrical potential energy* $W_{El} = Q \cdot \varphi$, i.e., equal to the product of the *ionic charge* Q and the local *electric potential* φ.

That is the *electrochemical potential energy* of a charged (ionic) particle is a generalisation of its *chemical potential energy*, just to include the impact of the local *electric potential* on this particle. Namely, the equality between

- the *electrochemical potential* of metal ions in the electrode and
- that of metal ions in the electrolyte

yields the *electrochemical equilibrium* according to (3.4).

[4]A *steady state* of a system is defined in a way that *characteristic variables* of the system—specifying the behaviour of the system—*remain constant over time*, i.e., their *time derivatives* are zero (compare Footnote 41). Typically, a steady state requires an *active net energy supply* in order to maintain the state. It is important to recognise that *momentary values of system variables* may still show time dependences in a steady state but not characteristic variables (such as effective values or magnitudes of time-dependant variables).

In many systems, a steady state is only achieved after some time following the start or initialisation of the system; e.g., after a *characteristic time* determined by the time constant of the system from Footnote 41. This initial situation up to a steady state is known as a *transient state* or start-up period.

A *dynamic equilibrium* is a limiting case or a subset of a *steady state* (but the opposite is not true). *No net energy entering or leaving a system* is required to maintain the equilibrium within the system. For instance, the dynamic equilibrium requires a *reversible chemical reaction* on the electrode surface (3.3) and (3.12), in which no net change in amounts of reactants and products occurs. The two opposing reactions go on at *equal rates*. A system that is in a *steady state* may not be in a dynamic equilibrium, because the two reactions may go at *different rates* and/or involved partial *reactions may be even irreversible* in the steady state (when, for instance, formed gases within one of the reaction at the electrode surface have enough time to bubble away).

In fact, the *currentless situation* of the electrode/electrolyte boundary is a necessary condition for its *dynamic equilibrium*. However, when a *finite conductive current* passes the boundary (Section "Active Current or Voltage Application Between Electrodes") this *equilibrium is lost* while a *steady state of the boundary is achieved* with a certain *time delay* (Section "Dynamics of Electro-Kinetic Processes").

Homeostasis in the human body can also be seen as a *steady state*, in which different body parameters (such as intracellular concentrations of ions (Kaniusas 2012, Sect. 2.1.2), body temperature (Kaniusas 2012, Sect. 3.1.5), or arterial blood pressure (Kaniusas 2012, Sect. 3.1.3.1) are actively regulated, accounting for the body's activity (e.g., sleeping or exercising) and for inevitable changes in the body's environment (e.g., cold or hot).

becomes charged since spatial charge can not be built in good conductors; compare Fig. 2.25a). This is because dissolved *metal ions become oxidized* to form *cations* and give off free electrons to the metal, i.e., *electrons* are left with their negative charge $z \cdot e^-$ on the metal surface (e^- is the elementary negative charge, i.e., $e^- = -1.6 \cdot 10^{-19}$ C), see Fig. 3.4a and (3.3). These positive cations, or positive *counterions*, are kept close to the negatively-charged electrode surface by attractive electrostatic forces (Fig. 3.6a). That is, this *charge separation* yields *electrostatic forces opposing* and then ending the effective *metal dissolution*, which is known then as the *electrochemical equilibrium* (i.e., a *dynamic equilibrium* as a *steady state*, see below). It is interesting to note that with increasing *concentration of the electrolyte*, the *osmotic pressure* of ions in the electrolyte increases, which causes less metal ions to leave the electrode surface (see above) and thus causes *less charging of the metallic electrode* in contact with the solution.

For instance, this behaviour of *metal dissolution*—or *metal oxidation*—applies to Al and Fe as electrode materials, i.e., the dissolution applies to *base metals*. The associated *electrode reactions* are $Al \leftrightarrow Al^{3+} + 3e^-$ and $Fe \leftrightarrow Fe^{2+} + 2e^-$, respectively [in line with (3.3) and Fig. 3.4a]. The *oxidation* of Al and Fe dominates (with $Al \rightarrow Al^{3+} + 3e^-$ and $Fe \rightarrow Fe^{2+} + 2e^-$) and the resulting so-called *polarization voltage* U_{pol} is negative ($U_{pol} < 0$) because of *negatively charged electrodes* [in line with (3.4), see below]. The *least noble metals* have the most negative values of U_{pol}.

However, if the *osmotic pressure* acting on ions in the electrolyte dominates over that acting on metal ions in the electrode, positive ions from the electrolyte, metal cations, join the metal, i.e., electrolyte "vaporizes" metal ions onto the metal surface. That is, *metal ions* deposit on the electrode surface, *become reduced*, and turn into neutral atoms taking off free electrons from the metal (*metal deposition*), see Fig. 3.4b and (3.3). Then the metal *electrode becomes positively charged* while the negatively-charged *counterions* (*anions*) from the electrolyte become attracted close to the electrode surface due to *electrostatic forces*. In contrast to the negatively charged metallic electrodes (see above), increasing *concentration of the electrolyte* here causes more metal ions to deposit on the surface and thus *stronger charging of the electrode*.

For instance, this behaviour of *metal deposition*—or *metal reduction*—applies to Ag, Au, and Pt as electrode materials, i.e., these *noble metals* do not tend to give ions or to dissolve/oxidise into the surrounding solution, in strong contrast to *metal dissolution*.[5] The associated *electrode reactions* are $Ag^+ + e^- \leftrightarrow Ag$ and

[5]From a microscopic point of view, processes of *metal deposition and dissolution* operate mainly in two modes:

- with intermediate *adsorption* and
- without it.

In the case of *metal deposition with adsorption*, metal ions from the *outer Helmholtz layer* (Fig. 3.6a) become discharged via an intermediate adsorption on the *surface of the metal electrode*. Then adsorbed ions (still mobile) diffuse along the surface until their final fit into the crystal lattice (e.g., adhere to edges of single atom layers or to crystal growth centers). Typically, this transition

$Au^+ + e^- \leftrightarrow Au$ for Ag and Au, respectively. The *reduction* of Ag^+ and Au^+ dominates (with $Ag^+ + e^- \rightarrow Ag$ and $Au^+ + e^- \rightarrow Au$) and the resulting *voltage* U_{pol} is positive ($U_{pol} > 0$) because of *positively charged electrodes* (Fig. 3.4b).

Obviously, this process of *charge separation* goes until the opposing *electrical driving force* (or electrostatic force, see Kaniusas (2012, Footnote 44))—due to the arising *electric field* between the charged *electrode surface* and *counterions* which are oppositely charged (as shown in Fig. 3.6a)—becomes equal to the force of the *driving osmotic pressure*. For instance, ions diffuse into the electrolyte until the counter potential set up by their departure constrains this tendency. Likewise, the negatively charged electrode attracts already dissolved positive ions via electrostatic forces, so that these electrostatic forces oppose chemical forces which tend to dissolve the electrode. The aforementioned *electrochemical equilibrium* is then reached and the effective electrode dissolution ceases (or the effective deposition of metal ions on the electrode, see above); i.e., here the velocity of the metal

---

from the adsorbed state into the lattice is quite fast and thus does not slow down the *total reaction kinetics* (Hamann and Vielstich 1998); see the discussed kinetics in Section "Active Current or Voltage Application Between Electrodes". Alternatively, metal ions from the outer Helmholtz layer can directly reach—or can directly be discharged to—their permanent positions within the metal lattice. An analogous behaviour is applicable for the *metal dissolution*.

Please note that metal ions in the *adsorbed state* are only *partly solvated/hydrated*, whereas ions in the outer Helmholtz layer (and further down in the bulk) are *completely solvated/hydrated*, as can be observed in Fig. 3.6a. Therefore, the solvation/hydration energy of metal ions in the bulk is overcome and gained with this intermediate step of adsorption during metal deposition and metal dissolution, respectively.

It is instructive to observe that the deposition of metal ions prefers regions at the electrode surface, which show high levels of the local *electric stray field*. These fields are typically strong in regions close to *conducting corners, points, and edges* (formed microscopically by single metal atoms); in analogy with the *electrical point effect* from Fig. 2.25 and Footnote 58 in Chap. 2. Interestingly, a *low conductivity of electrolyte* favours the *compaction of electric field lines* around conducting corners, points, and edges and thus favours the *electrical point effect* (Hamann and Vielstich 1998); compare Footnote 26. Consequently, a *rugged metal surface* is preferably formed by electrolytes of a *low conductivity*, whereas electrolytes of a *high concentration and thus a high conductivity* favour the formation of a *smooth metal surface* (or, in other words, smooth the original surface of the metal electrode).

In addition, the formation of a *smooth metal surface* is favoured when adsorption of metal ions is inhibited on outstanding surface parts (known as *nucleation sites*) of the metal electrode. Such inhibition can be realized through *specific inhibitors* subjected to specific adsorption on the metal surface where the highest local *electric stray fields* prevail (i.e., subjected to adsorption on nucleation sites). Then metal ions from electrolyte are forced to build constantly *new nucleation sites* and thus to form a smooth metal surface.

It is also interesting to note that the *formation speed of new nucleation sites* (of adsorbed metal atoms) decreases exponentially with decreasing *polarization overvoltage* $|u_{pol,i} - U_{pol}|$ (Hamann and Vielstich 1998); compare Fig. 3.13. Likewise, a *low overvoltage* implies an *undisturbed growth of crystals* and correspondingly the formation of a *rugged metal surface* (or a granular crystalline surface). On the contrary, a *large overvoltage* disfavours a continuous growth of crystals but instead promotes the formation of *new nucleation sites* and thus favours the formation of a *fine crystalline surface*.

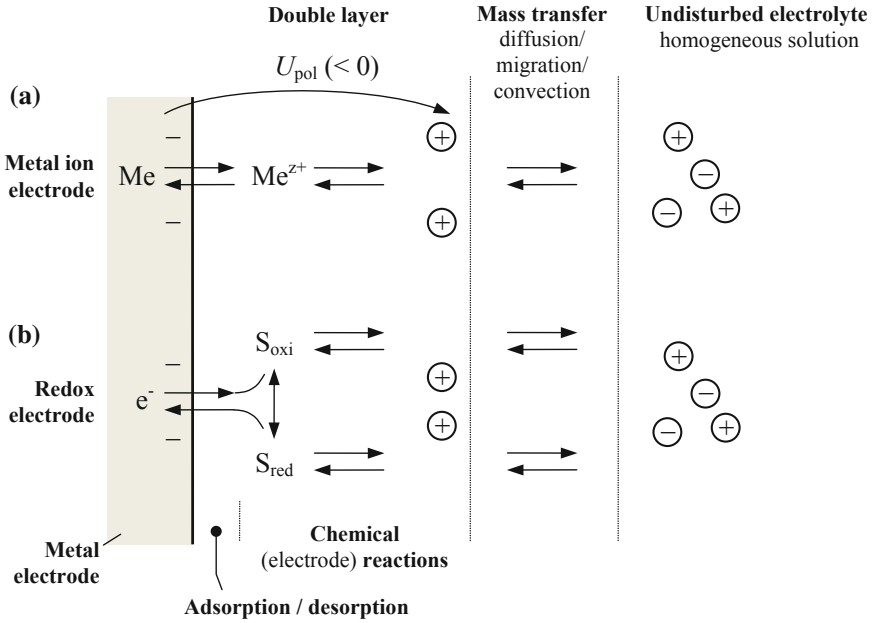

Fig. 3.5 The electrode/tissue boundary with the adsorption, chemical electrode reactions, and mass transfer; compare Fig. 3.20a. **a** The metal ion electrode with the predominant metal dissolution, see Figs. 3.4a and 3.6a. **b** The redox electrode with the predominant species oxidation, see Fig. 3.4c. Me and Me^{z+} denote the metal ion in the electrode and tissue/electrolyte, respectively (3.3). The substance S_{oxi} indicates the oxidized state of the substance S, whereas S_{red} indicates the associated reduced state (3.12). The assumed charge distribution is shown for the polarization voltage $U_{pol} < 0$ (and $i_{DC} = 0$)

dissolution is equal to that of the metal deposition in terms of a *dynamic equilibrium* as a *steady state* (Hamann and Vielstich 1998), see (3.3) and Footnote 4.

The relatively high *electric field* between the electrode surface and counterions (Footnote 13) yields the aforementioned *polarization voltage*[6] U_{pol} in the latter *electrochemical equilibrium* with the balanced *chemical and electrical forces*—and *without any active application of direct voltages or direct currents* on the

[6]It should be noted that the single *polarization voltage* U_{pol} can be hardly *experimentally* measured in *isolation* and in a straightforward way (Wagner 1993). Since (at least) two electrodes are needed to *register voltage*, e.g., a voltage between the *sensing and reference electrode* in Fig. 3.6, only the difference $U_{pol} - U'_{pol}$ between U_{pol} from the sensing electrode and U'_{pol} from the reference electrode can be experimentally assessed. This registered voltage equals $U_{pol} - U'_{pol}$ only if *currentless situation* prevails with $i_{DC} = 0$ (Fig. 3.6).

In fact, only the difference $U_{pol} - U'_{pol}$, but not the absolute value of U_{pol} or U'_{pol}, influences *diagnostic and therapeutic applications* of electrodes, as shown in (3.38) (in line with Fig. 3.24c, d) and (3.40) (Fig. 3.25c, d), respectively. For instance, the output voltage $u = U_{pol} - U'_{pol}$ results for $i = 0$ and $U_0 = 0$ in Fig. 3.24c, d.

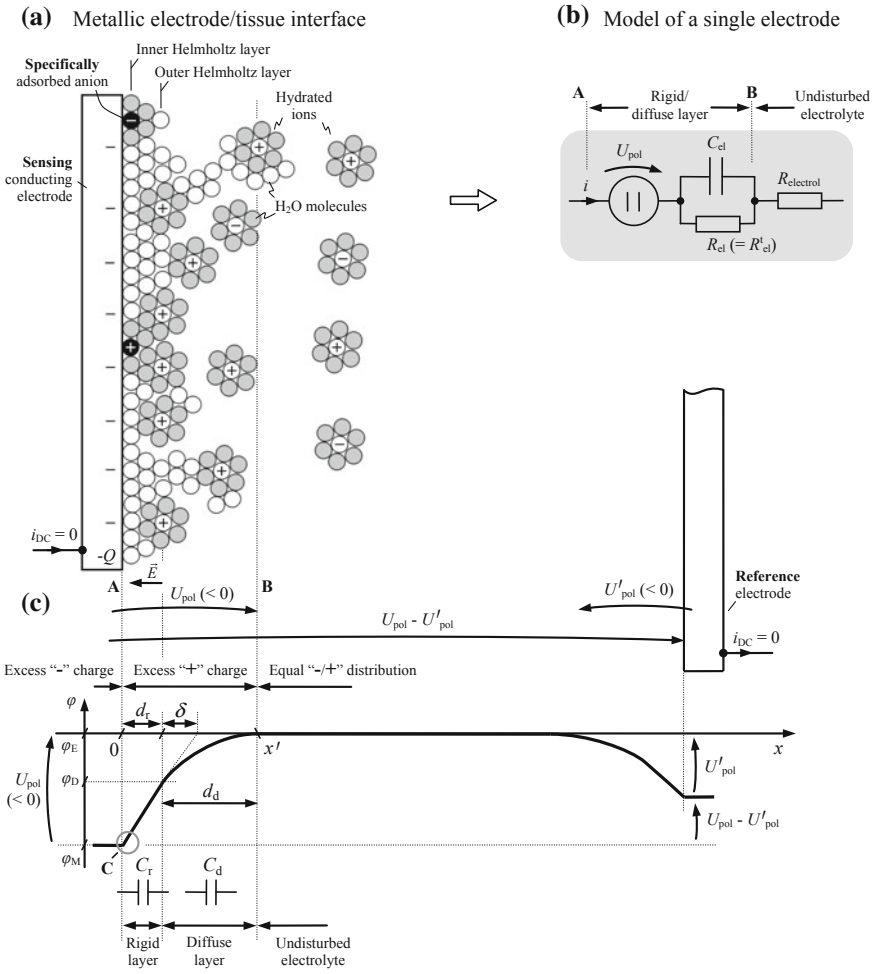

Fig. 3.6 The model of the electrode/tissue boundary of the metal ion electrode in the currentless situation (with the direct current $i_{DC} = 0$) and in its electrochemical equilibrium; compare Fig. 3.5. **a** Charged double layer results directly at the boundary of the sensing electrode, composed out of negative electron charges in the metallic electrode and positive ionic charges in the tissue/electrolyte (residing very close to the electrode surface, within a few nm) due to metal dissolution (Fig. 3.4a), with the associated electric field E in-between. **b** Electrical equivalent circuit model of the electrode/tissue boundary is shown, whereas a charge-transfer-limited reaction is assumed (Fig. 3.20b). **c** The resulting course of the electric potential φ across the boundary of the considered sensing electrode and across another boundary of the reference electrode. The polarization voltages U_{pol} (<0) and U'_{pol} (<0) result that are pertinent to the respective electrode/tissue boundary

electrodes, i.e., $i_{DC} = 0$ in Fig. 3.6a—as the *voltage drop between the electrode and undisturbed electrolyte* (Figs. 3.5a and 3.6a). In other words, U_{pol} can be interpreted as the *voltage drop* between the electrode and counterion layer; to be precise, between the electrode and the most distant end of the counterion layer from the electrode surface, see marked U_{pol} in Fig. 3.6c. Likewise, the electric potentials of the electrode and the undisturbed electrolyte must differ.

This voltage U_{pol}—as the difference of the electric potential φ_M of the metal electrode and φ_E of the *undisturbed electrolyte*—is expressed by the *Nernst equation* [for its derivation see Footnote 3, compare also (Kaniusas 2012, Footnote 46)], to give

$$U_{pol} = \varphi_M - \varphi_E = U^0_{pol} + \frac{R \cdot T}{z \cdot F} \cdot \ln \frac{a_{Me+}}{a_{Me}} = U^0_{pol} + \frac{R \cdot T}{z \cdot F} \cdot \ln \frac{a_{Me+}}{1\ \text{mol/l}} = U^{00}_{pol} + \frac{R \cdot T}{z \cdot F} \cdot \ln \frac{c_{Me+}}{1\ \text{mol/l}}. \tag{3.4}$$

Here a_{Me+} ($=f_{Me+} \cdot c_{Me+}$) is the *activity* of metal ions Me^{z+} in the electrolyte *close to the electrode surface*, f_{Me+} the associated *activity coefficient*[7] of ions, and c_{Me+} the concentration of these ions in the electrolyte. Here the constant R denotes the gas

[7]Please note that the *activity coefficient* f_{Me+} of the *ions* Me^{z+} approaches 1 only in *ideally diluted solutions* without any *inter-ionic interactions* (known as *ideal solution*). That is, the *electrochemical reactivity* a_{Me+} ($=f_{Me+} \cdot c_{Me+}$)—determining the *chemical energy* of Me^{z+} (Footnote 3)—is maximum for *isolated ions* where a_{Me+} approaches the ionic *concentration* c_{Me+} in the solution. In such ideally diluted solutions, there are no interactions of the considered ions Me^{z+} with other complementary structures in the solution (e.g., complementary ions Me^{z-} or even *polar water molecules*). In contrast to charged ions in the solution, *electrically-neutral non-interacting and dissolved substances* always show $f = 1$.

Likewise, the *coefficient* f_{Me+} *tends to decrease* ($f_{Me+} < 1$) with increasing *ionic* c_{Me+} *in the solution*. As described in Footnote 28 in Chap. 2, this is because *electrostatic forces* of *inter-ionic interactions*—forces which progressively increase with decreasing distances between charged ions in the solution—*mutually hinder ions in their directed migration* within the solution (migration in response to the directed local electric field).

For instance, a *NaCl solution* at 25 °C with $c = 0.001$ mol/l, 0.01 mol/l, or 0.1 mol/l shows the estimated $f = 0.96$, 0.9, or 0.78, respectively (according to different sources). However, in *highly concentrated solutions*, e.g., above about 1 mol/l (Hamann and Vielstich 1998), f_{Me+} *tends to raise* and even to surpass 1. Thus, the *NaCl solution* from above with $c = 1$ mol/l or 5 mol/l yields to $f = 0.66$ or 0.87, respectively. This increase in f_{Me+} with increasing c_{Me+} can be due to

- *insufficient solvent molecules* to build complete solvation shells around ions of the solute, which implies an increased reactivity of the almost bare ions (see below), or due to
- increased repelling forces between solvated ions with their *non-zero volumes* at high ionic concentrations, which rise an independent acting of ions and thus rise their f_{Me+}.

In addition,

- build-up of *ion-associations* of oppositely charged ions at high concentrations (the associated small inter-ionic distances lead to strong inter-ionic attractive forces between oppositely charged ions) tends to decrease the net level of f_{Me+}. This is because such ion associations act as *neutral particles* which do not contribute to the ionic activity a_{Me+} or the ionic conductivity (2.54). Lastly,

constant [R = 8.31 J/(K mol)], F the Faraday's constant ($F = 9.65 \cdot 10^4$ A s/mol), z the valence of the involved ions, and T the absolute temperature; compare (Kaniusas 2012, Eq. 2.5). Please note that a differentiation between the concentration of ions on the electrode surface and that within the undisturbed electrolyte is not appropriate in (3.4) because a *steady state without diffusion* (Section "Diffusion and Diffusion Overvoltage") is considered here, which yields equal latter concentrations.

As shown in (3.4), the activity a_{Me} of metal ions in the electrode was arbitrarily set to 1 mol/l (activity of the pure phase). In particular, the voltage U^0_{pol} (or U^{00}_{pol}) presents an *offset* for U_{pol} which takes into account the basic difference in the solid and liquid media being in direct contact. Please note that $U_{pol} = U^0_{pol}$ for

---

- bound solvent molecules in the *solvation shell* decrease the effective amount of the available solvent, which can be interpreted as an increase in the effective c_{Me+} or f_{Me+} with increasing ionic concentration.

In particular, attractive *electrostatic forces* between complementary charged ions *disfavour their dissociation* and isolation in the solution. Interestingly, *electrostatic forces/interactions* are effective over relatively *long atomic distances*, in contrast to *chemical forces/interactions* effective over *short distances* only. Therefore, *inter-ionic electrostatic interactions* should be considered even for strongly *diluted electrolytes*; likewise, significant deviations from an *ideal solution* already occur for *low electrolyte concentrations*. It should be recalled that for long-range electrostatic interactions between charged ions, the associated attractive and repelling electrostatic forces depend only on the *ionic charge and the distance in-between ions* but not on their *chemical identity*.

In contrast to *electrostatic forces*, the *thermal motion* of ions favours their dissociation and thus the independent spatial distributions of cations and anions in the solution with increasing *temperature*. Interestingly, the estimated *ratio* of the thermal energy to the electrostatic energy of attraction is only <2 for two monovalent ions dissociated in water at 25 °C. This implies still significant *electrostatic inter-ionic interactions* and shows that anions still prefer to reside close to cations despite of their relative dissociation. Please note that such *inter-ionic interactions hinder the opposite migration* of cations and anions in the electric field—as illustrated in Fig. 2.16a—and thus *reduce the resulting ionic conductivity* of the electrolyte with dissociated cations and anions within; as discussed in Footnote 28 in Chap. 2.

This means also that the activity a_{Me+} of a *charged ion* Me^{z+} in the aqueous solution with *polar water* molecules (as solvent) becomes reduced in comparison with a_{Me+} of an *isolated ion*, with the resulting $f_{Me+} < 1$ in the non-ideal solution. This is because the *ion's hydration shell* around Me^{z+} (Kaniusas (2012, Footnote 21)) should be stripped away before this ion can *react* with the electrode surface (e.g., before ions Me^{z+} can deposit on the electrode surface as Me). This process of the *ion's liberation* requires some *potential energy* ($=ze^- \cdot \varphi$ with φ as the local electric potential) at the expense of the *reduced reactivity* of the single (dehydrated) ion and thus at the expense of its reduced a_{Me+}. In other words, some *energy* must be submitted in order to liberate the ion from its hydration shell, whereas exactly this amount of energy is released when the shell is formed (due to reduction of *electric stray fields* between the charged ion and water molecules in the shell, see Kaniusas (2012, Footnote 13)).

In general, this behaviour of the reduced reactivity also applies to an ion surrounded by a *cloud of counterions*, as discussed in Footnote 17 with respect to Fig. 3.9b. This central ion should get rid of its cloud before chemical *reaction* (on the electrode surface). The *thicker and denser the hydration shell or the cloud of counterions*, the larger is the loss of *reactivity* of the ion (coated by the hydration shell or being in the centre of the cloud) and the lower is its f_{Me+} ($f_{Me+} < 1$).

$a_{Me+} = 1$ mol/l or $U_{pol} = U_{pol}^{00}$ for $c_{Me+} = 1$ mol/l in (3.4), which is usually referred to as U_{pol} under *standard thermodynamic conditions*.[8] In other words, the liquid can never be *saturated* as strongly as the metal with its metal ions Me^{z+} so that U_{pol}^{0} (or U_{pol}^{00}) is never zero. For instance, (3.4) yields that a change in the *concentration* c_{Me+} by a factor 10 at the body temperature of 37 °C and $z = 1$ results in the corresponding change of U_{pol} by about 61 mV; compare (Kaniusas 2012, Eq. 2.5). In fact, this polarization voltage occurs in close analogy with the origin of the resting membrane potential from Kaniusas (2012, Sect. 2.1.3.1). Please recall that (3.4) and the ongoing discussion still assume a *currentless situation*.

The qualitative meaningfulness of (3.4) can be easily seen in the light of the *metal deposition* on the electrode surface (Fig. 3.4b), as discussed above. Here the electrode becomes positively charged implying inequalities $\varphi_M > \varphi_E$ and $U_{pol} > 0$. An increasing concentration of the electrolyte around the electrode, i.e., an increasing c_{Me+} in (3.4), causes more metal ions to deposit on the electrode surface, the positive charge on the electrode to increase, and thus the voltage U_{pol} to increase, as conveyed principally by (3.4).

Electrical Double Layer

When *metallic electrode* is in contact with *tissue/electrolyte* (or with a cell suspension), an *ion exchange* takes place between the metal and tissue/electrolyte, and thus a *counterion layer* is formed outside but adjacent to the electrode surface within the *ional/molecular distance* of typically less than 1 nm (Fig. 3.6a). The electrostatic attractive forces force counterions to approach the inversely-charged surface as close as possible, whereas the thickness of the counterion layer is determined by the *Debye length* (Footnote 17).

This counterion layer and the *accumulated charge Q* on the electrode surface—of *opposite sign* and *equal amount*—are in parallel and form the so-called *electrical double layer* or *charge double layer*; i.e., *charge neutrality* applies to the whole double layer. Since the double layer—as an approximation—is *depleted inside from charges* (due to the discussed charge separation), with conductive media (or conductive adjoining phases) on both sides of the double layer, it resembles a *plate capacitor*[9] with the *capacitance*[10] C_{el} (Fig. 3.6b) given as

---

[8] *Standard thermodynamic conditions* imply solute activities of 1 mol/l, gas pressures of 1 bar (atmospheric pressure), and the temperature of 25 °C.

[9] The approximation of the *double layer* as a *plate capacitor* is rather valid for the *Helmholtz double layer* (with *rigid double layer* of charges only) and less valid for the diffuse *Gouy-Chapman double layer*, i.e., the model of the plate capacitor is appropriate for the relatively *high concentration of ions* only (see text).

[10] In fact, the *real double layer* does not behave as a *perfect capacitor* in experimental data. The double layer behaves rather as a *leaky capacitor with imperfect dielectrics*. In contrast to the *capacitive impedance* $1/(j\omega C_{el})$ of a *perfect capacitor* from (2.42), the *capacitive impedance* $\underline{Z}_C^{CPE}$ of the *double layer* acting as an *imperfect capacitor* often behaves as a *constant phase element*, to give

$$C_{\mathrm{el}} = \frac{Q}{U_{\mathrm{pol}}}; \tag{3.5}$$

compare (2.40). The capacitance C_{el} is also known as *interfacial capacitance*. Figure 3.6a demonstrates such double layer with the positively charged counterion layer residing close to the negatively charged electrode surface. Typically, the *differential* C_{el} ($=\mathrm{d}Q/\mathrm{d}U_{\mathrm{pol}} = \mathrm{d}Q/\mathrm{d}(\varphi_{\mathrm{M}} - \varphi_{\mathrm{E}}) = \mathrm{d}Q/\mathrm{d}\varphi_{\mathrm{M}}$ with φ_{E} in the undisturbed electrolyte assumed to be constant for varying U_{pol}) resides in the range of 5–50 μF per cm^2 of the electrode area (Hamann and Vielstich 1998) and depends on different physical properties, as discussed below.

Please note that the above *proportionality between Q and* U_{pol} (3.5) is not constant over the varying U_{pol} [$=\varphi_{\mathrm{M}} - \varphi_{\mathrm{E}}$, see (3.4)]. The capacitance C_{el} varies with U_{pol} which implies a *non-linear* C_{el} and thus a *non-linear behaviour between Q and* U_{pol}. This is because

- a *varying electric potential* φ_{M} of the electrode reorients water molecules (as *electric dipoles*) within rigid and diffuse layers (in terms of the *orientation polarization*, see Fig. 2.19c) (Hamann and Vielstich 1998). Consequently, the permittivity of this water may even change due to *varying electric fields* within the boundary (at fields which are already quite strong, see the following Section "Water Relevance") and so the contribution of the water permittivity to C_{el} (3.7) may change as well. For instance, the permittivity tends to decrease with increasing (and already strong) electric fields, which then manifests as a decrease in C_{el} (see Footnote 45 in Chap. 2 and Section "Water Relevance").
- An increase in $|U_{\mathrm{pol}}|$ tends to increase the *electrostatic attraction force counterions* are subjected to and thus to reduce the effective distance between the metal electrode surface and counterions within the double layer, which, in turn, would increase C_{el} (3.8); compare Section "Polarization of the Electrode/Tissue Boundary". Likewise, both rigid and diffuse layers can become reoriented with varying U_{pol}.
- In addition, *adsorption and deadsorption*—the type and number of *specifically adsorbed ions*—may change in response to the varying φ_{M} and thus may contribute to the non-linear C_{el} (Hamann and Vielstich 1998).

Obviously, the composition of this counterion layer is determined by both the electrode material and the suspension composition. Please note that the double layer at the *boundary of two phases*—metal and the undisturbed electrolyte—possesses

---

$$\underline{Z}_{\mathrm{C}}^{\mathrm{CPE}} = \frac{1}{(\mathrm{j}\cdot\omega)^{\alpha}\cdot C_{\mathrm{el}}} = \frac{1}{\omega^{\alpha}\cdot C_{\mathrm{el}}}\cdot \mathrm{e}^{-\mathrm{j}\cdot\frac{\pi}{2}\cdot\alpha}. \tag{3.5}$$

Here α is the exponent constant ($0 \leq \alpha \leq 1$) that determines the *resulting phase shift* $-\alpha \cdot \pi/2$ of $\underline{Z}_{\mathrm{C}}^{\mathrm{CPE}}$. Please note that this phase shift is *independent on the angular frequency* ω and equals to

- $-\pi/2$ ($=-90°$) in the case of an *ideal capacitor* [with $\alpha = 1$, see (2.42)] and, on the other hand,
- 0 (0°) for an *ideal resistor* [with $\alpha = 0$ and the resistance $R = 1/C_{\mathrm{el}}$, see (2.36)].

properties which are completely different from matter extending in either of the continuous phases (separated by this boundary); compare different charge distributions within the diffuse counterion layer (see below) and within the undisturbed electrolyte, as shown in Fig. 3.6a.

- Some of *counterions are rigidly held* at the surface and *resist thermal motion*, which is known as *Helmholtz double layer* or *rigid layer*.
- Following the Helmholtz double layer, other *counterions* (space charges) *are mobile*, tend to diffuse into the electrolyte by *thermal motion* and build a *cloud of space charge*, which is known as *Gouy-Chapman double layer* or *diffuse layer*.

Figure 3.6 demonstrates the *rigid layer* (Helmholtz layer) with its capacitance C_r inversely related to the *thickness of the rigid layer* (2.41). Here one virtual capacitor plate is built by the surface layer of the charged electrode and another plate by the charge layer of rigidly held counterions, whereas the distance between these plates is determined by the distance between *charge centers* within each layer. The so-called *outer Helmholtz layer* crosses the charge centre of counterions in the rigid layer (Fig. 3.6a). The subsequent *diffuse layer* (Gouy-Chapman layer) has its capacitance C_d inversely related to the *thickness of the diffuse layer*. Both rigid and diffuse layers will be referred to as *double layer*.

The *total capacitance* C_{el} is given as the *series connection* of C_r and C_d, to give

$$C_{el} = \frac{C_r \cdot C_d}{C_r + C_d}. \tag{3.6}$$

In the *diffuse layer*, the concentration of *counterions* (i.e., the amount of local excess charge)—see *surplus of cations* and *shortfall of anions* in Fig. 3.6a—decreases towards their *normal concentration* within the undisturbed electrolyte with increasing distance from the surface. In contrast, ions of the same sign as the metallic surface charge—see negative anions in Fig. 3.6a—increase in their number with distance from the metallic surface towards their normal concentration within the undisturbed electrolyte. This is because *charge neutrality* applies for the *undisturbed electrolyte* with balanced numbers of *cations and anions* within, see Fig. 3.6a.

The *total thickness of the double layer* is mainly affected by the kinetic/thermal energy of ions within the *diffuse layer*. Please note that the total thickness is related to the *distance from the metal surface* at which ions can already escape to the bulk by *thermal motion* (Grimnes and Martinsen 2008).

The *thickness* d_r *of the rigid layer*—see Fig. 3.6c—can be approximated as the *effective radius of solvated counterions* (a few 0.1 nm, see Fig. 2.16a and Footnote 22 in Chap. 2), residing directly on the electrode surface. This thickness d_r is rather independent on the concentration of counterions, whereas the *solvent*—such as *water* with its relatively low *permittivity* ε *within the double layer* (see below)—is important in terms of the solvation shell of counterions, with the shell

co-determining d_r. Thus, the value of the *(electrode) area-related* C_r can be estimated as

$$\frac{C_r}{A} = \frac{\varepsilon_r \cdot \varepsilon_0}{d_r}; \tag{3.7}$$

in numerical terms, $C_r / A = 10 \cdot 8.85 \cdot 10^{-12}$ F/m / 0.2 nm $\approx$ 44 μF/cm^2 with the assumed $d_r = 0.2$ nm and $\varepsilon_r = 10$.

In contrast, the *thickness* d_d *of the diffuse layer* increases

- with increasing *temperature*,
- with decreasing *concentration* of counterions, and
- with decreasing *valance* of involved counterions (because the decreasing valence reduces the net charge per single counterion and thus reduces the potential energy per single counterion ($=ze^- \cdot \varphi$) (compare Footnote 3); likewise, the decreasing valence means more counterions in the diffuse layer in order to compensate for the surface charge of the metal electrode, see below).

The *thickness* d_d can be described by means of the *Debye length* δ (strictly applicable to diluted electrolytes in line with Footnote 17), as the space constant of the exponential decay of the electric potential within the diffuse layer (3.9); see δ in Fig. 3.6c and (3.10). The exponential decay implies that d_d amounts to about 3–5 times δ ($<d_d$). Equation (3.10) confirms qualitatively the aforementioned dependence of d_d on temperature, concentration, and valence of ions. Likewise, the capacitance C_d is inversely related to δ—acting as the distance between capacitor plates in the *diffuse layer*—as if *all excess charge* of the diffuse layer would reside in a surface layer located at δ from the *outer Helmholtz layer*. Thus, the value of the *(electrode) area-related* C_d can be estimated as

$$\frac{C_d}{A} = \frac{\varepsilon_r \cdot \varepsilon_0}{\delta} \tag{3.8}$$

(in diluted electrolytes). Please note that C_d decreases with increasing *thickness* d_d *of the diffuse layer*. In analogy, C_d and the total C_{el} (3.6) decrease with increasing *temperature* and with decreasing *concentration*.

Interestingly, the *total thickness of the double layer* decreases with increasing *concentration of ions* in the solution (close to the electrode), i.e., diluted solutions show a less abrupt transition from the electrode surface into the undisturbed electrolyte.

- The thickness of the double layer is *about 0.5 nm* (in the range of ion size or of the thickness of the rigid layer) in *strong electrolytes* (roughly $\geq$ 0.1 mol/l (Hamann and Vielstich 1998)) with the *rigid layer* dominating the *double layer* [i.e., $C_d \gg C_r$ implying $C_{el} \approx C_r$, see (3.6)]; i.e., the diffuse layer results to be very thin with the associated high C_d. In other words, the rigid layer—as the only double layer present—is valid only for electrolytes of high concentration and very low temperature.

- In *dilute electrolytes* (with roughly <0.001 mol/l), the total thickness is *about 10 nm* while the *diffuse layer* dominates over the rigid layer ($\delta \gg d_r$ and thus $C_d \ll C_r$ implying $C_{el} \approx C_d$).

In other words,

- C_d increases with increasing ionic concentration because the effective d_d decreases. In contrast,
- C_r is independent on this concentration (in the absence of the specific ionic adsorption, see below). It follows that
- the total C_{el} (3.6) increases with increasing *ionic concentration*.

Specific Adsorption

In addition, some *specific ions* (non-water species)—charged or uncharged, especially *anions* (Dörfler 1994) such as Cl^- anions—can also be *specifically adsorbed*[11] by the metallic surface of the electrode and stay in *direct contact with the electrode surface*. In fact, such ions reside within the *rigid layer*, especially known as *inner Helmholtz*

[11]Interestingly, the *specific adsorption* can also lead to formation of a *charge double layer* on the surface of *non-conducting/non-charged bodies*. As illustrated in Fig. 3.8a, adsorbed negative anions attract positive cations from the electrolyte—acting as *counterions* to adsorbed ions—so that the double layer with the *resulting non-zero* $U_{pol} < 0$ is built.

- In analogy with Fig. 3.6a with the *negative excess charge within the electrode surface* (due to a *surplus of electrons* within the conducting electrode with electrons typically residing very close to the electrode surface),
- the *negative excess charge* in Fig. 3.8a resides *on the electrode surface* (due to a *surplus of adsorbed anions*).

Typically, *inorganic and organic bodies* form on their surface such *electric double layers* based on the specific adsorption.

Another important effect of the *specific adsorption* is illustrated in Fig. 3.8b, in the course of which *charge-neutral dissolved particles* with adsorbed *ions on their surface* attract the *oppositely charged counterions* from the electrolyte. A *charge double layer* is built around every neutral particle, in close analogy with Fig. 3.8a. Moreover, such neutral particle loaded with a significant amount of the net charge can even start to *migrate* when subjected to an *external electric field*, e.g., as induced by positively and negatively charged electrodes (compare Fig. 2.16a). The *counterions*, e.g., with the positive net charge in Fig. 3.8b, are obviously attracted by the external electric field in the *direction* opposite to the migration direction of loaded neutral particles, e.g., loaded with the negative net charge in Fig. 3.8b. If only *anions* are adsorbed on neutral particles (Fig. 3.8b), these loaded particles would *deposit* on the surface of the *positive electrode* during their migration in the electric field.

Otherwise, *neutral particles without adsorbed ions* or, on the other hand, *neutral particles with an equal number of adsorbed anions and cations* (per single particle)—which can usually be adjusted via the *pH-value* of the solution (Kaniusas 2012, Footnote 178)—*would not migrate* at all along the external electric field due to missing electrostatic attraction. Please note that the *dynamic behaviour of the counterions cloud* around a charged structure—or around a *loaded particle* as in Fig. 3.8b—is already described within the scope of α-dispersion (Fig. 2.19a), in analogy with the dynamic behaviour of the ionic cloud around the central ion (Footnote 40 in Chap. 2 and Fig. 3.9b).

layer that crosses the charge centre of the *specifically adsorbed* ions (see Fig. 3.6a). Such adsorption is *independent of the sign of the surface charge* residing on the electrode and is based on *short-range chemical adhesive forces* leading to direct bonding to the surface. In other words, the associated adhesive forces (e.g., van der Waals bonds) may have a different origin than the pure *electrostatic interaction*. In particular, ions tend to be adsorbed at specific regions of the metal surface where local chemical bonding forces are not saturated because of the local specific crystallographic structure or due to local defects of the crystal lattice. Likewise, adsorption sites of ions are usually defect-like sites such as local edges and/or corners, see Footnote 5.

Figure 3.7 provides an instructive *example of specific adsorption* in relation to *electrostatic attraction*. The electrolyte surrounding a metal electrode is composed out of neutral particles and charged particles (ions), whereas *only neutral particles are subjected to the specific adsorption*. Provided that the metal *electrode is uncharged*, i.e., its electric potential is zero as well as that of the electrolyte (e.g., $\varphi_M = \varphi_E = 0$ in Fig. 3.6c), *neutral particles* tend to cover the electrode surface because of their specific adsorption. Here neutral particles do not have to compete with charged ions in terms of the surface coverage. Figure 3.7 quantifies the surface coverage by the *degree of coverage* Θ, defined as the fraction of the electrode surface covered by adsorbed particles (i.e., $0 \leq \Theta \leq 1$ with $\Theta = 0$ for lacking coverage and $\Theta = 1$ for complete coverage). However, when the electrode becomes *negatively charged*, *positive cations* are attracted from electrolyte into the outer and eventually inner Helmholtz layers and displace the previously adsorbed neutral particles. Consequently, the coverage Θ of cations increases with decreasing

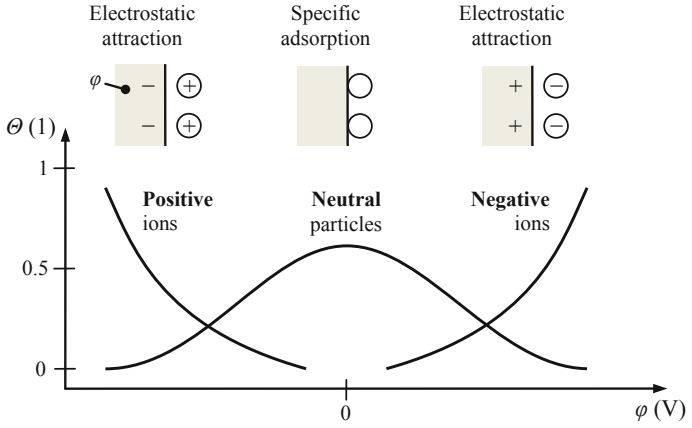

Fig. 3.7 Specific adsorption of charge-neutral particles and electrostatic attraction of charged particles (not subjected to specific adsorption) from electrolyte as a function of the electric potential φ of the metal electrode. The resulting surface coverage is qualitatively indicated by the degree of coverage Θ for neutral particles, positive and negative ions. Data is partly taken from (Hamann and Vielstich 1998)

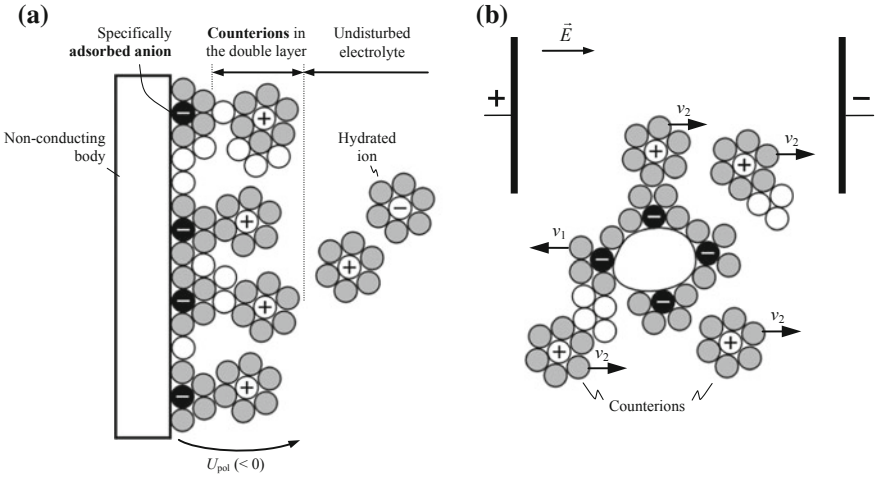

Fig. 3.8 Specific adsorption of anions on the surface of a non-conducting body. **a** Establishment of the charged double layer with the polarization voltage U_{pol} (<0). Adsorbed anions form one side of the double layer while cations as counterions form the other side which includes the rigid and diffuse layers; compare Fig. 3.6a. **b** Migration of a charge-neutral dissolved particle with adsorbed anions on its surface in response to the ambient electric field E; compare Fig. 2.16a

electrode potential. The reverse is true for the *positive charge of the electrode* which then attracts *negative anions* from electrolyte towards the electrode surface.

The specific adsorption is also illustrated in Fig. 3.6a by adsorbed positive and negative ions on the negatively charged metallic surface. Neutral particles could also be adsorbed on the surface due to chemical bonds. Please note that specifically adsorbed (charged) ions may interfere with *chemical reactions* [e.g., redox reactions, see (3.12)] taking place on the electrode surface (within the *rigid layer*, see Footnote 24), catalyse chemical reactions on the surface, or even block the electrode surface for other ions from the electrolyte. In general, *molecules* from the solution can also be specifically adsorbed within the rigid layer, in addition to ions from above.

Please note that a part of the *solvation/hydration shell* (Kaniusas 2012, Footnote 21)—the part facing the electrode surface—of ions to be adsorbed on the surface should be stripped away before their direct contact-based adsorption. When adsorbed, the ion is only partly solvated, see Fig. 3.6a. Therefore, the *specific adsorption* is favoured by *small solvation/hydration energy* of ions (which should be provided and is consumed while removing the solvation shell). The solvation sheath tends to prevent contact adsorption while hindering bare ions to approach closer the electrode surface, even though the surface may carry the opposite charge to the ion's charge which would principally favour the electrostatic attraction (compare Footnote 7). In addition, *solvent molecules*—which usually cover the electrode surface (Fig. 3.6a)—should be displaced by adsorbed ions. Please note that

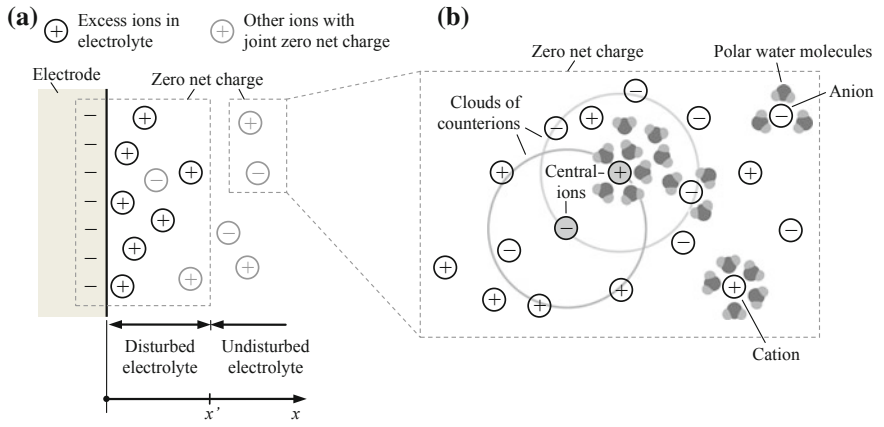

Fig. 3.9 Distribution of ions in the disturbed electrolyte close to the charged electrode surface (namely, in the rigid and diffuse layers of the double layer, see Fig. 3.6) in comparison with the distribution of ions in the undisturbed electrolyte (outside the double layer within the bulk). **a** The surface charge of the electrode is compensated by inversely charged excess ions in the disturbed electrolyte so that zero net charge results for the distance $x \geq x'$ from the electrode surface. Please note that the local electric potential φ—plotted as a function of x in Fig. 3.6c—equals to φ_E of the bulk/undisturbed electrolyte for $x \geq x'$ only. **b** Distribution of hydrated ions (Fig. 2.16a) in the undisturbed electrolyte with water as solvent. Each ion acts as a central ion of its own ionic cloud with dominating counterions within the cloud, which yields overlapping clouds. Cations and anions are balanced in their respective number and thus zero net charge results in the bulk/undisturbed electrolyte. The local φ and the net/excess electric charge as a function of the radial distance from any central ion are depicted in Fig. 3.10

- *cations* are usually more strongly solvated[12] with polar water molecules than
- *anions* (see Fig. 3.9b).

Hence cations are less likely to be specifically adsorbed given a negatively charged electrode surface than anions given a positively charged surface. Likewise, the weaker is the *solvation shell*, the less energy is consumed for its removal, and the stronger is usually the *specific adsorption*. It should be recalled that the ionic radius (of a bare ion) determines the thickness of the hydration shell so that a relatively small *ionic radius* yields a relatively large *effective radius* of the hydrated ion, see Fig. 2.16a and Footnote 22 in Chap. 2.

In addition to these

- *specifically adsorbed* ions (i.e., anions and cations, in general), other
- *non-specifically adsorbed counterions* (i.e., with ions charge in opposite to that of the surface charge)

reside within the *rigid layer* and are also *hydrated*, as illustrated in Fig. 3.6a. The *outer Helmholtz layer* crosses the charge centre of these *non-specifically adsorbed*

[12]Cations such as Na^+ or K^+ immobilise completely about 3 water molecules (Kaniusas 2012, Footnote 21), whereas only a single water molecule typically sticks on an anion.

ions. Please note that the non-specifically adsorbed ions are not subjected to any chemical interactions with the electrode material (in contrast to specifically adsorbed ions from above). In fact, these ions are simply attracted by the aforementioned *far-reaching electrostatic forces* generated by the complementary-charged electrode surface. In contrast to specifically adsorbed ions, these non-specifically adsorbed and completely solvated ions are thus spaced away from the electrode surface by solvent molecules, usually *water molecules*.

As illustrated in Fig. 3.9a, the *net charge* of the *outer Helmholtz layer* together with the *net/excess charge* of the adjacent *diffuse layer* compensate the *surface charge of the metal electrode*. This compensation can be compared with the *screening of the central ion by its counterions cloud* from the rest of solution in the *undisturbed electrolyte*, as shown in Fig. 3.9b and described in Footnote 17. In addition, Fig. 3.6c illustrates this phenomenon of the zero net charge outside the diffuse layer in that the *local electric potential* φ—as a function of the distance x from the electrode surface—converges towards the potential φ_E of the *bulk/undisturbed electrolyte* at $x = x'$ (φ_E is constant in the bulk/undisturbed electrolyte), i.e., at the end of the diffuse part of the double layer.

Water Relevance

Water molecules—as the typical *solvent*—fill gaps *between the electrode surface*, specifically adsorbed ions, and counterions in rigid and diffuse layers (Fig. 3.6a); the *charged electrode surface* is also hydrated with *polar water molecules* due to electrostatic interaction. It implies that *permanent dipoles* of water molecules *influence strongly* the *dielectric properties* of the *double layer*, in terms of their *orientation polarization* (Figs. 2.16b, c and 2.19c). That is, water molecules (their number and structure) determine the *effective permittivity of the double layer* which, in turn, determines the size of the capacitance C_{el} (3.6). Interestingly, the value of C_{el}, especially that of C_r, depends only weakly on the nature of ions as long as these ions are not specifically adsorbed (Schmickler 1993), which stresses the relevance of water in the double layer.

Interestingly, water molecules (as *electric dipoles*) are almost maximally reoriented (aligned or *polarized*) in the relatively *strong electric field*[13]—in line with Footnote 45 in Chap. 2—present *between the electrode surface and counterions* in the solution, especially counterions in the rigid layer. Primarily, *water molecules* on and in the vicinity of the *electrode surface* and those in the *hydration shells* of counterions experience this strong electric field and thus are subjected to a preferred strong reorientation. Consequently, with increasing local charge density

[13]The estimated *strength of the electric field* within the *double layer* is *quite high* and amounts to the order of 10^4 kV/cm (=2 V / 2 nm). Interestingly, such high fields are even able to weaken electrostatic binding forces in molecules so that, for instance, the degree of local dissociation can even increase within the double layer (Hamann and Vielstich 1998). Please note that this level is even two orders of magnitude higher than the relatively high inner electric field within the membrane of the cell (100 kV/cm), as discussed in Kaniusas (2012, Footnote 49).

(on the electrode surface and that of counterions) and thus with increasing local electric field acting on these water molecules (Kaniusas 2012, Footnote 21), an *incremental reorientation* of water molecules becomes progressively less with *increasing electric field* because the net reorientation of molecules is already highly dominant. In addition, *electrostriction*[14] of water molecules occurs. That is, the normal *structure of water is disrupted* in the *double layer* because of the *strong electric fields* the water molecules are exposed to and the electrostriction.

Hence, because of the *strong dielectric saturation* of water molecules (Footnote 45 in Chap. 2) with their *decreased ability to polarize* even more with increasing local electric field, the associated *relative permittivity of water molecules*—residing *close to the electrode surface* within the double layer—decreases. It decreases from about 74 (for normal *bulk water* structure *without any alignment* of water dipoles by (distant) charged surface or counterions, see Fig. 2.20) to only 30 (as average for the *rigid layer* with *partial alignment* only) or even down to 6–8 (for water molecules directly on the *electrode surface* being *completely aligned* by the surface) (Hamann and Vielstich 1998). The disrupted structure of water decreases its contribution to the *permittivity of the double layer* or, in analogy, decreases the effective value of C_{el}.

This reduced permittivity applies particularly to (*polar*) water molecules residing directly at the (*charged*) electrode surface, i.e., *water bound strongly to the surface* by *strong electrostatic forces* over the very short atomic distance (Fig. 3.6a). These water molecules are subjected to *very strong local electric fields*. The saturation in the polarization is strongest in the *first layer of water molecules* right at the electrode surface and then diminishes in the subsequent water layers towards the bulk of the electrolyte (Dörfler 1994).

In addition, the local reorientation of water molecules is strongly influenced by the local presence of *counterions* and their *strong electric fields*, whereas *hydration shells* of counterions are composed out of these water molecules (Fig. 2.16a). These fields in the vicinity of ions are in the order of 100 kV/cm; e.g., at a radial distance r of 0.5 nm from the centre of a monovalent ion with its elementary charge e, as can be easily estimated from $e/(4\pi\varepsilon_0 \cdot \varepsilon_r \cdot r^2)$ with $\varepsilon_r = 74$ of bulk water (Footnote 13). Here the field strength may be underestimated since water molecules in the shell are also subjected to dielectric saturation, with the resulting net ε_r of only 2–4 (Wright 2007). The smaller the ion and the larger its charge, the greater will be the saturation effect of this ion on water molecules located at small distances. In other words, *hydration shells* interact continuously with the charged electrode surface and, on the other hand, with the oppositely charged counterions within the *double layer*.

[14] *Electrostriction* refers to a relatively slight change of shape of (polar) dielectrics under the application of the *electric field*. Namely, the positive end of the polar structure (such as the hydrogen side of the *polar water molecule*, see Footnote 12) is displaced in the direction of the electric field while the negative end (such as the oxygen side of water molecule) is displaced in the opposite direction. An overall strain (or *elongation*) of the polar structure results along the direction of the applied electric field.

Hydrated ions close to the electrode surface (forming the *rigid layer*) can also displace *water molecules* adsorbed directly on the *electrode surface* and thus come closer to the surface. In fact, it depends whether *electrochemical interactions* between these hydrated ions and the surface are strong enough to favour this more close spatial binding between the ions and the surface. In terms of the equivalent circuit model, this close binding of ions to the surface tends to increase the *total capacitance* C_{el} because of the decreased distance d_r and thus increased C_r (3.7). To be more precise, the distance d_r decreases between the negatively charged electrode surface and positively charged counterions layer (within the *outer Helmholtz layer*) according to Fig. 3.6a, b.

Mass Transfer

In the *transitional space* between the double layer (*heterogeneous solution* close to the electrode surface) and the undisturbed electrolyte (*homogeneous solution* following the diffuse layer) a *mass transfer* can take place, as illustrated in Figs. 3.5a, b and 3.20a. In particular, different mechanisms contribute to this mass transfer:

- *Diffusion*[15] of substances due to their spatial concentration gradients; compare (Kaniusas 2012, Footnote 24). It is especially relevant for *neutral substances*

[15]Interestingly, *diffusion of a substance* composed out of different *dissolved ions*, e.g., its diffusion due to a spatial *concentration gradient* of this substance, generates different *electric diffusion potentials* and thus a non-zero *diffusion voltage* along the diffusion path. In fact, *anions and cations*—or, in general, any charged structures, such as shown in Fig. 3.8b—of the substance *diffuse along their concentration gradient*, i.e., from the *concentrated ionic solution towards the diluted ionic solution*, as described by Ficks first law (Kaniusas 2012, Footnote 24). Please note that no semi-permeable membrane is assumed here in-between both regions of the high and low concentrated solutions (in contrast to considerations in Footnote 1).

Since the *ionic mobilities* and *diffusion coefficients of anions and cations always differ*, it implies that anions or cations can rush ahead of cations or anions, respectively. The mobility is a function of the diffusion coefficient and the individual ion properties such as its effective size, as illustrated in (2.53) and Kaniusas (2012, Footnote 24). In analogy, anions and cations attain different drift velocities for a given electrical driving force or a given strength of the applied electric field (2.53).

That is, the diffusion starts with independent movements of cations and anions in their *neutral solution* along their *concentration gradient* or, to be precise, along the *gradient of the chemical potential energy* (see Footnote 3). Later, the spatial charge (i.e., negative and positive charges in diffusion along the concentration gradient) is not balanced anymore—in view of different mobilities of involved ions—and the *electric charge becomes separated along the diffusion direction*. A non-zero *diffusion voltage* arises with a *non-zero gradient of the electric potential* and the associated *non-zero electric field* (2.28).

For instance, if anions are more mobile than cations, the negative excess charge precedes in the direction of the diffusion while the positive excess charge lags behind. This charge separation implies a finite *diffusion voltage* across the imaginary *phase boundary* perpendicular to the direction of the (driving) *concentration gradient*. Obviously, the diffusion voltage is necessarily coupled with the inner electric field pointing normally to the latter phase boundary. This electric field then accelerates cations and their diffusion (originally, the relatively slow and lagging behind) and slows down anions (originally, the relatively fast and hurrying ahead). In the *steady state*, the

which can be reduced or oxidized at the electrode surface (3.12), i.e., relevant for *uncharged substances* which can not be transported by *migration* to electrodes.

- *Migration* of substances, i.e., movement of *charged substances* in response to the local electric field, compare with the force F_E in Kaniusas (2012, Fig. 2.6), Kaniusas (2012, Footnote 44), and Footnote 7.
- *Convection* of substances. These substances are dragged along with the mechanical stream that results in response to either active stirring (*forced convection*) or diffusion of another dissolved substance, as provoked by a spatial concentration gradient of this another substance (*natural convection*).

In particular, a *net mass transfer* takes place when *chemical reactions* on the electrode surface become *unbalanced* [e.g., metal deposition outweighs its dissolution (3.3) or oxidation dominates over reduction (3.12)] with the resulting *finite direct current* across the boundary metal/electrolyte; see unbalanced electrode/redox reactions in Fig. 3.13b, c.

Please note that in the case of the *metal ion electrode*, metal ions can leave the electrode surface out of the metal lattice into biological tissue and then may *contaminate tissue* if acting as *toxic ions*. This is in contrast to the *electrodes of the second type*, where metal ions—when left the electrode surface—precipitate mostly as a hardly soluble salt and thus do not enter or interfere with biological tissue, see the reference electrode in Section "Reference Ag/AgCl Electrode".

Electric Potential and Debye Length

Figure 3.6a illustrates that the *surface charge* is neutralised by opposite sign *counterions* in the electrolyte. Some counterions are located in a close distance of a few water molecules from the surface (composing the *rigid layer*) while others are located further away from the surface (within the *diffuse layer*). Spatial *concentration gradients* of anions and cations can be observed within the diffuse layer, whereas the local concentrations of anions and cations do not change anymore in the *undisturbed electrolyte* (at $i_{DC} = 0$ in Fig. 3.6). Please note the change in the sign and density of the local *net/excess charge* with increasing distance from the electrode surface (as discussed above).

Figure 3.6c illustrates the associated spatial course of the *electric potential* φ. The potential changes within a very short distance of a few nm so that an extremely *high electric field* results within the *double layer* (Footnote 13). In particular, the *electric potential* φ_M of the *surface charge* is dissipated from the metallic electrode surface to the counterions, whereas the dissipation is relatively

resulting *diffusion voltage* is just high enough to *equalise both drift velocities of cations and anions*; the resulting flows of cations and anions across the phase boundary (between high and low concentrated solutions) become identical. Typically, the diffusion potentials are in the range of 10 mV (Hamann and Vielstich 1998).

- steep and *linear* in the *rigid layer* (with more counterions per distance unit from the surface) and
- progresses more smoothly and *exponentially* in the *diffuse layer* (with diffuse and less dense distribution of ions per distance unit from the surface) according to

$$\varphi = (\varphi_D - \varphi_E) \cdot e^{-(x-d_r)/\delta} + \varphi_E \tag{3.9}$$

towards the *target potential* φ_E of the undisturbed electrolyte. Here φ_D is the potential right at the onset of the diffuse layer—at the *outer Helmholtz layer*—at the distance d_r (thickness of the rigid layer) from the electrode surface, see Fig. 3.6c.

Please note that the *potential* φ_E is constant within the *undisturbed electrolyte* in Fig. 3.6c because the currentless situation with $i_{DC} = 0$ within the electrolyte and homogeneous undisturbed electrolyte are assumed. In other words, a locally varying concentration of the solute in the electrolyte, for instance, would already yield varying φ_E in the electrolyte (Footnote 15). Figure 3.9b demonstrates *undisturbed electrolyte* with a specific order of cations and anions, which results out of an *energetically optimal distribution of counterions around a central ion*, as detailed in Footnote 40 in Chap. 2 and Footnote 17 in this section. Please note that such order yields a *zero net charge of the bulk electrolyte*, implying a constant φ_E throughout the electrolyte.

In (3.9), the *Debye*[16] *length*[17] δ is the space constant of the *exponential part of the potential* φ *change* towards the bulk/undisturbed solution—i.e., the distance at

[16]Peter Joseph William Debye (1884–1966) was a Dutch-American physical chemist with significant contributions to the understanding of strong ionic/electrolyte solutions as non-ideal solutions with limited activity coefficients (Footnote 7). His major investigations included also dipole moments in molecules and pioneer contributions in the mapping of molecular structures.

[17]The rationale of the *Debye length* results from the consideration of *charged ions in electrolyte* and their mutual *electrostatic interactions*. The Debye length is a measure how far the ion's net electrostatic effect persists. In line with Footnote 40 in Chap. 2, a *hydrated* ion (*central ion*) in electrolyte is primarily approached by *hydrated* ions of the opposite charge (*counterions*) because of attractive *electrostatic forces*. Consequently, a diffuse *cloud of ions*—including *all ions* residing in the electrolyte, not only counterions—is composed around the central ion, whereas *counterions* with their *net/excess charge* dominate *within the cloud*, as illustrated in Fig. 3.9b. In fact, *electrostatic and thermal forces* determine the formation of the cloud with *spherical symmetry* (Footnote 40 in Chap. 2). This cloud *screens* electrically the central ion with its non-zero charge from the bulk (see below). Please note that *charge neutrality* applies for the total/undisturbed electrolyte, as shown in Fig. 3.9; compare with charge neutrality in Kaniusas (2012, Table 2.1).

In comparison, an *isolated ion* with its electric charge Q without any other ions close to this ion (i.e., without any counterions in the vicinity)—but with *solvent molecules* around, typically water with its permittivity ε—yields the following electric potential φ as a function of the *radial distance* r from this (assumed as a point) charge

$$\varphi(r) = \frac{Q}{4\pi \cdot \varepsilon \cdot r},$$

as illustrated in Fig. 3.10a. For the associated electric field of the isolated ion, compare (2.28) and (Kaniusas 2012, Footnote 21). Provided that the isolated ion (bare unsolvated) has a finite ionic radius, the equation from above is valid only for r larger than this bare ion radius. Strictly speaking, the discrete molecular structure of water as solvent should be considered for small distances r close to the ion because the microscopic solvent structure would be modified by the intense field of the ion, yielding, for instance, a reduced macroscopic ε of water (as discussed in Section "Water Relevance").

In contrast to the isolated ion, the spatial potential φ for the *central ion* with its charge Q *enclosed by its cloud of ions* can be approximated as Hamann and Vielstich (1998)

$$\varphi(r) = \frac{Q}{4\pi \cdot \varepsilon \cdot r} \cdot \mathrm{e}^{-r/\delta},$$

with δ as the *Debye length* or *screening length* in line with (3.10). The resulting φ of the *central ion* is *exponentially screened* from the bulk with increasing r *by the excess charge of counterions* in the cloud; in addition to $1/r$ decrease given by a bare isolated ion. That is, φ of the uninsulated ion decreases faster with r than φ of the isolated ion. Figure 3.10 compares the decline of φ with r for the single isolated ion with φ for the central ion surrounded by counterions.

Please note that the latter approximation for the unisolated (central) ion is valid for strongly *diluted solutions* only, where the involved ionic radius (of a bare unsolvated ion) is smaller than δ. In addition, a relatively large thermal energy with the inequality $k \cdot T \gg |Q_\mathrm{C} \cdot \varphi|$ is assumed (with k as the Bolzmann constant ($k = 1.38 \cdot 10^{-23}$ J/K), T the absolute temperature, and Q_C the charge of a single counterion (or other ion) in the cloud exposed to φ field). This inequality indicates large interionic distances in the diluted solution, i.e., the local φ is already relatively weak at the distance r at the locations of counterions/ions within the cloud. Therefore, a large r implies a relatively small product $|Q_\mathrm{C} \cdot \varphi|$. On the other hand, the relatively small directional electrostatic energy is still sufficient to *establish a cloud with predominant counterions* around the central ion, despite the relatively strong but *unidirectional thermal energy*.

The length δ (3.10) is considered as the *radius of the ionic cloud*. To be precise, δ corresponds to the radial distance from the considered central (point) ion to the site $r = \delta$ within the ionic cloud, where the *highest density of counterions* resides. To illustrate this behaviour, Fig. 3.10b shows the accumulated *net/excess charge* Q_A within the sphere of the radius r and its decrease with r. The charge Q_A according to

$$Q_\mathrm{A}(r) = Q + \int_0^r \rho_\mathrm{Q}(r)\,\mathrm{d}V = Q \cdot \mathrm{e}^{-r/\delta} \cdot \left(1 + \frac{r}{\delta}\right)$$

is determined by Q (>0) of the central ion (at $r = 0$ with Q_A ($r = 0$) = Q), by Q_C (<0) of counterions (at $r > 0$), and remaining charges of other ions (at $r > 0$) within the *ionic cloud*. Here ρ_Q is the *charge spatial density* (Q/m^3) of the ionic cloud. The highest density of counterions is indicated by the *local maximum* of the depicted radial change $-\mathrm{d}Q_\mathrm{A}/\mathrm{d}r$ in Fig. 3.10b, right at $r = \delta$. Here $\mathrm{d}Q_\mathrm{A}/\mathrm{d}r$ can be interpreted as the maximum charge $\mathrm{d}Q_\mathrm{A}$ within the spherical shell with the radius δ and a small thickness $\mathrm{d}r$ (Hamann and Vielstich 1998). In fact, $\mathrm{d}Q_\mathrm{A}$ screens the central ion with its Q—i.e., $\mathrm{d}Q_\mathrm{A}$ and Q show opposite polarities—so that the accumulated Q_A decreases with increasing r because of the assumed positive Q and negative Q_C (Fig. 3.10b). In other words, the maximum contribution to Q_A by counterions is found at $r = \delta$.

Please note that ρ_Q, modelled as,

$$\rho_\mathrm{Q}(r) = -\frac{Q}{4\pi \cdot \delta^2} \cdot \frac{\mathrm{e}^{-r/\delta}}{r}$$

which φ has decreased by 1/e of ($\varphi_D - \varphi_E$) [compare Fig. 2.7 and (Kaniusas 2012, Fig. 2.8c)]—to give

$$\delta = \sqrt{\frac{\varepsilon \cdot k \cdot T}{e^2 \cdot \sum_i z_i \cdot \rho_i}}, \tag{3.10}$$

as illustrated in Fig. 3.6c. Here k is the Bolzmann constant, T the absolute temperature, e the elementary charge, z_i the valence of ith ion species in the electrolyte with the associated number density ρ_i (1/m^3) of this ion species.

In fact, all three the inner and outer Helmholtz layers as well as the Gouy-Chapman layer—with their non-zero inner net charges—influence the local spatial course of φ across the total double layer. Figure 3.9a illustrates these non-compensated *excess charges* in the *double layer*, which *screen* progressively the *surface charge* of the metal electrode *from the bulk*.

In particular, the *specific adsorption* influences significantly the local course of φ. Namely, adsorbed *anions* (only) would result in *local minima* within this course,

---

within the ionic cloud around the central ion *does not show any extreme values* with increasing r, has *inverse polarity* with respect to Q (in order to *screen the central ion* with its Q), and decreases in size with increasing r.

Likewise, the *screening length* δ shows how far the net *electrostatic effect of the central ion* in solution persists, i.e., a sphere with the radius δ is a volume, in which this electrostatic effect dominates. In line with Fig. 3.10b, the net/excess charge Q_A within the sphere of the radius $r = \delta$ amounts to about *74% of Q*, a still significant percentage; likewise, only 26% of Q are already screened by oppositely charged counterions.

Outside this sphere with $r > \delta$, the electrostatic effect of the central ion is already substantially screened from the bulk. As illustrated in Fig. 3.10b, the level of Q_A within the sphere of the radius $r = 5 \cdot \delta$ amounts to only about *4% of Q*, i.e., Q_A shows still the same polarity as Q of the central ion. At this radial distance, the central ion is almost completely screened by its diffuse cloud of counterions from the rest of solution. The spatial *excess charge* around the central ion—given by *predominant counterions* in addition to other ions within the cloud—*compensates* completely the *charge Q of the central ion*. Likewise, the net charge of the central ion and the net charge of all ions within the cloud of the central ion sum to zero outside this cloud.

Please note that this *mutual screening of ions* by neighbouring counterions, i.e., the *screening effect on the electric field from individual ions*—even in strongly diluted solutions with large distances between ions—implies the *reduced activity of ions* and thus their *reduced activity coefficient* (in line with Footnote 7). In other words, electrostatic interactions of the central ion with counterions in the cloud reduce the *electric stray fields of the central ion* (Kaniusas 2012, Footnote 13) and thus reduce the *potential energy* as well as the *activity* of the *central ion*.

For instance, the length δ amounts to $\delta \approx 1$ nm in *NaCl 0.1 mol/l solution* (this concentration is comparable to the *physiological NaCl concentration* of 0.15 mol/l with its $\delta \approx 0.8$ nm, see Footnote 27 in Chap. 2) or to $\delta \approx 0.3$ nm in stronger NaCl 1 mol/l solution (at 25 °C). The higher the *ionic concentration*—and, on the other hand, the higher the *ionic charge per ion* or the *valence*—the less δ is; as can also be derived from (3.10). This is because we have more counterions per radial distance unit with increasing concentration and thus a more compact screening of the central ion. In addition, the length δ increases with increasing *temperature* (3.10) because the heightened thermal motion yields a more smeared ionic cloud around the central ion (Footnote 40 in Chap. 2).

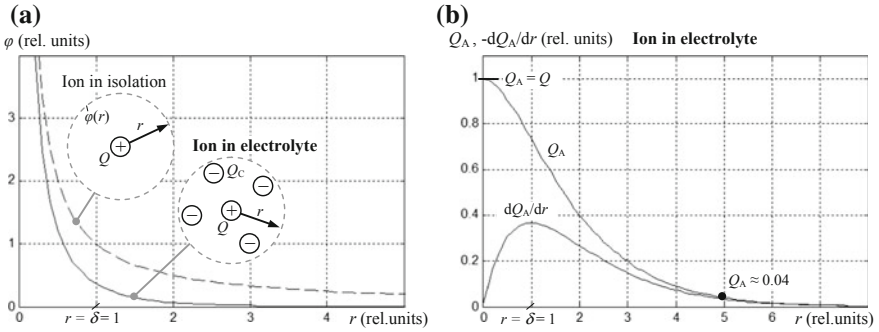

Fig. 3.10 Ionic clouds in electrolyte and their implications. **a** The electric potential φ as a function of the radial distance r from the (point) ionic charge Q (>0), in accordance with Footnote 17. An isolated single ion shows φ with $1/r$ dependence. In contrast to isolated ion, an uninsulated ion (central ion) in electrolyte is mainly enclosed by counterions, composing the spheric ionic cloud together with other ions from electrolyte (Fig. 3.9b). The total ionic cloud shows φ with even stronger $1/r \cdot e^{-r/\delta}$ dependence. Here the Debye length δ was assumed to be 1. **b** The accumulated net/excess electric charge Q_A within the sphere of the radius r—i.e., Q_A ($r = 0$) = Q (>0) of the central ion—and its radial change $-dQ_A/dr$ within the ionic cloud as a function of r (Footnote 17). The maximum of $-dQ_A/dr$ is located right at the distance $r = \delta$ which defines effectively the radius of the cloud (in diluted solutions only). Thus the maximum local charge or the maximum density of counterions in the cloud resides at $r = \delta$ within the spherical shell of the thickness dr

whereas adsorbed *cations* (only) would result in *local maxima*. Obviously, *non-specific adsorption* determines the composition of the electrolyte close to the electrode surface and thus determines also the spatial course of φ. Figure 3.6c depicts the case where a single anion and a single cation are adsorbed on the electrode surface, so that the net charge of these specifically adsorbed ions totals to zero and thus has no influence on the depicted local φ course (at the point C in Fig. 3.6c).

Half-Cell Voltage

Here we have analysed the so-called *half-cell concept*, in which a *single electrode* and its surrounding tissue/electrolyte are discussed, as illustrated in Fig. 3.4. However, any real application of electrodes—e.g., in terms of an electrolytic cell or a diagnostic measurement of electric biosignals with metallic electrodes on the skin—involves at least *two electrodes*, a *sensing electrode* and another *reference electrode*. Likewise, *two half-cells* (or simply a cell) are always involved in any practical set-up, as illustrated in Fig. 3.6 or Fig. 3.11c. In other words, it is not possible to measure experimentally U_{pol} (3.4) from a single half-cell using a single electrode only (Footnote 6).

Therefore, the so-called standard *half-cell voltage* U_h (also known as *standard reduction potential*) for any *sensing electrode* is introduced. The voltage U_h is the potential difference (or the *voltage drop*) between two electrodes without any active application of direct voltages or direct currents (i.e., *currentless situation* is assumed with $i_{DC} = 0$ in Fig. 3.6a) and equals

$$U_h = U_{pol} - U'_{pol} = U_{pol}, \tag{3.11}$$

where U_{pol} is the polarization voltage from the *sensing electrode* and U'_{pol} from a specific but arbitrary chosen *reference electrode*, usually from the *standard hydrogen electrode*.[18] In (3.11), both electrodes are subjected to *standard thermodynamic conditions* (Footnote 8). In fact, the reference U'_{pol} for the *standard hydrogen electrode* (Footnote 18) is arbitrarily assumed to be zero ($U'_{pol} = 0$) under the latter *standard conditions*, which then justifies the interpretation of the total voltage drop between the sensing and reference electrodes as U_h *of the sensing electrode* only [$U_h = U_{pol}$ in (3.11)]. Here it should be recalled that these *standard conditions* (especially, of the sensing electrode) imply the relevant equality $U_{pol} = U^0_{pol}$ in (3.4) (since $a_{Me+} = 1$ in the electrolyte under standard conditions, see Footnote 8).

Figure 3.6 illustrates this experimentally accessible difference $U_{pol} - U'_{pol}$. Consequently, any metal ion or redox electrode (e.g., Au/Au^+ or Fe/Fe^{2+} electrode) has its own unique U_h (e.g., $U_{h,Au} = +1.42$ V or $U_{h,Fe} = -0.41$ V, respectively (Hamann and Vielstich 1998)) under *standard conditions*; please note that U_h is in the voltage range and is therefore relatively high. Obviously, the *standard hydrogen electrode* itself has $U_h = 0$ by definition if used as the sensing electrode. Please note that *absolute values of* U_{pol} ($=U_h + U'_{pol}$) for specific sensing electrodes can also be

[18]The *standard hydrogen electrode* is a *redox electrode* which consists of a *Pt electrode* (as catalyser) dipped in *acid solution* and bubbled with pure H_2 *gas* at atmospheric pressure. In line with the principle redox reaction from (3.12), here the relevant *redox reaction* (Footnote 25) is

$$2 \cdot H^+ + 2 \cdot e^- \leftrightarrow H_2 \quad \text{or} \quad 2 \cdot H_3O^+ + 2 \cdot e^- \leftrightarrow H_2 + 2 \cdot H_2O;$$

see Footnote 24 in Chap. 2 for the genesis of H_3O^+ ions out of H^+ ions with water molecules H_2O as solvent. For the resulting ionic *acid solution*, the behaviour of *ideal solution* (Footnote 7) under *standard conditions* (Footnote 8) is assumed to apply, i.e., $a_{H_3O^+} = c_{H_3O^+} = 1$ mol/l. Interestingly, the *absolute* U'_{pol} of the standard hydrogen electrode is *negative* and is around −4.7 V up to −4.4 V (according to different sources). Therefore, the resulting inequality $U'_{pol} < 0$ applies which means that the electrolyte close to the Pt electrode surface has a positive potential with respect to the electrode itself. In fact, the consumption and formation of H_2 on the Pt surface can also appear in *basic or neutral solutions*; however, different redox reactions and thus different U_{pol} ($\neq U'_{pol}$) of these reactions apply here (Hamann and Vielstich 1998).

It is instructive to observe that if the *polarization voltage* $u'_{pol,i}$—as the applied voltage drop between the Pt electrode and the electrolyte, *outside the currentless situation* with $i_{DC} \neq 0$ (Fig. 3.13)—exceeds U'_{pol} ($<u'_{pol,i}$) then the *oxidation reaction* $H_2 + 2H_2O \rightarrow 2H_3O^+ + 2e^-$ dominates at the Pt surface (H_2 *is consumed*). In contrast, the *reduction reaction* $2H_3O^+ + 2e^- \rightarrow H_2 + 2H_2O$ dominates at the Pt surface for $u'_{pol,i} < U'_{pol}$ (H_2 *is formed*); compare Footnote 25.

Please note that the *standard hydrogen electrode* acts as a *non-polarizable electrode* with a relatively *high exchange current density* (see Fig. 3.14 and Footnote 22). Obviously, only a non-polarizable electrode can be used as a *reference electrode* with a relatively *constant* $u_{pol,i}$ (Footnote 30).

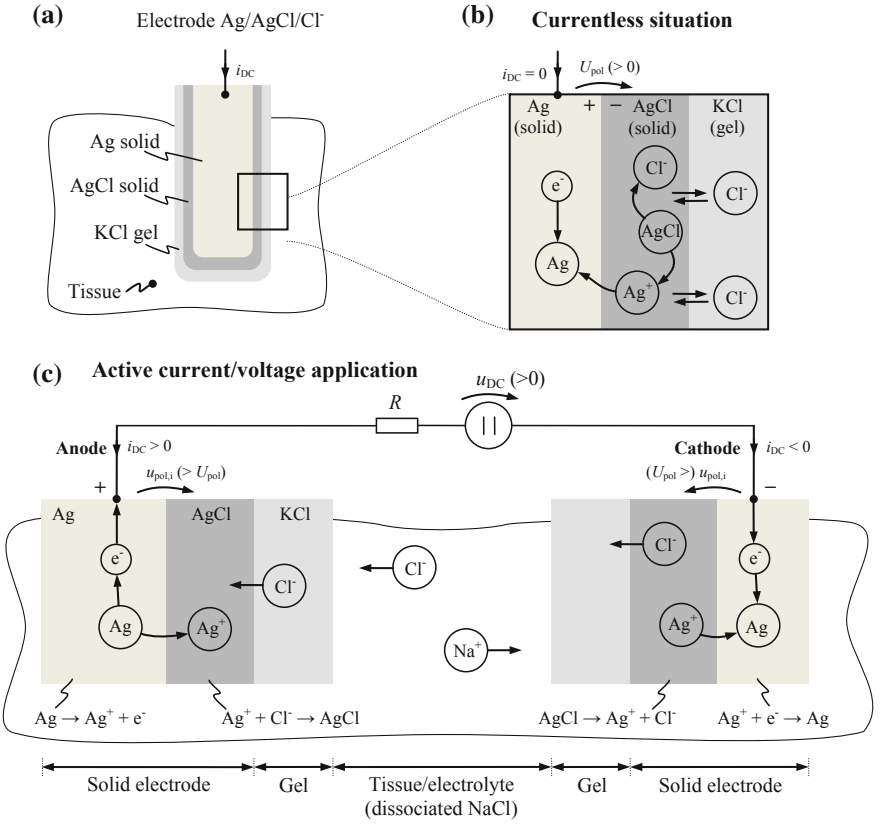

Fig. 3.11 The reference Ag/AgCl electrode. **a** Structural realization of the electrode covered with the conducting gel. **b** Basic chemical dissociation processes are depicted within the electrode in the currentless case (with the zero direct current $i_{DC} = 0$) and the resulting non-zero polarization voltage $U_{pol} > 0$. Chemical structures of primary importance are shown only. **c** The active application of the voltage u_{DC} and $i_{DC} \neq 0$ between two Ag/AgCl electrodes in contact with tissue/electrolyte which is approximated as the physiological aqueous NaCl solution (with its strong dissociation $NaCl \rightarrow Na^+ + Cl^-$, see Footnote 29 in Chap. 2). The associated chemical reactions are given for each electrode layer

estimated out of tabulated U_h [with (3.11)] if the absolute value of U'_{pol} of the standard hydrogen electrode is considered (as provided in Footnote 18).

A higher *level of* U_h *of electrode material* means that there is a greater tendency for *reduction of electrode ions* to occur; in analogy, the oxidation of this electrode material is hardly likely through electrolyte in contact with this material (e.g., Au electrode with deposited/reduced Au^+ ions, see Fig. 3.4b). In contrast, a lower level of U_h means there is a greater tendency for *oxidation of electrode ions* to occur (e.g., Fe electrode with dissolved/oxidized Fe^{2+} ions, see Fig. 3.4a). It follows that $U_{h,Au} > U_{h,Fe}$.

For instance, if Zn and Cu electrodes are used in a cell—i.e., Zn in one half-cell dipped into its ionic solution (such as $ZnSO_4 \leftrightarrow Zn^{2+} + SO_4^{2-}$) and Cu in another half-cell immersed within its ionic solution (such as $CuSO_4 \leftrightarrow Cu^{2+} + SO_4^{2-}$)—with the respective $U_{h,Zn} = -0.76$ V (for the reduction reaction $Zn^{2+} + 2e^- \rightarrow Zn$) and $U_{h,Cu} = +0.34$ V (for the reduction reaction $Cu^{2+} + 2e^- \rightarrow Cu$)—then the total dominating electrode reaction Zn (solid) + Cu^{2+} (solution) → Zn^{2+} (solution) + Cu (solid) applies, but not in the reverse direction. That is, Cu with $U_{h,Cu} > U_{h,Zn}$ becomes predominantly deposited/reduced within the total cell while Zn dissolves/oxidises.

Likewise, a *positive* $U_h > 0$ implies that the associated electrode substance is more easily reduced than is hydrogen (within the *standard hydrogen electrode*, operating as the *reference electrode*) while the associated electrode accepts electrons from the reference electrode (see the inflow of e^- in Fig. 3.4b). In contrast, a *negative* $U_h < 0$ implies that the associated substance is less easily reduced than is hydrogen while the associated electrode donates electrons to the reference electrode (see the outflow of e^- in Fig. 3.4a).

As a practical case, the *Pt electrode* as the *sensing electrode* and *Ag/AgCl electrode* as the *reference electrode* (Fig. 3.11) should be considered as *two half-cells in series*. The total *voltage drop in between both electrodes*—i.e., the voltage drop from Pt electrode to Ag/AgCl electrode—results then as the difference of the relevant U_h ($U_{h,Pt} = +1.12$ V for the reduction reaction $Pt^{2+} + e^- \rightarrow Pt$ and $U_{h,AgCl} = +0.22$ V for the reduction reaction $AgCl + e^- \rightarrow Ag + Cl^-$) in the *currentless case* and under *standard conditions of both electrodes*. Consequently, this voltage drop equals $U_{h,Pt} - U_{h,AgCl} = +1.12\ V - (+0.22\ V) = 0.9$ V and is thus positive. In analogy, *Fe electrode* (with its reaction $Fe^{2+} + 2e^- \leftrightarrow Fe$) and *Ag/AgCl electrode* yield the voltage drop—directed from Fe electrode to Ag/AgCl electrode—which is equal to $U_{h,Fe} - U_{h,AgCl} = -0.41\ V - (+0.22\ V) = -0.63$ V and is negative in sign. Likewise, *two identical Ag/AgCl electrodes* yield 0 V as the voltage drop in the currentless case. The aforementioned Zn and Cu electrodes—operating as a *galvanic cell* (Footnote 23)—yield −1.1 V (=−0.76 − 0.34) as the voltage drop from Zn to Cu electrode.

Redox Electrode and Its Double Layer

The *metal electrode* which is *inert and noble* with respect to the surrounding solution/electrolyte can also build another *electrochemical equilibrium* (i.e., a *dynamic equilibrium* as a *steady state*, see Footnote 4) with this electrolyte, in addition to that shown in Fig. 3.4a, b. Here a finite *polarization voltage* U_{pol} results between the electrode and electrolyte, in this case of the so-called *redox electrode*; see Figs. 3.4c, d and 3.5b. Here *chemical species* S in the electrolyte (or tissue acting as electrolyte) should be present, which can merge into one another through electron transfer in-between, i.e.,

- the *oxidized species* S_{oxi}, gaining z electrons, can be reduced to
- the *reduced species* S_{red}, and vice versa;

(z could also be defined as the valence of the electrode reaction). Likewise, S_{oxi} has given away its electrons while S_{red} has accepted electrons. This electrode reaction, i.e., the coupled *oxidation* and *reduction*, to give

$$S_{red} \leftrightarrow S_{oxi} + z \cdot e^{-}, \tag{3.12}$$

is known as the reciprocal *redox reaction*, see this reaction in Fig. 3.5b. Namely, the *oxidation* $S_{red} \rightarrow S_{oxi} + ze^{-}$ manifests as the shift of the equilibrium in (3.12) towards its left side, i.e., there are more species in oxidized form ready to accept electrons (and herewith become reduced in line with Fig. 3.4d). The reverse is true for the *reduction* $S_{oxi} + ze^{-} \rightarrow S_{red}$. A typical example of the redox reaction is $Fe^{2+} \leftrightarrow Fe^{3+} + e^{-}$ with Fe^{2+} as S_{red} and Fe^{3+} as S_{oxi}.

In fact, here the *redox electrode*[19] acts as a *catalyser* of the latter reaction *donating or accepting electrons* to or from S in the solution right at the *electrode surface*; consequently, the *electrode* becomes *charged or discharged* in the course of (3.12), as illustrated in Fig. 3.4c, d. This is in clear contrast to (3.3) of the metal ion electrode, where the electrode metal dissolves or deposits (Fig. 3.4a, b), i.e., the metal ion electrode does not act as catalyser here. In short,

- *metal ions* are exchanged between both phases, metal and electrolyte, of the *metal ion electrode*, whereas
- *electrons*, not ions, are exchanged between both phases of the *redox electrode*.

Please note that these electrons are never freely available in the electrolyte, electrons are either bound to S (3.12) or become solvated in the electrolyte (with a relatively short lifetime of the solvated state, e.g., in water <1 ms (Hamann and Vielstich 1998)).

To be precise, *strongly oxidized* S_{oxi} in the electrolyte would tend to gain or accept electrons from the metallic electrode, which, in turn, would imply lost electrons in the electrode and thus an accumulated *positive charge on the electrode surface*, as illustrated in Fig. 3.4d. Consequently, both the positive charge and the positive electric potential of the electrode would increase, given strongly oxidized S_{oxi}. This means also that the voltage U_{pol} (as defined in (3.13) and shown in Fig. 3.4d) increases with increasing *oxidative effects of the electrolyte* (the electrode is in contact with), i.e., U_{pol} increases with increasing desire of the electrolyte to accept electrons. The reverse is true for the *strongly reduced* S_{red} in the electrolyte,

[19]Here it should be recalled that the *electrode donating electrons* to S is called *cathode*, i.e., cathode reduces S (*reduction reaction*) while the (positive) *electric current* flows *out of the electrode*—in contact with S—into the wire connected to this electrode, see Fig. 3.11c. In contrast, the electrode *accepting electrons* from S is called *anode*, i.e., anode oxidizes S (*oxidation reaction*) while the (positive) *electric current* flows out of the wire *into this electrode* down to S, see Fig. 3.11c; compare Footnote 23.

which would tend to donate or give electrons to the metallic electrode and herewith become oxidized, as shown in Fig. 3.4c.

In analogy with Footnote 3, the *chemical potential energy* of *electrons* in the metal electrode and that in the electrolyte are different at the time instance of the electrode contact with (or immersion into) the electrolyte. A balancing *redox reaction*, according to (3.12), starts to equalise the latter chemical potentials towards a state of a *chemical equilibrium*. However, this chemical equilibrium can not be reached since, when electrons leave the electrode or accumulate on the electrode surface (3.12), the *electrode surface becomes electrically charged*. The involved species S from (3.12) close to the surface gain the net opposite charge (Fig. 3.5b).

Consequently, this *charge separation* due to electron transport yields the *electric field*, directed normal to the electrode surface, the resulting non-zero *polarization voltage* $U_{\mathrm{pol}} \neq 0$, and thus *non-zero electrostatic forces* on charged S (Fig. 3.4c, d). Please note that a charged electrode also tends to interact electrostatically with oppositely charged ions or dipoles residing close to the electrode surface. In particular, these forces oppose the further approach of S to be reduced or oxidized on the electrode surface (and attracts already reduced or oxidized S towards the electrode surface) and thus antagonise the further electron exchange in terms of (3.12). In other words, the induced *electrostatic forces* oppose the *chemical forces* of the redox reaction (i.e., oppose the predominantly oxidative or predominantly reductive forces). This opposition ends the effective *redox reaction* (3.12) in a way that further reduction and oxidation start to balance each other. Again, this balance between electrostatic forces and chemical forces is known as the *electrochemical equilibrium* with the associated build-up of a *double layer* at the *electrode surface* (Fig. 3.4c, d). This is in close analogy with the discussion of the *electrochemical equilibrium* of the *metal ion electrode* (Fig. 3.4a, b).

The relatively high *electric field* (Footnote 13) determines the *polarization voltage* U_{pol} which is governed by the *Nernst equation* in the *currentless situation* (with $i_{\mathrm{DC}} = 0$ in Fig. 3.4c, d), to give

$$U_{\mathrm{pol}} = \varphi_{\mathrm{M}} - \varphi_{\mathrm{E}} = U_{\mathrm{pol}}^{0} + \frac{R \cdot T}{z \cdot F} \cdot \ln \frac{a_{\mathrm{oxi}}}{a_{\mathrm{red}}}. \tag{3.13}$$

In analogy with (3.4), a_{oxi} and a_{red} are the *activities* of S_{oxi} and S_{red}, respectively, *close to the electrode surface* (or within the undisturbed electrolyte when there is no diffusion of S to and/or from the electrode surface). Please note that the activity is determined not only by the associated ionic concentration but also by the relevant activity coefficient, as discussed in Footnote 7. Please note that U_{pol} is the function of the ratio $a_{\mathrm{oxi}}/a_{\mathrm{red}}$ but not the absolute value of a_{oxi} or a_{red}. Likewise, U_{pol} increases with increasing concentration and/or increasing activity coefficient of oxidized (or oxidising) substances in the electrolyte, as discussed above.

It should be reiterated that a direct *experimental assessment* of U_{pol} from (3.13) is also not possible in isolation using typical measurements of the electric potential difference between two electrodes; as discussed in Footnote 6. Since both electrodes must be in contact with the biological tissue/electrolyte, two (but not one)

electrode/tissue boundaries are involved in the measurement. Therefore, U_{pol} and U'_{pol} of both electrodes determine the measured potential difference $U_{pol} - U'_{pol}$ in the *currentless situation*, as illustrated in Fig. 3.6 with the sensing and reference electrode.

Please note that *half-cell voltages* U_h (3.11) are also defined for *redox reactions* (3.12), which describe the reduction and oxidation strength of chemical species in the tissue/electrolyte surrounding the *redox electrode*. Therefore, the *absolute values of* U_{pol} [from (3.13)] can be *estimated* out of U_h with the absolute reference U'_{pol} from the standard hydrogen electrode (Footnote 18) when *standard thermodynamic conditions* apply (Footnote 8).

Reference Ag/AgCl Electrode

The *electrode polarization* of both aforementioned electrodes, namely, *metal ion electrode* and *redox electrode* (Fig. 3.4), depends strongly and directly on the composition of the *biological tissue/electrolyte* (i.e., tissue acting as electrolyte), the metal electrode is in contact with. Such electrodes are known as *electrodes of the first type*. Since the associated polarization voltage U_{pol} is then determined directly by the tissue/electrolyte composition, i.e., by the associated activities of metal ions (3.4) or activities of dissolved chemical species (3.13), such electrodes are clearly not suitable as *reference/indifferent electrodes* in biomedical sensing.

This is because *reference electrodes* require a relatively *small but constant and stable* U_{pol} regardless of the surrounding biological tissue/electrolyte. Interestingly, this independence of U_{pol} from the electrolyte in tissue can be attained by introducing *another phase boundary within the electrolyte* of the reference electrode, in addition to the inner boundary of the metal/electrolyte (Fig. 3.4). Such electrodes are known as *electrodes of the second type*.

An important reference electrode is given by *Ag/AgCl electrode*, as will be described here. As shown in Fig. 3.11a, Ag metal is covered with its *poorly soluble salt AgCl* (poorly soluble in aqueous solution) including the common cation Ag^+, with its relatively weak *dissociation/association reaction*

$$AgCl \leftrightarrow Ag^+ + Cl^-. \tag{3.14}$$

Likewise, the metal of the electrode of the second type exists in three different phases: solid metal (Ag), metal ions (Ag^+) in the dissolved salt, and as salt (AgCl) precipitated.

The covered electrode is bathed within a solution of a *readily soluble salt KCl* (readily soluble in aqueous solution)—Fig. 3.11a—of *defined concentration* with the same anion Cl^- as contained within AgCl; i.e., KCl is completely dissociated into K^+ and Cl^-. This is, by the way, why Ag/AgCl electrode is usually referred to as *Ag/AgCl/Cl*$^-$ *electrode*.

In line with (3.4), the cationic activity a_{Me+} of metal ions in the electrolyte right at the metal boundary determines U_{pol} in the *currentless situation* (with $i_{DC} = 0$ in Fig. 3.11b). In the present case of Ag/AgCl electrode, the equality $a_{Me+} = a_{Ag+}$ applies in (3.4) (with a_{Ag+} as the activity of Ag^+ ions within AgCl layer) because the *salt AgCl* acts as an *electrolytic saturated solution* to the Ag metal (Fig. 3.11b), to give

$$U_{pol} = U^0_{pol} + \frac{R \cdot T}{z \cdot F} \cdot \ln \frac{a_{Ag+}}{1\ \text{mol/l}} = U^{00}_{pol} - \frac{R \cdot T}{z \cdot F} \cdot \ln \frac{a_{Cl-}}{1\ \text{mol/l}}. \tag{3.15}$$

In particular, the voltage U^0_{pol}—in analogy with (3.4)—presents an offset for the phase boundary Ag/Ag^+. Likewise, Ag atoms in the metal surface are in the *electrochemical equilibrium* (i.e., a *dynamic equilibrium* as a *steady state*, see Footnote 4) with Ag^+ ions within AgCl layer, whereas this equilibrium of Ag^+ determines U_{pol}. Since Ag belongs to noble metals, *Ag^+ ions tend to deposit on Ag metal surface*, which means that the resulting *polarization voltage* U_{pol} of the reference Ag/AgCl electrode is positive ($U_{pol} > 0$) in the *currentless situation*; see Figs. 3.11b and 3.4b.

In the assumed *absence of Cl^- ions*, the activity a_{Ag+} in (3.15) (or the concentration of Ag^+ ions, see Footnote 7) would be subjected to *large variations* due to *ions adsorption at the electrode surface* (Fig. 3.11b). This would imply *unfavourable and undefined changes of* U_{pol} in the light of the aimed reference electrode (with U_{pol} as constant as possible). In addition, toxic Ag^+ ions would be able to leave the electrode and *contaminate biological tissue* in contact with the electrode that should obviously be avoided.

That is, the presence of both the *poorly soluble salt AgCl* and the *readily soluble KCl* gets rid of these disadvantages. That is, the aforementioned adsorbed Ag^+ ions at the Ag metal surface become instantly substituted (or compensated) in the electrolyte by other Ag^+ ions from the dissociated salt AgCl (3.14), as shown in Fig. 3.11b. On the other hand, *Ag^+ cations* can hardly leave—as an important advantage in terms of the mentioned *toxicity*—the vicinity of the electrode towards tissue because Ag^+ ions tend to *bound ionically* to *Cl^- anions* in the electrolyte and then precipitate as a *hardly soluble AgCl* on the electrode surface. In fact, this almost absent contamination of tissue is an advantage of *electrodes of the second type* over the metal ion electrodes (i.e., electrodes of the first type, see Fig. 3.4a, b).

The *question* left to answer is how to control the *amount of dissolved Ag^+ ions*—as elaborated below—since this *amount and its stability* over time defines the size of U_{pol} (3.15). An important note for this *question* is that—since the salt *AgCl is poorly soluble* and is present as a *solid body* within its *saturated solution*—the associated *product* $a_{Ag+} \cdot a_{Cl-}$ *is constant* over time when dissociation and

association arrived at their *equilibrium*[20] (Hamann and Vielstich 1998). The latter product is also known as *solubility product*. Thus an *inverse relationship* between the cationic activity a_{Ag+} and the anionic activity a_{Cl-} (of Cl^- ions) results within the dissociated salt AgCl, i.e., both activities or, alternatively, the associated concentrations of Ag^+ and Cl^- ions (Footnote 7) are *mutually coupled*. It means that the activity a_{Ag+} (or the amount of *dissolved* Ag^+ *ions*) can be *controlled and stabilized* with the activity a_{Cl-} (or with the amount of *dissolved* Cl^- *ions*); compare Footnote 21. For instance, when the concentration of Ag^+ ions becomes smaller as its *saturation concentration*—e.g., due to the aforementioned *deposition* of Ag^+ ions on the *metal surface* (Fig. 3.11b)—the *solubility of the salt AgCl into its ions increases* and the associated concentration of Cl^- ions within the AgCl layer increases (according to the constant product $a_{Ag+} \cdot a_{Cl-}$ but with the resulting inequality $a_{Cl-} > a_{Ag+}$, see Footnote 20).

Consequently, as shown in (3.15) (right side), the constant product $a_{Ag+} \cdot a_{Cl-}$ implies that the *polarization voltage* U_{pol} for the *reference Ag/AgCl electrode* becomes a function of the *anionic activity* a_{Cl-} of the AgCl layer only, i.e., this electrode acts practically as *chlorine-electrode*. For instance, increasing a_{Cl-} implies decreasing U_{pol}. The *offset* U_{pol}^{00} in (3.15) (right side) considers not only U_{pol}^{0} but also the size of the constant product $a_{Ag+} \cdot a_{Cl-}$.

In order to control a_{Cl-} [within the *poorly soluble salt AgCl* in line with (3.15)] and thus to stabilise the voltage U_{pol}, another *readily soluble salt KCl* with the *defined concentration of the anion* Cl^- is used (Fig. 3.11a). Here the activity a_{Cl-} is

[20]When the *reversible dissociation/association* reaction $AgCl \leftrightarrow Ag^+ + Cl^-$ (3.14) is given at its *dynamic equilibrium* (Footnote 4), the equality of

- $\alpha_d \cdot a_{AgCl}$ (i.e., the *rate of dissociation*) for the *dissociation reaction* ($AgCl \rightarrow Ag^+ + Cl^-$) and
- $\alpha_r \cdot a_{Ag+} \cdot a_{Cl-}$ (i.e., the *rate of association*) for the *association reaction* ($Ag^+ + Cl^- \rightarrow AgCl$)

applies, as can be derived from the *law of mass action*. At this equilibrium, both dissociation and association run with the same speed so there is no net change in the amount of solid AgCl and its ions Ag^+ and Cl^- within the solution.

Here α_d and α_r are the reaction speed constants for the dissociation and association reactions, respectively. Please note that the equality $a_{Ag+} = a_{Cl-}$ applies if the salt AgCl is only present in the considered solution (with the mole ratio of the dissociated Ag^+ and Cl^- equal to 1:1 which yields equal concentrations $c_{Ag+} = c_{Cl-}$) and this solution is highly diluted (i.e., the associated activity coefficients f of ions Ag^+ and Cl^- approach 1), so that $c_{Ag+} = c_{Cl-}$ requires $a_{Ag+} = f_{Ag+} \cdot c_{Ag+} = f_{Cl-} \cdot c_{Cl-} = a_{Cl-}$ (see Footnote 7).

The equality of $\alpha_d \cdot a_{AgCl}$ and $\alpha_r \cdot a_{Ag+} \cdot a_{Cl-}$ yields that the ratio $a_{Ag+} \cdot a_{Cl-} / a_{AgCl}$ or even the product $a_{Ag+} \cdot a_{Cl-}$ is constant and equals to the so-called *thermodynamic equilibrium constant*. In the latter ratio, the activity a_{AgCl} remains effectively constant because the salt *AgCl is poorly soluble* and is present as a *solid body*. In addition, the product $a_{Ag+} \cdot a_{Cl-}$ refers to ionic activities within the *saturated solution* which is in its *dynamic equilibrium* with the *solid body* of AgCl.

It is instructive to observe that if *high ionic activities* (e.g., of Ag^+ and Cl^- ions) are required for their precipitation to form a salt complex (e.g., AgCl) then *binding strength between these ions is low* and the associated *thermodynamic equilibrium constant is high*. The reverse is true for the low equilibrium constant.

kept *constant* through a *relatively high but defined concentration of Cl^- anions* within the completely dissociated KCl, which also implies a *relatively low but defined concentration of Ag^+ ions*[21] close to the electrode surface (since the product $a_{Ag+} \cdot a_{Cl-}$ is constant). Therefore the voltage U_{pol} *becomes constant and stable*, as required for *reference electrodes*. In practice, Cl^- anions within dissociated *KCl salt of defined concentration* are usually applied as an *electrode gel* (or paste) on the Ag/AgCl electrode, as illustrated in Fig. 3.11a, b.

The *absolute level of* U_{pol} (3.15) of Ag/AgCl electrode under *standard thermodynamic conditions* (i.e., $a_{Cl-} = 1$ mol/l according to Footnote 8) can be *estimated* out of the associated half-cell voltage $U_{h,AgCl} = +0.22$ V based on (3.11) with the absolute reference $U'_{pol} = 0$ from the standard hydrogen electrode (Footnote 18). Likewise, for the *physiological concentration* of Cl^- ions of 0.15 mol/l at 25 °C (Footnote 27 in Chap. 2) and with the relevant activity coefficient of 0.78 (Footnote 7), (3.15) yields a higher $U_{pol} = +0.22\ V - (-0.055\ V) = +0.275$ V than $U_{pol} = +0.22$ V under standard conditions.

Active Current or Voltage Application Between Electrodes

Figure 3.12a illustrates the *sensing and reference electrodes* in contact with tissue/electrolyte, with the associated simple circuit model for the *direct voltage/current application* shown in Fig. 3.12b. The *direct voltage* u_{DC} *across both electrodes*—as could be recalled from Footnote 6—fulfils $u_{DC} = U_{pol} - U'_{pol}$ only if *currentless situation* prevails with the *direct current* $i_{DC} = 0$. Here both electrodes are in their *electrochemical equilibrium* (Fig. 3.6). That is, there is no active application of u_{DC} (to be precise, different from $U_{pol} - U'_{pol}$) between electrodes so that a finite i_{DC} can not start to flow from one electrode to another. This currentless situation implies also *zero voltage drop* u_b [$=i_{DC} \cdot R_b = 0$, see (3.1)] *within tissue* with its ohmic resistance R_b or within the *undisturbed electrolyte* between electrodes (Fig. 3.12a, b). Here U_{pol} is the *polarization voltage* from the *sensing electrode*—estimated for $i_{DC} = 0$ only with (3.4) for metal ion electrode or with (3.13) for redox electrode—whereas U'_{pol} is that from the *reference electrode*.

However, when u_{DC} different from $U_{pol} - U'_{pol}$ is applied (i.e., u_{DC} is forced away from its value $U_{pol} - U'_{pol}$ at *open circuit*, see Fig. 3.13a) which actively changes electric potentials of both electrodes or, in analogy, when a non-zero $i_{DC} \neq 0$ is forced to cross the electrode/electrolyte boundary then a *new*

[21] Please note that the *solubility* of the poorly soluble *ionic compound AgCl* into its Ag^+ and Cl^- ions [in line with (3.14)] should be considered under the presence of *common ions*, such as Cl^- ions from the readily soluble salt KCl. In fact, the *solubility of AgCl decreases* when the total *number of Cl^- ions increases*. The associated *equilibrium* in (3.14) shifts then towards the right side while the *dissociation speed (or solubility) of AgCl decreases*. Consequently, if there is a relatively high concentration of Cl^- ions (primarily from KCl, in addition to a few Cl^- ions from the poorly dissolved AgCl), only a few Ag^+ ions become dissociated from AgCl. A relatively low concentration of Ag^+ ions results with an obvious *advantage for toxicity* (see text).

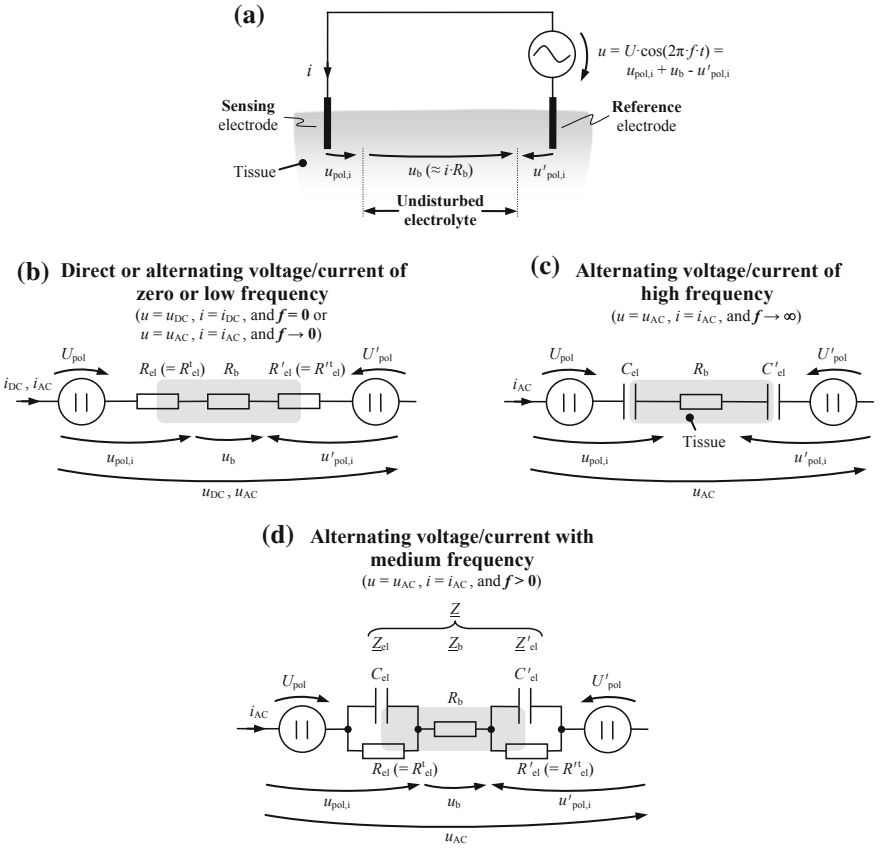

Fig. 3.12 Models of the sensing and reference electrodes (in contact with tissue/electrolyte) and their associated electrode/tissue boundaries; compare Fig. 3.17. Here a charge-transfer-limited electrode reaction is assumed, with the simplified electrode model from Fig. 3.20c. **a** The experimental set-up with an actively applied voltage u between both electrodes and the resulting current i. **b** Simplified electrical equivalent circuit model for the direct voltage application with $u = u_{DC}$ or the alternating voltage application with $u = u_{AC}$ at relatively low frequencies f (fulfilling $|1/j\omega C_{el}| \gg R_{el}$). Here R_{el} ($=R^t_{el}$) is the non-linear ohmic electrode resistance and R_b the ohmic bodily tissue resistance, whereas U_{pol} is the polarization voltage of the boundary at $i = 0$ (at its electrochemical equilibrium) and $u_{pol,i}$ is the resulting polarization voltage of the boundary at $i \neq 0$ (the latter equilibrium is lost). **c** Circuit model for u_{AC} application at high f ($|1/j\omega C_{el}| \ll R_{el}$) with C_{el} as the electrode capacitance. **d** Circuit model for u_{AC} application at medium f ($|1/j\omega C_{el}| \approx R_{el}$), see (3.26)

polarization voltage $u_{pol,i}$ results *across this boundary*. This voltage $u_{pol,i}$ is a *function of* i_{DC} *and* u_{DC}. The latter *electrochemical equilibrium* loses its balance and the discussed electrical double layer (Fig. 3.6) becomes disturbed. In analogy to the definition of U_{pol} (3.4), the current-dependent voltage $u_{pol,i}$ is the *voltage drop between the electrode and undisturbed electrolyte*. That is, an *extra*

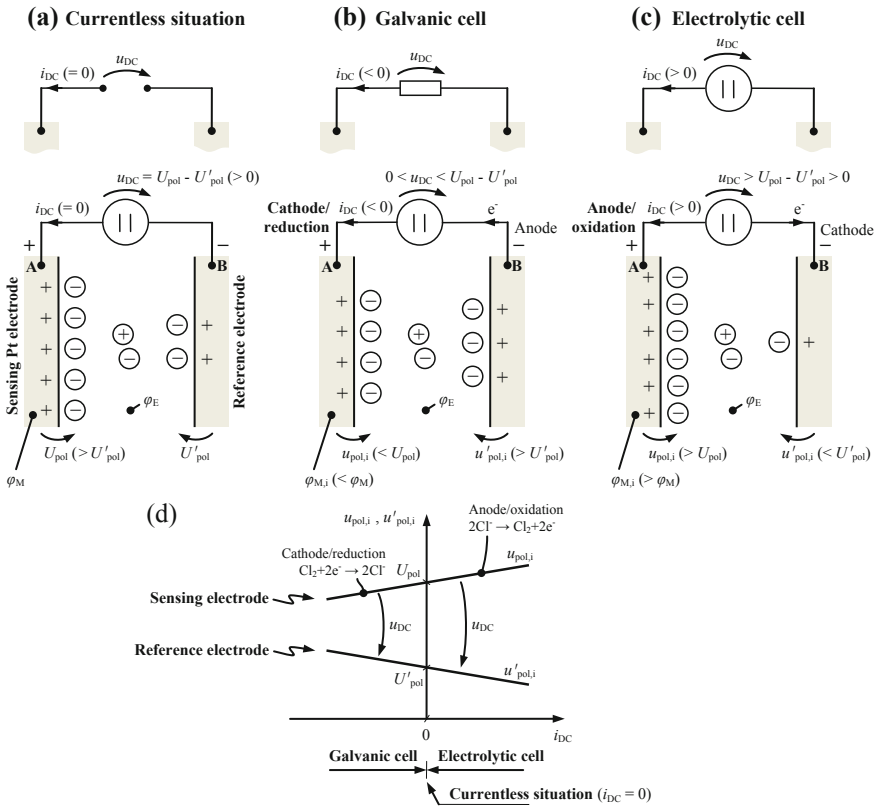

Fig. 3.13 Activation overvoltage $u^{t}_{pol,i} = u_{pol,i} - U_{pol}$ as the change of the polarization voltage from U_{pol} (relevant for the currentless case, Fig. 3.6) into another $u_{pol,i}$ (relevant for a finite direct current $i_{DC} \neq 0$ across the boundary metal/electrolyte). The direct voltage u_{DC} is applied between the sensing and reference electrodes, i.e., $u_{DC} = u_{pol,i} - u'_{pol,i}$, whereas the voltage drop in the highly conducting electrolyte between electrodes [proportional to i_{DC}, see (3.1)] is assumed to be zero. **a** Currentless case with $i_{DC} = 0$. **b** Galvanic cell with $i_{DC} < 0$ and $u_{DC} < U_{pol} - U'_{pol}$. **c** Electrolytic cell with $i_{DC} > 0$ and $u_{DC} > U_{pol} - U'_{pol}$. **d** The resulting $u_{pol,i}$ and $u'_{pol,i}$ as a function of i_{DC} and u_{DC} for small values of i_{DC}; compare Fig. 3.15b

overvoltage $(u_{pol,i} - U_{pol})$ must be applied across the boundary to initiate the *unbalanced electrode reaction* with $i_{DC} \neq 0$. Likewise, besides a finite voltage drop u_b $(=i_{DC} \cdot R_b \neq 0)$ across the undisturbed electrolyte between electrodes, this finite i_{DC} induces the extra overvoltage which acts as an *extra resistance* [in addition to R_b, see (3.31)] in the total *direct current circuit* (Fig. 3.12a).

The resulting difference $(u_{pol,i} - U_{pol})$, which is known as the *polarization overvoltage*, can be considered as a measure for the *unbalance in the electrode reaction* or even as a *measure for the inhibition of* i_{DC} given a certain applied overvoltage $(u_{pol,i} - U_{pol})$. Here numerous *electro-kinetic processes* of the *electrode/electrolyte boundary*—at least three as discussed below—are involved in

(or contribute to) this *kinetic inhibition* of a certain reaction step of the whole electrochemical process, as illustrated in Fig. 3.5. This inhibition, in fact, determines the aforementioned *extra resistance*, namely, the effective local *differential electrode resistance* R_{el} due to *all electro-kinetic processes* (Hamann and Vielstich 1998), to give

$$R_{el} = \frac{\Delta(u_{pol,i} - U_{pol})}{\Delta i_{DC}}. \tag{3.16}$$

Mainly *three electro-kinetic processes* are involved, as described below.

- *Speed of the charge transfer* (electron transfer) across the boundary electrode/electrolyte (within the *Helmholtz rigid layer*) is *finite* and so the reaction speed is finite. The charge transfer is the determining step of the electrode reaction speed, which leads to a *kinetic inhibition* of i_{DC}. Likewise, the so-called *activation overvoltage* $u^{t}_{pol,i} = u_{pol,i} - U_{pol}$ (known also as *charge transfer overvoltage* or *activation overpotential*) is needed to achieve a certain level of i_{DC}, with $u_{pol,i}$ as the polarization voltage due to the charge transfer only. As detailed in Footnote 22, this activation overvoltage depends on species involved in reactions, desolvation energies of reactive ions, used metals in electrodes, temperature, concentrations of reactants and reaction products on the electrode surface, and other factors. The associated *differential electrode resistance* R^{t}_{el} due to *constrained charge transfer*, which is known as *reaction resistance* or *charge-transfer resistance*, to give

$$R^{t}_{el} = \frac{\Delta(u_{pol,i} - U_{pol})}{\Delta i_{DC}} = \frac{\Delta u^{t}_{pol,i}}{\Delta i_{DC}} \tag{3.17}$$

  is very high for *constrained chemical reactions*, as applicable in *polarizable electrodes*. On the other hand, this resistance R^{t}_{el} is very low for *unconstrained chemical reactions*, as applicable in *non-polarizable electrodes* (see Fig. 3.14 and Footnote 22).
- *Diffusion-based transport* of substances (reactants and reaction products) from/to the undisturbed electrolyte to/from the site of the redox reaction (the electrode surface) is relatively *inert in its speed* and is the determining step of the electrode reaction speed, which thus inhibits i_{DC} as well. That is, *reactants* impoverish while reaction products enrich at the *electrode surface* over time, which necessarily triggers mass diffusion to equalise both surface and bulk concentrations. Provided that the diffusion is slow, depleted reactants at the surface necessarily *slow down the downstream charge transfer* process, i.e., reduce i_{DC} (due to the unbalanced electrode/redox reaction) for a given value of $(u_{pol,i} - U_{pol})$ (i.e., reduce i_{DC} from Footnote 22). Likewise, in order to keep i_{DC} constant or not to reduce i_{DC} due to the inert diffusion, a higher overvoltage $(u_{pol,i} - U_{pol})$ is necessary. This needed *surplus overvoltage* $u^{d}_{pol,i} = u_{pol,i} - U_{pol}$ is called *diffusion overvoltage*, known also as *diffusion*

overpotential. The associated *differential electrode resistance* R_{el}^{d} due to *inert diffusion*, which is known as *diffusion resistance*, is given by

$$R_{el}^{d} = \frac{\Delta(u_{pol,i} - U_{pol})}{\Delta i_{DC}} = \frac{\Delta u_{pol,i}^{d}}{\Delta i_{DC}}. \tag{3.18}$$

Typically, this diffusional transport is much more inert than the aforementioned charge transfer across the boundary. Therefore, *slow transport processes*—such as passive diffusion essential to maintain electrode reaction at a certain rate—usually determine the *total reaction kinetics* and thus determine the final size of the resulting i_{DC} across the boundary. In general, *mass transfer* of substances—due to not only *diffusion*, but also *migration* and *convection*—is here the rate determining step (see below).

- *Speed of coupled chemical reactions* at the electrode surface is finite. Such coupled reactions are upstream and downstream of the actual electrode/redox reaction (i.e., precede and follow the actual charge transfer) and, for instance, comprise reactions as *adsorption*, *deadsorption*, and/or even *dissociation*. Coupled reactions are steps determining the electrode reaction speed and also leading to a *kinetic inhibition* of i_{DC}. If the actual electrode/redox reaction and the diffusion are relatively fast, then the relatively slow coupled reactions may also determine the *total reaction kinetics*. A *surplus overvoltage* $u_{pol,i}^{c} = u_{pol,i} - U_{pol}$ to keep i_{DC} constant—because of the relatively slow coupled reactions—is called *reaction overvoltage*, known also as *reaction overpotential*. The associated *differential electrode resistance* R_{el}^{c} due to *inert coupled reactions* is given by

$$R_{el}^{c} = \frac{\Delta(u_{pol,i} - U_{pol})}{\Delta i_{DC}} = \frac{\Delta u_{pol,i}^{c}}{\Delta i_{DC}}. \tag{3.19}$$

For instance, when the supply of ions to the electrode reaction site (e.g., via a *constant current source*) does not meet the demand created by the actual potential drop $u_{pol,i}$ across the boundary, the total resistance $R_{el}^{t} + R_{el}^{d} + R_{el}^{c}$ increases, and the *boundary* is then said to be *polarized* at that electrode (Fig. 3.19b). In short, this total resistance arises from limitations on availability and mobility of ions whose motion between the electrolyte and electrode constitutes the *conductive current* across the boundary (see the conductive current $i_{AC,E}$ in Fig. 3.19c).

In fact, an *interplay* among the charge transfer (or the electrode reaction) at the electrode surface, the diffusion with its inert delivery of reactants and its inert removal of reaction products, as well as coupled reactions compose electro-kinetic processes within the electrode/electrolyte boundary and thus determine the actual $u_{pol,i}$. It should be noted that the aforementioned *electro-kinetic processes are mutually interrelated* so that, strictly speaking, the respective activation, diffusion, and reaction *overvoltages* $u_{pol,i}^{t}$, $u_{pol,i}^{d}$, and $u_{pol,i}^{c}$—as well as the associated *differential resistances* R_{el}^{t}, R_{el}^{d}, and R_{el}^{c}—can not be simply summed up to get the total overvoltage or total differential resistance (Hamann and Vielstich 1998). However,

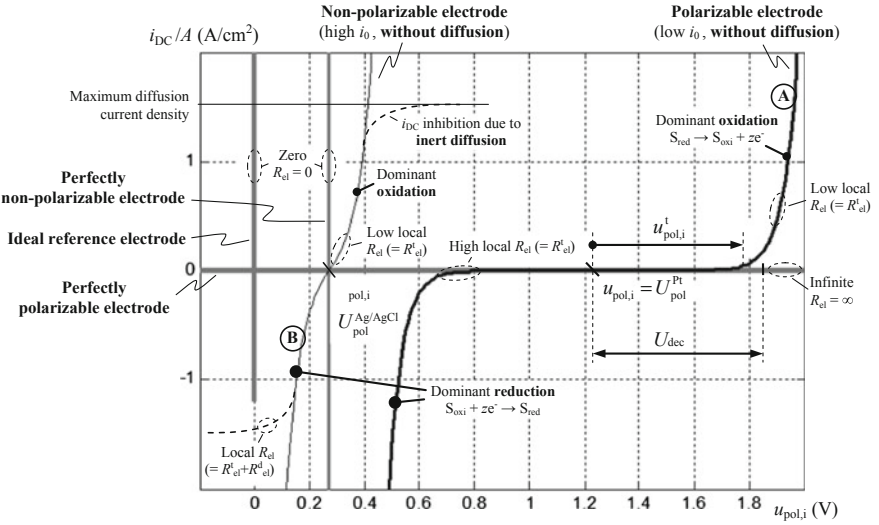

Fig. 3.14 The dependence of the direct current i_{DC} across the boundary electrode/electrolyte upon the polarization voltage $u_{pol,i}$ of this electrode (Fig. 3.13) in accordance with the activation overvoltage $u^t_{pol,i} = u_{pol,i} - U_{pol}$; see Butler-Volmer equation in Footnote 22. The depicted polarizable electrode approximates Pt electrode with the oxygen reduction/formation reaction $O_2 + 4 \cdot H^+ + 4 \cdot e^- \leftrightarrow 2 \cdot H_2O$ on its surface (compare Fig. 3.15c), with the associated $U^{Pt}_{pol} = 1.23\,V$ of this reaction and the associated relatively low exchange current density $i_0/A = 1 \cdot 10^{-6}$ A/cm^2 (Hamann and Vielstich 1998). In contrast, the shown non-polarizable electrode approximates the reference Ag/AgCl electrode, with the associated $U^{Ag/AgCl}_{pol} = 0.27\,V$ and the relatively high $i_0 = 0.1$ A/cm^2. The impact of the inert diffusion is indicated, which determines the total reaction kinetics and thus the level of i_{DC} for the relatively high amplitude of the polarization overvoltage $|u_{pol,i} - U_{pol}|$. The qualitative size of the differential electrode resistance R_{el} (3.16) is indicated

as an *approximation*, these overvoltages and these resistances are usually summed up [Fig. 3.19b and (3.31)]. For instance, the reaction and diffusion resistances R^t_{el} and R^d_{el} are summed up in Fig. 3.14.

Consequently, the contact *direct voltage* u_{DC} between the *sensing and reference electrodes* in contact with tissue/electrolyte (Fig. 3.12a) can be approximated as

$$\begin{aligned} u_{DC} &= u_{pol,i} + U_b - u'_{pol,i} \\ &= \left(U_{pol} + \sum_{k=1}^{3} (u^k_{pol,i} - U_{pol}) \right) + U_b - \left(U'_{pol} + \sum_{k=1}^{3} (u'^k_{pol,i} - U'_{pol}) \right); \end{aligned} \tag{3.20}$$

compare (3.31). Here sum symbols refer to the *sum of three polarization overvoltages* (from $k = 1$ to 3) of the respective *electro-kinetic processes* considered within each electrode/tissue boundary of electrodes. Equation (3.20) considers processes such as

- *the charge transfer* with the *activation overvoltage* $u^{t}_{pol,i} = u^{1}_{pol,i} - U_{pol}$,
- *the diffusion* with the *diffusion overvoltage* $u^{d}_{pol,i} = u^{2}_{pol,i} - U_{pol}$, and
- *coupled reactions* with the *reaction overvoltage* $u^{c}_{pol,i} = u^{3}_{pol,i} - U_{pol}$.

Figure 3.19c illustrates some of the latter overvoltages based on an *electrical equivalent circuit model*.

It is instructive to amend here that the *ohmic voltage drop* $u_b = U_b$ in the undisturbed *tissue/electrolyte* between electrodes equals to the product $i_{DC} \cdot R_b$ (see (3.1) and Fig. 3.12b) and is known as *resistance overvoltage* or *resistance overpotential*. Likewise, the *overvoltage amplitude* U_b as well as the finite R_b have their origins in the finite electrical *conductivity of the tissue/electrolyte* and, on the other hand, in limited (not infinite) geometrical dimensions of the *interphase area*, in line with (2.36). The size of this area determines not only R_b but also the resulting *current density* at the electrode/electrolyte boundary (2.23). In contrast to U_b, please note that U_{pol} or the *half-cell voltage* (3.11) *does not depend* on this *interphase area* since the *currentless state* is assumed in the definition of U_{pol} [(3.4) and (3.13)].

Charge Transfer and Activation Overvoltage

The *electro-kinetic process*[22] leading to *activation overvoltage* is shown in Fig. 3.13. Here *Pt metal electrode* is used as the *sensing electrode* (marked as A)

---

[22] In fact, the *activation energy of redox reaction* [oxidation and reduction, see (3.12)] on the *electrode surface* is a linear function of the *electric potential of the electrode* so that both the resulting *reaction speed* as well as the resulting i_{DC} across the boundary depend exponentially on this potential (according to *Arrhenius equation*).

To be more precise, the level of i_{DC} across a *single electrode/electrolyte boundary* (or across a *single double layer*) can be modelled as a function of the associated *activation overvoltage* $u^{t}_{pol,i} = u_{pol,i} - U_{pol}$ according to

$$i_{DC} = i_0 \cdot \left(e^{\frac{\alpha \cdot z F}{RT} \cdot (u_{pol,i} - U_{pol})} - e^{-\frac{(1-\alpha) \cdot z F}{RT} \cdot (u_{pol,i} - U_{pol})} \right)$$

only if the *charge-transfer kinetics* determine the polarization of the boundary. It is known as *Butler-Volmer equation*. Here $(u_{pol,i} - U_{pol})$ is the *activation overvoltage*, i_0/A the *exchange current density* (with A as the electrode area), α the charge transfer coefficient (usually around 0.5), z the number of electrons involved in the considered redox reaction (3.12) on the electrode surface, F the Faraday's constant, R the gas constant, and T the absolute temperature. In short, the rate of the electrode reaction is an exponential function of the voltage $(u_{pol,i} - U_{pol})$ between the electrode and electrolyte; likewise, when the electrode is at rest with $u_{pol,i} = U_{pol}$ there is no reaction and $i_{DC} = 0$.

The first term of this equation describes the *oxidation contribution* to the total i_{DC}, whereas the second term the *reduction contribution*. The oxidation contribution has a positive exponent for $(u_{pol,i} - U_{pol}) > 0$ (or for $\varphi_{M,i} > \varphi_M$, see Fig. 3.13c) and thus dominates the total i_{DC} for $(u_{pol,i} - U_{pol}) > 0$, with the relevant electrode acting as *anode*. In analogy, the reduction contribution dominates for $(u_{pol,i} - U_{pol}) < 0$ (or for $\varphi_{M,i} < \varphi_M$, see Fig. 3.13b), with the relevant electrode acting as *cathode*; see text. Figure 3.14 illustrates both exponential increases in the amplitude of i_{DC} for $u_{pol,i} > U_{pol}$ (dominant oxidation of the polarizable electrode) and for $u_{pol,i} < U_{pol}$ (dominant reduction).

Please note that Butler-Volmer equation in the above form *does not consider any diffusion processes or concentration gradients* within the electrode/electrolyte boundary, see Footnote 29.

dipped in *electrolyte containing Cl^- ions* within. The associated *redox reaction* on Pt electrode is $2 \cdot Cl^- \leftrightarrow Cl_2 + 2 \cdot e^-$ with the associated $U_{h,Cl} = +1.37$ V; compare (3.12). In the *currentless situation* with $i_{DC} = 0$—see Fig. 3.13a with the *applied direct voltage* $u_{DC} = U_{pol} - U'_{pol}$—the discussed *electrochemical equilibrium* is

In fact, this equation assumes *equal concentrations* c^s on the *electrode surface* and c^0 within the *bulk* of the substance S_{red} to be oxidized (3.12) at anode ($c^s_{red} = c^0_{red}$) and, on the other hand, of S_{oxi} to be reduced at cathode ($c^s_{oxi} = c^0_{oxi}$).

Please note that the total i_{DC} amounts to zero ($i_{DC} = 0$) for $u_{pol,i} = U_{pol}$ in the equation from above, i.e., the *redox reaction is balanced* here and stays in its *electrochemical equilibrium*, see Fig. 3.14. That is, the one component of i_{DC} due to oxidation reaction (anodic current) and the other one due to reduction reaction (cathodic current) are equal in size but have opposite directions, so both components (anodic and cathodic currents) cancel each other (as discussed above).

Please note that i_0/A is a characteristic measure for the *charge exchange* or ongoing *current* in each of the both directions of the redox reaction [i.e., oxidation and reduction, see (3.12)] at $u_{pol,i} = U_{pol}$, even though there is *no net current* ($i_{DC} = 0$). Likewise, i_0 is a measure for the kinetic reversibility or the *speed of the ongoing redox reaction*. The level of i_0 depends on the electrode (surface) composition, increases with T, and is proportional to *concentrations of involved species* in the redox reaction *on the electrode surface*.

The *local slope of* i_{DC} *increases* with increasing $u_{pol,i}$ (>U_{pol}, during *dominant oxidation*) and the *local slope of* i_{DC} *increases* with decreasing $u_{pol,i}$ (<U_{pol}, *dominant reduction*) are strong functions of i_0 (and of α, for details see Hamann and Vielstich (1998)), since i_0 acts as a multiplicative factor in the above equation. In fact, the higher i_0, the larger are both slopes, as illustrated in Fig. 3.14. Consequently, as described in Section "Electrode Impedance Model" in more detail,

- *high* i_0 indicates *small activation barriers* of electrode reactions that require small *activation overvoltages* $u^t_{pol,i} = u_{pol,i} - U_{pol}$ to produce large i_{DC}. Such electrodes act as so-called *non-polarizable electrodes* (Fig. 3.14). Interestingly, for relatively *small* $|u_{pol,i} - U_{pol}|$ (namely, $|u_{pol,i} - U_{pol}| \ll RT/nF \approx 25$ mV at 25 °C and $z = 1$), the exponential dependence from the above equation mutates into a linear dependence (according to the truncated series expansion $e^x = 1 + x$). Then the course of i_{DC} over $(u_{pol,i} - U_{pol})$ becomes a *straight line* according to

$$i_{DC} = i_0 \cdot \frac{zF}{RT} \cdot (u_{pol,i} - U_{pol}) = \frac{u_{pol,i} - U_{pol}}{R^t_{el}} \quad \text{with} \quad R^t_{el} = \frac{RT}{zF \cdot i_0},$$

  with the line's slope being clearly dependant on i_0. Likewise, the *non-polarizable electrode* acts as a *linear ohmic resistor* with its (differential) *charge-transfer resistance* R^t_{el} (3.17) due to *only slightly constrained charge transfer* across the boundary. It should be recalled that diffusion processes are not considered within R^t_{el}, see the relevant diffusion resistance R^d_{el} *due to inert diffusion* only (3.18). By contrast,
- *low* i_0 indicates *large activation barriers* that require large $u^t_{pol,i} = u_{pol,i} - U_{pol}$ to produce large i_{DC}. Such electrodes act as so-called *polarizable electrodes* (Fig. 3.14). For a relatively large $|u_{pol,i} - U_{pol}|$, the respective counter-reaction in the above equation can be neglected, i.e., either the dominant oxidation (the first term in the equation from above) determines i_{DC} or the dominant reduction (the second term). The current i_{DC} then becomes an *exponential function* of $(u_{pol,i} - U_{pol})$, whereas the associated *differential* R^t_{el} (3.17) then is highly dependent on $u_{pol,i}$ (as shown in Fig. 3.14). That is, the *polarizable electrode* has a highly *non-linear ohmic* R^t_{el}, in contrast to the non-polarizable electrode.

It should be stressed that the equations from above do not consider i_{DC} limitation due to diverse transport phenomena such as the *diffusion-based transport* or *migration-based transport* (Fig. 3.5); see Footnote 29.

established, which determines U_{pol} (3.13). For instance, the standard hydrogen electrode as the *reference electrode* with its $U_{h,H} = 0$ and standard conditions (Footnote 8) on both electrodes yield $u_{DC} = U_{pol} - U'_{pol} = U_{h,Cl} - U_{h,H} = +1.37$ V. In this equilibrium, both directions of the *redox reaction*, i.e., *reduction and oxidation*, are *equally fast and balanced* in their *respective non-zero mass and current transfer* across the boundary. However, in total, there is *no net mass transfer* and *no net direct current* $i_{DC} = 0$ across the metal/electrolyte boundary (Footnote 22).

However, the applied $u_{DC} \neq U_{pol} - U'_{pol}$ (Fig. 3.13b, c) *disrupts* the latter *electrochemical equilibrium*. The applied u_{DC} changes *electric potentials* of the sensing and reference electrodes (both electrodes are recharged via an external low-ohmic u_{DC} source), whereas the potential inside the undisturbed electrolyte remains constant and independent on u_{DC} (see section polarization of the electrode/tissue boundary). Likewise, the potential φ_M at the electrode surface (in Figs. 3.6c or 3.13a) moves to another value $\varphi_{M,i}$ (Fig. 3.13b, c) while φ_E does not change. Consequently, the voltage drop across the boundary electrode/electrolyte changes from U_{pol} ($=\varphi_M - \varphi_E$) to this *new polarization voltage* $u_{pol,i}$ ($=\varphi_{M,i} - \varphi_E$). The energy of charged particles/ions right on the surface changes by $e \cdot (\varphi_{M,i} - \varphi_M)$ and so the *electrode/redox reaction*[23] at the sensing Pt electrode *becomes unbalanced* with the associated *non-zero net mass transfer* across the boundary.

[23]It is instructive to observe that

- *redox reactions* are *non-spontaneous* in the *electrolytic cell*, i.e., electrical energy or *electric current* must be submitted to the electrolyte for these reactions to occur (electrical energy is converted into chemical energy). In contrast,
- *redox reactions* are *spontaneous* in the *galvanic cell*, i.e., electrical energy or *electric current* is derived from these redox reactions in terms of a battery (chemical energy is converted into electrical energy).

Provided that the *redox reaction is reversible* (3.12), the *applied voltage* u_{DC} across the electrodes determines the dominant direction of this redox reaction—i.e., either predominant oxidation or predominant reduction—and thus determines if the cell acts as an *electrolytic cell* or *galvanic cell*, as illustrated in Fig. 3.13. In fact, it depends whether the resulting voltage drop $u_{pol,i}$ (a part of u_{DC}) across the electrode/electrolyte boundary exceeds the polarization voltage U_{pol} (as applicable to the boundary of the sensing electrode in Fig. 3.13c, which shows *electrolytic cell*) or falls below U_{pol} (as in Fig. 3.13b, which shows *galvanic cell*). It should be recalled that U_{pol} (3.13) is applicable to the currentless situation only.

Please recall that the *net current flow* in the electrolytic or galvanic cell is always coupled with the *net transfer or conversion of chemical species* at the electrode surface. This conversion goes in accordance with *unbalanced electrode reactions* from (3.3) and (3.12).

As illustrated in Fig. 3.13b, c, the *plus pole* is the *anode* in the *electrolytic cell* (device that consumes electric power). In contrast, the *plus pole* is the *cathode* in the *galvanic cell* (device that provides power); see Footnote 19 for definitions of anode and cathode.

In fact, this unbalance yields a *finite* $i_{DC} \neq 0$ with the associated *net charge* starting to *permeate*[24] *the boundary*:

- In terms of a *galvanic cell* (*galvanic reaction*)—see Fig. 3.13b with the applied $u_{DC} < U_{pol} - U'_{pol}$—the *reduction reaction* $Cl_2 + 2 \cdot e^- \rightarrow 2 \cdot Cl^-$ is favoured (over the associated simultaneous oxidation) at the considered Pt electrode surface (acting as *cathode* with $u_{pol,i} < U_{pol}$) with the associated *non-zero net mass transfer* across the boundary and with the *finite* $i_{DC} \neq 0$ (we assume that there is sufficient Cl_2 gas at the surface for this galvanic cell to work). The *electric potential* $\varphi_{M,i}$ of the Pt electrode becomes more negative than φ_M due to e^- inflow (from $i_{DC} = 0$ in Fig. 3.13a to $i_{DC} \neq 0$ in Fig. 3.13b), so that the difference $\varphi_{M,i} - \varphi_E = u_{pol,i}$ decreases in comparison with U_{pol}. In contrast,
- in terms of an *electrolytic cell* (*electrolytic reaction*)—as depicted in Fig. 3.13c with the applied $u_{DC} > U_{pol} - U'_{pol}$—the *oxidation reaction* $2 \cdot Cl^- \rightarrow Cl_2 + 2 \cdot e^-$ is favoured (over reduction) at this Pt surface (acting as *anode* with $u_{pol,i} > U_{pol}$) with the associated *non-zero net mass transfer* across the boundary and with the *finite* $i_{DC} \neq 0$. Likewise, the potential $\varphi_{M,i}$ of the Pt electrode becomes more positive than φ_M (Fig. 3.13c) due to e^- outflow, so that the difference $\varphi_{M,i} - \varphi_E = u_{pol,i}$ increases with respect to U_{pol} (Fig. 3.13a, c).

Please note that the more positive is the *electrode potential* $\varphi_{M,i}$ (above φ_M, see Fig. 3.13c)—e.g., due to an externally charged sensing electrode via u_{DC}—the faster is the *oxidation* (and correspondingly the slower is the simultaneous reduction) at the *anode*, the faster is e^- transfer from the oxidized substance to the metal electrode, and the larger is the resulting i_{DC}, mainly due to the *oxidation process* (Fig. 3.13c); compare Footnote 22. Likewise, negative Cl^- ions are stronger attracted to the positively charged surface of the anode (Fig. 3.13c) and the faster is their oxidation ($2 \cdot Cl^- \rightarrow Cl_2 + 2 \cdot e^-$). The reverse is true for the *reduction* at the *cathode*, accelerated through a more negative $\varphi_{M,i}$ (below φ_M, see Fig. 3.13b) with the resulting i_{DC} being mainly due to the *reduction process*. Please note that an analogous behaviour of the *Ag/AgCl electrode* is illustrated in Fig. 3.11c, where $u_{pol,i} < U_{pol}$ is valid for the *reduction* process at the *cathode* and $u_{pol,i} > U_{pol}$ is valid for the *oxidation* at the *anode* (see below).

[24]Interestingly, *electrons* from/to the conduction band (Kaniusas 2015, Footnote 5 in Chap. 5) of metal *tunnel*

- to/from ions (or neutral particles) adsorbed right on the electrode surface (*specific adsorption*) or, on the other hand,
- to/from ions (or neutral particles) residing directly in front of the electrode surface within the *rigid layer* of the double layer (*non-specific adsorption*), see Fig. 3.6a.

Thus, quantum-mechanic *tunnelling processes* are responsible for *electrons transfer* across the *electrode/electrolyte interface*, over *atomic distances* from the *electrode surface* to the *inner Helmholtz layer* (within the *rigid layer*) or even from the *electrode surface* to the *outer Helmholtz layer* (within the *rigid layer*).

While U_{pol} and U'_{pol} apply across the boundaries metal/electrolyte for *balanced redox reactions*, for zero $i_{DC} = 0$, and for $u_{DC} = U_{pol} - U'_{pol}$ (Fig. 3.13a), *unbalanced redox reactions* on both electrodes with the changed electrode potentials ($u_{DC} \neq U_{pol} - U'_{pol}$) and finite $i_{DC} \neq 0$ necessarily yield other *polarization voltages* $u_{pol,i}$ and $u'_{pol,i}$. The boundary condition $u_{DC} = u_{pol,i} - u'_{pol,i}$ still applies under the assumption that the *voltage drop in electrolyte between electrodes is zero* even though $i_{DC} \neq 0$. However, this assumption is applicable only for electrolytes with high conductivities and thus with a *negligible ohmic voltage drop* in it (see below), as also assumed in Fig. 3.13b, c.

As detailed in Fig. 3.13b, c, these voltages $u_{pol,i}$ and $u'_{pol,i}$ depend on i_{DC} and its direction, in line with discussed redox reactions. Figure 3.13d illustrates $u_{pol,i}$ and $u'_{pol,i}$ as a function of i_{DC} and u_{DC}, as being applicable for relatively small i_{DC} (Hamann and Vielstich 1998). Likewise, an increasing current load (i.e., increasing i_{DC}) decreases u_{DC} (i.e., the *total voltage drop* across the sensing and reference electrodes) in the *galvanic cell* or increases u_{DC} in the *electrolytic cell*.

Figure 3.15 illustrates the change in u_{DC}—as the voltage drop between the *sensing Pt electrode* and the *reference Ag/AgCl electrode* in contact with tissue/electrolyte (Fig. 3.15a)—in relation to the associated current i_{DC} through both electrodes. Here the charge transfer and the *activation overvoltage* are considered only. In analogy with Fig. 3.13d, not only the case of

- the relatively *small* i_{DC} with a *proportional change* in $u_{pol,i}$ and $u'_{pol,i}$ over i_{DC} is shown in Fig. 3.15b but also the case of
- the relatively *large* i_{DC} with a highly *non-linear change* in $u_{pol,i}$ and $u'_{pol,i}$ over i_{DC} is depicted here in Fig. 3.15c.

Please note that the *voltage drop within tissue/electrolyte*—proportional to the product $R_b \cdot i_{DC}$ (3.1)—is *neglected* in Fig. 3.15 because the tissue conductivity is assumed to be quite high (i.e., $|R_b \cdot i_{DC}| \ll |u_{pol,i}|, |u'_{pol,i}|$).

In line with Section "Pt Electrodes", Fig. 3.15b, c reflects *O_2 cathodic reduction reaction* ($O_2 + 4H^+ + 4e^- \rightarrow 2H_2O$) and *$O_2$ anodic oxidation/formation reaction* ($2H_2O \rightarrow O_2 + 4H^+ + 4e^-$) on *Pt surface* of the sensing electrode (acting as catalyser), with quantitative data taken from Fig. 3.14. Likewise, *Ag reduction reaction* ($AgCl + e^- \rightarrow Ag + Cl^-$) and *Ag oxidation reaction* ($Ag + Cl^- \rightarrow AgCl + e^-$) of the *Ag/AgCl reference electrode*[25] apply for the denoted curve sections in Fig. 3.15b, c, with quantitative data also taken from Fig. 3.14.

It can be observed that u_{DC} *varies in proportion to* i_{DC} *only for small* i_{DC} (Fig. 3.15b), whereas this variation is highly *non-linear for large* i_{DC} (Fig. 3.15c) due to an *exponential* increase in $|i_{DC}|$ with rising *activation overvoltage* $|u^t_{pol,i}| = |u_{pol,i} - U_{pol}|$ (Footnote 22). Figure 3.15c delineates the size of the polarization/

[25] An instructive case would also result in Fig. 3.15b, c with the *standard hydrogen electrode* (Footnote 18) used as the *reference electrode*. Here *H_2 oxidation reaction* according to $H_2 + 2H_2O \rightarrow 2H_3O^+ + 2e^-$ would dominate at the *anodic branch* of the *polarization curve*, whereas *H_2 reduction/formation reaction* $2H_3O^+ + 2e^- \rightarrow H_2 + 2H_2O$ would dominate at the *cathodic branch*.

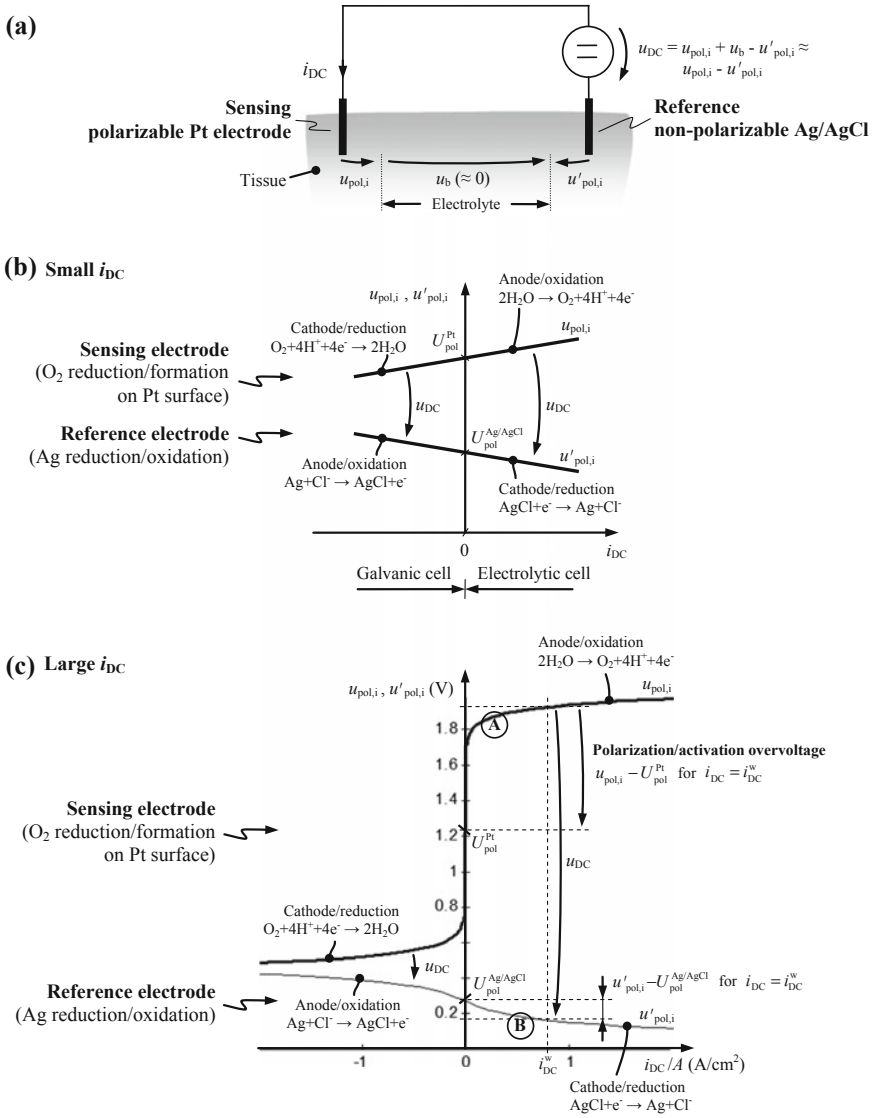
(a)
i_{DC}
$u_{DC} = u_{pol,i} + u_b - u'_{pol,i} \approx u_{pol,i} - u'_{pol,i}$
Sensing
polarizable Pt electrode
Reference
non-polarizable Ag/AgCl
Tissue
$u_{pol,i}$
u_b (≈ 0)
$u'_{pol,i}$
Electrolyte
(b) Small i_{DC}
$u_{pol,i}$, $u'_{pol,i}$
Anode/oxidation
$2H_2O \rightarrow O_2+4H^+ +4e^-$
Cathode/reduction
$O_2+4H^+ +4e^- \rightarrow 2H_2O$
U_{pol}^{Pt}
$u_{pol,i}$
Sensing electrode
(O_2 reduction/formation
on Pt surface)
u_{DC}
u_{DC}
Reference electrode
(Ag reduction/oxidation)
$U_{pol}^{Ag/AgCl}$
$u'_{pol,i}$
Anode/oxidation
$Ag+Cl^- \rightarrow AgCl+e^-$
Cathode/reduction
$AgCl+e^- \rightarrow Ag+Cl^-$
0
i_{DC}
Galvanic cell
Electrolytic cell
(c) Large i_{DC}
Anode/oxidation
$2H_2O \rightarrow O_2+4H^+ +4e^-$
$u_{pol,i}$, $u'_{pol,i}$ (V)
$u_{pol,i}$
1.8
A
Polarization/activation overvoltage
$u_{pol,i} - U_{pol}^{Pt}$ for $i_{DC} = i_{DC}^w$
1.6
1.4
Sensing electrode
(O_2 reduction/formation
on Pt surface)
1.2
U_{pol}^{Pt}
u_{DC}
1
0.8
Cathode/reduction
$O_2+4H^+ +4e^- \rightarrow 2H_2O$
u_{DC}
$U_{pol}^{Ag/AgCl}$
$u'_{pol,i} - U_{pol}^{Ag/AgCl}$ for $i_{DC} = i_{DC}^w$
Reference electrode
(Ag reduction/oxidation)
Anode/oxidation
$Ag+Cl^- \rightarrow AgCl+e^-$
0.2
B
$u'_{pol,i}$
-1
0
i_{DC}^w
1
i_{DC}/A (A/cm^2)
Cathode/reduction
$AgCl+e^- \rightarrow Ag+Cl^-$

◂**Fig. 3.15** The dependence of the direct voltage u_{DC} between the sensing and reference electrodes (in contact with tissue/electrolyte) upon the direct current i_{DC} across the associated electrode/electrolyte boundaries. The activation overvoltage is considered only (Footnote 22). **a** The experimental set-up with Pt electrode as the sensing electrode and Ag/AgCl electrode as the reference electrode. **b** The polarization voltages $u_{pol,i}$ and $u'_{pol,i}$ are qualitatively shown as a function of i_{DC} with the resulting u_{DC} ($=u_{pol,i} - u'_{pol,i}$) for small i_{DC}; in close analogy with Fig. 3.13d. Please note that the voltage drop in the highly conducting electrolyte between electrodes [proportional to i_{DC}, see (3.1)] is assumed to be zero. The associated redox reactions are specified. **c** For large i_{DC}, the quantitative courses of $u_{pol,i}$ and $u'_{pol,i}$ over i_{DC} become highly non-linear, as well as the resulting course of u_{DC} as a function of i_{DC}. Numerical data of both electrodes are taken from Fig. 3.14. The polarization/activation overvoltages ($u_{pol,i} - U_{pol}$) of both electrodes are indicated for the electrolytic mode; namely, for O_2 formation at the anode (plus electrode) and Ag reduction at the cathode (minus electrode). Symbols of encircled A and B indicate the associated curve sections from Fig. 3.14

activation overvoltage for the formation of O_2 (at the anode) and for the reduction of Ag (at the cathode) at the operating point with $i_{DC} = i^{w}_{DC}$. Please note that identical curve sections in both Figs. 3.14 and 3.15c are marked by encircled symbols A and B for instructive purposes; i.e., the *polarization curve* of Ag/AgCl electrode in Fig. 3.14 is inverted (around its center at U_{pol}) and then re-plotted in Fig. 3.15c.

It should be amended that not only *redox electrodes* (Fig. 3.4c, d) are subjected to the behaviour from Fig. 3.13 when a finite i_{DC} is applied but also *metal ion electrodes* (Fig. 3.4a, b). Here the *electrochemical equilibrium* implies *equal rates of metal dissolution (or metal oxidation)* and, on the other hand, *metal deposition (or metal reduction)*—according to (3.3) and Footnotes 4, 5—with the associated U_{pol} (3.4) for $i_{DC} = 0$ only. In contrast, a finite $i_{DC} \neq 0$ across the boundary metal/electrolyte yields a *net mass transfer* due to *dominant metal dissolution/oxidation* (at the *anode*) *or dominant metal deposition/reduction* (at the *cathode*), respectively. That is, a metal electrode becomes *dissolved* at *positive potentials* of this electrode, whereas metal *deposition* on the electrode surface requires *negative potentials*.

Diffusion and Diffusion Overvoltage

Interestingly, the model for the *activation overvoltage* ($u_{pol,i} - U_{pol}$) (Butler-Volmer equation in Footnote 22) is valid only for *equal concentrations* of reactants (involved species in the redox reaction) within the *undisturbed electrolyte* (bulk solution) and, on the other hand, reactants on the *electrode surface* (the reaction site). Please note that the exchange current (i_0 in Footnote 22) is proportional to the latter concentration within the bulk so that with increasing concentration level the size of i_{DC} raises for a given overvoltage ($u_{pol,i} - U_{pol}$). In fact, this simplified model *without diffusion* applies only when the diffusion-based transport is much faster than the charge transfer across the boundary. Likewise, the diffusion

here manages to equalize both concentrations (on the electrode surface and in the bulk) and thus does not limit the electrode reaction in its dynamic behaviour (or does not limit the speed of the charge transfer), as illustrated in Fig. 3.14.

However, these aforementioned concentrations c typically differ when the *electrode reaction is fast* and the simultaneous *diffusion is inert*. It occurs when the electrode reaction is sufficiently rapid to lower the *surface concentration* of reactants below that of *bulk solution*, whereas the diffusion from the bulk is unable to replenish reactive species at the electrode surface quickly enough and thus a gradient in c results. The rate of reaction and thus the resulting i_{DC} across the boundary is then dependent on the ability of reactants to reach the electrode surface[26] in time. Likewise, the *diffusion tends to decrease* i_{DC}—in line with a tangible example in Footnote 29 and with the *associated differential electrode resistance* R_{el}^{d} *due to inert diffusion* (3.18)—if the charge transfer across the boundary is faster than the diffusion process.

Here we have a *diffusion-limited electrode reaction*[27] on the electrode surface, whereas the *diffusion resistance* R_{el}^{d} dominates the *total electrode resistance* R_{el} [see Fig. 3.19b and (3.31) as well as (3.16)]. The diffusion-limited electrode reaction

[26]The relevance of *migration* should be highlighted in comparison with *diffusion*, as a contributing factor to the *mass transfer* of reactants and reaction products to and from the electrode surface, respectively. In fact, the *electrical current density* (2.54) and *diffusion current density* (Kaniusas 2012, Footnote 24) should be quantitatively compared.

As already discussed, charged substances such as ions experience attractive *forces*—in proportion to the local *electric field* and the *ionic charge*—towards an inversely charged electrode. Consequently, migration can contribute to the total mass transfer only if the local electric field or the *gradient of the electric potential* is quite high in electrolyte (2.28). However, most *electrolytes* have *high electrical conductivities*, whereas a high conductivity implies a negligible electric field within the associated electrolyte, in analogy with the discussion of Fig. 2.25. In fact, the resulting electric field depends on the applicable boundary conditions, compare (2.122), and the applicable dynamics of the ionic charge redistribution in electrolyte to zero the inner electric field (or to compensate the outer electric field), see Figs. 2.29c and 3.16a. Therefore,

- the *migration component, proportional to* $\mathrm{d}\varphi/\mathrm{d}x$, is usually much less in its amplitude than
- the *diffusion component, proportional to* $\mathrm{d}c/\mathrm{d}x$.

For the sake of simplicity, we assume here migration and diffusion in x direction only. In other words, migration can be expected to play a significant role in the mass transfer only if the effective conductivity of electrolyte is relatively small.

As a paradox as it sounds, charged ions can even move against the *electrical force* when a strong *diffusional force* opposes this weak electrical force (Hamann and Vielstich 1998). In general, ions always move along the *gradient of their electrochemical potential energy* which—in line with Footnote 3—considers both the gradient of their activity (or of their concentration) and the gradient of the electric potential.

[27]The *diffusion-limited electrode reaction* is characterized by a relatively *fast and unconstrained charge transfer* as related to an *inert diffusion process* (or a *slow mass transport* to/from the electrode surface); compare Footnote 28.

stands in clear contrast to a *charge-transfer-limited electrode reaction*,[28] in which the *charge-transfer resistance* R_{el}^{t} (3.17) dominates the total R_{el}.

- If we assume *dominant oxidation* only (at *anode*), i.e., dominant $(u_{pol,i} - U_{pol}) > 0$ applies from Footnote 22, it turns out that the *diffusion overvoltage*, i.e., the surplus $(u_{pol,i} - U_{pol})$ to compensate for the slow diffusion and to keep i_{DC} constant, is *positive* in its amplitude [i.e., $(u_{pol,i} - U_{pol}) > 0$] and is proportional to $\ln(c_{red}^{0}/c_{red}^{s})$ (Hamann and Vielstich 1998). Here c_{red}^{s} *is the concentration* of the substance S_{red} to be oxidized [in the oxidation reaction, see (3.12)] *on the electrode surface*, whereas c_{red}^{0} *is the concentration* of S_{red} within *undisturbed electrolyte* (bulk solution). Obviously, with progressing time, the ongoing *oxidation reaction* (consumption of S_{red}) and inert diffusion with delayed delivery of reactants yield $c_{red}^{0} > c_{red}^{s}$ and thus a positive function $\ln(c_{red}^{0}/c_{red}^{s})$ (>0). Likewise,
- if we assume *dominant reduction* only (at *cathode*) with $(u_{pol,i} - U_{pol}) < 0$, the *diffusion overvoltage* $(u_{pol,i} - U_{pol})$ turns to be *negative* (i.e., $(u_{pol,i} - U_{pol}) < 0$) and is proportional to $-\ln(c_{oxi}^{0}/c_{oxi}^{s})$ (Hamann and Vielstich 1998).

Please note that, strictly speaking, besides *diffusion overvoltage* there is also *concentration overvoltage*. In fact, the diffusion overvoltage assumes the relatively fast charge transfer (within the scope of the electrode reaction) in comparison with the relatively slow diffusion, whereas the *concentration overvoltage*[29] assumes different values of c_{red}^{0} and c_{red}^{s} (or c_{oxi}^{0} and c_{oxi}^{s}) only.

---

[28]The *charge-transfer-limited electrode reaction* is characterized by a *slow and constrained charge transfer* and a relatively *fast diffusion process* (or a *fast mass transport* to/from the electrode surface); compare Footnote 27.

[29]The *inert diffusion* as the process which limits or *decreases* i_{DC} (across the electrode surface) can be illustrated by an *advanced Butler-Volmer equation* (from Footnote 22) rewritten for *different concentrations* $c_{red}^{s} \neq c_{red}^{0}$ and $c_{oxi}^{s} \neq c_{oxi}^{0}$ (Hamann and Vielstich 1998), to give

$$i_{DC} = i_0 \cdot \left(\frac{c_{red}^{s}}{c_{red}^{0}} \cdot e^{\frac{\alpha \cdot zF}{RT} \cdot (u_{pol,i} - U_{pol})} - \frac{c_{oxi}^{s}}{c_{oxi}^{0}} \cdot e^{-\frac{(1-\alpha) \cdot zF}{RT} (u_{pol,i} - U_{pol})} \right).$$

For the relatively small $|u_{pol,i} - U_{pol}|$ ($\ll RT / zF$) and $\alpha = 0.5$ the latter equation yields an instructive relationship, to give

$$\begin{aligned} i_{DC} &= i_0 \cdot \left(\frac{zF}{RT} \cdot (u_{pol,i} - U_{pol}) + \frac{c_{red}^{s} - c_{red}^{0}}{c_{red}^{0}} - \frac{c_{oxi}^{s} - c_{oxi}^{0}}{c_{oxi}^{0}} \right) \\ &= \frac{u_{pol,i} - U_{pol}}{R_{el}^{t}} + i_0 \cdot \left(\frac{c_{red}^{s} - c_{red}^{0}}{c_{red}^{0}} - \frac{c_{oxi}^{s} - c_{oxi}^{0}}{c_{oxi}^{0}} \right). \end{aligned}$$

Please note that the assumed *concentration differences* $(c_{red}^{s} - c_{red}^{0})$ and $(c_{oxi}^{s} - c_{oxi}^{0})$ *determine the size of* i_{DC}—in addition to R_{el}^{t} due to charge transfer—in the above equation, which stresses the relevance of the diffusion for i_{DC}. Given a *diffusion-limited electrode reaction* (with a large R_{el}^{t} or small $|u_{pol,i} - U_{pol}|$, i.e., the associated charge transfer contributes little directly to the total i_{DC}), the differences $(c_{red}^{s} - c_{red}^{0})$ and $(c_{oxi}^{s} - c_{oxi}^{0})$ are clearly proportional to i_{DC}.

The spatial profile of the continuous concentration change, for instance, from c^{s}_{red} to c^{0}_{red} (>c^{s}_{red}, for oxidation reaction) extends from the electrode surface into the undisturbed solution over a distance of up to about 0.5 mm in the *resting solution* and down to 1 µm during *forced convection* (Hamann and Vielstich 1998). This region in the vicinity of the electrode surface where local c are different from their values c^0 in the bulk is known as *diffusion layer* (or *Nernst diffusion layer*) with its *effective thickness* δ_D (Figs. 3.5 and 3.20a). Please note that δ_D is usually defined as a *space constant*, in analogy with the definition of δ in Fig. 2.7, i.e., δ_D is the distance from the electrode surface to the point of intersection of the horizontal line corresponding to c^0 with the tangent to the curve of c at the surface. Please note that δ_D is typically much larger than the thickness of the *diffuse layer* d_d or the thickness of the *whole double layer* ($d_r + d_d$) (typically < 10 nm, see Fig. 3.6).

The difference between c^{s}_{red} and c^{0}_{red} rises with increasing i_{DC}. In fact, after the onset of i_{DC} with its constant amplitude (e.g., at $t = 0$), this difference-profile in

---

The *proportionality* between ($c - c^0$) and i_{DC} applies also *within the diffusion layer*, i.e., with c as the concentration of the electroactive substance within the diffusion layer (Fig. 3.5), besides the aforementioned proportionality between ($c^s - c^0$) and i_{DC} with c^s as the concentration on the electrode surface (reaction site).

To give a qualitative example, a positive difference ($u_{pol,i} - U_{pol}$) (>0) indicates *dominant oxidation* on the electrode surface (Fig. 3.14), in which S_{red} *is consumed* while S_{oxi} *is produced* (3.12). Consequently, the concentration c^{s}_{red} decreases below c^{0}_{red} ($c^{s}_{red} - c^{0}_{red} < 0$) while c^{s}_{oxi} increases above c^{0}_{oxi} ($c^{s}_{oxi} - c^{0}_{oxi} > 0$). Now, it can be derived from the above equation that the total *current* i_{DC} *decreases during oxidation* in comparison with the *diffusion-independent case* with $c^{s}_{red} = c^{0}_{red}$ and $c^{s}_{oxi} = c^{0}_{oxi}$. This diffusion-independent case considers only the charge transfer and does not consider the inert diffusion (i.e., neglects the *concentration overvoltage* or assumes a very fast diffusion), as elaborated in Footnote 22.

The above equation can also be rewritten as

$$\frac{u_{pol,i} - U_{pol}}{i_{DC}} = R^{t}_{el} + R^{d}_{el},$$

where the *constrained charge transfer and inert diffusion effects are additively separated* that contribute to the total i_{DC} in response to the *polarization overvoltage* ($u_{pol,i} - U_{pol}$); compare Fig. 3.19b. That is, the discussed *decrease* Δi_{DC} *in* i_{DC} *due to inert diffusion* only—given a certain constant overvoltage ($u_{pol,i} - U_{pol}$)—can also be expressed as a corresponding *increase in the (differential) diffusion resistance* R^{d}_{el} only (3.18), to give

$$R^{d}_{el} = \frac{\Delta(u_{pol,i} - U_{pol})}{\Delta i_{DC}} = \frac{RT}{zF \cdot i_{DC}} \cdot \left(\frac{c^{s}_{oxi} - c^{0}_{oxi}}{c^{0}_{oxi}} - \frac{c^{s}_{red} - c^{0}_{red}}{c^{0}_{red}} \right).$$

That is, the *dominant oxidation* from above yields negative ($c^{s}_{red} - c^{0}_{red}$) < 0 and positive ($c^{s}_{oxi} - c^{0}_{oxi}$) > 0, which means an *increased* R^{d}_{el} due to finite concentration differences. Likewise, this resistance fulfils $R^{d}_{el} = 0$ for $c^{s}_{red} = c^{0}_{red}$ and $c^{s}_{oxi} = c^{0}_{oxi}$; compare with the estimation of the charge-transfer resistance R^{t}_{el} (3.17) due to charge transfer only from Footnote 22.

concentration grows with progressing time ($t > 0$) from the electrode surface into the solution until the resulting δ_D ceases to increase. Then *steady-state conditions* are established, whereas this process can take up to 30–60 s in the *resting solution* and 0.1–1 s during *forced convection* (Hamann and Vielstich 1998).

The inert diffusion will limit the delivery speed of electroactive material to the electrode surface over time in order to fuel the electrode reaction and, on the other hand, will limit the removal speed of reaction products. In other words, the *diffusion* determines the *total reaction kinetics* for *high* i_{DC}. Then, for high i_{DC}, the rate of the electrode reaction and therefore the actual level of i_{DC}, become proportional to the *bulk concentration* of the electroactive material in electrolyte. To be precise, *Fick's first law*—as described in Kaniusas (2012, Footnote 24)—shows that the diffusion rate or *diffusion current density* is proportional to $D_F \cdot (c^0_{red} - c^s_{red})/\delta_D$ (with D_F as the *diffusion coefficient*). Consequently, the *maximum/limiting diffusion current density* is proportional to $D_F \cdot c^0_{red}/\delta_D$ with $c^s_{red} \to 0$ for maximum charge transfer across the boundary and thus *maximum consumption of reactants* on the electrode surface (i.e., species S_{red} are completely oxidized as soon as they arrive at the electrode/anode surface). Given these limitations, the maximum current i_{DC} can even become independent of the applied, relatively high, overvoltage $|u_{pol,i} - U_{pol}|$, as illustrated in Fig. 3.14 for the non-polarizable electrode with inert diffusion.

Mainly the *diffusion overvoltage* governs the *total overvoltage* in the case of *maximum/limiting diffusion current density* since the associated charge transfer is quite fast (or the associated R^t_{el} quite low) and is not the limiting factor of the total electrode kinetics; compare (3.20). On the contrary, when the mass transport is quite fast (e.g., due to *forced convection* or *stirring*) and the effective i_{DC} is much less than the maximum/limiting diffusion current then the *diffusion overvoltage* can be neglected with respect to the *activation overvoltage*. In this case, the *activation overvoltage*—according to Butler-Volmer equation from Footnote 22—governs the *total overvoltage*.

Coupled Reactions and Reaction Overvoltage

As summarized above, *coupled reactions*—such as *adsorption*, *deadsorption*, and/or *dissociation*—that precede and follow the charge transfer within the scope of the electrode/redox reaction tend to hinder the *total reaction kinetics* and thus tend to inhibit i_{DC}. In particular, this inhibition of i_{DC} is relevant when these coupled reactions are relatively slow in respect to the charge transfer and/or diffusion processes on the electrode surface.

For instance, *adsorption and deadsorption* of *hydrogen atoms* on the surface of the Pt electrode are highly relevant steps of the *redox reaction* of the *standard hydrogen electrode* (in line with Footnote 18). That is, such *coupled reactions* are typically linked with *catalysing effects* of metal surfaces with their special *surface structure*. To be precise, adsorption of a hydrogen atom on a conducting surface is due to *van der Waals bonds*. Such bonds are based on mutual interaction of

transient electric dipoles, i.e., interaction between this hydrogen atom and its *image charges* (induced charges of opposite signs, compare with the electrostatic induction in Fig. 2.25a) of both the *nucleus and electron shell* within the *conductor*.

The associated *reaction overvoltage* ($u_{pol,i} - U_{pol}$) which compensates for the above inhibition, can be quantitatively defined as the logarithmic change in the resulting *concentration of species* at the electrode surface—species involved directly in the charge transfer—in consequence of the *limited kinetics of coupled reactions* (Hamann and Vielstich 1998). Obviously, the reaction overvoltage is then a function of i_{DC}. This quantitative definition of the reaction overvoltage is similar to that of the *diffusion overvoltage* from above.

Dynamics of Electro-Kinetic Processes

All involved *electro-kinetic processes*—i.e., the *charge transfer*, *mass diffusion*, and *coupled reactions* (as described above)—are balanced and are within their individual *steady states* (Footnote 4) for only relatively *small currents* i_{DC} across the electrode/electrolyte boundary. That is, only *small local charge changes* per time unit (2.25) are assumed within the boundary.

Since all three *electro-kinetic processes are limited in their speed*, it is instructive to conclude that any *step-wise change* in either the applied i_{DC} or $u_{pol,i}$ ($\neq U_{pol}$) necessarily yields a delayed setting in the resulting $u_{pol,i}$ or i_{DC}, respectively. That is, this resulting $u_{pol,i}$ or i_{DC} is subjected to a *transient response*. In other words, *steady-state conditions* in

- the *voltage* $u_{pol,i}$ across,
- the *current* i_{DC} through the electrode/electrolyte boundary, and
- *concentrations* c^s of reactive ions/species on the electrode surface

are only reached after a certain *time delay*.

If the *applied* i_{DC} (via an external current source) *is relatively small* and the associated *charge transfer* across the electrode/electrolyte boundary is relatively *fast and unconstrained*, it follows from above that the resulting $u_{pol,i}$ between the electrode and electrolyte can become an instantaneous function of the resulting ionic/species concentrations c^s_{red} or c^s_{oxi} at the *electrode surface* in line with the *Nernst equation* from (3.4) and (3.13) (but not as a function of c^0_{red} or c^0_{oxi} from the bulk, see diffusion process from above). Conversely, if the *voltage* $u_{pol,i}$ *is applied* (via external voltage source), the resulting i_{DC} is relatively small, and the *charge transfer is unconstrained*, then the arising c^s_{red} or c^s_{oxi} at the electrode surface also follows the *Nernst equation* in their *steady state, without any time delay* as related to $u_{pol,i}$ changes.

In contrast to the *unconstrained charge transfer* across the boundary in its *steady state*, the *constrained charge transfer* implies a *strongly delayed setting* of reactive c^s_{red} or c^s_{oxi} at the electrode surface when i_{DC} or $u_{pol,i}$ is *abruptly applied* in a step-wise manner (Hamann and Vielstich 1998). Here the aforementioned *Nernst behaviour* is valid only for the relatively slow *temporal changes* of $u_{pol,i}$ (either applied externally or resulting from an external i_{DC} application).

Typically, the *charge transfer* is

- *unconstrained* for *slow changes* in $u_{\mathrm{pol,i}}$ and
- *constrained* for *fast changes* in $u_{\mathrm{pol,i}}$.

Since the Nernst behaviour is reached for *small* i_{DC} only, the *maximum* i_{DC} which can pass from the electrode into the electrolyte and thus through the double layer is determined by the *slowest link/instance* of all involved *electro-kinetic processes* along the current flow. As already discussed, the *charge transfer*—in terms of ongoing *electrochemical processes* on the electrode surface [(3.3) and (3.12)]—is usually much faster than the concurrent (diffusion-based) *mass transfer* (Fig. 3.5) so that this *mass transfer usually constitutes this slowest link*.

Figure 3.14 depicts i_{DC} as a function of $u_{\mathrm{pol,i}}$ when the *activation overvoltage* is considered due to the *finite reaction speed* on the electrode surface. Both *real polarizable electrode and real non-polarizable electrode* are depicted, as detailed in Footnote 22. For comparison, a *perfectly non-polarizable electrode* and an *ideal reference electrode* are shown in Fig. 3.14. Here the voltage drop $u_{\mathrm{pol,i}}$ across the boundary electrode/electrolyte is independent on the actual current i_{DC} crossing this boundary, with the associated *differential electrode resistance* $R_{\mathrm{el}} = 0$ (3.16).

In addition, the effect of the *diffusion-based transport* is schematically indicated in Fig. 3.14 for the *non-polarizable electrode*.

- For the relatively *low overvoltage* $|u_{\mathrm{pol,i}} - U_{\mathrm{pol}}|$, the *charge transfer* across the boundary (or the electrode reaction) is still relatively slow so that the needed *mass transfer* to/from the electrode surface (to fuel the reaction) is relatively small. The associated inert diffusion is still fast enough to assure $c^{0}_{\mathrm{red}} \approx c^{\mathrm{s}}_{\mathrm{red}}$. Therefore, the dependence between i_{DC} and $(u_{\mathrm{pol,i}} - U_{\mathrm{pol}})$ (3.16) is determined by *Buttler-Volmer equation* with $R_{\mathrm{el}} = R^{\mathrm{t}}_{\mathrm{el}}$ and $(u_{\mathrm{pol,i}} - U_{\mathrm{pol}})$ as the activation overvoltage only (Footnote 22). In contrast,
- for the relatively *high overvoltage* $|u_{\mathrm{pol,i}} - U_{\mathrm{pol}}|$, the *charge transfer* is already quite fast while the required *mass transfer* to fuel the reaction is also quite high. Now the inert *diffusion process* acts as the slowest link and thus determines the *total reaction kinetics*. Namely, the current i_{DC} becomes *limited by diffusion* with increasing $|u_{\mathrm{pol,i}} - U_{\mathrm{pol}}|$ and then saturates towards the *maximum/limiting diffusion current* (Fig. 3.14), as described above. Obviously,
- for the *medium overvoltage* $|u_{\mathrm{pol,i}} - U_{\mathrm{pol}}|$, both the limited speed of the charge transfer and the inert kinetics of the diffusion determine the relationship between i_{DC} and $(u_{\mathrm{pol,i}} - U_{\mathrm{pol}})$ with the effective electrode resistance $R_{\mathrm{el}} \approx R^{\mathrm{t}}_{\mathrm{el}} + R^{\mathrm{d}}_{\mathrm{el}}$ [(3.16) and Footnote 29].

Polarization of the Electrode/Tissue Boundary

In contrast to the discussed metallic electrode from Fig. 3.6 without any active application of direct voltages or direct currents, Fig. 3.16 illustrates a metallic

polarizable electrode with an externally applied electric potential. Here a *voltage u* from an external source *is applied* between the sensing and *reference*[30] electrodes in contact with *tissue/electrolyte*.

When *u* in Fig. 3.16a, b is *switched on* (at the time instance $t = 0$) to a *small and constant value*, both the sensing and reference electrodes attain their *non-zero electric potentials* and become *oppositely charged* by the applied *u* (like two charged capacitor plates from Fig. 2.8). Here a *transient current*[31] $i \neq 0$ results to charge both electrodes; however, this process of *charging is very quick* because the low-ohmic *u* source is directly connected to both electrodes in Fig. 3.16a.

Subsequently, the *(external) electric field* $\vec{E}_{\text{ext}}$—generated between both *charged electrodes*—forces electrically charged ions[32] in electrolyte (between both electrodes) to approach the oppositely charged electrode surfaces. This is indicated in the left subfigure in Fig. 3.16a with shown directions of ion's movements. For instance, if we consider *physiological solution* as electrolyte then Na^+ ions migrate to the minus pole (cathode) while Cl^- ions migrate to the plus pole (anode). These *ion species*, both relatively *inert in migration* [with different mobilities, see (2.53)],

---

[30]The *reference electrode* in Fig. 3.16 can be assumed to have a *negligible and constant* $u'_{\text{pol,i}} \approx U'_{\text{pol}} \approx 0$ and thus to behave as a *perfectly non-polarizable electrode* because of *unconstrained chemical reactions* (for both $i_{\text{DC}} = 0$ and $i_{\text{DC}} \neq 0$) on its surface. This is in full contrast to $u_{\text{pol,i}} \neq U_{\text{pol}}$ of the *polarizable sensing electrode*, see Fig. 3.14.

In addition, the assumed *large surface area* of the *reference electrode*—in relation to that of the sensing electrode—implies a small current density on the surface of the reference electrode and thus implies a *small ohmic voltage drop* across the electrolyte at this surface; compare the area-related discussion in Section "Electrode Impedance Model". If we additionally assume that the tissue/electrolyte in-between both sensing and reference electrodes has a high conductivity, then the external *u* drops mainly across the *electrode/tissue boundary* of the *polarizable sensing electrode* only. Then the equality $u \approx u_{\text{pol,i}} - u'_{\text{pol,i}} \approx u_{\text{pol,i}}$ applies [compare Fig. 3.13 and (3.22)]. In particular, this equality is even more valid after a relatively long time when a constant *u* is applied, namely, after a multiple of the *time constant* τ (e.g., after $3 \cdot \tau$ in Fig. 3.16b).

[31]A *transient current* $i \neq 0$ across the *electrode/tissue boundary* results in Fig. 3.16a, b during a sudden change of a voltage *u* across the *sensing and reference electrodes*—with the original (preceding) voltage between electrodes being different from the applied *u* (or being zero). That is, a finite time-limited *i* results in Fig. 3.16a, b during the recharge of both electrodes, to be precise, of metallic surfaces of both electrodes (as a *recharge of plate capacitor* in Fig. 2.8). This current *i* ceases after the recharge process has been completed and the generated *electric field* $\vec{E}_{\text{ext}}$ between electrodes does not change anymore.

During the *recharge*, this current *i*, the *transient conductive current along the wire* in Fig. 3.16a, equals the associated *current between both electrodes* throughout tissue. Because of the very quick recharge of both electrodes we can neglect the conductive current in tissue/electrolyte during the recharge since inert ion species in electrolyte can not be abruptly set in mechanical motion. Therefore, the latter *current between electrodes* in tissue/electrolyte is the *transient displacement current* which amplitude equals that of *i* along the wire. In line with (2.66), this displacement current is proportional to the *rate of change of* E_{ext}, in other words, as soon as E_{ext} levels off this *displacement current* disappears.

[32]Obviously, charged ions in the tissue/electrolyte are necessarily surrounded by polar and mobile structures (e.g., by *hydration shells* built out of *polar water molecules*, see Fig. 3.9b), so that the *surface charge* of the solid will attract *counterions individually surrounded* by these polar structures (Fig. 3.16a, c); compare Fig. 3.6a.

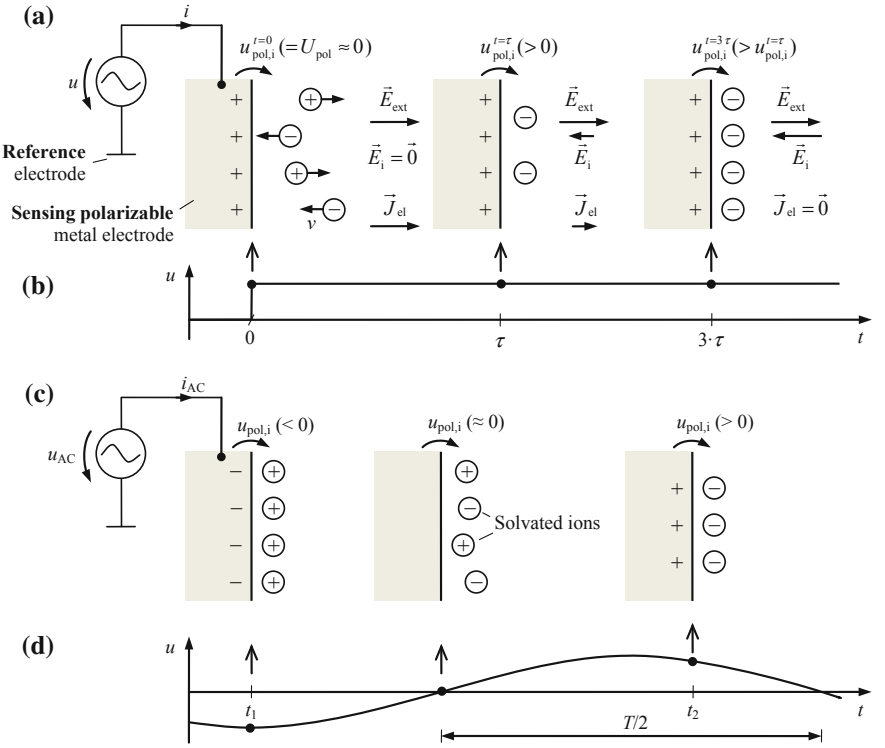

Fig. 3.16 Recharging of the polarizable electrode/tissue boundary in the course of the active application of the voltage u across this boundary and the adjacent tissue. The electrolytic double layer is formed, **a** the electrode surface charge and the opposite/balancing ionic counter-charge in the tissue/electrolyte close to the electrode surface are shown in synchrony with **b** the step-wise application of a constant u. For comparison, **c** the formation of the double layer is shown in response to **d** the varying instantaneous amplitude and polarity of the alternating u with its relatively long period T ($\gg\tau$). The resulting polarization voltage $u_{pol,i}$ is proportional to u with the approximation $u_{pol,i} \leq u$ (Footnote 30). Arrows indicate the associated time instances of u and subfigures of double layers

compose a *transient conductive current density* $\vec{J}_{el}$ *in electrolyte* [compare with discussions of (2.54)], as illustrated in Fig. 3.16a.

After the arrival at the *surface of the sensing electrode* (Fig. 3.16a), there is *no exchange of electrons between the arrived ions and the metal surface* [e.g., no redox/electrode reaction, (3.12)] as long as the *activation energy* of a relevant redox/electrode reaction on the electrode surface is not reached by the actual level of the external u. To be more precise, the associated $u \approx u_{pol,i}$ (Footnote 22) should not reach exceedingly high levels while the resulting *polarization overvoltage* $u_{pol,i}^{t} = u_{pol,i} - U_{pol}$ should stay below the *decomposition voltage* U_{dec} (Figs. 3.14 and 3.17b).

Instead, a *balancing ionic counter-charge accumulates* progressively near the *surface of the sensing electrode*, at the solid/liquid boundary. The *boundary*

behaves like a capacitor in which the stored electrical charge on both sides of the boundary is linearly dependent on the size of $u_{pol,i}$ (3.5). Solvated counter-charge ions are typically separated from the electrode surface by a *monolayer of solvent molecules*; compare Footnote 32 and Fig. 3.6a. The *true thickness* of the *counter-charge layer* outside the surface is described by the *Debye length* (in the typical range of 1 nm, see Footnote 17).

Because of *inert motions of ions* in electrolyte [due to *finite drift velocity*, see (2.53)], the counter-charge accumulates with a certain *time delay*, i.e., with the *relaxation time constant* τ. After this time, accumulated counter-charge has progressively balanced the oppositely charged surface of the metal electrode—see the right subfigure in Fig. 3.16a—and

- an *(inner) electric field* $\vec{E}_i$ has been progressively induced within electrolyte. This induced field has its origin in the accumulated ionic counter-charges, whereas the final $\vec{E}_i$ opposes and equals the applied $\vec{E}_{ext}$ (Fig. 3.16a). Then
- the *net electric field* $E_{ext} - E_i$ in electrolyte between both charged electrodes *becomes zero*,
- the associated *electrostatic driving force* acting on ions and their flow in electrolyte *ceases*, and thus
- the *transient ionic* $\vec{J}_{el}$ *disappears* in electrolyte. Correspondingly, the zero net electric field implies that
- the *electric potential* within electrolyte between electrodes *becomes constant* (2.28).

The latter process is in close analogy with the phenomenon of *induced surface charges*, as described in Fig. 2.25.

That is, the so-called *electrolytic double layer* is formed at the electrode surface after a few τ (approximately after $3 \cdot \tau$ in Fig. 3.16a, b)—the *electrode becomes polarized*—by the aforementioned *transient conductive current in electrolyte* which accumulates *ionic counter-charges*. Likewise, the charged metal surface of the polarizable electrode becomes neutralized (or balanced) by the neighbouring ionic counter-charge.

In the course of the described *polarization of the sensing electrode* (Fig. 3.16a), a certain *polarization voltage*[33] $u_{pol,i}$ results across its electrode/tissue boundary with the associated non-zero *polarization overvoltage* $(u_{pol,i} - U_{pol})$. For the

[33]Please note that the *voltage* U_{pol} *or* $u_{pol,i}$ *across the electrode/tissue boundary*—as the voltage drop across capacitor plates, see (3.5)—is *continuous in its time course* and can not jump in a step-wise manner, as long as the capacitance C_{el} of the boundary does not jump (or stays constant), the current charging this boundary is finite, and thus the accumulated electric charge $U_{pol} \cdot C_{el}$ or $u_{pol,i} \cdot C_{el}$ varies continuously over time without any step-wise changes [(2.25) and (2.40)].

For instance, as illustrated in the left subfigure of Fig. 3.16a, the equality $U_{pol} = u_{pol,i}$ applies for the switch-on time $t = 0$, even though $\vec{J}_{el}$ in electrolyte can be already assumed to be non-zero. Please note that the latter assumption neglects an *inert acceleration of ions* in electrolyte from the zero to a finite velocity at $t = 0$, whereas a finite velocity and a finite time are needed for a finite $\vec{J}_{el}$ [(2.53) and (2.54)]. Strictly speaking, the ionic drift velocity of *inert ions* is necessarily zero at both time instances $t = 0-$ just before the switch-on and $t = 0+$ just after the switch-on.

switch-on time $t = 0$ in Fig. 3.16a, the equality $u_{pol,i} = U_{pol}$ applies because *inert ionic/species concentrations* at the electrode surface remain in their *electrochemical equilibrium* for this short moment.

In contrast to an abrupt application of a constant voltage in Fig. 3.16a, b, the applied *alternating voltage* u_{AC} yields an *electrostatic driving force* (proportional to the instantaneous difference $E_{ext} - E_i$) acting on ions in electrolyte, which now *varies in its magnitude and direction*. As shown in Fig. 3.16c, d, inert ions in the counterion layer on the sensing electrode surface are then subjected to periodic and inert rearrangements in synchrony with u_{AC}. In particular, the amount of the *surface charge of the metal electrode* and the amount of the ionic *counter-charge close to the metal surface* (charges with opposite polarity) increase with increasing amplitude of u_{AC} or with increasing amplitude of the electrode potential. For instance, these charges are larger in their magnitudes at the time instance t_1 than t_2 because the inequality $|u_{AC}(t_1)| > |u_{AC}(t_2)|$ applies.

Please note that the inequality $T \gg \tau$ was assumed in Fig. 3.16c, d. That is, the oscillation period T of u_{AC} is much longer than τ so that there is sufficient time for inert ionic counter-charges to accumulate on the electrode surface. Consequently, as the oscillation *frequency* $f = 1/T$ of u_{AC} increases while the associated period T decreases down to the range of τ; inert ions are progressively less able to follow quick changes of u_{AC} (or to follow quick changes of the associated driving force); compare with the *inert redistribution* of charges in Fig. 3.16a. Consequently, the *voltage drop* $u_{pol,i}$ across the electrode/tissue boundary—and thus the *electrode polarization*—tends to *decrease with increasing f*. At *very high f* ($T \ll \tau$), the accumulation of the ionic counter-charge at the electrode surface ceases.

The application of the *alternating* u_{AC}—as shown in Fig. 3.16c, d—requires a continuous and *alternating recharge* of the *electrolytic double layer* on the electrode surface throughout the oscillation period of u_{AC}. The instantaneous surface charges of the metal electrode and *ionic counter-charges* close to the surface *vary* periodically in their *size* and *polarity*. These varying charges—in line with (2.25)—imply an *alternating* i_{AC} across the electrode/tissue boundary. Since *electric charges/electrons do not permeate this phase boundary* because a potential *redox/electrode reaction* is still absent (i.e., is assumed to be absent), it is the *displacement* i_{AC} *current* (but not the conductive current) which crosses this boundary; see discussions of (2.66) on the nature of the displacement current and Footnote 31. It is as if a *capacitor* would be charged, discharged, and then recharged again (in a periodic way) when connected to an alternating voltage source u_{AC}. Since the inequality $T \gg \tau$ applies, this current i_{AC} within tissue/electrolyte is mainly carried by ionic migration, i.e., by a *conductive current* within *electrolyte*. Please note that the periodic waveform of i_{AC} precedes that of u_{AC} in terms of the capacitor re-charge (Fig. 2.8), as can be derived from (2.40).

In contrast to the *charge double layer* in Fig. 3.6a subjected to the discussed *electrochemical equilibrium*, this equilibrium in Fig. 3.16 is *disrupted* by the externally applied u_{AC} ($\neq U_{pol} - U'_{pol}$) in the course of which the *charge loading* of the double layer increases, decreases, and even changes its polarity in synchrony with the time-varying u_{AC}. Obviously, this *disrupted equilibrium* implicates significant consequences on the *electrode reaction*, as discussed with respect to Fig. 3.13.

Please note that the *capacitance* C_{el} of the *electrolytic double layer* (Figs. 3.6b and 3.19) *depends also on f* of u_{AC}. According to Fig. 3.16c, the boundary—especially of a *polarizable electrode*—is charged, discharged, and recharged in synchrony with the time-varying u_{AC}. Since the ionic *counter-charge* accumulates with the *delay* τ on the electrode surface (Fig. 3.16a, b), we can expect a greater charge accumulation with increasing half-period $1/(2f)$ of u_{AC} and thus with decreasing f. This greater counter-charge accumulated across C_{el} for a given amplitude of u_{AC} (or for a given amplitude of $u_{pol,i}$ across C_{el}) implies—in line with the definition of C_{el} from (3.5)—a greater C_{el} with decreasing f; experimental data in Schwan (1992) confirms this frequency-dependent behaviour.

It is also instructive to observe that the *capacitance* C_{el} strongly *changes with the varying potential* of the associated metal electrode (while the potential of the undisturbed electrolyte stays constant). That is, the size of C_{el} changes when an *external voltage* is applied and varied between the sensing and reference electrodes; compare the discussion related to (3.5). Charged ions of the *counterion layer*—surrounding the electrode surface—become electrostatically attracted more or less strongly to the *metal surface* depending on the size and polarity of the applied electric potential of the electrode. The higher the absolute potential, the stronger this attraction of counterions will be. Consequently, the *distance* between the associated counterion layer and the metal surface changes, as well as the resulting size of C_{el} [in line with (3.7) and (3.8)]. As a tendency, C_{el} increases with increasing absolute potential of the electrode, as can be derived from Hamann and Vielstich (1998).

In addition, the number of *specifically adsorbed ions* also changes according to the *varying potential of the electrode surface* through specific adsorption and deadsorption as a function of this potential, as illustrated in Fig. 3.7. In consequence, the accumulated *electric charge* on the metal surface as well as the associated C_{el} (3.5) change in a step-wise way; in fact, a *finite size of the charge* of a single adsorbed/deadsorbed ion yields this step-wise change. Therefore, the *electrolytic double layer* acts as a *non-linear capacitor* which C_{el} *depends on the applied voltage* $u_{pol,i}$ across this double layer (Fig. 3.16).

Direct Voltage Application

Figure 3.17a illustrates the *sensing and reference electrodes* in contact with the biological tissue/electrolyte. Please note that the *polarization voltage* $u'_{pol,i}$ of the *perfectly non-polarizable reference electrode* is assumed here to be zero ($u'_{pol,i} \approx U'_{pol} \approx 0$), in line with explanations in Footnote 30. On the other hand, a current-dependant *ohmic voltage drop* u_b [$=i \cdot R_b$, see (3.1)] is assumed in *tissue/electrolyte* (in line with the *simplified tissue model* from Fig. 3.2a), i.e., the conductivity of electrolyte is assumed to be finite. *Diffusional processes* are assumed to be relatively *fast* and thus their influence is neglected in Fig. 3.17. Likewise, a *charge-transfer-limited electrode reaction* (Footnote 28) is assumed according to the simplified model in Fig. 3.20c.

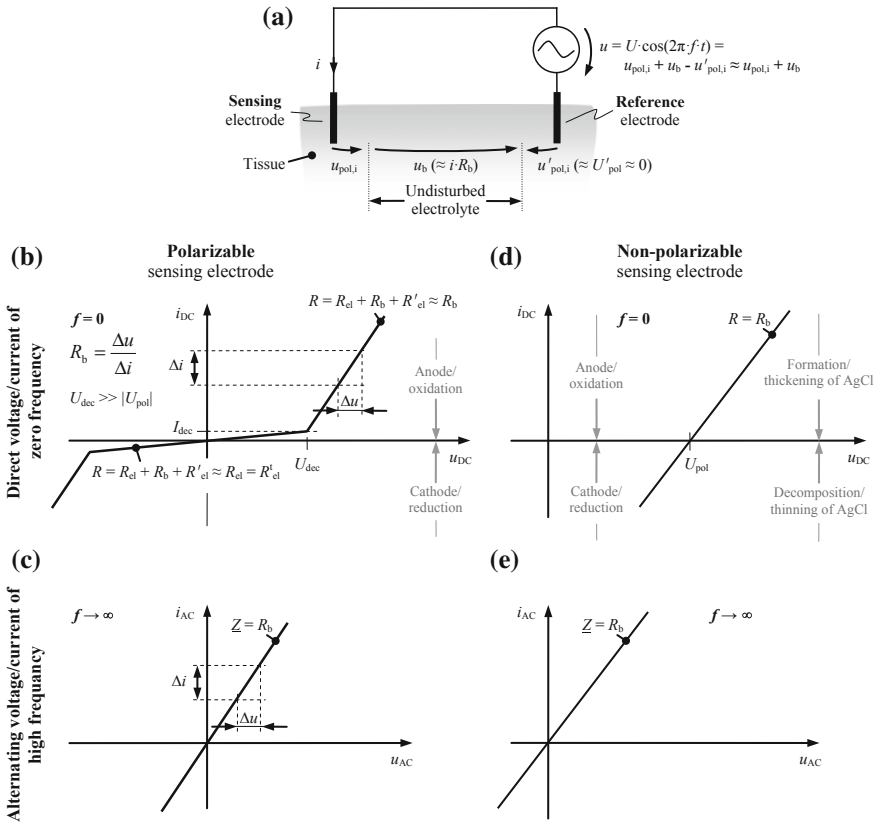

Fig. 3.17 Transfer functions $i = f(u)$ of the sensing and reference electrodes (in contact with tissue) and their associated electrode/tissue boundaries; compare Fig. 3.12. Here a charge-transfer-limited electrode reaction is assumed on the surface of the sensing electrode (with the model from Fig. 3.20c). **a** The experimental set-up with an actively applied voltage u between both electrodes and the resulting current i. The polarizable sensing electrode with **b** the direct current $i = i_{DC}$ as a function of the direct voltage $u = u_{DC}$ (Fig. 3.12b) and with **c** the alternating current $i = i_{AC}$ as a function of the alternating voltage $u = u_{AC}$ at high frequencies f (Fig. 3.12c). The non-polarizable sensing electrode with **d** i_{DC} as a function of u_{DC} and with **e** i_{AC} as a function of u_{AC} at high f. In the case (**b**), the relatively small u_{DC} ($\approx u_{pol,i}$) yields a very small i_{DC} across the boundary, as long as the activation barrier U_{dec}—known as the decomposition voltage—of the charge-transfer-limited electrode reaction is not reached (Footnote 22). In fact, this reaction starts with $u_{DC} > U_{dec}$ and with a steep increase in i_{DC}. Here the polarization voltage $|U_{pol}|$ of the sensing electrode is neglected with respect to U_{dec} ($\gg |U_{pol}|$). The local non-linear resistance ($=\Delta u/\Delta i$) between electrodes is inversely related to the local varying slope of shown $i = f(u)$; compare Fig. 3.14. In cases (**c**) and (**e**), the capacitive behavior of the boundary dominates with only displacement currents crossing the electrode impedance $\underline{Z}_{el}$ (as in Fig. 3.12c with $|1/j\omega C_{el}| \ll R_{el}$). Here the tendencies $|\underline{Z}_{el}| \ll R_b$ (3.26) and even $|\underline{Z}_{el}| \to 0$ apply for very high f (2.42) so that the total impedance $\underline{Z}$ between electrodes is then determined by the bodily tissue resistance R_b only. In the case (**d**), the non-polarizable electrode (Fig. 3.11) acts approximately as a very small ohmic resistor (with $|\underline{Z}_{el}| \ll R_b$) in series with U_{pol} because the activation barrier of the electrode reaction is small; consequently, R_b determines the slope of the resulting $i = f(u)$

The *transfer function* between the *externally applied direct voltage* u_{DC} *across both electrodes* and the *resulting direct current* i_{DC} is depicted in Fig. 3.17b, d. In the case of the *polarizable sensing electrode* in Fig. 3.17b, the transfer function is *highly non-linear*. That is, small values of u_{DC} yield quite small i_{DC} as long as u_{DC} does not exceed the so-called *decomposition voltage* U_{dec} ($>u_{DC}$) of the *polarizable electrode*.

According to the *activation overvoltage* $u^t_{pol,i} = u_{pol,i} - U_{pol}$ of the *polarizable electrode* from Fig. 3.14 (with $u_{pol,i}$ as the *polarization voltage* due to the charge transfer only), the associated *charge transfer* across the electrode/electrolyte *boundary of the sensing electrode* is strongly *constrained* for the relatively *small* $|u^t_{pol,i}| < U_{dec}$ or for the relatively small $|u_{DC}| < U_{dec}$ (see below). Therefore, the associated *differential electrode resistance* R_{el} (3.17)

$$R_{el} = \frac{\Delta(u_{pol,i} - U_{pol})}{\Delta i_{DC}} \approx \frac{\Delta u^t_{pol,i}}{\Delta i_{DC}} = R^t_{el} \tag{3.21}$$

is *quite high*. Please note that $R_{el} \approx R^t_{el}$ (3.17), $\Delta u_{pol,i} = \Delta u^t_{pol,i}$, and $u_{pol,i} = u^t_{pol,i}$ (with neglected $U_{pol} = 0$) apply here since we consider the *constrained charge transfer* only (i.e., *without inert diffusion*, compare Footnote 22). In other words, the *charge-transfer resistance* R^t_{el} dominates here in R_{el} over the *diffusion resistance* R^d_{el} [see (3.18) and (3.31)]; likewise, the inequality $u^t_{pol,i} \gg u^d_{pol,i}, u^c_{pol,i}$ holds (3.20).

Please note that the *effective level of* U_{dec} (Fig. 3.14) is determined by the size of the *exchange current density* (i_0/A according to Footnote 22) and thus differs for different electrodes. The higher this density, the lower U_{dec} is. Therefore,

- *polarizable electrodes* have *large* U_{dec},
- *non-polarizable electrodes* have *small* U_{dec}, and
- *perfectly non-polarizable electrodes* have *zero* U_{dec}, as exemplified in Fig. 3.14.

In fact, this *high local* R_{el} for $u_{DC} < U_{dec}$ (Fig. 3.17b) is much higher than the *tissue* R_b ($\ll R_{el}$) so that the *applied* u_{DC}—in terms of a voltage divider—drops mainly across the electrode/electrolyte *boundary of the sensing electrode*. Therefore, the approximate equality

$$u_{DC} = u_{pol,i} + u_b - u'_{pol,i} \approx u_{pol,i} \tag{3.22}$$

applies here with $u_{pol,i} \gg u_b$ (due to $R_{el} \gg R_b$) and $u'_{pol,i} \approx 0$; compare Figs. 3.12b and 3.14. The *slope of the transfer function* between i_{DC} and u_{DC} in Fig. 3.17b is then determined by $R_{el} + R_b \approx R_{el}$ ($=\Delta u_{DC}/\Delta i_{DC} = U_{dec}/I_{dec}$) for $u_{DC} < U_{dec}$. Likewise, the strict equality $u_{DC} = u_{pol,i}$ applies for zero $i_{DC} = 0$ (and thus zero $u_b = i_{DC} \cdot R_b = 0$ and $I_{dec} = 0$ in Fig. 3.17b). With the neglected $U_{pol} = 0$—as assumed in Fig. 3.17b (see below)—the condition $u_{DC} < U_{dec}$ for the constrained charge transfer can be rewritten as $u_{DC} \approx u_{pol,i} = u^t_{pol,i} < U_{dec}$.

In contrast to $u_{DC} < U_{dec}$, increasing u_{DC} ($>U_{dec}$) yields a steep increase in i_{DC} of the *polarizable electrode*, as shown in Fig. 3.17b. This is because the associated *charge transfer* across the electrode/tissue phase boundary *becomes unconstrained* and *electric charges start to permeate this boundary* (see Fig. 3.14, Footnotes 22 and 24). There is a continuous *exchange of the net charge* between the *sensing electrode* and the surrounding tissue/electrolyte. The speed of the associated chemical *electrode/redox reaction* (Footnote 23) on the surface of the sensing electrode rises. In particular, the *electrolytic reaction* starts to take place on the electrode surface for $u_{DC} > U_{dec}$ in Fig. 3.17b, whereas the *sensing electrode acts here as anode* (compare Fig. 3.13c).

It is instructive to observe that, at the electrode/electrolyte *boundary* of the *sensing electrode* for $u_{DC} > U_{dec}$, chemical *species or negative ions* from electrolyte give their electrons to this *positive electrode*, namely, to *anode* with the more positive $u_{pol,i}$ than U_{pol} (see Fig. 3.13c), and then become *oxidized*; compare Figs. 3.4 and 3.11c. In contrast, at the boundary of the sensing electrode for $u_{DC} < -U_{dec}$, electrons from this *negative electrode*, from *cathode* with the more negative $u_{pol,i} < U_{pol}$ (see Fig. 3.13b), *reduce now species or positive ions* arrived to the electrode surface from the undisturbed electrolyte.

The *local differential resistance* R_{el} (3.21) *decreases* for $u_{DC} > U_{dec}$ (compare Fig. 3.14) and falls below R_b ($\gg R_{el}$). Thus, the resistance R_{el} *of the polarizable electrode turns to be highly non-linear* with respect to u_{DC} (Footnote 22). Likewise, the *applied* u_{DC} drops now mainly across the *electrolyte* between electrodes with

$$u_{DC} = u_{pol,i} + u_b - u'_{pol,i} \approx u_{pol,i} + u_b \approx U_{dec} + u_b \tag{3.23}$$

and thus the approximate equality $\Delta u_{DC} \approx \Delta u_b$ now applies. Consequently, the *slope of the transfer function* between i_{DC} and u_{DC} is determined only by R_b ($=\Delta u_{DC} / \Delta i_{DC}$) for $u_{DC} > U_{dec}$, see Fig. 3.17b.

According to the description from above, the *total differential resistance R between the polarizable sensing and non-polarizable reference electrodes*—i.e., the *ratio* $\Delta u_{DC} / \Delta i_{DC}$ (Fig. 3.17b)—for the *application of the direct* u_{DC} (or, in analogy, of the direct i_{DC}) can be modelled as a *series connection* of

- the *non-linear differential electrode resistances* R_{el} and R'_{el} [from (3.21)] of both *electrode/tissue boundaries* (or *phase boundaries*)—with high R_{el} for $u_{DC} < U_{dec}$ and low R_{el} for $u_{DC} > U_{dec}$—and
- the *linear bodily tissue resistance* $R_b = u_b / i_{DC}$ [simplified model from (3.1) and Fig. 3.2a] of the tissue/electrolyte between both electrodes (i.e., with tissue acting as electrolyte), to give

$$R = \frac{\Delta u_{DC}}{\Delta i_{DC}} = R_{el} + R_b + R'_{el}. \tag{3.24}$$

Figure 3.12b illustrates this *series connection* in terms of the *equivalent circuit model*. In other words, the discussed condition $u_{DC} < U_{dec}$ in Fig. 3.17b implies $R \approx R_{el}$ in Fig. 3.12b because $R_{el} \gg R_b$ and $R'_{el} \approx 0$ (due to the assumed $u'_{pol,i} \approx 0$). Here the phase boundary of the *polarizable sensing electrode* determines the *total* R. On the contrary, the discussed condition $u_{DC} > U_{dec}$ of the *polarizable electrode* implies $R \approx R_b$ because $R_{el} \ll R_b$; here *tissue* between electrodes starts to dominate the total R. In other words, the total R decreases abruptly after u_{DC} exceeds U_{dec}, as can be observed from the increased *slope of the transfer function* for $u_{DC} > U_{dec}$ in Fig. 3.17b.

In contrast to the *transfer function* between i_{DC} and $u_{pol,i}$ of the *polarizable electrode* from Fig. 3.14 considering the *charge transfer* under *finite* $U_{pol} \neq 0$, it can be observed that the shown *transfer function* between i_{DC} and u_{DC} of the *polarizable sensing electrode* in Fig. 3.17b *neglects this finite* U_{pol} ($\neq 0$) of the sensing electrode. In other words, the plot in Fig. 3.17b assumes $U_{pol} = 0$ and $u_{pol,i} = u^t_{pol,i}$. Please recall that $u_{DC} \approx u_{pol,i} = u^t_{pol,i}$ applies for $u_{DC} < U_{dec}$ and $U_{pol} = 0$. In fact, the simplified transfer function in Fig. 3.17b crosses the horizontal u_{DC} axis at $u_{DC} = 0$ but not at the biophysically correct value $u_{DC} = U_{pol}$ (i.e., at U_{pol} of the sensing electrode) where i_{DC} is zero. This is because a *reasonable assumption* is met here that the absolute U_{dec} is much higher than $|U_{pol}|$ ($\ll U_{dec}$) so U_{pol} can be neglected in Fig. 3.17b. The better the *polarizability of the electrode*, the higher U_{dec} is, and thus the more appropriate this assumption is.

While the discussed *transfer function* between u_{DC} (across the *polarizable sensing* and the *perfectly non-polarizable reference electrodes*) and the resulting i_{DC} is *strongly non-linear*, i.e., u_{DC} and i_{DC} are *non-linearly coupled* with each other (Fig. 3.17b), please note that this is in strong contrast to the *linear transfer function of bodily tissue* with its ohmic and linear R_b [simplified model from (3.1)]. In tissues, there is a *linear coupling* between u_b and i_{DC} (Fig. 3.12b) or, in analogy, between the inner *direct electric field* [proportional to u_b across tissue, see (2.30)] and the resulting inner *direct current density* [proportional to i_{DC} through this tissue, see (2.23)] according to (2.54).

In the case that the *sensing electrode* is a *non-polarizable electrode*, the *transfer function* between i_{DC} and u_{DC} in Fig. 3.17d turns to be a *straight line* crossing $u_{DC} = U_{pol}$ at $i_{DC} = 0$. The *charge transfer* across the electrode/electrolyte boundary is unconstrained and the associated *exchange current density* is very high (Footnote 22). Therefore *small activation barriers* of electrode reactions render the associated *local* R_{el} (3.21) to be *quite small and linear*, as can also be observed from the course of the *activation overvoltage of the non-polarizable electrode* in Fig. 3.14 at low $|u_{pol,i} - U_{pol}|$.

Then the relatively high tissue R_b ($\gg R_{el}$ of the *non-polarizable sensing electrode*) governs the resulting i_{DC} in response to the applied u_{DC}. Likewise, R_b governs the total R in accordance with (3.24) (with $R'_{el} \approx 0$ due to $u'_{pol,i} \approx 0$). The *slope of the transfer function* between i_{DC} and u_{DC} in Fig. 3.17d with the involved *non-polarizable sensing electrode* is then determined by R_b ($=\Delta u_{DC} / \Delta i_{DC}$) only. This slope *does not change with varying* u_{DC} in clear contrast to Fig. 3.17b with the involved *polarizable electrode*.

The *non-polarizable electrode* acts for $u_{DC} > U_{pol}$ and $i_{DC} > 0$ as *anode* with its *oxidising properties*, whereas this electrode acts for $u_{DC} < U_{pol}$ and $i_{DC} < 0$ as *cathode* with its *reducing properties*. Please note that U_{pol} of the *non-polarizable electrode* is not neglected in Fig. 3.17d, in contrast to the neglected U_{pol} of the *polarizable electrode* in Fig. 3.17b (see above).

Alternating Voltage Application

In contrast to the direct u_{DC} application from above, the *external application* of the *alternating voltage* u_{AC} (or, in analogy, of the *alternating current* i_{AC}) with its *field frequency f* across the *sensing and reference electrodes* (in contact with tissue, see Fig. 3.17a) subjects all involved *electro-kinetic processes* (charge transfer, diffusion, and coupled reactions) on the electrode surface to an *oscillatory rhythm* with its period 1/*f*. In fact, the temporal dynamic of u_{AC} oscillation is highly relevant with respect to *finite dynamics of all electro-kinetic processes*. In qualitative terms, the slower are the temporal periodic changes of the applied u_{AC} (with its low *f*), the more *hindering involvement* of *inert electro-kinetic processes* (such as inert diffusion) we expect in determining the *total reaction kinetics* and thus in determining the *dynamic behaviour of the electrode/tissue boundary*. Since all these kinetic processes have their own *temporal inertia* in view of the *imprinted oscillation period 1/f*, the *transfer function* between the *applied* u_{AC} across the boundary and the *resulting* i_{AC} through this boundary—as illustrated in Fig. 3.17a and discussed in the following—becomes a strong function of *f*. The polarization voltage $u_{pol,i}$ and the polarization overvoltage $(u_{pol,i} - U_{pol})$ become *functions not only of the time-varying* i_{AC} *and* u_{AC} *but also of time*; compare with the application of the time-constant/direct u_{DC} or i_{DC} from Section "Active Current or Voltage Application Between Electrodes".

In fact, the *electrode reaction* alternates on the electrode surface. The *reaction changes from anodic to cathodic* (and vice versa) when the *positive half-wave* of u_{AC} changes into its *negative half-wave* (and vice versa), in synchrony with *f*; compare Figs. 2.75a and 3.14. The *electrode reaction* is typically *reversible* over the oscillation period 1/*f* of i_{AC} at rather *low f* (e.g., at 0.1 Hz), whereas the reaction can even disappear at rather *high f* due to a *non-infinite reaction speed*. Of course, if, for instance, the *electrode reaction* forms *gases* (e.g., O_2 gas on Pt anode, see Section "Pt Electrodes") and these gases have enough time to *bubble away* from the electrode surface (e.g., at quite *low f*), then the alternating electrode reaction becomes *irreversible* (as in the case of the direct i_{DC} application).

To begin with the detailed discussion on the application of u_{AC} across the sensing and reference electrodes (Fig. 3.17a) the following difference in-between u_{DC} and u_{AC} applications should be highlighted. The resulting *stationary* i_{DC} from one electrode to another *in response to the applied* u_{DC}—with *necessarily conductive currents* passing the *electrode/tissue boundary* and *tissue/electrolyte*—requires an *electrolytic or galvanic reaction* on the electrode surface (for the exchange of electric charges between both phases, metal electrode and tissue/electrolyte, with substance transfer and/or conversion at the boundary, see Footnote 23). Figure 3.19b

demonstrates this *conductive current* $i_{DC,E}$ across the boundary, which equals to i_{DC} in the *steady state* outside any switching events (Footnote 41).

On the contrary, the resulting *stationary* i_{AC} *in response to the applied* u_{AC} does not necessarily require such *electrolytic or galvanic reaction* because both

- *the conductive current* $i_{AC,E}$ (carried by migration of free *unbound charges*, see Fig. 2.16a) and
- *the displacement current* $i_{AC,C}$ (carried by local movements of *bound charges*, see Fig. 2.16b).

can cross the electrode/tissue boundary and thus compose additively the total i_{AC}, to give

$$i_{AC} = i_{AC,E} + i_{AC,C}. \tag{3.25}$$

Please note that the *alternating conductive* $i_{AC,E}$ with *real charge transfer* across the boundary is necessarily determined by the discussed *electro-kinetic processes* of the electrode reaction. In contrast, the *alternating displacement* $i_{AC,C}$ across the boundary is due to the *time-varying polarization* of the medium within the double layer, i.e., the *polarization of mainly water molecules* on and close to the electrode surface (Section "Water Relevance"). Within the tissue, *conductive currents* dominate over displacement currents in line with the *simplified tissue model* (Fig. 3.2a).

Figure 3.19c demonstrates $i_{AC,E}$ across the *modelled electro-kinetic processes* of the boundary in parallel to $i_{AC,C}$ across the *double layer capacitor* with its capacitance C_{el}, whereas (3.25) obviously applies. Please note that this $i_{AC,E}$ is principally comparable with the current i_E through R in Fig. 2.9b, whereas the associated $i_{AC,C}$ is comparable with the current i_C through C.

In fact, when we move from a *direct current* i_{DC} with the associated *unidirectional migration* of charged particles/ions in tissue/electrolyte to an *alternating current* i_{AC} (applied also between two electrodes in contact with tissue, see Fig. 3.17a), the *migration process* of charged particles/ions still takes place—i.e., *back and forth migration* in synchrony with the applied electric field within tissue/electrolyte—but *bidirectionally* and to a *smaller spatial extent*. The higher is f, the less is the travelled/migrated distance of charged ions due to their *migrational inertness*; compare with the frequency dependence of the effective conductivity in biological tissues from Section "Relaxation and Dispersion Effects on Conductivity and Polarization". At very *high* f, an effective *migration ceases* and *counterions do not accumulate* anymore at the electrode surface (Fig. 3.16a); here, the inequality $i_{AC,C} \gg i_{AC,E}$ applies and the displacement $i_{AC,C}$ dominates across the electrode/tissue boundary.

In analogy to the definition of the *total differential resistance* R for u_{DC} application between two electrodes (3.24), the *total differential complex impedance* $\underline{Z}$ *between the sensing and reference electrodes* (Fig. 3.12a) can be given as the *ratio* $\Delta\underline{U}_{AC} \;/\; \Delta\underline{I}_{AC}$ (2.34). That is, for the *application of* u_{AC} *between both electrodes* with its *complex amplitude* $\underline{U}_{AC}$—or, in analogy, for the application of

i_{AC} with its *complex amplitude* $\underline{I}_{AC}$—the total $\underline{Z}$ can be modelled as a *series connection* of

- the *non-linear electrode impedances* $\underline{Z}_{el}$ and $\underline{Z}'_{el}$ of *electrode/tissue boundaries* (or *phase boundaries*) of both *sensing and reference electrodes*, and
- the *linear bodily tissue impedance* $\underline{Z}_b \approx R_b = u_b / i_{AC}$ (the simplified model from (3.1) and Fig. 3.2a) of tissue residing between these two electrodes, to give

$$\underline{Z} = \frac{\Delta \underline{U}_{AC}}{\Delta \underline{I}_{AC}} = \underline{Z}_{el} + \underline{Z}_b + \underline{Z}'_{el} \approx \underline{Z}_{el} + R_b + \underline{Z}'_{el}. \tag{3.26}$$

Figure 3.12d illustrates this *series connection*. The approximation in (3.26) implies $\underline{Z}_b \approx R_b$ according to the *simplified tissue model* (Fig. 3.2a).

In the following discussion, we still assume $u'_{pol,i} \approx U'_{pol} \approx 0$ of the *perfectly non-polarizable reference electrode* (Footnote 30) and thus $\underline{Z}'_{el} \approx 0$. The *ohmic voltage drop* u_b [$=i_{AC} \cdot R_b$, see (3.1)] within *tissue/electrolyte* is assumed to depend on the current i_{AC} but not on the frequency f according to the *simplified tissue model* (Fig. 3.2a).

We start with the discussion of rather simple cases of u_{AC} application at a rather *high or low f*. Then we continue with a *medium f* of u_{AC}, which gives us a more complete and instructive picture of the *electrode/tissue boundary* behaviour.

High Field Frequency

A simple but instructive case results when the frequency f *of the applied* u_{AC} between the sensing and reference electrodes *is quite high* so that mainly *alternating displacement current* $i_{AC,C}$ ($\gg i_{AC,E}$) crosses the electrode/electrolyte boundary of the *sensing electrode*. It should be reiterated that, in contrast to u_{DC} application, there are almost *no real electric charges* permeating the boundary for u_{AC} *application* at this high f. Here the displacement $i_{AC,C}$ across the boundary (across C_{el} in Fig. 3.12c) dominates over the conductive $i_{AC,E}$ (across R_{el} in Fig. 3.12c); see (3.25). To be precise, for $f \to \infty$, only the *displacement* $i_{AC,C}$ crosses the boundary which then behaves as a pure short-circuited *capacitor* with its *double layer capacitance* C_{el}.

In addition, the finite *dynamics of electro-kinetic processes* within the boundary, such as the inert *diffusion-based transport*, can also be *neglected* (Footnote 35). In other words, inert directional processes have no time to form themselves during short half-waves of u_{AC} with the duration of $1/(2f)$; e.g., the direction of diffusion alternates from one half-wave to another half-wave for reversible electrode reactions. Consequently, the associated *diffusion impedance* $\underline{Z}^d_{el}$ is very small and can be ignored (Footnote 35).

For high f, the *capacitive behaviour of the boundary* with its *low interfacial capacitive impedance* $1/(j \cdot 2\pi \cdot f \cdot C_{el})$ [see (2.42)] dominates over its *resistive behaviour*. This is because the *relatively high resistance* $R_{el} \approx R^t_{el}$ [with $\underline{Z}^c_{el}$, $\underline{Z}^d_{el} \approx 0$ in Fig. 3.19c due to high f, see (3.32)] lays in *parallel* to C_{el} and thus does not effectively determine *the total electrode impedance* $\underline{Z}_{el}$ (3.36) *for this high f*. Figures 3.12c and 3.19c illustrate the associated *equivalent circuit models*.

The latter dominance implies the inequality $|\underline{Z}_{el}| \approx |1/(j \cdot 2\pi \cdot f \cdot C_{el})| \ll R_{el}$ in Fig. 3.12c [with the assumed $R_{electrol} \approx 0$ in Fig. 3.19c and (3.32)]. In fact, this inequality yields a quantitative measure for f to be considered as quite high; namely, the derived inequality $f \gg 1/(2\pi \cdot f \cdot R_{el} \cdot C_{el})$ should be fulfilled.

Interestingly, infinitely high $f \to \infty$ tends to yield negligibly small $|\underline{Z}_{el}| \to 0$ so that the dominance of the *bodily tissue* with its resistance R_b can even be assumed over the *electrode/tissue boundary* with its $|\underline{Z}_{el}|$ ($\ll R_b$) for this high f. In accordance with (3.26), the *total* $\underline{Z}$ *between the sensing and reference electrodes* can then be approximated as $\underline{Z} \approx R_b$ for high f since the relationships $|\underline{Z}_{el}| \ll R_b$ and $\underline{Z}'_{el} \approx 0$ (in line with the assumed $u'_{pol,i} \approx 0$) apply. Then the resistance R_b ($=u_{AC} / i_{AC} = \Delta u_{AC} / \Delta i_{AC}$) determines the relationship between i_{AC} and u_{AC} for this *high f*. In other words, only the *bodily tissue resistance* between electrodes determines the *total* $\underline{Z}$ *for high f*.

Correspondingly, the resistance R_b determines the *slope of the transfer function of the polarizable sensing electrode* for *high f* (Fig. 3.17c) and, on the other hand, determines the *slope of the transfer function of the non-polarizable sensing electrode* for *high f* (Fig. 3.17e). Please note that these slopes do not change with the varying amplitude of u_{AC} (or i_{AC}) which, in turn, means that the resulting *transfer functions are linear*; in clear contrast to the application of the direct u_{DC} in polarizable electrodes (Fig. 3.17b).

Low Field Frequency

For *quite low f of the applied* u_{AC} between the sensing and reference electrodes, the oscillatory period $1/f$ of u_{AC} is quite long so that the electrode/electrolyte boundary can be assumed to behave as that at the *direct voltage* application (as discussed in Section "Direct Voltage Application"). During the *positive half-wave* of u_{AC}, the *anodic behaviour* applies (from Fig. 3.17b, c with $u_{DC} = u_{AC} > 0$ and the assumed $u_{DC} > U_{pol}$). In analogy, the *negative half-wave* of u_{AC} yields *cathodic behaviour* (from Fig. 3.17b, c with $u_{DC} = u_{AC} < 0$ and $u_{DC} < U_{pol}$).

For low f, the *capacitive behaviour of the boundary* can be neglected because its *capacitive impedance* $1/(j \cdot 2\pi \cdot f \cdot C_{el})$ tends to be very large. Likewise, the *alternating conductive* $i_{AC,E}$ across the boundary dominates over the displacement $i_{AC,C}$ [$\ll i_{AC,E}$, see (3.25)]. In the borderline case, this impedance satisfies $|1/(j \cdot 2\pi \cdot f \cdot C_{el})| \to \infty$ for $f \to 0$ while only the *conductive* $i_{AC,E}$ crosses the boundary. This is because the finite *electrode resistance* $R_{el} \approx R^t_{el} + R^c_{el} + R^d_{el}$ [from Fig. 3.19b according to (3.31) with the neglected $R_{electrol} \approx 0$ for the sake of simplicity] lays in parallel to C_{el} and thus determines effectively the total $\underline{Z}_{el}$ (3.36) *for this low f*. Figures 3.12b and 3.19b illustrate the associated *equivalent circuit models*. In fact, the inequality $\underline{Z}_{el} \approx R_{el} \ll |1/(j \cdot 2\pi \cdot f \cdot C_{el})|$ applies in Figs. 3.12b and 3.19b (with $R_{electrol} \approx 0$), which highlights the derived inequality $f \ll 1/(2\pi \cdot f \cdot R_{el} \cdot C_{el})$ for f to be considered as quite low.

In accordance with (3.26), the condition of *low f* forces the *total* $\underline{Z}$ *between the sensing and reference electrodes* to satisfy $\underline{Z} \approx \underline{Z}_{el} + R_b \approx R_{el} + R_b$. Here relationships $\underline{Z}_{el} \approx R_{el}$ (due to low f and $i_{AC,E} \gg i_{AC,C}$) and $\underline{Z}'_{el} \approx 0$ (due to the assumed $u'_{pol,i} \approx 0$) apply. Consequently, the resistances R_{el} and R_b determine the resulting total i_{AC} ($\approx i_{AC,E}$)—according to (3.24)—in response to the applied u_{AC}

for this low f, as described within the scope of u_{DC} application (Section "Direct Voltage Application"). Likewise, with the slowly varying u_{AC} level with respect to the level of U_{dec}, both $\underline{Z}_{el}$ and R_{el} change non-linearly in a way as anticipated from the discussed *direct voltage behaviour* of the electrode/tissue boundary of the *polarizable sensing electrode* (Fig. 3.17b). In the case of the *non-polarizable sensing electrode*, both $\underline{Z}_{el}$ and R_{el} do not change with varying u_{AC} (Fig. 3.17d). That is, the *bodily tissue and electrode resistances* determine the *total* $\underline{Z}$ *for low f*.

Medium Field Frequency

For *medium f of the applied* u_{AC}, the *dynamics of electro-kinetic processes* of the electrode/electrolyte boundary, especially of *diffusional processes* (see below) play a crucial role.

Charge Transfer Process

The *charge transfer processes* are typically relatively fast so that the associated *activation overvoltage* $u^t_{pol,i} = (u_{pol,i} - U_{pol})$ can be assumed as frequency-independent. It implies that the ohmic *charge-transfer resistance* R^t_{el} [from (3.17)] remains *real, ohmic, and non-linear* (for polarizable electrodes), *does not change with f*, and equals to [in line with Ohm's law in (2.34)]

$$\underline{Z}^t_{el} = \frac{\Delta \underline{U}^t_{pol,i}}{\Delta \underline{I}_{AC,E}} = \frac{\Delta U^t_{pol,i}}{\Delta I_{AC,E}} = R^t_{el} \tag{3.27}$$

when the alternating u_{AC} (or i_{AC}) is applied across the electrode/electrolyte boundary (Fig. 3.19c). Here $\underline{U}^t_{pol,i}$ is the complex amplitude of $u^t_{pol,i}$ and $\underline{I}_{AC,E}$ the complex amplitude of the time course of the *conductive* $i_{AC,E}$ across the boundary (3.25).

Diffusion Process

The *alternating conductive* $i_{AC,E}$ across the electrode/electrolyte boundary—as a part of the actively applied i_{AC} (3.25) or resulting in response to the active u_{AC} application—yields an *alternating anodic and cathodic reaction*, i.e., the *charge transfer back and forth* across the boundary. This alternating reaction, in turn, yields a prominent *oscillation of the reactive species concentrations c* on *the electrode surface*. For instance, these concentrations c of *electroactive particles* refer to

- the *concentration* c_{red} of species S_{red} to be oxidized with z electrons on the surface (*anodic reaction* with $S_{red} \rightarrow S_{oxi} + z \cdot e^-$) and to
- the *concentration* c_{oxi} of species S_{oxi} to be reduced (*cathodic reaction* with $S_{oxi} + z \cdot e^- \rightarrow S_{red}$)

if a reversible *redox reaction* (3.12) occurs on the electrode surface (Fig. 3.14). This oscillation in c is especially dominant when a *diffusion-limited electrode reaction* is given with a relatively *slow mass transport* (Footnote 27). If the *electrode/redox reaction is reversible*, reactants (e.g., S_{oxi} for cathodic reaction) diffuse in one direction while reaction products diffuse in the opposite direction (e.g., S_{red}) during one *half-wave* of i_{AC}, whereas these species diffuse in their respective opposite directions during the subsequent half-wave of i_{AC} with the opposite amplitude.

This *spatial oscillation of c over time* propagates from the electrode surface towards the undisturbed electrolyte (down into the *bulk with its concentration* c^0) in terms of an *attenuated wave* [in line with (2.20)] along the *total thickness* δ_D^T of the *diffusion layer* (Figs. 3.5 and 3.20a). Correspondingly, this wave disappears completely at the distance δ_D^T from the electrode surface.

Since the concentration c may only *slowly and asymptotically converge* to its final value c^0 (e.g., the thickness δ_D^T is semi-infinite for a *resting electrode* and *diffusion-limited electrode reaction*, see Footnote 35), a finite *effective thickness* δ_D ($<\delta_D^T$) of the *diffusion layer* can be usually defined. In analogy with (2.20) and Fig. 2.7, this *thickness* δ_D of a resting electrode equals to the *penetration depth* of the spatial c wave or, in other words, equals to the *space constant* of this wave according to Hamann and Vielstich (1998)

$$\delta_D = \sqrt{\frac{D_F}{\pi \cdot f}}, \tag{3.28}$$

where D_F is the *diffusion coefficient*.

The depth δ_D is the *normal distance from the electrode surface* to the region within electrolyte at which the local c wave becomes attenuated by 1/e (Fig. 2.7). Equation (3.28) signifies that the *higher frequency f*—i.e., the higher the dynamics of i_{AC} with respect to the *inert diffusion process*—the more close is the *temporal variation of c* (to be more precise, of c_{red} and c_{oxi}) to the *electrode surface*. Likewise, with increasing f, the influence of the *inert diffusion progressively diminishes*.

Interestingly, the *difference* $(c^s - c^0)$, with c^s as the *concentration on the electrode surface*, is *proportional*[34] *to the amplitude of the conductive* $i_{AC,E}$, given a *diffusion-limited electrode reaction*. Furthermore, the *difference* $(c - c^0)$ *within the diffusion layer*, with c as the *local concentration* within the diffusion layer, is also *proportional to the amplitude of* $i_{AC,E}$.

The temporal courses of the *concentration differences* $(c^s - c^0)$ and $(c - c^0)$ are *delayed* with respect to the *temporal course of* $i_{AC,E}$ (when the *transport inhibition throughout the whole diffusion layer* is considered and not only the difference

[34]If we consider c^s and c^0 only—i.e., these *boundary conditions only* without the specific diffusion process inside of the diffusion layer—then Footnote 29 illustrates the *proportionality of*

- *the difference* $(c^s - c^0)$ (in particular, of the difference $(c_{red}^s - c_{red}^0)$ or $(c_{oxi}^s - c_{oxi}^0)$ of reduced and oxidized species, respectively) and
- the *amplitude of the resulting conductive* $i_{AC,E}$ ($\approx i_{DC}$ from Footnote 29) in a *diffusion-limited electrode reaction* (Footnote 27). In this *approximation which follows the discussed direct voltage behaviour*, there is *zero phase delay* between temporal courses of $(c^s - c^0)$ and $i_{AC,E}$ (Hamann and Vielstich 1998). Please note that this approximation also assumes a relatively *small overvoltage* $|u_{pol,i} - U_{pol}| \ll RT/zF$ (Footnote 22) across the electrode/electrolyte boundary, which can be seen as a *small* u_{AC} *oscillating around* U_{pol} (i.e., around the *electrochemical equilibrium* of the boundary). Likewise, the resulting $(u_{pol,i} - U_{pol})$ is then obviously proportional to the applied u_{AC}.

between the boundary values c^s and c^0, as assumed in Footnote 34). That is, the temporal course of the local c is *delayed* with respect to the temporal course of $i_{AC,E}$ due to a *finite diffusion speed*; likewise, this delay has its origin in a *finite time* which is needed to change the local level of c.

This *phase delay* between $(c - c^0)$ and $i_{AC,E}$ equals to $\pi/4 + \sqrt{\pi \cdot f/D_F} \cdot x$ (Hamann and Vielstich 1998), with x as the normal distance from the electrode surface into the bulk. In fact, this phase delay as a function of x can be principally equated with the phase shift $k \cdot r$ of the *lossy wave propagation* [in (2.20)] while the term $1/\delta_D$ [from (3.28)] corresponds to the *attenuation coefficient* α (2.20). Consequently, the oscillatory change in $(c^s - c^0)$ directly at the *electrode surface* (at $x = 0$) lags behind that in $i_{AC,E}$ by *45°* (or $\pi/4$).

Please note that this present *delay* between the time-varying local $(c^s - c^0)$ or $(c - c^0)$ and, on the other hand, the *alternating* $i_{AC,E}$ with $f \neq 0$ is in clear contrast to the application of the *direct current* i_{DC} with $f = 0$. As discussed in Footnote 29, there is obviously *no temporal delay* of $(c^s - c^0)$ or $(c - c^0)$ with respect to i_{DC} due to the assumed time-invariance of kinetic processes within the boundary.

This distinct difference between the application of the conductive $i_{AC,E}$ and the conductive i_{DC} through the electrode/electrolyte boundary implies that the *differential electrode resistance due to inert diffusion* [or *diffusion resistance* from (3.18)] is

- a *real quantity* R_{el}^d *for the direct* i_{DC} and must be
- a *complex and frequency-dependent number* $\underline{Z}_{el}^d$ *for the alternating conductive* $i_{AC,E}$

in a *diffusion-limited electrode reaction*. In other words, the discussed *non-zero phase delay* between the time profiles of the *local* c within the diffusion layer and $i_{AC,E}$ *through the boundary* forces the *differential diffusion impedance* $\underline{Z}_{el}^d$

$$\underline{Z}_{el}^d = \frac{\Delta \underline{U}_{pol,i}^d}{\Delta \underline{I}_{AC,E}} \tag{3.29}$$

to stay complex, which is known as *Warburg impedance*.[35] In (3.29), the complex amplitude $\underline{U}_{pol,i}^d$ of the time course of the *diffusion overvoltage*

[35]The *Warburg impedance* $\underline{Z}_{el}^d$ of the *electrode/electrolyte boundary* is defined for a *diffusion-limited electrode reaction* (Footnote 27) given an *alternating* i_{AC} *across the boundary*. Here the *diffusion layer* of the boundary has a *semi-infinite total thickness* δ_D^T, as applicable to a *resting electrode* in resting solution.

It should be recalled that $\delta_D^T \to \infty$ applies for the local concentration c within the diffusion layer to become exactly equal with c^0 in the bulk solution outside the diffusion layer (Fig. 3.20a), i.e., c converges asymptotically towards c^0. Likewise, the *spatial oscillation of c has a semi-infinite extent* from the *electrode surface* down into the *bulk*.

The impedance $\underline{Z}_{el}^d$ is a *constant phase element* (Footnote 10)—i.e., with its *phase arg*$(\underline{Z}_{el}^d)$ *independent on the frequency f*—according to

$$\underline{Z}_{\mathrm{el}}^{\mathrm{d}} = \frac{RT}{z^2F^2 \cdot A \cdot c^0 \cdot \sqrt{\pi \cdot D_{\mathrm{F}}}} \cdot \frac{(1-\mathrm{j})}{\sqrt{f}} = \tilde{R}_{\mathrm{el}}^{\mathrm{d}} + \frac{1}{\mathrm{j} \cdot 2\pi \cdot f \cdot \tilde{C}_{\mathrm{el}}^{\mathrm{d}}},$$

where A is the surface area of the electrode and z the number of electrons involved in the considered redox reaction on the electrode surface (3.12). This expression for $\underline{Z}_{\mathrm{el}}^{\mathrm{d}}$ applies for equal $c_{\mathrm{red}}^0 = c_{\mathrm{oxi}}^0$ and equal D_{F} of both *reactive species* $\mathrm{S_{red}}$ and $\mathrm{S_{oxi}}$. In addition, a relatively *small overvoltage* $|u_{\mathrm{pol,i}} - U_{\mathrm{pol}}|$ across the boundary and thus a *small conductive* $i_{\mathrm{AC,E}}$ through the boundary are assumed.

Please note that

- at *high f*, the impedance magnitude $|\underline{Z}_{\mathrm{el}}^{\mathrm{d}}|$ is small since *diffusing reactants* don't have to diffuse far within the diffusion layer during the relatively *short half-periods* $1/(2f)$ of i_{AC}.
- At *low f*, the reactants have to move farther which increases $|\underline{Z}_{\mathrm{el}}^{\mathrm{d}}|$.

In other words, *temporal and spatial oscillation of c disappears* at *the electrode surface* and *within the diffusion layer* for quick changes in the direction of the *alternating electrode reaction* (anodic to cathodic and vice versa) at quite *high f*. With disappearing $\underline{Z}_{\mathrm{el}}^{\mathrm{d}}$ (i.e., $\underline{Z}_{\mathrm{el}}^{\mathrm{d}} \to 0$ for $f \to \infty$), the associated diffusion overvoltage disappears also for this high f [compare (3.20)], i.e., the *diffusion overvoltage* is *frequency-dependent*. This is in clear contrast to the *activation overvoltage* which is *frequency-independent*, i.e., the associated charge-transfer resistance $R_{\mathrm{el}}^{\mathrm{t}}$ (3.17) does not change with increasing f.

As a *constant phase element*, the impedance $\underline{Z}_{\mathrm{el}}^{\mathrm{d}}$ shows its positive *real value* $\mathrm{Re}(\underline{Z}_{\mathrm{el}}^{\mathrm{d}})$ (>0) and negative *imaginary value* $\mathrm{Im}(\underline{Z}_{\mathrm{el}}^{\mathrm{d}})$ (<0), which are equal in their size at any f. It means that the electric current through $\underline{Z}_{\mathrm{el}}^{\mathrm{d}}$, or the *conductive current* $i_{\mathrm{AC,E}}$ *through the boundary*, precedes the associated voltage drop across $\underline{Z}_{\mathrm{el}}^{\mathrm{d}}$, or the *diffusion overvoltage* $(u_{\mathrm{pol,i}} - U_{\mathrm{pol}})$ across the boundary, by the *phase shift of 45°* at all f.

The consequence of this relationship is as follows: when $\underline{Z}_{\mathrm{el}}^{\mathrm{d}}$ *dominates the total electrode impedance* $\underline{Z}_{\mathrm{el}}$ at low f, this total $\underline{Z}$ (3.33) in the *complex plot*, namely, the *Nyquist plot* of $\underline{Z}$, converges for decreasing f towards a straight *diagonal line* (determined by $\underline{Z}_{\mathrm{el}}^{\mathrm{d}} \approx \underline{Z}_{\mathrm{el}}$) with its slope of 45°. This line is known as *Warburg line* and is demonstrated in Fig. 3.20d. The latter dominance of $\underline{Z}_{\mathrm{el}}^{\mathrm{d}}$ within $\underline{Z}_{\mathrm{el}}$ prevails especially for *low f* when *reactants have to diffuse over large distances* during the relatively *long half-periods* $1/(2f)$, increasing the effective size of $\underline{Z}_{\mathrm{el}}^{\mathrm{d}}$.

Since the assumed *diffusion-limited reaction* implies a *fast and unconstrained charge transfer* (Footnote 27), the *Nernst behaviour* (Section "Dynamics of Electro-Kinetic Processes") applies with a *direct and instantaneous coupling between* $u_{\mathrm{pol,i}}$ *and the concentration* c^{s} on the *electrode surface* (3.13). This direct coupling shows *no phase delay between the time-varying courses of* $u_{\mathrm{pol,i}}$ *and* c^{s} for a given $i_{\mathrm{AC,E}}$. Consequently, the temporal delay of both the course of $(c^{\mathrm{s}} - c^0)$ and the course of the diffusion overvoltage $(u_{\mathrm{pol,i}} - U_{\mathrm{pol}})$ with respect to the course of $i_{\mathrm{AC,E}}$ is reflected by the *Warburg line* and amounts to the discussed *phase shift* of 45°.

The *Warburg impedance* $\underline{Z}_{\mathrm{el}}^{\mathrm{d}}$ can be represented as a *series connection* of

- a *pseudo-resistance* $\tilde{R}_{\mathrm{el}}^{\mathrm{d}}$ (due to positive $\mathrm{Re}(\underline{Z}_{\mathrm{el}}^{\mathrm{d}}) > 0$, also known as *polarization resistance*) and
- a *pseudo-capacitance* $\tilde{C}_{\mathrm{el}}^{\mathrm{d}}$ (due to negative $\mathrm{Im}(\underline{Z}_{\mathrm{el}}^{\mathrm{d}}) < 0$, also known as *polarization capacitance*).

Please recall that $\mathrm{Im}(\underline{Z}_{\mathrm{C}})$ of a capacitive impedance $\underline{Z}_{\mathrm{C}}$ is negative by definition according to $\mathrm{Im}(-\mathrm{j}/(\omega C)) < 0$ (2.42). However, this $\tilde{R}_{\mathrm{el}}^{\mathrm{d}}$ and $\tilde{C}_{\mathrm{el}}^{\mathrm{d}}$ *do not represent a real resistor and a real capacitor*, respectively, because the values of $\tilde{R}_{\mathrm{el}}^{\mathrm{d}}$ and $\tilde{C}_{\mathrm{el}}^{\mathrm{d}}$ are frequency-dependent; in contrast to a frequency-independent resistance and capacitance of the real resistor and capacitor, respectively [(2.36) and (2.41)]. In fact, both $\tilde{R}_{\mathrm{el}}^{\mathrm{d}}$ and $\tilde{C}_{\mathrm{el}}^{\mathrm{d}}$ vary with $1/\sqrt{f} = f^{-0.5} = f^{-\alpha}$, i.e., decrease with increasing f, as can be seen from the above equation. Interestingly, the exponent constant α is not constant in experimental measurements and varies from 0.3 to 0.5, which implies that the

$u^{\mathrm{d}}_{\mathrm{pol,i}} = (u_{\mathrm{pol,i}} - U_{\mathrm{pol}})$ (3.18) is related to the complex amplitude $\underline{I}_{\mathrm{AC,E}}$ of $i_{\mathrm{AC,E}}$ through the boundary.

Please note that the same *phase delay*—as reflected by the complex $\underline{Z}^{\mathrm{d}}_{\mathrm{el}}$ and its $arg(\underline{Z}^{\mathrm{d}}_{\mathrm{el}})$—separates the *time courses of the polarization voltage* $u_{\mathrm{pol,i}}$ *due to diffusion and the current* $i_{\mathrm{AC,E}}$ or, in analogy, separates the time courses of the associated *overvoltage* $u^{\mathrm{d}}_{\mathrm{pol,i}} = (u_{\mathrm{pol,i}} - U_{\mathrm{pol}})$ and $i_{\mathrm{AC,E}}$. As elaborated in Footnote 35, this is because a *fast und unconstrained charge transfer prevails* in the

---

discussed *phase shift* equals $\alpha \cdot \pi/2$ and varies in the range from 27° to 45° (Schwan 1992). Please note that for $\alpha < 0.5$ and phase shifts <45°, the resulting frequency-dependencies of $\tilde{R}^{\mathrm{d}}_{\mathrm{el}} \propto f^{-(1-\alpha)}$ and $\tilde{C}^{\mathrm{d}}_{\mathrm{el}} \propto f^{-\alpha}$ would be different.

Please note that an *infinite* $\underline{Z}^{\mathrm{d}}_{\mathrm{el}} \to \infty$ *results for* $f \to 0$, i.e., for the direct current application, provided that a *semi-infinite* $\delta^{\mathrm{T}}_{\mathrm{D}} \to \infty$ is given. From a practical point of view, the *total thickness* $\delta^{\mathrm{T}}_{\mathrm{D}}$ *is usually finite* and is physically limited to $\delta^{\mathrm{T}}_{\mathrm{D}} = \delta_{\mathrm{D}}$. That is, the *diffusion layer is typically bounded* with a homogeneous solution outside the normal distance $\delta^{\mathrm{T}}_{\mathrm{D}}$ from the electrode surface. For instance, a finite $\delta^{\mathrm{T}}_{\mathrm{D}}$ is applicable for coated samples/electrodes or when *convection/stirring* is present, which *accelerates mass transport* to/from the electrode surface. Likewise,

- a *still electrode* in the solution has a *semi-infinite* $\delta^{\mathrm{T}}_{\mathrm{D}}$, whereas
- a *moving electrode* (rotating or non-resting electrode) has a *finite* $\delta^{\mathrm{T}}_{\mathrm{D}}$ (Hamann and Vielstich 1998).

For *finite thickness* $\delta^{\mathrm{T}}_{\mathrm{D}} = \delta_{\mathrm{D}}$, the so-called *finite length Warburg impedance* $\underline{Z}^{\mathrm{d,f}}_{\mathrm{el}}$ (also known as *Nernst impedance*) applies, to give

$$\underline{Z}^{\mathrm{d,f}}_{\mathrm{el}} = \underline{Z}^{\mathrm{d}}_{\mathrm{el}} \cdot \tanh\left(\sqrt{\frac{\mathrm{j} \cdot 2\pi \cdot f}{D_{\mathrm{F}}}} \cdot \delta_{\mathrm{D}}\right) = \frac{RT}{z^2F^2 \cdot A \cdot c^0 \cdot \sqrt{\pi \cdot D_{\mathrm{F}}}} \cdot \frac{(1-\mathrm{j})}{\sqrt{f}} \cdot \tanh\left(\sqrt{\frac{\mathrm{j} \cdot 2\pi \cdot f}{D_{\mathrm{F}}}} \cdot \delta_{\mathrm{D}}\right).$$

For *finite* $\delta^{\mathrm{T}}_{\mathrm{D}} = \delta_{\mathrm{D}}$, a *finite* $\underline{Z}^{\mathrm{d,f}}_{\mathrm{el}}$ *results for* $f \to 0$. In fact, the equality $\underline{Z}^{\mathrm{d,f}}_{\mathrm{el}} = 2RT \cdot \delta_{\mathrm{D}}/((zF)^2 \cdot A \cdot c^0 \cdot D_{\mathrm{F}})$ applies for $f \to 0$. Here the *impedance* $\underline{Z}^{\mathrm{d,f}}_{\mathrm{el}}$ becomes even *real* (because $\tanh(\sqrt{\mathrm{j} \cdot f})/\sqrt{\mathrm{j} \cdot f} \to 1$ for $f \to 0$ with the correspondence $1 - \mathrm{j} = \sqrt{2}/\sqrt{\mathrm{j}}$). Figure 3.20d demonstrates this real-valued $\underline{Z}^{\mathrm{d,f}}_{\mathrm{el}}$ for $f \to 0$. Please note that the ratio $\delta_{\mathrm{D}}/\sqrt{D}$ in the above equation characterises the *time reactants take to diffuse* through the spatially limited *diffusion layer* with its finite thickness $\delta^{\mathrm{T}}_{\mathrm{D}} = \delta_{\mathrm{D}}$.

It is instructive to observe that for *ideally fast mass transport* (e.g., with a strong *convective diffusion*), the thickness δ_{D} goes to zero ($\delta_{\mathrm{D}} \to 0$) and so the impedance $\underline{Z}^{\mathrm{d,f}}_{\mathrm{el}}$ ($\to 0$). In other words, a *diffusion-limited electrode reaction* at *no or weak convection* mutates into a *charge-transfer-limited electrode reaction* when a *strong convection* is given. Correspondingly, as illustrated within the complex plane of Fig. 3.20d, the model A for finite $\delta^{\mathrm{T}}_{\mathrm{D}} = \delta_{\mathrm{D}}$ mutates into the shown model A for $\underline{Z}^{\mathrm{d,f}}_{\mathrm{el}} = 0$ (or into the model B in Fig. 3.20e).

It can be observed that the *finite length Warburg impedance* $\underline{Z}^{\mathrm{d,f}}_{\mathrm{el}}$ (for $\delta^{\mathrm{T}}_{\mathrm{D}} = \delta_{\mathrm{D}}$) is indistinguishable from the *Warburg impedance* $\underline{Z}^{\mathrm{d}}_{\mathrm{el}}$ (for $\delta^{\mathrm{T}}_{\mathrm{D}} \to \infty$) at

- high f ($\gg D_{\mathrm{F}}/(2\pi \cdot \delta^2_{\mathrm{D}})$) or
- high δ_{D}

(since the function $\tanh(\cdot)$ approaches unity for large values of its argument). Figure 3.20d illustrates this similarity for high f based on both A models for semi-infinite and finite $\delta^{\mathrm{T}}_{\mathrm{D}}$. From a biophysical point of view, the time for an ion to diffuse across the distance δ_{D} is much longer than the half-period $1/(2f)$ of i_{AC} at this high f. So that this moving ion throughout the half-period (or electrode) does not 'see' that the diffusion layer is bounded (i.e., does not 'see' that $\delta^{\mathrm{T}}_{\mathrm{D}}$ is not semi-infinite) or that the film or coating has a finite thickness.

diffusion-limited reaction (Footnote 27), which requires the *Nernst behaviour* of the boundary with the logarithmically coupled c^s and $u_{pol,i}$ [(3.4) and (3.13)] *without any time delay* in-between the associated *time courses of* c^s *and* $u_{pol,i}$.

As discussed in Footnote 35, the *influence of the diffusion* decreases with increasing f (3.28). Thus, the diffusion impedance $\underline{Z}^d_{el}$ is small at *high* f since diffusing reactants don't have to diffuse far during the relatively *short half-periods* $1/(2f)$ of i_{AC}. By contrast, the reactants travel over great distances at *low* f, which increases $\underline{Z}^d_{el}$. In other words, the longer the half-wave of u_{AC}, the more significant is the *inert diffusion process to fuel the surface electrode reaction* within the scope of the *total reaction kinetics*.

Coupled Reactions

The *processes of coupled chemical reactions* are typically subjected to *inertia*, so that the associated *reaction overvoltage* $u^c_{pol,i} = (u_{pol,i} - U_{pol})$ as well as the *associated differential impedance* $\underline{Z}^c_{el}$

$$\underline{Z}^c_{el} = \frac{\Delta \underline{U}^c_{pol,i}}{\Delta \underline{I}_{AC,E}} \tag{3.30}$$

do also depend on f; compare with (3.19) for the direct voltage/current application. Here $\underline{U}^c_{pol,i}$ is the complex amplitude of $u^c_{pol,i}$ and $\underline{I}_{AC,E}$ the complex amplitude of $i_{AC,E}$.

For *adsorption processes* on electrodes (Hamann and Vielstich 1998), the impedance $\underline{Z}^c_{el}$ is finite at low f and even at $f \to 0$, whereas $\underline{Z}^c_{el}$ decreases towards zero for $f \to \infty$; compare Fig. 3.19c. From a physical point of view, the extent of *adsorption on the electrode surface* is quite small during the relatively *short half-periods* $1/(2f)$ of i_{AC} because the *available time* for adsorption, i.e., for the *inert adsorption* with its finite speed, is quite short at high f. Consequently, the associated *net inhibition* of the electrode reaction kinetics due to adsorption is quite small at this high f. The reverse is true for low f.

Electrical Equivalent Circuit Model

The *electrical equivalent circuit model* in Fig. 3.19c illustrates the effects of R^t_{el}, $\underline{Z}^d_{el}$, and $\underline{Z}^c_{el}$ in view of the time-varying $u_{pol,i}$ [$=U_{pol} + u^t_{pol,i} + u^c_{pol,i} + u^d_{pol,i}$, see (3.20)] and $i_{AC,E}$ [$=i_{AC} - i_{AC,C}$, see (3.25)]. Here the resistance R^t_{el} determines—in line with (3.27)—the temporal course of the *activation overvoltage* $u^t_{pol,i} = (u^1_{pol,i} - U_{pol})$ as a function of the *conductive component* $i_{AC,E}$ *of the total* i_{AC} through the electrode/electrolyte boundary. In analogy, the impedance $\underline{Z}^d_{el}$ (3.29) and $\underline{Z}^c_{el}$ (3.30) determine the *diffusion overvoltage* $u^d_{pol,i} = (u^2_{pol,i} - U_{pol})$ and the *reaction overvoltage* $u^c_{pol,i} = (u^3_{pol,i} - U_{pol})$, respectively, in response to $i_{AC,E}$.

In fact, another component of i_{AC}, the *displacement component* $i_{AC,C}$ (3.25) permeates the double layer capacitance C_{el} being in parallel to the sum impedance $R^t_{el} + \underline{Z}^d_{el} + \underline{Z}^c_{el}$, as shown in Fig. 3.19c. In particular, the time course of $i_{AC,C}$ is determined by $i_{AC,C} = C_{el} \cdot d(u_{pol,i} - U_{pol})/dt$ (2.40). Please recall that the *sum of both conductive* $i_{AC,E}$ *and displacement* $i_{AC,C}$ *components* gives the total i_{AC} (3.25)

across the boundary of the sensing electrode, as can be observed in the relevant (3.32) [and is discussed with respect to $i = i_E + i_C$ in Figs. 2.9b and (2.45)].

A *diffusion-limited electrode reaction* (Footnote 27) changes into a *charge-transfer-limited electrode reaction* (Footnote 28) for *high f*, as also elaborated in the following examples of Figs. 3.18c and 3.20d. That is, the *diffusion-limited reaction* requires consideration of the *frequency-independent* R_{el}^{t} *in series with* both the *frequency-dependent* $\underline{Z}_{el}^{d}$ and *frequency-dependent* $\underline{Z}_{el}^{c}$ to consider the *conductive* $i_{AC,E}$ *pathway* within the total *electrode impedance* $\underline{Z}_{el}$ [(3.32) and Fig. 3.19c]. For *high f*, both *impedances* $\underline{Z}_{el}^{d}$ *and* $\underline{Z}_{el}^{c}$ *disappear* so that only the *frequency-independent* R_{el}^{t} *is left* in the latter series connection (Fig. 3.20b). And this is the model of the *charge-transfer-limited reaction* which is characterized by *constrained charge transfer* but not constrained diffusion or constrained coupled reactions.

The latter observation has a significant implication on the resulting *structure of electrical equivalent circuit models of* $\underline{Z}_{el}$—as discussed in Section "Electrode Impedance Model" in detail—for *different electrode reactions* when an alternating i_{AC} or u_{AC} is applied across the *electrode/tissue boundary*. In fact, these models should account for both *conductive* $i_{AC,E}$ *and displacement* $i_{AC,C}$ *pathways* of the total i_{AC} (3.25) through $\underline{Z}_{el}$. That is, the phase boundary with

- the ongoing *diffusion-limited electrode reaction* can be modelled as a *parallel circuit* of the sum *impedance* $R_{el}^{t} + \underline{Z}_{el}^{d} + \underline{Z}_{el}^{c}$ (to consider the *conductive* $i_{AC,E}$) and the *capacitance* C_{el} (to consider the *displacement* $i_{AC,C}$). Figure 3.19c shows the associated model with the relevant (3.32), whereas all three *electro-kinetic processes* of the *charge transfer*, *diffusion*, and *coupled reactions* are taken into account. In analogy, Fig. 3.20a and (3.33) depict a *simplified boundary model* with the neglected $\underline{Z}_{el}^{c}$ (=0). The phase boundary with
- the ongoing *charge-transfer-limited electrode reaction* can be modelled as a *parallel circuit* of the *resistance* R_{el}^{t} and C_{el}, as shown in Fig. 3.20b with the associated (3.35) ($\underline{Z}_{el}^{c}$ is also neglected here). For instance, Fig. 3.12d takes this circuit as its basis with $R_{el} = R_{el}^{t}$ and with the applicable (3.36).

Linearity and Frequency Dependence

Please recall that the resistance R_{el}^{t} is *linear for the non-polarizable electrode* while R_{el}^{t} is highly *non-linear for the polarizable electrode* (Footnote 22). It is also important to stress here that not only $\underline{Z}_{el}^{d}$ and $\underline{Z}_{el}^{c}$ represent *frequency-dependent components* of the total $\underline{Z}_{el}$ (due to the discussed *temporal inertia* of the associated *electro-kinetic processes*) but also C_{el} (Fig. 3.19c).

That is, as discussed with respect to Fig. 3.16c, the *effective value of* C_{el} *tends to increase with decreasing f*. Very briefly, since *counter-charges* accumulate with a certain *time delay* on the electrode surface (the delay τ in Fig. 3.16a, b), we can expect a greater charge accumulation and thus a greater C_{el} [in line with (3.5)] with decreasing *f* for a given amplitude of u_{AC}. In addition, C_{el} *depends also on the absolute instantaneous level of* u_{AC}, as already described in terms of the *non-linear capacitor of the double layer* (Fig. 3.16). In short, higher instantaneous levels of

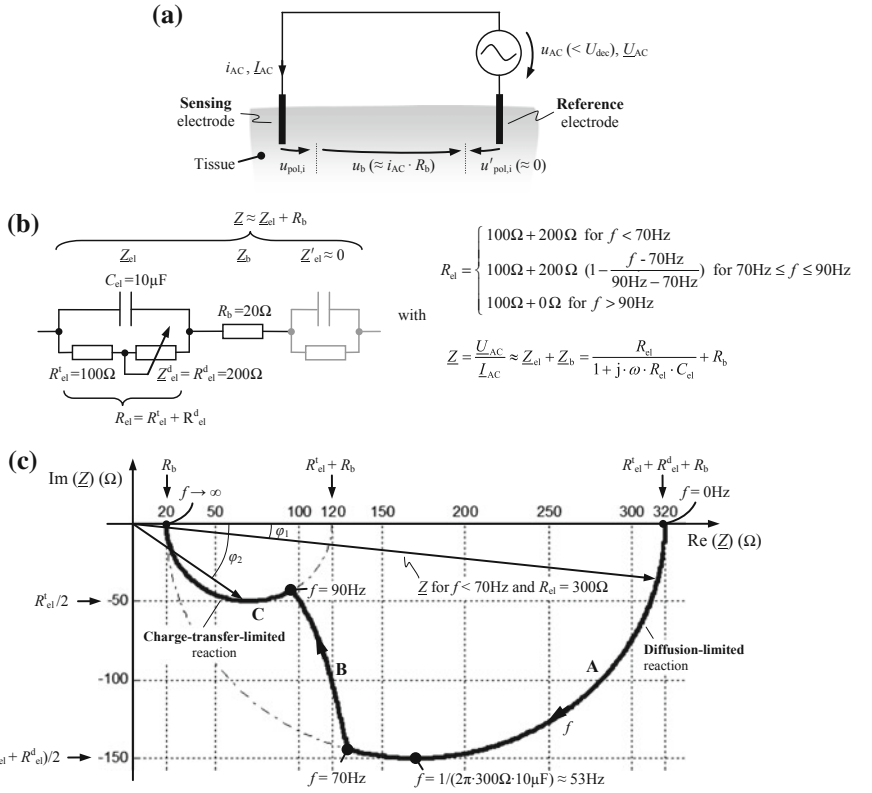

Fig. 3.18 The total complex impedance $\underline{Z}$ between the sensing and reference electrodes and its change in the complex plane as a function of the field frequency f. **a** The experimental set-up with the applied alternating voltage u_{AC} (<U_{dec}) and the resulting alternating current i_{AC} (Fig. 3.17a). The kinetics of the electrode reaction at the surface of the sensing electrode is determined through both charge transfer and diffusion processes. **b** The electrical equivalent circuit model of $\underline{Z}$ (3.26) with the associated arbitrary values of model parameters, as used in (**c**). For the electrode impedance $\underline{Z}_{el}$ of the sensing electrode, a simplified model from Fig. 3.20a and (3.33) is assumed here (with neglected $R_{electrol}$ and an assumed real-valued $\underline{Z}^d_{el} = R^d_{el}$). While the charge-transfer resistance R^t_{el} (=100 Ω) does not change with increasing f, the diffusion resistance R^d_{el} is assumed to decrease from 200 Ω down to zero with increasing f from 70 to 90 Hz (in line with Footnote 35). The electrode impedance $\underline{Z}'_{el}$ (≈0) of the reference electrode is neglected (due to $u'_{pol,i} \approx 0$, see Footnote 30). **c** The Nyquist plot of $\underline{Z}$. For low f (<70 Hz), the diffusion inhibits the electrode reaction and thus constrains the charge transfer process across the boundary of the sensing electrode (i.e., the diffusion-limited electrode reaction dominates). The associated total electrode resistance R_{el} (=R^t_{el} + R^d_{el} = 300 Ω) is relatively high; see the large semi-circle A. For medium f (70 Hz ≤ f ≤ 90 Hz), the size of R_{el} decreases towards R^t_{el} along the line segment B, i.e., the diffusion-limited reaction mutates into a charge-transfer-limited reaction. For high f (>90 Hz), the charge-transfer-limited reaction dominates. Here the plot of $\underline{Z}$ follows the small semi-circle C and then converges to a real-valued $\underline{Z}$ = R_b = 20 Ω for semi-infinite $f \to \infty$

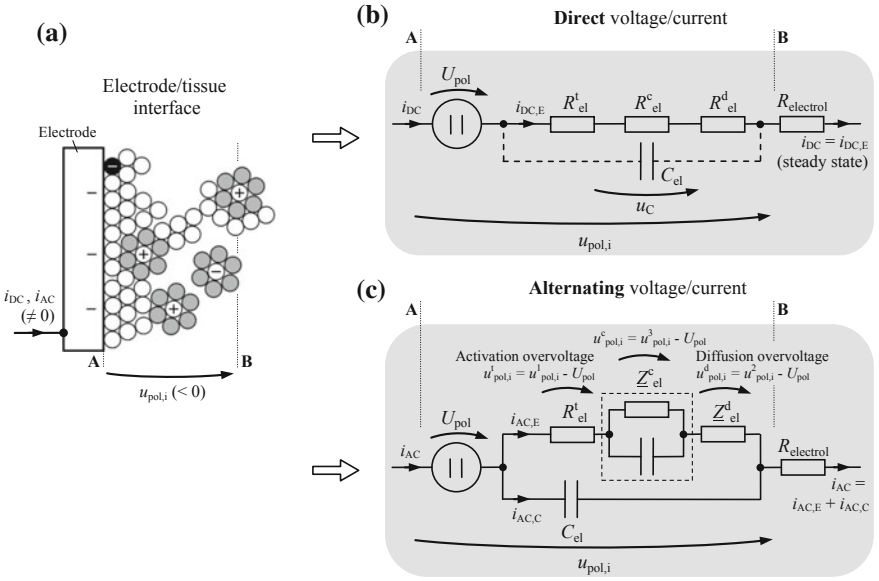

Fig. 3.19 The electrical equivalent circuit models of **a** the electrode/tissue boundary. **b** Physical boundary model for the direct voltage/current application. **c** Physical boundary model for the alternating voltage/current application, with simplified versions given in Fig. 3.20 [compare (3.20)]

u_{AC} lead to a stronger *attraction of inert counterions*, their shorter distances to the electrode/metal surface, and thus to an increased C_{el} (2.41). In addition, the number of *specifically adsorbed ions* may change as a function of the varying electrode potential (Fig. 3.7)—as governed by u_{AC}—and thus the associated C_{el} (3.5).

Please note that the *finite decomposition voltage* U_{dec} ($\neq 0$) of the *polarizable sensing electrode* (Fig. 3.14) co-determines the resulting *non-linear relationship*[36] between the *applied alternating* u_{AC} and the *resulting* i_{AC} (between the sensing and reference electrodes); see Fig. 3.17a. This is in analogy with the discussed cases of the *applied direct* $u_{DC} < U_{dec}$ and $u_{DC} > U_{dec}$ (from Fig. 3.17b, c).

In fact,

[36]Please note that the *non-linearity in-between* i_{AC} *and* u_{AC} (to be precise, between $i_{AC,E}$ and the activation overvoltage $u^t_{pol,i} = u_{pol,i} - U_{pol}$, see Fig. 3.14 and text) implies the presence of a non-linear *electrode impedance*. That is, if i_{AC} is applied (current clamp), then the resulting u_{AC} will be *distorted* (rectified) including both a *steady component* and *higher harmonics* within u_{AC}. In analogy, if u_{AC} is applied (voltage clamp), the resulting i_{AC} will be distorted accordingly.

To give a simple example, let us assume that a *harmonic voltage* $u_{AC} = c_1 \cdot \cos(\omega t)$ is applied across the electrode/electrolyte boundary with its schematic *non-linear relationship* $i_{AC} = c_2 \cdot (u_{AC})^2$ (with c_1 and c_2 as constants). As a result, a *direct current component* $(c_1^2 \cdot c_2)/2$ as well as a *second current harmonic* with its amplitude $(c_1^2 \cdot c_2)/2$ are generated according to $i_{AC} = (c_1^2 \cdot c_2)/2 + (c_1^2 \cdot c_2/2) \cdot \cos(2\omega t)$.

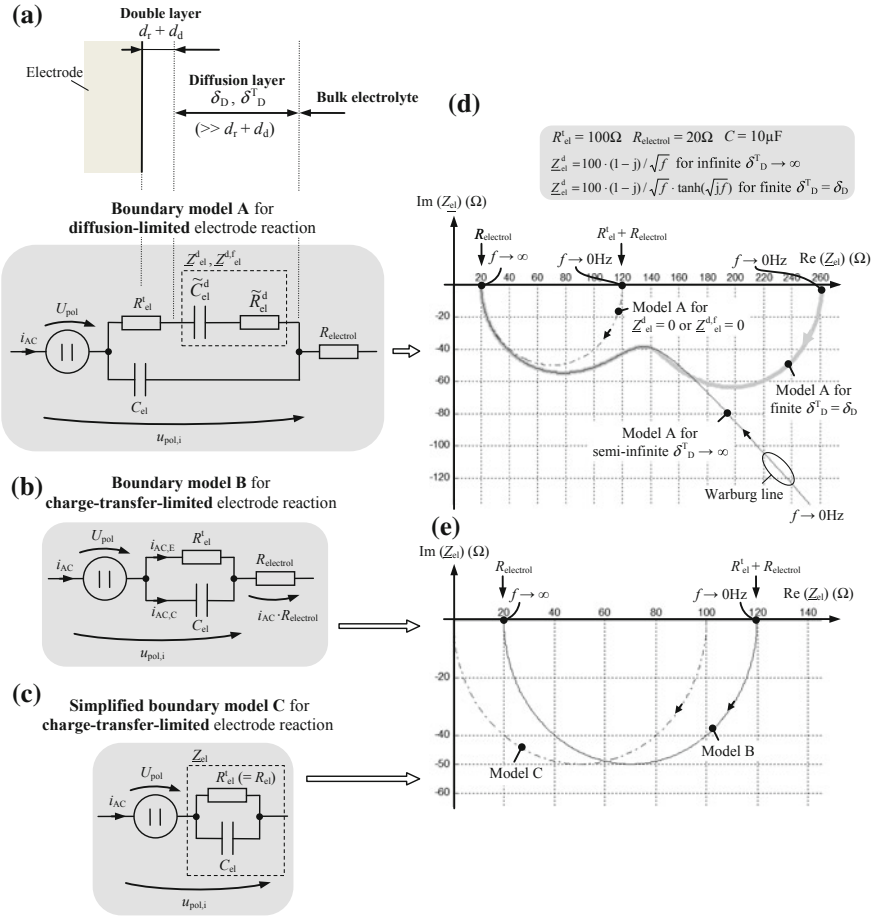

Fig. 3.20 Specific electrical equivalent circuit models of the electrode/tissue boundary (Fig. 3.19a) for the application of the alternating voltage/current (in line with the general model from Fig. 3.19c). The kinetic inhibition of the electrode reaction is only considered with respect to the charge transfer and diffusion processes, i.e., potentially inert coupled reactions are neglected here. **a** The boundary model A of the diffusion-limited electrode reaction (3.33). **b** The boundary model B of the charge-transfer-limited electrode reaction (3.35). **c** The simplified boundary model C of the charge-transfer-limited electrode reaction (3.36), as used in Fig. 3.12d and other figures. **d** The complex electrode impedance $\underline{Z}_{el}$ of the model A, which is given as a Nyquist plot in the complex plane. The diffusion impedance $\underline{Z}^d_{el}$ (Warburg impedance) is calculated and plotted for a semi-infinite diffusion layer thickness δ^T_D (→∞) and limited $\delta^T_D = \delta_D$ (Footnote 35). **e** Nyquist plots of the models B and C

- the *inequality* $u_{AC} < U_{dec}$ may mean a relatively *low* $u^{t}_{pol,i} < U_{dec}$ (please note that $u^{t}_{pol,i} < u_{AC}$ if $U_{pol} > 0$ according to Fig. 3.19c), featuring *constricted charge transfer* and thus a *high* R^{t}_{el} (Fig. 3.14) and a *low conductive* $i_{AC,E}$ through R^{t}_{el} (or through the boundary of the *polarizable sensing electrode*). We assume here $u_{AC} \approx u_{pol,i} = U_{pol} + u^{t}_{pol,i} + u^{d}_{pol,i} + u^{c}_{pol,i}$, i.e., the applied u_{AC} drops mainly across the *boundary of the sensing electrode*, in close analogy with (3.22) and its assumptions. The reverse is true for
- increasing $u_{AC} > U_{dec}$ with the assumed relatively *high* $u^{t}_{pol,i} > U_{dec}$ (once again, please note that $u^{t}_{pol,i} < u_{AC}$ with $U_{pol} > 0$, see Fig. 3.19c), which *lowers* R^{t}_{el} and *increases* $i_{AC,E}$. To be precise, the latter changes apply for time periods only when instantaneous values of the *time-varying* $u^{t}_{pol,i}$ exceed the *time-constant* U_{dec}. The applied u_{AC} drops mainly across the electrolyte between electrodes for time instants with $u^{t}_{pol,i} > U_{dec}$ and drops mainly across the boundary of the sensing electrode for time instants with $u^{t}_{pol,i} < U_{dec}$; that is, we assume here $u_{AC} \approx u_{pol,i} + u_b = U_{pol} + u^{t}_{pol,i} + u^{d}_{pol,i} + u^{c}_{pol,i} + u_b$ [in close analogy with (3.23)].

Interestingly, the onset of this non-linearity around U_{dec} depends on the smoothness of the *electrode surface*.[37] Please note that the applied $u_{AC} \approx u_{pol,i}$ can be seen as an oscillating signal either around U_{pol} of the sensing electrode (i.e., the applied u_{AC} has then a direct offset equal to U_{pol} and the approximation $u_{AC} - U_{pol} \approx u^{t}_{pol,i}$ applies when charge transfer dominates; compare Footnote 34) or around the zero voltage if U_{pol} can be neglected with respect to U_{dec} (i.e., then $|U_{pol}| \ll U_{dec}$ and $u_{AC} \approx u^{t}_{pol,i}$ apply while u_{AC} has no offset).

A *low* $u^{t}_{pol,i}$ and thus a *high* R^{t}_{el} especially apply for *low* f of u_{AC} when $\underline{Z}^{d}_{el}$ and $\underline{Z}^{c}_{el}$—in series with R^{t}_{el} (Fig. 3.19c)—are quite high (Footnote 35). Then the voltage

[37] It is instructive to consider that if the *electrode surface* is irregular or porous (with *sharp local edges*), the *current density distribution* can not be expected to be *homogeneous* along the surface (compare with the *electrical point effect* from Fig. 2.25). Therefore, *sharp surface regions* with the associated relatively *high local current densities* may already operate *above* U_{dec} *in the non-linear range* while other surface regions with the relatively low densities still *below* U_{dec} *in the linear range*, in close analogy with Footnote 137 in Chap. 2. As the *total current* through the whole electrode surface increases, these non-linear regions will grow in size until the whole electrode area operates under non-linear conditions. Thus, the *onset of the non-linearity varies spatially* (Schwan 1992).

Please note that the *shift of a particular surface region from linear to non-linear behaviour* implies that the associated *local electrode impedance* decreases (since a significant charge amount starts to permeate the boundary at this region, see Fig. 3.14 and Footnote 22). Thus, this particular *non-linear region* will *receive an additional current*, which, in turn, widens the spatial extent of this non-linear region and influences the aforementioned distribution of the current density along the whole surface (in terms of *a positive feedback cycle*).

When the *alternating* i_{AC} is applied, the discussed *onset and spreading of the spatial non-linearity* becomes a function of the *frequency* f. As f increases, the *limit current density of linearity* increases (see text), so that the onset and spreading of the non-linearity occur later for higher levels of i_{AC} at high f than at low f.

drop $u^{t}_{pol,i}$ across R^{t}_{el} is only a small *fraction* (<1) of the total voltage drop $u_{AC} - U_{pol} \approx u_{pol,i} - U_{pol}$ across the total series connection $R^{t}_{el} + \underline{Z}^{d}_{el} + \underline{Z}^{c}_{el}$ [acting as a voltage divider, see (3.20)]. Likewise, the fractional voltage $u^{t}_{pol,i}$ may not exceed U_{dec} (while the *charge transfer remains constricted*) even though u_{AC} or even ($u_{AC} - U_{pol}$) already exceeds U_{dec}. For *high f*, the latter *fraction of the voltage divider* across R^{t}_{el} increases due to the decreased sum $\underline{Z}^{d}_{el} + \underline{Z}^{c}_{el}$ and so both $u^{t}_{pol,i}$ (across R^{t}_{el}) and $i_{AC,E}$ (through R^{t}_{el}) increase for a given u_{AC} and may compromise the inequality $u^{t}_{pol,i} < U_{dec}$ for the *constricted charge transfer*. The associated total $\underline{Z}_{el}$ also decreases with rising f (3.32).

If we *compare external* i_{DC} *and* i_{AC} *applications* across the electrode/electrolyte boundary, it can be concluded that U_{dec} as well as the associated conductive $i_{DC,E}$ ($=i_{DC}$, see Fig. 3.19b) across the boundary are readily reached for the relatively small i_{DC} currents. In contrast to i_{DC}, the application of i_{AC} yields both currents $i_{AC,E}$ and $i_{AC,C}$ across this boundary (Fig. 3.19c), so that the *conductive* $i_{AC,E}$ is always less than the total i_{AC} [$=i_{AC,E} + i_{AC,C}$, see (3.25)]. Likewise, the level of U_{dec} as well as the associated level of the *partial current* $i_{AC,E}$ are reached for higher levels of the total i_{AC} as compared with i_{DC} levels necessary to rise $u^{t}_{pol,i}$ up to U_{dec}. To be precise, provided that amplitudes of the applied i_{AC} or i_{DC} are equal, the *activation overvoltage* $u^{t}_{pol,i} = u_{pol,i} - U_{pol}$ reaches more readily U_{dec} (Fig. 3.14) in the case of i_{DC} application.

Consequently, Ohm's behaviour of the electrode/electrolyte boundary—i.e., before U_{dec} is reached and before the *non-linear behaviour* of the boundary becomes prominent, see Footnote 22 and Fig. 3.14—is only valid for the relatively *small current levels* (of i_{DC} or i_{AC}), named as the *limit current density of linearity* [according to Schwan (1992)]. However, it is even more important to derive from the above discussion that this limit current density depends on *f*.

In particular, the *limit current density decreases with decreasing f* and, as an approximation, is *proportional to* $\sqrt{f}$ (Schwan 1992). Both following mechanisms contribute to this frequency dependence:

- the lower *f*, the lower is the shunt current $i_{AC,C}$ [$=(u_{pol,i} - U_{pol}) \cdot 2\pi \cdot f \cdot C_{el}$ in line with Fig. 3.19c] and thus the higher is the residual $i_{AC,E}$ through R^{t}_{el}; on the other hand,
- the lower *f*, the smaller is the voltage fraction across R^{t}_{el} and thus the smaller is $i_{AC,E}$ through R^{t}_{el} (see above).

Electrode Impedance as a Nyquist Plot

The influence of the limited *dynamics of electro-kinetic processes* within boundary on the *complex electrode impedance* $\underline{Z}_{el}$ (3.33) is schematically illustrated in Fig. 3.18 *for the varying f* of the applied u_{AC} (or i_{AC}). Here the *electrode reaction* of the *sensing electrode* (Fig. 3.18a) is kinetically limited by both *inert charge-transfer* and *inert diffusion processes*, i.e., none of these processes determines exclusively the *total reaction kinetics*. In order to model $\underline{Z}_{el}$, a *simplified electrical equivalent circuit model* from Fig. 3.20a (3.33) is used here (Fig. 3.18b),

whereas $\underline{Z}^{c}_{el}$ (=0) along with $R_{electrol}$ (=0) are neglected and $\underline{Z}^{d}_{el}$ (=R^{d}_{el}) is assumed to be real-valued for instructive purposes.

The variation of the total $\underline{Z} = \underline{Z}_{el} + R_b + \underline{Z}'_{el} \approx \underline{Z}_{el} + R_b$ (3.26) between the sensing and reference electrodes is depicted in Fig. 3.18c with increasing f within the *complex plane* as a *Nyquist*[38] *plot*. That is, the *imaginary part* of $\underline{Z}$ is plotted over its *real part* as a function of f. In the plotted $\underline{Z}$, the impedance $\underline{Z}'_{el}$ of the *perfectly non-polarizable reference electrode* is also neglected (Fig. 3.18a, b), i.e., $\underline{Z}'_{el} \approx 0$ applies due to the assumed $u'_{pol,i} \approx U'_{pol} \approx 0$ (Footnote 30). The body impedance $\underline{Z}_b$ is approximated as a real-valued R_b (Fig. 3.18b) according to the *simplified tissue model* from Fig. 3.2a and (3.1). Furthermore, we assume the inequality $u_{AC} < U_{dec}$ in order to *exclude a possible non-linearity of* R^{t}_{el} (see above), especially that pertaining to the *polarizable sensing electrode* (Fig. 3.17b).

In Fig. 3.18, the arbitrarily assumed size of R^{t}_{el} (=100 Ω) does not change with f while that of R^{d}_{el} does, in line with the discussed theory. According to Footnote 35, reactants have to diffuse to/from the electrode surface over relatively long distances for *low f* (<70 Hz, as arbitrarily assumed in Fig. 3.18) so that the associated diffusion resistance R^{d}_{el} (=200 Ω) is assumed to be quite high in this range of f. This *inert diffusion inhibits the total reaction kinetics* on the surface of the sensing electrode and limits the inherently fast *alternating charge transfer process*, i.e., limits the downstream charge transfer process across the boundary of this electrode. The diffusion inhibits the associated *alternating conductive* $i_{AC,E}$ across the boundary due to the high $R^{d}_{el} > R^{t}_{el}$ (of this boundary's $\underline{Z}_{el}$, see Fig. 3.18b).

- Thus, the resulting total *electrode resistance* R_{el} (=$R^{t}_{el} + R^{d}_{el}$ = 300 Ω) is relatively high for *low f* (<70 Hz), see the *circuit model* in Fig. 3.18b. This large R_{el} causes the total $\underline{Z}$ to move along the *large semi-circle A* in Fig. 3.18c with increasing f. The *circle's diameter* equals to $R^{t}_{el} + R^{d}_{el}$ and its *center* is located at coordinates $\mathrm{Re}(\underline{Z}) = (R^{t}_{el} + R^{d}_{el})/2 + R_b$ and $\mathrm{Im}(\underline{Z}) = 0$.
- With increasing f above 70 Hz, the *diffusion inhibits progressively less and less* the downstream charge transfer and thus the *total reaction kinetics*. Correspondingly, at *medium f* (70 Hz $\leq f \leq$ 90 Hz), the resistance R^{d}_{el} disappears progressively within the circuit model (Fig. 3.18b) while the total resistance $R_{el} = R^{t}_{el} + R^{d}_{el}$ decreases towards R^{t}_{el} (i.e., R_{el} decreases from 300 to 100 Ω). Therefore, the resulting magnitude of the total $\underline{Z}$ decreases as well, as we move along the *line segment B* in Fig. 3.18c.
- For *high f* above 90 Hz, the influence of the *diffusion is assumed to disappear* and the least constrained downstream *charge transfer across the boundary dominates* with its smallest $R_{el} = R^{t}_{el}$ (<$R^{t}_{el} + R^{d}_{el}$). Here the complex $\underline{Z}$ follows

[38]Harry Nyquist (1889–1976) was a Swedish born American physicist and electrical engineer after which the *Nyquist plot* was named. The Nyquist plot depicts the imaginary part of a complex quantity, complex impedance, or even a complex transmission function over its real part as a function of another parameter such as frequency (Fig. 3.18c). He also laid foundations of the information and signal sampling theories.

the *small semi-circle C* in Fig. 3.18c with its *diameter* equal to R_{el}^{t} and its center located at $\mathrm{Re}(\underline{Z}) = R_{el}^{t}/2 + R_b$ and $\mathrm{Im}(\underline{Z}) = 0$. For the *semi-infinite* $f \to \infty$, the impedance $\underline{Z}$ converges towards a real-valued $\underline{Z} = R_b$ of the bodily tissue.

In general, when *f of* u_{AC} *increases*, the *magnitude* $|\underline{Z}|$ *of* $\underline{Z}$ (3.26) decreases. Figure 3.18 illustrates this behaviour in that the magnitude $|\underline{Z}| = R_{el}^{t} + R_{el}^{d} + R_b = 320\ \Omega$ has its maximum at $f = 0$ and then decreases steadily with increasing f to its minimum $|\underline{Z}| = R_b = 20\ \Omega$ at $f \to \infty$.

It can be observed in Fig. 3.18c that the total $\underline{Z}$ is *predominantly real* for both the *very low f* with the associated $\underline{Z} \approx R_{el}^{t} + R_{el}^{d} + R_b$ and the *very high f* with $\underline{Z} \approx R_b$. A relatively *small phase angle* $\arg(\underline{Z}) = \varphi_1$ applies at these two extremes. The impedance $\underline{Z}$ is *strictly real* (i.e., $\arg(\underline{Z}) = 0$) at $f = 0$ with the associated $\underline{Z} = R_{el}^{t} + R_{el}^{d} + R_b = 320\ \Omega$ [i.e., the double layer capacitance C_{el} does not play any role in $\underline{Z}_{el}$ due to its infinite interfacial capacitive impedance $1/(j\omega C_{el}) \to \infty$ at $f = 0$, see (2.42)] and at $f \to \infty$ with $\underline{Z} = R_b = 20\ \Omega$ (here C_{el} acts as a short-circuit to $R_{el} = R_{el}^{t} + R_{el}^{d}$ with its zero $1/(j\omega C_{el}) = 0$ at $f \to \infty$). For *intermediate f*, significant *real and imaginary components* arise in $\underline{Z}$ with the relatively *large phase angle* $\arg(\underline{Z}) = \varphi_2 > \varphi_1$ (Fig. 3.18c).

Ag/AgCl and Pt Electrodes

Ag/AgCl Electrodes

The *active application of* u_{DC} (or i_{DC}) across two *Ag/AgCl electrodes—non-polarizable reference electrodes* in contact with *tissue/electrolyte*—is shown in Fig. 3.11c. Here tissue is approximated as *NaCl physiological solution* (Footnote 27 in Chap. 2). Charged ions within the AgCl electrodes (3.14) and ions within tissue are subjected to driving forces leading to *migration* and *electrode reactions* (with their relatively *small activation barriers*, see Footnote 22) due to the applied *electric fields* within Ag/AgCl electrode layers and within tissue.

In fact, provided that a *finite current* $i_{DC} \neq 0$ is applied between two Ag/AgCl electrodes in contact/series with tissue/electrolyte (Fig. 3.11c),

- *AgCl* at the *cathode* (minus pole; see Fig. 3.13c) is *decomposed* through neutralisation (or *reduction*) of Ag^+ cations (3.14); i.e., Cl^- anions leave the electrode towards the electrolyte while pure *metallic silver* appears on the electrode surface. The reduction of Ag^+ ions consumes electrons while these *electrons* carry the electric charge through the connected lead wire. Consequently, a *positive conductive current leaves the cathode* or, in analogy, the negative i_{DC} (<0) from Fig. 3.11c enters the cathode. Here the *total dominating electrolytic reaction* is $AgCl + e^- \to Ag + Cl^-$, i.e., the cathode reduces AgCl (in line with Footnote 19) with both contributing reactions shown in Fig. 3.11c. This *decomposition* of AgCl is also indicated in Fig. 3.17d for $i_{DC} < 0$ and in Fig. 3.15c.

- At the *anode* (plus pole), metallic Ag is *oxidized* into Ag^+ cations by this electrode and an additional *AgCl is formed* with Cl^- anions coming from the electrolyte (3.14). The oxidation of Ag^+ ions provides *electrons* to the connected lead wire, i.e., the positive *conductive current* i_{DC} *enters the anode*. Here the *total dominating electrolytic reaction* is $Ag + Cl^- \rightarrow AgCl + e^-$, i.e., the anode accepts e^- from Ag (Footnote 19) with both contributing reactions shown in Fig. 3.11c. In analogy, the *formation* of AgCl is indicated in Fig. 3.17d for $i_{DC} > 0$ and in Fig. 3.15c.
  Please note that, in contrast to the metal ion electrode (Fig. 3.4a, b), *toxic metal ions* Ag^+ of Ag advantageously do not enter biological tissue at the anode, but instead bind to Cl^- anions and then *precipitate as poorly soluble AgCl* at the anode (Footnote 20).

Please recall that the *decomposition voltage* U_{dec} is rather small for *non-polarizable electrodes* (see Section "Direct Voltage Application") and thus is not applicable to the *non-polarizable Ag/AgCl electrode*. This is because the *charge transfer* across the Ag/AgCl electrode boundary is rather *unconstrained* with the associated *high exchange current density* and a *low charge-transfer resistance* R_{el}^t (see Footnote 22 and Fig. 3.14). From a practical point of view, even a small change in u_{DC} between two Ag/AgCl electrodes yields an already finite and markable change in i_{DC} through these electrodes, whereas changes in u_{DC} and i_{DC} are mutually interrelated via the *effective differential resistance* $R_b \approx \Delta u_{DC} / \Delta i_{DC}$ ($\gg R_{el}^t$) of the bodily tissue, as discussed in Fig. 3.17d.

Pt Electrodes

In comparison with *non-polarizable Ag/AgCl electrodes*, *polarizable Pt electrodes* in contact with *tissue/electrolyte* (again approximated as *NaCl physiological solution* in water) should be discussed below. In fact, we assume an *active application of* u_{DC} (or i_{DC}) across two *Pt electrodes* in contact with *tissue/electrolyte*, as illustrated in Fig. 3.12a. Here a *finite current* $i_{DC} \neq 0$ is carried by *electrode reactions* based on different mechanisms (with their relatively *large activation barriers*, see Footnote 22), i.e., reactions based on *different discharge processes* (Grimnes and Martinsen 2008; Hamann and Vielstich 1998):

- At the Pt *cathode* (minus pole), Na^+ ions are typically not reduced due to a low electronegativity of Na^+ ions according to the associated reaction $Na^+ + e^- \rightarrow Na$ with its quite low $U_{pol} = -2.71$ V. In other words, a very low potential of the cathode would be needed to reduce Na^+ ions with the associated $u_{pol,i} < U_{pol} = -2.71$ V (compare the cathode in Fig. 3.13c). Pt atoms are not reduced as well since Pt^+ ions are absent within the electrolyte.

Instead, *reduction*[39] *of dissolved neutral oxygen* O_2—typically present only in low concentrations in tissue/electrolyte—(at the relatively low u_{DC} or i_{DC} with the reaction $O_2 + 4 \cdot H^+ + 4 \cdot e^- \rightarrow 2 \cdot H_2O$ and its $U_{pol} = 1.23$ V) and *decomposition of water molecules* H_2O take place (at even lower u_{DC} or higher i_{DC} with the decomposition reaction $2 \cdot H_2O + 2 \cdot e^- \rightarrow H_2 + 2 \cdot OH^-$ and its $U_{pol} = -0.41$ V in *neutral solutions* (Hamann and Vielstich 1998)). This *water decomposition*—known as *water reduction*—leads to formation of *H_2 gas* bubbles and to a *basic solution* with OH^- anions at the cathode when $u_{pol,i} < -0.41$ V (i.e., along the cathodic/reduction branch of Butler-Volmer equation, compare Fig. 3.15c). It should be recalled that relative amounts of the reduced O_2 and decomposed H_2O—i.e., relative levels of the associated i_{DC} at a given u_{DC} level—depends not only on the respective U_{pol} of the above electrode reactions but also on the respective exchange current densities (Footnote 22). The latter dependence of i_{DC} on the *exchange current density* is particularly strong for polarizable electrodes such as Pt electrodes (Fig. 3.14 and see below). Please note that in neutral solutions a direct reduction of H^+ ions (see its redox reaction with $U_{pol} = 0$ V in Footnote 18) can not be expected due to their low concentration and, moreover, due to a very weak *autodissociation* of water molecules (Footnote 29 in Chap. 2). Figure 3.15c demonstrates also the *reduction of O_2* on the cathode based on the charge transfer process.

- At the Pt *anode* (plus pole), Cl^- ions are typically oxidized to form *Cl_2 gas* ($2 \cdot Cl^- \rightarrow Cl_2 + 2 \cdot e^-$ with $U_{pol} = 1.37$ V). With increasing u_{DC} or i_{DC}, OH^- ions may be discharged/oxidized to carry an additional amount of i_{DC} ($4 \cdot OH^- \rightarrow O_2 + 2 \cdot H_2O + 4 \cdot e^-$ with $U_{pol} = 0.4$ V). With even higher u_{DC} or i_{DC}, *water is decomposed*—known as *water oxidation*—according to $2 \cdot H_2O \rightarrow O_2 + 4 \cdot H^+ + 4 \cdot e^-$, which leads to *formation*[40] *of O_2 gas* bubbles

[39] *Pt surface* acts as a *catalyser* for the *reduction of neutral and dissolved oxygen O_2*; compare Footnote 40. *Specific adsorption* and *deadsorption* of oxygen atoms on Pt surface comprise highly important *intermediate reaction steps* for the *following reduction of oxygen* (Hamann and Vielstich 1998). To be precise, *specific adsorption* of both oxygen atoms on Pt surface—with a particular spatial orientation of these oxygen atoms on the surface—yields mechanical stretching forces between these atoms (*bond stretching*). These forces, in turn, weaken the covalent bond between the two oxygen atoms. Consequently, the weakened bond allows hydrogen atoms to reduce both oxygen atoms (e.g., with a successive formation of water molecules in acid solution, see below).

- In *acid solution*, the dissolved O_2 is *directly reduced* according to the total reaction $O_2 + 4 \cdot H^+ + 4 \cdot e^- \rightarrow 2 \cdot H_2O$ (with $U_{pol} = 1.23$ V), whereas
- O_2 in *basic solution* is *directly reduced* according to the total reaction $O_2 + 2 \cdot H_2O + 4 \cdot e^- \rightarrow 4 \cdot OH^-$ ($U_{pol} = 0.4$ V).

Please note that here is also an *indirect way* of O_2 reduction to H_2O via an intermediate product H_2O_2 (hydrogen peroxide) in acid solution; alternatively, O_2 can be reduced to OH^- via HO_2^- (peroxide ion) in basic solution.

[40] In close analogy with Footnote 39, *Pt surface* acts as a *catalyser* for the *formation of O_2* (or, in other words, oxidation of oxygen atoms). Here *specific adsorption* and *deadsorption* of $OH^\bullet$ *radicals* (formed out of H_2O or OH^-, respectively; see below) on Pt surface—as *intermediate reactions steps*—play an important role in the *following formation of O_2* (Hamann and Vielstich 1998).

and to an *acid solution* with H^+ cations at the anode. Figure 3.15c demonstrates this *oxidation/formation of* O_2 on the anode based on the charge transfer process only.

The range of $u_{pol,i}$—or, in analogy, the range of the applied u_{DC}—between the *water reduction and water oxidation* is frequently called the *water window* (Cogan et al. 2016). If the polarization of an electrode, such as Pt electrode during a *stimulation pulse*, remains positive of the water reduction potential (with $u_{pol,i} > -0.41$ V when the pulse is at its minimum) and negative of the water oxidation potential (with $u_{pol,i} < 1.23$ V when the pulse is at its maximum)—that is the polarization remains within the water window—the resulting charge density of the pulse is often considered as *safe*. Within the water window, the rates of the water reduction and oxidation are negligible, whereas outside this window reactions proceed at sufficient rates and may cause damage to tissue.

Please note that *reaction products* (e.g., OH^- or H^+ ions) obtained from the aforementioned reactions can be potentially *damaging to tissue* and electrode material (e.g., in terms of the varying *pH-value*). In general,

- *reversible electrode reactions* can be usually regarded as biologically safe because reaction products do not leave the electrode and can be transferred back to the original substance by reversal of $u^t_{pol,i}$. Please note that the *safe charge injection limit* is associated with the voltage range of $u_{pol,i}$ (across the electrode/electrolyte boundary) within which only *reversible reactions* occur (Weissenrieder 2009); see Sections "Charge Transfer During Stimulation and Neural Stimulation" for more detailed and critical discussion on this limit. For instance, this limit can be favorably increased by increasing the *surface area of the electrode* (Section "Electrode Impedance Model") and thus decreasing the effective *charge density and current density* (2.158). In other words, charge density and/or electrode potential have to be kept within certain limits to avoid irreversible reactions. In contrast,
- *irreversible reactions*—e.g., with *gas evolution* and bubbling out—are undesirable since they form irreversible products that escape from the electrode, may accumulate and *harm tissue* (e.g., increase the risk of tissue inflammation via changes of the pH-value). In addition, irreversible reactions may cause *corrosion of the electrode* (degradation or *dissolution of the metal*, see Fig. 3.4a) and may form *insulating oxides* on the electrode surface.

- In *acid solution*, O_2 is formed with the *total reaction* $2 \cdot H_2O \rightarrow O_2 + 4 \cdot H^+ + 4 \cdot e^-$ (with $U_{pol} = 1.23$ V), whereas
- in *basic solution* O_2 is formed with the *total reaction* $4 \cdot OH^- \rightarrow O_2 + 2 \cdot H_2O + 4 \cdot e^-$ ($U_{pol} = 0.4$ V).

In general, effective *metal catalysers* for O_2 *formation* are also effective for O_2 *reduction*. Please note that by-products of oxygen reduction and oxygen formation can be damaging to tissue.

It is instructive to add that most *radicals* are highly chemically reactive (because of unpaired valance electrons) and thus show a very short lifetime (in the range of ns) and abreact directly from their adsorbed state right on the metal surface.

In fact, redox reactions at the surface of the Pt electrode may involve the *electrode material* itself (or its coating) and surface confined species. For instance, *Pt oxide can be formed* (at anode) and *Pt oxide reduced* (at cathode) within the reversible reaction $Pt + H_2O \leftrightarrow PtO + 2 \cdot H^+ + 2 \cdot e^-$ (with $U_{pol} = 0.75$ V), or *H-atoms can be plated* according to $Pt + H_2O + e^- \leftrightarrow Pt\text{-}H + OH^-$ (Cogan et al. 2016). Please note that these reactions are accompanied by the release or consumption of H^+ and OH^- ions and thus by associated changes of the *pH-value* of tissue/electrolyte, which may be harmful.

As discussed above, the following *factors* could cause *damage to tissue and/or electrode material*:

- formation of *gas bubbles*, e.g., formation of H_2 on Pt cathode and O_2 on Pt anode;
- changing of *pH-value*, e.g., formation of Pt oxide at anode;
- generation of *toxic by-products*, e.g., OH^- or H^+ ions (from above) or through oxidation of the saline as present in the physiological solution at Pt anode according to the reaction $Cl^- + H_2O \rightarrow ClO^- + 2 \cdot H^+ + 2 \cdot e^-$ (at about $U_{pol} = 0.8$ V), or even through oxidation of organic molecules in the solution;
- *formation of Pt oxide* (see above); and
- *dissolution of Pt* electrode, e.g., through oxidation reaction at Pt anode with involved Cl^- ions from the physiological solution according to the reaction $Pt + 6 \cdot Cl^- \rightarrow [PtCl_6]^{2-} + 4 \cdot e^-$ (at about $U_{pol} = 0.7$ V).

To give a practical example, let us consider a strong rectangular *biphasic current pulse* which is applied to a Pt electrode in contact with tissue/electrolyte, with the preceding *cathodic phase* and the following *anodic phase*, as illustrated in Fig. 2.75a. With the *onset of the cathodic phase*, *non-Faradaic reaction begins*. That is, the *capacitive charging of the double layer begins* because the activation overvoltage $u_{pol,i} - U_{pol} = u^t_{pol,i}$—determining *Faradaic reactions* within the boundary (Footnote 22)—is zero at the time of the phase onset. In fact, $u^t_{pol,i}$ is steady in its temporal course and thus can not abruptly change because $u^t_{pol,i}$ drops across C_{el} in parallel to R^t_{el} according to Fig. 3.20c; please note that the voltage across a capacitor is always steady as long as the current through the capacitor is finite (2.40). Afterwards, given a finite $u^t_{pol,i} \neq 0$, *Faradaic reactions* can start and run during the ongoing cathodic phase such as H-atom plating, evolution of H_2 (decomposition of water), reduction of Pt oxide and other (Rattay 1990). After the end of the cathodic phase and with the *onset of the anodic phase*, i.e., with the reversal of the current through the boundary, double layer recharging starts (non-Faradaic reactions), followed by a formation of Pt oxide, evolution of O_2 (decomposition of water) and other (Faradaic reactions).

The voltage U_{dec} is applicable to the *polarizable Pt electrode*. This is because the discussed *charge transfer processes* (or specific *discharge processes*) across the phase boundary of this electrode have typically *large activation barriers* with their correspondingly *low exchange current densities* (Footnote 22). Likewise, the *charge transfer remains constrained* for the relatively low *activation overvoltage* $|u_{pol,i} - U_{pol}| = |u^t_{pol,i}| < U_{dec}$ (of a particular *discharge process*, see Fig. 3.14) with the associated *high* R^t_{el} (3.17). This charge transfer becomes *unconstrained* only for

the relatively high $|u_{pol,i} - U_{pol}| = |u^t_{pol,i}| > U_{dec}$ with the associated *low* R^t_{el} (Figs. 3.14 and 3.17b, d). Furthermore, it is instructive to observe that

- the *onset of the effective contributions* of the different *electrode reactions* (or discharge processes)—such as the reduction of O_2 and decomposition of H_2O at the Pt cathode—*to the total* i_{DC} across the electrode/tissue boundary is a dedicated *function of* U_{pol} of the respective electrode reaction, provided that u_{DC} *is applied*. That is, the inequality $u_{pol,i} \neq U_{pol}$ (of a particular electrode reaction) determines this *reaction's onset* and its type (i.e., oxidation reaction for $u_{pol,i} > U_{pol}$ or reduction for $u_{pol,i} < U_{pol}$), as illustrated in Fig. 3.14 and detailed in Footnote 22. However,
- the *absolute extent of the effective contributions* of the different *electrode reactions to the total* i_{DC} is proportional to both the magnitude $|u^t_{pol,i}| = |u_{pol,i} - U_{pol}|$ of the *activation overvoltage* and the *exchange current* i_0 of a particular electrode reaction (Footnote 22), as can be observed in Fig. 3.14. Likewise, the larger i_0 of a certain electrode reaction, the larger is its associated contribution to the total i_{DC} for a given $|u^t_{pol,i}|$.

Recording Versus Stimulation

Please note that *AgCl electrodes* are usually used as *surface electrodes* on the skin (Fig. 3.1b) for *recording/diagnostic purposes*. *Pt electrodes* are usually used as *implanted electrodes* within the body (Fig. 3.1c) for *stimulating/therapeutic purposes* (Footnote 136 in Chap. 2).

In the case of an *active application of voltages* in terms of *therapy*, i.e., the *application of a voltage stimulus u* through the skin into tissue with (at least) two *contact electrodes*, the *polarization voltages* $u_{pol,i}$ and $u'_{pol,i}$ of both electrodes (Fig. 3.12a) diminish the *therapeutic voltage drop* u_b within tissue, as illustrated in Fig. 3.25c. In analogy, the applied u is larger than the voltage u_b within the *undisturbed electrolyte* according to Fig. 3.12a. In fact, the output u of the *therapeutic device* drops across the *series connection* of $u_{pol,i}$, $u'_{pol,i}$, and u_b (Figs. 3.12a and 3.25d). Consequently, the effective sizes of $u_{pol,i}$ and $u'_{pol,i}$ influence also the resulting *therapeutic current i* available in the bulk suspension of tissue cells, as shown in (3.40). Please recall that the size of $u_{pol,i}$ is also the discussed *non-linear function* of both i and the *field frequency f* (when an alternating $u = u_{AC}$ is applied). In short, the magnitude $|u_{pol,i}|$ tends to increase with increasing $|i|$ (see Figs. 3.14 and 3.19) and with decreasing f (Fig. 3.18c), so that the therapeutic i and u_b become strong non-linear functions of the applied u and f. Likewise, an efficient *coupling of therapeutic fields into the bodily tissue* can be expected for small i and/or for high f (and thus for small $u_{pol,i}$ in series with u_b).

In analogy to therapy, in terms of *diagnostic and passive recording of voltages* on the skin, the polarization voltages $u_{pol,i}$ and $u'_{pol,i}$ of both *contact electrodes* can also be seen in series with the output voltage of the relevant biosignal's source within the body, in line with Fig. 3.24d. Therefore, the effective sizes of $u_{pol,i}$ and $u'_{pol,i}$ influence also the resulting *diagnostic outcome*, e.g., the *diagnostic current i* in Fig. 3.24d according to (3.38).

Electrode Impedance Model

When designing and operating a *diagnostic or therapeutic system* with *electrodes* in contact with *biological tissue*, the *electrode/electrolyte boundary* is critical to the proper operation of electrodes. For instance, electrical properties of the boundary change over time due to *tissue encapsulation* close to electrodes. Movements of electrodes typically change boundary properties as well.

Therefore, an appropriate *model of the electrode/electrolyte boundary* is of paramount practical and scientific importance. Foundations for this model are already given by the described behaviour of the *electrode/electrolyte boundary* in the course of an active application of the *direct and alternating voltage/current* across two electrodes in contact with tissue (Section "Active Current or Voltage Application Between Electrodes").

In particular, the *polarization voltage* U_{pol} across the boundary (defined for different activities on the phase boundary, see (3.4) and (3.13), and for the *currentless case* with $i = 0$ through this boundary, see Fig. 3.6) in series with the *complex electrode impedance* $\underline{Z}_{\mathrm{el}}$ (with its *magnitude* $|\underline{Z}_{\mathrm{el}}|$ and *phase* $\arg(\underline{Z}_{\mathrm{el}})$) should be considered within this *boundary model*. This series connection accounts for the *total polarization voltage* $u_{\mathrm{pol,i}}$ ($>U_{\mathrm{pol}}$) across the boundary when *finite current* i (>0) is given, as illustrated in Figs. 3.12 and 3.19.

Figure 3.19 illustrates *electrical equivalent circuit models* of the electrode/tissue boundary for the *direct and alternating voltage/current application*. These models consider all three discussed *electro-kinetic processes* which form and determine the *electrode reaction*, i.e.,

- from the *mass transport* to/from the electrode surface,
- to *coupled reactions* on the surface (e.g., adsorption), and
- up to the real *charge transfer* across the boundary.

Please note that additional reaction steps, such as successive reaction steps or parallel processes of complex electrode reactions, could be considered by additional circuit elements, connected in series or in parallel, respectively.

To begin with, Fig. 3.19b shows the *boundary model* for the *direct voltage/current* u_{DC} / i_{DC} *application*. Obviously, the complex $\underline{Z}_{\mathrm{el}}$ mutates into the *real electrode resistance* R_{el} which can be approximated as a series connection [compare (3.20)] according to

$$R_{\mathrm{el}} \approx R_{\mathrm{el}}^{\mathrm{t}} + R_{\mathrm{el}}^{\mathrm{c}} + R_{\mathrm{el}}^{\mathrm{d}} + R_{\mathrm{electrol}}. \tag{3.31}$$

Here $R_{\mathrm{el}}^{\mathrm{t}}$ is the *charge-transfer resistance* (3.17), $R_{\mathrm{el}}^{\mathrm{c}}$ the resistance contribution due to inert *coupled reactions* (3.19), $R_{\mathrm{el}}^{\mathrm{d}}$ the *diffusion resistance* (3.18), and R_{electrol} the relatively small ohmic *resistance of the undisturbed electrolyte* close to the electrode surface (typically, the resistance of *electrode gel or paste*). Please note that the

double layer capacitance C_{el} (3.5)—as indicated in Fig. 3.19b—does not play any role in (3.31) as long as *voltages and currents* are in their *steady state*.[41]

For the *alternating voltage/current* u_{AC} / i_{AC} *application* with the *field frequency* f, Fig. 3.19c depicts the associated *boundary model*. Here the *electrode impedance* $\underline{Z}_{el}$ obeys

$$\underline{Z}_{el} = \frac{1}{\frac{1}{R^t_{el} + \underline{Z}^c_{el} + \underline{Z}^d_{el}} + j \cdot \omega \cdot C_{el}} + R_{electrol}, \tag{3.32}$$

where $\underline{Z}^d_{el}$ is the *complex diffusion impedance* [*Warburg impedance*, see Footnote 35 and (3.29)] and $\underline{Z}^c_{el}$ the *complex impedance due to inert coupled reactions* (3.30). For *adsorption processes* on the electrode surface, this impedance $\underline{Z}^c_{el}$ is typically represented as a *parallel connection of a resistor and capacitor*, as illustrated in Fig. 3.19c and discussed qualitatively with respect to (3.30) (Hamann and Vielstich 1998).

This model of Fig. 3.19c and (3.32) for the *alternating* u_{AC} / i_{AC} *application* is quite complex and can be reasonably simplified/differentiated into two specific cases

- the *diffusion-limited electrode reaction* (Footnote 27) and
- the *charge-transfer-limited electrode reaction* (Footnote 28),

as illustrated in Fig. 3.20. In particular, the *diffusion-limited electrode reaction* of the boundary (Fig. 3.20a) *yields* $\underline{Z}_{el}$ according to

$$\underline{Z}_{el} \approx \frac{1}{\frac{1}{R^t_{el} + \underline{Z}^d_{el}} + j \cdot \omega \cdot C_{el}} + R_{electrol} = \frac{(R^t_{el} + \underline{Z}^d_{el})/j \cdot \omega \cdot C_{el}}{R^t_{el} + \underline{Z}^d_{el} + 1/j \cdot \omega \cdot C_{el}} + R_{electrol}. \tag{3.33}$$

In contrast to the complete circuit in Fig. 3.19c and (3.32), the impedance $\underline{Z}^c_{el}$ is *neglected* in (3.33) (i.e., $\underline{Z}^c_{el} = 0$) and thus a potential kinetic inhibition of the total electrode reaction due to *coupled reactions*. The associated circuit model of the

[41] A *steady state*—see Footnote 4—implies that *amplitudes of all voltages and currents* in the *electrical equivalent circuit model* of the *electrode/tissue boundary* (Fig. 3.19b) *do not change in time*, i.e., their *time derivatives* are zero. In particular, it means that the capacitive *current* i_C *though* C_{el} *must be zero*, otherwise the voltage u_C across the capacitor would accordingly change in line with (2.40).

In other words, C_{el} does play a decisive role during *transient states* of voltages and currents, e.g. when they are switched on or off. After such switching processes, the circuit in Fig. 3.19b stays in its *transient state*—in order to recharge C_{el}—for a certain *characteristic time* of about $5 \cdot \tau$ with τ as the *time constant* of this circuit. Consequently, after about $5 \cdot \tau$ from the last switching activity, a *steady state* can again be assumed in the circuit model of Fig. 3.19b.

As an approximation, the constant τ can be estimated from Fig. 3.19b as $\tau = C_{el} \cdot (R^t_{el} + R^c_{el} + R^d_{el})$ with an assumed external *current source* connected to the electrode. For an external *voltage source*, this constant τ would be lower and mainly determined by the relatively low $R_{electrol}$ in series with the body resistance (with the assumed $R_{electrol} \ll R^t_{el} + R^c_{el} + R^d_{el}$).

diffusion-limited reaction in Fig. 3.20a is also known as *Randles circuit*,[42] a *Faradaic impedance* ($=R_{el}^{t} + \underline{Z}_{el}^{d}$, see below) *shunted by* an interfacial *capacitive impedance* ($=1/(j2\pi \cdot f \cdot C_{el})$, in series with $R_{electrol}$. Please note that the Randles circuit assumes a semi-infinite spatial extension of the *diffusion layer* (the *diffusion layer thickness* $\delta_D^T \rightarrow \infty$). As elaborated in Footnote 35, the impedance $\underline{Z}_{el}^{d}$ in Fig. 3.20a is approximated as a series connection of a *pseudo-resistance* and *pseudo-capacitance* in line with the semi-infinite δ_D^T.

For the relatively *low f*, the *impedance* $\underline{Z}_{el}$ of the *diffusion-limited reaction* [from (3.33)] simplifies to

$$\underline{Z}_{el} \approx R_{el}^{t} + \underline{Z}_{el}^{d} + R_{electrol}. \tag{3.34}$$

In terms of this *low f*, the inequality $f \ll 1/(2\pi \cdot (R_{el}^{t} + |\underline{Z}_{el}^{d}|) \cdot C_{el})$ applies in Fig. 3.20a as an approximation (when an external current source supplies i_{AC}, compare Footnote 41). Provided that the *thickness* δ_D^T is semi-infinite ($\delta_D^T \rightarrow \infty$) and *f is low*, the associated $\underline{Z}_{el}$ converges towards $\underline{Z}_{el}^{d}$ ($\gg R_{el}^{t} + R_{electrol}$) and thus to the shifted *Warburg line* of $\underline{Z}_{el}^{d}$ (Footnote 35). This is illustrated in the *complex plane* of Fig. 3.20d; see the *model A for semi-infinite* δ_D^T.

In contrast to $\delta_D^T \rightarrow \infty$, a *finite thickness* $\delta_D^T = \delta_D$ of the *diffusion layer* yields finite values of $\underline{Z}_{el}^{d}$ for *low f* (and even a real value of $\underline{Z}_{el}^{d}$ for $f \rightarrow 0$ according to Footnote 35) and thus yields a quite different course of $\underline{Z}_{el}$ for low *f*. Figure 3.20d illustrates this case; see the *model A for finite* $\delta_D^T = \delta_D$. From a biophysical point of view, the lower *f*, the stronger is the influence of the *diffusion* within the total *kinetics of the electrode reaction*, i.e., the *diffusion-limited electrode reaction* dominates at *low f*.

Please note that the *Nyquist plot* from Fig. 3.18c *mimics the plot of the model A* for finite $\delta_D^T = \delta_D$ in Fig. 3.20d. In fact, Fig. 3.18c assumes a real-valued $\underline{Z}_{el}^{d}$ ($=R_{el}^{d}$)—for the sake of simplicity—which decreases from 200 Ω to zero with increasing *f*, in *qualitative analogy* with the theory-based proportionality $\underline{Z}_{el}^{d} \propto 1/\sqrt{f}$ (from Footnote 35) shown *quantitatively* in Fig. 3.20d. Both plots from Figs. 3.18c and 3.20d demonstrate *shape similarities* with two *interconnected semi-circles*.

With *increasing f* of the *diffusion-limited electrode reaction*, the *diffusion influence vanishes* (Footnote 35) while the contributing electro-kinetic process of the *charge transfer starts to dominate* the total kinetics of the electrode reaction. That is, the *diffusion-limited electrode reaction* mutates into a *charge-transfer-limited electrode reaction* with increasing *f*.

Since the *impedance* $\underline{Z}_{el}^{d}$ *disappears* for *high f* (i.e., $\underline{Z}_{el}^{d} = 0$ for $f \rightarrow \infty$), it leads to the following *simplification of* $\underline{Z}_{el}$ [from (3.33)] with neglected $\underline{Z}_{el}^{d}$ according to

[42]John Edward Brough Randles (1912–1998) was an English electrochemist who laid the seeds of the electrochemical impedance considering diffusion and interfacial electron transfer, as well as introduced linear sweep voltammetry, which opened up a new method to study fast electrode reactions.

$$\underline{Z}_{\mathrm{el}} \approx \frac{1}{\frac{1}{R^{\mathrm{t}}_{\mathrm{el}}} + \mathrm{j}\cdot\omega\cdot C_{\mathrm{el}}} + R_{\mathrm{electrol}} = \frac{R^{\mathrm{t}}_{\mathrm{el}}/\mathrm{j}\cdot\omega\cdot C_{\mathrm{el}}}{R^{\mathrm{t}}_{\mathrm{el}} + 1/\mathrm{j}\cdot\omega\cdot C_{\mathrm{el}}} + R_{\mathrm{electrol}}. \tag{3.35}$$

In other words, the parallel connection of $R^{\mathrm{t}}_{\mathrm{el}}$ and C_{el} in series with R_{electrol} effectively determines $\underline{Z}_{\mathrm{el}}$ for high *f*. This is illustrated within the *model A* for $\underline{Z}^{\mathrm{d}}_{\mathrm{el}} = 0$ in Fig. 3.20d and within the *model B* in Fig. 3.20e. It should be stressed that (3.35) is applicable for the relatively *high f* of the *diffusion-limited electrode reaction* and, on the other hand, for the *charge-transfer-limited electrode reaction* (see below).

Correspondingly, as depicted in the *complex plane* of Fig. 3.20d, the low-frequency course of $\underline{Z}_{\mathrm{el}}$ (i.e., the *model A* for semi-infinite $\delta^{\mathrm{T}}_{\mathrm{D}}$ and the model A for finite $\delta^{\mathrm{T}}_{\mathrm{D}}$), including the *Warburg line*, *approaches and merges into a semi-circle* with *increasing f* (i.e., merges into the *model A* for $\underline{Z}^{\mathrm{d}}_{\mathrm{el}} = 0$). For *very high* $f \to \infty$, the impedance $\underline{Z}_{\mathrm{el}}$ converges towards a real valued $\underline{Z}_{\mathrm{el}} = R_{\mathrm{electrol}} = 20\ \Omega$. The latter semi-circle is determined by the *charge transfer process* only. Namely, the *circle's shape* is determined by $R^{\mathrm{t}}_{\mathrm{el}}$ and C_{el}, the *circle's diameter* equals $R^{\mathrm{t}}_{\mathrm{el}}$ (=100 Ω) while this semi-circle itself is shifted by R_{electrol} to the right (Fig. 3.20d).

This *semi-circle* (the *model A* for $\underline{Z}^{\mathrm{d}}_{\mathrm{el}} = 0$ in Fig. 3.20d) enlarges when the *charge transfer* across the boundary *slows down* and thus $R^{\mathrm{t}}_{\mathrm{el}}$ increases. With increasing $R^{\mathrm{t}}_{\mathrm{el}}$, the course of $\underline{Z}_{\mathrm{el}}$ would gradually cover this complete semi-circle with increasing *f* (3.33). For ideally *fast charge transfer* and thus disappearing $R^{\mathrm{t}}_{\mathrm{el}} \to 0$, in contrast to high $R^{\mathrm{t}}_{\mathrm{el}}$, the latter semi-circle in Fig. 3.20d would disappear and the *Warburg line* would directly connect to $\underline{Z}_{\mathrm{el}} = R_{\mathrm{electrol}}$ at $f \to \infty$, as can be derived from (3.33).

The *charge-transfer-limited electrode reaction* for the alternating u_{AC} / i_{AC} application (including zero $f = 0$) and its *boundary model* of $\underline{Z}_{\mathrm{el}}$ are shown in Fig. 3.20b and (3.35). In addition to the neglected $\underline{Z}^{\mathrm{c}}_{\mathrm{el}}$, the impedance $\underline{Z}^{\mathrm{d}}_{\mathrm{el}}$ is omitted here ($\underline{Z}^{\mathrm{c}}_{\mathrm{el}} = 0$ and $\underline{Z}^{\mathrm{d}}_{\mathrm{el}} = 0$ from Fig. 3.19c) because the *charge transfer* with its resistance $R^{\mathrm{t}}_{\mathrm{el}}$ determines the *total reaction kinetics* but not the relatively fast diffusion processes and/or fast coupled reactions (Footnote 28). In other words, $R^{\mathrm{t}}_{\mathrm{el}}$ determines the relationship between $i_{\mathrm{AC,E}}$ and $u_{\mathrm{pol,i}}$ in Fig. 3.20b. The *complex plot* of the *charge-transfer reaction* is shown in Fig. 3.20e (see the *model B*). The resulting *semi-circle* has a *diameter* $R^{\mathrm{t}}_{\mathrm{el}}$, starts at the real valued $\underline{Z}_{\mathrm{el}} = R^{\mathrm{t}}_{\mathrm{el}} + R_{\mathrm{electrol}}$ for zero $f = 0$, and ends at the real valued $\underline{Z}_{\mathrm{el}} = R_{\mathrm{electrol}}$ for semi-infinite $f \to \infty$ with increasing *f* (compare Fig. 3.18c). As already mentioned, the *radius of the semi-circle* (=$R^{\mathrm{t}}_{\mathrm{el}}$ / 2) decreases with faster charge transfer and thus with decreasing $R^{\mathrm{t}}_{\mathrm{el}}$.

Finally, a *simplified boundary model* of the *charge-transfer-limited electrode reaction* is shown in Fig. 3.20c. Here the resistance R_{electrol} from Fig. 3.20b is neglected. That is, the ohmic voltage drop $i{\cdot}R_{\mathrm{electrol}}$ across R_{electrol} within the *electrode gel* is neglected for a finite $i \neq 0$. This implies that this *gel has a quite high ionic conductivity* and/or the *electrode surface area is quite large*, which leads to *small* R_{electrol} (2.36). Therefore, the drop $i{\cdot}R_{\mathrm{electrol}}$ can be assumed to be much smaller than the voltage drop ($u_{\mathrm{pol,i}} - U_{\mathrm{pol}}$) across the parallel connection of $R^{\mathrm{t}}_{\mathrm{el}}$ and

C_{el} (Fig. 3.20b). In other words, the *simplified boundary model* (Fig. 3.20c) neglects the *resistance overvoltage* $i{\cdot}R_{electrol}$ across the *electrode gel*.

The resulting *impedance* $\underline{Z}_{el}$ of this *simplified electrode model* (Fig. 3.20c) follows then from (3.35) and yields

$$\underline{Z}_{el} \approx \frac{R_{el}^{t}/j \cdot \omega \cdot C_{el}}{R_{el}^{t} + 1/j \cdot \omega \cdot C_{el}} + R_{electrol} \approx \frac{R_{el}}{1 + j \cdot \omega \cdot R_{el} \cdot C_{el}}. \tag{3.36}$$

Please note that we apply the equality $R_{el} = R_{el}^{t}$ in (3.36) due to neglected $\underline{Z}_{el}^{c}$ and $\underline{Z}_{el}^{d}$, for the sake of simplicity. In short, the impedance $\underline{Z}_{el}$ of the *simplified electrode model* from Fig. 3.20c and (3.36) includes

- a resistor with its *non-linear resistance* $R_{el} = R_{el}^{t}$, determined by the highly *voltage-dependant charge transfer* of the electrode reaction (Footnote 22) within the double layer [i.e., high R_{el}^{t} for low $u_{AC} < U_{dec}$ (strictly speaking, for $u_{pol,i}^{t} < U_{dec}$, see Fig. 3.14) and low R_{el}^{t} for high $u_{AC} > U_{dec}$ (strictly speaking, for $u_{pol,i}^{t} > U_{dec}$), as discussed in Section "Alternating Voltage Application" with (3.22) and (3.23)], *connected in parallel* to
- the *capacitor* with its capacitance C_{el} (strictly speaking, also *non-linear* with respect to the levels of u_{AC} and f, as discussed in Section "Alternating Voltage Application"), determined by the (re)formation of the *charged double layer* on the electrode surface (Fig. 3.16).

Please note that this *simplified model* of Fig. 3.20c [with (3.36)] was already used in Fig. 3.12b–d (with $R_{el} = R_{el}^{t}$).

The *complex plot* of the *simplified boundary model* of the *charge-transfer-limited reaction* (3.36) is depicted in Fig. 3.20e (see the *model C*). In fact, the resulting *semi-circle* appears as a *laterally dislocated semi-circle* from (3.35) or as a laterally dislocated *model B*; with the boundary conditions $\underline{Z}_{el} = R_{el}^{t} = R_{el} = 100\ \Omega$ at $f = 0$ and $\underline{Z}_{el} = 0$ for $f \to \infty$.

This *omission of the relatively small* $R_{electrol}$ in (3.36) is especially valid for the relatively *low* f [for $f \ll 1/(2\pi \cdot R_{el}^{t} \cdot C_{el})$], which yields a relatively high impedance magnitude of the parallel connection of R_{el}^{t} and C_{el} in relation to the resistance $R_{electrol}$. This consideration implies the discussed *inequality* $u_{AC} < U_{dec}$ (Fig. 3.17b), i.e., the *non-linear* R_{el}^{t} is still relatively high due to the constrained charge transfer (especially for *polarizable electrodes*). Otherwise, the inequality $u_{AC} > U_{dec}$ and thus the relatively low R_{el}^{t}—which yield a relatively low total impedance of the parallel connection of R_{el}^{t} and C_{el}—may not justify the neglect of $R_{electrol}$.

According to Fig. 3.19,

- the *series connection of resistances* $R_{el}^{t} + R_{el}^{d} + R_{el}^{c}$ for the *direct* u_{DC} / i_{DC} application (see Fig. 3.19b) or
- the *series connection of impedances* $R_{el}^{t} + \underline{Z}_{el}^{d} + \underline{Z}_{el}^{c}$ for the *alternating* u_{AC} / i_{AC} application (see Fig. 3.19c)

represents the *transition resistance or transition impedance*, respectively, of the double layer. It is the barrier to

- *conductive current* flow between the electrode and electrolyte and is known as *Faradaic impedance*. In analogy, the latter *conductive current* through the Faradaic impedance—or across the electrode interface—is referred to as *Faradaic current* which is generated by *oxidation or reduction* of species on or very close to the electrode surface (Footnote 24). Here an electron transfer reaction—an *electrochemical reaction*—mediates the change from electronic conduction within the electrode to ionic conduction within the electrolyte across the electrode/electrolyte boundary (Fig. 3.4).
- Likewise, pure charging or discharging of the *double layer*—with a *displacement current* across C_{el}—but without any conductive current across the interface and *without any chemical reactions* within the boundary is a *non-Faradaic process*. In other words, *electrostatic reactions* occur, in contrast to electrochemical reactions composing Faradaic processes.

Therefore, the total *electrode impedance* $\underline{Z}_{el}$—in line with Fig. 3.19c and (3.32)—is given as the Faradaic impedance in parallel with C_{el}, and this combination in series with $R_{electrol}$.

It is instructive to observe that the interfacial *capacitance* C_{el} is proportional to the *electrode surface area* A [i.e., large electrodes have large C_{el}, see (3.7) and (3.8)], whereas the associated *capacitive impedance* $1/(j \cdot 2\pi \cdot f \cdot C_{el})$ is then inversely proportional to A [(2.41) and (2.42)]. Furthermore, all three series components of the *Faradaic impedance* R^t_{el}, $\underline{Z}^d_{el}$, and $\underline{Z}^c_{el}$ are also inversely proportional to A (2.36). In fact, the resistance R^t_{el} is proportional to $1/i_0$ while the exchange current i_0 increases with increasing A (2.23) for a given characteristic current density i_0 / A (Footnote 22). Consequently, R^t_{el} decreases with increasing A. The impedances $\underline{Z}^d_{el}$ and $\underline{Z}^c_{el}$ decrease with increasing A because an increased diffusion area expedites the diffusion process (Footnote 35) while an increased absorption area eases the absorption process (Fig. 3.19c), respectively. As an important conclusion of these mechanisms, it becomes clear that

- the *capacitive impedance*,
- the *Faradaic impedance*, and thus
- the *total electrode impedance* $\underline{Z}_{el}$ [as the parallel connection of the latter impedances according to (3.32)],

all three *decrease for large electrodes* with their *large* A; see the associated practical possibilities in Footnote 43 when A is intentionally varied (compare also Footnote 30). In close analogy, the resistance R_{el} (=R^t_{el}) from Fig. 3.6b decreases and the associated C_{el} increases with increasing A of the electrode.

The impact of $\underline{Z}_{el}$ becomes less within the *total measured impedance* $\underline{Z}$ (3.26) when the *physical size* of the used *electrodes* rises. That is, a *large* A diminishes the dominance of $\underline{Z}_{el}$, especially at *low* f when the magnitude of $\underline{Z}_{el}$ tends to be quite large (Fig. 3.20d); as discussed in Section "Alternating Voltage Application". Obviously, a *low* $\underline{Z}_{el}$ is favourable in diagnostic and therapeutic applications to

minimise losses of biosignals to be passively recorded and actively applied, respectively; compare Figs. 3.24 and 3.25.

For instance, it is a common praxis to *rough the electrode surface* (or introduce porosity) in order to increase this A, especially in *microelectrodes* that show a relatively small *contact/surface area* A, and thus to reduce effects of the associated $\underline{Z}_{el}$. When increasing A, *irreversible reactions* are typically reduced so that the safe charge deliver capacity of electrodes is increased as well as the *safe charge injection limit*; compare the associated discussion in Section "Pt Electrodes". On the other hand, if the impedance $\underline{Z}_{el}$ *is of interest*—e.g., in terms of an instructive and specific interaction between the electrode surface and tissue cells, as used in diagnostics—then a small A leading to a quite large $\underline{Z}_{el}$ within the measured $\underline{Z}$ is favourable. In general, such considerations have significant *practical consequences* for the electrode design in *diagnostic* and *therapeutic applications* (see below).

It is also interesting to note that the *capacitive behaviour* of $\underline{Z}_{el}$, namely, the *capacitive impedance* $1/(j \cdot 2\pi \cdot f \cdot C_{el})$, dominates in *strong electrolytes* (Footnote 29 in Chap. 2) the electrode is in contact with. As discussed in Section "Electrical Double Layer", the associated *concentrated solutions* show an *abrupt transition* (in the local concentration/composition) from the electrode surface into the undisturbed electrolyte. This implies a *small total thickness of the double layer*, a high C_{el} ($\approx C_r$ (3.7), i.e., the diffuse layer almost disappears), and thus a low resulting impedance $1/(j \cdot 2\pi \cdot f \cdot C_{el})$. This *low capacitive impedance* determines the total electrode impedance $\underline{Z}_{el}$ because $\underline{Z}_{el}$ is mainly given as the parallel circuit of the capacitive impedance and Faradaic impedance [(3.32) and (3.36)]. In other words, electrical properties of the *electrode/electrolyte boundary* in *concentrated solutions* can be well *approximated with* C_{el} *only* (Figs. 3.6b and 3.19c).

In analogy with the *simplified boundary model* (Fig. 3.20c), the *complex electrode impedance* (3.36) creates a natural *RC-filter* at the input of the measurement amplifier (of a *diagnostic device*) or at the output of the driver stage (of a *therapeutic device*), as illustrated and discussed with respect to Figs. 3.24 and 3.25. Therefore, there is an *intrinsic filtering* of incoming or outgoing biosignals, which can either limit the performance of the diagnostic/therapeutic device or can even be used in a favourable way. For instance, *polarizable electrodes* acting as *coupling capacitors* (Fig. 3.21b) can be used for *galvanic isolation* of the diagnostic device from the human body (Fig. 3.24).

Polarizable Electrode

The *polarizable electrode* (Footnote 22) is also known as *non-reversible electrode*. There is an *absent net charge transfer* across the electrode/electrolyte boundary, across the *electrical double layer* at the electrode surface, or across the *phase transition layer* for a relatively *high polarization voltage* $u_{pol,i}$—to be precise, for a relatively *high polarization overvoltage* $u^t_{pol,i} = (u_{pol,i} - U_{pol})$ but still *below* U_{dec} ($>u^t_{pol,i}$), see Fig. 3.14. The charge transfer is absent due to *large activation barriers* of the associated *electrode/redox reactions*. The associated *exchange current density*

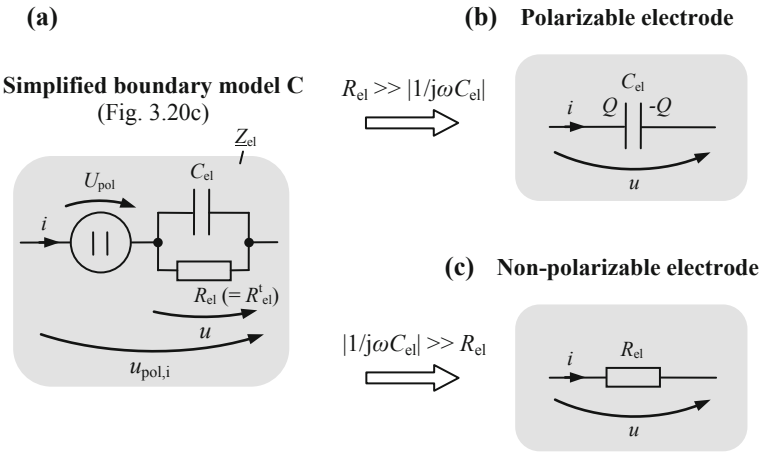

Fig. 3.21 Simplified electrical equivalent circuit models of the electrode/tissue boundary. **b** Model of the polarizable electrode and **c** that of the non-polarizable electrode, both derived from **a** the simplified boundary model C for the charge-transfer-limited electrode reaction (Fig. 3.20c)

(Footnote 22) is *very small* while the *charge-transfer resistance* $R_{el} = R^t_{el}$ [or the *electrode resistance* due to the inert charge transfer, see (3.17)] of the *electrode/redox reaction* on the electrode surface is *very high* (see Fig. 3.14). In fact, in order to *induce the electrode/redox reaction* to proceed with a considerable *net charge transfer* across the boundary, the *kinetic inhibition* of this reaction can only be overcome by applying a *quite high* ($u_{pol,i} - U_{pol}$) already *above* U_{dec} ($<u^t_{pol,i}$), as illustrated in Figs. 3.14 and 3.17b (for $u_{DC} > U_{dec}$). However, it should be stressed that the classical polarizable electrode assumes moderately high overvoltages below *activation barriers* satisfying $u^t_{pol,i} < U_{dec}$; otherwise, its simplified model from Fig. 3.21b would not apply (see below).

That is, charged species on the electrode side, the *electrons*, can not enter the electrolyte, while charged species on the electrolyte side, the *ions*, can not cross into metal. The *double layer* in-between the electrode and solution, the electrode/electrolyte boundary, serves as a *barrier for the redistribution of charges* and thus *for the net conductive current* through the boundary. Obviously, a charge can cross this interface from one side to the other but it *never gets out of the interphase* (Wagner 1993). In fact, the latter happens during the *build-up of the double layer* before the *electrochemical equilibrium* is reached (see Fig. 3.6a and the associated discussion). Please note that this *transient process of the double layer formation* requires the associated *charge transfer* across the boundary which then ceases after the double layer has been completed (as described with respect to Fig. 3.6a).

Likewise, there are no accessible electronic acceptor and/or donor states in the bulk electrolyte and there is a null concentration of transferable electrons in the

solution. An externally-applied change in the *electrode electric potential* $\varphi_{M,i}$—still under the assumption of $u_{pol,i} - U_{pol} = (\varphi_{M,i} - \varphi_E) - U_{pol} < U_{dec}$, with φ_E as the *electric potential of the undisturbed electrolyte* (Fig. 3.13b, c)—therefore does not lead to the electron transfer across the metal/electrolyte boundary and to any *net transfer of electric charges* across this boundary. Instead, this change in $\varphi_{M,i}$ (e.g., an increase in $\varphi_{M,i}$ in Fig. 3.13b, c) leads rather to the *boundary polarization*, namely, to an associated change (i.e., an increase) in the amount of the accumulated *electric charge Q on the metal surface*, balanced by an identical change (i.e., an increase) in the concentration of the *ionic counter-charge* $-Q$ in the near-surface region of the electrolyte (compare Fig. 3.6a). The *polarization phenomenon* manifests itself as the relatively high $u_{pol,i}$ of the phase transition layer. Likewise, the *size of* $u_{pol,i}$ ($=\varphi_{M,i} - \varphi_E$, see Fig. 3.13b, c) *changes* in response to the varying potential $\varphi_{M,i}$.

In fact, this is the behaviour of a *capacitor* with its *capacitance* C_{el}, as illustrated in Fig. 3.21b for the *polarizable electrode*. An increase in the voltage drop u across the capacitor plates raises the amount of surface charges Q and $-Q$ on both plates; see (3.5) and (2.39). Likewise, the *capacitive coupling* dominates for the relatively *high but not exceedingly high overvoltages* ($u_{pol,i} - U_{pol}) < U_{dec}$ and thus without any *electrolytic chemical reactions* at the electrode surface (Fig. 3.13b, c). There is just a dense build-up of charges across the boundary. In fact, these dense charges imply a major disadvantage of polarizable electrodes: namely, their sensitivity to movement artefacts, see Section "Movement Artefacts". It means that there are

- no *conductive currents* across the electrode/electrolyte boundary of the *polarizable electrode*. Neither *steady conductive currents* ($i_{DC} = 0$) nor *alternating conductive currents* ($i_{AC,E} = 0$) can cross this boundary. Instead, the *polarizable electrode* connects a *technical device and bodily tissues* via
- *displacement currents* only ($i_{AC,C} \neq 0$), as long as ($u_{pol,i} - U_{pol}$) is not exceedingly high, as discussed above.

The *perfectly polarizable electrode* is illustrated in Fig. 3.14. It exhibits a semi-infinite U_{dec} because of *ideally constrained electrode/redox reactions*. There is *ideally no net transfer of electric charges* ($i_{DC} = 0$ and $i_{AC,E} = 0$) across the boundary, *irrespective of the actual level of* $u_{pol,i}$ (the inequality ($u_{pol,i} - U_{pol}) < U_{dec}$ always applies because $U_{dec} \to \infty$). Consequently, the perfectly polarizable electrode shows a semi-infinite R_{el}^{t} and implies only the *capacitive coupling of displacement currents* ($i_{AC,C} \neq 0$) across the boundary for any level of $u_{pol,i}$.

Non-polarizable Electrode

The *non-polarizable electrode*, known also as *reversible electrode*, exhibits behaviour essentially opposite to that of polarizable electrode (Footnote 22). An *unconstrained exchange of electric charges* between the metal electrode and electrolyte takes place across the *electrical double layer*. There are accessible electronic acceptor and/or donor states in the bulk electrolyte, whereas the *electrode*

chemical reaction (ionic or redox) on the *electrode surface* is *always present* and is close to its *electrochemical equilibrium*. Because of the *fast and unconstrained electrode reaction*, an externally-applied *electrode potential* $\varphi_{M,i}$ yields changes in the *concentration* of at least one (ionic) species in the electrolyte at the electrode surface according to the Nernst equation; compare Section "Dynamics of Electro-Kinetic Processes". Likewise, in clear contrast to the polarizable electrode, the *equilibrium* in the non-polarizable electrode is *established quite fast* due to a *missing kinetic inhibition* of the charge transfer processes involved in the electrode/redox reaction.

The *unconstrained and rapid electrode/redox reaction* yields a relatively *low polarization overvoltage* $(u_{pol,i} - U_{pol})$ across the electrode/electrolyte boundary, as illustrated in Fig. 3.14. This low $(u_{pol,i} - U_{pol})$ already allows considerable *conductive currents*, namely, steady i_{DC} and/or alternating $i_{AC,E}$, to cross easily the boundary, with the current's transition being *energetically unconstrained* and with a *net transfer of charge* over the interface. This is in line with the relatively low *electrode resistance*, namely, the *low charge-transfer resistance* $R_{el} = R_{el}^{t}$ of this electrode/redox reaction (as compared with the relatively high R_{el}^{t} of the polarizable electrode at $(u_{pol,i} - U_{pol}) < U_{dec}$); see qualitatively indicated R_{el} levels in Fig. 3.14. According to Footnote 22, the associated *exchange current density* is quite *large*.

It should be reiterated that there is a *very small surplus polarization* $(u_{pol,i} - U_{pol})$ of the *non-polarizable electrode* away from its equilibrium-related U_{pol} (valid for the *electrochemical equilibrium* at $i_{DC} = 0$) due to the *finite* $i_{DC} \neq 0$ and/or *finite* $i_{AC,E} \neq 0$ (Fig. 3.14). That is, the discussed *electrochemical equilibrium* within the boundary approximately prevails in spite of these finite *conductive currents*. In an approximation, the rough equality $u_{pol,i} \approx U_{pol}$ applies for the relatively small i_{DC} and/or $i_{AC,E}$ due to *unconstrained electrode/redox reactions*.

The boundary behaves as a *resistor* with its relatively small *resistance* R_{el}, as illustrated in Fig. 3.21c for the *non-polarizable electrode*. The *galvanic coupling* dominates, whereas conductive i_{DC} and/or $i_{AC,E}$ can cross the electrode/electrolyte boundary.

The *perfectly non-polarizable electrode* is depicted in Fig. 3.14. It exhibits $R_{el} = 0$ and $u_{pol,i} = U_{pol}$ (or *zero overvoltage* $(u_{pol,i} - U_{pol}) = 0$) due to *absent surplus polarization* of the boundary for finite $i_{DC} \neq 0$ and/or finite $i_{AC,E} \neq 0$ across the boundary. Electrode/redox reactions and thus the *charge transfer* across the electrode/electrolyte boundary are *ideally unhindered and infinitely fast*, given *finite conductive currents* across this boundary.

Please note that the equality $u_{pol,i} = U_{pol} = 0$ applies only if the *charge separation* at the electrode/electrolyte boundary is *completely absent*. Here *electrode/redox reactions* are *ideally unconstrained* for both zero $i_{DC} = 0$ and zero $i_{AC,E} = 0$ (yielding $U_{pol} = 0$ at the *electrochemical equilibrium*) as well as for finite $i_{DC} \neq 0$ and/or finite $i_{AC,E} \neq 0$ (yielding $u_{pol,i} = U_{pol} = 0$). In this *ideal case*, the boundary can not be polarized at all, which would serve as a basis of an *ideal reference*

electrode with its *zero polarization* for both the currentless case and finite conductive currents across the boundary (Footnote 30), as illustrated in Fig. 3.14.

Polarizable Versus Non-polarizable Electrodes

Figure 3.21 illustrates both discussed *models of the polarizable and non-polarizable electrodes*. These models are derived from the *simplified boundary model for the charge-transfer-limited electrode reaction* (the model C from Fig. 3.20c).

- The *polarizable electrode* in Fig. 3.21b assumes $(u_{pol,i} - U_{pol}) < U_{dec}$ (i.e., electrode reactions with a net charge transfer are absent, as discussed above) and thus a relatively high $R_{el} = R_{el}^{t}$ exceeding the magnitude $|1/(j\omega C_{el})|$ of the *capacitive impedance* (2.42). Thus, the resulting inequality $R_{el} \gg |1/(j\omega C_{el})|$ in combination with the observation that the circuit component with its lower impedance (i.e., C_{el} with its $1/(j\omega C_{el})$) mainly determines the total impedance of the parallel circuit of two components (i.e., C_{el} and R_{el}; compare Fig. 2.14a, c) yields the *capacitor* with its C_{el} as the only component left of the *model of the polarizable electrode*. This capacitance C_{el} is quite large. This is because the *polarization* of the electrode/electrolyte boundary is *quite strong*, in line with the *absent net charge transfer* across this boundary, which would effectively diminish this polarization. Likewise, the large C_{el} turns the associated $1/j\omega C_{el}$ to be quite small, whereas $1/j\omega C_{el}$ determines the total current, namely, the displacement current, across the electrode/electrolyte boundary.
- The *non-polarizable electrode* in Fig. 3.21c assumes a relatively low $R_{el} = R_{el}^{t}$ below $|1/(j\omega C_{el})|$ ($\gg R_{el}$), so that the *resistor* with its R_{el} comprises the *model of the non-polarizable electrode*. The discussed *small surplus polarization* $(u_{pol,i} - U_{pol})$ means a *weak polarization* of the boundary and thus a quite small C_{el}. This is in line with the *unconstrained charge transfer* across this boundary and an easy going electrode/redox reaction which *reduces the polarization* of the boundary. Likewise, the small C_{el} implies a large $1/(j\omega C_{el})$, whereas R_{el} determines the total current, namely, the conductive current, across the electrode/electrolyte boundary.

Both *simplified models* of the polarizable and non-polarizable electrodes *neglect* U_{pol}, i.e., these models assume $|u| \gg |U_{pol}|$ (Fig. 3.21). Obviously, this assumption is rather valid for the polarizable electrode due to its strong boundary polarization (Fig. 3.14).

According to these models of polarizable and non-polarizable electrodes, please note that the use of *polarizable electrodes* with their *capacitive coupling* (Fig. 3.21b) does not permit passive measurements and active applications of *steady and/or slowly varying biosignals* from and into biological tissues (Figs. 3.24 and 3.25), respectively. This is in clear contrast to *non-polarizable electrodes* with their *galvanic coupling* (Fig. 3.21c), favouring measurements and applications of steady and/or alternating biosignals from and into tissues, respectively.

Pure *noble metal electrodes*, such as *Pt electrodes*, act as *polarizable electrodes* and are typically used for neuromuscular *stimulation purposes*. This is because such stimulation requires a high temporal dynamic of stimulating signals (see Section "Electrical Stimulation Effects") which thus can easily cross the *capacitive boundary* of the polarizable electrode as displacement currents. As an advantage in terms of *toxicity*, noble metals are inert and it is difficult for them to oxidise, dissolve (Fig. 3.4a) and then to contaminate tissue. However, if a *metal electrode is coated with its salt* (e.g., Ag with its poorly soluble salt AgCl, see Fig. 3.11), where the same anion is found in the *electrode gel* (e.g., Cl^- ion in the readily soluble KCl within the gel) as well as found in *tissue/electrolyte* (e.g., Cl^- in the dissociated salt NaCl superfluous within body fluids), a *non-polarizable electrode* results with its relatively low and stable U_{pol}. Non-polarizable electrodes with their *galvanic coupling* are typically used for *recording purposes* so that they register steady and alternating biosignals. In contrast to polarizable electrodes, non-polarizable electrodes involve some form of chemical reaction, so that its reaction products—if they left the electrode surface into tissue—can be *toxic* to the underlying tissue and may have adverse impacts.

Different other metal electrodes, such as *gold or stainless steel electrodes*, are located somewhere in-between the two extremes of polarizable and non-polarizable electrodes. To be precise, all real electrodes fall between perfectly polarizable and perfectly non-polarizable electrodes, which depends on the degree of the charge transfer across the boundary.

Experimental Issues

Measurement of Tissue Impedance

When *two surface electrodes* are in contact with *biological tissue of interest*—for instance, in order to *estimate experimentally the bodily tissue impedance* $\underline{Z}_b$ (Fig. 3.12a)—*electrode/tissue interfaces* of both electrodes have to be considered. In particular, the *electrode polarization voltage* $u_{pol,i}$ ($\neq U_{pol}$, i.e., apart from the currentless situation, see Figs. 3.14 and 3.16) in series with the voltage drop u_b across tissue affects the estimation of $\underline{Z}_b$ (Fig. 3.12d). In other words, the associated *electrode impedance* $\underline{Z}_{el}$ *in series with the wanted* $\underline{Z}_b$ (Fig. 3.12d) influences significantly this estimation of $\underline{Z}_b$ out of the *total measured impedance* $\underline{Z}$ [$=\underline{Z}_{el} + Z_b + \underline{Z}'_{el}$, see (3.26)]. Particular effects of the *electrode polarization* depend strongly on the *electrode material* and its *geometrical properties* as well as particular *tissue properties* (e.g., dissociated salts). In addition, *homogeneous current density distributions* around electrodes in contact with tissue should be aimed at; compare Footnote 37.

The dominance of $\underline{Z}_{el}$ within the total $\underline{Z}$ is particularly high for relatively *low field frequencies f* of the applied u_{AC} (or i_{AC})—all the more, for $f = 0$ of the applied u_{DC} (or i_{DC})—and/or for a *small area A of the electrode surface*, which imply a

large $\underline{Z}_{el}$ (see (3.32) and the associated discussion in Section "Electrode Impedance Model"). In particular, this *large* $\underline{Z}_{el}$ is due to

- a relatively *large double-layer capacitive component* $1/(j \cdot 2\pi \cdot f \cdot C_{el})$ (with the prominent *electrode polarization*, see Fig. 3.16) for *low f* and *small A* (2.42),
- a relatively *large diffusion impedance* $\underline{Z}_{el}^{d}$ (Footnote 35) for *low f* and *small A*, and
- a relatively *large impedance* $\underline{Z}_{el}^{c}$ *due to coupled reactions* (3.30) for *low f* and *small A*.

That is, low values of f and/or A stand for a relatively large $\underline{Z}_{el}$ in relation to $\underline{Z}_b$ within the *total measured* $\underline{Z}$ (3.26). This is especially true for f below about 1 kHz when *biological tissues* with their typical $\underline{Z}_b$ are considered. This inequality $|\underline{Z}_{el}| \gg |\underline{Z}_b|$ becomes even more significant below about 100 Hz (Gabriel et al. 1996).

Therefore, in order to minimize the *electrode polarization* (Fig. 3.16) and to keep $\underline{Z}_{el}$ as low as possible, the interfacial *capacitive impedance* $(=1/(j2\pi \cdot f \cdot C_{el}))$ of the *electrode/tissue boundary* should be kept as low as possible (Fig. 3.19b, c). This can be done either through a *relatively high f* and/or a *large A* yielding a *low capacitive impedance* and/or a *high* C_{el}, respectively. In *experimental measurements*, various *theory-based approaches*[43] can be additionally used to eliminate both impedances $\underline{Z}_{el}$ and $\underline{Z}'_{el}$ out of the measured $\underline{Z}$ in order to derive $\underline{Z}_b$.

---

[43]There are numerous theory-based experimental methods for the elimination of the *electrode/tissue boundary impedance*, the *electrode impedance* $\underline{Z}_{el}$. For instance, the application of *two similar electrodes* (with $\underline{Z}_{el} \approx \underline{Z}'_{el}$) with the *varying electrode area A* can be used to deduce $\underline{Z}_{el}$ out of the *total measured impedance* $\underline{Z}$ [$=\underline{Z}_{el} + \underline{Z}_b + \underline{Z}_{el}$, see (3.26)] in order to *estimate the bodily tissue impedance* $\underline{Z}_b$ of interest. To be more precise, the halving of A (the measurement with A and $A/2$) using raster electrodes doubles $\underline{Z}_{el}$ ($\underline{Z}_{el}$ and $2 \cdot \underline{Z}_{el}$, respectively, in line with (2.36) and (2.42), and with the associated discussion in Section "Electrode Impedance Model") and thus yields two different total $\underline{Z}$ ($\underline{Z}_A$ and $\underline{Z}_{A/2}$, respectively) out of which $\underline{Z}_b$ can be easily estimated. Please recall that $\underline{Z}_{el}$ is determined by the *double-layer capacitive impedance* $1/(j \cdot 2\pi f \cdot C_{el})$ and other *impedances* due to all *three electro-kinetic processes*, i.e., $R_{el}^{t} + \underline{Z}_{el}^{d} + \underline{Z}_{el}^{c}$ from Fig. 3.19c.

Under the assumption that $\underline{Z}_b$ remains almost constant while varying A (i.e., the current density distribution within tissue does not significantly change for varying A), it can be deduced from Fig. 3.12d that

$$\underline{Z}_A = \underline{Z}_{el} + \underline{Z}_b + \underline{Z}_{el} \quad \text{and} \quad \underline{Z}_{A/2} = 2 \cdot \underline{Z}_{el} + \underline{Z}_b + 2 \cdot \underline{Z}_{el}.$$

These two equations with two unknown quantities ($\underline{Z}_{el}$ and $\underline{Z}_b$) can be easily solved and yield $\underline{Z}_b = 2 \cdot \underline{Z}_A - \underline{Z}_{A/2}$.

In analogy, the *distance d between the electrodes* can also be changed to vary $\underline{Z}_b$ in a definite way (compare Fig. 2.9a). For instance, the halving of d halves also $\underline{Z}_b$ (2.36) and yields

$$\underline{Z}_d = \underline{Z}_{el} + \underline{Z}_b + \underline{Z}_{el} \quad \text{and} \quad \underline{Z}_{d/2} = \underline{Z}_{el} + \frac{\underline{Z}_b}{2} + \underline{Z}_{el},$$

Alternatively, *electrical equivalent circuit models* of the electrode/tissue boundary from Fig. 3.20a–c can be used for the *experimental estimation* of $\underline{Z}_{el}$ out of the *total measured* $\underline{Z}$ (3.26). Firstly, the *complex plot* of $\underline{Z}$—as illustrated in Figs. 3.18 and 3.20d, e—is experimentally captured. Then the impedance $\underline{Z}_{el}$ is identified within $\underline{Z}$; namely, *parameters of circuit elements* (of passive resistive and capacitive elements) of the selected equivalent circuit model of the boundary are extracted out of the measured $\underline{Z}$. For instance, as illustrated within the discussion of Fig. 3.18, the resulting complex plot of $\underline{Z}$ can be used to extract R_b and R_{el}^t (and then to estimate the exchange current i_0 from R_{el}^t, see Footnote 22) in a graphical way out of the resulting foot points and the resulting diameter of the *semi-circle of a charge-transfer-limited electrode reaction* (for the relatively *high* f >90 Hz in Fig. 3.18c).

It is instructive to observe that the resulting *geometrical shape* of the *semi-circle* within the complex plot of $\underline{Z}$ for *all* f [with a real tissue $\underline{Z}_b = R_b$, see (3.26)] indicates the presence of a *charge-transfer-limited electrode reaction*. In analogy, the presence of the *Warburg line* within the complex plot of the measured $\underline{Z}$ at the relatively *low* f (Footnote 35) indicates a *diffusion-limited electrode reaction*.

Please note that if the frequency f *is selected to be quite high* to *minimize the electrode polarization* (see above), *leads connected to electrodes* (in contact with biological tissue of interest) may impose additional difficulties; especially above 50 kHz (Hamann and Vielstich 1998) or above a few MHz (Gabriel et al. 1996; Miklavcic et al. 2006). The selected f should not be too high because the non-zero *inductance* L of *leads* (2.86) would affect an experimental estimation of $\underline{Z}_b$ out of the total measured $\underline{Z}$. In fact, the *inductive impedance* ($=j2\pi \cdot f \cdot L$) of electrode leads is *proportional to* f *and* L, and can be seen *in series with* $\underline{Z}_{el}$ *and* $\underline{Z}_b$, i.e., the total $\underline{Z}$ fulfils $\underline{Z} = j2\pi \cdot f \cdot L + \underline{Z}_{el} + Z_b + \underline{Z}'_{el}$ [compare (3.26)].

---

where the measured Z_d and $Z_{d/2}$ at the distance d and $d/2$, respectively, offer a convenient basis to estimate $\underline{Z}_b$ according to $\underline{Z}_b = 2 \cdot (\underline{Z}_d - \underline{Z}_{d/2})$. Obviously, it demands that the variation of the distance does not change $\underline{Z}_{el}$, i.e., does not change the electrode surface properties and its polarization.

Furthermore, *different oscillation frequencies* f of the applied *alternating* u_{AC} can also be used for the elimination of $\underline{Z}_b$ or $\underline{Z}_{el}$ out of the total $\underline{Z}$, to give

$$\underline{Z}\,(f \to \infty) = \underline{Z}_{el} + \underline{Z}_b + \underline{Z}_{el} \approx \underline{Z}_b \quad \text{and} \quad \underline{Z}(f \to 0) \approx 2 \cdot \underline{Z}_{el}.$$

The former approximation is based on the discussed disappearance of $\underline{Z}_{el}$ for very high f (i.e., $1/(j \cdot 2\pi f \cdot C_{el}) \to 0$ yields $|\underline{Z}_{el}| \to 0$, see Fig. 3.19c), whereas the latter approximation shows the typical dominance of $\underline{Z}_{el}$ over $\underline{Z}_b$ for very low f (i.e., $|\underline{Z}_{el}| \gg |\underline{Z}_b|$). Please note that $\underline{Z}_{el}$ disappears also for very high A [(2.36) and (2.42)]. In analogy, a systematic variation of f in an experimentally reasonable range may be used for the extrapolation of the measured $\underline{Z}$ towards $f \to \infty$ and thus for the subsequent estimation of $\underline{Z}_b$ ($=\underline{Z}$ at $f \to \infty$, see the equation from above).

In summary,[44]

- the phenomenon of *electrode polarization* is prominent at the relatively *low f*, whereas
- the phenomenon of *lead inductance* becomes an important factor at the relatively *high f* (see above).

Tissue Conductivity/Cell Concentration

The *concentration c of tissue cells* at the electrode surface *influences greatly the electrode impedance* $\underline{Z}_{el}$. It should be recalled that a *cell suspension* (e.g., erythrocytes) is typically a poor conductor at *low f* (below β-dispersion, i.e., below about 1 MHz, see Fig. 2.21) with *conductive currents* (i.e., i_{DC} and $i_{AC,E}$) flowing only through narrow *extracellular spaces* while bypassing individual *poorly conducting cells*. Please compare current pathways for low and high *f* in the course of β-dispersion from Fig. 2.22.

Therefore, the *ionic current* passing through the cell suspension reaches only a *certain part of the electrode surface* because cells shield a part of the electrode surface from this current (Schwan 1992). With *increasing c of cells*, i.e., with increasing volume fraction of cells in tissue, this *shielding effect becomes more pronounced* and thus the *polarization of the electrode/tissue boundary rises*. The poorly conducting cells strengthen polarization effects as compared with a homogeneous ionic solution equivalent in its conductivity to the extracellular fluid between cells.

Likewise, the slope of the resulting $u_{pol,i}$ (across the boundary) raises over the applied i (through the boundary) with increasing c. That is, the *impedance* $\underline{Z}_{el}$ *increases* with *increasing c*, which can be interpreted as decreasing C_{el} (or increasing capacitive impedance $1/(j \cdot 2\pi \cdot f \cdot C_{el})$) and/or increasing $\underline{Z}^{d}_{el}$ (i.e., obstructed diffusion) with increasing c of poorly conducting cells in tissue (Fig. 3.19c); the associated experimental data is illustrated in Schwan (1992).

Consequently, the manifestation of (solvated) *ionic charge accumulation* at the electrode surface (i.e., of charges carried by ionic currents in tissue to/from the electrode surface, see Fig. 3.16) tends to *become less dominant* (i.e., C_{el} decreases) *at low f* with *decreasing tissue sample conductivity* (Gabriel et al. 1996) or, in other words, with *increasing c of poorly conducting cells*.

[44] From a practical point of view, it is a good practice to *test the impedance measurement system* (of the tissue impedance) in a *saline solution*, *identify*

- *electrode polarization and*
- *lead induction effects*

and then eliminate them in a way that the measured electrical properties of the saline solution do not vary anymore with frequency until the GHz frequency range (Miklavcic et al. 2006), i.e., until γ-dispersion occurs (Section "Relaxation and Dispersion Effects on Conductivity and Polarization").

Movement Artefacts

By definition, the *polarizable electrode* shows a *strongly charged double layer* (Fig. 3.21b). If such *electrode is physically moved* with respect to its *adjacent electrolyte* at the *electrode surface*, the steady-state *distribution of ionic counter-charges* (or of local ional activities) *within this electrolyte layer*—the mobile layer of the dense build-up of charge—becomes mechanically disturbed (Fig. 3.16). Please note that this *electrolyte* can be given either by *tissue* (i.e., tissue itself can act as an electrolyte; for instance, when well-perfused tissue is in a direct contact with an implanted metal electrode, see Fig. 3.1c) or by an intermediate *conductive electrode paste* between the skin surface electrode and the body skin (Fig. 3.1b).

The mechanical *disturbance of counter-charges* changes momentarily *the polarization voltage* U_{pol} [i.e., changes the *half-cell voltage*, see (3.11)] and the *polarization overvoltage* ($u_{pol,i} - U_{pol}$) of the electrode/electrolyte boundary. That is, the local amount of *counter-charges* changes that forces—in line with (3.5)—the voltage drops U_{pol} and $u_{pol,i}$ to vary in size. In analogy, mechanically *agitated electrode paste* yields altered *metallic ion gradients* at the electrode surface and thus a varying U_{pol} [according to (3.4)] and $u_{pol,i}$.

After this disturbance due to movements, the original *electrochemical equilibrium of the boundary* (in its currentless state with $u_{pol,i} = U_{pol}$, see Footnote 4) or the original *steady state of the boundary* (with a finite current through the boundary and $u_{pol,i} \neq U_{pol}$) can be re-established with a certain *time delay* only. This is due to *inert movements of counter-charges* within the electrolyte layer and is principally comparable with the *relaxation time constant* from (2.73).

Consequently, the *contact voltage drop* u ($=u_{pol,i} + u_b - u'_{pol,i} \approx u_{pol,i} - u'_{pol,i}$ for small i, see Fig. 3.17a) *between two electrodes* (e.g., implanted polarizable electrodes) in contact with electrolyte varies disadvantageously *in response to movements* of any of these electrodes. These movement-related changes in the voltage u are known as *movement artefacts* (or movement noise). These artefacts can seriously *interfere*[45] *with the measurement of biosignals* up to their complete masking by this movement noise. Please note that *movement-related changes* in U_{pol} and $u_{pol,i}$ may even lead to *saturation of the input amplifier* operating the associated electrode.

Since the *overvoltage* ($u_{pol,i} - U_{pol}$) and thus the *charge accumulation* within the double layer are quite small in the *non-polarizable electrode* (Figs. 3.14 and 3.21c), it can be expected that potential mechanical disturbances of the *distribution*

[45]Since *motion artefacts* are mainly caused by *relative motions* between the electrode surface and the adjacent layer of the electrode paste (in a *direct contact with the skin*), artefacts can be minimised by the use of the so-called *floating electrodes*. Here the *metal electrode* is spaced away from the (moving) skin by a *buffer layer*, a *pre-gelled sponge*, or a *flat washer* (in contact with the *skin*), whereas the sponge or washer is filled by an isotonic electrolyte for the electrode to bath within the electrolyte. This *buffer layer absorbs movements* of the electrode in relation to the skin surface and thus contributes to the targeted *constancy of* $u_{pol,i}$ *and* U_{pol} over time, irrespective of the aforementioned *relative motions*.

of ionic counter-charges are *minimal in the non-polarizable electrode*. Therefore, the associated *movement artefacts* are weaker here than in the polarizable electrode. Perfectly non-polarizable electrodes have an unhindered exchange of charge across the electrode/electrolyte boundary and there is no such mechanical disturbance.

Likewise, a *low electrode impedance* $\underline{Z}_{el}$ ($\approx R_{el}^{t}$, see Fig. 3.21a, c) of the non-polarizable electrode tends to reduce the electrode's *susceptibility to movement artefacts*. Here a mechanical displacement of this electrode with respect to the surrounding electrolyte yields only relatively *small absolute changes* in $\underline{Z}_{el}$ and thus relatively small absolute variations in $u_{pol,i}$ (Fig. 3.21a). For instance, a definite electrolyte layer between the electrode and tissue (as an *electrode paste*) establishes a clearly defined contact with an advantageously *low contact impedance* and thus with a low absolute susceptibility of this contact impedance to movement artefacts.

Please note that *stray resistances* and *stray capacitances* at the input of a biomedical amplifier—which operates electrode leads connected to electrodes, compare Fig. 3.26—are also influenced by *electrode's motions*, *lead's motions*, and *subject's motions*. Consequently,

- the *coupling of biosignal* from the inner body to surface electrodes, to electrode leads, and then down into the amplifier is subjected to *movement artefacts*. But also
- the *coupling of any interference/noise* from the surroundings into the amplifier underlies *movement artefacts*.

In general, the output of the amplifier shows a *motion-related modulation of the registered biosignal* and a *motion-related noise*.

The biosignal's *source resistance* (R_U in Fig. 3.27a) as well as the biosignal's *source capacitance* (then with a complex *source impedance* $\underline{Z}_U$ instead of R_U in Fig. 3.27a) are also subjected to temporal changes due to *body's motions*. These changes modulate the voltage drop on the body surface that originates from the biosignal's source and is of diagnostic interest (i.e., modulate u_S in Figs. 3.26 and 3.27a). Consequently, the motion-related changes in R_U (or $\underline{Z}_U$) yield associated changes in the *voltage divider* in front of the differential input of the *biomedical amplifier*, as described by (3.42)–(3.44) and shown in Fig. 3.27a. The motion-related changes in the voltage divider lead to

- *gain distortion* (namely, lead to a distorted transfer function from the source open-circuit voltage amplitude $\underline{U}_0$ to the amplitude $\underline{U}_B$ of the differential voltage u_B at the amplifier's input, see Fig. 3.27a) and to
- *baseline wandering* of u_B;

both contributing to *movement artefacts*. In addition, the motion-related changes in R_U (or $\underline{Z}_U$) also modulate the coupling strength from ambient interference sources—such as power lines in Fig. 3.26—into the *conductive human body*.

It should be amended that the shown circuit in Fig. 3.27a applies not only to *contact electrodes* (e.g., surface electrodes with *galvanic coupling*, see Fig. 3.1b, c) but also to *non-contact electrodes* (with *capacitive coupling*, see Fig. 3.1a). In the

latter case, high levels of the capacitive source impedance $\underline{Z}_U$ as well as of impedances $\underline{Z}_{el}$ and $\underline{Z}'_{el}$ prevail [especially for relatively low frequencies, see (2.42)]. This requires an even higher *input impedance of the biomedical amplifier*—i.e., requires its high $\underline{Z}_{diff}$ in Fig. 3.27a (especially for low frequencies)—to minimize attenuating effects of the *voltage divider* and to minimize the aforementioned *motion-related changes of the divider*.

In particular, the *motion-related change in the distance between non-contact electrodes and the body surface* (Fig. 3.1a) varies substantially the capacitive components of $\underline{Z}_{el}$ and $\underline{Z}'_{el}$. Simply speaking, the *coupling capacitance* between metal electrodes and conductive body—see the capacitance C_C in Fig. 3.1a—varies over time due to motions. Thus the time-varying $\underline{Z}_{el}$ and $\underline{Z}'_{el}$ comprise a substantial *source of movement artefacts* which may totally disrupt the biosignal of interest.

Charge and Discharge of Monitoring Electrodes

The *polarizability of electrodes* plays an important role when electrodes are incidentally exposed to a powerful *electrical discharge*, such as from *defibrillation* (Footnote 125 in Chap. 2). In particular,

- a *polarizable electrode* (on the skin) can be strongly polarized by this discharge, namely, by the large *discharge current* (typically >10 A within about 4 ms). The polarizable electrode can even retain a residual charge within its electrode/tissue boundary due to its *high electrode resistance* R^t_{el} (Fig. 3.21b) and thus can become useless in the subsequent diagnostic transmission of relatively small *biosignals* (e.g., of electrocardiogram). In contrast,
- a *non-polarizable electrode* would rapidly dissipate any charge imbalance within the boundary induced by the defibrillator's discharge due to its *low* R^t_{el} short-circuiting this potential excess/residual charge (Fig. 3.21c). Absent residual charge enables a timely and correct transmission of *biosignals* (e.g., to the electrocardiogram monitor). Here non-polarizable electrodes are clearly in favour of polarizable electrodes when used in *intensive care units*.

The aforementioned *polarizability of electrodes* is also an important issue with respect to *direct bias currents* of a biomedical device (i.e., direct input currents of a *biomedical amplifier*; compare Fig. 3.27a) which operates electrodes, especially when electrodes are applied for long-term monitoring. These *small but finite currents* (e.g., of only about 200 nA (Khandpur 2005)) across the electrode/tissue boundary may yield quite *large offset voltages*, i.e., large $u_{pol,i}$ (exceeding 200 mV, see Fig. 3.19b) within minutes of monitoring. Notably, *polarizable electrodes* can become strongly polarized/charged by these currents in view of their high R^t_{el}, which may disadvantageously *drive the amplifier to its saturation*. In contrast, *non-polarizable electrodes* show minimal changes in their $u_{pol,i}$ due to their low R^t_{el} in response to 200 nA even after many days (Khandpur 2005).

3.1.1.4 Whole-Body Impedance

The *whole-body impedance* $\underline{Z}_{wb}$ is given as a sum of

- *skin impedances* $\underline{Z}_s$ of both electrodes and
- the relevant *inner body impedance* $\underline{Z}_b$ (=R_b). For instance,

$$\underline{Z}_{wb} = \underline{Z}_s + R_b + R_b + \underline{Z}_s = 2 \cdot \underline{Z}_s + 2 \cdot R_b \tag{3.37}$$

applies for *hand to hand pathway* in line with Fig. 3.22; compare also (3.39) and see below for more examples. In the latter approximation, any effects of the electrode/skin boundary are neglected, i.e., *electrode impedances* $\underline{Z}_{el}$ of both electrodes *are not considered*; the complete expression with $\underline{Z}_{el}$ is given in (3.38) (Fig. 3.24d).

In fact, the *impedance* $\underline{Z}_{wb}$ is highly relevant since it determines the *resulting current* $\underline{I} = \underline{U}_C / \underline{Z}_{wb}$ through the body (Fig. 3.22c), given a certain *contact voltage* $\underline{U}_C$ (or *touch voltage*); compare Fig. 2.90. In other words, a high *magnitude* Z_{wb} of $\underline{Z}_{wb}$ would advantageously limit the current and thus its *adverse effects* within the body in the case of an *electrical accident* (Sect. 2.3.2.5). Please note that since we do not consider the current-limiting $\underline{Z}_{el}$ in series with $\underline{Z}_s$ and R_b (Fig. 3.24d), the impedance $\underline{Z}_{wb}$ from (3.37) represents rather a worst-case scenario in terms of the

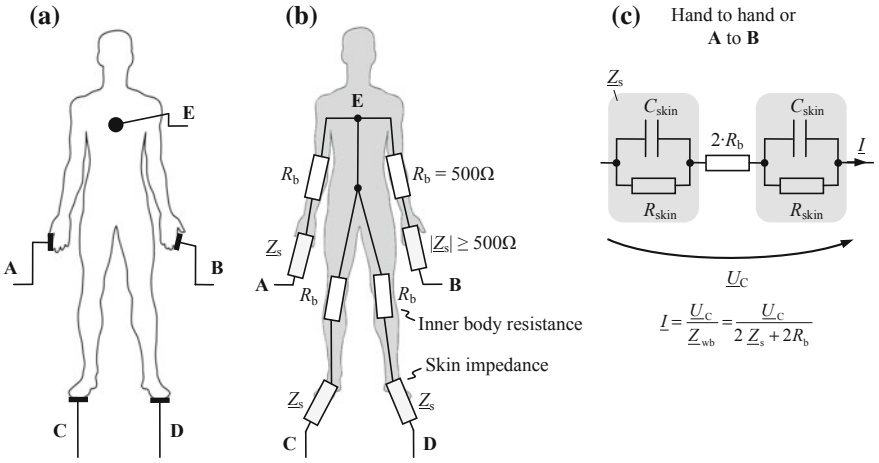

Fig. 3.22 Approximation of the whole-body impedance between **a** any two electrodes A–E applied on hands or feet (or touching live parts) in terms of **b** an equivalent circuit model for the mains frequency of 50 Hz, as partly adopted from Leitgeb (2010). Here the skin is modelled by a complex impedance $\underline{Z}_s$ with its magnitude usually $|\underline{Z}_s| \geq 500\ \Omega$. The inner body is modelled by a simple network of real impedances or electrical resistances R_b (each of about 500 Ω) at 50 Hz; i.e., the conductive behavior dominates in the inner body (see examples from Section "Biological Boundaries"). Any effects of the electrode/tissue interface are neglected here. **c** The detailed circuit model of the whole-body impedance between both hands (between A and B), as derived from (**b**)

electrical accident and the resulting relatively high I. On the other hand, a high Z_{wb} would disadvantageously impair the *stimulating effects* of the current in the case of an electrical *therapy* (Section "Electrical Stimulation Effects" and Footnote 115 in Chap. 2).

The *skin* contributes significantly to Z_{wb} (3.37) when live parts or live electrodes contact the body. In particular,

- the conductive electrode and *different layers of the skin* such as dry horny skin surface, isolating epidermis (especially, corneum when intact and dry), conducting dermis (well perfused), and isolating subcutaneous fat [see the skin's structure in Kaniusas (2015, Fig. 5.23)] form a *capacitor* (Fig. 3.22c) which impedance decreases in magnitude with increasing field frequency (3.2). In addition, the resistive components of the skin layers form a *resistor* connected *in parallel to the capacitor* [(2.47) and Fig. 3.22c]. Consequently, the *skin impedance* is primarily responsible for the frequency dependence of Z_{wb} (3.37). Therefore, the impedance magnitude Z_s—as well as Z_{wb}—*is highest for direct current* (at zero frequency) and *decreases with increasing field frequency*.
- Obviously, *wet skin* decreases the resistance of the horny skin layer as compared with *dry skin* and thus decreases the effective skin impedance.
- It is important to note that the skin impedance shows a voltage-dependant behaviour; namely, the *skin impedance* tends to decrease (highly *non-linearly*) with increasing U_C. This is because spots of local *electric breakdown* accumulate progressively in the insulating skin layers with increasing voltage, whereas these layers can withstand their inner electric fields only up to a certain limit (Kaniusas 2012, Footnote 49). Consequently, the skin resistance decreases with diminishing *isolation of the skin*. In addition, a sudden *breakdown* is seen in the skin impedance of dry skin above a critical voltage of about 500 V, whereas current through the skin becomes concentrated in *discrete channels* permeating the skin.

  Figure 3.23 demonstrates the decrease of Z_{wb}—as the sum of skin and body impedances (3.37)—with increasing U_C. Since the *body impedance* can be assumed to be *independent on* U_C, it is the *skin impedance which decreases with* U_C and thus determines the decrease of Z_{wb} with U_C. It is instructive to observe from Fig. 3.23 that the *voltage-dependant behaviour* of the skin impedance is especially prominent at relatively *low* U_C. Likewise, with *increasing* U_C, the impedance Z_{wb} becomes progressively less dependent on the skin impedance and thus *converges towards the body impedance* for high U_C.

  Please note that the decrease of Z_{wb} with increasing U_C becomes less with increasing *contact area* (of electrodes with the body). With increasing area, the total current becomes more widely distributed within the skin and thus the local current density decreases (2.23). Likewise, the *skin impedance* decreases with increasing *contact area* (2.36) as well as the *contribution of this skin impedance to* Z_{wb} (3.37) and so Z_{wb} decreases less steeply with increasing U_C for larger contact area.

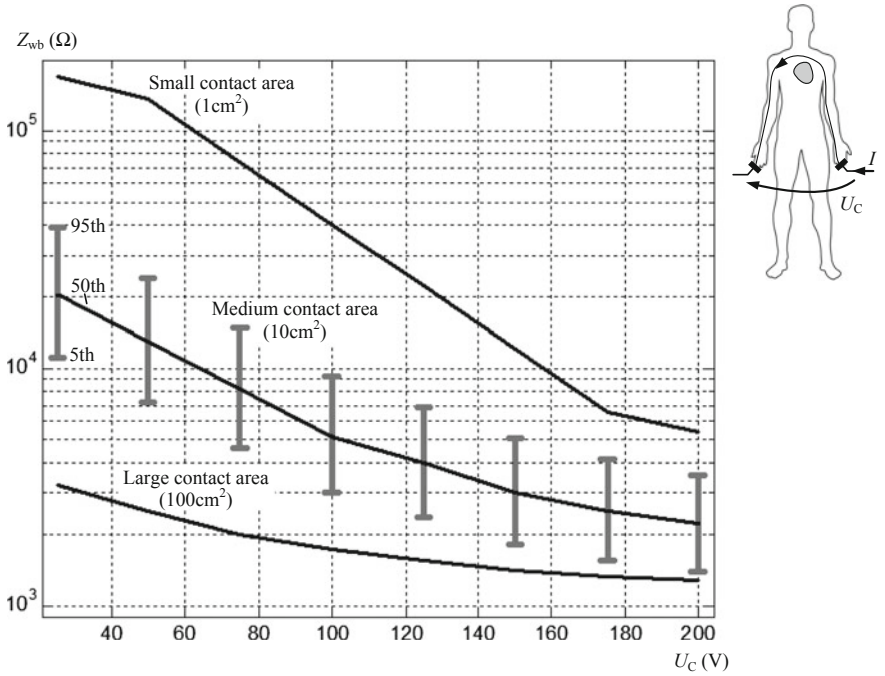

Fig. 3.23 Dependence of the whole-body impedance magnitude Z_{wb} on the contact voltage amplitude U_C between both hands (Fig. 3.22) and the size of the dry contact area. The alternating current at the mains frequency 50 Hz flows from on hand to another. Depicted values of Z_{wb} refer to 50th percentile values of adult persons while grey bars indicate the variability of Z_{wb} from its 5th up to 95th percentile for the medium contact area. Image data extracted from DIN 60479-1 (2007)

On the other hand, this *voltage-dependant behaviour* has an important consequence that *exposure limits* against electric shock should consider not only the current strength and the duration of exposure (Fig. 2.89) but also the applicable skin impedance (DIN 60479-1 2007). That is, practicable limits of exposure restrict usually $|\underline{U}_C|$ (given as the product of the current $|\underline{I}|$ through the body and $|\underline{Z}_{wb}|$) so that the voltage-dependant behaviour of the skin also becomes reflected by the exposure limits.

- The *size of the contact area* on the skin—the skin area in contact with live parts—impacts critically the *skin impedance*. For instance, if the contact area is reduced from the palm area (about 100 cm^2) to the fingertip area (about 1 cm^2), the skin impedance is theoretically expected to increase by a factor of 100 (2.36). However, the author in (Leitgeb 2010) reports a much lower factor of the latter increase; namely, only a 4-fold increase at U_C of 200 V and 40-fold increase at 20 V, as can also be derived from *experimental data* in Fig. 3.23. That is, the skin impedance is more sensitive to changes in the contact area (and to changes in the wetness and temperature of the skin) for *low* U_C (DIN 60479-1 2007).

Figure 3.23 demonstrates an increase of Z_{wb}, to be precise, an increase of the *skin impedance* (see above), with decreasing size of the *contact area* for different values of U_C.

- The *time* after an electrode is placed on the skin surface plays also a role. The skin impedance tends to fluctuate within *first minutes*, then *drops* in the range of *tenth of minutes*, and reaches an apparent asymptotic value after about *20–30 min* (Reilly 1998). A gradual hydration of the corneum from *sweat* buildup under the electrode contributes to this decrease over time.

Inner body impedances comprise another determinant of $\underline{Z}_{wb}$ (Fig. 3.22) and depend mainly on the effective current pathway through the inner body. In particular, *narrow body sections* within the inner body contribute significantly to the inner body impedance, as already discussed in Section "Charge and Current Induction". Decreasing cross-section area for the current flow through a body part increases the associated impedance (2.36). Therefore, *joints* which are *limited in space* and, on the other hand, are composed out of only poorly conducting bones, tendons, and cartilage with little conducting muscles around contribute most to the inner body impedance. In particular, small joints such as *wrist and ankle in the extremities* determine the inner body impedance. Likewise, the impedance of the torso can be neglected. Please note that the inner body impedance is only weakly affected by the field frequency at low frequencies; i.e., as long as the conductive behaviour dominates in tissue (compare Fig. 2.21 and some examples in Section "Biological Boundaries").

Figure 3.22 illustrates an approximation of $\underline{Z}_{wb}$ between extremities in *contact with live parts or live electrodes* at the points from A to E for the mains frequency of 50 Hz. For instance, the total *magnitude* Z_{wb} (3.37) of

- $Z_{wb} = |2 \cdot R_b + 2 \cdot \underline{Z}_s| \approx 2 \cdot R_b + 2 \cdot Z_s \approx 2000\ \Omega$ (3.37) results approximately for *hand to hand* pathway (from the point A to B in Fig. 3.22c),
- $Z_{wb} \approx (R_b + R_b/2) + 2 \cdot Z_s \approx 1750\ \Omega$ results approximately for the current pathway from one *hand to both (grounded) feet* (from A to short-circuited C and D), and
- $Z_{wb} \approx R_b/2 + 2 \cdot Z_s \approx 1250\ \Omega$, a lower value, results approximately for the pathway from the *chest to both feet* (from E to short-circuited C and D).

Here the magnitude Z_s of the *skin impedance* was assumed to be constant for all extremities and equal to 500 Ω (with the *phase arg($\underline{Z}_s$) of* $\underline{Z}_s$ approximated to be zero for 50 Hz). This level is approximately applicable, for instance, to *dry skin* with the contact area of about 10 cm^2 and U_C of 200 V, as derived from Leitgeb (2010). In general, *dry skin* shows greater variance in Z_{wb} than *wet skin*, whereas Z_{wb} in *children* is greater than in *adults* (Reilly 1998).

Each extremity in Fig. 3.22b was modelled with the *inner body resistance* R_b equal to 500 Ω (Leitgeb 2010), as a *stickman* with resistors. Please note that the conductive behaviour of tissue dominates at the relatively low frequency of 50 Hz (Section "Biological Boundaries"), so that the inner body impedance can be assumed to be real. *Experimental data* in Fig. 3.23 confirms the latter assumptions.

That is, the depicted Z_{wb} is about 2 kΩ for contact area of 10 cm^2 and U_C of 200 V, which then yields $Z_s \approx 500\ \Omega$ and $R_b \approx 500\ \Omega$ in line with $Z_{wb} \approx 2 \cdot R_b + 2 \cdot Z_s$ for *hand to hand pathway* (Fig. 3.22c).

Interestingly, the cited value of 500 Ω is in the similar range as the resistance of *NaCl physiological solution* (Footnote 27 in Chap. 2) and of geometrical dimensions of the considered body region (Reilly 1998). For instance, the assumed homogeneous conductivity of 2 S/m of NaCl solution of a cylindrical body region with a cross-section area of 25 $cm^2 = 25 \cdot 10^{-4}\ m^2$ and length 1 m yields $R_b = 1\ m / (2\ S/m \cdot 25 \cdot 10^{-4}\ m^2) = 200\ \Omega$ (2.36) without considering any narrow body sections (see above).

As already discussed, *extremities* determine the inner body resistance. In contrast, in the *thoracic area*, the inner resistance can be neglected (Fig. 3.22b) because the cross-section area in the thorax is quite large and mostly highly conductive tissues reside within; i.e., the level of R_b decreases with increasing area A and increasing conductivity γ in (2.36). In other words,

- mostly the *skin* and
- *body extremities* (arms, legs, and fingers) with their *limited cross-section areas* restraining the current flow in the inner body

determine Z_{wb} and thus *limit the resulting currents I* within the body in contact with live parts or live electrodes for the mains frequency. In particular, when the applied (contact) *voltage is moderately low* (<200 V according to Reilly (1998)) and the skin is undamaged, the skin impedance is the primary factor that limits the body currents. To give a practically relevant example, a *single index finger* has an estimated contribution to Z_{wb} of about 1 kΩ at the relevant U_C of 200 V at 50 Hz (i.e., the *mains voltage*), whereas a relatively small dry contact area of about 2.5 cm^2 of the index finger was given here (DIN 60479-1 2007). Please note that Z_{wb} is defined to be 2 kΩ at the mains frequencies 50/60 Hz for *safety considerations*, with the skin impedances from both contact sites contributing 50% to this value (defined for healthy users but not for patients who might be injured or have wet skin) (Leitgeb 2010) and neglected electrode impedances $\underline{Z}_{el}$. During surgery, the applicable Z_{wb} may be as low as 10 Ω (without skin).

Obviously, the *effective value of* Z_{wb} depends on the *field frequency* (2.47), the *contact area* (2.36), and even on the absolute value of U_C *of live parts or electrodes* (see above). Likewise, the level of $\underline{Z}_{wb}$ *converges towards the inner body impedance* $\underline{Z}_b$

- for *high* U_C (>200 V) due to skin breakdown and for *large skin contact areas* ($\geq 100\ cm^2$) diminishing $\underline{Z}_s$, as estimated from DIN 60479-1 (2007) and indicated in Fig. 3.23 (see above);
- for *large contact area* (for contact area $\geq 100\ cm^2$, see Fig. 3.23);
- for *hydrated or wet skin*; and
- for *high field frequencies* (>5 kHz) short-circuiting the skin and $\underline{Z}_s$.

For high U_C and/or high frequency, Z_{wb} *depends weakly* on the effective *contact area* and the *wetness* of the skin since mainly $\underline{Z}_b$ *determines* Z_{wb}. Thus, for instance, high-voltage *spark discharges* can be practically used to short-circuit $\underline{Z}_s$—the skin impedance breaks down—in order to measure $\underline{Z}_b$.

3.1.2 Signal Coupling in Diagnosis and Therapy

3.1.2.1 Diagnosis

A *diagnostic approach* with *surface electrodes* in contact with the *skin* is shown in Fig. 3.24 in order to illustrate contact-related effects on biosignals to register. For instance, the permanent electric biosignal, electrocardiogram, is registered here (Fig. 3.24b). The *resulting time-varying voltage u* between the skin electrodes and the associated *effective current amplitude* $\underline{I}$ in the external diagnostic device (used here as the *output biosignal*)—with respect to the *open-circuit effective voltage amplitude* $\underline{U}_0$ of the *biosignal's source* within the body (acting as the *input biosignal*)—determine the efficiency of the diagnostic device (Fig. 3.24c, d). In fact, the equivalent circuit model from Fig. 3.24d yields

$$\underline{I} = \frac{\underline{U}_0 + (U_{pol} - U'_{pol})}{R_U + R_b + R'_b + \underline{Z}_s + \underline{Z}'_s + \underline{Z}_{el} + \underline{Z}'_{el} + R_I} \approx \frac{\underline{U}_0}{\underline{Z}_{wb} + 2 \cdot \underline{Z}_{el} + R_I} = \frac{\underline{U}_0}{\underline{Z}_T + R_I}, \tag{3.38}$$

whereas U_{pol} and U'_{pol} are the respective polarization voltages (direct voltages) of both electrodes applied on the skin (Fig. 3.6c), R_U the inner resistance of the biosignal's source (assumed as a *voltage source*), R_b and R'_b the respective inner body resistances (simplified model from Fig. 3.2a), $\underline{Z}_s$ and $\underline{Z}'_s$ the respective complex skin impedances (simplified model from Fig. 3.2b), $\underline{Z}_{el}$ and $\underline{Z}'_{el}$ the respective complex electrode impedances (the impedances of the electrode/tissue interface according to the simplified model from Fig. 3.20c), and R_I the inner resistance of the diagnostic ammeter.

The approximation in (3.38) assumes reasonably that $R_U \ll |\underline{Z}_{wb}|$, $\underline{Z}_{el} = \underline{Z}'_{el}$, and $|U_{pol} - U'_{pol}| \ll |\underline{U}_0|$ (two identical electrode/tissue boundaries yield $U_{pol} = U'_{pol}$), whereas the *whole-body impedance* $\underline{Z}_{wb}$ is given as

$$\underline{Z}_{wb} = R_b + R'_b + \underline{Z}_s + \underline{Z}'_s. \tag{3.39}$$

Of these contributions in $\underline{Z}_{wb}$, the skin impedance $\underline{Z}_s$ (and $\underline{Z}'_s$) is the most difficult to characterise or to control in praxis.

It should be noted that the *efficiency of the diagnostic device* is governed by the size of the *total circuit impedance* $\underline{Z}_T = \underline{Z}_{wb} + 2 \cdot \underline{Z}_{el}$ (3.38) which determines practically the *output current* $\underline{I}$ in the diagnostic device for a given *input voltage* $\underline{U}_0$ in the body. In particular, $\underline{Z}_T$ is composed out of *series components* of the

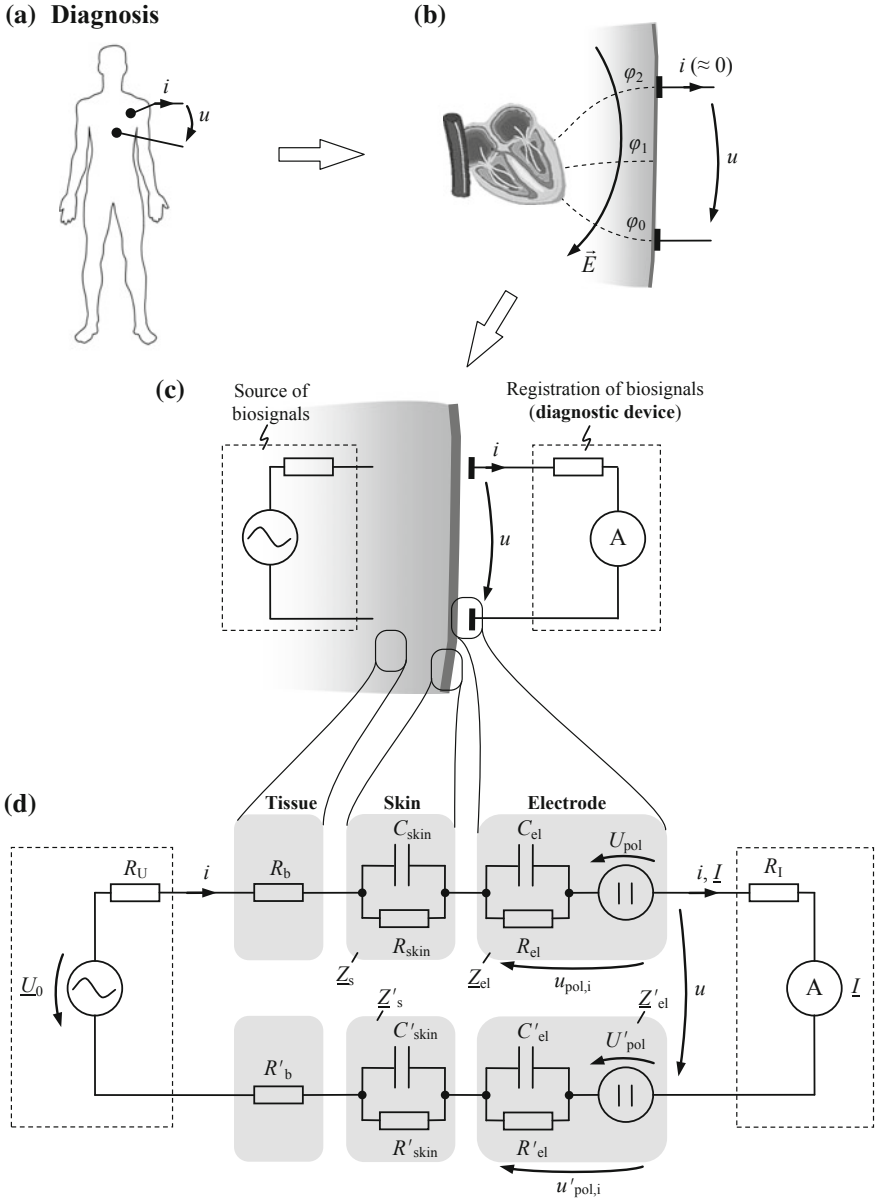
(a) Diagnosis
i
u
(b)
φ2
i (≈ 0)
φ1
u
φ0
E
(c)
Source of biosignals
Registration of biosignals (diagnostic device)
i
u
A
(d)
Tissue
Skin
Electrode
R_U
i
R_b
C_skin
R_skin
C_el
U_pol
R_el
i, I
R_I
U_0
Z_s
Z_el
u_pol,i
u
A
I
Z'_s
Z'_el
C'_skin
C'_el
U'_pol
R'_b
R'_skin
R'_el
u'_pol,i

◂**Fig. 3.24** Diagnosis with surface electrodes on the skin and the resulting electrical equivalent circuit model; compare Fig. 3.25. **a** Electrodes on the chest are applied to register a permanent electric biosignal, electrocardiogram. **b** The registered time-varying voltage u $(=\varphi_2 - \varphi_0)$ corresponds to the difference between two equipotential surfaces of the electric potential φ in tissue and thus is related to the local electric field $\vec{E}$ in tissue [in line with (2.28)]. **c** Simplified equivalent circuit model. **d** Advanced equivalent circuit model considering the source of biosignals (given as the voltage source with the open-circuit effective voltage $\underline{U}_0$ and the inner resistance R_U), the inner body resistance R_b, the skin impedance $\underline{Z}_s$ (Fig. 3.2), the electrode impedance $\underline{Z}_{el}$ (considering the charge-transfer-limited electrode reaction, see the model in Fig. 3.20c), and the diagnostic device to register biosignals (as an ammeter with its inner resistance R_I)

whole-body impedance $\underline{Z}_{wb}$ and the *electrode impedance* $\underline{Z}_{el}$, whereas the impedance $\underline{Z}_T$ includes contributions from

- the *biosignal's source*,
- the internal bodily *tissues*,
- the *skin*, and
- the *electrode interface*.

Namely, the best diagnostic efficiency is attained when the registered $\underline{I}$ becomes independent on $\underline{Z}_T$ and on the polarization voltage $u_{pol,i}$ (Fig. 3.24d), i.e., when the inequality $|\underline{Z}_T| \ll R_I$ applies in (3.38). In other words, an efficient *diagnostic device* should exhibit a *large input resistance* R_I, i.e., a *high impedance recording amplifier* is needed. However, then the magnitude of $\underline{I}$ in the device becomes very small in size, i.e., $|\underline{I}| \to 0$ for $R_I \to \infty$ (3.38). Likewise, the *voltage u between electrodes* should be ideally recorded with small $\underline{I} \to 0$ (Fig. 3.24c) to *minimize/avoid* both the *polarization overvoltage* $(u_{pol,i} - U_{pol})$ across $\underline{Z}_{el}$ with its complex amplitude $\underline{Z}_{el} \cdot \underline{I}$ and the voltage drop $\underline{Z}_{wb} \cdot \underline{I}$ across $\underline{Z}_{wb}$ proportional to $\underline{I}$. In addition, weak biosignals (in the range of mV and even μV) to be recorded may be lost in the noisy, ion-based electric fluctuations of the electrolyte at the electrode surface if U_{pol} and U'_{pol} as well as $\underline{Z}_{el}$ and $\underline{Z}'_{el}$ are not low enough. For instance, *large electrode surfaces* of skin electrodes are beneficial for low $\underline{Z}_{el}$ and $\underline{Z}'_{el}$, as discussed in Section "Electrode Impedance Model".

3.1.2.2 Therapy

A *therapeutic approach* with *surface electrodes* is demonstrated in Fig. 3.25. The *effective amplitude* $\underline{I}$ of the *resulting time-varying current i* through the body in response to the applied *open-circuit effective voltage amplitude* $\underline{U}_0$ of the therapeutic device (Fig. 3.25a) is crucial for the *therapeutic efficiency* or *therapeutic safety*. Here the electrical stimulation of tissue—e.g., of the heart region, as shown in Fig. 3.25b—by $\underline{I}$ could be relevant, whereas electrodes are directly applied on the skin. On the other hand, a limitation of the unwanted $\underline{I}$ in tissue could also be relevant to prevent adverse stimulation effects of currents within the body (e.g., to avoid ventricular fibrillation, see Section "Cardiac Interference").

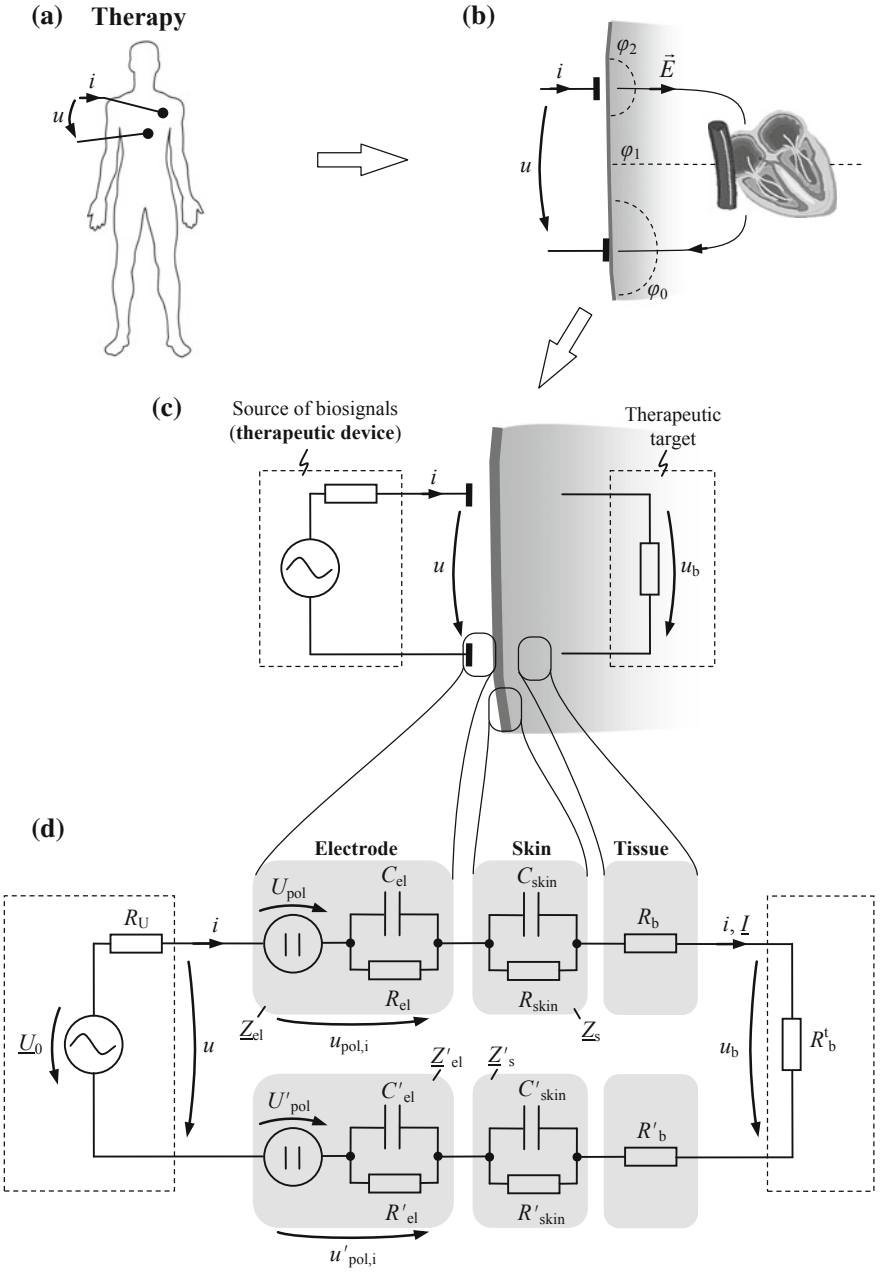
(a) Therapy
i
u
(b)
φ2
i
E
φ1
u
φ0
(c)
Source of biosignals
(therapeutic device)
Therapeutic
target
i
u
ub
(d)
Electrode
Skin
Tissue
Upol
Cel
Cskin
RU
i
Rb
i, I
Rel
Rskin
U0
Zel
upol,i
Zs
u
Z'el
Z's
ub
Rtb
U'pol
C'el
C'skin
R'b
R'el
R'skin
u'pol,i

◀**Fig. 3.25** Therapy with surface electrodes on the skin and the resulting electrical equivalent circuit model; compare Fig. 3.24. **a** Electrodes on the chest are applied to perform electrical stimulation of the heart region. **b** The externally-applied time-varying voltage u yields the equipotential surfaces of the electric potential φ and the corresponding local electric field $\vec{E}$ in tissue [in line with (2.28)]. **c** Simplified equivalent circuit model. **d** Advanced equivalent circuit model considering the source of biosignals, i.e., the external therapeutic device (given as the voltage source with the open-circuit effective voltage $\underline{U}_0$ and the inner resistance R_U), the electrode impedance $\underline{Z}_{el}$ (considering the charge-transfer-limited electrode reaction, see the model in Fig. 3.20c), the skin impedance $\underline{Z}_s$, the inner body resistance R_b, and the resistance R_b^t of the therapeutic target in the body (Fig. 3.2)

In line with Fig. 3.25d and in analogy with (3.38), the *total circuit impedance* $\underline{Z}_T = \underline{Z}_{wb} + 2 \cdot \underline{Z}_{el}$ determines mainly this *output current* $\underline{I}$ in tissue for a given *input voltage* $\underline{U}_0$, to give

$$\underline{I} = \frac{\underline{U}_0 - (U_{pol} - U'_{pol})}{R_U + R_b + R'_b + \underline{Z}_s + \underline{Z}'_s + \underline{Z}_{el} + \underline{Z}'_{el} + R_b^t} \approx \frac{\underline{U}_0}{\underline{Z}_{wb} + 2 \cdot \underline{Z}_{el}} = \frac{\underline{U}_0}{\underline{Z}_T}. \quad (3.40)$$

Here R_b^t denotes the resistance of the therapeutic target within the body. The latter approximation in (3.40) assumes reasonably that R_U, $R_b^t \ll |\underline{Z}_{wb}|$, $\underline{Z}_{el} = \underline{Z}'_{el}$, and $|U_{pol} - U'_{pol}| \ll |\underline{U}_0|$.

An efficient *therapeutic device* (designed as a voltage source, see Fig. 3.25c, d) should exhibit a *small inner resistance* R_U in order to maximise the output $\underline{I}$. In addition, the *therapeutic efficiency* increases with decreasing $|\underline{Z}_T|$ that favours a large $\underline{I}$, according to (3.40). In other words, since a certain current density ($\propto |\underline{I}|$) is needed within the body to induce a targeted therapeutic activity, a high $\underline{Z}_{el}$ and/or $\underline{Z}'_{el}$ would result in a large voltage drop $u_{pol,i}$ across the electrode/electrolyte boundary (Fig. 3.25) given a required $\underline{I}$, eventually leading to unwanted electrolytic reactions at this boundary that may be harmful to tissue (Fig. 2.84).

Please note that if the applied *therapeutic device* acts as a *current source* with a constant output current (i.e., its current is "clamped" to a certain level)—while this particular current level is required within the body—then both contact $\underline{Z}_{el}$ and $\underline{Z}'_{el}$ as well as $\underline{Z}_{wb}$ do not play any role in terms of the resulting current level within the body. This is because the therapeutic current source has a *high inner output impedance* (like R_U in Fig. 3.25d) which can be seen as connected in series with $\underline{Z}_{el}$, $\underline{Z}'_{el}$, and $\underline{Z}_{wb}$ (Fig. 3.25d) and which is typically higher than the sum $\underline{Z}_{el} + \underline{Z}'_{el} + \underline{Z}_{wb}$ (3.39). It should be recalled that an ideal current source has infinite inner output impedance to *keep the output current constant* irrespective of the size of the load impedance (i.e., of the sum $\underline{Z}_{el} + \underline{Z}'_{el} + \underline{Z}_{wb}$) connected to this source. However, large clamped currents through electrodes with their non-zero $\underline{Z}_{el}$ and $\underline{Z}'_{el}$ may lead to large levels of $u_{pol,i}$ (Figs. 3.14 and 3.24d) and thus to unfavourable electrolytic reactions of various types at the electrode/electrolyte boundary (Section "Ag/AgCl and Pt Electrodes").

3.1.2.3 Non-contact Diagnosis

Besides sensing using

- surface *contact electrodes* in *direct contact* with the body skin, known as *conductive sensing* (compare electrodes from Figs. 1.1 and 3.1b, c),
- *non-contact electrodes* located at a certain distance from the body can also be used for sensing using this *indirect contact*, known as *capacitive sensing* (compare electrodes from Figs. 3.1a and 3.31b).

In the latter case, each *non-contact metallic electrode* and, on the other hand, the skin of the body act as opposite plates of capacitor (Fig. 2.8), i.e., as plates separated by an insulator such as the air. In this capacitive coupling, *displacement currents* are registered, which are caused by the inner (endogenous) electric fields on the body surface.

The obvious *advantages of capacitive coupling* over conductive coupling are *missing skin infection/irritation* (eventually, due to adhesive electrodes in direct contact with the body skin) and *absent signal deterioration* in the long-term monitoring (due to a progressive worsening of the adhesive contact with the skin). The associated *disadvantages of capacitive coupling* comprise very *high contact impedance* (due to indirect and air-borne contact of electrodes with the body's sources of electric biosignals) and high *susceptibility to movement artefacts* (due to varying distance between the electrode and the body leading to *low signal-to-noise ratio*). Capacitive coupling is used for monitoring of diverse biosignals such as electrocardiogram or electroencephalogram, whereas the capacitive metallic electrodes are usually located in the bed cushion, chair backrest, underwear, or shirt (Zheng et al. 2014).

3.2 Biosignal and Interference Coupling

Figure 3.26 illustrates *biosignal coupling* using *two electrodes measurement* (shown in black) along with the coupling of *power line interference* (or *noise*, shown in grey). The power lines are unavoidably present in any clinical situation, if for no other purpose than to light the room or operate outlets. Here electrodes are applied on the *skin* of an *isolated human body*, i.e., on a *conductive body* surrounded by *isolating air* (compare Fig. 2.27b). These *surface electrodes* with their respective *electrode impedances* $\underline{Z}_{el}$ and $\underline{Z}'_{el}$ are connected via electrode leads (*sensing lines*) with an isolated *differential biomedical amplifier*. The amplifier's isolation is given via the capacitance C_{iso} connecting the amplifier's ground with power line's ground, see Fig. 3.26. The *differential voltage* u at the input of the amplifier—see (3.41)—reflects

- the *biosignal* u_B to be registered (Fig. 3.27a),
- the *common-mode interference voltage* u_{CI}, and
- the *differential-mode interference voltage* u_{DI} (Fig. 3.27b), as discussed in the following.

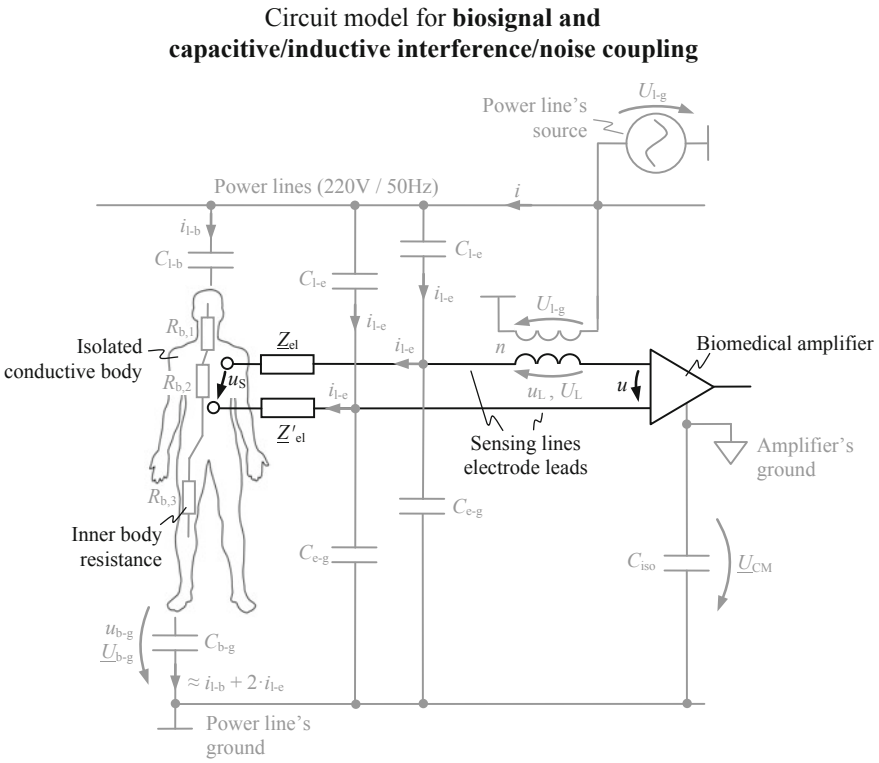

Fig. 3.26 Classical electrical equivalent circuit model for the coupling of (wanted) biosignal and (unwanted) power line interference, using two electrodes located on an isolated human body. The interference (or noise) is capacitively coupled into the conductive human body in terms of the displacement current i_{l-b} across the capacitance C_{l-b}, and, on the other hand, into both unshielded electrode leads in terms of the displacement currents i_{l-e} across the capacitances C_{l-e}. The inductive coupling of the power line interference yields a finite interference voltage u_L along leads with its amplitude U_L (=U_{l-g} / n with n as the turns ratio of the transformer). Detailed models are depicted in Figs. 3.27 and 3.28. The circuit elements shown have the following typical values (for 50 Hz): $C_{iso} \approx 10$ pF, $C_{l-b} \approx 2$ pF, $C_{b-g} \approx 200$ pF (with $C_{b-g} \gg C_{l-b}$ due to the large ground area), $C_{l-e} < C_{e-g} \approx 0.05$ pF, and 100 Ω < $\underline{Z}_{el}$ < 100 kΩ. The interference source and current pathways for the capacitive and inductive coupling are plotted in grey

3.2.1 *Capacitive Coupling of Interference*

The source of *power line interference* yields an *alternating displacement current* i_{l-b} in the air (at the power line frequency of 50 Hz), which is *capacitively coupled from wires of power lines into the conductive human body* across the *line-body stray capacitance* C_{l-b} towards the *low-ohmic power line's ground*, as shown in Fig. 3.26. Here the surface of the body acts as one capacitor plate while the wire's surface of power lines acts as another capacitor plate (Fig. 2.8). This coupling arises

(a) Detailed circuit model for **biosignal coupling**

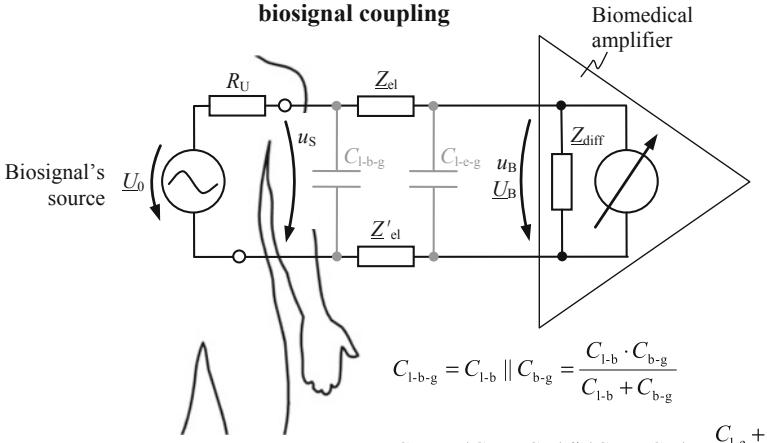

$$C_{l\text{-}b\text{-}g} = C_{l\text{-}b} \,||\, C_{b\text{-}g} = \frac{C_{l\text{-}b} \cdot C_{b\text{-}g}}{C_{l\text{-}b} + C_{b\text{-}g}}$$

$$C_{l\text{-}e\text{-}g} = (C_{l\text{-}e} + C_{e\text{-}g}) \,||\, (C_{l\text{-}e} + C_{e\text{-}g}) = \frac{C_{l\text{-}e} + C_{e\text{-}g}}{2}$$

(b) Detailed circuit model for **capacitive interference/noise coupling**

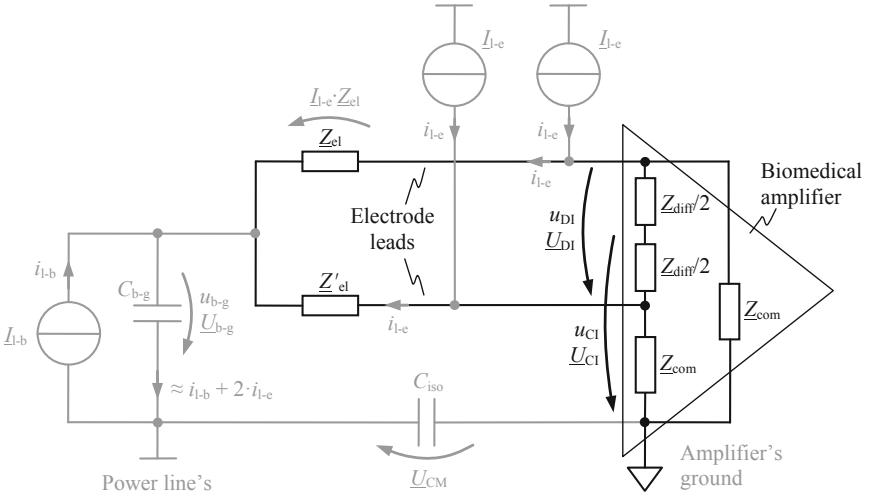

$$\underline{U}_{DI} \approx \underline{I}_{l-e} \cdot (\underline{Z}_{el} - \underline{Z}'_{el}) - (\underline{U}_{b-g} - \underline{U}_{CM}) \cdot \frac{\underline{Z}_{el} - \underline{Z}'_{el}}{\underline{Z}_{com}}$$

$$\underline{U}_{CI} = \underline{U}_{b-g} + \underline{I}_{l-e} \cdot \frac{\underline{Z}_{el} + \underline{Z}'_{el}}{2} - \underline{U}_{CM}$$

◀**Fig. 3.27** Detailed electrical equivalent circuit models of Fig. 3.26. **a** Model for the coupling of (wanted) biosignal using two electrode measurements. The resulting voltage divider reduces the input voltage $\underline{U}_B$ as related to the source voltage $\underline{U}_0$ [see $|\underline{U}_B| < |\underline{U}_0|$ from (3.42)]. **b** Model for the capacitive coupling of power line interference (or noise) into an isolated human body (see the current i_{l-b}) and into both unshielded electrode leads (see both currents i_{l-e}). The common-mode interference voltage $\underline{U}_{CI}$ and differential-mode interference voltage $\underline{U}_{DI}$ result at the amplifier's input. Please note that R_U is in the order of Ω while $\underline{Z}_{diff}$ and $\underline{Z}_{com}$ are in the order of GΩ; for values of other parameters consult Fig. 3.26. Inner body resistances, lead inductances, and inductive coupling of power line interference are neglected. Interference sources and current pathways for the capacitive coupling are plotted in grey

because *electric fields* between metallic wires of power lines, the conductive body, and the low-ohmic ground are subjected to *temporal changes or oscillations*. These changes lead necessarily to *displacement currents* in the air [according to (2.66)], which *flow* through the system *towards the ground*; compare Figs. 2.26 and 2.27b.

Please note that i_{l-b} (typically in the *range* of 0.1–1 μA (Huhta and Webster 1973)), as any *current* produced by *alternating electric potential above the ground*, will *flow to this ground* along the *path of least impedance* (or *least resistance* for direct currents, see Fig. 2.13a, c). Therefore, as illustrated in Fig. 3.26, the *largest portion of* i_{l-b} within the body does not cross $\underline{Z}_{el}$ and $\underline{Z}'_{el}$ (as *conductive currents*) to enter the *biomedical amplifier* with its typically very high[46] *differential-mode impedance* $\underline{Z}_{diff}$ *and common-mode input impedances* $\underline{Z}_{com}$ (Fig. 3.27b), but instead i_{l-b} crosses the *relatively large body-ground stray capacitance* C_{b-g} (as *displacement current*) with its *relatively low impedance* $1/(j\omega C_{b-g})$ on its way towards the power line's ground. In general, the coupling of ambient displacement currents into the body and accumulated static electric charges on this *conductive isolated body* cause a finite *interference voltage* u_{b-g} with its amplitude $\underline{U}_{b-g}$ across C_{b-g} (Fig. 3.26, compare also Fig. 2.29).

This current i_{l-b} across C_{b-g} contributes mainly to u_{b-g} and thus to a *common-mode input-referred interference voltage* u_{CI} at the amplifier's inputs (3.45), known as *common-mode electromagnetic interference*. This interference acts on the *input of the amplifier*—affecting its effective input u in line with (3.41), see Sect. 3.2.4—and thus should be suppressed by a preferably high *common-mode rejection ratio CMRR* of this *real differential amplifier*. In addition, the *residual portion of* i_{l-b} flowing through the high $\underline{Z}_{diff}$ and $\underline{Z}_{com}$ (Fig. 3.27b) can also produce another significant contribution to u_{CI} which may even *saturate the amplifier of the input stage*.

Other *displacement currents* i_{l-e} in the air are *capacitively coupled from power lines into both electrode leads* across the *line-lead stray capacitance* C_{l-e}, as shown in Fig. 3.26. Obviously, we must assume here that the two *leads are unshielded*

[46]It should be further supplemented that we want $\underline{Z}_{diff}$ *and* $\underline{Z}_{com}$ *to be large* enough to *avoid loading effects* on the differential and common potentials at the amplifier's input. In addition, large $\underline{Z}_{com}$ compared to $\underline{Z}_{el}$ and $\underline{Z}'_{el}$ *minimizes disadvantageous effects of the typical unbalance* $\underline{Z}_{el} \neq \underline{Z}'_{el}$, i.e., minimizes the associated effects of the *potential divider*, see Footnote 49 and Sect. 3.2.5.

(see Sect. 3.2.8). Both *currents* i_{l-e} (in the *range* of a few nA (Huhta and Webster 1973)) coupled into each lead are assumed here to be approximately *equal in their size* because both leads are presumed to run close together, their lengths are the same, and power lines are not very near one lead and not the other. Obviously, the longer is the lead, the larger is i_{l-e} entering this lead. Again, since both i_{l-e} follow the *path of least impedance* (2.51), *most of* i_{l-e}—as illustrated in Fig. 3.26—flow through the associated $\underline{Z}_{el}$ or $\underline{Z}'_{el}$ (as *conductive currents*) into the body and then cross C_{b-g} (as *displacement currents*) down to the *low-ohmic power line's ground*.

The total current through C_{b-g} amounts then to $i_{l-b} + 2 \cdot i_{l-e}$ and determines the interference u_{b-g} (Fig. 3.26). It should be reiterated that as soon as *displacement currents* i_{l-b} *and* i_{l-e} *in the air* enter the conductive body and/or conductive electrode leads, they become *conductive currents* (Fig. 2.8).

There is also an *alternative path* for both currents i_{l-e} to flow along leads into the amplifier with its quite high $\underline{Z}_{diff}$ and $\underline{Z}_{com}$ on their way to the power line's ground (Fig. 3.27b). However, since the inequality $\underline{Z}_{diff}, \underline{Z}_{com} \gg \underline{Z}_{el}, \underline{Z}'_{el}, 1/(j\omega C_{b-g})$ applies, this path can be expected to carry only a *minor amount of* i_{l-e} in terms of a *current divider* (2.51); i.e., the current divider between the one current branch down into the body for the *major* amount of i_{l-e} and the other branch down into the amplifier for the *minor* amount of i_{l-e}.

Both coupled currents i_{l-e} contribute not only to the *common-mode input-referred interference voltage* u_{CI} but also may contribute to a *differential-mode input-referred interference voltage* u_{DI} at the amplifier's input, known as *differential-mode electromagnetic interference*; see Sect. 3.2.5. In fact, both *interference voltages* u_{CI} and u_{DI} act on the total *input u of the differential amplifier* according to (Fig. 3.26)

$$u = u_B + u_{DI} + \frac{u_{CI}}{CMRR} \tag{3.41}$$

and—if not suppressed—clearly add *noise to the output of the real differential amplifier*; as described below in more detail. In formal terms, the *coupling impedance* as the ratio of the *input-referred interference voltage* (including both fractions u_{CI} and u_{DI} at the input of the amplifier) to *capacitively coupled displacement currents* should be preferably low in order to reduce *interference effects* (Spinelli and Mayosky 2005).

It is instructive to note that any *large grounded conductive object* next to the *human body* and/or to *electrode leads* tends to *reduce displacement currents* into the body and/or into leads, respectively (Huhta and Webster 1973). The reason for this is that such a conductive object *distorts the ambient electric field*—as induced by interference sources—and especially *reduces this electric field* in spatial regions close to *charge-free boundaries* of this object (compare Figs. 2.30, 2.49 and the associated discussions), aside from the electrical point effect (involving *charged boundaries*, see Figs. 2.25, 2.26a, and Footnote 58 in Chap. 2).

3.2.2 *Inductive Coupling of Interference*

In addition to capacitive coupling, Fig. 3.26 depicts also the *inductive coupling from power lines into the two electrode leads*. As illustrated in Fig. 3.28a in more detail, both *leads* and the *conductive body surface* can build *conductive loops* in the vicinity of *power lines* residing close to the leads. Since *current-bearing*[47] *power lines* (or other noise sources around) *emit time-varying magnetic fields* (at 50 or 60 Hz, depending on the country), it can be expected that these fields would permeate the latter conductive loops. As a result, a *time-varying electric field is induced* along these leads with the resulting *time-varying voltage drop along these leads*, in terms of the *electromagnetic induction*; compare Fig. 2.31.

In general—in accordance with (2.86) and (2.87)—the *induced interference voltage* u_L with its amplitude U_L at the amplifier's input (Figs. 3.26 and 3.28) grows in proportion to

- the *area of the formed conductive loop* which surface is *perpendicular* to the direction of the incident *time-varying magnetic field* (Fig. 2.32); and in proportion to
- the *magnitude and frequency of this magnetic field*.

As illustrated in Fig. 3.26, the induced u_L contributes to the time-varying *differential-mode input-referred interference voltage* u_{DI} at the amplifier's input, which *unfavourably adds to the total input u*, see (3.41). Thus u_L has to be minimized or avoided. Likewise, as shown in Fig. 3.28, if there is no biosignal-related input u_B (=0) and the capacitive coupling is neglected (with i_{l-b}, $i_{l-e} = 0$ in Fig. 3.26) then $u = u_L$ applies and u_L alone determines the amplifier's input.

A *transformer* in Fig. 3.26 models this *inductive coupling* and determines the relationship between the power line voltage amplitude U_{l-g} and the induced U_L. Likewise, the *turns ratio n* ($=U_{l-g}$ / U_L) of the transformer decreases while U_L increases with increasing strength of the inductive coupling.

From a practical perspective, the voltage u_L is *sensitive to rotation* of the *plane of the conductive loop* (with respect to the stationary power lines) and is usually minimized by

[47]It is *instructive* to observe that the *inductive coupling* requires *time-varying currents i*(*t*) flowing along *power lines* in order to induce *time-varying magnetic fields* $\vec{\dot{B}}$ around these lines; e.g., $\vec{\dot{B}} = \frac{\mu_0}{2\pi \cdot r} \cdot \frac{di(t)}{dt} \cdot \vec{e}_B$ applies for an infinitely long wire of power lines with $di(t)/dt \neq 0$ in Fig. 3.28 (Footnote 13 in Chap. 2). Likewise, the inductive coupling dominates in regions close to *transformers* (within the power supplies of most equipment) where typically large *i*(*t*) flows (Fig. 3.28a).

This is in clear contrast to the discussed *capacitive coupling* from power lines, which does not require any *i*(*t*). Power lines will still produce *alternating electric fields* and thus *alternating displacement currents* (2.66) entering the *body* and/or *electrode leads* even though *no i(t) flows along power lines* (Fig. 3.26). The voltage drop (U_{l-g} in Fig. 3.26) and the alternating electric field are still present between power lines and the power line's ground, irrespective of the current's *i*(*t*) presence (up to the on-off switch).

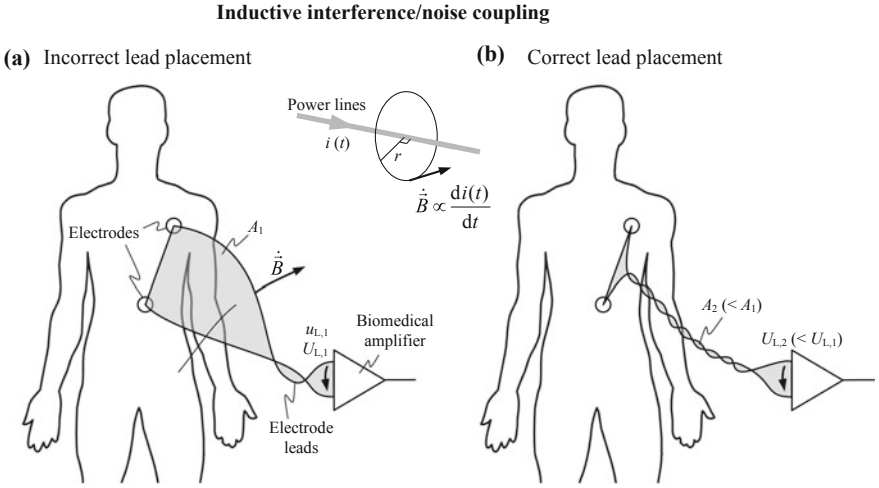

Fig. 3.28 Inductive coupling of the ambient time-varying magnetic field with its magnetic flux density $\vec{B}$—as originating from power lines—for two electrode measurements on the body surface; compare Fig. 3.26. The electromagnetic induction occurs across the surface area A (perpendicular to the direction of the vector $\vec{B}$) confined by a conductive loop which segments are formed by the conductive body and conductive electrode leads. **a** Disadvantageous lead placement forming a relatively large A_1 and thus a relatively large differential interference voltage $u_{L,1}$ at the amplifier's input with its amplitude $U_{L,1}$. **b** Favorable placement of electrode leads close to the body and their twisting forming a smaller A_2 ($<A_1$) and thus a smaller $U_{L,2}$ ($<U_{L,1}$)

- *lead twisting* and
- *running leads close the body*

in order to *reduce areas* of conductive loops exposed to the incident magnetic field. Figure 3.28 compares the inductive coupling for *untwisted leads* (Fig. 3.28a) and *twisted leads* (Fig. 3.28b) with different loop areas. Namely, the smaller area A_2 for twisted leads yields a reduced $U_{L,2}$ at the amplifier's input in comparison with the larger area A_1 ($>A_2$) for untwisted leads with the associated large $U_{L,1}$ ($>U_{L,2}$).

In order to prevent time-varying magnetic fields to enter conductive loops, *ferromagnetic materials* of high permeability (such as mu-metal) can be used to *shield the entire measurement environment*. However, please note that *shielding of each single electrode lead* does not prevent the inductive coupling, see Sect. 3.2.8.

3.2.3 Biosignal Coupling—Voltage Divider

Figure 3.27a illustrates the *relevance of* $\underline{Z}_{el}$ *and* $\underline{Z}'_{el}$ of both electrodes for an efficient *coupling of biosignals* from the inner human body along electrode leads into the biomedical amplifier, following Fig. 3.26. *Inner body resistances* have been assumed to be zero. In fact, the *open-circuit voltage amplitude* $\underline{U}_0$ of the *biosignal's source* within the body—to be registered by the amplifier, preferably undistorted and undamped—is obviously subjected to a *voltage divider* with respect to the *registered* u_B *with its amplitude* $\underline{U}_B$ at the input of the amplifier. The voltage divider—as illustrated in Fig. 3.27a—results from

- the *inner resistance* R_U of the biosignal's source (assumed as a *voltage source* with $\underline{U}_0$);
- *electrode impedances* $\underline{Z}_{el}$ and $\underline{Z}'_{el}$ of both electrodes applied on the body's skin, in series with the respective *lead wire* of *neglected wire's resistance*;
- the *capacitive current shunt* from the body to the ground (across C_{l-b}, see Fig. 3.26) and then back to the body (across C_{b-g}) over the resulting *total coupling stray capacitance* C_{l-b-g} ($=C_{l-b} \parallel C_{b-g}$), which *capacitively short-circuits differential biosignals* on the body's skin;
- the *capacitive current shunt* from electrode leads to the ground (across $C_{l-e} + C_{e-g}$, see Fig. 3.26) and then back to leads (across $C_{l-e} + C_{e-g}$) over the resulting *total coupling stray capacitance* C_{l-e-g} ($=(C_{l-e} + C_{e-g})/2$), which *capacitively short-circuits both leads* just after the electrode/skin boundary.

The *voltage divider* reduces the source-related $\underline{U}_0$ to the input-related $\underline{U}_B$ across $\underline{Z}_{diff}$ at the input of the amplifier according to

$$\begin{aligned} \underline{U}_B &= \underline{U}_0 \cdot \frac{\underline{Z}_{diff}}{(\underline{Z}_{diff} + R_U + \underline{Z}_{el} + \underline{Z}'_{el}) + j\omega \cdot A + (j\omega)^2 \cdot B} \quad \text{with} \\ A &= (\underline{Z}_{el} + \underline{Z}'_{el}) \cdot (\underline{Z}_{diff} C_{l-e-g} + R_U C_{l-b-g}) + \underline{Z}_{diff} R_U \cdot (C_{l-e-g} + C_{l-b-g}) \quad \text{and} \\ B &= \underline{Z}_{diff} R_U C_{l-b-g} C_{l-e-g} \cdot (\underline{Z}_{el} + \underline{Z}'_{el}). \end{aligned} \tag{3.42}$$

When C_{l-b-g} *is neglected* (i.e., $C_{l-b-g} = 0$), (3.42) simplifies to

$$\underline{U}_B = \underline{U}_0 \cdot \frac{\underline{Z}_{diff}}{(\underline{Z}_{diff} + R_U + \underline{Z}_{el} + \underline{Z}'_{el}) + j\omega \cdot \underline{Z}_{diff} \cdot C_{l-e-g} \cdot (R_U + \underline{Z}_{el} + \underline{Z}'_{el})}. \tag{3.43}$$

When C_{l-e-g} *is additionally neglected* ($C_{l-e-g} = 0$), a simple *voltage divider* results from (3.43)

$$\frac{\underline{U}_B}{\underline{U}_0} = \frac{\underline{Z}_{diff}}{\underline{Z}_{diff} + R_U + \underline{Z}_{el} + \underline{Z}'_{el}} = \frac{1}{1 + \frac{R_U}{\underline{Z}_{diff}} + \frac{\underline{Z}_{el} + \underline{Z}'_{el}}{\underline{Z}_{diff}}} \approx \frac{1}{1 + \frac{\underline{Z}_{el} + \underline{Z}'_{el}}{\underline{Z}_{diff}}} < 1; \qquad (3.44)$$

compare with Fig. 3.24 and (3.38). Since the inequality $R_U \ll |\underline{Z}_{el}|, |\underline{Z}'_{el}|, |\underline{Z}_{diff}|$ can be reasonably assumed, it can be seen from (3.42) to (3.44) that *capacitive current shunts* and *electrode impedances*[48] determine $\underline{U}_B$ in response to $\underline{U}_0$. That is, an appreciable portion of the available $\underline{U}_0$ may appear across the electrode/tissue boundary and probably less than the desired amplitude $\underline{U}_B$ (with $|\underline{U}_B| < |\underline{U}_0|$) may result at the amplifier's input.

In *quantitative terms*, $\underline{Z}_{el}$ of the skin *surface electrodes* occupies typically the *range from 100 Ω to 100 kΩ*. *Lower values* of $\underline{Z}_{el}$ are applicable for *rubbed skin* (e.g., with fine abrasive paper when the isolating corneal layer of the epidermis is removed; compare Fig. 3.3d), whereas *higher values* of $\underline{Z}_{el}$ apply to the skin without preparation. While $\underline{Z}_{diff}$ is in the order of GΩ, the *capacitive shunt impedances* $1/(j\omega C_{l-b-g})$ and $1/(j\omega C_{l-e-g})$ (2.42) can be expected to decrease down to the order of MΩ, especially for *higher frequencies* of u_B. For instance, capacitances C_{l-b-g} and C_{l-e-g} reside in the estimated range of pF (according to numerical data from Spinelli and Mayosky (2005)) so that the associated *capacitive impedances* turn to be around GΩ for the relatively *low mains frequency* of 50 or 60 Hz. As shown in Fig. 3.27a, even though $\underline{Z}_{diff}$ is quite high, the shunt impedance $1/(j\omega C_{l-e-g})$ can considerably reduce the total impedance of their parallel connection ($=\underline{Z}_{diff} \parallel (1/(j\omega C_{l-e-g}))$). Consequently, a relatively high total *electrode impedance* ($\underline{Z}_{el} + \underline{Z}'_{el}$) in series with $\underline{Z}_{diff} \parallel (1/(j\omega C_{l-e-g}))$ can also considerably and disadvantageously *reduce the input voltage* $\underline{U}_B$ across $\underline{Z}_{diff} \parallel (1/(j\omega C_{l-e-g}))$ in terms of the *voltage divider* (3.43), especially for *higher frequencies* when $1/(j\omega C_{l-e-g})$ decreases.

3.2.4 Common-Mode Interference

Figure 3.27b details the *capacitive coupling of the power line interference* and the associated *relevance of* $\underline{Z}_{el}$ *and* $\underline{Z}'_{el}$, based on Fig. 3.26. Again, *inner body resistances* are neglected here and thus assumed to be zero. It can be observed that the aforementioned *interference voltage* u_{b-g} results in the course of capacitively

[48] At the time of string galvanometers for recording of electrocardiogram, the applied electrodes consisted of buckets of saline in order to have a *large area of the electrode/skin boundary*. The large area was needed to attain a *small* $\underline{Z}_{el}$ (Section "Electrode Impedance Model") compared to the relatively low value of the *input impedance of string galvanometers* acting as *biomedical amplifiers*. In fact, the impedance $\underline{Z}_{el}$ should be kept small so that the recorded electrocardiogram is not reduced in its amplitude (because of the presented *voltage divider* at the amplifier's input, see Fig. 3.27a) and is not distorted in its waveform (because of the *frequency-dependent* $\underline{Z}_{el}$, see Fig. 3.19). As amplifiers improved, their input impedances increased much above typical $\underline{Z}_{el}$ values so that *small area electrodes* with relatively large $\underline{Z}_{el}$ can be used today.

coupled *displacement currents* i_{l-b} and i_{l-e}; namely, in response to the total $i_{l-b} + 2 \cdot i_{l-e}$ crossing the stray capacitance C_{b-g}. This u_{b-g} contributes to the *common-mode input-referred interference voltage* u_{CI} *with its amplitude* $\underline{U}_{CI}$ at the amplifier's inputs (Fig. 3.27b).

It is instructive to discuss that the human body offers a relatively low resistance to the currents i_{l-b} and i_{l-e} since the body is a *good conductor*, especially with respect to the surrounding air. Therefore, the body surface can be *approximated* to form a *single electric equipotential plane*. Under this approximation, it is clear that i_{l-b} and i_{l-e} of the power line interference mainly contribute to u_{b-g} from the body to the power line's ground and thus to the *common-mode voltage drop* u_{CI} *with respect to the amplifier's ground* (Fig. 3.26). In other words, *one fraction* of this interference voltage u_{b-g} is determined by the *capacitive voltage divider* across C_{l-b} and C_{b-g} (accounting for i_{l-b}), as shown in Fig. 3.26. The *other fraction* of this u_{b-g} is given via the voltage divider composed out of C_{b-g}, C_{l-e}, and C_{e-g} (accounting for $2 \cdot i_{l-e}$). Of course, the assumed additivity of both fractions assumes that the *superposition principle* applies (Kaniusas 2012, Footnote 195). It is also instructive to reiterate that most bioelectric phenomena within the body contribute to the *differential-mode biosignal voltage* on the body surface (Fig. 1.1) but not to the *common-mode interference voltage*. Please note that the above approximation of the *single equipotential surface* is in clear *contrast to a stickman representation of the body* (with the non-zero resistances $R_{b,1}$ to $R_{b,3}$ in Fig. 3.26 or Fig. 3.22b), as discussed later in Sect. 3.2.6.

In particular, both *inputs of the amplifier* experience the *common-mode interference voltage* (Fig. 3.27b)

$$\underline{U}_{CI} = \underline{U}_{b-g} + \underline{I}_{l-e} \cdot \frac{\underline{Z}_{el} + \underline{Z}'_{el}}{2} - \underline{U}_{CM} = \frac{\underline{I}_{l-b} + 2 \cdot \underline{I}_{l-e}}{j\omega C_{b-g}} + \underline{I}_{l-e} \cdot \frac{\underline{Z}_{el} + \underline{Z}'_{el}}{2} - \underline{U}_{CM} \tag{3.45}$$

with respect to the *amplifier's ground*. Here $\underline{U}_{CM}$ is the common-mode voltage created between the local ground of the amplifier and the power line's ground (see Figs. 3.26 and 3.27b) while $\underline{I}_{l-e}$ is the complex amplitude of i_{l-e} (Fig. 3.27b).

This *interference amplitude* $\underline{U}_{CI}$ has a considerable strength and is typically 2–3 orders larger than the *amplitude* $\underline{U}_B$ *of electric biosignals* (due to $\underline{U}_0$ only, see Fig. 3.27a) to be recorded. For instance, the magnitude of $\underline{U}_{CI}$ is typically in the order of a few volts while that of $\underline{U}_B$ ranges typically from μV to mV (e.g., from weak electroencephalogram signal to stronger electrocardiogram signal, respectively).

The latter *difference in magnitudes* signifies the necessity to consider *this interference* u_{CI} at the *amplifier's inputs*. This is because a *real differential amplifier* exhibits a small but *non-zero common-mode gain* (typically in the range of 1–2) and thus the *output of the amplifier* also depends on u_{CI} (and not only on u_B). Therefore, a *high common-mode rejection ratio CMRR* of the amplifier—defined as the *differential gain* over the *common-mode gain*—is needed to *suppress the influence*

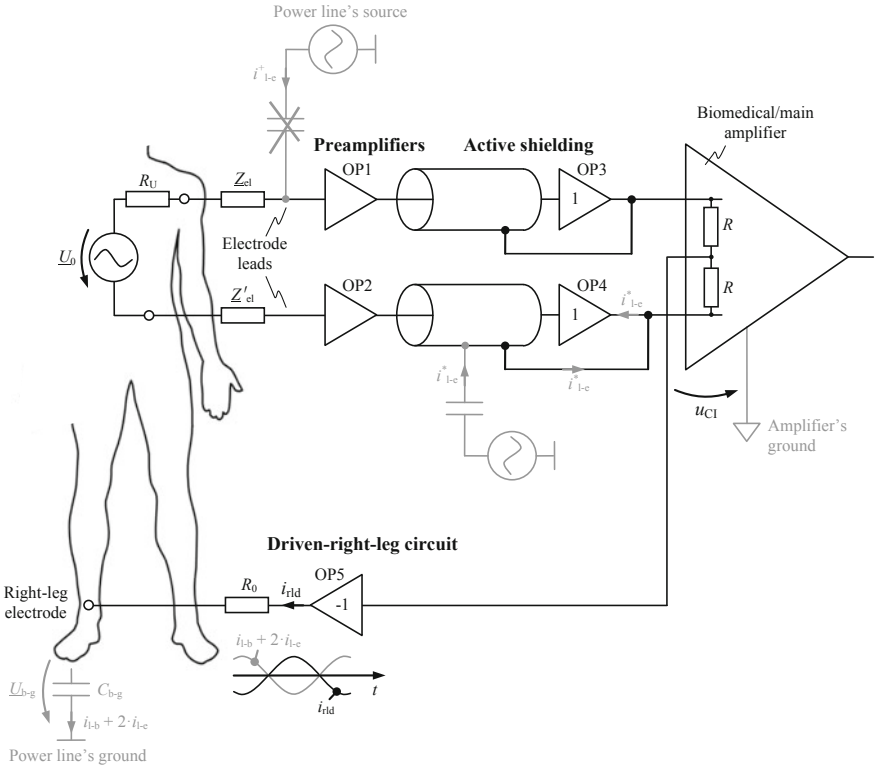

Fig. 3.29 Principle circuit models of countermeasures against the capacitive interference; compare Fig. 3.26. Preamplifiers (OP1 and OP2) close to each electrode reduce displacement currents i^{+}_{l-e} entering the respective short lead from the surface electrode to the preamplifier and thus reduce disadvantageous effects of the impedance unbalance $\underline{Z}_{el} - \underline{Z}'_{el} \neq 0$. The associated differential-mode interference is strongly reduced. The shown active shielding short-circuits the ambient i^{*}_{l-e} to the low-ohmic shield and then to the amplifier's ground (in OP3 and OP4); the common-mode and differential-mode interferences are strongly reduced. The driven-right-leg circuit (with OP5) diminishes effects of the capacitively coupled i_{l-b} and i_{l-e} (Fig. 3.26); the associated common-mode interference voltage u_{CI} is strongly reduced. Pathways for capacitively coupled currents are plotted in grey

of the relatively high u_{CI} and thus to *avoid masking* (or interference) of the *biosignal-related portion* u_B *of* u by the *interference-related portion* u_{CI} *of* u, see (3.41).

To give a tangible example, *CMRR* of any *real differential amplifier* is always *finite* and is typically about 100 dB. For instance, a typical $|\underline{U}_{CI}|$ level of 1 V still acts as a *differential input-referred interference voltage* of 10 µV [=$|\underline{U}_{CI}|/CMRR$ = 1 V/10^5, see (3.41)]. It acts as an *interference-related portion of the differential u*, which is then *amplified with the differential gain* and subsequently *appears as an augmented interference* at the amplifier's output. Equation (3.41) illustrates the latter effect of u_{CI} on the total u in an instructive way.

Please note that these estimated 10 μV are already in the range of the biosignal's amplitude U_B. Likewise, the typical *CMRR* of about 100 dB is too low for most practical cases and composes a problem. In other words, the *signal-to-interference* or *signal-to-noise ratio* at the amplifier's input is usually very low and it yields a need to implement amplification circuits with a high *CMRR*.

In addition, a high common-mode u_{CI} may even limit the *amplification gain of input circuits* in order to avoid *clipping* (or *saturation*) of the associated *amplifiers* due to this high input-referred u_{CI}. It requires to keep the *common-mode interference* u_{CI} at the amplifier's input as low as possible, in order to reduce its impact on the amplifier's output. Alternatively, special *countermeasures* can be applied, as discussed in Fig. 3.29.

For instance, the magnitude of $\underline{U}_{CI}$ (3.45) can be favourably *reduced* by

- *inhibited capacitive coupling*, i.e., reduced $i_{l-b} + 2 \cdot i_{l-e}$ and thus reduced $\underline{U}_{b-g}$ (see shielding from Fig. 3.29);
- a *high* C_{b-g}, i.e., a low impedance $1/(j\omega C_{b-g})$ and thus a low resulting $\underline{U}_{b-g} = (\underline{I}_{l-b} + 2 \cdot \underline{I}_{l-e})/(j\omega C_{b-g})$;
- *low values of* $\underline{Z}_{el}$ *and/or* $\underline{Z}'_{el}$ (i.e., a reduced product $\underline{I}_{l-e} \cdot (\underline{Z}_{el} + \underline{Z}'_{el})$); and by
- a *low value of* $\underline{Z}_{com}$ for *high interference environments* with a strong capacitive coupling. In fact, a low $\underline{Z}_{com}$ *admits large displacement currents* to be coupled and thus eliminates the risk that the *input of the amplifier becomes saturated* due to otherwise high u_{CI}. This condition of low $\underline{Z}_{com}$ can be realised with, for instance, balanced current sources at the amplifier's input (Dobrev and Daskalov 2002).

It must be stressed that, as stated above, *high* $\underline{Z}_{el}$ *and* $\underline{Z}'_{el}$ imply a *strong common-mode interference* u_{CI} with power lines, and on the other hand, a *strong attenuation of the biosignal-related portion* u_B at the amplifier's input (3.44). Consequently, the *frequency dependence of* $\underline{Z}_{el}$—see associated discussions of (3.27), (3.29), (3.30) as well as of Fig. 3.19—causes the dominance of the interference-related u_{CI} with respect to u_B at the amplifier's input to vary with both the *frequency of interference* and the *frequency of biosignal*.

For instance, *low frequency components of biosignal* (from $\underline{U}_0$, see Fig. 3.27a) are subjected to a *stronger interference* (due to the associated high $\underline{Z}_{el}$ in Fig. 3.27b) and to a *stronger attenuation* (also due to the high $\underline{Z}_{el}$ in Fig. 3.27a) than *high frequency components of biosignal* (with the associated low $\underline{Z}_{el}$). This comparison assumes that the *ambient interference*—in terms of coupled i_{l-b} and i_{l-e}—*is equally strong at all frequencies*. However, *frequency-dependent capacitive shunts* across C_{b-g}, C_{l-b-g}, and C_{l-e-g} (in Fig. 3.27a, b) co-influence the above comparison in that the input-referred interference u_{CI} tends to decrease with increasing frequency of the interference [i.e., $\underline{U}_{b-g}$ and $\underline{U}_{CM}$ decrease with increasing frequency in Fig. 3.27b and (3.45)], whereas the input-referred biosignal u_B tends also to decrease with increasing frequency of the biosignal (i.e., $\underline{U}_B$ decreases in Fig. 3.27a due to decreasing $1/(j\omega C_{l-b-g})$ and $1/(j\omega C_{l-e-g})$).

3.2.5 *Differential-Mode Interference*

Figure 3.27b demonstrates that the *capacitive coupling of the power line interference* can also yield the *differential-mode input-referred interference voltage* u_{DI} at the input of the amplifier. In particular, the coupling yields the *interference-related portion* u_{DI} *of* u (3.41), as already mentioned with respect to capacitively coupled i_{l-e} (Sect. 3.2.1). In particular, this *interference* u_{DI} arises when there is

- a *mismatch* $\Delta\underline{Z}_{el} = \underline{Z}_{el} - \underline{Z}'_{el} \neq 0$ between both *electrode impedances* $\underline{Z}_{el}$ and $\underline{Z}'_{el}$; e.g., due to poor electrode to skin contact, poor skin preparation, dry electrode paste, or partly detached electrodes (Huhta and Webster 1973). Please note that $\Delta\underline{Z}_{el}$ can be particularly high for *non-contact capacitive electrodes* (Fig. 3.1a) where a perfect matching of $\underline{Z}_{el}$ and $\underline{Z}'_{el}$ is very difficult.
  Namely, the *amplitude* $\underline{U}_{DI}$ of u_{DI} *at the amplifier's input* (Fig. 3.27b) obeys

$$\underline{U}_{DI} = \underline{I}_{l-e} \cdot \Delta\underline{Z}_{el} - (\underline{U}_{b-g} - \underline{U}_{CM}) \cdot \frac{\Delta\underline{Z}_{el}}{\underline{Z}_{com}}. \tag{3.46}$$

  and thus is composed out of

  - one *differential voltage contribution* $\underline{I}_{l-e} \cdot \Delta\underline{Z}_{el}$ in response to finite coupled $\underline{I}_{l-e}$ and
  - another *differential voltage contribution* $(\underline{U}_{b-g} - \underline{U}_{CM}) \cdot \Delta\underline{Z}_{el} \,/\, \underline{Z}_{com}$ in response to finite $(\underline{U}_{b-g} - \underline{U}_{CM})$ or, to be more precise, in response to coupled $\underline{I}_{l-b} + 2 \cdot \underline{I}_{l-e}$ determining $\underline{U}_{b-g}$. The voltage $(\underline{U}_{b-g} - \underline{U}_{CM})$ is subjected to *potential dividers*[49] across $\underline{Z}_{el}$ and $\underline{Z}_{com}$ as well as across $\underline{Z}'_{el}$ and

[49]The resulting contribution $\underline{U}^*_{DI}$ to $\underline{U}_{DI}$ due to the *potential divider* across $\underline{Z}_{el}$ and $\underline{Z}_{com}$ as well as across $\underline{Z}'_{el}$ and $\underline{Z}_{com}$ of the voltage $(\underline{U}_{b-g} - \underline{U}_{CM})$ (Fig. 3.27b) can be approximated in a straightforward way under a *reasonable assumption of* $|\underline{Z}_{diff}| \to \infty$, to give

$$\underline{U}^*_{DI} = (\underline{U}_{b-g} - \underline{U}_{CM}) \cdot \left(\frac{\underline{Z}_{com}}{\underline{Z}_{el} + \underline{Z}_{com}} - \frac{\underline{Z}_{com}}{\underline{Z}'_{el} + \underline{Z}_{com}} \right) \approx -(\underline{U}_{b-g} - \underline{U}_{CM}) \cdot \frac{\Delta\underline{Z}_{el}}{\underline{Z}_{com}}.$$

The latter approximation assumes relatively high $|\underline{Z}_{com}| \gg |\underline{Z}_{el}|, |\underline{Z}'_{el}|$ with $\Delta\underline{Z}_{el} = \underline{Z}_{el} - \underline{Z}'_{el}$ that yields the factor $\Delta\underline{Z}_{el} \,/\, \underline{Z}_{com}$ (3.46). It is also instructive to observe that $\underline{U}^*_{DI} \to 0$ *for quite high* $\underline{Z}_{com} \to \infty$.

The *complete solution for* $\underline{U}^*_{DI}$ in response to $(\underline{U}_{b-g} - \underline{U}_{CM})$ requires a longer calculus and yields

$$\underline{U}^*_{DI} = -(\underline{U}_{b-g} - \underline{U}_{CM}) \cdot \left(\frac{\Delta\underline{Z}_{el}}{\underline{Z}_{el} \cdot \underline{Z}'_{el}} \Big/ \frac{1}{\underline{Z}_{diff}} \cdot \left(\frac{\underline{Z}_{com}}{\underline{Z}_{el}} + 2 + \frac{\underline{Z}_{com}}{\underline{Z}'_{el}} \right) + \frac{1}{\underline{Z}_{com}} \cdot \left(1 + \frac{\underline{Z}_{com}}{\underline{Z}_{el}} \right) \cdot \left(1 + \frac{\underline{Z}_{com}}{\underline{Z}'_{el}} \right) \right)$$

$\underline{Z}_{com}$, whereas these dividers define the fraction $\Delta\underline{Z}_{el}$ / $\underline{Z}_{com}$ (Fig. 3.27b). Thereby, a low $\underline{Z}_{com}$ unfavourably increases the size of u_{DI}.

An additional contribution to $\underline{U}_{DI}$ [from (3.46)] arises when there is

- an *unbalance* of the two *coupled currents* i_{l-e} entering each lead; i.e., a mismatch in their amplitudes $\underline{I}_{l-e}$. Such unbalance can be due to an asymmetric/improper placement of electrode leads with respect to near interference sources (such as power lines) so that the displacement current into one lead is much greater than that into the other (Sect. 3.2.1). However, Figs. 3.26 and 3.27b assume equal i_{l-e} entering each lead for the sake of simplicity.

In terms of the capacitive coupling it is important to recognise that a *disturbed symmetry of the body/amplifier interface* ($\Delta\underline{Z}_{el} \neq 0$)—or, in general, *any resistive and/or capacitive asymmetry in the input circuit* of the amplifier—is the origin of u_{DI}. Please note that the interference u_{DI} owes not only to

- the *capacitive coupling* (Fig. 3.26) but also to
- the *inductive coupling* (Fig. 3.28)

so that the induced u_L unfavourably adds to the total u_{DI} as well.

Please note that this interference u_{DI} contributes to the amplifier's input u [Fig. 3.26 and (3.41)] and would be amplified as if this voltage would stem from a biosignal's source. Likewise, these *capacitive and inductive interferences* in terms of the induced *interference-related portion* u_{DI} *of* u may eventually fade out the true *biosignal-related portion* u_B *of* u—see (3.41)—and thus should be *minimized or supressed*.

For instance, an *unbalance in* $\Delta\underline{Z}_{el}$ (3.46) and an *unbalance in both* i_{l-e} *entering each lead* should be minimized or avoided. From a practical point of view, $\Delta\underline{Z}_{el}$ is usually in the same range as $\underline{Z}_{el}$ (Sect. 3.2.3), i.e., $\Delta\underline{Z}_{el}$ can go up to quite high values of 100 kΩ or can be as low as 100 Ω for rubbed skin. When low values of $\Delta\underline{Z}_{el}$ are given, a low $\underline{Z}_{com}$ is recommended for *minimal capacitive interference*, whereas for high values of $\Delta\underline{Z}_{el}$ a high $\underline{Z}_{com}$ is favourable (Huhta and Webster 1973; Spinelli and Mayosky 2005) which is in line with (3.46); compare Footnote 46.

3.2.6 Inner Body Resistance

As illustrated in Fig. 3.22b, the *human body* with its finite inner conductivity can be represented as a *stickman with resistors* in his arms, legs, and torso. This is in clear contrast to the approximation of the body surface as a single electric equipotential plane, as discussed in Sect. 3.2.4. If these *inner body resistances* are not neglected—as indicated in Fig. 3.26 by grey coloured resistances $R_{b,1}$ to $R_{b,3}$ within the human body—*displacement currents* i_{l-b} and i_{l-e} *within the air* entering the body through arms, legs, and torso (compare Fig. 2.27b) will cause different body regions to be at *slightly different electric potentials* in response to *induced*

conductive currents i_{l-b} and i_{l-e} *within the inner body*. Attached *surface electrodes* with a certain distance in-between will obviously *sense* these different *interference-related potentials* which then will be amplified together with the *biosignal-related potentials*.

- The *total induced potential difference* between electrodes (the voltage u_S in Fig. 3.26) is then composed out of a *biosignal-related portion* (due to $\underline{U}_0$ from Fig. 3.27a) and another *differential-mode interference-related portion* u_{DI}^{+}

$$u_{DI}^{+} = (i_{l-b} + i_{l-e}) \cdot R_{b,2} \tag{3.47}$$

  in Fig. 3.26, with (i_{l-b} + i_{l-e}) flowing through $R_{b,2}$ as the inner body resistance between the regions of electrode attachment. These portions—if located in the same amplitude and frequency range—may become inseparable from each other. In other words, the potential difference that stems from the biosignal's source and is of diagnostic interest may be masked out. This phenomenon of the non-zero inner body resistances, namely, the portion u_{DI}^{+} (3.47), contributes to the discussed *differential-mode interference* u_{DI} at the amplifier's input (Fig. 3.27b).
- On the other hand, induced interference potentials will also add to the *average potential of the two skin electrodes*. In particular, the *common-mode interference-related portion* u_{CI}^{+}

$$u_{CI}^{+} = (i_{l-b} + i_{l-e}) \cdot \frac{R_{b,2}}{2} + (i_{l-b} + 2 \cdot i_{l-e}) \cdot R_{b,3} \tag{3.48}$$

  is introduced in Fig. 3.26. That is, interference potentials, namely, the portion u_{CI}^{+} (3.48), contribute to the *common-mode interference* u_{CI} at the amplifier's inputs (Fig. 3.27b).

An advantage comes from the relatively *high body conductivity* that keeps gradients of the *induced interference potentials* within the body *low in amplitude* (2.54). However, the sensed differential interference potentials (u_{DI}^{+} within u_S in Fig. 3.26) rise with *increasing spatial distance* in-between surface electrodes [i.e., with increasing $R_{b,2}$, see (3.47) and (2.30)]. Likewise, the associated differential-mode interference u_{DI}^{+} from interference potentials almost disappears when electrodes are placed close together. This interference largely depends on the *electrode's orientation* with respect to the induced current distribution within the body (Fig. 2.11) as well as depends on the *inhomogeneity* of this current distribution (as discussed in Section "Charge and Current Induction").

Please note that the position of the *low-ohmic power line's ground* (i.e., the effective current sink for i_{l-b} and i_{l-e} originating from the power line's source) or the position of any other *low-ohmic electrode on the body* (e.g., the *right-leg electrode* if present, see Fig. 3.29) dictates the major spatial path the induced conductive current (i_{l-b} + 2 · i_{l-e}) will take through the body towards the ground and dictates what interference potentials will appear at each *surface electrode*.

Consequently, *interference potentials could be minimized* by changing the *position of the low-ohmic electrode*, e.g., by changing the *right-leg electrode* position from the *right leg to the stomach or chest* when the patient's electrocardiogram is considered (Huhta and Webster 1973).

3.2.7 Electrode Area

The *area A of a surface electrode* applied on the human body affects the capacitive coupling of interference in many ways. The larger A means its *increased stray capacitance* (2.41) and its *decreased capacitive impedance* (Section "Electrode Impedance Model") to a distant noise source or distant power lines that act as an interference source. Therefore, *large electrodes* tend to capacitively couple *more interference-related displacement currents* down into the body and/or down into electrode leads than *small electrodes*.

However, this dependence on A is not really dominant in practice since *electric fields* created by *interference sources* near the *conductive human body* are greatly reduced in certain large regions of the *body surface*. In particular, electric fields are reduced where these external fields are in parallel to the body surface; compare Figs. 2.49 and 2.51, and the associated discussions. Consequently, the associated *interference-related displacement currents* (2.66) are also greatly reduced in these body regions above the skin and the current's growth with increasing A of the electrode is practically absent (Huhta and Webster 1973).

On the other hand, an *increased A* implies a *decreased electrode impedance* $\underline{Z}_{el}$ and thus decreases both (Fig. 3.27b)

- the product $\underline{I}_{l-e} \cdot \underline{Z}_{el}$ (3.45) contributing to the *common-mode interference* u_{CI} and
- the product $\underline{I}_{l-e} \cdot \Delta\underline{Z}_{el}$ (3.46) contributing to the *differential-mode interference* u_{DI}.

Given both mechanisms from above, it can be concluded that *larger electrodes decrease the capacitive interference* and, conversely, small area electrodes increase this interference (Huhta and Webster 1973).

3.2.8 Countermeasures Against Interference

There are a few *common approaches*—as illustrated in Fig. 3.29—how to effectively *attenuate noise or power line interference coupled capacitively and/or inductively* into the *human body* and/or into *electrode leads* connecting skin electrodes with a biomedical amplifier, see Figs. 3.26 and 3.27b.

3.2.8.1 Shielding

Shielding of *electrode leads* with a *conductive screen/shield* (such as aluminium foil) which separately surrounds each lead—as illustrated in Fig. 3.29—reduces both the *common-mode interference* and *differential-mode interference*. In the case of

- a *passive shielding*, the shield is directly wired with the low-ohmic amplifier's ground. In the case of
- an *active shielding*, each shield is wired with the low-ohmic output of a *buffer amplifier* connected to a single electrode lead (see the amplifiers OP3 and OP4 in Fig. 3.29). Since buffer amplifiers have amplification gain of one, the resulting *electric potentials* of the shield and the associated lead become equal. Alternatively, the *common-mode input-referred interference voltage*—i.e., the voltage u_{CI} with respect to the amplifier's ground, see Fig. 3.27b—can be sampled to drive the shield voltage (with respect to the amplifier's ground) through a buffer amplifier.

The shielding *inhibits capacitive coupling* to electrode leads by short-circuiting the ambient displacement current in the air (the current i_{l-e} in Fig. 3.26 or, in analogy, the current i^*_{l-e} in Fig. 3.29) directly to the *low-ohmic shield* and then to the *low-ohmic amplifier's ground*; namely, to the low-ohmic output ground of OP3 and OP4 in Fig. 3.29. In fact, the current i^*_{l-e} in Fig. 3.29 (without shown preamplifiers in Fig. 3.29) follows the *path of least impedance* (2.51), in that i^*_{l-e} flows to the *low-ohmic power line's ground* instead of entering *high-ohmic electrode leads* connecting the human body (with its relatively *high-ohmic impedance* $1/(j\omega C_{b-g})$ *to the power line's ground*) with the biomedical amplifier (with its *high-ohmic input impedance to the power line's ground*).

However, please note that *shielded and grounded leads*—in terms of the *passive shielding*—tend to *degrade* $\underline{Z}_{com}$ of the amplifier (Fig. 3.27b). This is because the *lead-to-shield capacitive impedance* is in parallel to $\underline{Z}_{com}$. The practical consequence is that the *capacitance of the shielded and grounded cable*—which increases with increasing length of this cable according to its typical *distributed capacitance* of about 50–100 pF/m—*limits the cable length* that can be used in praxis.

On the other hand, the active driving of the shields—in terms of the *active shielding* from Fig. 3.29—raises the effective *lead-to-shield capacitive impedance* and thus *does not degrade* $\underline{Z}_{com}$. Therefore, the active shielding raises the *effective input impedance of the amplifier*. The aforementioned effects of the finite cable capacitance are strongly reduced—to be precise, reduced by the relatively large factor of the *differential gain* of the buffer amplifier—which then allows for the relatively *long electrode cables*, in contrast to the passive shielding. Since the active shielding improves the effective *input impedance of the amplifier*, it also *reduces the potential divider effects* (Footnote 49); similar to preamplifiers as another countermeasure (see below).

Please note that the *inductive coupling* (Sect. 3.2.2) is still present irrespective of shielded electrode leads, even when a *conductive and high-permeability shield* is used. This is because the incident alternating magnetic field enters the area of conductive loops, the area which does not depend on the shield's presence.

As an option, the patient can be covered with a *grounded conductive blanket*. The blanket shields both the patient and electrode leads against displacement currents i_{l-b} and i_{l-e}, respectively (Fig. 3.26); i.e., it *shields against the capacitive interference*.

3.2.8.2 Driven-Right-Leg Circuit

The *driven-right-leg circuit*—as shown in Fig. 3.29—is a special circuit in which an alternating signal is actively applied to the conductive body (via the amplifier OP5 in Fig. 3.29), usually applied to the ankle of the right leg with the so-called *right-leg electrode* (Huhta and Webster 1973; Winter and Webster 1983). This electrode is usually positioned at the most distant region from the biosignal source within the body, as the heart when denoising of the electrocardiogram is considered. However, the driven-right-leg circuit can also be applied for other biopotential measurements. The *applied signal* is formed in a way that it is *out-of-phase* with the sampled and amplified *common-mode input-referred interference voltage* u_{CI} (compare Fig. 3.27b). That is, the applied signal is shifted by 180°—or inverted by OP5 in Fig. 3.29—with respect to the input u_{CI}. The applied signal drives a certain conductive current into the right leg (i.e., the current i_{rld} in Fig. 3.29), which approximately equals and thus *destructively interferes* with capacitively coupled *currents* i_{l-b} *and* i_{l-e} passing through the body towards the power line's ground. Please recall that i_{l-b} and i_{l-e} are responsible for the common-mode u_{CI} [Fig. 3.27b and (3.45)]. This applied current i_{rld} destructively interferes with $i_{l-b} + 2 \cdot i_{l-e}$. Figure 3.29 illustrates an instructive inset with the *out-of-phase time courses* of i_{rld} and $(i_{l-b} + 2 \cdot i_{l-e})$. Please note that u_{CI} can be sampled (or sensed) by *averaging potentials* of both sensing electrodes with the use of a simple resistors network; see two resistors R in Fig. 3.29 (compare Fig. 3.27b).

The discussed destructive interference means that the *driven-right-leg circuit lowers significantly* u_{CI} at the amplifier's input and thus minimises the discussed effects of the *common-mode interference* (Sect. 3.2.4). In other words, a *low impedance path* is established between the body and the amplifier's ground by attaching the right-leg electrode. The *total common-mode rejection ratio* of the whole circuit, including the *driven-right-leg circuit* and the *biomedical amplifier*, is *significantly increased*. Likewise, a disconnected right-leg electrode may easily lead to clipping of the amplifier.

In addition, the driven-right-leg circuit reduces the *potential divider* effects (which are proportional to $\underline{U}_{b-g} = (\underline{I}_{l-b} + 2 \cdot \underline{I}_{l-e})/(j\omega C_{b-g})$, see Footnote 49). In terms of control engineering, the body acts here as the summing junction of a *negative feedback loop*, with the applied signal i_{rld} acting as a *feedback signal*.

Obviously, the driven-right-leg circuit works only if the *patient is galvanically isolated from the ground* (Figs. 2.27 and 3.29).

In general, a *passive and active approach* can be distinguished in the establishment of the *driven-right-leg circuit* (Winter and Webster 1983):

- The *passive approach*, in which a *wired connection* is established between the *right-leg electrode* and the *amplifier's ground*; and
- The *active approach*, in which the electric potential of the *right-leg electrode is actively governed* by an amplifier (the amplifier OP5 in Fig. 3.29).

However, the *passive but simple approach* is undesirable from safety considerations. That is because *large currents* could flow through the right-leg electrode and the body if the amplifier's circuit is not isolated. On the other hand, a poor electrode/skin contact of the right-leg electrode may show a quite large and *time-varying electrode impedance*—with its magnitude up to 100 kΩ, see Sect. 3.2.3—which would hinder an effective reduction of the common-mode u_{CI} by the passive approach. In contrast, the *active approach* overcomes both latter disadvantages. Here the output current i_{rld} of the driving amplifier can be easily limited (e.g., with a *current-limiting resistor* R_0 after OP5 in Fig. 3.29) while the effective electrode impedance of the right-leg electrode is reduced by several orders of magnitude due to the *negative feedback loop*.

3.2.8.3 Notch Filter

A *notch filter* can be used, i.e., a band-stop filter, analogous or even digital after the analogue-to-digital conversion. The filter *attenuates power line interference* (or *noise*) around the *interference frequency* (50 or 60 Hz, depending on the country) or, to be more precise, around the frequency of the coupled i_{l-b}, i_{l-e}, and/or u_L (Fig. 3.26). Therefore, the filter diminishes the discussed effects of i_{l-b}, i_{l-e}, and u_L related to *common-mode and differential-mode interferences* u_{CI} and u_{DI}.

However, since the electromagnetic interference can reside within the biosignal's u_B spectral band, such notch filter *attenuates unfavourably spectral components of* u_B around the interference frequency. Consequently, *diagnostic errors* may result out of deteriorated spectral content of u_B to be recorded. On the other hand, it is important to make sure that the interference is not strong enough to *saturate an amplifier of the input stage* before this interference arrives at the notch filter.

3.2.8.4 Preamplifier

A preamplifier located near each electrode on the body—as depicted in Fig. 3.29—is used to *eliminate the differential-mode and common-mode interferences* caused by capacitively coupled *displacement currents* into electrode leads (applicable to i_{l-e} in Fig. 3.26 or, in analogy, to i^{+}_{l-e} in Fig. 3.29). That is, the wired *connection from the electrode to the preamplifier is very short* with almost no displacement

currents entering this connection, as described in Sect. 3.2.1. For instance, the associated product $\underline{I}_{l-e} \cdot \Delta\underline{Z}_{el}$ (3.46) or, in analogy, $\underline{I}^{+}_{l-e} \cdot \Delta\underline{Z}_{el}$ is negligible here; see also (3.45).

In addition, preamplifiers have a high $\underline{Z}_{com}$ so that the aforementioned *potential divider effect* is not dominant *between the electrode and the respective preamplifier* (see Footnote 49 with the condition $\underline{Z}_{com} \to \infty$). In fact, preamplifiers are *buffer amplifiers* (the amplifiers OP1 and OP2 in Fig. 3.29) with a precisely *matched gain* (otherwise more interference could be introduced into electrode leads than preamplifiers eliminate) and very *low output impedances* (in the range of a few ohms).

The *differential-mode interference* is reduced by eliminating the discussed effects of the *electrode impedance unbalance* $\Delta\underline{Z}_{el} = \underline{Z}_{el} - \underline{Z}'_{el} \neq 0$. In particular, $\Delta\underline{Z}_{el}$ is high when $\underline{Z}_{el}$ is high, e.g., when *small-area surface electrodes* are applied (as in electroencephalography recordings) or when *non-contact capacitive electrodes* (Fig. 3.1a) are used; see Sect. 3.2.3 for the typical size of $\underline{Z}_{el}$.

The *low output impedance of preamplifiers* prevents the discussed *differential voltage contributions* to u_{DI} [both contributions proportional to $\Delta\underline{Z}_{el}$, see (3.46)], i.e.,

- prevents the effect of a *finite* $\underline{I}_{l-e}$ entering (relatively long) electrode leads *between preamplifiers and the biomedical/main amplifier* (diminishes $\underline{I}_{l-e} \cdot \Delta\underline{Z}_{el}$ in (3.46), see Fig. 3.26) and, on the other hand,
- prevents the effect of a *potential divider between each preamplifier and the biomedical/main amplifier* [diminishes $(\underline{U}_{b-g} - \underline{U}_{CM}) \cdot \Delta\underline{Z}_{el} / \underline{Z}_{com}$ in (3.46), see Footnote 49].

In other words, the *low output impedance* of preamplifiers in series with the *low impedance of leads* (between preamplifiers and the biomedical/main amplifier) in the order of ohms makes any potential unbalance or asymmetry of the input circuit of the biomedical/main amplifier negligible. In addition, *lead-flexing artefacts* are eliminated as well as the *length limitation of shielded cables* from preamplifiers to the biomedical/main amplifier (Huhta and Webster 1973); compare with effects of the passive and active shielding on the acceptable cable length.

Lastly, it should be mentioned that *limiting of length of unshielded electrode leads*—e.g., up to 1 m (Huhta and Webster 1973)—reduces the capacitance C_{l-e} and thus reduces the associated displacement currents i_{l-e} (Fig. 3.26).

3.2.9 Triboelectricity

Triboelectricity (or *contact electrification*) may result in strong movement artefacts, especially when *non-contact capacitive electrodes* (Fig. 3.1a) are used. The following describes the underlying concept and possible countermeasures for

- *global triboelectric effects and*
- *local triboelectric effects*.

Triboelectricity originates at the boundary of *two different uncharged objects in mechanical contact*, where an interaction between atoms and their electrons occur. Depending on the different *thermodynamic energies* of electrons within objects (different work functions)—as illustrated in Fig. 3.30a, b—one object may lose electrons from its outer surface at the boundary in favour of the other object, until *electrochemical potentials* (Footnote 3) of both objects are equalised. Consequently, the other object accumulates electrons on its surface (Fig. 3.30b). As a result, an *electrical double layer* will appear at the boundary, with a certain *contact voltage* between both surfaces in contact; compare Fig. 3.4. Now, when these two *objects are swiftly separated*, the respective *surface charges* remain, equal in their absolute size but opposite in their sign (Fig. 3.30c). Consequently, both objects lose their net charge neutrality from their original state (Fig. 3.30a) after the separation event. Namely, the object which has lost electrons becomes positively charged while that which has gained electrons becomes negatively charged. A non-zero *electrostatic voltage U* will now appear *between both objects* [compare (3.5)], i.e., the voltage U (>0) appears in Fig. 3.30c, which can be as high as kilovolts in many cases. A *fast touch and separation*—in terms of *rubbing both objects* together—favours this U because of low electron back-flow across the boundary after the onset of the separation (Wartzek et al. 2011). For instance, this *back-flow* can go as electric breakdown or discharge; namely, as a *spark relaxing excess surface charges*.

In fact, this *back-flow* is slow and excess surface charges are stored for quite a long time when rubbing of an *isolator to another isolator* is considered. The associated *discharge time constant* is large. In contrast, a *metal-isolator contact* or a *metal-metal contact* yields a lower U since electrons can more easily flow back across the *last existing contact* during the separation process. It is instructive that the voltage U increases with increasing *contact area* while rubbing, so that U is mainly determined by

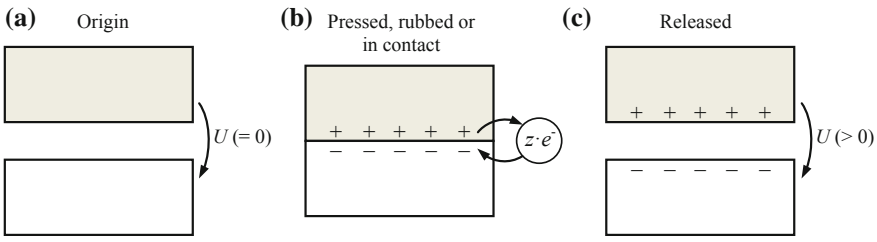

Fig. 3.30 Triboelectricity in which **a** two charge-neutral materials **b** after contact with each other **c** become charged with opposite signs and a non-zero electrostatic voltage U appears between both materials [in line with (3.5)]

- both *materials in contact*,
- the *separating speed*,
- the *contact surface size* and
- the *surface roughness* (the number of contact points).

Global Triboelectric Effects

In terms of *global triboelectric effects*, the *conductive human body* itself can *accumulate triboelectrically induced charge* only if the body is *isolated from the ground* (Fig. 2.27b). This electrostatic induction can happen when walking over a carpet or lifting a foot from the ground. The induced *electrostatic voltage from the body to ground* acts as a *common-mode input-referred interference voltage* u_{CI} to the *biomedical amplifier* (compare Fig. 3.27b), which should be obviously rejected in order to avoid the associated *movement artefacts* (as discussed in Section "Movement Artefacts"). In other words, a *transient* u_{CI} can be simply induced by lifting a foot from the ground, with the associated transient response at the amplifier's output due to its *limited common-mode rejection ratio* [*CMRR* in (3.41)].

The *driven-right-leg circuit* (Fig. 3.29) is an effective measure against the *electrostatic voltage from the body to ground*, in addition to the circuit's favourable effect on the total common-mode rejection ratio (Sect. 3.2.8). Namely, the low-ohmic output of the circuit's amplifier (the amplifier OP5 in Fig. 3.29), which drives the *right-leg electrode* on the body, *discharges quickly* the accumulated charge and thus facilitates short-circuiting of induced surface charges between the body and ground. In other words, the right-leg electrode short-circuits excess charges on the body surface to the ground. On the contrary, a *disconnected right-leg electrode* increases the *impedance from the body to ground* and thus *aggravates the charge counterbalancing* between the body and ground; here the resulting *electrostatic voltage* (acting as u_{CI}) turns to be quite high.

Local Triboelectric Effects

Besides *contact galvanic electrodes* (Fig. 3.1b), measurements performed with *non-contact capacitive electrodes* (Fig. 3.1a) are particularly sensitive to the triboelectrically induced electrostatic voltage. In terms of *local triboelectric effects*, here transient surface charges can be *triboelectrically induced* at the capacitive *electrode/tissue boundary*; e.g., charges result from rubbing of the electrodes on the subject's clothing. Non-contact measurements are critical because a *high isolation resistance* dominates between the electrodes and the subject's clothing the electrodes are rubbing on (Wartzek et al. 2011) so that the induced *surface charges* can not be easily short-circuited (across a low-ohmic path with a favourably small electrostatic voltage).

- The *induced charges and their temporal changes* within contact surfaces (while rubbing of the electrode on clothes) as well as
- the *time-dependent coupling capacitance* [i.e., the capacitance C_C in Fig. 3.1a subjected to temporal changes due to a *motion-induced displacement* of the metal electrode with respect to the conductive body, see (2.41)]

may significantly contribute to the *transient common-mode* u_{CI} and thus contribute to the associated *movement artefacts*. It should be recalled that a *varying capacitance* of the coupling capacitor with a *constant charge* on it still yields a *varying voltage drop* across this capacitor (3.5) and thus yields a varying u_{CI} at the amplifier's input.

Such artefacts originating from the *electrode/tissue boundary* are particularly strong when capacitive electrodes as well as the human body are well *isolated*, from each other and towards the ground. Then even *very small currents*, as generated by transient triboelectrically induced charges (in the typical range of μA down to nA (Wartzek et al. 2011)), may yield *severe common-mode* u_{CI} (in the range of kV) when crossing this isolation. Microscopically small contact areas are formed and disrupted during rubbing (e.g., in the course of respiration), leading to these small currents. Furthermore, this proper isolation implies large *discharge time constants* which are proportional to the product of the isolation resistance and isolation capacitance. Correspondingly, higher levels of u_{CI}, many more movement artefacts, and longer discharge times (of C_C in Fig. 3.1a) occur on *cold dry days* than on *hot humid days*. This is because low humidity makes it difficult for the charge build-up to dissipate gradually.

In addition, please note that even though decreasing *isolation impedance* [with its resistive and capacitive components, see (2.47)] weakens *triboelectric effects*, the decreasing *isolation resistance* and/or decreasing *isolation capacitance* increase the *cut-off frequency* of the circuit in front of the biomedical amplifier. The increased *cut-off frequency of the total measurement system* may add more noise to the output of the amplifier. Therefore, there is always a *compromise* between the affinity to triboelectric effects and the resulting cut-off frequency.

The *triboelectricity* of the *electrode/tissue boundary* can be reduced by a proper *design of this boundary*:

- The *surface type of the electrode* (i.e., the electrode's top layer) should be matched to the surface this electrode is in transient contact with, in terms of the *triboelectric series*. For instance, the electrode surface should be matched to the human skin if the electrode is directly applied to the skin or matched to clothes if the electrode resides on clothes. To give a more tangible example, a smaller electrostatic voltage is generated in-between *silver* (as electrode material) and *cotton* (as clothes) in comparison with *silver and silk*.
- Triboelectrically induced charges on the contact surfaces should have a low-ohmic *discharge path* within the boundary, instead of flowing through a *high-ohmic discharge path* and then generating a *high common-mode* u_{CI}. For instance, a low-ohmic grid on the surface of a *non-contact electrode* can efficiently drain off excess charges (Wartzek et al. 2011).
- *Rubbing of electrodes and subject's movements* should be avoided.

3.3 Body Area Networks

Electric biosignals can also be used as information carrier in ubiquitous *body area networks* in order to collect data from different medical sensors worn on the body. Besides the traditional wireless communication over the *air channel* (such as Bluetooth transmission at 2.4 GHz), the *body channel* can also be used for data exchange with the human *body itself as a transmission medium* for electric signals (Seyedi et al. 2013; Xu et al. 2012). In the latter case of the body channel, as demonstrated in Fig. 3.31a, all *signal electrodes* and *ground electrodes* (of multiple sensor outputs or, simply speaking, of transmitter and receiver) can be attached on the body (skin), which is known as *galvanic coupling* (compare Fig. 3.1b). Here an electric signal is differentially applied between the signal and ground electrodes of the transmitter (voltage u_T in Fig. 3.31a) and then received as a differential (but attenuated) signal between the signal and ground electrodes of the receiver (voltage u_R in Fig. 3.31a). There are predominantly *conductive pathways* for the currents in the body (carried by ions in tissue), i.e., for the forward and return currents necessarily building a *closed loop*; see indicated field lines in Fig. 3.31a.

The applied *alternating electric signals* at relatively *low frequencies* (<200 kHz in accordance with (Callejon et al. 2012)) are mainly confined to the surface of the body (to the person's proximity) by means of the *near-field* component. Only little energy is radiated into the surrounding environment outside of the human body, so that there is *no interference* with external electromagnetic fields (which implies also *natural security* of wireless communication). However, *increasing frequency of these electric signals* increases *radiated signal* components (into and from the environment), such that the *human body acts as antenna* (transmitting and receiving electric signals, respectively). Likewise, the signal confined to the surface of the body is partly radiated into the surroundings; in particular, when the signal wavelength becomes comparable with the human body channel length (2.5).

As an alternative to the galvanic coupling, only the *signal electrodes* (of transceivers) can be attached on the body, whereas the respective *ground electrodes* can float in the air without any direct contact with the conductive body; it is known as *capacitive coupling* (compare Fig. 3.1a). In this case, as demonstrated in Fig. 3.31b, the *forward current* pathway between the respective signal electrodes is a *conductive pathway*, whereas the *return current* pathway between the respective ground electrodes is a (parasitic) *capacitive pathway*. Usually, the external ground (and other environmental structures) is dominantly included in the return current pathway, see Fig. 3.31b, with the human body acting as a conductive body (Section "Charge and Current Induction"). In contrast to the *galvanic coupling* suited for the communication of both *on-body and in-body* implanted devices, the *capacitive coupling* addresses only *on-body* devices.

It turns out that the *galvanic coupling* is more strongly dependant on the *distance* between the pair of the receiving electrodes (i.e., the signal electrode plus the respective ground electrode) and the pair of the transmitting electrodes than the *capacitive coupling* (Callejon et al. 2012). Consequently, the capacitive coupling is

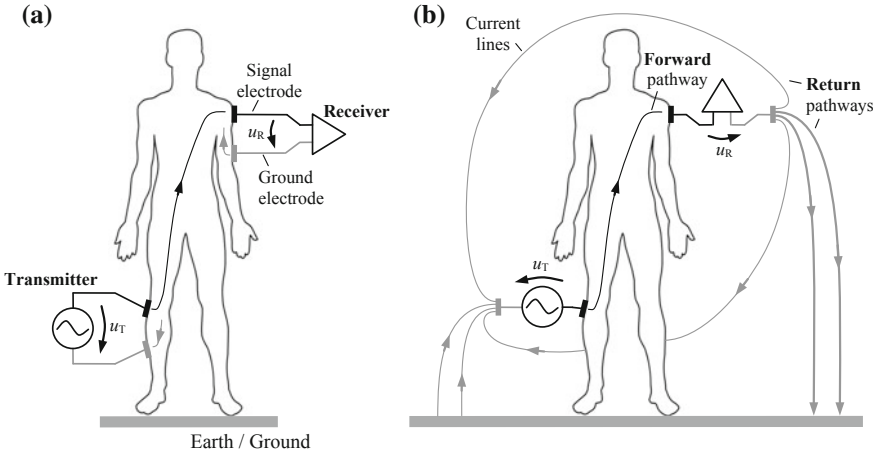

Fig. 3.31 Body area communication with **a** galvanic coupling (compare Fig. 2.16a) and **b** capacitive coupling (compare Figs. 2.26a and 2.51a)

the advantageous coupling for relatively long distances (>15 cm in accordance with (Callejon et al. 2012)). It should also be noted that the capacitive coupling is primarily dependent on the aforementioned capacitive return pathway (dominating at relatively *high frequencies* above 1 MHz), whereas the galvanic coupling is primarily dependent on the skin properties (at relatively *low frequencies* up to 200 kHz). The galvanic coupling shows better transmission results through the body channel for short distances (<15 cm) and low frequencies (<200 kHz); likewise, the capacitive coupling is more suitable for long distances and high frequencies.

It should be noted that

- the *galvanic coupling* behaves rather as a *low-pass filter* due to the low-pass behaviour of tissue (Fig. 2.9).
- The *capacitive coupling* behaves rather as a *high-pass filter* (2.42) due to the capacitive return pathway, which applies in the frequency range below approximately 4 MHz or for short distances between the signal electrodes (for short length of the conductive pathway), i.e., as long as the *signal losses* in the closed loop are relatively low (Cho et al. 2007); see below.

In general, as the *length of the conductive pathway* (i.e., the *length of the body channel*) increases, both the (unwanted) *resistance* of this pathway and the (unwanted) coupling *capacitance* from this pathway (in the body) to the external ground increase (Cho et al. 2007). The former effect is due to increasing effective length of the current pathway through tissues [compare (Kaniusas 2012, Footnote 30)], whereas the latter effect is due to increasing effective area of the aforementioned parasitic capacitance (Kaniusas 2012, Eq. 2.2). Both effects cause *signal loss* which amount depends obviously on the length of the resulting body channel.

In particular, the signal loss increases a lot more at relatively *high frequencies*—beyond 10 MHz in accordance with Cho et al. (2007)—as the body channel length increases; this is because of increased capacitive coupling between the body and the external ground [see complex and *frequency-related impedance of the capacitor*, (2.42)]. In analogy, *high frequency components* of the transmitted signal attenuate significantly with increasing length of the conductive pathway in the body or increasing distance between the signal electrodes on the skin.

In terms of the *capacitive coupling*, the *body impedance* can be ignored for relatively *low frequencies* [below 1 MHz in accordance with Cho et al. (2007)] because the impedance of the capacitive return pathway [through the air with $\varepsilon_r = 1$, (2.42)] is much higher than that of the conductive pathway (through the body with $\varepsilon_r \gg 1$); compare Footnote 53 in Chap. 2. Likewise, the electrical properties of body tissues have little effect on the efficiency of the capacitive coupling technology provided low frequencies are applied. However, as the signal *frequency increases*, the (absolute) coupling capacitances have less effect and the body impedance can not be neglected any more (Cho et al. 2007). In fact, large ground electrodes (large planes) for the return current pathway tend to reduce the impedance of the capacitive pathway [due to increased capacitance, see Kaniusas (2012, Footnote 33)] and thus to enhance the signal-to-noise ratio of the transmitted signal.

It should be noted that if the human body itself acts as a communication route, quite *low frequencies* in range of kHz up to MHz are employed because *body losses* increase with frequency. Figure 2.6 illustrates that the body penetration decreases strongly with increasing frequency. That is, the propagation of these low frequencies *along the body* is superior to that *through the air* around the body. In other words, typical telecommunication frequencies within GHz range (e.g., 2.4 GHz) are not favourable for the signal transmission throughout the body channel which then would simply short-circuit this *high frequency communication signal*.

References

M.A. Callejon, D.N. Hernandez, J.R. Tosina, L.M. Roa, Distributed circuit modeling of galvanic and capacitive coupling for intrabody communication. IEEE Trans. Biomed. Eng. **59**(11), 3263–3269 (2012)

N. Cho, J. Yoo, S.J. Song, J. Lee, S. Jeon, H.J. Yoo, The human body characteristics as a signal transmission medium for intrabody communication. IEEE Trans. Microw. Theory Tech. **55**(5), 1080–1086 (2007)

S.F. Cogan, D.J. Garrett, R.A. Green, Electrochemical principles of safe charge injection, in *Neurobionics: The Biomedical Engineering of Neural Prostheses*, ed. by R.K. Shepherd (Wiley, Hoboken, 2016), pp. 55–88

D. Dobrev, I. Daskalov, Two-electrode biopotential amplifier with current-driven inputs. Med. Biol. Eng. Comput. **40**(1), 122–127 (2002)

H.D. Dörfler, in *Interface and Colloid Chemistry* (in German: Grenzflächen- und Kolloidchemie) (VCH Publisher, 1994)

S. Gabriel, R.W. Lau, C. Gabriel, Gabriel: the dielectric properties of biological tissues: II. Measurements in the frequency range 10 Hz to 20 GHz. Phys. Med. Biol. **41**(11), 2251–2269 (1996)

S. Grimnes, O.G. Martinsen, *Bioimpedance and Bioelectricity Basics* (Elsevier Publisher, Amsterdam, 2008)
C.H. Hamann, W. Vielstich, in *Electrochemistry* (in German: Elektrochemie). Wiley-VCH Publisher (1998)
J.C. Huhta, J.G. Webster, 60-Hz interference in electrocardiography. IEEE Trans. Biomed. Eng. **20**(2), 91–101 (1973)
E. Kaniusas: Clinical versus portable monitoring: possibilities, pitfalls, and future vision, in *Invited Expert Commentary to "Sleep Apnea Syndrome: Research Trends"*, ed. by A.O. Lang (Nova Science Publishers, 2007), pp. 3–5
E. Kaniusas, in *Biomedical Signals and Sensors I: Linking Physiological Phenomena and Biosignals* (Springer Publisher, 2012)
E. Kaniusas, in *Biomedical Signals and Sensors II: Linking Acoustic and Optic Biosignals and Biomedical Sensors* (Springer Publisher, 2015)
R.S. Khandpur, in *Biomedical Instrumentation: Technology and Applications* (McGraw-Hill Publisher, 2005)
N. Leitgeb, in *Safety of Electromedical Devices* (Springer Publisher, 2010)
D. Miklavcic, N. Pavselj, F.X. Hart, Electric properties of tissues, in *Wiley Encyclopedia of Biomedical Engineering* (2006), pp. 1–12
A.C. Patil, N.V. Thakor, Implantable neurotechnologies: a review of micro- and nanoelectrodes for neural recording. Med. Biol. Eng. Comput. **54**(1), 23–44 (2016)
F. Rattay, in *Electrical Nerve Stimulation: Theory, Experiments and Applications* (Springer Publisher, 1990)
J.P. Reilly, in *Applied Bioelectricity: From Electrical Stimulation to Electropathology* (Springer Publisher, 1998)
P. Roach, D. Eglin, K. Rohde, C.C. Perry, Modern biomaterials: a review—bulk properties and implications of surface modifications. J. Mater. Sci. Mater. Med. **18**(7), 1263–1277 (2007)
Safety Publication and Preliminary Standard DIN IEC/TS 60479-1 (VDE V 0140-479-1): effects of current on human beings and livestock (2007)
W. Schmickler, Models for the interface between a metal and an electrolyte solution, in *Structure of Electrified Interfaces*, ed. by J. Lipkowski, P.N. Ross (VCH Publisher, 1993)
H.P. Schwan, Linear and nonlinear electrode polarization and biological materials. Ann. Biomed. Eng. **20**(3), 269–288 (1992)
M. Seyedi, B. Kibret, D.T.H. Lai, M. Faulkner, A survey on intrabody communications for body area network applications. IEEE Trans. Biomed. Eng. **60**(8), 2067–2079 (2013)
E.M. Spinelli, M.A. Mayosky, Two-electrode biopotential measurements: power line interference analysis. IEEE Trans. Biomed. Eng. **52**(8), 1436–1442 (2005)
F.T. Wagner, Simulation of the electrical double-layer in ultrahigh vacuum, in *Structure of Electrified Interfaces*, ed. by J. Lipkowski, P.N. Ross (VCH Publisher, 1993)
T. Wartzek, T. Lammersen, B. Eilebrecht, M. Walter, S. Leonhardt, Triboelectricity in capacitive biopotential measurements. IEEE Trans. Biomed. Eng. **58**(5), 1268–1277 (2011)
A.N. Weissenrieder, in *Stimulation Electrodes for Pacemaker Applications: Electrochemistry of Bioelectrodes* (VDM Publisher Dr. Müller, 2009)
B.B. Winter, J.G. Webster, Driven-right-leg circuit design. IEEE Trans. Biomed. Eng. **30**(1), 62–66 (1983)
M.R. Wright, An introduction to aqueous electrolyte solutions (Wiley, 2007)
R. Xu, W.C. Ng, H. Zhu, H. Shan, J. Yuan, Equation environment coupling and interference on the electric-field intrabody communication channel. IEEE Trans. Biomed. Eng. **59**(7), 2051–2059 (2012)
Y.L. Zheng, X.R. Ding, C.C.Y. Poon, B.P.L. Lo, H. Zhang, X.L. Zhou, G.Z. Yang, N. Zhao, Y.T. Zhang, Unobtrusive sensing and wearable devices for health informatics. IEEE Trans. Biomed. Eng. **61**(5), 1538–1554 (2014)

Index

A
Abdomen, 234
Abdominal fat, 23
Abdominal uterine electromyogram, 14
Abolish excitation, 285
Abolishing action potential, 286
Abolition of excitation in fewer fibers, 287
Abolition threshold, 285, 286
Above β-dispersion, 113, 114, 256, 258
Above the basic restrictions, 358
Above the dispersion region, 125
Above U_{dec}, 503
Above U_{dec} in the non-linear range, 487
Absent necrosis, 71
Absent net charge injection, 274
Absent net charge transfer, 502, 506
Absent reflection, 204
Absent signal deterioration, 524
Absent surplus polarization, 505
Absolute amplitudes of sinc courses of the electric field, 201
Absolute electrical impedance tomography, 24
Absolute level of U_{pol}, 445
Absolute refractory period, 294, 305, 374
Absolute temperature-time profile, 342
Absolute values of U_{pol}, 437, 442
Absorbed at the body surface, 349
Absorbed energy, 171
Absorbed power, 109
Absorbing corners, 199
Absorbs some energy, 163
Absorption of the electromagnetic energy, 348
Accelerates mass transport, 481
Acceptable margin of safety, 354
Accepting electrons, 440
Accommodating mechanisms, 134, 244, 245, 247, 293, 304, 305, 317
Accumulated by conductive currents, 174
Accumulated charge, 362, 421
Accumulated depolarization, 324
Accumulated equalizing currents outside countless muscle cells, 10
Accumulated excess charge, 278
Accumulated polarization charge, 92
Accumulated surface charge, 135, 149, 362, 363
Accumulates spatial planes, 41
Accumulate triboelectrically induced charge, 545
Accumulating wavefronts, 217
Acid, 339, 437, 492, 493
Acoustically slow medium, 41
Acoustic, optic, and electric biosignals, 171
Across the capacitor, 62
Across the opposite membranes, 258
Across the organelle, 116
Across the resistor, 61
Across the tissue section, 65
Across the whole cell, 259
Action impulse, 18, 266, 285, 294, 316, 335
Activated fibers, 296
Activated in synchrony, 14
Activated nerve-to-nerve synapses, 14
Activating function, 254, 263–267, 269, 282, 311, 314, 323, 324, 326, 331
Activation barriers, 503
Activation energy, 465
Activation energy of redox reaction, 451

© Springer Nature Switzerland AG 2019

E. Kaniusas, *Biomedical Signals and Sensors III*, Biological and Medical Physics, Biomedical Engineering, https://doi.org/10.1007/978-3-319-74917-4

Activation inside the axon, 265
Activation overvoltage, 448, 451, 455, 457, 461, 463, 472, 477, 480, 495
Active application of u_{DC}, 490, 491
Active application of voltages, 495
Active cell response, 243, 250
Active electrode, 332, 404
Active electrode near to biological tissue, 331
Active medical implants, 353
Active net energy supply, 414
Active response threshold, 345
Active shielding, 540
Active thermoregulatory mechanisms, 344
Active ungrounded catheter, 364
Activity coefficient, 419
Acute exposure, 388
Adaptation effects, 245
Additional multiplication factor, 192
Adjacent electrolyte, 511
Adjacent tissue layers, 216
Adjusted reference level, 361
Administrative controls, 358
Admits large displacement currents, 535
Adsorption and deadsorption, 411, 416, 422, 449, 461, 482, 497
Adult, 358, 517
Advanced Butler-Volmer equation, 459
Advantage for toxicity, 445
Advantages of capacitive coupling, 524
Adverse biological effects, 353
Adverse effects, 10, 13, 28, 49, 240, 348, 354, 381, 386, 514
A fibers, 329
After the stimulus, 326
After the vulnerable period, 375
Ag/AgCl electrode, 439, 442, 443, 445, 455, 490, 495
Ag^+ cations, 443
Aggravates the charge counterbalancing, 545
Ag^+ ions tend to deposit on Ag metal surface, 443
Agitated electrode paste, 511
Ag oxidation reaction ($Ag + Cl^- \rightarrow AgCl + e^-$), 455
Ag reduction reaction ($AgCl + e^- \rightarrow Ag + Cl^-$), 455
Air behaves as a dielectric, 192
Air channel, 547
Air/fat boundary, 192
Air to fat boundary, 217
Air to muscle or to fat, 204
Air/muscle boundary, 192, 207
Air/tissue boundary, 190, 208
Air ventilation/aeration, 24
Aligned electric fields, 91
Alignment of polar structures, 159
All electro-kinetic processes, 448
All excess charge, 424
All heart muscles, 373
All ions, 433
All-or-none action potentials, 243
All polarizations, 167
All thick fibers, 317
All three excitation-related quantities, 246
Alpha dispersion, 103
Alternating anodic and cathodic reaction, 477
Alternating charge transfer process, 489
Alternating conductive currents, 504
Alternating conductive $i_{AC,E}$, 474, 476, 477
Alternating current, 20, 25, 79, 146, 150, 245, 335, 336
Alternating current i_{AC}, 473
Alternating current impedance, 403
Alternating current in the body, 146
Alternating diffusion, 104
Alternating displacement current, 525
Alternating displacement current $i_{AC,C}$ (>> $i_{AC,E}$), 475
Alternating displacement $i_{AC,C}$, 474
Alternating electric currents, 146
Alternating electric field, 228, 240, 529
Alternating electric potential above the ground, 527
Alternating electric signals, 547
Alternating electrode reaction, 480
Alternating field, 100
Alternating i_{AC}, 467
Alternating i_{AC} across the boundary, 479
Alternating $i_{AC,E}$, 479
Alternating ionic diffusion, 104
Alternating magnetic fields, 240
Alternating recharge of the electrolytic double layer, 467
Alternating u_{AC}, 467, 509
Alternating u_{AC}/i_{AC} application, 497
Alternating voltage, 20
Ambient E_{ext} outside the body, 384
Ambient electric field, 100, 137, 243, 354, 361, 362
Ambient electromagnetic field, 352
Ambient fields are significantly perturbed, 240
Ambient magnetic field, 354
Ambient power density, 354
Ambient time-varying electric and magnetic fields, 379
Ambient interference, 535
Amount of dissolved Ag^+ ions, 443
Amplification, 386

Amplification factor, 227
Amplification gain of input circuits, 535
Amplification of input signals, 386
Amplified with the differential gain, 534
Amplifiers, 535
Amplifier's ground, 533, 542
Amplifier's inputs, 533
Amplitude, 14, 52, 54, 57, 61, 298, 332, 372
Amplitude and phase, 361
Amplitude change, 59
Amplitude/magnitude change, 59
Amplitude-modulated, 351
Amplitude-modulated electromagnetic fields, 351
Amplitude-modulated high frequency electromagnetic fields, 352
Amplitude of the resulting conductive $i_{AC,E}$, 478
Amplitude of the stimulation current, 389
Amplitudes of all voltages and currents, 497
Amplitude $\underline{U}_B$ of electric biosignals, 533
Amplitudes, 36, 39, 40, 54
Analysis of bioimpedance, 23
Angles φ_C^+ and φ^- differ, 182
Angles φ_E^+ and φ^- differ, 177
Angular frequency, 33, 60, 64, 95, 122
Animals, 167, 350
Anionic activity, 444
Anions, 78, 425, 428, 435
Anions and cations, 431
Anions migrate usually faster than cations, 78
Anisotropic excitation, 250, 259
Anisotropy, 73, 82, 143
Anisotropy in electrical properties, 73
Anisotropy in its structure, 73
Anisotropy of muscle, 132
Ankle and knee, 143
Ankles and wrist, 169
Annoyance, 378
Anodal break, 338
Anodal surround block, 315
Anode, 78, 314, 335, 336, 339, 440, 451, 453, 471, 473, 491
Anode and cathode, 288
Anode electrode, 338
Anodic, 261, 302, 313
Anodic and cathodic currents, 261
Anodic behaviour, 476
Anodic branch, 455
Anodic current, 260, 281, 320, 338
Anodic current ceases, 338
Anodic current stimulus, 271, 323
Anodic depolarization, 311
Anodic excitation, 339
Anodic excitation and propagation, 321
Anodic monophasic pulse, 288
Anodic phase, 277, 278, 284, 285, 287, 293, 314, 494
Anodic reaction with $S_{red} \rightarrow S_{oxi} + z \bullet e^-$, 477
Anodic sphere, 320
Anodic stimulation, 247, 270, 273, 309, 313, 321, 323
Anodic stimulation depolarizes, 270
Anodic stimulation threshold, 313
Anodic stimulus, 321
Anodic threshold stimulus, 323
Another phase boundary within the electrolyte, 442
Antinodes, 210, 211
Any resistive and/or capacitive asymmetry in the input circuit, 537
Aorta with the conductive blood, 21
Aperiodic firing, 281
Apnea, 370
A positive feedback cycle, 487
Appears as an augmented interference, 534
Application of a voltage stimulus u, 495
Application of i, 21
Application of the direct u_{DC}, 471
Application of u_{AC} between both electrodes with its complex amplitude $\underline{U}_{AC}$, 474
Applied alternating u_{AC}, 485
Applied charge, 280
Applied current leaks away, 307
Applied direct $u_{DC} < U_{dec}$, 485
Applied direct voltage $u_{DC} = U_{pol} - U'_{pol}$, 451
Applied field is partially compensated, 92
Applied i_{DC}, 462
Applied j, 260
Applied signal, 541
Applied u_{AC}, 473
Applied u_{DC}, 471
Applied voltage u_{DC}, 453
Approaching anodic currents, 257
Approaching currents, 247
Approximated anatomical models, 360
Approximated as a conductor, 59
Approximated with C_{el} only, 502
Approximations without dispersions, 68
A preamplifier located near each electrode, 542
Arbitrary fiber diameters, 321
Arbitrary geometries of the stimulation electrodes, 334
Area, 350
Area A of a surface electrode, 66, 539
Area of the formed conductive loop, 529
Area-related quantity, 349
Arrhenius equation, 451

Artefacts, 15, 16
Artefacts in electroencephalogram, 16
Artificial electric source, 6, 9
Artificial field, 386
Artificially produced, 283
Artificial stimulation, 274
Artificial stimulus, 4
As buzzing, clicking, or popping sounds, 350
As deliberately used in therapy, 28
As favourably used in diagnosis, 28
A single action impulse, 311
Associated current density field, 50
Associated differential electrode resistance R_{el}^{d} due to inert diffusion, 458
Associated differential impedance $\underline{Z}_{el}^{c}$, 482
Associated electric fields, 51
Associated sinusoidal, 32
Association reaction, 443
Asymmetric charge distribution, 103, 108, 112
Asymmetric cloud, 110
Asymmetric cloud of charges, 106
Asymmetric counterion distribution, 103, 107
Asymmetry, 109, 239
Asynchronous activation, 14
Asynchronous firing, 296
At rest before stimulation, 319
At the amplifier's input, 536
Atomic and molecular dipoles, 92
Atomic bonds, 87
Atomic diameter, 87, 94
Atomic dipole, 88
Atomic distances, 454
Atrial and ventricular fibrillation, 375
Atrial fibrillation, 375
Attenuated plane TEM wave, 43
Attenuated spherical TEM wave, 42, 44
Attenuated wave, 478
Attenuate noise or power line interference coupled capacitively and/or inductively, 539
Attenuates power line interference, 542
Attenuates unfavourably spectral components of u_B, 542
Attenuation, 42
Attenuation coefficient α, 44, 208, 479
Attenuation factor, 142, 194, 195, 224
Attenuation of electromagnetic fields, 47
Attenuation of the wave, 170
Attraction of inert counterions, 485
Attractive and repulsive electrostatic forces, 90
Attractive electrostatic force, 87, 106
Autodissociation, 492
Average body tissue, 73, 74
Average drift velocity, 77
Average man, 170
Average potential of the two skin electrodes, 538
Average power density, 351
Average unipolar polarization overvoltage, 278
Averaging and spread, 332
Averaging distance, 356
Averaging potentials, 541
Averaging volume, 356
Avoid heat stroke, 387
Avoiding or minimizing any direct current, 277
Avoid loading effects, 527
Avoid masking, 534
Away from the anode, 335
Axial direction, 267
Axial ratio, 148
Axial time constant of the membrane, 329
Axon activation, 311
Axonal injury, 389
Axon diameter, 273, 328
Axon lying in parallel to the skin, 262
Axon's firing, 315
Axon's membrane, 264
Aα fibers, 329
Aβ fibers, 329
Aδ fibers, 329

B

Back and forth migration, 474
Back-flow, 544
Balanced redox reactions, 455
Balance the delivered charge, 284
Balancing ionic counter-charge accumulates, 465
Bare perception, 366
Barrier for the redistribution of charges, 503
Based on a physical contact, 240
Baseline drifts, 401
Baseline wandering, 512
Base metals, 415
Basic or neutral solutions, 437
Basic restriction, 147, 161, 251, 341, 349, 354, 356, 357, 360, 365, 379, 380, 382, 384, 387, 388
Basic restriction is not exceeded, 356
Basic restriction of the current density, 241
Basic restriction of the inner electric field, 241
Basic restrictions are not exceeded, 354
Basic restrictions will not be exceeded, 356
Basis for guidelines, 354
Battery, 300
Behavioural responses, 346, 350

Bell-like shape, 262
Below the gamma relaxation frequency, 83
Below the resonance frequency, 167
Below the resonance region, 167
Below the thresholds for nerve or muscle stimulation, 383
Below U_{dec} in the linear range, 487
Below whole-body and partial-body resonances, 142
Bend axon regions, 262
Bending, 197, 207
Bend mode, 261, 288
Bend of the axon, 261
Bend regions, 261
Benign prostate tissue, 71
Benign tissues, 71
β-dispersion, 66, 72, 103, 111, 113, 128, 131, 132, 174, 176, 256, 257, 259, 305
Beta relaxation frequency, 258
Between preamplifiers and the biomedical/main amplifier, 543
Between the electrode and the respective preamplifier, 543
Between the electrode surface and counterions, 429
Between two electrodes, 511
Between two neighbouring stimulating pulses, 279
Bias voltage, 292
Bidirectional, 279, 474
Bifurcation, 273, 323, 335
Binding strength between these ions is low, 444
Biocompatible and safe, 392
Biocompatible metals, 390, 403
Bioelectrically inactive area, 332, 404
Biological bodies, 60, 75, 83, 192, 212, 352
Biological body as a conductor, 68
Biological body as a dielectric, 68
Biological effects, 351, 353, 354, 357, 382, 386, 388
Biological effects with the associated response windows, 351
Biological media, 59
Biological processes, 413
Biological structure, 89
Biological tissue/electrolyte, 442
Biological tissue of interest, 507
Biological tissues, 3, 12, 20, 31, 34, 37, 38, 42, 43, 46, 49, 50, 60, 62, 65, 66, 74, 75, 85, 87, 98–100, 124, 152, 250, 339, 390, 400, 406, 412, 496, 508
Biological water, 132
Biomedical amplifiers, 512, 513, 527, 532, 541, 545
Biophysics, 328
Biosignal, 513, 524
Biosignal coupling, 524
Biosignal-related portion u_B of u, 534, 537
Biosignal-related portion, 538
Biosignal-related potentials, 538
Biosignal's diagnostic power, 9
Biosignal's source, 519, 521, 531
Biphasic charge-balanced stimulus, 289
Biphasic current pulse, 269, 277, 278, 284, 393, 494
Biphasic current stimulation, 280, 285, 289
Biphasic excitation threshold, 287
Biphasic mode, 335
Biphasic pulses, 291
Biphasic rectangular pulse, 293
Biphasic rectangular stimulus, 287
Biphasic sinusoidal pulse, 293
Biphasic stimulation, 279, 284, 289, 301
Biphasic waveform, 2, 13, 288, 309
Bipolar and tripolar modes, 334
Bipolar cardiac pacemaker, 385
Bipolar case, 335
Bipolar mode, 15, 332, 334
Bipolar pacemaker, 385
Bipolar recording mode, 332
Bipolar stimulation mode, 332
Bipolar wired systems, .386
Bivalent ions, 78
Blink response, 16
Blockade, 296
Blocking, 321
Blocking phenomena, 243
Blocking threshold, 296
Block is less likely for short current pulses, 315
Block propagating action impulses, 314
Block the delivery of any direct current, 278
Blood-filled aorta, 22
Blood perfusion, 24, 84, 243, 344, 346, 359
Blood section, 68
Blood shift, 21
Blood vessels embedded within muscular tissue, 84
Blurred, 334
Bodily tissue, 191, 412, 476
Bodily tissue and electrode resistances, 477
Bodily tissue resistance, 476
Body area networks, 547
Body behaves as a conductor, 192

Body capacitance C_b, 406
Body channel, 547
Body cross-section, 140
Body extremities, 518
Body height, 164
Body impedance, 23, 515, 549
Body is exposed, 240
Body is grounded, 139, 141, 362
Body is insulated, 139
Body is ungrounded, 140
Body itself as a transmission medium, 547
Body losses, 549
Body mass, 350
Body resistance R_b, 406, 407
Body resonance phenomena, 359
Body resonances, 164
Body's exposure, 194, 399
Body size, 362
Body's motions, 512
Body surface, 164, 170, 357, 539
Body temperature to less than 1°C, 387
Bond stretching, 492
Both electrodes located near the target tissue, 332
Both feet, 377
Bottoms of the feet, 140
Boundaries are continuous, 239
Boundary, 41, 117, 172, 174, 239, 449
Boundary behaves like a capacitor, 466
Boundary conditions, 49, 84, 117, 136, 148, 149, 155, 172, 173, 180, 190, 201, 230, 231, 233, 381, 478
Boundary from the air to muscle or to fat, 203
Boundary model, 496, 497
Boundary model of $\underline{Z}_{el}$, 499
Boundary of the body, 156
Boundary of the conductive body, 136
Boundary of the sensing electrode, 470, 487
Boundary of the sensing electrode for $u_{DC} > U_{dec}$, 471
Boundary of the tissue section, 89–91
Boundary of two phases, 422
Boundary polarization, 504
Boundary surface, 210
Bound charge Q_p and $-Q_p$ on tissue boundaries, 92
Bound charges, 62, 85, 89, 94, 96, 99, 124, 159, 180, 229, 341, 474
Bounded media, 49
Bound ionically to Cl^- anions, 443
Bound water molecules, 118
Brain, 379
Brain tissue, 390
Braking forces, 108
Breakdown, 401, 515
Breakdown of cell membranes, 71, 72, 244, 256
Breakdown of membranes, 373
Breast to the left hand, 376, 377
Breathing difficulties, 366, 370
Breathing muscles, 369
Bubble away, 473
Buffer amplifiers, 540, 543
Buffer layer, 511
Buffer layer absorbs movements, 511
Buildup of polarization, 295
Build-up of the double layer, 503
Bulk concentration, 461
Bulk electrical properties, 70
Bulk permittivity, 127
Bulk solution, 458
Bulk/undisturbed electrolyte, 429
Bulk water, 430
Bulk with its concentration c^0, 478
Bunch of nerve fibers, 280
Burns, 364, 366, 368, 373
Butler-Volmer equation, 451
Buttler-Volmer equation with $R_{el} = R_{el}^t$ and $(u_{pol,i} - U_{pol})$, 463

C

Cable equation, 259, 260, 265
Cable equation for weak subthreshold stimulus, 260
Can block propagation, 335
Cancer therapies, 359
Can cross the electrode/tissue boundary, 474
Can not drive any net transmembrane currents, 253
Capacitance, 50, 62, 65, 139, 280, 297, 363, 403, 421, 504, 548
Capacitance C, 254
Capacitance C_{el}, 468, 483, 501
Capacitance C_{el} of the electrolytic double layer, 468
Capacitance of the muscle cell membrane, 113
Capacitance of the shielded and grounded cable, 540
Capacitance size, 363
Capacitance to the power line, 139
Capacitive and inductive interferences, 537
Capacitive behaviour, 274
Capacitive behaviour of the boundary, 475, 476
Capacitive behaviour of $\underline{Z}_{el}$, 502
Capacitive boundary, 277, 390, 507
Capacitive charging of the double layer begins, 494

Capacitive coating C, 267
Capacitive component, 406
Capacitive coupling, 15, 19, 403, 504, 506, 512, 529, 537, 547–549
Capacitive coupling of displacement currents, 504
Capacitive coupling of the power line interference, 532, 536
Capacitive current divider, 64
Capacitive current shunts, 531, 532
Capacitive/displacement current, 94, 305
Capacitive/displacement current density, 54, 95
Capacitive/displacement current density field, 172
Capacitive impedance, 19, 63, 142, 226, 407, 421, 498, 501, 506, 508, 532
Capacitive impedance of the body, 228
Capacitive impedance $1/(j \cdot 2\pi \cdot f \cdot C_{el})$, 476, 501, 502
Capacitively coupled displacement currents, 528
Capacitively coupled from power lines into both electrode leads, 527
Capacitively coupled from wires of power lines into the conductive human body, 525
Capacitively short-circuits both leads, 531
Capacitively short-circuits differential biosignals, 531
Capacitive mechanisms, 400
Capacitive pathway, 547
Capacitive sensing, 524
Capacitive shunt impedances, 532
Capacitive voltage divider, 533
Capacitor, 62, 65, 504, 506, 515
Capacitor is charged or discharged, 63
Capacitors, 278
Capacitor with its double layer capacitance C_{el}, 475
Capacity, 307
Carbonisation, 384
Cardiac activity, 6
Cardiac and/or respiratory arrest, 372
Cardiac and thorax surgery, 376
Cardiac arrest, 373
Cardiac component, 21, 22
Cardiac cycle, 378
Cardiac failure, 373
Cardiac information, 6
Cardiac muscle, 306, 382
Cardiac muscle cells repolarize and relax together, 374
Cardiac output, 346, 347
Cardiac pacemaker, 44, 192, 385
Cardiac surgery, 376
Cardiorespiratory, 21
Cardiovascular, 21
Cardiovascular and cardiorespiratory activity, 27
Cardiovascular system, 347
Cartilage degeneration, 18
Catalyser, 440, 492
Catalysing effects, 461
Cathodal make, 338
Cathode, 78, 261, 335, 336, 339, 440, 451, 453, 471, 473, 490
Cathode-anode distance, 332
Cathode electrode, 338
Cathodic, 302, 313, 314
Cathodic and anodic, 289
Cathodic and anodic phases, 271
Cathodic and anodic pulses, 288
Cathodic and anodic stimulation, 314, 321
Cathodic behaviour, 476
Cathodic block, 271, 273, 296, 315, 317, 320, 321, 323, 335
Cathodic blocking phenomenon, 319
Cathodic branch, 455
Cathodic current, 260, 281, 319
Cathodic current stimulus, 271, 323
Cathodic excitation and propagation, 321
Cathodic inhibition, 339
Cathodic monophasic pulse, 288
Cathodic monophasic rectangular pulse, 292
Cathodic monophasic thresholds, 288
Cathodic or anodic, 289
Cathodic phase, 277, 278, 284, 314, 494
Cathodic phase balances the charge, The, 285
Cathodic phase in extracellular stimulation, 293
Cathodic phase is relatively short, 284
Cathodic reaction with $S_{oxi} + z \bullet e^- \rightarrow S_{red}$, 477
Cathodic spherical rings, 320
Cathodic stimulation, 247, 270, 273, 309, 313, 314, 321, 323, 328, 330
Cathodic stimulation threshold, 313
Cathodic stimulus, 321, 335
Cathodic threshold stimulus, 323
Cathodic blocking phenomenon, 319
Cations, 18, 78, 428, 436
Cations and anions, 79, 80, 423
Cations and anions behave differently with increasing z, 81
Cations and anions contribute differently to the total conductivity, 81
C_{el} depends also on the absolute instantaneous level of u_{AC}, 483
Cell-based dipoles, 12
Cell membranes, 111

Cell radius, 115
Cells need some time, 245
Cell's orientation, 250
Cell's spatial extension, 250
Cell suspension, 406, 510
Cellular level, 13
Cellular tissue, 115
Center of gravity of counterions, 107
Central axon's region, 311
Central charged particle or ion, 109
Central depolarized region, 335
Central fiber region, 326
Central ion, 433
Central ion is exponentially screened, 434
Central mode, 253, 261, 263, 269, 308
Central nerves, 380
Central nervous system, 157, 194, 245, 379, 382, 386
Central single ion, 106
Centre of the head, 153
Centre of the legs, 153
Centre of the trunk, 153
Cerebral activity, 19
C fibers, 297, 329
Change in the electrical tissue properties, 20
Change in the spatial current distribution, 20
Changes after death, 72
Changes of the surface charge, 146
Change the excitability of cells, 277
Characterise nerve and muscle pathologies, 309
Characteristic time, 414, 497
Characteristic variables, 414
Charge, 278, 280
Charge accumulation, 148, 255, 281, 287, 305, 511
Charge-balance, 278
Charge-balanced biphasic current pulse, 272
Charge-balanced current pulses, 392
Charge-balanced pulse, 278, 279, 391, 393
Charge-balanced waveform, 251, 289
Charge-balancing phase, 278
Charge can be transferred, 274
Charge centers, 423
Charged at its inner boundaries, 116
Charged body is ungrounded, 362
Charged boundaries, 528
Charged cellular structures, 103
Charged conducting object is ungrounded, 362
Charged conducting objects, 147
Charged cornea, 16
Charged double layer, 500
Charged electrodes, 75, 87, 89–91, 464
Charged electrode surface, 429
Charge density, 91–93, 135, 175, 179, 185, 187–189, 390
Charge density and current density, 493
Charge density change, 187
Charge density limit, 391–393
Charge density Q/A, 393
Charged intracellular structures, 103
Charged ion, 419
Charged ions in electrolyte, 433
Charge dipole, 16, 17
Charged membrane-related structures, 104
Charged or discharged, 440
Charge double layer, 421, 425, 467
Charged structures, 75, 103
Charged substances, 432
Charged surfaces, 103, 104
Charge exchange, 452
Charge-free boundaries, 528
Charge levels, 313
Charge loading, 467
Charge monopol, 17
Charge movements, 133
Charge-neutral dissolved particles, 425
Charge neutrality, 275, 421, 423, 433
Charge-neutral non-polar and polar structures, 87, 88
Charge of stimulus, 279, 280
Charge of the central ion, 106
Charge per phase, 278, 314
Charge Q of the central ion, 433
Charge separation, 415, 441, 505
Charge size, 363
Charge spatial density, 434
Charges within the structure, 87
Charge transfer, 462, 470, 471, 491, 496, 499, 503, 505
Charge transfer across the boundary dominates, 489
Charge transfer back and forth, 477
Charge transfer is unconstrained, 462
Charge-transfer kinetics, 451
Charge-transfer-limited electrode reaction, 459, 468, 481, 483, 497–499, 509
Charge-transfer-limited reaction, 483
Charge transfer, mass diffusion, and coupled reactions, 462
Charge transfer overvoltage or activation overpotential, 448
Charge transfer processes, 477, 494, 505
Charge-transfer reaction, 499
Charge transfer remains constrained, 494

Charge transfer remains constricted, 488
Charge-transfer resistance R_{el}^{t}, 459, 470, 477, 496, 503
Charge transfer starts to dominate, 498
Charge transfer with the activation overvoltage $u_{pol,i}^{t} = u_{pol,i}^{l} - U_{pol}$, 451
Charge transfer under finite $U_{pol} \neq 0$, 472
Charge transport, 80
Charge transport and dipole reorientation, 127
Charge-unbalanced biphasic current pulse, 271
Charge-unbalanced pulses, 394
Charging, 464
Charging of interfaces, 111
Charging of the boundary, 278
Charging of the cell membrane capacitance, 113
Checkerboard pattern, 210
Chemical and electrical forces, 417
Chemical electrolytic reactions, 79
Chemical energy, 419
Chemical equilibrium, 414, 441
Chemical equilibrium can not be reached, 414
Chemical equilibrium state, 414
Chemical forces, 441
Chemical forces/interactions, 420
Chemical identity, 420
Chemically rough environment, 403
Chemical potential energy, 413
Chemical potential energy of electrons, 441
Chemical reactions, 427, 432
Chemical species, 439
Chest to both feet, 517
Children, 365, 371, 517
Chlorine-electrode, 444
Chronaxie, 280, 307, 372
Chronic electrical stimulation, 319
Chronic stimulations, 289, 300
Circumvent the inverse recruitment order, 318
Clinical neuromodulation, 339
Closed loop, 55, 266, 547
Closest node, 269
Closest node of Ranvier, 267
Closest to the stimulation electrode, 280, 326
Close to excitable structures, 314
Close to the electrode surface, 419, 430, 441
Close to the skin surface, 318
Close to the stimulation electrode, 281
Cloud of counterions, 109, 111, 420
Cloud of counterions becomes rearranged, 110
Cloud of ions, 106, 433
Cloud of space charge, 423
Clouds of counterions, 82
Cochlea potentials, 18
Cold environment, 347
Cole-Cole expression, 127
Collective effect, 380
Collision and friction, 359
Collision block, 271, 273, 283, 295, 296, 311, 323
Collisions decelerate, 109
Collisions of travelling ions, 79
Combined effects, 358
Comfortable level, 389
Common eye movements, 18
Common features of acoustic, optic, and electric biosignals, 171
Common ions, 445
Common-mode and differential-mode interferences, 542
Common-mode electromagnetic interference, 527
Common-mode gain, 533
Common-mode input-referred interference voltage, 527, 528, 540, 541, 545
Common-mode input-referred interference voltage u_{CI} with its amplitude U_{CI}, 533
Common-mode interference, 534, 538–541
Common-mode interference-related portion, 538
Common-mode interference voltage, 524, 533
Common-mode rejection ratio, 527
Common-mode voltage drop u_{CI} with respect to the amplifier's ground, 533
Compaction of electric field lines, 416
Compare external i_{DC} and i_{AC} applications, 488
Comparison between car and truck, 362
Complex amplitude, 59, 60, 63, 65, 95, 98, 205, 406, 408
Complex amplitude $\underline{I}_{AC}$, 475
Complex and frequency-dependent number $\underline{Z}_{el}^{d}$ for the alternating conductive $i_{AC,E}$, 479
Complex angles, 208
Complex diffusion impedance, 497
Complex electrode impedance, 502
Complex electrode impedance $\underline{Z}_{el}$, 488, 496
Complex form of Snell's refraction law, 208
Complex impedance, 59, 65, 68
Complex impedance due to inert coupled reactions, 497
Complex peak value, 43
Complex permittivity ε, 99, 124
Complex plane, 127, 498, 499
Complex plane as a Nyquist plot, 489
Complex plot, 480, 499, 509
Complex plot of the simplified boundary model of the charge-transfer-limited reaction, 500
Complex quantity, 32, 54

Complex structure and composition, 128
Complex-valued number, 43, 48, 205
Complex vector amplitudes, 128
Compressive loading, 18
Concentrated solutions, 502
Concentration, 419, 505
Concentration c_{oxi}, 477
Concentration c_{red}, 477
Concentration c of tissue cells, 510
Concentration c of 0.15 mol/l, 80
Concentration differences $(c^s - c^0)$ and $(c - c^0)$, 478
Concentration gradients, 79, 431, 432
Concentration of ions, 107, 424
Concentration of species, 462
Concentration of the electrolyte, 415
Concentration on the electrode surface, 478
Concentration overvoltage, 459
Concentrations c^s, 462
Concentrations of involved species, 452
Conceptual model of the grounded body, 139
Conceptual origin of the electric and magnetic fields, 52
Condition for extracellular activation, 263
Condition for normal components, 148
Condition for tangential components, 148
Conductance G, 254, 341
Conducting corners, points, and edges, 416
Conducting dermis, 410
Conducting electrode, 410
Conducting electrolyte, 407, 410
Conducting human body, 362
Conducting (metallic) electrode, 407
Conducting object, 164, 362, 364
Conducting object is grounded, 362
Conducting sharp corners, 138
Conducting subcorneal medium, 410
Conduction, 49
Conduction and dielectric spectrum, 101
Conduction block, 295
Conduction current, 64
Conduction current amplitude, 65
Conduction losses, 42
Conduction of the inner body heat to the body surface, 346
Conduction/propagation velocity, 273
Conduction velocities, 329
Conductive and dielectric body, 54, 59, 60
Conductive and dielectric losses, 98, 129
Conductive and dielectric phenomena, 173, 183, 185
Conductive and dielectric properties, 59, 65, 67, 98, 161, 229, 406
Conductive and displacement current, 239
Conductive and displacement current density, 60, 235
Conductive and displacement currents, 157, 183, 189, 348
Conductive and high-permeability shield, 541
Conductive behaviour, 20, 73, 131, 183, 186, 191, 257
Conductive blood insert, 237
Conductive body, 52, 54, 57, 59, 135, 136, 139, 152, 154, 158, 159, 178, 225, 226, 230, 234, 524
Conductive body insert, 228
Conductive body in the electric field, 137
Conductive body surface, 529
Conductive component, 65, 300
Conductive component $i_{AC,E}$ of the total i_{AC}, 482
Conductive condition, 184
Conductive coupling, 402
Conductive current, 75, 52, 54, 60, 61, 64, 84, 89, 95, 97, 112, 114, 135, 139, 146, 147, 160, 174–177, 184–186, 231, 233, 234, 245, 251, 341, 359, 407, 449, 467, 474, 501, 505, 510, 527, 528
Conductive current $i_{AC,E}$, 474
Conductive current i_{DC} enters the anode, 491
Conductive current component, 298, 305
Conductive current density, 61, 96, 136, 146, 175, 184, 225, 251
Conductive current density field, 172, 177, 237, 381
Conductive current density with the vector amplitude, 80
Conductive current entering or leaving a capacitor plate, 63
Conductive current $i_{AC,E}$ through the boundary, 480
Conductive current $i_{DC,E}$, 474
Conductive currents dominate, 226
Conductive effects, 96
Conductive electrode paste, 511
Conductive human body, 362, 512, 539, 545
Conductive human body—charged, 147
Conductive $i_{AC,E}$, 476, 477, 483, 488
Conductive $i_{AC,E}$ and displacement $i_{AC,C}$ pathways, 483
Conductive $i_{AC,E}$ pathway, 483
Conductive i_E, 254
Conductive impedance, 61, 65
Conductive impedance of the body, 228
Conductive insert, 237, 239
Conductive insets, 4, 155
Conductive inward transmembrane currents, 252

Conductive ionic current, 79
Conductive isolated body, 527
Conductive loops, 154, 529
Conductive losses, 99, 124, 341
Conductive mechanisms, 400
Conductive medium, 112
Conductive object, 367, 400
Conductive outward transmembrane currents, 252
Conductive pathway, 547
Conductive phenomena, 173, 175–177
Conductive properties prevail over dielectric, 230
Conductive regions, 154, 159
Conductive resistance, 407
Conductive screen/shield, 540
Conductive sensing, 402, 524
Conductive spherical body, 136
Conductive tissue, 75, 95, 96, 100, 152, 227, 407, 410
Conductive tissue section, 61, 77, 97
Conductivity, 21, 81, 96, 122, 381, 407
Conductivity γ_{eff} is relatively small, 109
Conductivity of the spheroid determines the size of the internal field, 148
Conductivity of the tissue/electrolyte, 451
Conductor, 70
Conductor and dielectric, 20
Conductor condition, 191
Configuration of electrodes, 386
Connected cables, 403
Connected in parallel, 500
Connection from the electrode to the preamplifier is very short, 542
Conservation of the electric current, 311
Conservative and unreliable exposure assessment, 360
Constancy of $u_{\text{pol,i}}$ and U_{pol}, 511
Constant, 91
Constant and time-varying electric fields, 386
Constant characteristics v, λ, and Z, 31
Constant charge, 546
Constant charge Q and $-Q$ on the respective electrode, 91
Constant current source, 449
Constant electric field, 261
Constant electric potential, 135
Constant exposure, 218
Constant hyperpolarization or depolarization, 295
Constantly moving body tissues, 390
Constant outer voltage, 178
Constant over time, 414
Constant P_{SAR}, 343
Constant phase element, 421, 479
Constant phase planes, 208
Constant plateau, 292
Constant stimuli, 244
Constant temperature, 135
Constrained charge transfer, 448, 470, 483
Constrained charge transfer and inert diffusion effects are additively separated, 460
Constrained chemical reactions, 448
Constrained for fast changes in $u_{\text{pol,i}}$, 463
Constricted charge transfer, 487, 488
Constructive interference, 199, 360
Constructive interference lowering the excitation threshold, 292
Constructive superposition, 210, 333
Contact area, 367, 383, 515, 517–519, 544
Contact-based approach, 400
Contact-based coupling, 10, 26, 49, 240, 383
Contact coupling, 405
Contact current, 147, 234, 235, 240, 355, 356, 361–363, 370, 373, 380, 394, 400
Contact currents and contact voltages, 353
Contact electrification, 543
Contact electrodes, the polarization voltages $u_{\text{pol,i}}$ and $u'_{\text{pol,i}}$, 495
Contact electrodes, 402, 403, 495, 512, 524
Contact galvanic electrodes, 545
Contact impedance, 25, 363
Contact-less approach, 400
Contact-less coupling, 26, 27, 49, 240, 242, 243, 352, 383
Contact-less transmission line, 154
Contact-less way, 51
Contact/surface area A, 502
Contact surface size, 545
Contact voltage, 370, 376, 410, 514, 544
Contact voltage drop, 511
Contact with live parts or live electrodes, 517
Contaminate biological tissue, 443
Contaminate tissue, 432
Content of tissue water, 119
Continuity of the electric field, 148
Continuity requirement, 204
Continuous direct current, 245
Continuous exposure, 350
Continuous high frequency current, 245
Continuous in its time course, 466
Continuous redistribution of charges, 146
Continuous sinusoidal stimulus, 303
Contractions of muscles, 372
Contrasts in electric properties, 25
Contrast to a stickman representation of the body, 533
Contrast to isolated electrodes, 91

Contributing factors, 367
Contribution of this Skin impedance to Z_{wb}, 515
Controlled environments, 358
Controlled number of excited fibers, 319
Control of the delivered stimulus charge, 319
Control the recruited volume, 332
Convection, 432, 449
Convection/stirring, 479
Convective diffusion, 481
Conventional heating, 347
Converges to a plane wave, 41
Converges towards the body impedance, 515
Converges towards the inner body impedance $\underline{Z}_b$, 518
Conversion of the coupled biosignal, 399
Coordinated excitation and contraction of ventricles, 374
Core body temperature, 345–347
Cornea, 16
Corneal capacitor, 407
Corneum layer, 407
Corrosion of the electrode, 493
Cortical neurons, 15
Cotton, 546
Counteracting inner field, 149
Counteracting mechanisms, 243
Counter-charge, 411, 468, 483, 511
Counter-charge close to the metal surface, 467
Counterion layer, 106, 421, 468
Counterion polarization, 103, 104, 120, 132
Counterions, 415, 416, 423, 425, 430, 432, 433
Counterions (anions), 415
Counterions are rigidly held, 423
Counterions do not accumulate, 474
Counterions individually surrounded, 464
Counterions will redistribute, 106
Counter measure, 278, 535
Coupled, 6, 29
Coupled currents, 537
Coupled fields, 357
Coupled reactions, 461, 496, 497
Coupled reactions with the reaction overvoltage $u^{c}_{pol,i} = u^{3}_{pol,i} - U_{pol}$, 451
Coupling, 3, 4, 6, 9, 240
Coupling and joint propagation, 36
Coupling capacitance, 513
Coupling capacitors, 502
Coupling effects, 357
Coupling efficiency, 383
Coupling impedance, 528
Coupling mechanisms, 49, 240, 353
Coupling of any interference/noise, 512
Coupling of biosignals, 399, 404, 512, 531
Coupling of electric biosignals, 399
Coupling of electromagnetic energy, 165
Coupling of energy, 360
Coupling of the outer field, 240
Coupling of therapeutic fields into the bodily tissue, 495
Created and destructed, 111
Created by conductive currents, 175
Creation and destruction of its ionic cloud, 110
Critical mass of the heart, 306
Crossing outwards the membrane, 260
Cross-section area, 52, 65, 115, 146, 152, 383
Cross-section surface, 52, 53, 63, 66
Crucial physical quantities, 354
Curls of the electric field, 55
Current, 26, 61, 143, 220, 404, 527
Current amplitude I, 146, 280, 281, 319, 340
Current-bearing power lines, 529
Current between electrodes, 464
Current brands, 384
Current ceases, 338
Current densities above 1000 mA/m^2, 386
Current densities are different, 279
Current density, 48, 139, 142, 161, 229, 234, 246, 260, 332, 343, 356, 359, 363, 377, 383, 384, 451
Current density distribution, 487
Current density field, 138, 244, 250, 405
Current density magnitudes, 65
Current dipole is non-zero, 13
Current dipole is zero, 13
Current dipole vector, 12, 13
Current-distance relationship, 319, 321
Current distribution, 140, 307
Current divider, 179, 528
Current electrode, 5, 21, 235, 263, 313
Current flow, 139, 401
Current flowing through the limbs, 355
Current flow is not homogeneous, 53
Current frequency, 366, 371
Current i_C though C_{el} must be zero, 497
Current i_{DC}, 462
Current i_{DC} decreases during oxidation, 460
Currentless, 135
Currentless and conductive body, 136
Currentless case, 439
Currentless case with $i = 0$, 496
Currentless conductive body, 133
Currentless conductive tissue, 92, 97
Currentless conductor, 133
Currentless situation, 411, 414, 417, 421, 436, 442, 443, 445, 452
Currentless state, 451
Current level, 383

Current-limiting barrier, 370
Current-limiting resistor, 542
Current pathway, 370, 377
Current pattern, 155
Current point source, 263, 264, 315, 319, 321, 328, 330, 334
Current pulse, 322, 375
Current reversal, 287, 316
Currents i_{l-b} and i_{l-e}, 541
Currents i_{l-e}, 528
Current sensing metal electrode, 235
Current sink, 254, 309, 314
Currents leakage, 307
Current source, 25, 253, 309, 497, 523
Current spreads, 363
Current strength, 314, 367, 375
Current threshold, 289, 291, 328, 330
Current threshold amplitude, 286
Current-voltage diagram, 370, 376
Current waveform is not important, 280
Curved implants, 353
Cut-off frequency, 546
Cut-off frequency of the total measurement system, 546

D

$d^2\varphi_e/dx^2$ is the forcing function, 265
Damage biological tissues, 340
Damaging to tissue, 493
Damped harmonic waves, 43
Damage tissue, 388
Damage tissue and fibers, 315
Damage to tissue and/or electrode material, 494
Deadsorption, 492
Debye expression, 125, 128
Debye-Falkenhagen effect, 107, 110
Debye length, 421, 424, 434, 466
Decay of instantaneous amplitudes, 41
Decomposed, 490
Decomposition of AgCl, 490
Decomposition of water molecules H_2O, 492
Decomposition voltage, 465, 470, 491
Decoupled, 29
Decoupled fields, 74
Decrease $\Delta\varepsilon$ is very large, 130
Decrease Δi_{DC} in i_{DC} due to inert diffusion, 460
Decreased ability to polarize, 430
Decreased capacitive impedance, 539
Decreased electrode impedance, 539
Decreased excitability of the cell, 243
Decrease for large electrodes, 501
Decrease with increasing f, 467
Decreasing exposure duration, 378
Decreasing interphase interval, 286
Decreasing stimulation frequency, 391
Decreasing tissue sample conductivity, 510
Decreasing wavelength, 162
Decreasing with frequency, 63
Deep heating, 165, 349, 350, 359
Deep penetration, 46, 358
Deep-seated electrodes, 402
Defibrillation, 373, 374, 513
Defibrillation shock, 375
Defibrillators, 389
Defined concentration, 442
Defined concentration of the anion Cl, 444
Deflated lungs, 70
Degrade $\underline{Z}_{com}$, 540
Degree of coverage, 426
Degree of perturbation, 359
Delay is maximal, 283
Delineation frequency, 241
Delta dispersion, 118
Denature proteins, 364
Dendrites, 15
Denervated muscle, 309
Denervated muscle fibers, 308
Dense vascular network, 346
Departing cathodic currents, 257
Depends also on f of u_{AC}, 468
Depends on the applied voltage $u_{pol,i}$, 468
Depends strongly on the oscillatory frequency, 85
Depleted inside from charges, 421
Depolarization, 12, 243, 247, 252, 254–256, 264, 266, 270, 271, 280, 284, 298, 301, 311, 313, 319, 328, 336, 339
Depolarization and hyperpolarization, 313
Depolarization close to excitation, 292
Depolarization of membranes, 243
Depolarization of the axon, 311
Depolarization or hyperpolarization, 266
Depolarization rate, 267, 317
Depolarize and excite the fiber, 284
Depolarize and hyperpolarize, 261
Depolarized, 261, 311
Depolarized membrane region, 257, 316
Depolarized region, 257
Depolarizing, 280, 285
Depolarizing bias voltage, 292
Depolarizing cathodic phase, 285
Depolarizing cathodic stimulus, 316
Depolarizing component, 298
Depolarizing current, 338
Depolarizing effect, 284
Depolarizing half-period, 245, 281, 293
Depolarizing inflow of Na^+ ions, 316
Depolarizing maximum, 335

Depolarizing monophasic pulse, 287
Depolarizing phase, 278, 280, 293
Depolarizing phase needs less charge, 286
Depolarizing phase of biphasic pulse, 287
Depolarizing stimuli, 254
Deposited energy, 70
Deposited (induced) power, 156
Deposit electromagnetic energy, 358
Deposition, 457
Deposition of Ag^+ ions, 444
Deprivation of oxygen, 374
Derivation, 298
Derivatives of fields act as sources, 162
Derived ratio, 66
Dermis, 407
Design of this boundary, 546
Destructive interference, 199, 284, 285, 287, 292, 360
Destructively interferes, 541
Destructive superposition, 210, 333
Determining τ, 299
Detrimental health effects, 349
Diagnosis, 1, 71
Diagnostic aims, 405
Diagnostic and passive recording of voltages, 495
Diagnostic and therapeutic applications, 417, 502
Diagnostic approach, 519
Diagnostic current *i*, 495
Diagnostic device, 502, 521
Diagnostic errors, 542
Diagnostic generation, 399
Diagnostic or therapeutic system, 496
Diagnostic outcome, 495
Diagnostic purposes, 399
Diagnostic sensing, 399, 400
Diagonal line, 480
Diameter, 261
Diameter of the ionic atmosphere, 107
Diameter of the ionic cloud or atmosphere, 108
Diameter R_{el}^{t}, 499
Dictate pathways of the local current density, 60
Dictates the current, 60
Dielectric, 66, 99, 203
Dielectric and conductive tissues slow down propagating waves, 34
Dielectric behaviour, 70, 131, 183, 186, 191, 258
Dielectric body, 54, 62, 228
Dielectric losses, 42, 99, 121, 124, 125, 127, 129
Dielectric losses are absent, 122
Dielectric losses are present, 122
Dielectric non-conductive space, 64
Dielectric permittivity, 34, 60, 70, 92, 128, 174, 203
Dielectric phenomena, 180, 182
Dielectric polarization, 65
Dielectric processes, 128
Dielectric properties of the double layer, 429
Dielectric regions, 159
Dielectrics, 85
Dielectric saturation, 120
Dielectric tissue, 37, 100, 152, 229
Dielectric tissue section, 63
Differential biomedical amplifier, 524
Differential diffusion impedance $\underline{Z}_{el}^{d}$, 479
Differential electrode resistance, 449
Differential electrode resistance due to inert diffusion, 479
Differential electrode resistance R_{el}^{c}, 449
Differential electrode resistance $R_{el} = 0$, 463
Differential electrode resistance R_{el}^{t}, 448, 470
Differential equation, 65, 344
Differential gain, 533, 540
Differential input-referred interference voltage, 534
Differential in the solute-concentrations, 413
Differential-mode biosignal voltage, 533
Differential-mode electromagnetic interference, 528
Differential-mode impedance, 527
Differential-mode input-referred interference voltage, 528, 529, 536
Differential-mode interference, 538–540, 543
Differential-mode interference-related portion, 538
Differential-mode interference voltage, 524
Differential picture, 12, 13
Differential resistances R_{el}^{t}, R_{el}^{d}, and R_{el}^{c}, 449
Differential voltage, 524
Differential voltage contribution, 536, 543
Different instants of time, 210
Different kinetics, 275
Different layers of the skin, 515
Different magnitudes, 173
Different media, 201
Different orientations of the body, 153
Different oscillation frequencies, 509
Different percentiles in men, 371
Different perception levels, 365
Different rates, 414
Different regions, 261
Different relaxation time constant, 127
Different strengths, 216
Different thresholds, 370

Different time delays, 314
Different time instants, 215
Differing conductivity of the membrane, 292
Diffracting elements, 360
Diffraction, 49, 171, 197, 199, 200
Diffraction of electromagnetic waves, 195
Diffraction pattern, 199
Diffuse along their concentration gradient, 431
Diffuse distribution of extracellular potentials, 308
Diffuse heating, 46
Diffuse layer, 423–425, 429, 432, 433
Diffuse layer d_d, 460
Diffuse spatial information, 15
Diffusing reactants, 480
Diffusion, 289, 431, 449, 498
Diffusional force, 458
Diffusional processes, 468, 477
Diffusion-based transport, 448, 452, 463, 475

Diffusion coefficient, 478
Diffusion component, proportional to dc/dx, 458
Diffusion current density, 458, 461
Diffusion impedance $\underline{Z}_{el}^{d}$, 475
Diffusion-independent case, 459
Diffusion inhibits progressively less and less, 489
Diffusion is assumed to disappear, 489
Diffusion is inert, 458
Diffusion layer, 479
Diffusion layer is typically bounded, 481
Diffusion layer (or Nernst diffusion layer), 460
Diffusion layer (the diffusion layer thickness $\delta_D^T \rightarrow \infty$, 498
Diffusion-limited electrode reaction, 458, 477–479, 483, 497–499, 509
Diffusion-limited electrode reaction at no or weak convection, 481
Diffusion-limited electrode reaction (with a large R_{el}^{i} or small $|u_{pol,i} - U_{pol}|$, 459
Diffusion-limited reaction, 480, 482, 483, 497
Diffusion of a substance, 431
Diffusion overvoltage, 448, 459, 461, 462
Diffusion overvoltage is frequency-dependent, 480
Diffusion process, 463
Diffusion resistance, 449, 479, 496
Diffusion resistance R_{el}^{d}, 458, 470
Diffusion tends to decrease i_{DC}, 458
Diffusion overvoltage $(u_{pol,i} - U_{pol})$, 459, 479
Diffusion overvoltage $u_{pol,i}^{d} = (u_{pol,i}^{2} - U_{pol})$, 482
Diffusion overvoltage $u_{pol,i}^{d} = (u_{pol,i} - U_{pol})$, 481
Diffusion voltage, 431
Diffusion with the diffusion overvoltage $u_{pol,i}^{d} = u_{pol,i}^{2} - U_{pol}$, 451
Diluted electrolytes, 420, 424
Diluted solutions, 434
Dimensions of the biological body, 74
Dimensions of the body, 160
Dimensions of the exposed body, 160
Dipolar behaviour, 17
Dipolar dielectric losses, 341
Dipolar effects, 83
Dipolar losses, 83, 121
Dipolar losses disappear, 122
Dipolar losses within tissue water, 122
Dipolar model, 17
Dipolar relaxation, 117, 119, 120, 128
Dipole electrode, 332, 334
Dipole inertness, 121
Dipole rotation, 359
Direct u_{DC}/i_{DC}, 500
Direct and alternating voltage/current, 496
Direct and alternating voltage/current application, 496
Direct and instantaneous coupling between $u_{pol,i}$ and the concentration c^s, 480
Direct bias currents, 513
Direct contact, 364, 524
Direct contact with the electrode surface, 425
Direct contact with the skin, 511
Direct coupling, 240, 348, 352, 400
Direct current, 79, 245, 277, 278, 304, 336–339, 391, 445
Direct current i_{DC}, 474
Direct current i_{DC} with $f = 0$, 479
Direct current circuit, 447
Direct current component $(c_1 \bullet c_2)/2$, 485
Direct-current conductivity, 74
Direct current density, 472
Direct current impedance, 403
Direct currents, 25, 339, 378
Direct currents above 500 mA, 378
Direct electric field, 110, 338, 472
Direction, 379, 425
Directional change of the electric field, 231
Directional difference, 73
Direction of the induced conductive currents, 157
Direction of the ionic drift, 78
Direction of the refraction, 208
Direction of the surface normal, 208
Direction of wave propagation, 40

Direction x of the axon, 265
Directly into the heart, 376
Direct voltage, 476
Direct voltage behaviour, 477
Direct voltage/current application, 445
Direct voltage/current u_{DC}/i_{DC} application, 496
Direct voltage u_{DC}, 450
Direct voltage u_{DC} across both electrodes, 445
Disadvantages of capacitive coupling, 524
Discharge, 380
Discharge current, 381, 513
Discharged through physical contact, 147
Discharge path, 546
Discharge process, 494
Discharges quickly, 545
Discharge time constant, 544, 546
Discharge via currents, 378
Discharging of the boundary, 278
Disconnected right-leg electrode, 545
Discontinuity, 230
Discontinuity of the electric field, 149
Discrete channels, 410, 515
Diseased heart, 374
Disorientation angle, 54, 56
Dispersed and widened, 228
Dispersion, 66, 75, 124
Dispersion, charge and current induction, electromagnetic induction, 49
Dispersion-dependent increase, 130
Dispersion dissipates, 121
Dispersion mechanism, 66, 68, 79, 117
Dispersion of conduction, 101
Dispersion of polarization, 101
Dispersion phenomena, 60
Dispersion phenomena are disregarded, 68
Dispersion regions, 131
Dispersive dielectric permittivity, 59
Dispersive electrical properties, 54
Dispersive function, 68
Dispersive properties, 61, 63
Dispersive region, 239
Dispersive τ, 68
Displaced towards the boundary of the (predominantly) conductive tissue, 158
Displacement angle, 90
Displacement current $i_{AC,C}$, 474
Displacement i_{AC} current, 467
Displacement $i_{AC,C}$, 475, 483
Displacement i_C, 254
Displacement component, 65, 300
Displacement component $i_{AC,C}$, 482
Displacement current, 19, 22, 27, 54, 59, 62–64, 97, 114, 124, 129, 139, 140, 147, 160, 174, 175, 180, 184, 186, 188, 233, 234, 245, 247, 256, 258, 341, 403, 407, 464, 501, 504, 524, 527, 528, 533, 537, 542
Displacement current amplitude, 65
Displacement current component, 298, 305
Displacement current density, 64, 97, 180, 184, 228
Displacement current density field, 182, 188
Displacement currents i_{l-b} and i_{l-e} in the air, 528
Displacement dispersion, 89, 123
Displacement magnitudes, 123
Displacement phenomena, 173
Displacement polarization, 122
Displacement relaxation, 123
Disproportionately smaller increase, 345
Disrupted equilibrium, 467
Disruption of cells, 72
Dissipated energy, 121
Dissipated power, 179
Dissociated ions concentration, 81
Dissociation, 449
Dissociation/association reaction, 442
Dissociation of NaCl, 86
Dissociation reaction, 82, 444
Dissociation speed (or solubility) of AgCl decreases, 445
Dissolution of Pt, 494
Dissolution of the metal, 493
Dissolved Ag^+ ions, 444
Dissolved at positive potentials, 457
Dissolved Cl^- ions, 444
Dissolved ions, 431
Distance, 3, 281, 308, 314, 316, 356, 547
Distance between electrodes, 26
Distance d between plates, 63
Distance d between the electrodes, 508
Distance from the metal surface, 423
Distance of the electrode, 307
Distance of this fiber from the electrode, 307
Distance r from the source to the onset of far field, 30
Distance to the power line, 139
Distance x, 156
Distance y, 321, 330
Distance y between the fiber and electrode, 266
Distance y to an axon, 336
Distant contact electrode, 404
Distant electrode, 336
Distant fibers, 281, 286, 287
Distant non-contact electrodes, 19
Distorts the ambient electric field, 528
Distributed capacitance, 540

Distribute regionally, 135
Distribution of cations and anions, 78
Distribution of charges, 146
Distribution of electric currents, 186
Distribution of induced fields and currents, 359
Distribution of ionic counter-charges, 511, 512
Distribution of P_{SAR}, 169, 213
Distribution of the conductive current density, 143, 373
Distribution of the tissue conductivity, 143
Distribution of transmembrane currents, 308
Distribution parameter, 127
Disturbance of counter-charges, 511
Disturbed symmetry of the body/amplifier interface, 537
Diverse interactions with tissue, 150
Dominance of conductance, 233
Dominance of dielectric properties, 233
Dominant conductor, 191
Dominant dielectric, 191
Dominant effect, 118
Dominant metal dissolution/oxidation (at the anode) or dominant metal deposition/reduction (at the cathode), 457
Dominant oxidation, 452, 459
Dominant oxidation only (at anode), 459
Dominant reduction, 452
Dominant reduction only (at cathode), 459
Donating or accepting electrons, 440
Double firing, 282
Double layer, 401, 421, 423, 424, 429, 430, 432, 501, 503
Double layer at the electrode surface, 441
Double layer capacitance, 391
Double layer capacitance C_{el}, 497
Double-layer capacitive impedance, 508
Double layer capacitor, 474
Doubling the distance, 330
Drift velocity, 77–79
Driven-right-leg circuit, 541, 542, 545
Driven-right-leg circuit lowers significantly u_{CI}, 541
Drive the amplifier to its saturation, 513
Driving force, 251, 262
Driving osmotic pressure, 413, 416
Driving voltage, 362, 363
Dry electrodes, 402
Dry skin, 515, 517
Due to coupled reactions, 508
Duration of a cathodic current impulse, 315
Duration of action impulses, 282
Duration of the depolarizing half-period, 246
Duration of the depolarizing phase, 293
Duration of the monophasic current stimulus, 281
Duration of the stimulus pulse, 275
Durations of less than 100 ms, 378
During a single phase, 279
During the stimulus, 284
Duty cycle, 241, 389
Dying tissue, 72
Dynamic, 24
Dynamic and peaks, 383
Dynamic behaviour of the counterions cloud, 425
Dynamic behaviour of the electrode/tissue boundary, 473
Dynamic change, 244
Dynamic equilibrium, 414, 415, 439, 443
Dynamic in the stimulus, 336
Dynamic properties, 21
Dynamic response, 100
Dynamics, 246
Dynamics of electro-kinetic processes, 475, 477, 488

E

Each and every ion, 106
Each space point of tissue, 60
E and B doubles, 40
Early phase of atrial or ventricular recovery, 306, 375
Easy stimulation of thick fibers, 317
$\vec{E}$ and $\vec{B}$ become coupled, 29
Eddy currents, 48, 152
Eddy electric field, The, 160
Eddy fields, 239
Edges of the beam, 200
Effective amplitude, 521
Effective area, 143
Effective conductivity, 34, 36, 42, 70, 74, 82, 83, 98, 99, 101, 111, 128, 129, 131, 142, 158, 191, 193, 205, 341
Effective current amplitude I, 519
Effective current pathway, 377
Effective diameter of its ionic cloud, 110
Effective differential resistance $R_b \approx \Delta u_{DC}/\Delta i_{DC}$ ($\gg R'_{el}$), 491
Effective electric field, 133, 148, 159
Effective field, 210, 211
Effective height, 142
Effective input impedance of the amplifier, 540
Effective level of U_{dec}, 470
Effectively disappear, 271
Effective permittivity of the double layer, 429

Effective radius, 77, 78, 119, 423, 428
Effective stimulation time constant, 307
Effective thickness δ_D, 460
Effective thickness $\delta_D (< \delta_D^T)$, 478
Effective value, 242, 341
Effective value of C_{el} tends to increase with decreasing f, 483
Effective value of the exposure, 241
Effective value of Z_{wb}, 518
Effects have their own thresholds, 382
Effects of the typical unbalance $Z_{el} \neq Z'_{el}$, 527
Efficiency of the diagnostic device, 519
Efficient excitation, 275, 286
Electrochemically safe limit, 391
Energy absorption, 169
Electrical accident, 514
Elastically bound, 89
Electrical behaviour of the skin, 407
Electrical boundary, 225, 230
Electrical circuit, 338
Electrical circuit model, 3, 6, 249, 297
Electrical conduction, 65, 135, 174, 176, 297
Electrical conductor, 60
Electrical current density, 458
Electrical discharge, 513
Electrical double layer, 421, 425, 502, 504, 544
Electrical driving force, 416
Electrical energy of stimulus, 340
Electrical equivalent circuit model, 29, 115, 407, 451, 482, 496, 497, 509
Electrical excitation, 7, 10, 13, 14, 242, 340, 374
Electrical field plethysmography, 4, 19
Electrical force, 458
Electrically exited heart, 10
Electrically-neutral non-interacting and dissolved substances, 419
Electrically slow medium, 41
Electrical model of the skin, 408
Electrical point effect, 135, 136, 138, 155, 159, 192, 195, 220, 221, 224, 226–228, 234, 239, 359, 360, 378, 393, 405, 415, 487
Electrical polarization, 245
Electrical potential energy, 414
Electrical properties, 42, 45, 49, 71, 73, 82, 144, 225, 230, 264
Electrical stimulation, 9, 240, 242, 243, 267, 374
Electric and/or magnetic field, 49, 74, 359
Electric and current density fields, 15, 16, 163, 241, 243, 400, 405
Electric and magnetic properties, 33
Electric biosignals, 1, 547
Electric breakdown, 515
Electric charge Q, 51, 55, 75, 174, 280, 340, 467, 468, 504
Electric conduction, 100
Electric consequences, 152
Electric current density, 152, 187
Electric currents, 51, 152, 360, 440, 453
Electric diffusion potentials, 431
Electric dipole, 88, 90, 92, 106, 422, 429
Electric displacement field, 93
Electric field and magnetic field, 10, 28, 48–51, 54, 60, 74, 75, 79, 80, 91, 96, 106, 108, 122, 133, 135, 136, 138, 142, 145, 150, 152, 158, 161, 162, 165, 171, 172, 174, 182, 187, 190, 194, 200, 201, 220, 226, 228, 229, 231, 233–235, 237, 244, 251, 261, 353, 356–358, 360, 362, 379, 385, 388, 405, 407, 416, 417, 430, 441, 458, 464, 490, 527, 539
Electric field effects, 379
Electric field lines, 136, 137, 235
Electric fields in peripheral sites, 383
Electric field within the body, 226–229
Electric field within tissue, 91, 96
Electric flux, 175, 178, 179
Electric flux density, 91, 93, 122, 125, 172, 174, 176, 177, 184, 187
Electric or magnetic far field, 360
Electric or magnetic near field, 360
Electric polarization, 100, 406
Electric polarization density, 92, 97
Electric potential $\varphi_{M,i}$, 15, 16, 18, 135, 220, 235, 264, 362, 363, 413, 432, 451, 453, 454, 466, 504, 505, 540
Electric potential sensors, 19
Electric source, 28
Electric stray field, 63, 78, 86, 106, 415, 419, 433
Electric susceptibility, 93
Electroactive particles, 477
Electrobiological interactions, 344
Electrocardiogram, 3, 4, 10, 11, 13
Electrochemical and metabolic stress, 390
Electrochemical damage, 392
Electrochemical driving force, 316
Electrochemical electrode reactions, 391
Electrochemical equilibrium, 277, 414–417, 439, 441, 443, 445, 446, 452, 453, 457, 467, 478, 503, 505, 511
Electrochemical interactions, 431
Electrochemical potential, 414, 544
Electrochemical potential energy, 413
Electrochemical processes, 463

Electrochemical reaction, 275, 277, 278, 391, 393, 402, 501
Electrochemical reactivity, 419
Electrochemical safety, 393
Electrochemical stress, 388, 390, 391, 393, 394, 405
Electrode's distance, 269
Electrode's geometry, 393
Electrode's motions, 512
Electrode's orientation, 538
Electrode/electrolyte boundary, 391, 440, 447, 479, 496, 502
Electrode/electrolyte interface, 250, 406, 413, 454
Electrode/redox reaction, 453, 471, 477, 503, 505
Electrode/tissue boundary, 235, 399, 401, 464, 471, 473, 475, 483, 497, 508, 545, 546
Electrode/tissue boundary with its $|\underline{Z}_{el}|$ ($\ll R_b$), 476
Electrode/tissue interfaces, 507, 521
Electrode, 10, 16, 91, 390, 393, 399, 401, 406, 414, 415, 426, 440, 466, 496, 511
Electrode axis, 12
Electrode charge, 93, 94
Electrode chemical reaction, 505
Electrode condition, 402
Electrode-cornea line, 17
Electrode current, 266, 316, 412
Electrode distance, 317, 319, 334
Electrode donating electrons, 440
Electrode electric potential, 504
Electrode exchanges charges, 401
Electrode gel, 445, 496, 499, 500, 507
Electrode impedance Z_{el}, 402, 403, 412, 483, 485, 497, 501, 507, 508, 514, 521, 524, 531, 532, 536, 543
Electrode leads, 528, 529, 539, 540
Electrode location, 393
Electrode material, 388, 390, 494, 507
Electrode paste, 412, 511
Electrode polarization, 411, 412, 442, 467, 507, 508, 510
Electrode positons, 264
Electrode reaction, 287, 415, 458, 473, 488, 491, 495, 496
Electrode reactions to the total i_{DC}, 495
Electrode resistance, 476, 489, 503, 505
Electrode resistance $R_{el} \approx R_{el}^{t} + R_{el}^{c} + R_{el}^{d}$, 476
Electrode shape, 266
Electrode sites or target organs, 406
Electrode size, 332
Electrodes of the first type, 442
Electrodes of the second type, 432, 442, 443
Electrodes rises, 501
Electrode surface, 339, 416, 429–431, 440, 441, 451, 452, 454, 457, 462, 478, 479, 487, 499, 505, 511
Electrode surface area A, 390, 501
Electrodynamic forces, 162
Electroencephalogram, 14, 15
Electrohysterogram, 14
Electro-kinetic processes, 447, 449, 450, 462, 463, 473, 474, 483, 496
Electrolyte, 81, 407, 412, 413, 452, 458, 467, 471, 511
Electrolyte concentration, 81
Electrolyte layer, 412
Electrolyte section, 61
Electrolytic cell or galvanic cell, 453–455
Electrolytic double layer, 104, 466, 468
Electrolytic effects, 25, 339
Electrolytic or galvanic reaction, 471, 473, 474, 504
Electrolytic saturated solution, 443
Electromagnetically-induced displacement currents, 161
Electromagnetically-induced electric field, 159
Electromagnetic exposure, 347
Electromagnetic field, 29, 162, 163, 171, 201, 240, 351, 362
Electromagnetic induction, 55, 75, 150, 161, 251, 356, 366, 379, 529
Electromagnetic stimulation, 379
Electromagnetic wave, 29, 32, 36, 37, 42, 162, 170, 171, 201
Electromyogram, 3, 13
Electromyography, 2
Electronegative oxygen atoms, 85
Electroneural anatomy, 393
Electronic bilayers, 103, 112
Electronic current, 401
Electronic or atomic polarization, 122
Electrons, 415, 440, 454, 490, 491, 503
Electrons transfer, 454
Electrooculogram, 16, 17
Electroporation, 256
Electropositive hydrogen atoms, 86
Electrostatic, 55
Electrostatically bound, 106, 110
Electrostatic and thermal forces, 433
Electrostatic attraction, 422, 426
Electrostatic conditions, 55
Electrostatic dragging force, 75, 77
Electrostatic driving force, 466, 467
Electrostatic effect of the central ion, 435

Electrostatic forces, 81, 106, 415, 420, 433, 441
Electrostatic induction, 75, 133, 255, 356
Electrostatic inter-ionic interactions, 87, 106, 128, 419, 426, 433
Electrostatic or quasi-electrostatic conditions, 55, 57
Electrostatic reactions, 501
Electrostatic voltage, 544, 545
Electrostriction, 430
Eliminate the differential-mode and common-mode interferences, 542
Elongated body, 148, 149, 165, 220, 221, 224
Elongated cells, 259
Elongated muscle bundles or nerve fibers, 73
Elongated pulse trains, 294
Elongation, 430
Emit time-varying magnetic field, 529
Empirical time constant, 292, 306, 394
Enclosed by its cloud of ions, 434
End mode and bend mode, 261, 253, 263, 288, 308, 313
End of expiration, 6
End of inspiration, 6
Endogenous current density fields, 383, 386
Endogenous electric fields, 382, 386
Endogenous electric sources, 3, 15, 28
End value, 409
Energetically optimal distribution of counterions around a central ion, 433
Energetically optimal near-order, 106
Energetically unconstrained, 505
Energized or charged conductive objects, 362
Energy, 375
Energy absorption, 163, 165, 169
Energy absorption decreases with increasing frequency, 170
Energy absorption rate P_{SAR}, 354, 387
Energy coupling and data exchange, 154
Energy density per single pulse, 351
Energy deposition and heat generation, 348, 357
Energy dissipated, 124
Energy flow, 39
Energy levels, 352
Engineering controls, 358
Engineering perspective, 287
Enhanced recruitment, 289
Entering inwards more distant axon's regions, 311
Enters an exposed biological body, 171
Enters perpendicularly, 177
Entire voltage, 258
Envelope of the standing wave, 216
Environmental conditions, 347
Epidermis, 407
Epileptic seizures, 15
E-polarization, 165, 167, 168, 170
Equal concentrations c^s, 451, 457
Equal excitation thresholds, 288
Equal in their respective magnitudes, 67
Equal in their size, 528
Equalizing currents, 3, 10, 13–15, 253
Equal rates, 414
Equal rates of metal dissolution (or metal oxidation), 457
Equilibrium, 109, 414, 416, 443, 445, 505
Equilibrium voltage, 316
Equipotential surfaces, 10, 14, 136, 222, 228, 229, 234
Equivalent circuit models, 472, 475, 476
Erythrocytes, 113
Establish a cloud with predominant counterions, 434
Estimated depth δ, 158
Estimated out of tabulated U_h, 437
Estimate P_{SAR}, 340
Estimate the bodily tissue impedance, 507, 508
Estimate the level of the resistance R and capacitance C, 67
Estimate the risk, 377
Estimation of the resulting temperature change $\Delta\vartheta$, 343
Every spatial point within the conductive body, 57
Example of specific adsorption, 426
Excess charge, 62, 277
Excess charges in the double layer, 435
Excessive heating, 357
Excess of positive nucleus charge, 414
Excess polarization, 277
Excess polarization charges Q_p and $-Q_p$, 91
Excess positive charge, 91
Exchange current density, 470, 472, 492, 502, 505
Exchange current i_0, 495
Exchange of the net charge, 471
Excitability, 154, 306
Excitability-related effects, 339
Excitable cells, 243, 245, 250, 254, 338, 339, 373, 382
Excitable structures, 263
Excitation and breakdown, 7, 251, 252, 256, 257, 259, 298, 319, 321
Excitation condition, 300
Excitation of a fiber, 285, 306
Excitation probability, 317, 319
Excitation propagation, 372

Excitation-related quantities, 247
Excitation threshold, 154, 267, 281, 285, 289, 293, 298
Excitation thresholds of nerves and muscles, 12, 154
Excitation wave, 374
Excitatory, 245
Excitatory threshold charge, 279, 281
Excited at once, 373
Excited in greater distances, 320
Excited region, 10
Exclude, 358
Existence of φ field, 55
Experimental P_{SAR} estimation, 343
Experimental and clinical systems, 24
Experimental assessment, 441
Experimental conditions, 302
Experimental current thresholds for physiological effects, 368
Experimental data, 130, 300, 306, 356, 516, 517
Experimental estimation, 509
Experimental fibrillation risk, 377
Experimental measurements, 355, 508
Experimental point of view, 128
Experimental set-up, 263, 267, 302
Experimental value, 132
Expiration, 22
Exponential anodic phase, 287
Exponential changes in the local charges, 135
Exponential damping, 217
Exponential decay, 41, 44, 45, 158, 215, 287
Exponential factor, 394
Exponential falling phase, 315
Exponential fashion, 48
Exponential fit, 300, 306
Exponential function, 100
Exponential function of $(u_{pol,i} - U_{pol})$, 451
Exponential increase
Exponential increase of ϑ, 344
Exponential increase or decrease, 125, 284, 283, 345
Exponentially decreasing currents, 135
Exponential part of the potential φ change, 433
Exposed biological tissue, 49
Exposed body, 356, 359
Exposed tissue section, 49
Exposure conditions and assessment, 354, 359
Exposure duration, 367, 368, 372, 375, 376
Exposure guidelines, 161, 384
Exposure limits, 49, 349, 353, 516
Exposure restrictions, 358
Exposure situation, 356
Exposure time, 369
Extent of depolarization or hyperpolarization, 266
External application of the alternating voltage u_{AC}, 473
External current, 266
External E_{ext}, 257
External electrical stimulation, 374
External electric field, 75, 87, 252, 385, 425
External electric field vector E_{ext}, 168
External electric field vector, 148
External electric sources, 28
External electrodes, 14
External electromagnetic fields, 163
External field, 133, 142, 353, 361
External field meter, 400
External field source, 240, 400
External impact on polarizable tissue, 93
Externally applied direct voltage u_{DC} across both electrodes and the resulting direct current i_{DC}, 470
Externally applied electric field, 90, 96
External magnetic field, 156
External sinks, 15
External stimulation, 329
External time-varying magnetic fields, 385
External to a conductive body, 133
External voltage, 468
Extracellular activation, 260
Extracellular and intracellular, 114, 256, 313
Extracellular anodic stimulation, 311, 314, 316
Extracellular cathodic stimulation, 311, 314
Extracellular conductivity, 115, 270
Extracellular electrical stimulation—spatial gradient, 264
Extracellular electrodes, 318
Extracellular equalizing currents, 14
Extracellular excitation, 263
Extracellular experimental set-up, 269
Extracellular fields, 264
Extracellular heating, 349
Extracellular potential φ_e, 260, 264, 267
Extracellular potential, 269, 328
Extracellular space, 71, 80, 113, 250, 339, 510
Extracellular stimulation, 247, 253, 254, 261, 263, 264, 271, 281, 284, 285, 287, 288, 291, 295, 307, 309, 311, 314–316, 328, 338
Extra overvoltage, 447
Extra resistance, 447, 448
Extrasystole, 374, 375
Extremities, 518
Eyeball rotation, 16
Eyelid movements, 16

F
Failure of thermoregulatory mechanisms, 347
Faint flashes of light, 379
Falls off as the inverse of frequency, 116
Faradaic impedance R_{el}^{t}, Z_{el}^{d}, and Z_{el}^{c}, 501
Faradaic reactions, 275, 391, 494
Far field, 30, 39, 40, 169, 200, 356, 360
Far field condition, 30
Far from the susceptible organ, 363
Far-reaching electrostatic forces, 429
Fast activation gates, 338
Fast and unconstrained charge transfer, 458, 480
Fast and unconstrained electrode reaction, 505
Fast charge transfer, 499
Fast diffusion process, 459
Fast fatigue, 317
Fast mass transport, 459
Fast medium, 207
Fast thermoregulation, 346
Fast touch and separation, 544
Fast-twitch muscles, 317
Fast und unconstrained charge transfer prevails, 481
Fast wave, 14
Fat/muscle boundary, 207, 217, 218, 344, 346, 358
Fatalities, 373
Fatigue, 246, 294
Fat to muscle boundary, 217
Fatty tissues, 72
Favourable current pathway, 376
Favourably used in practice, 243
Favour excitation, 252
Feedback effect, 157
Feedback signal, 541
Fe electrode, 439
Femtoseconds, 103
Ferromagnetic materials, 530
Few hundred mV, 256
Few nodes, 269
Few reverberations, 48
Fiber, 281, 314
Fiber diameter, 265, 308
Fiber parameters, 270
Fiber properties, 306
Fiber resting, 265
Fibrillation risk, 377
Fibrillation threshold, 370, 376, 382
Fick's first law, 461
Field and tissue properties, 85
Field distortion factor, 192
Field divergence, 359
Field energy, 242
Field exposure, 49
Field frequency f, 27, 60, 79, 85, 129, 140, 142, 144, 160, 162, 163, 167, 174, 186, 193, 201, 211, 242, 348, 357, 358, 362, 368, 379, 384, 473, 495, 497, 518
Field just outside the body surface, 220
Field lines, 139, 140
Field lines are perpendicular to the body surface, 139
Field parameters, 141
Field penetration, 45
Fields, 155
Field source, 356
Filter function, 361
Final state in the charge distribution, 134
Fine crystalline surface, 416
Fine spatial control, 332
Finite δ_D^T, 481
Finite conductive current, 414, 505
Finite cross-section area, 155
Finite current i, 412, 496
Finite current $i_{DC} \neq 0$, 490, 491
Finite decomposition voltage U_{dec} ($\neq$0), 485
Finite diffusion speed, 479
Finite direct current, 432
Finite drift velocity, 466
Finite dynamics of all electro-kinetic processes, 473
Finite electric field, 136, 255
Finite field frequencies, 183
Finite I_{l-e}, 543
Finite length Warburg impedance $\underline{Z}_{el}^{d,f}$, 481
Finite mobility, 174
Finite phase shift, 98
Finite reaction speed, 463
Finite relaxation time constant, 174
Finite size of the charge, 468
Finite thickness $\delta_D^T = \delta_D$ of the diffusion layer, 498
Finite time constant, 391
Finite volume of the axon, 269
Fire once and lately, 281
Firing rate, 281, 291
First cathodic phase depolarizes, 291
First cross the capacitor, 260
First derivative $d\varphi/dx$, 262
First derivative of φ_e, 261
First electrode, 318
First layer of water molecules, 430
First order of the Debye expression, 128
Floating electrodes, 511
Flow, 527
Flow around alveoli, 22
Flow of electromagnetic energy, 39, 48

Fluid content, 72
Fluid redistribution, 72
Flux density, 94
Focus low frequency fields, 404
Focussed electric field, 231
Focussed stimulation, 336
Focussed superficial applications, 404
Focussing, 359
Focussing capability, 404
Following anodic phase, 284, 285
Following each stimulation pulse, 278
Following formation of O_2, 492
Following medium, 173
Following reduction of oxygen, 492
Foot-to-foot current path, 23
Footwear, 167
Force application, 353
Forced convection, 432, 460, 461
Force magnitude, 90
Formation aspects, 9
Formation of AgCl, 491
Formation of O_2 gas, 492
Formation of Pt oxide, 494
Formations aspects, 28
Formation speed of new nucleation sites, 416
Forming polarization, 101
Forming relaxation, 101
Forward current, 547
Fourier analysis, 361
Fourier series, 64
Four skin electrodes, 21
Four-tenths of the free-space wavelength, 164
Fraction of milliseconds, 488, 103
Fraction of the voltage divider, 488
Frame rate, 24, 26
Free and bound charges, 129, 106, 159, 174–177, 229
Free ionic charges, 85
Free of any fields, 158
Free unbound charges
Frequencies below 100 kHz, 158, 364
Frequency f, 29, 64, 70, 192, 256, 304, 350, 358, 361, 367, 381, 467, 487
Frequency components, 4
Frequency content, 14
Frequency dependence, 101, 240, 245, 303, 532, 534
Frequency-dependent γ and ε_r, 68
Frequency-dependent $\underline{Z}^{c}_{el}$, 483
Frequency-dependent $\underline{Z}^{d}_{el}$, 483
Frequency-dependent, 66, 129, 131, 353, 363
Frequency-dependent capacitive shunts, 535
Frequency-dependent component, 99, 483
Frequency-dependent conductivity, 100
Frequency-dependent contribution, 83
Frequency-dependent measure, 96, 97
Frequency-dependent permittivity, 100
Frequency-dependent portion, 129
Frequency-dependent relaxation, 101
Frequency domain, 23, 249
Frequency domain analysis
Frequency increases, 549
Frequency-independent, 83, 99, 129, 483, 479
Frequency-independent non-dispersive τ, 68
Frequency of 2.5 GHz, 44
Frequency of biosignal, 535
Frequency of interference, 535
Frequency of stimulus, 341
Frequency range, 25, 245
Frequency-related impedance of the capacitor, 549
Friction, 124
Frictional braking force, 77
Frictional effects, 86
Friction losses, 121
Friction-related heat losses, 129
From the bulk, 435
Full blockade, 295
Full-spherical surface, 330
Fully recovered, 374
Functional electrical impedance tomography, 24
Functional electrical stimulation, 317
Functional interference, 354
Functionalisation of the electrode surface, 402
Function of i_{DC} and u_{DC}, 446
Function of U_{pol}, 495
Functions not only of the time-varying i_{AC} and u_{AC} but also of time, 473
Fundamental processes, 65
Fundamental quantity, 33
Future electrodes, 402

G

Gain distortion, 512
Gain in entropy, 86
Galvanic cell, 439, 453–455
Galvanic coupling, 505–507, 512, 547, 548
Galvanic isolation, 502
Gamma dispersion, 103, 117
Gas bubbles, 494
Gases, 473
Gas evolution, 493
Gaussian, 365
Gel has a quite high ionic conductivity, 499
General boundary conditions, 173
General public exposure, 358, 366, 379, 381, 384, 387, 388

General tendencies, 190
Generate different physiological effects, 28
Generation of action impulses, 316
Genesis of endogenous biosignals, 9
Genesis of ventricular fibrillation, 374
Geometrical and electrical properties, 61, 63
Geometrical and medium factors, 266
Geometrical distance, 385
Geometrical optics, 201
Geometrical projection, 12
Geometrical properties, 141, 507
Geometrical relation, 270
Geometrical shape, 509
Geometrical spread, 42
Geometric dimensions, 60
Geometry-related damping, 17, 36, 40, 42
Gestation, 14
Global electrical impedance, 60
Global electrical quantities, 60
Global electric behaviour, 60
Global homeostasis, 344
Global Ohm's law, 60
Global quantities, 57, 59, 60, 407
Global scalar quantity, 53, 56
Global triboelectric effects, 544, 545
Glossokinetic potential, 16
Gold or stainless steel electrodes, 402, 507
Good blood perfusion, 71
Good conductors, 45, 111, 124, 135, 208, 533
Gouy-Chapman double layer or diffuse layer, 421, 423
Graded postsynaptic potentials, 14
Gradient of the electric potential, 250, 252, 269, 458
Gradual bend, 261
Gradual changes, 337
Gradual control, 319
Gradual neural response, 319
Greater amplitudes, 286
Greater depths, 321
Greater excitability of thicker fibers, 320
Greater loss of excitation, 287
Greatest values of P_{SAR}, 170
Grey regions, 320
Ground/reference electrode, 234, 278
Grounded and ungrounded body, 139, 167, 234, 363
Grounded catheter, 364
Grounded conductive blanket, 541
Grounded conductive body, 144, 403
Grounded feet, 139
Grounded human, 137
Grounded human body, 147
Grounded object, 147
Grounded person, 140, 363, 380
Ground electrode, 186, 263, 332, 547
Grounding, 166
Guidelines, 301, 354

H

H_2 gas, 437, 492
H_2 oxidation reaction, 455
H_2 reduction/formation reaction $2H_3O^+ + 2e^- \rightarrow H_2 + 2H_2O$, 455
Half-cell concept, 436
Half-cell voltage, 392, 436, 442, 451, 511
Half cycle, 90
Half of the original rheobase, 308
Half-spherical surface, 330
Half-wave dipole, 164, 170
Half-wave of i_{AC}, 477
Halved, 330
Hand to both (grounded) feet, 517
Hand to hand, 376, 377, 514, 518, 517
Hard abiotic interface, 390
Hardly apparent, 105
Hardly soluble AgCl, 443
Harmful, 275, 277, 279, 347
Harmonic voltage $u_{AC} = c_1 \bullet \cos(\omega t)$, 485
Harmonic waveform, 64, 95, 98, 209
Harm tissue, 493
H-atoms can be plated, 494
Hazard assessment, 241, 305
Head and shoulders, 137, 139, 140, 347
Healing of wounds, 359
Health effects, 366
Heart current factor, 234, 370, 376–378
Heart rate, 346, 347
Heart region, 373
Heat, 129, 171, 241, 243, 282, 344, 364
Heat exchange, 346
Heating effects, 364
Heat in tissue, 79, 357, 359, 389
Heat transfer mechanisms, 343
Height of the person, 140
Height-to-radius ratio, 140
Helmholtz double layer or rigid layer, 421, 423, 448
Heterogeneity of tissues, 100, 131
Heterogeneous body, 143, 154, 159, 164, 168–170, 177, 180, 237, 239
Heterogeneous patterns, 349
Heterogeneous permittivities, 182
Heterogeneous solution, 431
Heterogeneous tissue, 61, 67, 82, 83, 116, 159, 348
High and very non-uniform, 163, 164
High body conductivity, 538

High but not exceedingly high overvoltages, 504
High cathodic current, 315
High common-mode rejection ratio CMRR, 533
High common-mode u_{CI}, 546
High concentration of ions, 416, 421
High-conductivity lossy medium, 43
High contact impedance, 524
High contact voltage, 375
High contrasts, 72
High current, 293, 372
High current blockade, 315, 318
High electric field, 432
High electrode resistance, 513
High energy, 352
Higher frequency f, 82, 99, 216, 380, 381, 478, 532
Higher heating rate in fat than in muscle, 190
Higher local absorption, 48
Higher oscillation frequencies, 291
Higher stimulating currents, 281
Higher stimulation levels, 243
Higher water content, 71
Highest current densities, 143
Highest density of counterions, 434
Highest reference level, 364
High exchange current density, 437, 491
High excitation threshold, 266
High frequencies relaxation processes, 341
High-frequency β-dispersion, 71
High frequency blockade, 295, 318
High frequency communication signal, 549
High frequency components, 534, 549
High frequency conduction blockade, 245, 295, 305
High frequency current, 364
High frequency field, 29, 404
High frequency stimulation, 295, 296
High impedance recording amplifier, 521
High inner electric field, 120
High input impedance, 405, 523
High interference environments, 535
High ionic activities, 444
High isolation resistance, 545
High levels of electric fields, 246
High local P_{SAR}, 169
High local R_{el} for $u_{DC} < U_{dec}$, 470
High local current densities, 487
High losses, 48, 72
Highly concentrated solutions, 419
Highly conductive objects, 45
Highly frequency-dependent, 82
Highly non-linear, 470
High-ohmic discharge path, 546
High-ohmic electrode leads, 540
High-ohmic input impedance to the power line's ground, 540
High overvoltage $|u_{pol,i} - U_{pol}|$, 463
High-pass behaviour, 409
High-pass filter, 548
High-permittivity medium, 37, 41, 43
High polarization voltage, 502
High positive value, 266
High power, 364
High-power stimulation, 389
High-risk exposure times, 370
High-solute-concentration solution, 413
High stimulation currents, 318
High U_C, 518
High values of γ_{eff} and ε of bodily tissue, 191
High voltages, 373
High-water and high-salinity content, 72
High water content, 130, 132
High Z_{el} and Z'_{el}, 535
Histological evaluations, 392
Homeostasis, 345, 359, 389, 414
Homogeneous and heterogeneous media, 9, 487
Homogeneous body, 63, 239
Homogeneous conductivity, 61
Homogeneous current density distributions, 507
Homogeneous distribution, 53, 54, 63
Homogeneous field, 56
Homogeneous isotropic tissue, 263, 269, 319, 334
Homogeneously distributed, 61, 63, 66
Homogeneous permittivity, 63
Homogeneous properties, 66
Homogeneous regions, 116
Homogeneous section, 61
Homogeneous solution, 431
Homogeneous tissue, 83, 157, 178, 342
Homogenous, 50
Homogenous anisotropic ionic conductivity, 154
Homogenous body, 156, 168, 169
Homogenous conductive body, 154
Homogenous electric field, 133
Homogenous media, 170
Hot and humid environment, 347
Hot humid days, 546
Hot spot effect, 138
Hot spots, 169
Household devices, 194
Human body, 133, 145, 156, 180, 191, 224, 348, 364, 383, 528, 537, 539, 547

Humans, 167, 350
Hydrated, 78, 413, 428, 433
Hydrated ions, 86, 128, 431
Hydrated or wet skin, 518
Hydrated proteins, 86
Hydration of polar proteins, 86
Hydration shell, 77, 78, 81, 106, 118, 427, 429, 430, 464
Hyperbolic fit, 300
Hyperpolarization, 243, 244, 247, 252, 253, 255–257, 261, 264, 266, 270, 271, 273, 278, 280, 281, 285, 297, 301, 311, 313–315, 335, 336, 338, 339
Hyperpolarization breaks down, 338
Hyperpolarizing anodic phase, 285
Hyperpolarizing current, 338
Hyperpolarizing effect, 284
Hyperpolarizing minimum, 335
Hyperpolarizing outflow of Na^+ ions, 316
Hyperpolarizing phase, 278, 286
Hyperpolarizing stimuli, 254
Hypersensitive, 246
Hyperthermia, 201
Hyperthermia treatment, 404
Hypothalamus, 347, 348

I

Ideal capacitor, 422
Ideal conductors, 45
Ideally conductive body, 135, 136, 206, 226
Ideally constrained electrode/redox reactions, 504
Ideally diluted solutions, 81, 419
Ideally fast mass transport, 481
Ideally no net transfer of electric charges, 504
Ideally unconstrained, 505
Ideally unhindered and infinitely fast, 505
Ideal reference electrode, 405, 505
Ideal resistor, 422
Ideal solution, 419, 437
Identical electrical properties, 230
Image charges, 462
Imaginary ε, 126
Imaginary conductivity, 98, 191
Imaginary part, 59, 68, 124, 125, 129, 489
Imaginary value $\mathrm{Im}(\underline{Z}_{\mathrm{el}}^{\mathrm{d}})$ (<0), 480
Immobile/bound charges, 65
Immobile polarization centers, 62
Impair normal breathing, 369
Impedance, 20, 363, 406, 508, 514, 545
Impedance cardiography, 19, 21
Impedance divider, 67
Impedance pneumography, 22
Impedance $R_{\mathrm{el}}^{\mathrm{t}} + Z_{\mathrm{el}}^{\mathrm{d}} + Z_{\mathrm{el}}^{\mathrm{c}}$, 483
Impedance tomography, 5, 19, 366
Impedance $\underline{Z}_{\mathrm{el}}^{\mathrm{d,f}}$, 479
Impedance $\underline{Z}_{\mathrm{el}}^{\mathrm{d}}$ disappears for high f, 498
Impedance $\underline{Z}_{\mathrm{el}}$ increases, 510
Impedance $\underline{Z}_{\mathrm{b}}$ of biological tissue, 406
Impedance $\underline{Z}_{\mathrm{el}}$ of this simplified electrode model, 500
Impedances $\underline{Z}_{\mathrm{el}}^{\mathrm{d}}$ and $\underline{Z}_{\mathrm{el}}^{\mathrm{c}}$ disappear, 483
Imperfect capacitor, 421
Implanted electrodes, 13, 44, 330, 402, 495
Implanted monopolar electrode, 330
Implanted monopolar stimulation electrode, 328
Imprinted oscillation period $1/f$, the transfer function, 473
Improved model, 410
Impulse duration, 316
Incident angle, 177, 182, 185, 189, 201
Incident angle and refraction angle, 203
Incident direction, 203
Incident electric field, 168
Incident field, 49
Incident homogenous power density, 200
Incident magnetic field, 168
Incident medium, 216
Incident normal field component, 221
Incident wave, 41, 202
Incident wavefront, 199
Incorporating metals, 390
Increase and approach a common value, 82
Increased effective conductivity, 110
Increased excitability, 243, 339
Increased magnitude of the resulting, 137
Increased γ of the body insert, 225
Increased $R_{\mathrm{el}}^{\mathrm{d}}$, 460
Increased resonance frequency, 170
Increased stray capacitance, 539
Increase in the body temperature of less than 1 °C, 387
Increase in the (differential) diffusion resistance $R_{\mathrm{el}}^{\mathrm{d}}$, 460
Increase in the strength, 314
Increase of electric fields, 353
Increase progressively, 304
Increases γ_{eff}, 72
Increases in proportion to increasing distance y, 270
Increases with increasing frequency, 404
Incremental reorientation, 430
Independent interactions, 75
Independent of the sign of the surface charge, 426
Independent on the angular frequency, 422
Independent on the fiber depth y, 270

Independent on the size of $i(t)$, 270
Independent on U_c, 515
Indifferent electrode, 404
Indirect contact, 524
Indirect coupling, 240, 348, 353, 363, 400
Indirect effects, 356
Indirect or contact-based coupling, 385
Indirect way of O_2, 492
Individual cells sum up, 14
Individual susceptibility, 368
Induced and orientation polarization, 120
Induced and reorientation polarizations, 160
Induced biosignals, 1, 7, 28
Induced charges and their temporal changes, 545
Induced conductive currents, 538
Induced current, 139, 146, 167, 365
Induced current density, 142, 152, 154
Induced currents should enter the axon, 254
Induced direct current, 79
Induced electric biosignals, 5–7, 9, 20
Induced electric field, 91, 152, 168, 195, 250
Induced electric fields and currents, 49
Induced equalizing currents, 3
Induced field which is constant throughout the interior, 148
Induced heating, 388
Induced inner electric field, 379
Induced interference potentials, 538
Induced interference voltage, 529
Induced polarization and orientation polarization, 75, 90, 91, 94
Induced surface charges, 133, 220, 466
Induced voltage across the membrane, 257
Induced voltage drop, 113, 115
Induce mutually each other, 162
Induces the electric field, 150
Induce the electrode/redox reaction, 503
Inductance, 509
Induction of electric dipoles ceases, 107
Inductive coupling, 529, 537, 541
Inductive impedance, 509
Ineffective, 375
Inert acceleration of ions, 466
Inert adsorption, 482
Inert and noble, 439
Inert behaviour of the boundary, 275
Inert charge redistribution, 135
Inert charge-transfer and inert diffusion processes, 449, 458, 459, 478, 482, 488, 489
Inert coupled reactions, 449
Inert dynamics, 391
Inert excitation process, 290
Inert fiber's excitation, 285
Inertia, 482
Inert in its speed, 448
Inert in migration, 464
Inert intracellular charges, 255
Inert ionic/species concentrations, 467
Inert ions, 466
Inert mechanical process, 125
Inert mechanisms, 103
Inert motions of ions, 466
Inert movements of counter-charges, 511
Inertness, 100
Inertness of bound charges, 100
Inertness of unbound charges, 100
Inert process, 284, 345
Inert redistribution, 467
In excess of 1–2 °C, 347
Infinite delay, 288
Infinitely long wire, 51
Infinite $\underline{Z}_{el}^{d} \to \infty$ results for $f \to 0$, 481
Inflammatory responses, 390
Inflated and deflated lungs, 22, 70
Influence strongly, 429, 482, 510
Infrared and visible range, 103
Infrared region, 122
Inhibited capacitive coupling, 535, 540
Inhibit formation of action impulses, 291
Inhomogeneity, 155, 538
Inhomogeneity effects, 28, 49
Inhomogeneous anatomical structures, 17
Inhomogeneous conductivity, 83
Inhomogeneous electric fields, 180
Inhomogeneous field, 145, 356
Inhomogeneous in space, 385
Inhomogeneous magnetic field, 385
Inhomogeneous properties, 71
Inhomogeneous tissue, 186
Initial cathodic phase, 284
Initial hyperpolarization, 285
Initial linear part, 284
Initially anodic biphasic pulse, 288
Initially cathodic biphasic pulse, 288
Initial membrane depolarization rate, 269
Initial rate $d\vartheta/dt$, 343, 344
Initial rectangular pulse or phase, 290
Initial time-varying magnetic field, 157
Inneraxional current leaking, 297
Inner biosignals, 405
Inner body fields, 240
Inner body impedance Z_b, 363, 514, 517
Inner body resistance, 517, 531, 532, 537
Inner conductivity, 265, 383
Inner current density, 195, 241, 384, 386, 387
Inner currents, 147, 383

Inner ear activity, 19
Inner electric field, 116, 149, 161, 194, 226, 228, 241, 379, 382, 466
Inner electric fields
Inner field, 92, 133, 240
Inner Helmholtz layer, 426, 454
Inner J_E inside the body, 381, 384
Inner region of the conductive body, 158
Inner resistance, 25, 531
Innervated muscle, 309
Inorganic and organic bodies, 425
Inorganic ions, 81
In parallel to the capacitor, 515
In-phase movement velocity of unbound charges, 98
In-phase propagation, 38
In-phase relationship, 59, 98
In-phase without any temporal, 58
Input biosignal, 519
Input impedance of string galvanometers, 532
Input impedance of the amplifier, 540
Input impedance of the biomedical amplifier, 513
Input of the amplifier, 527, 528, 533, 535
Input-referred interference voltage, 528
Input voltage, 519, 523
Insets of different conductivities, 155
Inspiration, 22
Instantaneous absorption rate, 84
Instantaneous electric conductive current, 57
Instantaneous electric conductive current density, 52
Instantaneous electric voltage, 55, 57
Instantaneous frequency, 340
Instantaneous value, 84
Insufficient solvent molecules, 419
Insulating inclusions, 113
Insulating oxides, 493
Intactness, 70
Integral form, 1, 151
Integration distance, 252, 292
Integration time, 394
Integrity of the electrode and biological tissue, 394
Intensive care units, 513
Interaction mechanism, 101, 241
Interactions, 50
Interactions between electric and magnetic fields, 50
Intercellular channels, 15
Interconnected semi-circles, 498
Interfaces, 116, 401
Interfacial capacitance, 422
Interfacial polarization, 112, 118
Interference, 171, 199, 406, 533, 534, 536, 537, 539
Interference amplitude U_{CI}, 533
Interference effects, 528
Interference frequency, 542
Interference pattern, 199
Interference-related potentials, 538
Interference sources, 539
Interference voltage, 385, 511, 527, 528, 538
Inter-ionic electrostatic interactions, 420
Inter-ionic forces, 81
Inter-ionic interactions, 77, 80, 81, 419, 420
Intermediate plateaus, 131
Intermediate reaction steps, 492
Intermolecular interactions, 128
Internal conductivity distribution, 24
Internal current density, 354, 357
Internal electric field, 148, 149, 152, 354, 356, 357
Internal electric field E_1, 168
Internal electric field E_2, 168
Internal fields, 353
Internal heating, 337
Internal membranes, 116
Internal thermal energy of the solvent, 413
Internodal distance, 253, 264, 267
Internodal length, 328
Interphase area, 451
Interphase delay, 285–288
Interphase interval, 285–289
Interplay, 449
Inter-pulse interval, 278
Inter-pulse potential control, 279
Interval size, 332
In the longitudinal orientation, 82
Intimately coupled, 29
Intolerable, 367
Intolerable pain, 366
Intracardial electrocardiogram, 13
Intracardial electrodes, 13, 376
Intracellular, 260, 313
Intracellular anodic stimulation, 310
Intracellular cathodic stimulation, 309
Intracellular conductivity, 115, 267
Intracellular electrode, 260, 281, 285
Intracellular heating, 349
Intracellular organelles, 116
Intracellular potential, 269
Intracellular resistance R_I, 254
Intracellular space, 71, 86, 115, 259
Intracellular stimulation, 247, 252, 254, 263, 278, 281, 284, 285, 289, 293, 295, 297, 301, 302, 307, 309, 315
Intrinsic filtering, 502

Invasive transtympanic, 40, 18
Inversely proportional to squared distance, 382
Inverse neutralization reaction, 340
Inverse of α, 44, 294
Inverse polarity, 435
Inverse problem, 26
Inverse recruitment order, 318, 320
Inverse relationship, 204, 205, 444
Inverse square law, 30, 31, 36, 40, 42, 44, 200
In-vitro evidence, 351
Involuntary muscle contraction, 244, 369
Inward and outward currents, 292, 297, 309
Inward transmembrane currents, 261
Ional/molecular distance, 421
Ion-associations, 419
Ion exchange, 421
Ionic and displacement dispersion, 103
Ionic charge, 78, 81, 255, 414, 419, 435, 458, 510
Ionic cloud, 434
Ionic compound AgCl, 445
Ionic concentration, 77, 425, 433
Ionic conduction, 129
Ionic conductivity, 70, 83, 85, 86, 99, 122
Ionic counter-charge $-Q$, 466, 467, 504
Ionic current, 264, 401, 510
Ionic diffusion, 105
Ionic dispersion, 122
Ionic effects, 83
Ionic electrical conductivity, 80
Ionic mobility, 77, 79
Ionic polarization, 122
Ionic radius, 428
Ionic relaxation, 122
Ionised and neutralised, 401
Ions, 107, 419, 425, 503
Ions collide, 109
Ion's hydration shell, 420
Ion's liberation, 420
Ions mobility, 86
Ion species, 464
Iridium, 392, 403
Irrespective of the actual level of $u_{pol,i}$, 504
Irreversible, 256, 279, 295, 389
Irreversible reactions, 274, 275, 281, 388, 391, 493, 502
Ischemia, 374
Isolated, 136, 545, 546
Isolated conductive body, 135, 136, 144
Isolated conductor, 177, 178
Isolated electrodes, 92
Isolated human body, 227, 228, 524
Isolated ion, 419, 433
Isolated passenger car, 380
Isolated truck, 380
Isolating air, 133, 234, 524
Isolating barrier, 406
Isolating corneum, 410
Isolating insert, 155, 237, 239
Isolating layer of the corneum, 407
Isolating subcutaneous fat, 410
Isolating tissue, 225
Isolation, 417, 515, 544
Isolation capacitance, 546
Isolation impedance, 546
Isolation resistance, 546
Isotropic, 54, 60, 230
Isotropic excitation, 250
Isotropic fat, 188
Isotropic media, 177, 182, 185, 188
Isotropic tissue, 82, 93

J

$\vec{J}_C$ across the membrane's surface, 253
$\vec{J}_E$ along the membrane's surface, 253
Joint propagation, 29

K

K^+ channels, 295
KCl salt of defined concentration, 445
Kinetic inhibition, 448, 449, 503
Kinetics of ion channel gating, 295
Kinetics of the electrode reaction, 498
K-polarization, 165, 167, 168, 170

L

Lack blood supply, 348
Large activation barriers, 491, 494, 502
Large antennas, 30
Large area of the electrode/skin boundary, 532
Large biological tissues, 161
Large blood volume, 71
Large body surface, 152
Large capacity, 283
Large charge densities, 279
Large clouds, 108
Large contact area, 518
Large contraction forces, 318
Large cross-section, 157
Large current, 143, 542
Large current densities, 279
Large diffusion impedance, 508
Large distances in tissue, 109
Large double-layer capacitive component, 508
Large electrode-eyeball distances, 17
Large electrodes, 393, 539

Large electrode surfaces, 521
Large fibers, 320
Large grounded conductive object, 528
Large i_{DC}, 455
Large impedance, 508
Large input resistance, 521
Large membrane region, 283
Large myelinated axons, 329
Large offset voltages, 513
Large overvoltage, 416
Large particle, 111
Large phase angle $\arg(\underline{Z}) = \varphi_2 > \varphi_1$, 490
Large polar proteins, 118
Larger delay, 281
Larger energies, 341
Large required energy deposition, 241
Large resistor, 407
Larger people, 153
Larger recruitment volume, 261
Larger than the geometrical size, 162
Larger than the wavelength, 169
Large-scale structures, 109
Large semi-circle A, 489
Large skin contact areas, 518
Largest capacitance, 186
Largest portion of i_{l-b}, 527
Large structures, 103
Large surface area, 405, 464
Large surface charges, 180
Large time constant, 283
Large time delay, 283
Large total P_{SAR} resulting from E-polarization, 168
Large variations due to ions adsorption at the electrode surface, 443
Last existing contact, 544
Late atrial or ventricular systole, 375
Late diastole, 6
Lateral depolarized regions, 335
Laterally confined beam, 200
Laterally dislocated semi-circle, 500
Late systole, 6
Law of mass action, 444
Layered skin, 84
Lead-flexing artefacts, 543
Lead inductance, 510
Lead induction effects, 510
Leading edge, 283
Leads, 509, 529
Leads are unshielded, 527
Leads connected to electrodes, 509
Lead's motions, 512
Lead-to-shield capacitive impedance, 540
Lead twisting, 530
Lead wire, 531
Leakage currents, 292, 304, 364
Leakage effects, 307
Leakage resistance, 298, 307
Leaky capacitor with imperfect dielectrics, 421
Least impedance, 186
Least inductance, 186
Least noble metals, 415
Least ohmic resistance, 186
Least resistance, 527
Least stimulation energy, 263
Leaving outwards the closest axon's regions, 311
Lectrostatic forces, 415
Left arm, 234
Left arm and both feet, 234
Left hand, 150, 234
Left hand and any foot, 377
Left hand to both feet, 376, 377
Left side, The, 253
Left side of the cell, 255, 258
Length constant, 158, 252, 296, 309, 356
Length limitation of shielded cables, 543
Length of the body channel, 548
Length of the conductive pathway, 548
Lens, 348
Lesions, 347
Let-go, 366, 370
Let-go current, 366, 371, 372
Let-go thresholds, 372
Lethal risk, 373
Level of U_h of electrode material, 438
Life-threatening effects, 386
Lightning, 377
Limbs, 347
Limit an increase in the tissue temperature by less than 1°C, 349
Limit current density of linearity, 487, 488
Limited accumulation speed, 174
Limited by diffusion, 463
Limited common-mode rejection ratio, 545
Limited compliance, 403
Limited conductivity, 164
Limited cross-section areas, 518
Limited in space, 517
Limited kinetics of coupled reactions, 462
Limited validity, 274
Limit increase in the tissue temperature, 345
Limiting of length of unshielded electrode leads, 543
Limits the cable length, 540
Limit the resulting currents, 518
Limit to the metabolic harm, 389
Linear, 62, 345, 433

Linear approximation, 267, 272
Linear bodily tissue impedance $\underline{Z}_b \approx R_b = u_b / i_{AC}$, 475
Linear bodily tissue resistance $R_b = u_b / i_{DC}$, 471
Linear body, 58
Linear change in the membrane voltage, 323
Linear coupling, 472
Linear decrease, 283, 323
Linear for the non-polarizable electrode, 483
Linear increase, 283, 323
Linearly controlled, 280
Linearly dependent, 39
Linearly proportional, 280
Linear responses, 120
Linear scaling, 220
Linear transfer function of bodily tissue, 472
Line-body stray capacitance, 525
Line dipole, 382
Line integral, 55
Line integral of the amplitude of the tangential component, 56
Line integral of the normal projection, 56
Line-lead stray capacitance, 527
Line segment B, 489
Live conductor, 234
Live parts or electrodes, 370, 518
Loaded particle, 425
Local body temperature, 345
Local burn, 364
Local circular loops, 155
Local concentration, 478
Local conductivity changes, 71
Local current density, 54, 154, 157
Local curvature, 221, 227
Local differential resistance R_{el} decreases for $u_{DC} > U_{dec}$, 471
Local electrical conductivity, 57
Local electrical properties, 60
Local electrical quantities, 60
Local electric behaviour, 60
Local electric field, 54
Local electric field within tissue, 75
Local electric potential, 54, 429
Local electrode impedance, 487
Local energy absorption, 170
Local energy deposition, 341
Local envelope width, 84
Local form, 150, 157
Local form of Ohm's law, 57, 60, 80
Local heating, 241
Local homeostasis, 344
Localized applicator, 403, 404
Localized effects, 360
Localized energy deposition, 201
Localized P_{SAR}, 365
Local lossy currents, 341
Locally restricted, 89
Locally restricted energy absorption, 46
Local maximum, 434, 436
Local mechanical and electrical stimuli, 379
Local movements, 94
Local non-uniform absorption, 164
Local Ohm's law, 60
Local polarizability changes, 71
Local P_{SAR} (x) can also vary from point to point, 84
Local quantities, 60
Local quantities of tissue, 407
Local R_{el}, 472
Local resonances, 168
Local slope of i_{DC} increases, 452
Local strength of stimulation, 332
Local time-varying vector quantities, 57
Local tissue, 96, 97
Local tissue heating, 341
Local triboelectric effects, 544, 545
Local vector quantity, 53, 56, 172
Local volume changes, 71
Location, 350
Location of the major current pathway, 367
Logarithmic scaling, 131, 220
Long atomic distances, 420
Long axis, 266
Long axis of an elongated cell, 250
Long axis of the body, 148, 168, 360
Long duration, 289, 375
Long electrode cables, 540
Long enough, 290
Longer and thinner bodies, 167
Longer reverberations, 49
Long half-periods $1/(2f)$, 480
Longitudinal, 252
Longitudinal axis, 378
Longitudinal body orientation, 222
Longitudinal currents, 73, 246, 302
Longitudinal electric field, 257
Longitudinal orientation, 132, 195
Long pulse durations, 315
Long range displacements, 110
Long settling times, 403
Long suprathreshold stimulus, 281
Long-term and chronic biological effects, 353
Long-term application, 390, 394, 403
Long-term chronic applications, 277
Long-term current application, 340
Long time constants, 287
Loosely bound and mobile, 75

Loss angle, 127
Losses, 341
Losses slow down, 43
Loss factor, 122
Loss in entropy, 86
Lossless, 9
Lossless and isotropic media, 177
Lossless and lossy media, 31
Lossless and weak dielectric, 41
Lossless biological tissue, 203
Lossless case, 34
Lossless current, 97, 98
Lossless dielectric, 97, 215
Lossless dielectric materials, 125
Lossless interaction, 124
Lossless materials, 124
Lossless media, 31, 32, 36–38, 40, 43, 45, 202, 204, 205, 207, 208
Lossless muscle, 36
Lossless oscillation, 124
Lossless penetration, 45
Lossless polarization, 93, 99
Lossless propagation, 36, 38
Lossy and heterogeneous sections, 48
Lossy and predominant dielectric medium, 215
Lossy and strong dielectric, 41
Lossy biological tissues, 205
Lossy case, 34
Lossy current, 98
Lossy current component, 97
Lossy dielectric materials, 125
Lossy dielectric medium, 27, 43
Lossy dielectrics, 54, 59, 60, 99, 101, 124, 152, 216
Lossy dielectric tissue, 43, 125
Lossy interactions, 79, 85, 109
Lossy materials, 124
Lossy media, 32, 36, 37, 41–44, 47, 48, 205, 208
Lossy muscle, 36
Lossy propagation, 3, 42, 43, 205
Lossy tissue, 45
Lossy wave propagation, 479
Low capacitive impedance, 502, 508
Low charge-transfer resistance R_{el}^{t}, 491, 505
Low conductive $i_{AC,E}$, 487
Low conductivity, 258, 416
Low conductivity of electrolyte, 416
Low contact impedance, 412, 512
Low contrasts, 72
Low currents, 373
Low electrode impedance, 405, 512
Low electrolyte concentrations, 420
Low energy, 352
Lowers R_{el}^{t} and increases $i_{AC,E}$, 487
Lower thresholds, 291, 292
Lower values, 532
Lowest cross-section areas, 343
Lowest excitation threshold, 379
Lowest levels of stimulation, 242
Lowest reference level, 364
Lowest threshold values, 305
Low exchange current densities, 494
Low excitation threshold, 266
Low-frequency approximation, 192
Low frequency components, 10
Low frequency components of biosignal, 535
Low-frequency β-dispersion, 71
Low frequency electromagnetic fields, 351
Low frequency fields, 404
Low frequency process, 116
Low frequency range, 103, 380
Low frequency stimulation, 296
Low i_0 indicates large activation barriers, 452
Low impedance of leads, 543
Low impedance path, 541
Low in amplitude, 538
Low interfacial capacitive impedance $1/(j \bullet 2\pi \bullet f \bullet C_{el})$, 475
Low internal, 149
Low ionic concentrations, 108
Low losses, 73, 130
Low magnitude B, 154
Low mains frequency, 532
Low-ohmic amplifier's ground, 540
Low-ohmic electrode on the body, 538
Low-ohmic power line's ground, 525, 528, 538, 540
Low-ohmic shield, 540
Low oscillating frequencies, 274
Low output impedance, 543
Low output impedance of preamplifiers, 543
Low overvoltage, 416
Low overvoltage $|u_{pol,i} - U_{pol}|$, 463
Low-pass filter, 12, 250, 548
Low polarization overvoltage, 505
Low quality factor, 48
Low R_{el}^{t}, 495
Low signal-to-noise ratio, 524
Low-solute-concentration solution, 413
Low stimulation rate, 246
Low strengths, 109
Low U_C, 515, 516
Low $u_{pol,i}^{t}$, 487
Low $u_{pol,i}^{t} < U_{dec}$, 487
Low value of $\underline{Z}_{com}$, 535
Low values of $\underline{Z}_{el}$ and/or $\underline{Z}'_{el}$, 535
Low voltages, 373

Low $\underline{Z}_{el}$, 501
Low water content, 130, 133
Low-water content tissues, 73
Lung function, 22
Lung's polarization, 71
Lung volume, 22
Lying posture, 142

M
Macroscopic body, 161
Macroscopic bulk properties, 101
Macroscopic electrical properties of tissue, 96
Macroscopic electric polarization field, 88, 89, 91
Macroscopic excitations, 297
Macroscopic field, 90
Macroscopic impact, 91
Macroscopic point, 90, 135
Macroscopic polarization field, 92
Macroscopic structures, 155, 170
Macroscopic tissue property, 113
Macroshock, 363, 370, 376
Magnetic field, 49–51, 154, 156, 158, 161, 171, 379
Magnetic flux density, 50, 150
Magnetic flux density field, 28, 201
Magnetic origin, 152
Magnetic resonance imaging, 156
Magnetic stimulation, 251
Magnitude, 39, 40, 55, 80, 152, 172
Magnitude B, 154
Magnitude E_{ext}, 92
Magnitude J_E, 154
Magnitude of the electric field, 200
Magnitude of the resulting v, 78
Magnitudes E and J_E, 156
Magnitude S of the power density, 40
Magnitude Z, 68
Magnitude Z_{wb}, 514, 517
Magnitude $|\underline{Z}_{el}|$ and phase $\arg(\underline{Z}_{el})$, 496
Mains frequency, 368
Mains voltage, 376, 518
Major amount of i_{l-e}, 528
Major determinant of metabolic stress, 391
Major difference, 356
Major β-dispersion, 115
Major effect, 242
Malfunction, 354
Malignant prostate tissue, 71
Malignant tissues, 71
Manifold electric field, 138
Mass density, 73
Mass transfer, 431, 449, 458, 463
Mass transport, 496
Matched gain, 543
Materials in contact, 545
Mathematically calculated, 355
Mathematical modeling, 356
Maxima, 292
Maximally stimulated, 335
Maxima of the envelope, 216
Maximum $\Delta\vartheta$ is highly disproportional to both J_E and E, 343
Maximum absorption, 167
Maximum at the midsection of the body, 140
Maximum change, 130
Maximum consumption of reactants, 461
Maximum coupling, 356
Maximum current, 140
Maximum current densities, 234
Maximum electric field, 136
Maximum energy, 381
Maximum energy absorption, 48
Maximum field, 48, 356
Maximum firing frequency, 294
Maximum frequency, 25
Maximum hyperpolarization, 270
Maximum i_{DC}, 463
Maximum inner electric field, 379
Maximum/limiting diffusion current, 463
Maximum/limiting diffusion current density, 461
Maximum local, 146
Maximum local depolarization, 335
Maximum of the depolarization, 270
Maximum of the hyperpolarization, 270
Maximum P_{SAR}, 167
Maximum possible reflection, 204
Maximum probability, 250
Maximum projection, 12
Maximum values of U_{ind}, 258
Maximum voltage drop, 116
Maximum U_{ind}, 258
Maxwell-Ampere equation, 157
Maxwell-Faraday equation, 150
Mean dimension, 116
Mean threshold values, 366
Mean values, 366
Measure for the inhibition of i_{DC}, 447
Measures interact, 392
Mechanical changes, 21
Mechanical force, 51, 150
Mechanically and electrically excitable cells in the retina, 379
Mechanical phenomena, 7
Mechanical stimulation, 379
Mechanical stress, 388, 390
Mechanism of conduction, 79

Mechanoreception, 242
Medical devices, 385
Medical exposure, 358
Medical implants, 44, 134, 147, 150, 152, 154, 163, 165, 192, 349
Medium f (70 Hz $\leq f \leq$ 90 Hz), 489
Medium f of the applied u_{AC}, 477
Medium f of u_{AC}, 475
Medium is unbounded, 29
Medium overvoltage $|u_{pol,i} - U_{pol}|$, 463
Medium-related damping, 17, 42, 44
Membrane, 113, 307
Membrane-bound structures, 115
Membrane breakdown, 72
Membrane excitability, 257
Membrane hyperpolarization or depolarization, 254
Membrane integration effects, 292, 303
Membrane of the cell, 382
Membrane segments, 264
Membrane shields, 113
Membranes of intracellular organelles, 116
Membrane thickness, 115
Membrane time constant, 284, 299, 306
Membrane voltage, 251, 253, 255, 259, 272, 285, 292, 297
Memory, 245
Men, 365, 371
Metabolic heat production, 346, 347, 350
Metabolic origin, 392
Metabolic rate of the human body, 387
Metabolic safety, 393
Metabolic stress, 279, 280, 294, 295, 388, 389, 392–394
Metal case, 279
Metal catalysers for O_2 formation, 493
Metal cations, 413
Metal deposition, 415, 421, 457
Metal deposition with adsorption, 415
Metal dissolution, 413, 415
Metal electrode, 413, 439, 511
Metal electrode is coated with its salt, 507
Metal/electrolyte, 412
Metal/electrolyte interface, 412
Metal ion electrode, 412, 413, 432, 440, 442, 457
Metal ions, 413, 415, 440
Metal-isolator contact, 544
Metallic electrode, 405, 412, 421
Metallic ion gradients, 511
Metallic silver, 490
Metallic surface, 209, 210
Metal-metal contact, 544
Metal oxidation, 415
Metal reduction, 415
Metal surface, 413, 444, 468
Metal/tissue, 412
Microelectrodes, 502
Microscopic electric fields, 87–90
Microscopic friction, 110, 111
Microscopic interactions, 91, 101
Microscopic point, 161
Microscopic structures, 155, 170
Microseconds, 119
Microshock, 363, 370, 376
Microwave diathermy, 359
Microwave hearing, 342, 350
Middle of two neighbouring nodes, 269
Migration, 81, 425, 432, 449, 474, 490
Migrational inertness, 474
Migration-based transport, 451
Migration ceases, 474
Migration component, proportional to $d\varphi/dx$, 458
Migration v of H^+ and OH, 78
Mimics the plot of the model A, 498
Minima, 292
Minima and maxima, 210, 217
Minimal capacitive interference, 537
Minimal in the non-polarizable electrode, 512
Minimal let-go currents, 371
Minimal threshold values, 366
Minima of the envelope, 216
Minimise losses of biosignals, 502
Minimize any differences, 71
Minimize/avoid both the polarization overvoltage, 521
Minimized or supressed, 537
Minimizes disadvantageous, 527
Minimize the electrode polarization, 509
Minimize the total energy, 61
Minimum, 305
Minimum amplitude and duration, 298
Minimum distance, 315
Minimum duration, 245
Minimum frequency, 25
Minimum thresholds, 371
Minimum time interval, 294
Minimum value, 381
Minor amount of i_{l-e}, 528
Minor dispersions, 115
Mismatch, 536
Missing ionic cloud, 110
Missing kinetic inhibition, 505
Missing skin infection/irritation, 524
Mixed behaviour, 191
Mobile, 423
Mobile carriers, 60

Mobility *m* of free charge carriers, 83
Mobility *m* of hydrated ions is reduced, 86
Model, 379
Model A, 498, 499
Model B, 499, 500
Model C, 500
Modelled chronaxie, 307
Modelled data, 130
Modelled electro-kinetic processes, 474
Modelled rheobase, 306
Model of the electrode/electrolyte boundary, 496
Model of the non-polarizable electrode, 506
Model of the polarizable electrode, 506
Model of the skin, 410
Moderate activity, 348
Moderate environmental conditions, 387
Modified complex permittivity, 128
Modified conditions, 99
Modulated by physiological activities, 28
Modulation by respiration, 4
Modulation frequency, 351
Modulation frequency windows, 351
Molecular bonds, 87, 89
Molecular dipole, 88, 117
Momentary stimulus, 244
Momentary values of system variables, 414
Momentary waveform, 300
Monitored, 331
Monolayer of solvent molecules, 466
Monophasic cathodic rectangular stimulus, 287
Monophasic excitation threshold, 287
Monophasic pulse, 275, 291
Monophasic rectangular anodic current pulses, 277
Monophasic rectangular pulse, 293
Monophasic rectangular stimulus, 300
Monophasic rectangular waveform, 301
Monophasic stimulation pulse, 308
Monophasic stimulus, 279, 284, 289
Monophasic waveform, 3, 13, 288, 309
Monopolar behaviour, 17
Monopolar, bipolar, 334
Monopolar mode, 332, 334
Monopolar model, 17
Monopolar modus, 15
Monopolar recording mode, 331
Monopolar stimulation mode, 332
Monotonically increase with frequency, 296
Monovalent ions, 78
More electrochemical stress, 391
More interference-related displacement currents, 539
More reaction by-products, 391
Most excitable axon's region, 330
Most excitable point, 270
Mostly normally coupled, 226
Mostly tangential, 148
Most sensitive to excitation, 311
Most sensitive to this depolarization, 311
Motion artefacts, 511
Motion component, 124
Motion-induced displacement, 545
Motion-related changes of the divider, 513
Motion-related modulation of the registered biosignal, 512
Motion-related noise, 512
Motor efferent fibers, 329
Motor fibers and sensory fibers, 329
Motoric thresholds, 366
Motor nerves, 283
Motor neurons, 308
Motor unit, 14, 317
Move locally bound charges, 97
Movement artefacts, 25, 401, 511, 512, 545, 546
Movement of solvated ions, 79
Movement-related changes, 511
Movements, 339
Movements of unbound electric charges, 51
Movement velocity, 94, 99
Moving electric charges, 51
Moving electrode, 481
Moving ions, 162
Much lossier, 130
Much stronger excitatory current, 313
Multifrequency tomography, 24
Multiparametric monitoring, 1
Multiple cells, 387
Multiple dispersion, 127
Multiple electrodes, 26
Multiple firing, 281
Multiple frequencies, 26
Multiple frequency rule, 361
Multiple implanted electrodes, 336
Multiple $\lambda/2$ intervals, 210
Multiple leads, 24
Multiple passage, 48, 164
Multiple re-entry, 374
Multiple reflections, 48, 217
Multiple reflections and re-reflections, 216
Multiple reverberation, 164
Multiple steps, 127
Muscle, 119, 131, 186, 244, 305, 344, 346, 358
Muscle activity, 19
Muscle-air boundary, 239
Muscle and fat, 45
Muscle cramps, 369

Muscle disuse, 319
Muscle/fat boundary, 190, 216
Muscle fibers, 73, 302, 303
Muscle force, 318
Muscle into fat, 190
Muscle isotropy, 188, 189
Muscle reactions, 366
Muscle response, 246
Muscle's dimensions, 67
Muscle section, 68
Muscle's electrical properties, 67
Muscle to fat, 188, 189
Muscle towards fat, 186, 188
Muscle twitches, 246
Muscular contraction, 113
Muscular tissue, 237
Mutual coupling, 29, 444
Mutual friction, 47, 109
Mutual induction, 29
Mutual interactions, 49
Mutually interrelated, 127
Mutual obstruction of ions, 82
Mutual screening of ions, 435
Myelinated and unmyelinated, 315
Myelinated axon, 263, 267, 328
Myelinated cylindrical fibers, 264
Myelinated fibers, 265, 283, 284, 286, 288, 291, 293, 294, 296, 306, 307, 313, 332
Myelinated fibers A fibers, 329
Myelinated nerve fibers, 382
Myelination, 306
Myocardium of atria, 10
Myocardium of ventricles, 10

N

Na^+ channels, 295
NaCl 0.1 mol/l solution, 435
NaCl aqueous solution, 82
NaCl physiological solution, 490, 491, 518
NaCl solution, 419
NaCl solution (table salt solution), 80
NaCl water solution, 82
Nanoseconds, 119
Narrow body sections, 517
Narrow nodes, 283
Narrow range of the stimulation current, 317
Narrow regions of body extremities, 234
Natural activation and propagation, 259
Natural convection, 432
Natural endogenous current densities, 383
Natural endogenous current density fields, 386
Natural endogenous electric fields, 194, 383
Natural firing rates, 295
Naturalistic environments, 16
Natural stimulation, 254
Naturally evoked, 283
Naturally quite often used, 317
Naturally quite seldom used, 317
Natural operation, 294
Natural patterns, 295
Natural recruitment order, 318
Natural repertoire, 346
Natural security, 547
Natural stimulation, 273
Near field, 29, 30, 169, 200, 356, 360, 547
Near field declines, 30
Near recording electrodes, 17
Necessary but not sufficient, 279
Necessary gradient of the electric field, 323
Neck and ankles, 146
Necrosis, 71
Needle electrodes, 405
Negative anions, 427
Negative charge density, 178
Negative charges, 16, 87, 133, 255
Negative electrode, 87, 339, 471
Negative excess charge, 425
Negative extracellular potentials, 2
Negative $f(x)$, 266
Negative feedback loop, 541, 542
Negative half-wave, 473
Negative half-wave of u_{AC}, 476
Negative ions, 78, 339
Negatively charged, 16
Negatively charged electrodes, 415
Negatively charged groups, 18
Negatively charged, positive cations, 426
Negatively charged posterior part, 17
Negative net charge, 363
Negative OH^- ions, 339
Negative phase, 301
Negative polarization charge, 87
Negative potentials, 457
Negative reflection, 204
Negative sign, 129
Negative surface charge, 179
Negative $U_h < 0$, 439
Neglected, 99, 475, 497
Neglected wire's resistance, 531
Neglects this finite U_{pol} ($\neq 0$), 472
Neglect U_{pol}, 506
Negligible, 342
Negligible and constant $u'_{pol,i} \approx U'_{pol} \approx 0$, 464
Negligible displacement, 154
Negligible energy absorption, 163
Negligible ohmic voltage drop, 455
Neighbouring nodes of Ranvier, 263
Nernst behaviour, 462, 480, 482

Nernst equation, 419, 441, 462
Nerve, 244, 280
Nerve bundle, 73, 319
Nerve cells, 245
Nerve damage, 389
Nerve fiber, 302, 305, 307, 314, 315
Nerves and muscles, 241
Net/excess charge, 429, 432, 433
Net charge, 278, 429, 454
Net charge flow, 97
Net charge injection, 275
Net charge transfer, 274, 503
Net conductance of Na^+, 338
Net current flow, 97, 453
Net electric field $E_{ext} - E_i$, 466
Net field, 210
Net inhibition, 482
Net mass transfer, 432, 457
Net outflow of Na^+ ions, 316
Net transfer of charge, 505
Net transfer of electric charges, 504
Net transfer or conversion of chemical species, 453
Net transmembrane current, 253, 263
Neural stimulation, 389
Neuromuscular effects, 26, 180, 244, 336, 337, 372, 400
Neuromuscular excitation, 25, 49, 246, 336, 353, 357, 383, 386
Neuromuscular stimulation effects, 154, 156, 247, 338, 340, 380, 384
Neurostimulation effects, 384
Neurotechnological, 16
Neutral electrode, 404
Neutral environments, 348
Neutral particles, 419, 426
Neutral particles with an equal number of adsorbed anions and cations, 425
Neutral particles without adsorbed ions, 425
Neutral solutions, 492
Neutral substances, 431
Never becomes currentless, 135
Never gets out of the interphase, 503
Noble materials, 392
Noble metal electrodes, 507
Noble metals, 415
No chemical interactions, 50
Nodes, 210, 211
Noise, 524, 542
Noise immunity, 386
Noise susceptibility, 401
Noise to the output of the real differential amplifier, 528
Non-compromised cardiac function, 346
Non-conducting/non-charged bodies, 425
Non-conducting particles, 74, 86, 113
Non-conductive air, 139
Non-contact assessment, 19
Non-contact capacitive electrodes, 536, 543, 545
Non-contact coupling, 405
Non-contact electrodes, 402, 403, 512, 524, 546
Non-contact metallic electrode, 524
Non-continuous pulsed exposure, 241
Non-continuous pulsed stimulation, 372
Non-disturbed field regions, 226
Non-Faradaic process, 501
Non-Faradaic reactions, 274, 275
Non-homogenous field distributions, 359
Non-ideally conductive body, 135
Non-infinite reaction speed, 473
Non-integrated version of the electrocardiogram, 1
Non-invasive extratympanic, 18
Non-linear behaviour, 156, 243, 256, 422, 488
Non-linear capacitor, 468, 483
Non-linear C_{el}, 422
Non-linear change in $u_{pol,i}$, 455
Non-linear dependence, 81
Non-linear differential electrode resistances R_{el} and R'_{el}, 471
Non-linear electrode impedances Z_{el} and Z'_{el} of electrode/tissue boundaries, 475
Non-linear fashion, 292
Non-linear for large i_{DC}, 455
Non-linear for the polarizable electrode, 483
Non-linear function, 495
Non-linearity in-between i_{AC} and u_{AC}, 485
Non-linearly coupled, 472
Non-linearly increases, 330
Non-linear mechanisms, 351
Non-linear membrane mechanisms, 302
Non-linear region will receive an additional current, 487
Non-linear R^t_{el}, 500
Non-linear relationship, 485
Non-linear relationship $i_{AC} = c_2 \bullet (u_{AC})^2$, 485
Non-linear resistance $R_{el} = R^t_{el}$, 500
Non-local movements, 95
Non-monotonic behaviour, 296
Non-overlapping balance points, 88

Non-polarizable Ag/AgCl electrode, 491
Non-polarizable electrode, 250, 437, 448, 452, 463, 473, 491, 504–507, 511, 513
Non-polarizable electrode acts as a linear ohmic resistor, 452
Non-polarizable electrodes have small U_{dec}, 470
Non-polarizable electrode, the transfer function between i_{DC} and u_{DC}, 472
Non-polarizable sensing electrode, 472, 477
Non-polar structure, 87
Non-resonant, 124
Non-reversible electrode, 502
Non-sinusoidal ambient field, 361
Non-sinusoidal contact current, 361
Non-sinusoidal magnetic fields, 154
Non-specific adsorption, 428, 429, 436, 454
Non-spontaneous, 453
Non-synchronized action impulses, 294
Non-thermal, 351
Non-thermal effects, 244
Non-thermal mechanism, 373
Non-uniform absorption, 348
Non-uniform composition, 143
Non-uniform deposition, 163
Non-uniform distribution, 349, 360
Non-uniform distribution of $\vec{J}_E$, 143
Non-uniform distribution of local currents, 147
Non-uniform distribution of P_{SAR}, 169
Non-uniform fields, 405
Non-uniformities, 171
Non-uniformity in the absorption, 164
Non-uniformity in the recovery of excitability, 374, 375
Non-uniform P_{SAR}, 349
Non-uniform spatial distribution, 217
Non-uniform structure, 101
Non-uniform surface, 393
Non-uniform waves, 208
Non-zero common-mode gain, 533
Non-zero current, 77
Non-zero direct component, 277
Non-zero displacement currents, 234
Non-zero electric potentials, 464
Non-zero electrostatic forces, 441
Non-zero excitatory electric fields, 274
Non-zero frequency, 68
Non-zero gradient, 253, 254
Non-zero inertance, 89
Non-zero net charge, 77
Non-zero net mass transfer, 454
Non-zero net surface charge, 144
Non-zero phase delay, 479
Non-zero phase shift, 43
Non-zero spatial gradient, 261, 263
Non-zero surface charge, 112, 117
Non-zero volumes, 419
No phase delay between the time-varying courses of $u_{pol,i}$ and c^s, 480
No real electric charges, 475
Normal and tangential components, 172, 173
Normal component, 174–176, 180, 182, 184, 190, 226, 239
Normal components of the electric field, 137, 176
Normal concentration, 423
Normal coupling, 149, 180, 221
Normal distance from the electrode surface, 478
Normal environmental conditions, 347
Normal field component, 172
Normal incidence, 203–205, 209, 210
Normal tissue and tumor tissue, 71
Normal to the area, 152
Normal to the conductor's surface, 176
Normal to the plate's surface, 50
Normal to this boundary, 136
Notch filter, 542
No vortices or curls in electrostatic orquasi-electrostatic, 55
Nuclear membrane, 116
Nucleation sites, 416
Nucleus and electron shell within the conductor, 462
Nucleus and organelles, 258
Number of Cl^- ions increases, 445
Number of electrodes, 26
Number of firing fibers, 317
Number of pulses, 394
Numerical data, 321
Numerical example, 155
Numerous cycles, 292
Numerous muscle cells, 14
Nyquist plot, 127, 480, 489, 498

O

O_2 anodic oxidation/formation reaction ($2H_2O \rightarrow O_2 + 4H^+ + 4e^-$), 455
Objective stimulation intensity, 394
Objects are physically separated, 51
Objects are swiftly separated, 544
Object size, 362
Oblique incidence, 202, 203, 210
Observed change of u, 323
Obstruction of charged ions, 81

O_2 cathodic reduction reaction ($O_2 + 4H^+ + 4e^- \rightarrow 2H_2O$), 455
Occupational exposure, 358, 381, 387
Octahedral arrangement, 86
Offset U_{pol}^{00}, 444
Ohmic voltage drop $u_b = U_b$, 451, 468, 475
Ohm's law, 57
Omission of the relatively small $R_{electrol}$, 500
On-body and in-body, 547
One-half of the wavelength, 164
One hand to another hand, 376
One-way propagation, 273
Ongoing electrical activity, 245
Ongoing exposure, 218
Onset and spreading of the spatial non-linearity, 487
Onset and strengthening of inter-ionic interactions, 82
Onset of activation, 260
Onset of Faradaic reactions, 275
Onset of the anodic phase, 494
Onset of the cathodic phase, non-Faradaic reaction, 494
Onset of the direct current, 338
Onset of the effective contributions, 495
Onset of the exposure, 218
Onset of the non-linearity varies spatially, 487
Onset of the stimulus, 265
Onset or interruption, 304, 336
Open circuit, 445, 519, 521, 531
Opening angle, 270, 271
Open surgery, 370
Opposes the incident change dB/dt, 157
Opposing electric fields, 136, 148, 220, 221, 224
Opposing field
Opposing ions movements, 77
Opposite charges, 390, 425, 464
Opposite direction, 203
Opposite sign and equal amount, 421
Optical frequencies, 29, 103
Optically slow medium, 41
Optimal depolarization, 301
Optimal distance, 335
Optimise waveforms, 308
Optimization or design guideline, 300, 301
Optimum, 301
Order and bound water molecules, 86
Orders of magnitude, 192
O_2 reduction, 492
Orientated differently, 148
Orientation, 161, 262
Orientation angle, 152
Orientation energy, 120
Orientation of the human body, 147, 165
Orientation polarization, 90, 91, 94, 117, 128, 422, 429
Oscillate bound charges, 99
Oscillate in-phase, 31, 59
Oscillating threshold, 292
Oscillation frequency, 25, 26, 303
Oscillation of ions, 79
Oscillation of the reactive species concentrations c on the electrode surface, 477
Oscillatory frequency f, 246
Oscillatory motion of bound charges, 124
Oscillatory rhythm, 473
Oscillatory stimulus, 292
Osmosis, 413
Osmotic pressure, 413, 415
Outer boundaries, 91
Outer conductive shell, 138
Outer E_{ext}, 381
Outer electric fields, 149, 379
Outer field strength, 142
Outer Helmholtz layer, 415, 423, 424, 428, 429, 433, 454
Outer membrane surface, 257
Outermost body surfaces, 156
Outgas as H_2, 340
Outgrowth of the forebrain, 379
Out-of-phase, 124, 210, 541
Out-of-phase behaviour, 122
Out-of-phase movement velocity of bound charges, 98
Out-of-phase oscillation, 32
Out-of-phase propagation, 30
Out-of-phase relationship, 59, 60, 98, 205, 207
Out-of-phase time courses, 541
Out of the electrode, 440
Output biosignal, 519
Output current, 519, 523
Output of the amplifier, 533
Outside the body, 239, 243
Outside the currentless situation, 437
Outside the head, 138
Outside the loop, 157
Outside the quasi-electrostatic situation, 75
Outside the targeted region, 307
Outside the vulnerable period, 375
Outside this sphere, 435
Outward currents, 270, 297, 310
Outward direction, 260
Outwards, 301
Outward transmembrane currents, 261
Overall brain functions, 15
Overall performance, 401

Overestimate, 127
Overhead power transmission lines, 156, 194
Overheating, 48
Overlap in space, 87
Overlapping Debye-type dispersions, 127
Overstimulation, 48
Over the muscle, 14
Over time, 10
Overvoltage, 511
Overvoltage amplitude U_b, 451
Overvoltages $u^t_{pol,i}$, $u^d_{pol,i}$, 449
Overvoltage $u^d_{pol,i} = (u_{pol,i} - U_{pol})$, 481
Own cloud of counterions, 106
Own electric field, 133
Oxidation at the anode, 454
Oxidation contribution, 451
Oxidation/formation of O_2, 493
Oxidation of electrode ions, 438
Oxidation or reduction, 415, 501, 440
Oxidation process, 454
Oxidation reaction, 440, 454, 459
Oxidative effects of the electrolyte, 440
Oxidising properties, 473
Oxidized/dissolved, 401, 471, 491
Oxidized species, 440

P

Pain, 366, 372
Pain is relieved, 359
Pain masking any thermal sensation, 242
Pain on contact, 366
Pain perception, 308
Pain relieve therapy, 339
Paradoxically, 382
Parallel circuit, 483
Parallel combination, 65
Parallel connection, 65, 84, 178, 497, 227
Parallel orientation, 152
Parallel to C_{el}, 475
Parallel to the external, 259
Parallel to the incident electric field, 250
Parallel to the long axis of the body, 139, 147
Parameters, 159
Parameters of circuit elements, 509
Parameters of the neural stimulus, 390
Partial alignment, 430
Partial blockade, 296
Partial-body resonances, 163, 164, 166, 348, 350
Partial compensation, 97
Partial conductive currents, 61
Partial current $i_{AC,E}$, 67, 488
Partial displacement currents, 64
Partially compensated, 97
Partially-excited muscle cells, 12
Partially follow, 121
Partially recovered, 374
Partial reflection, 48, 204, 213, 214–217
Partial standing waves, 48, 84, 215–217
Particular fiber, 244
Particular time moment, 300
Partly recovered cardiac muscle, 306
Partly solvated/hydrated, 416
Part of the heart muscle, 374
Parturition, 14
Passive and active approach, 542
Passive conducting objects, 362
Passive depolarization and hyperpolarization, 272
Passive electrical circuit model, 410
Passive linear electrical properties, 243
Passive medical implants, 353
Passive repolarization, 284
Passive shielding, 540
Passive state, 392
Path of least impedance, 527, 528, 540
Path of least resistance, 21, 22, 64, 220
Path with largest capacitance, 64
Patient is galvanically isolated from the ground, 542
Pattern pulsates, 210
Peak electric field, 200
Peak P_{SAR}, 360
Peak value, 39, 293
Peak value of a time-varying sinusoidal field, 84
Penetration depth δ, 26, 44, 159, 163, 165, 348, 350, 359, 478, 403
Perception, 366, 367
Perception and annoyance, 362, 380
Perception levels, 372
Perception of a finger contact, 380
Perception of the stimulation, 389
Perception threshold, 341, 350, 369, 372, 381
Perfect capacitor, 421
Perfect conductor, 206, 209, 216
Perfect dielectrics, 124, 125, 205, 209, 216
Perfect lossless dielectric body, 59
Perfectly non-polarizable electrode, 464, 470, 505
Perfectly non-polarizable electrode and an ideal reference electrode, 463
Perfectly non-polarizable reference electrode, 468, 472, 475, 489
Perfectly polarizable electrode, 504
Perforation of cell membranes, 373

Perfusion, 346
Periodic biphasic rectangular pulses, 289, 291, 293
Periodic biphasic sinusoidal pulses, 293
Periodic current stimulus, 293
Periodic firing, 281
Periodic series, 278
Periodic stimuli, 245, 277, 274, 289, 296, 304
Peripheral, 156, 305, 354
Peripheral body regions, 156
Peripheral myelinated fibers, 380
Peripheral myelinated nerves, 380
Peripheral nerves, 380, 382, 390
Peripheral nervous system, 157, 194, 382
Permanent biosignals, 1, 7, 28, 383, 386
Permanent dipoles, 90, 429
Permanent electric biosignals, 1, 2, 7, 9
Permanent electric dipole, 89, 90
Permanently polar structures, 89
Permanent polarization charges, 89
Permeate the boundary, 454
Permissible amplitude, 26
Permittivity, 21, 96, 101, 120, 130, 191, 381
Permittivity change, 126
Permittivity ε within the double layer, 423
Permittivity of the double layer, 430
Perpendicular, 17, 152, 379, 529
Perpendicular and parallel polarizations, 203
Perpendicular entrance, 177
Perpendicular polarization, 203
Perpendicular to the body surface, 136
Perpendicular to the electric field, 136
Perpendicular to the field, 250
Perpendicular to the incident magnetic field, 153
Perpendicular to the long axis of the body, 221
Personalized therapy, 1
Personal protection measures, 358
Person's impedance, 367
Perturb, 136, 150
Pervasive monitoring, 403
Phase arg ($\underline{Z}_{el}^{d}$) independent on the frequency *f*, 479
Phase arg ($\underline{Z}_s$) of $\underline{Z}_s$, 517
Phase boundaries, 475
Phase constant, 33
Phase delay, 479, 481
Phase duration, 340
Phase lag, 125
Phase shift equals $\alpha \bullet \pi/2$, 481
Phase shift of 45°, 480
Phase shift φ_Z, 59, 60, 68, 98
Phase transition layer, 502
Phasor diagram, 59, 95, 98
Phosphenes, 379
PH-value, 425, 493, 494
Physical boundary, 116, 225, 230
Physical contact, 353, 362
Physical effects, 161
Physical limitations, 127
Physical perspective, 47
Physical point, 20
Physical quantity, 361
Physical size, 501
Physiological concentration, 445
Physiological conditions, 21
Physiological effects, 49, 240, 241, 366, 369, 370, 379, 387
Physiological NaCl concentration, 435
Physiological phenomena, 6
Physiological point, 21
Physiological responses, 346
Physiological solution, 81, 464
Picoseconds, 103, 118
Planar wavefront, 40
Plane of incidence, 202, 203
Plane of the conductive loop, 529
Plane or spherical TEM wave, 39, 36, 38, 40, 41
Plane-parallel conductive capacitor plates, 62
Plane-parallel plates of the capacitor, 50
Planes of constant phase, 37, 43
Plane wave, 29, 31, 165, 199
Plane wave and far field, 168
Plateaus, 319, 372
Plate capacitor, 421, 464
Platinum, 390, 392, 402
Plus pole, 453
Point contact currents, 363–366
Point field source, 199
Point in the same direction, 82
Point of the ground contact, 140
Point sources, 313
Polar, 430
Polarity, 135, 467
Polarity ratio, 308, 313
Polarizability of the electrode, 472, 513
Polarizable electrode, 250, 448, 451, 464, 468, 470–473, 500, 502, 504, 506, 507, 511, 513
Polarizable Pt electrode, 491, 494
Polarizable sensing, 472
Polarizable sensing electrode, 464, 470, 472, 477, 485, 487, 489
Polarizable tissue, 90, 92–95, 97
Polarization, 93, 126, 208, 279, 506
Polarization and conductive behaviour, 97
Polarization and dispersion, 70

Polarization charges, 117
Polarization curve, 455
Polarization curve of Ag/AgCl electrode, 457
Polarization density field, 92
Polarization effects, 96
Polarization field, 92, 94, 97
Polarization mechanism, 103, 111, 112, 117, 305
Polarization of membrane, 245
Polarization of non-polar structures, 159
Polarization of the electrode/tissue boundary rises, 510
Polarization of the sensing electrode, 466
Polarization of the transverse tubules, 132
Polarization of water molecules, 474
Polarization overvoltage $u^{t}_{pol,i} = u_{pol,i} - U_{pol}$, 275, 277, 278, 390, 391, 393, 402, 405, 416, 447, 460, 465, 466, 511
Polarization phenomenon, 504
Polarization process, 255
Polarization, relaxation, 49
Polarization resistance, 480
Polarization voltage, 277, 392, 405, 415, 417, 437, 439, 441, 443–445, 455, 466, 468, 470, 496, 511
Polarized, 305, 429, 449
Polarized dielectric, 92
Polarized structures, 89, 91
Polarizes a tissue section, 90
Polar proteins, 118, 121
Polar side-chains on protein molecules, 119, 121
Polar structure, 87, 89–91
Polar structure of solvent molecules, 86
Polar water molecule, 78, 117, 419, 429, 430, 464, 419
Poor conductors, 135
Poorly conducting cells, 510
Poorly soluble salt AgCl, 442–444
Positional changes, 94
Position of the human body, 146
Position of the low-ohmic electrode, 539
Positive and negative electric charges, 87
Positive cations Me^{z+} in the tissue/electrolyte, 413
Positive charge of the electrode, 427
Positive charge on the electrode surface, 440
Positive charges, 87, 133, 255
Positive conductive current leaves the cathode, 490
Positive electric charge, 16
Positive electrode, 87, 339, 425, 471
Positive extracellular potentials, 2
Positive H^{+} ions, 339
Positive half-wave of u_{AC}, 473, 476
Positive ions, 78, 339, 471
Positively charged electrodes, 416
Positively charged monopolar cornea, 17
Positive monopolar source, 17
Positive phase, 301
Positive polarization charge, 87
Positive $U_h > 0$, 439
Potential, 433
Potential differences, 253, 362, 377
Potential divider, 536, 540, 541, 543
Potential energy, 420, 435
Power, 344
Power density, 30, 39, 45, 48, 165, 200, 349, 351, 354, 357, 360, 388
Power density windows, 351
Power deposition, 85
Power increase factor, 167
Power line frequencies, 191, 194
Power line interference, 401, 524, 525
Power lines, 234, 371, 529
Power loss, 80
Power per unit area, 39
Power P is proportional to E, 84
Power P is proportional to γ, 83
Power transmission lines, 385
Poynting vector, 39
Practical advantage, 280
Practical and easy to establish association, 272
Practical applications, 263, 331
Practical computations, 267
Practical consequences, 329, 502
Practically derived chronaxie, 307
Practical physical quantities, 354
Preceding cathodic phase, 285
Preceding medium, 173, 188
Precipitate as poorly soluble AgCl, 491
Precise anatomical models, 360
Predominant conductive behaviour, 99, 176, 186, 225
Predominant conductive body, 158
Predominant conductive medium, 43, 44
Predominant counterions, 434
Predominant dielectric behaviour, 99, 188, 228
Predominant dielectric medium, 41, 43, 44
Predominantly real, 490
Pre-excitation state, 297
Pre-gelled sponge, 511
Premature ventricular contraction, 374
Presence of a biological conducting object, 360
Primary function, 284
Primary importance, 340
Primary solvation, 86
Prior to and at the onset of the stimulus, 265

Probability of excitation, 317
Probability of fibrillation, 375
Processes of coupled chemical reactions, 482
Produced displacement, 99
Produced magnetic field, 157
Product $a_{Ag+} \bullet a_{Cl-}$ is constant, 443
Product of the inner electric field and the nuclear radius, 116
Progressive gain, 101
Progressive loss, 101
Projection, 15, 16, 54
Projection factor, 57
Prolate spheroid, 148, 194, 195, 227
Prolonged exposure, 347, 372, 378
Prominent resonance, 170
Pronounced decrease, 130
Pronounced increase, 130
Propagation, 3, 6, 29, 75, 29, 31, 316, 319–321, 335, 374
Propagation constant, 208
Propagation direction, 13, 32, 335
Propagation direction of the wave, 29
Propagation of action impulses, 273
Propagation of already generated action impulses, 317
Propagation of electromagnetic waves, 161
Propagation vector, 165
Propagation velocity, 32, 37, 40, 42, 203, 207, 211, 265, 323
Proper mode and appropriate *d*, 333
Properties of excitable tissue, 340
Properties of incident and induced fields, 359, 383
Properties of the body, 359, 383
Properties of the exitable fiber, 302
Proportional, 62, 152, 321
Proportional increase, 345
Proportionality, 321, 344, 422, 460, 459, 478, 509
Prostheses, 18
P_{SAR}, 356, 357, 360
P_{SAR} for excitatory interactions, 241
P_{SAR} for thermal interactions, 241
P_{SAR} increases with f^2, 167
Pseudo-capacitance, 480, 498
Pseudo-resistance, 480, 498
Psychophysical relationship, 394
Pt anode, 492
Pt cathode, 491
Pt electrode as the sensing electrode and Ag/AgCl electrode as the reference electrode, 439
Pt electrodes, 392, 437, 439, 491, 495, 507
Pt metal electrode, 451
Pt needle electrode, 393
Pt oxide, 494
Pt surface, 455, 492
Pulsatile blood perfusion, 22
Pulsed electromagnetic exposure, 350
Pulse duration, 246, 279
Pulse magnitude, 246
Pulse/phase, 287
Pulses sequences, 292
Pulse timing, 389
Pulse width, 267, 271, 317
Pump failure, 386
Pure perception, 378
Pure standing wave, 216
Pure water, 119
Pyramidal neurons, 15

Q

Q/*A*, 393
Qualitatively, 99
Qualitative analogy, 498
Qualitative data, 403
Qualitative perspective, 404
Quality factor, 49, 164
Quantitative, 49, 99, 148, 156, 498, 532
Quantity, 391
Quasi-elastic movements, 89
Quasi-electrostatic conditions, 29, 55
Quasi-electrostatic situation, 74, 75
Quick, strong, and/or extended stimulation, 388
Quite simple models, 17
Quotient, 37, 43, 113

R

Radial currents, 328
Radial distance, 433
Radial extension of the body, 156
Radiated signal, 547
Radicals, 492
Radii of dehydrated ions, 78
Radius of the ionic cloud, 434
Radius of the semi-circle ($=R_{el}^{t}/2$), 499
Raising the temperature, 282
Raising the threshold, 292
Randles circuit, a Faradaic impedance ($=R_{el}^{t} + Z_{el}^{d}$), 498
Random Brownian motion, 79
Randomly oriented neurons, 263
Randomly oriented polar structures, 89
Random thermal agitation, 120
Rate of association, 444
Rate of change d*u*/d*t*, 95, 97, 152, 161, 185, 188, 189, 264, 267, 304, 305, 366, 464

Rate of dissociation, 444
Rate of rise, 292, 293
Rate of the local temperature change, 351
Rate of the temperature change, 342
Rates of growth, 394
Ratio, 61, 285, 328, 330
Ratio $\Delta U_{AC}/\Delta I_{AC}$, 474
Rationale, 44, 169, 222, 252, 259
Ratios of the air ventilation to blood perfusion, 24
RC behaviour of the membrane, 298
RC-filter, 502
RC model, 297, 302
R_{el}^{d} due to inert diffusion, 452
Reach maximal values, 168
Reactance, 59
Reactants, 275, 448, 480
Reaction, 339, 414, 473
Reaction overpotential, 449
Reaction overvoltage ($u_{pol,i} - U_{pol}$), 462
Reaction overvoltage $u_{pol,i}^{c} = (u_{pol,i} - U_{pol})$, 449, 482
Reaction overvoltage $u_{pol,i}^{c} = (u_{pol,i}^{3} - U_{pol})$, 482
Reaction products, 275, 388, 493
Reaction resistance or charge-transfer resistance, 448
Reaction's onset, 495
Reaction speed, 451
Reactive component, 298
Reactive species S_{red} and S_{oxi}, 480
Readily soluble salt KCl, 442–444
Real and imaginary components, 490
Real charge transfer, 474
Real conductivity, 98
Real differential amplifier, 527, 533, 534
Real double layer, 421
Real electrode resistance R_{el}, 496
Real ε, 126
Real impedance, 59
Realistic strength-duration curve, 302
Real, ohmic, and non-linear, 477
Real part, 59, 124, 489
Real polarizable electrode and real non-polarizable electrode, 463
Real quantity, 32, 98, 177
Real quantity R_{el}^{d} for the direct i_{DC}, 479
Real reference electrode, 405
Real resistance, 57
Real value Re ($\underline{Z}_{el}^{d}$) (>0), 480
Reasonable assumption of $|\underline{Z}_{diff}| \rightarrow \infty$, 536
Recharged and depolarized, 280
Recharging of membranes, 112, 113
Reciprocal movements, 95
Reconstruction, 26
Recording and stimulation modes, 331
Recording/diagnostic purposes, 495, 507
Recovery period, 280
Recruited nerves, 366
Recruited volume of muscles, 366
Recruitment, 317
Recruitment volume, 263, 288, 320
Rectangular pulse, 292, 328
Rectangular section of muscle, 67
Rectangular shape, 282, 289, 290
Rectangular stimulus, 282, 305
Reddens, 384
Redistribute induced surface charges, 135
Redistribution of charges, 135
Redistribution of the surface charge, 112
Redox electrode, 412, 437, 439, 440, 442, 457
Redox reaction, 437, 440, 441, 452, 453, 461, 467, 477, 452, 453, 505, 530
Reduce areas, 530
Reduced activity coefficient, 435
Reduced activity of ions, 435
Reduced/deposited, 401
Reduced excitability, 339
Reduced excitation threshold, 339
Reduced human size, 170
Reduced interference, 192
Reduce displacement currents, 528
Reduced membrane voltage, 264
Reduced products, 277
Reduced reactivity, 420
Reduced size of the ionic cloud, 110
Reduced species S_{red}, 440
Reduce the total, 81
Reducing properties, 473
Reduction, 440, 490
Reduction and oxidation, 453
Reduction at the cathode, 454
Reduction contribution, 451
Reduction factor, 226, 380
Reduction of depolarizing current amplitude, 289
Reduction of dissolved neutral oxygen O_2, 492
Reduction of electrode ions, 438
Reduction of neutral and dissolved oxygen O_2, 492
Reduction of O_2, 492
Reduction process, 454
Reduction reaction, 437, 440
Reduction reaction $Cl_2 + 2 \bullet e^- \rightarrow 2 \bullet Cl^-$, 454
Re-entrant excitation waves, 13
Re-entry mechanism, 374, 375
Re-excites, 374
Reference Ag/AgCl electrode, 444, 455
Reference current pathway, 376, 377

Reference distance, 330
Reference electrode, 385, 404, 405, 408, 412, 436, 437, 439, 442, 445, 450, 455, 464, 468, 473, 475
Reference electrode with its $U_{h,H} = 0$, 453
Reference/indifferent electrodes, 442
Reference level, 26, 147, 354, 356–358, 360, 361, 364, 366, 380, 381, 388
Reference value, 356, 379, 384, 385
Reflected direction, 203
Reflected wave, 41, 202
Reflection, 41, 49, 164, 169, 171, 201, 203, 215
Reflection and refraction laws, 201
Reflection angle, 201
Reflection factor, 202, 205
Reflection laws, 195, 201
Reflections and re-reflections, 217
Reflection strength Γ_E, 204, 207
Reflective surface, 202
Refracting surface, 207
Refraction, 49, 164, 172, 201
Refraction angle, 177, 182, 185, 187–189, 207
Refractoriness, 245
Refractory, 389
Refractory behaviour, 247, 305
Refractory period, 280–282, 289, 291, 294, 322, 374
Regional blood perfusion, 24
Regional pulmonary ventilation, 24
Registered u_B with its amplitude $\underline{U}_B$, 531
Register voltage, 417
Registration, 3, 6
Registration of u, 21
Relationship, 298
Relative permittivity ε_r of tissue, 91
Relative permittivity ε_r, 92, 97
Relative permittivity of water molecules, 430
Relative refractory period, 294, 305
Relative to the wavelength, 167
Relaxation, 100, 103, 122
Relaxation frequency f_r, 67, 100, 103, 112, 117, 118, 122–124, 130, 187–189
Relaxation frequency of γ-dispersion, 83
Relaxation mechanism, 112, 117
Relaxation of surface charges, 147
Relaxation of the ionic atmosphere, 110
Relaxation of the ionic cloud, 108
Relaxation processes, 100, 129
Relaxation time, 97, 107
Relaxation time constant τ, 66, 68, 100, 104, 107, 112, 117, 125, 135, 147, 110, 466, 511
Relaxes partly back, 111
Relaxing dipole, 119
Relevance of Z_{el} and Z'_{el}, 531, 532
Relevant boundary conditions, 231
Remote ground electrode, 331, 332
Remote-seated electrodes, 403
Repeated biphasic pulses, 291
Repeatedly capturing and averaging, 19
Repeatedly stimulated, 375
Repeated sinusoidal pulses, 292
Repetitive firing, 281, 293
Repolarization, 12, 89, 94, 286
Reproducibility, 16
Repulsive electrostatic force, 87
Required limits, 278
Required rate of change $du/dt > 0$, 259, 261
Reshapes the recorded biosignal, 406
Residual polarization, 93
Residual portion of i_{l-b}, 527
Resistance, 20, 59, 60, 65, 505, 548
Resistance of the undisturbed electrolyte, 496
Resistance overvoltage $i \bullet R_{electrol}$, 500
Resistance overvoltage or resistance overpotential, 451
Resistive at low f, 100
Resistive behaviour, 475
Resistive current divider, 61
Resistor, 60, 65, 410, 506, 515
Resist thermal motion, 423
Resonance, 49, 167, 172
Resonance absorption frequency, 165
Resonance frequency, 166–168
Resonance in objects, 164
Resonance is prominent, 167
Resonance phenomena, 48
Resonance range, 170
Resonant body, 48
Resonant polarization mechanisms, 123
Resonating wavelengths, 170
Respective non-zero mass and current transfer, 453
Respective plate, 62
Respiratory arrest, 370
Respiratory component, 21, 22
Respiratory tetanus, 370
Response, 23
Response delay, 350
Responses of a nerve fiber, 281
Responsiveness, 339
Resting and action membrane potentials, 269
Resting body, 348, 387
Resting cardiac muscle, 306
Resting charges, 134
Resting electrode, 478, 479
Resting membrane electric field, 255

Resting membrane voltage, 255, 264
Resting muscle cell, 12
Resting positions, 79
Resting regions, 10
Resting solution, 460, 461
Resting state, 297, 338
Restorative force, 123
Restoring electrostatic forces, 107, 108
Restoring force, 107, 109, 110
Resulting current, 409, 514
Resulting i_{AC}, 473, 485
Resulting membrane voltage u, 257
Resulting non-zero U_{pol}, 425
Resulting phase shift, 422
Resulting time-varying current, 521
Resulting time-varying voltage u, 519
Resulting transmitted wavefront, 199
Retina, 16, 379
Retinal phosphenes, 354, 379, 383, 386
Retino-corneal difference, 16
Return current, 334, 547
Return electrode or reference electrode, 331, 332
Returns, 374
Reversal of electrochemical reactions, 289
Reversal of the current, 316
Reversal of the sodium Na^+ ionic flow, 316
Reversal of the stimulation current, 335
Reverse electrochemical processes, 284
Reversibility of the reaction, 275
Reversible cardiac arrhythmia, 373
Reversible chemical reaction, 414
Reversible dissociation/association, 444
Reversible electrode, 504
Reversible electrode reactions, 493
Reversible electroporation, 256
Reversible Faradaic reactions, 274
Reversible reactions, 274, 493
Reversibly block action impulses, 295
Rheobase, 306–309, 372
Rheobase and chronaxie, 302
Rheobase current, 306
Right-angled, 31, 40, 41
Right arm, 234
Right at the boundary surface, 209
Right hand, 234
Right-handed, 31, 40, 41, 51, 150, 157
Right-leg electrode, 538, 539, 541, 542, 545
Right leg to the stomach or chest, 539
Right on the boundary, 205
Right side of the cell, 258
Rigid double layer, 421
Rigid layer, 423–425, 427, 428, 430–433, 454
Ring electrode, 334
R in the range of kΩ, 68
Rise and decay times, 154
Rise in the absolute temperature, 347
Rise in ϑ, 343
Rises with increasing I, 321
Rising contact currents, 366
Rising the threshold, 294
Risk of discharge, 381
Risks of breakdown and excitation, 256
Robustness, 385
Root mean square, 84
Rotate bound charges, 97
Rotational forces, 90
Rotational relaxation, 118
Rotational reorientation, 117
Rough the electrode surface, 502
Rounded corners, 405
Rubbed skin, 532
Rubbing both objects, 544
Rubbing of electrodes and subject's movements, 546
Rugged metal surface, 416
Rule of thumb, 279
Running leads close the body, 530

S

Saccade, 18
Safe area, 392
Safe charge injection limit, 274, 275, 391, 393, 493, 502
Safe limits, 392
Safety, 393
Safety considerations, 518
Safety factors, 358, 387
Safety limit for macroshocks, 364
Safety limit for microshocks, 364
Safety margin, 308
Safety parameter, 370
Safety publication, 369, 370
Saline NaCl solution, 410
Saline solution, identify, 510
Salt AgCl, 443
Same number of metal ions, 414
Same spatial direction, 58, 93, 95, 98
Saturate an amplifier of the input stage, 542, 527
Saturated solution, 443
Saturation, 421, 534
Saturation concentration, 444
Saturation of the input amplifier, 511
Sawtooth, 282
Scalars, 60
Scalar superposition, 135
Scattering, 49, 171

Screening effect on the electric field from individual ions, 435
Screening length, 434
Screen the central ion, 429, 435
Seated individuals, 165
Seawater, 131, 132
Second anodic phase hyperpolarizes, 291
Secondary spherical wave, 199
Second current harmonic, 485
Second derivative $d^2\varphi/dx^2$, 261
Second derivative of φ_e, 261
Second electrode, 318
Second spatial derivative $d^2\varphi_e/dx^2$, 265
Selection of biosignals, 10
Selective block, 295, 296
Selective diffusion, 413
Selective excitation of different fibers, 285
Selective fiber excitation, 318
Selective stimulation, 243
Selective transport, 413
Self-excitation, 294
Self-sustaining fibrillation, 374
Semi-circle, 499, 500, 509
Semi-infinite $\delta_D^T \to \infty$, 481
Semi-infinite $f \to \infty$, 490
Semi-infinite time, 100, 126
Semi-infinite total thickness δ_D^T, 479
Semi-permeable cell membrane, 413
Semi-permeable diaphragm, 410
Semi-permeable membrane, 413
Semi-permeable structure, 413
Sensations, 378
Sensation thresholds, 367
Sensing electrode, 385, 404, 408, 436, 437, 445, 450, 451, 464, 468, 471–473, 475, 538
Sensing lines, 524
Sensing of electric biosignals, 399
Sensing organs, 244
Sensing Pt electrode, 455
Sensitive direction of elongated fibers, 250
Sensitive organ, 348
Sensitive subpopulations, 358
Sensitive to rotation, 529
Sensorial endings, 259
Sensory afferent fibers, 329
Sensory and motor fibers, 329
Sensory prostheses, 389
Separate bound charges, 97
Separating speed, 545
Sequence of biphasic rectangular pulses, 291
Series components, 519
Series connection, 83, 178, 226, 363, 410, 423, 471, 472, 475, 480, 495
Series connection of impedances $R_{el}^t + Z_{el}^d + Z_{el}^c$, 500
Series connection of resistances $R_{el}^t + R_{el}^d + R_{el}^c$, 500
Several 100 mA/m^2, 386
Several individual, 23
Several ohms, 376
Several polarizing, 101, 127
Severe burns, 370, 372
Severe common-mode u_{CI}, 546
Severe shock, 366
Severity, 369
Shallower is the tissue heating, 130
Shape of the curve l, 55, 57
Shape similarities, 498
Sharp bend, 261
Sharp decrease, 381
Sharp local edges, 487
Sharp shadows, 199
Sharp surface regions, 487
Shielded and grounded leads, 258, 540
Shielding effect becomes more pronounced, 510
Shielding effect of the membrane, 115
Shielding of each single electrode lead, 530
Shields against the capacitive interference, 541
Shields the interior of the cell, 116
Shield the entire measurement environment, 530
Shift of a particular surface region from linear to non-linear behaviour, 487
Shock and burn hazards, 364
Short-circuit current, 140
Short current durations, 375
Short current impulse of 100 μs, 284
Short current pulses, 283, 315
Short current stimulus, 267, 280
Short distances, 109, 267, 420
Short duration, 290
Short electrode-eyeball distances, 17
Shorter phases, 291
Shorter pulses, 291
Shorter subjects, 165
Short exposure duration < 200 ms, 378
Short exposures, 373, 378
Shortfall of anions, 423
Short half-periods $1/(2f)$ of i_{AC}, 480, 482
Shorting, 278
Short interphase intervals, 291
Short monophasic current stimulus, 279
Short phases, 291
Short pulse durations, 315
Short pulse widths, 267
Short-range chemical adhesive forces, 426

Short range displacements, 110
Short suprathreshold stimulus, 280
Short-term biological effects, 353
Short-term health effects, 354
Short-term stimulation, 392, 394
Short time constants, 287
Shortwave diathermy, 358
Shunting effect of the wall, 22
Side of the membrane, 253
Sigmoid shaped recruitment curve, 319
Signal electrodes, 547
Signal loss, 548
Signal-to-interference, 535
Signal-to-noise ratio, 17, 19, 26, 535
Sign and size of induced surface charges, 146
Signed magnitude, 53, 56
Significant contrasts, 71
Significantly increased, 541
Silver and silk, 546
Simple model, 254
Simple tissue model, 65
Simplification of $\underline{Z}_{el}$, 498
Simplified boundary model, 483, 499, 500, 502, 506
Simplified electrical equivalent circuit model, 488
Simplified electric network, 264
Simplified electrode model, 500
Simplified tissue model, 406–408, 468, 474, 475, 489, 500, 506
Simulated data, 291
Simultaneous exposure, 361
Simultaneous hyperpolarization, 314
Single action impulse, 323
Single and periodic biphasic rectangular pulses, 291
Single and repeated electromagnetic pulses, 350
Single and straightforward passage, 48, 164
Single anodic pulse, 281
Single biphasic current stimulus, 285
Single biphasic pulse, 291
Single biphasic rectangular pulse, 289
Single cardiac cycle, 375, 376
Single cathodic pulse, 281
Single cells, 23, 387
Single cycle, 303
Single dispersion mechanism, 116, 125–127
Single double layer, 451
Single electric equipotential plane, 533
Single electrode/electrolyte boundary, 451
Single equipotential surface, 533
Single firing, 280, 282
Single frequency, 23
Single H^+ ion, 78, 79
Single index finger, 518
Single ion aims at inversely charged counterions, 106
Single monophasic current stimulus, 281
Single monophasic rectangular pulse, 289
Single monophasic stimulus, 280
Single monopolar electrode, 270
Single node, 269
Single organs, 153
Single rectangular pulse, 299
Single small electrode, 334
Single step, 127
Single stimulation electrode, 392
Sinks, 97
Sinks for the field lines of $\vec{E}$, 154
Sinoatrial node, 374
Sinusoidal, 20, 52, 98, 282
Sinusoidal electrical stimulus, 246, 281
Sinusoidal fields, 84, 98
Sinusoidal pulses, 292
Sinusoidal thresholds, 304
Sinusoidal time courses, 98
Sinusoidal waveforms, 64, 293
Size and shape of the biological body, 85, 145, 381, 467
Size l of considered structures, 74
Size of E equals to the slope of $\varphi(x)$, 55
Size of the applicator, 359
Size of the contact area, 516
Size of the contact electrode, 308
Size of the exposed body, 152
Size of $u_{pol,i}$, 504
Skeletal muscle, 82
Skin, 250, 406, 511, 515, 518, 519, 521, 524
Skin blood flow, 346
Skin depth δ, 41, 44, 158, 163, 164, 215, 358, 403
Skin effects, 45, 406
Skin electrode, 14, 15
Skin impedance, 375, 408, 514–517
Skin regions, 156
Skin stimulation, 242
Skin surface electrode, 269
Skin without corneum, 409
Slenderness, 147
Slightly aligned, 90
Slightly different electric potentials, 537
Slope of the transfer function, 470–472
Slope of the transfer function of the non-polarizable sensing electrode for high f, 476

Slope of the transfer function of the polarizable sensing electrode for high f, 476
Slow and constrained charge transfer, 459
Slow and fast thermoregulation, 346
Slow down the downstream charge transfer, 448
Slow down the wave propagation, 217
Slowest link/instance, 463
Slow inactivation gates, 338
Slowly and asymptotically converge, 478
Slow mass transport, 458, 477
Slow medium, 207
Slows down the wave propagation, 37
Slow subthreshold responses, 283
Slow thermoregulation, 346
Slow thermoregulatory mechanisms, 364
Slow transport processes, 449
Slow-twitch muscles, 317
Slow wave, 14
Small A, 508
Small absolute changes, 512
Small activation barriers, 452, 472, 490
Small amplitudes, 286
Small and constant value, 464
Small and large bodies, 199
Small antennas, 30
Small area electrodes, 507, 532
Small-area surface electrodes, 543
Small axons, 318
Small body surface, 153, 199
Small but constant and stable U_{pol}, 442
Small but finite currents, 513
Small conductive $i_{\mathrm{AC,E}}$, 480
Small contact area, 364
Small contraction forces, 318
Small cross-section, 143, 157
Small current, 405, 488
Small currents i_{DC}, 462
Small curvature $1/r_1$ ($<1/r_2$), 31
Small decrease in, 123
Small direct currents, 340
Small electrode, 264, 393, 539
Small energy deposition, 241
Smaller by a factor of 6, 381
Smaller current thresholds, 321
Smaller spatial extent, 474
Smaller spatial range, 296
Smaller than the wavelength, 169
Smaller the associated m and γ, 81
Small fibers, 320
Small geometrical size, 29, 74
Small i_{DC}, 455, 463
Small inner resistance, 523
Small ion, 110
Small local charge changes, 462
Small losses, 48
Small negative ions, 111
Small net polarization, 120
Small ohmic voltage drop, 464
Small opening, 195, 199
Small overvoltage $|u_{\mathrm{pol,i}} - U_{\mathrm{pol}}| \ll RT/zF$, 478
Small overvoltage $|u_{\mathrm{pol,i}} - U_{\mathrm{pol}}|$, 480
Small phase angle $\arg(Z) = \varphi_1$, 490
Small polarization overvoltage, 405
Small polar proteins, 119
Small positive ions, 111
Small positive value, 266
Small R_{electrol}, 499
Small resistor, 407
Small semi-circle C, 490
Small solvation/hydration energy, 427
Small surface charges, 180
Small surface or small implanted stimulation electrodes, 330
Small surplus polarization, 506
Small total thickness of the double layer, 502
Small unmyelinated axons, 329
Small voltages, 370
Small water molecules, 118
Small u_{AC} oscillating around U_{pol}, 478
Small $|u^{\mathrm{t}}_{\mathrm{pol,i}}| < U_{\mathrm{dec}}$, 470
Small $|u_{\mathrm{pol,i}} - U_{\mathrm{pol}}|$, 452
Small Z_{el}, 532
Smearing of the near-order, 106
Smooth contraction (tetanus), 246
Smooth metal surface, 416
Smooth muscle cells, 14
Snell's refraction law, 208
Soft and high water content tissues, 72, 74, 132
Soft biological tissues, 390
Solid body, 443
Solubility, 445
Solubility of AgCl decreases, 445
Solubility of the salt AgCl into its ions increases, 444
Solubility product, 444
Solution of mobile ions, 412
Solvated/hydrated by molecules/polar molecules, 85
Solvated ions, 75
Solvation shell, 77, 419, 427, 428
Solvent molecules, 106, 427, 429, 433
Some focussing, 404
Some penetration, 404
Sophisticated materials, 390
Sophisticated mechanisms, 391
Source, 3, 17, 97
Source antenna, 30

Source capacitance, 512
Source electric fields, 160
Source fields, 239
Source impedance, 512
Source of movement artefacts, 513
Source power, 40
Source-related, 160
Source resistance, 512
Space constant, 44, 460, 478
Space domain, 249
Space evolutions, 326
Spark discharge, 362, 363, 394, 400, 519
Spark relaxing excess surface charges, 544
Sparse vascular network, 346
Spatial angular frequency, 33
Spatial area, 296
Spatial averaging or spatial spread, 332, 356
Spatial correlations, 106
Spatial decay, 266
Spatial derivative, 259, 260, 265
Spatial direction, 94, 172
Spatial distribution, 145, 218, 240, 246, 297
Spatial distribution of induced electric fields and conductive currents, 155
Spatial distribution of the extracellular potential φ_e, 264
Spatial distribution of the stimulation current, 307
Spatial extension, 200, 273, 323
Spatial frequency, 37, 41
Spatial gradients of electric fields, 246
Spatial irregularities, 200
Spatially accumulated, 37, 43
Spatially heterogeneous, 161
Spatially-uniform, 154
Spatial migration, 107
Spatial oscillation of c has a semi-infinite extent, 479
Spatial oscillation of c over time, 478
Spatial parameters, 246, 247
Spatial path of largest conductivity, 61
Spatial path of largest permittivity, 64
Spatial path of least impedance, 64
Spatial path of least resistance, 61
Spatial power density, 83
Spatial redirection, 171
Spatial resolution, 22, 25, 26
Spatial variation of P_{SAR}, 169
Spatial width of the depolarized region, 332
Spatiotemporal transfer functions, 249
Species or negative ions, 471
Specific adsorption, 425, 427, 428, 435, 454, 492
Specifically adsorbed ions, 422, 425, 426, 428, 468, 485
Specific boundary conditions, 173
Specific energy absorption rate P_{SAR}, 30, 84, 129, 154, 212
Specific experimental set-up, 244
Specific frequencies, 164
Specific heat capacity, 218, 346
Specific inhibitors, 416
Specific ions, 425
Specific stimulus, 244
Spectral broadening, 127
Spectral components, 361
Speed of coupled chemical reactions, 449
Speed of the charge transfer, 448
Speed of the ongoing redox reaction, 452
Spherical body, 225
Spherical cells, 255, 257
Spherical electrode, 315
Spherical fields, 269
Spherical shape, 263
Spherical suprathreshold region B, 320
Spherical suprathreshold region C, 319
Spherical surface area, 39
Spherical symmetry, 106, 263, 433
Spherical TEM wave, 36, 39, 40
Spherical wavefront, 31, 40, 41, 199, 201
Spherical wave in lossless media, 40
Spheroids, 148
Spike, 409
Spontaneous, 453
Spontaneous discharge, 315
S quadruples, 40
Squared sinc courses of S, 201
Square of the effective value, 84
S_{red} is consumed while S_{oxi} is produced, 460
Stable recording interface, 390
Stainless steel, 403
Standard conditions, 437, 439
Standard hydrogen electrode, 437, 439, 455, 461
Standardized 10–20 system, 15
Standard reduction potential, 436
Standard thermodynamic conditions, 413, 421, 437, 442, 445
Standing body with grounded feet, 166
Standing ungrounded body, 166
Standing wave, 48, 84, 169, 210, 211, 213, 216
Start depolarization of the membrane, 265
Starting point, 384
Static electric fields, 135, 381
Static magnetic field, 145, 150, 158, 161, 162
Static permittivity, 126

Static properties, 21
Stationary conditions, 176, 178, 187, 278
Stationary i_{DC}, 473, 474
Steady and/or slowly varying biosignals, 506
Steady and time-varying electric and current density fields, 400
Steady component and higher harmonics, 485
Steady conductive currents, 504
Steady direct current, 304
Steady increase of $\Delta\vartheta$, 343
Steady state, 49, 414, 415, 417, 420, 439, 462, 497
Steady-state conditions, 461, 462
Steady-state level, 218
Steady state of the boundary, 414, 511
Steady-state response, 345
Step current pulse, 298
Step function, 100
Step input $P \cdot \varepsilon(t)$, 344
Step response ϑ(t), 344
Step voltage, 377
Step-wise behaviour, 239
Step-wise change, 462
Step-wise decrease, 126, 220
Step-wise increase, 125
Step-wise manner, 115, 122
Step-wise supply, 344, 345
Stickman with resistors, 517, 537
Still electrode, 481
Stimulate nerves or muscles, 171
Stimulating effects, 515
Stimulating electrodes, 392
Stimulating phase, 278
Stimulation, 23, 159, 332, 374, 385, 495
Stimulation charge per pulse, 246
Stimulation current threshold, 264, 281, 332
Stimulation effects on excitable cells, 251
Stimulation electrode, 263, 278, 393, 404, 405
Stimulation frequency, 317
Stimulation-induced nerve injury, 392
Stimulation of excitable tissues, 241, 242
Stimulation of muscles, 154, 354
Stimulation of nerves, 154, 354
Stimulation parameters, 246
Stimulation pattern, 262
Stimulation pulse, 493
Stimulation purposes, 507
Stimulation rates, 291, 294, 295, 389, 391
Stimulation set-up, 302, 306, 307
Stimulation slightly over the threshold, 335
Stimulation strength, 336
Stimulation threshold, 244, 321, 333, 334, 375, 380
Stimulation upper threshold, 316
Stimulus amplitude, 317
Stimulus charge, 319
Stimulus duration, 297, 368
Stimulus energy, 340
Stimulus frequencies, 292
Stimulus properties, 340
Stimulus-related recording, 18
Stimulus strength, 297, 304
Stop propagation, 314
Stored energy, 124
Straight axon region, 261, 263
Straight-line asymptotes, 300
Stray capacitances, 512
Stray resistances, 512
Streaming potentials, 18
Strength, 94, 244, 257, 332
Strength-duration curve, 279, 281, 288, 297–303, 306, 308, 309, 340, 372
Strengthened coupling, 162
Strengthens subjectively, 131
Strength-frequency curve, 25, 303, 372
Strength of cathodic stimulus, 314
Strength of the ambient electric field, 362
Strength of the dispersion, 126
Strength of the electric field, 429
Stress mechanisms, 390
Stroke volume, 21
Strong attenuation of the biosignal-related portion, 535
Strong but highly flexible electrodes, 402
Strong common-mode interference, 535
Strong convection, 481
Strong currents, 317
Strong depolarization, 316, 334
Strong dielectric saturation, 430
Strong electric field, 110, 429, 430
Strong electrolyte, 82, 424, 502
Stronger attenuation, 535
Stronger charging of the electrode, 415
Stronger destructive interference, 287
Stronger interference, 535
Strongest electric field, 382
Strong interaction, 46
Strongly attenuated field, 46
Strongly charged double layer, 511
Strongly delayed setting, 462
Strongly lossy medium, 216
Strongly non-linear, 472
Strongly oxidized S_{oxi}, 440
Strongly reduced S_{red}, 440
Strong membrane depolarization, 316
Strong oscillations of its local membrane voltage, 295
Strong stimulating current, 244

Strong suprathreshold stimulating current, 294, 335
Strong total current, 142
Structural heterogeneity, 101
Structure-bound electric field, 88, 89
Structure of electrical equivalent circuit models of Z_{el}, 483
Structure of water is disrupted in the double layer, 430
Structures rotate, 90
Structure with its certain mass, 89
Subcorneal medium, 408
Subject's motions, 512
Subjective perception amplitude, 394
Submitted energy, 84
Sub multiple of the stimulation rate, 294
Sub-resonance range, 170
Subsequent electrolyte/skin interface, 412
Substances, 161
Substantially elongated vulnerable period, 286
Substitutes, 64
Substituting metals, 390
Subthreshold, 319
Subthreshold behaviour, 272, 297, 323
Subthreshold depolarization, 300, 301, 315, 316
Sub-threshold prepulses, 319
Subthreshold region A, 320
Subthreshold relationships, 297, 302
Successful anodic stimulation, 316
Successful cathodic stimulation, 315, 316
Sudden changes, 337
Sufficient thermoregulatory capacity, 347
Sum field, 210
Summation, 127
Sum of both conductive $i_{AC,E}$ and displacement $i_{AC,C}$ components, 482
Sum of depolarizing/activating influences, 266
Sum of hyperpolarizing/deactivating influences, 266
Super-conductivity, 78
Superficial absorption, 357, 388
Superficial heating, 156, 242, 348, 349
Superficial not-perfused tissues, 348
Superficial penetration, 46, 358
Superposed electric field, 160
Superposition of $f_k(x)$, 334
Superposition of $f(x)$, 334–336
Superposition of permanent microscopic fields, 89
Superposition of these induced microscopic fields, 88
Superposition principle, 91, 253, 334, 533
Suppress the influence of the relatively high u_{CI}, 534
Supra-resonant frequencies, 350
Suprathreshold, 286
Suprathreshold blocking phenomenon, 315
Suprathreshold cathodic stimulus, 314
Suprathreshold depolarization, 300, 301, 314
Suprathreshold range, 316
Suprathreshold region, 320, 335
Suprathreshold stimulation, 319, 325
Suprathreshold stimuli, 286
Surface absorption range, 170
Surface area of the body skin, 139
Surface area of the electrode, 493
Surface area of wavefronts, 200
Surface charge, 77, 97, 133, 137, 142, 145, 149, 154, 159, 160, 177, 360, 362, 378, 380, 432, 435, 464, 544, 545
Surface charge density, 185
Surface charge of the metal electrode, 429, 467
Surface charges of opposite polarity, 144
Surface concentration, 458
Surface curvature, 136
Surface effects, 47
Surface electrodes, 271, 330, 399, 405, 407, 495, 519, 521, 524, 532, 538
Surface free of charge, 175
Surface heating, 165
Surface integral, 53, 54
Surface monopolar electrode, 330
Surface of the metal electrode, 415
Surface of the sensing electrode, 465
Surface overheating, 359
Surface roughness, 545
Surface-seated electrodes, 402
Surfaces of conductive polymers, 390
Surfaces of constant phase, 40
Surface structure, 461
Surface type of the electrode, 546
Surplus of adsorbed anions, 425
Surplus of cations, 423
Surplus of electrons, 425
Surplus overvoltage $u^{c}_{pol,i} = u_{pol,i} - U_{pol}$, 449
Surplus overvoltage $u^{d}_{pol,i} = u_{pol,i} - U_{pol}$, 448
Surplus polarization, 120
Surrounding tissue, 225
Susceptibility, 240
Susceptibility to movement artefacts, 512, 524
Sustained myocardial contraction, 373
Sweat, 346, 517
Sweat ducts (sweat glands), 410
Swelling, 72
Switched electric field, 135

Switched off, 315
Switched on, 289, 294, 296
Symmetric, 107
Symmetric atmosphere, 108
Symmetric cloud, 110
Symmetric cloud of counterions, 106
Synaptic junctions, 379, 380
Synchronization, 245, 293
Synchronization of synaptic activity, 15
Synchronized action impulses, 293, 294
Synchrony, 293
System input, 125
System output, 125
System response, 20
System stimulus, 20
Systolic inflow, 22

T
Tangential, 179, 203, 204, 209
Tangential component, 56, 136, 172–174, 176, 179, 180, 182, 184, 185, 190, 239
Tangential coupling, 148, 149, 180, 221, 226, 227
Tangential direction, 55
Tangential electric field is steady, 174
Tangential $\vec{E}$ coupling, 220
Tangential $\vec{E}$ field, 217
Targeted by the electrical stimulation, 329
Target potential, 433
Task performance, 350
Technical device and bodily tissues, 504
Technical electric fields, 194
Techniques, 318
TEM field, 29
TEM mode, 31
Temperature, 70, 118–120, 345
Temperature coefficient, 83
Temperature increase, 340, 341
Temperature rise, 345
Temporal and spatial dispersion of the recovery, 374
Temporal and spatial oscillation of c disappears at the electrode surface, 480
Temporal angular frequency, 33
Temporal inertia, 473, 483
Temporal parameters, 246, 247
Temporal variation of c, 478
TEM wave, 31, 44, 201
Tends to raise, 419
Tenth of minutes, 517
Terminal endings, 261
Termini and/or bend regions, 261
Terminus of the axon, 261
Test the impedance measurement system, 510
Tetanus, 366
Tetrahedral arrangement, 86
Theory-based approaches, 508
Therapeutic, 339
Therapeutic aims, 405
Therapeutic applications, 340
Therapeutic approach, 521
Therapeutic coupling, 399, 400
Therapeutic current, 403, 495
Therapeutic device, 495, 502, 523
Therapeutic efficiency, 521, 523
Therapeutic point, 165
Therapeutic purposes, 399, 495
Therapeutic safety, 521
Therapeutic thermal treatment, 130
Therapeutic treatments, 358
Therapeutic voltage drop u_b, 495
Therapy, 71, 154, 495, 515
Thermal, 49, 122
Thermal agitation, 120
Thermal conductance, 350
Thermal damage, 346, 350
Thermal effects, 26, 154, 156, 180, 242, 243, 247, 337, 338, 340, 342, 354, 372, 384, 400
Thermal energy, 120
Thermal equilibrium, 120
Thermal excitation, 340, 357
Thermal gradients, 351
Thermal impact, 242, 340
Thermal interaction, 85, 241, 242, 336, 347
Thermal losses, 47
Thermal motion, 89, 106, 420, 423
Thermal receptors, 349
Thermal regulatory functions, 344
Thermal stimulation, 9, 10, 240
Thermal stress, 347, 351, 388–390
Thermal treatment depth, 359
Thermodynamic energies, 544
Thermodynamic equilibrium constant, 444
Thermoelastic interactions, 350
Thermoregulation, 349
Thermoregulatory actions, 243
Thermoregulatory capacity, 347, 358
Thermoregulatory effects, 348
Thermoregulatory mechanisms, 218, 341, 343, 346
Thermoregulatory response, 344–348, 350, 388
Thick axons can be excited more easily than thin ones, 328

Thick efferent motor neurons, 317
Thicker and denser the hydration shell or the cloud of counterions, 420
Thickest to the thinnest fibers, 296
Thick fibers, 261, 296, 297, 308, 317, 319, 320
Thick motor fibers, 318
Thickness δ_D, 478
Thickness δ, 158
Thickness δ_D^T, 498
Thickness d, 61, 63, 66
Thickness d_d of the diffuse layer, 424
Thickness d_r of the rigid layer, 423
Thickness of the diffuse layer, 423
Thickness of the human body, 164
Thickness of the rigid layer, 423
Thickness of the solvation/hydration shell, 81
Thick neurons, 318
Thin efferent motor neurons, 317
Thin fibers, 296, 297, 308, 317, 318, 329
Thin neurons, 317
Thin tissue section, 87
Thin wire, 64
Third cathodic phase favours, 291
This approximate factor of five, 313
Thoracic area, 518
Thoracic impedance decreases, 22
Three action impulses, 281
Three-dimensional electrical impedance tomography, 24
Three electro-kinetic processes, 448, 508
Three excitation-related quantities, 244
Three mechanisms, 274
Three orders of magnitude, 259
Threshold, 287, 292, 294, 297, 317, 319, 322, 380, 384
Threshold amplitude, 299, 328
Threshold charge, 299
Threshold current, 273, 289, 321
Threshold depolarization, 300, 301
Threshold differences, 291
Threshold energy, 300
Threshold excitation, 300
Threshold for excitation elevates, 389
Threshold for synaptic activation, 317
Threshold of 150 mA, 378
Threshold-related, 300
Thresholds for stimulation, 304
Thresholds of current densities, 291
Thresholds of the point contact current, 365
Threshold stimulation, 283, 325
Threshold values, 365, 366
Through the air, 549
Through the dielectric body of the capacitor, 63
Through the resistor, 61
Through the tissue section, 65
Time and spatial gradients, 161, 517
Time average, 106
Time constant τ, 218, 267, 275, 287, 315, 322, 344–346, 464, 497
Time-constant U_{dec}, 487
Time constant of the membrane, 279, 280, 328
Time courses of c^s and $u_{pol,i}$, 482
Time courses of the polarization voltage $u_{pol,i}$ due to diffusion and the current $i_{AC,E}$, 481
Time delay, 273, 283, 284, 325, 326, 414, 462, 483, 511
Time-dependent coupling capacitance, 545
Time derivative, 29, 162, 414
Time-difference electrical impedance tomography, 24
Time domain analysis, 23
Time evolutions, 326
Time integral of the current, 278
Time rate of energy, 85
Time reactants take to diffuse, 481
Time resolution, 26
Time-spatial, 32
Time-varying, 47, 98, 161, 487
Time-varying behaviour, 19
Time-varying currents, 354
Time-varying electrical properties, 410
Time-varying electric field, 135, 162, 251, 378, 529
Time-varying electrode impedance, 542
Time-varying field, 48, 159
Time-varying magnetic field, 51, 55, 145, 150, 158, 159, 162, 237, 251, 379, 385, 529
Time-varying magnetic fields $\dot{\vec{B}}$, 529
Time-varying polarization, 474
Time-varying surface charges, 354
Time-varying voltages, 15, 16, 529
Time-varying waveform, 64
Timing of periodic stimulation pulses, 391
Tingling or prickling sensation, 364
Tingling sensation or warmth, 372
Tip of the tongue, 16
Tissue, 348, 470, 511, 521
Tissue and electrode material, 274, 392
Tissue/body temperature, 163
Tissue conductivity, 79, 80, 152, 359
Tissue damage, 251, 275, 289
Tissue/electrolyte, 412, 421, 451, 464, 468, 475, 490, 491, 507
Tissue encapsulation, 496
Tissue harm and/or electrode corrosion, 277

Tissue heating, 348, 353
Tissue morphology, 21
Tissue properties, 66, 129, 341, 507
Tissue regions, 97
Tissue section, 60, 62, 65, 89, 91
Tissue temperature, 83, 343, 388
Tissue trauma, 390
Tissue water, 119, 122
Titan, 403
Titanium, 392
To stay complex, 479
Total capacitance, 423, 431
Total charge of the ionic cloud, 106
Total charge per stimulation period, 391
Total circuit impedance $\underline{Z}_T$, 519, 523
Total common-mode rejection ratio, 541
Total concentration of ions, 79
Total conductivity, 81
Total coupling stray capacitance, 531
Total current, 54, 59, 61, 64, 65, 67, 141, 160, 487
Total current density $\vec{J}$, 54, 98, 184, 235
Total current is relatively weak, 142
Total current through the body, 377
Total differential complex impedance Z between the sensing and reference electrodes, 474
Total differential resistance R between the polarizable sensing and non-polarizable reference electrodes the ratio $\Delta u_{DC}/\Delta i_{DC}$, 471
Total differential resistance R for u_{DC}, 474
Total dominating electrolytic reaction, 490
Total dominating electrolytic reaction is $Ag + Cl^- \rightarrow AgCl + e^-$, 491
Total electric field, 255
Total electrode impedance Z_{el}, 475, 501
Total electrode resistance R_{el}, 458
Total excess polarization charge, 90
Total $f(x)$, 334
Total impedance, 115, 228
Total induced potential difference, 538
Total losses, 97
Total lossy interactions, 85
Total measured impedance Z, 501, 507–509
Total overvoltage, 461
Total peripheral resistance, 347
Total polarization voltage $u_{pol,i}$ ($>U_{pol}$), 496
Total R, 472
Total radiated power, 39
Total reaction kinetics, 416, 449, 461, 463, 473, 482, 488, 489, 499
Total recruitment volume, 288
Total reflection, 48, 204, 205, 209, 216
Total thickness δ_D^T is usually finite, 481
Total thickness δ_D^T of the diffusion layer, 478
Total thickness of the double layer, 423, 424
Total voltage, 55, 257, 455
Total Z between the sensing and reference electrodes, 476
Total Z for high f, 476
Total Z for low f, 477
To the total i_{DC}, 495
Touch perception, 366
Touch voltage, 514
Towards the anode, 335
Towards the ground, 527
Toxic by-products, 494
Toxic ions, 432
Toxicity, 443, 507
Toxic metal ions Ag^+, 491
Transcranial direct current stimulation, 339
Transfer function, 125, 249, 298, 470, 472, 476
Transformer, 529
Transient common-mode, 546
Transient conductive current along the wire, 464
Transient conductive current density $\vec{J}_{el}$ in electrolyte, 465
Transient conductive current in electrolyte, 466
Transient conductive currents, 133, 135
Transient current $i \neq 0$, 464
Transient depolarization, 338
Transient displacement current, 464
Transient electric dipoles, 462
Transient ionic $\vec{J}_{el}$ disappears, 466
Transient process of the double layer formation, 503
Transient response, 462
Transient state, 414, 497
Transitional space, 431
Transition resistance or transition impedance, 501
Translation, 79, 161
Translational ionic drift, 79
Transmembrane currents, 252, 253, 261, 264, 270, 271
Transmembrane displacement currents, 10
Transmission, 9
Transmission and propagation, 9
Transmission efficiency, 204
Transmission factor, 204, 205
Transmission lines, 194
Transmission of electric biosignals, 28
Transmitted field disappears, 205
Transmitted heterogeneous, 200

Transmitted wave, 41
Transport inhibition throughout the whole diffusion layer, 478
Transport or move unbound free charges, 96
Transversal body orientation, 222
Transversal currents, 73, 246, 302
Transversal direction, 407
Transversal injection, 251
Transversal orientation, 195
Transversed by the electromagnetic wave, 34
Transverse electric field, 254
Transverse electromagnetic (TEM) wave, 29
Transverse orientation, 132
Transversing lossless medium, 37
Transversing lossy medium, 42
Trapezoid stimulus, 282
Triboelectrically induced, 545
Triboelectric effects, 401, 403, 546
Triboelectricity, 543, 544, 546
Triboelectric series, 546
Triphasic mode, 335
Triple firing, 282
Tripolar mode, 334, 336
Tripolar recording and stimulation modes, 334
Tripolar stimulation mode, 334
True physical angle of refraction, 208
True thickness of the counter-charge layer, 466
Trunk, 347
Thermal motion, 423
Tumors, 71
Tungsten, 403
Tunnelling processes, 78, 111, 454
Turns ratio, 529
T wave, 375
Twisted leads, 530
Two action impulses, 281, 282
Two balance points, 87, 89
Two capacitors, 410
Two different uncharged objects in mechanical contact, 544
Two-dimensional plane, 24
Two electrodes, 2, 404, 436, 524
Two frequency decades, 126
Two half-cells, 436, 439
Two homogeneous tissue sections, 83
Two identical Ag/AgCl electrodes, 439
Two-layered biological body, 217
Two levels of guidance, 354
Two plane and large electrodes, 87
Two polarizations, 170
Two similar electrodes, 508
Two surface electrodes, 507
Two symmetrical action impulses, 273, 311
Two-thirds, 365
Two-way propagation, 273
Type and temporal pattern, 240
Type I motor units, 317
Type II motor units, 317

U

u_{AC} application, 475
$u_{AC} < U_{dec}$, 500
$u_{AC} > U_{dec}$, 500
Ultraviolet region, 122
Unaware of their exposure, 358
Unbalanced electrode reactions, 447, 453, 537
Unbalanced redox reactions, 455
Unbalance in both i_{l-e} entering each lead i_{l-e} entering each lead, 537
Unbalance in $\Delta \underline{Z}_{el}$, 537
Unbound charges, 60, 77, 89, 91, 92, 94–96, 98, 109, 111, 124, 135, 175, 187, 189, 341, 474
Unbounded media, 49
Unbound electric charge, 54, 91
Unbound ionic charges, 338
Uncertainties, 382
Uncharged substances, 432
Uncompensated charges, 91, 92
Unconstrained and rapid electrode/redox reaction, 491, 494, 505
Unconstrained charge transfer, 462, 506
Unconstrained chemical reactions, 448, 464
Unconstrained exchange of electric charges, 504
Unconstrained for slow changes in $u_{pol,i}$, 463
Uncontrolled environments, 358
Uncoordinated and irregular excitation and contraction of ventricles, 374
Uncoupled fields, 29, 162, 357
Undamped harmonic waves, 38
u_{DC} is applied, 495
u_{DC} varies in proportion to i_{DC} only for small i_{DC}, 455
Underlying physical mechanisms, 103
Under the stimulation electrode, 314
Undisturbed $\vec{E}_{ext}$, 148
Undisturbed electrolyte, 419, 423, 429, 432, 433, 445, 457, 459, 495
Undisturbed growth of crystals, 416
Unfavourable and undefined changes of U_{pol}, 443
Unfavourable current pathway, 376
Unfavourably adds to the total input, 529
Unfocussed deep applications, 404
Ungrounded body, 139, 144, 164

Ungrounded human body, 147, 165, 364
Ungrounded object, 147, 363
Unidirectional, 279
Unidirectional migration, 474
Unidirectional thermal energy, 434
Uniform along the flow, 63, 66
Uniform coverage of current, 405
Uniform cross-section area, 61
Uniform exposure, 163
Uniform plane wave, 29
Uniform radiation, 199
Unipolar cardiac pacemaker, 385
Unipolar pacemaker, 385
Unipolar systems, 386
Unit vectors, 173
Unmyelinated and myelinated fibers, 291, 328
Unmyelinated axon, 267, 269, 328
Unmyelinated cylindrical fibers, 260, 265
Unmyelinated fibers, 265, 267, 273, 283, 284, 286, 291, 293, 296, 306, 307, 313, 319, 321, 329
Unmyelinated nerve fiber, 321
Unmyelinated ones, 329
Unnatural nerve stimulation, 317, 388
Unnecessarily conservative, 361
Unperturbed homogenous field, 356, 359
Unrestricted water molecules, 118
Untwisted leads, 530
Unwanted stimulation, 332
Upper limit, 315, 316
Upright posture, 142
Uterus, 14

V

Valence, 424, 435
Van der Waals bonds, 461
Vanishing amplitudes, 36
Variation, 192, 300
Varies in its magnitude and direction, 467
Varies inversely, 146
Varies much less with frequency, 82
Various (adverse) effects, 384
Varying capacitance, 546
Varying distance, 323
Varying electric fields, 422
Varying electric potential, 422
Varying electrode area, 508
Varying face area, 146
Varying health status, 358
Varying potential of the electrode surface, 468
Varying spatial orientation, 17
Varying susceptibilities, 358
Varying voltage drop, 546
Varying *y*, 330
Vary with frequency, 244
Vascularity, 348
Vasodilation of vessels, 344
Vector amplitude, 52, 54, 57, 60, 80, 95–98
Vector average, 356
Vector field, 51
Vector superposition, 133, 159
Velocity, 273
Ventricles, 375
Ventricular fibrillation, 13, 306, 364, 369, 370, 372–377, 386
Ventricular heart fibrillation, 366
Vertical eye movements, 17
Very low self-conductivity, 82
Very small charge, 278
Very small currents, 546
Very small surplus polarization, 505
Very strong local electric fields, 430
Vicinity of current electrodes, 338
Virtual anode, 253, 254, 257
Virtual cathode, 254, 257
Virtual electrodes, 254
Virtual "forcing current density", 259, 260
Visual and motor cortices, 246
Visual processing and motor co-ordination, 246
Visual sensation, 379
Voltage, 2, 55, 56, 61, 62, 323, 404, 462, 464, 466, 497, 521
Voltage-dependant behaviour, 515, 516
Voltage-dependant charge transfer, 500
Voltage-dependence of the skin impedance, 410
Voltage divider, 179, 512, 513, 531, 532
Voltage drop, 116, 252–254, 328, 363, 406, 408, 411, 419, 436, 439, 446, 455, 467
Voltage electrode, 5, 21, 235
Voltage-gated K^+ channels, 338
Voltage-gated Na^+ channels, 338
Voltage-gated sodium channels of different speeds, 284
Voltage is moderately low, 518
Voltage sensing metal electrode, 235
Voltage source, 410, 497, 519, 531
Voltage stimulus, 60, 408
Volume, 21, 119, 349
Volume conductor, 12, 15
Volume density, 92
Volume effects, 28, 49
Volume fields, 15
Volume fraction, 74, 113, 115
Volume-related quantity, 165, 349
Voluminous heating, 242, 349
Voluntary control of muscles is just lost, 366

Vortices, 160
Vulnerable period, 286, 306, 369, 374–376, 378, 382

W
Warburg impedance $\underline{Z}_{el}^{d}$, 479, 497, 481
Warburg line, approaches and merges into a semi-circle with increasing f, 499
Warburg line of $\underline{Z}_{el}^{d}$, 480, 498, 499, 509
Warming of extracellular, 256
Warming up of conductive implants, 353
Water, 70, 72, 78, 119, 430
Water decomposition, 492
Water dipole, 78, 121
Water is decomposed, 492
Water molecule, 89, 106, 117, 128, 429, 431
Water of hydration, 86
Water oxidation, 492, 493
Water reduction, 492, 493
Water salinity, 128
Water window, 493
Waveform, 242, 282, 287, 304, 308, 340
Waveform of the activating function $f(x)$, 272
Waveform of the charge-balancing phase, 287
Waveform parameters, 298
Wavefronts, 31, 37, 40, 43, 207
Wave impedance, 30, 32, 37, 41, 43
Wave interference, 199
Wavelength, 37, 42, 74, 162, 163, 201, 207, 404
Wavenumber, 33, 37, 43
Wave polarization, 202
Wave shadow, 195
Wave's size, 34
Wave's speed, 34
Weak autodissociation, 82
Weak conductor, 216
Weak depolarization, 334
Weak electric fields, 120, 245, 380
Weakens subjectively the objective changes, 131
Weaker current, 244
Weak interaction, 46
Weakly attenuated field, 46
Weakly lossy medium, 216
Weak polarization, 506
Weak subthreshold stimulus, 260
Wearable technologies, vi
Weighted, 361
Weighting factor, 361
Well-conducting layers, 402
Well-conductive subcorneal medium, 408, 409
Well-established biological effects, 354
Wet electrodes, 402
Wetness, 367, 519
Wet skin, 515, 517
Which opposes the applied external, 91
Whitish discoloration of the skin, 383
Whole-body dimensions or head/torso dimensions, 163
Whole-body fat percentage, 73
Whole-body impedance Z_{wb}, 368, 370, 375, 514, 519, 521
Whole body is exposed, 156
Whole-body P_{SAR}, 170, 357, 360, 387
Whole-body resonance frequency, 163, 164, 167, 350
Whole conductive body, 57
Whole double layer ($d_r + d_d$), 460
Whole exposure duration, 336, 337
Whole heart simultaneously, 374
Whole human body, 23
Wide distribution, 15
Width, 336
Windows of response, 351
Wire carrying the electric current, 50
Wired connection, 542
Within and outside the conductive body, 133
Within polarizable tissue, 91
Within the air, 537
Within the cloud, 433
Within the conductive body, 154
Within the diffusion layer, 460, 480
Within the inner body, 538
Within the structure, 87
Within the tissue layer, 158
Within this electrolyte layer, 511
Without any active application of direct voltages or direct currents, 417
Without any alignment, 430
Without any blocking phenomenon, 320
Without any chemical reactions, 501
Without any electrochemical reactions, 274
Without any external electric fields, 106
Without any physical contact, 240
Without any potentially harmful reaction products, 274
Without any thermoregulatory mechanisms, 345
Without any time delay, 482
Without changing, 190
Without diffusion, 457
Without dispersions, 68
Without inert diffusion, 470
Without polarizable tissue, 91
Women, 365, 371
Workers, 358
Worst-case conditions, 356

Worst-case coupling, 142
Worst-case scenario, 142, 341, 369
Would not migrate, 425
Wrist and ankle in the extremities, 517
Wrist or ankles, 234

Y
Yields $\underline{Z}_{el}$, 497
Young's modulus, 390

Z
$\underline{Z}_b$ determines Z_{wb}, 519
$\underline{Z}_{diff}$ and $\underline{Z}_{com}$ to be large, 527
Z decreases step-wise, 68
$\underline{Z}_{el}^{d}$ dominates the total electrode impedance $\underline{Z}_{el}$, 480
Zero curvature, 40
Zero direct current, 391
Zero electric fields, 206
Zero initial state, 344
Zero inner electric field, 135
Zero net charge, 77, 363, 433
Zero net surface charge, 144
Zero overvoltage, 505
Zero phase, 205, 478
Zero phase delay
Zero points, 210
Zero polarization, 506
Zero PQ interval, 12
Zero projection, 12
Zero ST interval, 12
Z in muscle, 36